CEREBROVASCULAR AND NEURODEGENERATIVE DISEASES – NEW INSIGHTS INTO MOLECULAR CELL BIOLOGY AND THERAPEUTIC TARGETS

EDITED BY: Sikha Saha and Sriharsha Kantamneni
PUBLISHED IN: Frontiers in Neuroscience, Frontiers in Cellular Neuroscience and Frontiers in Neurology

frontiers Research Topics

frontiers

ISSN 1664-8714
ISBN 978-2-88963-442-2
DOI 10.3389/978-2-88963-442-2

About Frontiers

Frontiers is more than just an open-access publisher of scholarly articles: it is a pioneering approach to the world of academia, radically improving the way scholarly research is managed. The grand vision of Frontiers is a world where all people have an equal opportunity to seek, share and generate knowledge. Frontiers provides immediate and permanent online open access to all its publications, but this alone is not enough to realize our grand goals.

Frontiers Journal Series

The Frontiers Journal Series is a multi-tier and interdisciplinary set of open-access, online journals, promising a paradigm shift from the current review, selection and dissemination processes in academic publishing. All Frontiers journals are driven by researchers for researchers; therefore, they constitute a service to the scholarly community. At the same time, the Frontiers Journal Series operates on a revolutionary invention, the tiered publishing system, initially addressing specific communities of scholars, and gradually climbing up to broader public understanding, thus serving the interests of the lay society, too.

Dedication to Quality

Each Frontiers article is a landmark of the highest quality, thanks to genuinely collaborative interactions between authors and review editors, who include some of the world's best academicians. Research must be certified by peers before entering a stream of knowledge that may eventually reach the public - and shape society; therefore, Frontiers only applies the most rigorous and unbiased reviews.
Frontiers revolutionizes research publishing by freely delivering the most outstanding research, evaluated with no bias from both the academic and social point of view. By applying the most advanced information technologies, Frontiers is catapulting scholarly publishing into a new generation.

What are Frontiers Research Topics?

Frontiers Research Topics are very popular trademarks of the Frontiers Journals Series: they are collections of at least ten articles, all centered on a particular subject. With their unique mix of varied contributions from Original Research to Review Articles, Frontiers Research Topics unify the most influential researchers, the latest key findings and historical advances in a hot research area! Find out more on how to host your own Frontiers Research Topic or contribute to one as an author by contacting the Frontiers Editorial Office: researchtopics@frontiersin.org

CEREBROVASCULAR AND NEURODEGENERATIVE DISEASES – NEW INSIGHTS INTO MOLECULAR CELL BIOLOGY AND THERAPEUTIC TARGETS

Topic Editors:
Sikha Saha, University of Leeds, United Kingdom
Sriharsha Kantamneni, University of Bradford, United Kingdom

Citation: Saha, S., Kantamneni, S., eds. (2020). Cerebrovascular and Neurodegenerative Diseases – New Insights Into Molecular Cell Biology and Therapeutic Targets. Lausanne: Frontiers Media SA.
doi: 10.3389/978-2-88963-442-2

Table of Contents

frontiers in Neurology

EDITORIAL
published: 13 December 2019
doi: 10.3389/fneur.2019.01322

Editorial: Cerebrovascular and Neurodegenerative Diseases - New Insights Into Molecular Cell Biology and Therapeutic Targets

Sikha Saha[1]* *and Sriharsha Kantamneni*[2]

[1] Leeds Institute of Cardiovascular and Metabolic Medicine, University of Leeds, Leeds, United Kingdom, [2] School of Pharmacy and Medical Sciences, University of Bradford, Bradford, United Kingdom

Keywords: neurodegenerative disease, molecular biology, stroke, middle cerebral artery and common carotid artery occlusion, cerebrovascular disease, therapeutics

Editorial on the Research Topic

Cerebrovascular and Neurodegenerative Diseases - New Insights into Molecular Cell Biology and Therapeutic Targets

There is a significant gap in our understanding of the molecular and cellular biology of cerebrovascular and neurodegenerative diseases to identify new therapeutic targets and develop diagnostic tools to better understand the disease progression and treatment. The cellular and molecular events linking cerebrovascular pathology and neurodegeneration are also not fully understood. The research articles and review papers published in this topic aim at a multifaceted approach to evaluating recent progress in our understanding some of the underlying molecular mechanisms of disease process and potential therapeutics targeting these diseases. Here we summarize the contributing articles to our topic conveying the aim of the pertaining research. The articles in this Research Topic highlight the challenges inspiring future research to address some of the questions and to exploit new opportunities for development of novel therapeutics for cerebrovascular and neurodegenerative diseases.

Smith-Dijak et al. studied the effects of pridopidine, a drug that enhances brain derived neurotrophic factor (BDNF) signaling through stimulation of the sigma-1 receptor (S1R) and S1R agonist, in cortical neurons obtained from a mouse model of Huntington disease (HD). Several pathways implicated in synaptic functions are dysregulated in HD, including BDNF and calcium signaling. The data provide evidence for restoration of synaptic plasticity that maintain the stability of neuronal and synaptic function required for new learning and cognitive function. The results suggest a potential new direction for developing therapy to mitigate cognitive deficits in HD and may provide new avenues for neuroinflammation-related disorders treatment.

Agouni et al. provided a comprehensive analysis of circulating extracellular vesicles (EVs) from vascular wall, blood, and immune cells in transient ischemic attacks (TIA) and acute ischemic stroke (AIS) patients from Southeast Asia and the Middle East. This study showed that EVs of various origins, especially those associated with endothelial cell injury and platelet activation, are increased in TIA and AIS patients. The levels of EV continue to be high for up to 30-days post-attacks indicating a sustained cellular activation, which may be associated with an increased risk of recurrence of acute events in this population.

D'Angelo et al. carried out a review on antiphospholipid syndrome (APS) and multiple sclerosis (MS). APS and MS are both considered as anti-lipid autoimmune diseases with specific

OPEN ACCESS

Edited and reviewed by:
Wendy Noble,
King's College London,
United Kingdom

***Correspondence:**
Sikha Saha
s.saha@leeds.ac.uk

Specialty section:
This article was submitted to Neurodegeneration, a section of the journal Frontiers in Neurology

Received: *19 September 2019*
Accepted: *29 November 2019*
Published: *13 December 2019*

Citation:
Saha S and Kantamneni S (2019) Editorial: Cerebrovascular and Neurodegenerative Diseases - New Insights Into Molecular Cell Biology and Therapeutic Targets. Front. Neurol. 10:1322. doi: 10.3389/fneur.2019.01322

pathophysiological mechanisms and events. Isolated neurological APS represents a significant diagnostic challenge, as epidemiological, clinical, and neuroimaging features may overlap with those of MS. The review draws attention to the clinical relevance of diagnosing isolated neurological APS and suggests that prompt and accurate diagnosis and treatment of APS with anti-aggregant and anticoagulant could be vital to prevent or reduce APS-related morbidity and mortality.

Wei et al. examined the cellular mechanisms mediating the neuroprotective effects of Homer1a, a short form of a scaffold protein, which is upregulated in rat cortical neurones following oxygen and glucose deprivation (OGD) mimicking ischemia-reperfusion (I/R) injury. The results showed that overexpression of Homer1a reduced OGD-induced lactate dehydrogenase (LDH) release, cell death, and mitochondrial dysfunctions in cultured cortical neurons. Homer1a also protects against OGD-induced injury by preserving mitochondrial function through inhibiting the protein kinase R-like endoplasmic reticulum kinase (PERK) pathway. In addition, mitochondrial protection of Homer1a was blocked by the ER stress activator tunicamycin (TM) suggesting that Homer1a may be a promising target of protecting neurons from cerebral injury.

Yang et al. examined the effect of cyclooxygenase (COX2)/prostaglandin D2 (PGD2)-related autophagy on brain injury in diabetic rats suggesting that the COX2-PGD2 pathway is a potential therapeutic target for diabetic brain injury.

Xu et al., reported that low-moderate ethanol consumption may prevent ischemic stroke and reduce brain cerebral ischemia/reperfusion injury (I/R) by suppressing inflammation, whereas heavy alcohol consumption may induce ischemic stroke and worsen brain I/R injury by aggravating inflammation.

He et al. found that smilagenin, a steroidal sapogenin from traditional Chinese medicinal herbs, can have neuroprotective effect on dopaminergic neurons in a chronic mouse model of Parkinson's disease (PD) suggesting that this drug could prevent the impairment of dopaminergic neurons in PD.

Zhang et al. demonstrated that Naringenin (NAR), a grapefruit flavonoid promoted microglia M1/M2 polarization, thus conferring anti-neuroinflammatory effects via the inhibition of mitogen-activated protein kinase (MAPK) signaling activation. These findings provide new alternative avenues for neuroinflammation-related disorders treatment.

Hao et al. showed that heterozygous loss of activin receptor-like kinase 1 (Alk1) can lead to hereditary hemorrhagic telangiectasia, which is a vascular disease characterized by direct connections between arteries and veins leading to arteriovenous malformations (AVMs). The results of the study suggest that Alk1 induces the formation of sporadic human cerebral AVMs through affecting migration and proliferation of endothelial cells combined with vascular endothelial growth factor A.

Li et al. developed a flow cytometry protocol to identify microglia and monocyte-derived macrophages from mouse intracerebral hemorrhagic (ICH) stroke model induced by collagenase or blood injection. The authors also combined magnetic-activated cell separation system that allows eight tissue samples to be assessed together. This protocol represents a very important tool for biological functions of microglial and monocyte-derived macrophage in ICH stroke and related brain diseases.

Jin et al., showed that glucose-regulated protein (GRP78) a chaperone protein located in the endoplasmic reticulum (ER) is involved in the neuroglial response to neurotoxic insult in rats induced by mitochondrial toxin 3-nitropropionic acid (3-NP), which selectively damages striatal neurons. These data provide novel insights into the phenotypic and functional heterogeneity of GRP78-positive cells within the lesion core and the involvement of GRP78 in the activation/recruitment of activated microglia/macrophages and blood-brain-barrier impairment in response neurotoxic insult.

Song et al. reported that the knock down of myosin light chain kinase, a key enzyme in smooth muscle cell contraction, in human brain smooth muscle cells (SMCs) caused effects similar to those observed in cultured SMCs from intracranial aneurysm patients. These results indicate that myosin light chain kinase plays an important role in maintaining smooth muscle contractility, cell survival and inflammation tolerance and is crucial to the normal function of intracranial arteries.

Hoyk et al. showed elevated serum triglyceride levels, changes in functional and morphological gene expressions and blood brain barrier dysfunction in transgenic mice overexpressing the human APOB-100 protein, a mouse model of human atherosclerosis suggesting that these transgenic mice could be a useful model to study the link between cerebrovascular pathology and neurodegeneration.

Yu et al. reported that injection of hydroxysafflor yellow A (HSYA), a major active chemical component of the safflower via carotid artery improves cognitive impairment and synaptic plasticity in a rat model of stroke induced by middle cerebral artery occlusion.

Chen et al. showed that Gap19, a selective Connexin 43 (Cx43) -hemi -channel inhibitor, produces neuroprotective effects in cerebral ischemia/reperfusion injury induced by middle cerebral artery occlusion in mice via suppression of Cx43 and Toll-like receptor 4 (TLR4) mediated signaling pathways.

Chang et al. developed a new *in vitro* cerebral micro-bleed model to study the interactions between brain endothelial cells and red blood cells exposed to oxidative stress. Their findings demonstrate that erythrophagocytosis mediated by the brain endothelial monolayer and the passage of iron-rich hemoglobin and RBC, may be involved in the development of cerebral microbleeds that are not dependent on disruption of the microvasculature.

Faustino-Mendes et al. reviewed the current experimental models of immature ischemic brain and highlighted the need for new multifactorial experimental models to attain more efficient therapies to treat this complex vascular condition and related long-term conditions.

Chen et al. showed that the compound 22a, a promising neuroprotective compound derived from tetramethylpyrazine and widely used as active ingredient of traditional Chinese medicine, effectively prevented glutamate-induced excitotoxicity in cerebellar granule cells (CGNs) via involvement of the PI3K/Akt and PGC1α/Nrf2 pathways suggesting that this

compound might be useful in preventing neuronal death from ischemic stroke.

Du et al. tested a hypothesis that chemokine interleukin (IL) eight released by astrocytes and C-X-C motif chemokine receptor 1 (CXCR1) in neurons are involved in neuronal apoptosis induced by methamphetamine (METH), a widely abused illicit drug, which can cause dopaminergic neuron apoptosis and astrocyte-related neuroinflammation. The results suggest that CXCR1 may be a potential target for METH-induced neurotoxicity therapy.

Lu et al., aimed to explore the protective effects of rosuvastatin, a 3-hydroxymethyl-3-methylglutaryl coenzyme A (HMG-CoA) reductase inhibitor, against haemorrhagic transformation (HT) after recombinant tissue plasminogen activator (rt-PA) treatment in a mouse model of experimental stroke. The beneficial effects are related to inhibition of the inflammation-related nuclear factor kappa B (NF-κB) and mitogen-activated protein kinase (MAPK) pathways.

Wang et al. showed that mild ER stress ("preconditioning") induced by tunicamycin (TM), can alleviate LPS-induced astrocytic activation and BBB disruption. Their findings provide a better understanding for the regulatory role of ER stress in neuroinflammation and indicate that mild ER stress might have therapeutic value for the treatment of neurodegenerative diseases.

Yang et al., found that adapentpronitrile, a new adamantane-based dipeptidyl peptidase-IV (DPP-IV) inhibitor significantly ameliorated neuronal injury and decreased amyloid precursor protein (APP) and amyloid beta (Aβ) expression in the hippocampus and cortex of rat model of diabetes fed with high fat diet. These authors showed that adapentpronitrile protected against diabetic neuronal injury by inhibiting mitochondrial oxidative stress and the apoptotic pathway.

Jang et al. reported intrastriatal injection of adeno-associated viral vector serotype DJ containing N171-82Q mutant huntingtin *(HTT) gene* to juvenile mice produced Huntington's disease (HD)-like symptoms including mutant *HTT* aggregation, neurodegeneration, and Neuroinflammation. The authors suggested that this model will a useful tool to better understand neuropathological mechanisms of HD and develop new therapeutics for this disease.

Hao et al. established a stable method for the isolation of endothelial cells (ECs) from human cerebral arteriovenous malformation tissues, which play an important role in the manifestation and development of cerebral vascular malformation as well as haemorrhagic stroke and thrombogenesis. The protocol can also be adapted for other vascular diseases.

He et al. demonstrated that rosuvastatin treatment significantly increased neurite outgrowth in cortical neurons after oxygen-glucose deprivation (OGD)-induced damage, reduced the generation of reactive oxygen species, protected mitochondrial function and elevated the ATP levels via Notch1 pathway. These findings highlight Notch1 signaling as important player and novel therapeutic target in promoting brain plasticity.

In summary, the present Research Topic encompassed several cutting-edge techniques and models for investigating the cellular and molecular mechanisms of cerebrovascular dysfunction and neurodegeneration. Together, they provide a framework for understanding the way some of the diseases progress and potential pathways for therapeutic interventions. We acknowledged that collection of articles in a single topic cannot deal with this extremely vast subject characterized by complex conditions such as cerebrovascular dysfunction and neurodegeneration. The topics addressed, however, help developing clear ideas, not only in terms of recent studies but also the unmet needs for future research in these areas. We trust that the papers assembled in this Research Topic will prove useful in encouraging and stimulating future progress in research related to cerebrovascular and neurodegenerative diseases.

AUTHOR CONTRIBUTIONS

SS prepared the editorial and both SK and SS edited the final version. SS and SK made substantial contributions to the review and approved the manuscripts accepted on this topic.

Conflict of Interest: The authors declare that the research was conducted in the absence of any commercial or financial relationships that could be construed as a potential conflict of interest.

frontiers in Cellular Neuroscience

ORIGINAL RESEARCH
published: 17 January 2018
doi: 10.3389/fncel.2018.00006

Rosuvastatin Improves Neurite Outgrowth of Cortical Neurons against Oxygen-Glucose Deprivation via Notch1-mediated Mitochondrial Biogenesis and Functional Improvement

Weiliang He[1], *Yingping Liu*[2] *and Xiaochao Tian*[3]*

[1]Department of Neurology, Hebei General Hospital, Shijiazhuang, China, [2]Department of Cardiology, Beijing Shijitan Hospital, Capital Medical University, Beijing, China, [3]Department of Cardiology, The Second Hospital of Hebei Medical University, Shijiazhuang, China

Neurogenesis, especially neurite outgrowth is an essential element of neuroplasticity after cerebral ischemic injury. Mitochondria may supply ATP to power fundamental developmental processes including neuroplasticity. Although rosuvastatin (RSV) displays a potential protective effect against cerebral ischemia, it remains unknown whether it modulates mitochondrial biogenesis and function during neurite outgrowth. Here, the oxygen-glucose deprivation (OGD) model was used to induce ischemic injury. We demonstrate that RSV treatment significantly increases neurite outgrowth in cortical neurons after OGD-induced damage. Moreover, we show that RSV reduces the generation of reactive oxygen species (ROS), protects mitochondrial function, and elevates the ATP levels in cortical neurons injured by OGD. In addition, we found that, under these conditions, RSV treatment increases the mitochondrial DNA (mtDNA) content and the mRNA levels of mitochondrial transcription factor A (TFAM) and nuclear respiratory factor 1 (NRF-1). Furthermore, blocking Notch1, which is expressed in primary cortical neurons, reverses the RSV-dependent induction of mitochondrial biogenesis and function under OGD conditions. Collectively, these results suggest that RSV could restore neurite outgrowth in cortical neurons damaged by OGD *in vitro*, by preserving mitochondrial function and improving mitochondrial biogenesis, possibly through the Notch1 pathway.

Keywords: cortical neurons, neurite outgrowth, cerebral ischemia, rosuvastatin, mitochondria, notch1

OPEN ACCESS

Edited by:
Sriharsha Kantamneni, University of Bradford, United Kingdom

Reviewed by:
Lezi E, Duke University, United States
Selva Baltan, Cleveland Clinic Lerner College of Medicine, United States

***Correspondence:**
Xiaochao Tian
xiaochao_tian2009@126.com

Received: *09 November 2017*
Accepted: *05 January 2018*
Published: *17 January 2018*

Citation:
He W, Liu Y and Tian X (2018) Rosuvastatin Improves Neurite Outgrowth of Cortical Neurons against Oxygen-Glucose Deprivation via Notch1-mediated Mitochondrial Biogenesis and Functional Improvement. Front. Cell. Neurosci. 12:6. doi: 10.3389/fncel.2018.00006

INTRODUCTION

Stroke is one of the leading causes of long-term disability and death worldwide and affects the patients' emotional, mental and physical health (Thampy and Pais, 2016). Neurogenesis including the regulation of neurite outgrowth is believed to be vital as a mechanism of neuroplasticity after cerebral ischemic injury (Kitamura et al., 2009; Lin and Sheng, 2015). Therefore, targeting neurite outgrowth represents a prospective therapeutic strategy for stroke patients.

Neurite outgrowth is a developmental process that requires a heavy energy supply, provided by the mitochondria (Mattson and Partin, 1999). However, the disruption of oxygen

and glucose supply, which is caused by stroke and mimicked by the *in vitro* oxygen-glucose deprivation (OGD) model, can produce a large number of reactive oxygen species (ROS) and lead to the depletion of cellular ATP (Rousset et al., 2015). Mitochondria are highly dynamic organelles and continually undergo biogenesis, fission and fusion (Anne Stetler et al., 2013). Maintaining a proper mitochondrial function depends on correct mitochondrial biogenesis (Sbert-Roig et al., 2016). Numerous studies have shown that mitochondrial dysfunction, especially regarding biogenesis, plays a crucial role in ischemic injury (McLeod et al., 2005; Gutsaeva et al., 2008). Therefore, identifying pharmacological agents that preserve mitochondrial functions and promote neurite outgrowth against cerebral ischemic injury might be an ideal therapeutic strategy.

Statins are structural analogs of the 3-hydroxy-3-methylglutaryl coenzyme A (HMG-CoA), the substrate of HMG-CoA reductase, and have been used as potent cholesterol-lowering drugs for the treatment of hypercholesterolaemia and coronary heart disease (Stein, 2002; Rader, 2003). Many studies have shown that statins reduce stroke incidence and improve its outcome (Bösel et al., 2005). The role of statins in neurite outgrowth has been proposed by previous studies (Jin et al., 2012; Métais et al., 2015). Rosuvastatin (RSV) is considered as one of the most effective statins and is able to ability to form multiple polar covalent bonds with the HMG-CoA reductase. In mice, RSV was shown to have a neuroprotective effect following cerebral ischemia. Accumulating evidence suggests that statins decrease the oxidative phosphorylation capacity and membrane potential of mitochondria, thus impairing their function (Broniarek and Jarmuszkiewicz, 2016), However, a recent study reported that, in the kidneys of wild type C57BL/6 male mice, RSV increases the protein levels of Sirt1 and PGC-1a, two key players in mitochondrial biogenesis (Corsetti et al., 2014). Nevertheless, it is not completely clear whether RSV modulates mitochondrial function and biogenesis during neurite outgrowth.

The Notch pathway constitutes one of the most well-conserved developmental pathways throughout evolution. It controls both cell proliferation and apoptosis and is crucial for intercellular interactions in human development as well as in disease (Artavanis-Tsakonas et al., 1999; Bi and Kuang, 2015). A lot of attention has been paid to understanding how this pathway regulates cellular metabolism. Notch1, a well-studied protein, plays a significant role in this pathway (Kageyama et al., 2007). Recent studies have shown that the Notch1 pathway regulates mitochondrial fusion (Kasahara et al., 2013), but also affects their function (Basak et al., 2014), indicating that Notch1 is crucial in mitochondrial metabolism. Furthermore, the activation of Notch1 modulates the expression of important mitochondria-localized metabolic pathway proteins (Basak et al., 2014). Additionally, a previous study reported that Notch1 may exert a negative effect on neurite outgrowth (Berezovska et al., 1999). However, whether Notch1 mediates the protective effect of RSV on neurite outgrowth following ischemic injury is still not clear.

Based on this evidence, this study was designed to investigate the role of mitochondrial function and biogenesis in RSV-induced neurite outgrowth. We also attempted to determine the role of Notch1 in promoting the effects of RSV, in order to further elucidate the potential mechanism of its action.

MATERIALS AND METHODS

The experimental protocols were conducted in accordance with guidelines approved by the Animal Experimentation Ethics Committee of Hebei Medical University.

Primary Cortical Neuron Culture and OGD

Cortical neurons were obtained from the brains of embryonic day 15–18 (E15–18) C57BL/6 mice (Vital River Laboratory Animal Technology Co. Ltd., Beijing, China). The cerebral cortex was dissected and incubated at 37°C, for 15 min, in Hibernate-E solution (Sigma, Ronkonkoma, NY, USA), supplemented with papain (2.0 mg/ml, Sigma, Ronkonkoma, NY, USA). Then, the cortical tissues were neutralized and dissociated into single cells in Neurobasal medium containing 2% B-27 supplement (Invitrogen, Carlsbad, CA, USA) and 0.5 mM glutamine (Life Technologies, Carlsbad, CA, USA). Cells were plated at a density of 2×10^5 cells/cm^2 onto culture dishes, which had been coated with poly-L-lysine (Biocoat, BD Biosciences, San Jose, CA, USA), and grown in the same medium in a humidified 5% CO_2 incubator at 37°C. In the present study, OGD was used to induce ischemia. To initiate ischemia, we used the same incubator in combination with a Hypoxic Workstation (gas mixture of 0.1% O_2, 94.9% N_2 and 5% CO_2, 37°C).

Drug Application

Neurons were pre-exposed to OGD conditions for 1 h and subsequently treated with different concertrations of RSV (0.5, 5, or 50 μM) for 48 h. Cells not treated with RSV or OGD served as a negative control. To evaluate the effect of Notch1 on mitochondrial function and biogenesis, a potent and specific inhibitor of the Notch1 pathway, DAPT, N-[N-(3,5-difluorophenacetyl)-L-alanyl]-S-phenylglycinet-butyl ester, was added to the medium at 10 μM (in 0.1% dimethyl sulfoxide; Sigma, USA), 30 min before the RSV treatment.

Neurite Outgrowth Assay

After 48 h of drug application, primary cortical neurons were fixed with 4% paraformaldehyde for 20 min and then processed for immunocytochemistry. Briefly, neurons were incubated with the mouse monoclonal anti-β-III-tubulin antibody (Tuj-1, 1:500, Sigma, USA) overnight at 4°C, followed by the donkey anti-mouse IgG, FITC-conjugated secondary antibody (1:200, CWBIO, China) for 1 h at 37°C. Stained cells were imaged with an upright fluorescence microscope (Olympus, Japan). The length of the longest neurite of a Tuj-1-positive cell and the total neurite length per cell were measured using ImageJ software. Approximately 60 Tuj-1-positive cells per condition were measured.

Measurement of Mitochondrial Membrane Potential (MMP)

The Mitochondrial Membrane Potential (MMP) of cortical neurons in different conditions was measured by using the JC-1

assay kit (Beyotime, China), according to the manufacturer's instructions. In brief, after the described treatments, neurons were collected and incubated with JC-1 staining solution (5 μg/mL) for 20 min at 37°C. Cells were then rinsed twice with JC-1 staining buffer and centrifuged at 600× *g* at 4°C for 15 min. The cells were resuspended with JC-1 staining buffer and the fluorescence intensity was detected using a monochromator microplate reader (Tecan, Switzerland). Fluorescence images were also obtained in green or red channels using an upright fluorescence microscope (Olympus, Japan). The fluorescence at 529 (green) and 590 (red) nm was measured using the monochromator microplate reader. The ratio of red to green fluorescence in different conditions was normalized to the respective one in the control condition, which was considered to have 100% MMP, and plotted graphically. Data were presented as percent of control.

Measurement of ROS

Intracellular ROS levels were quantified with the ROS assay kit (Beyotime, China) as previously reported (He et al., 2017). In brief, cortical neurons were incubated with 10 μM 2,7-dichlorofluorescein diacetate (DCF-DA) for 1 h at 37°C in the dark and then resuspended in PBS. Intracellular ROS production indicated by the fluorescence intensity of the probe 2,7-dichlorodihydro-fluorescein diacetate (H_2DCF-DA) was detected using a luminescence spectrometer with the excitation source set at 488 nm and the emission one at 525 nm. The values obtained at various conditions were expressed as the percentage change compared to the control condition.

Detection of Cellular ATP Levels

The cellular ATP levels were determined using an ATP assay kit according to the manufacturer's instructions (Beyotime, China). Luminesence was measured with a monochromatic microplate reader (Tecan, Switzerland). Data were presented as percentages compared to the control condition.

Mitochondrial DNA (mtDNA) Quantification

Total DNA from cortical neurons was extracted using the DNeasy Blood and Tissue kit (Qiagen, Germantown, MD, USA) according to previous reports (Tian et al., 2017). Mitochondrial DNA (mtDNA) copy number was measured by real-time PCR using an ABI 7500 real-time PCR system (Applied Biosystems, Foster, CA, USA) with the SYBR Green detection method. The relative mtDNA copy number was determined by comparison to nuclear DNA (rRNA 18S). The primers for mtDNA were as follows: forward: 5′-AACACGA TCAGGCAACCAAA-3′, and reverse: 5′-GGTAGCGGGTGAGTTGTCAG-3′. The primers for rRNA 18S were: forward: 5′-GGACAGCGGGTGAGTTGTCA-3′, and reverse: 5′-ACCTTCGTTATCGGAATACC-3′.

Quantitative Real-Time PCR

Quantitative real-time PCR (qRT-PCR) was performed according to previous reports (Dai et al., 2014; He et al., 2016). Briefly, total RNA was isolated from cortical neurons using Trizol reagent (Invitrogen, Carlsbad, CA, USA). Reverse transcription was carried out using the First-strand cDNA synthesis kit (Fermentas International Inc., Burlington, Canada) and the cDNA was amplified by a real-time PCR system (Applied Biosystems, Carlsbad, CA, USA) in the presence of a fluorescent dye (SYBR Green I, CWBIO). The relative abundance of specific mRNAs was calculated after normalization with the glyceraldehyde 3-phosphate dehydrogenase mRNA. The samples were tested in triplicates. Primers for all qRT-PCR experiments were listed as follows:

NRF-1: forward: 5′-GAGTGACCCAAACCGAACA-3′,
reverse: 5′-GGAGTTGA GTATGTCCGAGT-3′;
TFAM: forward: 5′-GGTGTATGAAGCGGATTT-3′,
reverse: 5′-CTTTCTTCTTTAGGCGTTT-3′;
GAPDH: forward: 5′-AAGGTGAAGGTCGGAGTCAA-3′,
reverse: 5′-AATGAAGGGGTCATTGATGG-3′.

Statistical Analysis

Statistical analysis was performed using SPSS version 16.0. All data were presented as mean ± SEM. One-way analysis of variance (ANOVA) was performed for comparisons among groups, and SNK-q test was used for *post hoc* multiple comparisons. $^*p < 0.05$ was considered to be statistically significant.

RESULTS

RSV Restores Neuritogenesis in Cortical Neurons Damaged by OGD

First, we examined the effect of RSV on the neurite outgrowth of cortical neurons under OGD. As shown in **Figures 1A,B**, neurons under OGD showed a remarkable decrease in neurite outgrowth (27.86 ± 5.11 μm, $n = 60$), compared to control cells (43.84 ± 7.15 μm, $n = 60$, $p < 0.005$). On the other hand, the treatment with different concentrations of RSV (0.5, 5, or 50 μM), for a period of 48 h after OGD injury, resulted in a significant recovery of neurite outgrowth. Compared with the OGD-treated cells (27.86 ± 5.11 μm), the length of the longest neurite was 30.25 ± 5.60 μm ($n = 60$, $p = 0.016$), for neurons treated with 0.5 μM RSV, 37.36 ± 6.55 μm, for those treated with 5 μM RSV ($n = 60$, $p < 0.005$), and 34.24 ± 7.02 μm, for those treated with 50 μM RSV ($n = 60$, $p < 0.005$). The fold change in the total neurite length between the untreated OGD-exposed cells and the treated ones with 0.5, 5 and 50 μM of RSV was 1.15, 1.65 and 1.44, respectively ($n = 60$, $p < 0.005$, **Figure 1C**). These results indicated that RSV could effectively improve neuritogenesis in cortical cells, previously injured by OGD. We chose 5 μM RSV to carry out subsequent experiments, considering that this concentration demonstrated the highest potential in inducing neurite outgrowth compared with the one of 0.5 ($n = 60$, $p < 0.005$) or 50 μM ($n = 60$, $p < 0.005$).

RSV Preserves Mitochondrial Function in Cortical Neurons under OGD

We next investigated the involvement of mitochondrial function in RSV-induced neurite outgrowth. Indicators of mitochondrial function were assessed in primary cortical neurons exposed to RSV under OGD conditions. Exposure of neurons to OGD for

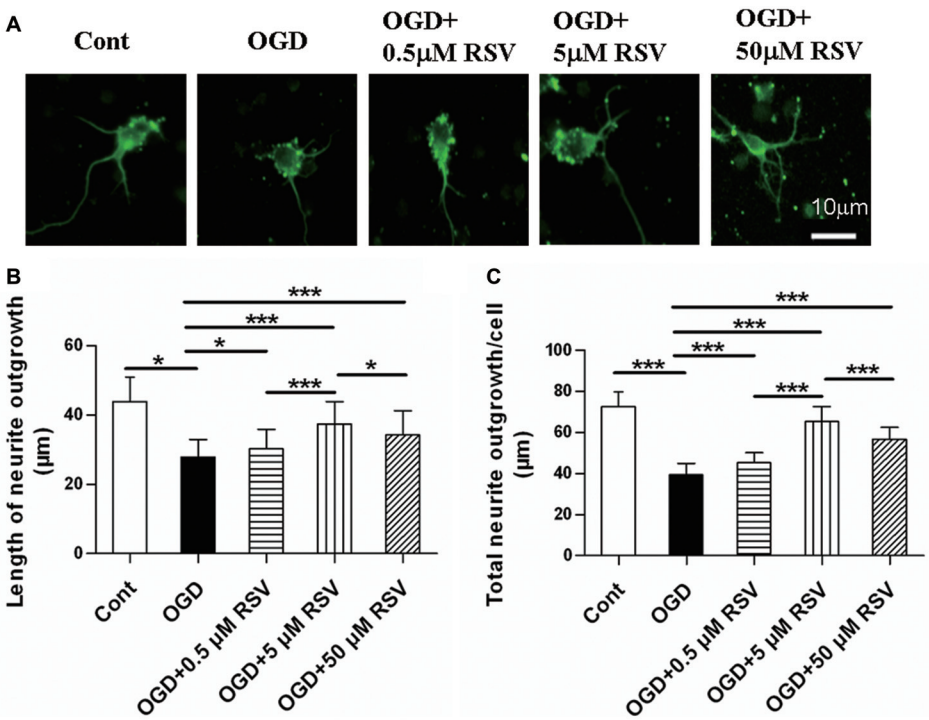

FIGURE 1 | Effect of rosuvastatin (RSV) on neurite outgrowth in cultured cortical neurons. Neurons were pre-exposed to oxygen-glucose deprivation (OGD) for 1 h and subsequently treated with or without RSV for 48 h. Cells were stained with anti-β-III-Tubulin (Tuj-1) antibody. **(A)** Representative images of Tuj-1-positive neurons (green) in different conditions. Scale bar represents 10 μm. **(B)** Quantitative analysis of the length of the longest neurite. Results are presented as the mean ± SEM. $^{*}p < 0.05$, $^{***}p < 0.005$, $n = 60$ per condition. **(C)** Quantitative analysis of the total neurite length per cell. Results are presented as the mean ± SEM. $^{*}p < 0.05$, $^{***}p < 0.005$, $n = 60$ per condition.

1 h resulted in dissipation of the MMP ($n = 6$, $p < 0.005$) and an increase in ROS production ($n = 6$, $p < 0.005$). On the other hand, the treatment of cells with RSV, counteracted these effects. The MMP recovered ($n = 6$, $p < 0.005$; **Figures 2A,B**) and ROS accumulation was significantly reduced ($n = 6$, $p < 0.005$; **Figure 2C**), in comparison to untreated OGD-exposed cells. The above-mentioned results suggest that RSV can reverse the mitochondrial dysfunction, induced by OGD.

RSV Elevates the Energy Metabolism of Primary Cultured Neurons Suppressed by OGD

As mitochondria are the main source of energy generation, we detected ATP levels, to assess the energy metabolism of primary cultured neurons. RSV significantly reversed the decrease in cellular ATP levels, which was observed following exposure to OGD ($n = 6$, $p < 0.005$; **Figure 2D**). These results indicate that RSV can increase the energy metabolism, impaired by OGD.

RSV Promotes Mitochondrial Biogenesis after OGD Exposure

To determine whether the altered mitochondrial function and energy metabolism are related to mitochondrial biogenesis, we also estimated the mtDNA content in different conditions (**Figure 3A**). The results showed that OGD exposure significantly decreased mtDNA content, whereas RSV treatment abrogated this effect ($n = 6$, $p < 0.005$; **Figure 3A**).

Mitochondrial transcription factor A (TFAM) and nuclear respiratory factor 1 (NRF-1) are major regulators of mitochondrial biogenesis. Therefore, we measured the expression of these factors, using qRT-PCR (**Figures 3B,C**). The results showed that RSV treatment after OGD exposure significantly increased the mRNA expression of TFAM and NRF-1 ($n = 6$, $p < 0.05$; **Figures 3B,C**).

Notch1 Mediates the Protective Effect of RSV on Mitochondrial Function and Biogenesis in Cortical Neurons Exposed to OGD

Based on our finding that RSV preserved the mitochondrial function in primary cultured neurons exposed to OGD, we explored whether Notch1 was involved in this process. The release of the Notch intracellular domain (NICD) is widely used as a marker for Notch1 pathway activation. In our study, we examined NICD expression via immunocytochemical analysis. We found that NICD was expressed in cortical neurons, exposed to OGD, which suggested that endogenous Notch1 might be activated upon neuronal injury and mediate OGD remodeling. In these conditions, we found that RSV treatment increased the expression of NICD (**Figure 4A**; data not shown). Next, we used

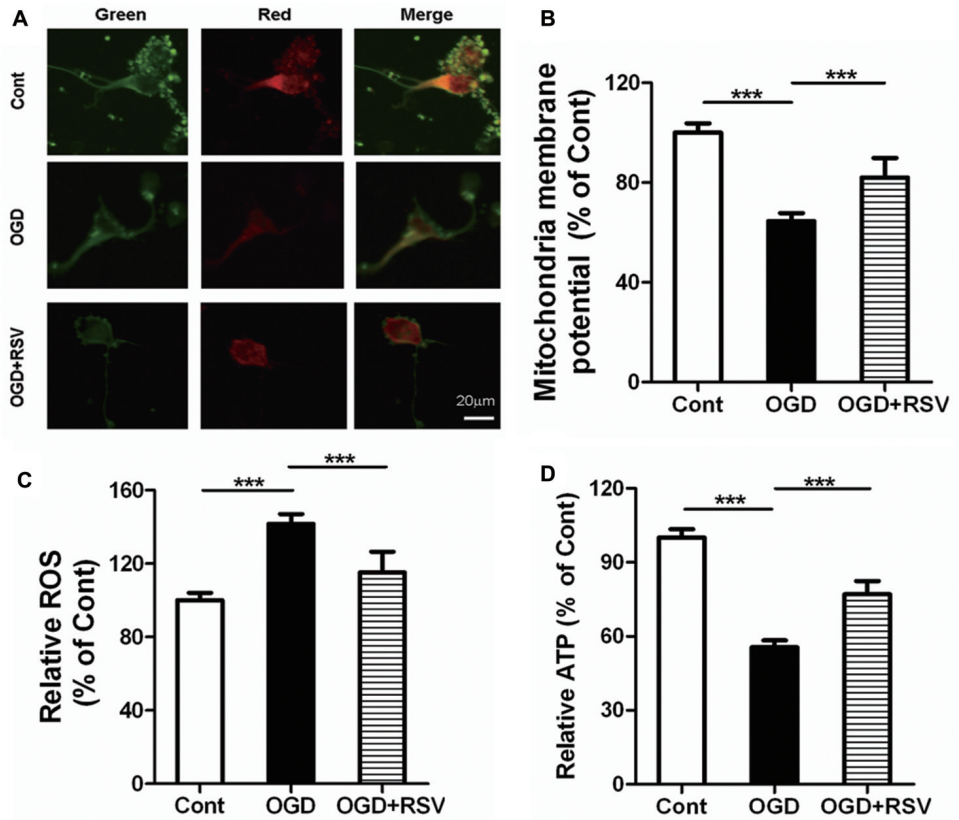

FIGURE 2 | Effects of RSV on mitochondrial function and ATP levels in cortical neurons exposed to OGD. Cells were exposed to OGD and incubated with the indicated concentrations of RSV. **(A)** Mitochondrial membrane potential (MMP) as determined using the JC-1 assay. Scale bar represents 20 μm. **(B)** MMP as determined using the JC-1 assay kit in different conditions (control, OGD-exposed and OGD-exposed plus RSV). The results are expressed as the mean ± SEM. ***$p < 0.005$, $n = 6$ per group. **(C)** Measurement of reactive oxygen species (ROS) generation in different conditions (control, OGD-exposed, and OGD-exposed plus RSV). Results are expressed as the mean ± SEM. ***$p < 0.005$, $n = 6$ per group. **(D)** ATP production measured in different conditions (control, OGD-exposed and OGD-exposed plus RSV). Results are expressed as the mean ± SEM. ***$p < 0.005$, $n = 6$ per condition.

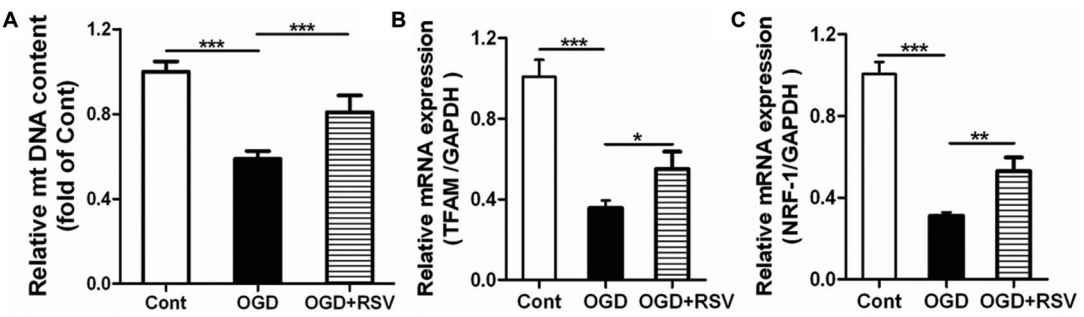

FIGURE 3 | Effect of RSV on mitochondrial biogenesis in cortical neuron cultures. Cells were pre-exposed to OGD for 1 h and subsequently treated with or without RSV for 48 h. **(A)** Mitochondrial DNA (mtDNA) content measurements. Results are expressed as the mean ± SEM. *$p < 0.05$, **$p < 0.01$, ***$p < 0.005$, $n = 6$ per condition. **(B,C)** mRNA expression of mitochondrial transcription factor A (TFAM) **(B)** and nuclear respiratory factor 1 (NRF-1; **C**) as measured using quantitative real-time PCR. Data are shown as the mean ± SEM. *$p < 0.05$, **$p < 0.01$, ***$p < 0.005$, $n = 6$ per condition.

the Notch1 pathway inhibitor DAPT to assess mitochondrial function. Compared to the RSV-treated OGD-exposed cells, DAPT partially reduced MMP ($n = 6$, $p < 0.005$; **Figure 4B**), boosted ROS production ($n = 6$, $p < 0.05$; **Figure 4C**), and decreased ATP levels ($n = 6$, $p < 0.05$; **Figure 4D**). Therefore, inhibition of the Notch1 pathway reverts the effects of RSV, at least to a certain extent. We also explored whether DAPT could affect mitochondrial biogenesis in primary cultured neurons

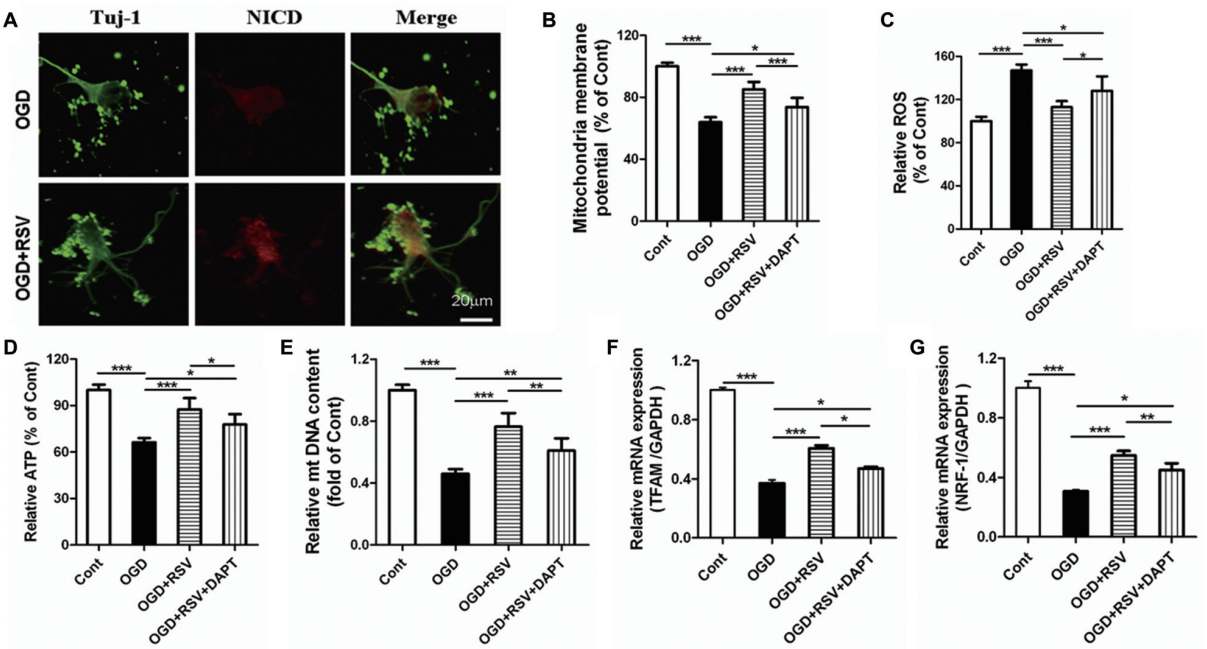

FIGURE 4 | Notch1 pathway is involved in the beneficial effects of RSV on neuronal function and mitochondrial biogenesis under OGD conditions. **(A)** Double immunofluorescence staining for anti-Notch intracellular domain (NICD) and anti-β-III-Tubulin (Tuj-1) antibodies. NICD (red), a marker for activation of Notch1 pathway, is expressed in Tuj-1-positive neurons (green) and its expression is increased in OGD-exposed cells treated with RSV compared to non-treated cells. **(B–D)** Effect of DAPT, a specific inhibitor of the Notch1 pathway, on the RSV-induced improvement of mitochondrial function as assessed by measuring MMP **(B)**, ROS levels **(C)**, and ATP levels **(D)**. Data are presented as mean ± SEM. $^{*}p < 0.05$, $^{**}p < 0.01$, $^{***}p < 0.005$, $n = 6$ per condition. **(E–G)** Effect of DAPT on RSV-induced mitochondrial biogenesis as assessed by measuring mtDNA **(E)** and the mRNA levels of TFAM **(F)** and NRF-1 **(G)**. Data are presented as mean ± SEM. $^{*}p < 0.05$, $^{**}p < 0.01$, $^{***}p < 0.005$, $n = 6$ per condition.

exposed to OGD. Compared to the RSV-treated cells, DAPT partialy decreased the mtDNA content ($n = 6$, $p < 0.01$; **Figure 4E**) and reduced the mRNA levels of TFAM ($n = 6$, $p < 0.05$; **Figure 4F**) and NRF-1 ($n = 6$, $p < 0.01$; **Figure 4G**).

Additional, we did the following experiments whether DAPT itself had detrimental effects. The length of the longest neurite, total neurite outgrowth per cell, MMP, ROS, ATP, mtDNA, TFAM and NRF-1 were detected. The data were shown in the supplementary data. The results showed that there were no signifcant diferences in the length of the longest neurite, total neurite outgrowth per cell, MMP, ROS, ATP, mtDNA, TFAM and NRF-1 between OGD+DAPT and OGD group (see **Supplementary Figures S1–S3** in Supplementary Data), suggesting that DAPT itself has no detrimental effects.

DISCUSSION

In this present study, we demonstrated that RSV restores neuritogenesis in primary cortical cells damaged by OGD. This action is possibly mediated by the improvement in mitochondrial function and biogenesis. Furthermore, we also elucidated that Notch1 is crucial for these RSV-dependent effects. To the best of our knowledge, this is the first report to provide evidence for the effect of RSV on cortical neuritogenesis following OGD and the involvement of Notch1 in RSV-induced mitochondrial biogenesis and functional improvement.

Statins act as inhibitors of the HMG-CoA reductase and have been extensively used for the treatment of hypercholesterolemia (Kahveci et al., 2014). Numerous studies have reported that statins may have neuroprotective properties, as demonstrated by the reduction of the affected region following focal cerebral ischemia and the protection of cortical neurons from excitotoxicity (Asahi et al., 2005; Bösel et al., 2005). Recent studies have shown that treatment of cortical neurons, cultured under OGD/reoxygenation conditions, with RSV, a novel HMG-CoA reductase inhibitor, was neuroprotective for the cells (Savoia et al., 2011). RSV exerts considerable protective effects on neural tissue against oxidative damage after spinal cord ischemia/reperfusion injury, improves cognitive functions in rats with diazepam-induced amnesia, and preserves long-term memory (Yavuz et al., 2013). Our results demonstrated that RSV, at a concentration of 5 μM, shows the maximum effects on enhancing neuritogenesis in cortical neurons exposed to OGD.

Neurite outgrowth is an energy-consuming process that primarily depends on mitochondria. Mitochondria may play a crucial role in controlling neuroplasticity, including neurite extension (Mattson, 2007; Cheng et al., 2010). It has been reported that modulating mitochondrial function may impact neurite outgrowth (Habash et al., 2015). Furthermore, impaired mitochondrial function may disturb neuroplasticity following stroke (Cheng et al., 2010). Additionally, mitochondria may influnce the generation of ROS (Onyango et al., 2011), whose

accumulation, caused by ischemia, could disrupt MMP and funcion. Damaged mitochondria can, in turn, generate more ROS (Bai et al., 2017). In this study, we found that the effects of RSV on neurite outgrowth correlated with improved mitochondrial function, as indicated by elevated MMP and ATP levels, as well as decreased ROS generation. These results suggest that mitochondrial function may be, at least in part, involved in RSV-induced neurite outgrowth.

Mitochondrial biogenesis is a highly regulated process, which occurs continuously in healthy cells and is crucial for cellular adaptation (Nikoletopoulou and Tavernarakis, 2014). Recent evidence has suggested a subtle link between mitochondrial biogenesis and neurological disorders (Mandemakers et al., 2007). Mitochondrial biogenesis has been found to counteract the detrimental effects of oxidative stress and has been suggested as a novel target of the repair mechanism (Cheng et al., 2010; Habash et al., 2015). *In vitro* studies have also suggested that impaired biogenesis contributes to the reduction of mitochondrial function after cerebral ischemia (Wang et al., 2014); however, its enhancement may reduce ischemic brain injury (Valerio et al., 2011). Although previous studies have indicated that RSV might impair mitochondrial function and biogenesis (Broniarek and Jarmuszkiewicz, 2016), our results show that RSV treatment restores the OGD-induced mtDNA loss in cortical neurons. TFAM and NRF-1 play an important role in the initiation of mtDNA replication and the transcription of mitochondrial encoded genes (Campbell et al., 2012). Therefore, we measured the mRNA levels of TFAM and NRF-1 in neurons exposed to OGD and treated with or without RSV. Our results revealed that RSV treatment significantly increased the mRNA levels of these factors. Collectively, our findings indicate that the RSV-induced neurite outgrowth against OGD exposure can be partially explained by the improved mitochondrial function and their enhanced biogenesis. Recent studies have provided convincing evidence that RSV exerts its protective effect by decreasing ROS levels, inhibiting the opening of the mitochondrial permeability transition pore, and promoting mitochondrial biogenesis (Corsetti et al., 2014; Liu et al., 2017). Nonetheless, further studies will be required to determine the exact mechanism of RSV effects on mitochondria.

The Notch pathway plays a vital role in the regulation of cell proliferation, self-renewal and differentiation, and is involved in several disorders of the central nervous system (Lundqvist et al., 2013). A previous study suggested that this pathway could regulate neurite outgrowth (Sestan et al., 1999; Levy et al., 2002). It also has been reported that Notch1 influences neurite morphology, and can activate its native signal transduction pathway in postmitotic neurons. Beyond neurogenesis, Notch1 plays a physiologically vital role in the central nervous system (Berezovska et al., 1999). In two recent studies, using M1 macrophages or cell lines *in vitro*, the Notch1 pathway was shown to enhance mtDNA transcription, ATP levels, and mitochondrial function (Basak et al., 2014; Xu et al., 2015). In addition, two statins, namely atorvastatin and simvastatin, have been shown to exert their effects, following stroke, through Notch signaling; the first, by increasing cell proliferation in the subventricular zone (Chen et al., 2008) and the second, by promoting arteriogenesis (Zacharek et al., 2009). Thus, we hypothesized that the Notch1 pathway was implicated in the regulation of RSV-induced mitochondrial biogenesis and function in cortical neurons. Our results show that, under OGD conditions, Notch1 signaling is active in primary cortical neurons and that its inhibition reverses the positive effects of RSV treatment on mitochondrial biogenesis and function. These results suggest that this pathway may, at least partially, contribute to the RSV-induced mitochondrial function and biogenesis in cortical neurons *in vitro*, which may represent a potent therapeutic strategy to promote brain plasticity after ischemic injury.

CONCLUSION

The present study has demonstrated that RSV promotes neurite outgrowth in primary cortical neurons, thus shielding them against OGD. RSV seems to be vital in preserving mitochondrial function and improving mitochondrial biogenesis and these effects are, at least in part, mediated by the Notch1 pathway. These findings highlight Notch1 signaling and mitochondria as important players and novel therapeutic targets in promoting brain plasticity.

AUTHOR CONTRIBUTIONS

WH and XT: study concept design and drafting of the manuscript. WH: collection of data. YL and XT: analysis and interpretation of data. All authors approved the final version of the manuscript.

SUPPLEMENTARY MATERIAL

The Supplementary Material for this article can be found online at: https://www.frontiersin.org/articles/10.3389/fncel.2018.00006/full#supplementary-material

FIGURE S1 | Effect of DAPT-only treatment on neurite outgrowth in primary cultured cortical neurons under oxygen-glucose deprivation (OGD). **(A)** Quantitative data of the longest neurite length of cultured cortical neurons. Results were presented as mean ± SEM. ns, non-significant, $n = 60$ per condition. **(B)** Quantitative data of total neurite length per cell. Results were presented as mean ± SEM. ns, non-significant, $n = 60$ per condition.

FIGURE S2 | Effect of DAPT-only treatment on mitochondrial function and ATP levels in cortical neurons exposed to OGD. **(A)** Mitochondrial membrane potential (MMP) was determined using JC-1 assay kit in different groups (OGD group, and DAPT group). Results were expressed as the mean ± SEM. ns, non-significant, $n = 6$ per condition. **(B)** The generation of ROS in different groups (OGD group and DAPT group). Results were expressed as the mean ± SEM. ns, non-significant, $n = 6$ per condition. **(C)** The ATP levels were measured in different groups (OGD group, and DAPT group). Results were expressed as the mean ± SEM. ns, non-significant, $n = 6$ per condition.

FIGURE S3 | Effect of DAPT-only treatment on mitochondrial biogenesis in cortical neurons exposed to OGD. **(A)** The mitochondrial DNA (mtDNA) content was measured. Results were expressed as the mean ± SEM. ns, non-significant, $n = 6$ per group. The expression of mitochondrial transcription factor A (TFAM; **B**), and nuclear respiratory factor 1 (NRF-1; **C**) at mRNA levels was measured by Quantitative Real-Time PCR. Data are shown as mean ± SEM. ns, non-significant, $n = 6$ per condition.

REFERENCES

Anne Stetler, R., Leak, R. K., Gao, Y., and Chen, J. (2013). The dynamics of the mitochondrial organelle as a potential therapeutic target. *J. Cereb. Blood Flow Metab.* 33, 22–32. doi: 10.1038/jcbfm.2012.158

Artavanis-Tsakonas, S., Rand, M. D., and Lake, R. J. (1999). Notch signaling: cell fate control and signal integration in development. *Science* 284, 770–776. doi: 10.1126/science.284.5415.770

Asahi, M., Huang, Z., Thomas, S., Yoshimura, S., Sumii, T., Mori, T., et al. (2005). Protective effects of statins involving both eNOS and tPA in focal cerebral ischemia. *J. Cereb. Blood Flow Metab.* 25, 722–729. doi: 10.1038/sj.jcbfm.9600070

Bai, F., Guo, F., Jiang, T., Wei, H., Zhou, H., Yin, H., et al. (2017). Arachidonyl-2-chloroethylamide alleviates cerebral ischemia injury through glycogen synthase kinase-3β-mediated mitochondrial biogenesis and functional improvement. *Mol. Neurobiol.* 54, 1240–1253. doi: 10.1007/s12035-016-9731-7

Basak, N. P., Roy, A., and Banerjee, S. (2014). Alteration of mitochondrial proteome due to activation of Notch1 signaling pathway. *J. Biol. Chem.* 289, 7320–7334. doi: 10.1074/jbc.M113.519405

Berezovska, O., McLean, P., Knowles, R., Frosh, M., Lu, F. M., Lux, S. E., et al. (1999). Notch1 inhibits neurite outgrowth in postmitotic primary neurons. *Neuroscience* 93, 433–439. doi: 10.1016/s0306-4522(99)00157-8

Bi, P., and Kuang, S. (2015). Notch signaling as a novel regulator of metabolism. *Trends Endocrinol. Metab.* 26, 248–255. doi: 10.1016/j.tem.2015.02.006

Bösel, J., Gandor, F., Harms, C., Synowitz, M., Harms, U., Djoufack, P. C., et al. (2005). Neuroprotective effects of atorvastatin against glutamate-induced excitotoxicity in primary cortical neurones. *J. Neurochem.* 92, 1386–1398. doi: 10.1111/j.1471-4159.2004.02980.x

Broniarek, I., and Jarmuszkiewicz, W. (2016). Statins and mitochondria. *Postepy Biochem.* 62, 77–84.

Campbell, C. T., Kolesar, J. E., and Kaufman, B. A. (2012). Mitochondrial transcription factor A regulates mitochondrial transcription initiation, DNA packaging, and genome copy number. *Biochim. Biophys. Acta* 1819, 921–929. doi: 10.1016/j.bbagrm.2012.03.002

Chen, J., Zacharek, A., Li, A., Cui, X., Roberts, C., Lu, M., et al. (2008). Atorvastatin promotes presenilin-1 expression and Notch1 activity and increases neural progenitor cell proliferation after stroke. *Stroke* 39, 220–226. doi: 10.1161/STROKEAHA.107.490946

Cheng, A., Hou, Y., and Mattson, M. P. (2010). Mitochondria and neuroplasticity. *ASN Neuro* 2:e00045. doi: 10.1042/AN20100019

Corsetti, G., D'Antona, G., Ruocco, C., Stacchiotti, A., Romano, C., Tedesco, L., et al. (2014). Dietary supplementation with essential amino acids boosts the beneficial effects of rosuvastatin on mouse kidney. *Amino Acids* 46, 2189–2203. doi: 10.1007/s00726-014-1772-5

Dai, S. H., Chen, T., Wang, Y. H., Zhu, J., Luo, P., Rao, W., et al. (2014). Sirt3 protects cortical neurons against oxidative stress via regulating mitochondrial Ca^{2+} and mitochondrial biogenesis. *Int. J. Mol. Sci.* 15, 14591–14609. doi: 10.3390/ijms150814591

Gutsaeva, D. R., Carraway, M. S., Suliman, H. B., Demchenko, I. T., Shitara, H., Yonekawa, H., et al. (2008). Transient hypoxia stimulates mitochondrial biogenesis in brain subcortex by a neuronal nitric oxide synthase-dependent mechanism. *J. Neurosci.* 28, 2015–2024. doi: 10.1523/JNEUROSCI.5654-07.2008

Habash, T., Saleh, A., Roy Chowdhury, S. K., Smith, D. R., and Fernyhough, P. (2015). The proinflammatory cytokine, interleukin-17A, augments mitochondrial function and neurite outgrowth of cultured adult sensory neurons derived from normal and diabetic rats. *Exp. Neurol.* 273, 177–189. doi: 10.1016/j.expneurol.2015.08.016

He, W., Cui, L., Zhang, C., Zhang, X., He, J., and Xie, Y. (2016). Sonic Hedgehog promotes neurite outgrowth of primary cortical neurons through up-regulating BDNF expression. *Neurochem. Res.* 41, 687–695. doi: 10.1007/s11064-015-1736-5

He, W., Cui, L., Zhang, C., Zhang, X., He, J., Xie, Y., et al. (2017). Sonic hedgehog promotes neurite outgrowth of cortical neurons under oxidative stress: involving of mitochondria and energy metabolism. *Exp. Cell Res.* 350, 83–90. doi: 10.1016/j.yexcr.2016.11.008

Jin, Y., Sui, H. J., Dong, Y., Ding, Q., Qu, W. H., Yu, S. X., et al. (2012). Atorvastatin enhances neurite outgrowth in cortical neurons *in vitro* via up-regulating the Akt/mTOR and Akt/GSK-3β signaling pathways. *Acta Pharmacol. Sin.* 33, 861–872. doi: 10.1038/aps.2012.59

Kageyama, R., Ohtsuka, T., and Kobayashi, T. (2007). The Hes gene family: repressors and oscillators that orchestrate embryogenesis. *Development* 134, 1243–1251. doi: 10.1242/dev.000786

Kahveci, R., Gökçe, E. C., Gürer, B., Gökçe, A., Kisa, U., Cemil, D. B., et al. (2014). Neuroprotective effects of rosuvastatin against traumatic spinal cord injury in rats. *Eur. J. Pharmacol.* 741, 45–54. doi: 10.1016/j.ejphar.2014.07.042

Kasahara, A., Cipolat, S., Chen, Y., Dorn, G. W. II., and Scorrano, L. (2013). Mitochondrial fusion directs cardiomyocyte differentiation via calcineurin and Notch signaling. *Science* 342, 734–737. doi: 10.1126/science.1241359

Kitamura, T., Saitoh, Y., Takashima, N., Murayama, A., Niibori, Y., Ageta, H., et al. (2009). Adult neurogenesis modulates the hippocampus-dependent period of associative fear memory. *Cell* 139, 814–827. doi: 10.1016/j.cell.2009.10.020

Levy, O. A., Lah, J. J., and Levey, A. I. (2002). Notch signaling inhibits PC12 cell neurite outgrowth via RBP-J-dependent and -independent mechanisms. *Dev. Neurosci.* 24, 79–88. doi: 10.1159/000064948

Lin, M. Y., and Sheng, Z. H. (2015). Regulation of mitochondrial transport in neurons. *Exp. Cell Res.* 334, 35–44. doi: 10.1016/j.yexcr.2015.01.004

Liu, C. W., Yang, F., Cheng, S. Z., Liu, Y., Wan, L. H., and Cong, H. L. (2017). Rosuvastatn postconditoning protects isolated hearts against ischemia-reperfusion injury: the role of radical oxygen species, PI3K-Akt-GSK-3β pathway, and mitochondrial permeability transiton pore. *Cardiovasc. Ther.* 35, 3–9. doi: 10.1111/1755-5922.12225

Lundqvist, J., El Andaloussi-Lilja, J., Svensson, C., Gustafsson Dorfh, H., and Forsby, A. (2013). Optimisation of culture conditions for differentiation of C17.2 neural stem cells to be used for *in vitro* toxicity tests. *Toxicol. In Vitro* 27, 1565–1569. doi: 10.1016/j.tiv.2012.04.020

Mandemakers, W., Morais, V. A., and De Strooper, B. (2007). A cell biological perspective on mitochondrial dysfunction in Parkinson disease and other neurodegenerative diseases. *J. Cell Sci.* 120, 1707–1716. doi: 10.1242/jcs.03443

Mattson, M. P. (2007). Mitochondrial regulation of neuronal plasticity. *Neurochem. Res.* 32, 707–715. doi: 10.1007/s11064-006-9170-3

Mattson, M. P., and Partin, J. (1999). Evidence for mitochondrial control of neuronal polarity. *J. Neurosci. Res.* 56, 8–20. doi: 10.1002/(sici)1097-4547(19990401)56:1<8::aid-jnr2>3.0.co;2-g

McLeod, C. J., Pagel, I., and Sack, M. N. (2005). The mitochondrial biogenesis regulatory program in cardiac adaptation to ischemia—a putative target for therapeutic intervention. *Trends Cardiovasc. Med.* 15, 118–123. doi: 10.1016/j.tcm.2005.05.001

Métais, C., Hughes, B., and Herron, C. E. (2015). Simvastatin increases excitability in the hippocampus via a PI3 kinase-dependent mechanism. *Neuroscience* 291, 279–288. doi: 10.1016/j.neuroscience.2015.02.023

Nikoletopoulou, V., and Tavernarakis, N. (2014). Mitochondrial biogenesis and dynamics in neurodegeneration, a causative relationship. *Neurochem. Res.* 39, 542–545. doi: 10.1007/s11064-013-0997-0

Onyango, I. G., Lu, J., Rodova, M., Lezi, E., Crafter, A. B., and Swerdlow, R. H. (2011). Regulation of neuron mitochondrial biogenesis and relevance to brain health. *Biochim. Biophys. Acta* 1802, 228–234. doi: 10.1016/j.bbadis.2009.07.014

Rader, D. J. (2003). Therapy to reduce risk of coronary heart disease. *Clin. Cardiol.* 26, 2–8. doi: 10.1002/clc.4960260103

Rousset, C. I., Leiper, F. C., Kichev, A., Gressens, P., Carling, D., Hagberg, H., et al. (2015). A dual role for AMP-activated protein kinase (AMPK) during neonatal hypoxic-ischaemic brain injury in mice. *J. Neurochem.* 133, 242–252. doi: 10.1111/jnc.13034

Savoia, C., Sisalli, M. J., Di Renzo, G., Annunziato, L., and Scorziello, A. (2011). Rosuvastatin-induced neuroprotection in cortical neurons exposed to OGD/reoxygenation is due to nitric oxide inhibition and ERK1/2 pathway activation. *Int. J. Physiol. Pathophysiol. Pharmacol.* 3, 57–64.

Sbert-Roig, M., Bauzá-Thorbrügge, M., Galmés-Pascual, B. M., Capllonch-Amer, G., García-Palmer, F. J., Lladó, I., et al. (2016). GPER mediates the effects of 17β-estradiol in cardiac mitochondrial biogenesis and function. *Mol. Cell. Endocrinol.* 420, 116–124. doi: 10.1016/j.mce.2015.11.027

Sestan, N., Artavanis-Tsakonas, S., and Rakic, P. (1999). Contact-dependent inhibition of cortical neurite growth mediated by notch signaling. *Science* 286, 741–746. doi: 10.1126/science.286.5440.741

Stein, E. A. (2002). Management of dyslipidemia in the high-risk patient. *Am. Heart J.* 144, S43–S50. doi: 10.1067/mhj.2002.130302

Thampy, A., and Pais, C. C. (2016). Early clinical implications of microalbuminuria in patients with acute ischaemic stroke. *J. Clin. Diagn. Res.* 10, OC29–OC31. doi: 10.7860/jcdr/2016/19690.8533

Tian, X., He, W., Yang, R., and Liu, Y. (2017). Dl-3-n-butylphthalide protects the heart against ischemic injury and H9c2 cardiomyoblasts against oxidative stress: involvement of mitochondrial function and biogenesis. *J. Biomed. Sci.* 24:38. doi: 10.1186/s12929-017-0345-9

Valerio, A., Bertolotti, P., Delbarba, A., Perego, C., Dossena, M., Ragni, M., et al. (2011). Glycogen synthase kinase-3 inhibition reduces ischemic cerebral damage, restores impaired mitochondrial biogenesis and prevents ROS production. *J. Neurochem.* 116, 1148–1159. doi: 10.1111/j.1471-4159.2011.07171.x

Wang, L., Chen, M., Yuan, L., Xiang, Y., Zheng, R., and Zhu, S. (2014). 14,15-EET promotes mitochondrial biogenesis and protects cortical neurons against oxygen/glucose deprivation-induced apoptosis. *Biochem. Biophys. Res. Commun.* 450, 604–609. doi: 10.1016/j.bbrc.2014.06.022

Xu, J., Chi, F., Guo, T., Punj, V., Lee, W. N., French, S. W., et al. (2015). Notch reprograms mitochondrial metabolism for proinflammatory macrophage activation. *J. Clin. Invest.* 125, 1579–1590. doi: 10.1172/JCI76468

Yavuz, C., Demirtas, S., Guclu, O., Karahan, O., Caliskan, A., Yazici, S., et al. (2013). Rosuvastatin may have neuroprotective effect on spinal cord ischemia reperfusion injury. *CNS Neurol. Disord. Drug Targets* 12, 1011–1016. doi: 10.2174/18715273113129990085

Zacharek, A., Chen, J., Cui, X., Yang, Y., and Chopp, M. (2009). Simvastatin increases notch signaling activity and promotes arteriogenesis after stroke. *Stroke* 40, 254–260. doi: 10.1161/STROKEAHA.108.524116

Conflict of Interest Statement: The authors declare that the research was conducted in the absence of any commercial or financial relationships that could be construed as a potential conflict of interest.

frontiers in Cellular Neuroscience

PROTOCOLS
published: 07 February 2018
doi: 10.3389/fncel.2018.00030

Procedure for the Isolation of Endothelial Cells from Human Cerebral Arteriovenous Malformation (cAVM) Tissues

*Qiang Hao[1,2], Xiao-Lin Chen[1], Li Ma[1], Tong-Tong Wang[3], Yue Hu[3] and Yuan-Li Zhao[1,3,4,5,6]**

[1] Department of Neurosurgery, Beijing Tiantan Hospital, Capital Medical University, Beijing, China, [2] Department of Neurosurgery, Peking University International Hospital, Peking University, Beijing, China, [3] Basic Medical Science Department, Capital Medical University, Beijing, China, [4] China National Clinical Research Center for Neurological Diseases, Beijing, China, [5] Stroke Center, Beijing Institute for Brain Disorders, Beijing, China, [6] Beijing Key Laboratory of Translational Medicine for Cerebrovascular Disease, Beijing, China

In this study, we successfully established a stable method for the isolation of endothelial cells (ECs) from human cerebral arteriovenous malformation (cAVM) tissues. Despite human cAVM tissues having a minor population of ECs, they play an important role in the manifestation and development of cAVM as well as in hemorrhagic stroke and thrombogenesis. To characterize and understand the biology of ECs in human cAVM (cAVM-ECs), methods for the isolation and purification of these cells are necessary. We have developed this method to reliably obtain pure populations of ECs from cAVMs. To obtain pure cell populations, cAVM tissues were mechanically and enzymatically digested and the resulting single cAVM-ECs suspensions were then labeled with antibodies of specific cell antigens and selected by flow cytometry. Purified ECs were detected using specific makers of ECs by immunostaining and used to study different cellular mechanisms. Compared to the different methods of isolating ECs from tissues, we could isolate ECs from cAVMs confidently, and the numbers of cAVM-ECs harvested were almost similar to the amounts present in vessel components. In addition to optimizing the protocol for isolation of ECs from human cAVM tissues, the protocol could also be applied to isolate ECs from other human neurovascular-diseased tissues. Depending on the tissues, the whole procedure could be completed in about 20 days.

Keywords: endothelial cells, cerebral arteriovenous malformation, isolation approach, purification, angiogenesis, *in vitro* culture

OPEN ACCESS

Edited by:
Sriharsha Kantamneni, University of Bradford, United Kingdom

Reviewed by:
Fabien Gosselet, Artois University, France
Alla B. Salmina, Krasnoyarsk State Medical University named after Prof. V.F.Voino-Yasenetski, Russia

****Correspondence:***
Yuan-Li Zhao
zhaoyuanli@126.com

Received: *01 November 2017*
Accepted: *24 January 2018*
Published: *07 February 2018*

Citation:
Hao Q, Chen X-L, Ma L, Wang T-T, Hu Y and Zhao Y-L (2018) Procedure for the Isolation of Endothelial Cells from Human Cerebral Arteriovenous Malformation (cAVM) Tissues. Front. Cell. Neurosci. 12:30. doi: 10.3389/fncel.2018.00030

INTRODUCTION

Cerebral arteriovenous malformations (cAVMs) are vascular lesions characterized by abnormal arteries and venous entanglement, which divert blood directly from the arteries to the venous circulation, instead of capillaries. cAVMs are rare and occur sporadically, which may be associated with genetic disorders (Consoli et al., 2013; Novakovic et al., 2013; Gross and Du, 2014; Young et al., 2015; **Figure 1**). The pathogenic mechanisms underlying cAVMs development are unknown. Currently, highly invasive procedures are the main medical treatment options for this vascular disease. However, the surgical access to cAVMs nidus can result in serious damage to adjacent brain areas and irreversible loss of neurological function. Therefore, alternative therapeutic strategies, which are safer and more efficient, are essential (Ferreira et al., 2014).

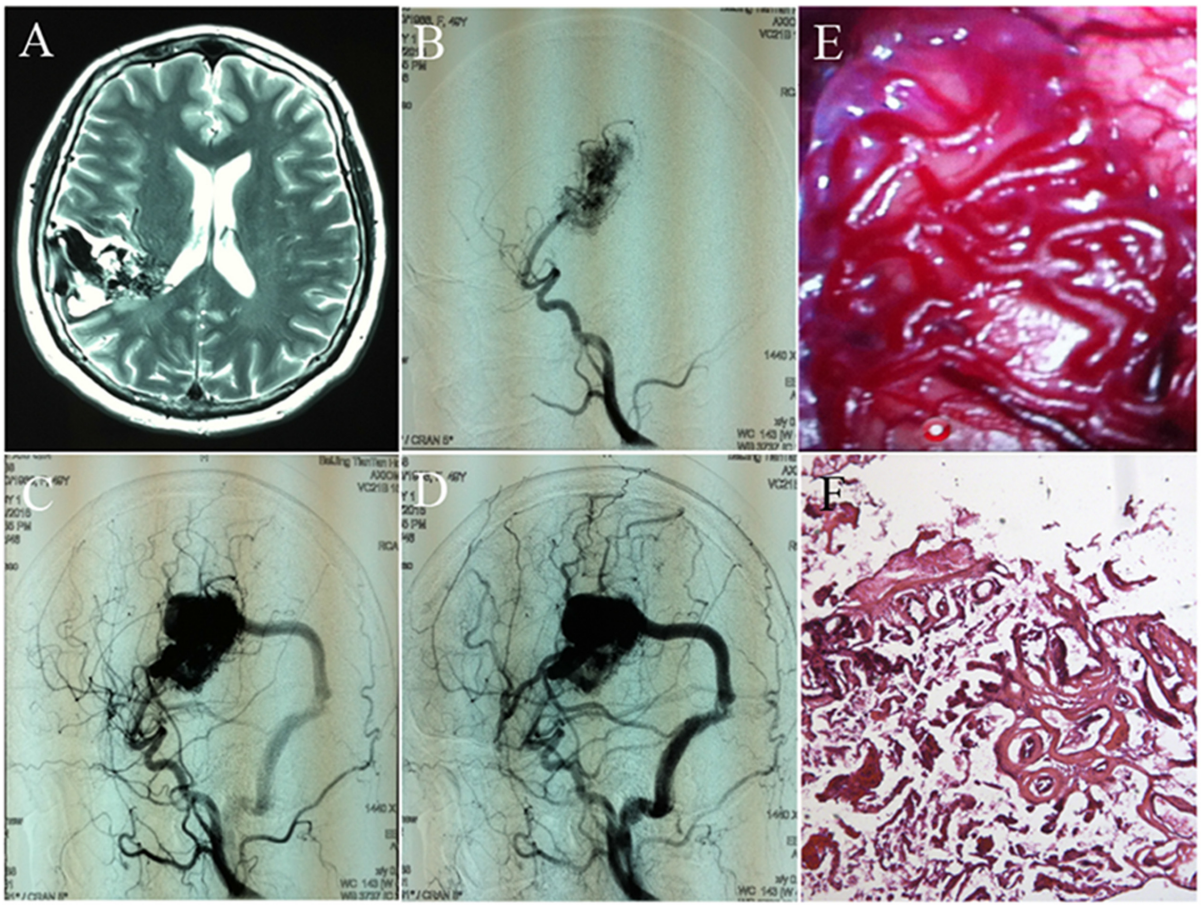

FIGURE 1 | Images and histology of cerebral arteriovenous malformation (cAVM). **(A)** T2WI of MRI imaging; **(B–D)** digital subtraction angiography (DSA) showed cerebral middle artery as the feeder artery provided blood to the cAVM nidus, which connected to the sigmoid sinus through a thick draining vessel; **(E)** morphology of cAVM viewed under the operational microscope; **(F)** photomicrograph of cAVM with deformed vascular walls from the nidus of the AVM. It had numerous collagen fibers, lacked smooth muscle and elastic fibers with incomplete wall demarcations.

Angiogenesis is the development of new blood vessels, and is a feature in different pathologies, such as atherosclerosis, cancer, arthritis, and particularly vascular diseases (Folkman, 1995; Griffioen and Molema, 2000). To understand the manifestations of these vascular diseases, a proper understanding of ECs biology is necessary. Hence, a method to isolate and purify ECs from cAVM tissues is essential.

Endothelial cells express a number of specific cell surface markers, including CD31, CD34, and von Willebrand factor (vWF), which have been used to isolate, purify and identify ECs in complex cell populations (Rakocevic et al., 2017). Using this method, isolation of ECs from cAVM (cAVM-ECs) tissues was carried out by creating a single-cell suspension of cAVMs through mechanical and biological digestion. These single-cell suspensions were then labeled with antibodies and isolated and purified through FACS (**Figures 2**, **3**). The purified cAVM-ECs could be used for different downstream applications, i.e., molecular profiling, genomic analysis, micro RNA analysis, proteomics, as well as for tissue engineering (Levenberg et al., 2010).

AVM-ECs Isolation and Culture

Endothelial cells accounts for about 1–2% of the total cells in cAVMs. They are located in the inner vessel cavity and surrounded by numerous cell types (Griffioen and Molema, 2000). Thus, ECs need to be purified before they can be used for further study. There are numerous methods for the isolation of ECs from the human brain (Baev and Awad, 1998; Bernas et al., 2010; Navone et al., 2013; Zhang et al., 2013). However, we compared the different methods, and found: (1) based on Professor Zhang' protocol, we could not harvest ECs from cAVMs reproducibly, and were only successful for 2 out of the 10 specimens; (2) we injected 0.25% Trypsin-EDTA into the cAVM nidus using a 1 ml injection syringe to digest the ECs, but the cells harvested were fibroblast-like cells and no ECs were found; (3) using the method established by us, we were able to confidently isolate ECs from cAVMs and passage them for 3–4 generations stably. These procedures included mincing and digestion, filtration, manual weeding, immunostaining, and isopycnic centrifugation of primary cultures or immortalized ECs.

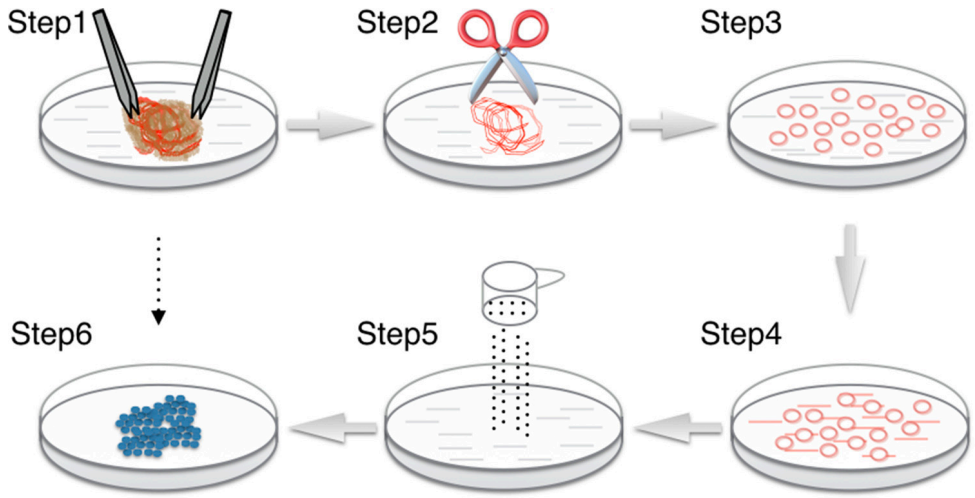

FIGURE 2 | Procedure for cAVM-EC isolation from cAVM lesioned tissues. (Step 1) Separate brain tissue from surrounding vessels; (Steps 2–4) AVMs were cut into small cubes and digested using 0.25% Trypsin-EDTA; (Step 5) filter cells; (Step 6) incubated cells for 7–14 days until colonies appeared.

Experimental Protocol

We exploited previously published methods for the isolation and passaging of ECs from normal human cerebral tissues and neurovascular tissues (Baev and Awad, 1998; Bernas et al., 2010; Navone et al., 2013; Zhang et al., 2013). This protocol used endothelial cell medium (ECM, ScienCell, United States), which could facilitate ECs to adhere to surfaces coated by collagen type I and result in a certain proportion of ECs adhering, compared to other cell types from cAVMs. The isolated cAVM-ECs were viable and could proliferate for an extended period. Even when cultured for more than 20 days *in vitro*, cAVM-ECs maintained their endothelial features and did not undergo fibroblast *trans*-differentiation. In addition, cAVM-ECs maintained high viability and were similar to thawed and cultured cryopreserved ECs.

Characterization of Isolated cAVM-ECs

After following our isolation and purification protocol, we verified the purity of the ECs. Specific endothelial cell markers were available to identify cells of endothelial origin, like vWF, CD31, and CD34 (van Beijnum et al., 2008; Rakocevic et al., 2017). Primary ECs were sorted by FACS for CD31 positive expression. The proportion of cAVM-ECs was estimated to be around (1.53 ± 0.13)% (**Figure 4**). cAVM-ECs were sorted before they reached four passages in cell culture. Under a phase-contrast microscope, the isolated cAVM-ECs were observed to have a classic round border and cobblestone appearance in morphology and displayed a flat ellipse shape when confluent with each other (**Figures 5A–C**).

Immunostaining demonstrated that more than 90% of cAVM-ECs expressed the classic EC markers, CD31 (91.6 ± 2.86) and CD34 (91.2 ± 2.96) (**Figures 5D–I**, **6**). In addition, cAVM-ECs were immunostained with negative EC markers, i.e., GFAP for astrocytes, SMA for smooth-muscle cells, and Tuj1 for neurons; however, no positive cells were observed. These results demonstrated that almost all the cultured cAVM-ECs purified using our protocol maintained the typical EC phenotype. In addition, the specific markers for ECs, vWF was also used to identify the origin of the cAVM-ECs (**Figure 7**). The cultured cAVM-ECs were functional, with the demonstrable ability to absorb Dil-Ac-LDL and form tube structures in 3D matrigel culture conditions. We found that Dil-Ac-LDL (labeled with red fluorescence) was in the cytoplasm of cAVM-ECs (**Figure 8A**) and the capillaries formed net-like structures (**Figure 8B**). However, the morphology of the isolated cAVM-ECs was not stable, and began to change into spindle-like cells after four generations of doubling (**Figure 9**).

Utility of Human cAVM-ECs

Endothelial cells are useful tools to understand the biological characteristics of cerebral endothelium in conditions of neuroinflammatory, neurodegeneration, as well as neurovascular diseases. During vascular disease, ECs undergo cellular, morphogenetic, and phenotypic changes, accompanied with the appearance of angiogenic vasculature. Understanding EC dysfunction during cAVMs occurrence and development will be helpful to craft new therapies for the treatment of cAVMs.

The protocol we have established for isolating ECs from cAVMs can be also performed for other vascular diseases, such as cavernous hemangioma and aneurysm. For efficient EC isolation and purification, the vascular density level of CD31 expression and cAVM composition are important. This new and optimized method for isolating ECs will be useful for the study of cerebrovascular diseases.

MATERIALS

Reagents

0.25% Trypsin-EDTA (Gibco, Cat. No. 25200072, United States);

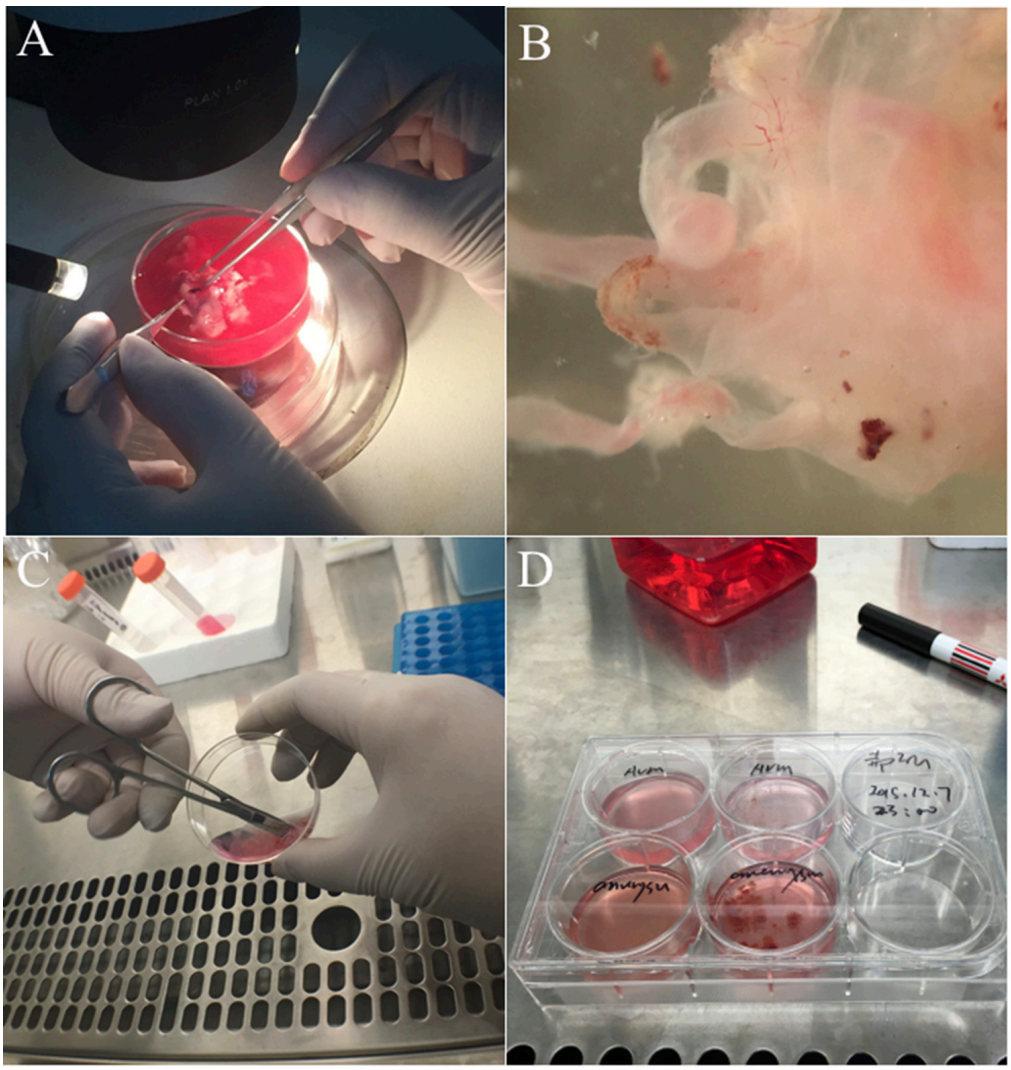

FIGURE 3 | Experimental procedure to isolate cAVM-ECs. **(A)** Original cAVM lesioned tissues were washed with Phosphate-buffered saline (PBS); **(B)** the disordered vessels in the cAVM nidus, showing thin and lucid vessel layers; **(C)** disordered vessels in the cAVM nidus were cut into small cubes and digested in Trypsin-EDTA; **(D)** The isolated cells were cultured in conditional medium.

FITC mouse anti-human CD31 antibody (BD, Cat. No. 557508, United States);
Rabbit polyclonal anti-CD31 (Abcam, Cat. No. Ab28364, United States);
Mouse monoclonal antibody of anti-CD34 (Abcam, Cat. No. Ab81289, United States);
Goat anti-vWF (Abcam, Cat. No. Ab 11713, United States);
Mouse anti-beta III Tubulin (Tuj1) (Abcam, Cat. No. Ab 78078, United States);
Rabbit anti-GFAP (Abcam, Cat. No. Ab 33922, United States);
Rabbit anti-alpha smooth-muscle Actin (α-SMA) (Abcam, Cat. No. Ab 5694, United States);
Donkey Anti-Rabbit IgG H&L (Alexa Fluor® 647) (Abcam, Cat. No. Ab150075, United States);
Goat Anti-Mouse IgG H&L (Alexa Fluor® 488) (Abcam, Cat. No. Ab150113, United States);
Donkey Anti-Goat IgG H&L (Alexa Fluor® 488) (Abcam, Cat. No. Ab150137, United States);
Vectashield mounting medium containing 4′, 6-diamidino-2-phenylindole (DAPI) (Vector Laboratories, Cat. No. H1200, United States);
Endothelial cell medium (ECM-NG, ScienCell, Cat. No. 1001NG, United States);
Fetal Bovine Serum (FBS, ScienCell, Cat. No. 0025, United States);
Penicillin / Streptomycin solution (P/S, ScienCell, Cat. No. 0503, United States);
Endothelial Cell Growth Supplement (ECGS, ScienCell, Cat. No. 1052, United States);
Phosphate-buffered saline (PBS) solution (Life Technologies, Cat No. 10010023, United States);
Bovine serum albumin (BSA, Jackson Immunoresearch Laboratories, Cat. No. BAH640050, United States);

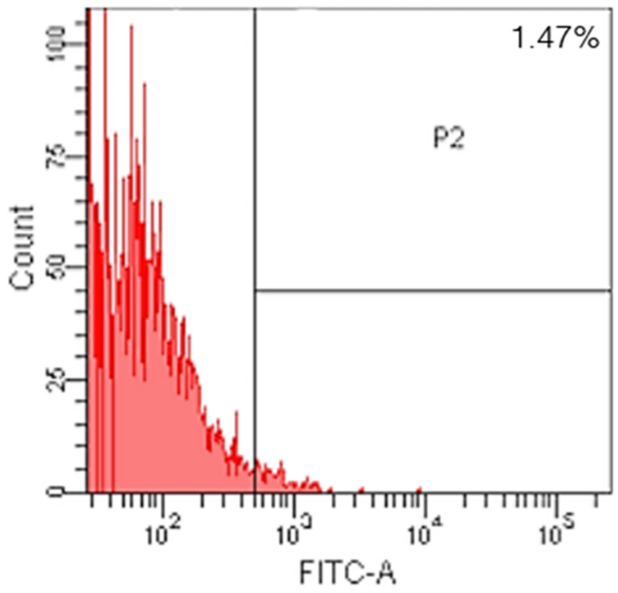

FIGURE 4 | Flow cytometry analysis of cAVM-ECs. Expression of CD31 in isolated human cAVM-ECs.

Dil-labeled acetylated LDL (Invitrogen, Cat No. L35353, United States);
Collagen type I (RD, Cat No. 3440-100-01, United States);
Heparin (Leo Pharma, Cat. No. 013192-02);
Cerebral AVM Tissues;
Matrigel (BD, Cat No. 354234, United States);
EC media;
FACS media;
LDL (Invitrogen, Cat No. L35353, United States)

Equipment

Centrifuge suitable for 15-ml and 1.7-ml tubes
FACS (Millipore);
Surgical blades;
Surgical scissor
Disposable Petri dishes;
50-ml Tubes (Corning, Cat. No. 431720, United States);
15-ml Tubes (Corning, Cat. No. 430052, United States);
1.7-ml Tubes (Corning, Cat. No. 3622, United States);
1-ml Syringes;
Cell strainers (BD, 70um, Cat. No. 352350, United States);
FACS tubes with caps;
Bovine Serum Albumin (BSA) (Solarbio, Cat. No. A8020, China);
Matrigel (Corning, Cat. No. 354248, United States);
PBS (pH7.4) (Life Technologies, Cat. No. 10010023, United States)

Reagent Setup

Patients and Tissues

Cerebral arteriovenous malformation samples were collected from eight patients who underwent surgical resection in the Department of Neurosurgery, Tian Tan Hospital, Beijing, China. Samples were collected between September 2015 and January 2016. Samples were collected from patients who had not previously received irradiation or embolization treatment. The Human Subject Review Committee of Tian Tan Hospital approved the experimental protocol. Tissue samples were collected immediately after surgical resection, which were placed in tubes with EC separation media and kept in the icebox for 6 h at most, before initiating the purification protocol.

Antibodies Used for Labeling and FACS

Titration of antibodies was crucial for isolating pure populations of cAVM-ECs. It was also recommended to titrate Ab that was EC-specific in the tissue of interest. We tested different titrations of Ab, and determined that 1:50 dilution of anti-CD31 was optimal for the isolation of cAVM-ECs. Human cAVM-ECs were sorted using FITC-labeled mouse anti-human CD31.

PBS/0.1%BSA
100 mg BSA was dissolved in 100 ml of PBS.

Collagen I (5 mg/ml)
100 mg Collagen I was dissolved in 20 mls of PBS.

Matrigel (80%wt/vol or 100%)
0.8 mg of Matrigel was dissolved in 0.2 ml EC culture medium.

EC Medium

Endothelial Cell Growth Supplement (ECGS, ScienCell, Cat. No. 1052, United States) was stored at −20°C. Once added to the media, it was stored at 4°C and protected from light. ECGS should be thawed only once and added to the media. ECGS was incubated at 37°C with occasional mixing until completely thawed before adding to the culture media in a BSC hood. The supplemented media should not be warmed using a 37°C water bath, and instead should be left to sit at room temperature protected from light before proceeding to cell culture. The reconstituted media was stable for 1 month.

FACS Medium

Cells were re-suspended in EC media supplemented with 0.1% BSA and were quickly sorted to prevent excessive cell death.

STEP-BY-STEP PROCEDURE FOR ISOLATING AND PURIFYING ECs FROM HUMAN CAVM SAMPLEs

Preparation of Human AVM Samples

wTime Required: 6 h

(1) Phosphate-buffered saline solution was prepared with heparin and stored on ice. After surgical removal of cAVMs, the samples were immediately immersed in PBS solution with heparin.

Critical Step

To avoid blood clotting and reduce injury to ECs, samples were placed in PBS supplemented with heparin, and addition of heparin also increased the efficiency of enzyme digestion. To maintain optimal viability, the samples should be processed within ∼6 h of surgical incision.

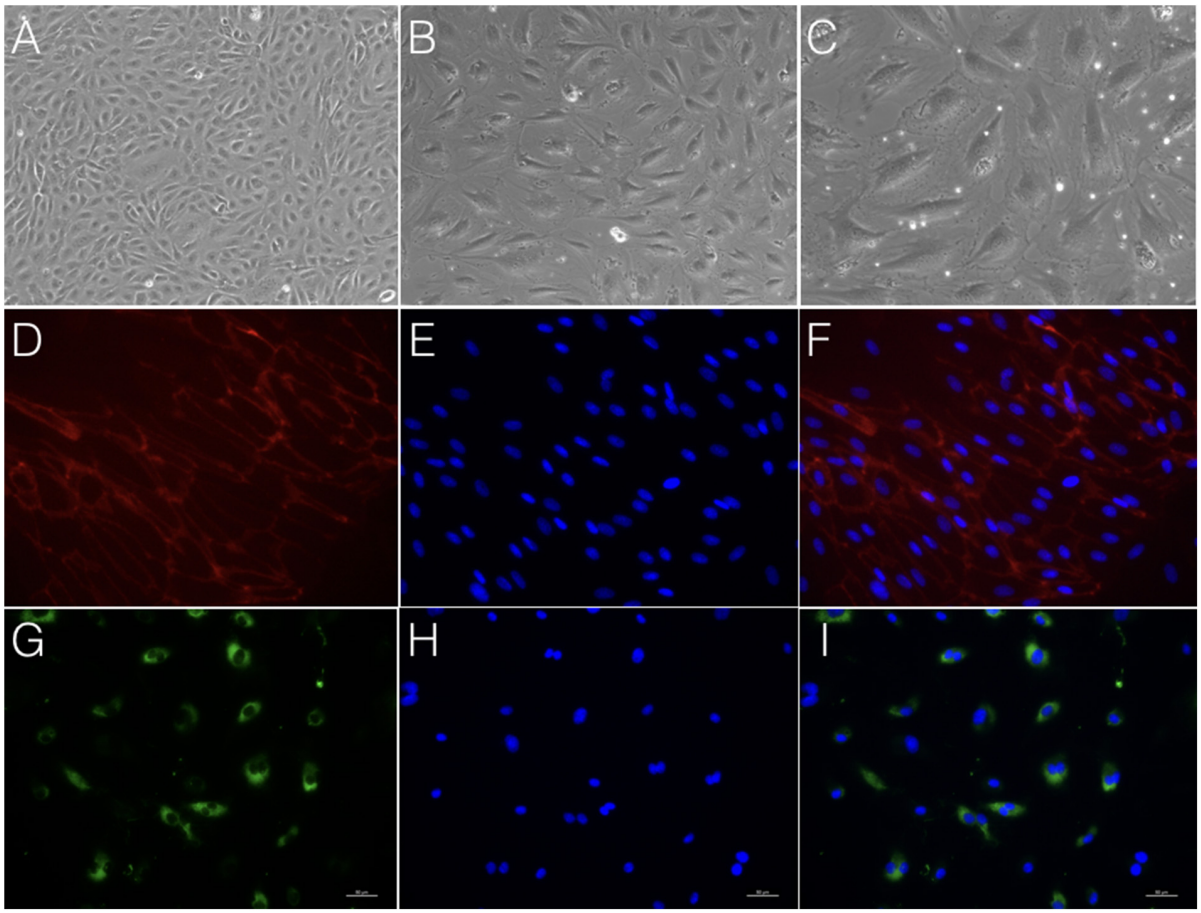

FIGURE 5 | Morphology and immunostaining of cAVM-ECs. **(A–C)** morphology of cAVM-ECs in different fields of view; **(A)** scale bar = 100 μm; **(B)** scale bar = 50 μm; **(C)** scale bar = 20 μm; **(D)** CD31 expression; **(E)** 4′, 6-diamidino-2-phenylindole (DAPI) staining; **(F)** Merge, scale bar = 50 μm; **(G)** CD34 expression; **(H)** DAPI staining; **(I)** Merge, scale bar = 50 μm.

Preparation of Single-Cell Suspensions for cAVM-ECs Isolation

wTime Required: 7–14 day

(2) Separated vasculature structures from human cAVM samples. cAVM samples contained abnormal vessels, surrounding brain tissues, blood cells, and some electro-coagulation materials. To remove unwanted cells, AVM nidus samples were soaked in PBS solution with heparin, and brain and surrounding tissues were separated under a micro-dissecting instrument. The electro-coagulation materials were removed in a similar manner. For the removal of intravascular blood cells, we injected PBS with heparin into the lumen using a 1-ml syringe, to exclude blood cells retained in the vessel's lumen (**Figures 2** Step 1, **3A,B**).

Critical Step

In order to avoid microbial contamination, the procedure should be carried out using sterile reagents and a laminar flow cabinet. The whole procedure was performed on ice.

(3) Cerebral arteriovenous malformations were cut into small cubes (**Figure 2** Step 2), and subsequently 0.25% Trypsin-EDTA was added. The tissues were further chopped and then incubated at 37°C with 5% CO_2 for 15 min (**Figures 2** Steps 3, 4, **3C,D**).

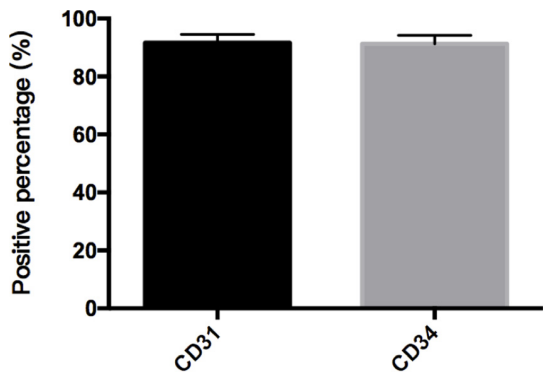

FIGURE 6 | Percent of CD31 and CD34 cells in cAVM-ECs. cAVM-ECs selected by FACS were immunostained for CD31 and CD34 antigens, respectively. The percent of CD31 positive cells was about (91.6 ± 2.86), and about (91.2 ± 2.96) for CD34.

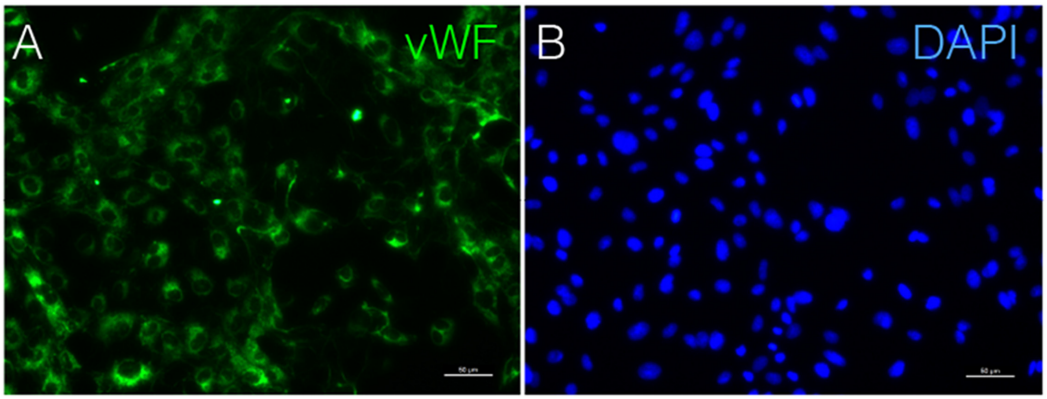

FIGURE 7 | Immunostaining of vWF in cAVM-ECs. **(A)** vWF expression; **(B)** DAPI staining, scale bar = 50 μm.

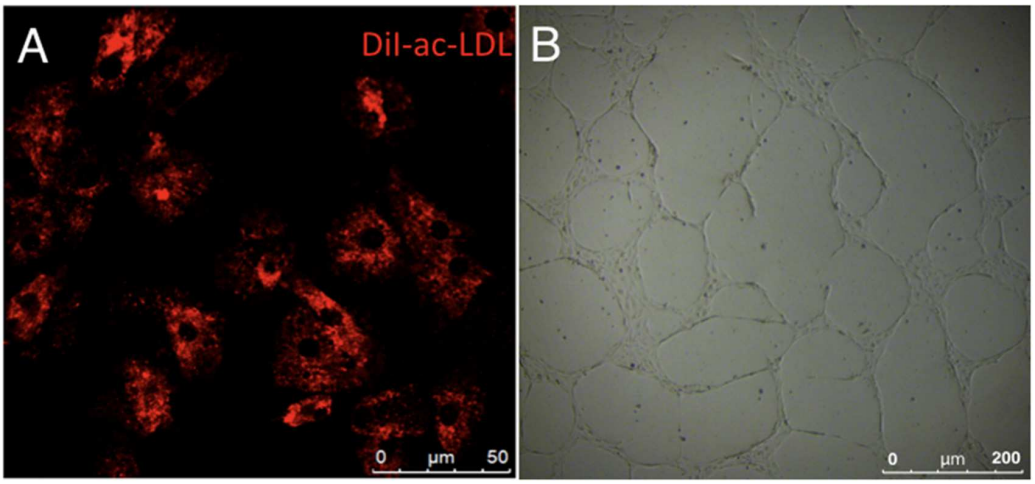

FIGURE 8 | Functional phenotypes of isolated human cAVM-ECs. **(A)** LDL uptake by human cAVM-ECs, scale bar = 50 μm; **(B)** Capillary tube-like structure formation by cAVM-ECs, scale bar = 200 μm.

Critical Step

Inefficient digestion of cAVMs with trypsin might cause cell clusters to not pass through cell filters and result in reduced cell yield. In order to avoid this, tissues should be gently pipetted up/down several times during the 15-min incubation.

(4) Neutralize Trypsin-EDTA with EC culture medium (please refer to solution 2:1). The digested cAVMs were then filtered twice using an additional 5 ml of EC culture media.

(5) The filtered cells were centrifuged at a speed of 1000 rpm for 5 min, then resuspended in EC culture media, and then centrifuged again. The cell pellets were then resuspended in fresh EC culture media (**Figure 2** Step 5).

(6) 6-well plates were coated with Collagen I (5 mg/ml). 2mls of Collagen I solution were added into wells and incubated under 37° C for 1 h. Then the Collagen I solution was removed and 6-well plates were washed three times with PBS. The cells were then seeded into 6-well plates. Large aggregates were removed from the culture media. The cells were incubated for 7–14 day until colonies were observed (**Figure 2** Step 6).

Critical Step

Collagen I could promote cell attachment and be reused three times at most.

EC Purification

wTime Required: 6 h

(7) cAVM-ECs were cultured in ECM and harvested after 7–14 days. The cells were washed three times with PBS, and digested by 0.25% Trypsin-EDTA. After 5–10 min digestion, the cells solution was added to ECM to neutralize Trypsin-EDTA. Then the cells solution was centrifuged at a speed of 1000 rpm for 5 min. cAVM-ECs were washed once with blocking buffer [1% BSA in 1× PBS with Calcium and Magnesium] and then suspended in blocking buffer to a density of 0.5×10^5 cells/ml at RT for 30 min. 1.0 μl of anti-human CD31 antibody (BD, Cat. No. 557508, United States) was then added to the cells and incubated for at least 30 min with gentle agitation. cAVM-ECs were kept protected from light and incubated on ice before being analyzed by FACS.

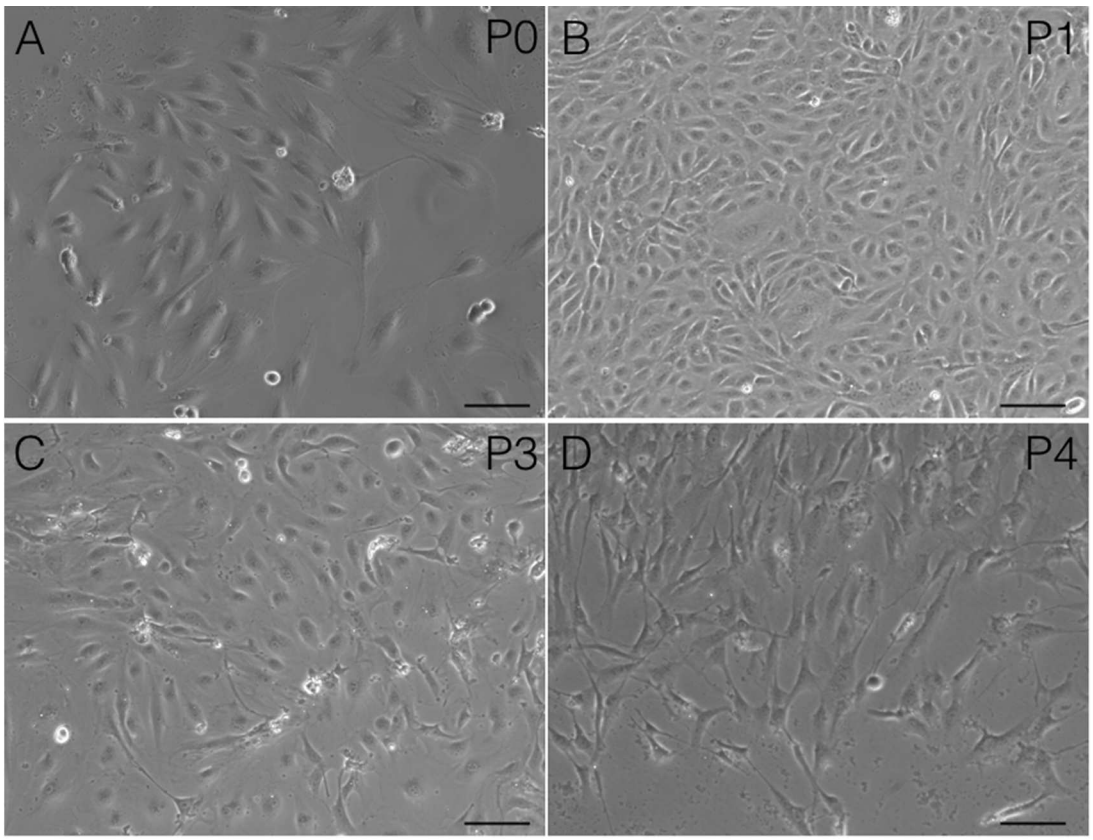

FIGURE 9 | Changes in cAVM-EC morphology when isolated and passaged. **(A)** morphology in P0; **(B)** morphology in P1; **(C)** morphology in P2; **(D)** morphology in P3. Scale bar = 50 μm

Critical Step

All procedures should be performed in the cell culture hood to maintain sterility. It was also recommended to perform anti-mycoplasma tests at the end of the protocol to be sure that the endothelial cells were mycoplasma free.

EC Immunocytochemistry

wTime Required: 20 h

(8) cAVM-ECs were fixed in 4% paraformaldehyde for 20 min at RT. Cells were then perforated permeabilized for 20 min using 0.3% Triton in PBS, and later washed three times with PBS, and subsequently blocked in 5% goat serum and incubated at 4°C with the following primary antibodies: Rabbit polyclonal anti-CD31 (1:200, Abcam, Cat No. Ab28364, United States), Mouse monoclonal antibody of anti-CD34 (1:100, Abcam, Cat No. Ab81289, United States), and Goat anti-Von Willebrand factor (vWF) (1:100, Abcam, Cat. No. Ab 11713, United States). The slides were then incubated with the appropriate secondary antibody, Donkey Anti-Rabbit IgG H&L (Alexa Fluor® 647) (1:200, Abcam, Cat No. Ab150075, United States), Goat Anti-Mouse IgG H&L (Alexa Fluor® 488) (1:200, Abcam, Cat No. Ab150113, United States), and Donkey Anti-Goat IgG H&L (Alexa Fluor® 488) (1:200, Abcam, Cat. No. Ab150137, United States) for 1 h. Immunostained cAVM-ECs were counted randomly using five microscope fields in a coverslip using a Nikon Eclipse inverted-fluorescence microscope.

EC DiI-Ac-LDL Uptake

wTime Required: 6 h

(9) The uptake of acetylated LDL served as a useful marker for identifying ECs. cAVM-ECs were incubated with DiI-labeled acetylated LDL (Invitrogen, Catalog No. L35353, United States) at RM for 4 h. Then cAVM-ECs were visualized and imaged using a Nikon Eclipse inverted-fluorescence microscope.

EC Capillary Tube-Like Structure Formation

wTime Required: 8 h

(10) To determine whether ECM-cultured cAVM-ECs retained angiogenic properties, cells were plated at a density of 0.4×10^5 onto surfaces coated with matrigel to detect formation of capillary tube-like structures. Reduced growth factor matrigel (BD, Cat No.354234, United States) was thawed at 4°C overnight in a refrigerator. 200 μl of matrigel was added into a 48-well plate, which was incubated at 37°C and under 5% CO_2 for 30 min. Then the cAVM-ECs were seeded into each well and cultured for 12 h.

Anticipated Results

Using the protocol we developed, isolated cAVM-ECs grew into separate colonies, with morphologies of round borders and cobblestone appearance. Observed under a microscope, cAVM-ECs showed flat and ellipse shape in morphology when confluent (**Figure 5**). After FACS, the proportion of cAVM-ECs was about 1.5% percentage of the total cell population (**Figure 4**). All primary ECs established from cAVMs were viable for a long period and expressed specific cell receptors, such as CD31, CD34, and vWF. In addition, AVM-ECs were with the demonstrable ability to absorb Dil-Ac-LDL and form tube structures in 3D matrigel culture conditions (**Figure 8**). These results demonstrated that cultured cAVM-ECs using our protocol were functional ECs, which had common cellular characteristics of ECs. The isolated cAVM-ECs should be used before four passages, because they would *trans*-differentiate into mesenchymal-like cells after four generations of doubling.

Statistical Analysis

All experimental data were presented as Mean ± SD, using GraphPad Prism 6 (United States).

ETHICS STATEMENT

This study was carried out in accordance with the recommendations of Bei Jing Tian Hospital of guidelines, Bei Jing Tian Tan Hospital of committee' with written informed consent from all subjects. All subjects gave written informed consent in accordance with the Declaration of Helsinki. The protocol was approved by the Bei Jing Tian Hospital of committee.

AUTHOR CONTRIBUTIONS

Y-LZ conceived and directed the project. QH designed the experiment and participated in the whole proceed, and wrote the manuscript. X-LC and LM participated in the discussion. T-TW and YH participated in the culture of cells.

FUNDING

This study was supported by grants (Nos. 81571110, 81271313, 81771234, and 81500995) to Y-LZ, from The National Natural Science Fund, China and Bai Qian Wan Talent Plan, 2017A07.

REFERENCES

Baev, N. I., and Awad, I. A. (1998). Endothelial cell culture from human cerebral cavernous malformations. *Stroke* 29, 2426–2434. doi: 10.1161/01.STR.29.11.2426

Bernas, M. J., Cardoso, F. L., Daley, S. K., Weinand, M. E., Campos, A. R., Ferreira, A. J., et al. (2010). Establishment of primary cultures of human brain microvascular endothelial cells to provide an *in vitro* cellular model of the blood-brain barrier. *Nat. Protoc.* 5, 1265–1272. doi: 10.1038/nprot.2010.76

Consoli, A., Renieri, L., Nappini, S., Limbucci, N., and Mangiafico, S. (2013). Endovascular treatment of deep hemorrhagic brain arteriovenous malformations with transvenous onyx embolization. *AJNR Am. J. Neuroradiol.* 34, 1805–1811. doi: 10.3174/ajnr.A3497

Ferreira, R., Santos, T., Amar, A., Tahara, S. M., Chen, T. C., Giannotta, S. L., et al. (2014). MicroRNA-18a improves human cerebral arteriovenous malformation endothelial cell function. *Stroke* 45, 293–297. doi: 10.1161/STROKEAHA.113.003578

Folkman, J. (1995). Angiogenesis in cancer, vascular, rheumatoid and other disease. *Nat. Med.* 1, 27–31. doi: 10.1038/nm0195-27

Griffioen, A. W., and Molema, G. (2000). Angiogenesis: potentials for pharmacologic intervention in the treatment of cancer, cardiovascular diseases, and chronic inflammation. *Pharmacol. Rev.* 52, 237–268.

Gross, B. A., and Du, R. (2014). Diagnosis and treatment of vascular malformations of the brain. *Curr. Treat. Options Neurol.* 16:279. doi: 10.1007/s11940-013-0279-9

Levenberg, S., Ferreira, L. S., Chen-Konak, L., Kraehenbuehl, T. P., and Langer, R. (2010). Isolation, differentiation and characterization of vascular cells derived from human embryonic stem cells. *Nat. Protoc.* 5, 1115–1126. doi: 10.1038/nprot.2010.31

Navone, S. E., Marfia, G., Invernici, G., Cristini, S., Nava, S., Balbi, S., et al. (2013). Isolation and expansion of human and mouse brain microvascular endothelial cells. *Nat. Protoc.* 8, 1680–1693. doi: 10.1038/nprot.2013.107

Novakovic, R. L., Lazzaro, M. A., Castonguay, A. C., and Zaidat, O. O. (2013). The diagnosis and management of brain arteriovenous malformations. *Neurol. Clin.* 31, 749–763. doi: 10.1016/j.ncl.2013.03.003

Rakocevic, J., Orlic, D., Mitrovic-Ajtic, O., Tomasevic, M., Dobric, M., Zlatic, N., et al. (2017). Endothelial cell markers from clinician's perspective. *Exp. Mol. Pathol.* 102, 303–313. doi: 10.1016/j.yexmp.2017.02.005

van Beijnum, J. R., van der Linden, E., and Griffioen, A. W. (2008). Angiogenic profiling and comparison of immortalized endothelial cells for functional genomics. *Exp. Cell Res.* 314, 264–272. doi: 10.1016/j.yexcr.2007.08.013

Young, A. M., Teo, M., Martin, S. C., Phang, I., Bhattacharya, J. J., and St George, E. J. (2015). The diagnosis and management of brain arteriovenous malformations in a single regional center. *World Neurosurg.* 84, 1621–1628. doi: 10.1016/j.wneu.2015.06.017

Zhang, H. F., Liang, G. B., Zhao, M. G., Song, Z. Q., and Xu, Z. H. (2013). An efficient and non-enzymatic method for isolation and culture of endothelial cells from the nidus of human cerebral arteriovenous malformations. *Neurosci. Lett.* 548, 21–26. doi: 10.1016/j.neulet.2013.05.050

Conflict of Interest Statement: The authors declare that the research was conducted in the absence of any commercial or financial relationships that could be construed as a potential conflict of interest.

frontiers in Cellular Neuroscience

ORIGINAL RESEARCH
published: 12 June 2018
doi: 10.3389/fncel.2018.00157

Adeno-Associated Viral Vector Serotype DJ-Mediated Overexpression of N171-82Q-Mutant Huntingtin in the Striatum of Juvenile Mice Is a New Model for Huntington's Disease

Minhee Jang[1], *Seung Eun Lee*[2] *and Ik-Hyun Cho*[1,3]*

[1]Department of Convergence Medical Science, College of Korean Medicine, Kyung Hee University, Seoul, South Korea, [2]Virus Facility, Research Animal Resource Center, Korea Institute of Science and Technology (KIST), Seoul, South Korea, [3]Brain Korea 21 Plus Program and Institute of Korean Medicine, College of Korean Medicine, Kyung Hee University, Seoul, South Korea

Huntington's disease (HD) is an autosomal-dominant inherited neurodegenerative disorder characterized by motor, psychiatric and cognitive symptoms. HD is caused by an expansion of CAG repeats in the huntingtin (*HTT*) gene in various areas of the brain including striatum. There are few suitable animal models to study the pathogenesis of HD and validate therapeutic strategies. Recombinant adeno-associated viral (AAV) vectors successfully transfer foreign genes to the brain of adult mammalians. In this article, we report a novel mouse model of HD generated by bilateral intrastriatal injection of AAV vector serotype DJ (AAV-DJ) containing N171-82Q mutant *HTT* (82Q) and N171-18Q wild type *HTT* (18Q; sham). The AAV-DJ-82Q model displayed motor dysfunctions in pole and rotarod tests beginning 4 weeks after viral infection in juvenile mice (8 weeks after birth). They showed behaviors reflecting neurodegeneration. They also showed increased apoptosis, robust glial activation and upregulated representative inflammatory cytokines (tumor necrosis factor-alpha (TNF-α) and interleukin (IL)-6), mediators (cyclooxygenase-2 and inducible nitric oxide synthase) and signaling pathways (nuclear factor kappa B and signal transducer and activator of transcription 3 (STAT3)) in the striatum at 10 weeks after viral infection (14 weeks after birth) via successful transfection of mutant *HTT* into neurons, microglia, and astrocytes in the striatum. However, little evidence of any of these events was found in mice infected with the AAV-DJ-18Q expressing construct. Intrastriatal injection of AAV-DJ-82Q might be useful as a novel *in vivo* model to investigate the biology of truncated N-terminal fragment (N171) in the striatum and to explore the efficacy of therapeutic strategies for HD.

Keywords: Huntington's disease, adeno-associated viral vector serotype DJ, mutant huntingtin, N171-82Q, polyglutamine expansion

OPEN ACCESS

Edited by:
Sikha Saha,
University of Leeds, United Kingdom

Reviewed by:
Michelle Gray,
University of Alabama at Birmingham, United States
Alba Di Pardo,
Centre for Neurogenetics and Rare Diseases, Italy

***Correspondence:**
Ik-Hyun Cho
ihcho@khu.ac.kr

Received: *18 December 2017*
Accepted: *18 May 2018*
Published: *12 June 2018*

Citation:
Jang M, Lee SE and Cho I-H (2018) Adeno-Associated Viral Vector Serotype DJ-Mediated Overexpression of N171-82Q-Mutant Huntingtin in the Striatum of Juvenile Mice Is a New Model for Huntington's Disease. Front. Cell. Neurosci. 12:157. doi: 10.3389/fncel.2018.00157

INTRODUCTION

Huntington's disease (HD) is an inherited progressive neurodegenerative disorder characterized by involuntary abnormal movements (chorea), cognitive decline and emotional as well as psychiatric disturbances (Damiano et al., 2010; Jacobsen et al., 2011; Gil-Mohapel et al., 2014). HD typically becomes apparent at 35–45 years of age and progresses toward death within 15–20 years after the

appearance of the first clinical symptoms (Ceccarelli et al., 2016). HD is caused by an abnormal expansion of a CAG codon ≥36 repeats located in exon one of the huntingtin gene (*HTT*) on chromosome 4 that confers a toxic function to the protein (Damiano et al., 2010; Jacobsen et al., 2011; Gil-Mohapel et al., 2014). The expansion encodes a prolonged polyglutamine sequence that results in conformational change of the *HTT* protein and induces the formation of intranuclear inclusions of mutant *HTT* in various areas of the brain. This mutation leads to neuronal loss and neuronal degeneration, most prominently in the striatum (Damiano et al., 2010; Jacobsen et al., 2011; Gil-Mohapel et al., 2014). On postmortem analysis, ubiquitinated intranuclear inclusions are observed, suggesting abnormal processing/folding of the polyglutamine domain in affected cells. However, the pathogenic mechanisms leading to neurodegeneration are unclear.

There is no established treatment to prevent or to delay the onset or forestall the progression of HD (Wyant et al., 2017). A critical aspect for drug discovery is the creation of *in vivo* models that recapitulating the genetic and molecular mechanisms underlying the neurodegenerative processes and that present symptoms of the HD patient. With the convergence of the genetic theory of the disease and gene transfer technology, various *in vivo* models of HD have been manufactured (Pouladi et al., 2013). Invertebrate models (*Drosophila and Caenorhabditis elegans*) have been used to effectively and rapidly screen potential therapeutic interventions and to investigate genetic/molecular pathogenesis of HD (Faber et al., 1999; Parker et al., 2001). Toxin models, which were the first animal models of HD, clarified the role of mitochondrial dysfunction and excitotoxicity, two events that have been characterized in the brains of individuals with HD (Beal et al., 1993; Pouladi et al., 2013). However, whether these models recapitulate HD biology is still uncertain (Pouladi et al., 2013). Transgenic (Tg) mouse models including R6/2, BACHD and YAC128 have been generated by introducing truncated N-terminal fragment or full-length of a juvenile HD patient's *HTT* gene into the mouse genome (Pouladi et al., 2013; Menalled and Brunner, 2014). The Tg models revealed behavioral deficits, such as motor symptoms, electrophysiological alterations, striatal neurodegenerations, presence of intranuclear *HTT* inclusions, or alteration of transcriptional factors. However, some Tg models have various phenotypes. They do not reproduce some major features of HD pathology, such as serious neuronal degeneration in the striatum (Crook and Housman, 2011; Pouladi et al., 2013; Menalled and Brunner, 2014). R6/2 mice are well known to have limited lifespan (Perry et al., 2010). Nonetheless, these models have been widely used to study HD pathogenesis and for therapeutic trials (Crook and Housman, 2011; Pouladi et al., 2013; Menalled and Brunner, 2014). Drug discovery trials using these models are a labor-, time-, and cost-intensive efforts. Recent advances in viral-vector technology have provided promising alternatives based on direct transfer of genes to selected sub-regions of the brain (Ruiz and Déglon, 2012; Blessing and Déglon, 2016; Saraiva et al., 2016).

Recombinant adeno-associated viral (AAV) vectors have been successfully used to locally or systemically enhance or silence gene expression in a variety of tissues, including brain tissues, in adult animals or human clinical trials (de Backer et al., 2010; Ruiz and Déglon, 2012; Blessing and Déglon, 2016; Saraiva et al., 2016). The AAV vectors are reportedly more effective than lentiviral vectors at regulating the expression of specific genes at specific brain regions (de Backer et al., 2010; Ruiz and Déglon, 2012; Blessing and Déglon, 2016; Saraiva et al., 2016). Thus far, 11 serotypes of AAV have been identified. These serotypes differ in their tropism or the type of cells they infect (Kwon and Schaffer, 2008). Hybrid capsids derived from multiple different serotypes can also alter viral tropism. AAV serotype DJ (AAV-DJ), one common hybrid example, contains a hybrid capsid derived from eight serotypes. AAV-DJ displays a higher transduction efficiency *in vitro* than any wild type serotype. *In vivo*, it displays very high infectivity across a broad range of cell types (Grimm et al., 2008).

An AAV-induced animal model was first manufactured to express expanded polyglutamine tracts (97Q) fused to green fluorescence protein (GFP) in the adult rat brain. The model revealed the rapid formation of fibrillar, cytoplasmic and ubiquitinated nuclear polyglutamine aggregates in neurons (Senut et al., 2000). Recently, a rat HD model obtained by AAV serotype 2/9 containing Exon 1-Q138 mutant *HTT* (Q138) was reported as a short-term model for *in vivo* studies in drug discovery (Ceccarelli et al., 2016). Although these models are useful in HD studies, more models would provide more options to researchers. In the present study, we used AAV-DJ expressing N-terminal truncated fragment (N171) carrying 82 or 18 CAG repeats (mutant *HTT* and wild type, respectively) to establish and optimize a mouse model of HD. AAV-DJ-N171-82Q (AAV-DJ-82Q) and AAV-DJ-N171–18Q (AAV-DJ-18Q) as control were stereotaxically injected in the bilateral striata of juvenile mice. As a result, we demonstrate that this AAV-DJ-82Q model could be valuable as a new tool for drug efficacy trials through confirming reduced motor activity, striatal cell death and increased *HTT* aggregation.

MATERIALS AND METHODS

AAV Vector Production

To generate AAV-*HTT*-N171-82Q, we used HD-N171-82Q cDNA construct in pBluescript to generate N171-82Q mouse model of HD (Schilling et al., 1999, 2004). The construct with first three exons (171 amino acids) of human *HTT* and 82 CAG gene repeats (*HTT*-N171-82Q) was obtained from Dr. David R. Borchelt (Santa Fe Health Care Alzheimer's Disease Research Center, University of Florida). The *HTT*-N171-82Q construct was double digested with EcoRI/XhoI and inserted into multi-cloning sites of an AAV-MCS expression vector (Cell Biolabs Inc., cat# VPK-410). This vector was created by expression under cytomegalovirus (CMV) immediate early enhancer and promoter. As a control vector, *HTT* cDNA containing 18Q CAG repeats was used. All plasmid constructs were verified by nucleotide sequencing. These viral vectors used in this study were pseudo-typed where the transgene was flanked by inverted terminal repeats of AAV2 packaged in an AAV-DJ capsid. AAV-DJ was engineered using a DNA

family shuffling technology to create a hybrid capsid from eight AAV serotypes. Additionally, AAV-DJ-*HTT*-N171-82Q and AAV-DJ-*HTT*-N171–18Q vectors were purified by iodixanol gradient ultracentrifugation by Korea Institute of Science and Technology (KIST) Virus Facility[1]. The production titer was 1.3×10^{13} genome copies/ml (GC/ml) for AAV-DJ-*HTT*-N171-82Q and 1.6×10^{13} GC/ml for AAV-DJ-*HTT*-N171–18Q.

Animals and Ethical Statement

Male C57BL/6 mice (Narabiotec Co., Ltd., Seoul, South Korea; Seed mice were originated from Taconic Biosciences Inc., Cambridge, IN, USA) were kept at a constant temperature of 23 ± 2°C with a 12-h light-dark cycle (light on 08:00–20:00) and fed food and water *ad libitum*. The animals were allowed to habituate to the housing facilities for 1 week before the experiments. This study was carried out in accordance with the recommendations of a NIH Workshop on preclinical models of neurological diseases (Landis et al., 2012). The protocol was approved by the Institutional Animal Care and Use Committee at Kyung Hee University. In this process, proper randomization of laboratory animals and handling of data were performed in a blinded manner.

Experimental Groups

To confirm the effect of AAV-DJ-82Q-infection, 4-week-old male juvenile mice were selected from a 5-day preliminary behavioral test. The selected mice were randomly divided into sham ($n = 5$), AAV-DJ-18Q (7.9×10^{12} GC/ml, $n = 7$), AAV-DJ-82Q (0.62×10^{12} GC/ml, $n = 7$), and AAV-DJ-82Q (1.23×10^{12} GC/ml, $n = 7$) groups.

Stereotactic Brain Surgery

Mice (4 weeks; body weight, 14–15 g) were deeply anesthetized (2%–3% isoflurane, 60% O_2, 40% N_2O), placed on a stereotaxic apparatus (myNeuroLab, St. Louis, MO, USA), and gently fixed with ear bars and head holder. Two microliters of AAV-DJ-18Q (7.9×10^{12} GC/ml) and AAV-DJ-82Q (0.62×10^{12} GC/ml and 1.23×10^{12} GC/ml) were injected at a speed of 0.5 μl/min into the mid-coronal level of the bilateral striatum (stereotaxic coordinates in mm with reference to the bregma were anteroposterior, +0.8; mediolateral, ±2.0; dorsoventral, −2.5; Paxinos and Watson, 1998) using a Hamilton syringe (Sigma-Aldrich, St. Louis, MO, USA) equipped with a 30 gauge sharp-tipped needle. After 5 min, the needle was removed in three intermediate steps for 3 min to minimize the backflow. After surgical suturing, the mice were kept on a warm pad until being awakened.

Behavioral Assessment

To investigate whether AAV-DJ-82Q injection induces neurological impairment (reduced motor coordination and imbalance), we measured body weight and accomplished pole and rota-rod performance tests (Choi et al., 2018) a weekly during 10 weeks from 1 day before AAV-DJ-82Q injection. Briefly, for the pole test, each mouse was placed on the top of a pole with a rough surface (1 cm in diameter and 50 cm in height) with its head facing upwards. The time in which the mouse completely turned downwards on the top of the pole and climbed down to the floor was recorded. At 1 h after pole test, each mouse was placed on the rotating rod (diameter = 4 cm) and tested at 16 rpm/s for 5 min. The latency to fall off the rota-rod apparatus within this time was recorded by magnetic trip plates. The assessment was accomplished by an experimenter who was unaware of the experimental condition under constant conditions of temperature (23 ± 2°C) and humidity (55 ± 5%) in a quiet room. Mice were acclimated to the pole and rota-rod apparatuses for 5 days before the first test. Mice that turned downwards on the top of the pole and climbed down to the floor within 2 min and that stayed on the rod without falling during training (for 5 min) were selected and randomly divided into the experimental groups.

Western Blot Analysis

Western blot analysis was performed as previously described (Jang et al., 2013, 2014; Jang and Cho, 2016; Lee et al., 2016a,b). Briefly, 10 weeks (14 weeks after birth) after the AAV-DJ-82Q-injection, mice ($n = 7$ per group) were anesthetized and the striatum was immediately removed with lysis buffer. The protein (30 μg) from each striatum was transferred to polyvinylidene fluoride membranes and blocked. These membranes were probed with mouse anti-*HTT* (1:500; catalog LS-C24591-100, a.a. 181–810, clone 2Q75; LifeSpan BioSciences, Seattle, WA, USA), mouse anti-*HTT* protein (1:200; catalog MAB5374, clone EM48; Millipore, Darmstadt, Germany), rabbit anti-NeuN (1:2000; Abcam, Cambridge, MA, USA), mouse anti-dopamine- and cAMP-regulated neuronal phosphoprotein (DARPP-32) (1:2000; BD Biosciences, San Jose, CA, USA), rabbit anti-cleaved caspase-3 (1:1000; Cell Signaling Technology, Beverly, MA, USA), rabbit anti-ionized calcium-binding adapter molecule 1 (Iba-1) (1:1000; WAKO, Chuo-Ku, Japan), rabbit anti-glial fibrillary acidic protein (GFAP) (1:2000; DACO, Carpinteria, CA, USA), rabbit anti-oligodendrocyte transcription factor 2 (Olig2) (1:500; Abcam), rabbit anti-tumor necrosis factor-alpha (TNF-α) (1:500; Cell Signaling Technology), rabbit anti-interleukin (IL)-6 (1:500; Cell Signaling Technology), mouse anti-inducible nitric oxide synthases (iNOS) (1:500; Santa Cruz Biotechnology, Santa Cruz, CA, USA), mouse anti-cyclooxygenase-2 (COX-2) (1:500, BD Biosciences), rabbit anti-phospho (p)-IkappaB-alpha (IκBα) (1:500; Cell Signaling Technology), rabbit anti-p-nuclear factor kappa B (NF-κB) (1:500; Cell Signaling Technology), rabbit anti-p-signal transducer and activator of transcription 3 (STAT3) (1:500; Cell Signaling Technology), and mouse anti-GFAP (1:2000; Millipore) followed by incubation with an horseradish peroxidase-conjugated secondary antibody prior to enhanced chemiluminescence (Amersham Pharmacia Biotech, Piscataway, NJ, USA). To normalize the level of protein expression, the membranes were stripped and reprobed with mouse anti-gyceraldehyde 3-phosphate dehydrogenase (GAPDH) (1:10,000; Cell Signaling Technology). After Western blots were performed three times, the density of each band was converted

[1]http://virus.kist.re.kr

into numerical values using the Photoshop CS2 program (Adobe, San Jose, CA, USA), subtracting background values from an area of film immediately adjacent to the stained band. Data are expressed as the ratio of protein to total GAPDH for each sample.

Tissue Preparation and Immunofluorescence Procedure

To examine the histopathological changes in the striatum, 10 weeks (14 weeks after birth) after AAV-DJ-82Q injection, the mice (n = 7 per group) were deeply anesthetized with diethyl ether and then intracardially perfused with saline and cold 4% paraformaldehyde in 0.1 M phosphate buffer (PB, pH 7.4). Brains were removed and post-fixed for 24 h and cryoprotected in 10, 20 and 30% sucrose in PBS serially at 4°C. Serial coronal slices (30-μm thickness) of striatum were acquired on a model CM3050S freezing microtome (Leica, Wetzlar, Germany) and collected in sequence as free-floating sections on PBS. The sections from the mid-coronal level of the striatum (Franklin and Paxinos, 2008) were processed for immunofluorescence stain as previously described (Lee et al., 2016a). Briefly, the brain sections from each group (n = 3 per brain) were incubated with mouse anti-*HTT* protein (1:400; catalog MAB5374, clone EM48; Millipore), rabbit anti-NeuN (1:5,000; Abcam), rabbit anti-cleaved caspase-3 (1:500; Cell Signaling Technology), rabbit anti-Iba-1 (1:2,000; WAKO), mouse anti-GFAP (1:5,000; Millipore) and rabbit anti-Olig2 (1:500; Abcam) overnight with gentle agitation at room temperature. The sections were followed with a mixture of secondary antibodies and examined with confocal imaging system (LSM five PASCAL; Carl Zeiss, Germany).

Statistical Analysis

Statistical analysis was performed by using the SPSS 21.0 package (SPSS Inc., Chicago, IL, USA) for Windows. Multiple comparisons were made using one-way ANOVA with Tukey *post hoc* test. All data are presented as means ± SEM and statistical difference was accepted at the 5% level unless otherwise indicated.

RESULTS

AAV-DJ-82Q-Injection Induces Neurological Impairment

First, to confirm whether AAV-DJ-82Q injection induced neurological symptoms and to select a more effective dose of the viral vector, motor coordination and balance activities were measured weekly after AAV-DJ-82Q-injetion using pole and rotarod performance tests. In the pole test, beginning at week 4 after AAV-DJ-82Q injection (8 weeks after birth), the average descent time to the bottom of the pole was increased (5.7 ± 0.3 and 6.3 ± 0.2 s in the 0.62 × 10^{12} GC/ml and 1.23 × 10^{12} GC/ml groups, respectively) 8 weeks after injection (12 weeks after birth) compared to the sham group (4.3 ± 0.5 s at 8 weeks after injection) and AAV-DJ-18Q (4.0 ± 0.3 s at 8 weeks after injection) groups (**Figure 1A**). In the rotarod test, the average latency to fall was reduced since week 4 after the AAV-DJ-82Q injection (282.9 ± 2.3 and 280.3 ± 1.7 s in the 0.62 × 10^{12} GC/ml and 1.23 × 10^{12} GC/ml groups, respectively, 8 weeks after injection) compared with the sham group (289.5 ± 1.9 s, 8 weeks after injection) and AAV-DJ-18Q (290.5 ± 1.3 s, 8 weeks after injection; **Figure 1B**). Body weight was significantly decreased since week 8 after AAV-DJ-82Q injection (1.23 × 10^{12} GC/ml), partially corresponding to both behavioral symptoms (**Figure 1C**). There were no significant differences in behavioral tests or change in body weight between low and high doses of vector groups (**Figures 1A–C**). At the end of experiment, all mice were alive. These results suggest that AAV-DJ-82Q-injection can successfully induce neurological impairment.

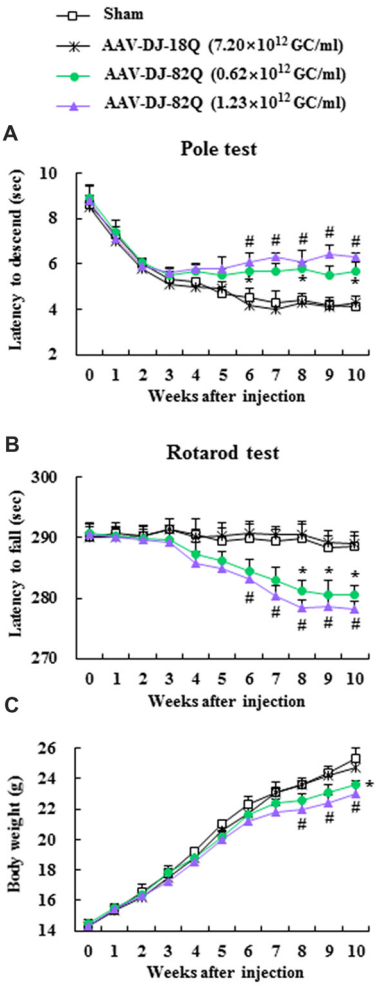

FIGURE 1 | Adeno-associated viral (AAV)-DJ-82Q-injection induces neurological impairment. Two microliters of AAV-DJ-82Q (0.62 × 10^{12} GC/ml and 1.23 × 10^{12} GC/ml) and AAV-DJ-18Q (7.9 × 10^{12} GC/ml) were stereotaxically injected into the mid-striatum of male juvenile mice (4 weeks old). Sham group received the same dose of vehicle. Pole **(A)** and rota-rod performance tests **(B)** and alteration of body weight **(C)** were measured weekly. ANOVA test; $^{*}p < 0.05$ and $^{\#}p < 0.05$ vs. sham group and AAV-DJ-18Q groups.

AAV-DJ-82Q Injection Enhances Mutant *HTT* Expression and Induces Neurodegeneration in Striatum

Since 1.23 × 10^{12} GC/ml of AAV-DJ-82Q more effectively induced neurological impairment than 0.62 × 10^{12} GC/ml of AAV, we further investigated whether the neurological impairments were associated with the level of AAV-DJ-82Q-infection into the striatum at the same dose. The level of AAV-DJ-82Q infection was measured by Western blot and immunohistochemical analysis against *HTT* and *HTT* aggregates with LS-C24591–100 and EM48 antibodies, respectively. Protein expression by anti-*HTT* antibody showed two bands. The *HTT* expression (∼75 KDa) was increased clearly in the striatum of sham and AAV-DJ-18Q groups while mutant *HTT* expression was increased clearly in the striatum of AAV-DJ-82Q group (**Figures 2A,D**). Expression level of mutant *HTT* aggregates by using EM48 antibody was not detected in the striatum from the sham or the AAV-DJ-18Q group. However, its expression was markedly increased in the striatum of the AAV-DJ-82Q group (**Figures 2B,D**). In agreement with these results, many EM48-immunnoreactive cells were detected in the striatum from the AAV-DJ-82Q group, while they were not detected in the striatum from the sham and AAV-DJ-18Q groups (**Figures 2E–G**). Subsequently, we confirmed whether the AAV-DJ-82Q-infection induced neurodegeneration in striatum. The protein expressions of NeuN (a neuron marker) AND DARPP-32 (a marker for medium spiny neurons) were significantly reduced and cleaved caspase-3 (apoptotic cell marker) were significantly enhanced in the striatum from the AAV-DJ-82Q group compared to the sham and AAV-DJ-18Q groups (**Figures 2C,D**) consistent with the expression pattern of NeuN and cleaved caspase-3-immunoreactive cells (**Figures 2E–M**). These results suggested that AAV-DJ-82Q-injection can over-express mutant *HTT* in the striatum, resulting in neurodegeneration associated with apoptosis.

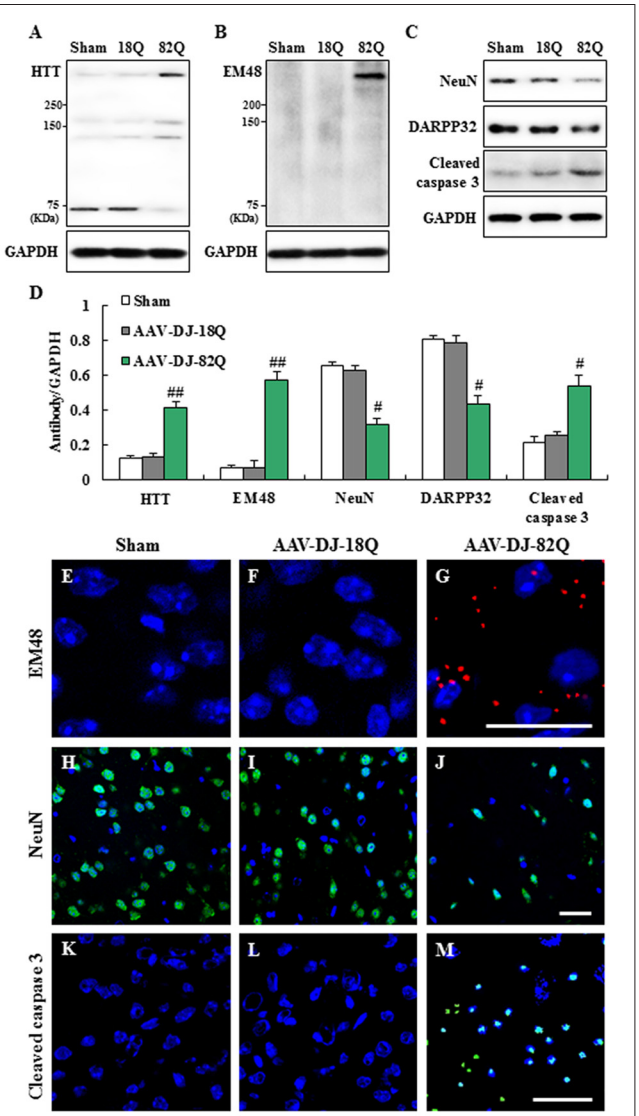

FIGURE 2 | AAV-DJ-82Q injection enhances mutant *huntingtin (HTT)* expression and induces neurodegeneration in the striatum. **(A–E)** Eight weeks after AAV-DJ-82Q-injection, the striata from sham, AAV-DJ-18Q, and AAV-DJ-82Q groups (n = 7 per group) were analyzed by Western blot to investigate change in protein expression of *HTT* (clone, 2Q75 and EM48), NeuN, DARPP32 and cleaved caspase-3 **(A–C)** and then quantified concerning the ratio of protein to total GAPDH for each sample **(D)**. **(A–C)** show a representative Western blot. ANOVA test; $^{\#}p < 0.05$ and $^{\#\#}p < 0.01$ vs. sham and AAV-DJ-18Q groups. **(E–M)** Striatal sections (n = 2 per brain) from each group (n = 7 per group) were accomplished by immunofluorescence stain using anti-*HTT* (clone, EM48, red) **(E–G)**, NenN (green) **(H–J)**, and cleaved caspase-3 (green) **(K–M)** antibodies. Scale bar denotes 100 μm.

AAV-DJ-82Q-Infection Induces Microglial and Astroglial Activation and Inflammation in Striatum

We examined whether AAV-DJ-82Q infection in the striatum affects the features of neuroglia (**Figure 3**). The protein expressions of Iba-1 (microglia marker) and GFAP (astrocyte marker) by Western blot analysis were significantly enhanced in striatal lesions from the AAV-DJ-82Q group compared to the sham and AAV-DJ-18Q groups (**Figures 3A,B**). In agreement with these results, the intensity of Iba-1-immunoreactive microglia was increased within or around striatal lesions from AAV-DJ-82Q group and the immunoreactive cells displayed activated forms with an enlarged cell body and short and thick processes, as compared to the sham and AAV-DJ-82Q groups, which generally displayed the typical morphology of resting cells with small cell bodies and thin processes (**Figures 3C–E**), as previous described (Cho et al., 2008; Jang et al., 2013, 2014; Jang and Cho, 2016; Lee et al., 2016a). The intensity of GFAP-immunoreactive astrocytes was also increased within or around striatal lesions from the AAV-DJ-82Q group, as compared with those of the sham and AAV-DJ-18Q groups (**Figures 3F–H**). However, AAV-DJ-82Q-injection did not significantly affect the protein expression of Olig2 (a marker of oligodendrocytes) (**Figures 3A,B**). Since activated microglia and astrocytes are involved in the inflammatory response (Lobsiger and Cleveland, 2007), we measured the level of expression of representative inflammatory mediators in the

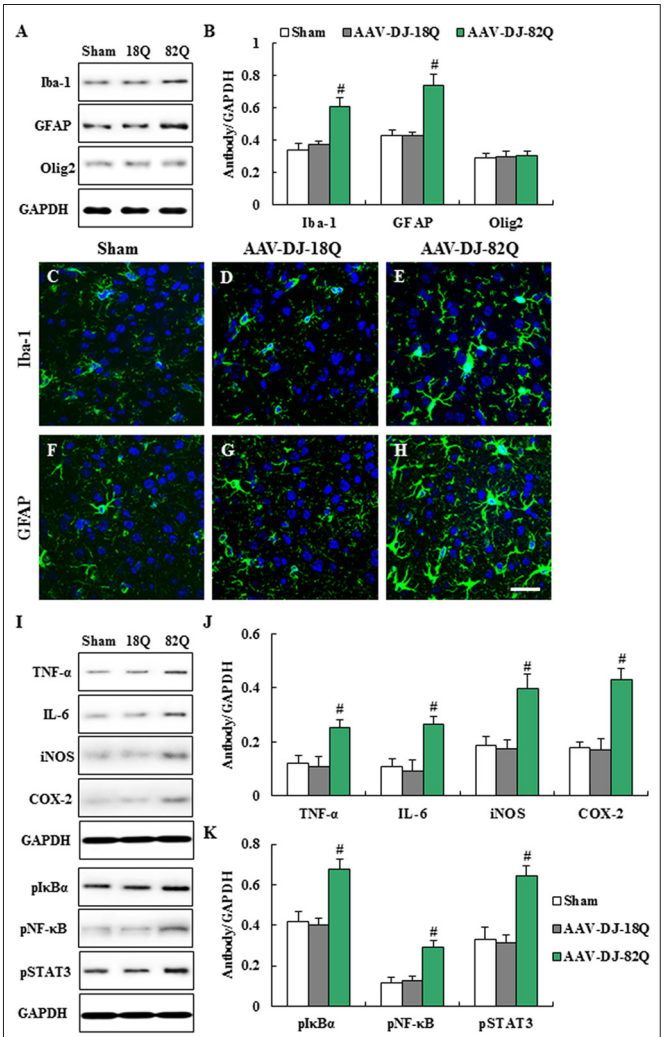

FIGURE 3 | AAV-DJ-82Q-infection induces microglial and astroglial activation and 263–270 inflammation in the striatum. **(A–F)** Eight weeks after the AAV-DJ-82Q-injection, the striata from sham, AAV-DJ-18Q, and AAV-DJ-/82Q groups (n = 7 per group) were analyzed by Western blot to investigate change in protein expression of Iba-1, glial fibrillary acidic protein (GFAP), and Olig2 **(A)** and then quantified as the ratio of protein to total GAPDH for each sample **(B)** ANOVA test; $^{\#}p < 0.05$ vs. sham and AAV-DJ-18Q groups. **(C–H)** Striatal sections (n = 2 per brain) from each group (n = 7 per group) were accomplished by immunofluorescence stain using anti-Iba-1 **(C–E)**, and GFAP **(F–H)** antibodies. Scale bar denotes 100 μm. **(I–K)** Eight weeks after AAV-DJ-82Q-injection, the striata from sham, AAV-DJ-18Q, and AAV-DJ-82Q groups (n = 7 per group) were analyzed by Western blot to investigate change in protein expression of TNF-α, IL-6, iNOS, COX-2, p-IκBα, p-NF-κB, p-signal transducer and activator of transcription (STAT3) and GAPDH **(I)** and then quantified concerning the ratio of protein to total GAPDH for each sample **(J,K)**. **(I)** show a representative Western blot. ANOVA test; $^{\#}p < 0.05$ vs. sham and AAV-DJ-18Q groups.

striatum 8 weeks after AAV-DJ-82Q injection by Western blot analysis (**Figures 3I–K**). Little or no expression of TNF-α, IL-6, iNOS and COX-2 proteins were detected in the striatum of sham and AAV-DJ-18Q groups, whereas their expressions were significantly enhanced in the striatum from the AAV-DJ-82Q group (**Figures 3I,J**). Additionally, we measured levels of activation of NF-κB and STAT3 pathways as representative inflammatory pathways. As expected, expression levels of p-IκBα, p-NF-κB, and p-STAT3 were significantly increased in the striatum of the AAV-DJ-82Q group (**Figures 3I–K**). These findings suggest that the AAV-DJ-82Q-infection may produce striatal cell death and neurological dysfunction by inducing the activation of microglia, astrocytes and the inflammatory response.

AAV-DJ-82Q Vector Infects Neurons, Microglia and Astrocytes, but Not Oligodendrocytes

The EM48-immunoreactive mutant *HTT* aggregates were densely spread in the striatal area from the AAV-DJ-82Q group (**Figure 2G**). However, it is unclear whether the aggregates are expressed in specific cell types. To investigate this, immunofluorescence staining was done using NeuN, Iba-1, GFAP, and Olig2 antibodies, as a marker of neurons, microglia, astrocytes, and oligodendrocytes, respectively. EM48-positive aggregates were predominantly expressed in the nucleus and cytoplasm of neurons, microglia, and astrocytes (**Figures 4A–C**). These aggregates were co-stained with NeuN (23.1 ± 1.5%; 45.4 ± 5.2 co-stained cells of 193.0 ± 8.7 NeuN-positive cells), Iba-1 (19.5 ± 1.3%; 14.0 ± 1.5 co-stained cells of 71.0 ± 3.6 Iba-1-positive cells), and GFAP (11.8 ± 1.1%; 8.1 ± 1.2 co-stained cells of 67.3 ± 3.9 GFAP-positive cells) antibodies (**Figures 4A–C**). However, these aggregates were not co-stained with Olig2 antibody (**Figure 4D**). These results indicate that AAV-DJ-82Q can infect specific cell types in striatum and induce HD-like pathology.

DISCUSSION

In the development of new therapeutic strategies for neurodegenerative disorders such as HD, animal models recapitulating the etiology, pathology and molecular mechanisms described in patients are positively necessary. However, currently a lot of animal models do not reproduce the critical therapeutic mechanisms/targets of the diseases (Crook and Housman, 2011; Pouladi et al., 2013; Menalled and Brunner, 2014). To help these challenges, various viral vectors for gene delivery and gene therapy within the nervous system have been developed over the past several decades. The studies have revealed the seemingly unlimited possibilities for viral vector systems in deciphering the nature of neurodegenerative disorders, such as HD, and so for the development of eradication regimens (Ruiz and Déglon, 2012). Despite several published reports using lentiviral and AAV vectors to model HD by over-expression of mutant *HTT*, neuroscientists in the field of HD have a much smaller selection of vectors to choose from. In the present study, we developed a novel animal model that was based on over-expression of human mutant *HTT* via a bilateral intrastriatal injection by AAV-DJ-82Q into juvenile mice. The mice over-express the transgene in the striatum beginning as juveniles and extending into adulthood. Our findings demonstrated that, after intrastriatal injection of mutant *HTT* into juvenile mice,

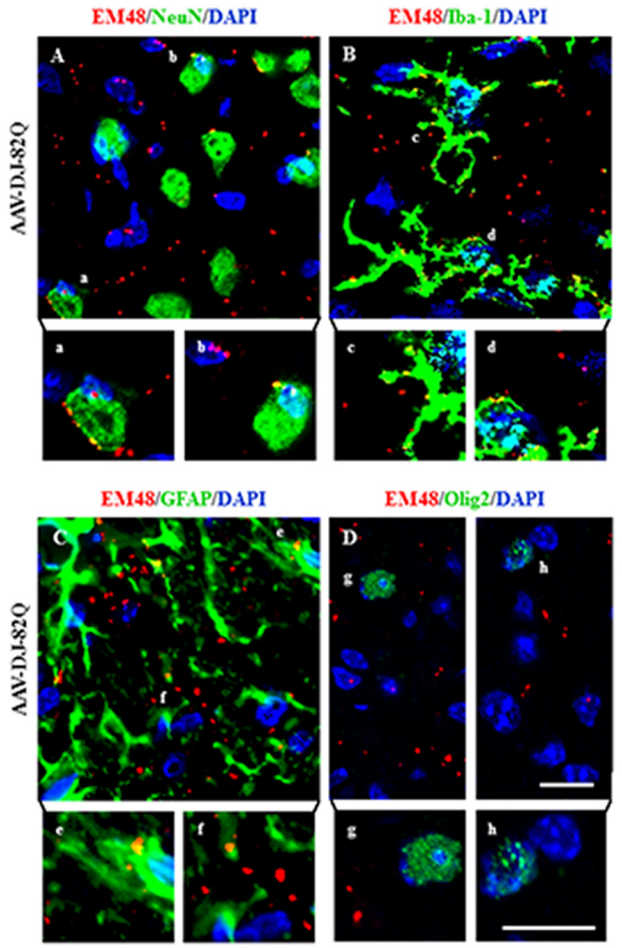

FIGURE 4 | AAV-DJ-82Q vector successfully infects neurons, microglia and astrocytes. Eight weeks after the AAV-DJ-82Q-injection, the striatal sections (n = 2 per brain) from sham, AAV-DJ-18Q and AAV-DJ-82Q groups (n = 7 per group) were analyzed by double immunofluorescence stain using anti-EM48, NeuN, Iba-1, GFAP and Olig2 antibodies **(A–D)**. Lower panels in **(A–D)** display high magnification micrographs of the areas marked with **(a–h)** in upper panels. Scale bar denotes 50 μm.

adult mice over-expressed mutant *HTT*, displayed neuronal loss, and showed striatal neuroinflammation, resulting in motor dysfunction. In particular, mutant *HTT* predominantly infected neurons, microglia, and astrocytes. Our findings suggest that the AAV-DJ-82Q-injected mouse model may be a helpful tool to study the pathophysiology of mutant *HTT*-associated disease and to develop efficacious therapeutic strategies in translational research.

Several types of N-terminal Tg (R6/1, R6/2, N171-82Q), full-length (YAC128, BACHD) and knock-in (Hdh^{Q111}) models have been generated to investigate the pathogenicity of HD and to discover therapeutic approaches (Pouladi et al., 2013; Menalled and Brunner, 2014). The *in vivo* models have revealed behavioral disorders including movement deficits, striatal neurodegeneration, electrophysiological dysfunctions, intracellular aggregates, and alteration of transcriptional factors (Pouladi et al., 2013; Menalled and Brunner, 2014). However, each model has different characteristics and so their results are not absolutely reproducible concerning some critical characteristics of HD pathology, such as clear neurodegeneration in the striatum or reduced life span (Crook and Housman, 2011). In addition, the research can experience difficulty in maintaining the animal strains. Problems include breeding failure and the high cost of maintaining the animals in the long-term. Our AAV-DJ-82Q model displayed clear motor deficits by pole and rota-rod tests, which were evident in the short term (at least 4–5 weeks following injection) by the onset of behavioral dysfunction as well as striatal degeneration and cellular aggregates. These results suggest that AAV-DJ-82Q model may be more helpful than others.

In the last two decades, there have been several attempts to develop the ideal vector (vehicle) for gene transfer to the central nervous system (CNS). Presently, recombinant AAVs are one of the preferred vectors, because their stable transduction of dividing and non-dividing cells, strong neural tropism, low risk of insertional mutagenesis, and reduced immune responses (Blessing and Déglon, 2016; Grieger et al., 2016; Saraiva et al., 2016). According to many studies that measured the ability of AAV serotypes to target the CNS, when administrated into the brain parenchyma of rodents, most of the serotypes (1, 2, 4, 5, 8 and 9) transduced neurons and glia in the CNS areas including striatum, hippocampus and neocortex (Ruiz and Déglon, 2012; Watakabe et al., 2015; Ceccarelli et al., 2016; Saraiva et al., 2016). Other serotypes, such as AAV-DJ, are potentially useful but have been less well examined (Cearley and Wolfe, 2006; Klein et al., 2008; Aschauer et al., 2013; Holehonnur et al., 2014). AAV-DJ is a synthetic serotype with a chimeric capsid of AAV-2, 8 and 9. AAV-DJ contains a heparin-binding domain in its capsid, which may efficiently transduce a broad range of cell types and escape from immune neutralization (Grimm et al., 2008). However, AAV-DJ has been available only recently and so relatively little is known about its optimal preparation/purification and application. In present study, we injected the striatum bilaterally with 0.62×10^{12} GC and 1.23×10^{12} GC in 2.0 ul of AAV-DJ-82Q per side, as is done with other vectors. The higher dose of viral injections produced more serious movement disorder in the pole and rota-rod performance tests (**Figures 1A,B**). The movement disorder progressively increased beginning 4–5 weeks following injection and lasted at least by 8 weeks after the injection. However, features of movement disorder were different to that of N171-82Q Tg mice (expressing a mutant N-terminal fragment of *HTT*), which displayed loss of coordination, hunched posture, tremors, abnormal gait, and clasping of hindlimbs (Schilling et al., 1999). In the present study, *HTT* aggregates were observed only in the striatum, similar to the *in vivo* rat HD model obtained by stereotaxic injection of AAV serotype nine containing Exon1-Q138 mutant *HTT* (AAV-9-Q138) (Ceccarelli et al., 2016). However, the expression pattern was different to that of N171-82Q Tg mice (Schilling et al., 1999). In the latter, nuclear inclusions were observed in various areas of the brain including the cerebral cortex, striatum, hippocampus, and amygdala. Furthermore, neuritic aggregates were seen in

several areas of the brain including the medial amygdala and subthalamic nucleus (Schilling et al., 1999). In the present study, *HTT* aggregates were observed in the nucleus and cytoplasm of neurons, microglia and astrocytes, but not in oligodendrocytes of striatum (**Figure 4**). However, in three HD mouse models that express either full-length *HTT* (Hdh^{Q150}, zQ175) or an N-terminal exon1 fragment (R6/2) of mutant HTT, the nuclear inclusions were observed in neurons, microglia, astrocytes, and oligodendrocytes (Jansen et al., 2017). In the present study, mutant *HTT* aggregates were observed in 23.1 ± 1.5% of the NeuN-positive neurons, 19.5 ± 1.3% of the Iba-1-positive microglia, and 11.8 ± 1.1% of the GFAP-positive astrocytes 8 weeks after AAV-DJ-82Q injection. However, in the three HD mouse models, at late stages of the disease, nuclear inclusions were found in 30%–50% of the neurons, 30% of the S100B-positive glial cells, 4%–10% of the GFAP-positive astrocytes, 3%–10% of the oligodendrocytes, and 0%–2% of the microglia (Jansen et al., 2017). Nuclear inclusions were also present in neurons and all studied glial cell types in human patient material (Jansen et al., 2017). Like this, in our AAV-DJ-82Q model, the expression pattern of mutant *HTT* aggregates was nearly the same with the Tg mouse models previous reported. The small differences may be explained by fundamental difference between Tg model (congenital) and AAV model (acquired) or among the AAV vector serotypes. Taken together, our results demonstrate that the AAV-DJ-82Q vector can possibly infect most functional classes of CNS, although our current data do not discriminate endothelial cell and immature/undifferentiated neural cells.

In the neurodegenerative diseases, microglia, resident immunocompetent and phagocytic cells, are activated and recruited/infiltrated around or into the lesions and serves as scavenger cell (Lobsiger and Cleveland, 2007; Kabba et al., 2018). Circulating peripheral immune cells (macrophages) may surpass a compromised blood–brain barrier and encounter neurons and microglia (Kadiu et al., 2005; Main and Minter, 2017). Although this response is initiated to protect the CNS from the harmful agents, the effect may be detrimental via releasing toxic mediators in neurodegenerative lesions (Lobsiger and Cleveland, 2007). Astrocytes can be activated by products from dead cells or infiltrated/activated immune cells within or around the lesion (Lobsiger and Cleveland, 2007). Interestingly, AAV-DJ-82Q injection clearly induced microglial and astroglial activation and protein expression of representative proinflammatory cytokines (TNF-α, IL-6) and inflammatory mediators (COX-2 and iNOS) in striatum at 14 weeks after injection, corresponding to enhanced expression of p-IκBα, p-NF-κB and p-STAT3 as representative inflammatory pathways. Whether glial activation protects against mutant *HTT* aggregates (toxicity) after the injection of AAV-DJ-82Q into normal mice is unclear. Nonetheless, our results provide the first demonstration that the AAV-DJ-82Q may induce neuroinflammatory response related to neurodegeneration in striatum.

CONCLUSION

An *in vivo* model recapitulating some cardinal pathogenesis of HD needs to be generated. Here, intrastriatal injection of AAV-DJ-82Q to juvenile mice successfully induced mutant *HTT* aggregation, neurodegeneration, and neuroinflammatory response in adult striatum, resulting in HD-like symptoms. Our findings suggest that AAV-DJ-82Q vector might be a helpful tool to better understand neuropathological mechanisms in the striatum of HD patients and develop new therapeutic strategies for HD-like symptoms.

AUTHOR CONTRIBUTIONS

MJ performed the stereotaxic injection, behavioral experiment, immunohistochemistry and Western blots and prepared the figures. SEL developed viral vector and produced AAV virus. I-HC conceived all experiments, analyzed the results and wrote the manuscript. All authors have read and approved the final manuscript.

FUNDING

This research was supported by Basic Science Research Program and Brain Research Program through the National Research Foundation of Korea (NRF) funded by the Ministry of Science and ICT (NRF-2017R1A2A2A05069493 and NRF-2016M3C7A1905074).

REFERENCES

Aschauer, D. F., Kreuz, S., and Rumpel, S. (2013). Analysis of transduction efficiency, tropism and axonal transport of AAV serotypes 1, 2, 5, 6, 8 and 9 in the mouse brain. *PLoS One* 8:e76310. doi: 10.1371/journal.pone.0076310

Beal, M. F., Brouillet, E., Jenkins, B. G., Ferrante, R. J., Kowall, N. W., Miller, J. M., et al. (1993). Neurochemical and histologic characterization of striatal excitotoxic lesions produced by the mitochondrial toxin 3-nitropropionic acid. *J. Neurosci* 13, 4181–4192. doi: 10.1523/jneurosci.13-10-04181.1993

Blessing, D., and Déglon, N. (2016). Adeno-associated virus and lentivirus vectors: a refined toolkit for the central nervous system. *Curr. Opin. Virol.* 21, 61–66. doi: 10.1016/j.coviro.2016.08.004

Cearley, C. N., and Wolfe, J. H. (2006). Transduction characteristics of adeno-associated virus vectors expressing cap serotypes 7, 8, 9, and Rh10 in the mouse brain. *Brain Mol. Ther.* 13, 528–537. doi: 10.1016/j.ymthe.2005.11.015

Ceccarelli, I., Fiengo, P., Remelli, R., Miragliotta, V., Rossini, L., Biotti, I., et al. (2016). Recombinant Adeno Associated Viral (AAV) vector type 9 delivery of Ex1-Q138-mutant huntingtin in the rat striatum as a short-time model for *in vivo* studies in drug discovery. *Neurobiol. Dis.* 86, 41–51. doi: 10.1016/j.nbd.2015.11.019

Cho, I. H., Hong, J., Suh, E. C., Kim, J. H., Lee, H., Lee, J. E., et al. (2008). Role of microglial IKKβ in kainic acid-induced hippocampal neuronal cell death. *Brain* 131, 3019–3033. doi: 10.1093/brain/awn230

Choi, J. H., Jang, M., Nah, S. Y., Oh, S., and Cho, I. H. (2018). Multitarget effects of Korean red ginseng in animal model of Parkinson's disease: antiapoptosis, antioxidant, antiinflammation and maintenance of blood-brain barrier integrity. *J. Ginseng Res.* In Press. doi: 10.1016/j.jgr.2018.01.002

Crook, Z. R., and Housman, D. (2011). Huntington's disease: can mice lead the way to treatment? *Neuron* 69, 423–435. doi: 10.1016/j.neuron.2010.12.035

Damiano, M., Galvan, L., Déglon, N., and Brouillet, E. (2010). Mitochondria in Huntington's disease. *Biochim. Biophys. Acta* 1802, 52–61. doi: 10.1016/j.bbadis.2009.07.012

de Backer, M. W., Fitzsimons, C. P., Brans, M. A., Luijendijk, M. C., Garner, K. M., Vreugdenhil, E., et al. (2010). An adeno-associated viral vector transduces the

rat hypothalamus and amygdala more efficient than a lentiviral vector. *BMC Neurosci.* 11:81. doi: 10.1186/1471-2202-11-81

Faber, P. W., Alter, J. R., MacDonald, M. E., and Hart, A. C. (1999). Polyglutamine-mediated dysfunction and apoptotic death of a *Caenorhabditis elegans* sensory neuron. *Proc. Natl. Acad. Sci. U S A* 96, 179–184. doi: 10.1073/pnas.96.1.179

Franklin, K. B. J., and Paxinos, G. (2008). *The Mouse Brain in Stereotaxic Coordinates*. San Diego, CA: Elsevier Academic Press.

Gil-Mohapel, J., Brocardo, P. S., and Christie, B. R. (2014). The role of oxidative stress in Huntington's disease: are antioxidants good therapeutic candidates? *Curr. Drug Targets* 15, 454–468. doi: 10.2174/1389450115666140115113734

Grieger, J. C., Soltys, S. M., and Samulski, R. J. (2016). Production of recombinant adeno-associated virus vectors using suspension HEK293 cells and continuous harvest of vector from the culture media for gmp fix and flt1 clinical vector. *Mol. Ther.* 24, 287–297. doi: 10.1038/mt.2015.187

Grimm, D., Lee, J. S., Wang, L., Desai, T., Akache, B., Storm, T. A., et al. (2008). *In vitro* and *in vivo* gene therapy vector evolution via multispecies interbreeding and retargeting of adeno-associated viruses. *J. Virol.* 82, 5887–5911. doi: 10.1128/JVI.00254-08

Holehonnur, R., Luong, J. A., Chaturvedi, D., Ho, A., Lella, S. K., Hosek, M. P., et al. (2014). Adeno-associated viral serotypes produce differing titers and differentially transduce neurons within the rat basal and lateral amygdala. *BMC Neurosci.* 15:28. doi: 10.1186/1471-2202-15-28

Jacobsen, J. C., Gregory, G. C., Woda, J. M., Thompson, M. N., Coser, K. R., Murthy, V., et al. (2011). HD CAG-correlated gene expression changes support a simple dominant gain of function. *Hum. Mol. Genet.* 20, 2846–2860. doi: 10.1093/hmg/ddr195

Jang, M., and Cho, I. H. (2016). Sulforaphane Ameliorates 3-Nitropropionic Acid-Induced Striatal Toxicity by Activating the Keap1-Nrf2-ARE pathway and inhibiting the MAPKs and NF-κB pathways. *Mol. Neurobiol.* 53, 2619–2635. doi: 10.1007/s12035-015-9230-2

Jang, M., Lee, M. J., and Cho, I. H. (2014). Ethyl pyruvate ameliorates 3-nitropropionic acid-induced striatal toxicity through anti-neuronal cell death and anti-inflammatory mechanisms. *Brain Behav. Immun.* 38, 151–165. doi: 10.1016/j.bbi.2014.01.015

Jang, M., Lee, M. J., Kim, C. S., and Cho, I. H. (2013). Korean Red Ginseng Extract Attenuates 3-Nitropropionic Acid-Induced Huntington's-Like Symptoms. *Evid. Based Complement Alternat. Med.* 2013:237207. doi: 10.1155/2013/237207

Jansen, A. H., van Hal, M., Op den Kelder, I. C., Meier, R. T., de Ruiter, A. A., Schut, M. H., et al. (2017). Frequency of nuclear mutant huntingtin inclusion formation in neurons and glia is cell-type-specific. *Glia* 65, 50–61. doi: 10.1002/glia.23050

Kabba, J. A., Xu, Y., Christian, H., Ruan, W., Chenai, K., Xiang, Y., et al. (2018). Microglia: housekeeper of the central nervous system. *Cell Mol. Neurobiol.* 38, 53–71. doi: 10.1007/s10571-017-0504-2

Kadiu, I., Glanzer, J. G., Kipnis, J., Gendelman, H. E., and Thomas, M. P. (2005). Mononuclear phagocytes in the pathogenesis of neurodegenerative diseases. *Neurotox Res.* 8, 25–50. doi: 10.1007/bf03033818

Klein, R. L., Dayton, R. D., Tatom, J. B., Henderson, K. M., and Henning, P. P. (2008). AAV8, 9, Rh10, Rh43 vector gene transfer in the rat brain: effects of serotype, promoter and purification method. *Mol. Ther.* 16, 89–96. doi: 10.1186/1471-2202-15-28

Kwon, I., and Schaffer, D. V. (2008). Designer gene delivery vectors: molecular engineering and evolution of adeno-associated viral vectors for enhanced gene transfer. *Pharm. Res.* 25, 489–499. doi: 10.1007/s11095-007-9431-0

Landis, S. C., Amara, S. G., Asadullah, K., Austin, C. P., Blumenstein, R., Bradley, E. W., et al. (2012). A call for transparent reporting to optimize the predictive value of preclinical research. *Nature* 490, 187–191. doi: 10.1038/nature11556

Lee, M. J., Bing, S. J., Choi, J., Jang, M., Lee, G., Lee, H., et al. (2016a). IKKβ-mediated inflammatory myeloid cell activation exacerbates experimental autoimmune encephalomyelitis by potentiating Th1/Th17 cell activation and compromising blood brain barrier. *Mol. Neurodegener.* 11:54. doi: 10.1186/s13024-016-0116-1

Lee, M. J., Jang, M., Choi, J., Lee, G., Min, H. J., Chung, W. S., et al. (2016b). Bee venom acupuncture alleviates experimental autoimmune encephalomyelitis by upregulating regulatory T cells and suppressing Th1 and Th17 responses. *Mol. Neurobiol.* 53, 1419–1445. doi: 10.1007/s12035-014-9012-2

Lobsiger, C. S., and Cleveland, D. W. (2007). Glial cells as intrinsic components of non-cell-autonomous neurodegenerative disease. *Nat. Neurosci.* 10, 1355–1360. doi: 10.1038/nn1988

Main, B. S., and Minter, M. R. (2017). Microbial immuno-communication in neurodegenerative diseases. *Front. Neurosci.* 11:151. doi: 10.3389/fnins.2017.00151

Menalled, L., and Brunner, D. (2014). Animal models of Huntington's disease for translation to the clinic: best practices. *Mov. Disord.* 29, 1375–1390. doi: 10.1002/mds.26006

Parker, J. A., Connolly, J. B., Wellington, C., Hayden, M., Dausset, J., and Neri, C. (2001). Expanded polyglutamines in *Caenorhabditis elegans* cause axonal abnormalities and severe dysfunction of PLM mechanosensory neurons without cell death. *Proc. Natl. Acad. Sci. USA* 98, 13318–13323. doi: 10.1073/pnas.231476398

Perry, G. M., Tallaksen-Greene, S., Kumar, A., Heng, M. Y., Kneynsberg, A., van Groen, T., et al. (2010). Mitochondrial calcium uptake capacity as a therapeutic target in the R6/2 mouse model of Huntington's disease. *Hum. Mol. Genet.* 19, 3354–3371. doi: 10.1093/hmg/ddq247

Pouladi, M. A., Morton, A. J., and Hayden, M. R. (2013). Choosing an animal model for the study of Huntington's disease. *Nat. Rev. Neurosci.* 14, 708–721. doi: 10.1038/nrn3570

Ruiz, M., and Déglon, N. (2012). Viral-mediated overexpression of mutant huntingtin to model HD in various species. *Neurobiol. Dis.* 48, 202–211. doi: 10.1016/j.nbd.2011.08.023

Saraiva, J., Nobre, R. J., and Pereira de Almeida, L. (2016). Gene therapy for the CNS using AAVs: The impact of systemic delivery by AAV9. *J. Control Release* 241, 94–109. doi: 10.1016/j.jconrel.2016.09.011

Schilling, G., Becher, M. W., Sharp, A. H., Jinnah, H. A., Duan, K., Kotzuk, J. A., et al. (1999). Intranuclear inclusions and neuritic aggregates in transgenic mice expressing a mutant N-terminal fragment of huntingtin. *Hum. Mol. Genet.* 8, 397–407. doi: 10.1093/hmg/8.3.397

Schilling, G., Savonenko, A. V., Klevytska, A., Morton, J. L., Tucker, S. M., Poirier, M., et al. (2004). Nuclear-targeting of mutant huntingtin fragments produces Huntington's disease-like phenotypes in transgenic mice. *Hum. Mol. Genet.* 13, 1599–1610. doi: 10.1093/hmg/ddh175

Senut, M. C., Suhr, S. T., Kaspar, B., and Gage, F. H. (2000). Intraneuronal aggregate formation and cell death after viral expression of expanded polyglutamine tracts in the adult rat brain. *J. Neurosci.* 20, 219–229. doi: 10.1523/jneurosci.20-01-00219.2000

Watakabe, A., Ohtsuka, M., Kinoshita, M., Takaji, M., Isa, K., Mizukami, H., et al. (2015). Comparative analyses of adeno-associated viral vector serotypes 1, 2, 5, 8 and 9 in marmoset, mouse and macaque cerebral cortex. *Neurosci. Res.* 93, 144–157. doi: 10.1016/j.neures.2014.09.002

Wyant, K. J., Ridder, A. J., and Dayalu, P. (2017). Huntington's disease-update on treatments. *Curr. Neurol. Neurosci. Rep.* 17:33. doi: 10.1007/s11910-017-0739-9

Conflict of Interest Statement: The authors declare that the research was conducted in the absence of any commercial or financial relationships that could be construed as a potential conflict of interest.

frontiers in Cellular Neuroscience

ORIGINAL RESEARCH
published: 18 July 2018
doi: 10.3389/fncel.2018.00214

Adapentpronitrile, a New Dipeptidyl Peptidase-IV Inhibitor, Ameliorates Diabetic Neuronal Injury Through Inhibiting Mitochondria-Related Oxidative Stress and Apoptosis

*Lu Yang[1†], Wenli Han[2†], Ying Luo[1], Xiangnan Hu[3], Ying Xu[4], Huan Li[1], Congli Hu[1], Dan Huang[5], Jie Ma[1], Yang Yang[1], Qi Chen[1], Yuke Li[1], Jiahua Zhang[1], Hui Xia[1], Zhihao Chen[1], Hong Wang[1], Dongzhi Ran[1] and Junqing Yang[1]**

[1] Department of Pharmacology, The Key Laboratory of Biochemistry and Molecular Pharmacology, Chongqing Medical University, Chongqing, China, [2] Laboratory Animal Center, Chongqing Medical University, Chongqing, China, [3] Department of Pharmacology, The Laboratory of Pharmaceutical Chemistry, Chongqing Medical University, Chongqing, China, [4] Department of Pharmaceutical Sciences, School of Pharmacy and Pharmaceutical Sciences, University at Buffalo, The State University of New York (SUNY), Buffalo, NY, United States, [5] Department of Pharmacology, The Laboratory of Pharmaceutical Analysis, Chongqing Medical University, Chongqing, China*

OPEN ACCESS

Edited by:
Sriharsha Kantamneni, University of Bradford, United Kingdom

Reviewed by:
Krishnan Prabhakaran, Norfolk State University, United States
Deep R. Sharma, SUNY Downstate Medical Center, United States

***Correspondence:**
Junqing Yang
cqyangjq@cqmu.edu.cn; cqjqyang2004@aliyun.com

[†]Co-first authors

Received: *18 March 2018*
Accepted: *28 June 2018*
Published: *18 July 2018*

Citation:
Yang L, Han W, Luo Y, Hu X, Xu Y, Li H, Hu C, Huang D, Ma J, Yang Y, Chen Q, Li Y, Zhang J, Xia H, Chen Z, Wang H, Ran D and Yang J (2018) Adapentpronitrile, a New Dipeptidyl Peptidase-IV Inhibitor, Ameliorates Diabetic Neuronal Injury Through Inhibiting Mitochondria-Related Oxidative Stress and Apoptosis. Front. Cell. Neurosci. 12:214. doi: 10.3389/fncel.2018.00214

Our previous studies indicated that adapentpronitrile, a new adamantane-based dipeptidyl peptidase-IV (DPP-IV) inhibitor, has a hypoglycemic effect and ameliorates rat pancreatic β cell dysfunction in type 2 diabetes mellitus through inhibiting DPP-IV activity. However, the effect of adapentpronitrile on the neurodegenerative diseases has not been studied. In the present study, we first found that adapentpronitrile significantly ameliorated neuronal injury and decreased amyloid precursor protein (APP) and amyloid beta (Aβ) expression in the hippocampus and cortex in the high fat diet/STZ rat model of diabetes. Furthermore, adapentpronitrile significantly attenuated oxidative stress, downregulated expression of the pro-apoptotic proteins BAX, cytochrome c, caspase-9, and caspase-3, and upregulated expression of the anti-apoptotic protein Bcl-2, although there was no effect on GLP-1R expression. At 30 min post-injection of adapentpronitrile (50 mg/kg) *via* the tail vein, its concentration in normal rat brain was 0.2034 ± 0.0094 μg/g. Subsequently, we further confirmed the neuroprotective effects and mechanism of adapentpronitrile in HT22 cells treated with high glucose (HG) and aluminum maltolate [Al(mal)$_3$] overload, respectively. Our results showed significant decreases in mitochondrial membrane potential (MTP) and Bcl-2 expression, accompanied by a significant increase in apoptosis, reactive oxygen species (ROS) generation, and the expression of pro-apoptotic proteins in HT22 cells exposed to these stimuli. Adapentpronitrile treatment protected against neuronal injury, suppressed ROS generation, and reduced MTP and mitochondrial apoptosis in HT22 cells; however, DPP-IV activity was not detected. Our results suggest that adapentpronitrile protects against diabetic neuronal injury, at least partially, by inhibiting mitochondrial oxidative stress and the apoptotic pathway in a DPP-IV-independent manner.

Keywords: adapentpronitrile, DPP-IV inhibitor, neuron injury, mitochondrial apoptosis pathway, reactive oxygen species

INTRODUCTION

Diabetes is a multifactorial metabolic disease characterized by hyperglycemia and high morbidity. The incidence of diabetes has increased sharply in the last decade. Cognitive impairment induced by neuronal injury is one of the chronic complications of diabetes (Maher and Schubert, 2009; Biessels and Reagan, 2015; Baglietto-Vargas et al., 2016). Epidemiological studies show that diabetes significantly increases the risk of dementia and may finally develop into Alzheimer's disease. β-Amyloid peptide (Aβ), a neuropathological hallmark of AD, is accumulated in specific brain regions (Hardy and Selkoe, 2002). Recent research demonstrates that insulin increases extracellular Aβ levels by elevating its secretion from neurons or modulating γ-secretase activity, and decreasing Aβ degradation by inhibiting Aβ-degrading enzymes (Gasparini et al., 2002; Phiel et al., 2003; Qiu and Folstein, 2006; Dineley et al., 2014). In addition, numerous studies have demonstrated that oxidative stress and mitochondrial abnormalities are common to the etiologies of both diabetes and Alzheimer's disease (Bosco et al., 2011; Moreira, 2012). Hence, anti-diabetic agents might have important clinical and social value in the treatment of AD.

Mitochondria are essential organelles with multiple functions in energy metabolism, reactive oxygen species (ROS) generation, and apoptosis induction. Neurodegenerative diseases, which are induced by inflammation, oxidative stress, and metal and glucose toxicity, are usually accompanied by mitochondrial dysfunctions (Lin and Beal, 2006; Kumar and Gill, 2009; Verdile et al., 2015; Kandimalla et al., 2016; Koliaki and Roden, 2016). Furthermore, abnormal Aβ and tau proteins were shown to have a direct impact on mitochondrial function (Schmitt et al., 2012). Amyloid precursor proteins (APP) accumulates in mitochondrial import channels, thereby resulting in mitochondrial dysfunction (Devi et al., 2006). DuBoff et al. (2012) revealed that mitochondrial elongation was significantly increased in hippocampal neurons from tau transgenic mice. Thus, mitochondrial dysfunction is implicated as a critical step toward neuronal death.

Although ROS play a vital role in cellular survival and signaling pathways at physiological condition (cellular cycle regulation, phagocytosis, and enzyme activation), excessive ROS lead to a series of harmful effects including DNA, lipid and protein damage, mitochondrial dysfunction, or even cell death (Knock and Ward, 2011; Verbon et al., 2012; Son et al., 2013). Because mitochondria are both targets and sources of ROS, oxidant-induced mitochondrial dysfunction may lead to an increased production of superoxide anion radicals by the electron transport chain, thereby triggering a "vicious cycle" (Wallace, 2005). Oxidative stress is an important causative factor in the pathogenesis of aging, diabetes, and neurodegenerative diseases, which also cause remarkable accumulation of Aβ (Smith et al., 2007; Valko et al., 2007; Chen et al., 2012; Manoharan et al., 2016). In fact, persistent mitochondrial dysfunction and oxidative stress contribute to apoptosis *via* the mitochondria-dependent caspase cascade induced by the release of cytochrome c into the cytosol (Wallace, 2005).

The incretin hormone glucagon-like-peptide 1 (GLP-1), secreted by enteroendocrine L-cells in response to ingestion of nutrients, plays an important role in stimulating insulin secretion, ameliorating glycemic control, and repairing β-cell function. Since GLP-1 is degraded rapidly by dipeptidyl peptidase-IV (DPP-IV), the inhibitors of which have been regarded as appropriate agents to maintain blood glucose levels. Pipatpiboon et al. (2013) found that DPP-IV inhibitor vildagliptin could increase GLP-1 levels in both plasma and brain, restore neuronal insulin receptor function, and prevent brain mitochondrial dysfunction, thus ameliorating cognitive function caused by high-fat diet (HFD) consumption. Saxagliptin ameliorates Aβ, tau phosphorylation, and inflammatory markers in a streptozotocin-induced model of Alzheimer's disease by increasing GLP-1 levels in the hippocampus (Kosaraju et al., 2013). Saxagliptin is also regarded as a novel therapeutic target for Parkinson's disease *via* antioxidant, anti-inflammatory, and antiapoptotic mechanisms (Nassar et al., 2015). However, the lack of evidence demonstrating the ability of these DPP-IV inhibitors to penetrate the blood–brain barrier (Golightly et al., 2012), and the role of DPP-IV inhibitors in the neuroprotective mechanisms remain to be clarified.

Our previous study showed that adapentpronitrile (APPN, CMD-05), an adamantane-based anti-diabetic agent synthesized in our laboratory, exerted DPP-IV inhibitory activity *in vitro*, and also mediated hypoglycemic functions in diabetic rats (Ma et al., 2017). Considering the neuroprotective effects of vildagliptin and saxagliptin, we hypothesized that the new DPP-IV inhibitor adapentpronitrile represents a novel agent for the protection against neurodegenerative disease and neuronal injury. The aim of the present study was to investigate the neuroprotective effect and mechanisms of adapentpronitrile in diabetic rat from the flowing aspects: (1) the effects of adapentpronitrile on the neuronal injury were observed in diabetic rat induced by HFD/STZ and in HT22 cells induced by HG/aluminum maltolate [$Al(mal)_3$]. (2) To primarily explore the mechanism of adapentpronitrile in neuronal injury. (3) Whether the neuroprotective mechanism of adapentpronitrile was related to the classic DPP-IV-dependent pathway, the adapentpronitrile concentration, and GLP-1R expression in rat brain and the DPP-IV activity in HT22 cells were detected.

MATERIALS AND METHODS

Chemicals

Adapentpronitrile (CMD-05; 98.9% purity) was synthesized by Laboratory of pharmaceutical chemistry, Chongqing Medical University (Patent apply number: 201610818878.5), and its purity was detected by high-performance liquid chromatography (HPLC).

Animals and Protocol

Sprague-Dawley (SD) male rats were obtained from Animal Laboratory Administrative Center, Chongqing Medical University (Chongqing, China), and housed in the barrier housing facility (SPF scale), which according with national

standard "Laboratory Animal-Requirements of Environment and Housing Facilities." The care and experimental operation of animal have conforming to "Chongqing Administration Rule of Laboratory Animal." The experimental procedures were approved by the animal laboratory administrative center and the institutional ethics committee of Chongqing Medical University (License number: SYXK YU 2012-0001) and also in accordance with the National Institutes of Health guidelines. All experiments reviewed and approved by the Instructional Animal Care and Use Committee (IACUC).

The experiments were performed in 70 male rats (aged 9 weeks, 80–100 g). The rats were housed in controlled conditions of temperature (22 ± 2°C), relative humidity (50 ± 10%), and 12/12-h light/dark cycle with water *ad libitum*. After a week of acclimation, 10 rats were randomly selected and fed with basal diet as the control group, 60 rats were fed a HFD (20% sugar, 10% lard, 10% egg yolk, and 60% basal feed) for 4 weeks to induce insulin resistance (Ma et al., 2017). Diabetes was induced by a single intraperitoneal injection of streptozotocin (Solarbio, China, S8050; STZ, 30 mg/kg), which is particularly toxic to pancreatic beta cells in mammals. Control rats were injected with the same volume of vehicle (citrate buffer solution). Hyperglycemia was defined as blood glucose >16.7 mmol/L, 72 h after STZ injection. Diabetic rats were maintained on the HFD for 4 weeks and randomly divided into following groups (n = 7): HFD/STZ group (0.5% CMC-Na), low dose group (adapentpronitrile 1.5 mg/kg), high dose group (adapentpronitrile 4.5 mg/kg). The dose of adapentpronitrile was based on our previous study (Ma et al., 2017). Diabetic rats in the adapentpronitrile groups were chronically administered adapentpronitrile (4.5 or 1.5 mg/kg) for 30 days *via* the intragastric route, while the control and model groups received the same amount of vehicle (0.5% CMC-Na; **Figure 1**).

After administration, three rats in each group were randomly selected and used for histopathological examination, and the remaining four rats were used for biochemical examination and Western blot.

HE Staining Observation

Three rats in each group were randomly selected and transcardially perfused with phosphate-buffered saline (PBS). Then, the brain tissues were isolated and fixed overnight in 4% paraformaldehyde. After embedded by paraffin, serial sections (5 μm) of brain tissue were obtained, which were stained by hematoxylin–eosin (HE). Proceed as follows: dewaxing in xylen, hydration in alcohols, HE staining, dehydration in alcohols, transparent in xylen and mounting with neutral resins. Ten consecutive fields were selected randomly from the hippocampal and cortical neurons, and the morphological changes were observed under an optical microscope (Olympus, Japan) at 400× magnification (Guo et al., 2016).

Measurement of SOD Activity and MDA Content

After anesthesia of another four rats in each group, the cortex and hippocampus were separated on an ice plate and washed by normal saline. Then the isolated tissues were dried and stored at −80°C until use. The superoxide dismutase (SOD) activity and malondialdehyde (MDA) content were measured using the Total Superoxide Dismutase Assay Kit (Beyotime, China, S0101) and the Lipid Peroxidation MDA Assay Kit (Beyotime, China, S0131), respectively. The protein content was determined using the BCA Protein Assay Kit (Beyotime, China, P0010S).

Measurement of Adapentpronitrile Concentration

Male SD rats (200–220 g) were injected a single dose of adapentpronitrile (50 mg/kg, n = 4) *via* tail vein after fasting 12 h. At 30 min post-injection, blood samples were collected from abdominal aorta and the brain tissues were isolated on ice (Ma et al., 2017). Plasma was obtained after centrifugation. Then the plasma and isolated brain tissues were stored at −80°C until used.

Pipette 100-μL plasma samples and 200-μL acetonitrile [containing 500-ng internal standard (IS)] into 1.5-ml eppendorf tube. After that, the mixture was centrifuged for supernatant at 12,000 × g for 15 min at 4°C.

The brain tissues were weighed and homogenized in a twofold volume of acetonitrile containing 500 ng. Briefly, acetonitrile was used to homogenize brain tissue according to a ratio of 2-mL acetonitrile to 1-g tissue sample. The homogenates were centrifuged for supernatant at 12,000 × g for 15 min at 4°C.

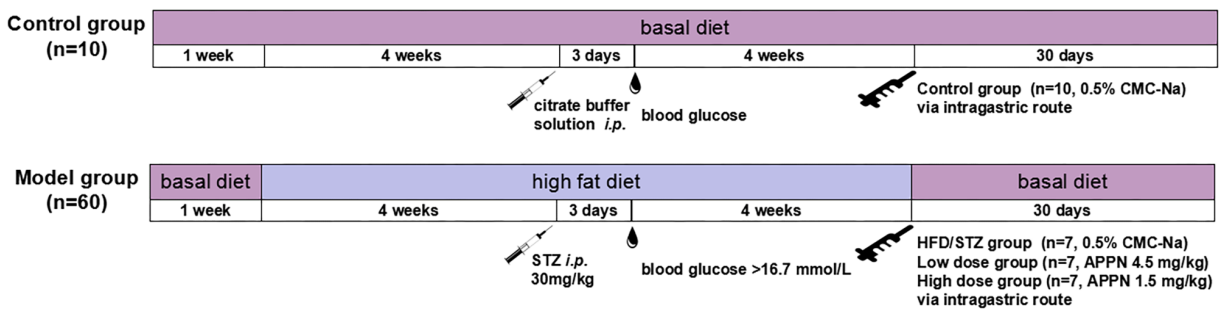

FIGURE 1 | The general procedure of this study *in vivo*.

Adapentpronitrile concentration in plasma and brain were determined using an HPLC system equipped with a UV detector. An octadecyl endcapped Phecda-C_{18} column (250 mm × 4.5 mm, 5-μm particle size) and Waters universal injector (100 μL capacity) were used. The optimum mobile phase was identified and consisted of acetonitrile and 10 mmol/L ammonium acetate (40:60, vol/vol). Samples (50 μL) were injected and a flow rate of 1 mL/min was equilibrated. The elution was monitored at 204 nm. The system was operated at the ambient temperature. Calibration curve was constructed by plotting standard peak area vs. concentration. Recoveries were calculated as the ratio of peak-area of the analyte from the fortified samples to the corresponding peak-area ratio of standard solutions.

Cell Culture

Immortalized murine hippocampal HT22 cell lines were obtained from BNCC, China. HT22 cells were cultured in DME/F12 medium (Hyclone, United States) supplemented with 10% fetal bovine serum (FBS; Hyclone, United States) and 1% 100× penicillin–streptomycin (Gibco, United States) at 37°C and 5% CO_2.

In Vitro Glucose (HG)/Al(mal)$_3$ Overload Model

HT22 cells were plated in 96-well plates (8×10^4 neurons/mL). The cells were divided into the control group (mannitol 100 mM) and four HG overloaded groups (glucose 25–100 mM). The cells were divided into the control group (maltol 600 μM) and four aluminum overloaded groups [Al(mal)$_3$ 50–400 μM; Ma et al., 2016]. After incubation, the relevant indicators were detected and the optimum concentrations of HG and Al(mal)$_3$ were selected in following experiments.

HT22 cells were divided into the control, HG overload and adapentpronitrile intervention groups induced by HG. HT22 cells were divided into the control group, Al(mal)$_3$ overloaded groups and adapentpronitrile intervention groups induced by Al(mal)$_3$. After incubation, the relevant indicators were detected in following experiments.

MTT Assay

HT22 cells were cultured in the 96-well plates at 8×10^4 cells/mL and subjected to HG or Al(mal)$_3$ as described above. After the intervention, 3-(4,5-dimethyl-thiazol-2-yl)-2,5-diphenyl-tetrazolium bromide (MTT, 20 μL, 5 mg/ml; Sigma, United States, M2128) was added per well. After 4 h of incubation, the medium was removed, and 150 μL dimethyl sulfoxide (DMSO) was added to solubilize the purple formazan. Then, the plate shook slowly on the horizontal shaking table free from light for 10 min at room temperature. Finally, optical density (OD) was detected at 490 nm using a microplate reader (BioTek, United States; Lobner, 2000).

LDH Leakage Rate Detection

Cell death was evaluated using the lactate dehydrogenase (LDH) Cytotoxicity Assay Kit (Beyotime, China, C0017). HT22 cells were cultured in 96-well plates at 5×10^4 cells/ml. After HG or Al(mal)$_3$ treatment for 36 h, the LDH leakage rate in the cell culture supernatant was measured according to the manufacturer's instruction.

Flow Cytometry Analysis

HT22 cells were seeded in six-well plates at 8×10^4 cells/mL and exposed to HG or Al(mal)$_3$ as described above. After the incubation period, cells were trypsinized without EDTA, collected and suspended in 1 ml PBS. Apoptosis was determined by flow cytometry using the Annexin V-FITC/propidium iodide (annexin V/PI) apoptosis detection kits according to the manufacturer's protocol. Three separate experiments were performed.

Transmission Electron Microscopy Observation

The changes in mitochondrial ultrastructure were confirmed by transmission electron microscopy (TEM) examination. After treatment, HT22 cells were collected and fixed in glutaraldehyde solution at 4°C. The fixed samples were sent to the electron microscope center of Chongqing Medical University for microscopic observed and photographed.

DPP-IV Activity Determination

Supernatant of HT22 cells and lysed HT22 cells were collected to measure DPP-IV activity in control group. Culture medium and equivoluminal lysis buffer were collected and regarded as blank group. DPP-IV enzyme assay was carried out according to the manufacturer's instructions. DPP-IV Activity Assay Kits (AnaSpec, United States, AS-24098) were used according the manufacturer's instructions. In this assay, DPP4 cleaves a substrate [H-Gly-Pro-7-amino-4-methyl coumarin (AMC)] to release a quenched fluorescent group, AMC, which can be easily detected using a fluorescence microplate reader at excitation and emission wavelengths of 354 and 442 nm, respectively.

TUNEL Assays

HT22 cells were cultured in cover slides and washed in ice-cold PBS. Samples were fixed with 4% paraformaldehyde for 15 min and permeabilized in PBS containing proteinase K for 3 min at room temperature. Apoptosis was determined using TUNEL FITC Apoptosis Detection Kits (Vazyme Biotech, China, A111-02) according to the manufacturer's protocol. Apoptotic cells were observed using a fluorescence microscopy. Four consecutive fields were selected randomly and the apoptosis rate was calculated as the ratio of the number of apoptotic cells to the total number of cells (expressed as a percentage).

Mitochondrial ROS Assay

Mitochondrial ROS levels were measured using ROS Assay Kits (Beyotime, China, S0033). 2′,7′-Dichloro-dihydro-fluorescein diacetate (DCFH-DA) is a non-fluorescent probe that can be oxidized to the highly fluorescent derivative DCF by intracellular

ROS. The cells were stained with 2-μM DCFH-DA and incubated at 37°C for 20 min. Four consecutive fields were selected randomly and the fluorescence intensity was measured under a fluorescence microscope after removal of the culture medium.

Mitochondrial Membrane Potential ($\Delta\psi_m$) Assay

The mitochondrial membrane potential (MMP, $\Delta\psi_m$) was measured using Mitochondrial Membrane Potential Assay Kits with JC-1 (Beyotime, China, C2006). JC-1, a cationic fluorescent dye, can be accumulated in the mitochondrial matrix to form polymer, which gives off a strong red fluorescence. At low MMP, JC-1 exists in the form of monomer in the cytoplasm and yields green fluorescence. The cells were strained with JC-1 dye at 37°C for 20 min. After washing with dilution buffer, four consecutive fields were selected randomly and the fluorescence intensity was measured under a fluorescence microscope.

Western Blot Analysis

After treatment, HT22 cells were washed in ice-cold PBS and lysed by RIPA lysis buffer containing phosphatase and protease inhibitors. The samples were collected and centrifuged at 12,000 × *g* and 4°C for 15 min, after incubated for 20 min on ice. The supernatant was collected and the total protein concentrations were measured with a BCA protein assay kit (Beyotime, China, P0010S). Loading buffer (Beyotime, China, P0015L) was added into the remaining supernatant and boiled at 100°C for 10 min. Ultimately, samples were stored at −20°C for further research.

Forty milligrams of rat cortex or hippocampus (n = 4) was added to 0.4 ml of RIPA Lysis Buffer for protein extraction and was centrifuged at 12,000 × *g* for 15 min at 4°C after homogenization. The supernatant was collected and determined with the BCA protein assay kit (Beyotime, China, P0010S) for protein concentrations. The remaining supernatant was mixed with Loading buffer (Beyotime, China, P0015L) and boiled at 100°C for 10 min. Finally, samples were stored at −20°C for further research.

According to the Cell Mitochondrial Isolation kit (Beyotime, China, C3601), the mitochondria can be separated quickly and conveniently, and the cytoplasmic protein can be obtained to study the release of mitochondrial proteins to the cytoplasm, such as cytochrome c.

Equal amounts of protein (20 mg) were separated by sodium dodecyl sulfate polyacrylamide gel electrophoresis (SDS–PAGE). The proteins were then transferred to PVDF membranes (Millipore, United States) and blocked with 5% bovine serum albumin (BSA) in Tris-buffered saline/Tween-20 (TBST) buffer for 4 h at room temperature. Membranes were probed overnight at 4°C with primary antibodies for specific detection of APP (dilution 1:500; Boster, China, BA0581), Aβ (dilution 1:1000; Abcam, United Kingdom, ab62658), GLP-1R (dilution 1:500, Bioss, China, bs-1559R), Bcl-2 (dilution 1:500; Abcam, United Kingdom, ab196495), Bax (dilution 1:400; Proteintech, China, 50599-2-Ig), cytochrome c (dilution 1:1000; Abcam, United Kingdom, ab133504), caspase-9 (dilution 1:1000; Abcam, United Kingdom, ab184786), caspase-3 (dilution 1:1000; Abcam, United Kingdom, ab184787), and β-actin (dilution 1:3000; Proteintech, United States, 60008-1-Ig; **Table 1**). The blots were incubated with HRP-conjugated secondary antibodies (dilution 1:2000; **Table 1**) at room temperature for 1 h. Finally, immunoreactive bands were visualized by ECL (Bio-Rad, United States) and quantified using Image Lab software (Bio-Rad, United States). All experiments were performed in triplicate.

Statistical Analysis

All investigators were complete randomization in the implementation process of experiments. All experiments were repeated at least four times, and representative results are shown. Data were presented as mean ± SD. Statistical analysis was carried out using SPSS 17.0 (SPSS Inc. Chicago, IL, United States). Normal distribution of data and homogeneity of variance were determined by Shapiro–Wilk test and one-way analysis of variance (ANOVA) test, respectively, followed

TABLE 1 | List of primary and secondary antibodies used in the study.

	Host	Dilution	Supply	Cat. No.	Application
Primary antibody					
APP	Rabbit	1:500	Boster	BA0581	WB
Aβ	Rabbit	1:1000	Abcam	ab62658	WB
GLP-1R	Rabbit	1:500	Bioss	bs-1559R	WB
Bcl-2	Rabbit	1:500	Abcam	ab196495	WB
Bax	Rabbit	1:400	Proteintech	50599-2-Ig	WB
Cytochrome c	Rabbit	1:1000	Abcam	ab133504	WB
Caspase-9	Rabbit	1:1000	Abcam	ab184786	WB
Caspase-3	Rabbit	1:1000	Abcam	ab184787	WB
β-Actin	Mouse	1:3000	Proteintech	60008-1-Ig	WB
Secondary antibody					
Anti-mouse HRP	Goat	1:2000	Proteintech	SA00001-1	WB
Anti-rabbit HRP	Goat	1:2000	Proteintech	SA00001-2	WB

by Dunnett-t type multiple comparison tests. $P < 0.05$ was considered to indicate statistical significance.

RESULTS

Effects of Adapentpronitrile on Pathomorphology and the Expression of APP and Aβ Proteins in Hippocampus and Cortex of Rat

Histopathological examination revealed that the neurons were in clear and intact structure, and arranged regularly in the control group. By contrast, HFD/STZ group showed severe hippocampal and cortical neurons injuries including karyopyknosis, hyperchromatic nuclei, and cell loss. Administration of adapentpronitrile (4.5 mg/kg) obviously ameliorated the pathomorphological injury in the hippocampus and cortex (**Figure 2A**).

As shown in **Figure 2B**, the expression of APP and Aβ proteins elevated significantly in HFD/STZ-treated rat, while adapentpronitrile (4.5 mg/kg) significantly blunted the changes of APP and Aβ protein expressions.

Effects of Adapentpronitrile on Oxidative Stress in the Hippocampus and Cortex of Rat

Both hippocampal and cortex SOD activity in HFD/STZ group significantly decreased compared with the control group. Adapentpronitrile treatment reversed the decrease of SOD activity (**Figure 3A**). Both hippocampal and cortex MDA content in HFD/STZ group significantly increased compared with the control group. Adapentpronitrile administration significantly blunted the increase of MDA content in HFD/STZ rats (**Figure 3B**).

Effects of Adapentpronitrile on GLP-1R and Mitochondria-Dependent Apoptosis Protein Expression Induced by HFD/STZ in the Rat Hippocampus and Cortex

Glucagon-like-peptide 1 is an incretin hormone, which plays a role in controlling synaptic plasticity and reversing memory impairment. As shown in **Figure 4**, there were no significant difference among these four groups in the protein expressions of GLP-1R. On the basis of this evidence, we deduced that the mechanism underlying the protective effects of adapentpronitrile may be GLP-1 independent.

Therefore, we also examined the impact of adapentpronitrile on the expression of the apoptosis-related proteins. The expression of the anti-apoptotic Bcl-2 was significantly decreased in HFD/STZ group, whereas the expressions of the pro-apoptotic proteins Bax, cytochrome c, caspase-9, and caspase-3 were significantly increased. However, all the alterations were significantly reversed by adapentpronitrile (4.5 mg/kg) treatment (**Figure 4**).

Concentration of Adapentpronitrile in the Rat Plasma and Brain Tissue

To confirm the ability of adapentpronitrile to permeate the BBB to protective against neuronal apoptosis, we used a HPLC method to determine the concentration of adapentpronitrile in rat plasma and brain tissue. According to HPLC methodology, the maximum ultraviolet absorption of adapentpronitrile is 204 nm, the quantitation limit and the detection limit were 0.03 μg/ml (S/N = 10) and 0.09 μg/ml (S/N = 3), respectively. The standard curve of adapentpronitrile had good linear relation in the range of 0.1–10 μg/mL in plasma, the equation was $Y = 0.5267X–0.0796$ ($r = 0.9997$, $n = 4$). The intra-day and inter-day precision RSD were 3.66–8.71 and 4.33–5.59%, respectively. The recovery of adapentpronitrile was 82.19 ± 6.57–118.21 ± 3.72%, and which has good stability in 48 h. The linear relation of adapentpronitrile was excellent within the range of 0.09–5 μg/ml in brain tissue; the equation was $Y = 0.325X–0.0125$ ($r = 0.9999$, $n = 4$). The intra-day and inter-day precision RSD were 1.71–5.69 and 3.77–4.54%, respectively. The recovery of adapentpronitrile was 106.68 ± 2.47–117.50 ± 5.10 and which has good stability in 48 h. These methods are stable, sensitive, and practicable for examination of adapentpronitrile distribution. As shown in **Figure 5**, HPLC-MS was confirmed to have good specificity to detect adapentpronitrile.

As shown in **Table 2**, the adapentpronitrile concentrations in plasma and brain were 2.8002 ± 0.5691 μg/100 μL and 0.2034 ± 0.0094 μg/g, respectively. Therefore, these data confirmed that adapentpronitrile permeates the BBB.

Establishment of HG Overload Model in HT22 Cells

To determine whether adapentpronitrile could protect neurons from HG injury, HT22 cells were treated with appropriate concentration of glucose (HG) to establish the neuronal damage model *in vitro*. As is shown in **Figure 6A**, treatment of glucose caused cytotoxicity in HT22 cells in a time- and concentration-dependent manner, showing that treatment of 200-μM glucose for 36 h resulted in a suitable neuronal injury model (66.24%).

The LDH leakage rate and apoptosis rate were elevated with the increase of glucose concentration, and treatment of 75-mM glucose led to a suitable LDH leakage rate (20.02%) and apoptosis rate (21.62%) for model establishment (**Figures 6B,C**).

As shown in **Figure 6D**, the cell number decreased with concentration of glucose from 25 to 100 mM, illustrating that cell proliferation was inhibited by HG.

Based on these results, the treatment of 75 mM glucose for 36 h was used in further experiments.

Adapentpronitrile Prevented HT22 Cells Against HG-Induced Cytotoxicity

Prior to explore the effect of adapentpronitrile on HG-induced cytotoxicity, the safety of adapentpronitrile on HT22 cells was evaluated by MTT assay. Treatment with adapentpronitrile at concentrations lower than 1×10^{-5} M did not caused significant cytotoxicity in HT22 cells (**Figure 7A**).

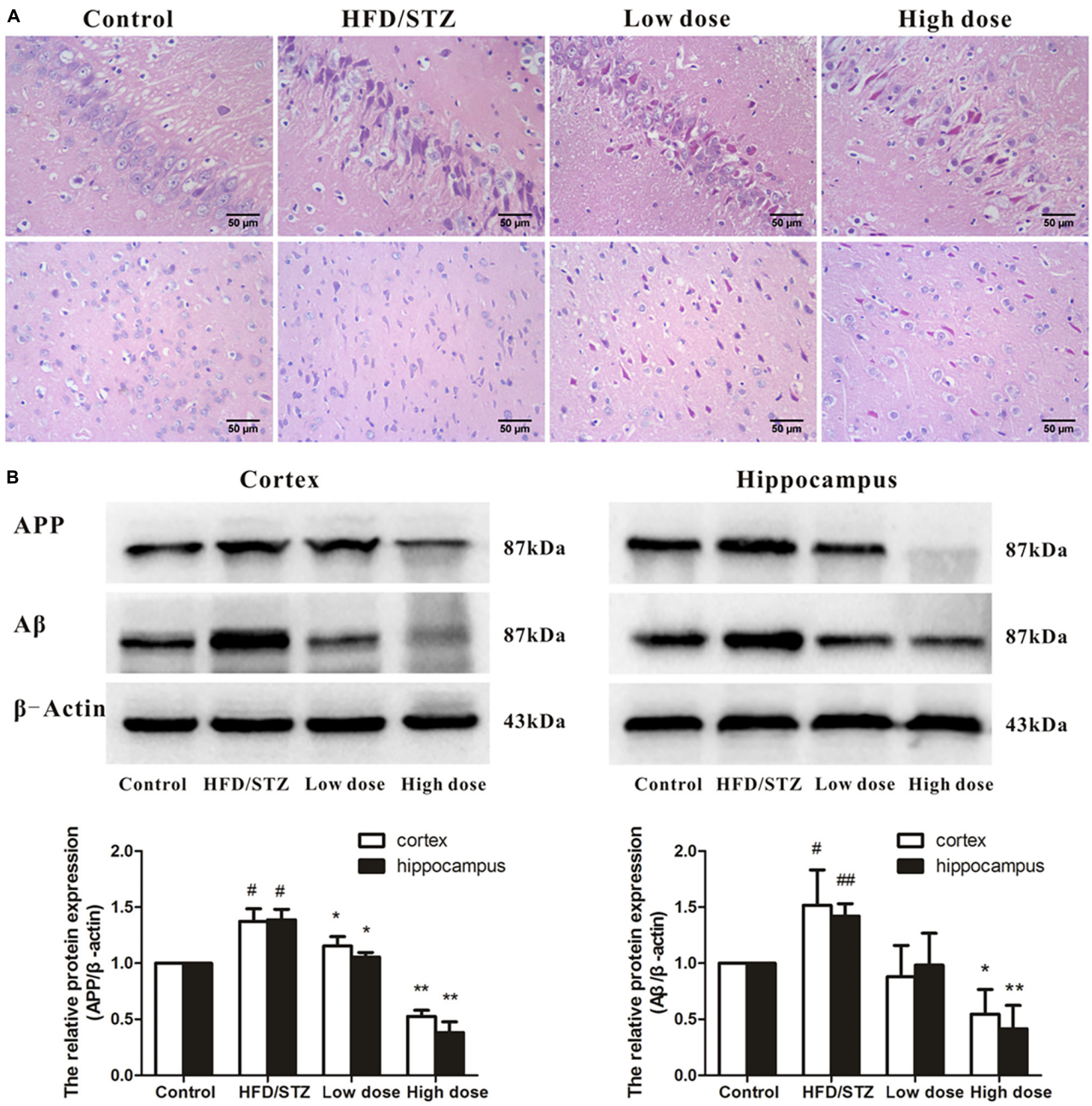

FIGURE 2 | Effects of adapentpronitrile on pathomorphology and the expression of APP and Aβ proteins in hippocampus and cortex of rat. **(A)** Representative neuronal pathomorphology in hippocampus and cortex. Sections were pictured at 400×. Scale bar = 50 μm. **(B)** The expressions of APP and Aβ proteins were measured by Western Blotting. Data were expressed as mean ± SD of four independent experiments, and were analyzed statistically using one-way ANOVA, followed by Dunnett-t type multiple comparison tests. $^{\#}P < 0.05$ and $^{\#\#}P < 0.01$ vs. Control group, respectively; $^{*}P < 0.05$ and $^{**}P < 0.01$ vs. HFD/STZ group, respectively.

The results showed that treatment with adapentpronitrile significantly increased the viability and reduced LDH leakage rate induced by HG overload in a concentration-dependent manner (**Figures 7B,C**). Treatment with adapentpronitrile (1×10^{-5} M) could ameliorate the apoptosis rate and pathomorphological change induced by 75-mM HG (**Figures 7D,E**). Therefore, these results together indicated that adapentpronitrile can inhibit neuronal apoptosis induced by HG overload *in vitro*.

DPP-IV Activity in HT22 Cells

To confirm whether dipeptidyl peptidase IV (DPP-IV) exists in HT22 cells. Supernatant from both HT22 cells incubation and the HT22 cells lysate were collected to measure DPP-IV activity

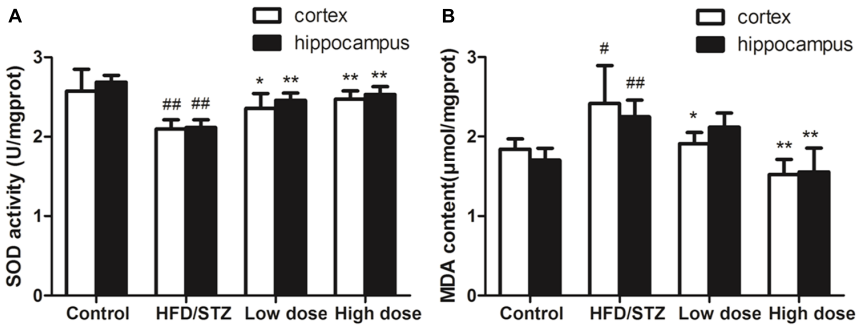

FIGURE 3 | Effects of adapentpronitrile on oxidative stress in the hippocampus and cortex of rat. **(A)** The change of SOD activity in hippocampus and cortex. **(B)** The alteration of MDA content in hippocampus and cortex. Data were expressed as mean ± SD of four independent experiments, and were analyzed statistically using one-way ANOVA, followed by Dunnett-t type multiple comparison tests. $^{\#}P < 0.05$ and $^{\#\#}P < 0.01$ vs. control group, $^{*}P < 0.05$ and $^{**}P < 0.01$ vs. HFD/STZ group, respectively.

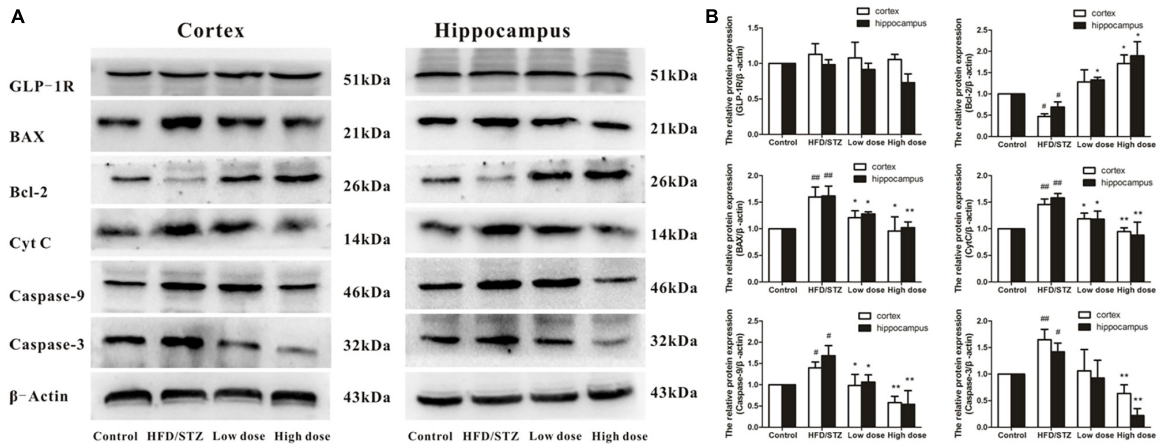

FIGURE 4 | Effects of adapentpronitrile on GLP-1R and mitochondria-dependent apoptosis protein expression induced by HFD/STZ in the rat hippocampus and cortex. **(A)** The expressions of GLP-1R and mitochondria-dependent apoptosis proteins were measured by Western Blotting. Representative images of experiments are shown. **(B)** The relative expression of GLP-1R and mitochondria-dependent apoptosis proteins were standardized to endogenous β-actin protein for each sample. Data were expressed as mean ± SD of four independent experiments, and were analyzed statistically using one-way ANOVA, followed by Dunnett-t type multiple comparison tests. $^{\#}P < 0.05$ and $^{\#\#}P < 0.01$ vs. Control group, respectively; $^{*}P < 0.05$ and $^{**}P < 0.01$ vs. HFD/STZ group, respectively.

as the control group. Equivoluminal culture medium and lysis buffer were collected and regarded as the blank group. As shown in **Figure 8**, there was no significant difference in the fluorescence intensity between the culture supernatant of HT22 cells and that of the cell-free control. There was also no significant difference in the fluorescence intensity between HT22 cell lysates and that of lysis buffer. Therefore, we concluded that DPP-IV activity was not present in HT22 cells, and indicating the protective effect of adapentpronitrile on neuronal injury *in vitro* is independent of DPP-IV.

Adapentpronitrile Protected Against HG-Induced Mitochondrial Apoptosis

As shown in **Figures 9A–C**, the numbers of TUNEL-positive cells and the ratio of green to red fluorescence of JC-1 and ROS level were significantly increased in the HG-overload group, while a reduction was noted in the adapentpronitrile-treated group.

The changes in mitochondrial ultrastructure were confirmed by TEM examination. As is shown in **Figure 9D**, in the control group, the nuclei of HT22 cells were round or oval with regular shape and evenly distributed chromatin, and the mitochondrial morphology was normal with a complete structure. In HG overload group, the chromatin was aggregated at the nuclear membrane, the mitochondrial cristae were thick and short accompanied with apoptotic bodies, thereby indicating the occurrence of mitochondrial fission; all alterations were ameliorated by adapentpronitrile treatment.

Effect of Adapentpronitrile on Mitochondria-Dependent Apoptosis-Related Protein Expression Caused by HG in HT22 Cells

As shown in **Figure 10**, exposure of HT22 cells to 75 mM HG for 36 h significantly decreased the expression of the

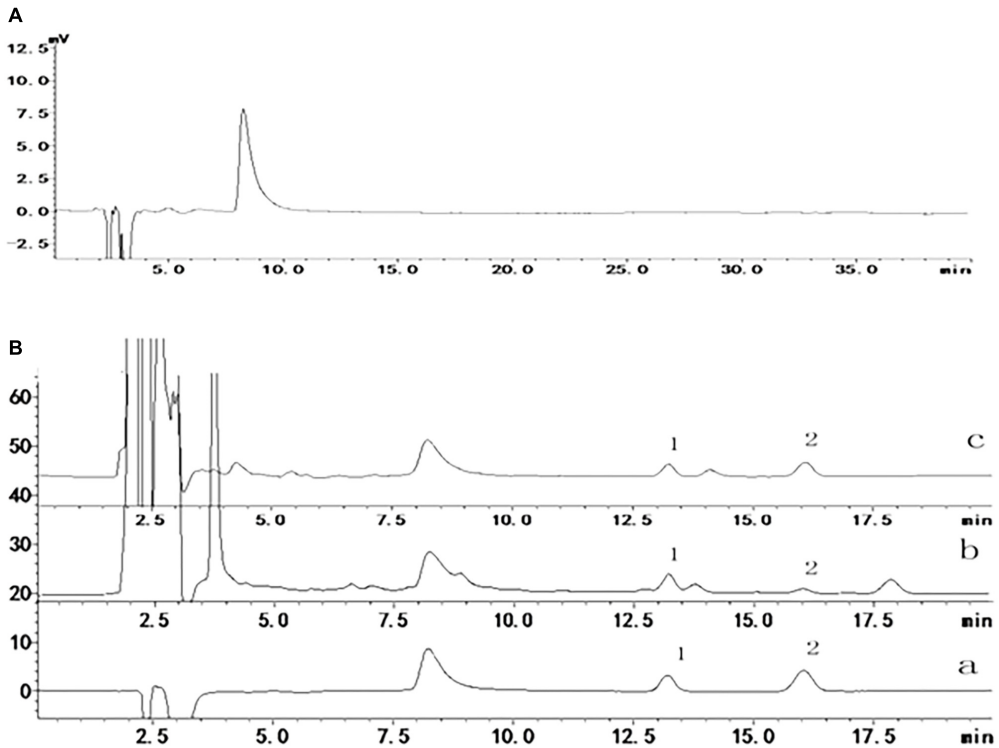

FIGURE 5 | The specificity of adapentpronitrile detected by HPLC-MS. **(A)** Acetonitrile **(B)** Sample (1) carbamazepine (2) adapentpronitrile (a) standard sample, (b) plasma, (c) brain.

anti-apoptotic protein Bcl-2 and increased the expression of the pro-apoptotic proteins Bax, cytochrome c, caspase-9, and caspase-3. All alterations in the expression of apoptosis-related proteins were reversed by adapentpronitrile treatment. Our results indicated that adapentpronitrile protects against HG-induced cell apoptosis *via* the mitochondrial apoptotic pathway.

Establishment of Al(mal)$_3$ Overload Model in HT22 Cells

To determine whether adapentpronitrile could protect neurons from non-HG injury, HT22 cells were treated with appropriate concentration of Al(mal)$_3$ to establish the neuronal damage model *in vitro*. As is shown in **Figure 11A**, treatment of Al(mal)$_3$ caused cytotoxicity in HT22 cells in a time- and concentration-dependent manner, showing that treatment of 200 μM Al(mal)$_3$ for 36 h resulted in a suitable neuronal injury model (66.24%).

The LDH leakage rate and apoptosis rates were elevated with the increase of Al(mal)$_3$ concentration, and treatment of 200 μM Al(mal)$_3$ led to a suitable LDH leakage rate (23.54%) and apoptosis rate (33.76%) for model establishment (**Figures 11B,C**).

As shown in **Figure 11D**, the cell number decreased with concentration of Al(mal)$_3$ from 50 to 400 μM, while only 400 μM Al(mal)$_3$ could contribute to a morphological change, illustrating that cell proliferation was inhibited by Al(mal)$_3$.

Based on these results, the treatment of 200 μM Al(mal)$_3$ for 36 h was used in further experiments.

TABLE 2 | Concentration of APPN in rat plasma and brain (mean ± SD, n = 4).

Sample	Unit	Concentration
Plasma	μg/ml	28.002 ± 5.691
Brain	μg/g	0.2034 ± 0.0094

Adapentpronitrile Prevented HT22 Cells Against Al(mal)$_3$-Induced Cytotoxicity

The results showed that treatment with adapentpronitrile significantly increased the viability and reduced LDH leakage rate induced by Al(mal)$_3$-overload in a concentration-dependent manner (**Figures 12A,B**). Treatment with adapentpronitrile (1×10^{-6} M) could ameliorate the apoptosis rate and pathomorphological change induced by 200 μM Al(mal)$_3$ (**Figures 12C,D**). Therefore, these results together indicated that adapentpronitrile can inhibit neuronal apoptosis induced by Al(mal)$_3$ overload *in vitro*.

Adapentpronitrile Protected Against Al(mal)$_3$-Induced Mitochondrial Apoptosis

As shown in **Figures 13A–C**, the numbers of TUNEL-positive cells, the ratio of green to red fluorescence of

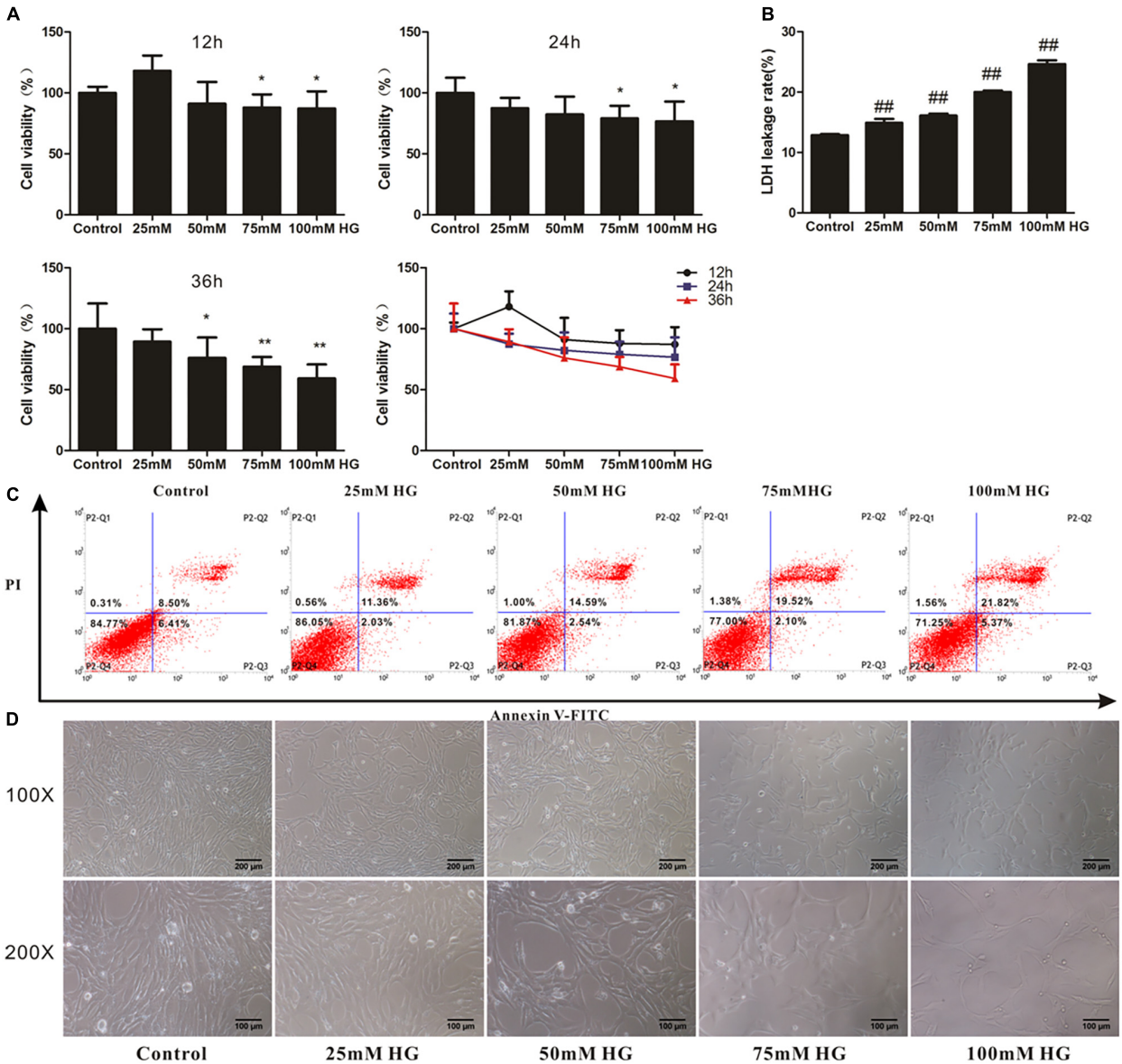

FIGURE 6 | The effects of HG overload on HT22 cells. **(A)** The viability of HT22 cells treated with different concentrations of glucose. Data were expressed as mean ± SD of six independent experiments, and were analyzed statistically using one-way ANOVA, followed by Dunnett-t type multiple comparison tests. $^{*}P < 0.05$, $^{**}P < 0.01$ vs. the control group. **(B)** The LDH leakage rate of HT22 cells treated with different concentration of glucose. Data were expressed as mean ± SD of six independent experiments, and were analyzed statistically using one-way ANOVA, followed by Dunnett-t type multiple comparison tests. $^{\#\#}P < 0.01$ vs. the control group. **(C)** The flow cytometry apoptosis analysis of HT22 cells were treated with high glucose for 36 h. The representative images of flow cytometry analysis are shown. **(D)** The cytomorphology changes in HT22 cells treated with different concentration of glucose. Representative images of experiments are shown. The magnification of images were 100× and 200×, respectively. Scale bars were 200 and 100 μm, respectively.

JC-1 and ROS level were significantly increased in the $Al(mal)_3$ overload group, while a reduction was noted in the adapentpronitrile-treated group. The photograph of TEM showed that the chromatin was aggregated at the nuclear membrane and the cristae of mitochondria was thick and short in the $Al(mal)_3$-overloaded group, which indicated that mitochondrial fission was broadly raised, while all alterations were ameliorated by adapentpronitrile treatment (**Figure 13D**).

Effect of Adapentpronitrile on Mitochondria-Dependent Apoptosis-Related Protein Expression Caused by $Al(mal)_3$ in HT22 Cells

As shown in **Figure 14**, the expression of Bcl-2 protein was significantly decreased in the $Al(mal)_3$-overload group, whereas the expressions of Bax, cytochrome c, caspase-9, and caspase-3 protein were significantly increased. All the alterations of

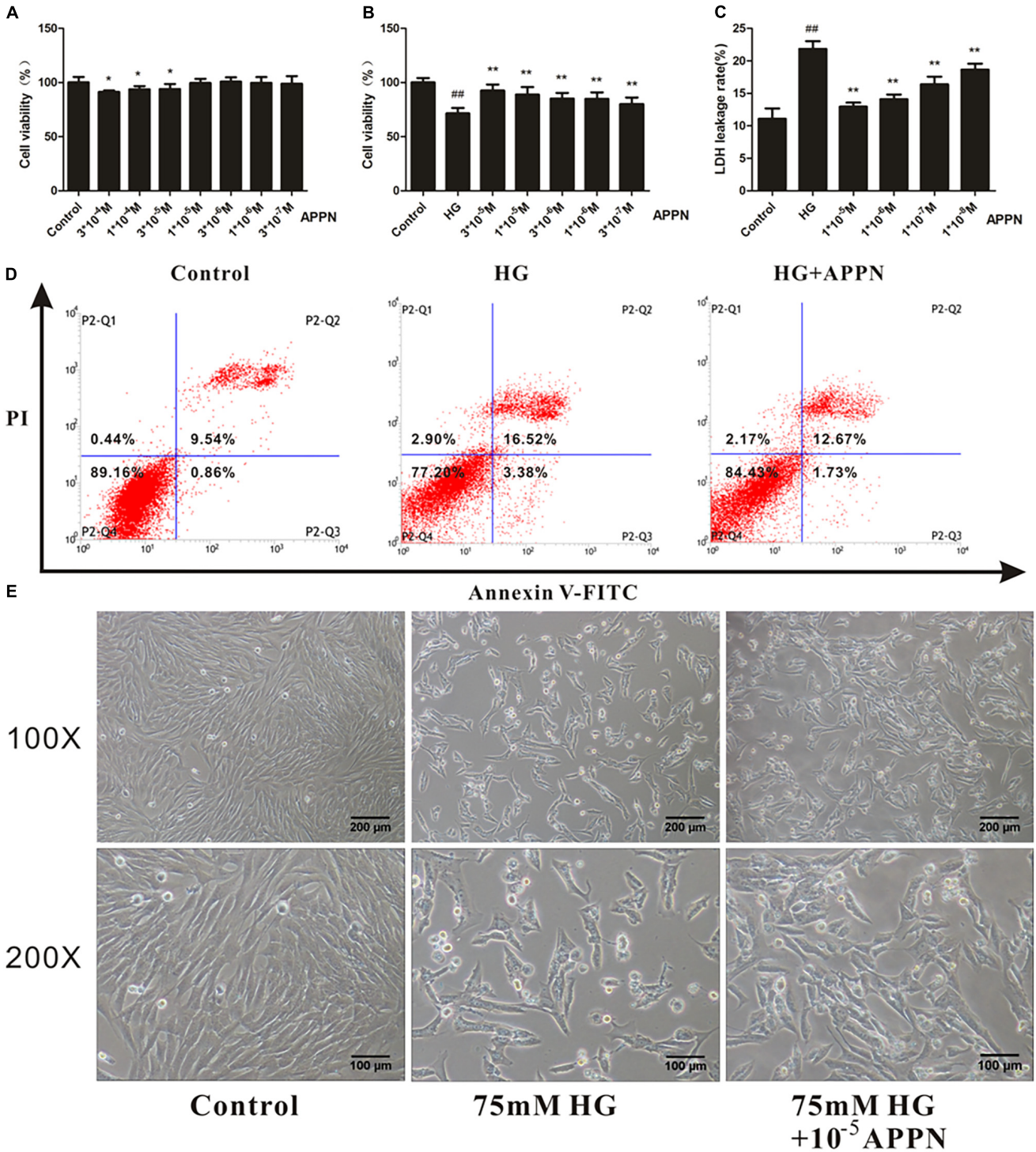

FIGURE 7 | The effect of adapentpronitrile on HG-induced cytotoxicity in HT22 cells. **(A)** The cytotoxicity of adapentpronitrile on HT22 cells. Data were expressed as mean ± SD of six independent experiments, and were analyzed statistically using one-way ANOVA, followed by Dunnett-t type multiple comparison tests. $^{*}P < 0.05$ vs. the control group. **(B)** The effect of adapentpronitrile on the viability in HT22 cells induced by HG-overload. **(C)** The effect of adapentpronitrile on the LDH leakage rate in HT22 cells induced by HG-overload. Data were expressed as mean ± SD of six independent experiments, and were analyzed statistically using one-way ANOVA, followed by Dunnett-t type multiple comparison tests. $^{\#\#}P < 0.01$ vs. the control group; $^{*}P < 0.05$ and $^{**}P < 0.01$ vs. the HG group, respectively. **(D)** The effect of adapentpronitrile on apoptosis in HT22 cells induced by HG-overload. The representative images of flow cytometry analysis are shown. **(E)** The effect of adapentpronitrile on the changes of cytomorphology in HT22 cells induced by HG overload. Representative images of experiments are shown. The magnification of images were 100× and 200×, respectively. Scale bars were 200 and 100 μm, respectively.

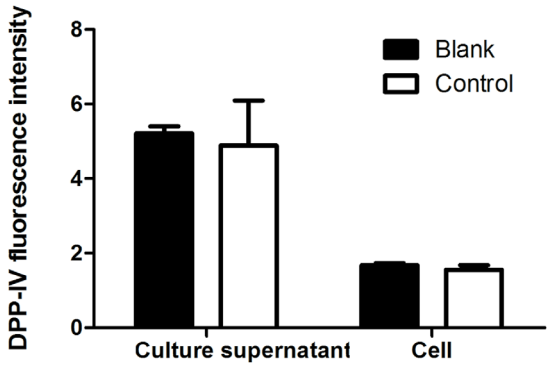

FIGURE 8 | The DPP-IV activity in HT22 cells. Data were expressed as mean ± SD of six independent experiments, and were analyzed statistically using one-way ANOVA, followed by Dunnett-t type multiple comparison tests.

apoptosis-related proteins were reversed by adapentpronitrile treatment.

DISCUSSION

Alzheimer's disease is an irreversible progressive neurodegenerative disorder characterized by cognitive deficits and memory loss. Despite various strategies have been explored, unfortunately, promising preclinical outcomes were generally disappointing (Mullard, 2016). In recent years, epidemiological studies suggest that diabetes mellitus is a risk factor for Alzheimer's disease, which may include three common pathological properties as follows, cerebrovascular inflammation, amyloid deposition, and impairment of brain insulin signaling (Takeda et al., 2010; De Felice and Ferreira, 2014). Antidiabetic agents, therefore, may have value in the treatment of AD.

In the present study, neuronal injury in rats was induced by a HFD combined with low-dose STZ (30 mg/kg). It is postulated that a persistent high-fat and high-sucrose diet contributes to an accumulation of glucolipotoxicity and β cell dysfunction, thereby leading to insulin resistance and hyperinsulinemia (Li et al., 2015). STZ is particularly toxic to islet cells in mammals and has been utilized to establish T2DM model, which accelerates β cell dysfunction and insulin deficiency (Lenzen, 2008). The pathology of HFD/STZ model reflects the progression from insulin resistance to hyperglycemia and hypoinsulinemia associated with diabetes (Reed et al., 2000; Li et al., 2015). In our previous study, we observed a reduction in β cell numbers by approximately 40% in HFD/STZ rats, which consistent with those observed in reports of patients with diabetes in the clinic (Butler et al., 2003; Ma et al., 2017). It is well known that hippocampus and cortex play an important role in the learning, cognition, and memory, and is also one of the earliest signs of neurodegenerative disorder such as Alzheimer's disease. Numerous investigations indicated that the atrophy and apoptosis of brain may occur in type 2 diabetes, especially in the hippocampus and cortex, and that may contribute to cognitive impairment (den Heijer et al., 2003; McCrimmon and Ryan, 2012; Ho and Sommers, 2013; Moran et al., 2013; Hirabayashi et al., 2016). In the present study, we observed significant pathomorphological changes and neuronal injury in the cortex and vulnerable hippocampal CA4 region following HFD/STZ insult. The protein expressions of APP and Aβ, which are a major hallmark in the pathologic progression of AD, were elevated significantly in both the hippocampus and cortex of the HFD/STZ rats. These results confirmed that the diabetic AD rat model was established successfully.

Treatment with adapentpronitrile, a new DPP-IV inhibitor, resulted in a dose-dependent amelioration of the pathological changes in the hippocampal CA4 region of T2DM rats. Furthermore, the abnormal protein expressions of APP and Aβ were reversed. These findings demonstrate the protective effects of adapentpronitrile against neuronal injury.

Glucagon-like-peptide 1, which is an incretin hormone secreted mainly by intestinal L-cells, plays a vital role in motivating insulin secretion, suppressing glucagon release, thus ameliorating glycemic control (Holst, 2007; Ma et al., 2014). In addition to the expression in peripheral tissues, the GLP-1 receptor is expressed in the brain, particularly in the hippocampus (Dunphy et al., 1998). Accumulating evidence demonstrates that GLP-1 analogs play a role in controlling synaptic plasticity and reversing memory impairment (Gault and Hölscher, 2008; McClean and Hölscher, 2014). Moreover, GLP-1 acts as a neurotropic factor by promoting proliferation and inhibiting apoptosis. The half-life of endogenous GLP-1 in the circulation is approximately 2 min due to its rapid degradation by DPP-IV (Drucker and Nauck, 2006; Ranganath, 2008). Therefore, DPP-IV inhibitors have been utilized to improve glycemic control in the treatment of T2DM since the first agent sitagliptin was approved by FDA in 2006 (Drucker and Nauck, 2006; Verspohl, 2009). DPP-IV inhibitors adapentpronitrile have been shown to stimulate insulin biosynthesis and secretion, improve glycemic control, and decrease HbA1c in diabetic rats induced by HFD/STZ (Ma et al., 2017). In the present study, adapentpronitrile significantly attenuated the neuronal injury in the hippocampus and cortex of rats caused by HFD/STZ. However, there was no significant difference among these groups in the protein expressions of the GLP-1R, indicating that the neuroprotective effects of adapentpronitrile are, at least partially, independent of the DPP-IV pathway. Therefore, the neuroprotective mechanism of adapentpronitrile remains to be fully elucidated.

The neurotoxic mechanism of HFD/STZ might be attributed to the overproduction of ROS. SOD is an important antioxidant enzyme, which functions primarily as a free radical scavenger to protect against oxidative stress. MDA, a biomarker of lipid peroxidation, is generated *via* a series of enzyme reactions (Del Rio et al., 2005). In the present study, we found that the SOD activity was significantly decreased and the MDA content was significantly increased in the brain of T2DM rat. Adapentpronitrile treatment reversed the abnormal decrease in SOD activity and increased MDA levels. These results further confirmed the involvement of oxidative stress in the rat model of diabetic neuronal injury induced by HFD/STZ, whereas adapentpronitrile treatment improved the oxidative imbalance.

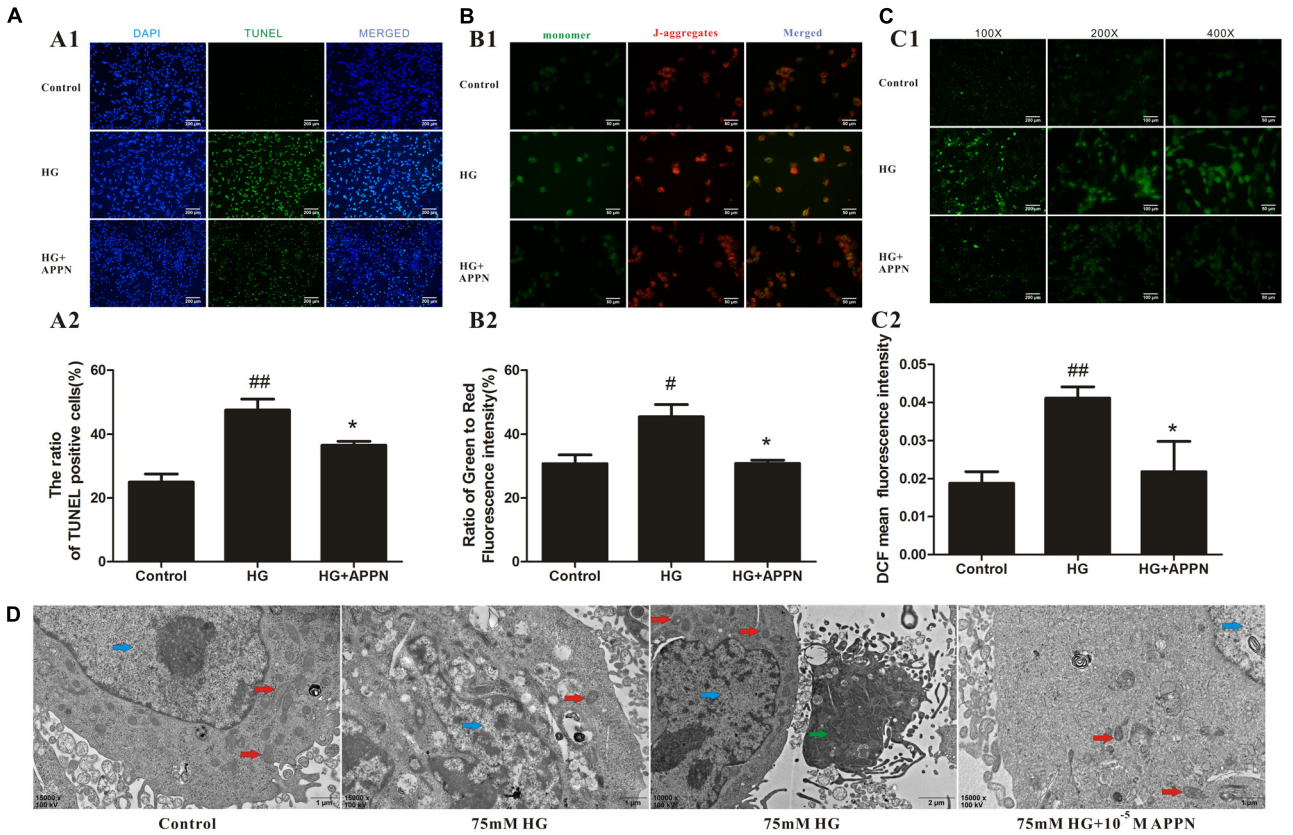

FIGURE 9 | Effects of adapentpronitrile on $\Delta\psi$m, ROS level, apoptosis, and mitochondria morphology in HT22 cells induced by HG overload. **(A)** Effects of adapentpronitrile on the TUNEL-positive cell number in HT22 cells induced by HG overload. **(B)** Effects of adapentpronitrile on mitochondrial membrane potential in HT22 cells induced by HG overload. **(C)** Effects of adapentpronitrile on ROS generation in HT22 cells induced by HG overload. Representative images of experiments are shown. Data were expressed as mean ± SD of four independent experiments, and were analyzed statistically using one-way ANOVA, followed by Dunnett-t type multiple comparison tests. $^{\#}P < 0.05$ and $^{\#\#}P < 0.01$ vs. the control group, respectively; $^{*}P < 0.05$ vs. the HG group. **(D)** The ultrastructure in HT22 cells detected by TEM. Representative images of experiments are shown. Sections were pictured at 15,000×. Scale bar = 1 μm. The blue, red, and green arrows were pointed to the nucleus, mitochondria, and apoptotic body, respectively.

Additionally, previous studies confirmed that oxidative stress promotes mitochondrial dysfunction. The mitochondrial respiratory chain can be impaired by mitochondrial dysfunction to produce excess ROS and exacerbate oxidative stress even further, forming a "vicious circle" (Vučetić-Arsić et al., 2013). Mitochondrial dysfunction initiates apoptosis by activating caspase-dependent or caspase-independent pathways (Arun et al., 2016). This process is regulated by the proteins of Bcl-2 family, including Bcl-2, Bcl-xL, Bax, and Bak. After a conformational shift, the pro-apoptotic proteins Bax and Bak insert themselves into mitochondrial membranes, where pro-apoptotic factors cytochrome c is released into the cytosol through the mitochondrial permeability transition pore (MPTP) or other channels (Tait and Green, 2010). Elevated cytosolic levels of soluble cytochrome c can lead to the increased cell mortality associated with neurodegeneration (Perier et al., 2005). In our present study, expression of the anti-apoptotic protein Bcl-2 was decreased significantly in the cortex and hippocampus of HFD/STZ rats, while the expression of mitochondria-associated pro-apoptotic proteins were increased significantly; these alterations were reversed by adapentpronitrile treatment. Thus, the current study indicates that the neuroprotective effects of adapentpronitrile are mediated *via* the mitochondrial apoptosis pathway.

Numerous studies suggest that disruption of the BBB is associated with age, obesity, and diabetes, and could contribute to early cognitive impairment (Tucsek et al., 2014; Montagne et al., 2015; van de Haar et al., 2016; Xu et al., 2016). Extensive research has revealed candidate drugs that have a better effect on CNS diseases in preclinical studies, while the clinical application has little or no effect. The main reason is that a candidate drug has to be administered directly into the cerebrospinal fluid, where it can enter the brain to mediate the neuroprotective effect (Pardridge, 2011). Therefore, it is necessary to determine whether a candidate drug can penetrate the BBB for the treatment of CNS diseases. In the present study, adapentpronitrile was detected in the brain of normal rats at 30 min after intravenous injection, indicating that adapentpronitrile can penetrate BBB. Hence, further studies are required to determine whether the neuroprotective effects of adapentpronitrile are mediated direct

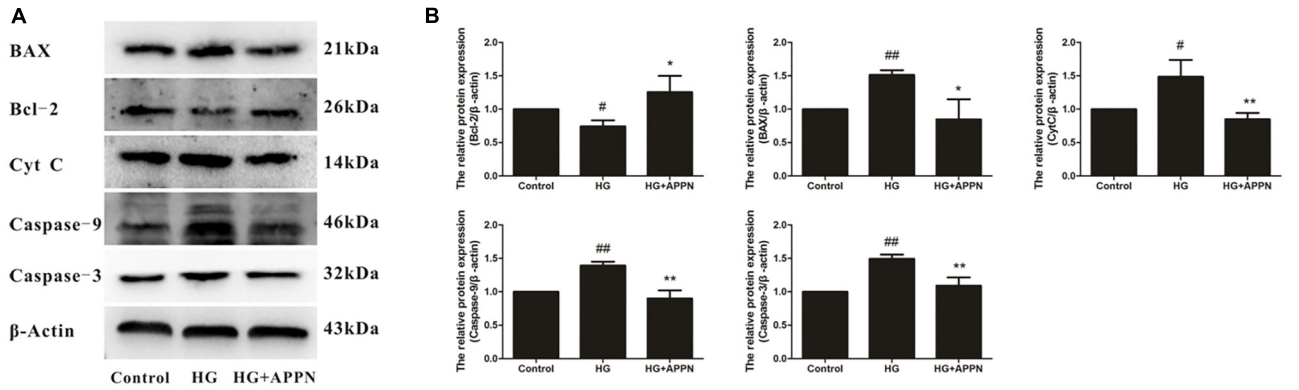

FIGURE 10 | Effect of adapentpronitrile on mitochondria-dependent apoptosis-related protein expression caused by HG in HT22 cells. **(A)** Representative blots of adapentpronitrile on the expressions of apoptosis-related proteins in HT22 cells induced by HG-overload. **(B)** The relative of protein expression were standardized to endogenous β-actin protein for each sample. Data were expressed as mean ± SD of four independent experiments, and were analyzed statistically using one-way ANOVA, followed by Dunnett-t type multiple comparison tests. $^{\#}P < 0.05$ and $^{\#\#}P < 0.01$ vs. the control group; $^{*}P < 0.05$, $^{**}P < 0.01$ vs. the HG group.

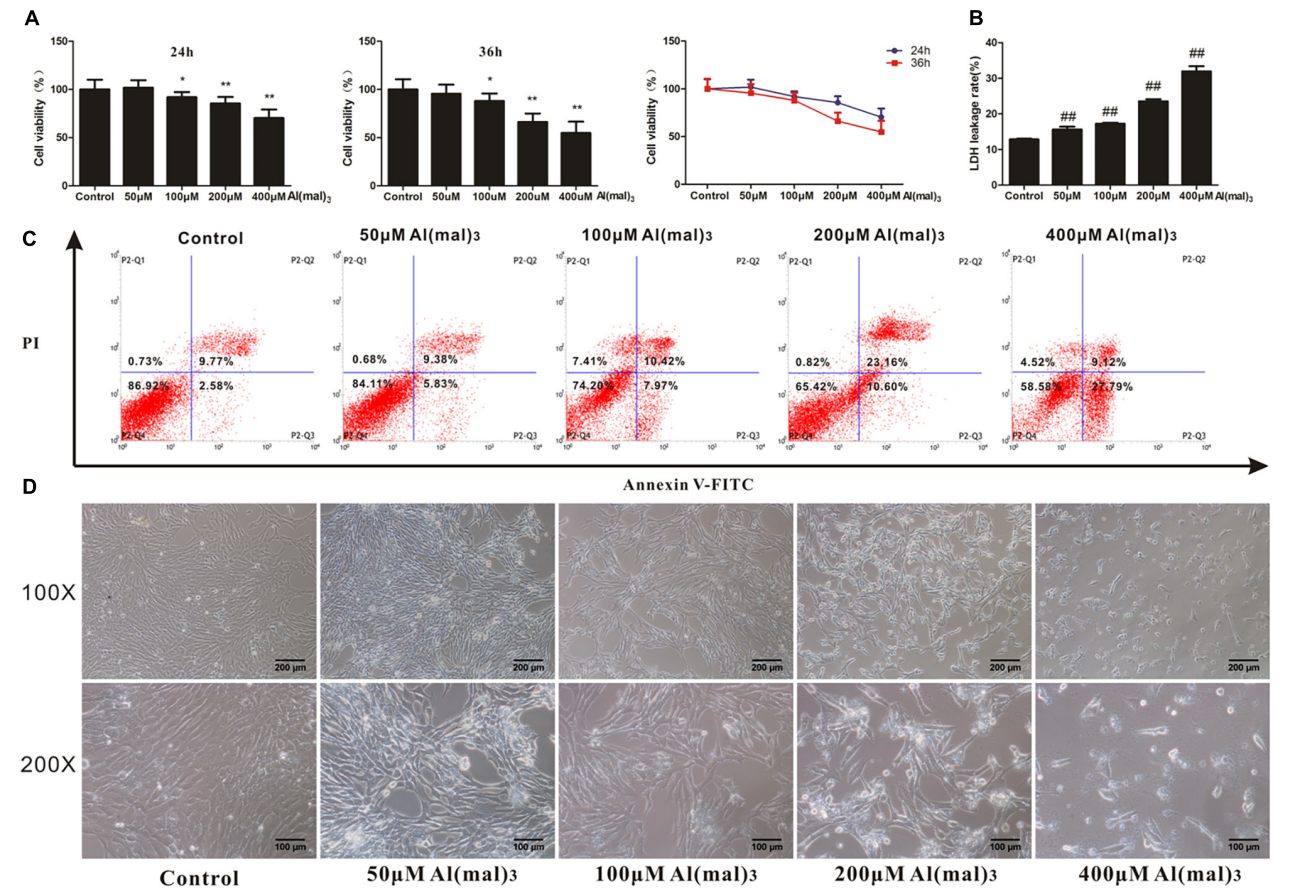

FIGURE 11 | The effects of $Al(mal)_3$ on HT22 cells. **(A)** The viability of HT22 cells treated with different concentrations of $Al(mal)_3$. Data were expressed as mean ± SD of 10 independent experiments, and were analyzed statistically using one-way ANOVA, followed by Dunnett-t type multiple comparison tests. $^{*}P < 0.05$, $^{**}P < 0.01$ vs. the control group. **(B)** The LDH leakage rate of HT22 cells treated with different concentration of $Al(mal)_3$. Data were expressed as mean ± SD of six independent experiments, and were analyzed statistically using one-way ANOVA, followed by Dunnett-t type multiple comparison tests. $^{\#\#}P < 0.01$ vs. the control group. **(C)** The flow cytometry apoptosis analysis of HT22 cells were treated with $Al(mal)_3$ for 36 h. The representative images of flow cytometry analysis are shown. **(D)** The cytomorphology changes of HT22 cells treated with different concentration of $Al(mal)_3$. Representative images of experiments are shown. The magnification of images were 100× and 200×, respectively. Scale bars were 200 and 100 μm, respectively.

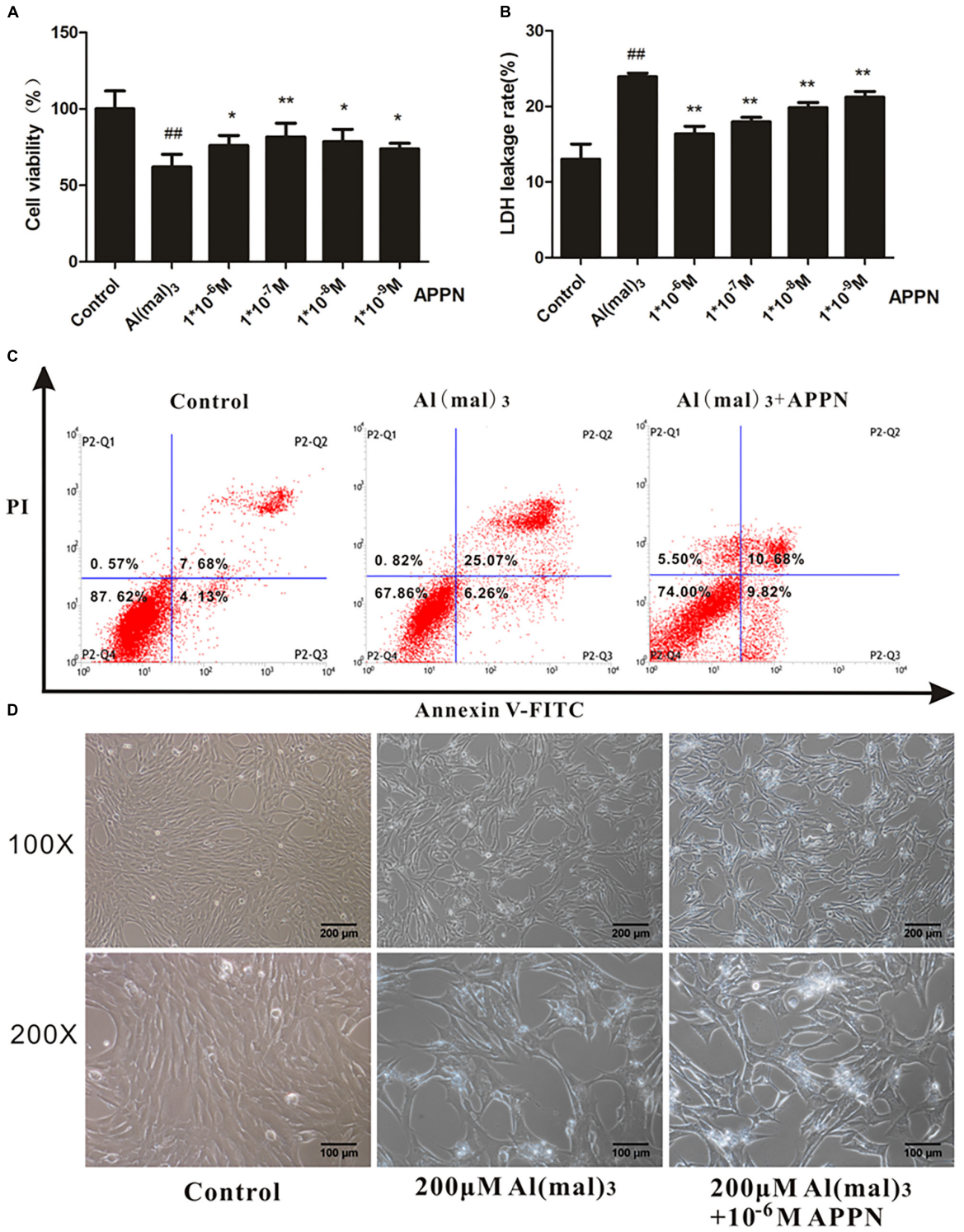

FIGURE 12 | The effect of adapentpronitrile on Al(mal)3-induced cytotoxicity in HT22 cells. **(A)** The effect of adapentpronitrile on the viability in HT22 cells induced by $Al(mal)_3$ overload. **(B)** The effect of adapentpronitrile on the LDH leakage rate in HT22 cells induced by $Al(mal)_3$ overload. Data were expressed as mean ± SD of six independent experiments, and were analyzed statistically using one-way ANOVA, followed by Dunnett-t type multiple comparison tests. $^{\#\#}P < 0.01$ vs. the control group; $^{*}P < 0.05$ and $^{**}P < 0.01$ vs. the $Al(mal)_3$ group, respectively. **(C)** The effect of adapentpronitrile on apoptosis in HT22 cells induced by $Al(mal)_3$-overload. The representative images of flow cytometry analysis are shown. **(D)** The effect of adapentpronitrile on the changes of cytomorphology in HT22 cells induced by $Al(mal)_3$-overload. Representative images of experiments are shown. The magnification of images were 100× and 200×, respectively. Scale bars were 200 and 100 μm, respectively.

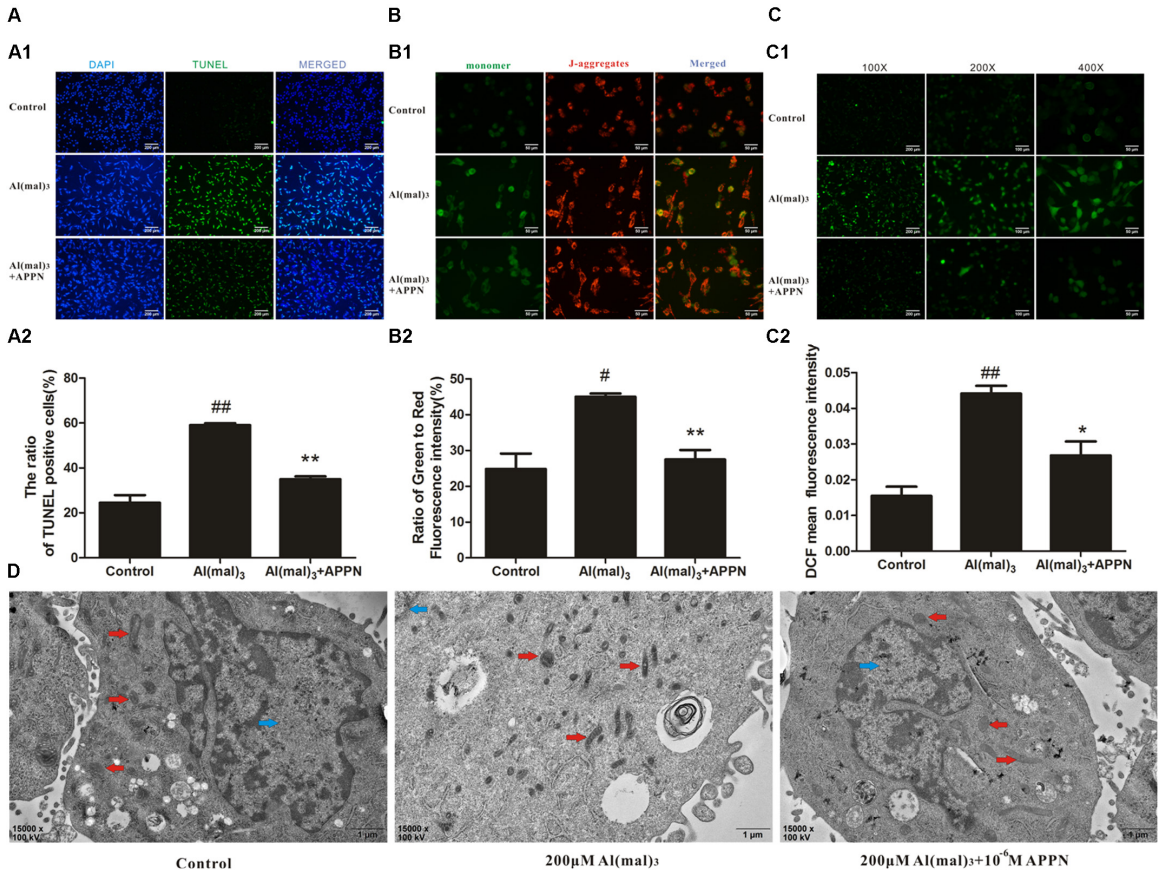

FIGURE 13 | Effects of adapentpronitrile on $\Delta\psi$m, ROS level, apoptosis, and mitochondria morphology in HT22 cells induced by Al(mal)$_3$ overload. **(A)** Effects of adapentpronitrile on the TUNEL-positive cell number in HT22 cells induced by Al(mal)$_3$ overload. **(B)** Effects of adapentpronitrile on mitochondrial membrane potential in HT22 cells induced by Al(mal)$_3$ overload. **(C)** Effects of adapentpronitrile on ROS generation in HT22 cells induced by Al(mal)$_3$ overload. Representative images of experiments are shown. Data were expressed as mean ± SD of four independent experiments, and were analyzed statistically using one-way ANOVA, followed by Dunnett-t type multiple comparison tests. $^{\#}P < 0.05$ and $^{\#\#}P < 0.01$ vs. the control group, respectively; $^{*}P < 0.05$ and $^{**}P < 0.01$ vs. the Al(mal)$_3$ group, respectively. **(D)** The ultrastructure in HT22 cells detected by TEM. Representative images of experiments are shown. Sections were pictured at 15,000×. Scale bar = 1 μm. The blue, red, and green arrows were pointed to the nucleus, mitochondria, and apoptotic body, respectively.

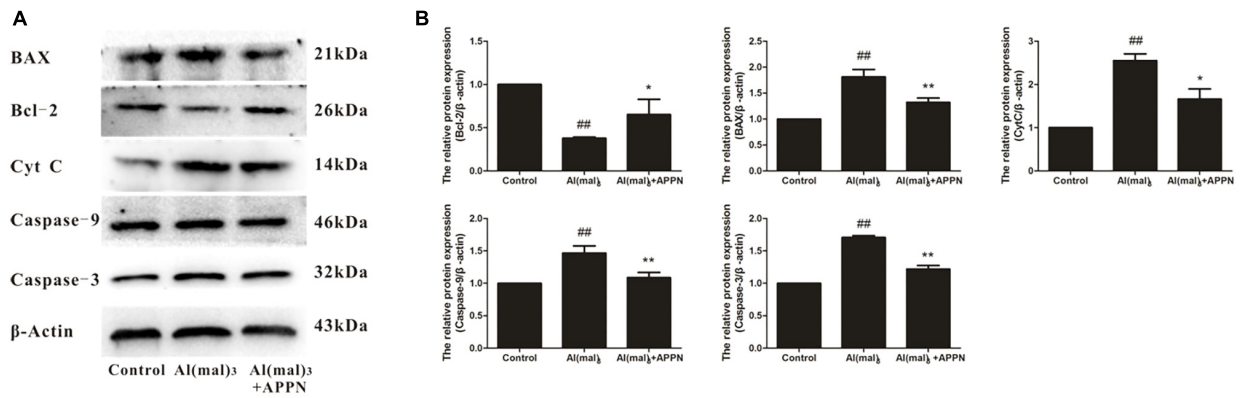

FIGURE 14 | Effect of adapentpronitrile on mitochondria-dependent apoptosis-related protein expression caused by Al(mal)$_3$ in HT22 cells. **(A)** Representative blots of adapentpronitrile on the expressions of apoptosis-related proteins in HT22 cells induced by Al(mal)$_3$. **(B)** The relative of protein expression were standardized to endogenous β-actin protein for each sample. Data were expressed as mean ± SD of four independent experiments, and were analyzed statistically using one-way ANOVA, followed by Dunnett-t type multiple comparison tests. $^{\#}P < 0.05$ and $^{\#\#}P < 0.01$ vs. the control group; $^{*}P < 0.05$, $^{**}P < 0.01$ vs. the Al(mal)$_3$ group.

or indirect action on neurons and whether the mechanism is related to DPP-IV dependent or independent.

To imitate the hyperglycemic state in the CNS of diabetic patients, we subjected HT22 cells, which are a neuronal cell line derived from murine hippocampus, to HG treatment *in vitro*. We found that neuronal injury aggravated with the HG concentration increasing, which was ameliorated by adapentpronitrile treatment.

In accordance with the results of our *in vitro* study, adapentpronitrile significantly abrogated the increase in ROS levels and neuronal apoptosis, and the decrease in MMP in HT22 cells following HG insult. Furthermore, adapentpronitrile treatment significantly increased Bcl-2 protein expression in HT22 cells, while the expression of Bax, cytochrome c, caspase 3, and caspase 9 proteins was decreased.

In order to further confirm the neuroprotection and mechanism of adapentpronitrile, the cell injury model was established by aluminum overload in HT22 cells. Metals play a risk role in AD *via* the production of free radicals, including iron, aluminum, mercury, copper, and zinc (Christen, 2000). Extensive literature illustrated that the neurotoxic effects of aluminum are beyond any doubt, and it cannot be discarded that aluminum may contribute to the development of AD (Gupta et al., 2005). Epidemiological evidence indicated that aluminum concentrations of drinking water is associated to the prevalence of AD with a dose–response relationship, and a similar link between exposure and the prevalence were also reported in elderly populations (Crapper et al., 1980; Rondeau et al., 2009). Furthermore, elevation of aluminum content were observed in the brains of patients with AD (Becaria et al., 2002), and it was also detected in *post mortem* neurofibrillary tangles and senile plaques of AD patients (Meiri et al., 1993). Both aluminum and aggregated β-amyloid stimulate free radicals production and contribute to mitochondrial dysfunction relating to the pathology of AD. $Al(mal)_3$ is a salt forms of aluminum used to imitate AD-like neuronal injury *in vivo* and *in vitro* for its stability at physiological pH (Johnson et al., 2005). Our experimental results showed that treatment of $Al(mal)_3$ decreased the viability and increase the LDH leakage rate in a concentration-dependent manner, which was ameliorated by adapentpronitrile treatment. Adapentpronitrile significantly blunted the reduction of mitochondrial membrane potential, ROS overproduction, of TUNEL-positive cell number and pro-apoptotic protein expressions triggered by $Al(mal)_3$-overload.

To explore the association of the neuroprotective effect of adapentpronitrile with DPP-IV inhibition, we determined DPP-IV activity in HT22 cells. We did not detect significant activity of DPP-IV in HT22 cells, indicating that the neuroprotective effects of adapentpronitrile are mediated *via* a DPP-IV-independent pathway *in vitro*.

CONCLUSION

The DPP-IV inhibitor adapentpronitrile effectively attenuates the neuronal injury caused by HG/$Al(mal)_3$ overload *in vitro* and ameliorates both the hippocampal and cortical neuron injury caused by HFD combined with low dose STZ *in vivo*. Pharmacokinetic studies confirmed the ability of adapentpronitrile to penetrate the blood–brain barrier *in vivo*, while no significant DPP-IV activity was detected in HT22 cells *in vitro*. These results together suggest that adapentpronitrile mediates obvious protection against diabetic neuronal injury, at least partially, by inhibiting mitochondrial oxidative stress and the apoptosis pathway *via* a DPP-IV-independent pathway. Thus, adapentpronitrile is implicated as a promising candidate for AD therapy in the clinical setting. However, the mechanism underlying the neuroprotective effects of adapentpronitrile and the potential of other whether the other DPP-IV inhibitors to mediate similar effects remain to be fully explored.

AUTHOR CONTRIBUTIONS

JY made substantial contribution to conception and design and performance of the study. LY, WH, YiL, HL, CH, DH, JM, YY, QC, YuL, JZ, HX, ZC, HW, and, DR participated in performance of all experiments and carried out the data analysis. XH provided adapentpronitrile and experimental guidance. YX participated in the grammar and writing instruction. LY participated in performance of the study and in writing the manuscript. All authors read and approved the final manuscript. JY is the guarantor of this work and, as such, had full access to all the data in the study and takes responsibility for the integrity of the data and the accuracy of the data analysis.

FUNDING

This work was supported by research grants from the Chongqing Science and Technology Commission Fund (cstc2015zdcy-ztzx120003).

REFERENCES

Arun, S., Liu, L., and Donmez, G. (2016). Mitochondrial biology and neurological diseases. *Curr. Neuropharmacol.* 14, 143–154. doi: 10.2174/1570159X13666150703154541

Baglietto-Vargas, D., Shi, J., Yaeger, D. M., Ager, R., and LaFerla, F. M. (2016). Diabetes and Alzheimer's disease crosstalk. *Neurosci. Biobehav. Rev.* 64, 272–287. doi: 10.1016/j.neubiorev.2016.03.005

Becaria, A., Campbell, A., and Bondy, S. C. (2002). Aluminum as a toxicant. *Toxicol. Ind. Health* 18, 309–320. doi: 10.1191/0748233702th157oa

Biessels, G. J., and Reagan, L. P. (2015). Hippocampal insulin resistance and cognitive dysfunction. *Nat. Rev. Neurosci.* 16, 660–671. doi: 10.1038/nrn4019

Bosco, D., Fava, A., Plastino, M., Montalcini, T., and Pujia, A. (2011). Possible implications of insulin resistance and glucose metabolism in Alzheimer's disease pathogenesis. *J. Cell. Mol. Med.* 15, 1807–1821. doi: 10.1111/j.1582-4934.2011.01318.x

Butler, A. E., Janson, J., Bonner-Weir, S., Ritzel, R., Rizza, R. A., and Butler, P. C. (2003). Beta-cell deficit and increased beta-cell apoptosis in humans with type 2 diabetes. *Diabetes Metab. Res. Rev.* 52, 102–110. doi: 10.2337/diabetes.52.1.102

Chen, X., Guo, C., and Kong, J. (2012). Oxidative stress in neurodegenerative diseases. *Neural Regen. Res.* 7, 376–385. doi: 10.3969/j.issn.1673-5374.2012.05.009

Christen, Y. (2000). Oxidative stress and Alzheimer disease. *Am. J. Clin. Nutr.* 71, 621S–629S. doi: 10.1093/ajcn/71.2.621s

Crapper, D. R., Quittkat, S., Krishnan, S. S., Dalton, A. J., and De Boni, U. (1980). Intranuclear aluminum content in Alzheimer's disease, dialysis encephalopathy, and experimental aluminum encephalopathy. *Acta Neuropathol.* 50, 19–24. doi: 10.1007/BF00688530

De Felice, F. G., and Ferreira, S. T. (2014). Inflammation, defective insulin signaling, and mitochondrial dysfunction as common molecular denominators connecting type 2 diabetes to Alzheimer disease. *Diabetes Metab. Res. Rev.* 63, 2262–2272. doi: 10.2337/db13-1954

Del Rio, D., Stewart, A. J., and Pellegrini, N. (2005). A review of recent studies on malondialdehyde as toxic molecule and biological marker of oxidative stress. *Nutr. Metab. Cardiovasc. Dis.* 15, 316–328. doi: 10.1016/j.numecd.2005.05.003

den Heijer, T., Vermeer, S. E., van Dijk, E. J., Prins, N. D., Koudstaal, P. J., Hofman, A., et al. (2003). Type 2 diabetes and atrophy of medial temporal lobe structures on brain MRI. *Diabetologia* 46, 1604–1610. doi: 10.1007/s00125-003-1235-0

Devi, L., Prabhu, B. M., Galati, D. F., Avadhani, N. G., and Anandatheerthavarada, H. K. (2006). Accumulation of amyloid precursor protein in the mitochondrial import channels of human Alzheimer's disease brain is associated with mitochondrial dysfunction. *J. Neurosci.* 26, 9057–9068. doi: 10.1523/JNEUROSCI.1469-06.2006

Dineley, K. T., Jahrling, J. B., and Denner, L. (2014). Insulin resistance in Alzheimer's disease. *Neurobiol. Dis.* 72(Pt A), 92–103. doi: 10.1016/j.nbd.2014.09.001

Drucker, D. J., and Nauck, M. A. (2006). The incretin system: glucagon-like peptide-1 receptor agonists and dipeptidyl peptidase-4 inhibitors in type 2 diabetes. *Lancet* 368, 1696–1705. doi: 10.1016/S0140-6736(06)69705-5

DuBoff, B., Götz, J., and Feany, M. B. (2012). Tau promotes neurodegeneration via DRP1 mislocalization in vivo. *Neuron* 75, 618–632. doi: 10.1016/j.neuron.2012.06.026

Dunphy, J. L., Taylor, R. G., and Fuller, P. J. (1998). Tissue distribution of rat glucagon receptor and GLP-1 receptor gene expression. *Mol. Cell. Endocrinol.* 141, 179–186. doi: 10.1016/S0303-7207(98)00096-3

Gasparini, L., Netzer, W. J., Greengard, P., and Xu, H. (2002). Does insulin dysfunction play a role in Alzheimer's disease? *Trends Pharmacol. Sci.* 23, 288–293.

Gault, V. A., and Hölscher, C. (2008). GLP-1 agonists facilitate hippocampal LTP and reverse the impairment of LTP induced by beta-amyloid. *Eur. J. Pharmacol.* 587, 112–117. doi: 10.1016/j.ejphar.2008.03.025

Golightly, L. K., Drayna, C. C., and McDermott, M. T. (2012). Comparative clinical pharmacokinetics of dipeptidyl peptidase-4 inhibitors. *Clin. Pharmacokinet.* 51, 501–514. doi: 10.2165/11632930-000000000-00000

Guo, Y., Lei, W., Wang, J., Hu, X., Wei, Y., Ji, C., et al. (2016). Misoprostol reverse hippocampal neuron cyclooxygenase-2 downstream signaling imbalance in aluminum-overload rats. *Curr. Alzheimer Res.* 13, 1006–1016. doi: 10.2174/1567205013666160401114601

Gupta, V. B., Anitha, S., Hegde, M. L., Zecca, L., Garruto, R. M., Ravid, R., et al. (2005). Aluminium in Alzheimer's disease: are we still at a crossroad? *Cell. Mol. Life Sci.* 62, 143–158. doi: 10.1007/s00018-004-4317-3

Hardy, J., and Selkoe, D. J. (2002). The amyloid hypothesis of Alzheimer's disease: progress and problems on the road to therapeutics. *Science* 297, 353–356. doi: 10.1126/science.1072994

Hirabayashi, N., Hata, J., Ohara, T., Mukai, N., Nagata, M., Shibata, M., et al. (2016). Association between diabetes and hippocampal atrophy in elderly japanese: the hisayama study. *Diabetes care* 39, 1543–1549. doi: 10.2337/dc15-2800

Ho, N., and Sommers, M. S. (2013). Effects of diabetes on hippocampal neurogenesis: links to cognition and depression. *Neurosci. Biobehav. Rev.* 37, 1346–1362. doi: 10.1016/j.neubiorev.2013.03.010

Holst, J. J. (2007). The physiology of glucagon-like peptide 1. *Physiol. Rev.* 87, 1409–1439. doi: 10.1152/physrev.00034.2006

Johnson, V. J., Kim, S. H., and Sharma, R. P. (2005). Aluminum-maltolate induces apoptosis and necrosis in neuro-2a cells: potential role for p53 signaling. *Toxicol. Sci.* 83, 329–339. doi: 10.1093/toxsci/kfi028

Kandimalla, R., Vallamkondu, J., Corgiat, E. B., and Gill, K. D. (2016). Understanding aspects of aluminum exposure in Alzheimer's disease development. *Brain Pathol.* 26, 139–154. doi: 10.1111/bpa.12333

Knock, G. A., and Ward, J. P. (2011). Redox regulation of protein kinases as a modulator of vascular function. *Antioxid. Redox Signal.* 15, 1531–1547. doi: 10.1089/ars.2010.3614

Koliaki, C., and Roden, M. (2016). Alterations of mitochondrial function and insulin sensitivity in human obesity and diabetes mellitus. *Annu. Rev. Nutr.* 36, 337–367. doi: 10.1146/annurev-nutr-071715-050656

Kosaraju, J., Gali, C. C., Khatwal, R. B., Dubala, A., Chinni, S., Holsinger, R. M., et al. (2013). Saxagliptin: a dipeptidyl peptidase-4 inhibitor ameliorates streptozotocin induced Alzheimer's disease. *Neuropharmacology* 72, 291–300. doi: 10.1016/j.neuropharm.2013.04.008

Kumar, V., and Gill, K. D. (2009). Aluminium neurotoxicity: neurobehavioural and oxidative aspects. *Arch. Toxicol.* 83, 965–978. doi: 10.1007/s00204-009-0455-6

Lenzen, S. (2008). The mechanisms of alloxan- and streptozotocin-induced diabetes. *Diabetologia* 51, 216–226. doi: 10.1007/s00125-007-0886-7

Li, L., Liao, G., Yang, G., Lu, Y., Du, X., Liu, J., et al. (2015). High-fat diet combined with low-dose streptozotocin injections induces metabolic syndrome in *Macaca mulatta*. *Endocrine* 49, 659–668. doi: 10.1007/s12020-015-0542-9

Lin, M. T., and Beal, M. F. (2006). Mitochondrial dysfunction and oxidative stress in neurodegenerative diseases. *Nature* 443, 787–795. doi: 10.1038/nature05292

Lobner, D. (2000). Comparison of the LDH and MTT assays for quantifying cell death: validity for neuronal apoptosis? *J. Neurosci. Methods* 96, 147–152. doi: 10.1016/S0165-0270(99)00193-4

Ma, J., Li, H., Hu, X., Yang, L., Chen, Q., Hu, C., et al. (2017). CMD-05, a novel promising clinical anti-diabetic drug candidate, in vivo and vitro studies. *Sci. Rep.* 7:46628. doi: 10.1038/srep46628

Ma, J., Yang, Q., Wei, Y., Yang, Y., Ji, C., Hu, X., et al. (2016). Effect of the PGD2-DP signaling pathway on primary cultured rat hippocampal neuron injury caused by aluminum overload. *Sci. Rep.* 6:24646. doi: 10.1038/srep24646

Ma, X., Guan, Y., and Hua, X. (2014). Glucagon-like peptide 1-potentiated insulin secretion and proliferation of pancreatic β-cells. *J. Diabetes* 6, 394–402. doi: 10.1111/1753-0407.12161

Maher, P. A., and Schubert, D. R. (2009). Metabolic links between diabetes and Alzheimer's disease. *Expert Rev. Neurother.* 9, 617–630. doi: 10.1586/ern.09.18

Manoharan, S., Guillemin, G. J., Abiramasundari, R. S., Essa, M. M., Akbar, M., and Akbar, M. D. (2016). The role of reactive oxygen species in the pathogenesis of Alzheimer's disease, Parkinson's disease, and Huntington's disease: a mini review. *Oxid. Med. Cell. Longev.* 2016:8590578. doi: 10.1155/2016/8590578

McClean, P. L., and Hölscher, C. (2014). Liraglutide can reverse memory impairment, synaptic loss and reduce plaque load in aged APP/PS1 mice, a model of Alzheimer's disease. *Neuropharmacology* 76(Pt A), 57–67. doi: 10.1016/j.neuropharm.2013.08.005

McCrimmon, R. J., and Ryan, C. M. (2012). Diabetes and cognitive dysfunction. *Lancet* 379, 2291–2299. doi: 10.1016/S0140-6736(12)60360-2

Meiri, H., Banin, E., Roll, M., and Rousseau, A. (1993). Toxic effects of aluminium on nerve cells and synaptic transmission. *Prog. Neurobiol.* 40, 89–121. doi: 10.1016/0301-0082(93)90049-X

Montagne, A., Barnes, S. R., Sweeney, M. D., Halliday, M. R., Sagare, A. P., Zhao, Z., et al. (2015). Blood-brain barrier breakdown in the aging human hippocampus. *Neuron* 85, 296–302. doi: 10.1016/j.neuron.2014.12.032

Moran, C., Phan, T. G., Chen, J., Blizzard, L., Beare, R., Venn, A., et al. (2013). Brain atrophy in type 2 diabetes: regional distribution and influence on cognition. *Diabetes Care* 36, 4036–4042. doi: 10.2337/dc13-0143

Moreira, P. I. (2012). Alzheimer's disease and diabetes: an integrative view of the role of mitochondria, oxidative stress, and insulin. *J. Alzheimers Dis.* 30(Suppl. 2), S199–S215. doi: 10.3233/JAD-2011-111127

Mullard, A. (2016). Symptomatic AD treatment fails in first phase III. *Nat. Rev. Drug Discov.* 15:738. doi: 10.1038/nrd.2016.225

Nassar, N. N., Al-Shorbagy, M. Y., Arab, H. H., and Abdallah, D. M. (2015). Saxagliptin: a novel antiparkinsonian approach. *Neuropharmacology* 89, 308–317. doi: 10.1016/j.neuropharm.2014.10.007

Pardridge, W. M. (2011). Drug transport in brain via the cerebrospinal fluid. *Fluids Barriers CNS* 8:7. doi: 10.1186/2045-8118-8-7

Perier, C., Tieu, K., Guégan, C., Caspersen, C., Jackson-Lewis, V., Carelli, V., et al. (2005). Complex I deficiency primes Bax-dependent neuronal apoptosis

through mitochondrial oxidative damage. *Proc. Natl. Acad. Sci. U.S.A.* 102, 19126–19131. doi: 10.1073/pnas.0508215102

Phiel, C. J., Wilson, C. A., Lee, V. M., and Klein, P. S. (2003). GSK-3alpha regulates production of Alzheimer's disease amyloid-beta peptides. *Nature* 423, 435–439. doi: 10.1038/nature01640

Pipatpiboon, N., Pintana, H., Pratchayasakul, W., Chattipakorn, N., and Chattipakorn, S. C. (2013). DPP4-inhibitor improves neuronal insulin receptor function, brain mitochondrial function and cognitive function in rats with insulin resistance induced by high-fat diet consumption. *Eur. J. Neurosci.* 37, 839–849. doi: 10.1111/ejn.12088

Qiu, W. Q., and Folstein, M. F. (2006). Insulin, insulin-degrading enzyme and amyloid-beta peptide in Alzheimer's disease: review and hypothesis. *Neurobiol. Aging* 27, 190–198. doi: 10.1016/j.neurobiolaging.2005.01.004

Ranganath, L. R. (2008). Incretins: pathophysiological and therapeutic implications of glucose-dependent insulinotropic polypeptide and glucagon-like peptide-1. *J. Clin. Pathol.* 61, 401–409. doi: 10.1136/jcp.2006.043232

Reed, M. J., Meszaros, K., Entes, L. J., Claypool, M. D., Pinkett, J. G., Gadbois, T. M., et al. (2000). A new rat model of type 2 diabetes: the fat-fed, streptozotocin-treated rat. *Metabolism* 49, 1390–1394. doi: 10.1053/meta.2000.17721

Rondeau, V., Jacqmin-Gadda, H., Commenges, D., Helmer, C., and Dartigues, J. F. (2009). Aluminum and silica in drinking water and the risk of Alzheimer's disease or cognitive decline: findings from 15-year follow-up of the PAQUID cohort. *Am. J. Epidemiol.* 169, 489–496. doi: 10.1093/aje/kwn348

Schmitt, K., Grimm, A., Kazmierczak, A., Strosznajder, J. B., Götz, J., and Eckert, A. (2012). Insights into mitochondrial dysfunction: aging, amyloid-β, and tau-A deleterious trio. *Antioxid. Redox Signal.* 16, 1456–1466. doi: 10.1089/ars.2011.4400

Smith, D. G., Cappai, R., and Barnham, K. J. (2007). The redox chemistry of the Alzheimer's disease amyloid beta peptide. *Biochim. Biophys. Acta* 1768, 1976–1990. doi: 10.1016/j.bbamem.2007.02.002

Son, Y., Kim, S., Chung, H. T., and Pae, H. O. (2013). Reactive oxygen species in the activation of MAP kinases. *Methods Enzymol.* 528, 27–48. doi: 10.1016/B978-0-12-405881-1.00002-1

Tait, S. W., and Green, D. R. (2010). Mitochondria and cell death: outer membrane permeabilization and beyond. *Nat. Rev. Mol. Cell Biol.* 11, 621–632. doi: 10.1038/nrm2952

Takeda, S., Sato, N., Uchio-Yamada, K., Sawada, K., Kunieda, T., Takeuchi, D., et al. (2010). Diabetes-accelerated memory dysfunction via cerebrovascular inflammation and abeta deposition in an Alzheimer mouse model with diabetes. *Proc. Natl. Acad. Sci. U.S.A.* 107, 7036–7041. doi: 10.1073/pnas.1000645107

Tucsek, Z., Toth, P., Sosnowska, D., Gautam, T., Mitschelen, M., Koller, A., et al. (2014). Obesity in aging exacerbates blood-brain barrier disruption, neuroinflammation, and oxidative stress in the mouse hippocampus: effects on expression of genes involved in beta-amyloid generation and Alzheimer's disease. *J. Gerontol. A Biol. Sci. Med. Sci.* 69, 1212–1226. doi: 10.1093/gerona/glt177

Valko, M., Leibfritz, D., Moncol, J., Cronin, M. T., Mazur, M., and Telser, J. (2007). Free radicals and antioxidants in normal physiological functions and human disease. *Int. J. Biochem. Cell Biol.* 39, 44–84. doi: 10.1016/j.biocel.2006.07.001

van de Haar, H. J., Burgmans, S., Jansen, J. F., van Osch, M. J., van Buchem, M. A., Muller, M., et al. (2016). Blood-Brain barrier leakage in patients with early Alzheimer Disease. *Radiology* 281, 527–535. doi: 10.1148/radiol.2016152244

Verbon, E. H., Post, J. A., and Boonstra, J. (2012). The influence of reactive oxygen species on cell cycle progression in mammalian cells. *Gene* 511, 1–6. doi: 10.1016/j.gene.2012.08.038

Verdile, G., Keane, K. N., Cruzat, V. F., Medic, S., Sabale, M., Rowles, J., et al. (2015). Inflammation and oxidative stress: the molecular connectivity between insulin resistance, Obesity, and Alzheimer's disease. *Mediators Inflamm.* 2015:105828. doi: 10.1155/2015/105828

Verspohl, E. J. (2009). Novel therapeutics for type 2 diabetes: incretin hormone mimetics (glucagon-like peptide-1 receptor agonists) and dipeptidyl peptidase-4 inhibitors. *Pharmacol. Ther.* 124, 113–138. doi: 10.1016/j.pharmthera.2009.06.002

Vučetić-Arsić, S., Radonjić, N. V., Jovanović, M., Selaković, V., Nikolić, T., Velimirović, M., et al. (2013). Oxidative stress precedes mitochondrial dysfunction in gerbil brain after aluminum ingestion. *Environ. Toxicol. Pharmacol.* 36, 1242–1252. doi: 10.1016/j.etap.2013.10.008

Wallace, D. C. (2005). A mitochondrial paradigm of metabolic and degenerative diseases, aging, and cancer: a dawn for evolutionary medicine. *Annu. Rev. Genet.* 39, 359–407. doi: 10.1146/annurev.genet.39.110304.095751

Xu, Z., Zeng, W., Sun, J., Chen, W., Zhang, R., Yang, Z., et al. (2016). The quantification of blood-brain barrier disruption using dynamic contrast-enhanced magnetic resonance imaging in aging rhesus monkeys with spontaneous type 2 diabetes mellitus. *Neuroimage* 158, 480–487. doi: 10.1016/j.neuroimage.2016.07.017

Conflict of Interest Statement: The authors declare that the research was conducted in the absence of any commercial or financial relationships that could be construed as a potential conflict of interest.

frontiers in Cellular Neuroscience

ORIGINAL RESEARCH
published: 27 July 2018
doi: 10.3389/fncel.2018.00222

Mild Endoplasmic Reticulum Stress Protects Against Lipopolysaccharide-Induced Astrocytic Activation and Blood-Brain Barrier Hyperpermeability

*Yiwei Wang†, Yinan Chen†, Qin Zhou, Jiawen Xu, Qingqing Qian, Pengfei Ni and Yanning Qian**

Department of Anesthesiology, The First Affiliated Hospital of Nanjing Medical University, Nanjing, China

Recent research has revealed that uncontrolled chronic neuroinflammation is closely associated with diverse neurodegenerative diseases, by impairing blood-brain barrier (BBB) function and astrocytic reaction. Endoplasmic reticulum (ER) stress is conventionally linked to the loss of neuronal structure and function and should be widely attenuated. This notion has been questioned by recent experimental studies, which have shown that non-harmful levels of ER stress had numerous beneficial roles against neurodegeneration, including neuroprotection and inhibition of cytokine production. Here, we investigated the mild ER stress-based regulation of LPS-induced inflammatory responses in astrocytes. Primary astrocytes were exposed to tunicamycin (TM), a compound that activates ER stress, with or without the ER-stress inhibitor sodium 4-phenylbutyrate (4-PBA) before LPS treatment. Astrocytic activation, proinflammatory factor production, and the extent of ER stress were assessed. In addition, the effect of mild ER stress on astrocytes and BBB function was determined *in vivo*. Male Sprague-Dawley rats received intracerebroventricular injections of TM with or without intraperitoneal 4-PBA before LPS administration. The levels of astrocytic activation and BBB permeability were measured after treatment. Our results showed that lower doses of TM resulted in a mild ER-stress response without inducing cytotoxicity and tissue toxicity. Non-toxic ER-stress preconditioning ameliorated LPS-induced overactivation and inflammatory responses in astrocytes. Moreover, pre-exposure to non-lethal doses of TM improved LPS-induced BBB impairment and cognitive ability dysfunction in rats. However, 4-PBA, reversed the protective effect of TM preconditioning *in vitro* and *in vivo*. We conclude that mild ER stress ("preconditioning") can alleviate LPS-induced astrocytic activation and BBB disruption. Our findings provide a better understanding for the regulatory role of ER stress in neuroinflammation and indicate that mild ER stress might have therapeutic value for the treatment of neurodegenerative diseases.

Keywords: endoplasmic reticulum stress, astrocytes, hormesis, blood-brain barrier, neuroinflammation, neurodegeneration

OPEN ACCESS

Edited by:
Sriharsha Kantamneni, University of Bradford, United Kingdom

Reviewed by:
Zhouguang Wang, Wenzhou Medical University, China
Hari S. Sharma, Uppsala University, Sweden

***Correspondence:**
Yanning Qian
yanning_qian@163.com

† These authors have contributed equally to this work.

Received: *22 April 2018*
Accepted: *09 July 2018*
Published: *27 July 2018*

Citation:
Wang Y, Chen Y, Zhou Q, Xu J, Qian Q, Ni P and Qian Y (2018) Mild Endoplasmic Reticulum Stress Protects Against Lipopolysaccharide-Induced Astrocytic Activation and Blood-Brain Barrier Hyperpermeability. Front. Cell. Neurosci. 12:222. doi: 10.3389/fncel.2018.00222

INTRODUCTION

Neurodegeneration is characterized by neuronal dysfunction and death in the central nervous system (CNS) (Estes and McAllister, 2016). Emerging evidence indicates that sustained inflammatory responses in the CNS associated with blood-brain barrier (BBB)-disruption contribute to neurodegenerative-disease progression (Glass et al., 2010; Broux et al., 2015). Systemic injection of lipopolysaccharide (LPS), a complex molecule containing both lipid and polysaccharide parts, can elicit neuroinflammation in the normal rat brain (Pintado et al., 2012). Animals with LPS-induced neuroinflammation are therefore frequently used as an experimental model for neurodegeneration and cognitive disorders (Qin et al., 2007).

Considering the many essential functions of astrocytes in the healthy CNS, astrocytic dysfunction might participate in the propagation and regulation of neuroinflammation. Astrocytes become activated in response to various stimuli, from subtle inflammatory changes in their microenvironment to massive neuronal damage (Sofroniew, 2015). Reactive astrocytes appear to play vital roles in mediating the production of proinflammatory effector molecules and amplifiers, such as chemokines, cytokines, and reactive oxygen species. These influence the state of surrounding cells (e.g., neurons, microglia, and other astrocytes), thereby triggering neuroinflammation leading to exacerbation of neurotoxicity and neurodegeneration (Gorina et al., 2011).

At least one-third of all proteins in the cell are first synthesized, folded, and structurally mature in the endoplasmic reticulum (ER); then, they are transported to the membrane compartment (Hetz and Mollereau, 2014). In astrocytes, the ER acquires a central role in sensing cellular stress after protein unfolding/misfolding in its lumen (known as ER stress), with the consequent activation of a cellular response termed the "unfolded protein response" (UPR). UPR is initiated by three principal stress sensors: the inositol-requiring protein 1α (IRE1α)-spliced X-box-binding protein 1 (XBP1s) pathway, the activating transcription factor (ATF)-6α pathway, and the protein kinase RNA-like ER kinase (PERK)-eukaryotic translation initiation factor 2α (EIF2α) pathway (Martin-Jiménez et al., 2017).

Endoplasmic reticulum stress in astrocytes has sometimes been viewed as a response mainly contributing to neurodegeneration, which should therefore be broadly attenuated (Martin-Jiménez et al., 2017). This notion is refuted by rapidly growing evidence, which shows that non-harmful levels of ER stress exert numerous beneficial functions that improve outcomes in CNS inflammation (Hetz and Mollereau, 2014; Matus et al., 2014). These findings have been reinforced by an array of related studies. A recent study showed that pretreatment with ER stressors protected against amyloid-β toxicity to reverse memory impairment in Alzheimer's disease (AD) (Casas-Tinto et al., 2011). Similarly, maintaining ER stress at a moderate level inhibits neuronal death in mouse and *Drosophila* Parkinson disease (PD) models (Fouillet et al., 2014). It is significant to emphasize that the roles of ER stress in neurodegenerative conditions are not stereotypically linear, but instead context-specific and complex, as determined by the type, severity, time, and duration of the insult. Specific mechanisms need to be identified and addressed.

In cardiac surgery, myocardial ischemic preconditioning is favorable for improving heart function. There is growing awareness that low perturbations of ER function also trigger a hormetic response, known as "ER hormesis," which involves a biologically-favorable response induced by exposing a cell/organism to non-lethal pharmacological ER stressors (Matus et al., 2014). However, there have so far been few scientific studies on the involvement of ER hormesis in astrocytes. Therefore, in the current study, we aimed to elucidate the effects of mild ER stress on LPS-induced inflammatory responses in astrocytes and to investigate whether mild ER stress exerts a protective effect against LPS-induced BBB hyperpermeability.

MATERIALS AND METHODS

Animals

One hundred and seventy-four male Sprague-Dawley (SD) rats (weight: 180–220 g) were used in the current study. All experiments were performed according to the ethical guidelines of the National Institutes of Health (NIH) guide for the Care and Use of Laboratory animals (NIH Publications No. 8023, revised 1978) and approved by the Nanjing Medical University Animal Care and Use Committee (IACUC-14030126). The rats were housed under standardized conditions (12-h light/dark cycle, 22.0 ± 1.0°C, and 40% humidity), and water and food were provided *ad libitum*. Based on the 3R principle for the ethical use of animals in research, all efforts were made to reduce animal use and suffering.

Intracerebroventricular Cannula Implantation

Rats were implanted with an indwelling lateral intracerebroventricular (icv) catheter for brain injection of drugs as previously described (Zhang et al., 2016). The animals were anesthetized (isoflurane, 2.1% inspired concentration in 0.3 FiO2) and placed on a stereotaxic apparatus. Stereotaxic coordinates for the placement of the icv cannulas were 0.8 mm rostral, 1.5 mm lateral to the bregma, and 3.7 mm ventral from the dorsal surface of the skull. Rats were individually housed after surgery and handled daily to familiarize the animals with the investigators and to check the guide catheter. Rats were allowed a minimum of 14 days to recover prior to icv administration of pharmacological agents and/or other experimental measurements.

Behavioral Tests

Trace fear conditioning, contextual assessment, and the Y-maze test were performed. The molecular-biology tests and the behavioral experiments were conducted using different animals. The behavioral test design is briefly illustrated in Supplementary Figure 1A. The specific methods can be found in the Supplementary Material.

Drug Administration

The well-known ER-stress inducer tunicamycin (TM) was diluted in sterile saline containing 10% dimethyl sulfoxide (DMSO) to create a stock concentration of 15 μg/μl. Then, 4-phenylbutyric acid (4-PBA), a common ER-stress inhibitor, was diluted with sterile saline to a concentration of 10 mg/ml and injected intraperitoneally (ip) at a dose of 100 mg/kg according to a previous study (Wang et al., 2017). LPS was dissolved in sterile saline to the concentration of 50 μg/ml. Each rat was ip-injected at a dose of 500 μg/kg, according to our previous study (Sun et al., 2015).

Experimental Protocol and Pharmacological Treatments

Experiment 1 (*In Vivo*)

Rats were divided into five groups (groups A–E), with 16 animals in each group. Empty treatments were administered to the rats in group A. Rats received either icv injections of 2 μl of vehicle (group B), 2 μl of 0.15 μg/μl TM (group C), 2 μl of 1.5 μg/μl TM (group D), or 2 μl of 15 μg/μl TM (group E). These concentrations were based on previous work from our laboratory (Wang et al., 2017). The study design is briefly illustrated in Supplementary Figures 1B,C.

Experiment 2 (*In Vivo*)

Rats were randomly divided into five groups (groups A–E), with 16 animals in each group. Rats in groups B, C, D, and E received icv cannula implantation, while empty treatments were administered to the rats in group A. Rats were administered an intraperitoneal injection of 100 mg/kg 4-PBA (group E) or an equivalent volume of sterile saline (groups B–D). Next, a dose of 2 μl of 1.5 μg/μl TM (groups D and E) or 2 μl of vehicle (10% DMSO in saline) (group B and C) was injected through the brain cannulas. One hour after 4-PBA/TM treatment, intraperitoneal injections were administered (group B: normal saline; groups C, D, and E: 500 μg/kg LPS). The experimental design is briefly illustrated in Supplementary Figures 1D,E.

According to the "3R" principle of ethical animal use, the same rats were used for group A in both experiments 1 and 2.

Experiment 1 (*In Vitro*)

Primary astrocytes were incubated for 24 h at different concentrations of TM (0.1, 1, and 10 ng/ml). The study design is briefly shown in Supplementary Figure 1F.

Experiment 2 (*In Vitro*)

Astrocytes were pretreated transiently with TM at 1 ng/ml with or without 4-PBA for 1 h, followed by thorough washing to remove the TM and 4-PBA, and incubated in fresh medium with or without LPS for 24 h. The experimental procedure is briefly illustrated in Supplementary Figure 1G.

Primary Astrocyte Cultures

Primary astrocyte cultures were prepared from neonatal (P1–P2) rat brains as previously described (Xu et al., 2018). Briefly, the cerebral cortices were isolated and digested at 37°C for 10 min in phosphate-buffered saline (PBS) containing 0.25% trypsin-EDTA. The dissociated cells were passed through a 100-μm pore mesh to remove debris. The cell suspension was seeded on poly-D-lysine-coated flasks in high-glucose Dulbecco's Modified Eagle's medium supplemented with 10% fetal bovine serum. The culture medium was changed for fresh solution every 3 days. After 10 days of cultivation, astrocytes were separated from the microglia by shaking for 5 h at 150 rpm. The purity of the astrocytes was >95% as confirmed by anti-GFAP immunochemical staining.

Cell Counting Kit-8 (CCK-8) Assay

Astrocytic viability was quantified using a CCK-8 assay based on the manufacturer's instructions (Beyotime, Shanghai, China). Briefly, 10 μl of the CCK-8 solution was added to each well of a 96-well plate containing 3×10^4 astrocytes following treatment with different concentrations of reagents and the absorbance was measured after a 1-h incubation at 37°C at 450 nm using a DTX-880 multimode microplate reader. Each experiment was repeated at least three times.

Enzyme-Linked Immunosorbent Assay (ELISA)

IL-6 and IL-1β levels in the astrocytic supernatant were measured using ELISA kits from R&D Systems (Minneapolis, MN, United States) according to the manufacturer's instructions. See the Supplementary Material for more information.

Western Blot Analysis

Hippocampal tissues and astrocytes were homogenized in RIPA lysis buffer, which contained 50 mM Tris, 150 mM NaCl, 1% Triton X-100, 2 mM EDTA, 1.5 μg/mL leupeptin, and 1 mM phenylmethylsulfonyl fluoride. The lysate was centrifuged for 20 min at 12,000 × *g* at 4°C. The protein content was determined by BCA assay (Thermo Scientific, Waltham, MA, United States), and 20 μg of protein was loaded per lane on a modified sodium dodecyl sulfate polyacrylamide gel electrophoresis. Separated proteins were transferred onto polyvinylidene difluoride membranes (Milipore, Bedford, MA, United States) and blocked for 1 h with 5% non-fat milk in Tris-buffered saline with Tween 20. Blocked membranes were probed overnight with specific primary antibodies diluted in 5% non-fat milk according to the recommendation of the manufacturer. After washing, membranes were incubated with anti-rabbit or anti-mouse IgG-HRP secondary antibodies, washed, and incubated with ECL reagent before exposure to film. Densitometry analysis was performed with the Image Lab software (Bio-Rad, Richmond, CA, United States) and quantified using the gel analysis plugin for Image J (NIH, Bethesda, MD, United States).

Immunohisto/Cytochemistry

The astrocyte culture medium was removed, and cells were fixed with 4% paraformaldehyde (PFA) for 30 min. The cells were then blocked with 5% bovine serum albumin containing 0.1% Triton X-100 for 1 h. Specific primary antibodies were added at an indicated concentration and incubated overnight

at 4°C. Following washes with PBS, the secondary antibodies (Alexa-Fluor-conjugated) were added and incubated for 1 h at 37°C. The images were captured using a confocal microscope (Zeiss LSM 510; Zeiss, Oberkochen, Germany).

Immunohistochemistry was used to determine the activation of the astrocytes in the hippocampus. Briefly, rats were perfused transcardially with 37°C saline followed by ice-cold 4% PFA. The ipsilateral hippocampal tissue was removed and fixed for 1 h in 4% PFA at 4°C. The tissue was sectioned at 15 μm with a cryostat. Sections were incubated overnight with specific primary antibodies followed by the appropriate secondary antibodies. Confocal images were obtained with a confocal microscope (Zeiss LSM 510).

The confocal microscope parameters were maintained constant across all samples, and samples of different groups were always processed in parallel. Fluorescence intensity was quantified using ImageJ and normalized to the fluorescence levels observed in untreated samples as described.

Evan's Blue (EB) Extravasation

Two percent of EB dye (Sigma-Aldrich, St. Louis, MI, United States) in 0.9% saline (5 mL/kg) was injected intravenously (right femoral vein), and 30 min later, the rats were perfused transcardially with 0.9% saline to remove the intravascular blood and EB. Then, the brains were harvested and homogenized in 0.5 ml of 50% trichloroacetic acid and centrifuged at 10,000 × *g* for 10 min. EB concentrations in supernatants were measured using spectrophotometry at 620 nm.

Statistical Analysis

Data are expressed as mean ± SEM. Two-tailed unpaired *t*-tests were used for comparisons between two groups, and multiple comparisons were evaluated using an appropriate ANOVA. *Post hoc* comparisons were performed using Tukey's test when appropriate. The alpha level was set at $P < 0.05$.

RESULTS

Low Concentrations of TM Generated Non-toxic, Mild ER Stress in Astrocytes

Many studies have shown that astrocytes may be vulnerable to ER stress-induced cell apoptosis. Consequently, primary cultured astrocytes were first exposed to different concentrations of TM for 24 h and their activities were tested using the CCK8 reagent. Our results indicate that TM (<10 ng/ml) had no effects on the cell viability of astrocytes compared to the control group (**Figure 1A**). Therefore, doses of 0.1, 1, and 10 ng/ml were selected for the subsequent experiments. The next experiment was conducted to explore whether lower concentrations of TM could also cause mild ER stress in astrocytes.

IRE1α initiates the most conservative signaling pathway of ER stress that, upon phosphorylation, cuts the non-conventional splicing of XBP-1 (XBP1u) mRNA into spliced-XBP1 (XBP1s) mRNA, which encodes a transcription activator that regulates ER protein folding (Gardner et al., 2013). Thus, to further determine the extent of IRE1-signaling activation, we measured the protein levels of p-IRE1α, XBP1s, and XBP1u using western blot analysis with specific antibodies (**Figure 1B**). TM (0.1, 1, and 10 ng/ml) significantly increased the expression levels of p-IRE1α and XBP1s, while the same treatment reduced XBP1u expression (**Figures 1C,D**). As a crucial stress sensor of ER stress, PERK is a transmembrane kinase that phosphorylates EIF2α at Ser51(Gardner et al., 2013). However, persistent EIF2α phosphorylation paradoxically upregulates translation of ATF4 mRNA, which in turn activates pro-apoptotic components such as the transcription of CCAAT/enhancer binding protein (C/EBP) homologous protein (CHOP) (Hetz and Mollereau, 2014).

To characterize the activation kinetics of PERK signaling of ER stress, we examined the expression of p-PERK and its downstream products: p-EIF2α, ATF4, and CHOP using western blot analysis. Compared with the control group, p-PERK and p-EIF2α phosphorylation was modestly elevated at concentrations of 0.1, 1, and 10 ng/ml TM (**Figure 1C**). It is worth noting that lower doses of TM (0.1 and 1 ng/ml) were no longer effective at increasing ATF4 and CHOP expression levels but that high concentrations (10 ng/ml) did increase ATF4 and CHOP expression (**Figure 1E**).

Similar results were also observed in the immunofluorescence assay (**Figures 2A,B**). Consistent with the previous data, increases of IRE1α phosphorylation were observed following TM treatment (0.1, 1, and 10 ng/ml) in the primary cultured astrocytes (**Figure 2C**). CHOP levels, in contrast, were not changed in primary cultured astrocytes treated with TM at doses of 0.1 or 1 ng/ml. The CHOP expression was only elevated in response to the highest dose of TM (10 ng/ml) (**Figure 2D**). These findings showed that lower concentrations of TM (0.1 and 1 ng/ml) triggered benign and mild ER-stress responses in the astrocytes.

Mild ER Stress Attenuated LPS-Induced Astrocytic Inflammatory Responses and Overactivation

We observed that low concentrations of TM (0.1 and 1 ng/ml) caused mild ER stress in the astrocytes but did not induce cell death. In the following experiment, we therefore selected a dosage of TM (1 ng/ml) to generate mild ER stress in the astrocytes. Next, we investigated the effects of mild ER stress in LPS-stimulated astrocyte activation.

TM Inhibited IL-1β and IL-6 Production in Primary Cultured Astrocytes

Astrocytes were treated with LPS in the absence or presence of TM. Because astrocytes participate in neuroinflammation via the excessive secretion of proinflammatory factors, IL-6 and IL-1β were analyzed with ELISA. As the results shown in **Figure 3** illustrate, LPS enhanced the expression of IL-1β and IL-6. Additionally, 1 ng/ml TM did not enhance, but instead suppressed, LPS-induced proinflammatory factor expression.

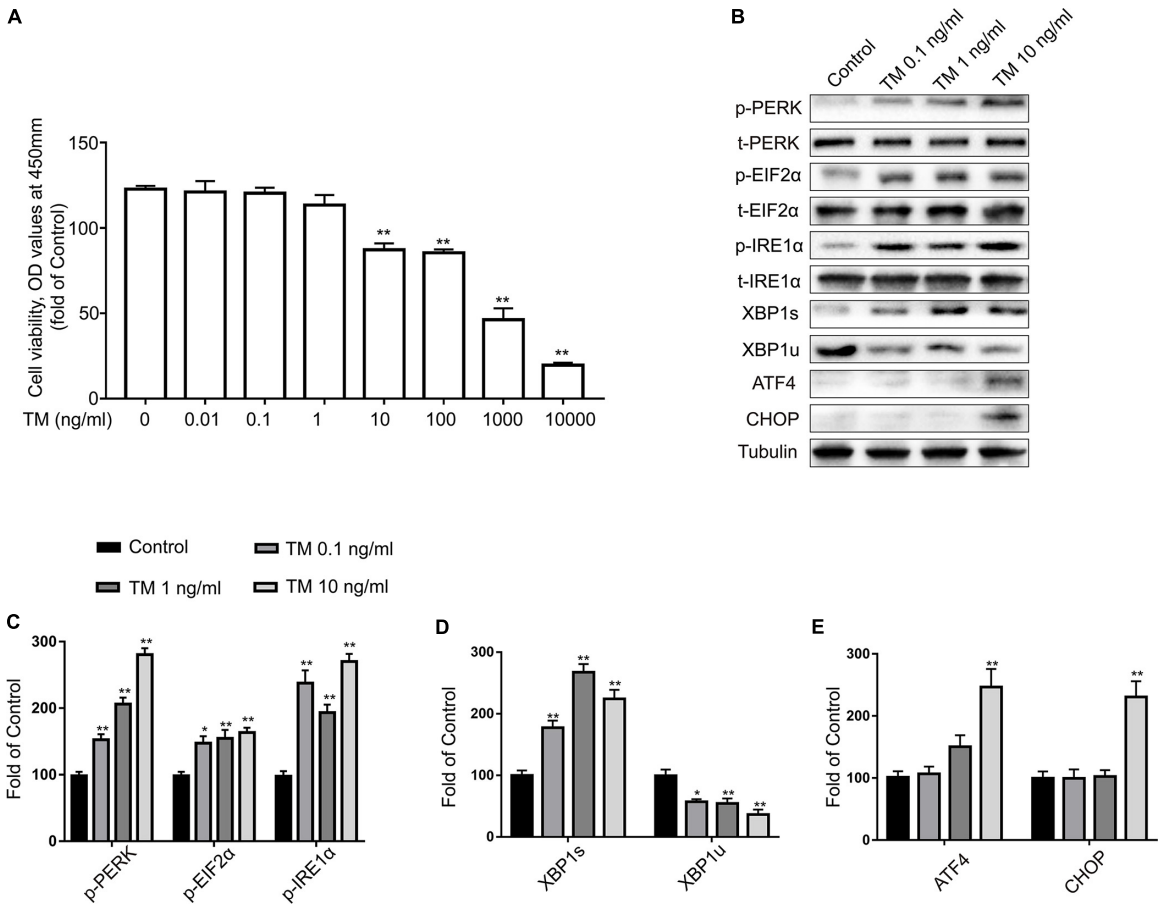

FIGURE 1 | Low doses of TM activated a non-toxic, mild ER stress in primary cultured astrocytes. **(A)** Primary astrocytes were treated with TM (0.01 to 10000 ng/ml) for 24 h followed by assessment of cell viability using the CCK-8 assay. **(B)** The expression levels of p-PERK, p-EIF2α, p-IRE1α, XBP1s, XBP1u, ATF4, and CHOP in primary cultured astrocytes were detected by Western blotting using specific antibodies. **(C)** Phosphorylated levels of PERK, EIF2α, and IRE1α were quantified and normalized to corresponding total levels. **(D)** Expression of XBP1s and XBP1u was quantified and normalized to Tubulin expression. **(E)** Expression of ATF4 and CHOP was quantified and normalized to Tubulin expression. Each value was then expressed relative to that of the control group, which was set to 100. All experiments were repeated three times. $^{*}P < 0.05$, $^{**}P < 0.01$ vs. control group. The data are presented as the mean ± SEM.

TM Reversed LPS-Induced Astrocyte Activation

To further confirm the protective effects of TM on primary astrocytes, GFAP expression levels corresponding to activated astrocytes were tested with western blot analysis. LPS significantly increased the expression of GFAP in primary cultured astrocytes compared with the levels observed in the control group, but these elevations were remarkably inhibited by TM pretreatment (**Figures 4A,B**). To validate these findings, astrocytes were labeled with GFAP by immunofluorescence (**Figures 4C,D**), which also confirmed that TM can inhibit LPS-induced astrocytic activation.

4-PBA Reversed TM-Induced Suppression of Astrocytic IL-1β, IL-6, and GFAP Production

Next, we examined whether mild ER-stress activation is responsible for TM-mediated inhibition of astrocytic activation and anti-inflammatory responses.

To test this hypothesis, we used a chemical chaperone, 4-PBA, to reduce ER stress. Astrocytes were first subjected to TM (1 ng/ml), individually or in the presence of 4-PBA at progressive concentrations for 1 h before treatment with LPS (100 ng/ml) for 24 h. Our results indicate that treatment of the primary cultured astrocytes with 1 ng/ml TM and 100 ng/ml LPS in the presence of T 4-PBA (<1,000 μM) had no significant cytotoxicity (**Figure 5**). We therefore selected a dose of 100 μM 4-PBA to ameliorate ER stress in the astrocytes. The primary cultured astrocytes were subjected to TM (1 ng/ml) and 4-PBA (100 μM) treatment for 1 h. Reperfusion was then performed by refreshing the astrocytes with normal medium, containing 100 ng/ml LPS. As shown in **Figure 6A**, there was a clear effect of 4-PBA against ER stress, as it obviously decreased p-PERK, p-EIF2α, p-IRE1α, and XBP1s protein levels and increased XBP1u protein levels compared to non-PBA treated cells (**Figures 6B–D**).

Importantly, 4-PBA partially blocked the TM-mediated inhibition of astrocytic activation and anti-inflammatory effects, as reflected by the increased expression of IL-1β, IL-6, and GFAP. We wondered whether this opposite effect was caused by the cytotoxic effects of 4-PBA.

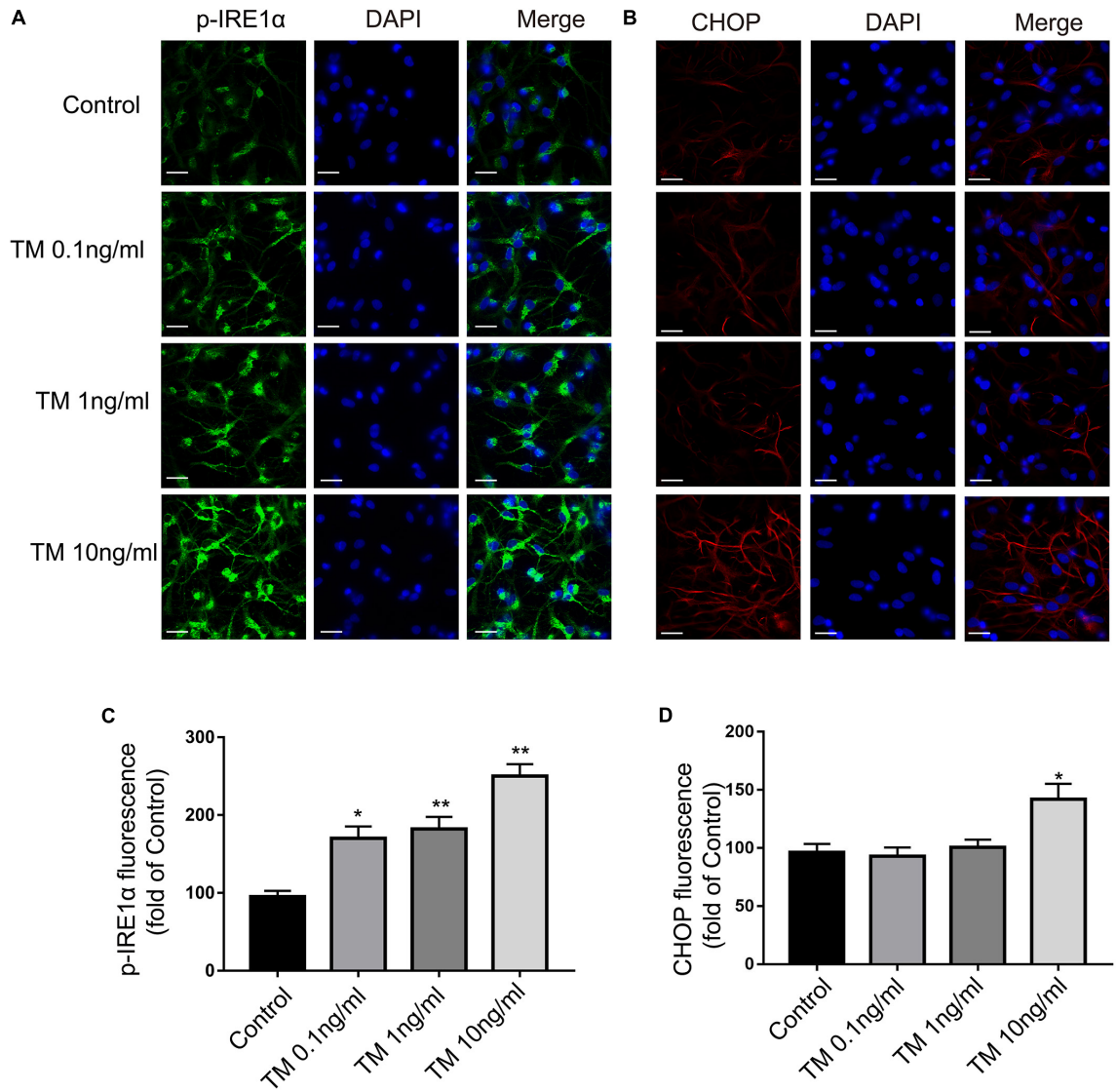

FIGURE 2 | Mild ER stress increased p-IRE1α expression but had no effect on CHOP expression in primary cultured astrocytes. **(A)** Astrocytes were stained with p-IRE1α antibody. p-IRE1α-immunopositivity in primary astrocytes was observed using confocal scanning. **(B)** Astrocytes were stained with CHOP antibody. CHOP-immunopositivity in primary astrocytes was observed using confocal scanning. Blue staining represents DAPI. Scale bar = 25 μm. **(C)** Quantitative data of the mean intensity of p-IRE1α fluorescence in primary astrocytes. **(D)** Quantitative data of the mean intensity of CHOP fluorescence in primary astrocytes. Each value was then expressed relative to that of the control group, which was set to 100. All experiments were repeated three times. $^{*}P < 0.05$, $^{**}P < 0.01$ vs. control group. The data are presented as the mean ± SEM.

Using the CCK-8 method, we excluded this possibility, as coincubation with LPS (100 ng/ml), TM (1 ng/ml), and 4-PBA (100 μM) for 24 h revealed no significant cytotoxicity and did not affect cell viability (**Figure 5**). Collectively, these data demonstrate that TM pretreatment protected astrocytes by, at least partly, inducing mild ER stress.

Mild ER Stress Ameliorated LPS-Induced Cognitive Decline

To confirm the *in vitro* findings, we also examined the effects of mild ER stress *in vivo*.

Our previous study showed that a 3-μg dose of TM triggered mild and benign perturbations of ER function in the rat hippocampus but did not induce drastic behavioral alterations or death (Wang et al., 2017). In the following experiment, rats were administered an icv injection of 3 μg TM to induce mild ER stress followed by systemic LPS administration.

Consistent with our previous experiment, LPS caused severe memory impairment in rats, as reflected by a significant reduction in freezing behavior and an improvement in the number of learning trials (Sun et al., 2015; Wang et al., 2017). Notably, TM pretreatment ameliorated

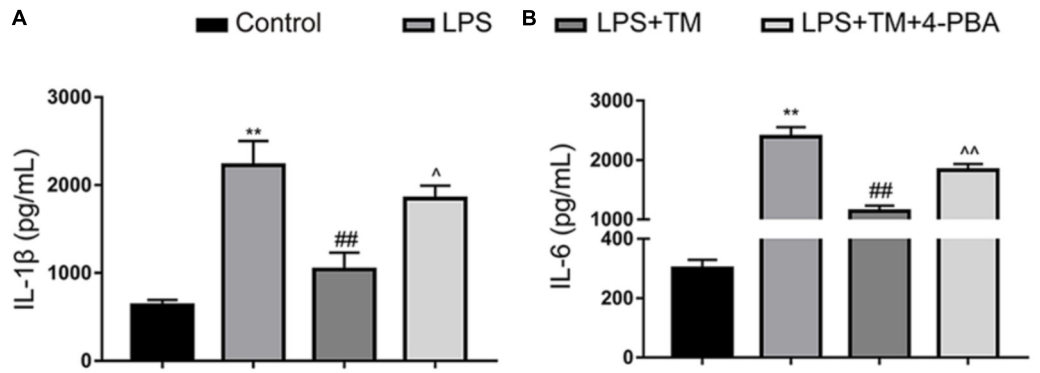

FIGURE 3 | Mild ER stress inhibits proinflammatory cytokine IL-1β and IL-6 production in primary cultured astrocytes. **(A)** The levels of the proinflammatory factors IL-1β were detected by ELISA. **(B)** The levels of the proinflammatory factors IL-6 were detected by ELISA. The data are representative of 3 independent experiments. $^{*}P < 0.05$, $^{**}P < 0.01$ vs. control group. $^{\#}P < 0.05$, $^{\#\#}P < 0.01$ vs. LPS treatment group. $^{\wedge}P < 0.05$, $^{\wedge\wedge}P < 0.01$ vs. TM treatment group. The data are presented as the mean ± SEM.

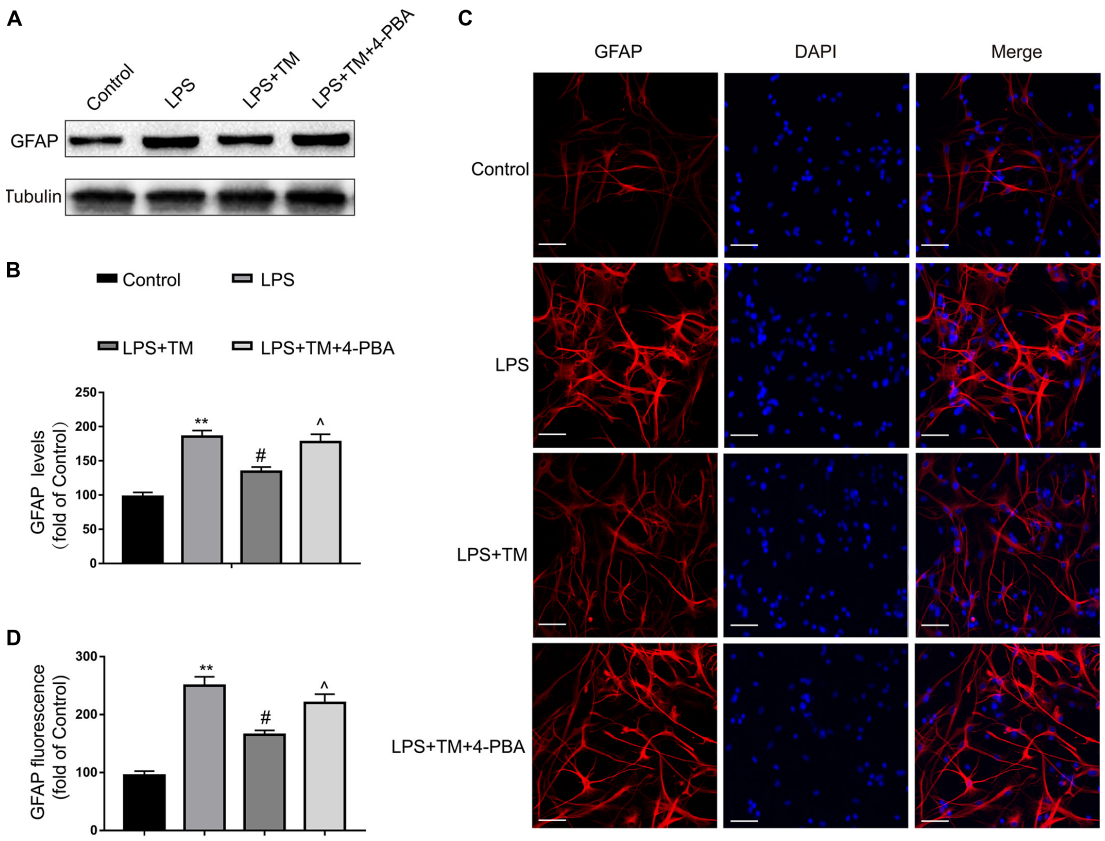

FIGURE 4 | Mild ER stress alleviated astrocyte activation. **(A)** The protein levels of GFAP were detected by Western blotting using specific antibody in the primary astrocytes. **(B)** Expression of GFAP was quantified and normalized to Tubulin levels. Each value is expressed relative to that in the control group, which was set to 100. **(C)** Astrocyte was stained with GFAP antibody as indicated. Blue staining represents DAPI. Scale bar = 25 μm. **(D)** Quantitative data of the mean intensity of GFAP fluorescence in primary astrocytes. Each value is expressed relative to that in the control group, which was set to 100. All experiments were repeated three times. $^{*}P < 0.05$, $^{**}P < 0.01$ vs. control group. $^{\#}P < 0.05$, $^{\#\#}P < 0.01$ vs. LPS treatment group. $^{\wedge}P < 0.05$, $^{\wedge\wedge}P < 0.01$ vs. TM treatment group. The data are presented as the mean ± SEM.

LPS-induced cognitive decline. However, concomitant administration of 4-PBA partially reversed the cognitive recovery conferred by TM (**Figure 7**). Therefore, these results further substantiate our previous findings that mild ER stress can protect against LPS-induced cognitive dysfunction.

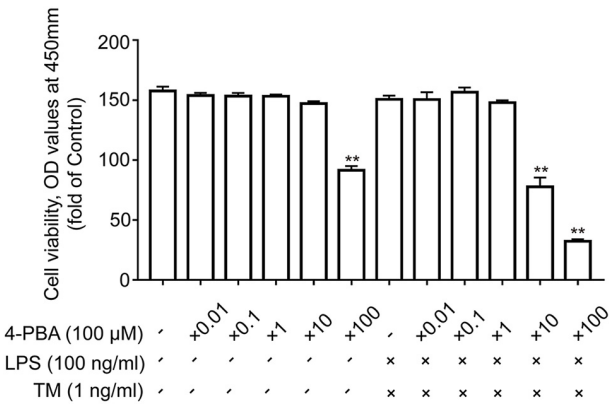

FIGURE 5 | The effects of 4-PBA on cell viability in primary astrocytes. Primary cultured astrocytes were subjected to LPS and TM and treated with the indicated dosage of 4-PBA. After 24 h of treatment, cell viability was determined using CCK-8. All experiments were repeated three times. $^{*}P < 0.05$, $^{**}P < 0.01$ vs. control group. The data are presented as the mean ± SEM.

Mild ER Stress Attenuated LPS-Induced Astrocytic Activation in the Hippocampus

The western blot analysis showed that systemic LPS administration enhanced the expression of GFAP in the hippocampi of rats, but these elevations were potently suppressed by TM pretreatment. Similar to the *in vitro* results, 4-PBA diminished the TM-mediated inhibition of astrocytic activation in the hippocampus (**Figures 8A,B**). These western blot findings were further validated by immunofluorescence (**Figures 8C,D**). Our results therefore further confirmed that mild ER stress was required for the TM-mediated protection.

Mild ER Stress Alleviated LPS-Induced BBB Hyperpermeability

Mild ER Stress Counteracted LPS-Induced Albumin Leakage in the Hippocampus

As BBB disruption leads to an extravasation of blood-borne proteins, we examined the leakage of albumin to confirm the integrity of the BBB. As shown in **Figure 9A**, LPS significantly increased albumin levels in the hippocampus of rats, compared with the naive group. Although TM administration induced a dramatic decrease in albumin expression, 4-PBA greatly diminished this effect (**Figure 9B**).

Mild ER Stress Inhibited the Decreases in Hippocampal Occludin and Claudin-5 Induced by LPS

Decreased tight-junction protein expressions are associated with alterations in BBB permeability. As occludin and claudin-5 are reportedly integral tight-junction membrane proteins (Qi et al., 2016), we examined the levels of occludin and claudin-5 in the hippocampus of rats with western blot analysis. LPS evoked significant decreases in occludin and claudin-5 protein expression compared with the naive group. Treatment with TM effectively negated the increases in hippocampal occludin and claudin-5 induced by LPS, while no elevated occludin and claudin-5 expression was detected after 4-PBA administration (**Figures 9C,D**).

Immunofluorescence staining was also used to analyze occludin and claudin-5 protein expression (**Figures 9E–H**), showing a marked decrease in occludin and claudin-5 protein levels in the LPS group compared with the naive group. Impressively, TM treatment significantly attenuated the occludin and claudin-5 protein expression decrease induced LPS, but 4-PBA cotreatment partially reversed the effect of TM. These results show that mild ER stress prevented BBB disruption by decreasing tight-junction protein levels.

Mild ER Stress Reversed the Increases in Hippocampal Matrix Metalloproteinase (MMP)-2 and MMP-9 Induced by LPS

Based on the recent observation that MMP activity is associated with the degradation of tight-junction proteins (Tasaki et al., 2014), we next monitored the expression of MMP-2 and MMP-9 upon mild ER stress induction. As expected, LPS treatment significantly increased MMP-2 and MMP-9 activity, while pretreatment with TM significantly attenuated LPS treatment-induced MMP-2 and MMP-9 activity. The expression levels of MMP-2 and MMP-9 were markedly increased after 4-PBA cotreatment, leading to significant reversal of these TM-evoked effects (**Figures 9I,J**). These results indicate that mild ER stress can inhibit LPS-induced MMP-2 and MMP-9 activation.

Mild ER Stress Reduced EB Extravasation in the LPS-Treated Rats

EB extravasation is a widely used marker for detecting breaches in the BBB. **Figure 10A** shows the EB extravasation in the extracted brains, indicating BBB disruption. As shown in **Figure 10B**, EB absorbance was increased in the LPS-treated rats compared with the naive group, which was apparently attenuated by TM treatment. Although TM alleviated LPS-induced BBB hyperpermeability, 4-PBA greatly diminished this effect as evidenced by increased EB content in the brain after 4-PBA administration.

DISCUSSION

Neurodegenerative diseases, exemplified by AD, PD, amyotrophic lateral sclerosis, and multiple sclerosis, pose the most pressing health and economic burden on developed societies with aging populations (Estes and McAllister, 2016). Neuroinflammation is an amplifier of neurodegenerative pathology, and thus, its influence is a subject of increasing interest (Glass et al., 2010).

In recent years, astrocytes have gained attention due to their pivotal role in brain homeostasis both in normal and pathological conditions (Haim and Rowitch, 2017). Long thought of as just supporting cells in the brain, astrocytes have in fact several

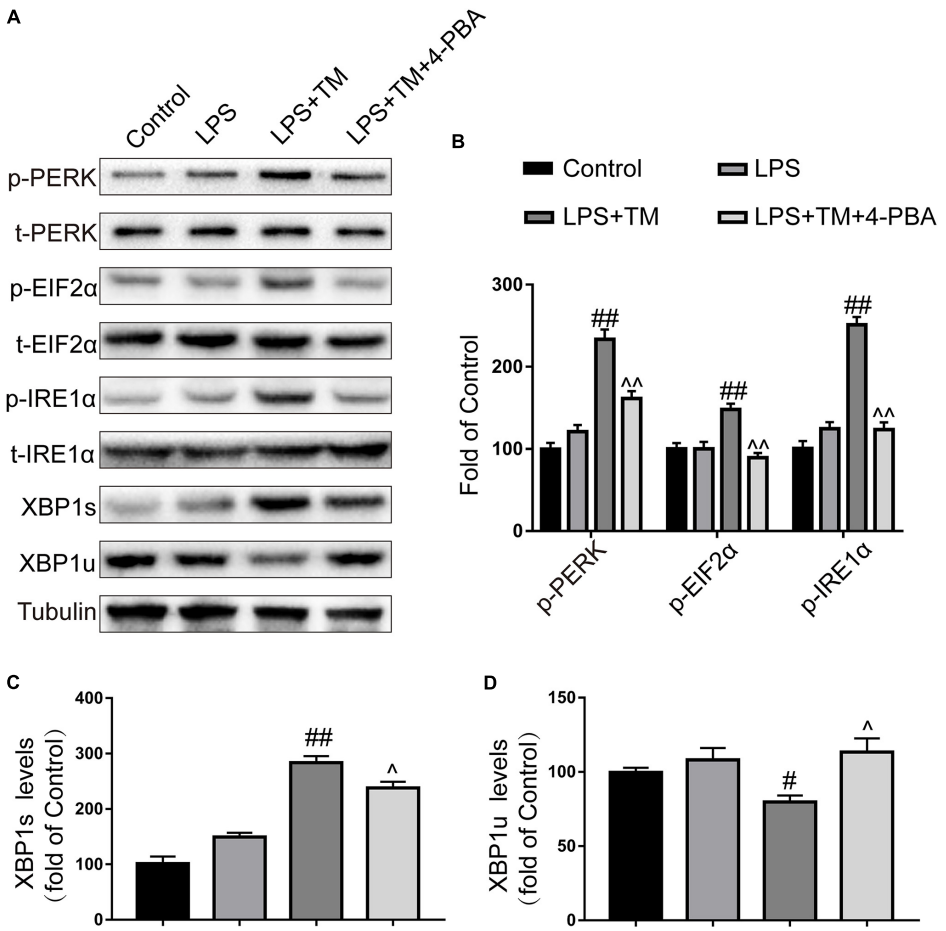

FIGURE 6 | 4-PBA partially inhibited mild ER stress in primary cultured astrocytes. **(A)** The expression levels of p-PERK, p-EIF2α, p-IRE1α, XBP1s, and XBP1u in primary cultured astrocytes were detected by Western blotting using specific antibodies. **(B)** Phosphorylated levels of PERK, EIF2α, and IRE1α were quantified and normalized to corresponding total levels. **(C)** Expression of XBP1s was quantified and normalized to Tubulin expression. **(D)** Expression of XBP1u was quantified and normalized to Tubulin expression. Each value is expressed relative to that in the control group, which was set to 100. All experiments were repeated three times. $^{\#}P < 0.05$, $^{\#\#}P < 0.01$ vs. LPS treatment group. $^{\wedge}P < 0.05$, $^{\wedge\wedge}P < 0.01$ vs. TM treatment group. The data are presented as the mean ± SEM.

housekeeping functions. Recently, astrocytes have become the focus of attention because of their metabolic coupling with neurons and the BBB (Cabezas et al., 2014).

The emerging evidence highlights the critical roles of astrocytes in regulating neuroinflammation through a process called "astrogliosis," (Sofroniew, 2015), which leads to an increase in the number, morphology, and motility of astrocytes and illustrates the role of the neuroinflammatory response in neurodegenerative diseases (Garwood et al., 2017). Astrogliosis is a well-characterized spectrum of cellular, molecular, and functional astrocytic changes in response to CNS damage. The cells in which astrogliosis occurs have the potential to be strongly reactive, thus contributing to the production of numerous proinflammatory molecules, such as cytokines, to exacerbate neuroinflammation (Khakh and Sofroniew, 2015; Bazargani and Attwell, 2016).

In recent years, numerous studies have shown that ER stress in astrocytes is associated with astrogliosis and the development of neuroinflammation (Cheng et al., 2013; Hong et al., 2016). However, these studies, which utilized high concentrations of pharmacological ER stressors to cause robust perturbation of ER function in experimental animals or cultured cells, failed to reproduce physiological and non-lethal levels of ER stress. ER stress activates the signaling events termed UPR. UPR is a heterogeneous and context-dependent cellular response, determined by the intensity or duration of the exposure to stress (Hetz and Mollereau, 2014). Under severe and robust ER stress, activation of the UPR operates as a pro-apoptotic program that reinforces the expression of pro-apoptotic components such as CHOP through ATF4; ER-related neurotoxicity consequently occurs. Under conditions of moderate and mild ER stress, ATF4 and CHOP are highly unstable at the mRNA and protein levels; these proteins are necessarily short-lived without a persistent and robust ER-stress signal transduction pathway (Matus et al., 2014). Therefore, mild perturbations of ER function may operate as an adaptive feedback mechanism of resistance against any possible further injuries.

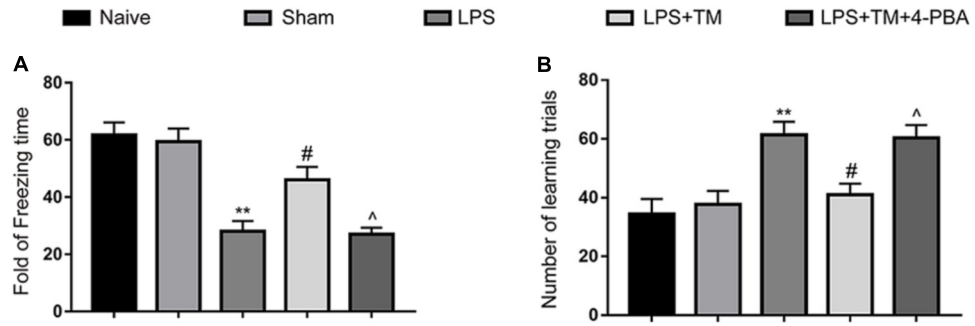

FIGURE 7 | Mild ER stress ameliorated LPS-induced cognitive impairment in the hippocampus. **(A)** Contextual fear response, as measured by freezing time, was determined in the rats (n = 12). **(B)** The number of learning trials was recorded to analyze the Y-maze test (n = 12). The data are presented as the mean ± SEM. $^{*}P < 0.05$, $^{**}P < 0.01$ vs. naïve group. $^{\#}P < 0.05$, $^{\#\#}P < 0.01$ vs. LPS treatment group. $^{\wedge}P < 0.05$, $^{\wedge\wedge}P < 0.01$ vs. TM treatment group. The data are representative of three independent experiments.

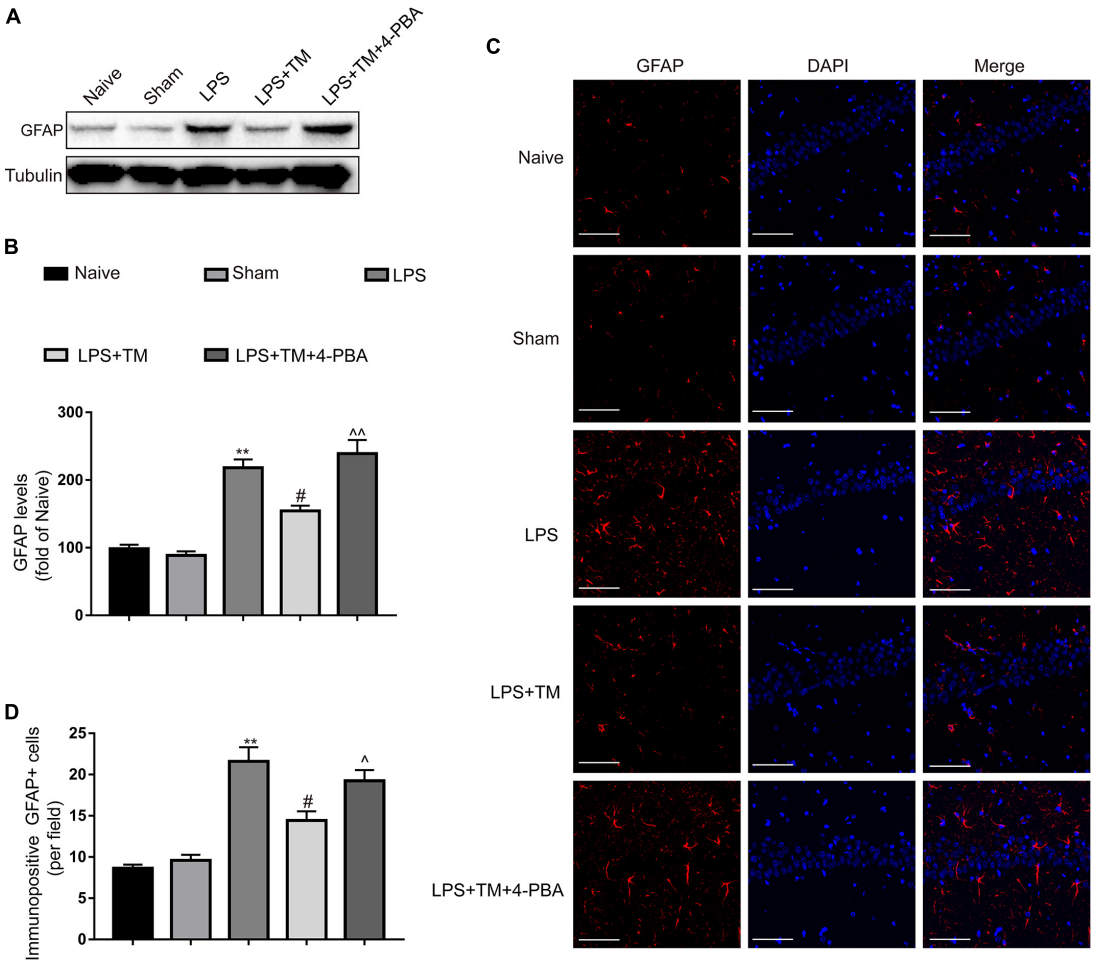

FIGURE 8 | Mild ER stress reduced the hippocampal astrocyte activation. **(A)** The protein levels of GFAP were detected by Western blotting using specific antibody in hippocampus. **(B)** Expression of GFAP was quantified and normalized to Tubulin levels. Each value was expressed relative to that of the naïve group, which was set to 100 (n = 6). **(C)** Immunofluorescent staining was used to detect GFAP, a maker of astrocytes, in hippocampal CA1 region. Blue staining represents DAPI. Scale bar = 200 μm. **(D)** Quantitative of GFAP-positive cells in the CA1 area of hippocampus. The data are representative of three independent experiments. $^{*}P < 0.05$, $^{**}P < 0.01$ vs. naïve group. $^{\#}P < 0.05$, $^{\#\#}P < 0.01$ vs. LPS treatment group. $^{\wedge}P < 0.05$, $^{\wedge\wedge}P < 0.01$ vs. TM treatment group. The data are presented as the mean ± SEM.

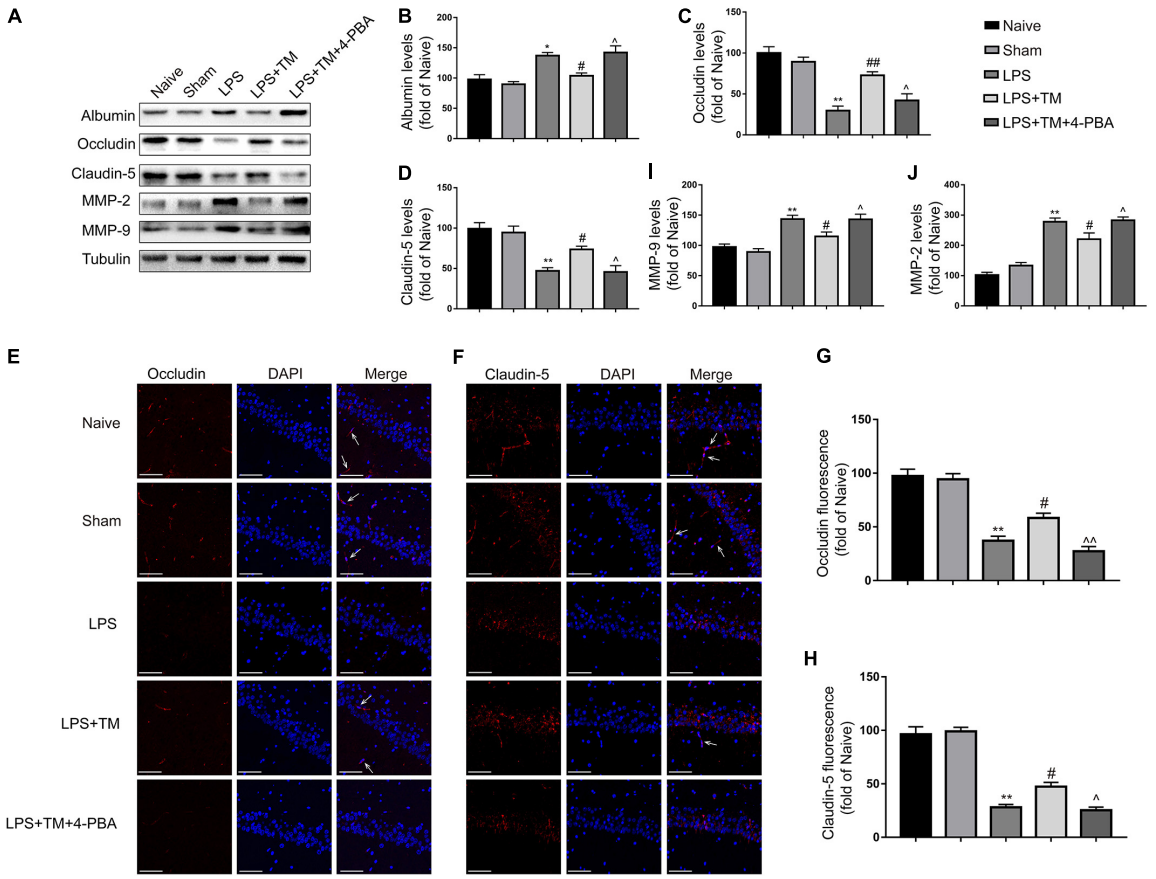

FIGURE 9 | Mild ER stress attenuated LPS-induced BBB hyperpermeability in hippocampus. **(A)** The expression levels of albumin, occludin, claudin-5, MMP-2, and MMP-9 were detected in the hippocampus of rats by Western blotting using specific antibodies. **(B–D)** Expression of albumin, occludin and claudin-5 was quantified and normalized to Tubulin levels. **(E,F)** Images acquired by confocal microscopy show the occludin and claudin-5 levels in the CA1 area of the hippocampus. The arrow in G points to an area in the CA1 area with high occludin immunoreactivity. The arrow in H points to an area in the CA1 area with high claudin-5 immunoreactivity. Scale bar, 100 μm. **(G,H)** Quantitative data of the mean intensities of occludin and claudin-5 fluorescence. **(I,J)** Expression of MMP-2 and MMP-9 was quantified and normalized to Tubulin levels. Each value was expressed relative to the values of the naïve group, which was set to 100 (n = 6). The data are representative of three independent experiments. $^{*}P < 0.05$, $^{**}P < 0.01$ vs. naïve group. $^{\#}P < 0.05$, $^{\#\#}P < 0.01$ vs. LPS treatment group. $^{\wedge}P < 0.05$, $^{\wedge\wedge}P < 0.01$ vs. TM treatment group. The data are presented as the mean ± SEM.

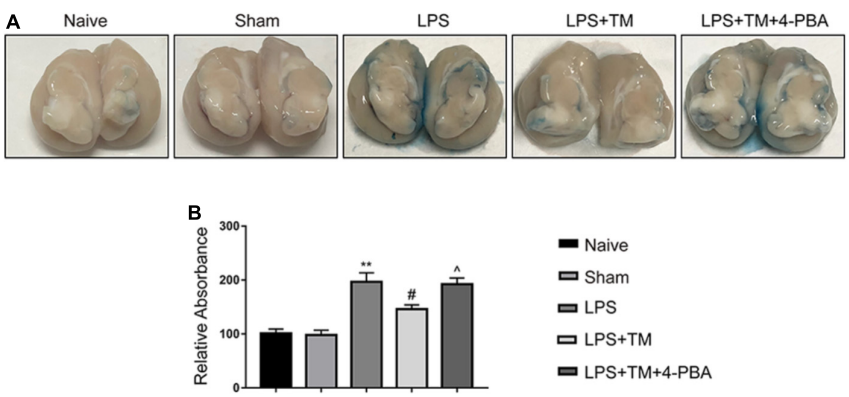

FIGURE 10 | Mild ER stress reduced EB extravasation in the LPS-treated rats. **(A)** Representative photographs of EB extravasation in the extracted brains of various groups. **(B)** The quantitative analysis of EB leakage. Each value was expressed relative to the values of the naïve group, which was set to 100 (n = 4). The data are presented as the mean ± SEM. $^{*}P < 0.05$, $^{**}P < 0.01$ vs. naïve group. $^{\#}P < 0.05$, $^{\#\#}P < 0.01$ vs. LPS treatment group. $^{\wedge}P < 0.05$, $^{\wedge\wedge}P < 0.01$ vs. TM treatment group.

We evaluated the levels of ATF4 and CHOP expression in astrocytes to further characterize the extent of ER stress in response to varying concentrations of TM. In the present investigation, activation of the PERK-EIF2α/IRE1-XBP1 pathway was detected at both high and low concentrations of TM. However, TM at the highest dose triggered a robust ER-stress response in astrocytes. Only at high concentrations (10 ng/ml) was TM able to trigger a robust ER-stress response in astrocytes, as evident by effective upregulation of ATF4 and CHOP, while lower doses of TM did not increase CHOP and ATF4 protein expression.

GFAP overexpression is a reliable marker for identifying reactive astrocytes under pathological conditions in the hypertrophic response of astrogliosis (Allaman et al., 2011). In this study, we observed that LPS altered the morphology of astrocytes, as demonstrated by terminal swelling filopodium-like processes, and induced the upregulation of GFAP expression. Additionally, LPS significantly induced the inflammatory cytokines, IL-1β, and IL-6, in cultured primary astrocytes. We defined *in vitro* and *in vivo* experimental conditions in which mild ER stress did not induce astrocytic lethality but rather suppressed LPS-induced overactivation and inflammatory responses in astrocytes. We demonstrated that astrocyte protection occurred as an intrinsic consequence of non-toxic, mild activation of ER stress.

It was reported that the heterogeneity between mild ER stress and robust ER stress pertains to differences in the expression of downstream proteins. Although less is known about this non-toxic ER stress in various models, current information points toward a concept that describes this adaptive reaction, which we refer to as "hormesis" (Matus et al., 2014). For instance, TM at a low dosage orchestrated neuroprotection in *Drosophila* and mouse models of PD (Fouillet et al., 2014), AD (Casas-Tinto et al., 2011), brain inflammation (Hosoi et al., 2014), and brain ischemia/reperfusion (Ibuki et al., 2012).

Our previous study revealed that preconditioning with the ER stress-inducer, TM, at a low dosage protected against LPS-induced cognitive decline and neuroinflammation, while 4-PBA partly counteracted this protective effect (Wang et al., 2017). We have proposed that ER-mediated hormesis (or ER hormesis) is responsible for protection after LPS challenge. This hypothesis is also supported by our current results that showed that mild doses of TM relieved LPS-stimulated BBB hyperpermeability.

Albumin is a vascular marker that crosses the BBB very slowly and is therefore often used to measure the loss of BBB integrity (Xaio et al., 2001). Using the albumin quota, we confirmed the role of mild ER stress in BBB function. We found more albumin leakage in the hippocampus following LPS injection, which was inhibited by pretreatment with TM. Furthermore, our study showed that TM treatment alleviated BBB dysfunction and hyperpermeability, evident by the increased levels of tight-junction proteins claudin-5 and occludin along with reduced expression of MMP-2 and MMP-9. It is becoming clear that, on one hand, astrocytes can exert proinflammatory effects by releasing molecules that enhance BBB permeability; on the other hand, however, astrocytes can promote BBB-structure repair by releasing trophic factors (Cabezas et al., 2014). It is difficult to determine the specific mechanism underlying the astrocytic influence on the BBB in our experiment. Further detailed work is required to address this issue in the future.

In summary, our results support a potential protective role of mild ER stress in alleviating LPS-induced astrocytic overactivation and BBB disruption. The central feature of this protective mild ER stress appears to be the triggering and maintenance of ER stress at a moderate level that facilitates survival, without increasing the levels of pro-apoptotic proteins such as CHOP and ATF4. While many crucial questions remain to be answered, our study findings provide not only a better understanding of the role of ER stress in neurodegeneration but also the basis for a prospective cure for neurodegeneration in the future.

AUTHOR CONTRIBUTIONS

YC, QZ, JX, QQ, and PN performed the experiments. YW and YQ designed the study. YW wrote the manuscript. All authors read and approved the final manuscript.

FUNDING

This project was funded by the National Natural Science Foundation of China (No. 81671387) and Postgraduate Research & Practice Innovation Program of Jiangsu Province (KYCX17_1250).

ACKNOWLEDGMENTS

We would like to thank Dr. Le-ting Zhou from Southeast University for his kind help of revising our manuscript.

SUPPLEMENTARY MATERIAL

The Supplementary Material for this article can be found online at: https://www.frontiersin.org/articles/10.3389/fncel.2018.00222/full#supplementary-material

REFERENCES

Allaman, I., Bélanger, M., and Magistretti, P. J. (2011). Astrocyte–neuron metabolic relationships: for better and for worse. *Trends Neurosci.* 34, 76–87. doi: 10.1016/j.tins.2010.12.001

Bazargani, N., and Attwell, D. (2016). Astrocyte calcium signaling: the third wave. *Nat. Neurosci.* 19, 182–189. doi: 10.1038/nn.4201

Broux, B., Gowing, E., and Prat, A. (2015). Glial regulation of the blood-brain barrier in health and disease. *Semin. Immunopathol.* 37, 577–590. doi: 10.1007/s00281-015-0516-2

Cabezas, R., Avila, M., Gonzalez, J., El-Bachã, R. S., Bãez, E., Garciã-Segura, L. M., et al. (2014). Astrocytic modulation of blood brain barrier: perspectives on Parkinson's disease. *Front. Cell. Neurosci.* 8:211. doi: 10.3389/fncel.2014.00211

Casas-Tinto, S., Zhang, Y., Sanchez-Garcia, J., Gomez-Velazquez, M., Rincon-Limas, D. E., and Fernandez-Funez, P. (2011). The ER stress factor XBP1s prevents amyloid-beta neurotoxicity. *Hum. Mol. Genet.* 20, 2144–2160. doi: 10.1093/hmg/ddr100

Cheng, L., Zhao, H., Zhang, W., Liu, B., Liu, Y., Guo, Y., et al. (2013). Overexpression of conserved dopamine neurotrophic factor (CDNF) in astrocytes alleviates endoplasmic reticulum stress-induced cell damage and inflammatory cytokine secretion. *Biochem. Biophys. Res. Commun.* 435, 34–39. doi: 10.1016/j.bbrc.2013.04.029

Estes, M. L., and McAllister, A. K. (2016). Maternal immune activation: implications for neuropsychiatric disorders. *Science* 353, 772–777. doi: 10.1126/science.aag3194

Fouillet, A., Levet, C., Virgone, A., Robin, M., Dourlen, P., Rieusset, J., et al. (2014). ER stress inhibits neuronal death by promoting autophagy. *Autophagy* 8, 915–926. doi: 10.4161/auto.19716

Gardner, B. M., Pincus, D., Gotthardt, K., Gallagher, C. M., and Walter, P. (2013). Endoplasmic reticulum stress sensing in the unfolded protein response. *Cold Spring Harb. Perspect. Biol.* 5:a13169. doi: 10.1101/cshperspect.a013169

Garwood, C. J., Ratcliffe, L. E., Simpson, J. E., Heath, P. R., Ince, P. G., and Wharton, S. B. (2017). Review: astrocytes in Alzheimer's disease and other age-associated dementias: a supporting player with a central role. *Neuropathol. Appl. Neurobiol.* 43, 281–298. doi: 10.1111/nan.12338

Glass, C. K., Saijo, K., Winner, B., Marchetto, M. C., and Gage, F. H. (2010). Mechanisms underlying inflammation in neurodegeneration. *Cell* 140, 918–934. doi: 10.1016/j.cell.2010.02.016

Gorina, R., Font-Nieves, M., Márquez-Kisinousky, L., Santalucia, T., and Planas, A. M. (2011). Astrocyte TLR4 activation induces a proinflammatory environment through the interplay between MyD88-dependent NFκB signaling, MAPK, and Jak1/Stat1 pathways. *Glia* 59, 242–255. doi: 10.1002/glia.21094

Haim, L. B., and Rowitch, D. H. (2017). Functional diversity of astrocytes in neural circuit regulation. *Nat. Rev. Neurosci.* 18, 31–41. doi: 10.1038/nrn.2016.159

Hetz, C., and Mollereau, B. (2014). Disturbance of endoplasmic reticulum proteostasis in neurodegenerative diseases. *Nat. Rev. Neurosci.* 15, 233–249. doi: 10.1038/nrn3689

Hong, Y., Wang, X., Sun, S., Xue, G., Li, J., and Hou, Y. (2016). Progesterone exerts neuroprotective effects against abeta-induced neuroinflammation by attenuating ER stress in astrocytes. *Int. Immunopharmacol.* 33, 83–89. doi: 10.1016/j.intimp.2016.02.002

Hosoi, T., Noguchi, J., Takakuwa, M., Honda, M., Okuma, Y., Nomura, Y., et al. (2014). Inhibition of inducible nitric oxide synthase and interleukin-1β expression by tunicamycin in cultured glial cells exposed to lipopolysaccharide. *Brain Res.* 1558, 11–17. doi: 10.1016/j.brainres.2014.02.035

Ibuki, T., Yamasaki, Y., Mizuguchi, H., and Sokabe, M. (2012). Protective effects of XBP1 against oxygen and glucose deprivation/reoxygenation injury in rat primary hippocampal neurons. *Neurosci. Lett.* 518, 45–48. doi: 10.1016/j.neulet.2012.04.053

Khakh, B. S., and Sofroniew, M. V. (2015). Diversity of astrocyte functions and phenotypes in neural circuits. *Nat. Neurosci.* 18, 942–952. doi: 10.1038/nn.4043

Martin-Jiménez, C. A., García-Vega, Á., Cabezas, R., Aliev, G., Echeverria, V., González, J., et al. (2017). Astrocytes and endoplasmic reticulum stress: a bridge between obesity and neurodegenerative diseases. *Prog. Neurobiol.* 158, 45–68. doi: 10.1016/j.pneurobio.2017.08.001

Matus, S., Castillo, K., and Hetz, C. (2014). Hormesis: protecting neurons against cellular stress in Parkinson disease. *Autophagy* 8, 997–1001. doi: 10.4161/auto.20748

Pintado, C., Gavilan, M. P., Gavilan, E., Garcia-Cuervo, L., Gutierrez, A., Vitorica, J., et al. (2012). Lipopolysaccharide-induced neuroinflammation leads to the accumulation of ubiquitinated proteins and increases susceptibility to neurodegeneration induced by proteasome inhibition in rat hippocampus. *J. Neuroinflammation* 9:87. doi: 10.1186/1742-2094-9-87

Qi, Z., Liang, J., Pan, R., Dong, W., Shen, J., Yang, Y., et al. (2016). Zinc contributes to acute cerebral ischemia-induced blood–brain barrier disruption. *Neurobiol. Dis.* 95, 12–21. doi: 10.1016/j.nbd.2016.07.003

Qin, L., Wu, X., Block, M. L., Liu, Y., Breese, G. R., Hong, J., et al. (2007). Systemic LPS causes chronic neuroinflammation and progressive neurodegeneration. *Glia* 55, 453–462. doi: 10.1002/glia.20467

Sofroniew, M. V. (2015). Astrocyte barriers to neurotoxic inflammation. *Nat. Rev. Neurosci.* 16, 249–263. doi: 10.1038/nrn3898

Sun, J., Zhang, S., Zhang, X., Zhang, X., Dong, H., and Qian, Y. (2015). IL-17A is implicated in lipopolysaccharide-induced neuroinflammation and cognitive impairment in aged rats via microglial activation. *J. Neuroinflammation* 12:165. doi: 10.1186/s12974-015-0394-5

Tasaki, A., Shimizu, F., Sano, Y., Fujisawa, M., Takahashi, T., Haruki, H., et al. (2014). Autocrine MMP-2/9 secretion increases the BBB permeability in neuromyelitis optica. *J. Neurol. Neurosurg. Psychiatry* 85, 419–430. doi: 10.1136/jnnp-2013-305907

Wang, Y., Zhou, Q., Zhang, X., Qian, Q., Xu, J., Ni, P., et al. (2017). Mild endoplasmic reticulum stress ameliorates lipopolysaccharide-induced neuroinflammation and cognitive impairment via regulation of microglial polarization. *J. Neuroinflammation* 14:223. doi: 10.1186/s12974-017-1002-7

Xaio, H., Banks, W. A., Niehoff, M. L., and Morley, J. E. (2001). Effect of LPS on the permeability of the blood-brain barrier to insulin. *Brain Res.* 896, 36–42.

Xu, J., Zhang, X., Qian, Q., Wang, Y., Dong, H., Li, N., et al. (2018). Histamine upregulates the expression of histamine receptors and increases the neuroprotective effect of astrocytes. *J. Neuroinflammation* 15:41. doi: 10.1186/s12974-018-1068-x

Zhang, X., Dong, H., Li, N., Zhang, S., Sun, J., Zhang, S., et al. (2016). Activated brain mast cells contribute to postoperative cognitive dysfunction by evoking microglia activation and neuronal apoptosis. *J. Neuroinflammation* 13:127. doi: 10.1186/s12974-016-0592-9

Conflict of Interest Statement: The authors declare that the research was conducted in the absence of any commercial or financial relationships that could be construed as a potential conflict of interest.

frontiers in Cellular Neuroscience

ORIGINAL RESEARCH
published: 02 August 2018
doi: 10.3389/fncel.2018.00225

Rosuvastatin Reduces Neuroinflammation in the Hemorrhagic Transformation After rt-PA Treatment in a Mouse Model of Experimental Stroke

Dan Lu[1,2†], Yanfang Liu[1,2†], Hongcheng Mai[1,2], Jiankun Zang[1,2], Lingling Shen[1,2], Yusheng Zhang[1] and Anding Xu[1,2]**

[1]Department of Neurology and Stroke Center, The First Affiliated Hospital, Jinan University, Guangzhou, China, [2]Clinical Neuroscience Institute of Jinan University, Guangzhou, China

Hemorrhagic transformation (HT) is a serious complication that stimulates inflammation during reperfusion therapy after acute ischemic stroke. Rosuvastatin, a 3-hydroxymethyl-3-methylglutaryl coenzyme A (HMG-CoA) reductase inhibitor, might improve the outcome of HT by inhibiting neuroinflammation. This study aimed to explore the protective effects of rosuvastatin against HT after recombinant tissue plasminogen activator (rt-PA) treatment in mice with experimental stroke via the attenuation of inflammation. A total of one hundred sixty-nine male BALB/c mice were used in the experiment. HT was successfully established in 70 mice that were subjected to 3 h of middle cerebral artery occlusion (MCAO) followed by a 10 mg/kg rt-PA injection over 10 min and reperfusion for 24 h. The mice were then administered rosuvastatin (1 mg/kg, 5 mg/kg) or saline (vehicle). The brain water content and neurological deficits (wire hang and adhesive removal somatosensory tests) were assessed at 24 h after rt-PA reperfusion following MCAO surgery. The morphology, blood-brain barrier (BBB) permeability and number of astrocytes and microglia were assessed by immunohistochemistry, electron microscopy and western blotting at 24 h after rt-PA reperfusion following MCAO surgery. Rosuvastatin protected against impaired neurological function and reversed the BBB leakage observed in the HT group. The increased activation of astrocytes and microglia and secretion of inflammatory factors caused by HT damage were significantly attenuated by high-dose rosuvastatin treatment vs. normal-dose rosuvastatin treatment. Related inflammatory pathways, such as the nuclear factor kappa B (NF-κB) and mitogen-activated protein kinase (MAPK) pathways, were downregulated in the rosuvastatin-treated groups compared with the HT group. In conclusion, our results indicate that rosuvastatin is a promising therapeutic agent for HT after rt-PA reperfusion following MCAO surgery in mice, as it attenuates neuroinflammation. Additionally, high-dose rosuvastatin treatment could have a greater anti-inflammatory effect on HT than normal-dose rosuvastatin treatment.

Keywords: rosuvastatin, hemorrhagic transformation, microglia, astrocytes, blood-brain barrier, NF-κB, MAPK pathway

OPEN ACCESS

Edited by:
Sikha Saha,
University of Leeds, United Kingdom

Reviewed by:
Mario Valentino,
University of Malta, Malta
Anna Maria Pugliese,
Università degli Studi di Firenze, Italy

****Correspondence:***
Yusheng Zhang
zhangys@jnu.edu.cn
Anding Xu
tlil@jnu.edu.cn

[†]These authors have contributed equally to this work.

Received: *16 April 2018*
Accepted: *11 July 2018*
Published: *02 August 2018*

Citation:
Lu D, Liu Y, Mai H, Zang J, Shen L, Zhang Y and Xu A (2018) Rosuvastatin Reduces Neuroinflammation in the Hemorrhagic Transformation After rt-PA Treatment in a Mouse Model of Experimental Stroke. Front. Cell. Neurosci. 12:225. doi: 10.3389/fncel.2018.00225

INTRODUCTION

Hemorrhagic transformation (HT) is a serious complication that occurs after acute ischemic stroke (Álvarez-Sabin et al., 2013; Wang et al., 2015). In clinical practice, after the administration of intravenous recombinant tissue plasminogen activator (IV-rt-PA) within the therapeutic window, the rate of type two parenchymal hemorrhage within 7 days is 6.8%, with a 90-day mortality rate as high as 17.9% (Emberson et al., 2014). Studies have shown that disturbances in the blood-brain barrier (BBB), which is composed mainly of endothelial cells, pericytes and astrocytes, occur throughout the process of HT (Kelly et al., 2006; Mishiro et al., 2012; Ozkul-Wermester et al., 2014). Emerging data have shown that the oxidative stress and overexpression and release of proinflammatory cytokines caused by rt-PA reperfusion are associated with BBB disruption (Wang et al., 2015). Furthermore, increasing studies in the literature have shown that inflammation related to the interaction between microglia and astrocytes but not astrocytes alone contributes to ischemia-induced HT and oedema (del Zoppo et al., 2012).

Statins, also known as 3-hydroxy-3-methylglutaryl-coenzyme A (HMG-CoA) reductase inhibitors, are well known for having beneficial effects on vascular events by lowering cholesterol levels (Postmus et al., 2014) and are used as neuroprotectants in experimental brain ischemia (Spence, 2014). *In vivo* studies have shown that statins induce time- and concentration-dependent reductions in Aβ production, and the reduced production of Aβ has been attributed to reductions in neuroinflammation (Hosaka et al., 2013). One study has suggested that reduced chronic neuroinflammation might be a key mechanism underlying statin-induced neuroprotection (McFarland et al., 2014). Furthermore, statins play a protective role against neurodegenerative conditions, including vascular dementia, Alzheimer's disease (AD) and Parkinson's disease (PD; Mandas et al., 2014). However, whether statins protect against HT and the related mechanisms in mice have not been determined.

Rats who were treated with rosuvastatin (a synthetically derived statin) immediately post-spinal cord injury demonstrated reduced inflammatory cell infiltration, tumor necrosis factor alpha (TNF-α) expression, myeloperoxidase activity, nitric oxide levels and caspase-3 activity in caudal spinal cord tissue (Kahveci et al., 2014). Pretreatment with rosuvastatin significantly reduced lipopolysaccharide (LPS)-induced interleukin 1 beta (IL-1β) and TNF-α release (Kahveci et al., 2014). Because the protective effect of rosuvastatin relies on the modulation of several signaling transduction pathways, including the nuclear factor kappa B (NF-κB), phosphatidylinositol 3-kinase and protein kinase B (PI3K/Akt) and c-Jun N-terminal kinase (JNK) pathways (Li et al., 2015; Liu et al., 2017), determining the potential role played by rosuvastatin in neuroinflammation-related diseases is critical.

In this study, experiments were performed to demonstrate our hypothesis that rosuvastatin protects against HT in middle cerebral artery occlusion (MCAO) mice by attenuating inflammation.

MATERIALS AND METHODS

Animals

A total of 169 male BALB/c mice (10–12 weeks old, weighing 22–25 g) were used. All animal procedures were performed in strict accordance with the National Institutes of Health guidelines (NIH publication no. 8023, revised 1978). Experimental protocols were approved by the Competent Ethics Committees of Jinan University, and efforts were made to reduce the total number of animals used as well as their potential pain and suffering.

Stroke Model, Experimental Design and Experimental Groups

One-hundred and forty-four mice were anesthetized with isoflurane in air (4% for inducing anesthesia, 1.5% for maintaining anesthesia; RWD Life Science, Shenzhen, China). The temperature of the mice was maintained at 37.0 ± 0.5°C using a heating pad, and focal ischemia was induced using an intraluminal filament (Mehra et al., 2012). A midline incision was made in the neck, and the left common carotid artery, external carotid artery and internal carotid artery were isolated. Briefly, the stump of the external carotid artery was cut, and a filament made of nylon string coated with silicon (MSMC23B104PK100, RWD Life Science, Shenzhen, China) was carefully inserted into the internal carotid artery and advanced 11 mm from the carotid artery bifurcation or until resistance was encountered. Changes in regional cerebral blood flow were monitored using a laser Doppler blood flow meter in the left MCA region (Mehra et al., 2012) to confirm successful MCAO. After 3 h of MCAO, thrombolysis was conducted via a tail vein injection of rt-PA (10 mg/kg, Actilyse, Boehringer Ingelheim Pharma GmbH and Co., UK) in saline for 10 min; then, the filament was carefully withdrawn to induce vascular recanalization/reperfusion for 24 h. The liquid was warmed to 37°C prior to intraperitoneal and tail vein injection. In addition, the mice remained on the heating pad in fresh air and were monitored (blood pressure, heart rate, and physical activity) until they showed movement. The operation time was kept to less than 10 min from the induction of anesthesia. During the 12 h of daytime, the mice were given 1 ml of jelly two times by oral feeding. Then, the mice were kept in a cage and allowed free access to jelly and water in a dish during the 12 h of night-time (Lourbopoulos et al., 2017). Mice in the sham-operated group served as controls and were treated with an equal volume of saline administered via the tail vein. At 24 h after reperfusion and the assessment of neurological deficits, the mice were deeply anesthetized with 5% isoflurane. After acute bleeding, tissue samples were collected for brain water content measurements and immunoblotting; other samples were collected after heart perfusion experiments for the assessment of BBB integrity and immunofluorescence, immunohistochemistry and electron microscopy (**Figure 1A**).

Mice in this experiment were divided randomly into four groups (**Figure 1B**): (1) SHAM: sham-operated mice treated

A Experimental design

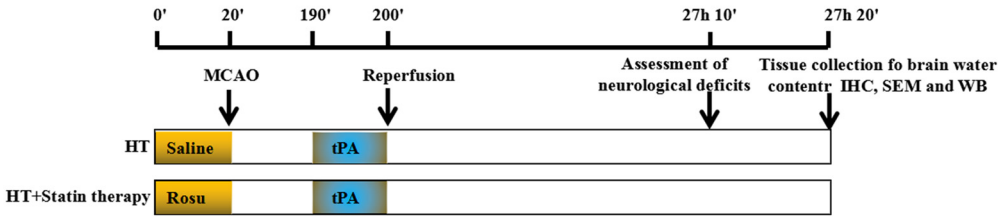

B Experimental groups

Grouping/Test	SHAM	HT	HT+LRO	HT+HRO
TTC staining	3	3	3	3
Wet/dry weight (Survival)	5	5	5	5
Biotin (Survival)	3	3	3	3
Immunocytochemistry (Survival)	5	5	5	5
SEM (Survival)	3	3	3	3
WB (Survival)	6	6	6	6
Death	0	9	8	9
Failure models	0	21	9	13
total	25	55	42	47

FIGURE 1 | Schematic overview of the stroke model and group allocation. **(A)** Timeline depicting the study design. The locomotor activity and sensory assessments were performed at 23 h and 50 min after reperfusion and 10 min prior to tissue collection at 24 h after reperfusion. **(B)** Summary of the mice in the various groups. The total number of mice does not include those excluded due to death by anesthesia, poor recovery after surgery, or model failure.

with saline as a control; (2) HT: mice pretreated with saline for 10 min before 3 h of MCAO followed by tPA treatment and 24 h of reperfusion; (3) normal-dose rosuvastatin therapy for HT-LRO: mice pretreated with 1 mg/kg rosuvastatin for 10 min before 3 h of MCAO followed by tPA treatment and 24 h of reperfusion; and (4) high-dose rosuvastatin therapy for HT-HRO: mice pretreated with 5 mg/kg rosuvastatin for 10 min before 3 h of MCAO followed by rt-PA treatment and 24 h of reperfusion. Twenty-six mice died because of failure to tolerate anesthesia or severe postoperative complications, such as subarachnoid hemorrhage and forty-three mice were excluded due to model failure; these mice are excluded from the following tests (**Figure 1B**).

Assessment of Neurological Deficits

Behavioral tests, including the wire hang and adhesive removal somatosensory tests, were conducted 24 h after reperfusion.

In the wire hang test (Wu et al., 2010), mice were placed midway on a wire (50 × 0.15 cm) mounted between two platforms 40 cm above the ground. Two days before formal experiments were conducted, all mice were familiarized with the technique of grasping the wire by the forelimbs. Their performance was observed for a maximum of 1 min, and exact scores were calculated. A mouse scored three points if it grasped the wire with both hind paws, two points if it grasped the wire with one hind paw, and one point if it did not grasp the wire with either hind paw. The suspension times were recorded and scored as follows: 0 points for 0–4 s; one point for 5–9 s; two points for 10–14 s; three points for 15–19 s; four points for 20–24 s; five points for 25–29 s; and six points ≥30 s. Each testing session consisted of three trials, and the interval between the trials was 5 min.

The adhesive removal somatosensory test is a sensitive method for assessing sensorimotor deficits (Modo et al., 2000; Bouet et al., 2009; Freret et al., 2009). All mice were familiarized with the testing environment before formal experiments were conducted. Two small, circular adhesive-backed paper patches (diameter: 10 mm) were used as bilateral tactile stimuli occupying the distal-radial region on the wrist of each forelimb. Each mouse was then returned to its respective home cage, and the time required to remove each stimulus was recorded (with a maximum limit of 120 s). Three trials were conducted per day, and individual trials were separated by at least 10 min.

Brain Water Content Measurement

The brain water content was measured using the wet/dry method (Manaenko et al., 2011). Briefly, after mice from each group were decapitated under deep anesthesia with 5% isoflurane, the whole brains were immediately removed. Each brain was weighed (wet weight [WW]) on an electronic analytical balance (Sartorius, Gottingen, Germany) and then dried at 100°C for 24 h to determine the dry weight (DW). The brain water content (%) was calculated as ([WW − DW]/WW) × 100%.

TTC Staining and Infarct Volume Measurement

At 24 h after reperfusion, following deep anesthesia with 5% isoflurane, four mice were selected randomly from each group and perfused transcardially with cold saline. The brains were

quickly removed and sectioned coronally into 1-mm slices and used for 2,3,5-triphenyltetrazolium chloride (TTC) staining. A Canon camera (Guangzhou, Guangdong, China) was used to capture images of the slices before they were stained with 2% TTC and incubated in a dark chamber at 37°C for 20 min. The infarct volumes were calculated as follows: infarct volume (%) = (contralateral hemisphere volume—ipsilateral hemisphere + infarct volume)/contralateral hemisphere volume × 100%. The hemispheric volumes were measured using Image-Pro® Plus (Version 6.0 for Windows™, National Institutes of Health, Bethesda, MD, USA; Zhu et al., 2016).

HE Staining

Brain tissue was collected and fixed in 4% paraformaldehyde (PFA) for 12 h after the heart perfusion experiments. The brains were cut into halves and immersed in 30% sucrose in distilled water overnight at 4°C before being embedded in optimal cutting temperature (OCT) compound. Cryosections with a thickness of 10 μm were dewaxed, dehydrated and stained with hemeatoxylin and eosin (H&E) for morphological evaluation. Each section was examined under 400× magnification using a Leica microscope (Vizna, Germany). The area of red blood that overflowed from the BBB into the brain tissues was obtained as average values and is expressed as the ratio of the area of red blood to the area of the corresponding high-power (HP) field.

Assessment of BBB Integrity

Mice were deeply anesthetized with 5% isoflurane. Fifty milliliters of 0.01 mol/l PBS containing EZ-link-sulfo-NHS-biotin (0.5 mg/ml; Thermo Fisher Scientific, Waltham, MA, USA) was used to perfuse the left ventricle of the heart over 5 min, followed by perfusion with 50 ml of ice-cold 1% PFA in 0.01 mol/l PBS. The brains were then dissected, fixed in 4% PFA for 1 h at room temperature, cut into halves and immersed in 30% sucrose in distilled water overnight at 4°C before being embedded in OCT compound. Cryosections with a thickness of 10 μm were blocked in 0.01 mol/l PBS + 10% normal goat serum + 0.3% Triton X-100 for 30 min at room temperature. The sections were then incubated with fluorescein isothiocyanate streptavidin (FITC-streptavidin; 1:200, Yeasen, Shanghai, China) for 1 h at room temperature; 4′,6-diamidino-2-phenylindole (DAPI; 1:250; Beyotime Biotechnology, Shanghai, China) was used to stain nuclei for 10 min before the slides were mounted. Images of the peri-infarct area, were captured using a confocal laser scanning microscope (Leica SP8, Vizna, Germany). The statistical data were generated from a total of three mice; these mice were used for three independent experiments, and three replicate slices were analyzed per group in each independent experiment.

Immunofluorescence

To assess the number of activated astrocytes, we used a cryostat (Thermo Fisher Scientific, Waltham, MA, USA) to prepare coronal cryosections (6 μm). After being permeabilized with 0.3% Triton X-100 in PBS for 30 min, the sections were blocked with 5% goat serum for 1 h. Then, the sections were incubated at 4°C overnight with the primary monoclonal anti-glial fibrillary acidic protein antibody (anti-GFAP; 1:250, Santa Cruz Biotechnology). After being washed with 0.01 mol/l PBS for 5 min, the sections were incubated three times with horseradish peroxidase-conjugated secondary antibodies (1:250; Yeason, Shanghai, China) at room temperature for 1 h. After being washed with 0.01 mol/l PBS for 5 min three times, DAPI was used to stain nuclei for 10 min before the slides were mounted. The number of positive cells was counted in the peri-infarct cortex (200× magnification) under a fluorescence microscope (Leica, Vizna, Germany), and the number of cells was analyzed as positive cells/total cells using ImageJ 1.50 software (National Institutes of Health, Bethesda, MD, USA).

Immunohistochemistry

To assess the number of activated microglia, we used a cryostat to obtain coronal cryosections (6 μm). The sections were permeabilized with 0.3% Triton X-100 in PBS for 30 min and then blocked with 5% goat serum for 1 h. The sections were then incubated at 4°C overnight with the primary anti-ionized calcium-binding adaptor molecule 1 antibody (Iba-1; 1:250, Santa Cruz Biotechnology, Dallas, TX, USA). The sections were incubated with horseradish peroxidase-conjugated secondary antibodies (1:250; Yeason, Shanghai, China) at room temperature for 1 h and then stained with 3,3-diaminobenzidin (Wanleibio, Shanghai, China) for 10 min. After the sections were washed three times with 0.01 mol/l PBS for 5 min, they were stained with hemeatoxylin for 10 min to label nuclei and were then dehydrated and mounted with neutral gum. The number of positive cells in the peri-infarct cortex was counted (200× magnification) under a fluorescence microscope (Leica, Vizna, Germany), and the number of cells was analyzed as positive cells/total cells using ImageJ 1.50 software (National Institutes of Health, Bethesda, MD, USA).

Electron Microscopy

Mice were anesthetized with 5% isoflurane and transcardially perfused with a cold saline solution followed by 2.5% glutaraldehyde in 0.1 M phosphate buffer. Then, the brains were isolated and dissected. The brains were sectioned, dehydrated, embedded in epoxy resin and then visualized using a HITACHI transmission electron microscope (HITACHI, Tokyo, Japan) at 80 kV. The sections were selected as previously described, and five areas in the ipsilateral peri-infarct cortex in each section were chosen.

Immunoblotting

At 24 h after recanalization, the cortex was obtained for immunoblotting as previously described. Proteins obtained from the peri-infarct cortex were subjected to sodium-dodecyl sulfate polyacrylamide gel electrophoresis and electrically transferred to a polyvinylidene difluoride membrane before being incubated with specific antibodies. Primary antibodies against the following mediators were used: TNF-α, cyclooxygenase 2 (Cox-2), inducible nitric oxide synthase (iNOS), IL-6, phospho-NF-κB p65 (p-p65), phospho-inhibitory subunit of NF-κB-α (p-IκBα), p-c-Jun, phosphorylated c-Jun-N-terminal kinase (p-JNK),

phosphorylated mitogen-activated protein kinase (MAPK) p38 (p-p38), β-actin (1:1000; all from Cell Signaling Technology, Danvers, MA, USA) and IL-1β (1:1000; Wanleibio, Shanghai, China). The membranes were incubated for 1 h with the appropriate secondary antibody (anti-rabbit IgG, anti-mouse IgG; 1:5000; Yeasen). The antibodies were visualized by enhanced chemiluminescence (ECL Plus; Beyotime Biotechnology). ImageJ (NIH, Bethesda, MD, USA) was used to analyze the band intensity. For individual samples, each value was normalized to that of β-actin.

Statistical Analyses

All data were analyzed using SPSS (Windows version 13.0; SPSS Inc., Chicago, IL, USA). Values are expressed as the mean ± SEM. Statistical differences among the groups were assessed by one-way ANOVA. All analyses were performed using GraphPad Prism six for Windows (GraphPad Software, Inc., La Jolla, CA, USA). In all tests, *P*-values of 0.05 or less were considered to indicate significance.

RESULTS

Rosuvastatin Attenuated HT in Mice

To examine whether rosuvastatin influenced the severity of cerebral hemorrhage, we evaluated locomotor activity using the wire hang test and assessed sensation by performing the adhesive removal test. The wire hang test was used to assess the strength and stamina of the mice. Deficit scores were assessed using the max hang duration in the HT group ($^{***}P < 0.001$ vs. the SHAM group). Neither normal- nor high-dose statin therapy significantly shortened the falling latency in the SHAM group compared to the HT group (**Figure 2Aa**). The adhesive removal test showed that mice in the HT group required more time than did those in the SHAM group ($^{*}P < 0.05$), while there were no significant differences between the statin-therapy groups and the HT group (**Figure 2B**). The grasp power assessment showed that the HT mice treated with saline achieved an average limb grasp score of 1.42 ± 0.16 ($^{***}P < 0.001$ vs. 2.95 ± 0.05 in the SHAM group), while those treated with normal-dose statin therapy showed an average grasp power score significantly higher than that of the HT mice (2.36 ± 0.21 vs. 1.42 ± 0.16, respectively, $^{\#\#}P < 0.01$). The mice treated with high-dose statin therapy showed a significantly higher grasp power score than did the HT mice (2.16 ± 0.19 vs. 1.42 ± 0.16, respectively, $^{\#}P < 0.05$; **Figure 2Ab**). Meanwhile, as shown in **Figures 2Ca–e**, more infarction was observed in the HT mice than in the SHAM mice ($^{*}P < 0.05$), while less infarction was observed in the HT+LRO and HT+HRO groups than in the HT group ($^{\#}P < 0.05$). In the gross slices of the brain dissected after saline perfusion, we found that the amount of bleeding was increased in the HT group, and the statin therapy improved the bleeding in the HT+LRO and HT+HRO groups (**Figures 2Da–d**). Furthermore, to verify the phenomenon, we then evaluated the water content 24 h after ischemia, which revealed that rt-PA reperfusion injury increased the brain water content compared with the sham operation. However, this effect was lower in the rosuvastatin-treated groups (1 mg/kg, water content: 1.05 ± 0.05, $^{\#}P < 0.05$;

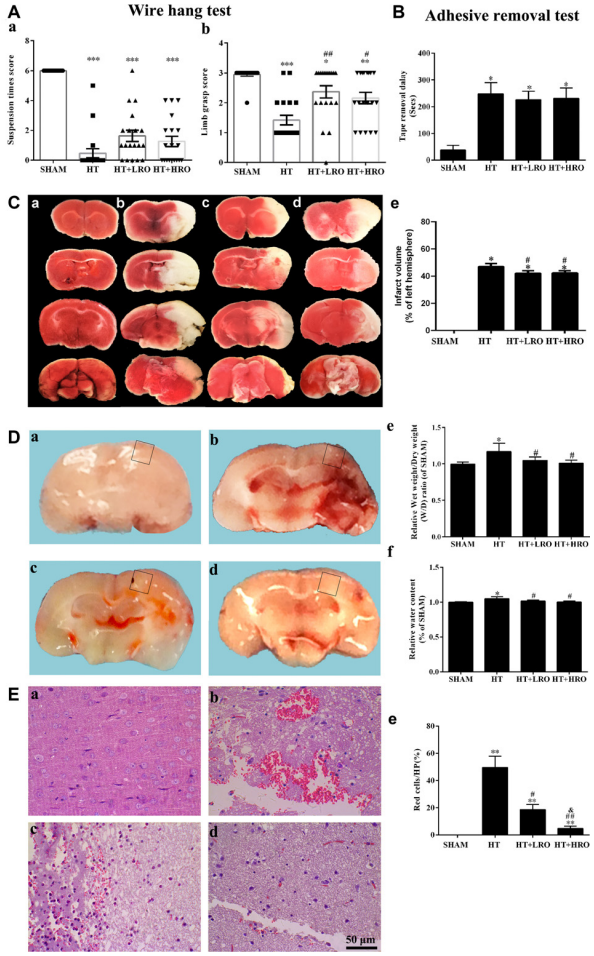

FIGURE 2 | Rosuvastatin attenuated hemorrhagic transformation (HT) after recombinant tissue plasminogen activator (rt-PA) reperfusion in mice. **(A)** Quantitative analysis of the wire hang test ($n = 5$ in each group) in the SHAM (sham-operated), HT (3 h of middle cerebral artery occlusion (MCAO) followed by tPA reperfusion), HT+LRO (rosuvastatin pretreatment for 10 min before MCAO followed by tPA reperfusion), and HT+HRO (rosuvastatin 5 mg/kg pretreatment for 10 min before MCAO followed by tPA reperfusion) groups. **(a)** The hang duration scores were expressed as the mean ± SEM, and between-group differences were assessed by one-way ANOVA followed by Tamhane's T2 test (homogeneity of variance was not determined), $n = 5$. $^{***}P < 0.001$ vs. the SHAM group. **(b)** The grasp power scores were expressed as the mean ± SEM, and between-group differences were assessed by one-way ANOVA followed by Tamhane's T2 test (homogeneity of variance was not determined), $n = 5$. $^{*}P < 0.05$, $^{**}P < 0.01$, and $^{***}P < 0.001$ vs. the SHAM group, $^{\#\#}P < 0.01$ vs. the HT group, $^{\#}P < 0.05$ vs. the HT group. **(B)** Adhesive removal test ($n = 5$ in each group) in the SHAM, HT, HT+LRO, and HT+HRO groups. The adhesive removal duration scores are expressed as the mean ± SEM, and between-group differences were assessed by one-way ANOVA followed by Tamhane's T2 test (homogeneity of variance was not determined), $n = 5$. $^{*}P < 0.05$ vs. the SHAM group. **(C)** Representative images of TTC staining from the four groups (**a–d** for the SHAM, HT, HT+LRO and HT+HRO groups, respectively). **(e)** The infarction volume scores were expressed as the mean ± SEM, and between-group differences were assessed by one-way ANOVA followed by the LSD test (homogeneity of variance was determined), $n = 3$ per group. $^{*}P < 0.05$ vs. the SHAM group, $^{\#}P < 0.05$ vs. the HT group. **(D)** Representative images of gross brain sections from the four groups (**a–d** for the SHAM, HT, HT+LRO and HT+HRO

(*Continued*)

FIGURE 2 | Continued
groups, respectively). **(e)** Relative wet weight/dry weight (WW/DW) ratios in the four groups. **(f)** Brain water contents (%) in the four groups. The values were expressed as the mean ± SEM, the determination of which was followed by the LSD test (homogeneity of variance was determined), $n = 5$. $^{*}P < 0.05$ vs. the SHAM group, $^{\#}P < 0.05$ vs. the HT group. **(E)** The pathological changes in the number of red blood cells in the ischemia penumbra determined under high-power (HP) microscopy in the four groups (**a–d** for the SHAM, HT, HT+LRO and HT+HRO groups, respectively). **(e)** The values were expressed as the mean ± SEM, and between-group differences were assessed by one-way ANOVA followed by Tamhane's T2 test (homogeneity of variance was not determined), $n = 5$. $^{**}P < 0.01$ vs. the SHAM group, $^{\#}P < 0.05$ and $^{\#\#}P < 0.01$ vs. the HT group, $^{\&}P < 0.05$ vs. the HT+LRO group.

5 mg/kg, water content: 1.00 ± 0.04, $^{\#}P < 0.05$) than in the HT group (water content: 1.17 ± 0.11) (**Figure 2De**). Similarly, the brain water content (%) in the HT group was significantly higher than that in the SHAM group, while the percentage in the HT+HRO group was lower than that in the HT group ($^{\#}P < 0.05$; **Figure 2Df**). Experiments of greater precision were used to assess the bleeding by HE staining (**Figures 2Ea–e**). Using HP microscopy, we found that the blood leakage in the HT group was significantly higher than that in the SHAM group (red blood percentage: 49.55 ± 8.33%, $^{**}P < 0.01$ vs. the SHAM group), while the blood leakage was significantly lower in the rosuvastatin-treated groups than in the HT group (1 mg/kg, red blood percentage: 18.59 ± 3.72%, $^{\#}P < 0.05$; 5 mg/kg, water content: 3.82 ± 1.70, $^{\#\#}P < 0.05$ vs. the HT group), especially in the high-dose rosuvastatin-treated group ($^{\&}P < 0.05$ vs. the HT+LRO group).

Thus, taken together, our results show that rosuvastatin substantially improved the HT-induced deficit in locomotor activity and attenuated the blood leakage resulting from HT-induced damage after rt-PA therapy reperfusion in mice. In addition, high-dose rosuvastatin treatment improved the attenuation of the HT-associated bleeding more than the normal-dose rosuvastatin treatment.

Rosuvastatin Decreased BBB Leakage

Disturbances in the BBB have been implicated in the HT process (Khatri et al., 2012; Ozkul-Wermester et al., 2014). We next utilized EZ-link-sulfo-NHS-biotin to examine the levels of BBB permeability, and if the BBB permeability increased, biotin leakage was examined. Biotin leakage images were captured in the peri-infarct areas of the brain slides (**Figure 3A**). Biotin leakage in the HT group was significantly higher than that in the SHAM group; however, the BBB permeability was significantly attenuated in the rosuvastatin-treated groups, especially in the high-dose rosuvastatin-treated group (**Figures 3B,C** <0.05).

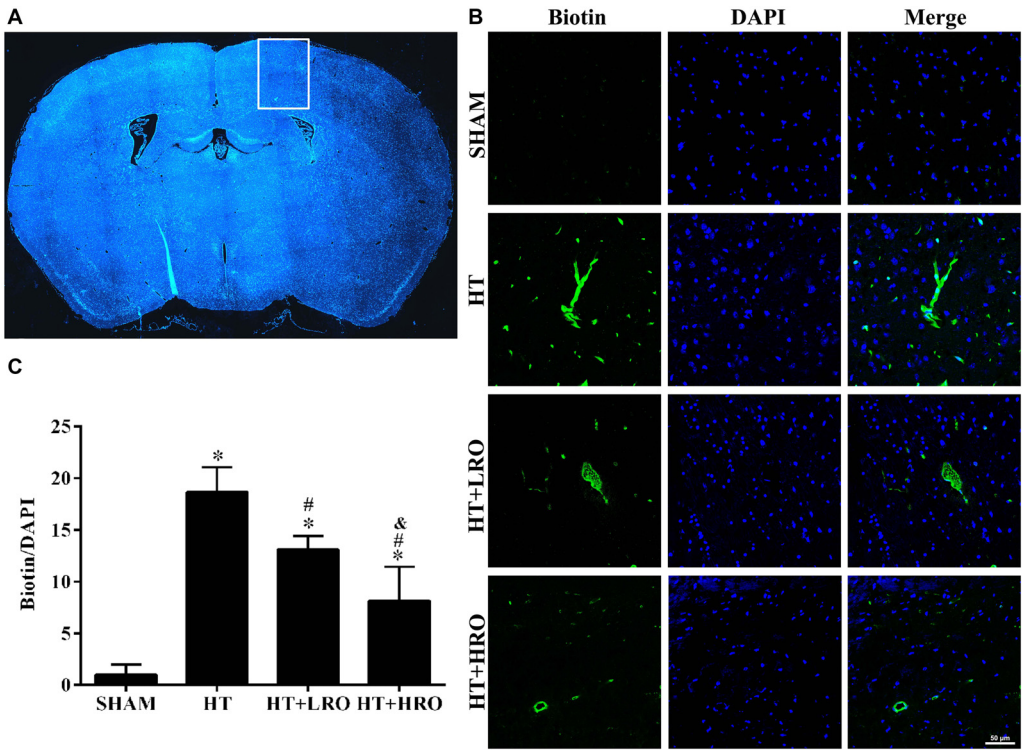

FIGURE 3 | Rosuvastatin decreased blood-brain barrier (BBB) leakage. **(A)** In the peri-infarct area indicated by the white box, images were captured and tissue samples were collected, as shown in the HT group as an example. **(B)** Representative photomicrographs of sections stained with 4′,6-diamidino-2-phenylindole (DAPI) and biotin from the peri-infarct areas of the brain at 24 h after reperfusion. Scale bar = 50 μm. **(C)** Relative biotin leakage ratios were analyzed by the ratio of biotin- to DAPI-positive cells in each group ($n = 3$ in each group). Values were expressed as the mean ± SEM, the determination of which was followed by the LSD test (homogeneity of variance was determined). $^{*}P < 0.05$ vs. the SHAM group, $^{\#}P < 0.05$ vs. the HT group, $^{\&}P < 0.05$ vs. the HT+LRO group.

These results indicate that rosuvastatin protects against HT by decreasing BBB leakage.

Rosuvastatin Attenuated Inflammation Levels

Reperfusion with rt-PA causes the release of proinflammatory cytokines that disturb the BBB permeability, and protective effects exerted by statins are associated with the reduced expression of neuroinflammatory mediators, such as TNF-α and IL-1β (McFarland et al., 2014, 2017; Wang et al., 2015). Thus, to further investigate whether rosuvastatin reduces HT via attenuating inflammation, we examined inflammation levels using western blotting. rt-PA reperfusion injury significantly increased the expression of the inflammatory cytokines TNF-α ($^{**}P < 0.01$), Cox-2 ($^{***}P < 0.001$), iNOS ($^{***}P < 0.001$), IL-1β ($^{***}P < 0.001$) and IL-6 ($^{***}P < 0.001$) relative to their expression levels in the SHAM group. However, the levels of TNF-α ($^{\#}P < 0.05$), Cox-2 ($^{\#\#\#}P < 0.001$), iNOS ($^{\#\#\#}P < 0.001$), IL-1β ($^{\#\#\#}P < 0.001$) and IL-6 ($^{\#\#\#}P < 0.001$) were significantly lower in the rosuvastatin-treated groups than in the HT group, and levels of TNF-α ($^{\&\&}P < 0.01$), iNOS ($^{\&}P < 0.05$), IL-1β ($^{\&\&\&}P < 0.001$) and IL-6 ($^{\&\&\&}P < 0.001$) were significantly lower in the high-dose rosuvastatin-treated group than in the normal-dose rosuvastatin-treated group (**Figure 4**). Therefore, these findings suggest that both a normal and a high dose of rosuvastatin exert neuroprotective effects by attenuating inflammation and that the high dose of rosuvastatin might reduce the release of proinflammatory factors more than the normal dose.

Rosuvastatin Inhibited Astrocyte Activation

Astrocytes participate in the formation of the BBB and act as major support cells in the central nervous system (CNS; Argaw et al., 2012; Colombo and Farina, 2016). The levels of GFAP, an astrocyte marker, in the HT group were significantly higher than those in the SHAM and rosuvastatin-treated groups (**Figures 5Aa–d** for the SHAM, HT, HT+LRO and HT+HRO groups, respectively, and **Figure 5B**, $P < 0.05$). The levels of GFAP in the rosuvastatin-treated groups were lower than those in the HT group (**Figure 5B**, $P < 0.05$). Ultrastructural analysis showed cell shrinkage, increased accumulation of abnormal electron-dense materials, nuclear condensation, and basement membrane thickening in the HT group. In comparison, less necrosis was observed in the rosuvastatin-treated groups (**Figures 5Ca–d** for the SHAM, HT, HT+LRO and HT+HRO groups, respectively). To further assess the number of astrocytes in peri-infarct areas at 24 h after reperfusion, GFAP expression levels were detected. Significantly inhibited astrocyte activation was observed in the rosuvastatin-treated groups compared with the HT group (**Figure 5D**, $^{\#\#\#}P < 0.001$), whereas significantly inhibited astrocyte activation was observed in the high-dose rosuvastatin-treated group compared with the normal-dose rosuvastatin-treated group (**Figure 5D**, $^{\&}P < 0.05$). Thus, these results indicate that rosuvastatin decreased BBB leakage via inhibiting astrocyte activation and that astrocyte activation was more inhibited by the high rosuvastatin dose than the normal rosuvastatin dose.

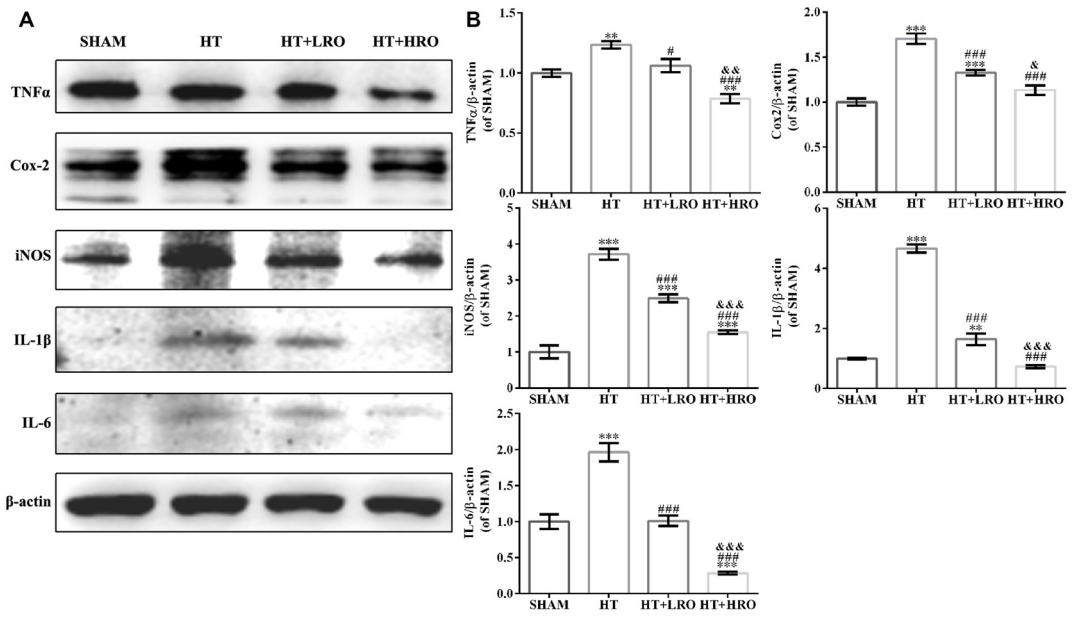

FIGURE 4 | Rosuvastatin attenuated inflammation levels. **(A)** Immunoblotting analysis of tumor necrosis factor alpha (TNF-α), cyclooxygenase 2 (Cox-2), inducible nitric oxide synthase (iNOS), interleukin 1 beta (IL-1β) and IL-6 expression levels at 24 h after reperfusion in each group ($n = 6$ in each group). **(B)** The results are normalized to β-actin. Values are expressed as the mean ± SEM, the determination of which was followed by the LSD test (homogeneity of variance was determined). $^{**}P < 0.01$ and $^{***}P < 0.001$ vs. the SHAM group, $^{\#}P < 0.05$ and $^{\#\#\#}P < 0.001$ vs. the HT group, $^{\&}P < 0.05$, $^{\&\&}P < 0.01$ and $^{\&\&\&}P < 0.01$ vs. the normal-dose rosuvastatin-treated group.

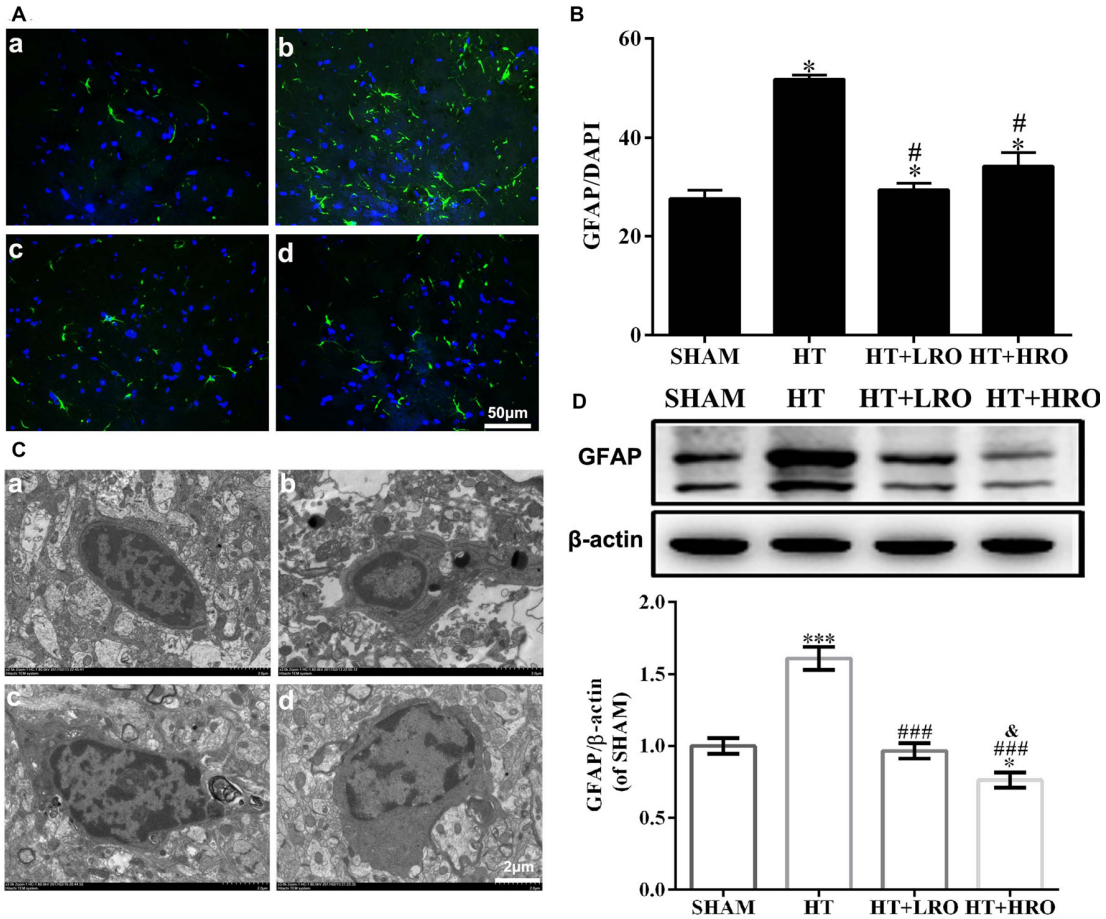

FIGURE 5 | Rosuvastatin inhibited astrocyte activation. **(A)** Representative images of DAPI and glial fibrillary acidic protein (GFAP) staining, as described above. Scale bars: 50 μm. **(B)** The quantified GFAP immunofluorescence intensity at 24 h after reperfusion; the results were normalized to DAPI. **(C)** Transmission electron microscopy image showing the ultrastructure of astrocytes. Scale bar: 200 nm. **(D)** GFAP expression levels, as determined by western blotting (n = 6 in each group); the results were normalized to β-actin. The values were expressed as the mean ± SEM (**a–d** for the SHAM, HT, HT+LRO and HT+HRO groups, respectively, as shown in **Figure 1**). $^{*}P < 0.05$ and $^{***}P < 0.001$ vs. the SHAM group, $^{\#}P < 0.05$ and $^{\#\#\#}P < 0.001$ vs. the HT group, $^{\&}P < 0.05$ vs. the normal-dose rosuvastatin-treated group.

Rosuvastatin Inhibited Microglial Activation

Previous studies have demonstrated that activated glia also play a vital role in CNS inflammation and behave as another major immune cell in the CNS; thus, we next examined microglial activation (Kettenmann et al., 2011; Xiao et al., 2013). Analysis of Iba-1, a microglial reactivity marker, was performed to verify microglial activation. The integrated density of Iba-1 staining was significantly higher in the HT group, while treatment with rosuvastatin significantly inhibited this increase (**Figures 6Aa–d** for the SHAM, HT, HT+LRO and HT+HRO groups, respectively, and **Figure 6B** <0.05). Ultrastructural analysis showed cell shrinkage, increased accumulation of abnormal electron-dense materials, and an increased nuclear-to-cytoplasmic ratio in the HT group compared with the rosuvastatin-treated groups, which showed less necrosis (**Figures 6Ca–d** for the SHAM, HT, HT+LRO and HT+HRO groups, respectively). To further assess the number of microglia in the peri-infarct areas at 24 h after reperfusion, Iba-1 expression levels were determined. Significantly inhibited microglial activation was observed in the rosuvastatin-treated groups relative to the HT group (**Figure 6D**, $^{\#\#}P < 0.01$ and $^{\#\#\#}P < 0.001$). Significantly inhibited microglia activation was also observed in the high-dose rosuvastatin-treated group relative to the normal-dose rosuvastatin-treated group (**Figure 6D**, $^{\&\&}P < 0.01$). Consistent with the above results, these findings indicate that rosuvastatin decreased BBB leakage via inhibiting microglial activation and that microglial activation was more inhibited in the high-dose rosuvastatin-treated group than in the normal-dose rosuvastatin-treated group.

Rosuvastatin Protected Against HT via Inhibiting the NF-κB Pathway

Considering the crucial influence of canonical NF-κB on glial cell activation and inflammatory responses following HT, we

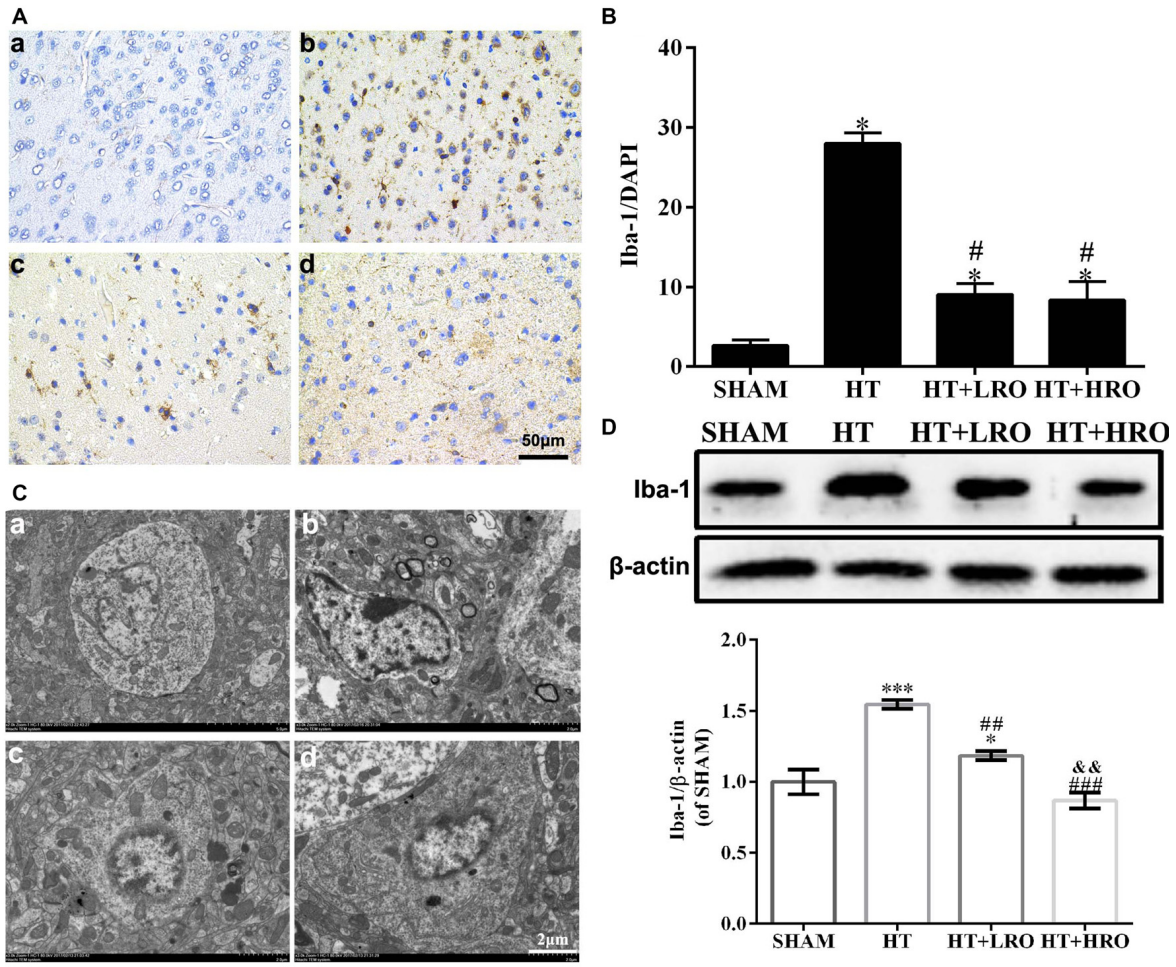

FIGURE 6 | Rosuvastatin inhibited microglial activation. **(A)** Representative images of DAPI and Iba-1 staining, as described above. Scale bars: 50 μm. **(B)** The quantified Iba-1 immunofluorescence intensity at 24 h after reperfusion; the results were normalized to DAPI. **(C)** Transmission electron microscopy image showing the ultrastructure of microglia. Scale bar: 200 nm. **(D)** Iba-1 expression levels, as determined by western blotting ($n = 6$ in each group); the results are normalized to β-actin. The values were expressed as the mean ± SEM, the determination of which was followed by the LSD test (homogeneity of variance was determined; **a–d** for the SHAM, HT, HT+LRO and HT+HRO groups, respectively, as shown in **Figure 1**). $^{*}P < 0.05$ and and $^{***}P < 0.001$ vs. the SHAM group, $^{\#}P < 0.05$, $^{\#\#}P < 0.01$ and $^{\#\#\#}P < 0.001$ vs. the HT group, $^{\&\&}P < 0.01$ vs. the normal-dose rosuvastatin-treated group.

measured the expression levels of proteins in the NF-κB pathway (Hayden and Ghosh, 2008; Sun and Ley, 2008). Blocking IκBα phosphorylation potentially inhibits the activation of molecules in the NF-κB pathway, such as p-NF-κB p65, thus downregulating inflammatory factors, including TNF-α, Cox-2, iNOS, IL-1β and IL-6. Thus, we determined the protein levels of the key NF-κB pathway factors p65 and IκBα. The levels of p-p65 and p-IκBα were substantially greater in the HT group than in the SHAM group (**Figure 7**, $^{\#}P < 0.05$), while these levels were significantly lower in the rosuvastatin-treated groups than in the HT group (**Figure 7**, $^{**}P < 0.01$ and $^{***}P < 0.01$). The levels of p-p65 and p-IκBα were significantly lower in the high-dose rosuvastatin-treated group than in the normal-dose rosuvastatin-treated group (**Figure 7**, $^{\&\&}P < 0.01$). Thus, these results indicate that rosuvastatin attenuated HT by inhibiting the NF-κB pathway.

Rosuvastatin Protected Against HT via Inhibiting the MAPK Pathway

As a member of the MAPK family related to neuronal survival, JNK has been shown to increase stroke injury upon activation, and p38 signaling has been shown to exacerbate stroke-induced inflammatory responses (Barone et al., 2001; Kuan et al., 2003; Cui et al., 2007; Nithianandarajah-Jones et al., 2012). Thus, we next investigated the role of rosuvastatin in the MAPK pathway using western blotting. Activated MAPKs can stimulate IκB kinase, release NF-κB dimers from the inactive cytoplasmic NF-κB/IκB complex and induce the nuclear translocation of NF-κB. The levels of p-c-Jun, p-JNK and p-p38 were higher in the HT group than in the SHAM group (**Figure 8**, $^{***}P < 0.05$) and the rosuvastatin-treated groups (**Figure 8**, $^{\#}P < 0.05$, $^{\#\#\#}P < 0.001$). The expression levels of p-c-Jun and p-p38 in the high-dose rosuvastatin-

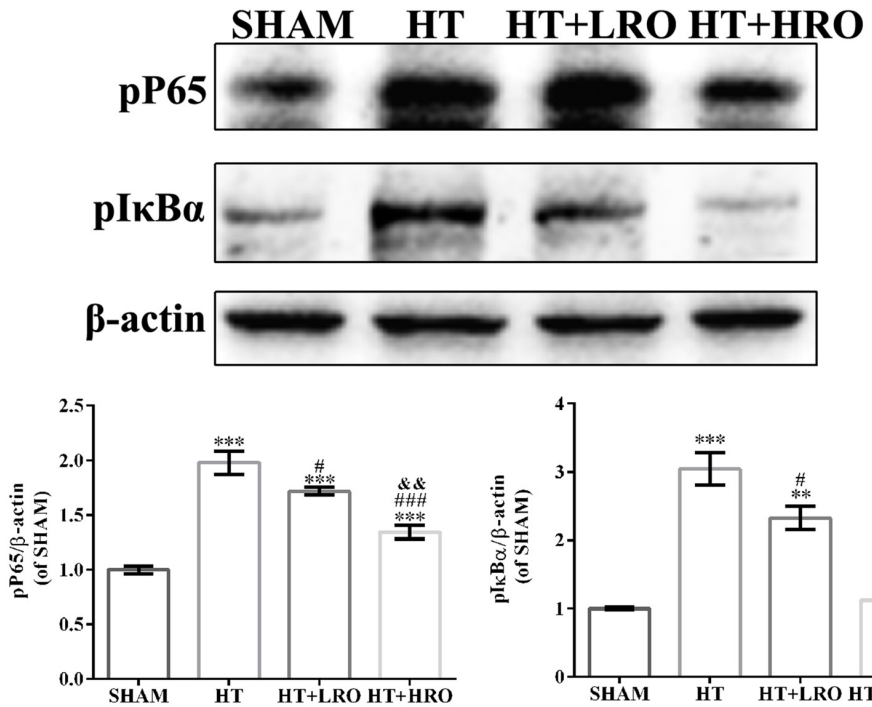

FIGURE 7 | Rosuvastatin protected against HT via inhibiting the NF-κB pathway. Western blot analysis of phospho-NF-κB p65 (p-p65) and phospho-inhibitory subunit of NF-κBα (p-IκBα) expression levels in the NF-κB pathway at 24 h after reperfusion (n = 6 in each group); the results are normalized to β-actin. The values are expressed as the mean ± SEM. $^{**}P < 0.01$ and $^{***}P < 0.001$ vs. the the SHAM group, $^{\#}P < 0.05$ and $^{\#\#\#}P < 0.001$ vs. the HT group, $^{\&\&}P < 0.01$ vs. the normal-dose rosuvastatin-treated group.

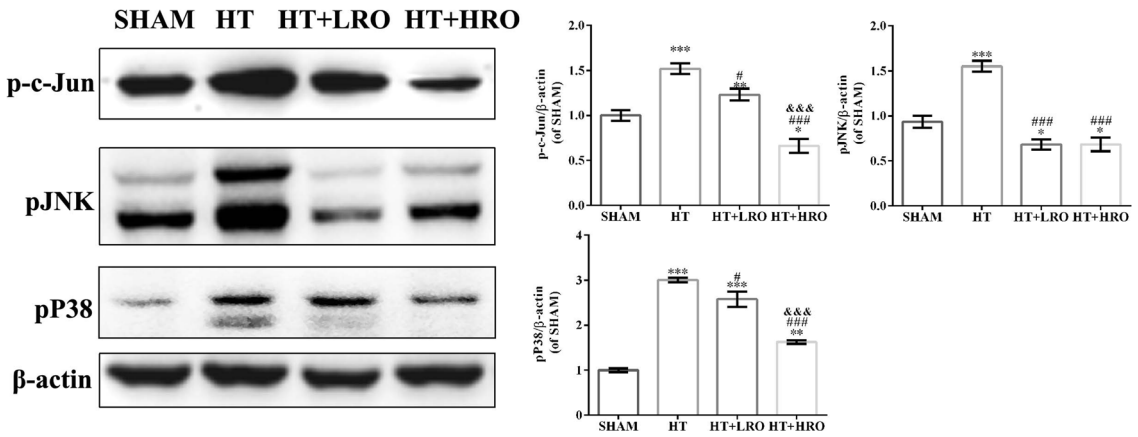

FIGURE 8 | Rosuvastatin protected against HT via inhibiting the mitogen-activated protein kinase (MAPK) pathway. Western blot analysis of p-c-Jun, phosphorylated c-Jun-N-terminal kinase (p-JNK) and p-p38 expression levels at 24 h after reperfusion (n = 6 in each group); the results are normalized to β-actin. The values are expressed as the mean ± SEM. $^{*}P < 0.05$, $^{**}P < 0.01$ and $^{***}P < 0.001$ vs. the SHAM group, $^{\#}P < 0.05$ and $^{\#\#\#}P < 0.001$ vs. the HT group, $^{\&\&\&}P < 0.05$ vs. the normal-dose rosuvastatin-treated group.

treated group were lower than those in the normal-dose rosuvastatin-treated group (**Figure 8**, $^{\&\&\&}P < 0.001$). Thus, taken together, these results suggest that the attenuation of the inflammatory response by rosuvastatin is involved in the MAPK pathway.

DISCUSSION

Inflammation is a major factor contributing to brain damage and nervous system dysfunction after intracerebral hemorrhage (ICH; Campos et al., 2013; Zhou et al., 2014). Rosuvastatin

has been used as a cholesterol-lowering drug for a long time and is more effective than other statins (McTaggart et al., 2001; Gullestad et al., 2012). Rosuvastatin has been demonstrated to exert neuroprotective effects by promoting anti-inflammatory responses in rat animal models of brain ischemia, thus improving their outcome. However, whether rosuvastatin exerts neuroprotective effects against secondary damage, including hemorrhaging after thrombolysis, is not clear. The major findings of this study are that rosuvastatin, at both normal and high doses, contributes to preventing HT after intravenous rt-PA thrombolysis in mice with brain ischemia by activating glial cells.

In addition to blood leakage due to disruption of the BBB, which significantly upregulates the activation of microglia/macrophages (Khatri et al., 2012; Ozkul-Wermester et al., 2014) and astrocytes (del Zoppo et al., 2012), the elevated expression of the proinflammatory cytokines IL-1β and IL-6, the activation of their transcription factor NF-κB, and the expression of the inflammatory enzymes Cox-2 and iNOS are considered the chief mechanisms underlying HT. Studies have shown that rosuvastatin can alleviate motor dysfunction and neuropathic pain detected by the wire hang and adhesive removal somatosensory tests (Bouet et al., 2009). Meanwhile, TNF-α, Cox-2, iNOS, IL-1β and IL-6 levels are ameliorated by NF-κB inactivation, and the numbers of microglia and astrocytes are decreased in rosuvastatin-treated mice. As proinflammatory cytokines produced by microglia and astrocytes, TNF-α and IL-1β are closely related to oedema formation and BBB dysfunction, leading to further brain injury in HT, as determined by increased WW/DW ratios (Ma et al., 2017). However, decreased WW/DW ratios after rosuvastatin treatment in HT mice resulted from the inhibition of TNF-α, Cox-2, iNOS, IL-1β and IL-6. Furthermore, NF-κB transcription factors are present in the cytosol in an inactive state complexed with inhibitory IκB proteins, and activation occurs via the phosphorylation of IκBα at Ser32 and Ser36, followed by proteasome-mediated degradation that results in the release and nuclear translocation of active NF-κB in HT mice. However, rosuvastatin might prohibit the activation of IκBα and NF-κB, thus suppressing the subsequent release of inflammatory cytokines (Asahi et al., 2005; Cordle and Landreth, 2005; Barone et al., 2011). We believe that treatment with rosuvastatin early in thrombolysis therapy will reduce the release of inflammatory cytokines, thus prohibiting oedema formation and BBB dysfunction.

The MAPK family is a group of serine/threonine protein kinases comprising several members, including extracellular signal-regulated kinases 1/2, JNK and p38 (Nithianandarajah-Jones et al., 2012). The importance of MAPKs in stroke, especially JNK and p38, is well documented in the literature. More specifically, JNK activation has been shown to increase stroke injury via the enhancement of neuronal apoptosis, and the genetic and pharmacological inhibition of JNK both improve the outcome after stroke (Kuan et al., 2003; Cui et al., 2007). p38 signaling activation exacerbates stroke-induced inflammatory responses and leads to poorer outcomes (Barone et al., 2011). IL-1β and other inflammatory cytokines can increase the phosphorylation of specific amino acid sequences in these components and then activate MAPKs. Activated MAPKs can stimulate IκB kinase, release NF-κB dimers from the inactive cytoplasmic NF-κB/IκB complex and induce the nuclear translocation of NF-κB (Kim et al., 2005; Joo et al., 2007). The activation of p38 and JNK in microglia and astrocytes via various pathways has also been demonstrated to be essential for IL-1β, IL-6, TNF-α, Cox-2 and iNOS expression (Koistinaho and Koistinaho, 2002). Indeed, the pharmacological inhibition of p38 and JNK by rosuvastatin inhibited the activation of microglia

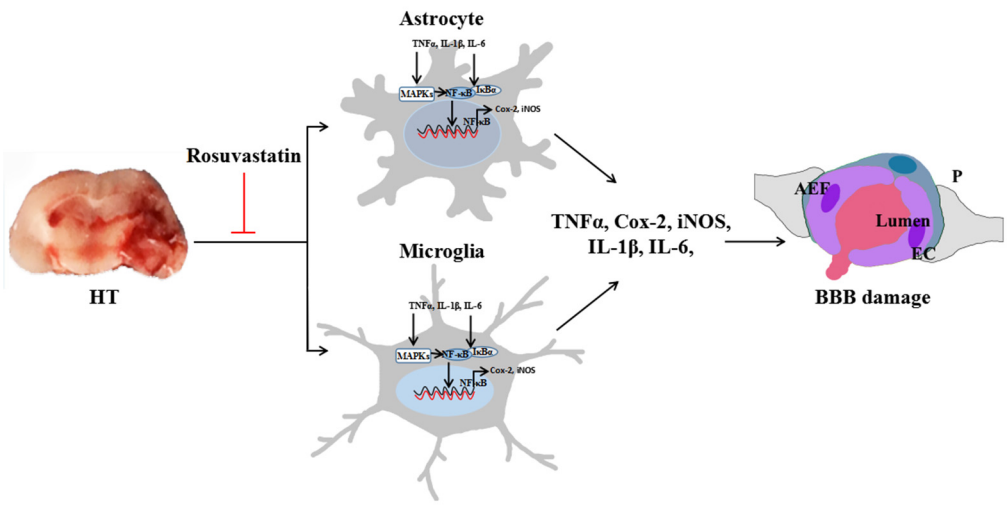

FIGURE 9 | Rosuvastatin protected against HT via decreasing BBB leakage by attenuating inflammation. Astrocytic and microglial activation increase the release of inflammatory cytokines, such as TNF-α, Cox-2, iNOS, IL-1β, and IL-6. The NF-κB and MAPK pathways are involved in glial inflammation. Activated MAPKs can stimulate IκB kinase, release NF-κB dimers from the inactive cytoplasmic NF-κB/IκB complex and induce the nuclear translocation of NF-κB, thus decreasing BBB leakage. AEF indicates the end foot of the astrocyte, P indicates the pericyte, EC indicates the endothelial cell, and blood is shown flowing from the lumen, indicating BBB leakage.

and astrocytes and reduced stroke injury (Piao et al., 2003) while also decreasing the expression of these inflammatory cytokines. Our results demonstrate that the pharmacological inhibition mediated by rosuvastatin attenuated HT, mainly via the NF-κB and MAPK pathways.

Our study does have some limitations. The possible neuroprotective mechanism of rosuvastatin in microglia and astrocytes, which might inhibit the inflammation mediated by MAPK phosphatase 1, salt-inducible kinase 2 (Ma et al., 2017) and low-density lipoprotein receptor-related protein 1 (Yepes et al., 2003; Cheng et al., 2006; Suzuki et al., 2009; Zhang et al., 2009), was not detected after ICH. In additional research, we will explore the potentially detailed molecular signaling pathway of rosuvastatin to further understand its potential clinical applications in HT therapy.

In conclusion, the major findings of this study are that rosuvastatin, at both normal and high doses, contributes to preventing HT after intravenous rt-PA thrombolysis in mice with brain ischemia by reducing glial cell activation. Meanwhile, the high-dose rosuvastatin treatment showed better anti-inflammatory effects in HT than did the normal-dose rosuvastatin treatment. The beneficial effects are related to inhibition of the inflammation-related NF-κB and MAPK pathways (**Figure 9**). These results indicate that rosuvastatin should be considered a promising therapeutic agent for rescuing HT, but further studies are necessary to elucidate the target of rosuvastatin and expand its clinical applications.

AUTHOR CONTRIBUTIONS

DL and YL wrote the article. DL, YL, HM, JZ and LS performed the experiments. DL and YL contributed to sample collection and data analyses. YZ and AX designed the study and revised the manuscript. All authors approved the final version of the manuscript. We also thank American Journal Experts for editing and polishing of the manuscript (Submission No. RTTNDBG2).

FUNDING

This work was supported by the National Natural Science Foundation of China (no. 81671167), the Natural Science Foundation of Guangdong Province (no. 2014A030313384) and the Science and Technology Program of Guangzhou, China (nos. 201508020004, 2014Y2-00505 and 2017A020215049).

REFERENCES

Álvarez-Sabin, J., Maisterra, O., Santamarina, E., and Kase, C. S. (2013). Factors influencing haemorrhagic transformation in ischaemic stroke. *Lancet Neurol.* 12, 689–705. doi: 10.1016/s1474-4422(13)70055-3

Argaw, A. T., Asp, L., Zhang, J., Navrazhina, K., Pham, T., Mariani, J. N., et al. (2012). Astrocyte-derived VEGF-A drives blood-brain barrier disruption in CNS inflammatory disease. *J. Clin. Invest.* 122, 2454–2468. doi: 10.1172/JCI60842

Asahi, M., Huang, Z., Thomas, S., Yoshimura, S., Sumii, T., Mori, T., et al. (2005). Protective effects of statins involving both eNOS and tPA in focal cerebral ischemia. *J. Cereb. Blood Flow Metab.* 25, 722–729. doi: 10.1038/sj.jcbfm.9600070

Barone, E., Cenini, G., Di Domenico, F., Martin, S., Sultana, R., Mancuso, C., et al. (2011). Long-term high-dose atorvastatin decreases brain oxidative and nitrosative stress in a preclinical model of Alzheimer disease: a novel mechanism of action. *Pharmacol. Res.* 63, 172–180. doi: 10.1016/j.phrs.2010.12.007

Barone, F. C., Irving, E. A., Ray, A. M., Lee, J. C., Kassis, S., Kumar, S., et al. (2001). Inhibition of p38 mitogen-activated protein kinase provides neuroprotection in cerebral focal ischemia. *Med. Res. Rev.* 21, 129–145. doi: 10.1002/1098-1128(200103)21:2<129::aid-med1003>3.0.co;2-h

Bouet, V., Boulouard, M., Toutain, J., Divoux, D., Bernaudin, M., Schumann-Bard, P., et al. (2009). The adhesive removal test: a sensitive method to assess sensorimotor deficits in mice. *Nat. Protoc.* 4, 1560–1564. doi: 10.1038/nprot.2009.125

Campos, F., Qin, T., Castillo, J., Seo, J. H., Arai, K., Lo, E. H., et al. (2013). Fingolimod reduces hemorrhagic transformation associated with delayed tissue plasminogen activator treatment in a mouse thromboembolic model. *Stroke* 44, 505–511. doi: 10.1161/strokeaha.112.679043

Cheng, T., Petraglia, A. L., Li, Z., Thiyagarajan, M., Zhong, Z., Wu, Z., et al. (2006). Activated protein C inhibits tissue plasminogen activator-induced brain hemorrhage. *Nat. Med.* 12, 1278–1285. doi: 10.1038/nm1498

Colombo, E., and Farina, C. (2016). Astrocytes: key regulators of neuroinflammation. *Trends Immunol.* 37, 608–620. doi: 10.1016/j.it.2016.06.006

Cordle, A., and Landreth, G. (2005). 3-Hydroxy-3-methylglutaryl-coenzyme A reductase inhibitors attenuate β-amyloid-induced microglial inflammatory responses. *J. Neurosci.* 25, 299–307. doi: 10.1523/jneurosci.2544-04.2005

Cui, J., Zhang, M., Zhang, Y. Q., and Xu, Z. H. (2007). JNK pathway: diseases and therapeutic potential. *Acta Pharmacol. Sin.* 28, 601–608. doi: 10.1111/j.1745-7254.2007.00579.x

del Zoppo, G. J., Frankowski, H., Gu, Y. H., Osada, T., Kanazawa, M., Milner, R., et al. (2012). Microglial cell activation is a source of metalloproteinase generation during hemorrhagic transformation. *J. Cereb. Blood Flow Metab.* 32, 919–932. doi: 10.1038/jcbfm.2012.11

Emberson, J., Lees, K. R., Lyden, P., Blackwell, L., Albers, G., Bluhmki, E., et al. (2014). Effect of treatment delay, age and stroke severity on the effects of intravenous thrombolysis with alteplase for acute ischaemic stroke: a meta-analysis of individual patient data from randomised trials. *Lancet* 384, 1929–1935. doi: 10.1016/S0140-6736(14)60584-5

Freret, T., Bouet, V., Leconte, C., Roussel, S., Chazalviel, L., Divoux, D., et al. (2009). Behavioral deficits after distal focal cerebral ischemia in mice: usefulness of adhesive removal test. *Behav. Neurosci.* 123, 224–230. doi: 10.1037/a0014157

Gullestad, L., Ueland, T., Kjekshus, J., Nymo, S. H., Hulthe, J., Muntendam, P., et al. (2012). The predictive value of galectin-3 for mortality and cardiovascular events in the controlled rosuvastatin multinational trial in heart failure (CORONA). *Am. Heart J.* 164, 878–883. doi: 10.1016/j.ahj.2012.08.021

Hayden, M. S., and Ghosh, S. (2008). Shared principles in NF-κB signaling. *Cell* 132, 344–362. doi: 10.1016/j.cell.2008.01.020

Hosaka, A., Araki, W., Oda, A., Tomidokoro, Y., and Tamaoka, A. (2013). Statins reduce amyloid β-peptide production by modulating amyloid precursor protein maturation and phosphorylation through a cholesterol-independent mechanism in cultured neurons. *Neurochem. Res.* 38, 589–600. doi: 10.1007/s11064-012-0956-1

Joo, J., Plimpton, S., Martin, S., Swiler, L., and Faulon, J. L. (2007). Sensitivity analysis of a computational model of the IKK NF-κB IκBα A20 signal transduction network. *Ann. N Y Acad. Sci.* 1115, 221–239. doi: 10.1196/annals.1407.014

Kahveci, R., Gökçe, E. C., Gürer, B., Gökçe, A., Kisa, U., Cemil, D. B., et al. (2014). Neuroprotective effects of rosuvastatin against traumatic spinal cord injury in rats. *Eur. J. Pharmacol.* 741, 45–54. doi: 10.1016/j.ejphar.2014.07.042

Kelly, M. A., Shuaib, A., and Todd, K. G. (2006). Matrix metalloproteinase activation and blood-brain barrier breakdown following thrombolysis. *Exp. Neurol.* 200, 38–49. doi: 10.1016/j.expneurol.2006.01.032

Kettenmann, H., Hanisch, U. K., Noda, M., and Verkhratsky, A. (2011). Physiology of microglia. *Physiol. Rev.* 91, 461–553. doi: 10.1152/physrev.00011.2010

Khatri, R., McKinney, A. M., Swenson, B., and Janardhan, V. (2012). Blood-brain barrier, reperfusion injury and hemorrhagic transformation in acute ischemic stroke. *Neurology* 79, S52–S57. doi: 10.1212/wnl.0b013e3182697e70

Kim, J. M., Oh, Y. K., Lee, J. H., Im, D. Y., Kim, Y. J., Youn, J., et al. (2005). Induction of proinflammatory mediators requires activation of the TRAF, NIK, IKK and NF-κB signal transduction pathway in astrocytes infected with *Escherichia coli*. *Clin. Exp. Immunol.* 140, 450–460. doi: 10.1111/j.1365-2249.2005.02804.x

Koistinaho, M., and Koistinaho, J. (2002). Role of p38 and p44/42 mitogen-activated protein kinases in microglia. *Glia* 40, 175–183. doi: 10.1002/glia.10151

Kuan, C. Y., Whitmarsh, A. J., Yang, D. D., Liao, G. H., Schloemer, A. J., Dong, C., et al. (2003). A critical role of neural-specific JNK3 for ischemic apoptosis. *Proc. Natl. Acad. Sci. U S A* 100, 15184–15189. doi: 10.1073/pnas.2336254100

Li, W., Li, Y., Zhu, S., Ji, Q., Shu, Y., Zhang, L., et al. (2015). Rosuvastatin attenuated the existing morphine tolerance in rats with L5 spinal nerve transection through inhibiting activation of astrocytes and phosphorylation of ERK42/44. *Neurosci. Lett.* 584, 314–319. doi: 10.1016/j.neulet.2014.11.003

Liu, C. W., Yang, F., Cheng, S. Z., Liu, Y., Wan, L. H., and Cong, H. L. (2017). Rosuvastatin postconditioning protects isolated hearts against ischemia-reperfusion injury: the role of radical oxygen species, PI3K-Akt-GSK-3β pathway and mitochondrial permeability transition pore. *Cardiovasc. Ther.* 35, 3–9. doi: 10.1111/1755-5922.12225

Lourbopoulos, A., Mamrak, U., Roth, S., Balbi, M., Shrouder, J., Liesz, A., et al. (2017). Inadequate food and water intake determine mortality following stroke in mice. *J. Cereb. Blood Flow Metab.* 37, 2084–2097. doi: 10.1177/0271678x16660986

Ma, L., Manaenko, A., Ou, Y. B., Shao, A. W., Yang, S. X., and Zhang, J. H. (2017). Bosutinib attenuates inflammation via inhibiting salt-inducible kinases in experimental model of intracerebral hemorrhage on mice. *Stroke* 48, 3108–3116. doi: 10.1161/strokeaha.117.017681

Manaenko, A., Fathali, N., Khatibi, N. H., Lekic, T., Hasegawa, Y., Martin, R., et al. (2011). Arginine-vasopressin V1a receptor inhibition improves neurologic outcomes following an intracerebral hemorrhagic brain injury. *Neurochem. Int.* 58, 542–548. doi: 10.1016/j.neuint.2011.01.018

Mandas, A., Congiu, M. G., Abete, C., Dessi, S., Manconi, P. E., Musio, M., et al. (2014). Cognitive decline and depressive symptoms in late-life are associated with statin use: evidence from a population-based study of Sardinian old people living in their own home. *Neurol. Res.* 36, 247–254. doi: 10.1179/1743132813y.0000000287

McFarland, A. J., Anoopkumar-Dukie, S., Arora, D. S., Grant, G. D., McDermott, C. M., Perkins, A. V., et al. (2014). Molecular mechanisms underlying the effects of statins in the central nervous system. *Int. J. Mol. Sci.* 15, 20607–20637. doi: 10.3390/ijms151120607

McFarland, A. J., Davey, A. K., and Anoopkumar-Dukie, S. (2017). Statins reduce lipopolysaccharide-induced cytokine and inflammatory mediator release in an *in vitro* model of microglial-like cells. *Mediators Inflamm.* 2017:2582745. doi: 10.1155/2017/2582745

McTaggart, F., Buckett, L., Davidson, R., Holdgate, G., McCormick, A., Schneck, D., et al. (2001). Preclinical and clinical pharmacology of Rosuvastatin, a new 3-hydroxy-3-methylglutaryl coenzyme A reductase inhibitor. *Am. J. Cardiol.* 87, 28B–32B. doi: 10.1016/S0002-9149(01)01454-0

Mehra, M., Henninger, N., Hirsch, J. A., Chueh, J., Wakhloo, A. K., and Gounis, M. J. (2012). Preclinical acute ischemic stroke modeling. *J. Neurointerv. Surg.* 4, 307–313. doi: 10.1136/neurintsurg-2011-010101

Mishiro, K., Ishiguro, M., Suzuki, Y., Tsuruma, K., Shimazawa, M., and Hara, H. (2012). A broad-spectrum matrix metalloproteinase inhibitor prevents hemorrhagic complications induced by tissue plasminogen activator in mice. *Neuroscience* 205, 39–48. doi: 10.1016/j.neuroscience.2011.12.042

Modo, M., Stroemer, R. P., Tang, E., Veizovic, T., Sowniski, P., and Hodges, H. (2000). Neurological sequelae and long-term behavioural assessment of rats with transient middle cerebral artery occlusion. *J. Neurosci. Methods* 104, 99–109. doi: 10.1016/s0165-0270(00)00329-0

Nithianandarajah-Jones, G. N., Wilm, B., Goldring, C. E., Muller, J., and Cross, M. J. (2012). ERK5: structure, regulation and function. *Cell. Signal.* 24, 2187–2196. doi: 10.1016/j.cellsig.2012.07.007

Ozkul-Wermester, O., Guegan-Massardier, E., Triquenot, A., Borden, A., Perot, G., and Gerardin, E. (2014). Increased blood-brain barrier permeability on perfusion computed tomography predicts hemorrhagic transformation in acute ischemic stroke. *Eur. Neurol.* 72, 45–53. doi: 10.1159/000358297

Piao, C. S., Yu, Y. M., Han, P. L., and Lee, J. K. (2003). Dynamic expression of p38β MAPK in neurons and astrocytes after transient focal ischemia. *Brain Res.* 976, 120–124. doi: 10.1016/s0006-8993(03)02579-4

Postmus, I., Trompet, S., Deshmukh, H. A., Barnes, M. R., Li, X., Warren, H. R., et al. (2014). Pharmacogenetic meta-analysis of genome-wide association studies of LDL cholesterol response to statins. *Nat. Commun.* 5:5068. doi: 10.1038/ncomms6068

Spence, J. D. (2014). Statins and ischemic stroke. *JAMA* 312, 749–750. doi: 10.1001/jama.2014.8357

Sun, S. C., and Ley, S. C. (2008). New insights into NF-κB regulation and function. *Trends Immunol.* 29, 469–478. doi: 10.1016/j.it.2008.07.003

Suzuki, Y., Nagai, N., Yamakawa, K., Kawakami, J., Lijnen, H. R., and Umemura, K. (2009). Tissue-type plasminogen activator (t-PA) induces stromelysin-1 (MMP-3) in endothelial cells through activation of lipoprotein receptor-related protein. *Blood* 114, 3352–3358. doi: 10.1182/blood-2009-02-203919

Wang, W., Li, M., Chen, Q., and Wang, J. (2015). Hemorrhagic transformation after tissue plasminogen activator reperfusion therapy for ischemic stroke: mechanisms, models and biomarkers. *Mol. Neurobiol.* 52, 1572–1579. doi: 10.1007/s12035-014-8952-x

Wu, B., Ma, Q., Khatibi, N., Chen, W., Sozen, T., Cheng, O., et al. (2010). Ac-YVAD-CMK decreases blood-brain barrier degradation by inhibiting caspase-1 activation of interleukin-1β in intracerebral hemorrhage mouse model. *Transl. Stroke Res.* 1, 57–64. doi: 10.1007/s12975-009-0002-z

Xiao, Y., Jin, J., Chang, M., Chang, J. H., Hu, H., Zhou, X., et al. (2013). Peli1 promotes microglia-mediated CNS inflammation by regulating Traf3 degradation. *Nat. Med.* 19, 595–602. doi: 10.1038/nm.3111

Yepes, M., Sandkvist, M., Moore, E. G., Bugge, T. H., Strickland, D. K., and Lawrence, D. A. (2003). Tissue-type plasminogen activator induces opening of the blood-brain barrier via the LDL receptor-related protein. *J. Clin. Invest.* 112, 1533–1540. doi: 10.1172/jci19212

Zhang, C., An, J., Haile, W. B., Echeverry, R., Strickland, D. K., and Yepes, M. (2009). Microglial low-density lipoprotein receptor-related protein 1 mediates the effect of tissue-type plasminogen activator on matrix metalloproteinase-9 activity in the ischemic brain. *J. Cereb. Blood Flow Metab.* 29, 1946–1954. doi: 10.1038/jcbfm.2009.174

Zhou, Y., Wang, Y., Wang, J., Anne Stetler, R., and Yang, Q. W. (2014). Inflammation in intracerebral hemorrhage: from mechanisms to clinical translation. *Prog. Neurobiol.* 115, 25–44. doi: 10.1016/j.pneurobio.2013.11.003

Zhu, H., Zhang, Y., Shi, Z., Lu, D., Li, T., Ding, Y., et al. (2016). The neuroprotection of liraglutide against ischaemia-induced apoptosis through the activation of the PI3K/AKT and MAPK pathways. *Sci. Rep.* 6:26859. doi: 10.1038/srep26859

Conflict of Interest Statement: The authors declare that the research was conducted in the absence of any commercial or financial relationships that could be construed as a potential conflict of interest.

frontiers in Cellular Neuroscience

ORIGINAL RESEARCH
published: 03 August 2018
doi: 10.3389/fncel.2018.00230

Role of CXCR1 and Interleukin-8 in Methamphetamine-Induced Neuronal Apoptosis

Si-Hao Du[1†], Wei Zhang[1†], Xia Yue[1], Xiao-Qing Luo[1,2], Xiao-Hui Tan[1], Chao Liu[3], Dong-Fang Qiao[1] and Huijun Wang[1]**

[1]School of Forensic Medicine, Southern Medical University, Guangzhou, China, [2]Nanfang Hospital, Southern Medical University, Guangzhou, China, [3]Guangzhou Forensic Science Institute, Guangzhou Public Security Bureau, Guangzhou, China

Methamphetamine (METH), an extremely and widely abused illicit drug, can cause serious nervous system damage and social problems. Previous research has shown that METH use causes dopaminergic neuron apoptosis and astrocyte-related neuroinflammation. However, the relationship of astrocytes and neurons in METH-induced neurotoxicity remains unclear. We hypothesized that chemokine interleukin (IL) eight released by astrocytes and C-X-C motif chemokine receptor 1 (CXCR1) in neurons are involved in METH-induced neuronal apoptosis. We tested our hypothesis by examining the changes of CXCR1 in SH-SY5Y cells and in the brain of C57BL/6 mice exposed to METH by western blotting and immunolabeling. We also determined the effects of knocking down CXCR1 expression with small interfering ribonucleic acid (siRNA) on METH-exposed SH-SY5Y cells. Furthermore, we detected the expression levels of IL-8 and the nuclear factor-kappa B (NF-κB) pathway in U87MG cells and then co-cultured the two cell types to determine the role of CXCR1 and IL-8 in neuronal apoptosis. Our results indicated that METH exposure increased CXCR1 expression both *in vitro* and *in vivo*, with the effects obtained *in vitro* being dose-dependent. Silencing of CXCR1 expression with siRNAs reduced the expression of cleaved caspase-3, cleaved poly (ADP-ribose) polymerase (PARP), and other related proteins. In addition, IL-8 expression and release were increased in METH-exposed U87MG cells, which is regulated by NF-κB pathway. Neuronal apoptosis was attenuated by siCXCR1 after METH treatment in the co-cultured cells, which can be reversed after exposure to recombinant IL-8. These results demonstrate that CXCR1 plays an important role in neuronal apoptosis induced by METH and may be a potential target for METH-induced neurotoxicity therapy.

Highlights

- Methamphetamine exposure upregulated the expression of CXCR1.
- Methamphetamine exposure increased the expression of interleukin-8 through nuclear factor-kappa B pathway.

OPEN ACCESS

Edited by:
Sriharsha Kantamneni, University of Bradford, United Kingdom

Reviewed by:
Michela Ferrucci, Università degli Studi di Pisa, Italy
James P. Kesby, University of Queensland, Australia

***Correspondence:**
Dong-Fang Qiao
qiaodf@163.com
Huijun Wang
hjwang@smu.edu.cn

†These authors have contributed equally to this work.

Received: *15 March 2018*
Accepted: *16 July 2018*
Published: *03 August 2018*

Citation:
Du S-H, Zhang W, Yue X, Luo X-Q, Tan X-H, Liu C, Qiao D-F and Wang H (2018) Role of CXCR1 and Interleukin-8 in Methamphetamine-Induced Neuronal Apoptosis. Front. Cell. Neurosci. 12:230. doi: 10.3389/fncel.2018.00230

Abbreviations: Bay 11–7082, ((E)3-[(4-methylphenyl)-sulfonyl]-2-propenenitrile; CNS, central nervous system; CXCR1, C-X-C motif chemokine receptor 1; DMEM, Dulbecco's modified Eagle's medium; FBS, Fetal bovine serum; IKK, IκB kinase; IL, Interleukin; METH, Methamphetamine; NF-κB, nuclear factor-kappa B; PARP, poly(ADP-ribose) polymerase; VDF, Polyvinylidenedifluoride; SDS-PAGE, Sodium dodecyl sulfate polyacrylamide gel.

– Activation of CXCR1 by interleukin-8 induces an increase in methamphetamine-related neuronal apoptosis.

Keywords: methamphetamine, CXCR1, IL-8, neurotoxicity, apoptosis, astrocytes

BACKGROUND

Methamphetamine (METH) is a highly addictive psychoactive drug that can have a significant injurious effect on the central nervous system (CNS). The abuse of METH has become more common than that of either heroin or cocaine and has thus placed great pressure on the economy and social order (Dinis-Oliveira et al., 2012).

Clinical and animal model studies of METH have shown that long-term consumption of METH results in significant damage to the dopaminergic system, including direct pharmacological damage of the sensitive brain region (Kita et al., 2009; Zhang et al., 2013), oxidative stress and inflammatory lesions, along with the destruction of dopaminergic neurons (Huang et al., 2015).

Our previous studies and other laboratories' research found that METH can cause neuronal apoptosis through P53 upregulated modulator of apoptosis (PUMA), insulin-like growth factor-binding protein 5 (IGFBP5), and other pathways (Qiao et al., 2014; Carmena et al., 2015; Chen C. et al., 2016; Mendieta et al., 2016). However, the treatment of primary astrocytes with METH showed that the nuclear import of nuclear factor-kappa B (NF-κB) could be increased through Toll-like receptor 4, leading increased release of pro-inflammatory cytokines, such as interleukin (IL)-1β and IL-18 (Du et al., 2017). Our recent study showed that the regulation of chemokines through a NF-κB/IL-8/C-X-C motif chemokine receptor 1 (CXCR1) pathway may play an important role in METH-induced neuronal apoptosis.

The pro-inflammatory IL-8 is a multi-functional CXC chemokine of about 75 amino acids in length (Waugh and Wilson, 2008; Citro et al., 2015). Numerous stresses, including inflammatory signals such as IL-1β and tumor necrosis factor alpha, environmental stresses (including hypoxia and/or reactive oxygen species) or surgical damage can induce IL-8 expression (Hoffmann et al., 2002; Sordillo and Helson, 2015). It turns out that both astrocytes and neurons produce IL-8 *in vitro*, stimulated by pro-inflammatory cytokines (Vlahopoulos et al., 1999; Waugh and Wilson, 2008; Kou et al., 2011). It has also been demonstrated that exposure of the cells to CpG oligodeoxynucleotides and lipopolysaccharides (LPS) increased the expression of IL-8 through mitogen-activated protein kinase (MAPK)-dependent and NF-κB-independent pathways (Kim et al., 2005). Two high-affinity receptors for IL-8 in humans are designated CXCR1 (also called IL-8R-A) and CXCR2 (Lee et al., 1992; Loetscher et al., 1994). The two receptors are expressed not only on leukocytes and tumor cells but also on neutrophils, monocytes, macrophages, basophils, natural killer T-cells and others normal cells; in addition, a lower percentage of T-cells express CXCR1/2 (Flynn et al., 2003; Brat et al., 2005). Additionally, it has been indicated that cells in CNS express chemokine receptors, including CXCR1 and CXCR2 (Dorf et al., 2000).

Chemokine IL-8, also known as CXCL8, exerts its biological effects by binding to the specific G protein-coupled receptors of CXCR1 and CXCR2 (Citro et al., 2015). After their internalization (i.e., via MAPK, phosphoinositide 3-kinase (PI3K), protein kinase c and Src tyrosine kinase, etc.), a wide range of intracellular pathways are activated (Takahashi et al., 2007; Citro et al., 2015). Therefore, in certain pathological conditions, CXCR1 is crucial in inflammatory injury and may be a promising target for neuronal apoptosis (Clunes and Boucher, 2007; Eltzschig and Eckle, 2011). However, the role of CXCR1 in neuronal apoptosis induced by METH remains to be investigated.

We hypothesized that CXCR1 would mediate METH-induced neuronal apoptosis and that the blockade of CXCR1 expression might partially protect against METH-induced neuronal apoptosis. In this study, we examined CXCR1 levels, and they showed elevated expression in METH poisoning models *in vivo* and *in vitro*. We also found that METH treatment of astrocytes resulted in increased expression of IL-8 through the activation of the NF-κB pathway. The apoptosis of neurons increased with the addition of exogenous IL-8, while the apoptosis of neurons was reduced after the silencing of CXCR1. These findings indicated that CXCR1 activation is important in the process of METH-induced neuronal apoptosis. Our study showed that CXCR1 may be a potential target in the mitigation of neuronal damage and apoptosis induced by METH.

MATERIALS AND METHODS

Materials

High Glucose Dulbecco's modified Eagle's medium (DMEM), fetal bovine serum (FBS), opti-MEM, Lipofectamine 3000 and trypsin were purchased from Gibco (Carlsbad, CA, USA). METH (>99% purity) was obtained from the National Institutes for the Control of Pharmaceutical and Biological Products (Beijing, China). Anti-cleaved poly (ADP-ribose) polymerase (PARP), anti-cleaved caspase3, anti-IKK-α, anti-IKK-β, anti-phospho-IKKα/β, anti-phospho-NF-κB, anti-IκB and anti-rabbit and mouse IgG (H + L), F(ab')2 fragment (Alexa Fluor 555 conjugated) were purchased from the Cell Signaling Technology (Boston, MA, USA). Anti-NeuN was purchased from Abcam (Cambridge, UK). Anti-NF-κB, anti-Bax, anti-Bcl-2 and anti-IL-8 were purchased from ABclonal Inc (College Park, MD, USA). Anti-β-actin and goat anti-mouse and rabbit IgG (H + L)-HRP were purchased from Beijing Ray Antibody Biotech (Beijing, China). Anti-CXCR1 was purchased from Bioss (Beijing, China). Fluorescein (FITC)-conjugated goat anti-mouse and rabbit IgG were purchased from DingGuo

(Beijing, China). siRNAs for CXCR1 was purchased from the Shanghai GenePharma Company Limited (Shanghai, China). Human IL-8 ELISA kit was purchased from Cusabio Biotech (Wuhan, China). Super ECL Assay was purchased from KeyGEN Biotech (Nanjing, China). Recombinant IL-8 was purchased from PerproTech (Rocky Hill, NJ, USA). Bay 11-7082 ((E)3-[(4-methylphenyl)-sulfonyl]-2-propenenitrile; a NF-κB inhibitor) was purchased from SelleckChem (Houston, TX, USA). Other reagents, unless specifically mentioned, were purchased from Sigma-Aldrich (St. Louis, MO, USA).

Animal Protocol

Healthy adult male C57BL/6 mice (18–22 g, 6–8 weeks old) were purchased from Southern Medical University Experimental Animal Center (Guangzhou, China) and placed individually in a temperature-controlled tub cage (approximately 22°C) with 12 h of light/dark cycle room. All procedures involving animals were performed in accordance with the ethical standards of Ethics Committee of Nanfang Hospital, Southern Medical University and with the 1964 Helsinki Declaration and its later amendments or comparable ethical standards. This article does not contain any studies with humans performed by any of the authors. Mice were placed in animal facilities for 1 week before use to make them accustomed. Mice were randomly divided into two groups (n = 3/group): saline control group and METH subacute exposure group. METH is dissolved in physiological saline. Mice in the subacute exposure group received an intraperitoneal (i.p.) METH injection (15 mg/kg/injection) every 12 h for a total of eight injections. This pattern of exposure is based on our and other previous studies (Cadet et al., 2003; Krasnova and Cadet, 2009; Qiao et al., 2014; Du et al., 2017). Saline control mice were injected i.p. with a similar volume of saline. Injections were performed at the same time as the subacute exposure group. All animals survived throughout the study. Mice were euthanized 2 h after the last injection (CO_2; followed by decapitation). Brain regions were rapidly isolated, and half hemispheres were cut and placed in 4% paraformaldehyde for 24 h for immunofluorescence experiments. The other half hemispheres were dissected to the prefrontal cortex, hippocampus, midbrain and striatum region on iced glass plates, rapidly frozen and stored at −80°C until analysis.

Cell Culture

SH-SY5Y cells, a human neuroblastoma cell line and U87MG cells, a human primary glioblastoma cell line were purchased from the Cell Bank of Shanghai Institute for Biological Center, Chinese Academy of Science (Shanghai, China). Cells were cultured in DMEM medium containing 10% FBS and placed in a 37°C constant temperature humidification, 5% carbon dioxide cell culture box. The culture medium was changed 1 or 2 days. Cells were passaged to 6-well plate when they reached about 80% to 90%.

Methamphetamine and Inhibitor Treatment

Once cells were reached about 80%, medium was changed to non-serum medium. Then cells were exposed to 0, 0.5, 1.0, 1.5, 2.0 and 2.5 mM METH in U87MG cells or SH-SY5Y cells for 24 h. This concentration range was selected based on our and others previous studies (Cisneros and Ghorpade, 2014; Zhang et al., 2015; Cao et al., 2016) and this concentration covers the non-toxic, sub-toxic and 50% lethal concentrations of METH (Chen C. et al., 2016). In the experiments with inhibitor Bay 11-7082, the cells were pre-cultured for 12 h with 10 μM Bay 11–7082 and then incubated with 2.0 mM METH for 24 h. The concentration of Bay 11–7082 was selected based on earlier studies (Pierce et al., 1997; Zanotto-Filho et al., 2011) and this concentration had optimal inhibition effects in our experiment.

Co-culture of U87MG Cells and SH-SY5Y Cells

U87MG cells and SH-SY5Y cells were cultured to a density of 90% and passaged into transwell dishes (0.4 μM; purchased from Corning (Corning, NY, USA)). SH-SY5Y cells were plated in the upper chamber of the transwell plate and U87MG cells were spread on the bottom of the transwell plate and cultured to a density of 70% to 80% respectively. The upper chamber was then placed above the lower chamber and exposed to 2.0 mM of METH for 24 h.

Western Blot Analysis

We used a Radio Immunoprecipitation Assay (RIPA) cleavage method to extract cell protein. Protein concentration was determined by BCA-100 protein quantification kit, which was purchased from Biosharp (Hefei, China). A sample of 50 μg of protein were taken and separated by 10% to 15% polyacrylamide gel electrophoresis. The protein was transferred to polyvinylidenefluoride (PVDF) membrane (Millipore, Billerica, MA, USA) and then the PVDF membranes were incubated for 1 h at room temperature (RT) in 5% (w/v) skim milk in tris-buffered saline containing 0.1% Tween 20 (TBST), followed by incubated overnight with a primary antibody at 4°C (1:500–1:1,000) in TBST. Next, the PVDF membranes were washed for three times with TBST and then incubated for 1 h at RT with secondary antibody (1:10,000) followed by three times washing with TBST. The membranes were developed with 200 μl of super ECL assay. The band intensities were quantitated by Gel-Pro analyzer (Media Cybernetics Inc., Rockville, MD, USA). We used β-actin as our reference index, and each experiment was repeated three times, with the most representative results presented in the current manuscript.

Small Interfering Ribonucleic Acid and Transient Cell Transfection

Transfection was performed as described previously (Du et al., 2017). The sequences of small interfering ribonucleic acid

TABLE 1 | The sequences of small interfering ribonucleic acids (siRNAs) used in the present study.

Gene	Number	The sequence of siRNA (5′-3′)
CXCR1	1	CCGCCAGGCUUACCAUCCAAACAAU
CXCR1	2	UCGUGCCGCUGUUUGUCAUGCUGUU
Negative control	1	UUCUCCGAACGUGUCACGUTT

(siRNA) are shown in **Table 1**. Twenty-four hours before transfection, 4−5 × 10^5 SH-SY5Y cells were seeded on 6-well culture plates, and 2 ml of DMEM medium containing 10% FBS was added to each well. Then, 20 μMol of CXCRl siRNA or control siRNA (siNC) (GenePharma, Shanghai, China) and 5 μl of lipofectamine 3000 reagent were added to 1 ml opti-MEM medium. The mixed solution was incubated at RT for 20 min, and then added to each well of the culture plate in conjunction with gentle shaking and mixing. The cell culture plates were placed in incubator for 6–12 h and then 1 ml complete medium was added in each well.

Double Immunofluorescence Labeling

Double immunofluorescence labeling was performed as described previously (Du et al., 2017). To determine CXCR1 expression levels in SH-SY5Y cells and mice midbrain samples, double immunofluorescence labeling on cells and frozen sections of adult mice midbrains was performed. For immunolabeling, SH-SY5Y cells were seeded on glass bottom cell culture dishes (NEST, Shanghai, China). Cells were fixated in 4% paraformaldehyde. Then cells were incubated with blocking buffer (10% BSA and 0.05% Triton X-100) for 30 min at RT, with the primary antibody (anti-NeuN dilution of 1:200 and anti-CXCR1 dilution of 1:100) overnight at 4°C, and then with the secondary antibody for 1 h at RT (FITC conjugated anti-mouse or rabbit IgG dilution of 1:50, Alexa Fluor 555 conjugated anti-mouse or rabbit IgG dilution of 1:200). All incubation solutions were prepared using PBS supplemented with 10% BSA and 0.05% Triton X-100. 4',6-diamidino-2-phenylindole (DAPI) was used to stain nucleus. The frozen tissue sections were incubated with cold acetone for 15 min to remove the embedding agent. The rest of the steps are the

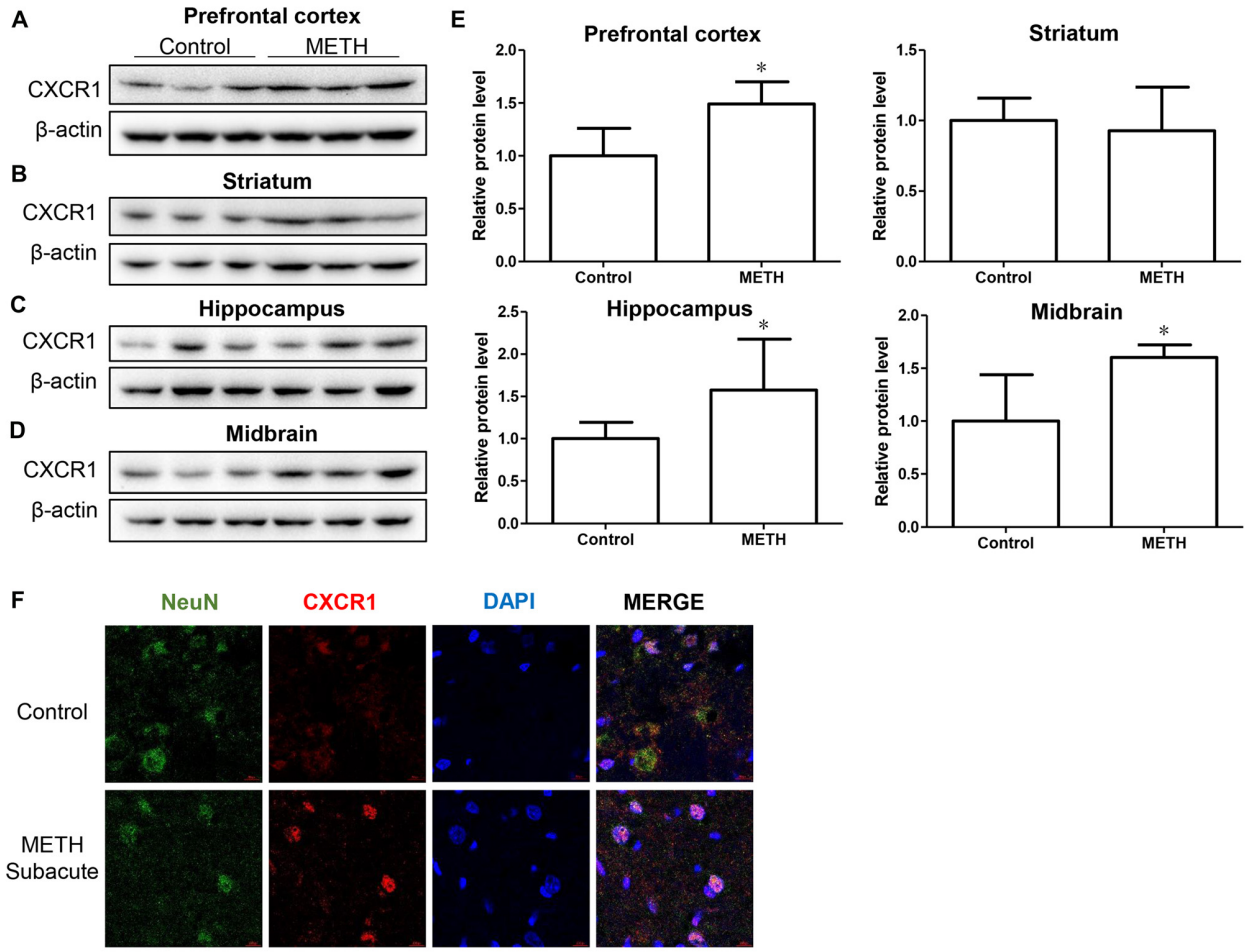

FIGURE 1 | Methamphetamine (METH) increased C-X-C motif chemokine receptor 1 (CXCR1) expression in the brain of male C57BL/6 mice. Male C57BL/6 mice were divided randomly into two groups: experimental group and control group (n = 3/group). Animals were injected intraperitoneally (i.p.) with METH (eight injections, 15 mg/kg/injection, at 12-h intervals) or saline. The prefrontal cortex, hippocampus, midbrain and striatum tissues were separated on ice at 2 h after the last dosing. Western blot **(A–D)** and quantitative analyses **(E)** were performed to determine CXCR1 expression. β-actin was used as a loading control. Fold induction relative to the control group is shown. *Represents a significant difference as compared with the control or vehicle-treated group, *$p < 0.05$. Results are expressed as the mean ± standard deviation (SD) of three experiments. Data were analyzed with Student's t-test. Immunolabeling and confocal imaging analyses **(F)** showed increased CXCR1 expression in the midbrain of METH-exposed mice in comparison with in the controls. Scale bar, 15 μM.

same as for the cells. Microphotographs were taken using fluorescence microscopy (A1+/A1R+; Nikon). All digital images were processed using the same settings to improve the contrast.

Enzyme Linked Immunosorbent Assay (ELISA)

ELISA was performed as Human IL-8 ELISA kit directions described (Cusabio Biotech, China). Briefly, add 100 μl of standard or test sample per well and incubate for 2 h at 37°C. Remove the liquid of each well and add 100 μl of primary antibody and incubate for 1 h at 37°C. Remove the liquid, wash the plate three times with PBS for 2 min each time, add 100 μl horseradish peroxidase labeled avidin secondary antibody, and incubate for 1 h at 37°C. Remove the liquid, wash the plate three times with PBS, add 90 μl of the substrate solution. Incubate for 15–30 min at 37°C to avoid light. Add 50 μl of stop solution to stop the reaction. Determine the optical density of each well within 5 min, using a microplate reader set to 450 nm.

Terminal Deoxynucleotidyl Transferase dUTP Nick End-Labeling (TUNEL) Staining

The DNA fragments of the apoptotic neurons were detected according to the instructions of a terminal deoxynucleotidyl transferase dUTP nick end labeling (TUNEL) fluorescent reagent. First, cells were fixed with 4% paraformaldehyde for 10 min at RT and then incubated for 1 h in cell culture incubator by adding terminal deoxynucleotidyl transferase enzyme conjugated to fluorescein, which was followed by the introduction of DAPI for nuclear count staining. The cross-sectional fragment was observed under a fluorescence microscope. Treatment in the control group was consistent with the addition of terminal deoxynucleotide transferase. TUNEL-positive cells and DAPI-positive cells were counted.

Statistical Analysis

Statistical analysis of data was performed with Student's *t*-test and one-way analysis of variance (ANOVA) followed by Least Significant Difference (LSD) *post hoc* analyses using SPSS 20.0 software (IBM Corporation, Armonk, NY, USA). Data given in the text are expressed as mean ± standard deviation (SD). The value of $P < 0.05$ was considered statistically significant.

RESULTS

Methamphetamine-Induced CXCR1 Expression in Neurons

In order to determine the role of CXCR1 in METH-triggered neurotoxicity, a mouse model treated with METH (eight injections, 15 mg/kg/injection, given at 12-h intervals) was used to detect the expression of CXCR1 *in vivo*. We separated the brain regions of prefrontal cortex, hippocampus,

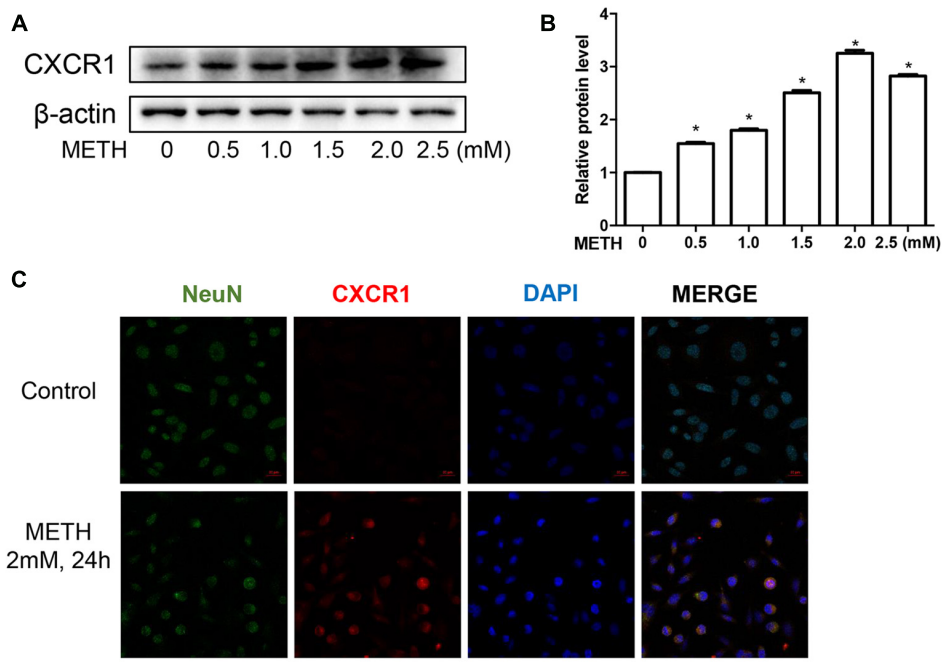

FIGURE 2 | METH increased CXCR1 expression in neurons. SH-SY5Y cells were exposed to 0.5 mM, 1 mM, 1.5 mM, 2 mM and 2.5 mM of METH for 24 h **(A)** or 2 mM of METH for 24 h **(C)**. Western blot **(A)** and quantitative analyses **(B)** were performed to determine CXCR1 protein expression. β-actin was used as a loading control. Fold induction relative to the control group is shown. *Represents a significant difference as compared with the control or vehicle-treated group, *$p < 0.05$. Results are expressed as the mean ± SD of three experiments. Data were analyzed with one-way ANOVA followed by least significant difference (LSD) *post hoc* analyses. Immunolabeling and confocal imaging analyses **(C)** showed elevated CXCR1 expression in the SH-SY5Y cells treated with METH in comparison with in the controls. Scale bar, 50 μM.

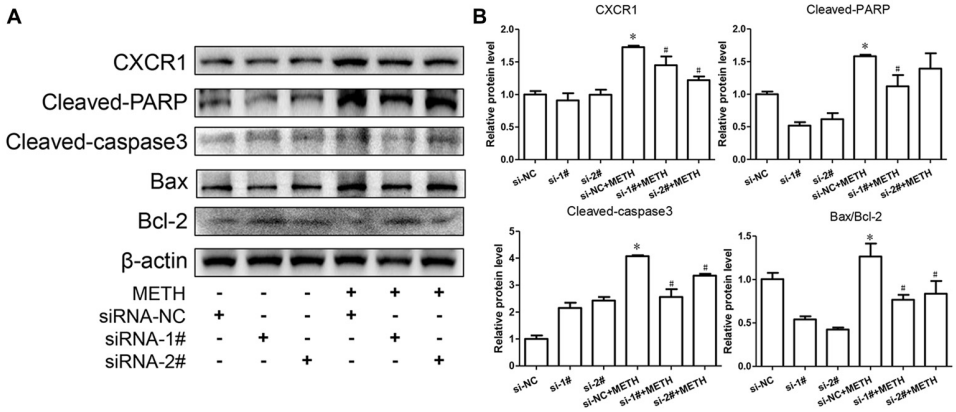

FIGURE 3 | Silencing of CXCR1 expression with small interfering ribonucleic acid (siRNA)-attenuated METH-induced neuronal apoptosis. SH-SY5Y cells were transfected with siRNA targeting CXCR1 or control siRNA for 24 h, followed by 2 mM of METH treatment for 24 h. Western blot **(A)** and quantitative analyses **(B)** were performed to determine CXCR1, cleaved caspase-3, cleaved PARP, Bax and Bcl-2 protein expression. β-actin was used as a loading control. Fold induction relative to the control group is shown. *Represents a significant difference as compared with the non-METH-treated group, $^{*}p < 0.05$. $^{\#}$Represents a significant difference as compared with the scrambled + METH treated group, $^{\#}p < 0.05$. Results are expressed as the mean ± SD of three experiments. Data were analyzed with one-way ANOVA followed by LSD *post hoc* analyses.

midbrain and striatum for further testing. Western blot results showed that CXCR1 protein levels in the prefrontal cortex, hippocampus and midbrain were higher in the subacute exposure group than in the control group (**Figures 1A,C–E**), while the expression of CXCR1 in the striatum showed no obvious effect between the two groups (**Figures 1B,E**). Immunofluorescence staining results also showed that the expression of CXCR1 was increased in the midbrain of METH-treated C57BL/6 mice (**Figure 1F**). In addition, we also observed co-localization of CXCR1 with neurons, indicating that CXCR1 is mainly expressed in the neurons of the midbrain.

To validate this phenomenon *in vitro*, we selected SH-SY5Y cells to determine the expression of CXCR1. SH-SY5Y cells were treated with different concentrations of METH—specifically, 0 mM, 0.5 mM, 1 mM, 1.5 mM, 2 mM, or 2.5 mM—and western blot analysis was performed to detect CXCR1 expression. The results showed that CXCR1 protein expression was increased in a dose-dependent manner in the SH-SY5Y cells (**Figures 2A,B**). CXCR1 protein expression was 3.25-fold higher in the 2.0 mM METH-treated SH-SY5Y cells for 24 h than in the control cells. Immunofluorescence staining results demonstrated the same results (**Figure 2C**). These findings suggest that METH exposure induces CXCR1 protein expression both *in vivo* and *in vitro*.

Importance of CXCR1 Induction in Neuronal Apoptosis Induced by Methamphetamine

To confirm the relationship of CXCR1 and neurotoxicity induced by METH, we designed two siRNA sequences for SH-SY5Y cells to silence CXCR1 expression. The results showed that both of the siRNA sequences could attenuate CXCR1 induction effectively in SH-SY5Y cells (**Figures 3A,B**). After pre-treatment with siRNA#1 or siRNA#2 of CXCR1, the cells were treated with METH (2 mM, 24 h). CXCR1 protein expression decreased respectively, as compared with in the siRNA-NC + METH treatment group (**Figures 3A,B**).

To evaluate the protective effect of CXCR1 silencing from METH-induced neuronal apoptosis, we determined the expression of cleaved caspase-3 and cleaved PARP by western blot analyses. We found that METH increased the level of cleaved caspase-3 and cleaved PARP obviously; this effect was significantly inhibited after CXCR1 silencing (**Figures 3A,B**). We then sought to examine whether Bcl-2/Bax are involved in METH-induced CXCR1-mediated neuronal apoptosis. Western blot analyses were performed to detect changes in Bcl-2 and Bax expression levels with and without CXCR1 knockdown. The results showed that the expression level of Bcl-2, an antiapoptotic factor, was increased following CXCR1 knockdown in comparison with in the si-NC + METH treatment group, while the expression level of Bax, a proapoptotic factor, was decreased (**Figures 3A,B**). Taken together, these results suggest that the silencing of CXCR1 inhibits the Bcl-2/Bax expression and that CXCR1 participates in the mitochondria-mediated apoptosis pathway triggered by METH.

Methamphetamine Increases the Expression of Chemokine IL-8 via Nuclear Translocation of NF-κB in Astrocytes

We have demonstrated that the expression of CXCR1 is upregulated in METH-treated SH-SY5Y cells and may be involved in METH-induced apoptosis. IL-8 is a cytokine secreted mostly by macrophages and epithelial cells. Studies have demonstrated that astrocytes can also secrete IL-8, so we applied METH in human-derived U87MG cells and found that the expression of IL-8 was increased in a dose-dependent

manner (**Figures 4A–C**). Specifically, at 2.0 mM, IL-8 protein expression in the U87MG cells was ∼1.77-fold higher than in the control cells. Similar effects were observed in the medium of the cells. The concentration of IL-8 in the medium was ∼1.38-fold higher than in the control (**Figure 4C**). According to our previous study, the expression of transcription factor NF-κB was upregulated in the METH-treated primary cultured C57BL/6 mouse astrocytes. To verify whether the NF-κB pathway is activated in U87MG cells, cells were exposed to 2.0 mM of METH and then western blot analysis was performed to detect the expressions of NF-κB and phosphor-NF-κB. The results showed that NF-κB protein expression was increased slightly and that phosphor-NF-κB protein expression was significantly increased (**Figures 4D,E**) in the METH-treated U87MG cells as compared with in the control. The expression of IκB kinase (IKK)-α did not change significantly, but the expressions of both IKK-β and phosphor-IKK-α/β were increased, respectively (**Figures 4D,E**). IκB was significantly decreased in the METH-treated U87MG cells. Taken together, these results showed that METH exposure induces the activation of the NF-κB pathway in U87MG cells. To confirm whether the release and expression of IL-8 is associated with NF-κB pathway activation in METH-treated U87MG cells, the inhibitor of NF-κB, Bay 11-7082, was administered to U87MG cells and western blot was performed. Results showed that a blockade of NF-κB reduces METH-induced IL-8 expression in U87MG cells (**Figures 4F,G**). We also detected the concentration of IL-8 in culture medium by ELISA; similar effects were observed (**Figure 4H**).

Co-culture of U87MG Cells and SH-SY5Y Cells Reduced the Apoptosis of SH-SY5Y Cells Induced by Methamphetamine

To explore the effects of METH on neurons in a co-culture mode of astrocytes and neurons, we constructed a cell co-culture model using transwell chambers (**Figure 5A**).

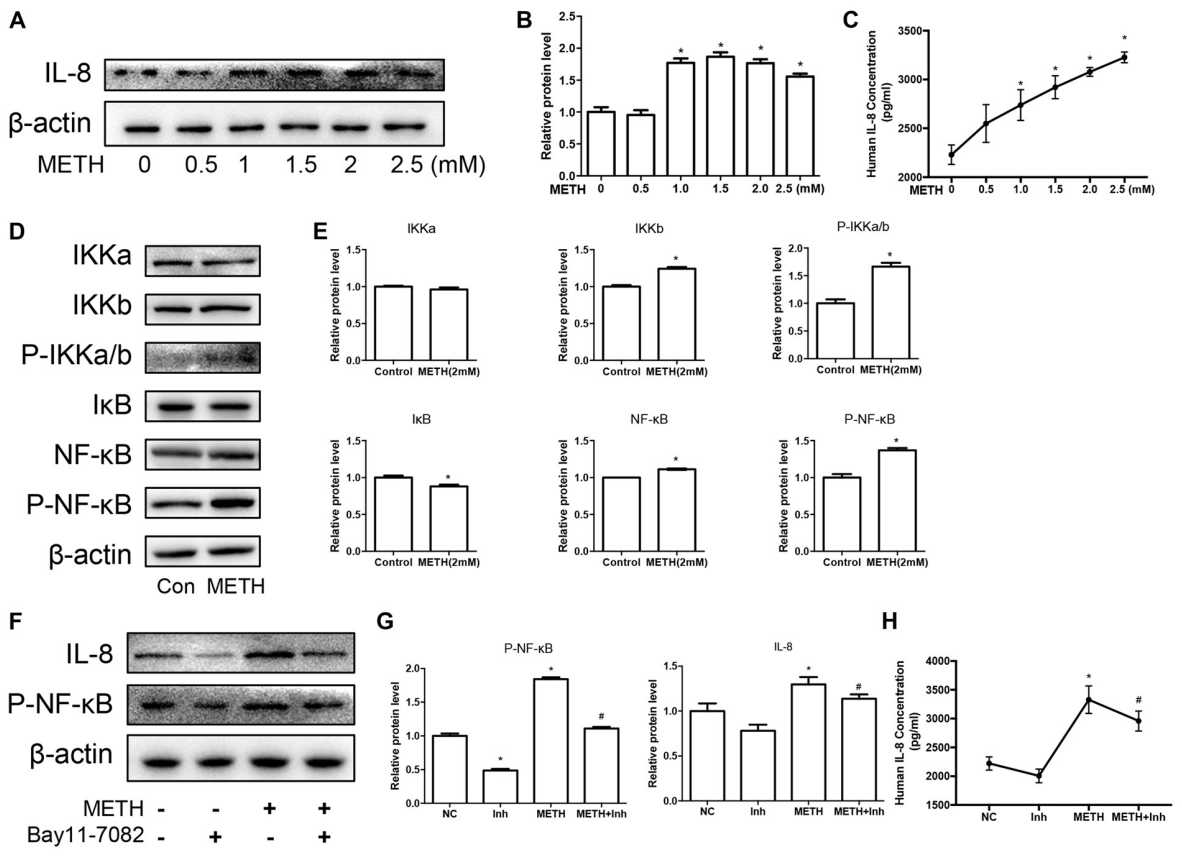

FIGURE 4 | METH increases the expression of chemokine interleukin (IL)-8 via nuclear translocation of NF-κB in astrocytes. U87MG cells were exposed to 0.5 mM, 1 mM, 1.5 mM, 2 mM and 2.5 mM of METH for 24 h **(A)** or 2 mM of METH for 24 h **(D)**. **(F)** U87MG cells were exposed to Bay 11–7082 (10 μM) for 12 h prior to METH (2 mM) treatment as indicated. Western blot **(A,D,F)** and quantitative analyses **(B,E,G)** were performed to determine IL-8, IKK-α, IKK-β, phospho-IKK-α/β, IκB, NF-κB and phospho-NF-κB protein expression. β-actin was used as a loading control. ELISA **(C,H)** was performed to detect the concentration of IL-8 in culture medium supernatant. Fold induction relative to the control group is shown. *Represents a significant difference as compared with the non-METH-treated group, $^{*}p < 0.05$. #Represents a significant difference as compared with the scrambled + METH treated group, $^{\#}p < 0.05$. Results are expressed as the mean ± SD of three experiments. Data in **(A,C,F,G)** were analyzed with one-way ANOVA followed by LSD *post hoc* analyses; data in **(D)** were analyzed with Student's *t*-test.

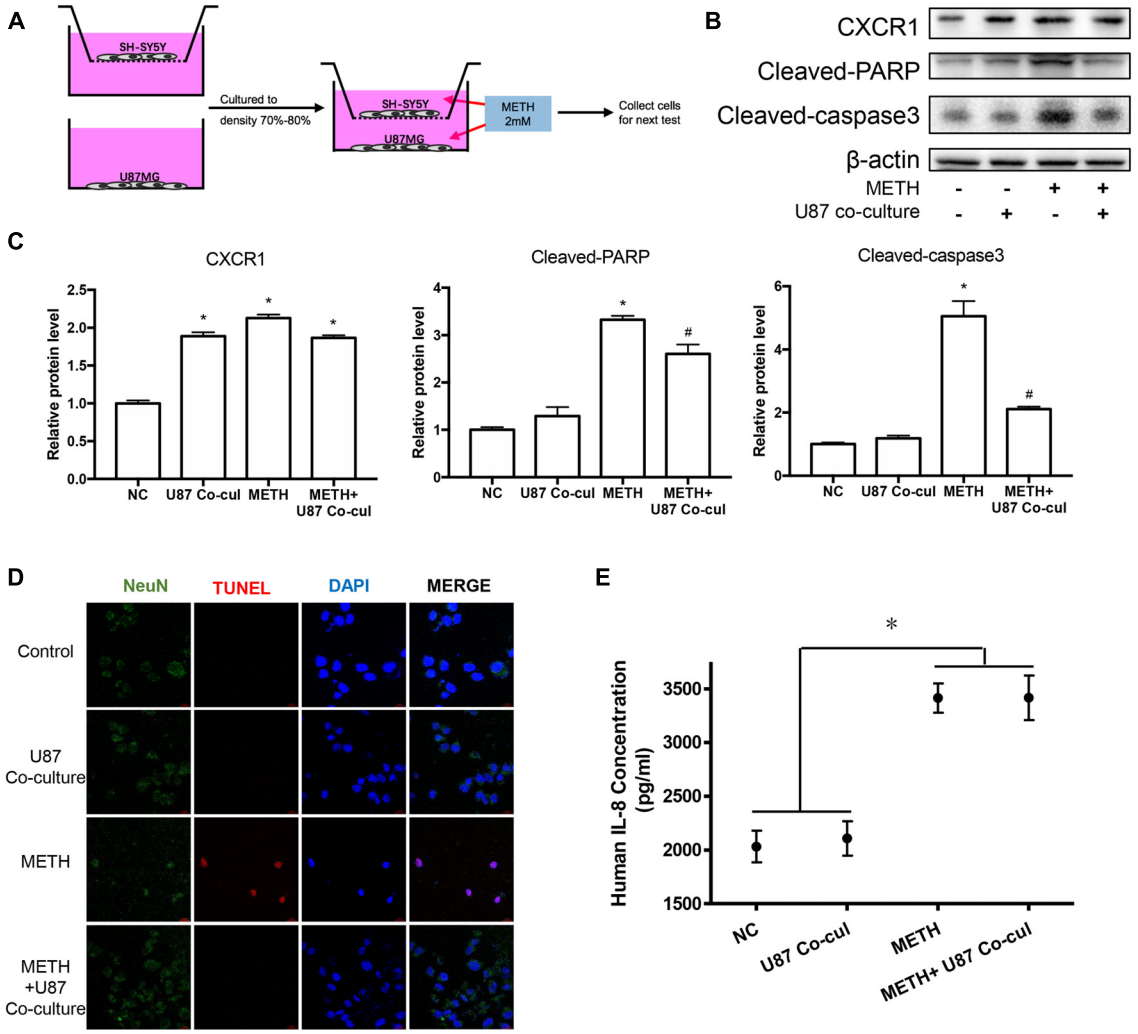

FIGURE 5 | Co-culture of U87MG cells and SH-SY5Y cells reduced the apoptosis of SH-SY5Y cells induced by METH. **(A)** Co-culture pattern diagram. U87MG cells and SH-SY5Y cells were cultured to a density of 90% and passaged into Transwell dishes. SH-SY5Y cells were plated in the upper chamber of the Transwell plate and U87MG cells were spread on the bottom of the Transwell plate and cultured to a density of 70% to 80% respectively. The upper chamber was then placed above the lower chamber and exposed to 2.0 mM of METH for 24 h. Western blot **(B)** and quantitative analyses **(C)** were performed to determine CXCR1, cleaved caspase-3 and cleaved PARP protein expression. β-actin was used as a loading control. Fold induction relative to the control group is shown. *Represents a significant difference as compared with the negative control group, $^{*}p < 0.05$. #Represents a significant difference as compared with the scrambled + METH treated group, $^{\#}p < 0.05$. Results are expressed as the mean ± SD of three experiments. Data were analyzed with one-way ANOVA followed by LSD *post hoc* analyses. terminal deoxynucleotidyl transferase dUTP nick end-labeling (TUNEL) staining and confocal imaging analysis **(D)** was performed to evaluate the SH-SY5Y cells apoptosis. Scale bar, 15 μM. ELISA **(E)** was performed to detect the concentration of IL-8 in culture medium supernatant.

Western blot analysis was performed to detect the expression of neuronal apoptosis-related protein cleaved caspase-3 and cleaved PARP. Our results revealed that cleaved caspase-3 and cleaved PARP expression was significantly attenuated in the co-cultured cells after METH exposure (**Figures 5B,C**). Apoptosis cells were also observed with TUNEL staining (**Figure 5D**). However, the expression of CXCR1 showed no significant difference between in the untreated co-culture group and in the METH-treated co-culture group, which indicated that CXCR1 protein expression is induced by another way in the co-culture model of U87MG cells and SH-SY5Y cells. We also detected the concentration of IL-8 in culture medium by ELISA (**Figure 5E**). Results showed that IL-8 expressions were increased in METH-exposed group, whether co-culture with SH-SY5Y or not.

Silencing of CXCR1 Expression With siRNA Reduced Methamphetamine-Induced Caspase-3 and PARP Activation in Co-cultured Cell Models

To assess the apoptosis levels of co-culture cell models treated by METH with or without CXCR1 siRNA transfection, western blot analysis was conducted. The results are shown

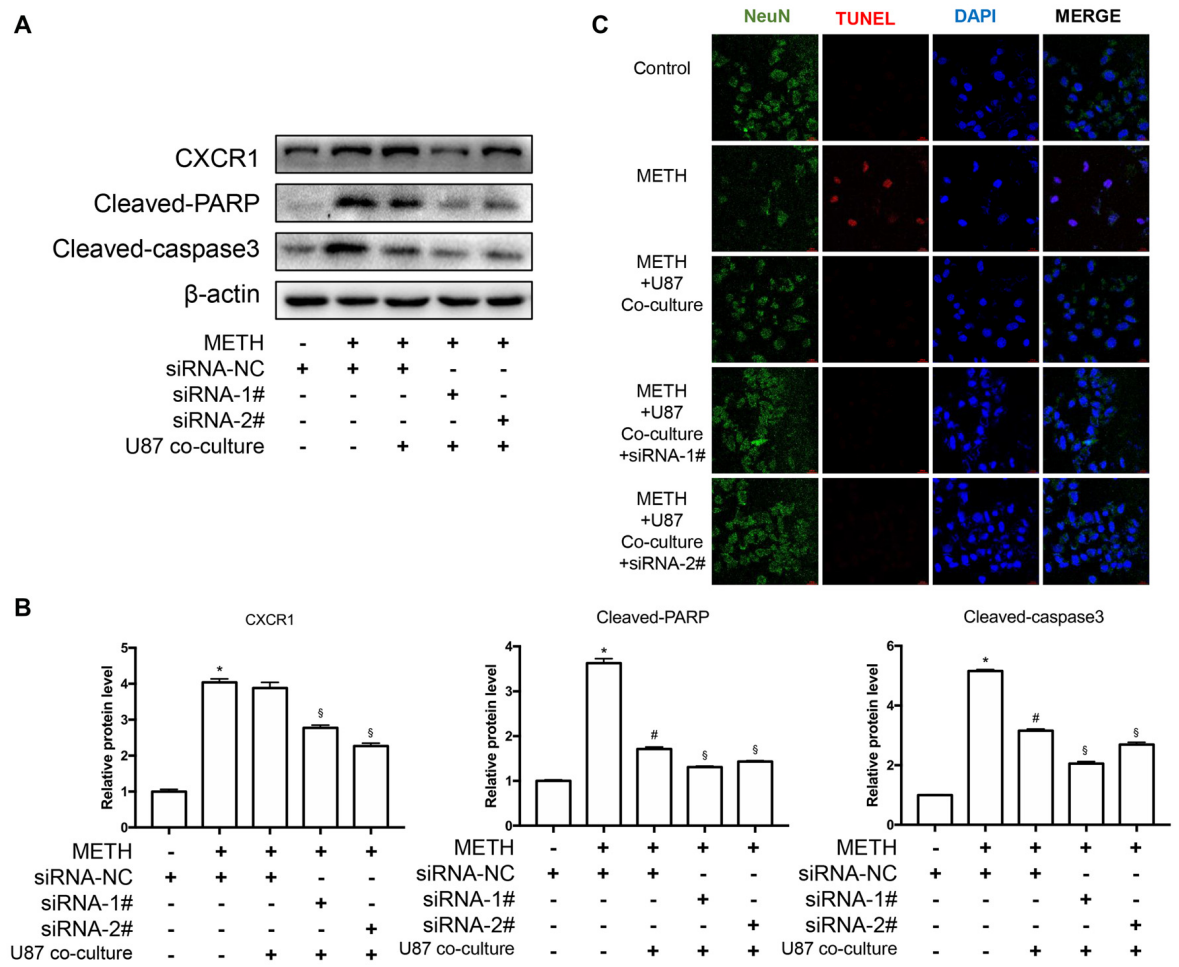

FIGURE 6 | Silencing of CXCR1 expression with siRNA-reduced METH-induced caspase-3 and PARP activation in co-cultured cell models. **(A)** U87MG cells and SH-SY5Y cells were co-cultured in the same manner as before. Before METH treatment, SH-SY5Y cells were transfected with siRNA targeting CXCR1 or control siRNA for 24 h followed by co-cultured with U87MG cells. Simultaneously, 2 mM of METH was added in the medium for 24 h. Western blot **(A)** and quantitative analyses **(B)** were performed to determine CXCR1, cleaved caspase-3 and cleaved PARP protein expression. β-actin was used as a loading control. Fold induction relative to the control group is shown. *Represents a significant difference as compared with the negative control group, $^{*}p < 0.05$. $^{\#}$Represents a significant difference as compared with siRNA NC + METH treated group, $^{\#}p < 0.05$. §Represents a significant difference as compared with siRNA NC + METH treated +U87MG cells co-culture group, $^{\S}p < 0.05$. Results are expressed as the mean ± SD of three experiments. Data were analyzed with one-way ANOVA followed by LSD *post hoc* analyses. TUNEL staining and confocal imaging analysis **(C)** was performed to evaluate the SH-SY5Y cells apoptosis. Scale bar, 15 μM.

in **Figures 6A,B**. The expression of CXCR1 in SH-SY5Y cells was increased in the METH-treated group with or without U87MG cells in the co-culture as compared with in the control group, while both of the siRNA sequences could effectively knockdown the expression of CXCR1. In addition, after the treatment of siRNA of CXCR1, cleaved caspase-3 and cleaved PARP protein expression were significantly decreased in comparison with in the negative control siRNA transfection group. To confirm that silence of CXCR1 protects against METH induced SH-SY5Y cells apoptosis, TUNEL staining was performed (**Figure 6C**). Results suggest that blockade of CXCR1 expression reduces METH-induced apoptosis in SH-SY5Y cells.

Interleukin-8 Increases PARP and Caspase-3 Protein Expression Induced by Methamphetamine *in Vitro*

To verify the effects of IL-8 on neurons in co-culture models treated by METH, exogenous recombinant IL-8 was added to SH-SY5Y cells. We chose two concentrations (10 and 100 ng/ml) to detect the effect of IL-8 on neurons, which were obtained from previous studies (Moriceau et al., 2009; Dwyer et al., 2012; De Buck et al., 2015). In our experiments, these two concentrations of IL-8 had no apparent toxic effects on neurons alone. Then, we checked the expression levels of CXCR1, cleaved caspase-3, and cleaved PARP by use of western blot analysis. Results are shown in **Figures 7A,B**. The expression of CXCR1, cleaved

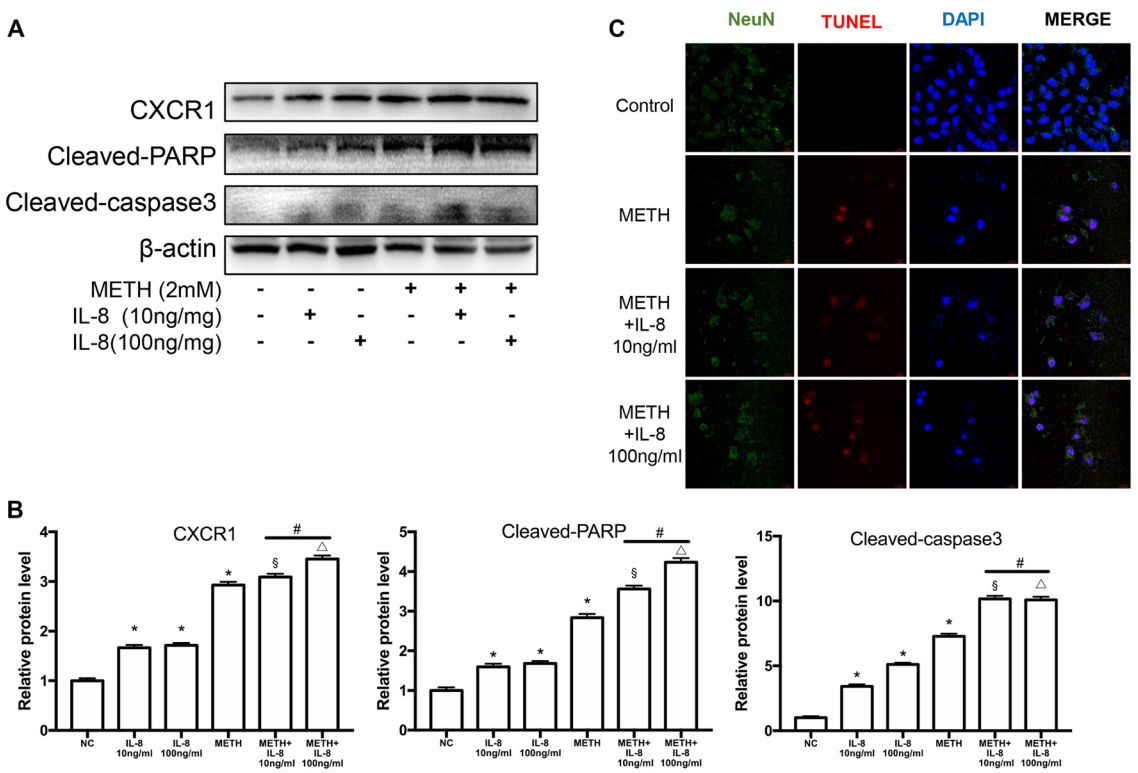

FIGURE 7 | IL-8 increases PARP and caspase-3 protein expression induced by METH *in vitro*. SH-SY5Y cells were treated with 10 ng/ml or 100 ng/ml recombinant human IL-8 for 24 h, given 2 mM of METH simultaneously. Western blot **(A)** and quantitative analyses **(B)** were performed to determine CXCR1, cleaved caspase-3 and cleaved PARP protein expression. β-actin was used as a loading control. Fold induction relative to the control group is shown. *Represents a significant difference as compared with the negative control group, $^{*}p < 0.05$. $^{\#}$Represents significant difference from METH treated group without IL-8 treatment, $^{\#}p < 0.05$. §Represents a significant difference as compared with IL-8 (10 ng/mg) treated group, $^{\S}p < 0.05$. $^{\triangle}$Represents a significant difference as compared with IL-8 (100 ng/mg) treated group, $^{\triangle}p < 0.05$. Results are expressed as the mean ± SD of three experiments. Data were analyzed with one-way ANOVA followed by LSD *post hoc* analyses. TUNEL staining and confocal imaging analysis **(C)** was performed to evaluate the SH-SY5Y cells apoptosis. Scale bar, 15 μM.

caspase-3 and cleaved PARP were increased following recombinant IL-8 treatment. Interestingly, METH and two concentrations of recombinant IL-8 exposure together increased the expression of CXCR1, and the expression of cleaved caspase-3 and cleaved PARP was much more increased. We also investigated whether the recombinant IL-8 affects METH-induced neuronal apoptosis using TUNEL staining (**Figure 7C**). These results further demonstrate that IL-8-CXCR1 is involved in METH-induced neuronal apoptosis.

DISCUSSION

In recent years, scholars have studied the direct effects of METH from the classical dopaminergic-related neurotoxicity to more aspects. Researches showed that METH also has direct toxic effects on other cells. The results of our institute and other investigators showed that METH mediates apoptosis of the brain's vascular endothelium through endoplasmic reticulum stress (Cai et al., 2016), mediates the opening of the blood-brain barrier (Xie et al., 2018), activation of astrocytes (Du et al., 2017), and even has some toxic effects to liver and cardiovascular system (Chen R. et al., 2016; Xie et al., 2018). Studies have shown that non-dopaminergic neuron systems play an important role in the development of Parkinson's disease (Guyenet and Crane, 1981; Bonnet, 2000; van der Heeden et al., 2014). METH exposure leads to the loss of neurons in the cerebral cortex and selectively damage pyramidal neurons in the CA3 region of the hippocampus and granule cells with dendritic cells activated by microglia (Kuczenski et al., 2007). In summary, these studies provide more potential targets for METH.

In the present study, we have demonstrated that CXCR1 expression is increased after METH exposure *in vivo* and *in vitro*. We also report that silence of CXCR1 expression using siRNA sequences can protect neuronal apoptosis caused by METH *in vitro* and promote the protective effect of astrocytes. We hypothesized that injury and protection coexist in the effect of astrocytes on METH-induced neuronal apoptosis. IL-8—CXCR1 may play an important role in this dynamic balance.

CXCR1 is a member of the G protein-coupled receptor family that is also a receptor for IL-8. CXCR1 binds IL-8 with high affinity and transduces the signal via the secondary

messenger system activated by the G protein (Park et al., 2012; Risnik et al., 2017). Studies have shown that stimulating the neutrophil surface of CXCR1 can lead to neutrophil chemotaxis and activation (Ocana et al., 2017; Tavares et al., 2017), and inhibition of CXCR1 and CXCR2 can reduce the migration of neutrophils to tumor regions (Tavares et al., 2017). Furthermore, oncology research has suggested that blocking CXCR1 can inhibit the differentiation of breast cancer stem cells (Jia et al., 2017), and that CXCR1 is overexpressed in the development of malignant melanoma and involved in cell growth and angiogenesis (Uen et al., 2015; Jacquelot et al., 2016). In the meantime, other study has demonstrated that CX3CR1 can mediate neuronal apoptosis in a cerebral ischemic model, thus potentially playing a role in the pathophysiology of stroke (Wang et al., 2018).

In the current study, we found that the METH exposure increased the expression of CXCR1 *in vivo* and *in vitro*. Immunofluorescence co-localization experiments showed that CXCR1 was mainly expressed on neurons in the midbrain of METH-exposed mice. Besides, the induction of CXCR1 expression by METH occurred in a dose-dependent manner. Inhibition of CXCR1 expression by siRNA sequences also attenuated METH-induced neuronal apoptosis. To verify the role of CXCR1 in METH-induced neuronal apoptosis, we examined two important molecules involved in mitochondrial apoptosis, Bax and Bcl-2. Bax, a water-soluble protein homologous to Bcl-2, is an apoptosis-promoting gene in the Bcl-2 gene family. Bax overexpression can antagonize the protective effect of Bcl-2 and cause cell death (Kuwana et al., 2005; Chen C. et al., 2016). In our previous study, we found that METH exposure can result in the overexpression of Bax and the silencing of Bcl-2 through PUMA, which leads to the mitochondrial apoptotic pathway by releasing cytochrome (Chen C. et al., 2016). The present results showed that, after CXCR1 was inhibited, the expression of Bax was downregulated and the expression of Bcl-2 was upregulated. Meanwhile, the expression of cleaved caspase-3 and cleaved PARP were downregulated, indicating that CXCR1 can mediate METH-induced neuronal apoptosis through the mitochondrial apoptosis pathway.

IL-8 is also known as neutrophil chemokine. It induces target cell chemotaxis, primarily in neutrophils and other granulocytes, causing them to migrate toward the site of infection. IL-8 also induces phagocytosis and is considered to be a potent promoter of angiogenesis (Han et al., 2018; Paulitti et al., 2018). IL-8 can be secreted by any cell that has a Toll-like receptor that is associated with an innate immune response. In our previous study, it was found that Toll-like receptor four mediates METH-induced activation of astrocytes through the NF-κB and caspase-11 signaling pathways (Du et al., 2017). Thus, we detected the expression of IL-8 in U87MG cells and in the culture medium. Results showed that METH application caused the production and secretion of IL-8 in U87MG cells. Furthermore, we also demonstrated that METH exposure induced activation of the NF-κB pathway in U87MG cells, which regulated the expression of IL-8. These findings are consistent with previous studies that suggested that the NF-κB pathway was activated in primary cultured astrocytes exposed to 2.0 mM of METH.

Previous studies have focused on the role of METH in the context of one type of cell, through PUMA, IGFBP5 and other ways to induce neuronal apoptosis (Qiao et al., 2014; Chen C. et al., 2016); METH through NF-κB, caspase-11 and other ways to the induce activation of astrocytes was also evaluated (Du et al., 2017). However, under the stimulation of METH, one question that has not been answered is regarding what happens to neurons when astrocytes and neurons are co-cultured. Studies have found that glial cells involved in the dopaminergic neurons damage (Krencik et al., 2017; Ugbode et al., 2017; Facci et al., 2018). Astrocytes may affect neuronal conditions through diverse molecules such as a-syn or glutamate, with the effect possibly being either protection or damage (Gustafsson et al., 2017; Lee et al., 2017; Madji Hounoum et al., 2017; Yu et al., 2018). In the present study, we used a noncontact, sandwich-type neuron-astrocyte co-culture to study the effects of astrocytes on neurons under the action of METH. Results showed that the neuronal apoptosis was significant reduced in the co-culture group with 2.0 mM of METH for 24 h. This effect is similar to the research of PD, astrocytes rapidly engulf α-syn oligomers resulting in impaired mitochondria, thereby protecting neurons (Gustafsson et al., 2017). According to current research and previous studies (Du et al., 2017), METH treatment of astrocytes alone can cause activation of the TLR4—NF-kB pathway and increased expression of IL 1, 8 and 18. But according to the results of co-culture, astrocytes in the co-culture system protected the damaged neurons. Therefore, we speculate that astrocytes present different states under different processing conditions, and their neuroprotective and injury effects are dynamically balanced. In the present study, the overall performance of astrocytes is the protection state. However, the specific mechanism needs further research.

Other novel findings are that knockdown CXCR1 expression can reduce neuronal apoptosis in an increased fashion. To test whether IL-8 plays a role in this process, we administered exogenous recombinant IL-8 to SH-SY5Y cells in combination with METH. As a result, IL-8 was found to enhance METH-induced apoptosis and to significantly up-regulate CXCR1 expression. These data demonstrated that CXCR1 plays an important role in METH-induced neuronal apoptosis and that the IL-8 secreted by astrocytes is involved in activating CXCR1. The role of astrocytes in neuronal repair may be a double-sided and dynamically balanced process, with damage and protection existing simultaneously. Further studies are needed to illustrate the role of astrocytes.

CONCLUSION

In summary, this study demonstrated that CXCR1 plays an important role in neuronal apoptosis induced by METH. The blockade of CXCR1 expression significantly attenuated METH-induced neuronal apoptosis and enhanced the protective effect of astrocytes on neurons. Moreover, we provide evidence

that IL-8 plays a role in neuronal injury. The underlying mechanisms about how astrocytes play a neuroprotective role in the fact of METH exposure and whether other effects could occur requires further research.

DATA AVAILABILITY

The authors declare that the data supporting the findings of this study are available within the article.

AUTHOR CONTRIBUTIONS

S-HD and WZ conducted all the experiments with the help of X-QL and X-HT. D-FQ and HW designed the research. S-HD, CL and XY analyzed and interpreted the results. D-FQ and S-HD wrote the manuscript.

FUNDING

This study was supported by the National Natural Science Foundation of China (Grant No. 81430045 to HW and Grant No.81172907 to D-FQ).

ACKNOWLEDGMENTS

We thank LetPub for its linguistic assistance during the preparation of this manuscript.

REFERENCES

Ashutosh, Kou, W., Cotter, R., Borgmann, K., Wu, L., Persidsky, R., et al. (2011). CXCL8 protects human neurons from amyloid-β-induced neurotoxicity: relevance to Alzheimer's disease. *Biochem. Biophys. Res. Commun.* 412, 565–571. doi: 10.1016/j.bbrc.2011.07.127

Bonnet, A.-M. (2000). Involvement of non-dopaminergic pathways in Parkinson's disease: pathophysiology and therapeutic implications. *CNS Drugs* 13, 351–364. doi: 10.2165/00023210-200013050-00005

Brat, D. J., Bellail, A. C., and Van Meir, E. G. (2005). The role of interleukin-8 and its receptors in gliomagenesis and tumoral angiogenesis. *Neuro Oncol.* 7, 122–133. doi: 10.1215/s1152851704001061

Cadet, J. L., Jayanthi, S., and Deng, X. (2003). Speed kills: cellular and molecular bases of methamphetamine-induced nerve terminal degeneration and neuronal apoptosis. *FASEB J.* 17, 1775–1788. doi: 10.1096/fj.03-0073rev

Cai, D., Huang, E., Luo, B., Yang, Y., Zhang, F., Liu, C., et al. (2016). Nupr1/Chop signal axis is involved in mitochondrion-related endothelial cell apoptosis induced by methamphetamine. *Cell Death Dis.* 7:e2161. doi: 10.1038/cddis.2016.67

Cao, L., Fu, M., Kumar, S., and Kumar, A. (2016). Methamphetamine potentiates HIV-1 gp120-mediated autophagy via Beclin-1 and Atg5/7 as a pro-survival response in astrocytes. *Cell Death Dis.* 7:e2425. doi: 10.1038/cddis.2016.317

Carmena, A., Granado, N., Ares-Santos, S., Alberquilla, S., Tizabi, Y., and Moratalla, R. (2015). Methamphetamine-induced toxicity in indusium griseum of mice is associated with astro- and microgliosis. *Neurotox. Res.* 27, 209–216. doi: 10.1007/s12640-014-9505-9

Chen, C., Qincao, L., Xu, J., Du, S., Huang, E., Liu, C., et al. (2016). Role of PUMA in methamphetamine-induced neuronal apoptosis. *Toxicol. Lett.* 240, 149–160. doi: 10.1016/j.toxlet.2015.10.020

Chen, R., Wang, B., Chen, L., Cai, D., Li, B., Chen, C., et al. (2016). DNA damage-inducible transcript 4 (DDIT4) mediates methamphetamine-induced autophagy and apoptosis through mTOR signaling pathway in cardiomyocytes. *Toxicol. Appl. Pharmacol.* 295, 1–11. doi: 10.1016/j.taap.2016.01.017

Cisneros, I. E., and Ghorpade, A. (2014). Methamphetamine and HIV-1-induced neurotoxicity: role of trace amine associated receptor 1 cAMP signaling in astrocytes. *Neuropharmacology* 85, 499–507. doi: 10.1016/j.neuropharm.2014.06.011

Citro, A., Cantarelli, E., and Piemonti, L. (2015). The CXCR1/2 pathway: involvement in diabetes pathophysiology and potential target for T1D interventions. *Curr. Diab. Rep.* 15:68. doi: 10.1007/s11892-015-0638-x

Clunes, M. T., and Boucher, R. C. (2007). Cystic fibrosis: the mechanisms of pathogenesis of an inherited lung disorder. *Drug Discov. Today Dis. Mech.* 4, 63–72. doi: 10.1016/j.ddmec.2007.09.001

De Buck, M., Berghmans, N., Pörtner, N., Vanbrabant, L., Cockx, M., Struyf, S., et al. (2015). Serum amyloid A1α induces paracrine IL-8/CXCL8 via TLR2 and directly synergizes with this chemokine via CXCR2 and formyl peptide receptor 2 to recruit neutrophils. *J. Leukoc. Biol.* 98, 1049–1060. doi: 10.1189/jlb.3A0315-085R

Dinis-Oliveira, R. J., Carvalho, F., Moreira, R., Duarte, J. A., Proenca, J. B., Santos, A., et al. (2012). Clinical and forensic signs related to opioids abuse. *Curr. Drug Abuse Rev.* 5, 273–290. doi: 10.2174/1874737111205040003

Dorf, M. E., Berman, M. A., Tanabe, S., Heesen, M., and Luo, Y. (2000). Astrocytes express functional chemokine receptors. *J. Neuroimmunol.* 111, 109–121. doi: 10.1016/s0165-5728(00)00371-4

Du, S., Qiao, D., Chen, C., Chen, S., Liu, C., Lin, Z., et al. (2017). Toll-like receptor 4 mediates methamphetamine-induced neuroinflammation through caspase-11 signaling pathway in astrocytes. *Front. Mol. Neurosci.* 10:409. doi: 10.3389/fnmol.2017.00409

Dwyer, J., Hebda, J. K., Le Guelte, A., Galan-Moya, E. M., Smith, S. S., Azzi, S., et al. (2012). Glioblastoma cell-secreted interleukin-8 induces brain endothelial cell permeability via CXCR2. *PLoS One* 7:e45562. doi: 10.1371/journal.pone.0045562

Eltzschig, H. K., and Eckle, T. (2011). Ischemia and reperfusion—from mechanism to translation. *Nat. Med.* 17, 1391–1401. doi: 10.1038/nm.2507

Facci, L., Barbierato, M., and Skaper, S. D. (2018). Astrocyte/microglia cocultures as a model to study neuroinflammation. *Methods Mol. Biol.* 1727, 127–137. doi: 10.1007/978-1-4939-7571-6_10

Flynn, G., Maru, S., Loughlin, J., Romero, I. A., and Male, D. (2003). Regulation of chemokine receptor expression in human microglia and astrocytes. *J. Neuroimmunol.* 136, 84–93. doi: 10.1016/s0165-5728(03)00009-2

Gustafsson, G., Lindstrom, V., Rostami, J., Nordstrom, E., Lannfelt, L., Bergstrom, J., et al. (2017). α-synuclein oligomer-selective antibodies reduce intracellular accumulation and mitochondrial impairment in α-synuclein exposed astrocytes. *J. Neuroinflammation* 14:241. doi: 10.1186/s12974-017-1018-z

Guyenet, P. G., and Crane, J. K. (1981). Non-dopaminergic nigrostriatal pathway. *Brain Res.* 213, 291–305. doi: 10.1016/0006-8993(81)90235-3

Han, J., Li, Y., Liu, X., Zhou, T., Sun, H., Edwards, P., et al. (2018). Metformin suppresses retinal angiogenesis and inflammation *in vitro* and *in vivo*. *PLoS One* 13:e0193031. doi: 10.1371/journal.pone.0193031

Hoffmann, E., Dittrich-Breiholz, O., Holtmann, H., and Kracht, M. (2002). Multiple control of interleukin-8 gene expression. *J. Leukoc. Biol.* 72, 847–855. doi: 10.1189/jlb.72.5.847

Huang, W., Xie, W. B., Qiao, D., Qiu, P., Huang, E., Li, B., et al. (2015). Caspase-11 plays an essential role in methamphetamine-induced dopaminergic neuron apoptosis. *Toxicol. Sci.* 145, 68–79. doi: 10.1093/toxsci/kfv014

Jacquelot, N., Enot, D. P., Flament, C., Vimond, N., Blattner, C., Pitt, J. M., et al. (2016). Chemokine receptor patterns in lymphocytes mirror metastatic spreading in melanoma. *J. Clin. Invest.* 126, 921–937. doi: 10.1172/jci80071

Jia, D., Li, L., Andrew, S., Allan, D., Li, X., Lee, J., et al. (2017). An autocrine inflammatory forward-feedback loop after chemotherapy withdrawal facilitates the repopulation of drug-resistant breast cancer cells. *Cell Death Dis.* 8:e2932. doi: 10.1038/cddis.2017.319

Kim, J. M., Kim, N. I., Oh, Y. K., Kim, Y. J., Youn, J., and Ahn, M. J. (2005). CpG oligodeoxynucleotides induce IL-8 expression in CD34+ cells

via mitogen-activated protein kinase-dependent and NF-κB-independent pathways. *Int. Immunol.* 17, 1525–1531. doi: 10.1093/intimm/dxh345

Kita, T., Miyazaki, I., Asanuma, M., Takeshima, M., and Wagner, G. C. (2009). Dopamine-induced behavioral changes and oxidative stress in methamphetamine-induced neurotoxicity. *Int. Rev. Neurobiol.* 88, 43–64. doi: 10.1016/s0074-7742(09)88003-3

Krasnova, I. N., and Cadet, J. L. (2009). Methamphetamine toxicity and messengers of death. *Brain Res. Rev.* 60, 379–407. doi: 10.1016/j.brainresrev.2009.03.002

Krencik, R., Seo, K., van Asperen, J. V., Basu, N., Cvetkovic, C., Barlas, S., et al. (2017). Systematic three-dimensional coculture rapidly recapitulates interactions between human neurons and astrocytes. *Stem Cell Reports* 9, 1745–1753. doi: 10.1016/j.stemcr.2017.10.026

Kuczenski, R., Everall, I., Crews, L., Adame, A., Grant, I., and Masliah, E. (2007). Escalating dose-multiple binge methamphetamine exposure results in degeneration of the neocortex and limbic system in the rat. *Exp. Neurol.* 207, 42–51. doi: 10.1016/j.expneurol.2007.05.023

Kuwana, T., Bouchier-Hayes, L., Chipuk, J. E., Bonzon, C., Sullivan, B. A., Green, D. R., et al. (2005). BH3 domains of BH3-only proteins differentially regulate Bax-mediated mitochondrial membrane permeabilization both directly and indirectly. *Mol. Cell* 17, 525–535. doi: 10.1016/j.molcel.2005.02.003

Lee, J., Horuk, R., Rice, G. C., Bennett, G. L., Camerato, T., and Wood, W. I. (1992). Characterization of two high affinity human interleukin-8 receptors. *J. Biol. Chem.* 267, 16283–16287.

Lee, M. L., Martinez Lozada, Z., Krizman, E. N., and Robinson, M. B. (2017). Brain endothelial cells induce astrocytic expression of the glutamate transporter GLT-1 by a Notch-dependent mechanism. *J. Neurochem.* 143, 489–506. doi: 10.1111/jnc.14135

Loetscher, P., Seitz, M., Clark-Lewis, I., Baggiolini, M., and Moser, B. (1994). Both interleukin-8 receptors independently mediate chemotaxis. Jurkat cells transfected with IL-8R1 or IL-8R2 migrate in response to IL-8, GRO α and NAP-2. *FEBS Lett.* 341, 187–192. doi: 10.1016/0014-5793(94)80454-0

Madji Hounoum, B., Mavel, S., Coque, E., Patin, F., Vourc'H, P., Marouillat, S., et al. (2017). Wildtype motoneurons, ALS-Linked SOD1 mutation and glutamate profoundly modify astrocyte metabolism and lactate shuttling. *Glia* 65, 592–605. doi: 10.1002/glia.23114

Mendieta, L., Granado, N., Aguilera, J., Tizabi, Y., and Moratalla, R. (2016). Fragment C domain of tetanus toxin mitigates methamphetamine neurotoxicity and its motor consequences in mice. *Int. J. Neuropsychopharmacol.* 19:pyw021. doi: 10.1093/ijnp/pyw021

Moriceau, S., Kantari, C., Mocek, J., Davezac, N., Gabillet, J., Guerrera, I. C., et al. (2009). Coronin-1 is associated with neutrophil survival and is cleaved during apoptosis: potential implication in neutrophils from cystic fibrosis patients. *J. Immunol.* 182, 7254–7263. doi: 10.4049/jimmunol.0803312

Ocana, A., Nieto-Jiménez, C., Pandiella, A., and Templeton, A. J. (2017). Neutrophils in cancer: prognostic role and therapeutic strategies. *Mol. Cancer* 16:137. doi: 10.1186/s12943-017-0707-7

Park, S. H., Das, B. B., Casagrande, F., Tian, Y., Nothnagel, H. J., Chu, M., et al. (2012). Structure of the chemokine receptor CXCR1 in phospholipid bilayers. *Nature* 491, 779–783. doi: 10.1038/nature11580

Paulitti, A., Andreuzzi, E., Bizzotto, D., Pellicani, R., Tarticchio, G., Marastoni, S., et al. (2018). The ablation of the matricellular protein EMILIN2 causes defective vascularization due to impaired EGFR-dependent IL-8 production affecting tumor growth. *Oncogene* 37, 3399–3414. doi: 10.1038/s41388-017-0107-x

Pierce, J. W., Schoenleber, R., Jesmok, G., Best, J., Moore, S. A., Collins, T., et al. (1997). Novel inhibitors of cytokine-induced IκBα phosphorylation and endothelial cell adhesion molecule expression show anti-inflammatory effects *in vivo*. *J. Biol. Chem.* 272, 21096–21103. doi: 10.1074/jbc.272.34.21096

Qiao, D., Xu, J., Le, C., Huang, E., Liu, C., Qiu, P., et al. (2014). Insulin-like growth factor binding protein 5 (IGFBP5) mediates methamphetamine-induced dopaminergic neuron apoptosis. *Toxicol. Lett.* 230, 444–453. doi: 10.1016/j.toxlet.2014.08.010

Risnik, D., Podaza, E., Almejún, M. B., Colado, A., Elías, E. E., Bezares, R. F., et al. (2017). Revisiting the role of interleukin-8 in chronic lymphocytic leukemia. *Sci. Rep.* 7:15714. doi: 10.1038/s41598-017-15953-x

Sordillo, P. P., and Helson, L. (2015). Curcumin and cancer stem cells: curcumin has asymmetrical effects on cancer and normal stem cells. *Anticancer Res.* 35, 599–614.

Takahashi, M., Ishiko, T., Kamohara, H., Hidaka, H., Ikeda, O., Ogawa, M., et al. (2007). Curcumin (1,7-bis(4-hydroxy-3-methoxyphenyl)-1,6-heptadiene-3,5-dione) blocks the chemotaxis of neutrophils by inhibiting signal transduction through IL-8 receptors. *Mediators Inflamm.* 2007:10767. doi: 10.1155/2007/10767

Tavares, L. P., Garcia, C. C., Machado, M. G., Queiroz-Junior, C. M., Barthelemy, A., Trottein, F., et al. (2017). CXCR1/2 antagonism is protective during influenza and post-influenza pneumococcal infection. *Front. Immunol.* 8:1799. doi: 10.3389/fimmu.2017.01799

Uen, W. C., Hsieh, C. H., Tseng, T. T., Jiang, S. S., Tseng, J. C., and Lee, S. C. (2015). Anchorage independency promoted tumor malignancy of melanoma cells under reattachment through elevated interleukin-8 and CXC chemokine receptor 1 expression. *Melanoma Res.* 25, 35–46. doi: 10.1097/cmr.0000000000000134

Ugbode, C. I., Smith, I., Whalley, B. J., Hirst, W. D., and Rattray, M. (2017). Sonic hedgehog signalling mediates astrocyte crosstalk with neurons to confer neuroprotection. *J. Neurochem.* 142, 429–443. doi: 10.1111/jnc.14064

van der Heeden, J. F., Marinus, J., Martinez-Martin, P., and van Hilten, J. J. (2014). Importance of nondopaminergic features in evaluating disease severity of Parkinson disease. *Neurology* 82, 412–418. doi: 10.1212/wnl.0000000000000087

Vlahopoulos, S., Boldogh, I., Casola, A., and Brasier, A. R. (1999). Nuclear factor-κB-dependent induction of interleukin-8 gene expression by tumor necrosis factor α: evidence for an antioxidant sensitive activating pathway distinct from nuclear translocation. *Blood* 94, 1878–1889.

Wang, J., Gan, Y., Han, P., Yin, J., Liu, Q., Ghanian, S., et al. (2018). Ischemia-induced neuronal cell death is mediated by chemokine receptor CX3CR1. *Sci. Rep.* 8:556. doi: 10.1038/s41598-017-18774-0

Waugh, D. J. J., and Wilson, C. (2008). The interleukin-8 pathway in cancer. *Clin. Cancer Res.* 14, 6735–6741. doi: 10.1158/1078-0432.ccr-07-4843

Xie, X. L., He, J. T., Wang, Z. T., Xiao, H. Q., Zhou, W. T., Du, S. H., et al. (2018). Lactulose attenuates METH-induced neurotoxicity by alleviating the impaired autophagy, stabilizing the perturbed antioxidant system and suppressing apoptosis in rat striatum. *Toxicol. Lett.* 289, 107–113. doi: 10.1016/j.toxlet.2018.03.015

Yu, W. W., Cao, S. N., Zang, C. X., Wang, L., Yang, H. Y., Bao, X. Q., et al. (2018). Heat shock protein 70 suppresses neuroinflammation induced by α-synuclein in astrocytes. *Mol. Cell. Neurosci.* 86, 58–64. doi: 10.1016/j.mcn.2017.11.013

Zanotto-Filho, A., Braganhol, E., Schröder, R., de Souza, L. H., Dalmolin, R. J., Pasquali, M. A., et al. (2011). NFκB inhibitors induce cell death in glioblastomas. *Biochem. Pharmacol.* 81, 412–424. doi: 10.1016/j.bcp.2010.10.014

Zhang, F., Chen, L., Liu, C., Qiu, P., Wang, A., Li, L., et al. (2013). Up-regulation of protein tyrosine nitration in methamphetamine-induced neurotoxicity through DDAH/ADMA/NOS pathway. *Neurochem. Int.* 62, 1055–1064. doi: 10.1016/j.neuint.2013.03.016

Zhang, Y., Lv, X., Bai, Y., Zhu, X., Wu, X., Chao, J., et al. (2015). Involvement of sigma-1 receptor in astrocyte activation induced by methamphetamine via up-regulation of its own expression. *J. Neuroinflammation* 12:29. doi: 10.1186/s12974-015-0250-7

Conflict of Interest Statement: The authors declare that the research was conducted in the absence of any commercial or financial relationships that could be construed as a potential conflict of interest.

frontiers in Neuroscience

ORIGINAL RESEARCH
published: 15 August 2018
doi: 10.3389/fnins.2018.00567

A Novel Tetramethylpyrazine Derivative Protects Against Glutamate-Induced Cytotoxicity Through PGC1α/Nrf2 and PI3K/Akt Signaling Pathways

Haiyun Chen[1,2], Jie Cao[2], Zeyu Zhu[2], Gaoxiao Zhang[2], Luchen Shan[2], Pei Yu[2], Yuqiang Wang[2], Yewei Sun[2] and Zaijun Zhang[2]**

[1] Institute of Biomedical and Pharmaceutical Sciences, Guangdong University of Technology, Guangzhou, China, [2] Institute of New Drug Research and Guangzhou Key Laboratory of Innovative Chemical Drug Research in Cardio-Cerebrovascular Diseases, Jinan University College of Pharmacy, Guangzhou, China

Glutamate-induced excitotoxicity is one of the main causes of neuronal cell death in stroke. Compound **22a** has been previously reported as a promising neuroprotective compound derived from tetramethylpyrazine, which is a widely used active ingredient of traditional Chinese medicine Chuanxiong (Ligusticum wallichii Franchat). Compound **22a** can protect neurons from oxidative stress-induced PC12 cell death and alleviates the infarct areas and brain edema in a rat permanent middle cerebral artery occlusion model. In the current work, we further investigated the neuroprotective effects and underlying mechanisms of compound **22a** against glutamate-induced excitotoxicity in primary culture of rat cerebellar granule neurons (CGNs). We found that pretreatment with compound **22a** prevented glutamate-induced neuronal damage by maintaining mitochondrial membrane potential and attenuating cellular apoptosis. Compound **22a** could also enhance peroxisome proliferator-activated receptor gamma coactivator 1-alpha (PGC1α) transcriptional activity and induce nuclear accumulation of Nrf2 in PC12 cells. Accordingly, pretreatment with compound **22a** reversed the glutamate-induced down-regulation of expression of the proteins PGC1α, transcriptional factor NF-E2-related factor 2 (Nrf2), and hemooxygenase 1 (HO-1). In addition, compound **22a** increased the phosphorylation of phosphoinositide 3-kinase (p-PI3K), phosphorylated protein kinase B (p-Akt), and glycogen synthase kinase 3β (p-GSK3β). Meanwhile, the small interfering RNA-mediated silencing of PGC1α expression and selective inhibitors targeting PI3K/Akt (LY294002 and Akt-iv) could significantly attenuate the neuroprotective effect of compound **22a**. Taken together, compound **22a** protected against glutamate-induced CGN injury possibly in part through regulation of PGC1α/Nrf2 and PI3K/Akt pathways.

Keywords: ischemic stroke, tetramethylpyrazine derivative 22a, excitotoxicity, neuroprotection, peroxisome proliferator-activated receptor gamma coactivator 1-alpha

OPEN ACCESS

Edited by:
Sikha Saha,
University of Leeds, United Kingdom

Reviewed by:
Margarida Castro-Caldas,
Universidade Nova de Lisboa, Portugal
Federico Herrera,
Instituto de Tecnologia Química e Biológica (ITQB-NOVA), Portugal

****Correspondence:***
Yewei Sun
yxy0723@163.com
Zaijun Zhang
zaijunzhang@163.com

Specialty section:
This article was submitted to Neurodegeneration, a section of the journal Frontiers in Neuroscience

Received: *27 December 2017*
Accepted: *27 July 2018*
Published: *15 August 2018*

Citation:
Chen H, Cao J, Zhu Z, Zhang G, Shan L, Yu P, Wang Y, Sun Y and Zhang Z (2018) A Novel Tetramethylpyrazine Derivative Protects Against Glutamate-Induced Cytotoxicity Through PGC1α/Nrf2 and PI3K/Akt Signaling Pathways. Front. Neurosci. 12:567. doi: 10.3389/fnins.2018.00567

Abbreviations: Akt, protein kinase B; CGN, cerebellar granule neurons; Cyt C, cytochrome c; GSK3β, glycogen synthase kinase 3β; HO-1, hemooxygenase 1; MMP, mitochondria membrane potential; Nrf2, transcriptional factor NF-E2-related factor 2; PGC1α, peroxisome proliferator-activated receptor gamma coactivator 1-alpha; PI3K, phosphatidylinositol 3-kinase; ROS, reactive oxygen species; TMP, tetramethylpyrazine.

INTRODUCTION

Ischemic stroke is one of the major causes of human death and disability worldwide (Donnan et al., 2008). Glutamate-induced excitotoxicity has been demonstrated to be involved in neuronal cell death in stroke (Lai et al., 2014). Physiologically, glutamate acts as one of the main excitatory neurotransmitters in the central nervous system (CNS), contributing to normal neural transmission, development, differentiation, and plasticity. Under pathological conditions, however, overproduction of extracellular glutamate leads to uncontrolled, continuous depolarization of neurons in a toxic process called excitotoxicity. Glutamate-induced excitotoxicity is associated with the over-stimulation of glutamate receptors, inducing the impairment of intracellular Ca^{2+} homeostasis and subsequently leading to overproduction of free radicals, overactivation of proteases and kinases, etc. (Wang and Qin, 2010; Lai et al., 2014). Particularly, the overloading intracellular Ca^{2+} and overproduction of free radicals have been shown to induce mitochondrial dysfunction by down-regulating PGC1α, which plays a protective role against neurodegenerative conditions (Sano and Fukuda, 2008; Wareski et al., 2009). Although great progress has been made, the exact mechanism underlying glutamate-induced cytotoxicity is still not clear. Nonetheless, it has been reported that dysregulation of PI3K/Akt and Nrf2 signaling pathways contributes to glutamate-induced excitotoxicity (Jing et al., 2012; Pang et al., 2016). Stimulation of the PI3K/Akt pathway is neuroprotective against hypoxic and excitotoxic neuronal death *in vitro* and ischemic neuronal death *in vivo*, and there is increasingly evidence to indicate cross talk between the Nrf2 and PI3K/Akt pathways in response to glutamate caused cell injury (Jo et al., 2012; Lee et al., 2015).

Since the exact causes of ischemic stroke have yet to be elucidated, currently there are no pharmacological treatments to ameliorate glutamate excitotoxicity and provide neuroprotection for brain ischemic stroke (Lau and Tymianski, 2010). Thrombolysis via the intravenous (i.v.) administration of recombinant tissue plasminogen activator remains the only treatment currently available for acute ischemic stroke. In addition, it is of great concern that clinical trials investigating neuroprotective agents for the development of new stroke therapies have generally been unsuccessful (Grupke et al., 2014). As a result, numerous researchers have been exploring potentially active plant-derived agents, hoping to meet this unmet need and discover a disease-modifying drug (Zhang et al., 2014). Traditional Chinese medicine focuses on the overall regulation of the pathophysiological condition of the entire body, a trait that makes these compounds particularly promising in the treatment of complex diseases (Ghosh et al., 2014). TMP is one of the mainly biologically active constituents derived from the traditional Chinese medicine Chuanxiong (Ligusticum wallichii Franchat) and has been widely used to treat cardio- and cerebro-vascular diseases in clinic (Liu et al., 2003; Xue et al., 2011). In our previous study, a TMP-derived compound **22a** was designed to combine caffeic acid (Touaibia et al., 2011) (another natural compound with versatile pharmacological activities) and a nitrone group (Floyd et al., 2013) (a strong free radical-trapping agent) with TMP. We found that compound **22a** exhibited strong ROS scavenging activity and exerted protective effects in models of ischemic stroke *in vivo* (Chen et al., 2017). In the present study, the neuroprotective effects of compound **22a** against glutamate-induced excitotoxicity on primary culture of rat CGNs, and the underlying mechanisms of action, were further investigated.

MATERIALS AND METHODS

Chemicals and Reagents

All media and supplements used for cell cultures were purchased from Gibco (Carlsbad, CA, United States), unless otherwise noted. ATP assay kit was obtained from Beyotime (Beyotime, China). LY294002 and Akt-iv was obtained from Sigma-Aldrich (St. Louis, MO, United States). PGC1α siRNA, scrambled siRNA and transfection reagent were purchased from Santa Cruz Biotechnology (Santa Cruz, CA, United States). RIPA lysis buffer, phenylmethanesulfonyl fluoride (PMSF), and halt phosphatase inhibitor cocktail were purchased from Pierce Biotechnology (Rockford, IL, United States). Antibodies against phospho-Ser473 Akt, phospho-Ser9 GSK3β, Bcl-2 and Bax were obtained from Cell Signaling Technology (Beverly, MA, United States). Antibodies against β-actin, PGC1α, Nrf2 and HO-1 were obtained from Santa Cruz Biotechnology (Santa Cruz, CA, United States). All other reagents were from Sigma-Aldrich (St. Louis, MO, United States) except where stated otherwise.

Primary Cell Cultures

Eight-day-old Sprague-Dawley rats were obtained from the Experimental Animal Center of Sun Yat-sen University. The detailed methodology used to separate the CGNs is described in our previous publication (Chen H.Y. et al., 2015). Briefly, neurons were seeded at a density of 1.0–1.5 × 10^5 cells/well in basal modified Eagle's medium supplemented with 10% fetal bovine serum, 25 mM KCl, 2 mM glutaMax and penicillin (100 U/mL)/streptomycin (100 μg/mL). The cultures were grown at 37°C for 24 h. The growth of non-neuronal cells was limited by adding cytosine arabinoside (10 μM). Using this protocol, 95–99% of the cultured cells were granule neurons. All experiments were performed in CGNs at 8 days *in vitro* (DIV).

All experiments were conducted in accordance with the guidelines of the Experimental Animal Care and Use Committee of Jinan University. The experimental protocols were approved by the Ethics Committee for Animal Experiments of Jinan University.

MTT Reduction Assay

The tetrazolium salt 3-(4,5-dimethylthiazol-2-yl)-2,5-diphenyltetrazolium bromide dye (MTT) assay was used to assess neurotoxicity. The assay was performed according to the procedure described in our previous work (Chen H.Y. et al., 2015). Briefly, neurons were cultured in 96-well plates for 8 DIV. Treatments of compound **22a** (0.1, 1, 10, 100 μM), TMP (100 μM) and memantine (5 μM) were used as controls for 2 h before 200 μM glutamate was added to the media. To determine the possible pathways involved in the effect of

compound **22a**, CGNs were pretreated with 1 μM LY294002 (a PI3K inhibitor) or 1 μM Akt-iv (an Akt inhibitor) for 30 min before administration of compound **22a** (10 μM), and were then challenged by glutamate. After 24 h, the media of each well was supplemented with 10 μL of 5 mg/mL MTT, and the plate was put in an incubator at 37°C for 4 h under humidified conditions. A microplate reader was used to measure the absorbance of the samples at 570 nm wavelength.

Lactate Dehydrogenase (LDH) Release

The activity of LDH released into the incubation medium was used as an indicator to determine cellular injury. CGNs were pretreated with compound **22a** (0.1, 1, 10, 100 μM) or TMP (100 μM) and memantine (5 μM) for 2 h, then 200 μM glutamate was added to incubated for 24 h. The cytotoxicity detection kit (Roche Applied Science, Germany) was used to determine LDH activity. LDH release was calculated according to the manufacturer's instructions. A microplate reader was used to measure the absorbance at 490 nm wavelength. Cytotoxicity (%) was calculated with the following equation:

$$\text{Cytotoxicity}\,(\%) = (\text{experimental LDH release} - \text{spontaneous LDH release}) / (\text{Maximum LDH release} - \text{spontaneous LDH release}) * 100$$

Experimental LDH release represents the activity of released LDH in cells pretreated with test compounds and glutamate, Spontaneous LDH release represents the activity of released-LDH in untreated normal cells, and Maximum LDH release represents maximum LDH activity determined by lysing the cells (100% dead cells) with Triton X-100 (final concentration 2% for 4 h at 37°C). All assays were performed in six-replicates and repeated three times.

Hoechst Staining

Chromatin condensation was detected by nucleus staining with Hoechst 33342 (Beyotime, China) as previously described (Chen H.Y. et al., 2015). CGNs of 4–5 × 10^5 cells/well were cultured in a 24-well plate for 8 DIV. Pretreatment of compound **22a** (100 μM) and memantine (5 μM) as the positive control at the indicated concentrations for 2 h before 200 μM glutamate was added into the media. After 24 h, cells were washed with ice-cold phosphate-buffered saline (PBS) and fixed with 4% formaldehyde in PBS. Hoechst 33342 (5 mg/mL) was added to the media for 5 min at 4°C. Samples were observed and photos were taken under a fluorescence microscope. The fluorescence images were photo-taken from three different fields of each experiment with a total of three independent experiments. The number of apoptotic nuclei was counted and expressed as a percentage of total 100 nuclei counted/field.

Measurement of Intracellular Reactive Oxygen Species (ROS)

Cerebellar granule neurons were cultured in 96-well plates at a density of 1.0–1.5 × 10^5 cells/well for 8 DIV. After pretreatment with compound **22a** (0.1, 1, 10, 100 μM) or memantine (5 μM) for 2 h, they were then exposed to 200 μM glutamate for 24 h. The total intracellular ROS were detected using H_2DCF-DA (10 μM), and a microplate reader was used to measure the fluorescence intensity. The fluorescence intensity/per well was normalized against the MTT absorption value of the same well. The fluorescence values of the treated group were calculated as a percentage of the fluorescence of the control cells.

Measurement of Mitochondrial Membrane Potential

Cerebellar granule neurons were placed in a 96-well plate at a density of 1.0–1.5 × 10^5 cells/well. After 8 DIV, compound **22a** or memantine was added to pretreat cells at the indicated concentrations for 2 h. After exposure to 200 μM glutamate for 24 h, the cells were washed three times and then stained with 2 μM JC-1 (Beyotime, China), a molecular probe to measure mitochondrial membrane potential (MMP), for 10 min. The microplate reader was used to measure the fluorescence intensity using 490 nm/530 nm excitation and 525 nm/590 nm dual emissions. The mitochondrial accumulation of JC-1 is dependent upon MMP, which is calculated as a decrease in the ratio of 590 nm to 525 nm emissions.

Measurement of Intracellular ATP Levels

Cerebellar granule neurons were placed in a 96-well plate at a density of 1.0–1.5 × 10^5 cells/well. After 8 DIV, **22a** or memantine was added to pretreat at the indicated concentrations for 2 h. After the following incubation with 200 μM glutamate for 24 h, a ATP Assay Kit was used to detect the intracellular ATP levels by using the (Beyotime, China) according to the manufacturer's protocol. The intracellular ATP levels of the treated group were normalized to the control cells'.

Western Blot Assay

Cerebellar granule neurons were cultured in a 6-well plate at a density of 2 × 10^6 per well in 1.5 mL. At 8 DIV, cells were pretreated with **22a** for 2 h before incubation with 200 μM glutamate for another 12 h. Cells were harvested in a cell lysis buffer supplemented with 1% PMSF (phenylmethanesulfonyl fluoride) as well as 1% protease inhibitor cocktail (Roche Applied Science). The cellular protein concentrations were determined by the BCA assay (Pierce, Rockford, IL, United States) after incubation for 15 min on ice and centrifugation (14,000 *g*) for 10 min at 4°C. SDS sample buffer was added to dilute the cell lysates, and the mixture was heated for 5 min at 100°C. The protein (30 μg) was separated on a 10% SDS–polyacrylamide gel. After transferring protein to polyvinyldifluoride membranes, 5% BSA was used as a blocking buffer to block the membranes. After incubation with the primary antibodies at 4°C overnight, signals were attained by binding a secondary antibody conjugated to horseradish peroxidase. Blots were detected using the chemiluminescence enhancer detection ECL plus kit (Fude Biological Technology Co., Ltd., China) and images captured using a detecting system (Carestream Health, United States). Quantitation of the digitalized images was analyzed based on their mean pixel density by using Carestream software system,

and described as an expression ratio of target protein to β-actin (a loading control protein).

Silencing of PGC1α by Small Interfering RNA (siRNA)

Cerebellar granule neurons at 8 DIV were transfected with siRNA using transfection reagent Opti-MEM I (Invitrogen, Carlsbad, CA, United States) and Lipofectamine2000 (Invitrogen) according to the manufacturer's instructions and the previous studies' (Kim et al., 2014). Experiments were carried out 24 h after the cells were transfected with PGC1α siRNA or scrambled siRNA.

PGC1α Transcriptional Activity

PC12 cells were plated in 24-well plates and transfected with a PGC1α luciferase reporter plasmid along with Renilla luciferase control vector by using the Amaxa Nucleofector II, which can be used for transfection of any DNA vectors (expression plasmids, shRNA vectors) into difficult-to-transfect cell lines and primary cells. Then 12 h after transfection, the cells were treated with compound **22a** at the indicated concentrations for 24 h. Cells were harvested and analyzed using a Dual-Glo luciferase assay kit (Promega, Madison, WI, United States) following the manufacturer's instructions. Firefly luciferase activity was normalized to Renilla luciferase activity.

Immunofluorescence

Cerebellar granule neurons of 4–5 $\times$ 10^5 cells/well were cultured in a 24-well plate for 8 DIV, and were treated with compound **22a** (100 μM). After 12 h, cells were washed with ice-cold phosphate-buffered saline (PBS) and fixed with 4% formaldehyde in PBS for 30 min at room temperature. The cells were washed with ice-cold PBS containing 5% BSA acting as a blocking buffer for 1 h at room temperature before being incubated with anti-Nrf2 antibody (1:500) overnight at 4°C. The cells were then washed with ice-cold PBS and incubated with FITC antibody (1:200) (Sigma-Aldrich, St. Louis, MO, United States) containing 200 nM DAPI for 2 h at room temperature. Samples were observed and photos were taken under a fluorescence microscope.

Statistical Analysis

All experiments were carried out at least three times with different neuronal preparations, data from which was presented as means ± SEM. Analysis of variance (ANOVA) and Bonferroni's

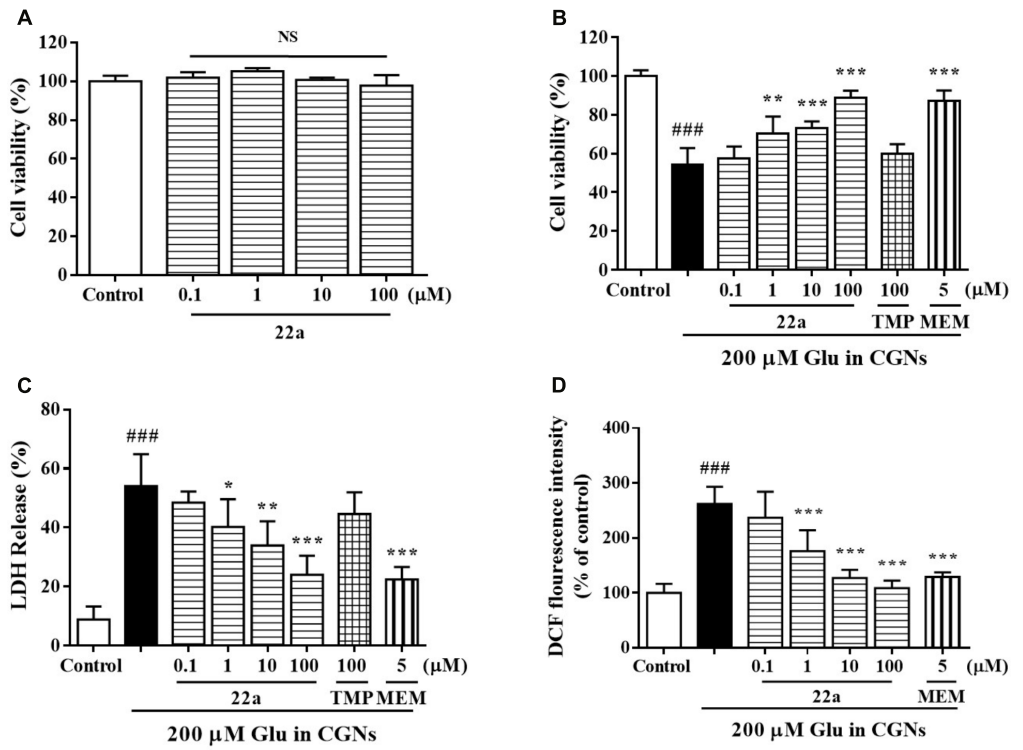

FIGURE 1 | Compound **22a** prevents glutamate-induced neurotoxicity. **(A)** Toxicity of compound **22a** on CGNs. CGNs were pre-incubated with compound **22a** for 24 h. Cell viability was measured using the MTT assay. **(B)** Compound **22a** prevents glutamate-induced neuronal death in CGNs. CGNs were pre-incubated with various agents for 2 h, then exposed to 200 μM glutamate. Cell viability was measured at 24 h post glutamate challenge using the MTT assay. **(C)** Compound **22a** prevents glutamate-induced increase of LDH in CGNs (% of control). CGNs were pre-incubated with various agents for 2 h, then exposed to 200 μM glutamate. LDH release was measured at 24 h after glutamate challenge. **(D)** Compound **22a** attenuates glutamate-induced increase of ROS in CGNs. CGNs were pre-incubated with various compounds for 2 h, then exposed to 200 μM glutamate for another 24 h. Intracellular hydrogen peroxide was measured by DCF-DA. Data were expressed as the mean ± SEM of three separate experiments; $^{###}p < 0.001$ versus control group; $^{*}p < 0.05$, $^{**}p < 0.01$, and $^{***}p < 0.001$ versus glutamate group. Ctrl means control. Glu, glutamate. MEM, memantine.

post-test were used for statistical comparisons, with $P < 0.05$ being considered as statistical significance.

RESULTS

Compound 22a Effectively Prevents Glutamate-Induced Neurotoxicity

At 8 DIV, CGNs were exposed to increasing concentrations of glutamate, which induced a concentration-dependent neuronal death from 50 to 1000 μM (data not shown). Since low doses of glutamate induced apoptosis instead of necrosis in primary CGNs (Du et al., 1997), a 200 μM glutamate concentration that produced approximately 54% neuronal loss was used for the subsequent experiments. Treatment with compound **22a** up to 100 μM for 24 h didn't cause any cytotoxicity to CGNs (**Figure 1A**). Pretreatment with serial concentrations of compound **22a** (1–100 μM) could prevent glutamate-induced toxicity and the maximum cell viability reached 88.7% at 100 μM, similar to that of positive control memantine (87.1%) and higher than that of TMP (60.0%) (**Figure 1B**). The neuroprotection of compound **22a** against glutamate triggered cytotoxicity was more potent than that of TMP.

To further confirm the protection of compound **22a** against glutamate-induced neurotoxicity, we measured the LDH release and intracellular ROS production in CGNs. Compound **22a** and memantine significantly prevented glutamate-induced LDH release. TMP (100 μM) had a marginal effect in this model (**Figure 1C**). Furthermore, pretreatment with compound **22a** from 1 to 100 μM and memantine significantly decreased the intracellular ROS overproduction caused by glutamate in CGNs (**Figure 1D**).

Compound 22a Inhibits Glutamate-Induced Cellular Apoptosis in CGNs

It has been reported that a 200 μM glutamate concentration induced neuronal damage via apoptosis (Du et al., 1997). Compound **22a** and memantine significantly reversed the cell counts of nuclear condensation induced by glutamate (**Figures 2A,B**). In **Figure 2C**, two apoptosis related proteins, Bcl-2 and Bax, were determined by Western blot analysis. It was found that pretreatment with compound **22a** reversed the Bcl-2 down-regulation and Bax up-regulation induced by glutamate. The Bcl-2/Bax ratio was increased by pretreatment with compound **22a** in a concentration-dependent manner (**Figure 2D**).

Compound 22a Improves the Mitochondrial Dysfunction Induced by Glutamate

To examine whether the neuroprotective effects of compound **22a** was due to preservation of mitochondrial function, we

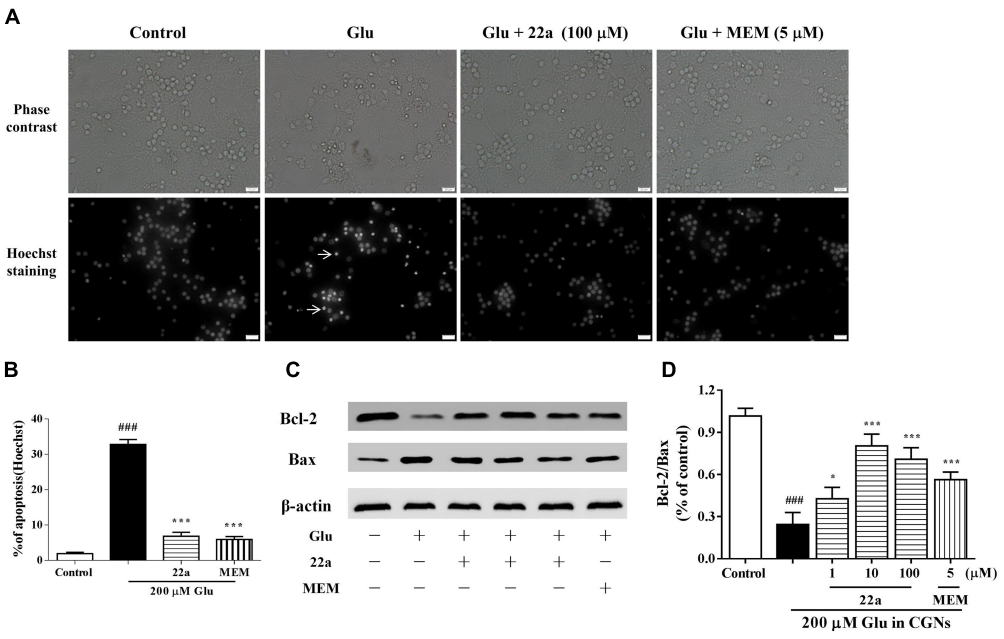

FIGURE 2 | 22a inhibits glutamate-induced cell apoptosis in CGNs. **(A)** Compound **22a** prevents glutamate-induced increase of pyknotic nuclei in CGNs. CGNs were pre-incubated with various agents for 2 h, then exposed to 200 μM glutamate. CGNs were stained with Hoechst 24 h after the glutamate challenge. Photographs were from a representative experiment; experiments were repeated three times (original magnification 400×). **(B)** Statistical analysis of the number of pyknotic nuclei. The number of pyknotic nuclei with condensed chromatin was counted from representative Hoechst staining photomicrographs and is represented as a percentage of the total number of nuclei counted. **(C)** Western blot of apoptosis related proteins Bcl-2 and Bax. **(D)** Densitometry analysis of protein expression ratios of Bcl-2 and Bax. Data were expressed as the mean ± SEM of three separate experiments; $^{###}p < 0.001$ versus control group; $^{*}p < 0.05$ and $^{***}p < 0.001$ versus glutamate group.

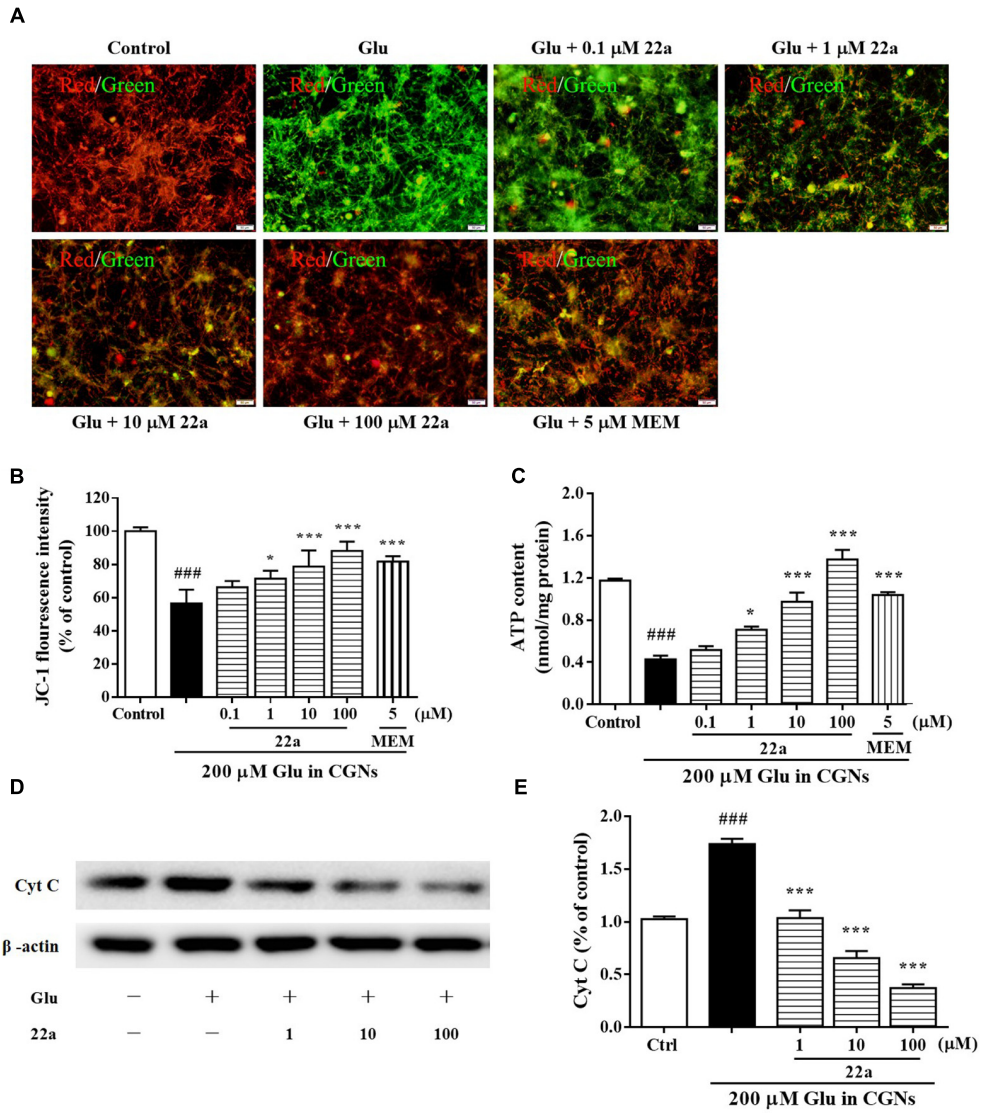

FIGURE 3 | Compound 22a improves mitochondrial dysfunction induced by glutamate. **(A)** Compound **22a** prevents glutamate-induced changes of MMP in CGNs. CGNs were pre-incubated with various agents for 2 h, then exposed to 200 μM glutamate. The MMP was evaluated by staining with the potential sensor JC-1. The fluorescence shift from red to green was detected by a microplate reader. **(B)** Quantitative analysis of the red fluorescence to green fluorescence (590 nm/529 nm) ratio in **(A)**. **(C)** Compound **22a** attenuates glutamate-induced ATP depletion in CGNs. **(D)** Immunoblot assay was performed with antibodies against Cyt C. **(E)** Densitometric analysis of **(D)**. Data were expressed as the mean ± SEM of three separate experiments; $^{###}p < 0.001$ versus control group; $^{*}p < 0.05$, $^{**}p < 0.01$, and $^{***}p < 0.001$ versus glutamate group.

measured the MMP collapse and mitochondrial ATP release. Changes of MMP were monitored by a JC-1 molecular probe, and the fluorescence shift from red to green reflected the depolarization of MMP (Chaoui et al., 2006). It was found that pretreatment with compound **22a** concentration-dependently and strongly restored MMP decrease (red fluorescence/green fluorescence) in glutamate-treated CGNs (**Figures 3A,B**). We also found that glutamate induced a significant decrease in mitochondrial ATP production, whereas pretreatment with compound **22a** significantly prevented glutamate-induced decreases in ATP levels (**Figure 3C**). Memantine was also effective ameliorating the decrease of MMP and ATP in glutamate-treated CGNs. In addition, when Cyt C release was measured by Western blot as shown in **Figures 3D,E**, it was found that **22a** concentration-dependently prevented glutamate-induced Cyt C release.

Compound 22a Up-Regulates PGC1α/Nrf2 Pathway Through Activation of PI3K/Akt

PGC1α was considered to be a major regulator of mitochondrial biogenesis. It is thought to regulate the expression of Nrf2 (Wareski et al., 2009; Robinson et al., 2014), a major transcription

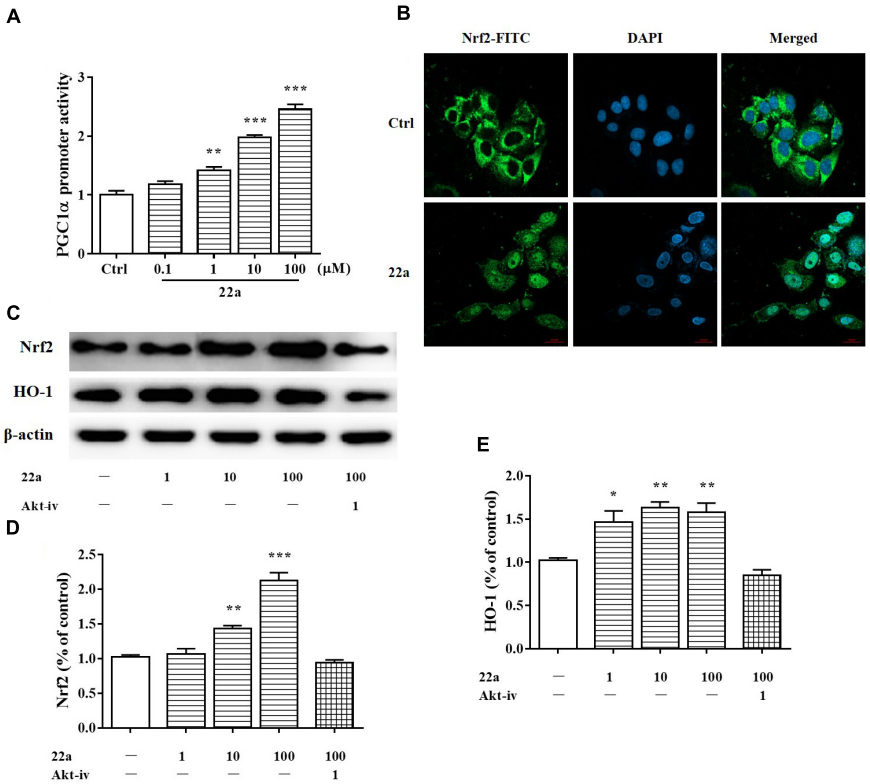

FIGURE 4 | Compound **22a** activates of PGC1α/Nrf2 signaling pathway. **(A)** Compound **22a** (0.1, 1, 10, 100 μM) increased the transcriptional activity of PGC1α determined by the luciferase reporter assay. **(B)** Compound **22a** (100 μM) induced the nuclear translocation of Nrf2 determined by immunofluorescence staining. Left panel: green fluorescence showing Nrf2 localization. Middle panel: stained nucleus with DAPI. Right panel: merged images from green and blue filters. Scale bar: 20 μm. **(C)** Immunoblot assay was performed with antibodies against Nrf2 and HO-1. **(D,E)** Densitometric analysis of the protein expression in **(C)**. CGNs were treated with compound **22a** (1, 10, 100 μM) for 12 h. Data were expressed as the mean ± SEM of three separate experiments; $^{*}p < 0.05$, $^{**}p < 0.01$, and $^{***}p < 0.001$ versus control group.

factor against oxidative stress (Nguyen et al., 2009). As shown in **Figure 4A**, Compound **22a** increased the transcriptional activity of PGC1α in a concentration-dependent manner. Nrf2 nuclear translocation was further investigated with PC12 cells after treatment with 100 μM compound **22a** for 12 h. As shown in **Figure 4B**, **22a** pretreatment increased Nrf2 accumulation in the nucleus. Nrf2 is a crucial regulator against oxidative stress and it is of interest to investigate the involvement of HO-1 protein expression. As shown in **Figures 4C–E**, CGNs treated with compound **22a** concentration-dependently increased Nrf2 and HO-1 expression. PI3K/Akt activation was reported to contribute to the up-regulation of the Nrf2 signal (Lee et al., 2015). We assessed if compound **22a**-induced Nrf2 and HO-1 expression was affected by Akt inhibitor Akt-iv. As shown in **Figures 4C–E**, compound **22a**-induced up-regulation of Nrf2 and HO-1 was completely abolished by Akt-iv.

Compound 22a Activates PGC1α/Nrf2 Signaling Pathway in CGNs Treated With Glutamate

To further elucidate whether the PGC1α/Nrf2 signaling pathways were involved in the protective effect of compound **22a** against glutamate-induced neuron injury, the two protein's expression levels were examined with Western blotting. We found that glutamate significantly decreased PGC1α, Nrf2, and HO-1 protein expression (**Figures 5A,B**); however, compound **22a** pretreatment reversed these decreases. To confirm the role of PGC1α activation in the neuroprotective effects of compound **22a**, we tested the blocking effect of PGC1α siRNA transfection. We found that PGC1α siRNA transfection dramatically decreased PGC1α protein expression (**Figures 5C,D**). In cell viability tests, PGC1α siRNA transfection considerably attenuated the neuroprotection of compound **22a**; however, a scrambled RNA transfection that was used as a negative control did not yield any significant effects on PGC1α expression or on cell viability (**Figure 5E**).

Compound 22a Reversed the Inhibition of PI3K/Akt/GSK3β Pathway Caused by Glutamate

To investigate the signaling pathways involved in the protective effects of compound **22a** against glutamate-caused excitotoxicity, we evaluated the correlation between cell viability and PI3K/Akt activation. The levels of p-PI3K, p-Ser473-Akt and p-Ser9-GSK3β

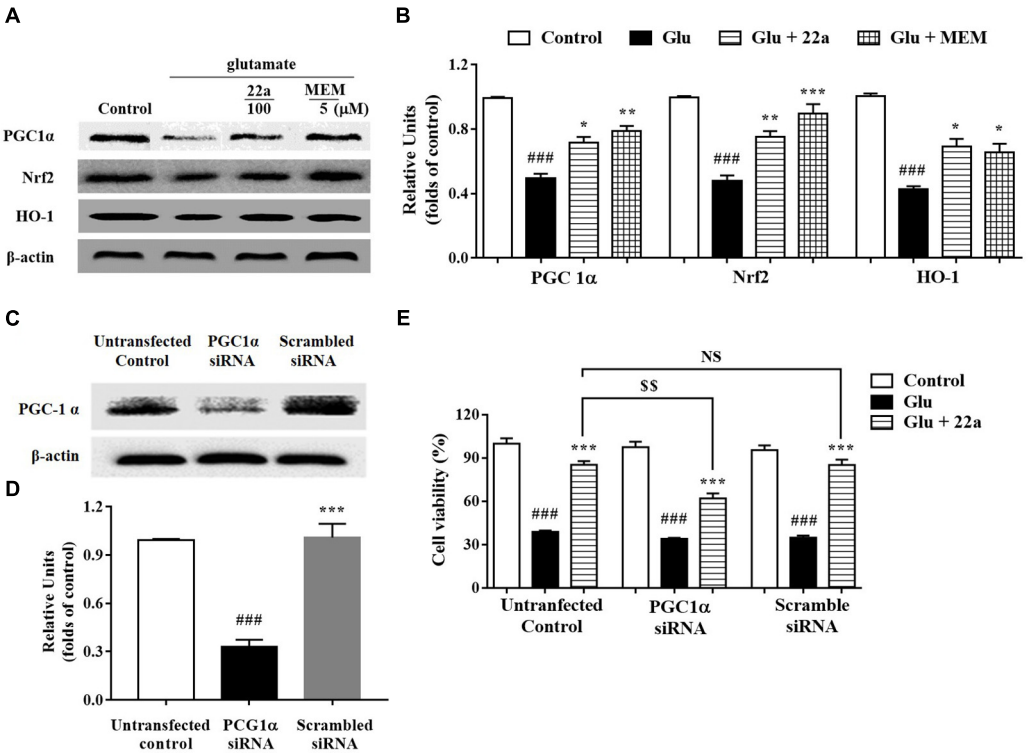

FIGURE 5 | Involvement of the PGC1α/Nrf2 pathway in neuroprotection exerted by compound **22a** in CGNs. **(A)** Representative blots showed the expression of proteins PGC1α, Nrf2 and HO-1 in CGNs after different treatments. **(B)** Densitometric analysis of the protein expression in **(A)**. **(C)** Representative blots showed the protein expression of PGC1α was silenced in CGNs pretreated with PGC1α siRNA, but not when pretreated with scrambled siRNA. **(D)** Densitometric analysis of **(C)**. **(E)** PGC1α siRNA significantly attenuated the neuroprotective effects of compound **22a** against glutamate-induced neuronal cell death in CGNs. CGNs were transfected with either PGC1α siRNA or scrambled siRNA for 24 h and then pretreated with compound **22a** (10 mM) for 2 h before exposure to 200 μM glutamate. Cell viability was measured at 24 h post glutamate exposure using the MTT assay. Data were expressed as the mean ± SEM of three experiments; $^{\#\#\#}p < 0.01$ versus control group; $^{*}p < 0.05$, $^{**}p < 0.01$, and $^{***}p < 0.001$ versus glutamate group; NS means no significance; $^{\$\$}p < 0.01$ versus **22a** in the not-transfected control group.

were analyzed by Western blot. As shown in **Figures 6A–D**, glutamate down-regulated the phosphorylation of PI3K and Akt, while pretreatment with both compound **22a** and memantine reversed the suppressed phosphorylation of PI3K and Akt. GSK-3β is the molecule downstream of PI3K/Akt and is phosphorylated by the PI3K/Akt pathway. As shown in **Figures 6E,F**, there was a significant increase in the phosphorylation of GSK-3β after treatment with compound **22a** in the presence of glutamate.

PI3K and Akt Inhibitors Attenuate the Neuroprotective Effects of Compound 22a

Activation of the pro-survival PI3K/Akt signaling pathway has been shown to be important for neuroprotection (Cantrell, 2001). Consistent with our previous study (Xu et al., 2016), when exposing the cells to a PI3K inhibitor, LY294002 (1 μM), 30 min prior to the addition of compound **22a**, phosphorylation of Akt and GSK3β was nearly completely blocked by LY294002 as shown in **Figures 7A–D**. Pretreatment with LY294002 reversed compound **22a**-prompted Bcl-2 up-regulation and Bax down-regulation; the Bcl-2/Bax ratio was decreased by LY294002 (**Figures 7E,F**). In line with previous reports that PI3K/Akt is involved in Nrf2 mediated HO-1 expression (Lee et al., 2015), when cells were exposed to an Akt inhibitor, Akt-iv (1 μM), 30 min prior to **22a** treatment, the up-regulation of PGC1α, Nrf2 and HO-1 proteins' expression by compound **22a** was almost completely suppressed by Akt-iv, as shown in **Figures 7G,H**.

To further confirm the involvement of the PI3K/Akt pathway in the neuroprotection exerted by compound **22a** in CGNs damaged by glutamate, a specific PI3K inhibitor LY294002 and an Akt inhibitor Akt-iv were applied in a cell viability assay. LY294002 and Akt-iv significantly attenuated the neuroprotection of compound **22a** against glutamate toxicity (**Figure 7I**).

DISCUSSION

Glutamate is the principal excitatory amino acid neurotransmitter with complex biological activities (Pita-Almenar et al., 2006; Paoletti, 2011). However, a high concentration of extracellular glutamate is toxic to nerve cells

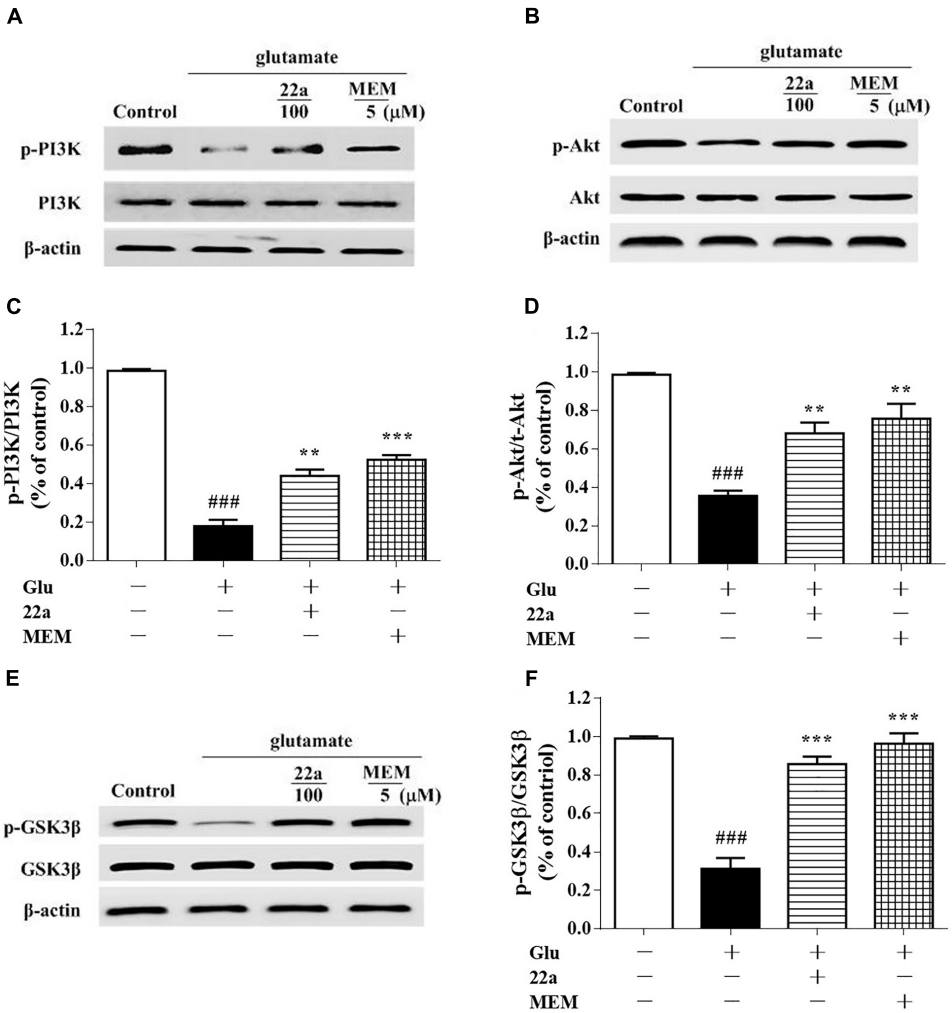

FIGURE 6 | Compound **22a** activates PI3K/Akt pathway in glutamate treated CGNs. **(A,C,E)** Representative blots showed the protein expression of p-PI3K/PI3K **(A)**, p-Akt/Akt **(C)**, and p-GSK3β/GSK3β **(E)** in CGNs. CGNs were pretreated with compound **22a** and memantine for 2 h before exposure to glutamate. **(B,D,F)** Densitometric analysis of the protein expression in **(A,C,E)**. Data were expressed as the mean ± SEM of three experiments; $^{###}p < 0.001$ versus control group; $^{**}p < 0.01$ and $^{***}p < 0.001$ versus glutamate treatment group.

and is considered to be a key contributor in the pathogenesis of neurodegenerative diseases such as ischemic stroke (Wahl et al., 1994). In our previous study, we reported that compound **22a** exhibited neuroprotective effects against oxidative stress-induced neuronal loss *in vitro* and protected against ischemic stroke *in vivo* (Chen et al., 2017). However, the exact mechanisms underlying the neuroprotection of compound **22a** is still unknown. Therefore, the neuroprotective effects of compound **22a** against glutamate-induced excitotoxicity were investigated in the current study. We demonstrated that compound **22a** protected against glutamate-induced neurotoxicity in CGNs. Meanwhile, we found that compound **22a** reversed the MMP collapse and alternation of Bcl-2 and Bax expression to attenuate glutamate-induced cellular apoptosis. Our research further demonstrated that the neuroprotective effects of compound **22a** were intermediated by the stimulation of PI3K/Akt and PGC1α/Nrf2 pathways.

Glutamate is one of the pathological factors in cerebral ischemic disease, and can cause cell apoptosis and MPP reduction, both of which are initiated by the interaction between pro- and anti-apoptotic Bcl-2 family members (Chen Q. et al., 2015). In addition, glutamate toxicity induces mitochondrial dysfunction. Mitochondria are recognized as a center of intracellular energy metabolism, and mitochondrial Ca^{2+} is a positive effector of ATP synthesis (Feissner et al., 2009). Ca^{2+} overload, however, results in free radical generation and mPTP opening, which in turn causes mitochondrial depolarization, matrix solute loss, and Cyt C release (Bernardi and Rasola, 2007). Moreover, the overproduction of ROS is also reported to be related to mPTP opening (Christophe and Nicolas, 2006). In our study, compound **22a** pretreatment significantly prevented intracellular ATP reduction and ROS aggregation, and mitigated MMP dissipation and Cyt C release. Our data further uncovered that compound **22a**

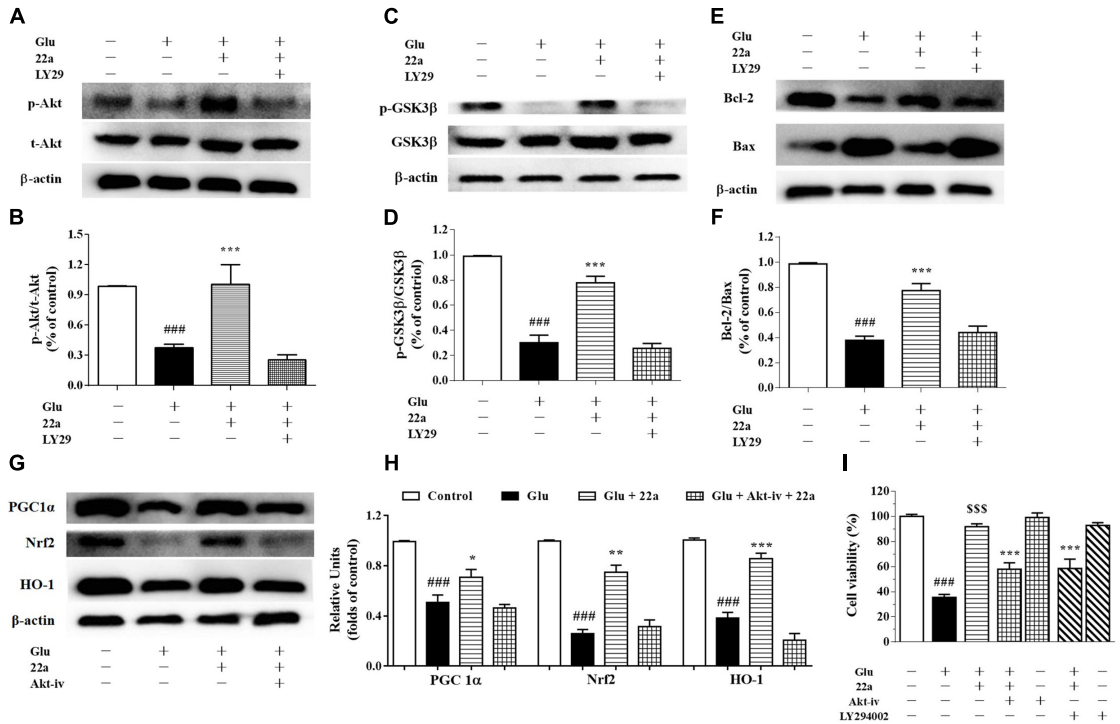

FIGURE 7 | Involvement of the PI3K/Akt pathway in neuroprotection exerted by compound **22a** in CGNs. **(A,C,E)** Representative blots showed the protein expression of p-Akt/Akt **(A)**, p-GSK3β/GSK3β **(C)**, Bcl-2 and Bax **(E)**. CGNs were pretreated with 1 μM LY294002 for 30 min before administration of compound **22a** (10 mM), followed by glutamate challenge. **(B,D,F)** Densitometric analysis of the protein expression in **(A,C,E)**. **(G)** Representative blots showed the protein expression of PGC-1α, Nrf2 and HO-1. **(H)** Densitometric analysis of the protein expression in **(G)**. **(I)** Pretreatment with an Akt inhibitor (Akt-iv) and a PI3K inhibitor (LY294002) attenuated the protective effects of compound **22a** on glutamate-treated CGNs. Data were expressed as the mean ± SEM of three experiments; $^{###}p < 0.001$ versus control group; $^{*}p < 0.05$, $^{**}p < 0.01$, and $^{***}p < 0.001$ versus glutamate treatment group; $^{\$\$\$}p < 0.001$ versus "**22a**+glutamate" treatment group. LY29 refers to PI3K inhibitor LY294002.

reversed the up-regulation of Bax and down-regulation of Bcl-2 expression induced by glutamate. Furthermore, the expression of Bcl-2, an integral membrane protein, is recognized as a hallmark of cell death associated with mitochondria dysfunction (Wallgren et al., 2013). Altogether, these results imply that increased Bcl-2 expression may represent an endogenous repair mechanism against apoptotic pathway, indicating that **22a** may block the Bax-mediated decrease of MMP or promote mitochondrial homeostasis against glutamate-caused CGNs damage.

As described above, mitochondria play a vital role in many fundamental cellular processes, ranging from energy production and metabolism to apoptosis (Robinson et al., 2014). PGC1α is a transcriptional co-activator that regulates the transcription of numerous genes involved in cellular metabolism, including mitochondrial biogenesis and respiration and ROS metabolism (Shin et al., 2011). PGC1α is also a potent stimulator of mitochondrial respiration and gene transcription that acts by activating nuclear respiratory factors Nrf1 and Nrf2, which in turn regulate expression of mitochondrial transcription factor A (Tfam) and other nuclear-encoded mitochondrial proteins (Wareski et al., 2009). Numerous studies indicate that Nrf2 combines with the promoter of ARE to create general antioxidant responses, which is recognized as a promising method to therapeutically reestablish the CNS redox balance in neurodegenerative disorders (Lim et al., 2014). Among the enzymes that are redox-sensitive inducible is HO-1, which can protect neurons from acute insults under stress conditions thanks to its antioxidant and anti-inflammatory properties (Chen, 2014). In line with previous studies, we found that compound **22a** could enhance PGC1α transcriptional activity and induce nuclear accumulation of Nrf2 in PC12 cells (**Figures 4A,B**). In addition, we found that glutamate treatment significantly down-regulated the protein expression of PGC1α and pretreatment with compound **22a** significantly reversed the down-regulated expressions of PGC1α, Nrf2 and HO-1 induced by glutamate in CGNs (**Figures 5A,B**). Several investigations present that Nrf2 is tightly regulated in neurons through signaling pathways such as PI3K/Akt, which is reported to have a Nrf2-dependent role in activating HO-1 expression (Wang et al., 2008; Zhang et al., 2012; Yin et al., 2015). In this sense, the present study was designed to investigate whether the PI3K/Akt pathway is involved in regulating the PGC1α and Nrf2/HO-1 activation resultant from compound **22a**'s presence, and what effect that has on compound **22a**'s subsequent protective against glutamate-induced neurotoxicity. Our results demonstrated that a specific Akt inhibitor significantly suppressed the enhanced

expression of PGC1α, Nrf2 and HO-1 induced by compound **22a** (**Figures 7G,H**). Moreover, to some extent, knockdown of PGC1α was found to reverse the neuro-protective effect of compound **22a** against toxic stress (**Figures 5C–E**). As such, compound **22a** may pave an effective and practical way to modulate PGC1α activity in neurons.

The PI3K/Akt pathway plays a critical role in preventing the neuronal cell death seen in hypoxic and excitotoxic conditions *in vitro*. Inhibiting the PI3K/Akt pathway exacerbates ischemic neuronal death (Lai et al., 2014). Previous reports indicate that neuroprotective strategies against glutamate-induced excitotoxicity in the cortex and hippocampus of postnatal brains can trigger the activation of PI3K/Akt (Shah et al., 2014). Additionally, Akt activation is capable of suppressing several pro-apoptotic proteins, including members of the Bcl-2 family and some signaling molecules such as GSK-3β (Maurer et al., 2014). In our study, phosphorylation of PI3K, Akt and GSK3β in CGNs was significantly down-regulated when cells were exposed to glutamate; however, compound **22a** pretreatment reversed these changes (**Figures 6A–F**). In addition, PI3K inhibitor LY29004 significantly inhibited the up-regulation of phosphorylated Akt and GSK3β expression while reversing compound **22a**-induced up-regulation of Bcl-2 and down-regulation of Bax expression (**Figures 7A–F**). Importantly, PI3K and Akt inhibitors completely abolished the neuroprotection conferred by compound **22a** pretreatment (**Figure 7I**). Summarily, our results indicate that PI3K/Akt pathway activation is involved in the neuro-protection of compound **22a** against CGNs injury induced by glutamate.

In summary, compound **22a** effectively prevented glutamate-induced excitotoxicity of CGNs via involvement of the PI3K/Akt and PGC1α/Nrf2 pathways. Our results suggest that compound **22a** might be of benefit in preventing neuronal death from ischemic stroke.

ETHICS STATEMENT

All animal studies were conducted following to the handbook of the Experimental Animal Care and Use Committee of Jinan University, and the experimental protocols were approved by the Ethics Committee for Animal Experiments of Jinan University.

AUTHOR CONTRIBUTIONS

HC conceptualized and designed the experiments, performed the research, analyzed and interpreted the results, and wrote the manuscript. JC and ZyZ helped design and performed the experiments. YW, ZjZ, YS, GZ, LS, and PY conceptualized and designed the experiments, analyzed and interpreted the results, and revised the manuscript.

FUNDING

This work was partially supported by the Natural Science Fund of China (81502908), the China Postdoctoral Science Foundation (2017M622646), the Science and Technology Project of Guangdong Province (2013A022100030, 2014A030310174, 2015A020211019, 2015B020232011, 2016A020217013, and 2016A030313107), GD-HK Cooperative Project (2016A050503030), the Key Laboratory Project of Guangzhou (151800010), the Science and Technology Program of Guangzhou (201704020181); as well as the Fundamental Research Funds for the Central Universities (21617469).

ACKNOWLEDGMENTS

We thank Ms. Linda Wang for proof-reading the manuscript.

REFERENCES

Bernardi, P., and Rasola, A. (2007). Calcium and cell death: the mitochondrial connection. *Subcell. Biochem.* 45, 481–506. doi: 10.1007/978-1-4020-6191-2_18

Cantrell, D. (2001). Phosphoinositide 3-kinase signalling pathways. *J. Cell Sci.* 114, 1439–1445.

Chaoui, D., Faussat, A. M., Majdak, P., Tang, R., Perrot, J. Y., Pasco, S., et al. (2006). JC-1, a sensitive probe for a simultaneous detection of P-glycoprotein activity and apoptosis in leukemic cells. *Cytometry B Clin. Cytom.* 70, 189–196. doi: 10.1002/cyto.b.20100

Chen, H., Tan, G., Cao, J., Zhang, G., Yi, P., Yu, P., et al. (2017). Design, synthesis, and biological evaluation of novel tetramethylpyrazine derivatives as potential neuroprotective agents. *Chem. Pharm. Bull.* 65, 56–65. doi: 10.1248/cpb.c16-00699

Chen, H. Y., Xu, D. P., Tan, G. L., Cai, W., Zhang, G. X., Cui, W., et al. (2015). A potent multi-functional neuroprotective derivative of tetramethylpyrazine. *J. Mol. Neurosci.* 56, 977–987. doi: 10.1007/s12031-015-0566-x

Chen, Q., Xu, H., Xu, A., Ross, T., Bowler, E., Hu, Y., et al. (2015). Inhibition of Bcl-2 sensitizes mitochondrial permeability transition pore (MPTP) opening in ischemia-damaged mitochondria. *PLoS One* 10:e0118834. doi: 10.1371/journal.pone.0118834

Chen, J. (2014). Heme oxygenase in neuroprotection: from mechanisms to therapeutic implications. *Rev. Neurosci.* 25, 269–280. doi: 10.1515/revneuro-2013-0046

Christophe, M., and Nicolas, S. (2006). Mitochondria: a target for neuroprotective interventions in cerebral ischemia-reperfusion. *Curr. Pharm. Des.* 12, 739–757. doi: 10.2174/138161206775474242

Donnan, G. A., Fisher, M., Macleod, M., and Davis, S. M. (2008). Stroke. *Lancet* 371, 1612–1623. doi: 10.1016/S0140-6736(08)60694-7

Du, Y., Bales, K. R., Dodel, R. C., Hamilton-Byrd, E., Horn, J. W., Czilli, D. L., et al. (1997). Activation of a caspase 3-related cysteine protease is required for glutamate-mediated apoptosis of cultured cerebellar granule neurons. *Proc. Natl. Acad. Sci. U.S.A.* 94, 11657–11662. doi: 10.1073/pnas.94.21.11657

Feissner, R. F., Skalska, J., and Gaum, W. E. (2009). Crosstalk signaling between mitochondrial Ca2+ and ROS. *Front. Biosci.* 14:1197–1218. doi: 10.2741/3303

Floyd, R. A., Castro, Faria Neto HC, Zimmerman, G. A., Hensley, K., and Towner, R. A. (2013). Nitrone-based therapeutics for neurodegenerative diseases: their use alone or in combination with lanthionines. *Free Radic. Biol. Med.* 62, 145–156. doi: 10.1016/j.freeradbiomed.2013.01.033

Ghosh, N., Ghosh, R., Bhat, Z. A., Mandal, V., Bachar, S. C., Nima, N. D., et al. (2014). Advances in herbal medicine for treatment of ischemic brain injury. *Nat. prod. commun.* 9, 1045–1055.

Grupke, S., Hall, J., Dobbs, M., Bix, G. J., and Fraser, J. F. (2014). Understanding history, and not repeating it. Neuroprotection for acute ischemic stroke: from review to preview. *Clin. Neurol. Neurosurg.* 129, 1–9. doi: 10.1016/j.clineuro.2014.11.013

Jing, Y., Liu, L. Z., Jiang, Y., Zhu, Y., Guo, N. L., Barnett, J., et al. (2012). Cadmium increases HIF-1 and VEGF expression through ROS, ERK, and AKT signaling

pathways and induces malignant transformation of human bronchial epithelial cells. *Toxicol. Sci.* 125, 10–19. doi: 10.1093/toxsci/kfr256

Jo, H., Mondal, S., Tan, D., Nagata, E., Takizawa, S., Sharma, A. K., et al. (2012). Small molecule-induced cytosolic activation of protein kinase Akt rescues ischemia-elicited neuronal death. *Proc. Natl. Acad. Sci. U.S.A.* 109, 10581–10586. doi: 10.1073/pnas.1202810109

Kim, H. K., Song, I. S., Lee, S. Y., Jeong, S. H., Lee, S. R., Heo, H. J., et al. (2014). B7-H4 downregulation induces mitochondrial dysfunction and enhances doxorubicin sensitivity via the cAMP/CREB/PGC1-α signaling pathway in HeLa cells. *Pflugers Arch.* 466, 2323–2338. doi: 10.1007/s00424-014-1493-3

Lai, T. W., Zhang, S., and Wang, Y. T. (2014). Excitotoxicity and stroke: identifying novel targets for neuroprotection. *Prog. Neurobiol.* 115, 157–188. doi: 10.1016/j.pneurobio.2013.11.006

Lau, A., and Tymianski, M. (2010). Glutamate receptors, neurotoxicity and neurodegeneration. *Pflugers Arch.* 460, 525–542. doi: 10.1007/s00424-010-0809-1

Lee, D. S., Cha, B. Y., Woo, J. T., Kim, Y. C., and Jang, J. H. (2015). Acerogenin a from acer nikoense maxim prevents oxidative stress-induced neuronal cell death through Nrf2-mediated heme oxygenase-1 expression in mouse hippocampal HT22 cell line. *Molecules* 20, 12545–12557. doi: 10.3390/molecules200712545

Lim, J. L., Wilhelmus, M. M., de, Vries HE, Drukarch, B., Hoozemans, J. J., and van, Horssen J (2014). Antioxidative defense mechanisms controlled by Nrf2: state-of-the-art and clinical perspectives in neurodegenerative diseases. *Arch. Toxicol.* 88, 1773–1786. doi: 10.1007/s00204-014-1338-z

Liu, X., Zhang, R., Xu, W., Li, C., Zhao, Q., and Wang, X. (2003). Synthesis of the novel liqustrazine derivatives and their protective effect on injured vascular endothelial cell damaged by hydrogen peroxide. *Bioorg. Med. Chem. Lett.* 13, 2123–2126. doi: 10.1016/S0960-894X(03)00359-7

Maurer, U., Preiss, F., Brauns-Schubert, P., Schlicher, L., and Charvet, C. (2014). GSK-3 - at the crossroads of cell death and survival. *J. Cell Sci.* 127, 1369–1378. doi: 10.1242/jcs.138057

Nguyen, T., Nioi, P., and Pickett, C. B. (2009). The Nrf2-antioxidant response element signaling pathway and its activation by oxidative stress. *J. Biol. Chem.* 284, 13291–13295. doi: 10.1074/jbc.R900010200

Pang, T., Wang, Y. J., Gao, Y. X., Xu, Y., Li, Q., Zhou, Y. B., et al. (2016). A novel GSK-3β inhibitor YQ138 prevents neuronal injury induced by glutamate and brain ischemia through activation of the Nrf2 signaling pathway. *Acta Pharmacol. Sin.* 37, 741–752. doi: 10.1038/aps.2016.3

Paoletti, P. (2011). Molecular basis of NMDA receptor functional diversity. *Eur. J. Neurosci.* 33, 1351–1365. doi: 10.1111/j.1460-9568.2011.07628.x

Pita-Almenar, J. D., Collado, M. S., Colbert, C. M., and Eskin, A. (2006). Different mechanisms exist for the plasticity of glutamate reuptake during early long-term potentiation (LTP) and late LTP. *J. Neurosci.* 26, 10461–10471. doi: 10.1523/JNEUROSCI.2579-06.2006

Robinson, A., Grösgen, S., and Mett, J. (2014). Upregulation of PGC-1α expression by Alzheimer's disease-associated pathway: presenilin 1/amyloid precursor protein (APP)/intracellular domain of APP. *Aging Cell* 13, 263–272. doi: 10.1111/acel.12183

Sano, M., and Fukuda, K. (2008). Activation of mitochondrial biogenesis by hormesis. *Circ. Res.* 103, 1191–1193. doi: 10.1161/CIRCRESAHA.108.189092

Shah, S. A., Lee, H. Y., Bressan, R. A., Yun, D. J., and Kim, M. O. (2014). Novel osmotin attenuates glutamate-induced synaptic dysfunction and neurodegeneration via the JNK/PI3K/Akt pathway in postnatal rat brain. *Cell Death Dis.* 5, e1026. doi: 10.1038/cddis.2013.538

Shin, J. H., Ko, H. S., Kang, H., Lee, Y., Lee, Y. I., Pletinkova, O., et al. (2011). PARIS (ZNF746) repression of PGC-1α contributes to neurodegeneration in Parkinson's disease. *Cell* 144, 689–702. doi: 10.1016/j.cell.2011.02.010S0092-8674(11)00124-3

Touaibia, M., Jean-Francois, J., and Doiron, J. (2011). Caffeic Acid, a versatile pharmacophore: an overview. *Mini Rev. Med. Chem.* 11, 695–713. doi: 10.2174/138955711796268750

Wahl, F., Obrenovitch, T. P., Hardy, A. M., Plotkine, M., Boulu, R., and Symon, L. (1994). Extracellular glutamate during focal cerebral ischaemia in rats: time course and calcium dependency. *J. Neurochem.* 63, 1003–1011. doi: 10.1046/j.1471-4159.1994.63031003.x

Wallgren, M., Lidman, M., Pedersen, A., Brännström, K., Karlsson, B. G., and Gröbner, G. (2013). Reconstitution of the anti-apoptotic Bcl-2 protein into lipid membranes and biophysical evidence for its detergent-driven association with the pro-apoptotic bax protein. *PLoS One* 8:e61452. doi: 10.1371/journal.pone.0061452

Wang, L., Chen, Y., Sternberg, P., and Cai, J. (2008). Essential roles of the PI3 kinase/Akt pathway in regulating Nrf2-dependent antioxidant functions in the RPE. *Invest. Ophthalmol. Vis. Sci.* 49, 1671–1678. doi: 10.1167/iovs.07-1099

Wang, Y., and Qin, Z. H. (2010). Molecular and cellular mechanisms of excitotoxic neuronal death. *Apoptosis* 15, 1382–1402. doi: 10.1007/s10495-010-0481-0

Wareski, P., Vaarmann, A., Choubey, V., Safiulina, D., Liiv, J., Kuum, M., et al. (2009). PGC-1α and PGC-1β regulate mitochondrial density in neurons. *J. Biol. Chem.* 284, 21379–21385. doi: 10.1074/jbc.M109.018911

Xu, D., Chen, H., Mak, S., Hu, S., Tsim, K. W. K., Hu, Y., et al. (2016). Neuroprotection against glutamate-induced excitotoxicity and induction of neurite outgrowth by T-006, a novel multifunctional derivative of tetramethylpyrazine in neuronal cell models. *Neurochem. Int.* 99, 194–205. doi: 10.1016/j.neuint.2016.07.006

Xue, Y., Tie, C. R., Li, J., Tian, T., and Li, Q. X. (2011). Ligustrazine inhibits lipopolysaccharide-induced proliferation by affecting P27, Bcl-2 expression in rat mesangial cells. *Eur. J. Pharmacol.* 665, 8–12. doi: 10.1016/j.ejphar.2011.05.004

Yin, X., Wang, X., Fan, Z., Peng, C., Ren, Z., Huang, L., et al. (2015). Hyperbaric oxygen preconditioning attenuates myocardium ischemia-reperfusion injury through upregulation of heme oxygenase 1 expression: PI3K/Akt/Nrf2 pathway involved. *J. Cardiovasc. Pharmacol. Ther.* 20, 428–438. doi: 10.1177/1074248414568196

Zhang, J., Li, Y., Chen, X., Pan, Y., Zhang, S., and Wang, Y. (2014). Systems pharmacology dissection of multi-scale mechanisms of action for herbal medicines in stroke treatment and prevention. *PLoS One* 9:e102506. doi: 10.1371/journal.pone.0102506

Zhang, R., Chae, S., Lee, J. H., and Hyun, J. W. (2012). The cytoprotective effect of butin against oxidative stress is mediated by the up-regulation of manganese superoxide dismutase expression through a PI3K/Akt/Nrf2-dependent pathway. *J. Cell. Biochem.* 113, 1987–1997. doi: 10.1002/jcb.24068

Conflict of Interest Statement: The authors declare that the research was conducted in the absence of any commercial or financial relationships that could be construed as a potential conflict of interest.

frontiers in Cellular Neuroscience

OPINION
published: 29 August 2018
doi: 10.3389/fncel.2018.00277

The Ischemic Immature Brain: Views on Current Experimental Models

Tânia Faustino-Mendes[1], *Marta Machado-Pereira*[1,2], *Miguel Castelo-Branco*[1,2,3] *and Raquel Ferreira*[1,2]*

[1] Faculty of Health Sciences, University of Beira Interior, Covilhã, Portugal, [2] Health Sciences Research Centre (CICS-UBI), University of Beira Interior, Covilhã, Portugal, [3] Hospital Center of Cova da Beira, Covilhã, Portugal

Keywords: perinatal, neonatal, stroke, experimental models, immature brain

STROKE IN PRETERM AND TERM NEWBORNS

Perinatal stroke occurs between the 20th week of gestation and the 28th day after birth (Nelson, 2007). Brain injury within this period can also lead to conditions such as neonatal encephalopathy or to encephalopathy of prematurity. Considering the complex diagnosis and limited data available, the incidence of 1/2,300 live births is a likely underestimation (Nelson and Lynch, 2004; Lee et al., 2005). Nevertheless, these numbers are comparable to those in the elderly (Fernández-López et al., 2014). The most common subtypes are arterial ischemic stroke (Fernández-López et al., 2014), which induces a focal lesion similar to adult stroke, and cerebral sinovenous thrombosis (Govaert et al., 2009). Focal interruption of arterial or venous cerebral blood flow is usually secondary to thrombosis or embolism, with a multifactorial pathophysiology. Importantly, in the fetal circulatory system, placental or systemic venous emboli may pass through a patent *ductus arteriosus* or *foramen ovale* directly to the left carotid artery and subsequently to the left MCA, facilitating occlusion (Gunny and Lin, 2012). Confirmation by imaging or neuropathological studies is always mandatory (Govaert et al., 2009). Different risk factors have been recognized for perinatal stroke (**Supplementary Table 1**; Kurnik et al., 2003; Mirabelli-Badenier et al., 2012; Kasdorf and Perlman, 2013; Basu, 2014; Fernández-López et al., 2014; Kratzer et al., 2014; Machado et al., 2015; Buerki et al., 2016) but inflammation seems to be a prevalent underlying mechanism (Vexler and Yenari, 2009; Hagberg et al., 2015). For instance, chorioamnionitis, a bacterial infection of the amniochorionic membranes (Kasdorf and Perlman, 2013; Buerki et al., 2016) often leads to a longer labor period and worse prognosis (Vexler and Yenari, 2009). Nevertheless, although there is a substantial number of studies concerning neonatal encephalopathy (or hypoxic-ischemia encephalopathy), human data on perinatal stroke can be disparate; some authors found a positive correlation with pro-inflammatory polymorphisms, others did not (Hagberg et al., 2015).

Adult and perinatal stroke also cause distinct presenting symptoms: adults tend to present unilateral symptoms and only 3% have seizures; seizures are one of the most common presentations after perinatal stroke (Fernández-López et al., 2014). Hemiplegic cerebral palsy is also the most frequent long-term motor outcome of the latter (Nelson, 2007). However, several aspects delay the suspicion of diagnosis, since (i) newborns with seizures may appear clinically well-between episodes; (ii) initially, newborns may present discrete non-specific symptoms like lethargy, apnea, difficult feeding and impaired chewing; (iii) and some cases may be asymptomatic, presenting lateralized symptoms only around the 5th month. In fact, lateralized symptoms are rare in neonates (Nelson, 2007; Fernández-López et al., 2014). In 2011, Harbert and colleagues conducted the first human study demonstrating the positive effect of therapeutic hypothermia on perinatal stroke: active whole-body cooling *via* a blanket cooling device led to a significantly lower frequency of seizures (Harbert et al., 2011). Since these symptoms are associated to a worse prognosis, the risk of long-term neurologic disability is likely reduced. Given the complex pathophysiology and difficulty in obtaining an early and accurate diagnosis, new therapies are being tested, alone

OPEN ACCESS

Edited by:
Sikha Saha,
University of Leeds, United Kingdom

Reviewed by:
Marta Fumagalli,
Università degli Studi di Milano, Italy
Marco Bacigaluppi,
San Raffaele Scientific Institute (IRCCS), Italy

***Correspondence:**
Raquel Ferreira
raquelmargarida@gmail.com

Received: *25 March 2018*
Accepted: *08 August 2018*
Published: *29 August 2018*

Citation:
Faustino-Mendes T, Machado-Pereira M, Castelo-Branco M and Ferreira R (2018) The Ischemic Immature Brain: Views on Current Experimental Models. Front. Cell. Neurosci. 12:277. doi: 10.3389/fncel.2018.00277

or in combination with hypothermia, to improve global outcome. Some include administration of growth factors, anticoagulant and antiplatelet agents, blood uric acid lowering medication, antioxidant and anti-inflammatory molecules, stem cells-based therapy and electrical stimulation (Cnossen et al., 2009; Gonzalez and Ferriero, 2009; Mirabelli-Badenier et al., 2012; Basu, 2014; Fernández-López et al., 2014; Kratzer et al., 2014).

IN VITRO APPROACHES

In vitro models resort to oxygen and glucose deprivation (OGD), followed by reoxygenation and nutrient replenishment. Since oxygen levels should be kept preferably under 2%, to represent the ischemic core, and around 7% if studying the ischemic penumbra (Tornabene and Brodin, 2016), these models can be very relatable while allowing easy assessment of cell activity, protein expression and release, and barrier properties of particular cell type(s). We have exposed either individualized cells or brain tissue, namely organotypic brain slice cultures (OSC), to very low O_2 rates (0.1%; Ferreira et al., 2016; Machado-Pereira et al., 2017). These tissue cultures provide unique characteristics and several advantages over cell models, since they preserve whole organ structure and maintain neuronal activity and synapse circuitry. OSC also maintain integrity *in vitro* for over 2 weeks allowing a series of pharmacological studies. Other advantages include the possibility of using younger animals if needed (e.g., 1–3-day-old mice), the refinement of experimental doses/conditions and the reduction of the number of animals for *in vivo* models. To the best of our knowledge only one group has used OSC, from P8-10 rats (Leonardo et al., 2009). A considerable drawback from OSC, and cell cultures, is the absence of blood flow and infiltrating immune cells. Nevertheless, they provide a snapshot of the neurovascular unit up to the time of brain isolation if a lesion and/or treatment is applied *a priori*. Younger animals such as 2-day-old mice still grant the ability to inject a therapeutic agent *via* the temporal vein, which is still visible at this age, to study its protective value (Machado-Pereira et al., 2018). Subsequently, therapeutic agents and stimuli can be further administered over tissue to evaluate their impact on neurovascular and glial activity.

ANIMAL MODELS OF PERINATAL STROKE

Experimental models are important to understand mechanisms of disease. Parameters like injury onset and duration, area of penumbra, reperfusion or therapeutic window are clearly defined, and symptoms can be easily identified and monitored. However, reproducing all the complex pathophysiological aspects of stroke in an otherwise healthy animal is challenging; typically, a stroke patient is elderly and has more than one health condition. One of the most frequently used adult models is induced by transient occlusion of the middle cerebral artery (MCA) with an intraluminal monofilament, blocking cerebral blood flow (usually 60 min) and causing reproducible infarcts in this territory (Carmichael, 2005; Sommer, 2017). A transient model allows the study of the significant effects of reperfusion. Regarding the perinatal period, the most common methodologies use unilateral ligation of the common carotid artery followed by hypoxia, or direct exposure to hypoxia alone. **Table 1** briefly describes procedures using rodents, rabbits, pigs and lambs. Animal models employing pigs, lambs or rabbits, are costly in terms of maintenance, in the sense that they have longer gestation periods and smaller litter size, while offering higher genetic dissimilarity with humans, comparing with mice (Leong et al., 2015). Importantly, most models use O_2 rates much higher (5–12%) than those believed to occur after an ischemic event. Only one group used a lower percentage (3.5–4%), albeit on rats of an age range comparable to a term and up to 2-years-old infant. In fact, normal brain tissue pO_2 is 33.8 ± 2.6 mmHg, which corresponds to $4.4 \pm 0.3\%$ O_2 in the microenvironment (Carreau et al., 2011). Three of the models used between 6 and 12% O_2: a fraction of inspired oxygen (FiO_2) of 0.06–0.12. Considering that atmospheric air is 21% O_2 or the equivalent to a FiO_2 of 0.21, these animals would be subjected to a third to a half O_2 available. Are lower O_2 rates fatal? Moreover, most models use 7-days-old or older animals, which offer a more reasonable size for surgery than younger pups. A week old rat, the most commonly used species, would represent a 2-months-old infant (well-beyond the 28th day post-birth) if considering peripheral organ systems (Sengupta, 2013; Titomanlio et al., 2015), and a term infant, if considering brain development (Titomanlio et al., 2015), raising further challenges on what age range to choose.

Age is very important, since the extent of ischemic injury is largely influenced by brain maturity (Sheldon et al., 1996; McQuillen et al., 2003; Webber et al., 2009). In preterm newborns, oligodendrocyte progenitor cells (OPC) are particularly more sensitive to ischemia (Back et al., 2002). Global ischemia, as in hypoxic-ischemia encephalopathy, disrupts OPC maturation, causing delayed or disrupted myelination, largely contributing to neuronal loss and periventricular white matter diffuse injury (periventricular leukomalacia; Back et al., 2007; Webber et al., 2009). Several experimental models have also been proposed to study this particular condition (Shen et al., 2010). For this reason, OPC constitute a potential target for the development of protective therapies focusing on the reduction of white matter loss in premature infants (Back et al., 2007). Subplate neurons, a transient neuronal population important for the formation of mature neuronal networks, are another vulnerable target. Additionally, interneuron migration to the neocortex is only completed at birth, in a process modulated by microglia activity (Leviton and Gressens, 2007; Xu et al., 2011). In term newborns, gray matter is focally affected, greatly impacting on motor function (Back et al., 2001; Fernández-López et al., 2014; Luhmann et al., 2016). The immature brain is also more susceptible to excitotoxicity and to free radicals considering the higher expression of receptors that signal for excitatory neurotransmitters and lower levels of anti-oxidant enzymes (Johnston, 2005; Lafemina et al., 2006). Overall, choosing the "right" age pertains to the fact that the perinatal period encompasses different stages of the circulatory and immune systems (Titomanlio et al., 2015; Lange et al., 2016). Accordingly, the therapeutic value of an agent directed at

TABLE 1 | Perinatal and neonatal animal models for ischemic injury, specifically rat, pig, mouse, rabbit, and lamb.

RAT		
P5-P17 Φ	Exposure to hypoxia (3.5–4% O_2 in N_2) until apnea or heart rate below 20% of baseline	Jensen, 1995
P10 Φ	Exposure to hypoxia (7, 5, 4% O_2 in N_2) for 8, 6, and 1 min, respectively	Dunn et al., 2017
P10 Φ	Left MCAO for 90 min by inserting a 6-0 nylon filament into the internal carotid artery; unilateral ligation of right CCA followed by hypoxia (8% O_2 in N_2) for 90 min	Ashwal et al., 2007
P7 ♀	MCAO for 180 min by inserting a 6-0 coated filament into the internal carotid artery	Fernández-López et al., 2013
P7 Φ	Unilateral ligation of right CCA followed by hypoxia (8% O_2 in N_2) for 60 min	Jantzie and Todd, 2010
P7 Φ	Unilateral ligation of CCA followed by hypoxia (8% O_2 in N_2) for 30, 60, 90, or 120 min	Silverstein and Johnston, 1984
P7 Φ	Unilateral ligation of left CCA followed by hypoxia (8% O_2 in 92% N_2) for 90 min	Bae et al., 2012
P7 Φ	Unilateral ligation of right CCA followed by hypoxia (8% O_2 in N_2) for 180 min	Jantzie et al., 2005
P7 Φ	Unilateral ligation of left CCA followed by hypoxia (8% O_2 in N_2) for 120 min	Lubics et al., 2005
P7 Φ	Unilateral ligation of CCA followed by hypoxia (8% O_2 in N_2) for 60–240 min	Vannucci and Vannucci, 2005
P4 ♂	Exposure to hypoxia (11% O_2 in N_2) for 360 min *per* day for 5 days	Schaeffer et al., 2013
P4 Φ	Exposure to hypoxia (11% O_2 in N_2) for 360 min *per* day for 5 days	Fendt et al., 2008
P2 Φ	Exposure to hypoxia (12% O_2 in N_2) for 14 days	Deruelle et al., 2006
P1 ♂	Exposure to hypoxia (12% FiO_2) for 10 days	Del Duca et al., 2009
P1 Φ	Unilateral ligation of right CCA followed by hypoxia (8% O_2 in N_2) for 210 min	Girard et al., 2009
P1 Φ	Exposure to hypoxia (5% O_2 in N_2) for 60 or 75 min	Slotkin et al., 1995
Newborn ♂/♀	Unilateral ligation of right CCA followed by hypoxia (8% O_2 in N_2) for 120 min	Kartal et al., 2016
PIG		
P3-P7 Φ	Exposure to a gas mixture (10% FiO_2) for 40 min, followed by 5 min of reoxygenation and 7 min of anoxia by clamping the endotracheal tube	Ni et al., 2011
P1-P4 ♂	Exposure to a gas mixture (FiO_2 6–8%) until hearth rate decreased to 60 beats/min (bradycardia) or mean arterial blood pressure decreased to 15 mmHg (severe hypotension)	Faa et al., 2012
P1-P3 Φ	Exposure to a gas mixture (12% O_2 in N_2) for 120 min to achieve a pO_2 of 30–40 mmHg	Stevens et al., 2008
Newborn Φ	Exposure to a gas mixture (8% O_2 in N_2) until the mean arterial blood pressure decreased to 20 mmHg or base excess reached −20 mmol/L	Garberg et al., 2017
MOUSE		
P9 Φ	Unilateral ligation of left CCA followed by hypoxia (10% O_2 in N_2) for 60 min	Kichev et al., 2014
P7 ♂	Exposure to hypoxia (10% O_2 in N_2) for 360 min *per* day (3 sessions of 120 min separated by 45 min intervals) for 6 days	Kameda et al., 2013
RABBIT		
E22 Φ	Uterine ischemia for 40 min, *via* arterial embolectomy catheter inserted through the maternal left femoral artery into the descending aorta	Yu et al., 2011
LAMB		
E126-141 Φ	Intrauterine hypoxia by induced maternal hypotension *via* infusion of trimetaphan camsylate glucose solution into a polyethylene catheter placed in the maternal femoral vein, for 60–90 min	Gersony et al., 1976

Rodent models usually resort to exposure to hypoxia alone (3.5–12% O_2) or to unilateral ligation of the common carotid artery, followed by hypoxia (8% O_2), in animals of varying ages. Pig models use exposure to a gas mixture ranging from 6 to 12% O_2 while lamb and rabbit models induce intrauterine ischemia. ♀, female; ♂, male; Φ undisclosed sex; CCA, common carotid artery E, embryonic days; MCAO, middle cerebral artery occlusion; min, minutes; P, post-natal days.

perinatal stroke would be better assessed using younger animals. Fundamentally, the brain vasculature during development is formed through two distinct processes: (i) vasculogenesis, in which angioblasts differentiate into endothelial cells forming the perineural vascular plexus, which in turn functions as a substrate for (ii) angiogenesis, the process of generating new vessels from pre-existing ones (Vasudevan and Bhide, 2008; Lee et al., 2009; Tam and Watts, 2010). These processes are consolidated by migrating mural cells, formation of an extracellular matrix and establishment of tight and adherens junctions that regulate permeability and transcellular transport (Lee et al., 2009; Tam and Watts, 2010). With increasing age, blood-brain barrier (BBB) functionality is less maintained after stroke since the expression of several of these proteins (e.g., occludin, claudins, zonula occludens proteins; Kratzer et al., 2014) that support the integrity of tight junctions is also changed. Another reason for a higher resistance of the BBB to ischemic injury in the early stages could be the maturation-dependent interplay between leukocytes and the endothelium and the less active pathophysiological role of the inflammatory process (Titomanlio et al., 2015). A restricted BBB opening may also account for limited neutrophil recruitment/infiltration. While regulatory T

cells seem to play a neuroprotective role, microglia cells promote phagocytosis and tissue recovery, or white matter damage, depending on the adopted phenotype (Hagberg et al., 2015). In fact, microglia migrate to the brain even before blood vessel formation possibly impacting on the development of these structural elements (Rymo et al., 2011; Arnold and Betsholtz, 2013). Hence, in the perinatal period, the neuroinflammatory response has a preponderant role in stroke outcome (and to diffuse pattern of injury), relying more on the activation of microglia than on the extrinsic recruitment of inflammatory cells such as macrophages and neutrophils (Hagberg et al., 2015). A more mature brain offers a BBB more vulnerable to ischemic injury and to immune cell infiltration, and therefore, these cells assume a greater role and become associated to a focal pattern of injury. Consequently, several pro-/anti-inflammatory molecules and growth factors are released and have been studied as part of the impactful secretome unleashed by ischemia. Vascular endothelial growth factor (VEGF) is responsible for several processes upon ischemic stroke, including disruption of endothelial cell junctions and endothelial cell endocytosis, followed by increased BBB permeability, and consequently intracranial hemorrhage and intracranial hypertension (Angelo and Kurzrock, 2007; Lange et al., 2016; Suzuki et al., 2016). However, VEGF also promotes endothelial cell proliferation and migration, and enhances perfusion (reduced infarct volume and penumbra were associated to increased neuroprotection, including in neonatal stroke; Titomanlio et al., 2015; Lange et al., 2016; Suzuki et al., 2016). There are other cell types responsible for the development, regulation and maintenance of central nervous system angiogenesis and BBB integrity such as pericytes and astrocytes (Tam and Watts, 2010). These cells control the production and release of several factors that regulate the aforementioned processes (Lee et al., 2009; Tam and Watts, 2010; Arnold and Betsholtz, 2013). Therefore, diminished quantities of pericytes and astrocytes alongside blood vessels are associated to a higher susceptibility to ischemic injury (Fernández-López et al., 2014; Kratzer et al., 2014).

On a final note, rodent strains may display different levels of vulnerability to injury. For instance, CD1 mice are more vulnerable to damage induced by 30 min of hypoxia, than C57BL/6 and 129Sv mice, with the latter being the most resistant strain (Sheldon et al., 1998). Other murine strains (BDF, CFW, and BALB/C) display varying infarct volumes following 24 h of focal ischemia possibly because of differences in the anatomy of the posterior communicating arteries. BALB/C mice showed a more significant infarct volume and were proposed as the most suitable strain to conduct pharmacological studies in cerebral ischemia (Barone et al., 1993). In addition to differences in vascular anatomy, humans and other animals also display significantly different nutrient and oxygen metabolism, hemodynamics, and neural cell population density/activity (Dirnagl et al., 1999).

An interesting but poorly studied subject is the fact that perinatal stroke appears to be gender-dependent with male neonates and children being more commonly affected and with poorer outcomes (Turtzo and McCullough, 2010; Fernández-López et al., 2014). Turtzo and McCullough have extensively reviewed the role of gender and sex hormones in the perinatal, infant and adult periods. Although *in vitro* data from female pups suggest higher protection from OGD, and neuronal cells from males seem more susceptible to hypoxic injury (Heyer et al., 2005; Li et al., 2005), clinical studies and mechanisms of action remain inconclusive. Overall, ischemic cell death occurs *via* a caspase-independent pathway in males, while this process is caspase-dependent in females; ultimately, both pathways lead to mitochondrial dysfunction. The protection provided by female sex hormones, such as estrogen and progesterone, is a possible explanation. However, estrogen and progesterone administration to post-menopausal women were found to raise the risk of stroke (Turtzo and McCullough, 2010). To further investigate this issue in the perinatal period, it is possible to divide pups, even after birth, by a distinct physical trait: male mice have a visible pigment spot on the scrotum (Wolterink-Donselaar et al., 2009).

CONCLUSIONS

In vitro models are useful for assessing the potential of a therapeutic agent and constitute an inescapable stepping stone for *in vivo* models. However, current animal models still hold key limitations regarding the level of hypoxia and extent of focal injury, age and costs associated to the selected animal species/strain, as well as their basic anatomy. Importantly and understandably, all fail to reproduce the exact mechanisms of injury that occur specifically in perinatal stroke. Hence, it is urgent to continue advancing newer (and multifactorial) experimental models to attain more efficient therapies to treat this complex vascular condition and long-term sequela.

AUTHOR CONTRIBUTIONS

All authors listed have made a substantial, direct and intellectual contribution to the work, and approved it for publication.

FUNDING

Work supported by FEDER through POCI-COMPETE 2020 (POCI-01-0145-FEDER-007491, FCOMP-01-0124-FEDER-041099), and through CENTRO 2020 (CENTRO-01-0145-FEDER-000013), Foundation for Science and Technology (UID/Multi/00709/2013, IF/00178/2015/CP1300/CT0001), L'Oréal-UNESCO Portugal for Women in Science, BD Biosciences Immunology Grant.

SUPPLEMENTARY MATERIAL

The Supplementary Material for this article can be found online at: https://www.frontiersin.org/articles/10.3389/fncel.2018.00277/full#supplementary-material

REFERENCES

Angelo, L. S., and Kurzrock, R. (2007). Vascular endothelial growth factor and its relationship to inflammatory mediators. *Clin. Cancer Res.* 13, 2825–2830. doi: 10.1158/1078-0432.CCR-06-2416

Arnold, T., and Betsholtz, C. (2013). The importance of microglia in the development of the vasculature in the central nervous system. *Vasc. Cell* 5, 4. doi: 10.1186/2045-824X-5-4

Ashwal, S., Tone, B., Tian, H. R., Chong, S., and Obenaus, A. (2007). Comparison of two neonatal ischemic injury models using magnetic resonance imaging. *Pediatr. Res.* 61, 9–14. doi: 10.1203/01.pdr.0000251612.16069.4b

Back, S. A., Han, B. H., Luo, N. L., Chricton, C. A., Xanthoudakis, S., Tam, J., et al. (2002). Selective vulnerability of late oligodendrocyte progenitors to hypoxia–ischemia. *J. Neurosci.* 22, 455–463. doi: 10.1523/JNEUROSCI.22-02-00455.2002

Back, S. A., Luo, N. L., Borenstein, N. S., Levine, J. M., Volpe, J. J., and Kinney, H. C. (2001). Late oligodendrocyte progenitors coincide with the developmental window of vulnerability for human perinatal white matter injury. *J. Neurosci.* 21, 1302–1312. doi: 10.1523/JNEUROSCI.21-04-01302.2001

Back, S. A., Riddle, A., and McClure, M. M. (2007). Maturation-dependent vulnerability of perinatal white matter in premature birth. *Stroke* 38, 724–730. doi: 10.1161/01.STR.0000254729.27386.05

Bae, S. H., Kong, T. H., Lee, H. S., Kim, K. S., Hong, K. S., Chopp, M., et al. (2012). Long-lasting paracrine effects of human cord blood cells on damaged neocortex in an animal model of cerebral palsy. *Cell Transplant.* 21, 2497–2515. doi: 10.3727/096368912X640457

Barone, F. C., Knudsen, D. J., Nelson, A., Feuerstein, G., and Willette, R. N. (1993). Mouse strain differences in susceptibility to cerebral ischemia are related to cerebral vascular anatomy. *J. Cereb. Blood Flow Metab.* 13, 683–692. doi: 10.1038/jcbfm.1993.87

Basu, A. P. (2014). Early intervention after perinatal stroke: opportunities and challenges. *Dev. Med. Child. Neurol.* 56, 516–521. doi: 10.1111/dmcn.12407

Buerki, S. E., Grandgirard, D., Datta, A. N., Hackenberg, A., Martin, F., Schmitt-Mechelke, T., et al. (2016). Inflammatory markers in pediatric stroke: an attempt to better understanding the pathophysiology. *Eur. J. Paediatr. Neurol.* 20, 252–260. doi: 10.1016/j.ejpn.2015.12.006

Carmichael, S. T. (2005). Rodent models of focal stroke: size, mechanism, and purpose. *NeuroRx* 2, 396–409. doi: 10.1602/neurorx.2.3.396

Carreau, A., El Hafny-Rahbi, B., Matejuk, A., Grillon, C., and Kieda, C. (2011). Why is the partial oxygen pressure of human tissues a crucial parameter? Small molecules and hypoxia. *J. Cell. Mol. Med.* 15, 1239–1253. doi: 10.1111/j.1582-4934.2011.01258.x

Cnossen, M. H., van Ommen, C. H., and Appel, I. M. (2009). Etiology and treatment of perinatal stroke; a role for prothrombotic coagulation factors? *Semin. Fetal Neonatal Med.* 14, 311–317. doi: 10.1016/j.siny.2009.07.004

Del Duca, D., Wong, G., Trieu, P., Rodaros, D., Kouremenos, A., Tadevosyan, A., et al. (2009). Association of neonatal hypoxia with lasting changes in left ventricular gene expression: an animal model. *J. Thorac. Cardiovasc. Surg.* 138, 538–546.e1. doi: 10.1016/j.jtcvs.2009.04.042

Deruelle, P., Balasubramaniam, V., Kunig, A. M., Seedorf, G. J., Markham, N. E., and Abman, S. H. (2006). BAY 41-2272, a direct activator of soluble guanylate cyclase, reduces right ventricular hypertrophy and prevents pulmonary vascular remodeling during chronic hypoxia in neonatal rats. *Neonatology* 90, 135–144. doi: 10.1159/000092518

Dirnagl, U., Iadecola, C., and Moskowitz, M. A. (1999). Pathobiology of ischaemic stroke: an integrated view. *Trends Neurosci.* 22, 391–397. doi: 10.1016/S0166-2236(99)01401-0

Dunn, R., Queenan, B. N., Pak, D. T. S., and Forcelli, P. A. (2017). Divergent effects of levetiracetam and tiagabine against spontaneous seizures in adult rats following neonatal hypoxia. *Epilepsy Res.* 140, 1–7. doi: 10.1016/j.eplepsyres.2017.12.006

Faa, A., Iacovidou, N., Xanthos, T., Locci, A., Pampaloni, P., Aroni, F., et al. (2012). Hypoxia/reoxygenation-induced myocardial lesions in newborn piglets are related to interindividual variability and not to oxygen concentration. *Clinics* 67, 503–508. doi: 10.6061/clinics/2012(05)16

Fendt, M., Lex, A., Falkai, P., Henn, F., and Schmitt, A. (2008). Behavioural alterations in rats following neonatal hypoxia and effects of clozapine: implications for schizophrenia. *Pharmacopsychiatry* 41, 138–145. doi: 10.1055/s-2008-1058107

Fernández-López, D., Faustino, J., Derugin, N., and Vexler, Z. S. (2013). Acute and chronic vascular responses to experimental focal arterial stroke in the neonate rat. *Transl. Stroke Res.* 4, 179–188. doi: 10.1007/s12975-012-0214-5

Fernández-López, D., Natarajan, N., Ashwal, S., and Vexler, Z. S. (2014). Mechanisms of perinatal arterial ischemic stroke. *J. Cereb. Blood Flow Metab.* 34, 921–932. doi: 10.1038/jcbfm.2014.41

Ferreira, R., Fonseca, M. C., Santos, T., Sargento-Freitas, J., Tjeng, R., Paiva, F., et al. (2016). Retinoic acid-loaded polymeric nanoparticles enhance vascular regulation of neural stem cell survival and differentiation after ischaemia. *Nanoscale* 8, 8126–8137. doi: 10.1039/C5NR09077F

Garberg, H. T., Solberg, R., Barlinn, J., Martinez-Orgado, J., Løberg, E.-M., and Saugstad, O. D. (2017). High-dose cannabidiol-induced hypotension after global hypoxia-ischemia in piglets. *Neonatology* 112, 143–149. doi: 10.1159/000471786

Gersony, W. M., Morishima, H. O., Daniel, S. S., Kohl, S., Cohen, H., Brown, W., et al. (1976). The hemodynamic effects of intrauterine hypoxia: an experimental model in newborn lambs. *J. Pediatr.* 89, 631–635. doi: 10.1016/S0022-3476(76)80406-4

Girard, S., Kadhim, H., Beaudet, N., Sarret, P., and Sébire, G. (2009). Developmental motor deficits induced by combined fetal exposure to lipopolysaccharide and early neonatal hypoxia/ischemia: a novel animal model for cerebral palsy in very premature infants. *Neuroscience* 158, 673–682. doi: 10.1016/j.neuroscience.2008.10.032

Gonzalez, F. F., and Ferriero, D. M. (2009). Neuroprotection in the newborn infant. *Clin. Perinatol.* 36, 859–880, vii. doi: 10.1016/j.clp.2009.07.013

Govaert, P., Ramenghi, L., Taal, R., de Vries, L., and Deveber, G. (2009). Diagnosis of perinatal stroke I: definitions, differential diagnosis and registration. *Acta Paediatr.* 98, 1556–1567. doi: 10.1111/j.1651-2227.2009.01461.x

Gunny, R. S., and Lin, D. (2012). Imaging of perinatal stroke. *Magn. Reson. Imaging Clin. N. Am.* 20, 1–33. doi: 10.1016/j.mric.2011.10.001

Hagberg, H., Mallard, C., Ferriero, D. M., Vannucci, S. J., Levison, S. W., Vexler, Z. S., et al. (2015). The role of inflammation in perinatal brain injury. *Nat. Rev. Neurol.* 11, 192–208. doi: 10.1038/nrneurol.2015.13

Harbert, M. J., Tam, E. W., Glass, H. C., Bonifacio, S. L., Haeusslein, L. A., Barkovich, A. J., et al. (2011). Hypothermia is correlated with seizure absence in perinatal stroke. *J. Child. Neurol.* 26, 1126–1130. doi: 10.1177/0883073811408092

Heyer, A., Hasselblatt, M., von Ahsen, N., Häfner, H., Sirén, A. L., and Ehrenreich, H. (2005). *In vitro* gender differences in neuronal survival on hypoxia and in 17beta-estradiol-mediated neuroprotection. *J. Cereb. Blood Flow Metab.* 25, 427–430. doi: 10.1038/sj.jcbfm.9600056

Jantzie, L. L., Cheung, P. Y., and Todd, K. G. (2005). Doxycycline reduces cleaved caspase-3 and microglial activation in an animal model of neonatal hypoxia-ischemia. *J. Cereb. Blood Flow Metab.* 25, 314–324. doi: 10.1038/sj.jcbfm.9600025

Jantzie, L. L., and Todd, K. G. (2010). Doxycycline inhibits proinflammatory cytokines but not acute cerebral cytogenesis after hypoxia–ischemia in neonatal rats. *J. Psychiatry Neurosci.* 35, 20. doi: 10.1503/jpn.090061

Jensen, F. (1995). An animal model of hypoxia-induced perinatal seizures. *Ital. J. Neurol. Sci.* 16, 59–68. doi: 10.1007/BF02229075

Johnston, M. V. (2005). Excitotoxicity in perinatal brain injury. *Brain Pathol.* 15, 234–240. doi: 10.1111/j.1750-3639.2005.tb00526.x

Kameda, S. R., Fukushiro, D. F., Wuo-Silva, R., Trombin, T. F., Procópio-Souza, R., Brandão, L. C., et al. (2013). Opposite effects of neonatal hypoxia on acute amphetamine-induced hyperlocomotion in adult and adolescent mice. *Psychiatry Res.* 208, 74–77. doi: 10.1016/j.psychres.2013.03.021

Kartal, Ö., Aydinöz, S., Kartal, A. T., Kelestemur, T., Caglayan, A. B., Beker, M. C., et al. (2016). Time dependent impact of perinatal hypoxia on growth hormone, insulin-like growth factor 1 and insulin-like growth factor binding protein-3. *Metab. Brain Dis.* 31, 827–835. doi: 10.1007/s11011-016-9816-z

Kasdorf, E., and Perlman, J. M. (2013). Hyperthermia, inflammation, and perinatal brain injury. *Pediatr. Neurol.* 49, 8–14. doi: 10.1016/j.pediatrneurol.2012.12.026

Kichev, A., Rousset, C. I., Baburamani, A. A., Levison, S. W., Wood, T. L., Gressens, P., et al. (2014). Tumor necrosis factor-related apoptosis-inducing ligand (TRAIL) signaling and cell death in the immature central nervous system after hypoxia-ischemia and inflammation. *J. Biol. Chem.* 289, 9430–9439. doi: 10.1074/jbc.M113.512350

Kratzer, I., Chip, S., and Vexler, Z. S. (2014). Barrier mechanisms in neonatal stroke. *Front. Neurosci.* 8:359. doi: 10.3389/fnins.2014.00359

Kurnik, K., Kosch, A., Sträter, R., Schobess, R., Heller, C., Nowak-Göttl, U., et al. (2003). Recurrent thromboembolism in infants and children suffering from symptomatic neonatal arterial stroke: a prospective follow-up study. *Stroke* 34, 2887–2892. doi: 10.1161/01.STR.0000103745.03393.39

Lafemina, M. J., Sheldon, R. A., and Ferriero, D. M. (2006). Acute hypoxia-ischemia results in hydrogen peroxide accumulation in neonatal but not adult mouse brain. *Pediatr. Res.* 59, 680–683. doi: 10.1203/01.pdr.0000214891.35363.6a

Lange, C., Storkebaum, E., de Almodóvar, C. R., Dewerchin, M., and Carmeliet, P. (2016). Vascular endothelial growth factor: a neurovascular target in neurological diseases. *Nat. Rev. Neurol.* 12, 439–454. doi: 10.1038/nrneurol.2016.88

Lee, H. S., Han, J., Bai, H. J., and Kim, K. W. (2009). Brain angiogenesis in developmental and pathological processes: regulation, molecular and cellular communication at the neurovascular interface. *FEBS J.* 276, 4622–4635. doi: 10.1111/j.1742-4658.2009.07174.x

Lee, J., Croen, L. A., Backstrand, K. H., Yoshida, C. K., Henning, L. H., Lindan, C., et al. (2005). Maternal and infant characteristics associated with perinatal arterial stroke in the infant. *J. Am. Med. Assoc.* 293, 723–729. doi: 10.1001/jama.293.6.723

Leonardo, C. C., Hall, A. A., Collier, L. A., Gottschall, P. E., and Pennypacker, K. R. (2009). Inhibition of gelatinase activity reduces neural injury in an *ex vivo* model of hypoxia-ischemia. *Neuroscience* 160, 755–766. doi: 10.1016/j.neuroscience.2009.02.080

Leong, X. F., Ng, C. Y., and Jaarin, K. (2015). Animal models in cardiovascular research: hypertension and atherosclerosis. *BioMed Res. Int.* 2015, 528–757. doi: 10.1155/2015/528757

Leviton, A., and Gressens, P. (2007). Neuronal damage accompanies perinatal white-matter damage. *Trends Neurosci.* 30, 473–478. doi: 10.1016/j.tins.2007.05.009

Li, H., Pin, S., Zeng, Z., Wang, M. M., Andreasson, K. A., and McCullough, L. D. (2005). Sex differences in cell death. *Ann. Neurol.* 58, 317–321. doi: 10.1002/ana.20538

Lubics, A., Reglodi, D., Tamás, A., Kiss, P., Szalai, M., Szalontay, L., et al. (2005). Neurological reflexes and early motor behavior in rats subjected to neonatal hypoxic–ischemic injury. *Behav. Brain Res.* 157, 157–165. doi: 10.1016/j.bbr.2004.06.019

Luhmann, H. J., Sinning, A., Yang, J. W., Reyes-Puerta, V., Stüttgen, M. C., Kirischuk, S., et al. (2016). Spontaneous neuronal activity in developing neocortical networks: from single cells to large-scale interactions. *Front. Neural Circuits* 10:40. doi: 10.3389/fncir.2016.00040

Machado, V., Pimentel, S., Pinto, F., and Nona, J. (2015). Perinatal ischemic stroke: a five-year retrospective study in a level-III maternity. *Einstein* 13, 65–71. doi: 10.1590/S1679-45082015AO3056

Machado-Pereira, M., Santos, T., Ferreira, L., Bernardino, L., and Ferreira, R. (2017). Anti-inflammatory strategy for M2 microglial polarization using retinoic acid-loaded nanoparticles. *Mediators Inflamm.* 2017, 6742427. doi: 10.1155/2017/6742427

Machado-Pereira, M., Santos, T., Ferreira, L., Bernardino, L., and Ferreira, R. (2018). Intravenous administration of retinoic acid-loaded polymeric nanoparticles prevents ischemic injury in the immature brain. *Neurosci. Lett.* 673, 116–121. doi: 10.1016/j.neulet.2018.02.066

McQuillen, P. S., Sheldon, R. A., Shatz, C. J., and Ferriero, D. M. (2003). Selective vulnerability of subplate neurons after early neonatal hypoxia-ischemia. *J. Neurosci.* 23, 3308–3315. doi: 10.1523/JNEUROSCI.23-08-03308.2003

Mirabelli-Badenier, M., Braunersreuther, V., Lenglet, S., Galan, K., Veneselli, E., Viviani, G. L., et al. (2012). Pathophysiological role of inflammatory molecules in paediatric ischaemic brain injury. *Eur. J. Clin. Invest.* 42, 784–794. doi: 10.1111/j.1365-2362.2012.02640.x

Nelson, K. B. (2007). Perinatal ischemic stroke. *Stroke* 38, 742–745. doi: 10.1161/01.STR.0000247921.97794.5e

Nelson, K. B., and Lynch, J. K. (2004). Stroke in newborn infants. *Lancet Neurol.* 3, 150–158. doi: 10.1016/S1474-4422(04)00679-9

Ni, X., Yang, Z.-J., Carter, E. L., Martin, L. J., and Koehler, R. C. (2011). Striatal neuroprotection from neonatal hypoxia-ischemia in piglets by antioxidant treatment with EUK-134 or edaravone. *Dev. Neurosci.* 33, 299–311. doi: 10.1159/000327243

Rymo, S. F., Gerhardt, H., Sand, F. W., Lang, R., Uv, A., and Betsholtz, C. (2011). A two-way communication between microglial cells and angiogenic sprouts regulates angiogenesis in aortic ring cultures. *PLoS ONE* 6:e15846. doi: 10.1371/journal.pone.0015846

Schaeffer, E. L., Kühn, F., Schmitt, A., Gattaz, W. F., Gruber, O., Schneider-Axmann, T., et al. (2013). Increased cell proliferation in the rat anterior cingulate cortex following neonatal hypoxia: relevance to schizophrenia. *J. Neural Transm.* 120, 187–195. doi: 10.1007/s00702-012-0859-y

Sengupta, P. (2013). The laboratory rat: relating its age with human's. *Int. J. Prev. Med.* 4, 624–630.

Sheldon, R. A., Chuai, J., and Ferriero, D. M. (1996). A rat model for hypoxic-ischemic brain damage in very premature infants. *Neonatology* 69, 327–341. doi: 10.1159/000244327

Sheldon, R. A., Sedik, C., and Ferriero, D. M. (1998). Strain-related brain injury in neonatal mice subjected to hypoxia–ischemia. *Brain Res.* 810, 114–122. doi: 10.1016/S0006-8993(98)00892-0

Shen, Y., Plane, J. M., and Deng, W. (2010). Mouse models of periventricular leukomalacia. *J. Vis. Exp.* 39, 1951. doi: 10.3791/1951

Silverstein, F., and Johnston, M. V. (1984). Effects of hypoxia-ischemia on monoamine metabolism in the immature brain. *Ann. Neurol.* 15, 342–347. doi: 10.1002/ana.410150407

Slotkin, T. A., Lappi, S. E., McCook, E. C., Lorber, B. A., and Seidler, F. J. (1995). Loss of neonatal hypoxia tolerance after prenatal nicotine exposure: implications for sudden infant death syndrome. *Brain Res. Bull.* 38, 69–75. doi: 10.1016/0361-9230(95)00073-N

Sommer, C. J. (2017). Ischemic stroke: experimental models and reality. *Acta Neuropathol.* 133, 245–261. doi: 10.1007/s00401-017-1667-0

Stevens, J. P., Churchill, T., Fokkelman, K., Haase, E., Idikio, H., Korbutt, G., et al. (2008). Oxidative stress and matrix metalloproteinase-9 activity in the liver after hypoxia and reoxygenation with 21% or 100% oxygen in newborn piglets. *Eur. J. Pharmacol.* 580, 385–393. doi: 10.1016/j.ejphar.2007.11.019

Suzuki, Y., Nagai, N., and Umemura, K. (2016). A review of the mechanisms of blood-brain barrier permeability by tissue-type plasminogen activator treatment for cerebral ischemia. *Front. Cell Neurosci.* 10:2. doi: 10.3389/fncel.2016.00002

Tam, S. J., and Watts, R. J. (2010). Connecting vascular and nervous system development: angiogenesis and the blood-brain barrier. *Annu. Rev. Neurosci.* 33, 379–408. doi: 10.1146/annurev-neuro-060909-152829

Titomanlio, L., Fernández-López, D., Manganozzi, L., Moretti, R., Vexler, Z. S., and Gressens, P. (2015). Pathophysiology and neuroprotection of global and focal perinatal brain injury: lessons from animal models. *Pediatr. Neurol.* 52, 566–584. doi: 10.1016/j.pediatrneurol.2015.01.016

Tornabene, E., and Brodin, B. (2016). Stroke and drug delivery–*in vitro* models of the ischemic blood-brain barrier. *J. Pharma. Sci.* 105, 398–405. doi: 10.1016/j.xphs.2015.11.041

Turtzo, L. C., and McCullough, L. D. (2010). Sex-specific responses to stroke. *Fut. Neurol.* 5, 47–59. doi: 10.2217/fnl.09.66

Vannucci, R. C., and Vannucci, S. J. (2005). Perinatal hypoxic-ischemic brain damage: evolution of an animal model. *Dev. Neurosci.* 27, 81–86. doi: 10.1159/000085978

Vasudevan, A., and Bhide, P. G. (2008). Angiogenesis in the embryonic CNS: a new twist on an old tale. *Cell Adh. Migr.* 2, 167–169. doi: 10.4161/cam.2.3.6485

Vexler, Z. S., and Yenari, M. A. (2009). Does inflammation after stroke affect the developing brain differently than adult brain? *Dev. Neurosci.* 31, 378–393. doi: 10.1159/000232556

Webber, D. J., Van Blitterswijk, M., and Chandran, S. (2009). Neuroprotective effect of oligodendrocyte precursor cell transplantation in a long-term model of periventricular leukomalacia. *Am. J. Pathol.* 175, 2332–2342. doi: 10.2353/ajpath.2009.090051

Wolterink-Donselaar, I. G., Meerding, J. M., and Fernandes, C. (2009). A method for gender determination in newborn dark pigmented mice. *Lab. Anim.* 38, 35–38. doi: 10.1038/laban0109-35

Xu, G., Broadbelt, K. G., Haynes, R. L., Folkerth, R. D., Borenstein, N. S., Belliveau, R. A., et al. (2011). Late development of the GABAergic system in the human cerebral cortex and white matter. *J. Neuropathol. Exp. Neurol.* 70, 841–858. doi: 10.1097/NEN.0b013e31822f471c

Yu, L., Derrick, M., Ji, H., Silverman, R. B., Whitsett, J., Vásquez-Vivar, J., et al. (2011). Neuronal nitric oxide synthase inhibition prevents cerebral palsy following hypoxia-ischemia in fetal rabbits: comparison between JI-8 and 7-nitroindazole. *Dev. Neurosci.* 33, 312–319. doi: 10.1159/000327244

Conflict of Interest Statement: The authors declare that the research was conducted in the absence of any commercial or financial relationships that could be construed as a potential conflict of interest.

frontiers in Cellular Neuroscience

ORIGINAL RESEARCH
published: 06 September 2018
doi: 10.3389/fncel.2018.00279

Brain Endothelial Erythrophagocytosis and Hemoglobin Transmigration Across Brain Endothelium: Implications for Pathogenesis of Cerebral Microbleeds

*Rudy Chang[1], Juan Castillo[2], Alexander C. Zambon[1], Tatiana B. Krasieva[3], Mark J. Fisher[4] and Rachita K. Sumbria[1,4]**

[1] Department of Biopharmaceutical Sciences, School of Pharmacy and Health Sciences, Keck Graduate Institute, Claremont, CA, United States, [2] Department of Neuroscience, Claremont McKenna College, Claremont, CA, United States, [3] Beckman Laser Institute, University of California, Irvine, Irvine, CA, United States, [4] Departments of Neurology and Pathology & Laboratory Medicine, University of California, Irvine, Irvine, CA, United States

OPEN ACCESS

Edited by:
Sikha Saha,
University of Leeds, United Kingdom

Reviewed by:
Ayman ElAli,
CHU de Québec Research Center, Canada
Ulrich Bickel,
Texas Tech University Health Sciences Center, United States

***Correspondence:**
Rachita K. Sumbria
rsumbria@kgi.edu

Received: 22 February 2018
Accepted: 08 August 2018
Published: 06 September 2018

Citation:
Chang R, Castillo J, Zambon AC, Krasieva TB, Fisher MJ and Sumbria RK (2018) Brain Endothelial Erythrophagocytosis and Hemoglobin Transmigration Across Brain Endothelium: Implications for Pathogenesis of Cerebral Microbleeds.
Front. Cell. Neurosci. 12:279.
doi: 10.3389/fncel.2018.00279

Peripheral endothelial cells are capable of erythrophagocytosis, but data on brain endothelial erythrophagocytosis are limited. We studied the relationship between brain endothelial erythrophagocytosis and cerebral microhemorrhage, the pathological substrate of MRI-demonstrable cerebral microbleeds. To demonstrate the erythrophagocytic capability of the brain endothelium, we studied the interactions between brain endothelial cells and red blood cells exposed to oxidative stress *in vitro*, and developed a new *in vitro* cerebral microbleeds model to study the subsequent passage of hemoglobin across the brain endothelial monolayer. Using multiple approaches, our results show marked brain endothelial erythrophagocytosis of red blood cells exposed to oxidative stress compared with control red blood cells *in vitro*. This brain endothelial erythrophagocytosis was accompanied by passage of hemoglobin across the brain endothelial monolayer with unaltered monolayer integrity. *In vivo* and confocal fluorescence microscopy studies confirmed the extravasation of RBC exposed to oxidative stress across brain endothelium. These findings, demonstrating erythrophagocytosis mediated by the brain endothelial monolayer and the subsequent passage of iron-rich hemoglobin *in vitro* and RBC *in vivo*, may have implications for elucidating mechanisms involved in the development of cerebral microbleeds that are not dependent on disruption of the microvasculature.

Keywords: erythrophagocytosis, cerebral microbleeds, brain endothelial cells, hemoglobin, red blood cells, transmigration

INTRODUCTION

Cerebral microhemorrhages are tiny deposits of blood degradation products in the brain and are the pathological substrate of cerebral microbleeds (CMB). CMB are associated with increasing age, cerebrovascular diseases, hypertension, and chronic kidney disease (Lau et al., 2017). Mechanistically, it is widely accepted that loss of vascular integrity due to an underlying disruption of the cerebral microvasculature causes CMB development, and these are classified as primary microbleeds (Fisher, 2014). Other mechanisms involved in CMB development include hemorrhagic infarction/microinfarction, and these are classified as secondary microbleeds (Fisher, 2013, 2014). Besides the involvement of hemorrhagic and ischemic processes in the development of CMB, there has been some indication that release of iron from oligodendrocytes during ischemia may result in MRI-demonstrable CMB (Janaway et al., 2014). Further, the existence of *pseudo-microbleeds*, a phenomenon in which iron-rich hemosiderin from red blood cells (RBC) produces signatures of CMB in the absence of vascular disruption, has been proposed (Fisher, 2014).

A recent study showed that brain endothelium have phagocytic properties and that brain vascular endothelial cells are capable of engulfing and translocating intracranial emboli into the brain extravascular space, a process termed angiophagy (Grutzendler et al., 2014). The concept of angiophagy has some similarities to endothelial erythrophagocytosis, a recently described process by which injured or aged erythrocytes are ingested by endothelial cells, undergo hemolysis, and are cleared from the blood circulation (Fens et al., 2010). Endothelial erythrophagocytosis has recently been reported by peripheral endothelial cells using human umbilical vein endothelial (HUVEC) and hepatic sinusoidal endothelial cells *in vitro,* and has further been confirmed *in vivo* (Fens et al., 2010, 2012; Lee et al., 2011).

In the cerebral milieu, macrophage-mediated erythrophagocytosis has been well-documented (Zhao et al., 2009), and the involvement of macrophages in CMB is known (Fisher et al., 2010). Besides macrophages, pericytes are known to have phagocytic function and there is some evidence of pericyte mediated erythrophagocytosis in the brain (Fisher et al., 2010). Phagocytosis of parasitized RBC by brain endothelium within an inflammatory milieu has been reported in *in vitro* studies of cerebral malaria (Jambou et al., 2010). Involvement of brain endothelium in phagocytosis of non-parasitized aged and/or injured RBC and subsequent transmigration of RBC or RBC degradation products (hemoglobin) into the brain has not been reported. It has been proposed that iron-rich extravasated RBC or RBC degradation products may produce MRI signatures of CMB in the absence of vascular disruption (pseudo-microbleeds) (Fisher, 2014).

The above prompted us to investigate the role of the brain endothelium in mediating erythrophagocytosis of aged and/or injured RBC, and subsequent passage of RBC and/or RBC degradation product hemoglobin into the brain. In the current proof-of-concept study to demonstrate brain endothelial erythrophagocytosis, RBC were treated with phosphate buffer saline (PBS) or tert-butylhydroperoxide (t-BHP), an oxidative stressor that results in the exposure of RBC phosphatidylserine (PS) to mimic aged and/or injured RBC marked for phagocytic removal from the circulation (Schroit et al., 1985). Using multiple approaches, our results show robust adhesion and engulfment (erythrophagocytosis) of t-BHP-RBC by brain endothelial cells (bEND3) compared with PBS-RBC. We developed a new CMB *in vitro* model system to study passage of RBC degradation product hemoglobin across bEND3 cells, and show passage of hemoglobin from t-BHP-treated RBC across the bEND3 monolayer with unaltered monolayer integrity. Our *in vitro* results were corroborated by our *in vivo* findings of extrusion of fluorescently-labeled RBC across the mouse brain endothelium. These results may have important implications for elucidating mechanisms involved in the development of CMB demonstrated on brain MRI.

MATERIALS AND METHODS

Red Blood Cell Preparation and Treatment

Purified RBC in Alsevers solution were derived from 2 to 3 month-old male BALB/c mice (BioReclamation IVT, New York, NY). RBC were washed and resuspended in sterile PBS (without $Ca^{2+}$and Mg^{2+}) before experimental treatment with PBS (control; incubation time: 30 min), lipopolysaccharide derived from gram negative bacterium Salmonella Typhimurium (LPS, 10 μg/mL; incubation time: 1 h; an inflammatory stimulus), neuraminidase enzyme from vibrio cholerae (0.125 U or 0.5 U; incubation time: 1 h; for senescence induction) or various concentrations (0.3, 1.0, 3.0 mM) of t-BHP (incubation time: 30 min; an oxidative stressor) at 37°C. LPS, neuraminidase, and t-BHP were selected for the current study based on previous studies using peripheral endothelial cells (Tissot Van Patot et al., 1996; Fens et al., 2012; Yang et al., 2014). After treatment, RBC were washed and resuspended in sterile PBS to desired concentrations described below. All the above materials were purchased from Sigma-Aldrich, St. Louis, MO.

Brain Endothelial Cell Culture

Murine brain microvascular endothelial cells (bEND3 cells; American Type Culture Collection, Manassas, VA) between passages 22 and 31 were grown on T75 flasks in Delbucco's Modified Eagle's Medium (DMEM) containing 0.45% glucose, 0.37% $NaHCO_3$, 4 mM Glutamine, 10% fetal bovine serum, and 100 μg/ml penicillin/streptomycin (Sigma, St. Louis, MO). After reaching 70–80% confluency, cells were subcultured in complete DMEM and seeded onto 6-well plates (5×10^5 bEND3 cells per well), 24 well plates with 0.2% gelatin coated glass cover slips (1×10^5 bEND3 cells per coverslip), or 12-well transwells with 3 μm pore polyester membrane inserts with a surface area of 1.12 cm^2 (Corning, New York, NY) (1×10^5 bEND3 cells per well). For all the experiments, 5×10^6 treated RBC were incubated with the seeded bEND3 cells for up to 24 h at 37°C in 5% CO_2. For initial experiments, 24 h after initial seeding of bEND3 cells grown on 24 well plates with 0.2% gelatin coated cover glass, bEND3 cells were primed with or without 100 ng/mL of LPS for another 24 h

before being incubated with treated RBC to determine the effect of endothelial activation on RBC-bEND3 interactions.

Annexin V-FITC Labeling

To quantify the percentage of treated RBC with PS exposure, t-BHP- and PBS-treated RBC were labeled with annexin-V-FITC (BioLegend, San Diego, CA) as per the manufacturer's instructions. Briefly, after wash and resuspension of RBC in sterile PBS, 1×10^6 RBC were incubated in FITC-labeled annexin-V and 1.2 mM Ca^{2+} for 30 min in the dark. After washing and resuspending in sterile PBS, RBC were quantified with a flow cytometer (Accuri C6 Plus, BD, Franklin lakes, NJ) using logarithmic gain for light scatter and fluorescence channels with gating and background settings defined through the PBS/control RBC.

Hematoxylin and Eosin Staining

Twenty-four hours after initial bEND3 seeding on 0.2% gelatin coated glass coverslips in 24 well plates, the cells were incubated with RBC treated either with PBS or t-BHP for 3 h, 18 h and 24 h. Glass cover-slips were then fixed with 4% paraformaldehyde (PFA) for 15 min on ice followed by hematoxylin and eosin (H&E) staining. Briefly, each coverslip was washed with ice cold PBS, stained with hematoxylin for 10 min followed by Scott's Tap Water wash, stained with eosin Y for 8 min, and washed with ethanol and dipped in xylene before mounting. Six fields of view per coverslip were manually quantified by an observer blinded to the treatment using light microscopy at a 20X magnification to estimate: RBC adhesion: RBC to bEND3 ratio (expressed as %) and engulfment: % of bEND3 that were positive for RBC engulfment.

Diaminofluorene Assay

H&E staining results were confirmed using a colorimetric assay which is based on the pseudoperoxidase activity of hemoglobin using 2,7-diaminofluorene (DAF) (Sigma, St. Louis, MO) substrate and hydrogen peroxide (Gebran et al., 1992). For this, bEND3 cells seeded onto 6-well plates at 5×10^5 cells per well for 72 h at 37°C in 5% CO_2 were used. After 72 h, cell media was changed from the FBS-supplemented DMEM to strictly FBS-free DMEM. After media change, RBC treated with PBS or t-BHP were incubated with the bEND3 cells for 24 h. bEND3 cells without RBC served as control (bEND3 only group). After incubation, the supernatant media of the wells was aspirated, wells were washed with distilled water to lyse attached RBC (RBC that are not engulfed by endothelial cells) and incubated with 0.2M Tris-HCl buffer containing 6M urea lysis solution for 30 min, followed by circular scrubbing with cell scrappers to further lyse bEND3 cells to release hemoglobin. DAF dye stock solution (10 mg/mL in 90% acetic acid) was added to 10 mL of 6M urea with 100 μL of hydrogen peroxide to make a DAF working solution which was used to react with 100 μL of supernatant of each well prepared above and immediately read on a SpectraMax 384 microplate reader (Molecular Devices, Sunnyvale, CA) at 620 nm. A hemoglobin standard (Lee Biosolutions, Maryland Heights, MO) was used to estimate the amount of hemoglobin which is an indicator of the extent of erythrophagocytosis. The amount of hemoglobin was expressed as % of hemoglobin detected with the bEND3 only group. Published studies have shown that high concentrations of t-BHP convert hemoglobin to methemoglobin (Murakami and Mawatari, 2003), which is not detected by the DAF assay. This was further confirmed in our lab (data not shown) and as a result, the DAF assay was performed using the lowest dose of t-BHP (0.3 mM).

Red Blood Cell Incubation Viability

The viability of PBS- and t-BHP-treated RBC in cell culture incubation environment was assessed by incubating treated RBC (5×10^6 cells per well) in DMEM or FBS-free DMEM into 24 well plates. After 24 h, 10 μL cells were collected and mixed with trypan blue at 1:1, and manually counted with a hemocytometer for both live and dead RBC based on trypan blue exclusion. Viable RBC were expressed as % of total RBC.

Confocal Microscopy

Brain endothelial cell tight-junctions were imaged and analyzed through Zonula Occludens-1 (ZO-1) staining and confocal microscopy. Twenty-four hours after initial bEND3 seeding on 0.2% gelatin coated glass coverslips in 24 well plates, the cells were incubated with RBC treated either with PBS or t-BHP for 24 h. Glass cover-slips were then fixed with 2% PFA, blocked in 5% bovine serum albumin (BSA) in PBS with 0.1% tritonX-100, incubated with ZO-1 antibody (1:100, ZO-1 Alexa Flour 488, SantaCruz Biotechnology, Dallas, TX; Antibody Registry Accession No. AB_628459) in PBS with 0.75% BSA overnight at 4°C, followed by endothelial nuclear staining with DRAQ5 (BioLegend, San Diego, CA). Cover-slips were mounted with VectaShield Hardset Mounting Medium (Vector Labs, Burlingame, CA) and imaged with a Leica SP5 confocal microscope (Leica, Wetzlar, Germany).

Live Imaging

To visualize the time-lapse of events that occurs between bEND3 cells and RBC, PBS- and t-BHP-treated RBC that were incubated with bEND3 cells on 6-well plates were placed in an incubator (37°C in 5% CO_2) with LumaScope 720 imaging microscope (EtaLuma, Carlsbad, CA) that captured images of each well every 2.5 min over a course of 24 h. The timestamped images were then compiled into an mpeg file that illustrated the time-lapse at 3 frames per second.

Transmigration of Hemoglobin Across the bEND3 Monolayer

To determine the appropriate time to initiate the transmigration experiments, the integrity of the bEND3 monolayer in the transwells was assessed by performing transendothelial electrical resistance (TEER) measurements using the EVOM2 Epithelial Volt/Ohm Meter and an STX-2 electrode system (World Precision Instruments LLC, Sarasota, FL) at various time points (3, 24, 48, and 72 h) in each well.

The experimental setup of the transmigration experiment is shown in **Figure 4A**. To assess whether hemoglobin from treated

RBC migrates through the endothelial monolayer, bEND3 cells were cultured onto the apical wells of the transwells with complete DMEM for 72 h (time at which maximum TEER was obtained; data not shown), followed by replacement of the complete DMEM with FBS-free DMEM. PBS- and t-BHP-treated RBC were then added to the apical wells, incubated undisturbed for 24 h at 37°C in 5% CO_2. Endothelial cells grown on transwell inserts without RBC served as controls (bEND3 only group). After incubation, media in the basolateral well was gently mixed and 200 μL of the media was collected and lysed with 200 μL of 0.2 M Tris-HCl buffer containing 6 M urea for 15 min at RT. The basolateral aliquot was then examined for hemoglobin passage across the bEND3 monolayer using the DAF and hemoglobin standard assay described above. Passage of hemoglobin across bEND3 monolayer-free transwell insert was used to assess spontaneous migration of hemoglobin across the transwell insert. Hemoglobin amount was expressed as % bEND3 only group (control).

TEER measurements were performed in triplicates per insert before addition of RBC to the apical well (0 h) and 24 h after RBC incubation to assess monolayer integrity during the transmigration experiment. All TEER values were corrected for the blank TEER of monolayer-free transwell inserts and represented at % PBS RBC values.

In vivo Passage of RBC Across the Brain Endothelium

All animal procedures were approved by UCI Institutional Animal Care and Use Committee and were carried out in compliance with University Laboratory Animal Resources regulations. Passage of t-BHP-treated RBC across the brain endothelium was visualized using postmortem confocal fluorescence microscopy. Adult male Tie2-GFP mice (10–12 week old, Jackson Laboratory, Bar Harbor, ME) with green fluorescent protein (GFP) labeled endothelial cells were used for imaging. Briefly, autologous blood (200–250 μL) was collected from Tie2-GFP mice ($n = 2$) and RBC were purified using Ficoll-Paque (GE Healthcare, Uppsala, Sweden) gradient. After several washes in PBS, RBC were treated with PBS or 3 mM t-BHP for 30 min at 37°C as described above and stained with PKH-26 Red Fluorescent Cell Linker Kit (Sigma, St. Louis, MO) according to manufacturer's instructions and re-injected into the mice intravenously. Mice were euthanized 24 h after RBC injection using a lethal dose of Euthasol (150 mg/kg, i.p.) and whole brains were harvested for postmortem confocal fluorescence microscopy to visualize passage of RBC across the brain endothelium.

Fluorescence images of whole brains were obtained using Zeiss LSM 510 microscopy system equipped with a longworking distance Zeiss 40x, 0.8 NA water immersion objective. Laser scanning did not induce any visible damage to the tissue or noticeable bleaching of the sample. Stacks of images were acquired with the z-step (distance between consecutive imaging planes) of 2.5 μm. The maximum depth for imaging was up to 80 μm from the brain surface. The probed 3D volume was reconstructed by Zeiss LSM original software.

Measurement of Free Hemoglobin From RBC

bEND3 cells (1×10^5) seeded onto 24 well plates were allowed to grow to confluence and incubated with PBS- or t-BHP-treated RBC in FBS free media for 3 h, 18 h, and 24 h. At the predetermined time intervals, media was collected from each well, and placed in Amicon-100K centrifuge tubes (Fisher Scientific, Hampton, NH). After spinning for 10 min at 14,000 RPM, the filtrate at the bottom containing the free hemoglobin was collected (RBC are retained on top) and processed using the DAF assay described above to determine free hemoglobin present in the media represented as % of hemoglobin from PBS RBC (% control).

Statistical Analysis

All statistical analysis was performed using GraphPad Prism 5 (GraphPad Software Inc., La Jolla, CA). Data are presented as mean ± SEM of at least 3 independent experiments done in duplicates based on power analysis which indicated that at least 3 experiments will be needed to detect a difference of 20% between groups with a power of 80% and significance level of 5%. To compare more than 2 independent groups, one-way ANOVA with Bonferroni's correction was used. For data with more than 2 independent groups and 2 independent variables, two-way ANOVA, with or without repeated measures, was used. A two-tailed $p < 0.05$ for the entire family of comparison was considered statistically significant.

RESULTS

Three-hour incubation of PBS-treated bEND3 cells with PBS-treated RBC resulted in negligible RBC adhesion to bEND3 cells. There was a significant ($p < 0.001$) increase in the adhesion of 3 mM t-BHP-treated RBC to PBS-treated bEND3 cells compared with PBS-treated RBC incubated with PBS-treated bEND3 cells **(Figure 1A)**. Treatment of RBC with LPS or neuraminidase (0.125U or 0.5U) did not significantly alter RBC adhesion to PBS-treated bEND3 cells compared with PBS-treated RBC incubated with PBS-treated bEND3 cells **(Figure 1A)**. Treatment of the bEND3 cells with LPS did not have a significant effect on RBC adhesion under any condition tested in the current study (**Figure 1A**) or with an increase in incubation time (data not shown).

Phosphatidylserine Exposure

Studies with annexin-V FITC showed that greater than 90% of t-BHP-treated RBC are annexin-V FITC positive confirming PS exposure on the surface of t-BHP-treated RBC compared with PBS-treated RBC **(Figure 1B)**.

Concentration and Time Dependent RBC-bEND3 Erythrophagocytosis (Adhesion and Engulfment)

RBC treatment with low and medium concentrations of t-BHP (0.3 and 1 mM) resulted in negligible RBC adhesion to the bEND3 cells following 3 h incubation. RBC treatment with high

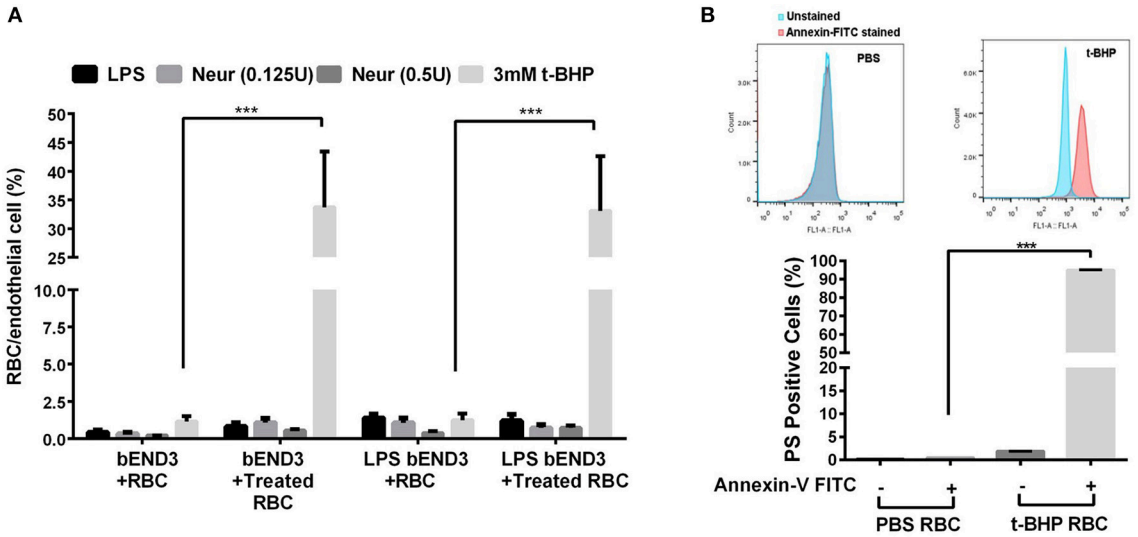

FIGURE 1 | RBC adhesion to brain endothelial (bEND3 cells) under different conditions **(A)** and PS exposure in t-BHP-treated RBC **(B)**. RBC treated with PBS (control), LPS (10 μg/mL) or neuraminidase (0.125 U or 0.5 U) did not significantly alter RBC adhesion to bEND3 cells following 3 h incubation, however, 3 mM t-BHP treatment of RBC resulted in a significant increase in RBC adhesion to bEND3 cells compared with respective PBS-treated RBC. LPS treatment of bEND3 cells did not further enhance RBC adhesion under any treatment conditions. >90% of 0.3 mM t-BHP-treated RBC were PS positive compared with PBS-treated RBC as determined by flow cytometry **(B)**. Data is presented as mean ± SEM of at least 3 independent experiments. ***$p < 0.001$.

concentration of t-BHP on the other hand resulted in significant RBC adhesion to the bEND3 cells as early as following 3 h incubation. Overall, adhesion of t-BHP-treated RBC to bEND3 cells, increased in a concentration and time dependent manner. Maximum RBC adhesion for the 0.3 mM t-BHP concentration was observed at 24 h and RBC adhesion plateaued at 18 h for 1 mM and 3 mM t-BHP concentrations **(Figure 2A,B)**.

Similarly, low and medium concentrations of t-BHP resulted in no engulfment of RBC by bEND3 cells following 3 h incubation. There was a trend toward an increase in the engulfment of 3 mM t-BHP-treated RBC following 3 h incubation. Engulfment of t-BHP-treated RBC also increased in a concentration and time dependent manner with maximum engulfment of t-BHP-treated RBC occurring following 24 h incubation **(Figure 2C)**. Overall, maximum adhesion and engulfment of t-BHP-treated RBC was observed with a concentration of 3 mM. As shown in **Figure 2D**, multiple 3 mM t-BHP-treated RBC are seen engulfed (red arrows) by a single bEND3 cell. The average number of bEND3 cells per field of view remained unchanged with adhesion and engulfment of t-BHP-RBC over the duration of the experiment **(Figure 2E)** for any experimental group and viability of the PBS- and t-BHP-treated RBC in cell culture media was > 90% at 24 h (data not shown).

DAF assay that relies on the pseudoperoxidase activity of hemoglobin was used to confirm erythrophagocytosis (adhesion and engulfment) observed by microscopy. There was no significant difference in the amount of hemoglobin detected in the bEND3 cells incubated with PBS-treated RBC compared with control (bEND3 monolayer only). However, bEND3 cells incubated with t-BHP-treated RBC had a significantly higher amount of hemoglobin, an indicator of erythrophagocytosis, compared with the control and PBS-treated RBC, confirming the light microscopy results **(Figure 2F)**.

Adhesion and engulfment of t-BHP-treated RBC by the bEND3 monolayer was further confirmed using live cell time-lapse imaging (see **Supplementary Video 1**), immunofluorescence and confocal microscopy. **Figure 3A** shows a maximum projection of a 6 μm depth z-stack image with a step size of 0.3 μm, and confirms the presence of tight junction protein ZO-1 in the confluent bEND3 monolayer (ZO-1 tight junction protein staining shown in green and bEND3 nuclei stained with DRAQ5 shown in blue). Both PBS- and t-BHP-RBC autofluoresce (green) as shown in the figure. Adhesion and engulfment of t-BHP-treated RBC is further confirmed by orthogonal and single z-stack projections **(Figure 3B)**.

Transmigration of Hemoglobin Across the bEND3 Monolayer

We developed a method to determine the passage of hemoglobin across the bEND3 monolayer using an *in vitro* transwell system. Experimental set-up for the transmigration experiment is shown in **Figure 4A**. Migration of hemoglobin across the bEND3 monolayer was determined using the DAF assay as described above. Spontaneous migration reflects the passage of hemoglobin from PBS-RBC across the 3 μm pore size transwell in the absence of a bEND3 monolayer. As expected, hemoglobin passage was observed in the absence of the bEND3 monolayer. However, in the presence of the bEND3 monolayer, the passage of hemoglobin from PBS-RBC across the bEND3 monolayer was the same as control (bEND3 only) indicating no passage of hemoglobin from PBS-RBC across the monolayer. There was a significant increase in the hemoglobin in the basolateral chamber of wells

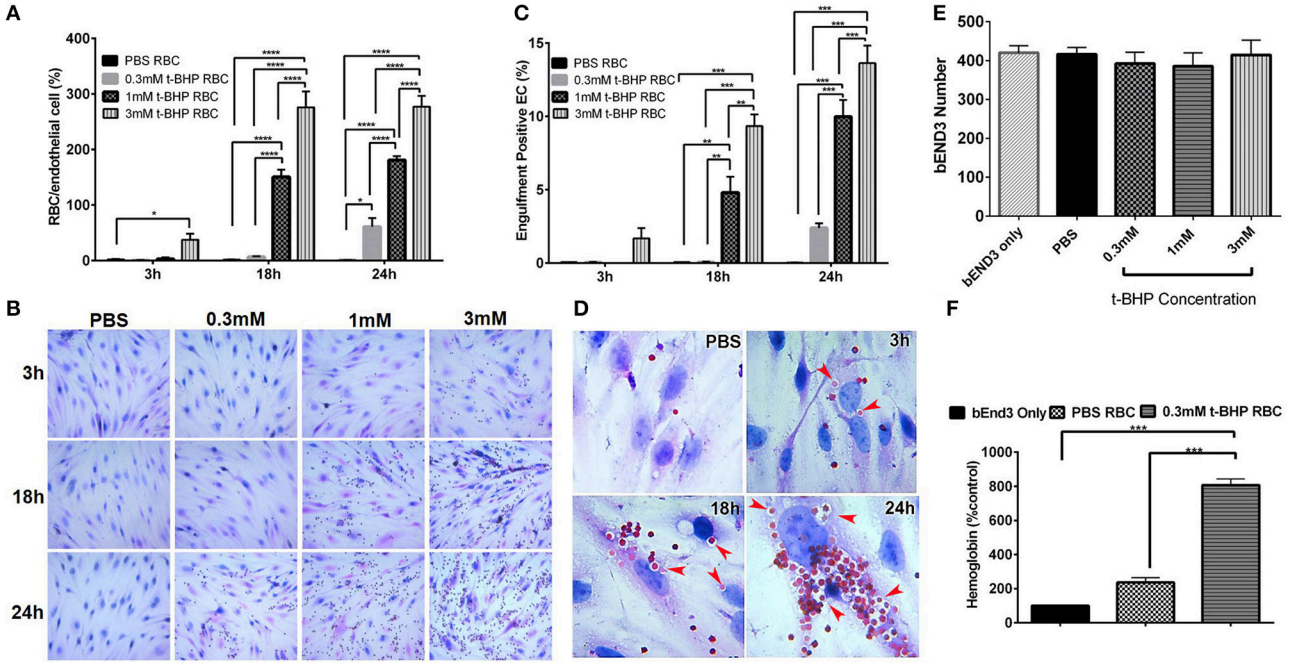

FIGURE 2 | Erythrophagocytosis by brain endothelial cells. Significant time- and concentration-dependent increase in adhesion **(A,B)** and engulfment **(C)** of t-BHP-treated RBC compared with PBS-treated RBC using light microscopy. Marked time dependent increase in engulfment of t-BHP-treated RBC by bEND3 cells indicated by red arrows **(D)**. Brain endothelial erythrophagocytosis at 24 h was not associated with bEND3 degradation or loss **(E)**. Significant increase in the amount of hemoglobin retained by the bEND3 cells incubated with t-BHP-treated RBC compared with PBS-treated RBC following 24 h incubation confirming erythrophagocytosis using the DAF colorimetric method **(F)**. Data is presented as mean ± SEM of at least 3 independent experiments. $^{*}p < 0.05$, $^{**}p < 0.01$, $^{***}p < 0.001$, $^{****}p < 0.0001$. EC, endothelial cells.

incubated with t-BHP-treated RBC compared with PBS-treated RBC confirming passage of hemoglobin from t-BHP-treated RBC across the bEND3 monolayer **(Figure 4B)**.

To determine if passage of hemoglobin from the t-BHP-treated RBC was associated with changes in bEND3 monolayer integrity, we measured TEER values, before and 24 h after RBC incubation. No changes in TEER were observed for all concentrations of t-BHP compared with PBS-RBC used as control, confirming that the passage of hemoglobin from t-BHP-RBC was not associated with altered bEND3 monolayer integrity **(Figure 4C)**. Further, to rule out the possibility of an increase in hemoglobin release with t-BHP in the apical chamber that may result in higher hemoglobin in the basolateral chamber, we determined the amount of free hemoglobin released by PBS- and t-BHP-treated RBC over the course of 24 h. We found that treating RBC with t-BHP did not increase the free hemoglobin released in the media compared with PBS-treated RBC **(Figure 4D)**.

Passage of RBC Across the Brain Endothelium *in vivo*

In vivo studies in Tie2-GFP mice showed that PKH-26 labeled PBS-treated RBC were confined to the cerebral vasculature. However, PKH-26 labeled t-BHP-treated RBC were found inside, outside, partially outside, and partially attached to the cerebral vasculature **(Figure 5)**.

DISCUSSION

In this study we demonstrate that RBC exposed to the oxidative stressor t-BHP undergo significant erythrophagocytosis (adhesion and engulfment) by the brain endothelial cells in an *in vitro* cell culture system. Further, this enhanced erythrophagocytosis was associated with an increased passage of RBC degradation product hemoglobin across the brain endothelial cells. No change in brain endothelium monolayer integrity was observed with passage of hemoglobin across the endothelial monolayer in the current study. *In vivo* studies using Tie2-GFP mice further verified the passage of t-BHP-treated RBC across the brain endothelium.

Under normal physiological conditions, the adhesion of RBC to the vascular endothelium is negligible. However, altered RBC-vascular endothelial adhesion has been observed in various pathological conditions including sickle cell disease (SCD), diabetes mellitus, malaria, and retinal vein occlusion (Wautier and Wautier, 2013). Pathological adherence of RBC to the vascular endothelium is associated with vascular complications including vaso-occlusive events observed in SCD (Wautier et al., 1985). Further, cytoadherence of plasmodium falciparum-infected RBC to the brain microvascular endothelium has been demonstrated in cerebral malaria (Jambou et al., 2010; El-Assaad et al., 2013; Howland et al., 2015). Besides abnormal adhesion of RBC to the vascular endothelium, recent studies report endothelial

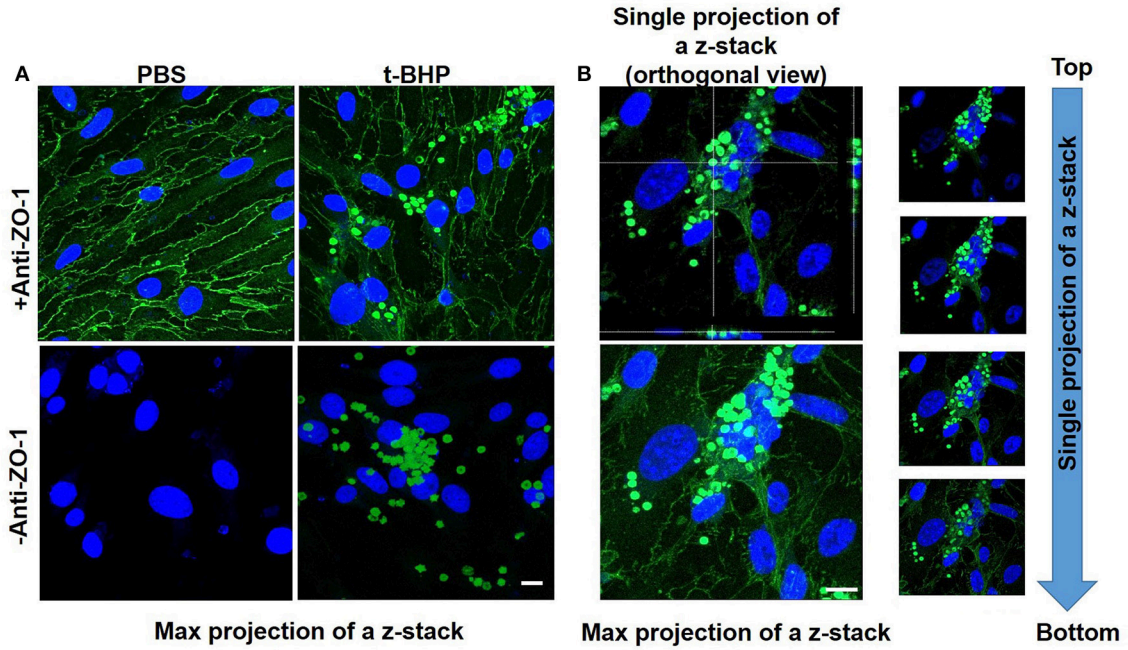

FIGURE 3 | Confocal microscopy of bEND3 cells and RBC to confirm erythrophagocytosis. Maximum projection of z-stack shows adhesion of t-BHP-treated RBC to bEND3 cells and no adhesion of PBS-treated RBC (Blue = DRAQ5 stain for the endothelial nucleus, green = tight junction ZO-1 protein and autofluorescence of RBC) **(A)**. Orthogonal view of a single projection, maximum projection of a z-stack and individual images of a z-stack moving from top to bottom of a cover glass confirm the internalization of t-BHP-treated RBC by bEND3 cells **(B)**. Scale bar = 10 μm.

erythrophagocytosis, a phenomenon by which aged and/or injured RBC adhere to and are engulfed by endothelial cells of peripheral origin including HUVECs and hepatic sinusoidal endothelial cells (Fens et al., 2010, 2012; Lee et al., 2011).

Among the first mechanisms shown to be involved in the phagocytic removal of aged, senescent, or injured RBC from the blood circulation (erythrophagocytosis) is membrane scrambling leading to the exposure of membrane PS to the outer leaflet of the RBC membrane (Bratosin et al., 1998). PS exposure serves as an "eat me" signal that triggers erythrophagocytosis by phagocytes, thereby facilitating erythrocyte clearance from the circulation (Schroit et al., 1985). Some of the seminal studies of RBC erythrophagocytosis showed that RBC with abnormal distribution of PS in the outer cell wall were phagocytized by macrophages more readily than normal or healthy RBC (Bratosin et al., 1998). PS-exposing cells are cleared from the circulation through recognition by receptors, including scavenger receptors, αvβ3 integrins, MerTK, TIM-1 and 4, BAI1, and Stabilin1 and 2, and subsequent attachment, cytoskeleton rearrangement and phagolysosomal processing (Ravichandran and Lorenz, 2007). The role of PS in endothelium-mediated erythrophagocytosis was also recently demonstrated (Lee et al., 2011; Fens et al., 2012). In these studies, PS-mediated endothelial erythrophagocytosis was mediated by the αvβ3 integrins (Fens et al., 2012) or stabilin 1 and 2 (Lee et al., 2011). Apart from endothelial erythrophagocytosis, PS exposure also plays a pivotal role in pathologic RBC adherence to vascular endothelium (Setty et al., 2002; Wautier et al., 2011).

In the current proof-of-concept study, PS exposure to mimic aged and/or injured RBC *in vivo* was triggered by treating RBC with t-BHP **(Figure 1B)** which, although an exogenous agent, is known to result in exposure of PS to the outer-leaflet of RBC (Fens et al., 2010), and is widely used as an external inducer of oxidative stress (Zou et al., 2001). Notably, oxidation of RBC plays an important role in erythrophagocytic clearance of aged and/or injured RBC (Kiefer and Snyder, 2000). As previously demonstrated by others, we found that a large percent of the t-BHP-treated RBC exposed PS (Fens et al., 2012). Consistent with studies using peripheral endothelial cells (Fens et al., 2012), in the current study we found that murine RBC treated with varying concentrations of t-BHP resulted in robust adhesion followed by engulfment of RBC by the murine brain endothelial cells (bEND3) (**Figures 2**, **3**), a well-characterized immortalized brain microvascular cell line known to retain many morphological and biochemical properties similar to *in vivo* conditions (Omidi et al., 2003). Adhesion and engulfment of t-BHP-RBC was confirmed using multiple approaches (H&E, DAF assay, confocal analysis and live imaging). Erythrophagocytosis of t-BHP-RBC was not associated with loss or degradation of brain endothelial cells in the current study and is in agreement with a recent study using HUVEC cells, in which erythrophagocytosis of oxidative stress-exposed RBC did not result in immediate signs of degradation and only a small fraction of HUVEC cells showed signs of apoptosis after 24 h incubation (Fens et al., 2012).

Treatment of RBC with other pathological stimuli such as LPS or neuraminidase did not result in brain endothelial

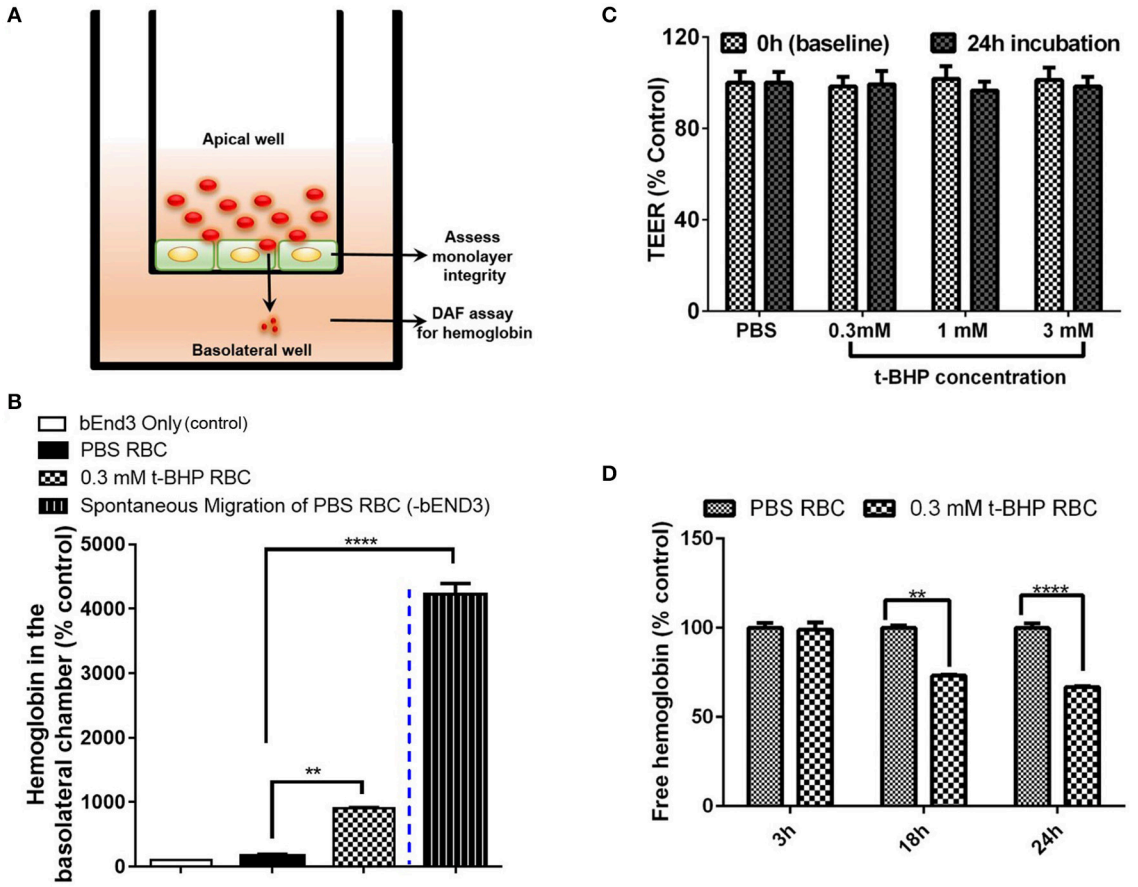

FIGURE 4 | Transmigration of hemoglobin across the bEND3 monolayer. Experimental set up to detect passage of hemoglobin across the bEND3 monolayer **(A)**. Significant increase in the passage of hemoglobin across the bEND3 monolayer incubated with t-BHP-treated RBC compared with PBS-RBC. Spontaneous migration reflects passage of hemoglobin from PBS-RBC across the 3 μm pore size transwell in the absence of a bEND3 monolayer **(B)**. Passage of hemoglobin across the bEND3 monolayer grown on transwells incubated with t-BHP-RBC was not accompanied by a change in TEER; TEER measurements are presented as % of PBS-RBC values **(C)**. Free hemoglobin released by t-BHP-treated RBC is significantly lower compared with PBS-treated RBC. The bEND3 monolayer was grown on standard cell culture wells **(D)**. Data is presented as mean ± SEM of at least 3 independent experiments. $^{**}p < 0.01$, $^{****}p < 0.0001$.

erythrophagocytosis or PS exposure (data not shown) in the current study. Further, activation of the brain endothelial cells with LPS did not augment erythrophagocytosis of t-BHP-treated RBC (**Figure 1**). These results are in contrast to previous studies in which treatment of RBC with LPS or neuraminidase resulted in significant adhesion to vascular endothelium (Tissot Van Patot et al., 1996; Eichelbrönner et al., 2000; Yang et al., 2014), and activation of endothelial cells with LPS further augmented such RBC-endothelial cell interactions *in vitro* (Tissot Van Patot et al., 1996; Eichelbrönner et al., 2000; Setty and Betal, 2008). The use of brain microvascular endothelial cells in the current study, as opposed to peripheral endothelial cells used in all the previous studies, may explain this difference in outcome.

After demonstrating robust erythrophagocytosis of RBC exposed to oxidative stress by the brain microvascular endothelial cells *in vitro*, the main question we wanted to address was whether brain endothelial erythrophagocytosis was associated with the passage of RBC or hemoglobin (RBC degradation product) across the brain endothelium. In the current study, we show significant passage of hemoglobin across the brain endothelial monolayer incubated with t-BHP-treated RBC (**Figure 4**). We further confirmed that the passage of hemoglobin was not associated with a change in the brain endothelial monolayer integrity since the TEER values remained unchanged for the duration of the experiment.

To evaluate the possibility of migration of free apical hemoglobin from t-BHP-treated RBC across the monolayer into the basolateral chamber, we determined the free hemoglobin released by t-BHP-RBC compared with PBS-RBC over 24 h in a separate series of experiments using bEND3 monolayers grown in standard cell culture plates (not transwells). We found that t-BHP-treated RBC did not release more free hemoglobin into the media compared with the PBS-RBC, and there was significantly less free hemoglobin in the media of brain endothelial cells incubated with t-BHP-RBC compared with PBS-RBC (**Figure 4**) following 18 h and 24 h incubation. This suggests that the

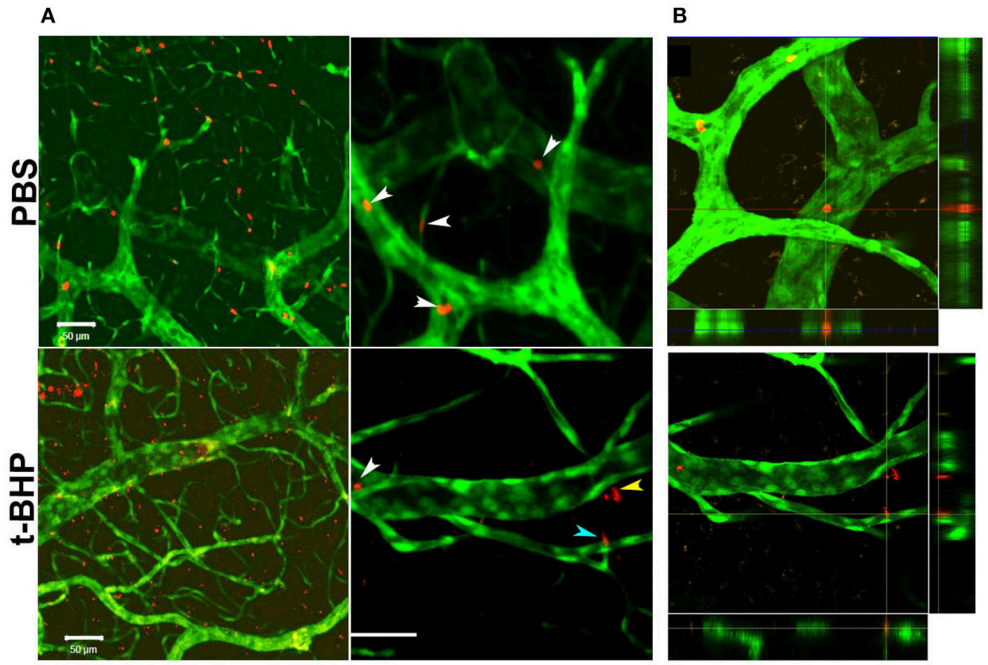

FIGURE 5 | Postmortem confocal microcopy images on mouse brains showing GFP-positive brain endothelium (green) and PKH-26-labeled RBC (red). (**A,** Top): PBS-RBC remain in the blood vessels (white arrows heads). (**A,** Bottom): t-BHP-treated RBC are inside (white arrow head) and outside the blood vessels (yellow arrow head), and also partially extravasated into the brain (blue arrow head). Orthogonal view showing PBS-treated RBC within the blood vessel (**B,** Top) and t-BHP-treated RBC partially and completely outside the blood vessel (**B,** Bottom). Scale bar = 50 µm.

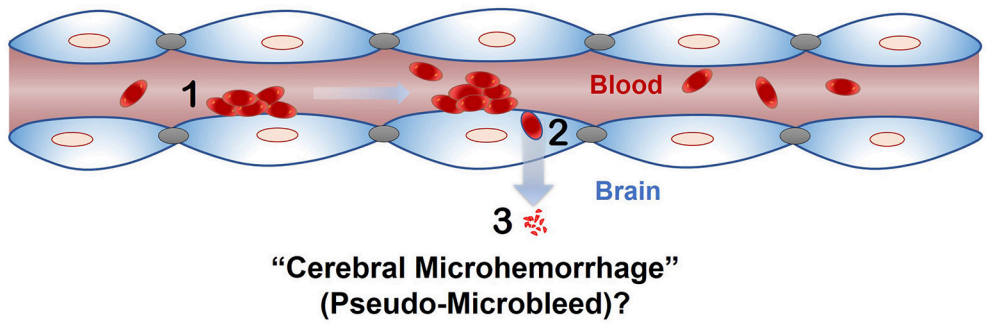

FIGURE 6 | Proposed role of endothelial erythrophagocytosis in cerebral microhemorrhage (pseudo-microbleeds) development. Aged and/or injured RBC adhere to (1) and are engulfed by (2) the brain endothelium. Iron rich RBC or degradation products (e.g., hemoglobin) are translocated across the brain endothelium (3), where they may produce signatures of CMB.

hemoglobin in the basolateral chamber does not represent the migration of free hemoglobin released in the apical chamber. The decrease in free hemoglobin with t-BHP-RBC at 18 h and 24 h is consistent with increased RBC erythrophagocytosis of t-BHP-RBC by brain endothelial cells, and thus lower free RBC available to release hemoglobin at these time points.

A limitation of our *in vitro* findings is the use of an immortalized brain endothelial cell line. Note, however, that passage of RBC degradation product (hemoglobin) across the brain endothelial monolayer were corroborated by our *in vivo* findings of extravasation of fluorescently-labeled t-BHP-treated RBC across the brain endothelium of Tie2-GFP mice using confocal microscopy **(Figure 5)**. We reported a similar finding of extravasation of fluorescently-labeled RBC across the brain endothelium of Tie2-GFP mice in an inflammation-induced mouse model of CMB (Sumbria et al., 2016). In the current study, the blood vessel adjacent to the extravasated RBC appeared intact with no visible rupture **(Figure 5)**.

Erythrophagocytosis mediated by macrophages involves RBC engulfment, endosomal processing and RBC degradation with subsequent release of hemoglobin and heme. It should be noted that not all engulfed RBC are subjected to

phagosomal degradation and that the fate of the engulfed RBC depends on the molecular machinery involved in erythrophagocytosis (Santarino et al., 2017). The intracellular mechanisms involved in the cellular trafficking of engulfed RBC and subsequent RBC processing by endothelial cells are understudied.

In the current study, we report the passage of RBC degradation product hemoglobin *in vitro* and the passage of fluorescently-labeled RBC across the brain endothelium *in vivo*. The possibility of passage of RBC fragments and not intact RBC cannot be ruled-out from the current data. We are unaware of prior reports of extravasation of non-parasitized RBC across the brain endothelium. Our findings are similar to the work done by Grutzendler and co-workers who reported engulfment and subsequent extravasation of emboli into the brain (termed as angiophagy; Grutzendler et al., 2014). Following passage across the brain endothelium, emboli were engulfed and degraded by pericytes and microglial cells. Future *in vitro* studies using co-cultures with pericytes and microglial cells will help elucidate the intracellular trafficking and the fate of the RBC involved in brain endothelial erythrophagocytosis.

The phenomenon of passage of intact RBC or RBC degradation products across an intact endothelial monolayer following endothelial erythrophagocytosis is a novel finding, and brain endothelial erythrophagocytosis is particularly relevant from the standpoint of non-hemorrhagic mechanisms involved in CMB development **(Figure 6)** (Fisher, 2014). This is because CMB are focal deposits of blood degradation products, predominately hemosiderin, which is derived from hemoglobin following hemolysis (Janaway et al., 2014). MRI detection of CMB relies on the paramagnetic properties of hemosiderin and any passage of hemoglobin across the brain endothelium into the perivascular space can thus produce signatures of CMB. Further investigation is required to determine whether brain endothelial erythrophagocytosis and subsequent passage of RBC or RBC degradation products across the brain endothelium occur under physiologically relevant conditions that induce oxidative stress *in vivo* to produce CMB signatures. Notably, PS exposure on erythrocytes and oxidative stress has been reported under several risk factors for CMB, such as chronic kidney disease (Bonomini et al., 1999, 2002; Tucker et al., 2015) and Alzheimer's disease (Nicolay et al., 2007; Gella and Durany, 2009). Further, CMB in the absence of gadolinium extravasation (marker of blood-brain barrier disruption) have been reported in patients with cerebral malaria (Potchen et al., 2018), and recent work showed engulfment of parasitized RBC by human brain endothelial cells in an *in vitro* model of cerebral malaria (Jambou et al., 2010), raising the possibility of erythrophagocytosis-dependent CMB in this disorder.

In conclusion, we show that brain endothelial cells express an erythrophagocytic phenotype for RBC exposed to oxidative stress *in vitro*. Further, brain endothelial erythrophagocytosis is associated with passage of hemoglobin across the brain endothelial monolayer *in vitro*, and passage of RBC exposed to oxidative stress across the brain endothelium *in vivo*. These results may have significant implications for mechanisms of CMB in the absence of frank vascular disruption.

DATA AVAILABILITY STATEMENT

All datasets for this study are included in the manuscript and the **Supplementary Video 1**. The raw data supporting the conclusions of this manuscript will be made available by the authors, without undue reservation, to any qualified researcher.

AUTHOR CONTRIBUTIONS

RC performed the experiments, collected and analyzed data, and contributed to manuscript writing. JC performed the experiments and collected data. TK performed confocal microscopy for *in vivo* studies. AZ helped with live imaging. MF helped conceive the study and edited the manuscript. RS conceived the study, designed, analyzed and coordinated the experiments, and drafted and edited the manuscript. All authors read and approved the final manuscript.

FUNDING

This work was partly supported by a grant from the Alzheimer's Association: RG-15-361188 (RS), NIH NS20989 (MF), and intramural support from the Keck Graduate Institute.

ACKNOWLEDGMENTS

Authors thank Russle Benson, Ruaab Patel, Kei-Lwun Yee, Jeffery Woods, and Abrar Al Maghribi for their assistance with the H&E quantification, and Leomar Patam for assistance with the live cell imaging. We also thank Dr. David Cribbs for his assistance with the *in vivo* experimentation. A part of this work was presented at the American Association of Colleges of Pharmacy. (2016).

SUPPLEMENTARY MATERIAL

The Supplementary Material for this article can be found online at: https://www.frontiersin.org/articles/10.3389/fncel.2018.00279/full#supplementary-material

Supplementary Video 1 | Live cell imaging of brain endothelial erythrophagocytosis. The highlighted region shows attachment and subsequent engulfment of two RBC by brain endothelium.

REFERENCES

American Association of Colleges of Pharmacy. (2016).Correction to 117th annual meeting of the American Association of Colleges of Pharmacy, Anaheim, California, July 23–27. *Am. J. Pharm. Educ.* 80:S22.

Bonomini, M., Sirolli, V., Gizzi, F., Di Stante, S., Grilli, A., and Felaco, M. (2002). Enhanced adherence of human uremic erythrocytes to vascular endothelium: role of phosphatidylserine exposure. *Kidney Int.* 62, 1358–1363. doi: 10.1111/j.1523-1755.2002.kid560.x

Bonomini, M., Sirolli, V., Settefrati, N., Dottori, S., Di Liberato, L., and Arduini, A. (1999). Increased erythrocyte phosphatidylserine exposure in chronic renal failure. *J. Am. Soc. Nephrol.* 10, 1982–1990.

Bratosin, D., Mazurier, J., Tissier, J. P., Estaquier, J., Huart, J. J., Ameisen, J. C., et al. (1998). Cellular and molecular mechanisms of senescent erythrocyte phagocytosis by macrophages. a review. *Biochimie* 80, 173–195. doi: 10.1016/S0300-9084(98)80024-2

Eichelbrönner, O., Sielenkämper, A., Cepinskas, G., Sibbald, W. J., and Chin-Yee, I. H. (2000). Endotoxin promotes adhesion of human erythrocytes to human vascular endothelial cells under conditions of flow. *Crit. Care Med.* 28, 1865–1870. doi: 10.1097/00003246-200006000-00030

El-Assaad, F., Wheway, J., Mitchell, A. J., Lou, J., Hunt, N. H., Combes, V., et al. (2013). Cytoadherence of *Plasmodium berghei*-infected red blood cells to murine brain and lung microvascular endothelial cells *in vitro*. *Infect Immun.*81, 3984–3991. doi: 10.1128/IAI.00428-13

Fens, M. H., Storm, G., Pelgrim, R. C., Ultee, A., Byrne, A. T., Gaillard, C. A., et al. (2010). Erythrophagocytosis by angiogenic endothelial cells is enhanced by loss of erythrocyte deformability. *Exp. Hematol.* 38, 282–291. doi: 10.1016/j.exphem.2010.02.001

Fens, M. H., van Wijk, R., Andringa, G., van Rooijen, K. L., Dijstelbloem, H. M., Rasmussen, J. T., et al. (2012). A role for activated endothelial cells in red blood cell clearance: implications for vasopathology. *Haematologica* 97, 500–508. doi: 10.3324/haematol.2011.048694

Fisher, M. (2014). Cerebral microbleeds: where are we now? *Neurology* 83, 1304–1305. doi: 10.1212/WNL.0000000000000871

Fisher, M., French, S., Ji, P., and Kim, R. C. (2010). Cerebral microbleeds in the elderly: a pathological analysis. *Stroke* 41, 2782–2785. doi: 10.1161/STROKEAHA.110.593657

Fisher, M. J. (2013). Brain regulation of thrombosis and hemostasis: from theory to practice. *Stroke* 44, 3275–3285. doi: 10.1161/STROKEAHA.113.000736

Gebran, S. J., Romano, E. L., Pons, H. A., Cariani, L., and Soyano, A. N. (1992). A modified colorimetric method for the measurement of phagocytosis and antibody-dependent cell cytotoxicity using 2,7-diaminofluorene. *J. Immunol. Methods* 151, 255–260. doi: 10.1016/0022-1759(92)90125-D

Gella, A., and Durany, N. (2009). Oxidative stress in Alzheimer disease. *Cell Adh. Migr.*3, 88–93. doi: 10.4161/cam.3.1.7402

Grutzendler, J., Murikinati, S., Hiner, B., Ji, L., Lam, C. K., Yoo, T., et al. (2014). Angiophagy prevents early embolus washout but recanalizes microvessels through embolus extravasation. *Sci. Transl. Med.* 6:226ra31. doi: 10.1126/scitranslmed.3006585

Howland, S. W., Poh, C. M., and Rénia, L. (2015). Activated brain endothelial cells cross-present malaria antigen. *PLoS Pathog.*11:e1004963. doi: 10.1371/journal.ppat.1004963

Jambou, R., Combes, V., Jambou, M. J., Weksler, B. B., Couraud, P. O., and Grau, G. E. (2010). *Plasmodium falciparum* adhesion on human brain microvascular endothelial cells involves transmigration-like cup formation and induces opening of intercellular junctions. *PLoS Pathog.* 6:e1001021. doi: 10.1371/journal.ppat.1001021

Janaway, B. M., Simpson, J. E., Hoggard, N., Highley, J. R., Forster, G., Drew, D., et al. (2014). Brain haemosiderin in older people: pathological evidence for an ischaemic origin of magnetic resonance imaging (MRI) microbleeds. *Neuropathol. Appl. Neurobiol.*40, 258–269. doi: 10.1111/nan.12062

Kiefer, C. R., and Snyder, L. M. (2000). Oxidation and erythrocyte senescence. *Curr. Opin. Hematol.* 7, 113–116. doi: 10.1097/00062752-200003000-00007

Lau, W. L., Huisa, B. N., and Fisher, M. (2017). The cerebrovascular-chronic kidney disease connection: perspectives and mechanisms. *Transl. Stroke Res.* 8, 67–76. doi: 10.1007/s12975-016-0499-x

Lee, S. J., Park, S. Y., Jung, M. Y., Bae, S. M., and Kim, I. S. (2011). Mechanism for phosphatidylserine-dependent erythrophagocytosis in mouse liver. *Blood* 117, 5215–5223. doi: 10.1182/blood-2010-10-313239

Murakami, K., and Mawatari, S. (2003). Oxidation of hemoglobin to methemoglobin in intact erythrocyte by a hydroperoxide induces formation of glutathionyl hemoglobin and binding of alpha-hemoglobin to membrane. *Arch. Biochem. Biophys.* 417, 244–250. doi: 10.1016/S0003-9861(03)00389-8

Nicolay, J. P., Gatz, S., Liebig, G., Gulbins, E., and Lang, F. (2007). Amyloid induced suicidal erythrocyte death. *Cell Physiol. Biochem.* 19, 175–184. doi: 10.1159/000099205

Omidi, Y., Campbell, L., Barar, J., Connell, D., Akhtar, S., and Gumbleton, M. (2003). Evaluation of the immortalised mouse brain capillary endothelial cell line, b.End3, as an *in vitro* blood-brain barrier model for drug uptake and transport studies. *Brain Res.* 990, 95–112. doi: 10.1016/S0006-8993(03)03443-7

Potchen, M. J., Kampondeni, S. D., Seydel, K. B., Haacke, E. M., Sinyangwe, S. S. Mwenechanya, M., et al. (2018). 1.5 Tesla magnetic resonance imaging to investigate potential etiologies of brain swelling in pediatric cerebral malaria. *Am. J. Trop. Med. Hyg.* 98, 497–504. doi: 10.4269/ajtmh.17-0309

Ravichandran, K. S., and Lorenz, U. (2007). Engulfment of apoptotic cells: signals for a good meal. *Nat. Rev. Immunol.*7, 964–974. doi: 10.1038/nri2214

Santarino, I. B., Viegas, M. S., Domingues, N. S., Ribeiro, A. M., Soares, M. P., and Vieira, O. V. (2017). Involvement of the p62/NRF2 signal transduction pathway on erythrophagocytosis. *Sci. Rep.*7:5812. doi: 10.1038/s41598-017-05687-1

Schroit, A. J., Madsen, J. W., and Tanaka, Y. (1985). *In vivo* recognition and clearance of red blood cells containing phosphatidylserine in their plasma membranes. *J. Biol. Chem.* 260, 5131–5138.

Setty, B. N., and Betal, S. G. (2008). Microvascular endothelial cells express a phosphatidylserine receptor: a functionally active receptor for phosphatidylserine-positive erythrocytes. *Blood* 111, 905–914. doi: 10.1182/blood-2007-07-099465

Setty, B. N., Kulkarni, S., and Stuart, M. J. (2002). Role of erythrocyte phosphatidylserine in sickle red cell-endothelial adhesion. *Blood* 99, 1564–1571. doi: 10.1182/blood.V99.5.1564

Sumbria, R. K., Grigoryan, M. M., Vasilevko, V., Krasieva, T. B., Scadeng, M., Dvornikova, A. K., et al. (2016). A murine model of inflammation-induced cerebral microbleeds. *J. Neuroinflammation* 13:218. doi: 10.1186/s12974-016-0693-5

Tissot Van Patot, M. C., MacKenzie, S., Tucker, A., and Voelkel, N. F. (1996). Endotoxin-induced adhesion of red blood cells to pulmonary artery endothelial cells. *Am. J. Physiol.* 270(1 Pt 1), L28–L36. doi: 10.1152/ajplung.1996.270.1.L28

Tucker, P. S., Scanlan, A. T., and Dalbo, V. J. (2015). Chronic kidney disease influences multiple systems: describing the relationship between oxidative stress, inflammation, kidney damage, and concomitant disease. *Oxid. Med. Cell Longev.* 2015:806358. doi: 10.1155/2015/806358

Wautier, J. L., Galacteros, F., Wautier, M. P., Pintigny, D., Beuzard, Y., Rosa, J., et al. (1985). Clinical manifestations and erythrocyte adhesion to endothelium in sickle cell syndrome. *Am. J. Hematol.* 19, 121–130. doi: 10.1002/ajh.2830190203

Wautier, J. L., and Wautier, M. P. (2013). Molecular basis of erythrocyte adhesion to endothelial cells in diseases. *Clin. Hemorheol. Microcirc.* 53, 11–21. doi: 10.3233/CH-2012-1572

Wautier, M. P., Héron, E., Picot, J., Colin, Y., Hermine, O., and Wautier, J. L. (2011). Red blood cell phosphatidylserine exposure is responsible for increased erythrocyte adhesion to endothelium in central retinal vein occlusion. *J. Thromb. Haemost.* 9, 1049–1055. doi: 10.1111/j.1538-7836.2011.04251.x

Yang, Y., Koo, S., Heng, L. T., Meiselman, H. J., and Neu, B. (2014). Non-adsorbing macromolecules promote endothelial adhesion of erythrocytes with reduced sialic acids. *Biochim. Biophys. Acta* 1840, 288–293. doi: 10.1016/j.bbagen.2013.09.031

Zhao, X., Grotta, J., Gonzales, N., and Aronowski, J. (2009). Hematoma resolution as a therapeutic target: the role of microglia/macrophages. *Stroke* 40 (Suppl. 3), S92–S94. doi: 10.1161/STROKEAHA.108.533158

Zou, C. G., Agar, N. S., and Jone, G. L. (2001). Oxidative insult in sheep red blood cells induced by T-butyl hydroperoxide: the roles of glutathione and glutathione peroxidase. *Free Radic. Res.* 34, 45–56. doi: 10.1080/10715760100300051

Conflict of Interest Statement: MF has received support from Boehringer-Ingelheim and Otsuka Pharmaceutical Company (research grants).

The remaining authors declare that the research was conducted in the absence of any commercial or financial relationships that could be construed as a potential conflict of interest.

frontiers in Cellular Neuroscience

ORIGINAL RESEARCH
published: 17 October 2018
doi: 10.3389/fncel.2018.00372

Inhibition of Connexin 43 Hemichannels Alleviates Cerebral Ischemia/Reperfusion Injury via the TLR4 Signaling Pathway

*Yingzhu Chen[1,2†], Liangzhu Wang[2,3†], Lingling Zhang[1,2], Beilei Chen[1,2], Liu Yang[2,3], Xiaobo Li[1,2,4], Yuping Li[1,2] and Hailong Yu[1,2,4,5]**

[1]Clinical Medical College of Yangzhou University, Yangzhou, China, [2]Department of Neurology, Northern Jiangsu People's Hospital, Yangzhou, China, [3]Dalian Medical University, Dalian, China, [4]Institute of Neuroscience, Northern Jiangsu People's Hospital, Yangzhou, China, [5]Drum Tower Hospital, Medical School of Nanjing University, Nanjing, China

Connexin 43 (Cx43) widely exists in all components of the neurovascular unit (NVU) and is a constituent of gap junctions and hemichannels. In physiological states, gap junctions are open for regular intercellular communication, and the hemichannels present low open probability in astrocytes. After cerebral ischemia, a large number of hemichannels are unusually opened, leading to cell swelling and even death. Most known hemichannel blockers also inhibit gap junctions and sequentially obstruct normal electrical cell-cell communication. In this study, we tested the hypothesis that Gap19, a selective Cx43-hemichannel inhibitor, exhibited neuroprotective effects on cerebral ischemia/reperfusion (I/R). An obvious improvement in neurological scores and infarct volume reduction were observed in Gap19-treated mice after brain ischemia induced by middle cerebral artery occlusion (MCAO). Gap19 treatment attenuated white matter damage. Moreover, Gap19 treatment suppressed the expression of Cx43 and Toll-like receptor 4 (TLR4) pathway-relevant proteins and prevented the overexpression of tumour necrosis factor-α (TNF-α) and interleukin-1β (IL-1β). To further explore downstream signaling, we established an *in vitro* model–oxygen glucose deprivation (OGD) to simulate ischemic conditions. Immunofluorescence staining showed that Cx43 co-existed with TLR4 in astrocytes. The hemichannel activity was increased after OGD and Gap19 could inhibit this effect on astrocytes. Gap19 substantially improved relative cell vitality and decreased the expression of Cx43, TLR4 and inflammatory cytokines *in vitro*. In addition, in the lipopolysaccharide (LPS) stimulation OGD model, Gap19 also exhibited a protective effect via inhibiting TLR4 pathway activation. In summary, our results showed that Gap19 exerted a neuroprotective effect after stroke via inhibition of the TLR4-mediated signaling pathway.

Keywords: cerebral ischemia/reperfusion, hemichannel, inflammation, toll-like receptor 4, neurovascular unit, neuroprotection

OPEN ACCESS

Edited by:
Sriharsha Kantamneni, University of Bradford, United Kingdom

Reviewed by:
Pablo Jose Saez, Institut Curie, France
Juan C. Saez, Pontificia Universidad Católica de Chile, Chile

****Correspondence:***
Hailong Yu
hailongyu1982tg@163.com

†These authors have contributed equally to this work

Received: *30 May 2018*
Accepted: *28 September 2018*
Published: *17 October 2018*

Citation:
Chen Y, Wang L, Zhang L, Chen B, Yang L, Li X, Li Y and Yu H (2018) Inhibition of Connexin 43 Hemichannels Alleviates Cerebral Ischemia/Reperfusion Injury via the TLR4 Signaling Pathway. Front. Cell. Neurosci. 12:372. doi: 10.3389/fncel.2018.00372

INTRODUCTION

Stroke is the most common neurological disease, and it causes high disability and high mortality (Lo, 2010). An epidemiological study revealed that 70%–80% of all strokes are ischemic (Mozaffarian et al., 2015). Currently, intravenous tissue plasminogen activator (t-PA) is recognized as the most effective therapy for acute ischemic stroke (Powers et al., 2018). However, its clinical use

is largely limited because of the narrow time window and strict inclusion criteria (Saver et al., 2013). Recent research has been devoted to the development of alternative neuroprotective agents, but almost no agents have been successful in clinical trials (Sahota and Savitz, 2011). The primary reason is that previous studies focus on single target neurons or white matter and ignore the communication between the components of the neurovascular unit (NVU; Girouard and Iadecola, 2006). NVU is a complex of neurons, astrocytes, and cerebrovascular endothelial cells, considered as the structural and functional unit of the brain (Zhang et al., 2012; Xue et al., 2013). NVU components are involved in the transport of substances via intercellular signal transduction and neurovascular coupling and regulate the steady state microenvironment of neurons (Guo et al., 2008). Abnormal NVU function may cause neurological disorders, such as stroke (Moskowitz et al., 2010).

Cell communication in the NVU primarily occurs via gap junctions (Islam and Mohamed, 2015). Gap junctional intercellular communication (GJIC) allows direct cell-to-cell communication, energy metabolites and diffusion of molecules to maintain homeostatic balance in the brain, such as K^+ or glutamate (Naus and Giaume, 2016). Gap junction is consisted by the aggregation of two connexons (or hemichannels), to form a direct pathway linking the cytoplasm of the neighboring cells (Bodendiek and Raman, 2010). Each hemichannel consists of six connexin proteins, and 11 subtypes are expressed in brain (Chew et al., 2010). The connexin 43 (Cx43) subtype is one of the most abundant connexin proteins in brain, widely exists in the component of NVU, predominately in astrocytes (Giaume et al., 2010). Connexins are four-time transmembrane proteins and exist on the plasma membranes. They own two extracellular loops (ELs) and one intracellular cytoplasmic loop (CL; Schulz et al., 2015). In the physiological state, gap junctions in astrocytes remain open, while the hemichannels still present low open probability (Kim et al., 2016). Hemichannels are primarily activated after cerebral ischemia, allowing the entry of Na^+ and Ca^{2+} and the release of adenosine triphosphate (ATP) and other small metabolites. These fluctuations cause Ca^{2+} overload, osmotic imbalance, energy exhaustion and even cell death (Sáez and Leybaert, 2014). Moreover, ATP released from hemichannels could mediate the microglia activation and induce inflammatory cytokines secretion from activated microglia, further upregulate the Cx43 hemichannels and form a vicious cycle (Shaikh et al., 2012; Sáez et al., 2013).

Hemichannels modulation was considered as a potential neuro-therapeutic target in cerebral ischemia/reperfusion (I/R) injury (De Bock et al., 2011). Connexin43 mimetic peptides could prevent the opening of hemichannels and further reduce the spread of harmful substance after ischemic injury (Evans and Leybaert, 2007; O'Carroll et al., 2008). Our previous study found that the Gap26 and Gap27 could significantly reduce infarct size and promote neurological function recovery after hypoxia/ischemia injury in neonatal rats (Li et al., 2015). However, when applied for several hours, these agents also prevented the joining of hemichannels and affected gap junction communication due to their poor specificity (Decrock et al., 2009). Another mimetic peptide, Gap19, consists of nine amino acids KQIEIKKFK (Schulz et al., 2015), and it inhibits the opening of hemichannels without interference the gap junction communication in astrocytes (Abudara et al., 2014). Selective inhibition of Cx43 hemichannels using Gap19 protects against myocardial I/R injury *in vitro* and *in vivo* (Wang N. et al., 2013). Given the higher specificity, we can hypothesis that Gap19 may alleviate cerebral I/R injury. Restoration of blood supply and reoxygenation are usually associated with deterioration of tissue injury and a profound inflammation called reperfusion injury (Kim et al., 2014). Subsequent reperfusion further activates of innate and adaptive immune responses and cell death programmes (Eltzschig and Eckle, 2011). Recently study shows that Cx43 hemichannel opening could be triggered by treatment with pro-inflammatory cytokines in astrocytes (Retamal et al., 2007). Nevertheless, whether Gap19 influences cerebral I/R injury via disruption of inflammatory responses is not clear.

In the present study, we established middle cerebral artery occlusion (MCAO) and oxygen glucose deprivation (OGD) models to assess the role and relevant mechanisms of Gap19 in cerebral ischemia. We found that Gap19 exerted a protective role in cerebral I/R injury via inhibition of Toll-like receptor 4 (TLR4) signaling *in vitro* and *in vivo*. Therefore, Gap19 is a promising new drug candidate for the treatment of ischemic stroke.

MATERIALS AND METHODS

Animals and Experimental Groups

Adult male ICR mice (8–10 weeks, 25–35 g) were purchased from the Comparative Medical Centre of Yangzhou University. Animals were housed in an appropriate environment at $22 \pm 2°C$ and 60% humidity with a 12-h light/dark cycle. All experiment protocols were approved by the Animal Ethics Committee of the Yangzhou University (license number: YIACUC-15-0013). Animals were randomly separated into five groups (n = 6–15 each): (I) sham; (II) Gap19 group; (III) I/R group; (IV) I/R + Gap19 group; and (V) I/R + Gap26 group. In the I/R group, the animals were assigned to several subgroups with different reperfusion time points (4 h, 12 h, 24 h, 72 h and 7 days).

The Middle Cerebral Artery Occlusion (MCAO) Model

The MCAO was established as described previously (Wang et al., 2014). Briefly, after anesthetize mice with 5.0% isoflurane, made a small incision on the neck skin, and carefully exposed the left common carotid artery (CCA), external carotid artery (ECA), and internal carotid artery (ICA). The ECA was ligated to block blood flow, and aneurysm clips were used to clamp the left CCA and ICA. A small incision was created at 2 mm proximal end of the CCA bifurcation. Through the incision, the filament was inserted into the ICA, and about 9–11 mm was inserted to block the MCA. The filament was gently removed (onset of reperfusion) after 45 min of focal cerebral ischemia. Tight the ICA with suture line and close the neck incision. Sham group only accepted neck incision and ligation of the

ECA without occluding MCA. The mice went back to the cages with closely monitored and keep the body temperature at 36.5–37.5°C by the electric blanket until they recovered from anesthesia.

Drug Preparation and Treatment Schedule

Gap19 was purchased from TOCRIS (catalog No. 5353) and dissolved in sterilized double distilled water (ddH_2O). Gap19 was injected into the right lateral cerebral ventricle (coordinates: 0.5 mm posterior to Bregma, 1.0 mm right of the midline, and depth is 2.5 mm) 1 h after MCAO as described previously (Meller et al., 2005). The optimal dose was selected based on previous studies (Li et al., 2015) and 10 μg Gap19/Gap26 in 10 μl ddH_2O was slowly injected over 10 min.

Evaluation of Neurological Deficit

A researcher who was unclear of animal grouping assessed neurological deficits at 24 h after reperfusion. A 5-point method of neurological deficit scores was applied to assess neurological behavior, as described previously (Yu H. et al., 2012): 0, no deficit; 1, failure to fully extend right paw; 2, circling to right; 3, falling to right; 4, no spontaneous walking with depressed consciousness. Score of 0–2 manifested mild neurological impairment, and 3–4 manifested severe neurological impairment. Remove the animals with no deficit after MCAO.

Measurement of Infarct Volume

Infarct volume was measured with 0.2% (w/v) 2,3,5-triphenyltetrazolium chloride (TTC, Sigma-Aldrich) as described previously (Tsubokawa et al., 2007; Yu H. et al., 2012). Briefly, mice were decapitated after neurological evaluation, and quickly removed and frozen the brain. After cut the brains into 2 mm coronal sections, slices were stained with 0.2% TTC for 30 min at 37°C, then fixed with 4% paraformaldehyde overnight. The infarct tissue area was not stained (white), and normal tissue was stained red. Then all brain slices were photographed in one picture and the infarct volume in each slice was determined by a computerized image analysis system (AlphaEase Image Analysis Software V 3.1.2). The percent hemispheric infarct volume was calculated as described previously (Xiong et al., 2011; Li et al., 2015), calculated the ratio (%) of the infarction area to the contralateral area of the same brain.

Luxol Fast Blue Myelin Staining

Luxol fast blue staining (Sigma) and Cresyl violet was used as a counterstain to assess the myelin damage at 7 days after reperfusion. Washed the slices in ddH_2O for 2 min, and incubated in 95% ethanol for 1 min. Sections were then incubated in a preheated solution of 1% LFB (60°C) for 2 h. After washed, differentiate sections with a 0.05% lithium carbonate solution and 70% ethyl alcohol each for 10 s. Repeated this step twice and stained with a 0.1% cresyl violet for 1 min. Tissues were gradually dehydrated in an ethanol gradient (70%, 95% and 100%) and fixed with xylene. Quantitative analyses of Luxol fast blue-stained sections were performed as described previously (Jing et al., 2014). White matter damage was calculated as the percentage of blue area in the ipsilateral striatum.

Isolation and Purification of Three Kinds of Mice Cerebral Cells

Brain microvascular endothelial cells (BMECs) were collected from 2-week-old mice, as previously described (Gauthier et al., 2012; Ruck et al., 2014). Briefly, gray matter was minced into small pieces in ice-cold 20 mM HEPES in Dulbecco's Modified Eagle Medium (DMEM). Tissue was digested at 37°C for 30 min in 0.05% collagenase/dispase. Isolated BMECs with 17% dextran and ultracentrifuged at 4°C 10,000× *g* for 30 min. Autoclaved glass beads were used to collect the cells. Precipitates were resuspended in DMEM supplemented with 10% FBS, 100 U/ml penicillin, 100 mg/ml streptomycin, 2 mM L-glutamine, 50 mg/ml DNase I and 0.1 mM nonessential amino-acids. Seed the cells on 6-well culture plates pre-coated with 1% gelatin and incubate at 37°C in 5% CO_2. The purified endothelial cells were used for following experiments.

Astrocytes were prepared from mice brain cortices within 24 h of birth, as previously described (Nakagawa et al., 2009). Gray cortices were minced, digested 0.25% trypsin and centrifuged. Sediments were resuspended in DMEM supplemented with 10% FBS and 100 U/ml penicillin, and 100 mg/ml streptomycin. Cells were seeded at a density of 4.5×10^6 cells/flask onto 75-cm^2 flasks pre-coated with 20 μg/ml poly-D-lysine. Change the culture medium every 2 days. After 12–14 days of culture, shake the flasks to discard microglia and collect the purified astrocytes. Astrocytes could be digested with 0.25% trypsin and seeded on different culture plates for further experiments.

Neurons were obtained from mice embryos at 15–16 days of gestation, as previously described, using a modified protocol (Zhu et al., 2014). Briefly, remove the embryos and separate the cerebral cortex quickly, strip meninges in the sterile filter papers. Put the acquired tissues into a Ca^{2+}/Mg^{2+}-free Hank's balanced saline solution (HBSS) solution. Then digest in 2-mg/ml papain for 30 min and centrifuged. Cells were seeded at 5×10^5 cells/cm^2 into 6-well culture plates pre-coated with 100 μg/ml poly-D-lysine and cultured with Neurobasal medium including 4.5 g/L glucose, Glutamax and 2% B27. Replace half of the medium with new medium after 2 days and maintain in culture 3 days prior to each experiment.

Establishment of *in vitro* NVU Model

NVU model was constructed by using the transwell system (Corning Incorporated) according to previous report (Xue et al., 2013; Tian et al., 2016). Briefly, the neurons were first seeded into the 6-well culture plate to 0.5×10^5 cells/cm^2 for 5 days. Then seed the purified astrocytes on the external of the transwell insert membrane with a density of 5×10^5 cells/cm^2. After astrocytes were adhered for 4 h, and the insert was transferred into the well to co-culture with neurons. After 1 day, BMECs were plated to the internal of the transwell insert membrane with 1.0×10^5 cells/cm^2 and co-cultured for 2–3 days. After co-culture, medium was replaced with DMEM-F12 supplemented with 10% FBS, L-glutamine, penicillin (100 U/ml) and streptomycin (100 mg/ml). The NVU model was prepared

for next experiments. Lipopolysaccharide (LPS; 1 μg/ml, Sigma) and Gap19 were added to the medium below the transwell at the beginning of OGD to construct the model.

Oxygen-Glucose Deprivation

To simulate ischemia *in vitro*, OGD treatment was established as described previously (Rowe et al., 2014) with small modification. First, removed the original culture medium and replaced with glucose/serum-free DMEM. Then, transfer the plates into an anaerobic chamber for 4 h at 37°C, which already balanced with 5% CO_2 and 95% N_2. Cells were returned to completely normal conditions for 24 h. Groups as follows: (1) control; (2) Gap19 group; (3) OGD group; (4) OGD + Gap19 group; (5) OGD + LPS group; and (6) OGD + LPS + Gap19 group. Control cells were incubated in the normoxic incubator. Gap19 (100 μM) were treated into system at the beginning of OGD.

Cytotoxicity Assay

The 3-(4,5-dimethyl-thiazol-2-yl)-2,5-diphenyltetrazolium bromide (MTT) assay was used to assess the cell viability (Jiang et al., 2014). Briefly, purified astrocytes were seeded in 96-well plates with DMEM without serum. Cells were disposed with different concentrations (10 μM, 50 μM, 100 μM, 150 μM and 200 μM) of Gap19 at the beginning of OGD. Then the medium was removed, and the MTT assay was conducted according to the manufacturer's protocols. The formation of formazan crystals was detected at 490 nm by a microplate reader. Cell viability was showed as a percentage of the control that had not undergone Gap19 treatment.

Immunofluorescence Staining

Immunofluorescence was performed as described in a previous study (Tian et al., 2016). Briefly, different cell types were seeded on coverslips. Cells were gently washed after reaching 70% confluency and fixed with 4% paraformaldehyde for 20 min. Then block with 3% bovine serum for 1 h and incubate with primary antibody at 4°C overnight. BMECs were incubated with CD31 (anti-rabbit, 1:20, Abcam), and neurons were incubated with tubulin β-III isoform (anti-mouse, 1:200, Millipore). Astrocytes were incubated with GFAP (anti-mouse, 1:100, Millipore; anti-rabbit, 1:500, Cell Signaling), Cx43 (anti-rabbit, 1:1,000, Cell Signaling; anti-mouse, 1:100, Abcam) and TLR4 (anti-mouse, 1:500, Proteintech). Cells were washed and incubated with anti-rabbit IgG labeled with Alexa-594 (Invitrogen) or anti-mouse IgG labeled with Alexa-488 (Invitrogen). Finally, stain the nuclei with 4',6-diamidino-2- phenylindole (DAPI, C1006; Beyotime, Shanghai, China). The coverslips were viewed by the fluorescence microscope (LSM780, Zeiss, Jena, Germany).

Ethidium Bromide Uptake

To evaluate the hemichannels activity after OGD and the effect of Gap19, astrocytes, neurons and BMECs were respectively cultured on 24-well plates. After OGD, the cultured cells were washed with HBSS twice and incubated with 5 μM ethidium bromide (EtBr; Giaume et al., 2012) in 37°C for10 min. Then washed the cells again, fixed with 4% paraformaldehyde and visualized by the fluorescence microscope. Pictures were analyzed through counting the number of EtBr-positive cells per field by ImageJ software.

Enzyme-Linked Immunosorbent Assay (ELISA) Analysis

Carefully collect the cell culture supernatants after OGD and centrifuge at 12,000× *g* 4°C for 15 min. Tumor necrosis factor-α (TNF-α) and interleukin-1β (IL-1β) concentrations were evaluated by Enzyme-Linked Immunosorbent Assay (ELISA) assay kits. All procedures were performed following the directions provided in the kit. The absorbance of each sample was detected by a microplate reader at 490 nm. The concentration of cell cytokines is described as picograms per milliliter.

Western Blot Analysis

At different reperfusion times, protein was extracted from the infarcted hemispheres and cultured cells by a protein extraction kit (Beyotime Biotech) as described in our previous report (Li et al., 2015). Protein samples were next electrophoresed and transferred to polyvinylidene difluoride filter (PVDF) membranes. Then block the membrane with 5% fat-free milk at room temperature for 2 h, and incubate with primary antibodies as follows: anti-Tubulin (Cell Signaling), anti-Cx43 (Cell Signaling), anti-TLR4 (Proteintech), anti-MyD88 (Cell Signaling), anti-NF-κB p65 (Proteintech), anti-IL-1β (Bioss), and anti-TNF-α (Bioss) at 4°C overnight. Next day, incubate with secondary horse anti-mouse or goat anti-rabbit antibodies conjugated with horseradish peroxidase (Cell Signaling) for 2 h and visualize by an enhanced chemiluminescence system (ECL). Relative protein levels were quantified after normalization to Tubulin.

Statistical Analysis

All data were described as the mean ± SEM. Pictures were analyzed by ImageJ software. Data from all experiments were quantified and analyzed by GraphPad Prism 7.0 software. $P < 0.05$ was regarded as statistically significant.

RESULTS

Gap19 Decreased Infarct Volume and Prevented the Deterioration of Neurological Deficit

Animals were euthanized after 24 h reperfusion, and the brain infarction volume was analyzed using TTC staining to determine whether Gap19 was protective after cerebral I/R injury. Results demonstrated I/R group has a large infarct volume (56.06 ± 1.77%). Gap26 and Gap19 treatment groups exhibited a significantly smaller infarct volume than I/R group ($P < 0.05$, **Figures 1A,B**). Furthermore, the infarct volume of the I/R + Gap19 group (27.9 ± 0.93%) was significantly smaller than that of the I/R + Gap26 group (40.12 ± 0.95%; $P < 0.05$, **Figures 1A,B**). This result demonstrated that Gap19 had a better neuroprotective effect. As shown in **Figure 1C**, no obvious neurological deficits were generated in the sham

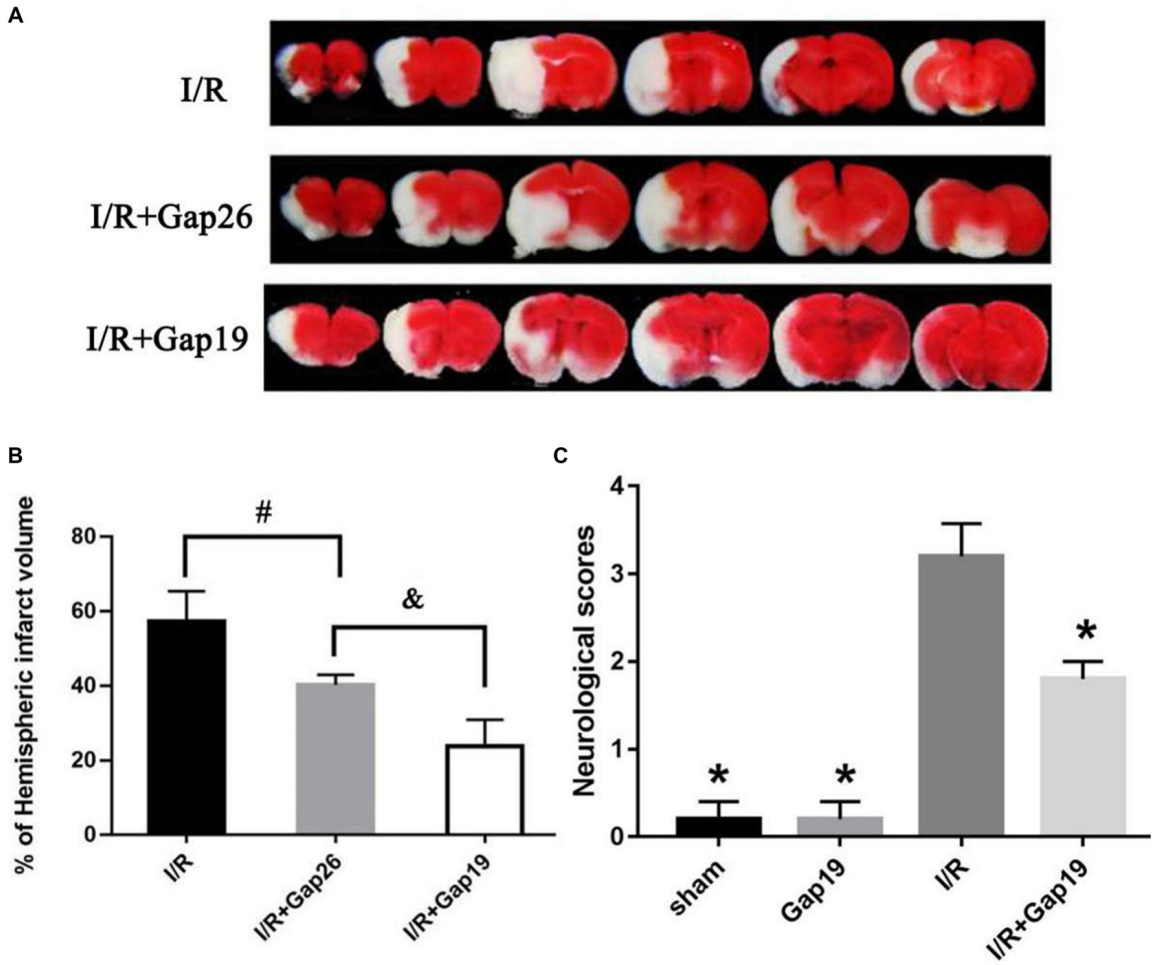

FIGURE 1 | Gap19 decreased infarct volume and prevented the deterioration neurological deficit after ischemia/reperfusion (I/R) injury. Mice were administered Gap26 or Gap19 1 h after middle cerebral artery occlusion (MCAO). 2,3,5-triphenyltetrazolium chloride chloride (TTC) staining and neurological scores were examined at 24 h after reperfusion. **(A)** Representative TTC-stained slices of different treatment groups after MCAO. The infarct tissue area was not stained (white), and normal tissue was stained (red). **(B,C)** Statistical analyses of infarct volume of different treatment groups were shown. **(C)** Neurological scores were assessed with a 5-point scale system. Gap19 treatment observably decreased neurological deficits. Data represent mean ± SEM of five brains. $^{*}P < 0.05$ vs. I/R group, $^{\#,\&}P < 0.05$.

or Gap19 groups, whereas severe deficits could be observed in I/R group. Consistent with this result, we also found that Gap19 treatment remarkably reduced neurological scores and prevented the deterioration of the neurological function ($P < 0.05$, **Figure 1C**).

Gap19 Ameliorated White Matter Injury After Cerebral I/R Injury

We euthanized mice at 7 days after reperfusion, and the brains were prepared for frozen sectioning, stained with LFB to examine the influence of Gap19 on white matter after I/R injury. We chose the white matter-enriched area of the striatum for LFB stain and analyzed the blue area in the striatum. Striatum staining was shallow in the I/R group, and the cells were swollen and disorganized (**Figures 2A,B**). The blue area in I/R + Gap19 group was obviously larger than the area in I/R group ($P < 0.05$, **Figure 2C**). This result demonstrated that Gap19 alleviated the white matter injury in the MCAO model.

The Relative Amount of Cx43 and TLR4 Increased After Cerebral I/R Injury

Western blots analyzed the expression levels of Cx43 and TLR4 at different reperfusion time points. The infarcted hemispheres were extracted from the sham group and groups with different reperfusion times (4 h, 12 h, 24 h, 72 h and 7 days). Upon I/R 4 h, it was observed an increase in the abundance of Cx43. Expression increased 4 h after reperfusion, peaked 24 h after reperfusion, and declined but remained higher than normal until 7 days ($P < 0.05$, **Figures 3A,C**). TLR4 level increased obviously in the infarcted region at 24 h after reperfusion and reached a maximum at 72 h post-reperfusion ($P < 0.05$, **Figures 3A,B**). This trend correlated with Cx43 expression. At 24 h after cerebral I/R injury, the level of Cx43 protein in I/R + Gap19 group was lower than that in the

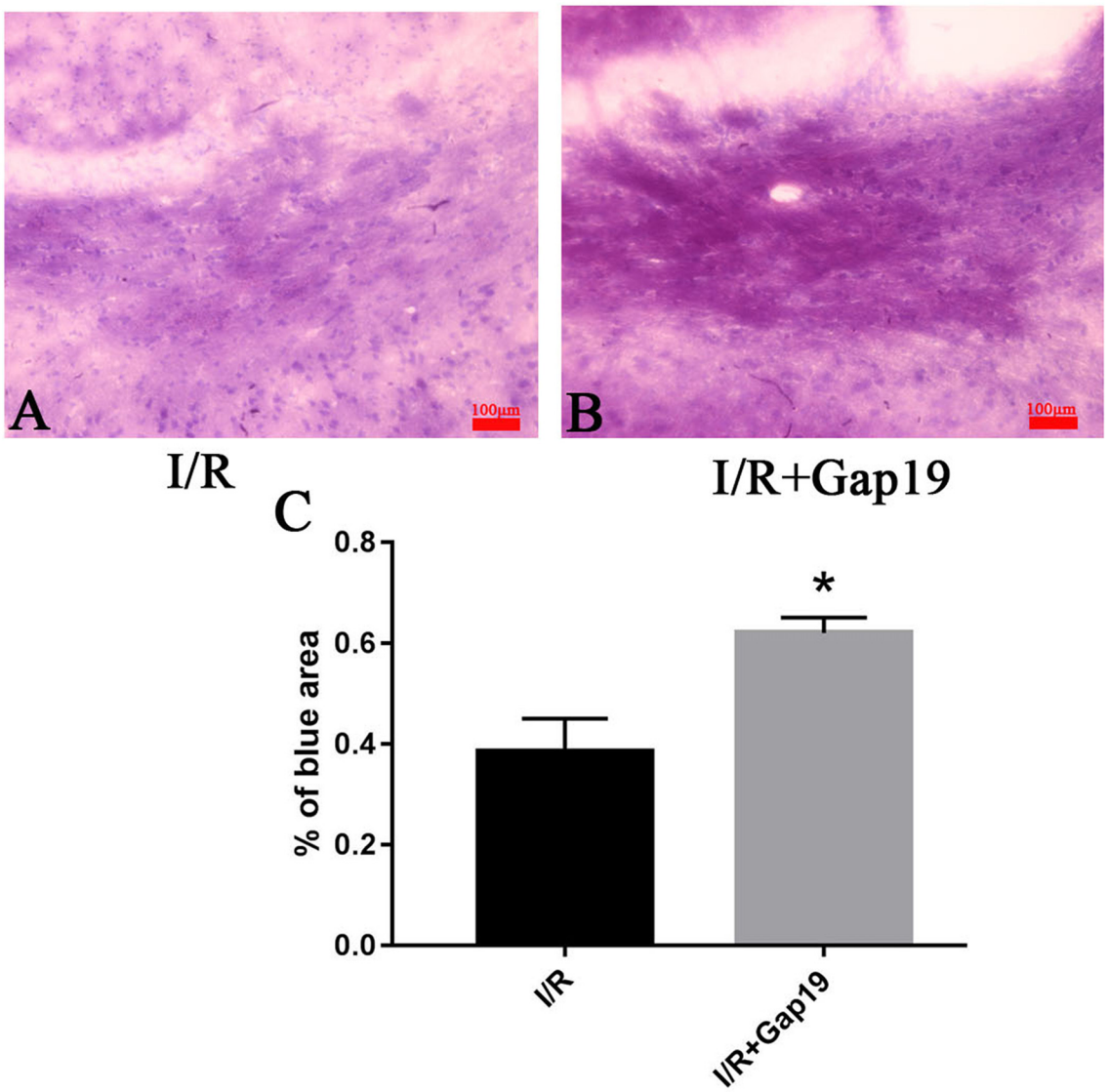

FIGURE 2 | Gap19 ameliorated white matter injury. **(A,B)** Representative pictures of LFB stain at 7 days after cerebral ischemia. **(C)** The percentage of blue area in I/R + Gap19 group was increased compared to I/R group. *$P < 0.05$ vs. I/R group. Data represent the mean ± SEM ($n = 3$ mice/group). Scar bar = 100 μm.

I/R group, which indicated that Gap19 effectively prevented the increase in the abundance of Cx43 ($P < 0.05$, **Figures 3D,E**).

Gap19 Inhibited Activation of the TLR4 Pathway and Reduced Inflammatory Cytokines *in vivo*

The secondary inflammatory response is the main reason for secondary injury after cerebral I/R, and TLR4-mediated innate immunity plays an important role (Wang Y. et al., 2013). We found that the expression of TLR4 was remarkably increased after MCAO than sham group or Gap19 group ($P < 0.05$, **Figures 4A,B**). TLR4 level was significantly lower in I/R + Gap19 group than I/R group. Gap19 also inhibited the expression of the TLR4 downstream protein MyD88 and NF-κB ($P < 0.05$, **Figures 4A,C,E**). Furthermore, proinflammatory cytokines as TNF-α and IL-1β released from ischemic tissue are associated with neurotoxic effects by inducing apoptosis of neuronal cells (Boutin et al., 2001; Shichita et al., 2012). Previous studies showed that these cytokines could also affect Cx43 abundance in both astrocytes (Même et al., 2006; Retamal et al., 2007) and microglia (Eugenín et al., 2001). Our study demonstrated that Gap19 treatment remarkably decreased the expression of IL-1β and TNF-α ($P < 0.05$, **Figures 4D,F,G**), which could further decreasing the Cx43 expression. These results revealed that Gap19 could effectively inhibited TLR4 pathway and decreased inflammation in a mouse cerebral I/R model.

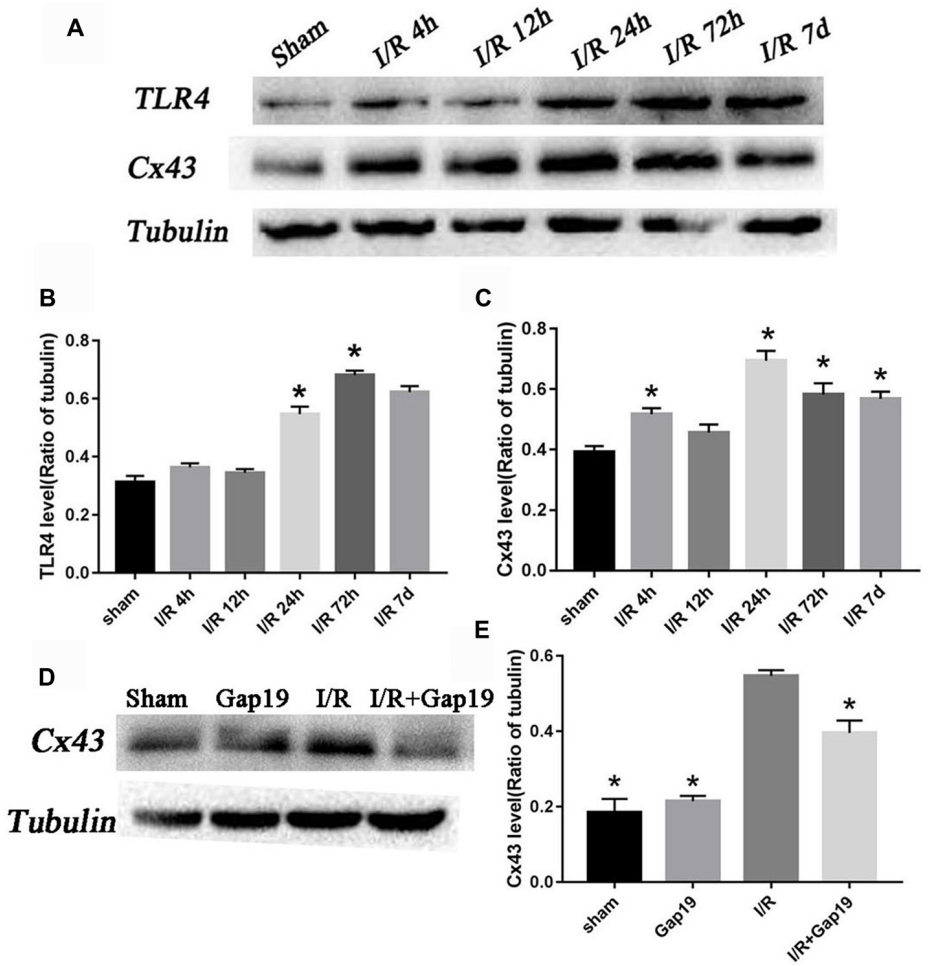

FIGURE 3 | The relative amount of connexin 43 (Cx43) and Toll-like receptor 4 (TLR4) increased after cerebral I/R injury. **(A)** Photomicrographs showed Cx43 and TLR4 tubulin levels in the sham group and 4 h, 12 h, 24 h, 72 h and 7 days after cerebral I/R injury. **(B,C)** Quantitative analyses revealed the variation tendency of Cx43 and TLR4 after cerebral I/R injury. **(D)** Photomicrographs showed Cx43 levels at 24 h after cerebral I/R injury. **(E)** Quantitative analysis of Cx43. Data represent the mean ± SEM (n = 3 mice/group). *$P < 0.05$ vs. I/R group.

Cx43 Co-existed With TLR4 in Astrocytes

We performed immunofluorescence staining for Cx43 and TLR4 in primary astrocytes to further determine the relationship between the protective effect of Gap19 and the TLR4 signaling pathway in cerebral ischemic injury. We could saw both TLR4 and Cx43 existed on astrocytes in the OGD model. Cx43 was primarily expressed in the cytoplasm (yellow arrow), and TLR4 was expressed in the cell membrane (red arrow; **Figure 5**).

Gap19 Increased Cell Viability After OGD and Inhibited Cx43 Expression

We performed MTT assay in primary astrocytes to determine the optimal concentration of Gap19 in the cell OGD model. Different concentrations of Gap19 were selected to intervention in the onset of OGD, and cell viability was determined. The results demonstrated that Gap19 effectively improved the relative vitality of co-cultured cells at 50 μM, 100 μM, 150 μM and 200 μM ($P < 0.05$, **Figure 6A**), and we chose optimal concentration—100 μM ($P < 0.01$) for subsequent experiments. The expression level of Cx43 was increased in the cell OGD model, and the expression was reduced after Gap19 intervention, which was consistent with the *in vitro* results ($P < 0.05$, **Figures 6B,C**).

Gap19 Decreased the Hemichannels Activity After OGD on Astrocytes

Previous study showed that Gap19 can inhibit Cx43 hemichannel activity in astrocytes after treatment with pro-inflammatory cytokines (Abudara et al., 2014). In this study, we targeted the Cx43 hemichannels after brain ischemia, so we conducted the EtBr uptake assay to evaluate the hemichannels activity in different cells after OGD. First, we identified the three cell types with specific cellular markers. Neuron was verified by anti-β-III tubulin antibody (**Figure 7A**), BMECs were characterized by anti-CD31 antibody (**Figure 7B**) and astrocytes

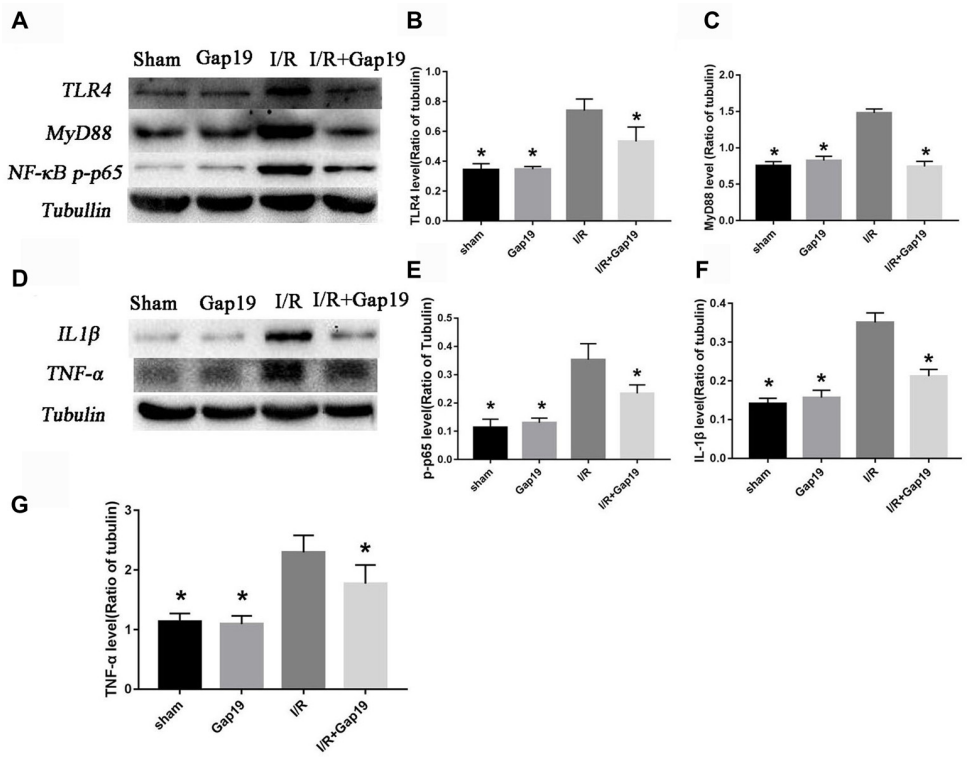

FIGURE 4 | Gap19 suppressed the TLR4 signaling pathway and inflammatory cytokines expression *in vivo*. **(A)** Brain tissues were collected after 24 h reperfusion, and TLR4, MyD88 and NF-κB p-p65 levels were determined by Western blot. Gap19 treatment inhibited the increment of TLR4 **(B)**, MyD88 **(C)** and NF-κB p-p65 **(E)** expression. **(D)** Interleukin-1β (IL-1β) and tumor necrosis factor-α (TNF-α) protein expression was also lower in Gap19-treated mice than I/R mice 24 h post-reperfusion **(F,G)**. Data represent the mean ± SEM (n = 3 mice/group). $^*P < 0.05$ vs. I/R group.

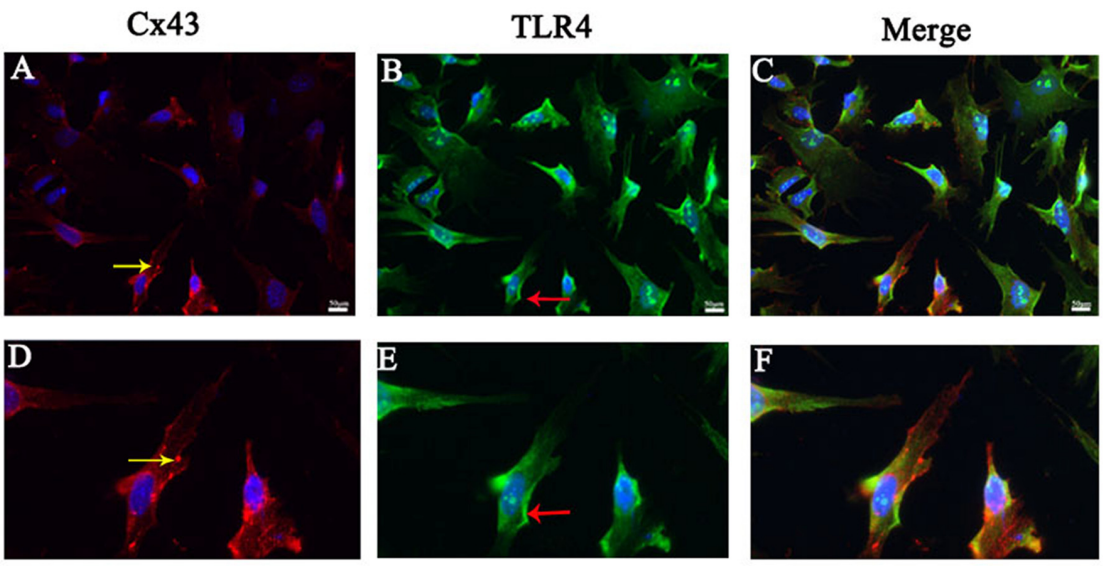

FIGURE 5 | Cx43 co-existed with TLR4 in astrocytes. **(A–C)** Double immunofluorescence staining showed the Cx43 (yellow arrow) and TLR4 (red arrow) in cultured astrocytes after oxygen glucose deprivation (OGD). **(D–F)** The pictures were the amplification of the cell with the arrow above. Scar bar = 50 μm.

were identified by anti-GFAP antibody (**Figure 7C**). Then, we observed that EtBr uptake was increased in three type cells after OGD (**Figures 7G–I**) than the control group (**Figures 7D–F**). There was slightly reduction of hemichannels

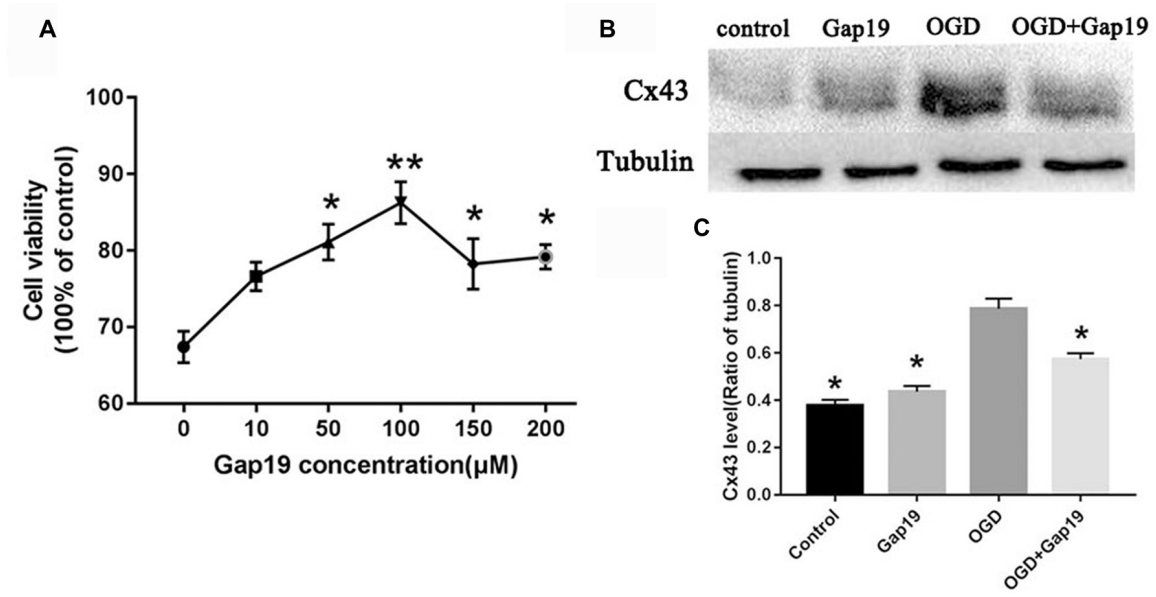

FIGURE 6 | Gap19 increased cell viability after OGD and inhibited Cx43 expression. **(A)** Cell viability following different concentrations of Gap19 after OGD. **(B)** Astrocytes were deprived oxygen-glucose for 4 h following 24 h reoxygenation, and the level of Cx43 was detected using Western blot. **(C)** Quantitative analysis confirmed that Gap19 treatment at the beginning of OGD significantly decreased Cx43 expression. Data represent the mean ± SEM (n = 3). *$P < 0.05$, **$P < 0.01$ vs. OGD group.

activity in neurons and BMECs after treatment with Gap19, but without statistical difference (**Figures 7J,K,M,N**). Meanwhile, Gap19 could obviously inhibit the hemichannels opening after OGD in astrocytes (**Figures 7L,O**). This result was consistent with a recently study. Walrave et al. (2018) found that Gap19 inhibited the hemichannels open induced by Pilocarpine and exerted anticonvulsant effects. Based on these result, we think astrocytes are the most critical cell type in this triple co-culture system.

Gap19 Also Prevented the Activation of TLR4 Pathway and Reduced Inflammatory Cytokines *in vitro*

We constructed a triple cell co-culture system to verify the role of Gap19 *in vitro* cerebral I/R model. Gap19 reduced the activation of TLR4 ($P < 0.05$, **Figures 8A,B**) compared to the levels in the triple cell co-culture OGD group. MyD88 and NF-κB level were also lower in the OGD + Gap19 group ($P < 0.05$, **Figures 8A,C,D**). We conducted ELISA to analyze the levels of inflammatory factors in the culture supernatant. The secretion of TNF-α and IL-1β in the Gap19 treatment group was decreased ($P < 0.05$, **Figures 8E,F**). These results were similar to those in the *in vitro* study. To further identify the anti-inflammation role of Gap19, we use the neutralizing antibodies of TNF-α to treat the astrocytes after OGD and detect the cell viability. We qualitatively found both TNF-α and p-P65 expression was inhibited through Western blot (**Figure 8G**). The MTT assay revealed that neutralization of TNF-α can also increase the astrocytes viability after OGD, just like Gap19 ($P < 0.05$, **Figure 8H**). This is a very interesting result, which further confirmed that Gap19 could alleviate the inflammatory response by inhibiting the opening of Cx43 hemichannels.

Gap19 Attenuated LPS-Induced TLR4 Activation and Inflammation *in vitro*

Based on the above results, we hypothesized that Gap19 protected against cerebral I/R injury via downregulation of TLR4 signaling. LPS is one of the pathogen-associated molecular pattern that can specifically activate TLR4 signaling (Shao et al., 2013), and increase Cx43 hemichannels activity in astrocytes (Retamal et al., 2007). We conducted the LPS-induced experiment to further verify this hypothesis. The expression of TLR4 after LPS treatment was increased compared to the OGD group in the triple cell co-culture system ($P < 0.05$, **Figures 9A,B**). Gap19 treatment significantly attenuated TLR4 expression after LPS stimulation in OGD model. We further detected proinflammatory cytokine levels in the cell supernatant using ELISA. Gap19 treatment decreased the release of TNF-α and IL-1β in the culture medium after LPS stimulation ($P < 0.05$, **Figures 9C,D**). These results further corroborate that the protective effect of Gap19 occurred via downregulation of the TLR4 pathway.

DISCUSSION

The concept of the NVU was first proposed in 2003 by Lo and colleagues (Lo et al., 2003). Cerebrovascular disease research has gradually shifted focus from merely neurons or astrocytes to the NVU integral components, and it is considered a precondition for the screening of novel drugs and therapeutic

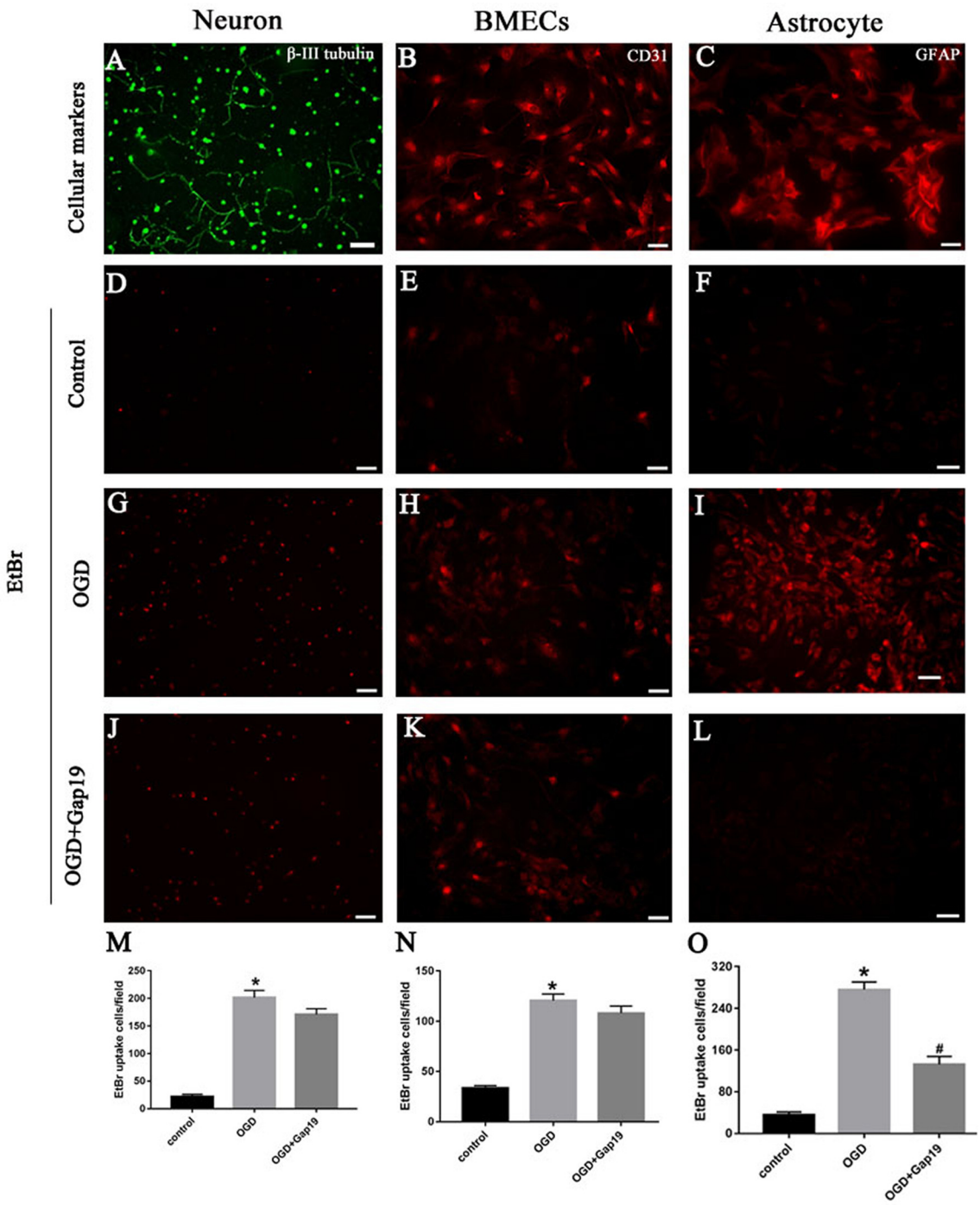

FIGURE 7 | Gap19 decreased the hemichannels activity after OGD on astrocytes. **(A–C)** Immunophenotyping of three cells were identified by β-III tubulin, CD31 and GFAP. **(D–L)** Representative pictures showed ethidium bromide (EtBr) uptake via hemichannels in the three groups of different cells. **(M–O)** EtBr uptake was increased after OGD injury, and Gap19 could remarkably inhibited hemichannels activity. $^{*}P < 0.05$ vs. control group. $^{\#}P < 0.05$ vs. OGD group. Scar bar = 100 μm.

target for stroke (Hu et al., 2017). Glial cells (astrocytes and oligodendrocytes) and BMECs are damaged via similar injury pathways, including glutamate toxicity, during ischemic injury (George and Steinberg, 2015). Ischemic damage also activates endogenous immune cells such as microglia (Kim et al., 2014). This study successfully established the cerebral I/R model *in vivo*/*vitro* and examined the role of Gap19 in cerebral I/R injury. Our results suggested that Gap19 reduced the infarct size and prevented the deterioration of the neurological function after cerebral ischemia and alleviated brain white matter damage.

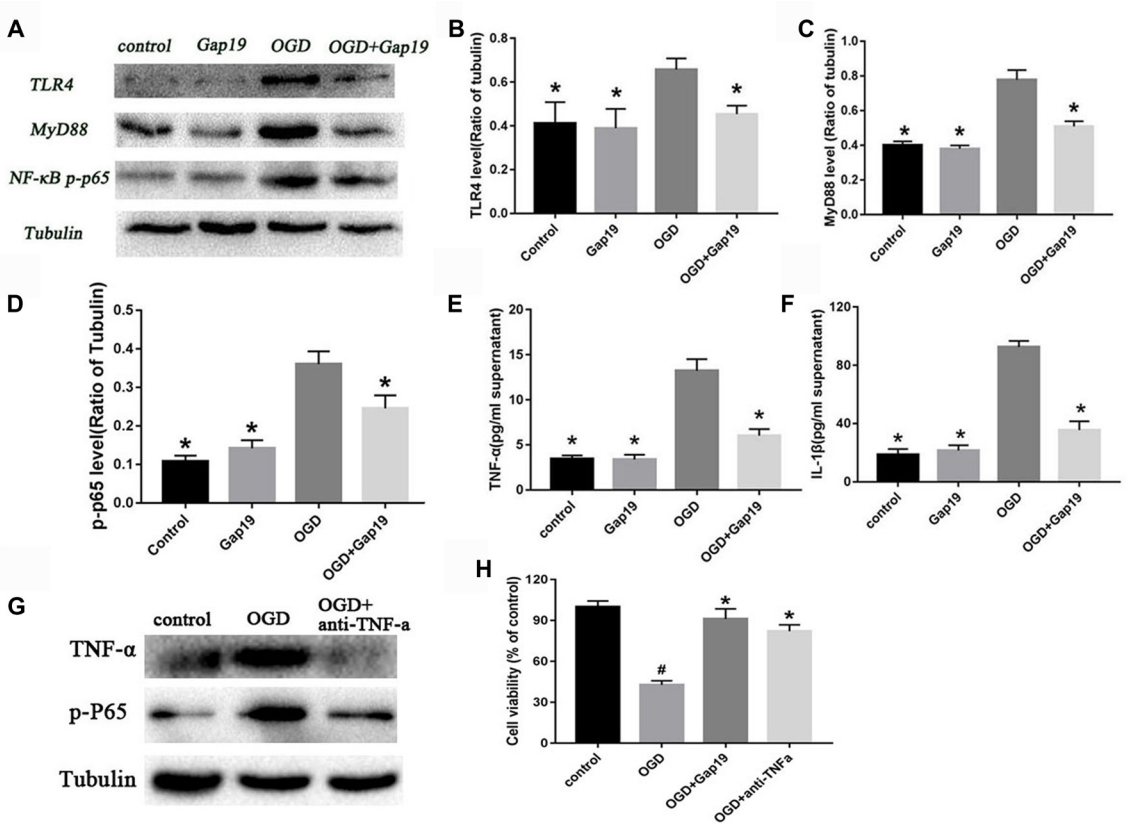

FIGURE 8 | Gap19 prevented the activation of TLR4 pathway and reduced inflammatory cytokines *in vitro*. **(A–D)** Western blot and quantitative analysis showed the expression of TLR4, MyD88 and NF-κB p-p65 were decreased by Gap19 after OGD. **(E,F)** Enzyme-linked immunosorbent assay (ELISA) revealed that Gap19-treated cells exhibited altered release of IL-1β and TNF-α 24 h after reoxygenation. **(G,H)** The neutralizing antibodies of TNF-α decrease the p-P65 expression and increased the astrocytes viability after OGD. Values (mean ± SEM) are representative of at least three independent experiments. $^{*}P < 0.05$ vs. the OGD group. $^{\#}P < 0.05$ vs. the control group.

We further investigated the protection mechanism of Gap19. Result showed that Gap19 reduced the expression levels of Cx43, TLR4, MyD88 and NF-κB after ischemic injury and reduced the inflammatory response secondary to reperfusion.

We also investigated the mechanism about how Gap19 alleviating inflammation following stroke. We cultured primary neurons, astrocytes and cerebrovascular endothelial cells and constructed an NVU model for OGD treatment to simulate the *in vivo* process of cerebral I/R injury. Our result showed that when the concentration of Gap19 over 150 μM, the cell viability decreased compared with 100 μM. We think that high concentration strongly inhibits the Cx43 expression and decrease the gap junction formation, further interfering cell-to-cell communication. We detected the change of hemichannels activity on different treatment by EtBr uptake assay. Results showed that the opening of hemichannels increased after OGD and Gap19 could inhibit this effect on astrocytes. We also observed that Gap19 inhibited activation of the TLR4 pathway after OGD and inhibited the expression of pathway-related proteins, reduced the release of TNF-α and IL-1β, which was similar with the role of neutralization of TNF-α. Gap19 also decreased the expression of TLR4 in the LPS administration OGD model. Our results are the first to demonstrate that specific blocker of Cx43 hemichannels-Gap19 plays a vital role in protecting cerebral ischemia via inhibition of activation of the TLR4 pathways.

NVU consists of neurons, astrocytes and cerebrovascular endothelial cells, pericytes, basal membranes, and extracellular matrix (Stanimirovic and Friedman, 2012). Nerve cells are primarily connected with each other via gap junctions to communicate electrical signals, transmit chemical signals and metabolites to support the normal function of NVU cells (Giaume et al., 2010). Our study considered the NVU as the main research object and gap junctions as the main target. Cx43 is the main connexin protein that forms the gap junctions and hemichannels, and these proteins are expressed abundantly in brain, especially in astrocytes (D'hondt et al., 2014). Large amounts of hemichannels are opened after ischemia, causing ion disorders, loss of important metabolic substances, cell swelling and even death. Previous studies have shown that the use of gap junction inhibitors, such as glycyrrhetinic acid and its derivative carbenoxolone, improve blood-brain barrier permeability in mice, but the specificity is poor, and glycyrrhetinic acid interferes with other types of junctions

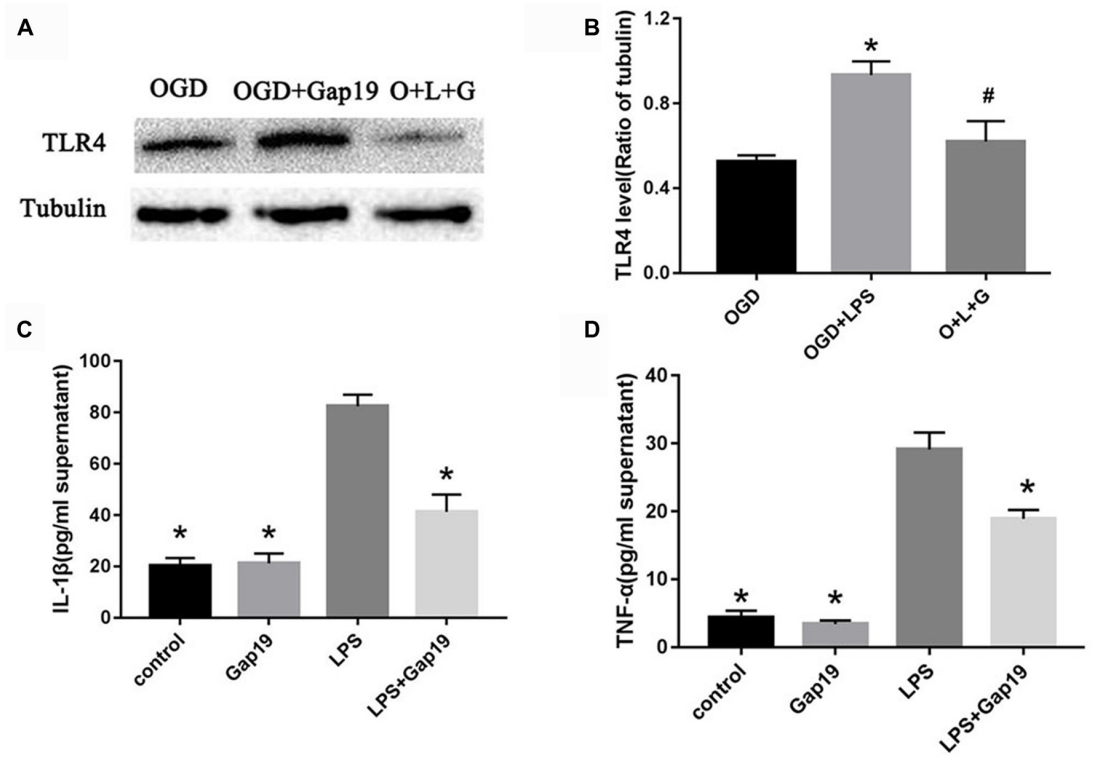

FIGURE 9 | Gap19 attenuated LPS-induced TLR4 activation and inflammation *in vitro*. **(A)** Photomicrographs show TLR4 levels after LPS treatment using Western blot. The group O + L + G means OGD + LPS + Gap19 group. **(B)** Quantitative analysis confirmed that Gap19 treatment decreased TLR4 expression after LPS stimulation. **(C,D)** ELISA showed that Gap19 inhibited the release of IL-1β and TNF-α after LPS administration. Data represent the mean ± SEM ($n = 3$). $^{*}P < 0.05$ vs. OGD group, $^{\#}P < 0.05$ vs. OGD + LPS group.

(Takeuchi et al., 2011). Our previous studies demonstrated that the Cx43 mimetic peptides Gap26/Gap27 exhibited protective effects on the hypoxia/ischemia model in neonatal rats (Li et al., 2015). Hawat et al. (2010) found that Gap26 reduced infarct volume in myocardial ischemia reperfusion injury in rats. However, Gap26/27 also affected the formation of gap junctions when hemichannels are blocked.

Gap19 is a mimetic peptide that corresponds to a sequence in the CL of Cx43, which may disturb the interaction of C-terminal tail and CL of Cx43 (Abudara et al., 2014). The peptide may keep the gap junction open and hemichannel closed after ischemia with high specificity (Delmar et al., 2004). Wang N. et al. (2013) verified that Gap19 decreased the infarct volume after myocardial I/R in mice and alleviated cell oedema. Vicario et al. (2017) found that Gap19 specifically inhibited damage to human neuroblastoma cells after hypoxia/reoxygenation injury. Walrave et al. (2016) reported that TAT-Gap19 impaired hippocampal short-term spatial memory via inhibition of Cx43 hemichannels. Treatment with Gap19 decreased Cx43 expression in our study, which could further decrease the formation of Cx43 hemichannels. Our previous study found that Gap26 could decrease both total and dephosphorylated Cx43, and promote the internalization of Cx43 and the degradation of Cx43 in cytoplasm through the ubiquitin proteasome pathway (Li et al., 2015). In this study, Gap19 reduced infarction volume more than Gap26, exhibited better specificity and played a neuroprotective role in brain ischemia, and our results identified that Gap19 could significantly decrease the hemichannels activity on astrocytes but not on neurons and BMECs. Previous studies showed that Cx43 mainly expressed in astrocytes, rarely on neurons (Liu et al., 2012; Schulz et al., 2015), and could increase in BMECs after inflammation (Danesh-Meyer et al., 2012). In this NVU model, astrocytes were the critical one as bridge to connect the different components.

I/R is a pathological process that interrupts the blood flow of an organ, subsequent with reperfusion and reoxidation. Blood recirculation further aggravates tissue damage, which leads to a more severe inflammatory response, known as reperfusion injury (Eltzschig and Eckle, 2011). This injury occurs in a sterile environment and involves signaling events through pattern-recognition receptors (PRRs), such as TLRs, and the infiltration of blood immune cells of the innate and adaptive immune systems (Shichita et al., 2012). As we all know, microglia is the primary immune effector and can be activated by ischemia, releasing inflammatory cytokines (Morioka et al., 1993). And in brain, TLRs are constitutively expressed in microglia, but also in astrocyte and can be activated by endogenous damage-associated molecular patterns (DAMPs), such as ATP (Zhang et al., 2010), high mobility group box 1 protein (Yang et al., 2011), heat shock proteins, extracellular matrix proteins and so

on. They are released from damaged brain cells after ischemia (Kim et al., 2014; Molteni et al., 2016). Increasing evidence suggests that TLR4 plays an important role in secondary brain injury following ischemia (Brea et al., 2011). A recent study demonstrated that TLR4$^{-/-}$ mice decreased neuronal damage and apoptosis after global cerebral I/R (Hua et al., 2007). Hua et al. (2015) found that TLR4 blocker TAK-242 alleviated the inflammation after brain ischemia and played a neuroprotective role. Although TLR4 was primarily expressed in microglia in the central nervous system, these receptors are also expressed in astrocytes (Carpentier et al., 2008), neurons (Tang et al., 2007), and cerebrovascular endothelial cells (Grace et al., 2014) in some pathological environments. Our study demonstrated that Gap19 inhibited activation of the TLR4 signaling by MyD88-dependent pathway. Previous studies showed that treatment with TNF-α or IL-1β could increase membrane permeability through Cx43 hemichannels in astrocytes (Retamal et al., 2007) and upregulate the expression of Cx43 in microglia (Shaikh et al., 2012; Sáez et al., 2013). Our results revealed that Gap19 attenuated the expression of TNF-α and IL-1β after cerebral I/R injury which further suggests that the protective effect may occur via inhibition of the inflammatory response after reperfusion. Previous researches showed that after inflammation stimulation, microglia can also express Cx43 and communicate with each other through the gap junction (Eugenín et al., 2001; Shaikh et al., 2012; Sáez et al., 2013). In the future study, it will be valuable to add the microglia in this system for further study.

A recent study demonstrated that the Cx43 hemichannel may be a novel mediator of sterile inflammatory diseases (Li et al., 2018), which is consistent with the results of our study. This research further indicates that Cx43 is associated with inflammation. LPS is the main component of the cytoderm of Gram-negative bacteria and specifically activated the TLR4 pathway to induce an inflammatory response (Kawai and Akira, 2010). The *in vitro* model found that Gap19 reduced TLR4 and inflammatory cytokines expression after LPS stimulation. Previous studies reported that IL-1β and TNF-α released by activated microglia can inhibit the gap junction communication and increase the hemichannels activity on astrocyte (Même et al., 2006; Retamal et al., 2007). In other words, Gap19 may also decrease the opening of Cx43 hemichannels. All these data demonstrated that the inhibitory effect of Gap19 on the inflammation secondary to I/R injury may be associated with the inhibition of TLR4 signaling pathway. However, how the interaction of Gap19 and Cx43 causes inhibition of the TLR4 pathway remains unknown. We think that the mechanism may be similar to the treatment with Gap26. Previous study showed that the decrease of Cx43 expression after DNA hyper-methylation further activates the transcriptional activation of apoptosis suppressor genes (Yu S. C. et al., 2012). Li et al. (2016) found that hypoxia during pregnancy may lead to continuous whole-brain hypo-methylation in the fetal brain. Hence, does it affect the methylation of Cx43 DNA promoter region? This still requires further study.

CONCLUSION

Our results indicate that Gap19 can decrease the brain infarct volume, prevent the deterioration of neurological deficit and alleviate white matter damage, and that Gap19 can also remarkably reduce the inflammatory response via inhibition of the TLR4 signaling pathway following *in vivo* MCAO and *in vitro* OGD. Therefore, Gap19 may be a potential therapeutic drug for cerebral ischemic injury which associated with NVU disruption.

However, whether Gap19 affects TRIF-mediated inflammatory responses, which is the other pathway of TLR4, is not known. Future experiments should address this relationship. We did not verify the inhibition of Gap19 on the TLR4 pathway at the gene expression level, and more studies are required to further validate these results.

AUTHOR CONTRIBUTIONS

YC, LW and HY: conceived and designed the experiments; contributed to the writing of the manuscript. LW, LZ and LY: performed the experiments. HY, YL and LW: analyzed the data. LW, XL and BC: contributed reagents, materials and analysis tools. All authors approved the final manuscript.

FUNDING

This study was supported by National Natural Science Foundation of China (Grant nos. 81400963 and 81371377), 333 project of Jiangsu Province (the grant number: BRA2015187 and BRA2017168) and Jiangsu Provincial Medical Youth Talent (Grant #QNRC2016327 and QNRC2016328, QNRC2016326) and Six big talent peak fund in Jiangsu Province (grant #2016-WSN-274).

ACKNOWLEDGMENTS

All authors have contributed significantly, and all authors are in agreement with the content of the manuscript. We gratefully thank YC, XL, BC, YL and HY for their generous assistance.

REFERENCES

Abudara, V., Bechberger, J., Freitas-Andrade, M., De Bock, M., Wang, N., Bultynck, G., et al. (2014). The connexin43 mimetic peptide Gap19 inhibits hemichannels without altering gap junctional communication in astrocytes. *Front. Cell. Neurosci.* 8:306. doi: 10.3389/fncel.2014.00306

Bodendiek, S. B., and Raman, G. (2010). Connexin modulators and their potential targets under the magnifying glass. *Curr. Med. Chem.* 17, 4191–4230. doi: 10.2174/092986710793348563

Boutin, H., LeFeuvre, R. A., Horai, R., Asano, M., Iwakura, Y., and Rothwell, N. J. (2001). Role of IL-1α and IL-1β in ischemic brain damage. *J. Neurosci.* 21, 5528–5534. doi: 10.1523/JNEUROSCI.21-15-05528.2001

Brea, D., Blanco, M., Ramos-Cabrer, P., Moldes, O., Arias, S., Perez-Mato, M., et al. (2011). Toll-like receptors 2 and 4 in ischemic stroke: outcome and therapeutic values. *J. Cereb. Blood Flow Metab.* 31, 1424–1431. doi: 10.1038/jcbfm.2010.231

Carpentier, P. A., Duncan D', A. S., and Miller, S. D. (2008). Glial toll-like receptor signaling in central nervous system infection and autoimmunity. *Brain Behav. Immun.* 22, 140–147. doi: 10.1016/j.bbi.2007.08.011

Chew, S. S., Johnson, C. S., Green, C. R., and Danesh-Meyer, H. V. (2010). Role of connexin43 in central nervous system injury. *Exp. Neurol.* 225, 250–261. doi: 10.1016/j.expneurol.2010.07.014

Danesh-Meyer, H. V., Kerr, N. M., Zhang, J., Eady, E. K., O'Carroll, S. J., Nicholson, L. F., et al. (2012). Connexin43 mimetic peptide reduces vascular leak and retinal ganglion cell death following retinal ischaemia. *Brain* 135, 506–520. doi: 10.1093/brain/awr338

De Bock, M., Culot, M., Wang, N., Bol, M., Decrock, E., De Vuyst, E., et al. (2011). Connexin channels provide a target to manipulate brain endothelial calcium dynamics and blood-brain barrier permeability. *J. Cereb. Blood Flow Metab.* 31, 1942–1957. doi: 10.1038/jcbfm.2011.86

Decrock, E., De Vuyst, E., Vinken, M., Van Moorhem, M., Vranckx, K., Wang, N., et al. (2009). Connexin 43 hemichannels contribute to the propagation of apoptotic cell death in a rat C6 glioma cell model. *Cell Death Differ.* 16, 151–163. doi: 10.1038/cdd.2008.138

Delmar, M., Coombs, W., Sorgen, P., Duffy, H. S., and Taffet, S. M. (2004). Structural bases for the chemical regulation of connexin43 channels. *Cardiovasc. Res.* 62, 268–275. doi: 10.1016/j.cardiores.2003.12.030

D'hondt, C., Iyyathurai, J., Himpens, B., Leybaert, L., and Bultynck, G. (2014). Cx43-hemichannel function and regulation in physiology and pathophysiology: insights from the bovine corneal endothelial cell system and beyond. *Front. Physiol.* 5:348. doi: 10.3389/fphys.2014.00348

Eltzschig, H. K., and Eckle, T. (2011). Ischemia and reperfusion—from mechanism to translation. *Nat. Med.* 17, 1391–1401. doi: 10.1038/nm.2507

Eugenín, E. A., Eckardt, D., Theis, M., Willecke, K., Bennett, M. V., and Saez, J. C. (2001). Microglia at brain stab wounds express connexin 43 and *in vitro* form functional gap junctions after treatment with interferon-γ and tumor necrosis factor-α. *Proc. Natl. Acad. Sci. U S A* 98, 4190–4195. doi: 10.1073/pnas.051634298

Evans, W. H., and Leybaert, L. (2007). Mimetic peptides as blockers of connexin channel-facilitated intercellular communication. *Cell Commun. Adhes.* 14, 265–273. doi: 10.1080/15419060801891034

Gauthier, S. A., Sahoo, S., Jung, S. S., and Levy, E. (2012). Murine cerebrovascular cells as a cell culture model for cerebral amyloid angiopathy: isolation of smooth muscle and endothelial cells from mouse brain. *Methods Mol. Biol.* 849, 261–274. doi: 10.1007/978-1-61779-551-0_18

George, P. M., and Steinberg, G. K. (2015). Novel stroke therapeutics: unraveling stroke pathophysiology and its impact on clinical treatments. *Neuron* 87, 297–309. doi: 10.1016/j.neuron.2015.05.041

Giaume, C., Koulakoff, A., Roux, L., Holcman, D., and Rouach, N. (2010). Astroglial networks: a step further in neuroglial and gliovascular interactions. *Nat. Rev. Neurosci.* 11, 87–99. doi: 10.1038/nrn2757

Giaume, C., Orellana, J. A., Abudara, V., and Saez, J. C. (2012). Connexin-based channels in astrocytes: how to study their properties. *Methods Mol. Biol.* 814, 283–303. doi: 10.1007/978-1-61779-452-0_19

Girouard, H., and Iadecola, C. (2006). Neurovascular coupling in the normal brain and in hypertension, stroke and Alzheimer disease. *J. Appl. Physiol.* 100, 328–335. doi: 10.1152/japplphysiol.00966.2005

Grace, P. M., Ramos, K. M., Rodgers, K. M., Wang, X., Hutchinson, M. R., Lewis, M. T., et al. (2014). Activation of adult rat CNS endothelial cells by opioid-induced toll-like receptor 4 (TLR4) signaling induces proinflammatory, biochemical, morphological and behavioral sequelae. *Neuroscience* 280, 299–317. doi: 10.1016/j.neuroscience.2014.09.020

Guo, S., Kim, W. J., Lok, J., Lee, S. R., Besancon, E., Luo, B. H., et al. (2008). Neuroprotection via matrix-trophic coupling between cerebral endothelial cells and neurons. *Proc. Natl. Acad. Sci. U S A* 105, 7582–7587. doi: 10.1073/pnas.0801105105

Hawat, G., Benderdour, M., Rousseau, G., and Baroudi, G. (2010). Connexin 43 mimetic peptide Gap26 confers protection to intact heart against myocardial ischemia injury. *Pflugers Arch.* 460, 583–592. doi: 10.1007/s00424-010-0849-6

Hu, X., De Silva, T. M., Chen, J., and Faraci, F. M. (2017). Cerebral vascular disease and neurovascular injury in ischemic stroke. *Circ. Res.* 120, 449–471. doi: 10.1161/circresaha.116.308427

Hua, F., Ma, J., Ha, T., Xia, Y., Kelley, J., Williams, D. L., et al. (2007). Activation of toll-like receptor 4 signaling contributes to hippocampal neuronal death following global cerebral ischemia/reperfusion. *J. Neuroimmunol.* 190, 101–111. doi: 10.1016/j.jneuroim.2007.08.014

Hua, F., Tang, H., Wang, J., Prunty, M. C., Hua, X., Sayeed, I., et al. (2015). TAK-242, an antagonist for toll-like receptor 4, protects against acute cerebral ischemia/reperfusion injury in mice. *J. Cereb. Blood Flow Metab.* 35, 536–542. doi: 10.1038/jcbfm.2014.240

Islam, M. M., and Mohamed, Z. (2015). Computational and pharmacological target of neurovascular unit for drug design and delivery. *Biomed Res. Int.* 2015:731292. doi: 10.1155/2015/731292

Jiang, M., Li, J., Peng, Q., Liu, Y., Liu, W., Luo, C., et al. (2014). Neuroprotective effects of bilobalide on cerebral ischemia and reperfusion injury are associated with inhibition of pro-inflammatory mediator production and down-regulation of JNK1/2 and p38 MAPK activation. *J. Neuroinflammation* 11:167. doi: 10.1186/s12974-014-0167-6

Jing, Z., Xing, J., Chen, X., Stetler, R. A., Weng, Z., Gan, Y., et al. (2014). Neuronal NAMPT is released after cerebral ischemia and protects against white matter injury. *J. Cereb. Blood Flow Metab.* 34, 1613–1621. doi: 10.1038/jcbfm.2014.119

Kawai, T., and Akira, S. (2010). The role of pattern-recognition receptors in innate immunity: update on toll-like receptors. *Nat. Immunol.* 11, 373–384. doi: 10.1038/ni.1863

Kim, Y., Davidson, J. O., Gunn, K. C., Phillips, A. R., Green, C. R., and Gunn, A. J. (2016). Role of hemichannels in CNS inflammation and the inflammasome pathway. *Adv. Protein Chem. Struct. Biol.* 104, 1–37. doi: 10.1016/bs.apcsb.2015.12.001

Kim, J. Y., Kawabori, M., and Yenari, M. A. (2014). Innate inflammatory responses in stroke: mechanisms and potential therapeutic targets. *Curr. Med. Chem.* 21, 2076–2097. doi: 10.2174/0929867321666131228205146

Li, W., Bao, G., Chen, W., Qiang, X., Zhu, S., Wang, S., et al. (2018). Connexin 43 hemichannel as a novel mediator of sterile and infectious inflammatory diseases. *Sci. Rep.* 8:166. doi: 10.1038/s41598-017-18452-1

Li, Y., Ma, Q., Halavi, S., Concepcion, K., Hartman, R. E., Obenaus, A., et al. (2016). Fetal stress-mediated hypomethylation increases the brain susceptibility to hypoxic-ischemic injury in neonatal rats. *Exp. Neurol.* 275, 1–10. doi: 10.1016/j.expneurol.2015.10.007

Li, X., Zhao, H., Tan, X., Kostrzewa, R. M., Du, G., Chen, Y., et al. (2015). Inhibition of connexin43 improves functional recovery after ischemic brain injury in neonatal rats. *Glia* 63, 1553–1567. doi: 10.1002/glia.22826

Liu, X., Sun, L., Torii, M., and Rakic, P. (2012). Connexin 43 controls the multipolar phase of neuronal migration to the cerebral cortex. *Proc. Natl. Acad. Sci. U S A* 109, 8280–8285. doi: 10.1073/pnas.1205880109

Lo, E. H. (2010). Degeneration and repair in central nervous system disease. *Nat. Med.* 16, 1205–1209. doi: 10.1038/nm.2226

Lo, E. H., Dalkara, T., and Moskowitz, M. A. (2003). Mechanisms, challenges and opportunities in stroke. *Nat. Rev. Neurosci.* 4, 399–415. doi: 10.1038/nrn1106

Meller, R., Stevens, S. L., Minami, M., Cameron, J. A., King, S., Rosenzweig, H., et al. (2005). Neuroprotection by osteopontin in stroke. *J. Cereb. Blood Flow Metab.* 25, 217–225. doi: 10.1038/sj.jcbfm.9600022

Même, W., Calvo, C. F., Froger, N., Ezan, P., Amigou, E., Koulakoff, A., et al. (2006). Proinflammatory cytokines released from microglia inhibit gap junctions in astrocytes: potentiation by β-amyloid. *FASEB J.* 20, 494–496. doi: 10.1096/fj.05-4297fje

Molteni, M., Gemma, S., and Rossetti, C. (2016). The role of toll-like receptor 4 in infectious and noninfectious inflammation. *Mediators Inflamm.* 2016:6978936. doi: 10.1155/2016/6978936

Morioka, T., Kalehua, A. N., and Streit, W. J. (1993). Characterization of microglial reaction after middle cerebral artery occlusion in rat brain. *J. Comp. Neurol.* 327, 123–132. doi: 10.1002/cne.903270110

Moskowitz, M. A., Lo, E. H., and Iadecola, C. (2010). The science of stroke: mechanisms in search of treatments. *Neuron* 67, 181–198. doi: 10.1016/j.neuron.2010.07.002

Mozaffarian, D., Benjamin, E. J., Go, A. S., Arnett, D. K., Blaha, M. J., Cushman, M., et al. (2015). Heart disease and stroke statistics—2015 update: a report from the American Heart Association. *Circulation* 131, e29–e322. doi: 10.1161/CIR.0000000000000152

Nakagawa, S., Deli, M. A., Kawaguchi, H., Shimizudani, T., Shimono, T., Kittel, A., et al. (2009). A new blood-brain barrier model using primary rat brain endothelial cells, pericytes and astrocytes. *Neurochem. Int.* 54, 253–263. doi: 10.1016/j.neuint.2008.12.002

Naus, C. C., and Giaume, C. (2016). Bridging the gap to therapeutic strategies based on connexin/pannexin biology. *J. Transl. Med.* 14:330. doi: 10.1186/s12967-016-1089-0

O'Carroll, S. J., Alkadhi, M., Nicholson, L. F., and Green, C. R. (2008). Connexin 43 mimetic peptides reduce swelling, astrogliosis and neuronal

cell death after spinal cord injury. *Cell Commun. Adhes.* 15, 27–42. doi: 10.1080/15419060802014164

Powers, W. J., Rabinstein, A. A., Ackerson, T., Adeoye, O. M., Bambakidis, N. C., Becker, K., et al. (2018). 2018 Guidelines for the early management of patients with acute ischemic stroke: a guideline for healthcare professionals from the American Heart Association/American Stroke Association. *Stroke* 49, e46–e110. doi: 10.1161/STR.0000000000000158

Retamal, M. A., Froger, N., Palacios-Prado, N., Ezan, P., Saez, P. J., Saez, J. C., et al. (2007). Cx43 hemichannels and gap junction channels in astrocytes are regulated oppositely by proinflammatory cytokines released from activated microglia. *J. Neurosci.* 27, 13781–13792. doi: 10.1523/jneurosci.2042-07.2007

Rowe, D. D., Collier, L. A., Seifert, H. A., Chapman, C. B., Leonardo, C. C., Willing, A. E., et al. (2014). Leukemia inhibitor factor promotes functional recovery and oligodendrocyte survival in rat models of focal ischemia. *Eur. J. Neurosci.* 40, 3111–3119. doi: 10.1111/ejn.12675

Ruck, T., Bittner, S., Epping, L., Herrmann, A. M., and Meuth, S. G. (2014). Isolation of primary murine brain microvascular endothelial cells. *J. Vis. Exp.* 93:e52204. doi: 10.3791/52204

Sáez, J. C., and Leybaert, L. (2014). Hunting for connexin hemichannels. *FEBS Lett.* 588, 1205–1211. doi: 10.1016/j.febslet.2014.03.004

Sáez, P. J., Shoji, K. F., Retamal, M. A., Harcha, P. A., Ramirez, G., Jiang, J. X., et al. (2013). ATP is required and advances cytokine-induced gap junction formation in microglia *in vitro*. *Mediators Inflamm.* 2013:216402. doi: 10.1155/2013/216402

Sahota, P., and Savitz, S. I. (2011). Investigational therapies for ischemic stroke neuroprotection and neurorecovery. *Neurotherapeutics* 8, 434–451. doi: 10.1007/s13311-011-0040-6

Saver, J. L., Fonarow, G. C., Smith, E. E., Reeves, M. J., Grau-Sepulveda, M. V., Pan, W., et al. (2013). Time to treatment with intravenous tissue plasminogen activator and outcome from acute ischemic stroke. *JAMA* 309, 2480–2488. doi: 10.1001/jama.2013.6959

Schulz, R., Görge, P. M., Görbe, A., Ferdinandy, P., Lampe, P. D., and Leybaert, L. (2015). Connexin 43 is an emerging therapeutic target in ischemia/reperfusion injury, cardioprotection and neuroprotection. *Pharmacol. Ther.* 153, 90–106. doi: 10.1016/j.pharmthera.2015.06.005

Shaikh, S. B., Uy, B., Perera, A., and Nicholson, L. F. (2012). AGEs-RAGE mediated up-regulation of connexin43 in activated human microglial CHME-5 cells. *Neurochem. Int.* 60, 640–651. doi: 10.1016/j.neuint.2012.02.023

Shao, J., Liu, T., Xie, Q. R., Zhang, T., Yu, H., Wang, B., et al. (2013). Adjudin attenuates lipopolysaccharide (LPS)- and ischemia-induced microglial activation. *J. Neuroimmunol.* 254, 83–90. doi: 10.1016/j.jneuroim.2012.09.012

Shichita, T., Sakaguchi, R., Suzuki, M., and Yoshimura, A. (2012). Post-ischemic inflammation in the brain. *Front. Immunol.* 3:132. doi: 10.3389/fimmu.2012.00132

Stanimirovic, D. B., and Friedman, A. (2012). Pathophysiology of the neurovascular unit: disease cause or consequence? *J. Cereb. Blood Flow Metab.* 32, 1207–1221. doi: 10.1038/jcbfm.2012.25

Takeuchi, H., Mizoguchi, H., Doi, Y., Jin, S., Noda, M., Liang, J., et al. (2011). Blockade of gap junction hemichannel suppresses disease progression in mouse models of amyotrophic lateral sclerosis and Alzheimer's disease. *PLoS One* 6:e21108. doi: 10.1371/journal.pone.0021108

Tang, S. C., Arumugam, T. V., Xu, X., Cheng, A., Mughal, M. R., Jo, D. G., et al. (2007). Pivotal role for neuronal toll-like receptors in ischemic brain injury and functional deficits. *Proc. Natl. Acad. Sci. U S A* 104, 13798–13803. doi: 10.1073/pnas.0702553104

Tian, X., Peng, J., Zhong, J., Yang, M., Pang, J., Lou, J., et al. (2016). β-Caryophyllene protects *in vitro* neurovascular unit against oxygen-glucose deprivation and re-oxygenation-induced injury. *J. Neurochem.* 139, 757–768. doi: 10.1111/jnc.13833

Tsubokawa, T., Jadhav, V., Solaroglu, I., Shiokawa, Y., Konishi, Y., and Zhang, J. H. (2007). Lecithinized superoxide dismutase improves outcomes and attenuates focal cerebral ischemic injury via antiapoptotic mechanisms in rats. *Stroke* 38, 1057–1062. doi: 10.1161/01.str.0000257978.70312.1d

Vicario, N., Calabrese, G., Zappala, A., Parenti, C., Forte, S., Graziano, A. C. E., et al. (2017). Inhibition of Cx43 mediates protective effects on hypoxic/reoxygenated human neuroblastoma cells. *J. Cell. Mol. Med.* 21, 2563–2572. doi: 10.1111/jcmm.13177

Walrave, L., Pierre, A., Albertini, G., Aourz, N., De Bundel, D., Van Eeckhaut, A., et al. (2018). Inhibition of astroglial connexin43 hemichannels with TAT-Gap19 exerts anticonvulsant effects in rodents. *Glia* doi: 10.1002/glia.23341 [Epub ahead of print].

Walrave, L., Vinken, M., Albertini, G., De Bundel, D., Leybaert, L., and Smolders, I. J. (2016). Inhibition of connexin43 hemichannels impairs spatial short-term memory without affecting spatial working memory. *Front. Cell. Neurosci.* 10:288. doi: 10.3389/fncel.2016.00288

Wang, N., De Vuyst, E., Ponsaerts, R., Boengler, K., Palacios-Prado, N., Wauman, J., et al. (2013). Selective inhibition of Cx43 hemichannels by Gap19 and its impact on myocardial ischemia/reperfusion injury. *Basic Res. Cardiol.* 108:309. doi: 10.1007/s00395-012-0309-x

Wang, P. F., Fang, H., Chen, J., Lin, S., Liu, Y., Xiong, X. Y., et al. (2014). Polyinosinic-polycytidylic acid has therapeutic effects against cerebral ischemia/reperfusion injury through the downregulation of TLR4 signaling via TLR3. *J. Immunol.* 192, 4783–4794. doi: 10.4049/jimmunol.1303108

Wang, Y., Ge, P., and Zhu, Y. (2013). TLR2 and TLR4 in the brain injury caused by cerebral ischemia and reperfusion. *Mediators Inflamm.* 2013:124614. doi: 10.1155/2013/124614

Xiong, X., Barreto, G. E., Xu, L., Ouyang, Y. B., Xie, X., and Giffard, R. G. (2011). Increased brain injury and worsened neurological outcome in interleukin-4 knockout mice after transient focal cerebral ischemia. *Stroke* 42, 2026–2032. doi: 10.1161/STROKEAHA.110.593772

Xue, Q., Liu, Y., Qi, H., Ma, Q., Xu, L., Chen, W., et al. (2013). A novel brain neurovascular unit model with neurons, astrocytes and microvascular endothelial cells of rat. *Int. J. Biol. Sci.* 9, 174–189. doi: 10.7150/ijbs.5115

Yang, Q. W., Lu, F. L., Zhou, Y., Wang, L., Zhong, Q., Lin, S., et al. (2011). HMBG1 mediates ischemia-reperfusion injury by TRIF-adaptor independent toll-like receptor 4 signaling. *J. Cereb. Blood Flow Metab.* 31, 593–605. doi: 10.1038/jcbfm.2010.129

Yu, S. C., Xiao, H. L., Jiang, X. F., Wang, Q. L., Li, Y., Yang, X. J., et al. (2012). Connexin 43 reverses malignant phenotypes of glioma stem cells by modulating E-cadherin. *Stem Cells* 30, 108–120. doi: 10.1002/stem.1685

Yu, H., Zhang, Z. L., Chen, J., Pei, A., Hua, F., Qian, X., et al. (2012). Carvacrol, a food-additive, provides neuroprotection on focal cerebral ischemia/reperfusion injury in mice. *PLoS One* 7:e33584. doi: 10.1371/journal.pone.0033584

Zhang, J. H., Badaut, J., Tang, J., Obenaus, A., Hartman, R., and Pearce, W. J. (2012). The vascular neural network—a new paradigm in stroke pathophysiology. *Nat. Rev. Neurol.* 8, 711–716. doi: 10.1038/nrneurol.2012.210

Zhang, Q., Raoof, M., Chen, Y., Sumi, Y., Sursal, T., Junger, W., et al. (2010). Circulating mitochondrial DAMPs cause inflammatory responses to injury. *Nature* 464, 104–107. doi: 10.1038/nature08780

Zhu, H. T., Bian, C., Yuan, J. C., Chu, W. H., Xiang, X., Chen, F., et al. (2014). Curcumin attenuates acute inflammatory injury by inhibiting the TLR4/MyD88/NF-κB signaling pathway in experimental traumatic brain injury. *J. Neuroinflammation* 11:59. doi: 10.1186/1742-2094-11-59

Conflict of Interest Statement: The authors declare that the research was conducted in the absence of any commercial or financial relationships that could be construed as a potential conflict of interest.

frontiers in Cellular Neuroscience

ORIGINAL RESEARCH
published: 18 October 2018
doi: 10.3389/fncel.2018.00371

Hydroxysafflor Yellow A (HSYA) Improves Learning and Memory in Cerebral Ischemia Reperfusion-Injured Rats via Recovering Synaptic Plasticity in the Hippocampus

Lu Yu[1†], Yanhong Duan[2†], Zheng Zhao[2], Wendi He[2], Ming Xia[1], Qiujuan Zhang[3] and Xiaohua Cao[2*]*

[1]*Comprehensive Department of Traditional Chinese Medicine, Putuo Hospital Affiliated to Shanghai University of Traditional Chinese Medicine, Shanghai, China,* [2]*Shanghai Key Laboratory of Brain Functional Genomics, Ministry of Education, School of Life Sciences, East China Normal University, Shanghai, China,* [3]*Department of Neurology, Yueyang Hospital of Integrated Chinese and Western Medicine Affiliated to Shanghai University of Traditional Chinese Medicine, Shanghai, China*

OPEN ACCESS

Edited by:
Sriharsha Kantamneni, University of Bradford, United Kingdom

Reviewed by:
Rodrigo A. Cunha, Universidade de Coimbra, Portugal
Nicola Berretta, Fondazione Santa Lucia (IRCCS), Italy

***Correspondence:**
Qiujuan Zhang
qiujuanzhang1014@163.com
Xiaohua Cao
xiaohua_cao@hotmail.com

[†]These authors have contributed equally to this work and should be considered co-first authors

Received: *15 July 2018*
Accepted: *28 September 2018*
Published: *18 October 2018*

Citation:
Yu L, Duan Y, Zhao Z, He W, Xia M, Zhang Q and Cao X (2018) Hydroxysafflor Yellow A (HSYA) Improves Learning and Memory in Cerebral Ischemia Reperfusion-Injured Rats via Recovering Synaptic Plasticity in the Hippocampus. Front. Cell. Neurosci. 12:371. doi: 10.3389/fncel.2018.00371

Hydroxysafflor yellow A (HSYA) is the major active chemical component of the safflower plant flower, which is widely used in Chinese medicine for cerebrovascular and cardiovascular disease treatment. Recent studies have demonstrated that HSYA exerts neuroprotective effect on cerebral ischemia, such as neuronal anti-apoptosis, antioxidant activity and oxygen free radical-scavenging. However, whether and how HSYA has a protective effect on cognitive impairment induced by cerebral ischemia reperfusion remains elusive. In the present study, by using the middle cerebral artery occlusion (MCAO) model, we found that 8 mg/kg and 16 mg/kg HSYA administration by common carotid artery (CCA) injection improved impaired cognitive function in Morris water maze (MWM) and passive avoidance tasks, but not 4 mg/kg HSYA treatment, suggesting that HSYA treatment in a certain concentration can improve cognitive impairment in MCAO rats. Furthermore, we found that 8 mg/kg HSYA treatment rescued the impaired long-term potentiation (LTP) in hippocampus of MCAO rats. Taken together, these results for the first time demonstrate that HSYA has the capacity to protect cognitive function and synaptic plasticity against cerebral ischemia-reperfusion injury, and provide a new insight that HSYA may be a promising alternative for recovery of cognitive dysfunction after brain ischemic injury.

Keywords: Hydroxysafflor yellow A, cerebral ischemia, memory, field potential recording, LTP

INTRODUCTION

Stroke is the third leading cause of death and adult disability worldwide, particularly of the elderly (Chen et al., 2012), which is broadly classified as ischemic stroke (approximately 80%–90%) and hemorrhagic stroke (approximately 10%–20%; Goldstein et al., 2006). Ischemic stroke occurs when an artery in the brain is blocked resulting from a transient or permanent reduction in cerebral blood

flow (Dirnagl et al., 1999). The stroke patients must not only survive the acute stage of infarction, but also cope with the ongoing neurological impairment. More than half of the stroke survivors experience residual physical disability and cognitive decline (Ivan et al., 2004). Although it has been reported that the impaired sensorimotor function after ischemic stroke could be recovered with time (DeVries et al., 2001; Fluri et al., 2017), cognitive and neuronal dysfunction is irreversible (Bayat et al., 2012, 2015).

The flower of the safflower plant, *Carthamus tinctorius* L. has been widely used in traditional Chinese medicine for cerebrovascular and cardiovascular disease treatment. In the Compendium of Materia Medica, it is described as being able "to invigorate the circulation of blood," which suggests it has potential benefits for the circulation system (Xu et al., 2012). Hydroxysafflor yellow A (HSYA), first isolated by Meselhy et al. in 1993 (Zhu et al., 2011), is the major active component of safflower which was confirmed that the structure is C-Glycosyl quinochalcones (Black, 2011; Li et al., 2016) and has proven to be water-soluble and penetrative to the blood brain barrier (Meselhy et al., 1993).

Previous studies have demonstrated that HSYA markedly extends coagulation time in mice, which raised the possibility that it might exert therapeutic actives on cerebral ischemia induced by thrombosis (Li et al., 2013). Furthermore, it is confirmed that HSYA could significantly decrease neurological deficit scores, reduce the percentage of infarction following ischemia-reperfusion injury in rats (Sun et al., 2013; Nazari et al., 2016). However, most of researches in this field to date have focused on neuronal anti-apoptosis (Shan et al., 2010), antioxidant activity (Wei et al., 2005) and oxygen free radical-scavenging (Tian et al., 2008) of HSYA in the cerebral ischemic injury. Whether HSYA has benefits on cognitive improvement after ischemia-reperfusion injury is unclear.

In recent years, with more and more studies focus on the neural mechanisms of the cerebral injury, it is demonstrated that brain ischemia impairs physiological form of synaptic plasticity (Feng et al., 2013; Christophe et al., 2017). Clinical symptoms of cognitive impairment such as learning disability, memory loss and lack of executive functioning resulting from ischemic stroke are associated with a loss of synapse number and function in the hippocampus (Jiang et al., 2010). Long-term changes in synaptic transmission, such as long-term potentiation (LTP), are thought to be an indicator of synaptic plasticity at the cellular level (Malenka and Nicoll, 1999; Martin et al., 2000), which is necessary for storage of information by modifying synaptic transmission efficiency. It has been confirmed that LTP can be induced after a short period of brain ischemic injury (Hammond et al., 1994). Also, it has been reported that HSYA improves cognitive function in the rat model of vascular dementia via increasing VEGF and NR1 (Zhang et al., 2014), and enhancing the endogenous expression of BDNF and NMDARs in the hippocampus (Xing et al., 2016). Thus, it is manifested that BDNF and NMDAR play an important role in synaptic plasticity and forming process of LTP in vascular dementia. In addition, it would almost be certain that HSYA has neuroprotective effect on ameliorating cognitive dysfunction. Therefore, it is necessary to study whether HSYA recovers cognitive impairment after brain ischemia via improvement of synaptic plasticity. So far, however, there has been little discussion about the impact of HSYA on synaptic plasticity and memory performance.

In the present work, we adopted middle cerebral artery occlusion (MCAO) model, which is considered to be a convenient, reproducible, and reliable rodent model of cerebral ischemia in humans, to investigate the effects of HSYA on cognitive function and hippocampus synaptic plasticity in cerebral ischemia reperfusion-injured rats. We found that HSYA significantly improved the learning and memory of rats subjected to MCAO model in the Morris water maze (MWM) and passive avoidance tasks. Furthermore, HSYA recovered the impaired LTP at hippocampus while leaving basal synaptic transmission unaffected.

MATERIALS AND METHODS

Animals and Drugs

Sprague-Dawley male rats (weighing 250–290 g, aged 9–11 weeks) were obtained from Shanghai Laboratory Animal Center of Chinese Academy of Sciences. The rats were housed in temperature (22–26°C) and humidity (40%–70%) controlled conditions with a 12/12 h light/dark cycle, and the rats had *ad libitum* access to food and water. All animal experiments described in this study were conducted according to Animals Act (2006; China) and approved by the Institutional Animal Care and Use Committee (IACUC approval ID #M07016) of the East China Normal University. All efforts were made to minimize animal suffering and reduced the number of animals used. In addition, HSYA was produced by Shanghai Yuanye Pharmaceutical Co., Ltd. (Shanghai, China), and its purity as analyzed by high performance liquid chromatography peak area normalization was 98.8%. Solution of drugs was always prepared afresh before use.

Focal Cerebral Ischemia/Reperfusion Procedure and HSYA Administration

Rats were randomly divided into five groups: (1) sham operated rats; (2) MCAO (vehicle-treated) group; (3) 4 mg/kg HSYA group; (4) 8 mg/kg HSYA group; and (5) 16 mg/kg HSYA group. Focal cerebral ischemia/reperfusion injury was induced by MCAO, based on the method developed by Longa et al. (1989). The rats were anesthetized with an intraperitoneal injection of 10% chloral hydrate (400 mg/kg; Sinopharm Group Chemical Reagent Co., Ltd., Shanghai, China). The right common carotid artery (CCA), external carotid artery (ECA) and internal carotid artery (ICA) were isolated via blunt dissection with a midline incision of the neck. The branches of the ECA were cut off, and the whole of the ECA was ligated. A monofilament nylon suture with a polylysine-coated tip (0.26 mm; Beijing Xinong BioTechnologies Co., Ltd., China) was inserted into the right side of ICA in the depth of 19 ± 0.5 mm from the CCA,

to occlude the origin of the (MCA). The monofilament nylon suture was fixed and the incision was closed. Occlusion was done for a period of 1.5 h. After 1.5 h occlusion, reperfusion achieved by withdrawing the monofilament nylon suture to restore blood supply to the MCA territory. After waiting for another 1.5 h, the incision of rat was reopened and HSYA (at a dose of 4 mg/kg, 8 mg/kg, and 16 mg/kg dissolved in 0.9% saline) was injected into the unilateral CCA at a constant speed (0.05 mL/min). The sham-operated rats received all surgical procedures but without the monofilament nylon suture inserted. Body temperature of rats were maintained at 37 ± 0.5°C throughout the surgery by means of a heating blanket and a lamp.

Evaluation Test of MCAO Model

Assessment of Neurological Deficits

Assessment of neurological deficits was performed on rats 24 h after reperfusion by using the Garcia test, which is a neurological examination that utilizes an 18-point scale (Garcia et al., 1995). The examiners were blind to the procedure that the rat had undergone. The neurobehavioral study items included spontaneous activity, symmetry in the movement of four limbs, forepaw outstretching, climbing, body proprioception.

Measurement of Edema (Brain Water Content)

Cerebral edema was determined 24 h after reperfusion via measuring brain water content by means of the standard wet/dry weight method (Hatashita et al., 1988). Brains were removed quickly under ice and weighted on an electronic balance to obtain wet weight and then were placed in an oven at (100 ± 2)°C for 24 h to get their dry weight. Brain water content percentage was calculated according to the following formula: [(wet weight − dry weight)/wet weight] × 100%.

Measurement of Infarct Volume

Triphenyltetrazolium chloride (TTC) staining was used to measure the infarct volumes 24 h after reperfusion. Rats were killed under deep anesthesia using 10% chloral hydrate and brains were rapidly took out and cut into 2-mm thick coronal sections using the brain matrix (Beijing Xinong BioTechnologies Co., Ltd., China). The fresh slices were incubated away from light in 2% 2,3,5-triphenyl-tetrazolium chloride solution at 37°C for 30 min to visualize in infarctions. Normal and damaged tissue were stained red and white, respectively. The brain slices were photographed with a digital camera and the size of the infarct area (unstained) was assessed by ImageJ software. The percentage of the infarct volume was calculated according to the following formula: {[contralateral volume − (ipsilateral volume−infarct volume)]/contralateral volume}·100%.

Behavioral Study

Open Field

After modeling and drug treatment, the rat was first tested by open field to assess its locomotor and exploratory activity. The apparatus (Gray et al., 1975) was a square black box (100 cm long × 100 cm wide × 50 cm high) and placed under dim light. The rat was placed in the box to explore the arena freely for 30 min, and all activities were recorded using a video camera mounted above the open field and recorded in real time. Move time and total distance were analyzed using the motion tracking system.

Morris Water Maze Test (MWM)

The ability of spatial learning and memory was evaluated by Morris water maze (MWM) test (Morris, 1984). All of five groups of rats after open field test were trained and tested in MWM for the purpose of the spatial cognition study. The water maze consists of a large circular pool (150 cm in diameter, 60 cm in height, filled to the depth of 45 cm with water at 22°C ± 1°C). The water is made opaque with black nontoxic ink. The pool is divided into four equal hypothetical quadrants and includes four points in each quadrant (North, East, South and West), plus a hidden circular platform (10 cm in diameter) painted black and submerged 1.5 cm beneath the surface of the water in the southwest quadrant. The position of the platform is unaltered throughout the training session. A digital camera was located above the MWM to record the rats' swimming pathways.

Acquisition Trial

The consecutive training days were commenced from the 4th day after the termination of the HSYA treatment described above. All of rats were trained through four trial sessions in the afternoon each day for five sequential days, and the southwest quadrant was maintained as the target quadrant in all acquisition trials. Facing against the maze wall, the rats were released into the pool randomly in one quadrant (North, East, South or West) for each trial without repetition. They should find the hidden platform according to the program's instructions. For memory acquisition, the location of the platform remained stable and the rats were given a maximum of 60 s to find the hidden platform. Once a rat climbed onto the platform and remained on it for 20 s, the trial was terminated. If the rat failed to reach the platform within 60 s, it would be gently guided to the hidden platform and allowed to stay on it for 20 s. The average swimming speed was recorded and escape latency time, the time required for the rats to climb the platform was recorded as well. After 5-day acquisition trial, the rat was subjected to the retrieval test in the 6th day.

Retrieval Trial

Memory retention was evaluated during a probe test. On the 6th day, the platform was removed from the pool. Each rat was placed in water maze and allowed to swim for 60 s to explore it. Every rat was subjected to one such trial, and each trial was started by placing the rat in the quadrant farthest from where the platform had previously been placed. The platform crossings and the time spent in the target quadrant for searching the missing platform were recorded. The experimenter always stood at the same position. Throughout the study, experimenter must be careful not to disturb the relative location of the pool with respect to other objects in the laboratory, which could be served as prominent visual clues.

Passive Avoidance Test

Passive avoidance test (PAT) which was conducted in another batch of rats used for evaluating learning and memory (Loureiro et al., 2012) was executed over 2 days and divided into acquisition trial and retention trial. The apparatus for the passive avoidance study consisted of light and dark chambers (20 cm × 20 cm × 20 cm) with stainless steel bars (2 mm in diameter and 1 cm in distance) on the floor, divided by a guillotine door (5 cm × 5 cm) that separated the two chambers. In the acquisition trial, each rat was placed in the light chamber and the door between the two chambers would be opened 30 s later. After the rat entering the dark chamber, the door was automatically closed, and an electrical shock (0.5 mA) was discharged through the floor grid for 2 s. If the rat did not enter the dark chamber within 60 s after the door opened, it had to be put into the dark chamber, and the latency was considered as 60 s. The retention trial was performed 24 h after the acquisition trial, in which the rat was allowed to enter into the dark chamber freely while the entrance time to the dark chamber was recorded as the step-through latency (STL). However, there was no electrical shock in the retention trial when rats entered the dark chamber. The maximum cut off time for the STL was 300 s.

Electrophysiological Study

Preparation

After the behavioral tests, rats were anesthetized using chloral hydrate and decapitated. The protocols were similar to those described previously (Tang et al., 1999; Duan et al., 2018). Rats were anesthetized with sodium pentobarbital (40 mg/kg, intraperitoneal) and killed by decapitation. The brain was removed immediately. Whole brain was cut into coronal slices (370 μm thickness) containing the hippocampus using a vibroslicer (Vibratome 3000; Vibratome, St. Louis, MO, USA) with cold (4°C) and oxygenated (95% O_2, 5% CO_2) modified artificial cerebrospinal fluid (section ACSF) containing (in mM): choline chloride, 110; KCl, 2.5; $CaCl_2$, 0.5; $MgSO_4$, 7; $NaHCO_3$, 25; NaH_2PO_4, 1.25; and D-(+)-glucose, 25; pH 7.4. The slices were recovered in an incubation chamber with normal ACSF (incubation ACSF) containing (in mM): NaCl, 119; $CaCl_2$, 2.5; KCl, 2.5; $MgSO_4$, 1.3; $NaHCO_3$, 26.2; Na_2HPO_4, 1.0; and Dglucose, 11; pH 7.4, 95% O_2 and 5% CO_2 for 60 min at 31°C before recording.

Field Potential Recording

For field potential recording, slices were transferred to a recording chamber filled with the oxygenated incubation ACSF, and the rate of ACSF superfusion was 0.5 mL/min. An unipolar tungsten stimulating electrode was placed in the stratum radiatum to activate the Schaffer-collateral pathway projecting to CA1 and the field excitatory post-synaptic potentials (fEPSPs) were recorded using a glass microelectrode filled with 0.1 M CH_3COONa (3–5 MΩ). A typical experiment began with an input-output curve ranging from subthreshold to maximal response. Fiber volley amplitude was measured from peak negative voltage to baseline. Paired-pulse facilitation (PPF) was assessed among inter-stimulus intervals ranging from 0.02 s to 0.4 s. The PPF was defined as the ratio of the amplitude of the second to that of the first fEPSP amplitude elicited by pairs of stimuli (pulse2/pulse1 × 100). Synaptic responses were monitored with stimuli consisting of constant current pulses of 0.05 ms duration at 0.033 Hz.

After obtaining a stable baseline response for at least 15 min, LTP was induced by theta burst stimulation (TBS; 10 bursts of four pulses at 100 Hz separated by 200 ms). fEPSP continued to be recorded for 60 min after TBS stimulation. Data were recorded using a Multiclamp 700B amplifier and digitized with a Digidata 1322A (Axon Instruments, Foster City, CA, USA). The fEPSP amplitude was used to measure the synaptic efficacy and LTP induction was expressed as the percentage of the increase of fEPSP amplitude compared with the average amplitude of the baseline period. If the change of fEPSP amplitude in sham group of rats exceeded 20%, it was defined as a successful induction of LTP.

Statistical Analysis

All data were shown as mean ± SEM. Student's *t*-test was used for comparison of two groups. For comparisons with multiple data sets, one-way analysis of variance was used. For input-output curve and PPF analysis, two-way repeated measures ANOVA followed was used. Differences were considered statistically significant at $p < 0.05$.

RESULTS

Evaluation of MCAO Model

The neurological scores, brain edema and infarct volume were evaluated at 24 h of MCAO. The results showed that neurological scores (**Figure 1A**, sham, 16.75 ± 0.16, $n = 8$; MCAO, 9.25 ± 0.16, $n = 8$; Student's *t*-test, $P < 0.0001$) was significantly decreased in MCAO rats. Brain water content (**Figure 1B**, sham, 16.75 ± 0.16, $n = 2$; MCAO, 82.28 ± 0.37, $n = 6$; Student's *t*-test, $P < 0.01$) was significantly increased in MCAO rats. Moreover, MCAO rats displayed an obvious manifestation of cerebral infarction (**Figures 1C,D** sham, 0.00 ± 0.00, $n = 2$; MCAO, 9.25 ± 0.16, $n = 8$; Student's *t*-test, $P < 0.0001$), whereas rats in the sham group did not show any signs of cerebral injury, indicating the success of the MCAO model.

Behavioral Experiments

Effect of HSYA on Locomotor Activity in the Open Field

To investigate whether HSYA can improve cognitive impairment after MCAO. We began by exploring modifications of the spontaneous locomotor activity of the different groups of rats. As shown in **Figure 2**, MCAO did not significantly affect the spontaneous locomotion of rats, as gauged by their move time (**Figure 2A**, move time: sham, 306.4 ± 95.94 s, $n = 7$; MCAO, 235.7 ± 138.8 s, $n = 12$) and distance (**Figure 2B**, distance: sham, 4,483 ± 2,177 cm, $n = 8$; MCAO, 3,974 ± 2,582 cm, $n = 13$) in the open field test. Moreover, after HSYA treatment,

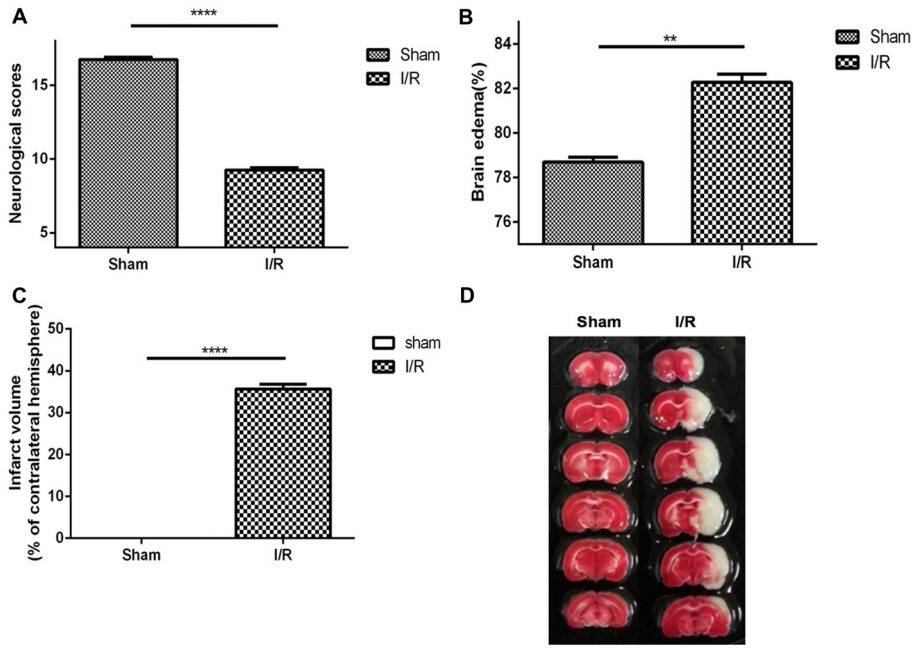

FIGURE 1 | Middle cerebral artery occlusion (MCAO) model was evaluated to be suitable for studying the pharmacology efficacy of Hydroxysafflor yellow A (HSYA). **(A)** Neurological scores, **(B)** brain edema, **(C)** infarct volume, **(D)** pictures of infarct volume. The values are shown as means ± SEM. Significant difference between sham group vs. MCAO group in neurological scores (sham, $n = 8$; MCAO, $n = 8$, $^{****}P < 0.0001$), brain edema (sham, $n = 2$; MCAO, $n = 6$, $^{**}P < 0.01$) and infarct volume (sham, $n = 2$; MCAO, $n = 8$, $^{****}P < 0.0001$).

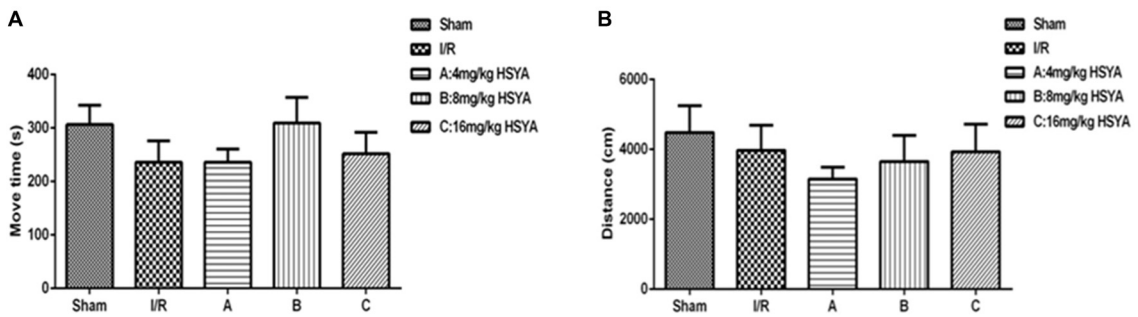

FIGURE 2 | Locomotor activity of HSYA on open field test. **(A)** Move time, **(B)** distance. The values are shown as means ± SEM.

it also showed that HSYA no matter in which dosage (4 mg/kg, 8 mg/kg, 16 mg/kg) has no effect on the spontaneous locomotor activity of control rats (**Figures 2A,B**, one-way ANOVA, $P > 0.05$).

Effect of HSYA on Brain Ischemia-Induced Memory Impairment in the Morris Water Maze Test

To determine the effects of HSYA on the rats' spatial learning acquisition and memory retention, MWM test was used. All rats learned to locate the hidden platform through 5 days of acquisition training. During this training, we found that the average swimming speed of rats in each and every group was similar, which suggested that every groups of rats have normal sensory-motor function and motivation for survival (**Figure 3A**, one-way ANOVA, $P > 0.05$). However, the escape latency of 8 mg/kg HSYA group and 16 mg/kg HSYA group significantly decreased compared to that of MCAO group (**Figure 3B**, MCAO 47.46 ± 6.14 s, $n = 5$; 8 mg/kg HSYA, 11.71 ± 3.61 s, $n = 9$, one-way ANOVA, $P < 0$ 0.01; 16 mg/kg HSYA, 16.27 ± 5.42 s, $n = 7$; one-way ANOVA, $P < 0.05$), but not of 4 mg/kg HSYA group (**Figure 3B**, MCAO, 47.46 ± 6.14 s, $n = 5$; 4 mg/kg HSYA, 35.52 ± 6.91, $n = 13$; one-way ANOVA, $P > 0.05$).

During the retrieval trial, platform crossings and time spent in the target quadrant were calculated for each rat to evaluate memory retention. As shown in **Figures 3E,F**, the swimmers' trajectories showed there were fewer platform region crossing times in MCAO group compared to sham group (**Figure 3C**,

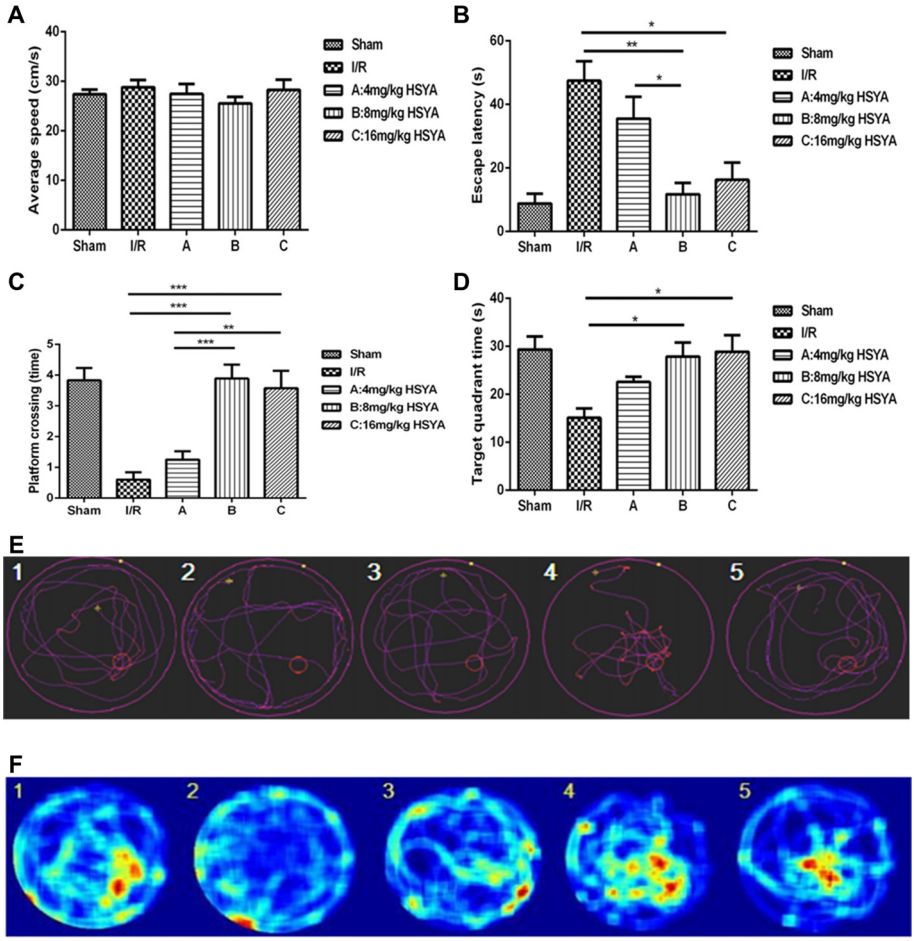

FIGURE 3 | Neuroprotective effects of HSYA on Morris water maze (MWM) test. **(A)** Average swimming speed, **(B)** escape latency, **(C)** platform crossing, **(D)** target quadrant time, **(E)** trajectory of swimming, **(F)** heat-variable images recording rats' stay in the target quadrant. The values are shown as means ± SEM. Significant difference between MCAO group vs. 8 mg/kg HSYA (*$P < 0.05$) and 16 mg/kg HSYA groups (**$P < 0.01$), 4 mg/kg HSYA group vs. 8 mg/kg HSYA group (*$P < 0.05$) in escape latency; MCAO group vs. 8 mg/kg HSYA (***$P < 0.001$) and 16 mg/kg HSYA groups (***$P < 0.001$), 4 mg/kg HSYA vs. 8 mg/kg HSYA (***$P < 0.001$) and 16 mg/kg HSYA groups (**$P < 0.01$) in platform crossing; MCAO group vs. 8 mg/kg HSYA (*$P < 0.05$) and 16 mg/kg HSYA groups (*$P < 0.05$) in target quadrant time.

crossing times: MCAO, 0.60 ± 0.24, $n = 5$; sham, 3.83 ± 0.40, $n = 6$; one-way ANOVA, $P < 0.001$). After HSYA treatment, 8 mg/kg HSYA group and 16 mg/kg HSYA group produced a significant increase in the retention phase, measured as platform crossings (**Figure 3C**, MCAO, 0.60 ± 0.55, $n = 5$; 8 mg/kg HSYA, 3.89 ± 0.45, $n = 9$; $P < 0.001$; 16 mg/kg HSYA, 3.57 ± 0.57, $n = 7$; $P < 0.001$), but there was no difference between 4 mg/kg HSYA group and MCAO group (**Figure 3C**, MCAO, 0.60 ± 0.55, $n = 5$; 4 mg/kg HSYA, 1.25 ± 0.97, $n = 12$; one-way ANOVA, $P > 0.05$). In addition, we found that with the increasing dose of HSYA, rats spent more time in the target quadrant. Target quadrant time in 8 mg/kg HSYA group and 16 mg/kg HSYA group was significant increased compared with that in MCAO group, and even reached values observed in the sham group (**Figure 3D**, MCAO, 15.13 ± 1.91 s, $n = 4$; 8 mg/kg HSYA, 27.86 ± 2.94 s, $n = 7$, one-way ANOVA, $P < 0.05$; MCAO, 15.13 ± 1.91 s, $n = 4$; 16 mg/kg HSYA, 28.89 ± 3.46 s, $n = 6$; one-way ANOVA, $P < 0.05$). There was still no difference between 4 mg/kg HSYA and MCAO group in time spent in the target quadrant (**Figure 3D**, MCAO, 15.13 ± 1.91 s, $n = 4$; 4 mg/kg HSYA, 22.58 ± 3.75, $n = 12$; one-way ANOVA, $P > 0.05$). These results suggest that 8 mg/kg HSYA group and 16 mg/kg HSYA can improve the reference memory after brain ischemic injury.

Effect of HSYA on Brain Ischemia-Induced Memory Impairment in the Passive Avoidance Test

To further investigate whether HSYA can improve the cognitive dysfunction after MCAO, passive avoidance task was used. We found that STL significantly declined in MCAO group compared with sham group (**Figure 4**, MCAO, 34.30 ± 17.90 s, $n = 3$; sham, 327.90 ± 27.79 s, $n = 6$; one-way ANOVA, $P < 0.001$), and 8 mg/kg HSYA group and 16 mg/kg HSYA group produced a significant increase of STL in comparison with MCAO group (**Figure 4**, MCAO, 34.30 ± 17.90 s, $n = 3$; 8 mg/kg HSYA, 189.80 ± 20.73 s, $n = 8$; one-way

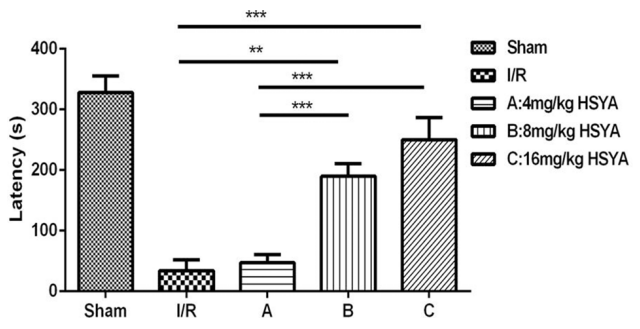

FIGURE 4 | Neuroprotective effects of HSYA on passive avoidance test (PAT). The values are shown as means ± SEM. Significant difference between MCAO group vs. 8 mg/kg HSYA (**$P < 0.01$) and 16 mg/kg HSYA groups (***$P < 0.001$), 4 mg/kg HSYA vs. 8 mg/kg HSYA (***$P < 0.001$) and 16 mg/kg HSYA groups (***$P < 0.001$) in latency.

ANOVA, $P < 0.01$; 16 mg/kg HSYA, 250.00 ± 36.48 s, $n = 6$; one-way ANOVA, $P < 0.001$), but not 4 mg/kg HSYA group (**Figure 4**, MCAO, 34.30 ± 17.90 s, $n = 3$; 4 mg/kg HSYA, 47.09 ± 13.74 s, $n = 14$; one-way ANOVA, $P > 0.05$). These data indicate that 8 mg/kg HSYA group and 16 mg/kg HSYA can improve the fear memory after brain ischemic injury.

Taken together, the results of behavioral experiments demonstrated that HSYA treatment in a certain concentration can improve cognitive impairment in MCAO rats. Since the effects of 8 mg/kg HSYA treatment were close to that of 16 mg/kg HSYA treatment, in the following electrophysiological experiments, we selected 8 mg/kg HSYA as an optimal dose to investigate the effects of HSYA on synaptic plasticity.

Electrophysiological Experiments

HSYA Has No Effect on Basal Synaptic Transmission After Brain Ischemic Insult

The cognitive facilitation exhibited by HSYA prompted us to investigate how HSYA facilitates the learning and memory after brain ischemic injury. Given that synaptic plasticity is one of the important cellular foundations of learning and memory, we first examined the basal excitatory synaptic transmission in Schaffer collaterals-CA1 synapse of hippocampus by *in vitro* fEPSP recording. However, no significant difference was observed in input-output curves (**Figure 5A**: two-way repeated-measures ANOVA, no significant effect of MCAO, $p > 0.05$) and PPF (**Figure 5B**: two-way repeated-measures ANOVA, no significant effect of MCAO, $p > 0.05$) between sham and MCAO group of rats. In addition, after 8 mg/kg HSYA treatment, there was also no significant difference was observed in input-output curves (**Figure 5A**: two-way repeated-measures ANOVA, no significant effect of HSYA, $p > 0.05$) and PPF (**Figure 5B**: two-way repeated-measures ANOVA, no significant effect of HSYA, $p > 0.05$) between HSYA treatment and MCAO group of rats. These results suggest that HSYA have no effect on the basal synaptic transmission after brain ischemic injury.

HSYA Rescues Long Term Plasticity Impairment Induced by MCAO Model

We then investigated whether synaptic plasticity in the hippocampus was improved by HSYA treatment after brain ischemic injury. As shown in **Figure 6**, we compared Schaffer collateral-CA1 LTP induced by TBS among the sham, MCAO and HSYA treatment groups. Forty-five minutes after the TBS, a significant reduction of LTP was found in the MCAO group compared to sham group (**Figures 6A,B**, sham, 153.89 ± 12.02%, $n = 6$; MCAO, 111.7 ± 4.86%, $n = 9$; Student's t-test, $P < 0.01$). After 8 mg/kg HSYA treatment, the LTP was significantly improved in the HSYA treatment group compared to that in the MCAO group (**Figures 6A,B**, 8 mg/kg HSYA, 142.28 ± 5.00%, $n = 6$; MCAO, 111.7 ± 4.86%, $n = 9$; Student's t-test, $P < 0.01$); and, there was no statistically difference of LTP between sham group and HSYA treatment group (**Figures 6A,B**, sham, 153.89 ± 12.02%, $n = 6$; 8 mg/kg HSYA, 142.28 ± 5.00%, $n = 6$; Student's t-test, $P > 0.05$). These data suggest 8 mg/kg HSYA can significantly improve the synaptic plasticity after brain ischemic injury.

DISCUSSION

Post-stroke cognitive dysfunction is one of the major consequences after stroke and chronic cerebral hypoperfusion can induce vascular cognitive impairment (Back et al., 2017). Currently, thrombolytic drug therapy is used for treating acute ischemic stroke, but the curative effect is limited (Heuschmann et al., 2004). HSYA is a major active component of safflower, which is described as being able to improve the circulation of blood for cerebrovascular and cardiovascular disease. MCAO in rodents is a well-known model of cerebral ischemia in humans to evaluate the progression of impaired spatial learning and memory performance after ischemic stroke (Li et al., 2013). In the present study, we firstly verified the applicability and stability of MCAO model for pharmacological study by assessment of neurological deficits, measurement of brain water content and infarct volume. Then, using this MCAO model, we found that HSYA has the capacity to protect cognitive function and synaptic plasticity against cerebral ischemia-reperfusion injury.

To study whether MCAO model induces cognitive impairment as reported and HSYA has a protective effect on cognitive impairment induced by cerebral ischemia reperfusion, we first carried out a serious behavioral experiment. Using the open field test, we found brain ischemia induced by MCAO did not influence spontaneous locomotor activities on the rats which was consistent with previous study (Chang et al., 2016; Zhang et al., 2017). However, Katsuta et al. (2003) showed that global ischemia induced in gerbils produced a significant increase in locomotor activity and administration of neuroprotective agents ameliorated locomotor hyperactivity. Carmo et al. (2014) showed that mice subject to pMCAO displayed a lower rearing activity. The inconsistency may be due to the difference in model animals, drug intervention and condition of experiment. In addition, in our present study, doses of HSYA were selected

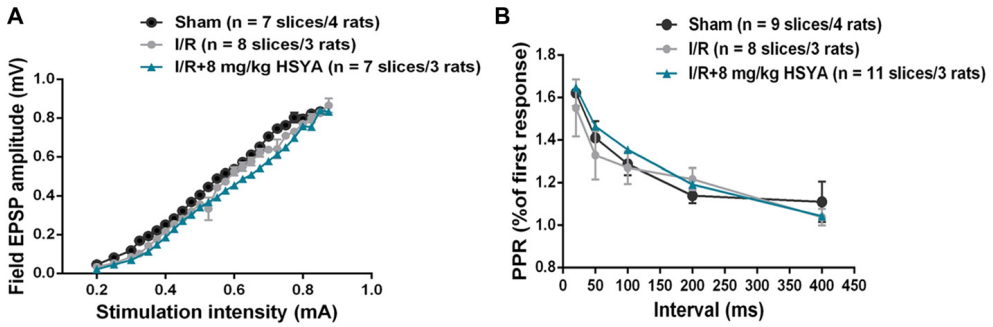

FIGURE 5 | Treatment with HSYA after MCAO did not change basal synaptic transmission. **(A)** HSYA treatment after MCAO have no effect on the input-output curve at Schaffer collateral-CA1 synapses. **(B)** HSYA treatment after MCAO have no effect on the paired-pulse facilitation (PPF) at Schaffer collateral-CA1 synapses.

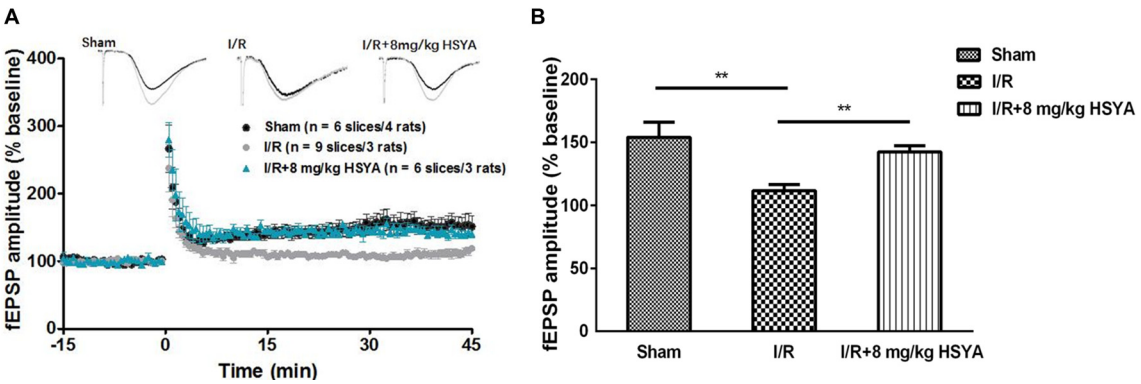

FIGURE 6 | Neuroprotective effects of HSYA on recovery of long-term potentiation (LTP) in MCAO rats. **(A)** Values are expressed as percentage of change relative to baseline. **(B)** The average percent change of field excitatory post-synaptic potential (fEPSP) amplitude 45 min after theta burst stimulation (TBS). The values are shown as means ± SEM. **Represent significant differences before and after tetanic stimulation for sham, MCAO and 8 mg/kg HSYA groups, respectively (**$P < 0.01$).

based upon pilot study conducted in our laboratory and from available literature which showed it has neuroprotective effects (Bliss and Collingridge, 1993; Meselhy et al., 1993; Ramagiri and Taliyan, 2016). In the open field test, HSYA treatment after MCAO, no matter in which dose (4 mg/kg, 8 mg/kg and 16 mg/kg), did not affect spontaneous locomotor activities on rats.

MWM is one of the classic behavioral test to study spatial learning and memory (Loureiro et al., 2012). The acquisition of spatial memory was reflected through rats' performance in training trial while the retrieval of spatial memory was reflected through test trial. Using MWM task, we found MCAO rats have normal swimming speed, but the spatial learning and memory was significantly impaired, which was consistent with previous study (Wei et al., 2018). After HSYA treatment, we found that both 8 mg/kg and 16 mg/kg HSYA treatment could significantly reduce the escape latency during acquisition trial, and increase platform crossings and target quadrant time during retrieval trial on MCAO rats, but not 4 mg/kg HSYA treatment. In addition, there was no significant difference between 8 mg/kg and 16 mg/kg HSYA on protection of spatial learning and memory impairment after MCAO. All of these results suggest that HSYA in a certain concentration can improve the impaired spatial learning and memory after brain ischemia.

Passive avoidance is a behavioral test to study fear learning and memory. Using this PAT, we found that the fear learning and memory was significantly impaired on MCAO rats, which was in agreement with previous study (Yang et al., 2015). After HSYA treatment, we found that both 8 mg/kg and 16 mg/kg HSYA treatment could significantly prolong the latency into the dark box on MCAO rats, but not 4 mg/kg HSYA treatment. In addition, there was no significant difference between 8 mg/kg and 16 mg/kg HSYA on protection of fear learning and memory impairment after MCAO. All of these results suggest that HSYA in a certain concentration can improve the impaired fear learning and memory after brain ischemia.

Through behavioral experiments, we found HSYA in a certain concentration improved cognitive function in MCAO rats. The cognitive improvement exhibited by HSYA treatment prompted us to further investigate the mechanism underlying the improvement by HSYA treatment in MCAO rats. Given that synaptic plasticity is one of the important cellular foundations of learning and memory (Esmaeili Tazangi et al., 2015), we first examined the basal excitatory synaptic transmission in

hippocampus CA3-CA1 pathway by *in vitro* fEPSP recording. No distinguishable difference was observed between MCAO and sham groups in input-output curves and PPF, suggesting that basal synaptic transmission was unchanged after brain ischemic insult. After HSYA treatment, whether basal synaptic transmission in MCAO rats was effected by HSYA, we found that 8 mg/kg of HSYA which could recover the cognitive impairment after MCAO has no effect on both input-output curves and PPF in MCAO rats. Impairment of synaptic plasticity has been thought of as the mechanism underlying cognitive impairment after stroke (Feng et al., 2013; Christophe et al., 2017). Moreover, the level of long-term potentiation induction is a well-known useful synaptic marker for studying learning and memory ability and is regarded as a basis of information storage (Morris, 1984; Lynch, 2004; Esmaeili Tazangi et al., 2015). Through inducing LTP in hippocampal CA1 region by TBS, we found that LTP at hippocampus was significantly impaired in MCAO group of rats, which was consistent with previous reports (Li et al., 2013; Nazari et al., 2016). It has been reported that HSYA has no effect on hippocampal LTP in sham group of rats (Zhang et al., 2014; Xing et al., 2016). In our present work, after HSYA treatment, we found that 8 mg/kg HSYA treatment could significantly improve the impaired LTP in MCAO rats, and the LTP amplitude almost reached values observed in the control group. Taken together, it suggests that HSYA treatment can recover the synaptic plasticity impairment after MCAO.

It's known that PPF is an indirect index for measurement of Glutamate release from pre-synaptic terminals (Dobrunz and Stevens, 1997). In our present study, no change was found in the PPF after HSYA treatment, suggesting that HSYA may have no effect on Glutamate release from pre-synaptic terminals. Together with the no changed input-output curves after HSYA treatment, it suggested that both the pre-synaptic transmitter release and the post-synaptic AMPA receptors function were normal after HSYA treatment on MCAO rats. How does LTP impair in MCAO rats, and how HSYA treatment improves this impaired LTP? Using *in vitro* field potential recording, we found that LTP at hippocampus was impaired in MCAO group of rats, which was consistent with previous reports (Li et al., 2013; Nazari et al., 2016). After 8 mg/kg HSYA treatment, the impaired LTP was improved in MCAO rats, and the LTP amplitude even reached values observed in the control group, suggesting that HSYA treatment can recover the impaired synaptic plasticity after MCAO. It has been reported that HSYA can enhance the endogenous expression of BDNF and GluN2B (Xing et al., 2016), VEGF and NR1 (Zhang et al., 2014). It's well known that all of these three proteins have important role in synaptic plasticity and learning and memory. Therefore, future work will be done to further investigate these protein expressions that related tightly with synaptic plasticity and learning and memory after HSYA treatment. In addition, most recently, LTD was found to couple with synaptic deficits upon aging and AD (Temido-Ferreira et al., 2018). Whether the LTD is also effected by MCAO, we need to detect it in our future work too.

CONCLUSION

In summary, we found that MCAO model of brain ischemia induced cognitive impairment and injection with a certain concentration of HSYA into the CCA promoted learning and memory after MCAO. One of the underlying mechanisms of HSYA's neuroprotective effect is about its capacity of recovery on synaptic plasticity impairment. Thus, our findings of the present study demonstrated that HSYA treatment may be a promising alternative to protect cognitive and synaptic function against brain ischemic injury.

AUTHOR CONTRIBUTIONS

LY carried out experiments and wrote the manuscript. YD carried out experiments and revised the manuscript. WH carried out experiments. ZZ analyzed experimental results. MX assisted with data analysis. QZ designed experiments. XC designed and instructed experiments.

FUNDING

This work was supported by grants from National Natural Science Foundation of China (No 81503370 and 31471077), and by MOST China-Israel cooperation (2016YFE0130500).

REFERENCES

Back, D. B., Kwon, K. J., Choi, D. H., Shin, C. Y., Lee, J., Han, S. H., et al. (2017). Chronic cerebral hypoperfusion induces post-stroke dementia following acute ischemic stroke in rats. *J. Neuroinflammation* 14:216. doi: 10.1186/s12974-017-0992-5

Bayat, M., Baluchnejadmojarad, T., Roghani, M., Goshadrou, F., Ronaghi, A., and Mehdizadeh, M. (2012). Netrin-1 improves spatial memory and synaptic plasticity impairment following global ischemia in the rat. *Brain Res.* 1452, 185–194. doi: 10.1016/j.brainres.2012.03.008

Bayat, M., Sharifi, M. D., Haghani, M., and Shabani, M. (2015). Enriched environment improves synaptic plasticity and cognitive deficiency in chronic cerebral hypoperfused rats. *Brain Res. Bull.* 119, 34–40. doi: 10.1016/j.brainresbull.2015.10.001

Black, S. E. (2011). Vascular cognitive impairment: epidemiology, subtypes, diagnosis and management. *J. R. Coll. Physicians Edinb.* 41, 49–56. doi: 10.4997/jrcpe.2011.121

Bliss, T. V., and Collingridge, G. L. (1993). A synaptic model of memory: long-term potentiation in the hippocampus. *Nature* 361, 31–39. doi: 10.1038/361031a0

Carmo, M. R., Simoes, A. P., Fonteles, A. A., Souza, C. M., Cunha, R. A., and Andrade, G. M. (2014). ATP P2Y1 receptors control cognitive deficits and neurotoxicity but not glial modifications induced by brain ischemia in mice. *Eur. J. Neurosci.* 39, 614–622. doi: 10.1111/ejn.12435

Chang, S. J., Cherng, J. H., Wang, D. H., Yu, S. P., Liou, N. H., and Hsu, M. L. (2016). Transneuronal degeneration of thalamic nuclei following middle cerebral artery occlusion in rats. *Biomed. Res. Int.* 2016:3819052. doi: 10.1155/2016/3819052

Chen, Y. C., Wu, J. S., Yang, S. T., Huang, C. Y., Chang, C., Sun, G. Y., et al. (2012). Stroke, angiogenesis and phytochemicals. *Front. Biosci.* 4, 599–610. doi: 10.2741/s287

Christophe, B. R., Mehta, S. H., Garton, A. L., Sisti, J., and Connolly, E. S. Jr. (2017). Current and future perspectives on the treatment of cerebral ischemia. *Expert Opin. Pharmacother.* 18, 573–580. doi: 10.1080/14656566.2017.1309022

DeVries, A. C., Nelson, R. J., Traystman, R. J., and Hurn, P. D. (2001). Cognitive and behavioral assessment in experimental stroke research: will it prove useful? *Neurosci. Biobehav. Rev.* 25, 325–342. doi: 10.1016/s0149-7634(01)00017-3

Dirnagl, U., Iadecola, C., and Moskowitz, M. A. (1999). Pathobiology of ischaemic stroke: an integrated view. *Trends Neurosci.* 22, 391–397. doi: 10.1016/s0166-2236(99)01401-0

Dobrunz, L. E., and Stevens, C. F. (1997). Heterogeneity of release probability, facilitation and depletion at central synapses. *Neuron* 18, 995–1008. doi: 10.1016/s0896-6273(00)80338-4

Duan, Y., Wang, Q., Zeng, Q., Wang, J., Chen, Z., Xu, M., et al. (2018). Striatal GluN2B involved in motor skill learning and stimulus-response learning. *Neuropharmacology* 135, 73–85. doi: 10.1016/j.neuropharm.2018.03.002

Esmaeili Tazangi, P., Moosavi, S. M., Shabani, M., and Haghani, M. (2015). Erythropoietin improves synaptic plasticity and memory deficits by decrease of the neurotransmitter release probability in the rat model of Alzheimer's disease. *Pharmacol. Biochem. Behav.* 130, 15–21. doi: 10.1016/j.pbb.2014.12.011

Feng, Z. M., He, J., Jiang, J. S., Chen, Z., Yang, Y. N., and Zhang, P. C. (2013). NMR solution structure study of the representative component hydroxysafflor yellow A and other quinochalcone C-glycosides from *Carthamus tinctorius*. *J. Nat. Prod.* 76, 270–274. doi: 10.1021/np300814k

Fluri, F., Malzahn, U., Homola, G. A., Schuhmann, M. K., Kleinschnitz, C., and Volkmann, J. (2017). Stimulation of the mesencephalic locomotor region for gait recovery after stroke. *Ann. Neurol.* 82, 828–840. doi: 10.1002/ana.25086

Garcia, J. H., Wagner, S., Liu, K. F., and Hu, X. J. (1995). Neurological deficit and extent of neuronal necrosis attributable to middle cerebral artery occlusion in rats: Statistical validation. *Stroke* 26, 627–634; discussion 635. doi: 10.1161/01.str.26.4.627

Goldstein, L. B., Adams, R., Alberts, M. J., Appel, L. J., Brass, L. M., Bushnell, C. D., et al. (2006). Primary prevention of ischemic stroke: a guideline from the American Heart Association/American Stroke Association Stroke Council: cosponsored by the Atherosclerotic Peripheral Vascular Disease Interdisciplinary Working Group; Cardiovascular Nursing Council; Clinical Cardiology Council; Nutrition, Physical Activity and Metabolism Council; and the Quality of Care and Outcomes Research Interdisciplinary Working Group. *Circulation* 113, e873–e923. doi: 10.1161/01.STR.0000223048.70103.F1

Gray, J. A., Drewett, R. F., and Lalljee, B. (1975). Effects of neonatal castration and testosterone injection on adult open-field behaviour in rats with atypical sex difference in defecation. *Anim. Behav.* 23, 773–778. doi: 10.1016/0003-3472(75)90105-0

Hammond, C., Crépel, V., Gozlan, H., and Ben-Ari, Y. (1994). Anoxic LTP sheds light on the multiple facets of NMDA receptors. *Trends Neurosci.* 17, 497–503. doi: 10.1016/0166-2236(94)90140-6

Hatashita, S., Hoff, J. T., and Salamat, S. M. (1988). Ischemic brain edema and the osmotic gradient between blood and brain. *J. Cereb. Blood Flow Metab.* 8, 552–559. doi: 10.1038/jcbfm.1988.96

Heuschmann, P. U., Kolominsky-Rabas, P. L., Roether, J., Misselwitz, B., Lowitzsch, K., Heidrich, J., et al. (2004). Predictors of in-hospital mortality in patients with acute ischemic stroke treated with thrombolytic therapy. *JAMA* 292, 1831–1838. doi: 10.1001/jama.292.15.1831

Ivan, C. S., Seshadri, S., Beiser, A., Au, R., Kase, C. S., Kelly-Hayes, M., et al. (2004). Dementia after stroke: the Framingham Study. *Stroke* 35, 1264–1268. doi: 10.1161/01.str.0000127810.92616.78

Jiang, J. S., He, J., Feng, Z. M., and Zhang, P. C. (2010). Two new quinochalcones from the florets of *Carthamus tinctorius*. *Org. Lett.* 12, 1196–1199. doi: 10.1021/ol902971w

Katsuta, K., Umemura, K., Ueyama, N., and Matsuoka, N. (2003). Pharmacological evidence for a correlation between hippocampal CA1 cell damage and hyperlocomotion following global cerebral ischemia in gerbils. *Eur. J. Pharmacol.* 467, 103–109. doi: 10.1016/s0014-2999(03)01573-5

Li, W., Huang, R., Shetty, R. A., Thangthaeng, N., Liu, R., Chen, Z., et al. (2013). Transient focal cerebral ischemia induces long-term cognitive function deficit in an experimental ischemic stroke model. *Neurobiol. Dis.* 59, 18–25. doi: 10.1016/j.nbd.2013.06.014

Li, F., Wu, X., Li, J., and Niu, Q. (2016). Ginsenoside Rg1 ameliorates hippocampal long-term potentiation and memory in an Alzheimer's disease model. *Mol. Med. Rep.* 13, 4904–4910. doi: 10.3892/mmr.2016.5103

Longa, E. Z., Weinstein, P. R., Carlson, S., and Cummins, R. (1989). Reversible middle cerebral artery occlusion without craniectomy in rats. *Stroke* 20, 84–91. doi: 10.1161/01.str.20.1.84

Loureiro, M., Lecourtier, L., Engeln, M., Lopez, J., Cosquer, B., Geiger, K., et al. (2012). The ventral hippocampus is necessary for expressing a spatial memory. *Brain Struct. Funct.* 217, 93–106. doi: 10.1007/s00429-011-0332-y

Lynch, M. A. (2004). Long-term potentiation and memory. *Physiol. Rev.* 84, 87–136. doi: 10.1152/physrev.00014.2003

Malenka, R. C., and Nicoll, R. A. (1999). Long-term potentiation—a decade of progress? *Science* 285, 1870–1874. doi: 10.1126/science.285.5435.1870

Martin, S. J., Grimwood, P. D., and Morris, R. G. (2000). Synaptic plasticity and memory: an evaluation of the hypothesis. *Annu. Rev. Neurosci.* 23, 649–711. doi: 10.1146/annurev.neuro.23.1.649

Meselhy, M. R., Kadota, S., Momose, Y., Hatakeyama, N., Kusai, A., Hattori, M., et al. (1993). Two new quinochalcone yellow pigments from *Carthamus tinctorius* and Ca^{2+} antagonistic activity of tinctormine. *Chem. Pharm. Bull.* 41, 1796–1802. doi: 10.1248/cpb.41.1796

Morris, R. (1984). Developments of a water-maze procedure for studying spatial learning in the rat. *J. Neurosci. Methods* 11, 47–60. doi: 10.1016/0165-0270(84)90007-4

Nazari, M., Keshavarz, S., Rafati, A., Namavar, M. R., and Haghani, M. (2016). Fingolimod (FTY720) improves hippocampal synaptic plasticity and memory deficit in rats following focal cerebral ischemia. *Brain Res. Bull.* 124, 95–102. doi: 10.1016/j.brainresbull.2016.04.004

Ramagiri, S., and Taliyan, R. (2016). Neuroprotective effect of hydroxy safflor yellow A against cerebral ischemia-reperfusion injury in rats: putative role of mPTP. *J. Basic Clin. Physiol. Pharmacol.* 27, 1–8. doi: 10.1515/jbcpp-2015-0021

Shan, L. Q., Ma, S., Qiu, X. C., Zhou, Y., Zhang, Y., Zheng, L. H., et al. (2010). Hydroxysafflor yellow A protects spinal cords from ischemia/reperfusion injury in rabbits. *BMC Neurosci.* 11:98. doi: 10.1186/1471-2202-11-98

Sun, L., Yang, L., Fu, Y., Han, J., Xu, Y., Liang, H., et al. (2013). Capacity of HSYA to inhibit nitrotyrosine formation induced by focal ischemic brain injury. *Nitric Oxide* 35, 144–151. doi: 10.1016/j.niox.2013.10.002

Tang, Y. P., Shimizu, E., Dube, G. R., Rampon, C., Kerchner, G. A., Zhuo, M., et al. (1999). Genetic enhancement of learning and memory in mice. *Nature* 401, 63–69. doi: 10.1038/43432

Temido-Ferreira, M., Ferreira, D. G., Batalha, V. L., Marques-Morgado, I., Coelho, J. E., Pereira, P., et al. (2018). Age-related shift in LTD is dependent on neuronal adenosine A_{2A} receptors interplay with mGluR5 and NMDA receptors. *Mol. Psychiatry* doi: 10.1038/s41380-018-0110-9 [Epub ahead of print].

Tian, J., Li, G., Liu, Z., and Fu, F. (2008). Hydroxysafflor yellow A inhibits rat brain mitochondrial permeability transition pores by a free radical scavenging action. *Pharmacology* 82, 121–126. doi: 10.1159/000141653

Wei, X., Liu, H., Sun, X., Fu, F., Zhang, X., Wang, J., et al. (2005). Hydroxysafflor yellow A protects rat brains against ischemia-reperfusion injury by antioxidant action. *Neurosci. Lett.* 386, 58–62. doi: 10.1016/j.neulet.2005.05.069

Wei, J., Sun, C., Liu, C., and Zhang, Q. (2018). Effects of rat anti-mouse interleukin-6 receptor antibody on the recovery of cognitive function in stroke mice. *Cell. Mol. Neurobiol.* 38, 507–515. doi: 10.1007/s10571-017-0499-8

Xing, M., Sun, Q., Wang, Y., Cheng, Y., and Zhang, N. (2016). Hydroxysafflor yellow A increases BDNF and NMDARs in the hippocampus in a vascular dementia rat model. *Brain Res.* 1642, 419–425. doi: 10.1016/j.brainres.2016.04.030

Xu, J., Wang, Y., Li, N., Xu, L., Yang, H., and Yang, Z. (2012). L-3-n-butylphthalide improves cognitive deficits in rats with chronic cerebral ischemia. *Neuropharmacology* 62, 2424–2429. doi: 10.1016/j.neuropharm.2012.02.014

Yang, L. C., Guo, H., Zhou, H., Suo, D. Q., Li, W. J., Zhou, Y., et al. (2015). Chronic oleoylethanolamide treatment improves spatial cognitive deficits through enhancing hippocampal neurogenesis after transient focal cerebral ischemia. *Biochem. Pharmacol.* 94, 270–281. doi: 10.1016/j.bcp.2015.02.012

Zhang, N., Xing, M., Wang, Y., Liang, H., Yang, Z., Shi, F., et al. (2014). Hydroxysafflor yellow A improves learning and memory in

a rat model of vascular dementia by increasing VEGF and NR1 in the hippocampus. *Neurosci. Bull.* 30, 417–424. doi: 10.1007/s12264-013-1375-2

Zhang, L., Zhao, M., and Sui, R. B. (2017). Cerebellar fastigial nucleus electrical stimulation alleviates depressive-like behaviors in post-stroke depression rat model and potential mechanisms. *Cell Physiol. Biochem.* 41, 1403–1412. doi: 10.1159/000467940

Zhu, H., Zhang, J., Sun, H., Zhang, L., Liu, H., Zeng, X., et al. (2011). An enriched environment reverses the synaptic plasticity deficit induced by chronic cerebral hypoperfusion. *Neurosci. Lett.* 502, 71–75. doi: 10.1016/j.neulet.2011.04.015

Conflict of Interest Statement: The authors declare that the research was conducted in the absence of any commercial or financial relationships that could be construed as a potential conflict of interest.

frontiers in Cellular Neuroscience

ORIGINAL RESEARCH
published: 25 October 2018
doi: 10.3389/fncel.2018.00380

Cerebrovascular Pathology in Hypertriglyceridemic APOB-100 Transgenic Mice

Zsófia Hoyk[1†], Melinda E. Tóth[2†], Nikolett Lénárt[2‡], Dóra Nagy[2], Brigitta Dukay[2], Alexandra Csefová[2], Ágnes Zvara[3], György Seprényi[4], András Kincses[1], Fruzsina R. Walter[1], Szilvia Veszelka[1], Judit Vígh[1], Beáta Barabási[1], András Harazin[1], Ágnes Kittel[5], László G. Puskás[3], Botond Penke[6], László Vígh[2], Mária A. Deli[1] and Miklós Sántha[2]**

[1] Institute of Biophysics, Biological Research Centre, Hungarian Academy of Sciences, Szeged, Hungary, [2] Institute of Biochemistry, Biological Research Centre, Hungarian Academy of Sciences, Szeged, Hungary, [3] Laboratory of Functional Genomics, Core Facilities, Biological Research Centre, Hungarian Academy of Sciences, Szeged, Hungary, [4] Department of Anatomy, Histology and Embryology, Faculty of Medicine, University of Szeged, Szeged, Hungary, [5] Laboratory of Molecular Pharmacology, Department of Pharmacology, Institute of Experimental Medicine, Hungarian Academy of Sciences, Budapest, Hungary, [6] Department of Medical Chemistry, Faculty of Medicine, University of Szeged, Szeged, Hungary

OPEN ACCESS

Edited by:
Sikha Saha,
University of Leeds, United Kingdom

Reviewed by:
Ryusuke Takechi,
Curtin University, Australia
Ibolya Andras,
University of Miami, United States
Mehmet Kaya,
Koç University, Turkey

***Correspondence:**
Mária A. Deli
deli.maria@brc.mta.hu
Miklós Sántha
santha.miklos@brc.mta.hu

[†]These authors have contributed equally to this work

[‡]**Present address:**
Nikolett Lénárt,
Laboratory of Neuroimmunology, Department of Molecular and Developmental Neuroscience, Institute of Experimental Medicine, Hungarian Academy of Sciences, Budapest, Hungary

Received: 13 June 2018
Accepted: 04 October 2018
Published: 25 October 2018

Citation:
Hoyk Z, Tóth ME, Lénárt N, Nagy D, Dukay B, Csefová A, Zvara Á, Seprényi G, Kincses A, Walter FR, Veszelka S, Vígh J, Barabási B, Harazin A, Kittel Á, Puskás LG, Penke B, Vigh L, Deli MA and Sántha M (2018) Cerebrovascular Pathology in Hypertriglyceridemic APOB-100 Transgenic Mice. Front. Cell. Neurosci. 12:380. doi: 10.3389/fncel.2018.00380

Hypertriglyceridemia is not only a serious risk factor in the development of cardiovascular diseases, but it is linked to neurodegeneration, too. Previously, we generated transgenic mice overexpressing the human APOB-100 protein, a mouse model of human atherosclerosis. In this model we observed high plasma levels of triglycerides, oxidative stress, tau hyperphosphorylation, synaptic dysfunction, cognitive impairment, increased neural apoptosis and neurodegeneration. Neurovascular dysfunction is recognized as a key factor in the development of neurodegenerative diseases, but the cellular and molecular events linking cerebrovascular pathology and neurodegeneration are not fully understood. Our aim was to study cerebrovascular changes in APOB-100 transgenic mice. We described the kinetics of the development of chronic hypertriglyceridemia in the transgenic animals. Increased blood-brain barrier permeability was found in the hippocampus of APOB-100 transgenic mice which was accompanied by structural changes. Using transmission electron microscopy, we detected changes in the brain capillary endothelial tight junction structure and edematous swelling of astrocyte endfeet. In brain microvessels isolated from APOB-100 transgenic animals increased *Lox-1, Aqp4*, and decreased *Meox-2, Mfsd2a, Abcb1a, Lrp2, Glut-1, Nos2, Nos3, Vim*, and in transgenic brains reduced *Cdh2* and *Gfap-σ* gene expressions were measured using quantitative real-time PCR. We confirmed the decreased P-glycoprotein (ABCB1) and vimentin expression related to the neurovascular unit by immunostaining in transgenic brain sections using confocal microscopy. We conclude that in chronic hypertriglyceridemic APOB-100 transgenic mice both functional and morphological cerebrovascular pathology can be observed, and this animal model could be a useful tool to study the link between cerebrovascular pathology and neurodegeneration.

Keywords: apolipoprotein B-100, astroglia, blood-brain barrier, brain endothelial cell, cerebrovascular pathology, hypertriglyceridemia, P-glycoprotein, tight junction

INTRODUCTION

There is growing preclinical and clinical evidence that pathological changes at the level of the neurovascular unit (NVU), comprising all the cell types of cerebral microvessels and the surrounding neural tissue, lead to secondary neuronal injury and neurodegenerative diseases, including Alzheimer's disease (AD) (Zhao et al., 2015). The key pathways of vascular dysfunction that are linked to neurodegenerative diseases include blood-brain barrier (BBB) breakdown, hypoperfusion-hypoxia and endothelial metabolic dysfunction (Zlokovic, 2008; Zhao et al., 2015). Morphologically the BBB is formed by the capillary endothelium, the basement membrane and the surrounding pericytes and astrocytic endfeet. The endothelial cells adhere tightly to one another, through junctional structures termed tight junctions (TJs), which restrict paracellular permeability of the BBB [3]. Several families of active influx and efflux transporters and transcytotic receptor systems regulate the exchange of small and large nutrients and metabolites across the BBB (Zlokovic, 2008). Both the structure and functions of the BBB are damaged in AD: the barrier function of TJs is impaired, the energy supply of neural cells is decreased, the entry of neurotoxic agents is elevated and the clearance of Aβ peptides is reduced (Zlokovic, 2008, 2011; Lyros et al., 2014; Di Marco et al., 2015; Zhao et al., 2015). Many studies suggest a direct link of atherosclerosis with not only vascular, but also AD dementia, although the relationship is still unclear (Nelson et al., 2016; Kapasi and Schneider, 2016). NVU and BBB pathologies have been increasingly investigated in genetic and other animal models of AD (Nicolakakis and Hamel, 2011), but there are very few models focusing on the link between atherosclerosis and dementia (Li et al., 2003; Lane-Donovan et al., 2016) or NVU changes.

Previously, we generated a mouse model of human atherosclerosis using transgenic mice overexpressing the human APOB-100 protein in different tissues such as the liver, heart and brain (Bjelik et al., 2006; Csont et al., 2007; Lénárt et al., 2012). Apolipoprotein B-100 (APOB-100) is a large, 512 kDa glycoprotein that circulates in the plasma as the major protein component of low density lipoprotein (LDL) and very low density lipoproteins (VLDL). The higher ratio of LDL and VLDL fractions compared to HDL in the blood of these transgenic animals is similar to the human plasma lipoprotein profile, therefore this mouse strain is more suitable to study the effects of hypercholesterinaemia and hypertriglyceridemia than the wild-type mice (Csont et al., 2007). Several studies have shown that the concentration of APOB is elevated in the serum of AD patients (Caramelli et al., 1999; Sabbagh et al., 2004) which correlates with β-amyloid (Aβ) deposition in AD brains (Kuo et al., 1998). Cholesterol and apolipoprotein accumulates in mature amyloid plaques in brains from both AD patients and animal models of AD (Puglielli et al., 2003). The processing of amyloid precursor protein (APP) is modulated by cholesterol which is enriched in the membrane microdomains of neurons (Ehehalt et al., 2003). The amount of 24S-hydroxycholesterol is increased in the plasma of AD and vascular dementia patients, indicating a change in the metabolism of cholesterol (Lutjohann et al., 2000). High levels of plasma triglyceride preceded the formation of amyloid plaques in transgenic mouse models of AD (Burgess et al., 2006). In our model, APOB-100 transgenic mice showed significantly elevated serum triglyceride and cholesterol level when fed with normal chow and cholesterol rich diet, respectively (Csont et al., 2007), and increased the rigidity of the plasma membrane of brain endothelial cells isolated from these transgenic animals (Lénárt et al., 2015). In the past 10 years we have described in detail the neurodegenerative processes occurring in the brain of hypertriglyceridemic APOB-100 transgenic mice. We detected widespread neuronal cell death and apoptosis of cortical and hippocampal neurons in this model (Lénárt et al., 2012). Synaptic dysfunction in the hippocampal region of APOB-100 transgenic mice using electrophysiolology and hyperphosphorylation of the tau protein (primarily at Ser^{262}, Ser^{396}, $Ser^{199/202}$, Ser^{404}phosphosites) were also shown (Lénárt et al., 2012). As a consequence of the extended neurodegeneration a pronounced enlargement of brain ventricles in transgenic brains was detected using MRI, which was transgene dose-dependent (Bereczki et al., 2008). Moreover, APOB-100 overexpression increased the level of lipid peroxidation in cortical and hippocampal brain regions and impaired cognitive function of the animals (Löffler et al., 2013).

Under cerebral ischemic conditions, decreased cortical microvascular density and increased brain capillary lumen diameter was found in our APOB-100 transgenic atherosclerosis model showing neurodegeneration (Süle et al., 2009). Cerebral ischemia also promoted the swelling of perivascular astrocytes and reduced the ratio of intact capillaries (Süle et al., 2009). Our aim was to further study neurovascular pathology and reveal structural and functional changes in the BBB of APOB-100 transgenic mice that may contribute to the neurodegeneration already described in this model.

MATERIALS AND METHODS

Animals

All animals were handled in accordance with approved procedures as defined by the EU Directive 2010/63/EU and all animal work was approved by the regional Station for Animal Health and Food Control (Csongrád-county, Hungary; project license: XVI/4136/2014). Mice were housed in groups of two to three under standard conditions (24°C, 12 h light–dark cycle) with food and water available *ad libitum*. APOB-100 transgenic mice were produced in our laboratory as described previously (Bjelik et al., 2006). Transgenic mice were backcrossed with C57B/6 strain six times to achieve a homogenous genetic background. Animals were maintained on a regular rodent chow diet. Animal surgeries were performed under sodium pentobarbital (Nembutal) anesthesia and all efforts were made to minimize pain and suffering. For genotyping, tail DNA of 10-day-old pups was purified as described earlier (Bjelik et al., 2006) and integrated transgenes were detected by PCR, using primers from the 5′ promoter region of the human *APOB* gene (Callow et al., 1994).

Materials

All reagents were purchased from Sigma-Aldrich Ltd. (St. Louis, MO, United States) except for those specifically mentioned.

Serum Triglyceride Measurement

Serum triglyceride levels in 7, 9, and 12-month-old APOB-100 transgenic (n = 5) and wild-type mice (n = 5) fed on a normal chow diet were measured using a colorimetric assay (**Supplementary Table S1**). Blood samples were collected through cardiac puncture under terminal anesthesia. After clot formation samples were centrifuged at 4°C, 1000 × g for 10 min, then serum was removed and stored at −80°C until use. Serum triglyceride levels were measured in triplicate using a commercially available enzymatic colorimetric assay kit (Diagnosticum Ltd., Budapest, Hungary) according to the manufacturer's instructions. Test accuracy was monitored using Standard Lipid Controls (Diagnosticum Ltd., Budapest, Hungary). Absorbance of the produced purple color product was measured at 560 nm using a microplate reader (Multiskan FC, Thermo Scientific, United States). Values were expressed in mmol/liter. Experimental groups, (APOB-100 transgenic mice and wild-type littermates) consisted of 5 animals each.

BBB Permeability

Permeability for sodium fluorescein (SF, mw: 376 Da), a marker of paracellular flux, and Evans blue (EB, mw: 67 kDa), a tracer which binds to serum albumin (Patterson et al., 1992), was measured as described in detail earlier (Veszelka et al., 2003). Six-month-old wild-type and transgenic mice (n = 10 animals/group) (**Supplementary Table S1**) were given a solution of both dyes (2%, 5 ml/kg) in an *iv*. injection to the tail vein for 1 h, and at the end of the experiments, the animals were perfused with 25 ml phosphate-buffered saline (PBS) for 15 min. Samples from two brain regions, cerebral cortex and hippocampus, were collected, weighed and stored at −80°C. Tissue pieces were homogenized in 650 μl PBS, then 650 μl of cold, 50% w/v, freshly prepared trichloroacetic acid was added and samples were centrifuged again with 10,000 × g for 12 min at 4°C. Dye concentrations were measured in supernatants by a PTI spectrofluorimeter (T-format, Quanta Master QM-1; Photon Technology International). Five hundred μl of the supernatants were diluted in ethanol (1:3) than emission of Evans blue was measured at 650 nm after excitation at 600 nm wavelength. For SF measurement 500 μl supernatants were diluted in distilled water (1:3) then 100 μl 10N NaOH was added to each sample. Emission of fluorescein was measured at 510 nm after excitation at 492 nm wavelength. BBB permeability was expressed as ng tracer/g brain tissue.

Transmission Electron Microscopy (TEM) and Image Analysis

Seven-month-old wild-type and transgenic mice (n = 4 animals/group) (**Supplementary Table S1**) were anesthetized with sodium pentobarbital (150 μg/g, i.p.), then transcardially perfused with 0.9% NaCl in 0.01 M phosphate buffer (PB), followed by 4% paraformaldehyde containing 2.5% glutaraldehyde in 0.1 M PB. Brains were removed and post-fixed in 4% paraformaldehyde in 0.1 M PB overnight at 4°C. Then, 40-μm-thick coronal sections were cut on an Oxford Vibratome (The Vibratome Company, St. Louis, MO, United States). Sections were washed with PBS and incubated in 1% OsO_4 for 30 min, then rinsed with distilled water and dehydrated in graded ethanol, block-stained with 1% uranyl acetate in 50% ethanol for 30 min and embedded in Taab 812 (Taab; Aldermaston, United Kingdom). Following polymerization at 60°C for 12 h, 60–70 nm ultrathin sections were cut using a Leica UCT ultramicrotome (Leica Microsystems, Milton Keynes, United Kingdom) and examined using a Hitachi 7100 transmission electron microscope (Hitachi Ltd., Tokyo, Japan). Electron micrographs were made by Veleta 2k × 2k MegaPixel side-mounted TEM CCD camera (Olympus, Tokyo, Japan). Contrast/brightness of electron micrographs was edited by Adobe Photoshop CS3 (Adobe Photoshop Inc., San Jose, CA, United States). Altogether 215 non-overlapping images representing 56 capillaries from the frontal cortex and 111 non-overlapping images representing 59 capillaries from the hippocampus were analyzed for morphological changes. All analyzed images were taken at 30,000× magnification. To calculate pericyte coverage on capillary profiles, the circumference of brain endothelial cells at their abluminal side facing the basal membrane was marked manually by a line with one color, and the length of pericytes with another. Only pericyte branches completely embedded in the capillary basement membrane were counted. The length of the lines was determined by Matlab. The background (the original image) was removed and the two colors were seperated to two channels. The pixel number of the two differently labeled lines is a good approximation of the pericyte to brain capillary endothelial circumference in each group. Thus, the ratio of the structures is the ratio of the two cumulative pixel numbers.

Brain Microvessel Isolation

Cortical microvessels were isolated from the brain of 6–7-month-old animals, as described earlier (Veszelka et al., 2007). The forebrains of APOB-100 overexpressing or wild-type mice (n = 6) (**Supplementary Table S1**) were collected in ice-cold sterile phosphate buffered saline (PBS). Meninges were taken off by rolling brains on a sterile wet filter paper. White matter and the choroid plexus were removed and the tissue was minced into 1 mm^3 pieces by scalpels. Samples then were homogenized in ice-cold Ringer-Hepes buffer (4 ml/g of tissue), and the resulting homogenates were centrifuged at 1000 g for 10 min. After centrifugation the microvessel enriched pellets were resuspended in 17.5% dextran (64–76 kDa) in Ringer-Hepes, and centrifuged at 4°C, 1500 × g for 15 min. The resulting pellets were suspended in 2 ml Ringer-Hepes buffer containing 1% BSA, while the supernatants were collected and centrifuged two more times. The resulting pellets were pooled and passed through a 100 μm and a 20 μm nylon mesh. The microvessels retained by the 20 μm mesh were washed off with 10 ml buffer and centrifuged at 4°C, 1000 g for 10 min. Finally, the pellets were resuspended in 1 ml buffer and centrifuged at 4°C, 10,000 g for 2 min, and stored in TRIZOL reagent until use. A small aliquot

of the brain microvessel preparation was observed with phase contrast microscopy, and similarly to our previously published data (Veszelka et al., 2007), these fractions only contained brain microvessel endothelial cells and pericytes.

Quantitative Real-Time PCR

Total RNA was extracted from primary cell cultures, cortical microvessel samples, or hippocampal and cortical brain regions using TRIZOL reagent according to the manufacturer's protocol. Hippocampal and cortical brain samples were derived from 6-month-old mice (n = 6 animals/group) (**Supplementary Table S1**). Briefly, samples were homogenized in the appropriate volume of TRIZOL reagent, then 1/5 volume chloroform was added to each mixture and the samples were incubated on ice for 5 min. After centrifugation at 12,000 × g for 15 min at 4°C, the RNA containing aqueous phase was separated from the organic phase. The RNA was precipitated with 100% isopropyl alcohol and incubated for 10 min at −20°C. After centrifugation for 10 min at 12,000 × g at 4°C, RNA was washed with 80% ethanol and samples were centrifuged for 5 min at 12,000 × g at 4°C. RNA pellets were dissolved in RNase free water and then bound to RNA Clean Up column (NucleoSpin RNA clean-up kit, Macherey-Nagel) where they were treated with DNase. RNA was finally eluted from the membrane with RNase-free water, and the concentrations of the samples were measured at 230 nm using a spectrophotometer (NanoDrop ND-1000).

mRNA samples were converted to cDNA by using a reverse transcriptase kit (High Capacity cDNA Reverse Transcription Kit, Applied Biosystems). Each reaction mix consisted of 2 μg RNA (15 μl); 1.5 μl reverse transcriptase; 3 μl primer; 1.2 μl dNTP; 3 μl buffer; 6.3 μl RNase free water. The temperature profile of the reaction was the following: 10 min at 25°C, 2 h at 37°C and 5 min at 85°C (using MJ Mini - Personal Thermal Cycler, BioRad). The cDNA was finally diluted 1:20, and 9 μl of this mix was used as a template in the PCR reaction that follows. Each reaction was performed in a total volume of 20 μl containing 10 μl of 2x Power SYBR Green PCR Master Mix (Applied Biosystems), 1 μl of 5 pmol/μl primer mix (forward + reverse) and 9 μl of cDNA sample. The amplification was carried out on a RotorGene 3000 instrument (Corbett Research) with the following cycling parameters: heat activation at 95°C for 10 min; followed by 45 cycles of denaturation at 95°C for 15 s, annealing at 56°C for 15 s, and extension at 60°C for 40 s in 45 cycles. Fluorescent signals were collected after each extension step at 72°C and at the end the registration of the melting curve was performed between 50 and 95°C. The expression level of target genes was normalized to an endogenous control gene *Gapdh* or *Actb* (ΔCt). Then ΔΔCt was calculated, i.e., the relative expression of the target genes in transgenic animals was compared with the expression levels observed in wild-type animals. Fold-differences were calculated using the $2^{-\Delta\Delta Ct}$ formula and were expressed in percents. Gene expression changes were considered significant if the expression level dropped below 50% or showed a two-fold increase compared with control values. We studied genes involved in different molecular mechanism, such as oxidative stress, transport pathways or endothelial dysfunction. Individual genes were selected based on literature data, especially those identified in BBB transcriptome analysis in mice (Daneman et al., 2010), related to AD pathology (Wu et al., 2005), or selected for our recently published gene expression analysis of different BBB models (Veszelka et al., 2018). Primer sequences used in this study are listed in **Supplementary Table S2**.

Immunohistochemistry and Confocal Microscopy

Standard immunofluorescence protocols were applied. 7–8-months-old mice (**Supplementary Table S1**) were terminally anesthetized with sodium pentobarbital (150 μg/g, i.p.), then transcardially perfused with 0.9% sodium chloride dissolved in 0.01 M PB, pH 7.4, followed by 3% paraformaldehyde in 0.1 M PB, pH 7.4. Brains were removed and postfixed for 4 h in the same fixative. Following fixation the brain samples were washed in 0.1 M PB, pH 7.4, and cryoprotected in 30% sucrose until saturation. Then, 30-μm-thick, hippocampus and frontal cortex containing coronal sections were cut on a cryostat (Floorstanding Cryostat MNT; Slee, Mainz, Germany), collected in 0.1 M PB, pH 7.4 containing 0.01% sodium azide (Fluka) (w/v) and were stored at 4°C.

Antigen retrieving for claudin-5 and occludin immunostainings was performed with 0.5 % Triton X-100 in PBS for 10 min, followed by an incubation in protease type XIV (1 μg/ml) dissolved in $CaCl_2$ (1 mg/ml) for 7 min. Antigen retrieving for the other primary antibodies used included only Triton X-100 treatment at concentrations based on our preliminary experiments [0.1% for Pdgfrβ, 0.2% for vimentin and Gfap, 0.3% for Lox-1, and 0.5% for *P*-glycoprotein (Pgp) for details of Lox-1 immunolabeling see **Supplementary Material**]. Primary antibodies used were rabbit anti-claudin-5, rabbit anti-occludin (Thermo Fisher Scientific, Waltham, MA, United States), goat anti-Gfap (Abcam, Cambridge, United Kingdom), mouse anti-vimentin [Agilent (DAKO), Santa Clara, CA, United States], mouse anti-Pgp (Merck Millipore, Burlington, MA, United States), and rabbit anti Lox-1 (Abcam, Cambridge, United Kingdom), (**Supplementary Table S3**). Appropriate secondary antibodies conjugated with DyLight™ 488 and Alexa Fluor™ 594 (Jackson ImmunoResearch Europe Ltd., Cambridgeshire, United Kingdom) were applied. Sections were counterstained with DAPI, coverslipped with Confocal Matrix® (Micro Tech Lab, Graz, Austria) and examined with a confocal laser scanning microscope (Olympus Fluoview FV1000, Olympus Life Science Europa GmbH, Hamburg, Germany). Images of 512 × 512 px were captured using the following microscope configuration: objective lens: UPLSAPO 60x, numeric aperture 1.35; sampling speed: 8 μs/pixel; scanning mode: sequential unidirectional. In order to obtain high resolution (1024 × 1024 px) images, Yokogawa W1/Olympus IX83-based spinning disk confocal microscope was also used for imaging Gfap, vimentin, and Pdgfrβ immunostainings using excitation and detection parameters optimized for DyLight™ 488, Alexa Fluor™ 594 and DAPI. 405nm (for DAPI), 488 nm (for DyLight™ 488) and 561 nm (for Alexa Fluor™ 594) laser excitation, and 60x objective were used for imaging. The contrast of these images showing Gfap

immunostaining was increased by inverting and displaying them as gray scale images using the public domain Fiji software.

Fluorescence Intensity Analysis

Immunostained coronal sections containing the hippocampus and cortical areas (5 animals per group, 3 sections per animal) were selected based on the principle of systematic random sampling (Gundersen and Osterby, 1981; Mayhew, 1991). Three images representing randomly selected parts of the hippocampus and frontal cortex in each section were taken with a laser scanning (for claudin-5, occludin and Pgp immunolabeling) or a spinning disk (for Gfap immunostaining) confocal microscope using a 60× objective lens and the same excitation and detection parameters for each image. Fluorescence intensity of claudin-5, occludin and Pgp immunolabelings was evaluated using the ImageQuant^{TM} software as follows: on every image 10 equally sized small rectangular areas (7 × 7 pixels) were placed randomly on the intensively highlighted immunolabeled structures, and five equal rectangles were placed randomly on areas lacking immunostaining representing the background. Then the average intensity/pixel values of each area were calculated, and the average intensity/pixel values representing the background intensity were subtracted from those of immunolabeled areas. The GFAP immunostained structures represented a more a complex pattern and occupied larger areas, therefore the integrated fluorescence intensity of Gfap immunolabeling was measured using the public domain Fiji software as follows: Grayscale 16-bit images were used. The integrated fluorescence intensity of the whole image and that of a small area lacking immunostained structures were measured, then the background fluorescence intensity of the whole image was calculated and subtracted from the integrated fluorescence intensity value of the whole image. The procedures were performed on each image, and the collected data were statistically analyzed (Farkas et al., 2008).

Statistical Analysis

GraphPad Prism 5.0 software (GraphPad Software Inc. LaJolla, CA, United States) was used for statistical analysis. Gaussian distribution of the data was tested with the Kolmogorov–Smirnov normality test. Data showing Gaussian distribution were analyzed with two-way analysis of variance followed by Bonferroni *post hoc* test. Data showing no Gaussian distribution were analyzed with Kruskal–Wallis and Dunn's multiple comparison tests. The level of statistical significance was taken as $p < 0.05$. Results are presented as means ± SEM.

RESULTS

Chronic Hypertriglyceridemia in APOB-100 Transgenic Mice

A statistically significant difference was detected in transgenic compared to wild-type animals at every time point (7, 9, and 12-month, $n = 5$ animals/group) indicating chronic hypertriglyceridemia in APOB-100 transgenic mice (**Figure 1A**).

Impairment of the BBB Integrity: Permeability Measurements

We measured a significant increase in the BBB permeability ($p < 0.05$) for the small molecular weight marker SF in the hippocampal region of transgenic mice, while alteration in the extravasation of the large serum protein albumin showed a non-significant trend (**Figure 1B**). However, there was no obvious change in the permeability for either of the markers in the cortex of transgenic mice compared to wild-type littermates.

BBB Dysfunction: Changes in Gene and Protein Expression in Brain Microvessels

Reduced expression (16%) of the vascular restricted and mesenchyme homeobox gene 2 (*Meox2*), a key regulator of BBB functions, particularly in AD, was measured in cerebral microvessels of APOB-100 transgenic mice compared to wild-type animals (**Figure 1C**). The gene expression of *Mfsd2a* (44%), the BBB transporter for unsaturated lipid docosahexaenoic acid (DHA), and the primary glucose transporter in brain endothelial cells, *Glut-1* (57%) were also decreased (**Figure 1C**).

Lox-1, a lectin-like protein expressed in endothelial cells in the periphery is considered as the major receptor for oxidized low-density lipoprotein. The level of oxidized LDL (oxLDL) receptor (*Lox-1*) has increased dramatically (297%) in the microvessels of APOB-100 transgenic mice (**Figure 1C**). In contrast to the periphery, where Lox-1 was detected in heart coronal vessels, Lox-1 immunolabeling was observed only in neuronal cell bodies and processes, but not in brain capillaries (**Supplementary Figure S1**). A significant increase in Lox-1 immunoreactive area was detected in the cortex, but no change was seen in the hippocampus of transgenic mice compared to wild-type animals (**Supplementary Figure S2**). While mRNA level of LDL receptor-related protein-1 (*Lrp1*, 70%) slightly decreased, the expression level of *Lrp2* dropped to 56% in transgenic microvessels (**Figure 1C**).

We measured two isoforms of nitric oxide (NO) synthases (NOS), the endothelial (*eNos/Nos3*) and the inducible form (*iNos/Nos2*), and found a significant decrease for both genes in brain microvessels of transgenic animals (**Figure 1C**). Expression of mRNA for caveolin-1 (*Cav-1*), a structural element of brain endothelial caveolae associated with Nos3, was also reduced (**Figure 1C**).

The expression of selected TJ proteins was analyzed at gene expressional level using quantitative real-time PCR, and at protein level using fluorescence immunohistochemistry, too. The mRNA level of transmembrane protein *Ocln*, and TJ cytoplasmic linker *Tjp-1*, was reduced to half in transgenic microvessels, while there was no change in the expression level of *Cldn-5*, the dominant claudin member at the BBB, compared to wild-type animals (100%) (**Figure 1C**). Fluorescence immunohistochemical stainings for claudin-5 (**Figure 2A**) and occludin (**Figure 3A**) showed that both immunolabelings were exclusively localized at endothelial TJs and appeared as continuous lines. There was no statistically significant change

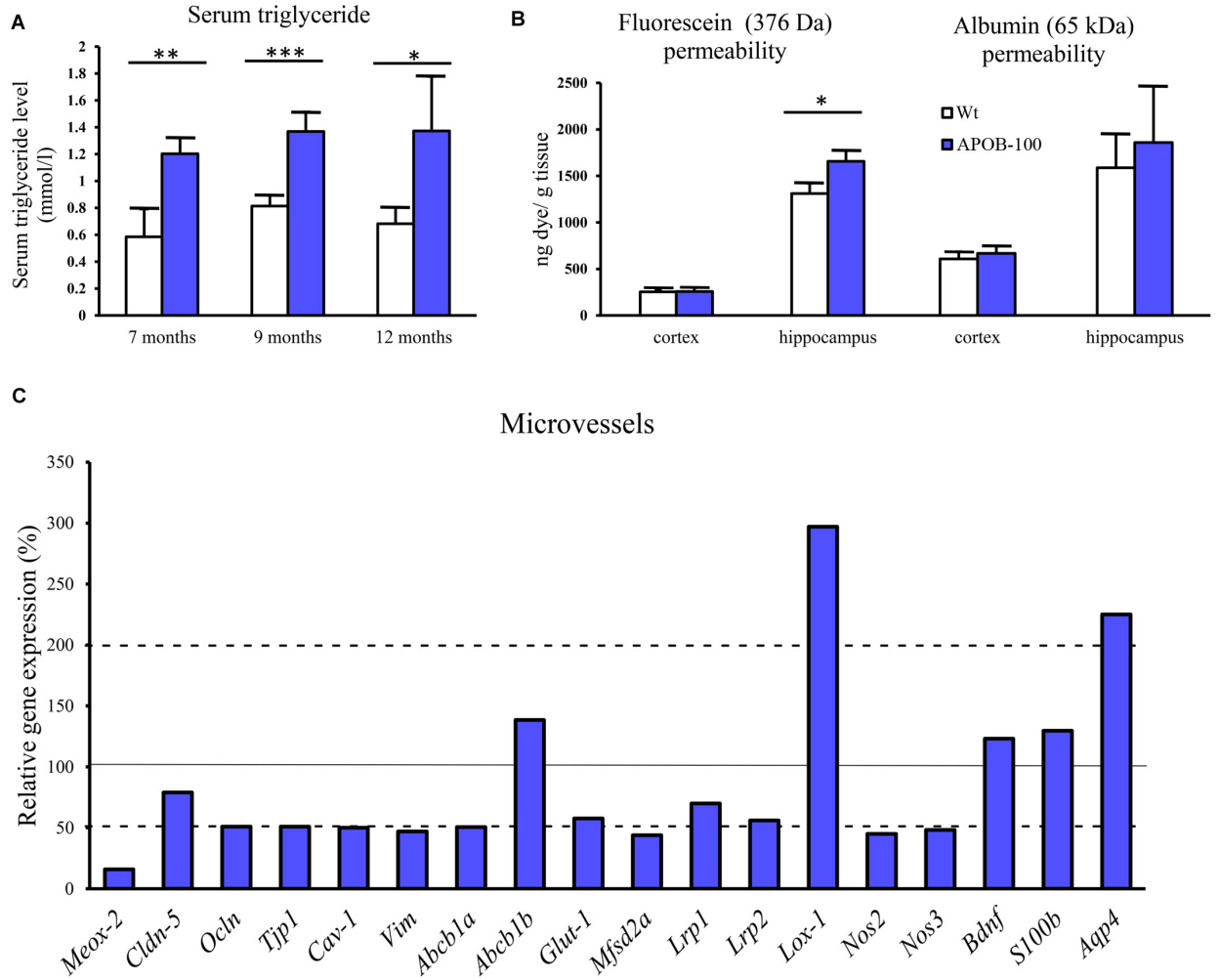

FIGURE 1 | Serum triglyceride levels **(A)**, BBB permeability for fluorescein and albumin in the brain of hypertriglyceridemic APOB-100 transgenic (APOB-100) and wild-type (Wt) mice **(B)**, and gene expression analysis of the microvessel fraction from APOB-100 transgenic mice using QPCR **(C)**. Continuous line indicates the expression level of the corresponding gene in wild-type mice (100%). Dashed lines indicate the levels of significant changes: a 2 fold (200%) increase or an 0.5 fold (50%) reduction in gene expression. $^{***}P < 0.001$, $^{**}P < 0.01$, $^{*}P < 0.05$, compared with Wt mice.

neither in claudin-5 nor in occludin immunostaining intensity in transgenic cortex and hippocampus compared to wild-type animals (**Figures 2B**, **3B**).

The gene expression of vimentin, a cytoskeletal protein, which labels reactive astrocytes (Pekny et al., 2007), but can be produced by pericytes (Bandopadhyay et al., 2001) and brain endothelial cells (Deracinois et al., 2013) too, showed a significant reduction in isolated brain microvessels (**Figure 1C**). At protein level, vimentin was localized along capillaries in the frontal cortex of wild-type mice as it can be observed in occludin-vimentin double immunofluorescence stainings (**Figure 3A**), where occludin immunolabeling delineates brain capillaries. Vimentin immunoreactivity was very rarely seen in the frontal cortex of APOB-100 transgenic animals, and it was not detected in the hippocampus of either genotype (**Figure 3A**). The vimentin immunolabeling showed no co-localization with epitopes recognized either by a Gfap antibody (an astroglia marker), or by a Pdgfrβ antibody (a pericyte marker) (**Supplementary Figure S3**). Furthermore, we have established primary pericyte, astrocyte and endothelial cell cultures from wild-type and transgenic mice and vimentin gene expression was measured using QPCR. The vimentin gene expressions normalized to the endogenous mouse actin gene were compared in wild-type animals (ΔCT values). Vimentin was expressed at high level in endothelial cells (ΔCT = 1.3), astrocytes (ΔCT = 2) and pericytes (ΔCT = 2.3) as well. Comparison of the vimentin expression level of wild-type and transgenic animals demonstrates that while the vimentin expression levels were not changed significantly in the transgenic endothelial cells and astrocytes (74 and 124%, respectively) transgenic pericytes showed significantly reduced vimentin level (33%) compared to wild-type cells (**Supplementary Figure S4**). The most widely studied, and AD related ABC transporter at the BBB, *Abcb1* or P-glycoprotein (P-gp) was also examined by QPCR in isolated

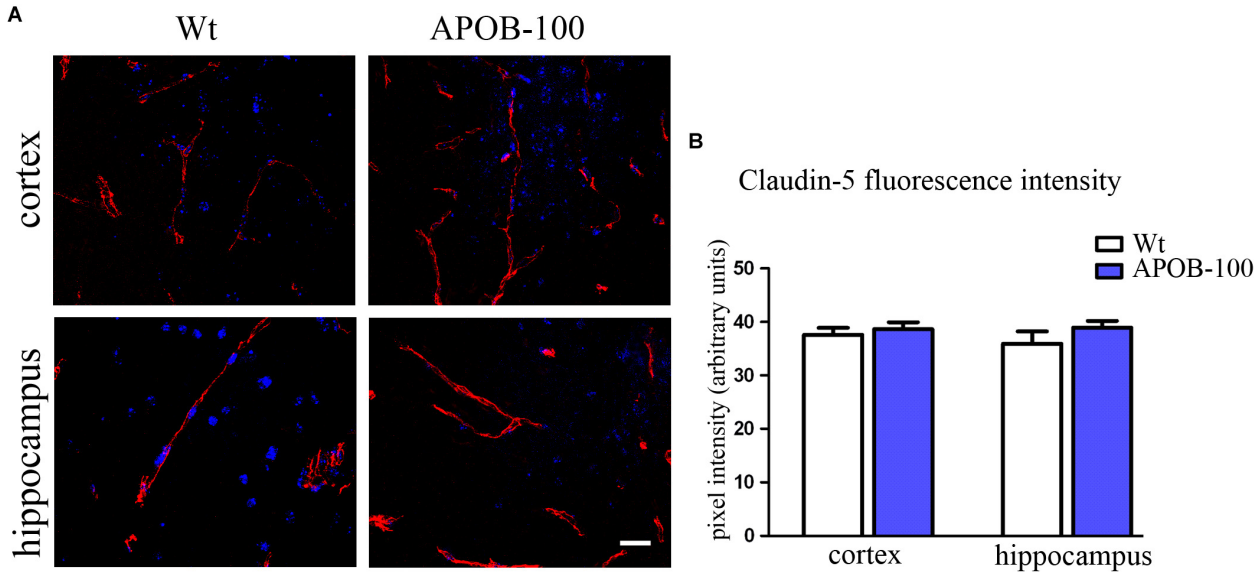

FIGURE 2 | Claudin-5 immunostaining pattern (red) in the cortex and hippocampus of wild-type (Wt) and APOB-100 transgenic mice (APOB-100), counterstained with DAPI (blue) **(A)**. Scale bar: 20 μm. Quantification of fluorescence intensity of claudin-5 immunolabeling in the frontal cortex and hippocampus of Wt and APOB-100 transgenic mice **(B)**.

brain microvessels and by immunohistochemistry in the frontal cortex and hippocampus of wild-type and APOB-100 transgenic mice. From the isoforms of P-gp coding genes, *Abcb1a* mRNA expression was significantly decreased (51%), while *Abcb1b* (138%) showed no significant change (**Figure 1C**). Using a monoclonal antibody recognizing both isoforms of P-gp the immunoreactivity pattern of P-gp was similar to that of TJ proteins delineating a large number of capillaries in the frontal cortex and hippocampus in wild-type animals. However, in the APOB-100 transgenic group, P-gp immunoreactivity could hardly be observed in either brain region examined (**Figure 4A**), which was reflected by a significant drop in P-gp fluorescence intensity in APOB-100 transgenic mice compared to wild-type animals in the cortex and hippocampus, too (**Figure 4B**).

Astroglial endfeet are important structural and functional elements of the BBB. The gene expression level of aquaporin-4 (*Aqp4*), a water channel and a marker of glial endfeet, has increased dramatically (225%) in isolated brain microvessels (**Figure 1C**), while no change was observed in brain samples (**Figure 6**). In the microvessel samples the glial specific calcium-binding cytoplasmic protein *S100b* (129%) and the astrocyte produced brain derived neurotrophic factor (*Bdnf*, 123%) levels showed no change (**Figure 1C**).

Ultrastructural Changes of the BBB in APOB-100 Transgenic Mice

Analysis of the ultrastructure of brain capillaries using TEM revealed several alterations in the NVU of APOB-100 transgenic mice compared to wild-type animals (**Figure 5** and **Table 1**). The most significant changes were observed in the morphology of TJs and astrocytic endfeet. Swollen astrocytic processes around capillaries were predominant in the transgenic group, indicating edema of glial endfeet (**Figure 5A** and **Supplementary Figure S5**). The intercellular junctions of capillary endothelial cells were characterized by a continuous electron dense material in wild-type mice (**Figure 5B**). In the transgenic group, in contrast, nearly half of the endothelial cell contacts displayed a discontinuous electron dense structure (**Figure 5B** and **Table 1**). Further ultrastructural differences include basal membrane alterations, like increased thickness, tortuosity, fragmentation, and alterations in luminal membrane characteristics, like increased number of protrusions in the transgenic group. No significant difference was found in the pericyte coverage of brain capillaries (**Table 1**). The described ultrastructural changes were detected in the frontal cortex and in the hippocampus as well.

Neuroinflammation and Neuron Related Changes in the Cortex and Hippocampus

From the genes of selected cytokines and neuroinflammatory markers the expression of cytokine *Tnfα* (152%) and the inflammation related nuclear factor *NF-κB* (167%) increased in the transgenic cortex but were not substantially changed in the hippocampus. No change was measured for *Il-1β* (**Figure 6**). Similarly, there was no notable change in the expression of other inflammatory markers in the cortex, except for *Tlr4*, the expression of which was dropped down to 60%. Of neuronal synaptic genes, which play an important role in remodeling CNS synapsis, the level of *Nlgn1* (152%) has slightly increased in the hippocampus but was not changed in the cortex. The expression level of *Nmdar* and *Nrxn1* was unchanged both in the hippocampus and in the cortex. However, a significant decrease in the expression level of a cell adhesion molecule, *Cdh2* (*N-cadherin)*, (32%) was detected in the hippocampus of

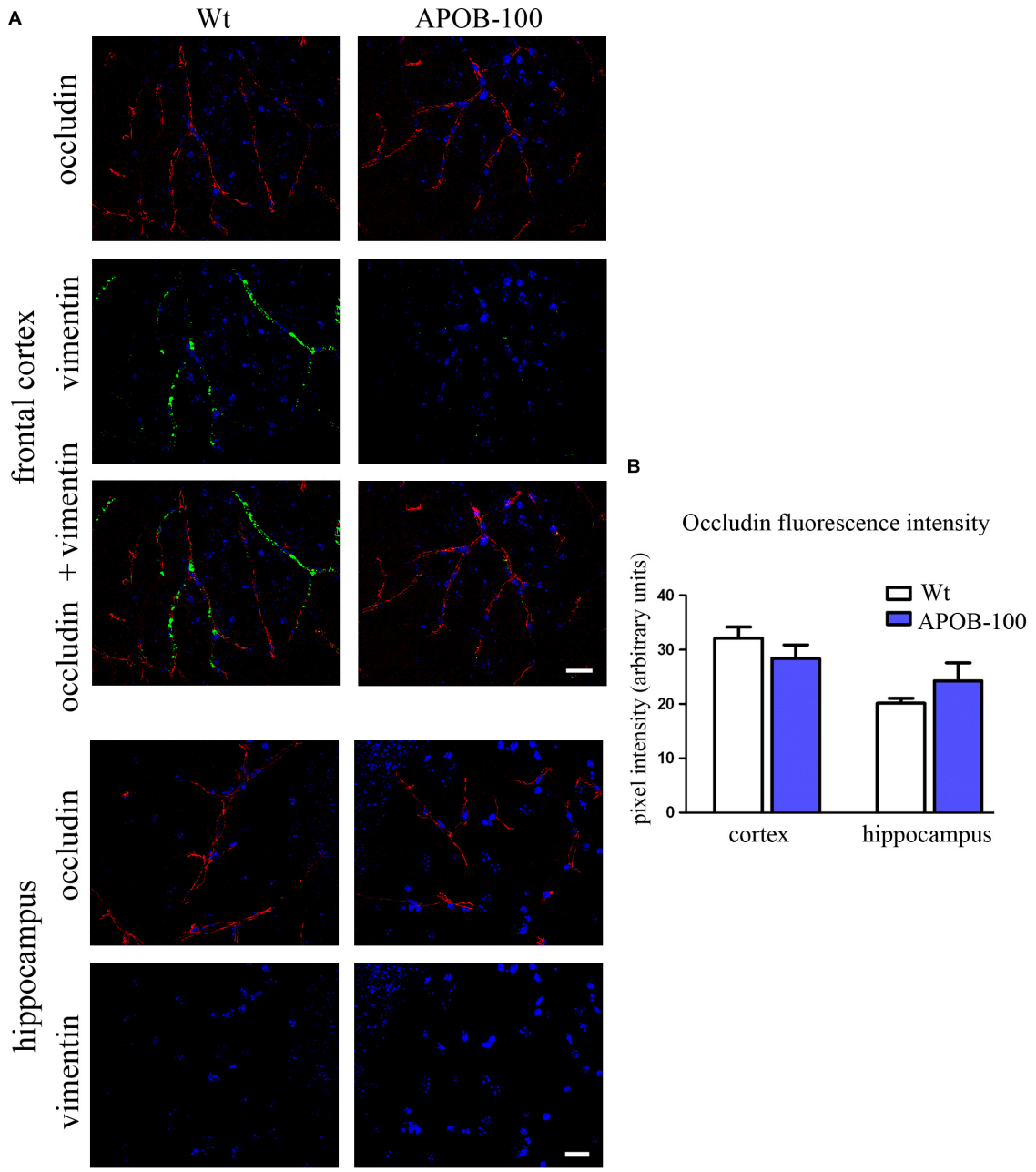

FIGURE 3 | Occludin (red) and vimentin (green) immunostaining pattern in the cortex and hippocampus of wild-type (Wt) and APOB-100 transgenic mice (APOB-100) counterstained with DAPI (blue) **(A)**. Scale bar: 20 μm. Quantification of fluorescence intensity of occludin immunolabeling in the frontal cortex and hippocampus of Wt and APOB-100 transgenic mice **(B)**.

transgenic brains (**Figure 6**). The results of gene expression analysis are summarized in **Table 2**.

Out of 600 miRNAs analyzed, we could detect 10 (1.67%) differentially expressed miRNA genes in APOB100 transgenic cortices (6 upregulated and 4 repressed). List of miRNA genes with altered expression level is shown in **Supplementary Table S4**. Overexpressed miRNAs were mmu-miR-669g, mmu-miR-222, mmu-miR-708, mmu-miR-26a, mmu-miR-1898, and mmu-miR-500, and repressed miRNAs were mmu-miR-7a, mmu-miR-7b, mmu-miR-187, and mmu-miR-1a. Although we found 10 miRNAs showing differential expression, only 4 miRNAs had experimentally validated targets in the IPA database (mmu-miR-1a, mmu-miR-222, mmu-miR-26a, mmu-miR-7b). Some of these target genes (n = 11) were expected to have relevance in neuronal changes. The expression level of these genes was further investigated by QPCR but no significant changes were detected (data not shown) with the exception of *Bdnf*. This gene may be regulated by two differentially expressed

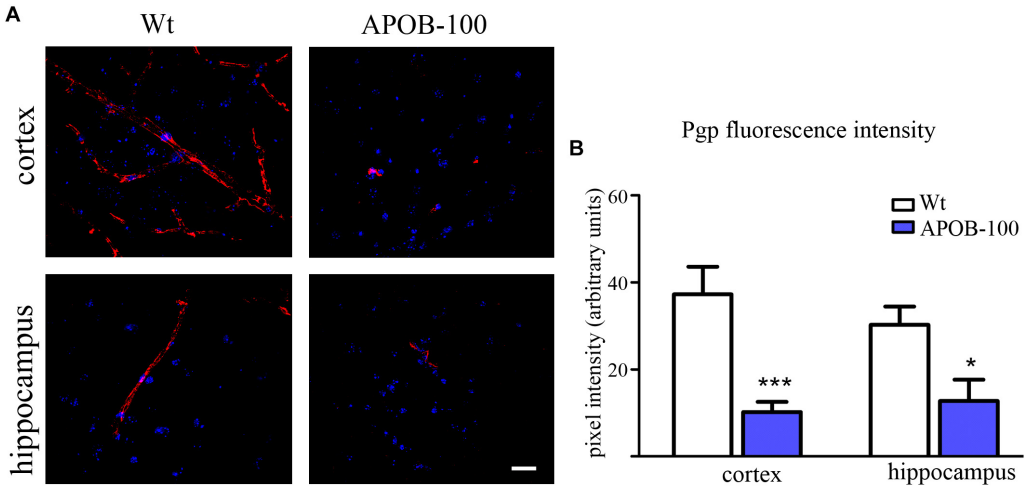

FIGURE 4 | P-gp (ABCB1) transporter immunostaining pattern (red) in cortical and hippocampal areas of wild-type (Wt) and APOB-100 transgenic mice (APOB-100), counterstained with DAPI (blue) **(A)**. Scale bar: 20 μm. Quantification of fluorescence intensity of P-gp immunolabeling in the frontal cortex and hippocampus of Wt and APOB-100 transgenic mice **(B)** ***$P < 0.001$, *$P < 0.05$, compared with Wt mice.

miRNAs: mmu-miR-26a (overexpressed), and mmu-miR-1a (repressed). QPCR data showed a two-fold overexpression of *Bdnf* gene in the transgenic cortex (**Supplementary Figure S6**).

Changes in Glial Cell Gene Expression and Morphology

The expression level of the microglial marker (*Iba-1/Aif1*) was slightly increased (145%) in the hippocampus of APOB-100 transgenic mice compared to wild-type animals (**Figure 6**). In contrast, the expression level of glial fibrillary acidic protein (*Gfap*), a cytoskeletal astroglial marker, was dropped down to 38% in transgenic hippocampus (**Figure 6**). The level of two *Gfap* isoforms, *Gfap*-α and *Gfap*-σ, was also reduced to 59 and 41%, respectively, in the hippocampus of APOB-100 transgenic mice compared to wild-type littermates (100%) (**Figure 6**). Gfap immunoreactive cells displayed several processes that were closely associated with microvessels in the cortex and in the hippocampus too, in both experimental groups (**Figure 7A**). The intensity of the fluorescent Gfap immunolabeling showed a significant decrease in the cortex of APOB-100 transgenic mice compared to wild-type animals (**Figure 7B**).

DISCUSSION

Here, we describe, that transgenic mice overexpressing the human APOB-100 protein show chronic hypertriglyceridemia, an increase in permeability for a small molecular marker, and gene expressional, immunohistochemical and ultrastructural alterations at the BBB. Several previous reports have already shown that hypertriglyceridemia is a serious risk factor in the development of neurodegeneration and dementia (Burgess et al., 2006; Raffaitin et al., 2009; Bowman et al., 2012; Klafke et al., 2015) and it was also demonstrated that dyslipidemia is more prevalent in AD subjects with BBB impairment (Bowman et al., 2012). Observations in aging rats, that a decrease in cerebral blood flow is linked to pathologies similar to those found in AD (De La Torre et al., 1992; De la Torre and Mussivand, 1993) and demonstration of brain microvascular injury and BBB leakage in AD patients (Zipser et al., 2007) led to the vascular concept of AD which became generally accepted by today (Zlokovic, 2008; Gosselet et al., 2013; Zhao et al., 2015; Kisler et al., 2017). Lipolysis products generated from triglyceride rich lipoproteins damage endothelial barrier function: perturb the expression of junctional proteins, induce apoptotic cell death *in vitro* in human aortic endothelial cells (Eiselein et al., 2007) and transiently elevate BBB permeability *in vivo* in mice (Lee et al., 2017). Hypertriglyceridemia may contribute to endothelial dysfunction likely through the generation of oxidative stress (Antonios et al., 2008). Indeed, in our recent study (Lénárt et al., 2015) we have shown that oxidized LDL treatment induced barrier dysfunction and increased reactive oxygen species production and membrane rigidity in primary brain endothelial cells.

In the present paper we studied BBB related functional and morphological characteristics as well as gene expression profiling of APOB-100 transgenic mice. We found APOB-100 transgenic mice are characterized by chronic hypertriglyceridemia. Regarding BBB function, a significantly increased extravasation for a small molecule marker, SF, was observed in the hippocampus of transgenic mice, which may suggest an increase in paracellular permeability. Gene expression changes suggesting endothelial dysfunction in APOB-100 transgenic animals include reduced expression of the homeobox regulator *Meox2*, and BBB transporters *Mfsd2a*, *Glut1*, *Lrp2*, *Abcb1a* genes in APOB-100 transgenic brain microvessels may indicate pathomechanisms similar to those observed in conditions of BBB dysfunctions (Zlokovic, 2011; Zhao et al., 2015). Low expression of *MEOX2* was demonstrated in cultured brain endothelial cells isolated from severely affected AD patients (Wu et al., 2005). In the same

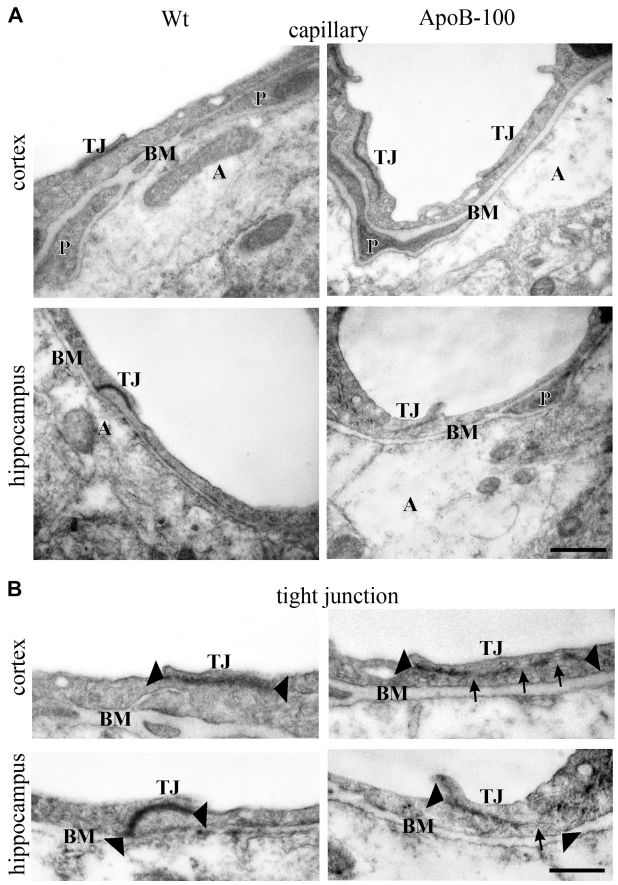

FIGURE 5 | Electron micrographs of brain capillaries **(A)** and tight junctions **(B)** in the frontal cortex and hippocampus of wild-type (Wt) and APOB-100 transgenic (APOB-100) mice. Tight junctions in **(B)** are larger magnifications of tight junctions seen in **(A)**. A, astrocyte; BM, basal membrane; P, pericyte; TJ, tight junction. Scale bars: 500 nm **(A)** and 800 nm **(B)**.

TABLE 1 | Summary of changes in BBB ultrastructure in the frontal cortex and hippocampus of wild-type (Wt) and APOB-100 transgenic (APOB-100) mice.

Frontal cortex		**Wt**	**APOB-100**
Number of capillaries		23	33
Number of images		91	124
Capillary endothelial cell			
Luminal membrane	Smooth	69%	48%
	Protrusions	31%	52%
Tight junctions	Intact	100%	56%
	Discontinuous	0%	44%
Basal membrane	Intact	78%	56%
	Altered	22%	44%
Pericyte			
	Capillary coverage	20%	17%
	Capillary wo pericyte	5%	22%
Astrocyte			
	Intact	77%	12%
	Edema	23%	88%
Hippocampus CA1		**Wt**	**APOB-100**
Number of capillaries		29	30
Number of images		92	129
Capillary endothelial cell			
Luminal membrane	Smooth	78%	46%
	Protrusions	22%	54%
Tight junctions	Intact	100%	29%
	Discontinuous	0%	71%
Basal membrane	Intact	89%	24%
	Altered	11%	76%
Pericyte			
	Capillary coverage	25%	23%
	Capillary wo pericyte	19%	23%
Astrocyte			
	Intact	89%	44%
	Edema	11%	56%

Values are shown as percent of all images analyzed in the group. Pericyte coverage was calculated as written in the Materials and methods section.

study Meox2 deletion in mice resulted in decreased density of brain capillaries, lower levels of cerebral blood flow during rest, a diminished hypoxia-induced angiogenic response in the brain. In addition, in these animals low levels of LRP were observed leading to reduced Aβ efflux. Our observations on the drastically reduced *Meox2* in transgenic brain microvessels might also support the link between Meox2 and neurovascular dysfunction. Beside *Meox2* the other gene for which a dramatic decrease was observed in brain microvessels from transgenic animals was *Mfsd2a,* which might have contributed to the increased BBB permeability in our study and the neurodegeneration in our model described previously (Bereczki et al., 2008). It has been recently discovered, that Mfsd2a is not only a DHA transporter at the BBB, but also a key regulator of BBB integrity and function (Zhao and Zlokovic, 2014). Mutations in *MFSD2A* gene leads to decreased DHA transport into the CNS and severe neurological symptoms (Betsholtz, 2015), and DHA can protect cells of the NVU against amyloid peptide toxicity (Veszelka et al., 2013). At the BBB GLUT1 is the main transporter of glucose, the primary energy source in the CNS. A reduction in Glut1 expression was linked to neurovascular dysfunction and AD in a mouse model (Winkler et al., 2015) emphasizing the importance of the present findings.

Additionally, the receptors Lrp1, Lrp2 and the transporter P-gp responsible for the clearance of Aβ from the brain (Shibata et al., 2000; Deane et al., 2003; Cirrito et al., 2005) are downregulated in AD pathology (Marques et al., 2013). In this study we showed a significant reduction in the expression of the *Abcb1a* gene coding the P-gp isoform predominantly expressed in brain capillary endothelial cells (Croop et al., 1989; Shoshani et al., 1998). In agreement with this finding, the P-gp immunolabeling could hardly be detected in APOB-100 transgenic mouse brains, which may be linked to the previously demonstrated increased accumulation of Aβ in this model (Bereczki et al., 2008).

A significant decrease in inducible *Nos2* and endothelial *Nos3*, and an increase in *Lox-1* expression were detected in microvessels isolated from APOB-100 transgenic animals.

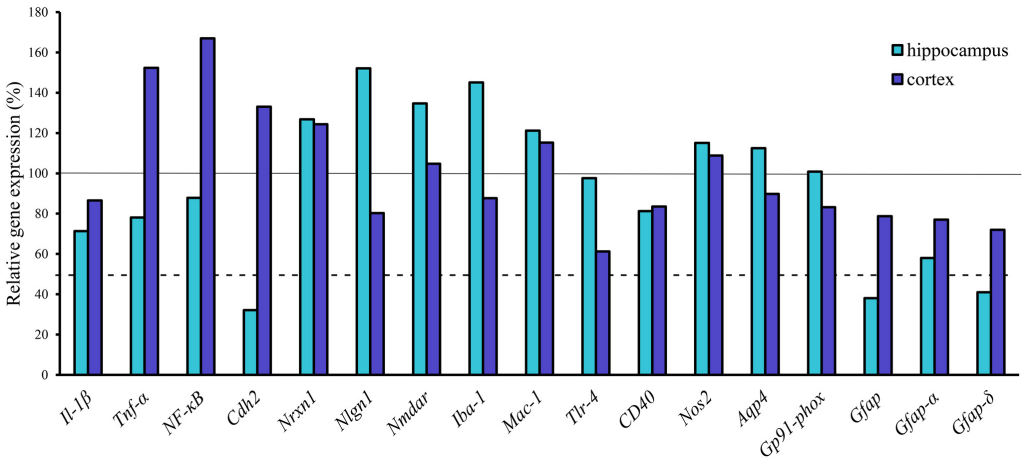

FIGURE 6 | Gene expression analysis of neuroinflammatory markers, transporters and Gfap isoforms in the hippocampus and cortex of APOB-100 transgenic mice. Continuous line indicates the expression level of the corresponding gene in wild-type mice (100%). Dashed line indicates the level of significant changes: a 0.5 fold (50%) reduction in gene expression.

TABLE 2 | Summary of gene expression changes in hypertriglyceridemic APOB-100 transgenic mice.

	mRNA		Protein	
	Tissue	**Level**	**Tissue**	**Level**
P-gp (Abcb1a)	Microvessel	Decreased	Hippocampus	Decreased
			Cortex	Decreased
iNOS	Microvessel	Decreased		n.d.
eNOS	Microvessel	Decreased		n.d.
Lox1	Microvessel	Increased	Cortex	Increased
Aqp4	Microvessel	Increased		n.d
Occludin	Microvessel	Decreased	Hippocampus	No change
			Cortex	No change
ZO-1	Microvessel	Decreased		n.d
Caveolin-1	Microvessel	Decreased		n.d
Vimentin	Microvessel	Decreased	Cortex	Decreased
Mfsd2A	Microvessel	Decreased		n.d
Meox-2	Microvessel	Decreased		n.d.
Glut-1	Microvessel	Decreased		n.d
Bdnf	Cortex	Increased		n.d.
Aif-1/Iba-1	Hippocampus	Increased*	Hippocampus	No change
Gfap	Hippocampus	Decreased	Hippocampus	No change
			Cortex	Decreased
Gfap alpha	Hippocampus	Decreased		n.d
Gfap delta	Hippocampus	Decreased		n.d.
IL-β	Hippocampus	Decreased*		n.d
Ncadh	Hippocampus	Decreased		n.d.
TNF-α	Cortex	Increased*		n.d
NF-κB	Cortex	Increased*		n.d.
Tlr4	Cortex	Decreased*		n.d

**Denotes less than two-fold change.*

The area fraction of Lox-1 immunoreactive structures was also significantly increased in the cortex of APOB-100 transgenic mice compared to wild-type animals. The upregulation of *Lox-1* and the downregulation of *Nos2* and *Nos3* mRNA levels confirmed atherosclerotic changes in APOB-100 transgenic mice reported earlier (Chen et al., 2002; Csont et al., 2007) The reduction in *Nos3* gene expression is in line with observations focusing on atherosclerosis-prone regions of the mouse aorta (Won et al., 2007) and on areas of human atherosclerosis (Buttery et al., 1996; Barry et al., 1998). Lox-1 upregulation is observed in atherosclerosis and linked to oxidative stress and inflammatory reactions leading to inhibition of Nos3 enzymatic activity via increased C-reactive protein production (Stapleton et al., 2010; Stancel et al., 2016) and, consequently, microvessel dysfunction in the periphery (Lubrano and Balzan, 2016). Our study suggests for the first time, that there may be a link between neurovascular changes and *Lox-1* upregulation, *Nos2* and *Nos3* downregulation in brain microvessels.

NO or NO donors at low concentrations do not modify the barrier function of BBB culture models, while both the blocking of basal NO production and high levels of NO induce barrier opening (Deli et al., 2005). NO is known to modulate cGMP-pathways which decrease resistance and increase permeability in culture models of the BBB and may mediate the effects of excess NO (Deli et al., 2005), but the exact mechanisms by which NO regulates different BBB permeability pathways are not known.

A significant decrease in *Cav-1* gene expression was detected in microvessels isolated from APOB-100 transgenic brains. Caveolin-1 is a structural protein playing a stabilizing role in caveolae, but it is reported to influence TJ morphology and the expression of junctional proteins occludin and ZO-1, too. Caveolin-1 knock-out mice are characterized by increased paracellular permeability, smaller TJs and defects in the adhesion of endothelial cells to the-basement membrane (Schubert et al., 2002). Knocking down caveolin-1 expression in brain endothelial cells resulted in a decrease in occludin and ZO-1 expression in western blots (Song et al., 2007). However, the effect of caveolin-1 on TJ protein expression is contradictory, since an increase in

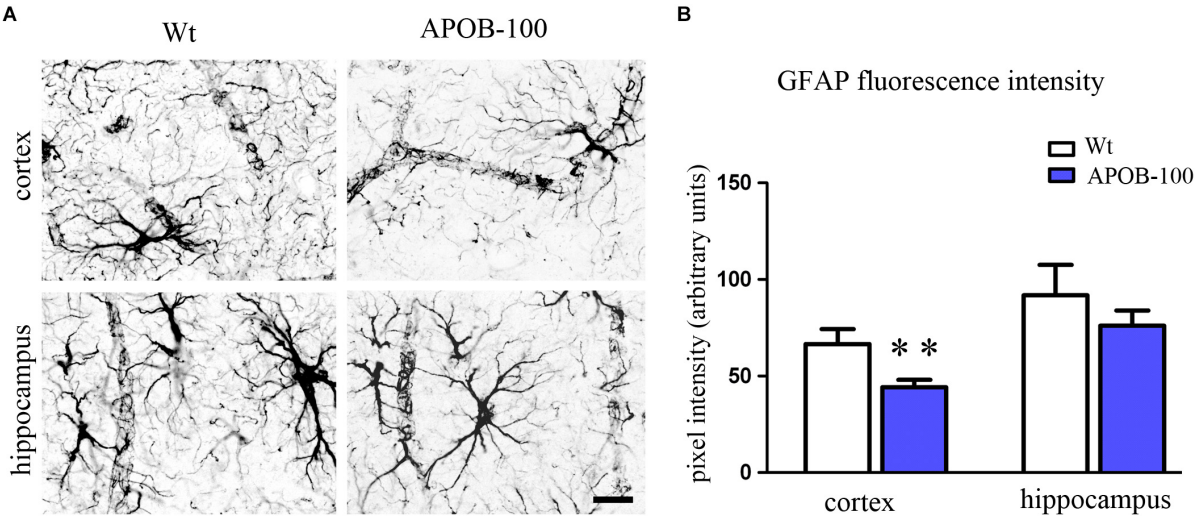

FIGURE 7 | Gfap immunostaining pattern in the cortex and hippocampus of wild-type (Wt) and APOB-100 transgenic mice (APOB-100) **(A).** Scale bar: 25 μm. Quantification of fluorescence intensity of Gfap immunolabeling in the frontal cortex and hippocampus of Wt and APOB-100 transgenic mice **(B)**. $^{**}P < 0.01$ compared with Wt mice.

caveolin-1 expression was also linked to a decrease in occludin and or claudin-5 protein expression related to BBB damage (Nag et al., 2007; Beauchesne et al., 2010). In our study a decrease was observed in both caveolin-1 and occludin gene expression using QPCR, which is in concordance with the western blot findings reported by Song et al. (2007).

The increase in BBB permeability in our model may be linked to reduced expression of genes coding important brain endothelial TJ proteins *Cldn-5, Ocln, Tjp-1*. However, the differences detected at mRNA level were not reflected by the immunofluorescent staining pattern of TJ proteins claudin-5 and occludin, suggesting no detectable changes of TJs between the experimental groups at light microscopic level. In contrast, regarding the ultrastructure, a great percentage of discontinuous TJs were observed in TEM images of transgenic brains. Data obtained by PCR and immunohistochemistry do not necessarily show direct positive correlation due to the complex regulation of the gene expression at transcriptional, posttranscriptional, and posttranslational levels resulting in divergences (Vogel and Marcotte, 2012). In addition, during tissue fixation some epitopes may suffer alterations resulting in changes in specific antibody binding. Consequently, both these possibilities may explain the differences between PCR data and the analysis of immunofluorescent TJ signals.

Our findings on functional and gene expressional alterations at the BBB in APOB-100 mice are in agreement with the neurovascular concept of AD. Barrier dysfunction in brain microvessels is well described in AD (Zipser et al., 2007; Nelson et al., 2016), and BBB breakdown was found in the hippocampus in aging human brain which may contribute to cognitive impairment (Montagne et al., 2015).

Due to the observed similarities in gene expression changes present in both AD pathology and in APOB-100 transgenic mice, we examined whether neuroinflammation and neuronal changes were also characteristic features of our model. An increase in the gene expression of *Tnfα*, *NF-κB* and *Aif-1*/*Iba-1* detected in the brain of APOB-100 transgenic mice suggested inflammation related changes. Among the other inflammatory markers examined, *Tlr4*, which is reported to participate in innate neuroprotective mechanisms (Conte et al., 2017), decreased to 60% in the cortex of APOB-100 transgenic mice. It may indicate a disturbance in neuroprotection. Furthermore, a significant decrease in *Cdh2* expression coding *N*-cadherin was observed in the hippocampus of APOB-100 transgenic animals. *N*-cadherin, as an adhesion molecule, plays an important role in connecting pericytes to endothelial cells, thus maintaining normal BBB integrity (Winkler et al., 2011). Consequently, a loss in *N*-cadherin might lead to the structural and functional disintegration of the BBB.

The miRNA analysis revealed 10 miRNAs showing altered expression in APOB-100 transgenic cortex compared with wild-type ones. Out of these miRNAs mmu-miR-1a, mmu-miR-222, mmu-miR-26a, mmu-miR-7b are correlated with validated target genes. Among the target genes only *Bdnf* can be related to neuronal changes. It is regulated by several miRNAs (Varendi et al., 2014), among others mir-1, miRNA-26a and 26b suppress endogenous BDNF protein levels (Caputo et al., 2011; Varendi et al., 2014) In our study, we measured elevated *Bdnf* mRNA level, while the expression level of two posttranscriptional regulator miRNAs was changed in the opposite direction, miR-1a was downregulated and inversely, miR-26b was upregulated. The reduced expression of miR-1a and the increased expression of miR-26a is in accordance with findings related to high cholesterol levels and AD, respectively. High-cholesterol diet induced a significant decrease of miR-1 expression in ApoE deficient mice (Wang et al., 2013). Blocking miR-1 with antagomir enhanced endothelial permeability, while miR-1 mimics attenuated endothelial barrier dysfunction, strongly

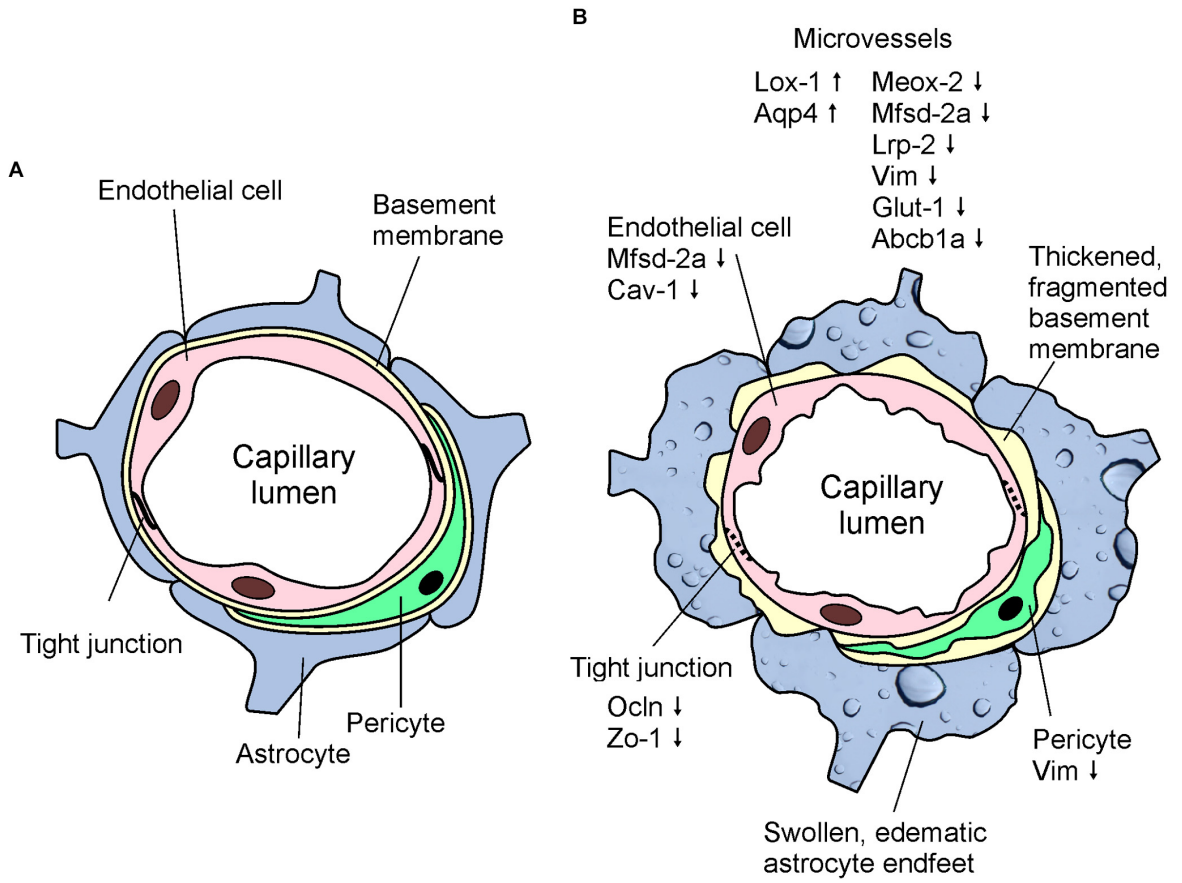

FIGURE 8 | Schematic drawings showing the basic structure of the BBB **(A)** and highlighting the most characteristic morphological and gene expression changes detected in cerebral microvessels of APOB-100 transgenic mice **(B)**.

indicating that miR-1 contributes to the regulation of endothelial barrier function (Wang et al., 2013). Similarly to our result, miR-26a was shown to be upregulated in AD brains (Cogswell et al., 2008) indicating that miR-26a might serve as a therapeutic target for patients with AD (Li and Sun, 2011).

In addition to brain capillary endothelial cells and neurons, alterations in other structural components of the NVU, such as astrocyte endfeet and pericytes may also contribute to BBB dysfunction. Astrocytes participate in the development and maintenance of BBB features, including tightening of TJs, inducing the expression of influx and efflux transporters, as well as specialized enzyme systems (Deli et al., 2005; Abbott et al., 2006; Deracinois et al., 2013). The expression level of Gfap, an astroglia marker, is critical in maintaining BBB integrity. Either an increase or a decrease in Gfap expression results in TJ protein expressional changes and BBB dysfunction (Willis, 2012). The fluorescence intensity of Gfap immunolabeling was significantly decreased in the cortex of APOB-100 transgenic mice compared to their wild-type littermates, which may contribute to the observed decrease in the expression of various TJ protein coding genes. It also may be in line with ultrastructural changes of astrocytes, characterized by edematic swellings around capillaries in the brain of APOB-100 transgenic mice. In a recent study (Ito et al., 2017), an increased sodium fluorescein permeability was reported following electroconvulsive stimulations. Regarding brain capillary ultrastructure, intact TJs were detected in this model of epilepsy, while astrocytic endfeet were swollen. In another paper (Haley and Lawrence, 2017) increased BBB permeability and astrocytic endfeet swelling occurred after cerebral ischaemia, but TJs remained intact and TJ proteins claudin-5 and occludin expression showed no change in western blots. Our study is in concordance with these data on both astroglia morphology and TJ protein expression. The abnormalities in astrocytic endfeet may be linked to the increased expression of *Aqp4* in brain microvessels isolated from APOB-100 transgenic animals. The loss of polarized expression of AQP4 in astrocyte foot processes has an important impact on development of BBB dysfunction and perivascular edema, and also disturbed homeostasis in the brain parenchyma in various pathologies (Wolburg et al., 2009).

S100b, another predominantly glial protein may also indicate BBB disruption. S100B is considered a plasma biomarker in traumatic brain injury (Halstrom et al., 2017), and cerebral small vessel disease, in which it is associated with cognitive impairment in patients (Gao et al., 2015). S100B is also linked to pathological changes observed in early AD (Mattsson et al., 2014).

In our model, no significant difference was found in *S100b* gene expression in the transgenic microvessels. In contrast, the gene expression of vimentin, another intermediate filament protein, dropped to less than 50% in the microvessel fraction of APOB-100 transgenic mice. The decrease in vimentin expression was observed at protein level too, based on immunohistochemical findings. Vimentin is expressed by endothelial cells, fibroblasts and α-smooth muscle actin producing cells in the middle cerebral artery of hyperlipidemic rabbits (Kacem et al., 2006). In an attempt to identify which cell type of the NVU is producing vimentin in our experimental animals, double immunolabeling studies were performed. Vimentin did not colocalize either with Gfap or Pdgfrβ, but a drop of vimentin mRNA expression was only observed in cultured pericytes from transgenic mice. Although cultures do not fully reflect the *in vivo* situation, the immunohistochemistry data together with the vimentin QPCR results on microvessels and cultured cells point to the possibility, that the change in the vimentin staining in brain microvessels of APOB-100 transgenic mice is related to pericytes. The reduction in vimentin immunostaining in the cortical microvessels of APOB-100 transgenic mice reflects that vimentin expression may react very sensitively to hypertriglyceridemic conditions.

Pericytes are embedded between endothelial cells and astrocyte endfeet in brain capillaries and they are crucial components of the NVU. They induce the expression of BBB-specific genes in cerebral endothelial cells and the polarization of glial endfeet which cover brain microvessels (Armulik et al., 2010). Pericyte deficiency leads to accelerated amyloid angiopathy and cerebral β-amyloidosis in a mouse AD model (Sagare et al., 2013). In our TEM analysis we detected an increase in the ratio of capillaries displaying no pericyte branches in the frontal cortex of APOB-100 transgenic mice compared with wild-type animals. It may suggest a decrease in pericyte number, which is in accordance with earlier findings demonstrating a reduction in the number of pericytes during neurodegeneration (Sagare et al., 2013).

CONCLUSION

In conclusion, we demonstrated here, that APOB-100 transgenic mice are characterized by elevated serum triglyceride levels and show functional, morphological, and gene expression alterations suggesting BBB dysfunction (**Figure 8**). Based on our findings we propose APOB-100 transgenic mice as a novel mouse model of vascular neurodegeneration. This model might provide researchers a useful tool to gain deeper insights into the pathomechanism of neurodegenerative diseases of vascular origin, which is fundamental for the development of efficient therapies.

AUTHOR CONTRIBUTIONS

MD, ZH, MT, and MS contributed to the conception and design of the study. DN, NL, and MT performed the BBB penetration study. ÁK, ZH, MT, and MD conducted the ultrastructural studies. ZH, MT, BD, FW, SV, JV, and BB performed the immunohistochemistry. MT, NL, DN, BD, and AZ investigated the QPCR analysis. AZ investigated and LP supervised the miRNA analysis. ZH, AH, GS, AK, BB, AZ, BD, AC, and MT performed the software analysis. MD, LP, LV, BP, and MS supervised the work. MD, LV, BP, and MS were the grant holders. MD, ZH, MT, and MS wrote the manuscript draft. LV, LP, and BP reviewed the manuscript. All authors approved the final manuscript.

FUNDING

This work was supported by funding from National Research, Development and Innovation Office, Hungary (GINOP 2.3.2.-15.2016-00060) and the Hungarian Basic Research Fund (OTKA NN111006).

ACKNOWLEDGMENTS

We thank I. Kis-Sebestyén for her technical assistance, M. Tóth for artwork preparation, T. Márkus-Vadóc and Dr. Marcus Mark Philip for reviewing the manuscript.

SUPPLEMENTARY MATERIAL

The Supplementary Material for this article can be found online at: https://www.frontiersin.org/articles/10.3389/fncel.2018.00380/full#supplementary-material

REFERENCES

Abbott, N. J., Rönnbäck, L., and Hansson, E. (2006). Astrocyte-endothelial interactions at the blood-brain barrier. *Nat. Rev. Neurosci.* 7, 41–53. doi: 10.1038/nrn1824

Antonios, N., Angiolillo, D. J., and Silliman, S. (2008). Hypertriglyceridemia and ischemic stroke. *Eur. Neurol.* 60, 269–278. doi: 10.1159/000157880

Armulik, A., Genové, G., Mäe, M., Nisancioglu, M. H., Wallgard, E., Niaudet, C., et al. (2010). Pericytes regulate the blood-brain barrier. *Nature* 468, 557–561. doi: 10.1038/nature09522

Bandopadhyay, R., Orte, C., Lawrenson, J. G., Reid, A. R., De Silva, S., Allt, G., et al. (2001). Contractile proteins in pericytes at the blood-brain and blood-retinal barriers. *J. Neurocytol.* 30, 35–44. doi: 10.1023/A:1011965307612

Barry, S. O., Marcel, R. T., Nelson, G., Victor, B., Tadeusz, M., Thomas, F. L., et al. (1998). Reduced endothelial nitric oxide synthase expression and production in human atherosclerosis. *Circulation* 97, 2494–2498. doi: 10.1161/01.CIR.97.25.2494

Beauchesne, E., Desjardins, P., Butterworth, R. F., and Hazell, A. S. (2010). Up-regulation of caveolin-1 and blood-brain barrier breakdown are attenuated by N-acetylcysteine in thiamine deficiency. *Neurochem. Int.* 57, 830–837. doi: 10.1016/j.neuint.2010.08.022

Bereczki, E., Bernát, G., Csont, T., Ferdinandy, P., Scheich, H., Sántha, M., et al. (2008). Overexpression of human apolipoprotein B-100 induces severe neurodegeneration in transgenic mice. *J. Proteome Res.* 7, 2246–2252. doi: 10.1021/pr7006329

Betsholtz, C. (2015). Lipid transport and human brain development. *Nat. Genet.* 47, 699–701. doi: 10.1038/ng.3348

Bjelik, A., Bereczki, E., Gonda, S., Juhasz, A., Rimanoczy, A., Zana, M., et al. (2006). Human apoB overexpression and a high-cholesterol diet differently modify the brain APP metabolism in the transgenic mouse model of atherosclerosis. *Neurochem. Int.* 49, 393–400. doi: 10.1016/j.neuint.2006.01.026

Bowman, G. L., Kaye, J. A., and Quinn, J. F. (2012). Dyslipidemia and blood-brain barrier integrity in Alzheimer's disease. *Curr. Gerontol. Geriatr. Res.* 2012:184042. doi: 10.1155/2012/184042

Burgess, B. L., McIsaac, S. A., Naus, K. E., Chan, J. Y., Tansley, G. H. K., Yang, J., et al. (2006). Elevated plasma triglyceride levels precede amyloid deposition in Alzheimer's disease mouse models with abundant A beta in plasma. *Neurobiol. Dis.* 24, 114–127. doi: 10.1016/j.nbd.2006.06.007

Buttery, L. D., Chester, A. H., Springall, D. R., Borland, J. A., Michel, T., Yacoub, M. H., et al. (1996). Explanted vein grafts with an intact endothelium demonstrate reduced focal expression of endothelial nitric oxide synthase specific to atherosclerotic sites. *J. Pathol.* 179, 197–203. doi: 10.1002/(SICI)1096-9896(199606)179:2<197::AID-PATH587>3.0.CO;2-D

Callow, M. J., Stoltzfus, L. J., Lawn, R. M., and Rubin, E. M. (1994). Expression of human apolipoprotein-B and assembly of lipoprotein (A) in transgenic mice. *Proc. Natl. Acad. Sci. U.S.A.* 91, 2130–2134. doi: 10.1073/pnas.91.6.2130

Caputo, V., Sinibaldi, L., Fiorentino, A., Parisi, C., Catalanotto, C., Pasini, A., et al. (2011). Brain derived neurotrophic factor (BDNF) expression is regulated by microRNAs miR-26a and miR-26b allele-specific binding. *PLoS One* 6:e28656. doi: 10.1371/journal.pone.0028656

Caramelli, P., Nitrini, R., Maranhao, R., Lourenco, A. C., Damasceno, M. C., Vinagre, C., et al. (1999). Increased apolipoprotein B serum concentration in Alzheimer's disease. *Acta Neurol. Scand.* 100, 61–63. doi: 10.1111/j.1600-0404.1999.tb00724.x

Chen, M., Masaki, T., and Sawamura, T. (2002). LOX-1, the receptor for oxidized low-density lipoprotein identified from endothelial cells: implications in endothelial dysfunction and atherosclerosis. *Pharmacol. Ther.* 95, 89–100. doi: 10.1016/S0163-7258(02)00236-X

Cirrito, J. R., Deane, R., Fagan, A. M., Spinner, M. L., Parsadanian, M., Finn, M. B., et al. (2005). P-glycoprotein deficiency at the blood-brain barrier increases amyloid-beta deposition in an Alzheimer disease mouse model. *J. Clin. Invest.* 115, 3285–3290. doi: 10.1172/JCI25247

Cogswell, J. P., Ward, J., Taylor, I. A., Waters, M., Shi, Y., Cannon, B., et al. (2008). Identification of miRNA changes in Alzheimer's disease brain and CSF yields putative biomarkers and insights into disease pathways. *J. Alzheimers Dis.* 14, 27–41. doi: 10.3233/JAD-2008-14103

Conte, C., Roscini, L., Sardella, R., Mariucci, G., Scorzoni, S., Beccari, T., et al. (2017). Toll like receptor 4 affects the cerebral biochemical changes induced by mptp treatment. *Neurochem. Res.* 42, 493–500. doi: 10.1007/s11064-016-2095-6

Croop, J. M., Raymond, M., Haber, D., Devault, A., Arceci, R. J., Gros, P., et al. (1989). The three mouse multidrug resistance (mdr) genes are expressed in a tissue-specific manner in normal mouse tissues. *Mol. Cell. Biol.* 9, 1346–1350. doi: 10.1128/MCB.9.3.1346

Csont, T., Bereczki, E., Bencsik, P., Fodor, G., Görbe, A., Zvara, A., et al. (2007). Hypercholesterolemia increases myocardial oxidative and nitrosative stress thereby leading to cardiac dysfunction in APOB-100 transgenic mice. *Cardiovasc. Res.* 76, 100–109. doi: 10.1016/j.cardiores.2007.06.006

Daneman, R., Zhou, L., Agalliu, D., Cahoy, J. D., Kaushal, A., and Barres, B. A. (2010). The mouse blood-brain barrier transcriptome: a new resource for understanding the development and function of brain endothelial cells. *PLoS One* 5:e13741. doi: 10.1371/journal.pone.0013741

De La Torre, J. C., Fortin, T., Park, G. A. S., Butler, K. S., Kozlowski, B. A., Pappas, B. A., et al. (1992). Chronic cerebrovascular insufficiency induces dementia-like deficits in aged rats. *Brain Res.* 582, 186–195. doi: 10.1016/0006-8993(92)90132-S

De la Torre, J. C., and Mussivand, T. (1993). Can disturbed brain microcirculation cause Alzheimer's disease? *Neurol. Res.* 15, 146–153.

Deane, R., Du Yan, S., Submamaryan, R. K., LaRue, B., Jovanovic, S., Hogg, E., et al. (2003). RAGE mediates amyloid-beta peptide transport across the blood-brain barrier and accumulation in brain. *Nat. Med.* 9, 907–113. doi: 10.1038/nm890

Deli, M. A., Abrahám, C. S., Kataoka, Y., and Niwa, M. (2005). Permeability studies on *in vitro* blood-brain barrier models: physiology, pathology, and pharmacology. *Cell. Mol. Neurobiol.* 25, 59–127. doi: 10.1007/s10571-004-1377-8

Deracinois, B., Pottiez, G., Chafey, P., Teerlink, T., Camoin, L., Davids, M., et al. (2013). Glial-cell-mediated re-induction of the blood-brain barrier phenotype in brain capillary endothelial cells: a differential gel electrophoresis study. *Proteomics* 13, 1185–1199. doi: 10.1002/pmic.201200166

Di Marco, L. Y., Venneri, A., Farkas, E., Evans, P. C., Marzo, A., and Frangi, A. F. (2015). Vascular dysfunction in the pathogenesis of Alzheimer's disease-A review of endothelium-mediated mechanisms and ensuing vicious circles. *Neurobiol. Dis. Rev.* 82, 593–606. doi: 10.1016/j.nbd.2015.08.01

Ehehalt, R., Keller, P., Haass, C., Thiele, C., and Simons, K. (2003). Amyloidogenic processing of the Alzheimer beta-amyloid precursor protein depends on lipid rafts. *J. Cell. Biol.* 160, 113–123. doi: 10.1083/jcb.200207113

Eiselein, L., Wilson, D. W., Lamé, M. W., and Rutledge, J. C. (2007). Lipolysis products from triglyceride-rich lipoproteins increase endothelial permeability, perturb zonula occludens-1 and F-actin, and induce apoptosis. *Am. J. Physiol. Heart Circ. Physiol.* 292, H2745–H2753. doi: 10.1152/ajpheart.00686.2006

Farkas, A. S., Acsai, K., Nagy, N., Tóth, A., Fülöp, F., Seprényi, G., et al. (2008). Na(+)/Ca(2+) exchanger inhibition exerts a positive inotropic effect in the rat heart, but fails to influence the contractility of the rabbit heart. *Br. J. Pharmacol.* 154, 93–104. doi: 10.1038/bjp.2008.83

Gao, Q., Fan, Y., Mu, L. Y., Ma, L., Song, Z. Q., and Zhang, Y. N. (2015). S100B and ADMA in cerebral small vessel disease and cognitive dysfunction. *J. Neurol. Sci.* 354, 27–32. doi: 10.1016/j.jns.2015.04.031

Gosselet, F., Saint-Pol, J., Candela, P., and Fenart, L. (2013). Amyloid-β peptides, Alzheimer's disease and the blood-brain barrier. *Curr. Alzheimer Res.* 10, 1015–1033. doi: 10.2174/15672050113106660174

Gundersen, H. J., and Osterby, R. (1981). Optimizing sampling efficiency of stereological studies in biology: or 'do more less well!'. *J. Microsc.* 121, 65–73. doi: 10.1111/j.1365-2818.1981.tb01199.x

Haley, M. J., and Lawrence, C. B. (2017). The blood-brain barrier after stroke: structural studies and the role of transcytotic vesicles. *J. Cereb. Blood Flow Metab.* 37, 456–470. doi: 10.1177/0271678X16629976

Halstrom, A., MacDonald, E., Neil, C., Arendts, G., Fatovich, D., and Fitzgerald, M. (2017). Elevation of oxidative stress indicators in a pilot study of plasma following traumatic brain injury. *J. Clin. Neurosci.* 35, 104–108. doi: 10.1016/j.jocn.2016.09.006

Ito, M., Bolati, K., Kinjo, T., Ichimura, K., Furuta, A., McLoughlin, D. M., et al. (2017). Electroconvulsive stimulation transiently enhances the permeability of the rat blood-brain barrier and induces astrocytic changes. *Brain Res. Bull.* 128, 92–97. doi: 10.1016/j.brainresbull.2016.11.011

Kacem, K., Sercombe, C., Hammami, M., Vicaut, E., and Sercombe, R. (2006). Sympathectomy causes aggravated lesions and dedifferentiation in large rabbit atherosclerotic arteries without involving nitric oxide. *J. Vasc. Res.* 43, 289–305. doi: 10.1159/000093010

Kapasi, A., and Schneider, J. A. (2016). Vascular contributions to cognitive impairment, clinical Alzheimer's disease, and dementia in older persons. *Biochim. Biophys. Acta* 1862, 878–886. doi: 10.1016/j.bbadis.2015.12.023

Kisler, K., Nelson, A. R., Rege, S. V., Ramanathan, A., Wang, Y., and Ahuja, A. (2017). Pericyte degeneration leads to neurovascular uncoupling and limits oxygen supply to brain. *Nat. Neurosci.* 20, 406–416. doi: 10.1038/nn.4489

Klafke, J. Z., Porto, F. G., Batista, R., Bochi, G. V., Moresco, R. N., da Luz, P. L., et al. (2015). Association between hypertriglyceridemia and protein oxidation and proinflammatory markers in normocholesterolemic and hypercholesterolemic individuals. *Clin. Chim. Acta* 448, 50–57. doi: 10.1016/j.cca.2015.06.013

Kuo, Y. M., Emmerling, M. R., Bisgaier, C. L., Essenburg, A. D., Lampert, H. C., Drumm, D., et al. (1998). Elevated low-density lipoprotein in Alzheimer's disease correlates with brain A beta 1-42 levels. *Biochem. Biophys. Res. Commun.* 252, 711–715. doi: 10.1006/bbrc.1998.9652

Lane-Donovan, C., Wong, W. M., Durakoglugil, M. S., Wasser, C. R., Jiang, S., Xian, X., et al. (2016). Genetic restoration of plasma ApoE improves cognition and partially restores synaptic defects in ApoE-deficient mice. *J. Neurosci.* 36, 10141–10150. doi: 10.1523/JNEUROSCI.1054-16.2016

Lee, L. L., Aung, H. H., Wilson, D. W., Anderson, S. E., Rutledge, J. C., and Rutkowsky, J. M. (2017). Triglyceride-rich lipoprotein lipolysis products increase blood-brain barrier transfer coefficient and induce astrocyte lipid

droplets and cell stress. *Am. J. Physiol. Cell Physiol.* 312, C500–C516. doi: 10.1152/ajpcell.00120.2016

Lénárt, N., Szegedi, V., Juhász, G., Kasztner, A., Horváth, J., Bereczki, E., et al. (2012). Increased tau phosphorylation and impaired presynaptic function in hypertriglyceridemic ApoB-100 transgenic mice. *PLoS One* 7:e46007. doi: 10.1371/journal.pone.0046007

Lénárt, N., Walter, F. R., Bocsik, A., Sántha, P., Tóth, M. E., Harazin, A., et al. (2015). Cultured cells of the blood-brain barrier from apolipoprotein B-100 transgenic mice: effects of oxidized low-density lipoprotein treatment. *Fluids Barriers CNS.* 12:17. doi: 10.1186/s12987-015-0013-y

Li, B., and Sun, H. (2011). MiR-26a promotes neurite outgrowth by repressing PTEN expression. *Physiol. Genomics* 43, 521–528. doi: 10.3892/mmr.2013.1534

Li, L., Cao, D., Garber, D. W., Kim, H., and Fukuchi, K. (2003). Association of aortic atherosclerosis with cerebral beta-amyloidosis and learning deficits in a mouse model of Alzheimer's disease. *Am. J. Pathol.* 163, 2155–2164. doi: 10.1016/S0002-9440(10)63572-9

Löffler, T., Flunkert, S., Havas, D., Sántha, M., Hutter-Paier, B., Steyrer, E., et al. (2013). Impact of APOB-100 expression on cognition and brain pathology in wild-type and hAPPsl mice. *Neurobiol. Aging* 34, 2379–2388. doi: 10.1016/j.neurobiolaging.2013.04.008

Lubrano, V., and Balzan, S. (2016). Roles of LOX-1 in microvascular dysfunction. *Microvasc. Res.* 105, 132–140. doi: 10.1016/j.mvr.2016.02.006

Lutjohann, D., Papassotiropoulos, A., Bjorkhem, I., Locatelli, S., Bagli, M., Oehring, R. D., et al. (2000). Plasma 24S-hydroxycholesterol (cerebrosterol) is increased in Alzheimer and vascular demented patients. *J. Lipid Res.* 41, 195–198.

Lyros, E., Bakogiannis, C., Liu, Y., and Fassbender, K. (2014). Molecular links between endothelial dysfunction and neurodegeneration in Alzheimer's disease. *Curr. Alzheimers. Res.* 11, 18–26. doi: 10.2174/1567205010666131119235254

Marques, F., Sousa, J. C., Sousa, N., and Palha, J. A. (2013). Blood-brain-barriers in aging and in Alzheimer's disease. *Mol. Neurodegener.* 8:38. doi: 10.1186/1750-1326-8-38

Mattsson, N., Insel, P., Nosheny, R., Trojanowski, J. Q., Shaw, L. M., Jack, C. R. Jr., et al. (2014). Effects of cerebrospinal fluid proteins on brain atrophy rates in cognitively healthy older adults. *Neurobiol. Aging* 35, 614–622. doi: 10.1016/j.neurobiolaging.2013.08.027

Mayhew, T. M. (1991). The new stereological methods for interpreting functional morphology from slices of cells and organs. *Exp. Physiol.* 76, 639–665. doi: 10.1113/expphysiol.1991.sp003533

Montagne, A., Barnes, S. R., Sweeney, M. D., Halliday, M. R., Sagare, A. P., Zhao, Z., et al. (2015). Blood-brain barrier breakdown in the aging human hippocampus. *Neuron* 85, 296–302. doi: 10.1016/j.neuron.2014.12.032

Nag, S., Venugopalan, R., and Stewart, D. J. (2007). Increased caveolin-1 expression precedes decreased expression of occludin and claudin-5 during blood-brain barrier breakdown. *Acta Neuropathol.* 114, 459–469. doi: 10.1007/s00401-007-0274-x

Nelson, A. R., Sweeney, M. D., Sagare, A. P., and Zlokovic, B. V. (2016). Neurovascular dysfunction and neurodegeneration in dementia and Alzheimer's disease. *Biochim. Biophys. Acta* 1862, 887–900. doi: 10.1016/j.bbadis.2015.12.016

Nicolakakis, N., and Hamel, E. (2011). Neurovascular function in Alzheimer's disease patients and experimental models. *J. Cereb. Blood Flow Metab.* 31, 1354–1370. doi: 10.1038/jcbfm.2011.43

Patterson, C. E., Rhoades, R. A., and Garcia, J. G. (1992). Evans blue dye as a marker of albumin clearance in cultured endothelial monolayer and isolated lung. *J. Appl. Physiol.* 72, 865–873. doi: 10.1152/jappl.1992.72.3.865

Pekny, M., Wilhelmsson, U., Bogestål, Y. R., and Pekna, M. (2007). The role of astrocytes and complement system in neural plasticity. *Int. Rev. Neurobiol.* 82, 95–111. doi: 10.1016/S0074-7742(07)82005-8

Puglielli, L., Tanzi, R. E., and Kovacs, D. M. (2003). Alzheimer's disease: the cholesterol connection. *Nat. Neurosci.* 6, 345–351. doi: 10.1038/nn0403-345

Raffaitin, C. H., Gin, J. P., Empana, J. P., Helmer, C., Berr, C., Tzourio, C., et al. (2009). Metabolic syndromeand risk for incident Alzheimer's disease or vascular dementia: the Three-City study. *Diabetes Care* 32, 169–174. doi: 10.2337/dc08-0272

Sabbagh, M., Zahiri, H. R., Ceimo, J., Cooper, K., Gaul, W., Connor, D., et al. (2004). Is there a characteristic lipid profile in Alzheimer's disease? *J. Alzheimers Dis.* 6, 585–589. doi: 10.3233/JAD-2004-6602

Sagare, A. P., Bell, R. D., Zhao, Z., Ma, Q., Winkler, E. A., Ramanathan, A., et al. (2013). Pericyte loss influences Alzheimer-like neurodegeneration in mice. *Nat. Commun.* 4:2932. doi: 10.1038/ncomms3932

Schubert, W., Frank, P. G., Woodman, S. E., Hyogo, H., Cohen, D. E., Chow, C. W., et al. (2002). Microvascular hyperpermeability in caveolin-1 (-/-) knock-out mice. Treatment with a specific nitric-oxide synthase inhibitor, L-NAME, restores normal microvascular permeability in Cav-1 null mice. *J. Biol. Chem.* 277, 40091–40098. doi: 10.1074/jbc.M205948200

Shibata, M., Yamada, S., Kumar, S. R., Calero, M., Bading, J., Frangione, B., et al. (2000). Clearance of Alzheimer's amyloid-beta (1-40) peptide from brain by LDL receptor-related protein-1 at the blood-brain barrier. *J. Clin. Invest.* 106, 1489–1499. doi: 10.1172/JCI10498

Shoshani, T., Zhang, S., Dey, S., Pastan, I., and Gottesman, M. M. (1998). Analysis of random recombination between human MDR1 and mouse mdr1a cDNA in a pHaMDR-dihydrofolate reductase bicistronic expression system. *Mol. Pharmacol.* 54, 623–630.

Song, L., Ge, S., and Pachter, J. S. (2007). Caveolin-1 regulates expression of junction-associated proteins in brain microvascular endothelial cells. *Blood* 109, 1515–1523. doi: 10.1182/blood-2006-07-034009

Stancel, N., Chen, C. C., Ke, L. Y., Chu, C. S., Lu, J., Sawamura, T., et al. (2016). Interplay between CRP, atherogenic LDL, and LOX-1 and its potential role in the pathogenesis of atherosclerosis. *Clin. Chem.* 62, 320–327. doi: 10.1373/clinchem.2015.243923

Stapleton, P. A., Goodwill, A. G., James, M. E., Brock, R. W., and Frisbee, J. C. (2010). Hypercholesterolemia and microvascular dysfunction: interventional strategies. *J. Inflamm.* 7:54. doi: 10.1186/1476-9255-7-54

Süle, Z., Mracskó, E., Bereczki, E., Sántha, M., Csont, T., Ferdinandy, P., et al. (2009). Capillary injury in the ischemic brain of hyperlipidemic, apolipoprotein B-100 transgenic mice. *Life Sci.* 84, 935–939. doi: 10.1016/j.lfs.2009.04.011

Varendi, K., Kumar, A., Härma, M. A., and Andressoo, J. O. (2014). miR-1, miR-10b, miR-155, and miR-191 are novel regulators of BDNF. *Cell. Mol. Life Sci.* 71, 4443–4456. doi: 10.1007/s00018-014-1628-x

Veszelka, S., Pásztói, M., Farkas, A. E., Krizbai, I., Ngo, T. K., Niwa, M., et al. (2007). Pentosan polysulfate protects brain endothelial cells against bacterial lipopolysaccharide-induced damages. *Neurochem. Int.* 50, 219–228. doi: 10.1016/j.neuint.2006.08.006

Veszelka, S., Tóth, A., Walter, F. R., Tóth, A. E., Gróf, I., Mészáros, M., et al. (2018). Comparison of a rat primary cell-based blood-brain barrier model with epithelial and brain endothelial cell lines: gene expression and drug transport. *Front. Mol. Neurosci.* 11:166. doi: 10.3389/fnmol.2018.00166

Veszelka, S., Tóth, A. E., Walter, F. R., Datki, Z., Mózes, E., Fülöp, L., et al. (2013). Docosahexaenoic acid reduces amyloid-β induced toxicity in cells of the neurovascular unit. *J. Alzheimers Dis.* 34, 487–501. doi: 10.3233/JAD-120163

Veszelka, S., Urbányi, Z., Pázmány, T., Németh, L., Obál, I., Dung, N. T., et al. (2003). Human serum amyloid P component attenuates the bacterial lipopolysaccharide-induced increase in blood-brain barrier permeability in mice. *Neurosci. Lett.* 352, 57–60. doi: 10.1016/j.neulet.2003.08.028

Vogel, C., and Marcotte, E. M. (2012). Insights into the regulation of protein abundance from proteomic and transcriptomic analyses. *Nat. Rev. Genet.* 13, 227–232. doi: 10.1038/nrg3185

Wang, H., Zhu, H. Q., Wang, F., Zhou, Q., Gui, S. Y., and Wang, Y. (2013). MicroRNA-1 prevents high-fat diet-induced endothelial permeability in apoE knock-out mice. *Mol. Cell. Biochem.* 378, 153–159. doi: 10.1007/s11010-013-1606-x

Willis, C. L. (2012). Imaging *in vivo* astrocyte/endothelial cell interactions at the blood-brain barrier. *Methods Mol. Biol.* 814, 515–529. doi: 10.1007/978-1-61779-452-0_34

Winkler, E. A., Bell, R. D., and Zlokovic, B. V. (2011). Central nervous system pericytes in health and disease. *Nat. Neurosci.* 14, 1398–1405. doi: 10.1038/nn.2946

Winkler, E. A., Nishida, Y., Sagare, A. P., Rege, S. V., Bell, R. D., Perlmutter, D., et al. (2015). GLUT1 reductions exacerbate Alzheimer's disease vasculo-neuronal dysfunction and degeneration. *Nat. Neurosci.* 18, 521–530. doi: 10.1038/nn

Wolburg, H., Noell, S., Wolburg-Buchholz, K., Mack, A., and Fallier-Becker, P. (2009). Agrin, aquaporin-4, and astrocyte polarity as an important feature of the blood-brain barrier. *Neuroscientist* 15, 180–193. doi: 10.1177/1073858408329509

Won, D., Zhu, S. N., Chen, M., Teichert, A. M., Fish, J. E., Matouk, C. C., et al. (2007). Relative reduction of endothelial nitric-oxide synthase expression and transcription in atherosclerosis-prone regions of the mouse aorta and in an *in vitro* model of disturbed flow. *Am. J. Pathol.* 171, 1691–1704. doi: 10.2353/ajpath.2007.060860

Wu, Z., Guo, H., Chow, N., Sallstrom, J., Bell, R. D., Deane, R., et al. (2005). Role of the MEOX2 homeobox gene in neurovascular dysfunction in Alzheimer disease. *Nat. Med.* 11, 959–965. doi: 10.1038/nm1287

Zhao, Z., Nelson, A. R., Betsholtz, C., and Zlokovic, B. V. (2015). Establishment and dysfunction of the blood-brain barrier. *Cell* 163, 1064–1078. doi: 10.1016/j.cell.2015.10.06

Zhao, Z., and Zlokovic, B. V. (2014). Blood-brain barrier: a dual life of MFSD2A? *Neuron* 82, 728–730. doi: 10.1016/j.neuron.2014.05.012

Zipser, B. D., Johanson, C. E., Gonzalez, L., Berzin, T. M., Tavares, R., Hulette, C. M., et al. (2007). Microvascular injury and blood-brain barrier leakage in Alzheimer's disease. *Neurobiol. Aging* 28, 977–986. doi: 10.1016/j.neurobiolaging.2006.05.016

Zlokovic, B. V. (2008). The blood-brain barrier in health and chronic neurodegenerative disorders. *Neuron* 57, 178–201. doi: 10.1016/j.neuron.2008.01.003

Zlokovic, B. V. (2011). Neurovascular pathways to neurodegeneration in Alzheimer's disease and other disorders. *Nat. Rev. Neurosci.* 3, 723–738. doi: 10.1038/nrn3114

Conflict of Interest Statement: The authors declare that the research was conducted in the absence of any commercial or financial relationships that could be construed as a potential conflict of interest.

frontiers in Cellular Neuroscience

ORIGINAL RESEARCH
published: 13 November 2018
doi: 10.3389/fncel.2018.00416

The Effect of Myosin Light Chain Kinase on the Occurrence and Development of Intracranial Aneurysm

Yaying Song[1†], Peixi Liu[2†], Zongwei Li[3], Yuan Shi[2], Jun Huang[4], Sichen Li[2], Yingjun Liu[2], Zhijun Zhang[3], Yongting Wang[3], Wei Zhu[2] and Guo-Yuan Yang[1,3]**

[1] Department of Neurology, Ruijin Hospital, Shanghai Jiao Tong University School of Medicine, Shanghai, China, [2] Department of Neurosurgery, Huashan Hospital of Fudan University, Shanghai, China, [3] Neuroscience and Neuroengineering Research Center, School of Biomedical Engineering, Med-X Research Institute, Shanghai Jiao Tong University, Shanghai, China, [4] Shanghai Key Laboratory of Hypertension, Department of Hypertension, Shanghai Institute of Hypertension, Ruijin Hospital, Shanghai Jiao Tong University School of Medicine, Shanghai, China

Myosin light chain kinase is a key enzyme in smooth muscle cell contraction. However, whether myosin light chain kinase plays a role in the occurrence or development of intracranial aneurysms is not clear. The present study explored the function of myosin light chain kinase in human intracranial aneurysm tissues. Five aneurysm samples and five control samples were collected, and smooth muscle cells (SMCs) were dissociated and cultured. A label-free proteomic analysis was performed to screen the differentially expressed proteins between aneurysm and control samples. The expression and function of myosin light chain kinase in aneurysms were examined. We found that 180 proteins were differentially expressed between the aneurysm and control samples, among which 88 were increased and 92 (including myosin light chain kinase) were decreased in aneurysms compared to control tissues. In a model of the inflammatory environment, contractility was weakened and apoptosis was increased in aneurysm SMCs compared to human brain SMCs ($p < 0.05$). The knock down of myosin light chain kinase in human brain SMCs caused effects similar to those observed in aneurysm SMCs. These results indicated that myosin light chain kinase plays an important role in maintaining smooth muscle contractility, cell survival and inflammation tolerance.

Keywords: aneurysm, myosin light chain kinase, phenotype switch, proteomic, smooth muscle cell

OPEN ACCESS

Edited by:
Sriharsha Kantamneni, University of Bradford, United Kingdom

Reviewed by:
Senthilkumar Rajagopal, Rayalaseema University, India
Michael G. Blennerhassett, Queen's University, Canada

***Correspondence:**
Wei Zhu
drzhuwei@fudan.edu.cn
Guo-Yuan Yang
gyyang@sjtu.edu.cn

† These authors have contributed equally to this work

Received: *18 July 2018*
Accepted: *24 October 2018*
Published: *13 November 2018*

Citation:
Song Y, Liu P, Li Z, Shi Y, Huang J, Li S, Liu Y, Zhang Z, Wang Y, Zhu W and Yang G-Y (2018) The Effect of Myosin Light Chain Kinase on the Occurrence and Development of Intracranial Aneurysm. Front. Cell. Neurosci. 12:416. doi: 10.3389/fncel.2018.00416

INTRODUCTION

Intracranial aneurysm (IA), as a cerebrovascular disease, has an annual incidence of approximately 1–2% and is characterized by the ballooning of the intracerebral artery with high mortality due to vascular rupture (Rinkel, 2008; Brown and Broderick, 2014). Ongoing studies characterize the process of IA formation as hemodynamic stress, thrombus formation, extracellular matrix degradation, inflammatory responses and structural changes, including SMC phenotypic modulation and consequently apoptosis (Frosen et al., 2012; Frosen, 2014). The current treatment for IA mainly involves clipping for surgical intervention and endovascular coiling based on its

Abbreviations: HBVSMC, human brain vascular smooth muscle cell; IA, intracranial aneurysm; IASMCs, intracranial aneurysm smooth muscle cells; MLCK, myosin light chain kinase; SMA, anti-SM-α actin; SMCs, smooth muscle cells; STA, superficial temporal artery.

special characteristics. Experimental aneurysm studies have mainly focused on endothelial cells, such as the autologous endothelial cell-seed stent (Zhu et al., 2008) and enhanced aneurysm neck endothelialization by erythropoietin-induced endothelial progenitor cell stimulation (Liu et al., 2016). In addition, endothelial injury may result from the reaction and migration of SMCs to the tunica intima (Etminan and Rinkel, 2016). Evidence has also indicated that SMCs might be involved in neo-intima formation in a ligation model (Yuan et al., 2017). Moreover, the dysfunction of endothelial cells and the apoptosis or phenotypic modulation of SMCs could accelerate the progression of aneurysms.

The phenotypic modulation or dedifferentiation of SMCs could be caused by genetic defects or stimulated by stress, which are involved in many vascular diseases (Frosen, 2014; Liu et al., 2015). SMCs alter the synthetic phenotype in the medial layer, thereby weakening the vessel wall, disturbing hemostasis and finally collapsing the vascular structure. Previous studies using microarray (Yu et al., 2014), mRNA sequencing analysis (Kleinloog et al., 2016), and proteomics (Wang et al., 2016) have implicated a group of reported genes, mRNAs and related proteins involved in the proliferation, migration, and apoptosis of SMCs. Previous studies have demonstrated that the injury or death of SMCs by inflammation results in the occurrence and development of aneurysms. Furthermore, SMCs are the main components of the walls of brain vessels and aneurysms (Kondo et al., 1998; Owens, 2007). Because IASMCs were isolated from aneurysm walls, these cells have been considered as a cell model to understand the phenotype and function of SMCs in the formation, progress and rupture of aneurysms (Dai et al., 2006; Bygglin et al., 2011).

The aim of the present study was to explore the role of SMC phenotypic modulation in IA pathogenesis. We used proteomic analysis to explore the specific protein functions in IA pathology. IASMCs were isolated to further explain the results of clinical samples and investigate the role of aneurysm SMCs in IA progression.

MATERIALS AND METHODS

Ethics Statement

This study was approved by the Institutional Review Board (IRB) and the Ethics Committee of Huashan Hospital, Fudan University, China. Each participant provided written informed consent to participate in this study.

Tissue Collection and Label-Free Proteomic

Ten patients with IA who underwent microsurgical clipping were enrolled, and the samples were collected. The control group included patients who underwent STA surgery, followed by unavoidable clipping. Among the 10 samples, 5 were used for label-free proteomics, 2 were used for immunostaining, and 3 were used for western blotting. These 10 samples were frozen immediately at −80°C for further experiments. In addition to these 10 samples, another 4 samples were used for IASMC isolation, of which 3 samples were successful. These 10 samples were all frozen immediately at −80°C for further experiments. Label-free proteomics was commissioned by the Shanghai Branch of the Chinese Academy of Sciences.

IASMC Isolation and Culture

Intracranial aneurysm tissues were obtained from the brain tissues of 3 IA patients during microsurgery. The modified isolation protocol was based on a previously described study (Bygglin et al., 2011; Huang et al., 2017). After clipping, the samples were immediately collected into DMEM supplemented with 5% penicillin/streptomycin. The tissue segments were washed three times with phosphate-buffered saline (PBS) supplemented with 1% penicillin/streptomycin. The surrounding connective tissue was separated, and the endothelial cell layer was scratched gently. Then, the tissues were dissected into 1 mm × 1 mm fragments that were evenly arranged on a dish and incubated in a humidified atmosphere of 5% CO_2 and 95% air at 37°C in a medium comprising DMEM supplemented with 20% fetal bovine serum and 1% penicillin/streptomycin. After 1–2 weeks, the cells grown from the IA explants reached semiconfluence and were subcultured in smooth muscle cell medium (Lonza, Basel, Switzerland) after trypsinization. Control human brain vascular SMCs were obtained from ScienCell Research Laboratories (Carlsbad, CA, United States) and cultured in smooth muscle cell medium. We used the markers anti-myosin-11 and SMA to identify the SMCs.

Immunostaining of Human Tissue Samples

The samples were fixed in 4% paraformaldehyde and embedded in paraffin. Following antigen retrieval by microwaving in pH 6.0 citrate buffer, the sections were incubated with anti-myosin-11 (1:50 dilution; Santa Cruz Biotechnology, Santa Cruz, CA, United States), anti-MLCK (1:200 dilution; Abcam, Cambridge, MA, United States), and anti-SMA (1:100 dilution; Abcam), followed by an immunofluorescent secondary antibody. The brain sections were then stained with DAPI and mounted. Images were taken at different magnifications with a microscope (Leica, Solms, Germany).

MLCK siRNA Interference

Human brain vascular smooth muscle cells (HBVSMCs, Zhongqiao Xinzhou Company, Shanghai, China) were seeded onto six-well plates. Then, 100 nmol/L siRNA was diluted with 250 μl of Opti-MEM (Gibco, Carlsbad, CA, United States) and incubated for 5 min. Next, 10 μl of Lipofectamine® 2000 (Invitrogen, Carlsbad, CA, United States) was diluted with 250 μl of Opti-MEM and incubated for 5 min. The above samples were mixed, generating a final 500 μl Opti-MEM solution, and incubated for 20 min. This medium was added to 2 ml of SMCM (ScienCell, Carlsbad, CA, United States) and incubated with the cells for 6 h. After changing to normal medium, the cells were cultured for 72 h. The interference was detected by real-time PCR and Western blot analysis. The following siRNA sequences

were used: si-*mlck*: 5′-3′ CCTGCTTTCATTTTGCCCCC, TCACAAGGCTGAAAGTCCCC.

Cell Viability Assay

Smooth muscle cells were plated in triplicate in 96-well plates at 4×10^3 cells per well. After 24 h, the cells were treated with TNF-α at different doses, including 0, 0.5, 5, 10, 20, and 40 ng/ml for 2 h. The cck-8 assay kit was prepared according to the manufacturer's instructions and then 100 μl was added to each well and incubated for 2 h at 37°C. The absorbance was measured at 450 nm with a spectrometer.

RNA Extraction and Real-Time PCR

Total RNA was isolated from the cells using TRIzol reagent (Invitrogen) according to the manufacturer's instructions. The integrity of the RNA was quantified by using the NanoDrop 1000 spectrophotometer (Thermo Fisher Scientific, UT, United States). The reverse transcription reaction and real-time PCR were performed according to the manufacturer's instructions for the ABScript II cDNA Synthesis Kit (ABclonal, Wuhan, China) and the SYBR Premix ExTaq II Kit (Takara, Dalian, China) by a real-time PCR system (7900HT, ABI). No non-specific amplification was observed based on the dissociation curve. Glyceraldehyde 3-phosphate dehydrogenase (GAPDH) was used as an internal control. The data were analyzed using the comparison Ct ($2^{-\Delta\Delta C_t}$) method and expressed as a fold change relative to the respective control. The following sequences were used for qPCR primers: ACTA2: 5′-3′ TTGAGAAGAGTTACGAGTTG, AGG ACATTGTTAGCATAGAG; MYL9: 5′-3′ CGGGCCACATCCA ATGTCTT, CCATGTTTGAGGATGCGGGT; MLCK: 5′-3′ GGGGACTTTCAGCCTTGTGA, CTGCTTCGCAAAACTTCC TTCT; and CNN1 5′-3′ GGCCCAGAAGTATGACCACC, CCGTCCATGAAGTTGTTGCC.

Western Blotting Analysis

Equal amounts of protein per lane (30 μg) were subjected to electrophoresis on a 12% SDS-PAGE gel. The proteins were electrotransferred onto a polyvinylidene difluoride membrane (PVDF, Millipore, Billerica, MA, United States). The membrane was blocked with 5% non-fat dry milk/0.1% Tween-20 in Tris-buffered saline for 1 h at room temperature. Thereafter, the membrane was incubated with different primary antibodies, including rabbit anti-MLCK (1:5000 dilution, Abcam), rabbit anti-SMA (1:200 dilution, Abcam) and rabbit anti-cleaved caspase-3 (1:1000 dilution, Cell Signaling Technology). Subsequently, the membrane was treated with secondary antibody for 2 h at room temperature. Immunoblots were probed using enhanced ECL substrate (Thermo, Rockford, IL, United States). The chemiluminescence level was recorded using an imaging system (Bio-Rad, Hercules, CA, United States). The results were normalized to β-actin.

Calcium Fluo-4 AM Assay and Contraction Study

Smooth muscle cells were preloaded with the calcium-sensitive fluorophore Fluo-4 AM in extracellular solution for 40 min at room temperature as described in a previous study (Granata et al., 2017). Then, the cells were washed for 30 min at room temperature. Intracellular calcium flux was monitored as a time series, and the acquisition rates were 1 frame every 0.1 ms over 1 min using a Leica confocal microscope before and after the addition of pilocarpine. To detect intracellular calcium release, the SMCs were incubated with calcein. A concentration of 20 mM calcein was used for stimulation. Calcium flux was detected in HBVSMCs (Zhongqiao Xinzhou Company, Shanghai, China), si-*mlck*SMCs, and IASMCs before and after TNF-α stimulation. Five cells were randomly selected from a field of view, and the fluorescent trace was analyzed using ImageJ pro plus software (Media Cybernetics, Bethesda, MD, United States).

Statistical Analysis

All data were expressed as the means ± SE. ANOVA with Student–Newman–Keuls multiple comparisons posttest was used for gene expression. Comparisons between two groups were made by Student's *t*-test. A $p < 0.05$ was considered significantly different. Statistical analysis was carried out with Prism GraphPad 6. Each *in vitro* experimental group was repeated three times, and the experiments were performed separately three times. These outcomes are from data averaged statistically.

RESULTS

Sample Collection and Label-Free Proteomic Analysis

Intracranial aneurysm ($n = 5$) and STA ($n = 5$) groups without significant differences in sex, age, or risk factors were compared. More information is shown in **Supplementary Table 1**. The location of sample collection was shown by HE and Masson staining (**Figure 1A**). The aneurysm wall showed less muscle and collagen compared with the STA wall. Among all 1908 proteins identified from 15426 peptides, 180 significantly differentially expressed proteins between IA and STA were identified, among which 88 were upregulated and 92 were downregulated in IA (**Figure 1B**). GO ontology analysis classified the proteins into "Molecular function," "Cellular component," and "Biological process" subcategories. Further protein expression data were obtained from the KEGG Mapper Pathway to illustrate changes in biological processes (**Figure 1C**). MLCK encodes a regulatory light chain of myosin II, known as myosin light-chain kinase, which was downregulated in IAs. In the vascular smooth muscle contraction pathway, MLCK was involved in the mechanism of smooth muscle contraction (**Figure 1D**).

MLCK Is Downregulated in Both Tissue Samples and Primary IASMCs

Tissue samples from STA and IA were double stained for SMA and MLCK. MLCK showed higher expression in the IA group, and SMA showed weaker expression in the STA group compared with the IA group. Myosin-11 is a marker of mature SMCs, and co-staining with SMA showed a reduction in contractile

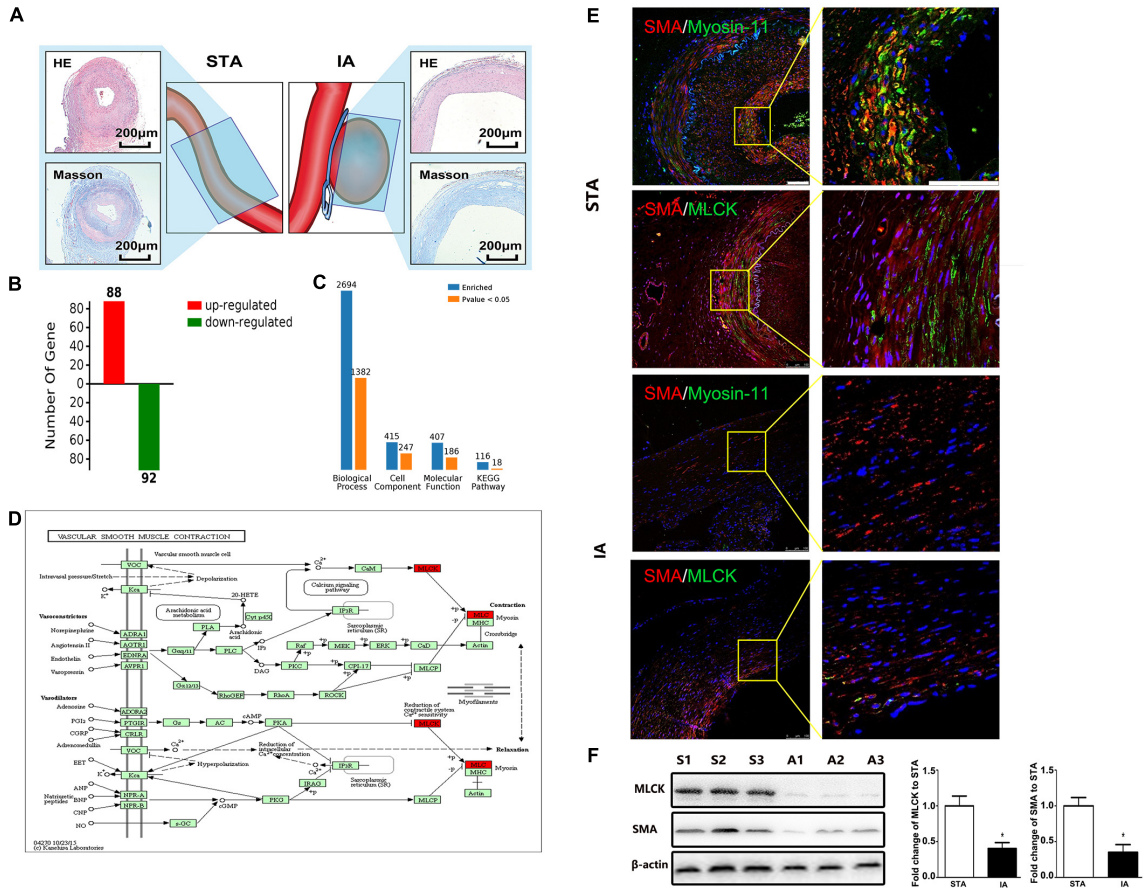

FIGURE 1 | Basic information from label-free proteomics and verification in tissue samples. **(A)** IA and STA illustration with HE and Masson staining show the specimen location for label-free proteomics. **(B)** Significant differences in protein levels between IA and STA. **(C)** GO ontology analysis between IA and STA. **(D)** KEGG pathway mapping of smooth muscle cells (SMCs). **(E)** Double staining for SMA/myosin-11 and SMA/MLCK in STA and IA, with 2× magnification for a closer view. **(F)** Western blot and quantification studies of MLCK and SMA in the tissue sample. S1–S3 represents proteins from three different STA samples, and A1–A3 represents IA samples. STA, superficial temporal artery; IA, intracranial aneurysm.

SMCs. Magnification also showed low SMA expression, which indicated the loss of SMCs in IA tissues. The SMC density showed a significant decrease in the IA sample, indicating that degeneration occurred in the aneurysm wall (**Figure 1E**). The IA samples showed a more significant downregulation of MLCK than STA, consistent with findings in proteomics. SMA was also downregulated, which suggested that functionally mature SMCs were lost in the aneurysm wall (**Figure 1F**). To examine whether the downregulation of MLCK in IA tissue has a similar effect in SMCs, we further isolated primary SMCs from IA walls (IASMCs). IASMCs were morphologically modulated and appeared as spider-like cells with the loss of mature SMC markers. These morphologic changes demonstrated that ductility decreased when stress suddenly increased. Cell viability was also weakened throughout the culture process. IASMCs appeared irregularly shaped and showed weak positivity for SMA, MLCK and myosin-11 compared with HBVSMCs. The results of immunostaining indicated that the IASMCs were in an immature state (**Figure 2**).

MLCK Downregulation in Primary IASMCs and Its Impact on SMC Function

To investigate the function of SMCs, we used siRNA to interfere with *mlck* in HBVSMCs to mimic the genetic defects in IASMCs. The level of *mlck* showed 50% interference, with no significant difference compared with IASMCs (**Figure 3A**). Western blot results showed that the expression of the mature SMC markers MLCK and SMA was decreased in both IASMCs and si-*mlck*SMCs compared with HBVSMCs. We then used cleaved caspase-3 to detect apoptosis. The results indicated that with the loss of mature SMC markers, SMCs probably progressed to apoptosis (**Figure 3B**).

We detected cell contractility in these three groups to further investigate the role of MLCK during SMC contraction. Pilocarpine is a cholinergic agent that can activate the cholinergic receptor. SMCs can respond to the stimulus and contract. When the SMCs were incubated with calcine, intracellular calcium release was detected. The influx of calcium is not the same as "contraction," but the cyclic calcium wave in response to

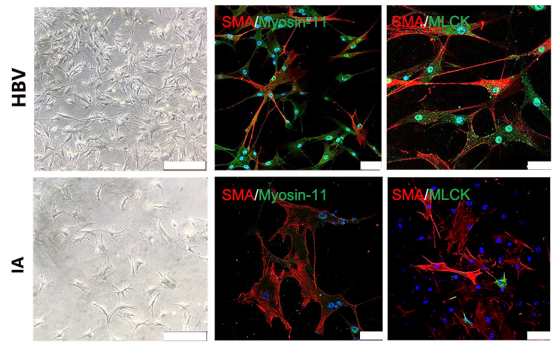

FIGURE 2 | Myosin light chain kinase primary SMCs. Bright field images show IASMCs with more irregular morphology than HBVSMCs. Double staining for SMA/myosin-11 and SMA/MLCK showed that IASMCs were less or weakly positive compared with HBVSMCs. Data are presented as the means ± SD, $*p < 0.05$, bar = 100 μm. HBVSMC, human brain vascular smooth muscle cell; IASMC, intracranial aneurysm smooth muscle cell.

an agonist may reflect cell contractility. SMCs with lower MLCK expression showed reduced contractility in response to stimulation with the cholinergic agent pilocarpine. The local cell morphology of these three groups was also different when simulated by pilocarpine. HBVSMCs showed a spindle shape, and cells with low expression of MLCK showed a more stellate pattern (**Figure 3C**). The intracellular calcium responses of HBVSMCs were different from those of both si-*mlck*SMCs and IASMCs. HBVSMCs generated cyclic calcium waves, whereas si-*mlck*SMCs and especially IASMCs did not generate propagating calcium waves and returned abruptly to basal levels (**Figure 3D**).

Genetic Loss of MLCK Impacts the Inflammatory Responses of SMCs

To mimic the IA environment, we administered TNF-α to explore the proliferation and contractility of SMCs. The mRNA levels of four mature SMC genes, *mlck*, *acta2*, *myl9*, and *cnn1*, were detected after treatment with different doses of TNF-α (**Figure 4A**). We found that mature SMC marker expression was reduced by stimulation with higher doses of TNF-α. The expression of mature SMC markers, such as ACTA2, MYL9, CNN1, and MLCK, was largely decreased after treatment with 40 ng/ml of TNF-α compared with that after treatment with other TNF-α concentrations in cultured SMCs. Therefore, we used a concentration of 40 ng/ml to treat HBVSMCs,

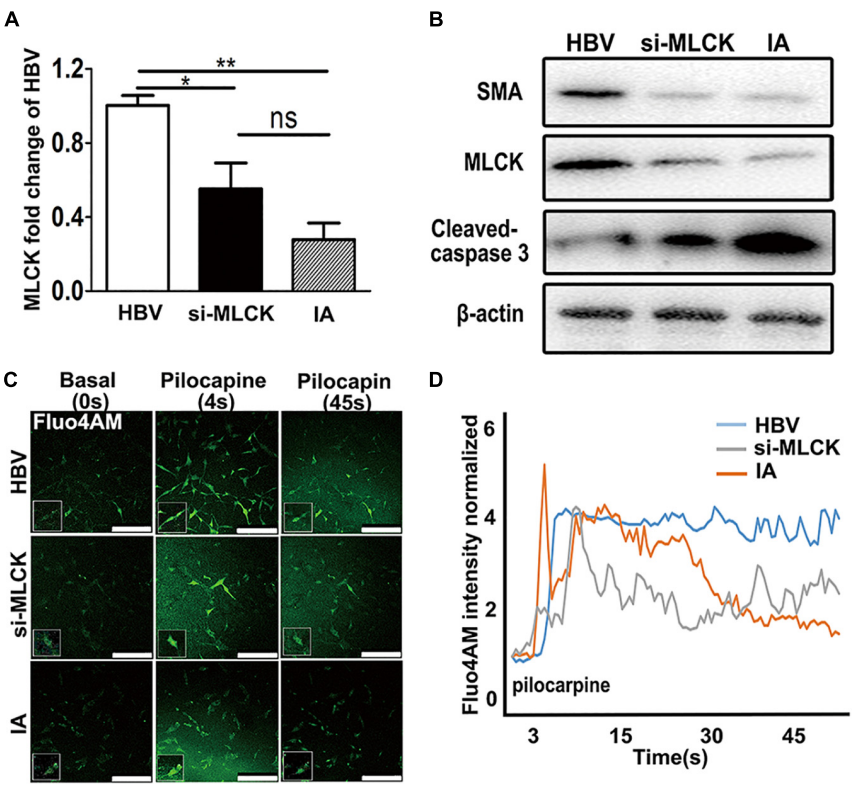

FIGURE 3 | Both si-*mlck*HBVSMCs and IASMCs show weak proliferation and contraction. **(A,B)** MLCK expression in HBVSMCs, si-*mlck*HBVSMCs and primary IASMCs was detected at the mRNA and protein levels. **(C)** Ca^{2+} flux measured by Fluo-4 AM loading and the intensity in HBVSMCs, si-*mlck*HBVSMCs, and IASMCs at a basal level (0 s), upon stimulation with pilocarpine (4 s) and at 45 s after stimulation. **(D)** Quantification of contractility measured as the fluorescence change in the cell surface area of HBVSMCs, si-*mlck*HBVSMCs, and IASMCs. The relative mRNA level was normalized to GAPDH. Data are presented as the means ± SD, $*p < 0.05$, $**p < 0.01$. HBVSMC, human brain vascular smooth muscle cell; IASMC, intracranial aneurysm smooth muscle cell; si-*mlck*SMC, HBVSMCs with interfered *mlck*.

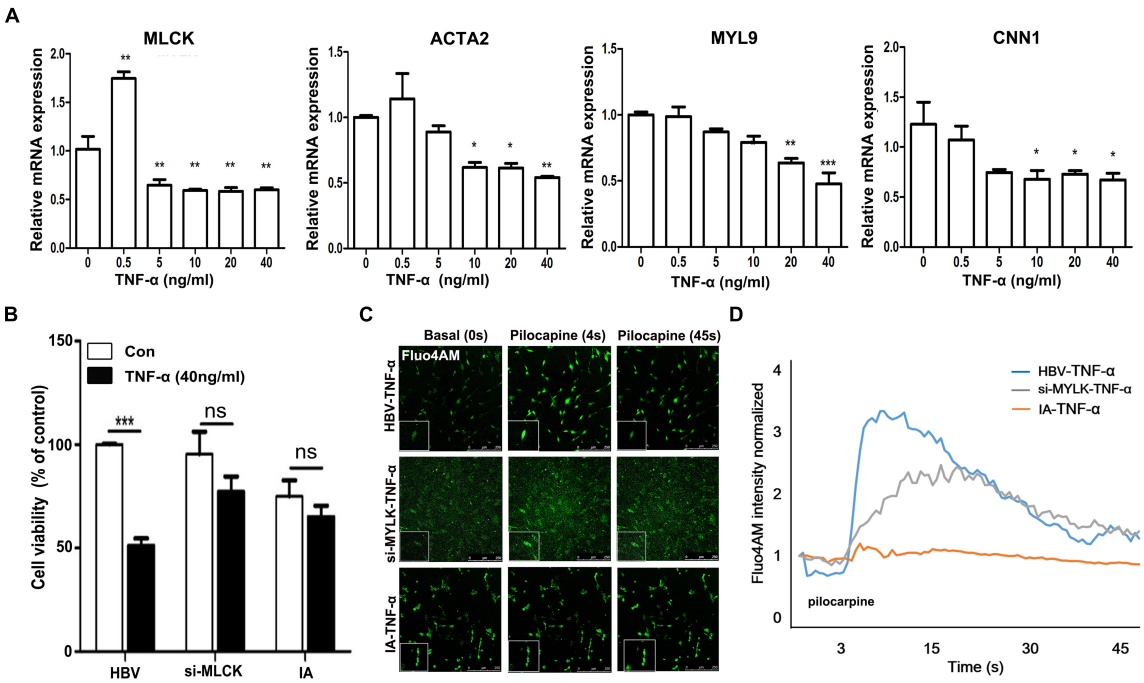

FIGURE 4 | Genetically downregulated MLCK affects cell function more with the stimulation of TNF-α. **(A)** HBVSMCs were treated with a gradient dose of TNF-α and the levels of the mature SMC markers MLCK, ACTA2, MYL9, and CNN1 were detected. **(B)** All three kinds of cells were detected for cell viability by cck-8. **(C)** Ca^{2+} flux measured by loading Fluo-4 AM. **(D)** Quantification of contractility measured as the fluorescence change in the cell surface area of HBVSMCs, si-*mlck*SMCs, and IASMCs. The relative mRNA level was normalized to the control. Data are presented as the means ± SD, $^{*}p < 0.05$, $^{**}p < 0.01$, $^{***}p < 0.001$. HBVSMC, human brain vascular smooth muscle cell; IASMC, intracranial aneurysm smooth muscle cell; si-*mlck*SMC, HBVSMCs with interfered *mlck*.

si-*mlck*SMC, and IASMCs. Interestingly, HBVSMCs stimulated with TNF-α showed lower cell viability than IASMCs and si-*mlck*SMCs. Thus, the effect of *mlck* deficiency at the genetic level on cell viability may differ from that on inflammation (**Figure 4B**). We redetected cell contractility to further investigate the impact on cell viability. All of the cells showed reduced contractility in response to pilocarpine stimulation, with altered cell morphology. However, HBVSMCs appeared as slim fusiform but still responded to pilocarpine. For IASMCs, the cell morphology was not clear and showed little response to stimulation. The si-*mlck*SMCs appeared as short rod shapes but with a weaker response to calcium stimulation (**Figure 4C**). It was clearly observed that with the reduction of MLCK, the contractility was reduced in all three groups, and IASMCs could hardly generate calcium waves, and cells that genetically lacked MLCK seemed more vulnerable to inflammatory attacks (**Figure 4D**).

DISCUSSION

This study observed the effects of MLCK downregulation in IA samples using a label-free proteomic analysis. SMCs with downregulated MLCK underwent phenotypic modulation and were vulnerable to apoptosis when stimulated with TNF-α. MLCK expression was also decreased in SMCs isolated from IA walls (**Figure 5**). Normal SMCs with downregulated MLCK showed disturbed contractile function and were vulnerable to inflammation. In the label-free proteomic analysis, proteins that play a role in IA pathology were found, which mirrored the results found in previous studies using iTRAQ (Wang et al., 2016). Using a DNA microarray, Chen et al. (2014) found that *myh11, acta2, mlck, and my19* were differentially expressed genes associated with VSMC contraction (Chen et al., 2014). Our study focused on SMCs and highlighted the impact of losing MLCK on IA formation.

After MLCK was downregulated, the contraction of SMCs was disturbed. SMCs undergo phenotypic modulation with less contractile gene expression and show a pro-inflammatory, dedifferentiated phenotype (Owens, 1998; Owens et al., 2004; Yoshida and Owens, 2005). Phenotypic modulation and eventual degeneration have been considered to promote the formation and progression of IA. IASMCs were first isolated by Bygglin et al. (2011), and the present study was the first to detect the functions of IASMCs and the contractile gene *mlck*. IASMCs were morphologically modulated and appeared as spider-like cells with the loss of mature SMC features. A study of rabbit aneurysm models showed large and stellate cells with long cytoplasmic extensions (Dai et al., 2006). The IASMCs no longer displayed tightly arranged spindle-like cells, and the morphology was replaced by a sparse disordered form whereby the cells dissociated from each other (Merei and Gallyas, 1980). This morphological change suggests a decrease in ductility when placed under sudden stress.

Smooth muscle cell contraction and relaxation are affected not only by how much Ca^{2+} is infused but also by oxidative stress and inflammation directly or indirectly (Carvalho-de-Souza et al., 2013). Previous studies have demonstrated that the myosin light chain phosphatase regulatory light chains were associated with myosin, whose contractions were dictated by the stimulation of myosin ATPase activity (Murthy, 2006). Calcium increased and bound to calmodulin, and the calcium/calmodulin complexes then combined with MLCK, leading to MLC phosphorylation. We also showed the morphological changes and detected the contractility of IASMCs and HBVSMCs with downregulated *mlck* in **Figures 3**, **4**. With increasing Ca^{2+} levels, calcium could bind to calmodulin and lead to MLC phosphorylation. In an aneurysm environment, the intracellular concentration of Ca^{2+}, as a second messenger, decreased. Therefore, the phosphorylation induced by calcium was also downregulated. Ca^{2+}/calmodulin-dependent MLCK phosphorylated MLC is essential for the initiation of smooth muscle contractions. Sustained MLC phosphorylation could be induced by Ca-independent MLCK. Thus, with downregulated MLCK, MLC phosphatase activity may also be downregulated. MLCK and MLC phosphatase activity can coregulate the relaxation of cells (Murthy, 2006). SMC relaxation can result from the activation of TGR5 by the inhibition of the RhoA/Rho kinase pathway. MLC phosphorylation via Ca^{2+}-independent MLCK can sustain G protein activation and regulate the inhibition of MLC phosphatase (Rajagopal et al., 2013).

The *mlck* gene is prominently differentially expressed in IA compared with control arteries. In our experiment, MLCK expression could also be decreased by inflammatory stimulation, and SMCs showed lower viability with a higher dose of TNF-α. During intracranial inflammation, MLCK expression was decreased in SMCs. Additionally, MLC phosphatase activity might also be downregulated (Murthy, 2006). It is largely unknown whether MLCK causes or results from the phenotypic and functional modulation of SMCs. Our results suggested that MLCK might promote SMC dysfunction; however, this is the first study to support this hypothesis. Although TNF-α could suppress the expression of mature SMC genes, normal SMCs could retain the ability of contraction under certain inflammatory conditions (Ali et al., 2013). When inflammation occurred in SMCs lacking MLCK, the contractions were profoundly suppressed, thus explaining why some IA failed to maintain stability throughout the lifetime of an individual.

Intracranial aneurysm pathology also involves apoptosis, which leads to the weakening intima and media of aneurysm walls. Inflammatory factors, such as TNF-α, could trigger an inductive signal in the initiation of apoptosis (Jamous et al., 2007; Sprague and Khalil, 2009; Ait-Oufella et al., 2011). TNF-α and IL-1 are the most important pro-inflammatory factors, which are often used to induce a focal inflammatory response. Numerous studies have demonstrated that TNF-α increases and plays a critical role in the occurrence and development of aneurysms. Therefore, we used TNF-α to mimic the environment of an aneurysm (Ali et al., 2013; Aoki et al., 2014; Starke et al., 2014). Under an inflammatory environment, smooth muscle relaxation was inhibited, which was caused by soluble guanylyl activity (Rajagopal et al., 2015). SMC dysfunction or apoptosis were considered the destructive events in a ruptured IA. Our results indicated that the loss of MLCK in SMCs could lead to apoptotic progression and promote injury in a pro-inflammatory environment. The continuous loss of SMCs and functional synthesis of collagen and matrix components resulted in aneurysm enlargement and rupture (Frosen, 2014). We found that there was a significant decrease in the expression of MLCK in IA by proteomic analysis. After interfering with MLCK RNA silencing, we found that SMC contractility decreased and apoptosis increased. In addition, SMA expression was downregulated. Therefore, we speculated that decreased MLCK could promote aneurysm development. Many other decreased proteins in IA and STA tissues, such as filamin-C, desmin, and aldehyde dehydrogenase, were found through proteomic analysis. We demonstrated that MLCK was less expressed in IASMCs and that other proteins were usually not expressed in SMCs. Therefore, we chose MLCK as a target in the current study.

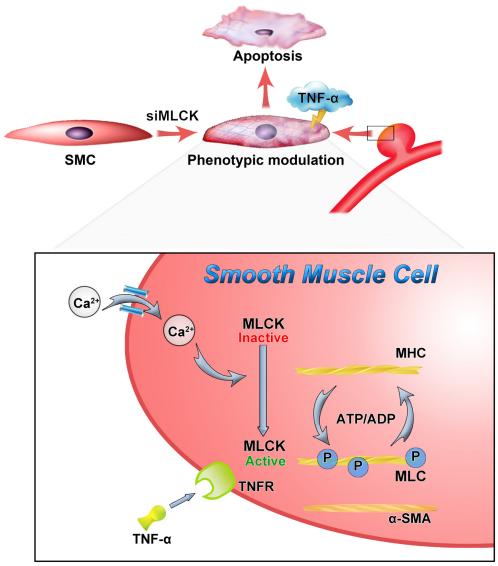

FIGURE 5 | Down-regulation of MLCK weaken the contractile function and with vulnerably reaction to inflammation. The loss of MLCK expressed as phenotypic modulation and calcium dependent phosphorylation was further disturbed. In the TNF environment, the morphologically altered smooth muscle is weaker and more susceptible to apoptosis.

There were also some limitations that need further improvement. IASMCs were isolated from IA tissues and cultured using SMCM. We isolated SMCs from the IA wall directly by cutting small pieces of IA tissues and only used cells within three passages to avoid the effects of *in vitro* culture conditions. The cells were derived with an apoptotic nature and could not be passed for several generations, thus limiting experiments *in vitro*. Whether the *mlck* gene plays a key role in IASMC dysfunction and whether *mlck* mutations exist still needs further exploration.

In summary, the present study provided novel evidence showing that the downregulation of MLCK in SMCs impacted the organization of mature and functional arteries. The lower

expression of MLCK further led to increased apoptosis during the inflammatory response, which resulted in the loss of SMCs and contractile dysfunction. This study is the first to use primary IASMCs to detect SMC function. Our results provide further support that MLCK is involved in SMC contraction, proliferation and apoptosis. Our results also showed that the homeostasis of SMCs is crucial to the normal function of intracranial arteries.

AUTHOR CONTRIBUTIONS

YaS and PL designed and performed the experiments, analyzed the data, and drafted the manuscript and figures. G-YY and WZ conceived the project, designed the experiments, and edited the final manuscript. ZL and YuS participated in the study design. JH, SL, and YL contributed to specimen collection. ZZ and YW helped to design the experiments and interpreted the data.

FUNDING

This study was supported by the Shanghai Sailing Program, project no. 16YF1401200 (PL), the NSF of China, no. 81571102 (WZ), the National Key Research and Development Program of China (2016YFC1300600), the National Natural Science Foundation of China (81771251, G-YY; 81771244, ZZ; 81471178, G-YY; and 81522015, YW), the K. C. Wong Education Foundation (G-YY), and the Science and Technology Commission of Shanghai Municipality (17ZR141 3600, ZZ).

ACKNOWLEDGMENTS

The authors would like to thank Yanye Feng for the proteomic analysis and the staff of the Neuroscience and Neuroengineering Center for collaborative support.

SUPPLEMENTARY MATERIAL

The Supplementary Material for this article can be found online at: https://www.frontiersin.org/articles/10.3389/fncel.2018.00416/full#supplementary-material

REFERENCES

Ait-Oufella, H., Taleb, S., Mallat, Z., and Tedgui, A. (2011). Recent advances on the role of cytokines in atherosclerosis. *Arterioscler. Thromb. Vasc. Biol.* 31, 969–979. doi: 10.1161/ATVBAHA.110.207415

Ali, M. S., Starke, R. M., Jabbour, P. M., Tjoumakaris, S. I., Gonzalez, L. F., Rosenwasser, R. H., et al. (2013). TNF-alpha induces phenotypic modulation in cerebral vascular smooth muscle cells: implications for cerebral aneurysm pathology. *J. Cereb. Blood Flow Metab.* 33, 1564–1573. doi: 10.1038/jcbfm.2013.109

Aoki, T., Fukuda, M., Nishimura, M., Nozaki, K., and Narumiya, S. (2014). Critical role of TNF-alpha-TNFR1 signaling in intracranial aneurysm formation. *Acta Neuropathol. Commun.* 2:34. doi: 10.1186/2051-5960-2-34

Brown, R. D. Jr., and Broderick, J. P. (2014). Unruptured intracranial aneurysms: epidemiology, natural history, management options, and familial screening. *Lancet Neurol.* 13, 393–404. doi: 10.1016/S1474-4422(14)70015-8

Bygglin, H., Laaksamo, E., Myllarniemi, M., Tulamo, R., Hernesniemi, J., Niemela, M., et al. (2011). Isolation, culture, and characterization of smooth muscle cells from human intracranial aneurysms. *Acta Neurochir.* 153, 311–318. doi: 10.1007/s00701-010-0836-x

Carvalho-de-Souza, J. L., Varanda, W. A., Tostes, R. C., and Chignalia, A. Z. (2013). BK channels in cardiovascular diseases and aging. *Aging Dis.* 4, 38–49.

Chen, L., Fan, Y., and Wan, J. (2014). Screening of key genes of unruptured intracranial aneurysms by using DNA microarray data analysis techniques. *Genet. Mol. Res.* 13, 758–767. doi: 10.4238/2014.January.31.2

Dai, D., Ding, Y. H., Kadirvel, R., Danielson, M. A., Lewis, D. A., Cloft, H. J., et al. (2006). A longitudinal immunohistochemical study of the healing of experimental aneurysms after embolization with platinum coils. *AJNR Am. J. Neuroradiol.* 27, 736–741.

Etminan, N., and Rinkel, G. J. (2016). Unruptured intracranial aneurysms: development, rupture and preventive management. *Nat. Rev. Neurol.* 12, 699–713. doi: 10.1038/nrneurol.2016.150

Frosen, J. (2014). Smooth muscle cells and the formation, degeneration, and rupture of saccular intracranial aneurysm wall–a review of current pathophysiological knowledge. *Transl. Stroke Res.* 5, 347–356. doi: 10.1007/s12975-014-0340-3

Frosen, J., Tulamo, R., Paetau, A., Laaksamo, E., Korja, M., Laakso, A., et al. (2012). Saccular intracranial aneurysm: pathology and mechanisms. *Acta Neuropathol.* 123, 773–786. doi: 10.1007/s00401-011-0939-3

Granata, A., Serrano, F., Bernard, W. G., Mcnamara, M., Low, L., Sastry, P., et al. (2017). An iPSC-derived vascular model of marfan syndrome identifies key mediators of smooth muscle cell death. *Nat. Genet.* 49, 97–109. doi: 10.1038/ng.3723

Huang, J., Song, J., Qu, M., Wang, Y., An, Q., Song, Y., et al. (2017). MicroRNA-137 and microRNA-195* inhibit vasculogenesis in brain arteriovenous malformations. *Ann. Neurol.* 82, 371–384. doi: 10.1002/ana.25015

Jamous, M. A., Nagahiro, S., Kitazato, K. T., Tamura, T., Aziz, H. A., Shono, M., et al. (2007). Endothelial injury and inflammatory response induced by hemodynamic changes preceding intracranial aneurysm formation: experimental study in rats. *J. Neurosurg.* 107, 405–411. doi: 10.3171/JNS-07/08/0405

Kleinloog, R., Verweij, B. H., Van Der Vlies, P., Deelen, P., Swertz, M. A., De Muynck, L., et al. (2016). RNA sequencing analysis of intracranial aneurysm walls reveals involvement of lysosomes and immunoglobulins in rupture. *Stroke* 47, 1286–1293. doi: 10.1161/STROKEAHA.116.012541

Kondo, S., Hashimoto, N., Kikuchi, H., Hazama, F., Nagata, I., and Kataoka, H. (1998). Apoptosis of medial smooth muscle cells in the development of saccular cerebral aneurysms in rats. *Stroke* 29, 181–188; discussion 189. doi: 10.1161/01.STR.29.1.181

Liu, P., Zhou, Y., An, Q., Song, Y., Chen, X., Yang, G. Y., et al. (2016). Erythropoietin stimulates endothelial progenitor cells to induce endothelialization in an aneurysm neck after coil embolization by modulating vascular endothelial growth factor. *Stem Cells Transl. Med.* 5, 1182–1189. doi: 10.5966/sctm.2015-0264

Liu, R., Leslie, K. L., and Martin, K. A. (2015). Epigenetic regulation of smooth muscle cell plasticity. *Biochim. Biophys. Acta* 1849, 448–453. doi: 10.1016/j.bbagrm.2014.06.004

Merei, F. T., and Gallyas, F. (1980). Role of the structural elements of the arterial wall in the formation and growth of intracranial saccular aneurysms. *Neurol. Res.* 2, 283–303. doi: 10.1080/01616412.1980.11739584

Murthy, K. S. (2006). Signaling for contraction and relaxation in smooth muscle of the gut. *Annu. Rev. Physiol.* 68, 345–374. doi: 10.1146/annurev.physiol.68.040504.094707

Owens, G. K. (1998). Molecular control of vascular smooth muscle cell differentiation. *Acta Physiol. Scand.* 164, 623–635. doi: 10.1111/j.1365-201X.1998.tb10706.x

Owens, G. K. (2007). Molecular control of vascular smooth muscle cell differentiation and phenotypic plasticity. *Novartis Found. Symp.* 283, 174–191; discussion 191–193, 238–241. doi: 10.1002/9780470319413.ch14

Owens, G. K., Kumar, M. S., and Wamhoff, B. R. (2004). Molecular regulation of vascular smooth muscle cell differentiation in development and disease. *Physiol. Rev.* 84, 767–801. doi: 10.1152/physrev.00041.2003

Rajagopal, S., Kumar, D. P., Mahavadi, S., Bhattacharya, S., Zhou, R., Corvera, C. U., et al. (2013). Activation of G protein-coupled bile acid receptor, TGR5, induces smooth muscle relaxation via both Epac- and PKA-mediated inhibition of RhoA/Rho kinase pathway. *Am. J. Physiol. Gastrointest. Liver Physiol.* 304, G527–G535. doi: 10.1152/ajpgi.00388.2012

Rajagopal, S., Nalli, A. D., Kumar, D. P., Bhattacharya, S., Hu, W., Mahavadi, S., et al. (2015). Cytokine-induced S-nitrosylation of soluble guanylyl cyclase and expression of phosphodiesterase 1A contribute to dysfunction of longitudinal smooth muscle relaxation. *J. Pharmacol. Exp. Ther.* 352, 509–518. doi: 10.1124/jpet.114.221929

Rinkel, G. J. (2008). Natural history, epidemiology and screening of unruptured intracranial aneurysms. *Rev. Neurol.* 164, 781–786. doi: 10.1016/j.neurol.2008.07.012

Sprague, A. H., and Khalil, R. A. (2009). Inflammatory cytokines in vascular dysfunction and vascular disease. *Biochem. Pharmacol.* 78, 539–552. doi: 10.1016/j.bcp.2009.04.029

Starke, R. M., Chalouhi, N., Jabbour, P. M., Tjoumakaris, S. I., Gonzalez, L. F., Rosenwasser, R. H., et al. (2014). Critical role of TNF-alpha in cerebral aneurysm formation and progression to rupture. *J. Neuroinflammation* 11:77. doi: 10.1186/1742-2094-11-77

Wang, J., Yu, L., Huang, X., Wang, Y., and Zhao, J. (2016). Comparative proteome analysis of saccular intracranial aneurysms with iTRAQ quantitative proteomics. *J. Proteomics* 130, 120–128. doi: 10.1016/j.jprot.2015.09.014

Yoshida, T., and Owens, G. K. (2005). Molecular determinants of vascular smooth muscle cell diversity. *Circ. Res.* 96, 280–291. doi: 10.1161/01.RES.0000155951.62152.2e

Yu, L., Fan, J., Wang, S., Zhang, D., Wang, R., Zhao, Y., et al. (2014). Gene expression profiles in intracranial aneurysms. *Neurosci. Bull.* 30, 99–106. doi: 10.1007/s12264-013-1398-8

Yuan, F., Wang, D., Xu, K., Wang, J., Zhang, Z., Yang, L., et al. (2017). Contribution of vascular cells to neointimal formation. *PLoS One* 12:e0168914. doi: 10.1371/journal.pone.0168914

Zhu, W., Tian, Y., Zhou, L. F., Wang, Y., Song, D., Mao, Y., et al. (2008). Development of a novel endothelial cell-seeded endovascular stent for intracranial aneurysm therapy. *J. Biomed. Mater. Res. A* 85, 715–721. doi: 10.1002/jbm.a.31592

Conflict of Interest Statement: The authors declare that the research was conducted in the absence of any commercial or financial relationships that could be construed as a potential conflict of interest.

frontiers in Cellular Neuroscience

ORIGINAL RESEARCH
published: 20 November 2018
doi: 10.3389/fncel.2018.00434

Spatiotemporal Expression of GRP78 in the Blood Vessels of Rats Treated With 3-Nitropropionic Acid Correlates With Blood–Brain Barrier Disruption

*Xuyan Jin[1,2], Tae-Ryong Riew[1], Hong Lim Kim[3], Soojin Kim[1] and Mun-Yong Lee[1,2]**

[1] Department of Anatomy, Catholic Neuroscience Institute, College of Medicine, The Catholic University of Korea, Seoul, South Korea, [2] Department of Biomedicine and Health Sciences, College of Medicine, The Catholic University of Korea, Seoul, South Korea, [3] Integrative Research Support Center, Laboratory of Electron Microscope, College of Medicine, The Catholic University of Korea, Seoul, South Korea

Glucose-regulated protein (GRP78) or BiP, a 78-kDa chaperone protein located in the endoplasmic reticulum (ER), has recently been reported to be involved in the neuroglial response to ischemia-induced ER stress. The present study was designed to study the expression patterns of this protein and the cell types involved in the induction of GRP78 expression in rats treated with the mitochondrial toxin 3-nitropropionic acid (3-NP). GRP78 immunoreactivity was almost exclusively localized to striatal neurons in saline-treated controls, but GRP78 expression was induced in activated glial cells, including reactive astrocytes and activated microglia/macrophages, in the striata of rats treated with 3-NP. In the lesion core, increased GRP78 immunoreactivity was observed in the vasculature; this was evident in the lesion periphery of the core at 3 days after lesion induction, and was evenly distributed throughout the lesion core by 7 days after lesion induction. Vascular GRP78 expression was correlated, both temporally and spatially, with infiltration of activated microglia into the lesion core. In addition, this was coincident with the time and pattern of blood–brain barrier (BBB) leakage, detected by the extravasation of fluorescein isothiocyanate-albumin, an established BBB permeability marker. Vascular GRP78-positive cells in the lesion core were identified as endothelial cells, smooth muscle cells, and adventitial fibroblast-like cells, in which GRP78 protein was specifically localized to the cisternae of the rough ER and perinuclear cisternae, but not to other organelles such as mitochondria or nuclei. Thus, our data provide novel insights into the phenotypic and functional heterogeneity of GRP78-positive cells within the lesion core, suggesting the involvement of GRP78 in the activation/recruitment of activated microglia/macrophages and its potential role in BBB impairment in response to a 3-NP-mediated neurotoxic insult.

Keywords: 78-kDa glucose-regulated protein, striatum, endoplasmic reticulum, 3-nitropropionic acid, blood vessels, blood–brain barrier

OPEN ACCESS

Edited by:
Sriharsha Kantamneni, University of Bradford, United Kingdom

Reviewed by:
Manoj K. Gottipati, Rensselaer Polytechnic Institute, United States
Mario Valentino, University of Malta, Malta

***Correspondence:**
Mun-Yong Lee
munylee@catholic.ac.kr

Received: *07 August 2018*
Accepted: *01 November 2018*
Published: *20 November 2018*

Citation:
Jin X, Riew T-R, Kim HL, Kim S and Lee M-Y (2018) Spatiotemporal Expression of GRP78 in the Blood Vessels of Rats Treated With 3-Nitropropionic Acid Correlates With Blood–Brain Barrier Disruption. Front. Cell. Neurosci. 12:434. doi: 10.3389/fncel.2018.00434

INTRODUCTION

The 78-kDa glucose-regulated protein (GRP78), also known as the immunoglobulin heavy-chain binding protein or BiP, is a multifunctional regulator of endoplasmic reticulum (ER) homeostasis and stress response (Bole et al., 1989; Zhang and Zhang, 2010; Ouyang et al., 2011). ER stress triggers a cell stress response, termed the unfolded protein response, which activates the apoptosis pathway, when ER stress is excessive or prolonged (for review, see Zhu and Lee, 2015; Casas, 2017). GRP78, a major upregulated target protein in the unfolded protein response, regulates the folding and assembly of newly synthesized proteins, facilitates protein translocation across the ER membranes, and acts as a calcium binding protein (for review, see Zhu and Lee, 2015; Casas, 2017). In addition, GRP78 can translocate from the ER to the cytosol, nucleus, mitochondria, and plasma membrane, and it can also be secreted, suggesting its involvement in the regulation of cell viability and signaling (Sun et al., 2006; Gonzalez-Gronow et al., 2009; Liu et al., 2010; Misra and Pizzo, 2010a,b; Misra et al., 2011; Ni et al., 2011; Ouyang et al., 2011).

The neuronal functions of GRP78 have been investigated in various central nervous system (CNS) disease models, including ischemic insults (Wang et al., 1993; Aoki et al., 2001; Ito et al., 2001; Shibata et al., 2003; Tajiri et al., 2004; Oida et al., 2008; Osada et al., 2010), epileptic seizures (Wang et al., 1993; Chen et al., 2013), spinal cord injury (Penas et al., 2007, 2011; Ohri et al., 2012; Matsuyama et al., 2014), diabetic encephalopathy (Zhao et al., 2015), and experimental subarachnoid hemorrhage (Liu et al., 2016). GRP78 overexpression can have a neuroprotective effect by inhibiting the unfolded protein response, promoting autophagy, buffering calcium unbalance, and activating pro-survival signaling pathways (Ouyang et al., 2011; Zhang et al., 2015; Casas, 2017). Although most studies investigating GRP78 have focused on neuron-specific functions, there is increasing evidence of alterations in GRP78 expression in activated glial cells after CNS insults. GRP78 expression is induced in reactive astrocytes following status epilepticus and ischemia (Osada et al., 2010; Ko et al., 2011), and in microglia/macrophages after spinal cord injury (Fan et al., 2015). In addition, *in vitro* evidence indicates that GRP78 overexpression in astrocytes protects against ER stress (Ouyang et al., 2011; Suyama et al., 2011). Furthermore, our recent *in vivo* study showed prominent induction of GRP78 expression within activated glial cells after transient focal cerebral ischemia, predominantly in microglia/macrophages and reactive astrocytes (Jin et al., 2018a). Thus, the aforementioned data indicate a phenotypic and functional heterogeneity of GRP78-positive cells in the injured CNS, suggesting a multifunctional role, possibly in the neuroglial reaction to CNS insults, in addition to its known neuroprotective role. However, the detailed expression pattern of GRP78 and the cell types involved in the induction of GRP78 expression have been analyzed only in the ischemic brain. Thus, these findings need to be further substantiated in other models of CNS insults.

To address these issues, we examined the temporal changes and cellular localization of GRP78 expression in the lesioned striatum following injection of the natural mitochondrial toxin 3-nitropropionic acid (3-NP), which selectively damages medium-spiny striatal neurons and thus mimics many of the histological and neurochemical features characteristic of Huntington's disease (Hamilton and Gould, 1987; Beal et al., 1993; Borlongan et al., 1997). This 3-NP model accurately mimics the dynamic spatiotemporal regulation of neuroglial activation in response to injuries, producing tissue lesions consisting of well-demarcated cores and perilesional areas with astroglial scar formation (Duran-Vilaregut et al., 2010; Mu et al., 2016; Riew et al., 2017).

MATERIALS AND METHODS

Animal Preparation

All experimental procedures were conducted in accordance with the Laboratory Animal Welfare Act, the Guide for the Care and Use of Laboratory Animals, and Guidelines and Policies for Rodent Survival Surgery, and were approved by the Institutional Animal Care and Use Committee at the College of Medicine, The Catholic University of Korea (Approval Number: CUMC-2017-0321-04). All efforts were made to minimize animal suffering and to reduce the number of animals used.

Adult, male Sprague-Dawley rats (250–300 g, aged 9–11 weeks) were used in this study. Animals were housed in groups of three per cage in a controlled environment at a constant temperature (22 ± 5°C) and humidity (50 ± 10%) with food (gamma ray-sterilized diet) and water (autoclaved tap water) available *ad libitum*. They were maintained on a 12-h light/dark cycle. 3-NP (Sigma-Aldrich, St. Louis, MO, United States) was dissolved in buffered saline (pH 7.0), and administered intraperitoneally (i.p.) at a dose of 15 mg/kg once daily for 3 days. All 3-NP-injected rats were evaluated daily for the presence of behavioral deficits, and only rats exhibiting neurological deficit symptoms, including hind limb impairment or a kyphotic posture, recumbency, and impaired postural adjustments, were included in the experimental group (Hamilton and Gould, 1987). Animals were sacrificed 1, 3, 7, and 14 days after the final injection of 3-NP (n = 6/time point). The control group (n = 3) received intraperitoneal injections of the same volume of normal saline for three consecutive days and were sacrificed 3 days after the final injection. The animals were anesthetized with 10% chloral hydrate, sacrificed, and then perfused transcardially with 4% paraformaldehyde in 0.1 M phosphate buffer (PB; pH 7.4) The brain tissues were equilibrated with 30% sucrose in 0.1 M PB and frozen whole.

Immunohistochemistry

For GRP78 immunohistochemistry, coronal cryostat sections (25-μm-thick) were incubated in blocking buffer solution (0.2% gelatin, 0.05% saponin, and 1% bovine serum albumin in phosphate-buffered saline) and then incubated overnight at 4°C with a rabbit polyclonal antibody to GRP78 (1:2000; Abcam, Cambridge, United Kingdom). Primary antibody binding was visualized using peroxidase-labeled goat anti-rabbit antibody (1:100; Jackson ImmunoResearch, West

Grove, PA, United States) and 0.05% 3,3′, -diaminobenzidine tetrahydrochloride (DAB) with 0.01% H_2O_2 as a substrate. The specificity of GRP78 immunoreactivity was confirmed by the absence of immunohistochemical staining in sections from which the primary or secondary antibody had been omitted. Tissue sections were scanned and photographed using a slide scanner (SCN400, Leica Microsystems Ltd., Mannheim, Germany). Images were converted to TIFF format, and contrast levels adjusted using Adobe Photoshop v. 13.0 (Adobe Systems, San Jose, CA, United States).

For the evaluation of tissue injury, serial sections from sham controls and experimental rats at 3 days post-lesion were processed for Fluoro-Jade B (FJB) histochemistry and immunohistochemistry for GRP78. For FJB staining, sections were stained with 0.0004% FJB (Millipore, Temecula, CA, United States) in distilled water containing 0.01% acetic acid for 30 min according to the manufacturer's protocol. After rinsing in distilled water, the sections were immersed in xylene and cover-slipped with DPX mounting medium (Sigma-Aldrich).

For triple-labeling, non-specific staining was blocked by preincubation of free-floating sections (25-μm-thick) in blocking buffer (3% normal goat serum, 1% bovine serum albumin, and 0.5% triton). Primary antibodies and dilutions were as follows: rabbit polyclonal antibody against GRP78 (1:2000; Abcam), mouse monoclonal antibody against rat endothelial cell antigen-1 (RECA1; 1:200; Bio-Rad, Hercules, CA, United States), mouse monoclonal antibodies against glial fibrillary acidic protein (GFAP; 1:700; Millipore), mouse monoclonal antibody against NeuN (1:500; Millipore), goat polyclonal antibody against ionized calcium-binding adaptor molecule 1 (Iba1; 1:500; Abcam), mouse monoclonal antibody against nestin (1:500; Millipore), goat polyclonal antibody against choline acetyltransferase (1:300; Millipore), mouse monoclonal antibodies to ED1 (1:50; Bio-Rad) or mouse monoclonal antibodies to CD45 (1:15; Bio-Rad). In addition, double labeling was performed using a mix of rabbit polyclonal antibody against GRP78 (1:2000; Abcam), and one of following antibodies: mouse monoclonal antibody to NG2 (1:500; Millipore) or to α-smooth muscle actin (α-SMA; 1:500; Sigma-Aldrich). This triple- or double-labeling was followed by a 2-h incubation with appropriate secondary antibodies, as follows: Cy3-conjugated donkey anti-goat antibody (1:2000; Jackson ImmunoResearch), Cy3-conjugated donkey anti-mouse antibody (1:2000; Jackson ImmunoResearch), Alexa Fluor 488-tagged donkey anti-rabbit antibody (1:300; Thermo Fisher, Waltham, MA, United States), Alexa Fluor 647-conjugated donkey anti-mouse antibody (1:300; Thermo Fisher), or Alexa Fluor 647-conjugated donkey anti-rabbit antibody (1:300; Thermo Fisher). Negative staining controls for the triple- or double-immunofluorescence were performed by omission of the primary or secondary antibodies. In addition, we compared the results of triple or double-labeling with those from single-labeling of all combinations of antibodies to ensure clear interpretation of results. Counterstaining of cell nuclei was carried out using DAPI (4′,6-diamidino-2-phenylindole; 1:2000; Roche, Mannheim, Germany) for 10 min.

In order to detect apoptotic cells simultaneously with GRP78 expression in neurons, we performed triple-labeling for terminal deoxynucleotidyl transferase dUTP nick end labeling (TUNEL) according to the manufacturer's protocol (Roche Diagnostics Corporation, Indianapolis, IN, United States) and the following antibodies: rabbit polyclonal antibody against GRP78 (1:2000; Abcam) and mouse monoclonal antibody against NeuN (1:500; Millipore). This was followed by a 2-h incubation with Alexa Fluor 488-tagged goat anti-rabbit antibody (1:300; Thermo Fisher), Alexa Fluor 647-tagged goat anti-mouse antibody (1:300; Thermo Fisher), and Cy3-conjugated streptavidin (1:1200; Jackson ImmunoResearch) for the TUNEL method. Counterstaining of cell nuclei was carried out with DAPI for 10 min. Slides were viewed under a confocal microscope (LSM 700; Carl Zeiss Co., Ltd., Oberkochen, Germany) equipped with four lasers (Diode 405, Argon 488, HeNe 555, and HeNe 639) under constant viewing conditions. Images were converted to TIFF format, and contrast levels and sizes were adjusted using Adobe Photoshop v.13.0.

Quantitative Analysis

To quantify time-dependent changes in GRP78 immunoreactivity associated with the vasculature after 3-NP injection, we analyzed the immunofluorescence intensities from the confocal data by using ZEN 2.1 Blue Edition software (Carl Zeiss Co., Oberkochen, Germany). Sections double-labeled for GRP78 and RECA1, a vascular endothelial cell marker, in sham-operated and experimental rats at days 1, 3, and 7 after reperfusion (n = 3 animals per time point) were obtained from three locations posterior to the bregma at approximately 0.2, 0.7, and 1.2 mm (Paxinos and Watson, 2006). Ten randomly selected areas (160 μm × 160 μm per field) were chosen in the lesion core of each section, and images of GRP78 and RECA1 immunoreactivity were then obtained from these areas at ×400 magnification under constant viewing conditions. Three days after 3-NP injection, two areas of the lesion core (the core-periphery and core-epicenter) were clearly distinguishable in the experimental rats on the basis of the presence of GRP78-positive cells; therefore, 10 areas were chosen from each of the two areas. The area covered by GRP78 and RECA-1 was estimated, and GRP78 coverage was expressed as a percentage of the total RECA1-positive vascular area. Differences in staining intensity between groups were assessed with one-way analysis of variance (ANOVA) followed by *post hoc* Bonferroni tests for multiple comparisons. Differences with P-values less than 0.05 were considered statistically significant. All statistical analysis was performed using GraphPad Prism version 5 (GraphPad Software Inc., San Diego, CA, United States).

In addition, to quantify the time-dependent changes in GRP78-positive microglia/macrophages in the striatum in rats treated with 3-NP, sections obtained from control and experimental rats (from the three locations described above) at 1, 3, and 7 days after 3-NP injection (n = 3 per time point) were double-labeled for GRP78 and Iba1. Ten areas (160 μm × 160 μm per field) were chosen in the lesion core of each section and the corresponding striatum from control sections, and GRP78/Iba1 double-labeled cells were counted only

when their nuclei could be clearly observed. The cell counts are presented as the mean ± standard error of the mean (SEM). Data analysis was performed as described above.

Assessment of Blood–Brain Barrier (BBB) Leakage

To detect BBB leakage in 3-NP-injected rats, experimental rats (n = 3 animals) were deeply anesthetized on days 3 and 7 after 3-NP injection and intravenously administered fluorescein isothiocyanate (FITC)-albumin (2 mg diluted in 0.1 ml saline; Sigma-Aldrich) via the tail vein. One hour after injection, animals were deeply anesthetized and perfused transcardially with fixative, as described above. Coronal cryostat sections (25-μm-thick) from animals injected with FITC-albumin were incubated overnight at 4°C with a mixture of rabbit polyclonal antibody against GRP78 (1:2000; Abcam) and one of following antibodies: goat polyclonal antibody against Iba1 (1:500; Abcam), mouse monoclonal antibody against RECA1 (1:200; Bio-Rad), or mouse monoclonal antibodies against GFAP (1:700; Millipore). This was followed by 2-h incubation with appropriate secondary antibodies as follows: Cy3-conjugated donkey anti-goat antibody (1:2000; Jackson ImmunoResearch), Cy3-conjugated goat anti-mouse antibody (1:2000; Jackson ImmunoResearch), or Alexa Fluor 647-tagged donkey anti-rabbit antibody (1:300; Thermo Fisher). Counterstaining of cell nuclei was carried out using DAPI for 10 min.

Immunoelectron Microscopy

For the correlative light- and electron-microscopic study, vibratome sections (300-μm-thick) from experimental rats at 3 days after 3-NP injection were cryoprotected with 2.3 M sucrose in 0.1 M PB and frozen in liquid nitrogen. Semi-thin cryosections (1-μm-thick) were cut at −100°C with a glass knife in a Leica EM UC7 ultramicrotome equipped with an FC7 cryochamber (Leica). The sections were double-labeled at 4°C overnight using a mix of rabbit polyclonal antibody against GRP78 (1:2000; Abcam) and one of following antibodies: goat polyclonal antibody against Iba1 (1:500; Abcam), mouse monoclonal antibody against RECA1 (1:200; Bio-Rad), or mouse monoclonal antibody to nestin (1:500; Millipore). Antibody staining was visualized using Alexa Fluor 488-FluoroNanogold-anti-rabbit Fab' (1:300; Nanoprobes; Yaphank, NY, United States) and either Cy3-conjugated goat anti-mouse antibody (1:2000, Jackson ImmunoResearch) or Alexa Fluor 647-tagged donkey anti-goat antibody (1:300; Thermo Fisher). Sections were counterstained with DAPI for 10 min. Coverslipped sections were examined with a confocal microscope and photographed at various magnifications with a differential interference contrast setting to find specific areas for later examination by electron microscopy. After the coverslips had been floated off the sections, silver enhancement was performed using the HQ silver enhancement kit (Nanoprobes) for 3 min, and the tissues were prepared further for electron microscopy. After post-fixation, dehydration, and embedding in Epon 812 (Polysciences, Warrington, PA, United States), areas of interest were excised and glued onto resin blocks. After being cut into ultrathin sections 70–90 nm thick, they were observed in an electron microscope (JEM 1010; JEOL, Tokyo, Japan) with slight uranyl acetate staining.

RESULTS

Spatial and Temporal Expression of GRP78 in the Striatum of Rats Treated With 3-NP

Consistent with our previous data (Choi et al., 2017; Riew et al., 2017; Jin et al., 2018b), approximately 70% of rats treated with 3-NP in our study developed characteristic neurological deficits including hindlimb impairment, recumbency, and impaired postural adjustments. In addition, all the animals examined in this study showed comparable expression patterns of GRP78 at each time point after 3-NP injection.

We first performed immunohistochemistry to examine the spatiotemporal distribution of GRP78-positive cells in the striata of rats treated with 3-NP. In the striata of saline-treated controls, we observed no specific staining for FJB, which labels degenerating neurons, and GRP78 immunoreactivity was observed in neuron-like cells (**Figures 1A,B**), as reported previously (Jin et al., 2018a). One day after the last 3-NP injection, a well-demarcated lesion core was evident in the lateral part of the striatum. GRP78-positive neurons had mostly disappeared in the lesion core, while neuronal GRP78 expression persisted in the peri-lesional area (**Figure 1C**). Three days after lesion induction, the lesion core, which was characterized by intense FJB staining, could be clearly divided into two areas according to the GRP78 expression profile: the epicenter and periphery of the lesion core (**Figures 1D,E**). A higher magnification image of the lesion core revealed that neuronal profiles were positive for the neuronal degeneration marker FJB (inset in **Figure 1D**). In the periphery of the lesion core, intense GRP78 immunoreactivity was observed in vascular profiles and cells with round cell bodies, while only weak GRP78 immunoreactivity was observed in the lesion epicenter. At day 7 after lesion induction, GRP78 immunoreactivity was evenly distributed throughout the lesion core, including the periphery and the center (**Figure 1F**). This expression pattern was maintained on day 14 (data not shown).

Characterization of GRP78-Positive Cells in the Striatum After 3-NP Injection

As described above, the pattern of GRP78 immunoreactivity in the lesion core changed during the post-injury period. Therefore, to clarify the phenotypes of GRP78-positive cells in the striata from control and experimental rats, we performed triple-labeling with GRP78 and cell type-specific markers. In the striata from control rats, GRP78 immunoreactivity was evident in almost all striatal neurons expressing NeuN, including large cholinergic interneurons expressing choline acetyltransferase, a specific marker for cholinergic neurons (**Figure 2A**), but not in

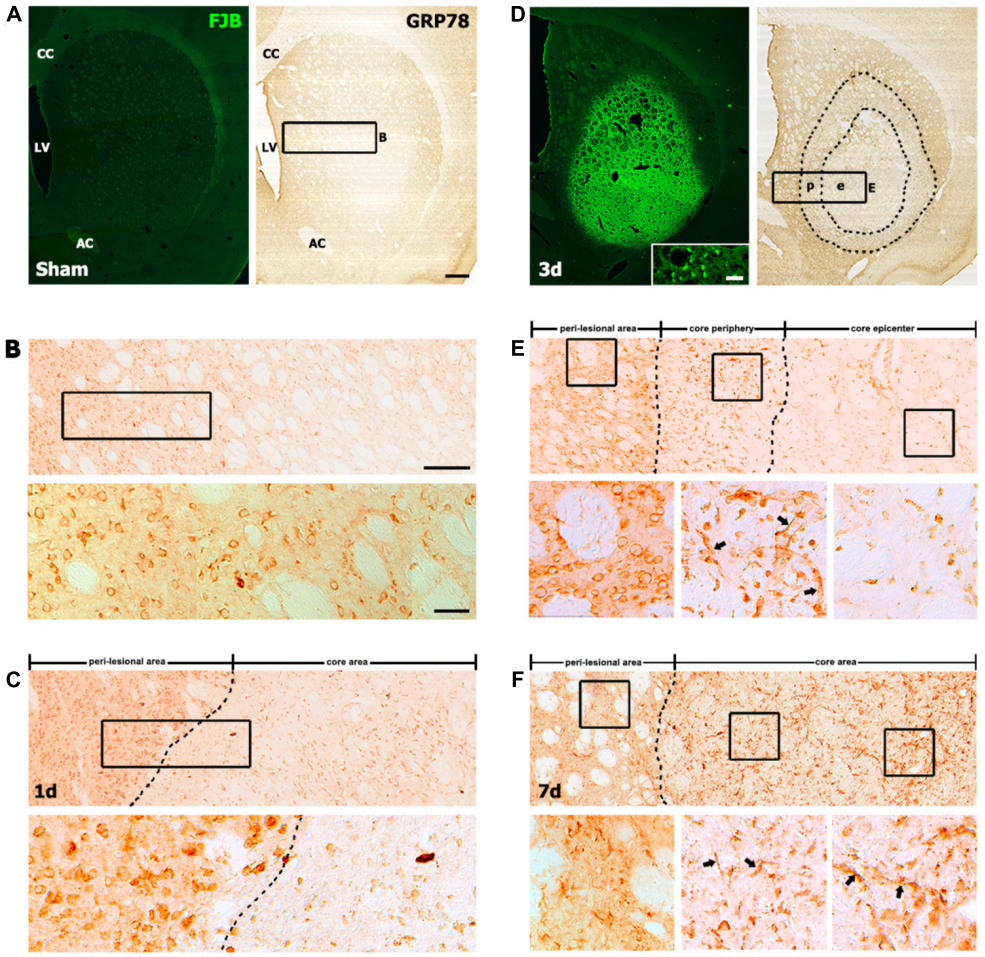

FIGURE 1 | Representative images showing the temporal expression of the 78-kDa glucose-regulated protein (GRP78) in striatal sections from saline-treated control and 3-nitropropionic acid-injected rats. **(A,B)** Lower- **(A)** and higher- **(B)** magnification views of coronal sections from saline-treated controls. **(A)** Serial striatal sections stained with Fluoro-Jade B (FJB) and anti-GRP78 antibody, showing no specific staining for FJB in the striatum. **(B)** Upper and lower panels of B are higher magnification images of the boxed area of A and upper panel of B, respectively, showing that GRP78 is present in neuron-like cells. **(C)** At day 1 after lesion induction, a spatial difference can be observed between GRP78 expression in the lesion core (right side of the broken line) and that in the peri-lesional area. The boxed area in upper panel is enlarged in the lower panel, showing that most neuronal profiles are absent in the lesion core, while intense GRP78 immunoreactivity is still evident in neurons in the peri-lesional area. **(D)** At 3 days after lesion induction, the core of the lesion, which is clearly distinguished by intense FJB staining, can be divided into two distinct areas on the basis of GRP78 immunoreactivity: the epicenter (e) and the lesion periphery (p); the border between these areas is indicated by the broken line. (Inset in left panel of **D**) Higher magnification image of an FJB-stained section, showing intense FJB staining within neuronal profiles in the lesion core. (**E**, Upper) Higher magnification image of the boxed area of **D**, showing the distinct expression patterns of GRP78 in the perilesional area, lesion periphery, and epicenter. Boxed areas in these three parts are enlarged in the corresponding lower panels of **E**. (**E**, Lower) Intense GRP78 expression is observed in vascular profiles (arrows in middle panel) and cells with round cell bodies in the lesion periphery, while no prominent GRP78 expression is visible in the lesion epicenter. (**F**, Upper) At day 7 after lesion induction, GRP78 expression is more densely distributed throughout the lesion core (right side of the broken line). (**F**, Lower) Higher magnification images of boxed areas in the three areas, i.e., the perilesional area, lesion periphery, and epicenter, from the corresponding images in the upper panel. Note that vessel-associated GRP78 immunoreactivity is evident in both the lesion periphery (arrows in middle panel) and the epicenter (arrows in right panel). CC, corpus callosum; LV, lateral ventricle; AC, anterior commissure. Scale bars represent 500 μm for **A**, **D**; 200 μm for upper panels in **B**, **C**, **E**, **F**; and 50 μm for the inset in the left panel in **D** and lower panels in **B**, **C**, **E**, **F**.

astrocytes or microglia (**Figure 2B**), consistent with the findings of our previous study (Jin et al., 2018a).

One day after lesion induction, most GRP78-positive neuronal profiles were absent from the lesion core, which was confirmed by triple-labeling of GRP78, NeuN, and TUNEL (**Figure 2C**). Striatal neurons in the lesion core, most of which were positive for TUNEL, were devoid of significant GRP78 immunoreactivity (**Figure 2E**), while neurons in the peri-lesional area showed evident GRP78 immunoreactivity (**Figure 2D**). At this time point, triple-labeling of GRP78, Iba1, and GFAP revealed that the lesion core was clearly demarcated by the absence of astrocytes and microglia with normal morphology, while both glial cell types were present in the peri-lesional area (**Figures 2F,H**). Observation of the peri-lesional area at higher magnification revealed weak GRP78 immunoreactivity in astrocytes and microglia, both

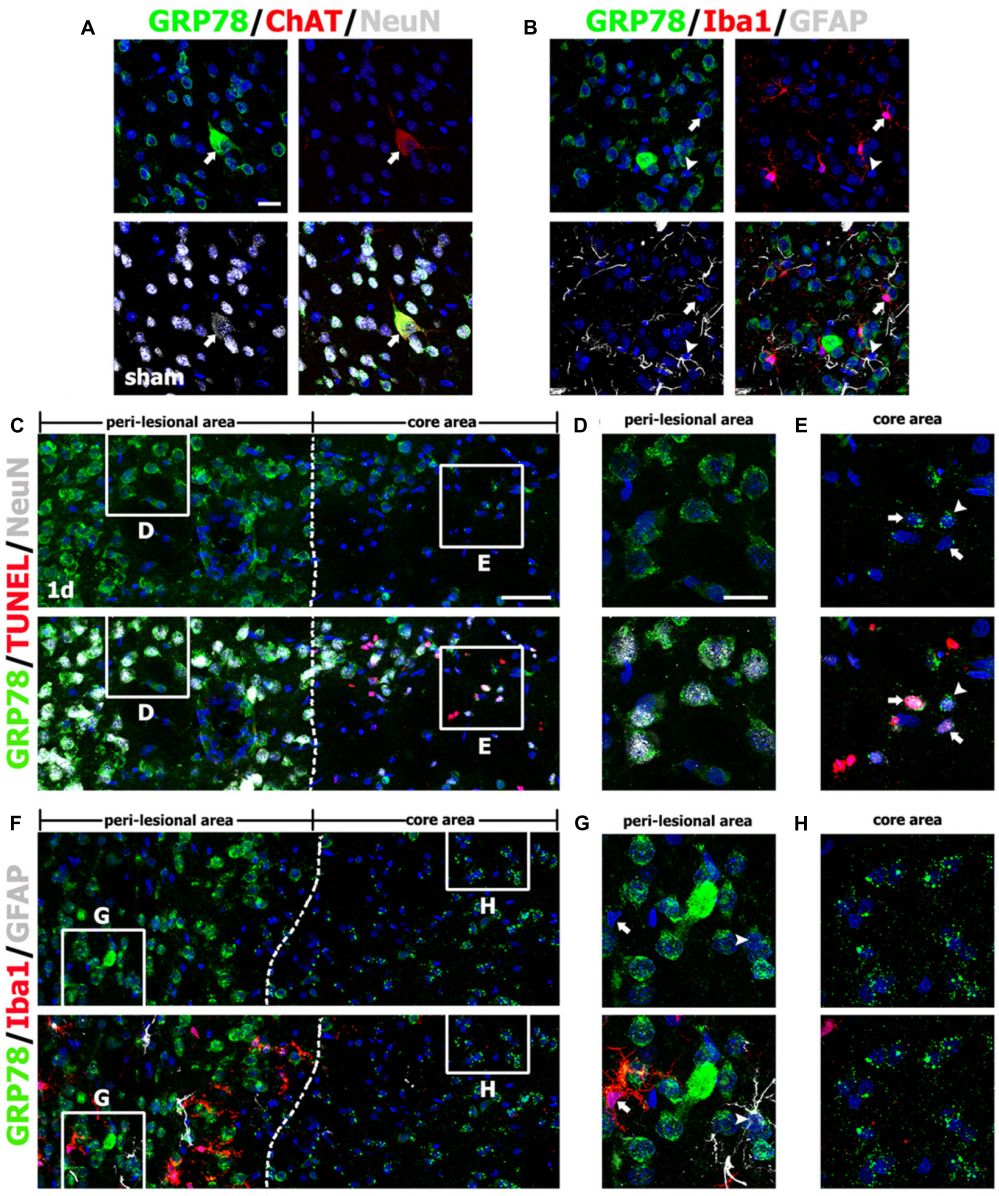

FIGURE 2 | Characterization of glucose-regulated protein (GRP78)-positive cells in the striata of saline-treated control and 3-nitropropionic acid-injected rats on day 1. **(A)** Triple-labeling of GRP78, neuronal nuclear protein (NeuN), and choline acetyltransferase (ChAT), a specific marker for cholinergic neurons, in control striatum, showing that GRP78 expression is localized in almost all NeuN-positive neurons and also in some cholinergic interneurons (arrows). **(B)** Triple-labeling of GRP78, ionized calcium-binding adaptor molecule 1 (Iba1), and glial fibrillary acidic protein (GFAP) in the striatum of a control rat, showing that neither microglia (arrows) nor astrocytes (arrowheads) show specific immunoreactivity for GRP78. **(C–E)** Lower- **(C)** and higher- **(D,E)** magnification views of sections triple-labeled for GRP78, NeuN, and terminal deoxynucleotidyl transferase dUTP nick end labeling (TUNEL) 1 day after lesion induction. The boxed areas of the peri-lesional area (left side of the broken line) and the lesion core in **C** are enlarged in **D** and **E**, respectively. Notably, GRP78 expression is very weak to negligible in nearly all TUNEL-positive (arrows in **E**) and TUNEL-negative (arrowheads in **E**) neurons in the lesion core, while neurons in the peri-lesional area show prominent GRP78 immunoreactivity. **(F–H)** Lower- **(F)** and higher- **(G,H)** magnification views of section triple-labeled for GRP78, Iba1, and GFAP 1 day after lesion induction. The boxed areas of the peri-lesional area (left side of the broken line) and the lesion core in **F** are enlarged in **G** and **H**, respectively. Note that astrocytes (arrowheads in **G**) and microglia (arrows in **G**) in the peri-lesional area show very weak immunoreactivity for GRP78. Cell nuclei are stained with 4′,6-diamidino-2-phenylindole. Scale bars represent 50 μm for **C**, **F**; and 20 μm for **A**, **B**, **D**, **E**, **G**, **H**.

of which had not yet shown typical reactive phenotypes (**Figure 2G**).

On day 3 after lesion induction, triple-labeling of GRP78, NeuN, and TUNEL revealed that specific GRP78 immunoreactivity was virtually absent in dying or dead neurons in the lesion core (**Figure 3A**). As mentioned above, the lesion core could be divided into two areas: the lesion periphery, in which intense GRP78 expression was localized within the

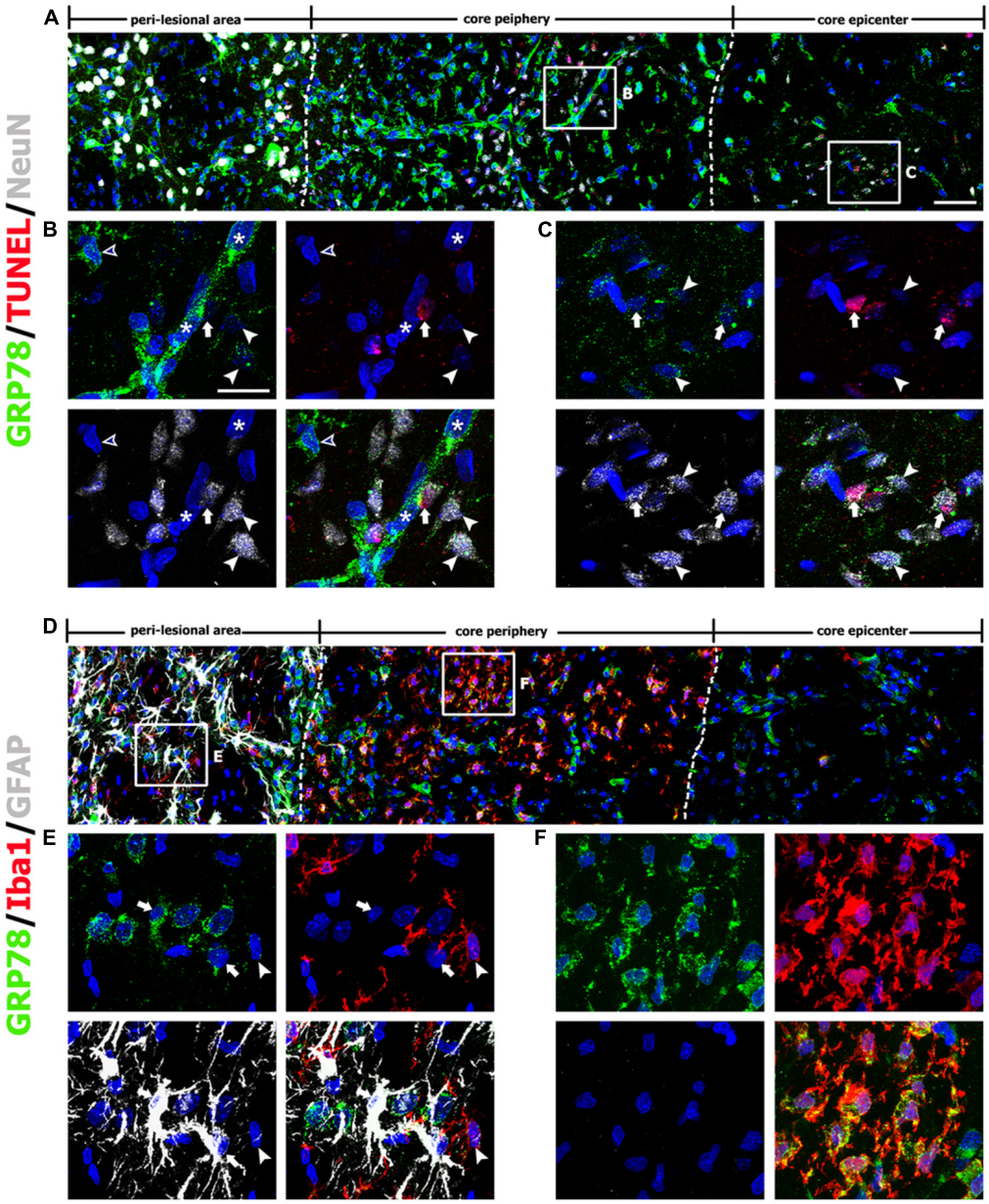

FIGURE 3 | Characterization of glucose-regulated protein (GRP78)-positive cells in lesioned striatum on day 3 after 3-nitropropionic acid injection. **(A)** Triple-labeling of GRP78, NeuN, and terminal deoxynucleotidyl transferase dUTP nick end labeling (TUNEL) showing that neuronal GRP78 expression is evident in the perilesional area, while GRP78 is virtually absent in dying or dead neurons in the lesion core. The two broken lines indicate the borders of three areas: the peri-lesional area, lesion periphery, and epicenter. The corresponding boxed areas in the lesion periphery and epicenter in **A** are enlarged in **B**, **C**. **(B,C)** In both the lesion periphery **(B)** and the epicenter **(C)**, both TUNEL-positive (arrows) and TUNEL-negative (arrowheads) neurons show negligible immunoreactivity. Notably, in the lesion periphery, intense GRP78 expression is localized within the vascular profiles (asterisks in **B**) and presumptive activated microglia (open arrowheads in **B**), while no specific GRP78 expression is detectable in the epicenter. **(D)** Triple-labeling of GRP78, Iba1, and GFAP showing that the lesion core can be divided into two areas: the core periphery, which is heavily infiltrated by activated microglia, and the epicenter, which is devoid of Iba1-positive microglia. Notably, GFAP immunoreactivity is absent in both the periphery and the epicenter. **(E,F)** Higher-magnification views of the corresponding boxed areas in **D**. **(E)** In the peri-lesional area, GRP78 expression can be observed in reactive astrocytes (arrows) and activated microglia (arrowheads). **(F)** In the lesion periphery, intense GRP78 expression is visible in almost all Iba1-positive cells. Cell nuclei are stained with 4′,6-diamidino-2-phenylindole. Scale bars represent 50 μm for **A D**; and 20 μm for **B**, **C**, **E**, **F**.

vascular profiles and cells with round cell bodies (**Figure 3B**), and the epicenter, which was devoid of specific GRP78 expression (**Figure 3C**). This finding was further supported by triple-labeling of GRP78, Iba1, and GFAP; in the lesion core that was devoid of GFAP immunoreactivity, GRP78 and Iba1 had overlapping regional distributions confined to the lesion periphery, while no Iba1-positive microglia were observed within the epicenter of the lesion core (**Figures 3D,F**). By contrast,

GRP78 immunoreactivity was more evident in reactive astrocytes and activated microglia in the peri-lesional area on day 3 when compared to GRP78 immunoreactivity at day 1 after lesion induction (**Figure 3E**).

Seven days after lesion induction, triple-labeling of GRP78, Iba1, and GFAP revealed that the lesion core was evenly populated with Iba1-positive cells, nearly all of which expressed GRP78, although GRP78 expression was also observed in the vascular profiles (**Figures 4A,C,D**). In the peri-lesional area, intense GRP78 expression was observed in astrocytes and microglia, both of which showed distinct reactive phenotypes (**Figure 4B**).

As described above, GRP78 expression was induced in almost all Iba1-positive cells, including activated microglia/macrophages in the lesion core, and they appeared to gradually increase in number over 7 days after lesion induction. Quantitative temporal analysis revealed a progressive increase in the number of GRP78-positive microglia/macrophages at 3–7 days post-lesion (**Figure 4E**). In particular, the number of GRP78-positive microglia/macrophages in the lesion periphery was significantly higher than that in the epicenter in the striatum 3 days post-lesion.

Induction of GRP78 Expression Within Vascular Structures in the Striatum After 3-NP Injection

The above findings prompted us to investigate the association between GRP78 and blood vessels. Therefore, we performed double-labeling of GRP78 and the vascular endothelial cell marker RECA1. In striata from control rats (**Figure 5A**) and rats after 1 day of lesion induction (**Figure 5B**), GRP78 expression was absent or very weak within vascular profiles. At 3 days after lesion induction, triple-labeling of GRP78, RECA1, and Iba1 revealed that vessel-associated GRP78 expression was prominent in the lesion periphery, where GRP78-positive activated microglia/macrophages had accumulated (**Figures 5C,D**). In contrast, GRP78 immunoreactivity was observed only in a small fraction of the vasculature in the lesion epicenter, where microglia had not yet infiltrated (**Figure 5E**). We further characterized these microglia/macrophages expressing GRP78 by triple-labeling of GRP78, Iba1, and either ED1, which is expressed in the membranes of phagolysosomes in microglia and macrophages (Damoiseaux et al., 1994), or CD45, which is expressed in all nucleated hematopoietic cells or leukocytes (Penninger et al., 2001). As shown in **Figures 5F,G**, a small fraction of the GRP78/Iba1 double-labeled cells in the lesion core expressed ED1 or CD45 and showed amoeboid macrophage-like phenotypes, indicating that they were likely to be blood-derived macrophages, as reported previously (Guillemin and Brew, 2004).

Seven days after lesion induction, GRP78 immunoreactivity was localized to nearly all vessels in both the epicenter and the periphery of the lesion (**Figures 5H–J**). Next, we determined the relative proportion of vascular profiles occupied by GRP78 among all RECA1-positive vessels in the lesion core over a 7-day period after lesion induction. As shown in **Figure 5K**, 9.2% and 19.2% of all RECA1-positive vascular areas were covered by areas of GRP78 immunoreactivity in control sections and in lesioned striata 1 day after lesion induction, respectively. At 3 days after lesion induction, this proportion in the lesion periphery rose to 46.5%, which was significantly higher than that in the epicenter (23.1% of all vessels). At 7 days after lesion induction, the GRP78-positive area comprised 37.8% of the vascular area in both the periphery and the epicenter of the lesion core.

Spatiotemporal Coincidence Between Vascular GRP78 Expression and BBB Leakage in the Lesion Core After 3-NP Injection

In order to determine whether vessel-associated GRP78 expression could be related to the impairment of the BBB that occurred in the striatum of 3-NP treated rats, we infused FITC-albumin into the circulation via the tail vein at days 3 and 7 after 3-NP injection, and allowed the tracer to circulate for 1 h. On day 3 after lesion induction, triple-labeling of FITC-albumin, GRP78, and GFAP revealed that vessels with FITC-albumin were exclusively confined to the lesion core, where GFAP immunoreactivity was absent, while no noticeable vascular fluorescence was observed in the peri-lesional area (**Figure 6A**). In particular, we found that FITC-labeled vessels were more apparent in the lesion periphery than in the epicenter. This observation was supported by the results of triple-labeling of GRP78, FITC-albumin, and RECA1, which showed that both FITC-albumin and GRP78 were co-expressed in almost all the same vessels in the lesion periphery (**Figure 6B**). In addition, triple-labeling of FITC-albumin, GRP78, and Iba1 showed that FITC-labeled vessels were more prominent in the lesion periphery, where GRP78-positive microglia/macrophages had infiltrated, than in the microglia-free epicenter (**Figure 6C**). Higher magnification revealed that, in close proximity to FITC-labeled vessels, FITC-albumin accumulated within amoeboid-like brain macrophages, but not in activated microglia with evident processes, indicating that leaked FITC-albumin could be sequestered by brain macrophages (**Figure 6C**). At 7 days after lesion induction, triple-labeling of GRP78, FITC-albumin, and Iba1 revealed that FITC-albumin could be detected in both the periphery and the epicenter of the lesion core, indicating the overlapping distribution of GRP78-positive microglia/macrophage and BBB leakage (**Figure 6D**).

Phenotypic Characterization of Vessel-Associated GRP78-Positive Cells in the Lesion Core After 3-NP Injection

For the phenotypic characterization of GRP78-expressing cells associated with the vasculature in the lesion core, we performed double-labeling using GRP78 and two smooth muscle cell markers, α-SMA or NG2, both of which label smooth muscle cells (Jin et al., 2018b). As shown in **Figures 7A,B**, GRP78-positive cells in vascular profiles were positive for both smooth muscle cell markers. Next, we performed triple-labeling of GRP78, Iba1, and nestin, because a subset of vascular wall cells that are distinct from endothelial cells, pericytes, or smooth

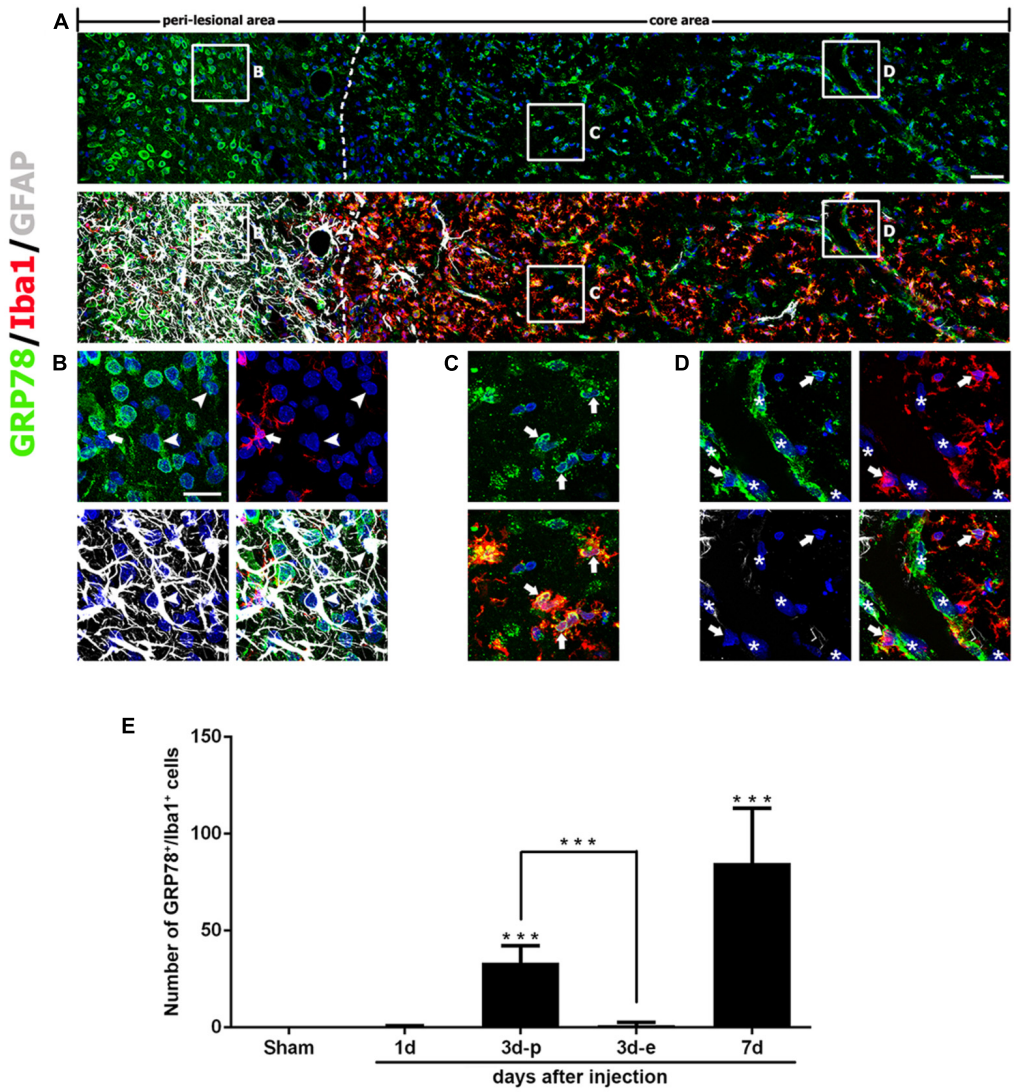

FIGURE 4 | Characterization of glucose-regulated protein (GRP78)-positive cells in lesioned striatum on day 7 after 3-nitropropionic acid injection. **(A)** Triple-labeling of GRP78, Iba1, and GFAP showing that the lesion core (right side of the broken line) is devoid of GFAP immunoreactivity, but is evenly filled with Iba1-positive cells, nearly all of which express GRP78. The boxed areas in the peri-lesional area and the lesion core are enlarged in the corresponding panels **B–D**. **(B)** In the peri-lesional area, evident GRP78 immunoreactivity is observed in reactive astrocytes (arrowheads) and activated microglia (arrows). **(C,D)** In the lesion core, intense GRP78 expression is observed in the vascular profiles (asterisks) and in activated microglia/macrophages (arrows). **(E)** Quantitative temporal analysis showing that the number of GRP78-positive microglia/macrophages increases progressively over a 7-day period after lesion induction. Note that the number of GRP78-positive microglia/macrophages is significantly higher in the lesion periphery than in the epicenter on day 3. The data are expressed as the mean ± standard error of the mean. ***$P < 0.001$ vs. saline-treated controls. Cell nuclei are stained with 4′,6-diamidino-2-phenylindole. Scale bars represent 50 μm for **A**; and 20 μm for **B–D**.

muscle cells express nestin, and can transform into fibroblast-like cells in the ischemic brain (Shin et al., 2013). As shown in **Figure 7C**, GRP78 expression was clearly detected in three types of vasculature-associated cells: endothelial cells, Iba1-positive microglia/macrophages, and nestin-positive perivascular cells that were devoid of Iba1 immunoreactivity. Thus, our data indicate a phenotypic heterogeneity of vascular GRP78-positive cells in the striatal lesions.

Light microscopic imaging alone was not sufficient to clarify the identity of vascular GRP78-positive cells and to establish the precise subcellular localization of GRP78 protein within these cells. Therefore, we performed correlative light- and immunogold-electron microscopic imaging to determine the precise localization of the light microscopic signals from subcellular structures. First, semi-thin sections double-labeled for GRP78 and RECA1 were observed using confocal microscopy, and the same semi-thin sections were subsequently subjected to electron microscopy (**Figures 8A–C,E,F**). Overlay of the confocal microscopy and transmission electron microscopy data confirmed that GRP78 protein, as indicated by silver-enhanced immunogold particles, was specifically localized to the cisternae of the rough ER in endothelial cells, but not to other organelles

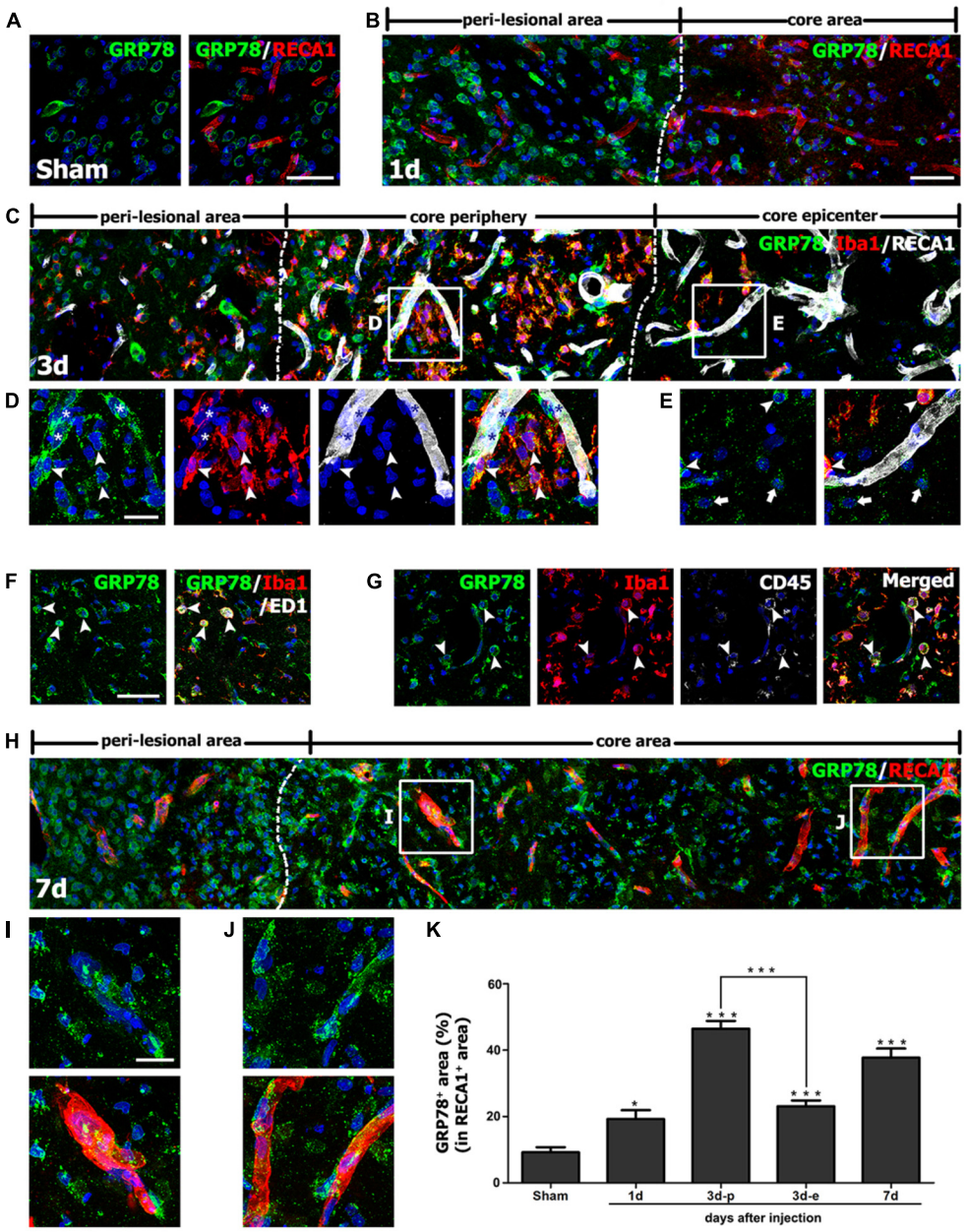

FIGURE 5 | Characterization of glucose-regulated protein (GRP78) expression associated with the vasculature in control and lesioned striata after 3-nitropropionic acid injection. **(A)** Double-labeling of GRP78 and the endothelial cell marker RECA1 in control striatum, showing that GRP78 immunoreactivity is negligible or absent within vessels. **(B)** Double-labeling of GRP78 and RECA1 1 day after lesion induction, showing that GRP78 immunoreactivity within vessels is negligible or very weak in the lesion core (right side of the broken line). **(C–E)** Lower- **(C)** and higher- **(D,E)** magnification views of sections triple-labeled for GRP78, Iba1, and RECA1 3 days after lesion induction. The boxed areas of the lesion periphery and the epicenter in **C** are enlarged in **D** and **E**, respectively. Notably, the lesion periphery is heavily infiltrated by GRP78/Iba1 double-labeled microglia/macrophages (arrowheads in **D**), while only some Iba1-positive microglia/macrophages can be detected in the epicenter (arrowheads in **E**). In addition, GRP78 expression is detectable in association with most of the vasculature (asterisks in **D**) in the lesion periphery. Arrows in **E** indicate presumptive dying or dead neurons that are devoid of significant GRP78 expression. **(F,G)** Triple-labeling of GRP78, Iba1, and either ED1 or CD45 on day 3 after lesion induction, showing that GRP78 is expressed in nearly all of ED1- (arrowheads in **F**) or CD45-positive cells (arrowheads in **G**), corresponding to only a small fraction of the GRP78/Iba1 double-labeled cells. Notably, these triple-labeled cells are frequently associated with blood vessels. **(H)** Double-labeling of GRP78 and RECA1 at 7 days after lesion induction, showing that GRP78 expression is evenly distributed throughout the lesion core (right side of the broken line). **(I,J)** Higher magnification images of the boxed areas in **H**, showing that GRP78 immunoreactivity is localized to nearly all vessels in both the lesion periphery **(I)** and epicenter **(J)**. **(K)** Quantitative temporal analysis of the proportion of vascular areas occupied by GRP78 immunoreactivity, within all RECA1-positive vessels. This proportion increases progressively by day 1, and then decreases slightly on day 7. Note that the vascular area covered by GRP78 is significantly higher in the lesion periphery than in the epicenter on day 3. The data are expressed as the mean ± standard error of the mean. $^{*}P < 0.05$ and $^{***}P < 0.001$ vs. saline-treated controls. Cell nuclei are stained with 4′,6-diamidino-2-phenylindole. Scale bars represent 50 μm for **A–C**, **F–H**; and 20 μm for **D**, **E**, **I**, **J**.

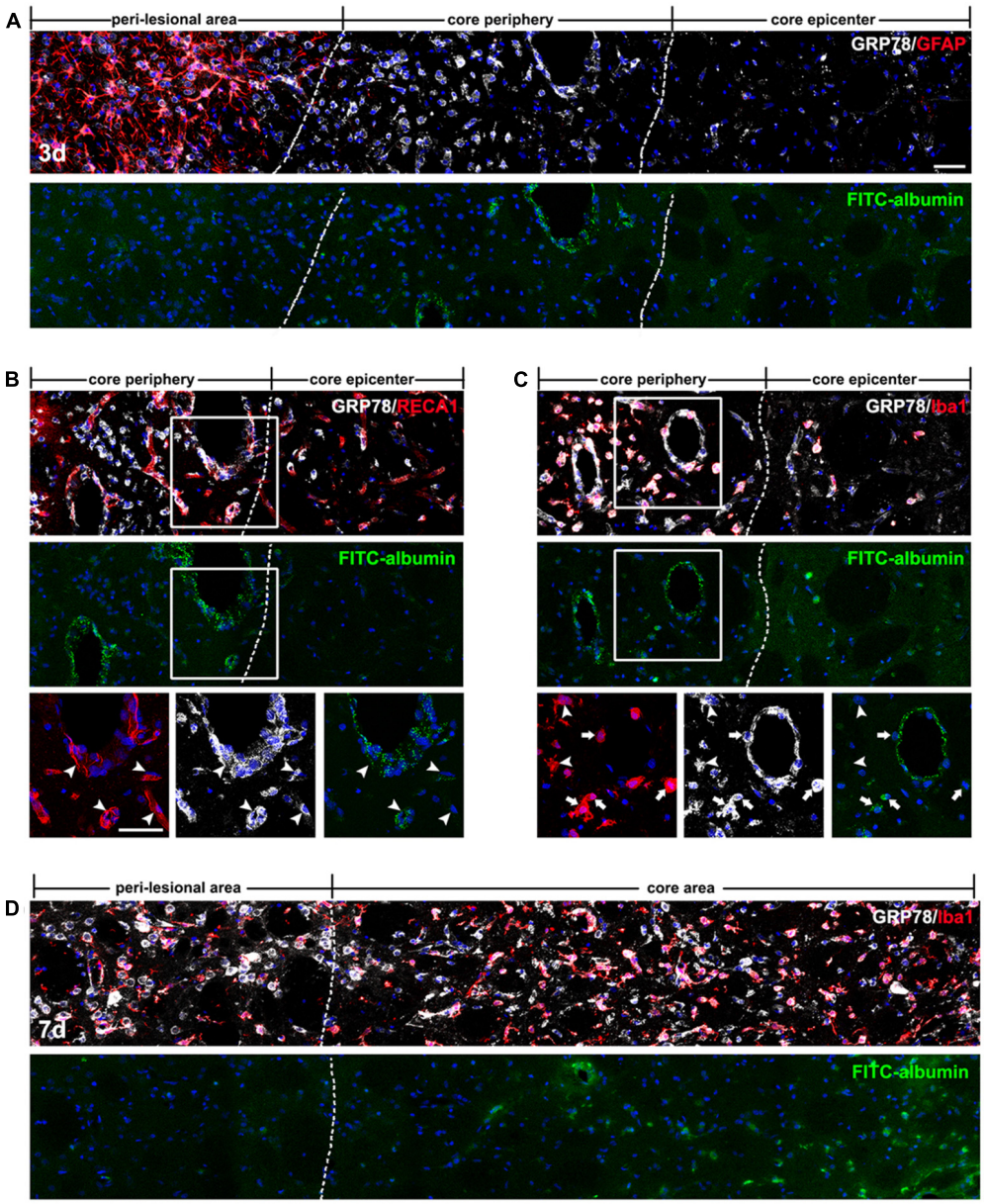

FIGURE 6 | Spatiotemporal coincidence between vascular glucose-regulated protein (GRP78) expression and blood–brain barrier (BBB) leakage, as indicated by extravasation of fluorescein isothiocyanate (FITC)-albumin in the striata lesion by 3-nitropropionic acid injection. **(A)** Triple-labeling of FITC-albumin, GRP78, and GFAP 3 days after lesion induction, showing that vessels labeled with FITC-albumin are distributed only in the periphery of the lesion core, and not in the peri-lesional area or the lesion epicenter. The two broken lines indicate the borders of the three areas: the peri-lesional area, lesion periphery, and epicenter. **(B)** Triple-labeling of FITC-albumin, GRP78, and RECA1 at day 3, showing that both FITC-albumin and GRP78 are detectable in nearly identical vessels (arrowheads) in the lesion periphery. **(C)** Triple-labeling of FITC-albumin, GRP78, and Iba1 at day 3, showing that in addition to vascular walls, FITC-albumin is detected in amoeboid-like brain macrophages (arrows), but not in activated microglia with evident processes (arrowheads). **(D)** Triple-labeling of FITC-albumin, GRP78, and Iba1 at 7 days after lesion induction, showing that tracer extravasation is detectable throughout the lesion core (right side of the broken line). Cell nuclei are stained with 4′,6-diamidino-2-phenylindole. Scale bars represent 50 μm for **A–D**.

such as mitochondria (**Figures 8B,C,F**). In addition, GRP78 protein was detected in cells that were closely apposed to the outer part of endothelial cells and smooth muscle cells (**Figures 8A,C**), indicating that these GRP78-expressing cells may correspond to nestin-positive cells, based on their location in the perivascular space. Thus, semi-thin sections triple-labeled for GRP78, nestin, and Iba1 were further analyzed with electron microscopy. As shown in **Figure 8D**, GRP78/nestin double-labeled cells that were devoid of Iba1 labeling were characterized by a large euchromatic nucleus with a prominent nucleolus and invariably lay outside the endothelial and smooth muscle cells, indicating that they may correspond to perivascular fibroblast-like cells, as described

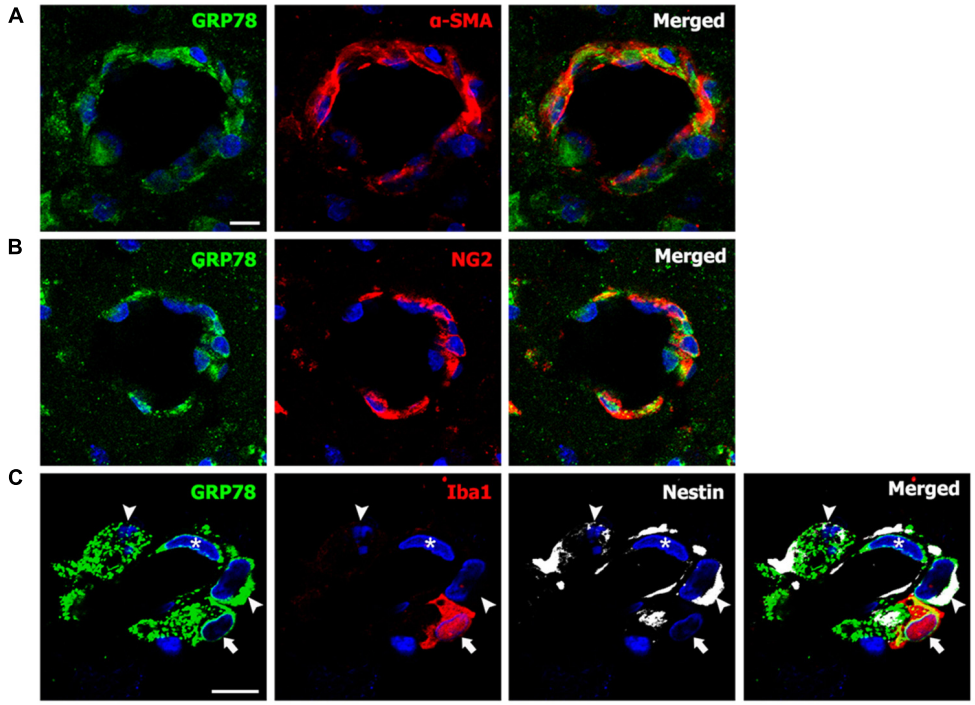

FIGURE 7 | Phenotypic characterization of vessel-associated glucose-regulated protein (GRP78)-positive cells in the lesion periphery on day 3 after lesion induction by 3-nitropropionic acid injection. **(A,B)** Double-labeling of GRP78 and two smooth muscle cell markers, alpha-smooth muscle actin (α-SMA) and NG2, showing that prominent GRP78 immunoreactivity is visible in smooth muscle cells. **(C)** Triple-labeling of GRP78, Iba1, and nestin showing that GRP78 expression can be detected in endothelial cells (asterisks), Iba1-positive microglia/macrophages (arrows), and nestin-positive perivascular cells (arrowheads). Cell nuclei are stained with 4′,6-diamidino-2-phenylindole. Scale bars represent 10 μm for **A–C**.

previously (Shin et al., 2013). GRP78 protein in these cells was mainly localized in the rough ER/perinuclear cisternae, some of which showed marked dilatation (**Figures 8C,D**). In smooth muscle cells, silver-enhanced immunogold particles targeted to GRP78 were specifically associated with the perinuclear cistern and the cisternae of the rough ER (**Figures 8E,F**).

DISCUSSION

We recently reported that, in a rat model of stroke, GRP78 expression is induced in activated glial cells, predominantly in brain macrophages and reactive astrocytes in the infarct and peri-infarct areas, respectively (Jin et al., 2018a). In the present study, by using a 3-NP injection model, we further investigated the induction of GRP78 expression in response to neurotoxic insults. In agreement with our previous findings (Jin et al., 2018a), constitutive GRP78 expression was observed in striatal neurons, and expression was induced in association with activated glial cells in the striata of rats treated with 3-NP. Glial induction of prominent GRP78 expression could be attributed to activated microglia/macrophages and reactive astrocytes. In addition, the present study provides new evidence for the prominent induction of GRP78 within vascular profiles in the striatal lesion. Although the model of ischemic stroke and the 3-NP model have commonalities including BBB breakdown and lead to the formation of striatal lesions consisting of a lesion core and peri-lesional area (Mu et al., 2016), the 3-NP model employed in the present study shows a better-preserved lesion core, because well-demarcated striatal lesions do not spread to the cerebral cortex (Duran-Vilaregut et al., 2010; Mu et al., 2016; Riew et al., 2017). Thus, this 3-NP model allows a detailed characterization of the time course of GRP78 expression in the lesion core, especially within vascular profiles that are difficult to observe when tissue damage is severe. Together with our previous findings (Jin et al., 2018a), our data demonstrate a strong correlation between GRP78 expression and an activated functional status of neuroglial cells during CNS insults, and provide novel evidence to show that cells of the vascular wall also contribute to the increased GRP78 expression in the lesion core (**Figure 9**).

Notably, we found that vascular induction of GRP78 showed characteristic spatiotemporal patterns during the post-injury period. GRP78 expression was negligible or very weak in the control striata and at 1 day after lesion induction. However, expression was detectable at the edge of the lesion core by day 3 after lesion induction, and was evenly distributed throughout the lesion core by day 7. The proportion of vascular area covered by GRP78 immunoreactivity within all RECA1-positive vessels was significantly higher in the lesion periphery than in the epicenter 3 days after lesion induction. Interestingly, vascular GRP78 expression was correlated temporally and spatially with infiltration of activated microglia into the lesion core.

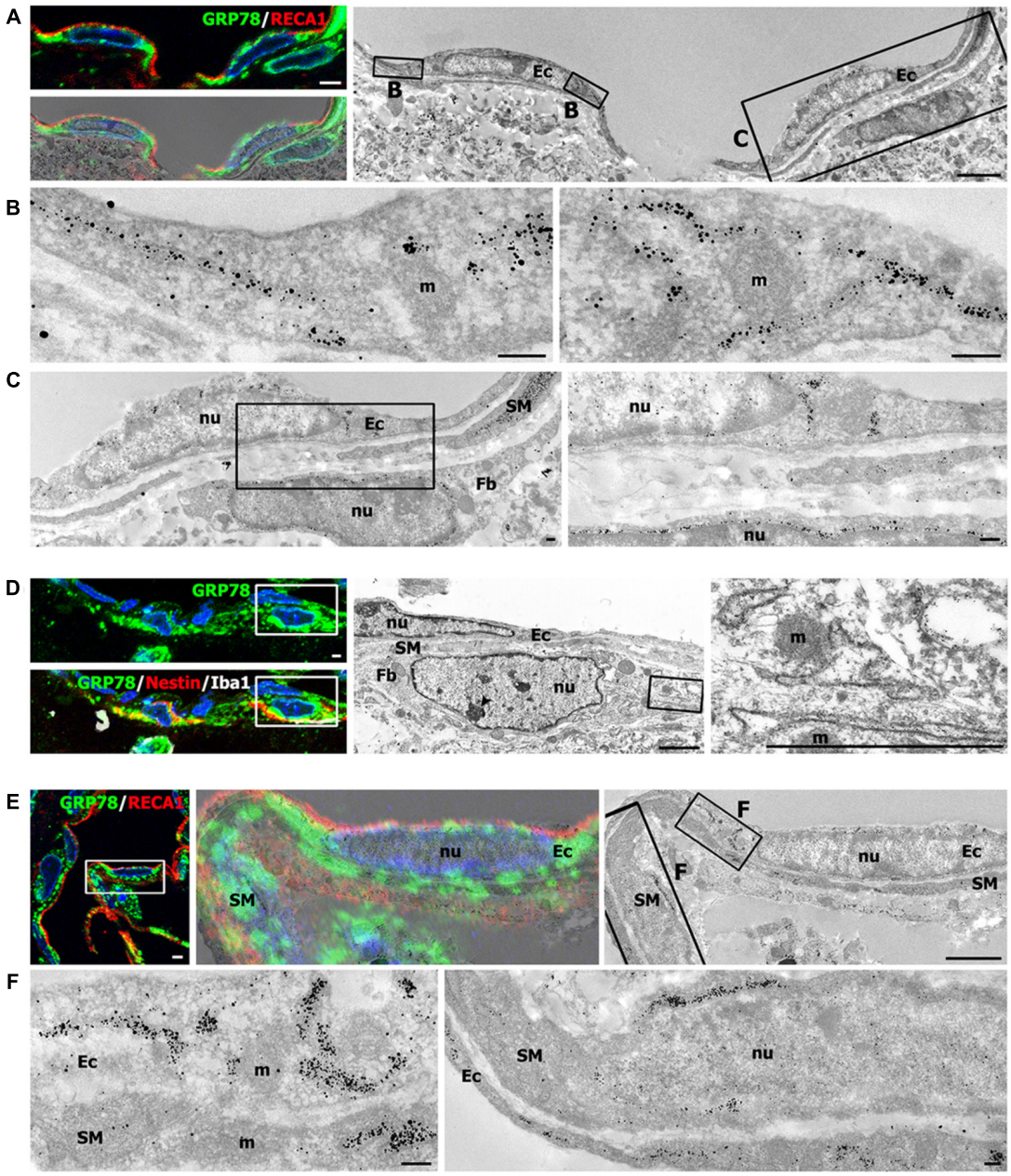

FIGURE 8 | Ultrastructural characterization of vascular glucose-regulated protein (GRP78)-positive cells in the lesion periphery at 3 days after lesion induction by 3-nitropropionic acid injection. **(A)** Confocal microscopic image of a semi-thin section double-labeled with GRP78 and RECA1 (left upper panel), image of confocal microscopic data overlaid onto the corresponding electron microscopic image (left lower panel), and the corresponding transmission electron microscopic image obtained from the same field (right panel). **(B,C)** Higher-magnification views of the boxed areas in **A**. The boxed area in the left panel of **C** is enlarged in the right panel of **C**. Notably, GRP78 protein, as indicated by silver-enhanced immunogold particles, is specifically localized to the cisternae of the rough endoplasmic reticulum (rER), but not to other organelles within endothelial cells (Ec), such as mitochondria (m) or nuclei (nu). In addition, GRP78 protein is detectable in perivascular cells (Fb) that are closely apposed to the outer part of endothelial cells and smooth muscle cells (SM). **(D)** Confocal microscopic image of a semi-thin section triple-labeled for GRP78, Iba1, and nestin (left panel), and the corresponding electron microscopic image of the boxed areas in the left panels (middle panel). The boxed area in the middle panel is enlarged in the right panel. Note that the GRP78/nestin double-labeled cell (Fb) has a large euchromatic nucleus (nu) with prominent nucleolus (arrowhead), and was invariably located outside the endothelial cells (Ec) and smooth muscle cells (SM). Furthermore, GRP78 protein is mainly localized in the rER/perinuclear cisternae, but not in the mitochondria (m) or nucleus (nu) of GRP78/nestin double-labeled cells. **(E)** Confocal microscopic image of a semi-thin section double-labeled for GRP78 and RECA1 (left panel), the corresponding transmission electron microscopic image of the boxed area in the left panel (right panel), and their overlay image (middle panel). **(F)** Higher-magnification images of the boxed areas in the right panel of **E**. Notably, the silver-enhanced immunogold particles targeted to GRP78 are specifically associated with the perinuclear cistern and the cisternae of the rER of endothelial cells (Ec) and smooth muscle cells (SM), but not with mitochondria (m). Cell nuclei are stained with 4′,6-diamidino-2-phenylindole. Scale bars represent 2 μm for **A**, **D**, **E**; 1 μm for **C**; and 0.2 μm for **B**, **F**.

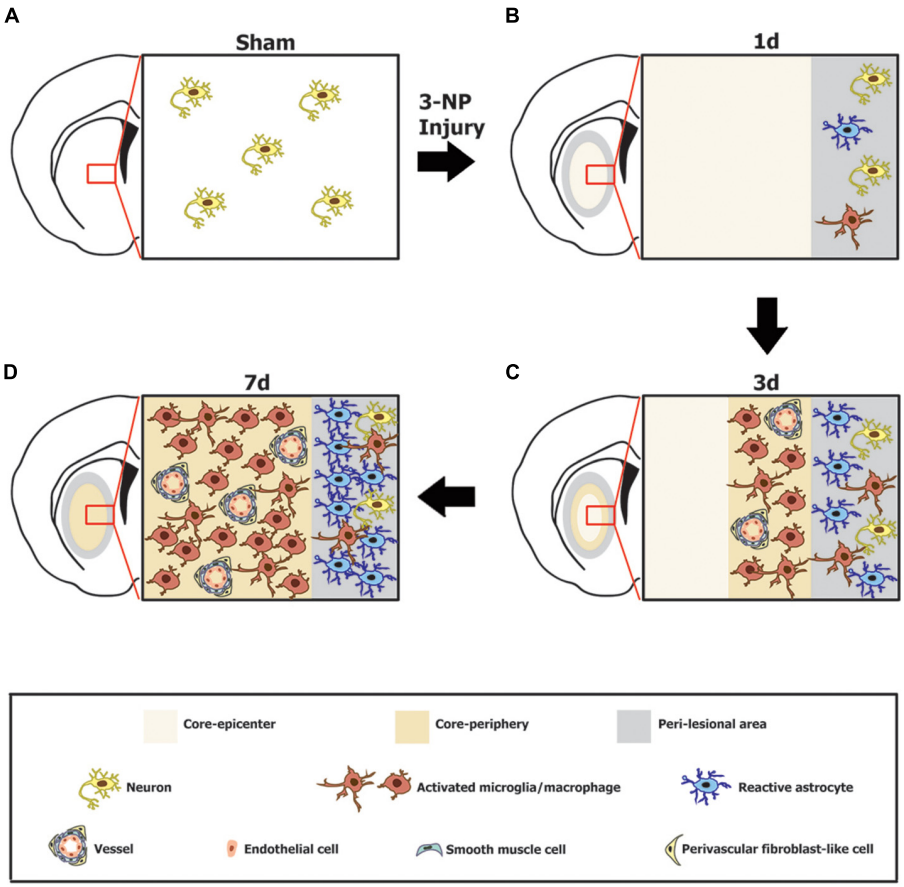

FIGURE 9 | Schematic representation of the phenotypic heterogeneity of GRP78-positive cells in the lesion core and perilesional area in the striata after lesion induction using 3-nitropropionic acid injection. **(A)** In the saline-treated control striatum, GRP78 immunoreactivity is almost exclusively localized to striatal neurons. **(B)** One day after 3-NP injection, neuronal profiles are absent from the lesion core, while neurons in the peri-lesional area show evident GRP78 immunoreactivity. In addition, astrocytes and microglia in the peri-lesional area show very weak immunoreactivity for GRP78. **(C)** Three days after lesion induction, GRP78 expression is induced in association with activated microglia/macrophages and the vascular wall, including endothelial cells, smooth muscle cells, and adventitial fibroblast-like cells in the lesion periphery, although these cell types are absent from the lesion epicenter. In addition, evident GRP78 immunoreactivity is observed in reactive astrocytes and activated microglia in the perilesional area. **(D)** Seven days after lesion induction, intense GRP78 expression is observed in the vascular profiles and in activated microglia/macrophages throughout the lesion core. In addition, intense GRP78 expression is observed in reactive astrocytes and activated microglia in the peri-lesional area.

In agreement with our previous reports (Jin et al., 2018b), activated microglia/macrophages appeared at the lesion edge 3 days after lesion induction, with infiltration throughout the lesion core being clearly observed by day 7. This distribution of reactive microglia is analogous with previously published data on their band-like accumulation in regions surrounding the ischemic core during the first week of ischemic stroke (Li et al., 2013, 2014), indicating that instead of containing pre-existing microglia, the lesion core was progressively infiltrated by microglia migrating from the peri-lesional area. These activated microglia/macrophages showed intense immunoreactivity for GRP78, as previously reported (Fan et al., 2015; Yang et al., 2015; Corsetti et al., 2017; Jin et al., 2018a). Thus, the temporal patterns of vascular GRP78 appeared to overlap with the period during which GRP78 was expressed by microglia/macrophages recruited into the lesion core. Recent studies have shown that under pathological conditions such as ischemic insults, BBB disruption is closely correlated with accumulation of activated microglia, suggesting that microglia are associated with blood vessel dysfunction and pro-inflammatory signaling (Matsumoto et al., 2012; Barkauskas et al., 2015; Jolivel et al., 2015; Dudvarski Stankovic et al., 2016). However, further studies using microglia/macrophage-specific GRP78-null or over-expressing mice are needed to determine whether GRP78 induction in activated microglia and macrophages indeed reflects its potential functions.

Our data revealed that vessel-associated GRP78 expression could be related to BBB impairment in the striatal lesion. Indeed, BBB breakdown in the striatum has been reported previously in rat models of 3-NP-induced Huntington's disease (Sarkar and Schmued, 2010; Duran-Vilaregut et al., 2011). Our data also showed that some of GRP78/Iba1 double-labeled cells with amoeboid macrophage-like phenotypes were often localized in the vicinity of blood vessels, and that they expressed CD45,

which is a marker of blood-derived macrophages (Guillemin and Brew, 2004). Given that microgliosis in the ischemic area is mainly due to proliferating resident microglia and not infiltrating macrophages (Li et al., 2013), GRP78/Iba1/CD45 triple-labeled cells, corresponding to only a small fraction of the GRP78/Iba1 double-labeled cells, might be infiltrating macrophages, and they may presumably infiltrate the lesion core through the compromised BBB induced by 3-NP. Moreover, the extravasation of the established BBB permeability marker FITC-albumin (Michalski et al., 2010; Krueger et al., 2015) was exclusively detectable in the lesion core, where astrocytes are virtually absent, but not in the peri-lesional area. In particular, vascular induction of GRP78 expression in the lesion core at days 3 and 7 days after 3-NP injection was coincident with the time and distribution of BBB leakage. Thus, vascular expression of GRP78 was correlated temporally and spatially with focal BBB breakdown and concomitantly occurring recruitment of activated microglia/macrophages induced by 3-NP. Considering that increased GRP78 could act as an inhibitor of macrophage adhesion (Bai et al., 2014) and enhance phagocytosis of amyloid-β peptides by microglia (Kakimura et al., 2001), GRP78 induction in activated microglia/macrophages might play a role in the activation/recruitment of these cells to the injured striatum, although the exact role played by GRP78 remains unclear.

A growing body of evidence suggests a novel role for GRP78 in the regulation of the BBB, despite its main function as a cellular chaperone protein. Alteration of GRP78 expression in vascular endothelial cells occurs in response to BBB disruption following subarachnoid hemorrhage (Yan et al., 2011). GRP78, associated with its cofactor HTJ-1, can be translocated and anchored to the cell surface by oxidized phospholipids, suggesting that GRP78 is a novel receptor initiating a protective vascular barrier response to oxidized phospholipids (Birukova et al., 2014). By contrast, lead exposure induces GRP78 expression in brain endothelial cells, which leads to Src activation and subsequent reduction of tight junctional proteins, with ensuing BBB disruption (Song et al., 2014). In addition, a recent study demonstrated that exposure to GRP78-specific recombinant antibodies results in increased BBB leakage, suggesting that GRP78 autoantibodies are associated with BBB disruption in neuromyelitis optica (Shimizu et al., 2017). Collectively, these results, including our present findings, suggest that GRP78 expression may be related to the development of BBB impairment in rats treated with 3-NP; however, the precise role of GRP78 in this process remains unclear. In addition, it remains to be clarified whether the increased GRP78 expression is a cause or a consequence of the BBB impairment. Thus, additional experiments, including two-photon microscopy for temporal and spatial *in vivo* imaging of BBB disruption, are required to clarify the role of GRP78 in BBB impairment.

Despite the potential relationship between GRP78 expression and BBB integrity, little is known about vessel-associated cells expressing GRP78 in the lesion core. Although a limited number of studies have reported GRP78 expression in vascular endothelial cells (Yan et al., 2011; Birukova et al., 2014; Song et al., 2014), to our knowledge, this is the first study to show that, in addition to endothelial cells, smooth muscle cells and adventitial cells also express GRP78. In particular, adventitial cells had the following features that were similar to those of perivascular fibroblast-like cells, reported in our previous study, although their exact cellular identity had not been elucidated: they were localized along the outer part of smooth muscle cells, had euchromatic nuclei with prominent nucleoli, and coexpressed GRP78 with nestin (Shin et al., 2013). A correlative approach using light and electron microscopy clearly demonstrated that, in these vasculature-associated cells, conspicuous silver-enhanced grains indicative of GRP78 were specifically localized in the rough ER/perinuclear cisternae, indicating that despite the phenotypic heterogeneity of vascular GRP78-positive cells, GRP78 was present as an ER protein in these cells. This ER localization of GRP78 in endothelial cells is unexpected considering that GRP78 is redistributed from the ER to the cytosol or plasma membrane of endothelial cells *in vitro*, where it acts as a receptor mediating for controlling cell viability and signaling (Birukova et al., 2014; Song et al., 2014). In our previous studies, however, GRP78 protein was almost exclusively localized to the rough ER in both constitutive cells (neurons) and cells induced by ER stress (reactive astrocytes and brain macrophages) after focal cerebral ischemia (Jin et al., 2018a). Interestingly, cells capable of GRP78 induction, such as activated microglia/macrophages, reactive astrocytes, and vessel-associated cells, particularly fibroblast-like adventitial cells, shared the following characteristics: they underwent marked morphological changes distinct from the cells in the control rats, and they had well-developed rough ER with prominent cisternal dilation, implying that protein synthesis was actively occurring in these cells. Thus, the previous findings and our observations indicate that although GRP78-positive cells in striatal lesions may represent a heterogeneous population of cells with functional diversity, GRP78 act as an ER-localized chaperone. However, further investigation is needed to determine the reason for GRP78 induction in these vascular cells, and to ascertain whether increased GRP78 expression reflects a specific function for this protein in the lesion core.

In summary, our data showed that constitutive GRP78 immunoreactivity was almost exclusively localized to striatal neurons, but it was induced in association with activated microglia/macrophages and reactive astrocytes in the striata of rats treated with 3-NP. In addition, GRP78 was induced in cells of the vascular wall, including endothelial cells, smooth muscle cells, and adventitial fibroblast-like cells, in which GRP78 protein was specifically localized in the rough ER/perinuclear cisternae. The vascular induction of GRP78 appeared to correlate temporally and spatially with infiltration of activated microglia into the lesion core, and coincided with BBB leakage, indicating that the expression of GRP78 was induced in vessels with BBB impairment in the lesion core. Thus, our data further support the link between GRP78 expression and an activated functional status of neuroglial cells during CNS insults, and provide a novel insight into the phenotypic and functional heterogeneity of GRP78-positive cells, suggesting GRP78 involvement in the activation/recruitment of activated microglia/macrophages and

its potential role in the BBB impairment that occurs in response to neurotoxic insults such as 3-NP.

AUTHOR CONTRIBUTIONS

All authors have contributed significantly to the research and the article preparation. XJ contributed to the treatment of the experimental animals, immunohistochemistry, immunoelectron microscopy, and quantitative analysis. T-RR and SK worked on the treatment of the experimental animals and immunohistochemistry. HK worked on the electron microscopy. M-YL worked on the design of the study, data analysis, and final manuscript preparation.

FUNDING

This research was supported by the Basic Science Research Program through the National Research Foundation of Korea (NRF) funded by the Ministry of Science, ICT and Future Planning (NRF2017R1A2B4002922).

REFERENCES

Aoki, M., Tamatani, M., Taniguchi, M., Yamaguchi, A., Bando, Y., Kasai, K., et al. (2001). Hypothermic treatment restores glucose regulated protein 78 (GRP78) expression in ischemic brain. *Brain Res. Mol. Brain Res.* 95, 117–128. doi: 10.1016/S0169-328X(01)00255-8

Bai, H., Li, N., Zhou, X., Wang, C., Zhang, Y., Zhu, X., et al. (2014). GRP78 inhibits macrophage adhesion via SR-A. *J. Biomed. Res.* 28, 269–274. doi: 10.7555/jbr.28.20130054

Barkauskas, D. S., Dixon Dorand, R., Myers, J. T., Evans, T. A., Barkauskas, K. J., Askew, D., et al. (2015). Focal transient CNS vessel leak provides a tissue niche for sequential immune cell accumulation during the asymptomatic phase of EAE induction. *Exp. Neurol.* 266, 74–85. doi: 10.1016/j.expneurol.2015.02.018

Beal, M. F., Brouillet, E., Jenkins, B. G., Ferrante, R. J., Kowall, N. W., Miller, J. M., et al. (1993). Neurochemical and histologic characterization of striatal excitotoxic lesions produced by the mitochondrial toxin 3-nitropropionic acid. *J. Neurosci.* 13, 4181–4192. doi: 10.1523/JNEUROSCI.13-10-04181.1993

Birukova, A. A., Singleton, P. A., Gawlak, G., Tian, X., Mirzapoiazova, T., Mambetsariev, B., et al. (2014). GRP78 is a novel receptor initiating a vascular barrier protective response to oxidized phospholipids. *Mol. Biol. Cell* 25, 2006–2016. doi: 10.1091/mbc.E13-12-0743

Bole, D. G., Dowin, R., Doriaux, M., and Jamieson, J. D. (1989). Immunocytochemical localization of BiP to the rough endoplasmic reticulum: evidence for protein sorting by selective retention. *J. Histochem. Cytochem.* 37, 1817–1823. doi: 10.1177/37.12.2685110

Borlongan, C. V., Koutouzis, T. K., and Sanberg, P. R. (1997). 3-Nitropropionic acid animal model and Huntington's disease. *Neurosci. Biobehav. Rev.* 21, 289–293. doi: 10.1016/S0149-7634(96)00027-9

Casas, C. (2017). GRP78 at the centre of the stage in cancer and neuroprotection. *Front. Neurosci.* 11:177. doi: 10.3389/fnins.2017.00177

Chen, J., Guo, H., Zheng, G., and Shi, Z. N. (2013). Region-specific vulnerability to endoplasmic reticulum stress-induced neuronal death in rat brain after status epilepticus. *J. Biosci.* 38, 877–886. doi: 10.1007/s12038-013-9391-y

Choi, J. H., Riew, T. R., Kim, H. L., Jin, X., and Lee, M. Y. (2017). Desmin expression profile in reactive astrocytes in the 3-nitropropionic acid-lesioned striatum of rat: characterization and comparison with glial fibrillary acidic protein and nestin. *Acta Histochem.* 119, 795–803. doi: 10.1016/j.acthis.2017.10.003

Corsetti, G., Romano, C., Stacchiotti, A., Pasini, E., and Dioguardi, F. S. (2017). Endoplasmic reticulum stress and apoptosis triggered by sub-chronic lead exposure in mice spleen: a histopathological study. *Biol. Trace Elem. Res.* 178, 86–97. doi: 10.1007/s12011-016-0912-z

Damoiseaux, J. G., Dopp, E. A., Calame, W., Chao, D., MacPherson, G. G., and Dijkstra, C. D. (1994). Rat macrophage lysosomal membrane antigen recognized by monoclonal antibody ED1. *Immunology* 83, 140–147.

Dudvarski Stankovic, N., Teodorczyk, M., Ploen, R., Zipp, F., and Schmidt, M. H. H. (2016). Microglia-blood vessel interactions: a double-edged sword in brain pathologies. *Acta Neuropathol.* 131, 347–363. doi: 10.1007/s00401-015-1524-y

Duran-Vilaregut, J., Del Valle, J., Manich, G., Junyent, F., Camins, A., Pallas, M., et al. (2010). Systemic administration of 3-nitropropionic acid points out a different role for active caspase-3 in neurons and astrocytes. *Neurochem. Int.* 56, 443–450. doi: 10.1016/j.neuint.2009.12.001

Duran-Vilaregut, J., Manich, G., del Valle, J., Pallas, M., Camins, A., Pelegri, C., et al. (2011). Neuronal apoptosis in the striatum of rats treated with 3-nitropropionic acid is not triggered by cell-cycle re-entry. *Neurotoxicology* 32, 734–741. doi: 10.1016/j.neuro.2011.07.009

Fan, H., Tang, H. B., Kang, J., Shan, L., Song, H., Zhu, K., et al. (2015). Involvement of endoplasmic reticulum stress in the necroptosis of microglia/macrophages after spinal cord injury. *Neuroscience* 311, 362–373. doi: 10.1016/j.neuroscience.2015.10.049

Gonzalez-Gronow, M., Selim, M. A., Papalas, J., and Pizzo, S. V. (2009). GRP78: a multifunctional receptor on the cell surface. *Antioxid. Redox Signal.* 11, 2299–2306. doi: 10.1089/ars.2009.2568

Guillemin, G. J., and Brew, B. J. (2004). Microglia, macrophages, perivascular macrophages, and pericytes: a review of function and identification. *J. Leukoc. Biol.* 75, 388–397. doi: 10.1189/jlb.0303114

Hamilton, B. F., and Gould, D. H. (1987). Nature and distribution of brain lesions in rats intoxicated with 3-nitropropionic acid: a type of hypoxic (energy deficient) brain damage. *Acta Neuropathol.* 72, 286–297. doi: 10.1007/BF00691103

Ito, D., Tanaka, K., Suzuki, S., Dembo, T., Kosakai, A., and Fukuuchi, Y. (2001). Up-regulation of the Ire1-mediated signaling molecule, bip, in ischemic rat brain. *Neuroreport* 12, 4023–4028. doi: 10.1097/00001756-200112210-00034

Jin, X., Kim, D. K., Riew, T. R., Kim, H. L., and Lee, M. Y. (2018a). Cellular and subcellular localization of endoplasmic reticulum chaperone GRP78 following transient focal cerebral ischemia in rats. *Neurochem. Res.* 43, 1348–1362. doi: 10.1007/s11064-018-2550-7

Jin, X., Riew, T. R., Kim, H. L., Choi, J. H., and Lee, M. Y. (2018b). Morphological characterization of NG2 glia and their association with neuroglial cells in the 3-nitropropionic acid-lesioned striatum of rat. *Sci. Rep.* 8:5942. doi: 10.1038/s41598-018-24385-0

Jolivel, V., Bicker, F., Biname, F., Ploen, R., Keller, S., Gollan, R., et al. (2015). Perivascular microglia promote blood vessel disintegration in the ischemic penumbra. *Acta Neuropathol.* 129, 279–295. doi: 10.1007/s00401-014-1372-1

Kakimura, J., Kitamura, Y., Taniguchi, T., Shimohama, S., and Gebicke-Haerter, P. J. (2001). Bip/GRP78-induced production of cytokines and uptake of amyloid-beta(1-42) peptide in microglia. *Biochem. Biophys. Res. Commun.* 281, 6–10. doi: 10.1006/bbrc.2001.4299

Ko, S. B., Ortega-Gutierrez, S., Choi, H. A., Claassen, J., Presciutti, M., Schmidt, J. M., et al. (2011). Status epilepticus-induced hyperemia and brain tissue hypoxia after cardiac arrest. *Arch. Neurol.* 68, 1323–1326. doi: 10.1001/archneurol.2011.240

Krueger, M., Bechmann, I., Immig, K., Reichenbach, A., Hartig, W., and Michalski, D. (2015). Blood-brain barrier breakdown involves four distinct stages of vascular damage in various models of experimental focal cerebral ischemia. *J. Cereb. Blood Flow Metab.* 35, 292–303. doi: 10.1038/jcbfm.2014.199

Li, Q., Dong, C., Li, W., Bu, W., Wu, J., and Zhao, W. (2014). Neuropeptide Y protects cerebral cortical neurons by regulating microglial immune function. *Neural Regen. Res.* 9, 959–967. doi: 10.4103/1673-5374.133140

Li, T., Pang, S., Yu, Y., Wu, X., Guo, J., and Zhang, S. (2013). Proliferation of parenchymal microglia is the main source of microgliosis after ischaemic stroke. *Brain* 136, 3578–3588. doi: 10.1093/brain/awt287

Liu, Q., Zhao, D., Ji, Y. X., Huang, X. Y., Yang, P., Wang, Y. Z., et al. (2016). Role of glucose-regulated protein 78 in early brain injury after experimental

subarachnoid hemorrhage in rats. *J. Huazhong Univ. Sci. Technol. Med. Sci.* 36, 168–173. doi: 10.1007/s11596-016-1561-3

Liu, X., Xu, K., Yan, M., Wang, Y., and Zheng, X. (2010). Protective effects of galantamine against abeta-induced PC12 cell apoptosis by preventing mitochondrial dysfunction and endoplasmic reticulum stress. *Neurochem. Int.* 57, 588–599. doi: 10.1016/j.neuint.2010.07.007

Matsumoto, J., Dohgu, S., Takata, F., Nishioku, T., Sumi, N., Machida, T., et al. (2012). Lipopolysaccharide-activated microglia lower P-glycoprotein function in brain microvascular endothelial cells. *Neurosci. Lett.* 524, 45–48. doi: 10.1016/j.neulet.2012.07.004

Matsuyama, D., Watanabe, M., Suyama, K., Kuroiwa, M., and Mochida, J. (2014). Endoplasmic reticulum stress response in the rat contusive spinal cord injury model-susceptibility in specific cell types. *Spinal Cord* 52, 9–16. doi: 10.1038/sc.2013.118

Michalski, D., Grosche, J., Pelz, J., Schneider, D., Weise, C., Bauer, U., et al. (2010). A novel quantification of blood-brain barrier damage and histochemical typing after embolic stroke in rats. *Brain Res.* 1359, 186–200. doi: 10.1016/j.brainres.2010.08.045

Misra, U. K., Payne, S., and Pizzo, S. V. (2011). Ligation of prostate cancer cell surface GRP78 activates a proproliferative and antiapoptotic feedback loop: a role for secreted prostate-specific antigen. *J. Biol. Chem.* 286, 1248–1259. doi: 10.1074/jbc.M110.129767

Misra, U. K., and Pizzo, S. V. (2010a). Ligation of cell surface GRP78 with antibody directed against the COOH-terminal domain of GRP78 suppresses Ras/MAPK and PI 3-kinase/AKT signaling while promoting caspase activation in human prostate cancer cells. *Cancer Biol. Ther.* 9, 142–152. doi: 10.4161/cbt.9.2.10422

Misra, U. K., and Pizzo, S. V. (2010b). Modulation of the unfolded protein response in prostate cancer cells by antibody-directed against the carboxyl-terminal domain of GRP78. *Apoptosis* 15, 173–182. doi: 10.1007/s10495-009-0430-y

Mu, S., Liu, B., Ouyang, L., Zhan, M., Chen, S., Wu, J., et al. (2016). Characteristic changes of astrocyte and microglia in rat striatum induced by 3-NP and MCAO. *Neurochem. Res.* 41, 707–714. doi: 10.1007/s11064-015-1739-2

Ni, M., Zhang, Y., and Lee, A. S. (2011). Beyond the endoplasmic reticulum: atypical GRP78 in cell viability, signalling and therapeutic targeting. *Biochem. J.* 434, 181–188. doi: 10.1042/bj20101569

Ohri, S. S., Maddie, M. A., Zhang, Y., Shields, C. B., Hetman, M., and Whittemore, S. R. (2012). Deletion of the pro-apoptotic endoplasmic reticulum stress response effector CHOP does not result in improved locomotor function after severe contusive spinal cord injury. *J. Neurotrauma* 29, 579–588. doi: 10.1089/neu.2011.1940

Oida, Y., Izuta, H., Oyagi, A., Shimazawa, M., Kudo, T., Imaizumi, K., et al. (2008). Induction of BiP, an ER-resident protein, prevents the neuronal death induced by transient forebrain ischemia in gerbil. *Brain Res.* 1208, 217–224. doi: 10.1016/j.brainres.2008.02.068

Osada, N., Kosuge, Y., Ishige, K., and Ito, Y. (2010). Characterization of neuronal and astroglial responses to ER stress in the hippocampal CA1 area in mice following transient forebrain ischemia. *Neurochem. Int.* 57, 1–7. doi: 10.1016/j.neuint.2010.03.017

Ouyang, Y. B., Xu, L. J., Emery, J. F., Lee, A. S., and Giffard, R. G. (2011). Overexpressing GRP78 influences Ca2+ handling and function of mitochondria in astrocytes after ischemia-like stress. *Mitochondrion* 11, 279–286. doi: 10.1016/j.mito.2010.10.007

Paxinos, G., and Watson, C. (2006). *The Rat Brain in Stereotaxic Coordinates*, 6th Edn. New York, NY: Academic Press.

Penas, C., Font-Nieves, M., Fores, J., Petegnief, V., Planas, A., Navarro, X., et al. (2011). Autophagy, and BiP level decrease are early key events in retrograde degeneration of motoneurons. *Cell Death Differ.* 18, 1617–1627. doi: 10.1038/cdd.2011.24

Penas, C., Guzman, M. S., Verdu, E., Fores, J., Navarro, X., and Casas, C. (2007). Spinal cord injury induces endoplasmic reticulum stress with different cell-type dependent response. *J. Neurochem.* 102, 1242–1255. doi: 10.1111/j.1471-4159.2007.04671.x

Penninger, J. M., Irie-Sasaki, J., Sasaki, T., and Oliveira-dos-Santos, A. J. (2001). CD45: new jobs for an old acquaintance. *Nat. Immunol.* 2, 389–396. doi: 10.1038/87687

Riew, T. R., Kim, H. L., Jin, X., Choi, J. H., Shin, Y. J., Kim, J. S., et al. (2017). Spatiotemporal expression of osteopontin in the striatum of rats subjected to the mitochondrial toxin 3-nitropropionic acid correlates with microcalcification. *Sci. Rep.* 7:45173. doi: 10.1038/srep45173

Sarkar, S., and Schmued, L. (2010). Kainic acid and 3-Nitropropionic acid induced expression of laminin in vascular elements of the rat brain. *Brain Res.* 1352, 239–247. doi: 10.1016/j.brainres.2010.07.011

Shibata, M., Hattori, H., Sasaki, T., Gotoh, J., Hamada, J., and Fukuuchi, Y. (2003). Activation of caspase-12 by endoplasmic reticulum stress induced by transient middle cerebral artery occlusion in mice. *Neuroscience* 118, 491–499. doi: 10.1016/S0306-4522(02)00910-7

Shimizu, F., Schaller, K. L., Owens, G. P., Cotleur, A. C., Kellner, D., Takeshita, Y., et al. (2017). Glucose-regulated protein 78 autoantibody associates with blood-brain barrier disruption in neuromyelitis optica. *Sci. Transl. Med.* 9:eaai9111. doi: 10.1126/scitranslmed.aai9111

Shin, Y. J., Kim, H. L., Park, J. M., Cho, J. M., Kim, S. Y., and Lee, M. Y. (2013). Characterization of nestin expression and vessel association in the ischemic core following focal cerebral ischemia in rats. *Cell Tissue Res.* 351, 383–395. doi: 10.1007/s00441-012-1538-x

Song, H., Zheng, G., Shen, X. F., Liu, X. Q., Luo, W. J., and Chen, J. Y. (2014). Reduction of brain barrier tight junctional proteins by lead exposure: role of activation of nonreceptor tyrosine kinase Src via chaperon GRP78. *Toxicol. Sci.* 138, 393–402. doi: 10.1093/toxsci/kfu007

Sun, F. C., Wei, S., Li, C. W., Chang, Y. S., Chao, C. C., and Lai, Y. K. (2006). Localization of GRP78 to mitochondria under the unfolded protein response. *Biochem. J.* 396, 31–39. doi: 10.1042/bj20051916

Suyama, K., Watanabe, M., Sakabe, K., Okada, Y., Matsuyama, D., Kuroiwa, M., et al. (2011). Overexpression of GRP78 protects glial cells from endoplasmic reticulum stress. *Neurosci. Lett.* 504, 271–276. doi: 10.1016/j.neulet.2011.09.045

Tajiri, S., Oyadomari, S., Yano, S., Morioka, M., Gotoh, T., Hamada, J. I., et al. (2004). Ischemia-induced neuronal cell death is mediated by the endoplasmic reticulum stress pathway involving CHOP. *Cell Death Differ.* 11, 403–415. doi: 10.1038/sj.cdd.4401365

Wang, S., Longo, F. M., Chen, J., Butman, M., Graham, S. H., Haglid, K. G., et al. (1993). Induction of glucose regulated protein (grp78) and inducible heat shock protein (hsp70) mRNAs in rat brain after kainic acid seizures and focal ischemia. *Neurochem. Int.* 23, 575–582. doi: 10.1016/0197-0186(93)90106-F

Yan, J., Li, L., Khatibi, N. H., Yang, L., Wang, K., Zhang, W., et al. (2011). Blood-brain barrier disruption following subarchnoid hemorrhage may be faciliated through PUMA induction of endothelial cell apoptosis from the endoplasmic reticulum. *Exp. Neurol.* 230, 240–247. doi: 10.1016/j.expneurol.2011.04.022

Yang, Y., Sun, M., Shan, Y., Zheng, X., Ma, H., Ma, W., et al. (2015). Endoplasmic reticulum stress-mediated apoptotic pathway is involved in corpus luteum regression in rats. *Reproduct. Sci. (Thousand Oaks, Calif.)* 22, 572–584. doi: 10.1177/1933719114553445

Zhang, L. H., and Zhang, X. (2010). Roles of GRP78 in physiology and cancer. *J. Cell. Biochem.* 110, 1299–1305. doi: 10.1002/jcb.22679

Zhang, Q., Li, Y., Liang, T., Lu, X., Zhang, C., Liu, X., et al. (2015). ER stress and autophagy dysfunction contribute to fatty liver in diabetic mice. *Int. J. Biol. Sci.* 11, 559–568. doi: 10.7150/ijbs.10690

Zhao, Y., Yan, Y., Zhao, Z., Li, S., and Yin, J. (2015). The dynamic changes of endoplasmic reticulum stress pathway markers GRP78 and CHOP in the hippocampus of diabetic mice. *Brain Res. Bull.* 111, 27–35. doi: 10.1016/j.brainresbull.2014.12.006

Zhu, G., and Lee, A. S. (2015). Role of the unfolded protein response, GRP78 and GRP94 in organ homeostasis. *J. Cell. Physiol.* 230, 1413–1420. doi: 10.1002/jcp.24923

Conflict of Interest Statement: The authors declare that the research was conducted in the absence of any commercial or financial relationships that could be construed as a potential conflict of interest.

frontiers in Cellular Neuroscience

PROTOCOLS
published: 09 January 2019
doi: 10.3389/fncel.2018.00520

Expression of *Tmem119/Sall1* and *Ccr2/CD69* in FACS-Sorted Microglia- and Monocyte/Macrophage-Enriched Cell Populations After Intracerebral Hemorrhage

*Qian Li†‡, Xi Lan‡, Xiaoning Han and Jian Wang**

Department of Anesthesiology and Critical Care Medicine, The Johns Hopkins University School of Medicine, Baltimore, MD, United States

OPEN ACCESS

Edited by:
Sriharsha Kantamneni, University of Bradford, United Kingdom

Reviewed by:
Ruben Lopez-Vales, Autonomous University of Barcelona, Spain
Mikhail A. Gavrilin, The Ohio State University, United States

***Correspondence:**
Jian Wang
jwang79@jhmi.edu

†Present address:
Qian Li, Department of Biochemistry and Molecular Biology, Beijing Key Laboratory of Neural Regeneration and Repair, School of Basic Medical Sciences, Capital Medical University, Beijing, China; Advanced Innovation Center for Human Brain Protection, Beijing, China

‡*These authors have contributed equally to this work*

Received: 28 August 2018
Accepted: 12 December 2018
Published: 09 January 2019

Citation:
Li Q, Lan X, Han X and Wang J (2019) Expression of Tmem119/Sall1 and Ccr2/CD69 in FACS-Sorted Microglia- and Monocyte/Macrophage-Enriched Cell Populations After Intracerebral Hemorrhage. Front. Cell. Neurosci. 12:520. doi: 10.3389/fncel.2018.00520

Activation and polarization of microglia and macrophages are critical events in neuroinflammation and hematoma resolution after intracerebral hemorrhage (ICH). However, distinguishing microglia and monocyte-derived macrophages histologically can be difficult. Although they share most cell surface markers, evidence indicates that the gene regulation and function of these two cell types might be different. Flow cytometry is the gold standard for discriminating between the two cell populations, but it is rarely used in the ICH research field. We developed a flow cytometry protocol to identify and sort microglia and monocyte-derived macrophages from mice that have undergone well-established ICH models induced by collagenase or blood injection. In addition, we combined a recently established magnetic-activated cell separation system that allows eight tissue samples to be assessed together. This protocol can be completed within 5–8 h. Sorted cells are fully preserved and maintain expression of microglia-specific (*Tmem119/Sall1*) and macrophage-specific (*Ccr2/CD69*) markers. They retain phagocytic ability, respond to lipopolysaccharide stimulation, and engulf fluorescent latex beads. Thus, this protocol represents a very important tool for researching microglial and monocyte-derived macrophage biologic function after ICH and other brain diseases.

Keywords: fluorescent-activated cell sorting, intracerebral hemorrhage, monocyte-derived macrophage, magnetic-activated cell separation, microglia

INTRODUCTION

Intracerebral hemorrhage (ICH), the second most common type of stroke, affects more than 1 million people each year (Kim and Bae, 2017; Thabet et al., 2017). As the most important innate immune cell types, microglia and infiltrating monocyte-derived macrophages play critical roles in neuroinflammation (Wang and Tsirka, 2005; Wang, 2010; Wu et al., 2010; Lan et al., 2017a),

Abbreviations: FACS, fluorescence-activated cell sorting; ICH, intracerebral hemorrhage; MACS, magnetic-activated cell separation; MMϕ, microglia/macrophages; PI, propidium iodide.

hematoma resolution (Flores et al., 2016; Chang et al., 2017; Lan et al., 2018), white matter injury (Li et al., 2017d, 2018), and neuronal toxicity (Wu et al., 2011; Yang J. et al., 2016; Zhang et al., 2017) after ICH. Recent studies have indicated that microglia and macrophages may have opposing functions after ICH: macrophage depletion exacerbates brain damage after experimental ICH (Min et al., 2016), whereas elimination of microglia improves ICH outcomes in the same animal model (Li et al., 2017a). Therefore, distinguishing microglial and macrophage function, activation, and polarization is critical to understanding ICH pathophysiology (Lan et al., 2017c, 2018).

Magnetic-activated cell separation (MACS) has been used to isolate microglia and monocyte-derived macrophages (MMϕ) in mouse models of Alzheimer's disease (Kronenberg et al., 2017), glioma (Szulzewsky et al., 2015), ischemic stroke (Yang B. et al., 2016), and ICH (Lan et al., 2017a). However, to our knowledge, no protocol exists for separating the two cell types after ICH. Here, we used a MACS tissue dissociation system to dissociate the brains of mice after collagenase-induced or blood-induced ICH. Then, after removing myelin and red blood cells (RBCs), we counted live cells and used fluorescence-activated cell sorting (FACS).

Flow cytometry can provide highly sensitive detection and accurate analysis of different cell populations. In our optimized procedure, we used fluorescent antibodies Ly6g, CD11b, and CD45 together with propidium iodide (PI) to stain brain cells, and subsequently sorted the cells by flow cytometry. The populations of $Ly6g^{-}/CD45^{high}/CD11b^{+}$ and $Ly6g^{-}/CD45^{Int}/CD11b^{+}$, which encompass infiltrating monocytes/macrophages and resident microglia, were sorted separately (Hellstrom Erkenstam et al., 2016; Varvel et al., 2016; Vinet et al., 2016). We confirmed that the expression of *Tmem119*/*Sall1* and *Ccr2*/*CD69* differed in FACS-sorted microglia- and monocyte/macrophage-enriched cell populations, respectively. These isolated cells had maximally preserved biologic characteristics after ICH, including inflammatory responses, phagocytosis, and dynamic polarization. They also can be applied to real-time PCR, RNA nanostring, mass spectrometry/proteomics, and *in vitro* cell culture.

This MACS and FACS-based method allows us to distinguish microglia and infiltrating monocytes/macrophages after ICH using MMϕ cell surface markers. This method is fast, efficient, simple, and accurate. Therefore, our optimized protocol provides an important tool for studying MMϕ function after ICH and other brain diseases.

MATERIALS AND EQUIPMENT

Animals

All animal experiments were conducted in accordance with guidelines from the National Institutes of Health and were approved by the Institutional Animal Care and Use Committee at The Johns Hopkins University School of Medicine. Adult male C57BL/6 mice (8–10 weeks old) were purchased from Charles River Laboratories (Frederick, MD).

ICH Mouse Models

- Collagenase VII-S, cat #C2399, Sigma-Aldrich
- 50-μL Hamilton syringe, cat #80100
- 1-μL Hamilton syringe, cat #80908
- Motorized microinjector,
- DC Temperature Controller 40-90-8D, FHC Inc., ME

Tissue Dissociation

- Neural Tissue Dissociation kit (P), cat #130-092-628, Miltenyi Biotec
- C Tubes, cat #130-096-334, Miltenyi Biotec
- gentleMACS Dissociator, cat #130-093-235, Miltenyi Biotec
- MACSmix Tube Rotator, cat #130-090-753, Miltenyi Biotec
- Myelin Removal Beads, cat #130-096-731, Miltenyi Biotec
- Myelin removal buffer: PBS solution containing 0.5% bovine serum albumin (BSA)
- Red Blood Cell Lysis Solution, cat #130-094-183, Miltenyi Biotec
- LS columns, cat #130-042-401, Miltenyi Biotec
- QuadroMACS Separator, cat #130-091-051, Miltenyi Biotec
- HBSS with Ca^{2+}/Mg^{2+}, cat #14025134, Thermo Fisher Scientific
- HBSS without Ca^{2+}/Mg^{2+}, cat #14170161, Thermo Fisher Scientific
- 70-micron cell strainer, cat #352350, Corning Inc.

Flow Cytometry and Fluorescence-Activated Cell Sorting (FACS)

- FITC-CD11b, cat #130-081-201, Miltenyi Biotec
- PE-CD45, cat #130-102-596, Miltenyi Biotec
- APC-Ly6g, cat #560599, BD Pharmingen
- BV421-CD45, cat #103133, Biolegend
- Flow buffer (HBSS without Ca^{2+}/Mg^{2+}, 10 mM HEPES, 1% BSA)
- Blocking buffer (1% goat serum, 0.5% BSA, and 2 mM EDTA in PBS)
- MoFlo cytometer, Beckman Coulter

Real-Time PCR and Cell Culture

- TRIzol reagent, cat #15596018, Thermo Fisher Scientific
- NanoDrop 2000 spectrophotometer, Thermo Fisher Scientific
- SuperScript VILO cDNA Synthesis kit, cat #11754250, Thermo Fisher Scientific
- TaqMan Universal Master Mix II, cat #4440038, Thermo Fisher Scientific
- Real-time PCR primers, TaqMan® Gene Expression Assay, Thermo Fisher Scientific
- QuantStudio™ 3 Real-Time PCR System, 96-well, 0.1 mL
- DMEM/F-12, cat #11330057, Thermo Fisher Scientific
- Fetal bovine serum (FBS), cat #10438026, Thermo Fisher Scientific
- Penicillin-streptomycin, cat #15140148, Thermo Fisher Scientific
- M-CSF, cat #315-02, PeproTech

- Culture medium: DMEM/F-12 with 10% FBS, 100 U/mL penicillin-streptomycin and 20 ng/μL M-CSF
- pHrodo Red Zymosan Bioparticles Conjugate for Phagocytosis, cat #P35364, Thermo Fisher Scientific

Step-By-Step Procedure

ICH Mouse Models: 20 min to 50 min/Each Mouse

Mice were anesthetized with 1–3% isoflurane and ventilated with oxygen-enriched air (20%:80%) via a nose cone. We used two well-established ICH mouse models – the collagenase-induced model and the blood-induced model – for this protocol (Li and Wang, 2017). For the collagenase-induced ICH model, we injected collagenase VII-S (0.0525 U in 0.35 μL sterile saline) into the striatum (0.1 μL/min) at the following coordinates relative to the bregma: 0.8 mm anterior, 2 mm lateral, and 2.8 mm deep (Li et al., 2017b; Yang et al., 2017; Zhu et al., 2018). For the blood-induced ICH model, we injected 20 μL of autologous whole blood at a rate of 1 μL/min at those the same coordinates (Zhu et al., 2014; Meng et al., 2017; Wu et al., 2017). We chose the injection volumes based on preliminary experiments in which we matched hematoma volume in the two models on day 1 post-ICH, when hematoma reaches its maximum (Wang et al., 2015), to ensure a fair comparison. Our results showed that the hematoma size induced by 0.0525 U collagenase (6.86 ± 1.11 mm^3, $n = 5$) was similar to that induced by 20 μL blood injection (6.92 ± 1.27 mm^3, $n = 5$) at 1 day post-ICH (**Figure 1**). Therefore, we used those dosages for our subsequent experiments.

Animal core body temperature was maintained at 37.0 ± 0.5°C throughout the surgery and recovery periods with a DC Temperature Controller 40-90-8D. Sham control mice underwent the same procedure, including needle insertion, but without collagenase or whole blood injection.

NOTE: Completion of the procedure requires 20 min per mouse for the collagenase-induced ICH model and 50 min per mouse for the blood-induced ICH model.

Brain Tissue Preparation: 10 min/Each Mouse

At 24 h after ICH induction, mice were sacrificed and perfused with ice-cold phosphate-buffered saline (PBS; Thermo Fisher Scientific, Waltham, MA). Based on our pre-calculated injury volume, we collected a 4 mm-thick sample from the ipsilateral caudate putamen (∼80 mg/sample) that included all of the injured area (Chang et al., 2015). Each sample was quickly transferred to 1 mL of cold Hanks' buffered salt solution (HBSS; without Ca^{2+}/Mg^{2+}) for the dissociation steps.

NOTE: Sacrifice the mice as soon as possible to keep brain tissue fresh and maximally maintain the live cell status. Delay may result in fewer live cells.

Tissue Dissociation With the gentleMACS^{TM} Dissociator: 40 min/up to 8 Mice

The automated dissociation system (Lee and Lufkin, 2012) was purchased from Miltenyi Biotec (Auburn, CA). The manufacturer's instructions were followed for reagent preparation and major steps (**Figure 2**).

(1) Transfer tissues into the C tubes containing 37°C pre-warmed enzyme mix 1 (50 μL Enzyme P and 1900 μL Buffer X).
(2) Run the gentleMACS program "m_brain_01" when C-tubes are attached onto the gentleMACS Dissociator.
(3) Incubate the samples for 15 min at 37°C, and then run on program "m_brain_02."
(4) Add 30 μL of enzyme mix 2 (20 μL Buffer Y and 10 μL Enzyme A) into each sample and re-incubate them for 10 min at 37°C.
(5) Run on program "m_brain_03" with another incubation for 10 min at 37°C; then spin down quickly (4000 rpm for 10–15 s at room temperature) and collect the cells.
(6) Resuspend the cells gently in 10 mL of HBSS (with Ca^{2+}/Mg^{2+}) and pass them through a 70-micron cell strainer to a new 50 mL tube.
(7) After washing the cells in 10 mL HBSS (with Ca^{2+}/Mg^{2+}), centrifuge them at 300 × *g* for 10 min at 4°C and then collect them for myelin and RBC removal.

NOTE:

(a) The gentleMACS^{TM} Dissociator can hold up to eight C tubes at once. Thus, more samples may take more than 40 min.
(b) Before attaching the C tubes to the dissociator, make sure they have been tightened.

Sample Clearing: 80 min

All procedures were carried out according to the manufacture's protocol.

Myelin removal:

- Incubate cells with Myelin Removal Beads (200 μL beads and 1800 μL buffer per sample) for 15 min at 4°C.
- Wash cells in 5 mL of myelin removal buffer and centrifuge at 300 × *g* for 10 min at 4°C.
- Suspend pellets in 1 mL buffer and apply them onto the LS column (3 columns for each 200 μL beads).
- Collect the unlabeled cells in a 15 mL tube.
- Centrifuge at 300 × *g* for 10 min at 4°C and collect cell pellets for the next steps.

RBC removal:

- Collect the cell pellets and suspend them in 20 times volume of 1 × Red Blood Cell Lysis Solution (∼1 mL per sample).
- After incubating the samples at 4°C for 10 min, add 10 mL of 0.5% BSA buffer and centrifuge them at 300 × *g* for 5 min. Cell pellets proceed to the FACS step.

NOTE:

(a) The volume of Myelin Removal Beads used depends on the tissue weight. If the mouse brain is greater than 500 mg, more beads may be needed to remove myelin debris.
(b) The LS column should be rinsed with 3 mL of buffer before the suspended cells are applied to it.

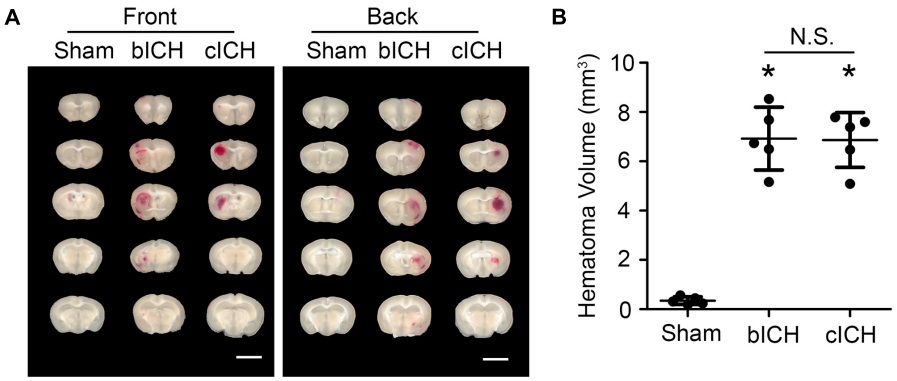

FIGURE 1 | Hematomas on day 1 after blood-induced intracerebral hemorrhage (bICH) and collagenase-induced ICH (cICH) were matched for size. Eight- to ten-week-old male C57BL/6 mice underwent collagenase injection, blood injection, or sham procedure. Mice were sacrificed at day 1 post-ICH. **(A)** Representative images from fresh brain coronal sections. **(B)** Quantification of hematoma volume. $^*p < 0.05$ vs. Sham; N.S., not significant; $n = 5$. Results are presented as scatter plots (mean ± SD). One-way ANOVA followed by Dunn's multiple comparison post-test. Scale bars: 1 mm.

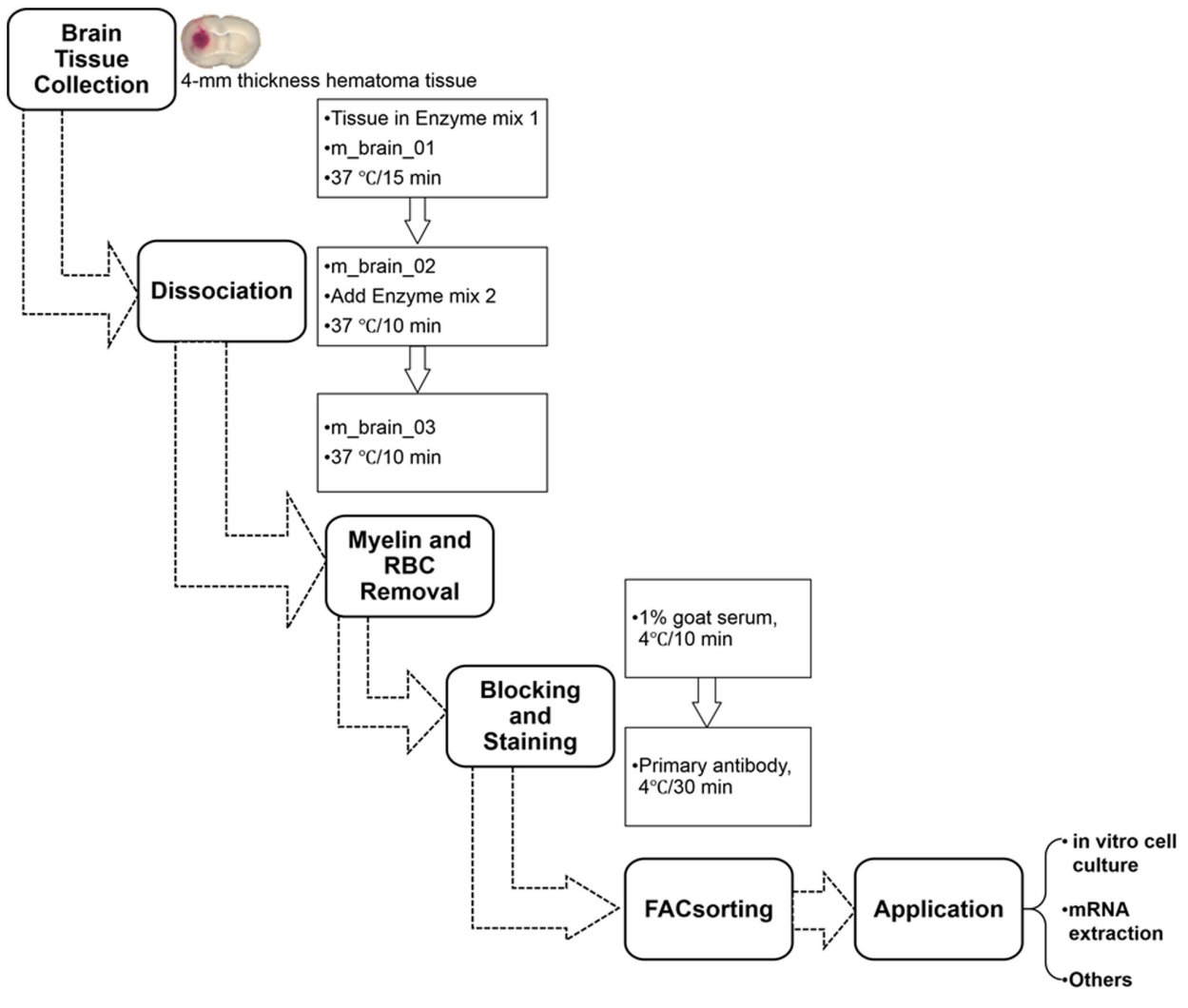

FIGURE 2 | Procedure for isolating mouse microglia and monocyte-derived macrophages after ICH. RBC, red blood cells.

(c) Carefully avoid air bubbles when eluting cells, as they may block columns.

Tissue Dissociation With Percoll

The manual Percoll dissociation procedure was performed based on a published protocol (Lelios and Greter, 2014). Briefly, fresh brain tissue was collected, cut, and digested in 0.4 mg/mL collagenase IV (Sigma-Aldrich) for 45 min at 37°C. Tissue was homogenized by passing it through a syringe with an 18G, 1½ inch needle. The cell suspension was then passed through a 70-micron cell strainer. Cells were washed in PBS, mixed with Percoll (Cat #17089102, GE Healthcare Life Sciences), and then centrifuged at 15,000 × *g* for 30 min. After the topmost layer was discarded, the remainder was filtered through a 70-micron cell strainer. Finally, the cell suspension was centrifuged at 450 × *g* for 5 min at 4°C and the cell pellet collected for the FACS step.

FACS

Cell surface staining: 50–60 min

- Incubate the cells in blocking buffer for 10 min at 4°C.
- Incubate cells with the primary antibodies for 30 min at 4°C.
  - To observe cell morphology and measure pro-inflammatory cytokines and mRNA, we used FITC-CD11b (1:10), PE-CD45 (1:10), and APC-Ly6g (1:10).
  - For evaluation of cell phagocytic function, we used FITC-CD11b (1:10) and BV421-CD45 (1:10).
- Use the corresponding isotype antibodies as negative controls (**Supplementary Figure 1**).
- Stained samples are washed three times and centrifuged at 300 × *g* for 5 min at 4°C. Resuspend cells in 0.5–1 mL filtered flow buffer. Add PI to distinguish dead cells.

NOTE:

(a) Cells should be kept on ice until being sorted on a MoFlo cytometer (Beckman Coulter).
(b) The volume of blocking buffer depends on the total cell number counted before staining. We recommend 1×10^6 cells/200 μL buffer for blocking.
(c) Antibodies can be added directly into blocking buffer at the ratio we suggested.
(d) Alternatives:
For *ex vivo* cell culture, cells can be sorted into culture medium.
For mRNA extraction and real-time PCR, cells can be sorted into TRIzol reagent.
(e) Cell sorting time depends on the live cell numbers; it usually takes 20–30 min to run each mouse sample.

Other Methods

mRNA Extraction and Real-Time PCR

TRIzol reagent was added to the pellets, which were triturated and incubated for 5 min at room temperature. Then, after 100 μL of chloroform was added to the lysate (200 μL/1 mL TRIzol), the samples were incubated for 2 min and centrifuged at 12,000 × *g* for 15 min at 4°C. We transferred the aqueous phase, which contained the RNA, to a new RNase/DNase-free tube and added 5 μg glycogen as a carrier and 250 μL isopropanol to each sample. The samples were incubated for 10 min and then centrifuged at 12,000 × *g* for 10 min at 4°C. We then discarded the supernatants, washed the pellets with 500 μL of 75% ethanol (1 mL/1 mL TRIzol), and centrifuged them again at 7,500 × *g* for 5 min at 4°C. Supernatants were discarded and the RNA pellets air dried. We used 10–15 μL warm (55°C) RNase/DNase-free water to dissolve the pellets. The RNA concentration was measured on a NanoDrop 2000 spectrophotometer.

For the real-time PCR assay, we followed the protocol provided by the manufacturer. Briefly, for the reverse transcription (RT) reaction, reaction mix (4 μL), enzyme mix (2 μL), RNA (500 ng), and DEPC-treated water were mixed to a total volume of 20 μL. We used the RT reaction program provided by the manufacturer. To measure mRNA, we prepared the reaction mix by combining 7.5 μL TaqMan Universal Master Mix II (2×), 1 μL primers, 50 ng cDNA template, and RNase/DNase-free water to a total volume of 15 μL. Mixtures were transferred to MicroAmp Fast Optical 96-Well Reaction Plates (cat #4346907) for use in the Applied Biosystems 7500 Fast Real-time PCR system (Thermo Fisher Scientific) (Li et al., 2017c). Reactions were incubated at 50°C for 2 min, 95°C for 10 min, and for 40 cycles of 95°C for 15 s and 60°C for 1 min. Relative mRNA expression was calculated by $2^{-\Delta\Delta Ct}$, and GAPDH was used as an internal control. The following TaqMan Gene Expression Assay Mixes (Applied Biosystems) were used: *IL-1β* (Mm00434228_m1), *CD32* (Mm004388875_m1), *IL-10* (Mm00439614_m1), *YM-1* (Mm00657889_m1), *Teme119* (Mm00525305_m1), *Sall1* (Mn00491266_m1), *Ccr2* (Mm00438270_m1), *CD69* (Mm01183378_m1), and *GAPDH* (Mm99999915_g1).

Microglial and Macrophage Culture

$CD11b^+/CD45^{Int}$ (microglia) and $CD11b^+/CD45^{high}$ (monocytes/macrophages) were sorted in DMEM/F-12 with FBS and penicillin-streptomycin at 4°C. Cell supernatants were centrifuged at 300 × *g* for 10 min and resuspended in culture medium. Cells were seeded at 5,000 per well on poly-l-lysine-coated Nunc Lab-Tek II Chamber Slides (Thermo Fisher Scientific, cat #154534) and cultured at 37°C in 5% CO_2. The medium was changed after 24 h. To detect the specific gene expression in cultured microglia and macrophages, we photographed cell morphology under a microscope and then collected cells for mRNA measurement on day 3. At the same time point, lipopolysaccharide (LPS; 25 ng/mL, Sigma-Aldrich, cat #L2630) was added to another set of microglia or monocytes/macrophages for 12 h (Lan et al., 2011). Cell supernatants were collected for ELISA (R&D Systems, Minneapolis, MN), and cells were fixed in 4% paraformaldehyde for immunofluorescence microscopy (Nikon Eclipse 90i fluorescence microscope) (Lan et al., 2017b).

TABLE 1 | Cell numbers by gentleMACS and Percoll methods.

	GentleMACS with Myelin Removal Beads (n = 6)		Tissue dissociation with Percoll (n = 3)	
	Sham	**ICH day 1**	**Sham**	**ICH day 1**
Cell counts before FACS	$(2.13 \pm 0.23) \times 10^6$	$(1.67 \pm 0.12) \times 10^6$	$(1.92 \pm 0.41) \times 10^6$	$(1.32 \pm 0.33) \times 10^6$
Total events collected by FACS (per mouse)	$(1.56 \pm 0.19) \times 10^6$	$(1.02 \pm 0.22) \times 10^6$	$(1.01 \pm 0.21) \times 10^6$	$(0.6 \pm 0.11) \times 10^6$
(FSC-H+SSC-H) subtype (% of total events)	27.9%	22.5%	31.2%	25.8%
No. of microglia	$(13.2 \pm 2.13) \times 10^3$	$(16.4 \pm 3.52) \times 10^3$	$(12.8 \pm 2.11) \times 10^3$	$(12.1 \pm 3.33) \times 10^3$
No. of monocytes/macrophages	$(2.12 \pm 0.52) \times 10^3$	$(6.8 \pm 1.52) \times 10^3$	$(2.91 \pm 0.24) \times 10^3$	$(4.13 \pm 0.92) \times 10^3$

ICH, intracerebral hemorrhage; FACS, fluorescent-activated cell sorting; FSC-H, forward scatter height; SSC-H, side scatter height.

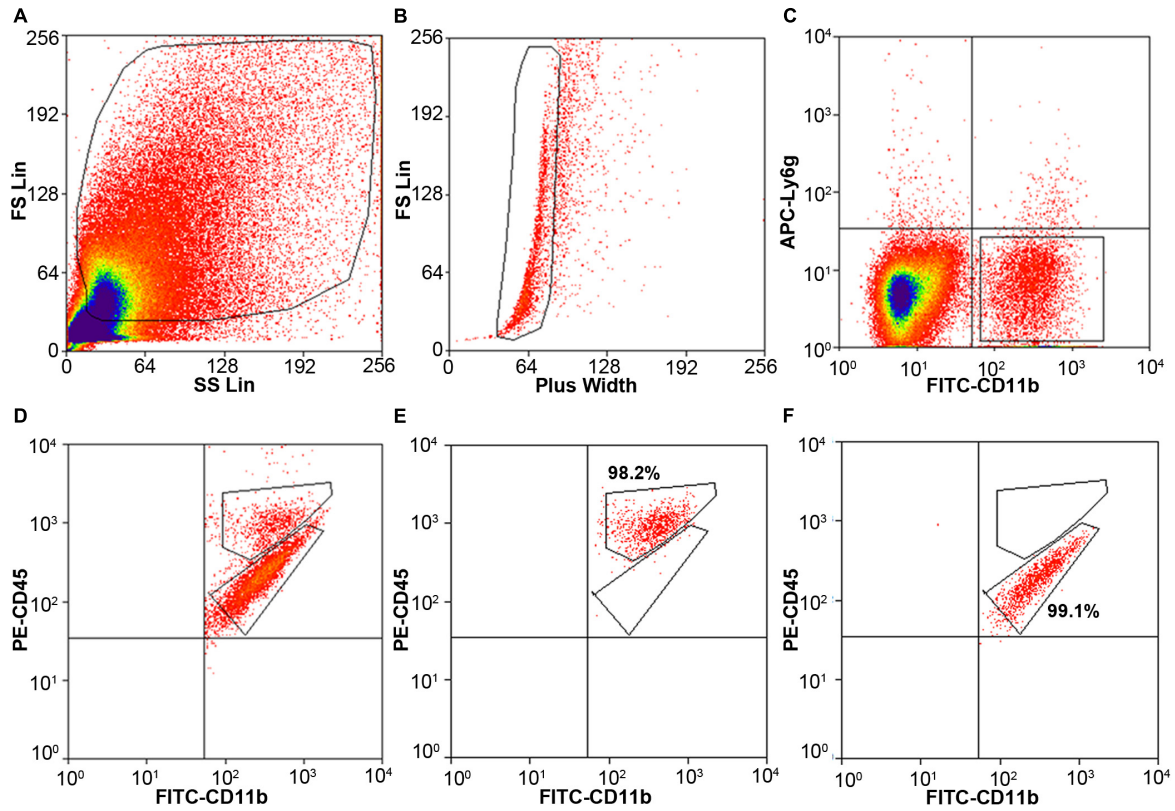

FIGURE 3 | Cell gating by flow cytometry. Eight- to ten-week-old male C57BL/6 mice underwent collagenase injection. Mice were sacrificed on day 1 post-ICH. Mouse brain was perfused with phosphate-buffered saline and dissociated into single cells. Cells were stained with APC-Ly6g, FITC-CD11b, PE-CD45, and propidium iodide (PI). **(A)** Representative gating of all cells. **(B)** Representative gating of singlets. **(C)** Representative gating of $Ly6g^-CD11b^+$ PI^- cells. **(D)** Representative gating of $CD11b^+CD45^{high}$ and $CD11b^+CD45^{Int}$ after gating from **(C)**. **(E,F)** the post-sort purity of monocytes/macrophages **(E)** and microglia **(F)**.

Phagocytosis Assay

pHrodo Red Zymosan Bioparticles Conjugates were dissolved in DMEM/F-12 at 100 μg/mL. Then each well of cells was incubated with 100 μL of the beads for 4–6 h at 37°C. Cells were then washed three times in PBS and fixed in 4% paraformaldehyde for immunofluorescence microscopy.

Statistics

Data are presented as bar graphs (mean ± SD) or dot plots. We made two-group comparisons with a two-tailed Student's t-test followed by Welch's correction. One-way ANOVA was used for comparisons among multiple groups; Dunn's *post hoc* analysis was used to determine where those differences occurred. All analyses were carried out with GraphPad Software (GraphPad Prism 5.0; GraphPad Software, Inc., La Jolla, CA). The criterion for statistical significance was $p < 0.05$.

RESULTS

Cell Counts After Brain Dissociation

After tissue dissociation and removal of myelin debris and red blood cells, we counted live cells in each group at the 24-h time point. Using our method (**Table 1**), we collected approximately

$2.13 \pm 0.23 \times 10^6$ cells from each sham mouse ($n = 6$), $1.51 \pm 0.22 \times 10^6$ cells from each mouse in the blood-induced ICH group ($n = 6$), and $1.67 \pm 0.12 \times 10^6$ cells from each mouse in the collagenase-induced ICH group ($n = 6$). Using the Percoll protocol (**Table 1**), we collected $1.92 \pm 0.41 \times 10^6$ cells from each sham mouse ($n = 3$) and $1.32 \pm 0.33 \times 10^6$ cells from each mouse in the collagenase-induced ICH group ($n = 3$).

Flow Cytometry and FACS

Cells stained for cell surface markers and with PI were analyzed by flow cytometry. We gated $Ly6g^-CD11b^+PI^-$ cells (**Figure 3**) and sorted the two populations of microglia and monocytes/macrophages into the culture medium. The post-sort purity was 98.2% for monocyte/macrophages (**Figure 3E**) and 99.1% for microglia (**Figure 3F**). APC-$Ly6g^-$FITC-$CD11b^+$BV421-$CD45^{Int}PI^-$ and APC-$Ly6g^-$FITC-$CD11b^+$BV421-$CD45^{high}PI^-$ cell populations were sorted for cell phagocytosis measurement; APC-$Ly6g^-$FITC-$CD11b^+$PE-$CD45^{Int}PI^-$ and APC-$Ly6g^-$FITC-$CD11b^+$PE-$CD45^{high}PI^-$ cell populations were sorted for other experiments. Our results showed that the $Ly6g^-CD11b^+CD45^{Int}$ population, which comprises microglia, and the $Ly6g^-CD11b^+CD45^{high}$ population, which comprises infiltrating monocytes/macrophages (Greter et al., 2015; Varvel et al., 2016), were clearly separated by CD11b and CD45 staining at 24 h post-ICH in both mouse models (**Figure 4**). Limited blood-brain barrier damage caused by needle insertion

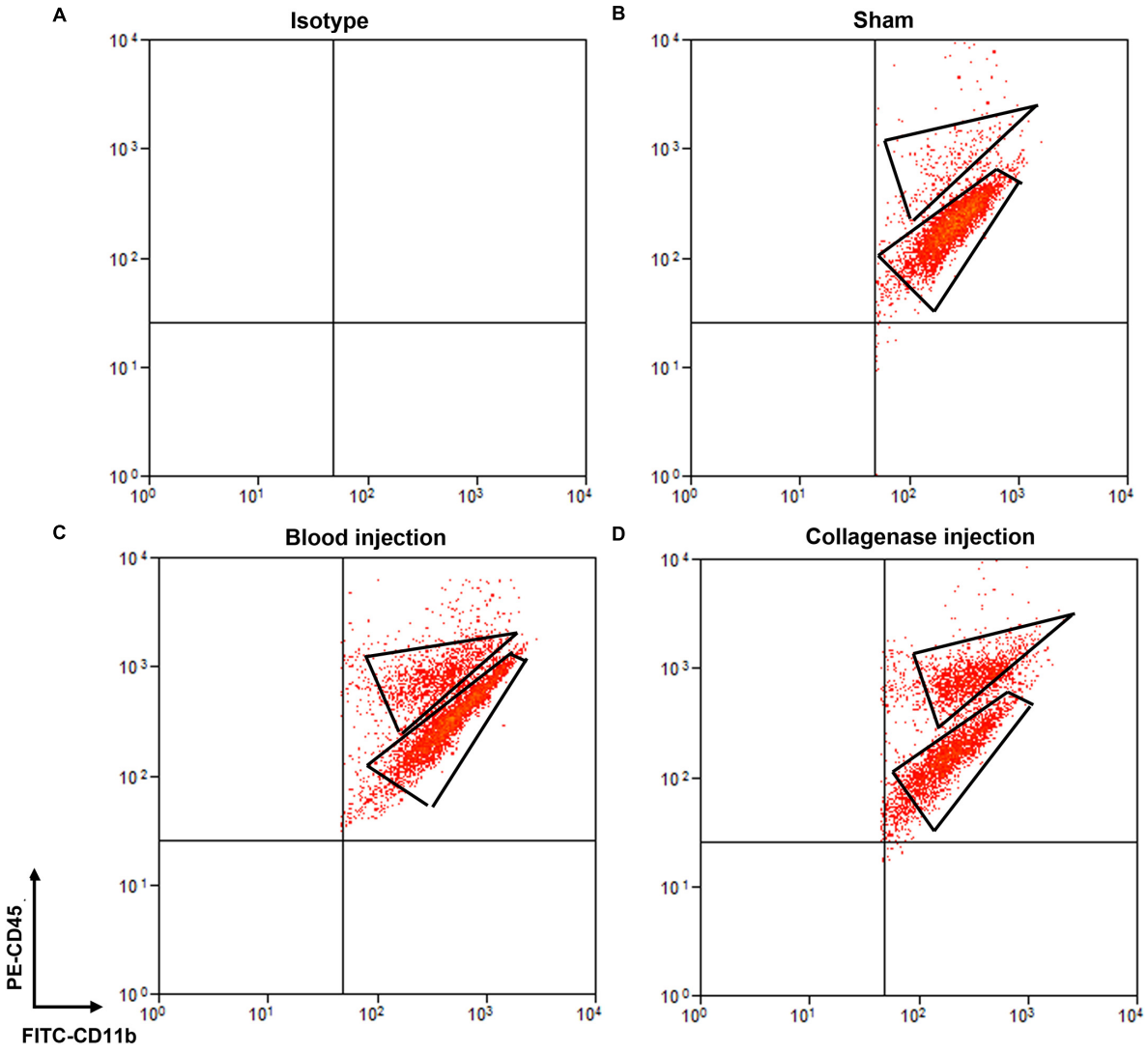

FIGURE 4 | Separation of microglia and monocytes/macrophages by flow cytometry on day 1 after blood-induced or collagenase-induced ICH. Eight- to ten-week-old male C57BL/6 mice underwent collagenase injection, blood injection, or sham procedure. Mice were sacrificed at day 1 post-ICH. Mouse brain was perfused with phosphate-buffered saline and dissociated into single cells. Cells were stained with propidium iodide (PI) and isotype **(A)** or APC-Ly6g, FITC-CD11b, and PE-CD45 **(B–D)** for flow cytometry. Representative images show cell populations in each group, and gates show cells sorted into $Ly6g^-CD11b^+CD45^{high}PI^-$ and $Ly6g^-CD11b^+CD45^{Int}PI^-$ populations.

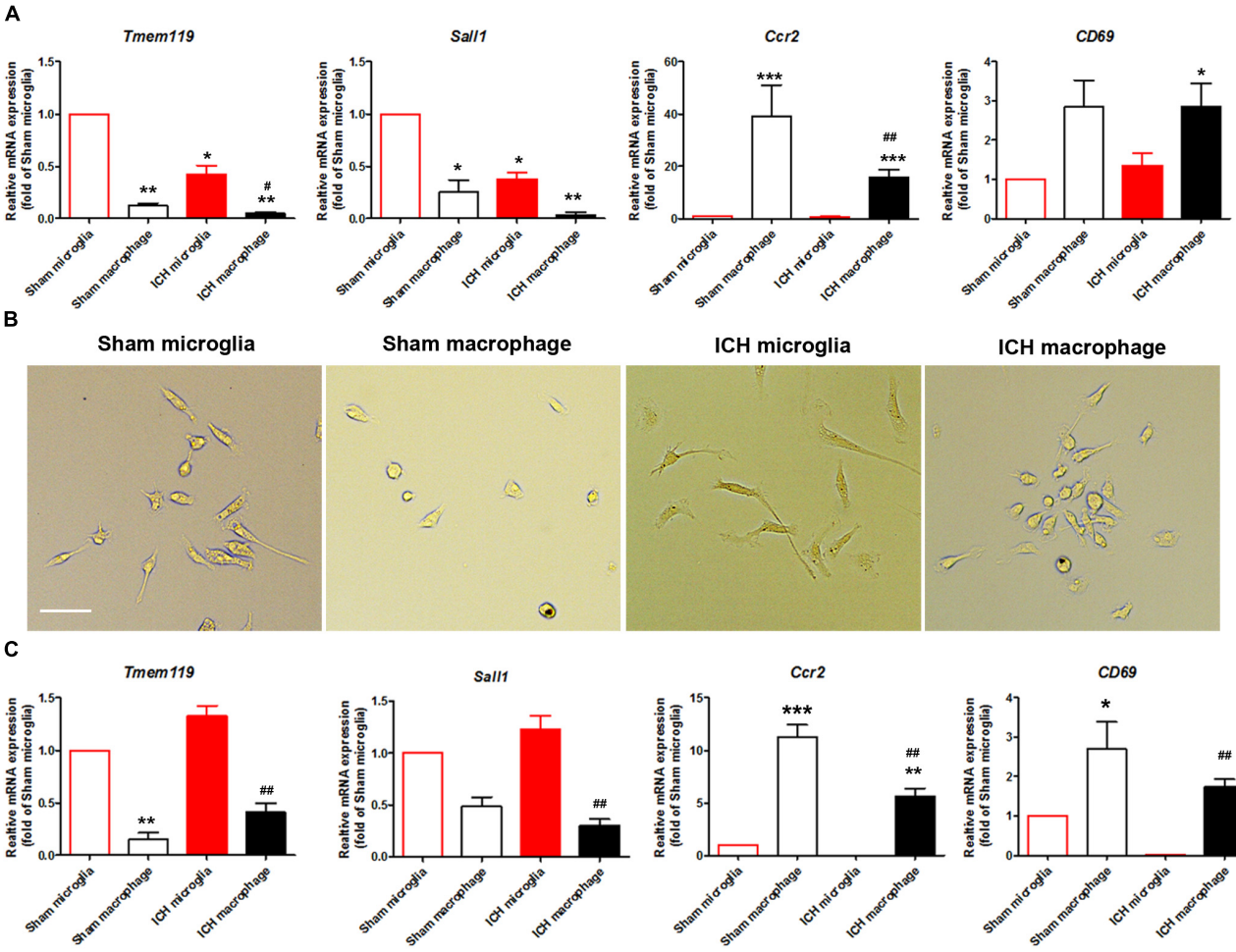

FIGURE 5 | Expression of microglia- and monocyte/macrophage-specific markers in sorted and cultured cells after ICH. Eight- to ten-week-old male C57BL/6 mice underwent collagenase injection or sham procedure. Mice were sacrificed at day 1 post-ICH. Mouse brain was perfused with phosphate-buffered saline and dissociated into single cells. Microglia (Ly6g$^-$CD11b$^+$CD45^{Int}PI$^-$) and monocytes/macrophages (Ly6g$^-$CD11b$^+$CD45^{high}PI$^-$) were isolated and sorted. **(A)** mRNA from cells was extracted and real-time PCR carried out with different primers. *GAPDH* was used as an internal control, and results are shown as fold of control. **(B)** Sorted cells were seeded and bright field images were taken after 3 days in culture. Representative images are shown. **(C)** mRNA was extracted after sorted cells were cultured for 3 days. Real-time PCR was carried out with different primers. *GAPDH* was used as an internal control, and results are shown as fold of sham microglia. $^*p < 0.05$, $^{**}p < 0.01$, $^{***}p < 0.001$ vs. corresponding control; $\#p < 0.05$, $\#\#p < 0.01$ vs. corresponding group in sham animals; $n = 3$. Results are presented as mean ± SD. One-way ANOVA followed by Dunn's multiple comparison post-test. Scale bars: **(B)** 20 μm.

accounts for the small number of CD11b$^+$CD45^{high} cells in the sham group (**Figure 4B**). No positive staining was observed in the isotype group (**Figure 4A**). Cells were then used for *in vitro* culture and mRNA measurement.

We also compared our method with the classic Percoll method. With our method (**Table 1**), 1.02 × 10^6 events were counted by flow cytometry for each collagenase-induced ICH mouse brain, and the (FSC height + SSC height) subtype, gated as live cells, was 22.5% of total counts (**Figure 3**). With the Percoll method (**Table 1**), the total number of events for each collagenase-induced ICH mouse brain was 0.6 × 10^6, and the (FSC height + SSC height) subtype was 25.8% (**Supplementary Figure 2**). After gentleMACS dissociation and cell sorting, 6.8 ± 1.52 × 10^3 Ly6g$^-$CD11b$^+$CD45^{high}PI$^-$ monocytes/macrophages and 16.4 ± 3.52 × 10^3 Ly6g$^-$CD11b$^+$CD45^{Int}PI$^-$ microglia were collected, respectively, from collagenase-induced ICH mouse brain (n = 6). By the Percoll method, 4.13 ± 0.92 × 10^3 monocytes/macrophages and 12.1 ± 3.33 × 10^3 microglia were sorted from the ICH mice (n = 3).

Purity of Microglia and Monocyte-Derived Macrophages in Sorted and Cultured Cells

The literature has reported that Tmem119 and Sall1 are microglia-specific markers (Bennett et al., 2016; Buttgereit et al., 2016), that Ccr2 is a monocyte/macrophage-specific marker (Gu et al., 2016), and that CD69 is enriched in monocytes/macrophages but does not change in activated

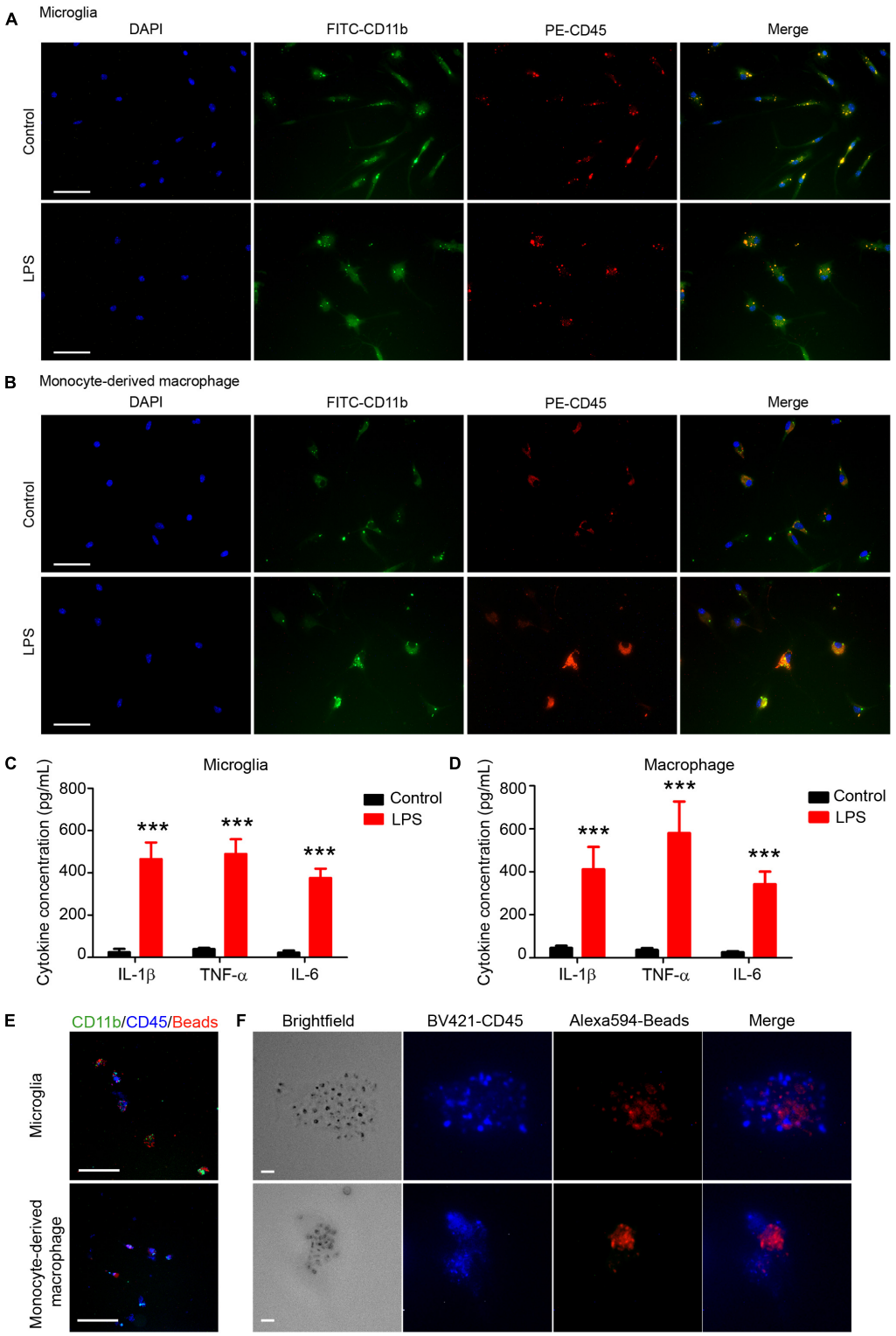

FIGURE 6 | Sorted microglia and monocytes/macrophages respond to lipopolysaccharide (LPS) stimulation and phagocytose beads *ex vivo*. At 1 day after mice were injected with collagenase, microglia ($Ly6g^{-}CD11b^{+}CD45^{int}PI^{-}$) and macrophages ($Ly6g^{-}CD11b^{+}CD45^{high}PI^{-}$) were isolated, sorted, and seeded onto slides. Cells recovered briefly and were incubated with LPS or vehicle for 12 h. Representative images of **(A)** microglia and **(B)** monocyte-derived macrophages are shown. **(C,D)** Conditioned medium was collected and ELISA assays were performed. $^{***}p < 0.001$ vs. corresponding control; $n = 3$. Results are presented as mean ± SD. Two tailed Student's *t*-test followed by Welch's correction. **(E,F)** Cells were incubated with fluorescence-conjugated latex beads for 4–6 h and fixed before imaging. Representative images are shown. Scale bars: **(A,B)** 50 μm; **(E)** 100 μm; and **(F)** 10 μm.

microglia (Lewis et al., 2014). To confirm the purity of the two sorted populations, we extracted mRNA and performed real-time PCR with sorted Ly6g$^-$CD11b$^+$CD45^{Int} and Ly6g$^-$CD11b$^+$CD45^{high} cells. As expected, *Tmem119* and *Sall1* were more highly expressed in the microglial cell population, whereas *Ccr2* and *CD69* were more highly expressed in the monocyte/macrophage cell population (**Figure 5A**). The expression levels of *Tmem119*, *Sall1*, and *Ccr2* were decreased at 1-day post-ICH compared with those in sham animals (**Figure 5A**). After the sorted cells had been cultured for 3 days, we observed morphologic differences between microglia and macrophages, and microglia from the ICH group exhibited morphology typical of activated microglia (**Figure 5B**). Subsequently, we performed real-time RT PCR and verified the specific markers of these two cell populations. As expected, *Tmem119* and *Sall1* were still expressed mainly in microglia, and *Ccr2* and *CD69* were expressed mainly in monocytes/macrophages (**Figure 5C**). However, the expression level of *Tmem119* and *Sall1* was higher in the ICH group than in the sham group, whereas the expression levels of *Ccr2* and *CD69* remained lower in the ICH group than in the sham group (**Figure 5C**). These results indicate that the expression of those genes is differentially regulated by ICH and by *in vitro* culturing.

LPS Response and Phagocytosis by Sorted Microglia and Macrophages *in vitro*

Microglia and monocyte-derived macrophages showed healthy morphology with FITC-CD11b, PE-CD45, and DAPI staining (**Figures 6A,B**, first row). After LPS stimulation (**Figures 6A,B**, second row), microglia (**Figure 6A**) and monocytes/macrophages (**Figure 6B**) exhibited reactivated morphologies, with larger cell bodies and more dendrite branches than the control group.

ELISA assays showed that levels of proinflammatory cytokines (IL-1β, TNF-α, and IL-6) were significantly higher in the LPS-induced microglia (**Figure 6C**) and macrophages (**Figure 6D**) than in the control groups. Furthermore, we used APC-Ly6g, FITC-CD11b, and BV421-CD45 to sort microglia and monocytes/macrophages in a parallel experiment. We found that sorted cells were able to phagocytose fluorescent latex beads *in vitro* (**Figures 6E,F**). These results indicate that the sorted microglia and monocytes/macrophages maintained their inflammatory reactivity to LPS and their phagocytic function.

M1 and M2 Marker mRNA Expression in Microglia and Monocytes/Macrophages

To evaluate whether our method can be used to observe MMϕ polarization after ICH, we extracted mRNA and performed real-time PCR with sorted Ly6g$^-$CD11b$^+$CD45^{Int}PI$^-$ and Ly6g$^-$CD11b$^+$CD45^{high}PI$^-$ cells. Our results showed that M1 markers, *IL-1β* and *CD32*, and M2 markers, *IL-10* and *YM-1*, were increased in both microglia and monocytes/macrophages (**Figure 7**). Notably, *YM-1* was significantly elevated in the monocyte/macrophage population on day 1 post-ICH (**Figure 7**).

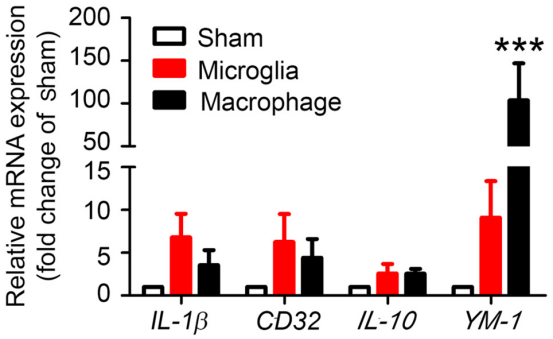

FIGURE 7 | Sorted microglia and monocytes/macrophages express M1 and M2 markers *ex vivo*. At 1 day after mice underwent collagenase injection or sham procedure, microglia (Ly6g$^-$CD11b$^+$CD45^{Int}PI$^-$) and monocytes/macrophages (Ly6g$^-$CD11b$^+$CD45^{high}PI$^-$) were isolated and sorted. mRNA from cells was extracted and real-time PCR carried out with different primers. *GAPDH* was used as an internal control, and results are shown as fold of sham. ***$p < 0.001$ vs. corresponding control; $n = 3$. Results are presented as mean ± SD. One-way ANOVA followed by Dunn's multiple comparison post-test.

Potential Pitfalls and Troubleshooting

Isolate Microglia/Macrophages at Different Time Points Post-ICH and From Sham-Operated Group

The number of infiltrating MMϕ differs at different time points after ICH. Therefore, sorted MMϕ may not be sufficient for mRNA extraction or cell culture. To isolate MMϕ more than 5 days after ICH, we recommend pooling two or more mouse brains together to collect enough cells. To collect enough macrophages from sham-operated mice, we suggest pooling at least three mouse brains together.

Maintain Cell Viability Before/During FACS

Brain cells are more vulnerable than other cells (tumor cells or blood cells), and hemorrhagic brain contains more debris than non-traumatic brain tissue. Thus, tissues/cells need to be kept on ice at all times except during enzyme incubation. All procedures require quick (perfusion) and gentle (incubation and resuspension) techniques. If the FACSorting takes more than 3 h, we suggest that cells be resuspended in Neurobasal medium (cat. 21103049, Thermo Fisher Scientific) with 1% BSA to maximally maintain cell viability.

Cell Collection After FACS

In some cases, the number of sorted cells may be small. To maximally preserve the viability and number of sorted cells, we recommend seeding cells directly onto poly-l-lysine–coated cover slips or 6- or 12-well plates. Cells can be sorted directly into TRIzol reagent and stored at −80°C for up to 6 months before mRNA is extracted.

DISCUSSION

Microglia and monocyte-derived macrophage activation and polarization play an important role in hematoma resolution

after ICH (Mracsko and Veltkamp, 2014; Zhou et al., 2014; Lan et al., 2017c; Zhang et al., 2017). In preclinical studies, upregulation of M2-like MMϕ has been shown to ameliorate outcomes after ICH (Wan et al., 2016; Yang J. et al., 2016; Chang et al., 2017; Pascual et al., 2017; Yu et al., 2017; Zhou et al., 2017). However, the concept of MMϕ phenotypes in these studies was unclear. Most evaluations of MMϕ polarization use whole brain homogenates in Western blotting, ELISA, or real-time PCR to detect changes in protein or mRNA expression. However, owing to the global expression of most proinflammatory and anti-inflammatory cell markers on neurons, astrocytes, MMϕ, and even oligodendrocytes (Ren and Dubner, 2008), these methods cannot be used to precisely determine the dynamic changes in MMϕ after ICH. Furthermore, recent studies indicated that the roles of microglia and monocyte-derived macrophages might differ after ICH: the infiltrating $CCR2^{+}Ly6c^{high}$ cells accelerated neurologic deficits in the acute phase after ICH (Hammond et al., 2014), and the activity of $CD11b^{+}/CD45^{high}$ cells was similar to that of monocytes, which contribute to brain injury post-ICH (Min et al., 2016). However, microglial depletion was beneficial for brain recovery on day 3 post-ICH (Li et al., 2017a). These results indicate that evaluating the functions of microglia and monocyte-derived macrophages separately is critical in preclinical and clinical studies of ICH (Lan et al., 2018). Therefore, a protocol is needed that can reliably sort microglia and monocyte-derived macrophages from the ICH brain.

Several methods have been developed to separate microglia and monocytes/macrophages in the mouse ICH brain. The traditional method for distinguishing resident microglia from infiltrating monocytes/macrophages is based on cell morphology (amoeboid, ramified or reactivated (Jeong et al., 2013; Li et al., 2018)) and CD45 staining (Perego et al., 2011). However, this method can only identify cellular location (in the hematoma core or perihematoma regions) and marker expression (by immunostaining other cell markers); the ability to assess cellular function is very limited. Another method is to generate bone marrow chimeras using $Cx3cr1^{gfp/+}$ transgenic (Ajami et al., 2007; Tashima et al., 2016) or other transgenic mice. This approach allows researchers to separate the infiltrating bone marrow-derived monocytes/macrophages ($Cx3cr1^{gfp/+}$) from resident microglia ($Cx3cr1^{-/-}$). Unfortunately, bone marrow transplantation has the potential to cause acute and chronic inflammatory responses (Mildner et al., 2007), which may affect the MMϕ function and even alter the expression of some cell surface markers (Moravan et al., 2016). Recently, researchers developed new tools based on cell surface markers to distinguish microglia and infiltrating monocytes/macrophages. The $CX3CR1^{CreER/+}$:$R26^{IDTR/+}$ transgenic mouse was developed to enable microglia and monocytes/macrophages to be observed separately (Parkhurst et al., 2013). Moreover, a new anti-TMEM119 antibody, which can specifically identify microglia in the brain, was applied to study microglia and monocyte-derived macrophage differences (Bennett et al., 2016). Nevertheless, even as new approaches and tools are developed to study MMϕ, flow cytometry-based FACS remains the gold standard to separate microglia and monocytes/macrophages for *ex vivo* and *in vitro* ICH study, as this method allows maximal retention of cell properties after brain damage.

In the present study, we used Ly6g, CD11b, and CD45 antibodies to label microglia and monocytes/macrophages, as these are classical cell markers of these two populations. As an alternative, CD44 is also a good marker to distinguish microglia, monocytes, and monocyte-derived macrophages after brain injury. Studies showed that the $CD11b^{high}CD44^{low}$ population was also $CD45^{Int}$ and $Ly6c^{low}$, and that the $CD11b^{high}CD44^{high}$ population was $CD45^{high}$ and $Ly6c^{high}$ in an experimental autoimmune encephalomyelitis (EAE) model (Lewis et al., 2014). Therefore, the combination of cell markers CD44, CD11b, CD45, and Ly6g could potentially be more reliable for separating microglia, monocytes, and macrophages. It will be valuable in the future to perform another series of experiments to show that this combination of markers is also useful after ICH.

The tissue dissociation efficiency is a key factor that affects the activity of sorted cells. In our optimized protocol, we chose the gentleMACS dissociation system, which is flexible and fast and allows the preparation of eight samples simultaneously. To isolate live cells from adult mouse brain, we used Myelin Removal Beads to decrease the debris content and maintain cell viability. Furthermore, because of the substantial bleeding in a hemorrhagic brain, we also added double volume of Red Blood Cell Lysis Solution to maximally eliminate the effect of autofluorescence. The dissociation process can be completed in approximately 2 h and is not affected by the sample number (up to 8); the whole procedure, including sorting, can be finished in 8 h. More importantly, the cell viability and status are not heavily dependent on the proficiency of the operator. Thus, variability between groups within and between experiments, even those carried out by different individuals, is minimal, making data reliable and reproducible. Additionally, the process produces approximately $1.5–3.0 \times 10^{6}$ live cells that can be collected for subsequent FACS. This number should be sufficient for follow-up experiments (e.g., immunostaining, real-time PCR, and nanostring) without needing to pool several brains together in most cases, which could potentially increase variability. Compared to the classic Percoll-based dissociation protocol, we found no significant differences in the percentage of FSC height + SSC height subtype or microglia/macrophage cell numbers by FACS. However, the total number of events collected for each sample was less with the Percoll method than with our method on day 1 post-ICH.

After flow cytometry, two populations of $CD11b^{+}CD45^{Int}$ (microglia) and $CD11b^{+}CD45^{high}$ (monocytes/macrophages) can be clearly separated from mice with ICH. However, we did observe a small macrophage population in sham mice. We also used Ly6g antibody to distinguish neutrophils from monocytes. We gated $Ly6g^{-}/CD11b^{+}$ and sorted microglia and monocytes/macrophages separately. One alternative approach is to use $Cx3cr1^{GFP/+}CCR2^{RFP/+}$ mice (Mizutani et al., 2012) and gate $Cx3cr1^{+}CCR2^{-}$ to separate monocytes

from MMϕ. To confirm the purity of the gated cells, we performed real-time RT PCR to examine specific markers: *Tmem119* and *Sall1* for microglia, *Ccr2* and *CD69* for monocyte/macrophages. As expected, *Tmem119* and *Sall1* were expressed mainly in the microglial ($CD11b^{+}CD45^{Int}$) population, and *Ccr2* and *CD69* were expressed mainly in the monocyte/macrophage population ($CD11b^{+}CD45^{high}$). Importantly, cultured cells retained the specific marker expression for days post-sorting.

We also found that the expression level of those markers changes after acute ICH. *Tmem119* is a recently discovered specific microglial marker in the brain (Bennett et al., 2016). However, its biologic function is unknown. *Tmem119* expression was shown to be elevated in the brains of patients with Alzheimer's disease, but not in those with amyotrophic lateral sclerosis or Parkinson's disease (Satoh et al., 2016). Interestingly, *Tmem119* is a target gene of TGFβ1 in postnatal microglia but cannot be regulated by TGFβ1 in mature microglia (Attaai et al., 2018). Our results showed that *Tmem119* expression significantly decreased on day 1 post-ICH, suggesting that it may participate in microglial function after acute brain injury. *Sall1* is another important transcriptional regulator that is required for microglia to retain a healthy phenotype and characteristics (Buttgereit et al., 2016). Similar to *Tmem119*, *Sall1* was significantly suppressed on day 1 post-ICH; however, after 3 days of culture, this reduction disappeared in ICH microglia, perhaps suggesting self-recovery. Therefore, whether the reduction of *Sall1* expression can be used as a biomarker for ICH diagnosis needs further investigation.

It has been reported that in an EAE animal model, Ccr2 was rarely expressed in microglia but highly expressed in monocyte-derived macrophages. Moreover, Ccr2 expression decreased in macrophages of mice with EAE scores of 0 and 3 compared with that of naïve mice (Lewis et al., 2014). Our data indicated that Ccr2 is a specific monocyte/monocyte-derived macrophage marker after ICH, and its expression was downregulated after ICH. Unlike Ccr2, CD69 was highly expressed in macrophages, but we did not observe a significant change in *CD69* expression on day 1 post-ICH. Therefore, a time-course experiment is needed to study the dynamic expression changes and function of CD69 after ICH.

For *in vitro* studies, researchers commonly use primary microglia from p0 mouse pups to investigate microglial function. However, these cells are not completely mature (Moussaud and Draheim, 2010). Moreover, astrocyte-contaminated microglia may have altered cytokine production after stimulation (Bohlen et al., 2017). With our protocol, the sorted cells are mature, can be cultured *in vitro*, retain a healthy morphology, and can be reactivated by stimulation with LPS for proinflammatory cytokine upregulation. Furthermore, the microglia we collected maintained the ability to engulf beads by phagocytosis. These results provide evidence that the sorted MMϕ have excellent viability, activity, and function. When we measured levels of extracted mRNA by real-time PCR, we were able to examine the changes in microglial activation and polarization more precisely, accurately, and efficiently than is possible with immunostaining. In a future study, we will apply nanostring technology and proteomics to further investigate the changes in microglia and monocyte-derived macrophages after ICH.

This protocol has several limitations. First, the MACS sorter, dissociation kit, and C tubes are relatively more expensive than components needed for the traditional method. Second, to achieve the best results, different dissociation kits need to be used for neonatal and adult mice. In addition, because massive bleeding is induced in the ICH model, it is difficult to completely remove red blood cells. Third, gating of the monocyte-derived macrophages would be different from gating of the monocytes because transformation of monocytes into macrophages alters cell size and changes surface marker expression in the ICH animals at different time points. Thus, to investigate the transformation of monocytes into macrophages after ICH, we will sort $Ly6c^{+}Ly6g^{-}CD11b^{+}CD45^{high}$ monocytes and $Ly6c^{-/-\text{and}+/-}Ly6g^{-}CD11b^{+}CD45^{high}$ macrophages separately in our future research.

CONCLUSION

In conclusion, we established a method based on MACS dissociation and sorting by FACS flow cytometry to separate microglia and monocyte-derived macrophages after ICH. The whole process can be achieved within 5–8 h, and the sorted microglia and monocyte-derived macrophages maintain their post-ICH characteristics, an attribute that is critical for ICH research. This fast, efficient, and precise protocol will be valuable for multiple applications and an important means by which to study the role of microglia and monocyte-derived macrophages after ICH and other brain diseases.

AUTHOR CONTRIBUTIONS

QL, XL, and JW designed the experiments and wrote the manuscript. QL, XL, XH, and JW analyzed the data.

FUNDING

The author(s) disclosed receipt of the following financial support for the research, authorship, and/or publication of this article: This research was supported by the National Institutes of Health (R01NS078026, R01AT007317, R56NS096549, and R01NS102583 to JW) and the American Heart Association (Grant-in-Aid, 17GRNT33660766 to JW; Postdoctoral Fellowship Awards 16POST29640010 to QL; Scientist Development Grant, 16SDG30980031 to XH), Award from the American Heart Association and the DC Women's Board 17POST3366019 to XL, and a Stimulating and Advancing ACCM Research (StAAR) grant from the Department of Anesthesiology and Critical Care Medicine, Johns Hopkins University.

ACKNOWLEDGMENTS

We thank Dr. Hao Zhang from Johns Hopkins Bloomberg School of Public Health for flow cytometry assistance and Claire Levine, MS, ELS, for editing the manuscript in draft form.

SUPPLEMENTARY MATERIAL

The Supplementary Material for this article can be found online at: https://www.frontiersin.org/articles/10.3389/fncel.2018.00520/full#supplementary-material

REFERENCES

Ajami, B., Bennett, J. L., Krieger, C., Tetzlaff, W., and Rossi, F. M. (2007). Local self-renewal can sustain CNS microglia maintenance and function throughout adult life. *Nat. Neurosci.* 10, 1538–1543. doi: 10.1038/nn2014

Attaai, A., Neidert, N., Von Ehr, A., Potru, P. S., Zoller, T., and Spittau, B. (2018). Postnatal maturation of microglia is associated with alternative activation and activated TGFbeta signaling. *Glia* doi: 10.1002/glia.23332 [Epub ahead of print].

Bennett, M. L., Bennett, F. C., Liddelow, S. A., Ajami, B., Zamanian, J. L., Fernhoff, N. B., et al. (2016). New tools for studying microglia in the mouse and human CNS. *Proc. Natl. Acad. Sci. U.S.A.* 113, E1738–E1746. doi: 10.1073/pnas.1525528113

Bohlen, C. J., Bennett, F. C., Tucker, A. F., Collins, H. Y., Mulinyawe, S. B., and Barres, B. A. (2017). Diverse requirements for microglial survival, specification, and function revealed by defined-medium cultures. *Neuron* 94, 759.e8–773.e8. doi: 10.1016/j.neuron.2017.04.043

Buttgereit, A., Lelios, I., Yu, X., Vrohlings, M., Krakoski, N. R., Gautier, E. L., et al. (2016). Sall1 is a transcriptional regulator defining microglia identity and function. *Nat. Immunol.* 17, 1397–1406. doi: 10.1038/ni.3585

Chang, C. F., Cai, L., and Wang, J. (2015). Translational intracerebral hemorrhage: a need for transparent descriptions of fresh tissue sampling and preclinical model quality. *Transl. Stroke Res.* 6, 384–389. doi: 10.1007/s12975-015-0399-5

Chang, C. F., Wan, J., Li, Q., Renfroe, S. C., Heller, N. M., and Wang, J. (2017). Alternative activation-skewed microglia/macrophages promote hematoma resolution in experimental intracerebral hemorrhage. *Neurobiol. Dis.* 103, 54–69. doi: 10.1016/j.nbd.2017.03.016

Flores, J. J., Klebe, D., Rolland, W. B., Lekic, T., Krafft, P. R., and Zhang, J. H. (2016). PPARgamma-induced upregulation of CD36 enhances hematoma resolution and attenuates long-term neurological deficits after germinal matrix hemorrhage in neonatal rats. *Neurobiol. Dis.* 87, 124–133. doi: 10.1016/j.nbd.2015.12.015

Greter, M., Lelios, I., and Croxford, A. L. (2015). Microglia versus myeloid cell nomenclature during brain inflammation. *Front. Immunol.* 6:249. doi: 10.3389/fimmu.2015.00249

Gu, N., Peng, J., Murugan, M., Wang, X., Eyo, U. B., Sun, D., et al. (2016). Spinal microgliosis due to resident microglial proliferation is required for pain hypersensitivity after peripheral nerve injury. *Cell Rep.* 16, 605–614. doi: 10.1016/j.celrep.2016.06.018

Hammond, M. D., Taylor, R. A., Mullen, M. T., Ai, Y., Aguila, H. L., Mack, M., et al. (2014). CCR2+ Ly6C(hi) inflammatory monocyte recruitment exacerbates acute disability following intracerebral hemorrhage. *J. Neurosci.* 34, 3901–3909. doi: 10.1523/JNEUROSCI.4070-13.2014

Hellstrom Erkenstam, N., Smith, P. L., Fleiss, B., Nair, S., Svedin, P., Wang, W., et al. (2016). Temporal characterization of microglia/macrophage phenotypes in a mouse model of neonatal hypoxic-ischemic brain injury. *Front. Cell. Neurosci.* 10:286. doi: 10.3389/fncel.2016.00286

Jeong, H. K., Ji, K., Min, K., and Joe, E. H. (2013). Brain inflammation and microglia: facts and misconceptions. *Exp. Neurobiol.* 22, 59–67. doi: 10.5607/en.2013.22.2.59

Kim, J. Y., and Bae, H. J. (2017). Spontaneous intracerebral hemorrhage: management. *J. Stroke* 19, 28–39. doi: 10.5853/jos.2016.01935

Kronenberg, G., Uhlemann, R., Schoner, J., Wegner, S., Boujon, V., Deigendesch, N., et al. (2017). Repression of telomere-associated genes by microglia activation in neuropsychiatric disease. *Eur. Arch. Psychiatry Clin. Neurosci.* 267, 473–477. doi: 10.1007/s00406-016-0750-1

Lan, X., Han, X., Li, Q., Li, Q., Gao, Y., Cheng, T., et al. (2017a). Pinocembrin protects hemorrhagic brain primarily by inhibiting toll-like receptor 4 and reducing M1 phenotype microglia. *Brain Behav. Immun.* 61, 326–339. doi: 10.1016/j.bbi.2016.12.012

Lan, X., Han, X., Li, Q., and Wang, J. (2017b). (-)-Epicatechin, a natural flavonoid compound, protects astrocytes against hemoglobin toxicity via Nrf2 and AP-1 signaling pathways. *Mol. Neurobiol.* 54, 7898–7907. doi: 10.1007/s12035-016-0271-y

Lan, X., Han, X., Li, Q., Yang, Q. W., and Wang, J. (2017c). Modulators of microglial activation and polarization after intracerebral haemorrhage. *Nat. Rev. Neurol.* 13, 420–433. doi: 10.1038/nrneurol.2017.69

Lan, X., Han, X., Liu, X., and Wang, J. (2018). Inflammatory responses after intracerebral hemorrhage: from cellular function to therapeutic targets. *J. Cereb. Blood Flow Metab.* doi: 10.1177/0271678X18805675 [Epub ahead of print].

Lan, X., Liu, R., Sun, L., Zhang, T., and Du, G. (2011). Methyl salicylate 2-O-beta-D-lactoside, a novel salicylic acid analogue, acts as an anti-inflammatory agent on microglia and astrocytes. *J. Neuroinflammation* 8:98. doi: 10.1186/1742-2094-8-98

Lee, M. Y., and Lufkin, T. (2012). Development of the "Three-step MACS": a novel strategy for isolating rare cell populations in the absence of known cell surface markers from complex animal tissue. *J. Biomol. Tech.* 23, 69–77. doi: 10.7171/jbt.12-2302-003

Lelios, I., and Greter, M. (2014). Isolation of leukocytes from mouse central nervous system. *Methods Mol. Biol.* 1193, 15–19. doi: 10.1007/978-1-4939-1212-4_2

Lewis, N. D., Hill, J. D., Juchem, K. W., Stefanopoulos, D. E., and Modis, L. K. (2014). RNA sequencing of microglia and monocyte-derived macrophages from mice with experimental autoimmune encephalomyelitis illustrates a changing phenotype with disease course. *J. Neuroimmunol.* 277, 26–38. doi: 10.1016/j.jneuroim.2014.09.014

Li, M., Li, Z., Ren, H., Jin, W. N., Wood, K., Liu, Q., et al. (2017a). Colony stimulating factor 1 receptor inhibition eliminates microglia and attenuates brain injury after intracerebral hemorrhage. *J. Cereb. Blood Flow Metab.* 37, 2383–2395. doi: 10.1177/0271678X16666551

Li, Q., Han, X., Lan, X., Gao, Y., Wan, J., Durham, F., et al. (2017b). Inhibition of neuronal ferroptosis protects hemorrhagic brain. *JCI Insight* 2, e90777. doi: 10.1172/jci.insight.90777

Li, Q., Han, X., Lan, X., Hong, X., Li, Q., Gao, Y., et al. (2017c). Inhibition of tPA-induced hemorrhagic transformation involves adenosine A2b receptor activation after cerebral ischemia. *Neurobiol. Dis.* 108, 173–182. doi: 10.1016/j.nbd.2017.08.011

Li, Q., Wan, J., Lan, X., Han, X., Wang, Z., and Wang, J. (2017d). Neuroprotection of brain-permeable iron chelator VK-28 against intracerebral hemorrhage in mice. *J. Cereb. Blood Flow Metab.* 37, 3110–3123. doi: 10.1177/0271678X17709186

Li, Q., and Wang, J. (2017). "Animal models: cerebral hemorrhage," in *Primer on Cerebrovascular Diseases,* eds K. M. Welch, L. R. Caplan, B. K. Siesjo, B. Weir, and D. J. Reis (Cambridge, MA: Academic Press), 306–311.

Li, Q., Weiland, A., Chen, X., Lan, X., Han, X., Durham, F., et al. (2018). Ultrastructural characteristics of neuronal death and white matter injury in mouse brain tissues after intracerebral hemorrhage: coexistence of ferroptosis. Autophagy, and Necrosis. *Front. Neurol.* 9:581. doi: 10.3389/fneur.2018.00581

Meng, Z., Zhao, T., Zhou, K., Zhong, Q., Wang, Y., Xiong, X., et al. (2017). A20 ameliorates intracerebral hemorrhage-induced inflammatory injury by regulating TRAF6 polyubiquitination. *J. Immunol.* 198, 820–831. doi: 10.4049/jimmunol.1600334

Mildner, A., Schmidt, H., Nitsche, M., Merkler, D., Hanisch, U. K., Mack, M., et al. (2007). Microglia in the adult brain arise from Ly-6ChiCCR2+ monocytes only under defined host conditions. *Nat. Neurosci.* 10, 1544–1553. doi: 10.1038/nn2015

Min, H., Jang, Y. H., Cho, I. H., Yu, S. W., and Lee, S. J. (2016). Alternatively activated brain-infiltrating macrophages facilitate recovery from collagenase-induced intracerebral hemorrhage. *Mol. Brain* 9:42. doi: 10.1186/s13041-016-0225-3

Mizutani, M., Pino, P. A., Saederup, N., Charo, I. F., Ransohoff, R. M., and Cardona, A. E. (2012). The fractalkine receptor but not CCR2 is present on microglia from embryonic development throughout adulthood. *J. Immunol.* 188, 29–36. doi: 10.4049/jimmunol.1100421

Moravan, M. J., Olschowka, J. A., Williams, J. P., and O'banion, M. K. (2016). Brain radiation injury leads to a dose- and time-dependent recruitment of peripheral myeloid cells that depends on CCR2 signaling. *J. Neuroinflammation* 13:30. doi: 10.1186/s12974-016-0496-8

Moussaud, S., and Draheim, H. J. (2010). A new method to isolate microglia from adult mice and culture them for an extended period of time. *J. Neurosci. Methods* 187, 243–253. doi: 10.1016/j.jneumeth.2010.01.017

Mracsko, E., and Veltkamp, R. (2014). Neuroinflammation after intracerebral hemorrhage. *Front. Cell. Neurosci.* 8:388. doi: 10.3389/fncel.2014.00388

Parkhurst, C. N., Yang, G., Ninan, I., Savas, J. N., Yates, J. R. III, Lafaille, J. J., et al. (2013). Microglia promote learning-dependent synapse formation through brain-derived neurotrophic factor. *Cell* 155, 1596–1609. doi: 10.1016/j.cell.2013.11.030

Pascual, G., Avgustinova, A., Mejetta, S., Martin, M., Castellanos, A., Attolini, C. S., et al. (2017). Targeting metastasis-initiating cells through the fatty acid receptor CD36. *Nature* 541, 41–45. doi: 10.1038/nature20791

Perego, C., Fumagalli, S., and De Simoni, M. G. (2011). Temporal pattern of expression and colocalization of microglia/macrophage phenotype markers following brain ischemic injury in mice. *J. Neuroinflammation* 8:174. doi: 10.1186/1742-2094-8-174

Ren, K., and Dubner, R. (2008). Neuron-glia crosstalk gets serious: role in pain hypersensitivity. *Curr. Opin. Anaesthesiol.* 21, 570–579. doi: 10.1097/ACO.0b013e32830edbdf

Satoh, J., Kino, Y., Asahina, N., Takitani, M., Miyoshi, J., Ishida, T., et al. (2016). TMEM119 marks a subset of microglia in the human brain. *Neuropathology* 36, 39–49. doi: 10.1111/neup.12235

Szulzewsky, F., Pelz, A., Feng, X., Synowitz, M., Markovic, D., Langmann, T., et al. (2015). Glioma-associated microglia/macrophages display an expression profile different from M1 and M2 polarization and highly express Gpnmb and Spp1. *PLoS One* 10:e0116644. doi: 10.1371/journal.pone.0116644

Tashima, R., Mikuriya, S., Tomiyama, D., Shiratori-Hayashi, M., Yamashita, T., Kohro, Y., et al. (2016). Bone marrow-derived cells in the population of spinal microglia after peripheral nerve injury. *Sci. Rep.* 6:23701. doi: 10.1038/srep23701

Thabet, A. M., Kottapally, M., and Hemphill, J. C. III (2017). Management of intracerebral hemorrhage. *Handb. Clin. Neurol.* 140, 177–194. doi: 10.1016/B978-0-444-63600-3.00011-8

Varvel, N. H., Neher, J. J., Bosch, A., Wang, W., Ransohoff, R. M., Miller, R. J., et al. (2016). Infiltrating monocytes promote brain inflammation and exacerbate neuronal damage after status epilepticus. *Proc. Natl. Acad. Sci. U.S.A.* 113, E5665–E5674. doi: 10.1073/pnas.1604263113

Vinet, J., Vainchtein, I. D., Spano, C., Giordano, C., Bordini, D., Curia, G., et al. (2016). Microglia are less pro-inflammatory than myeloid infiltrates in the hippocampus of mice exposed to status epilepticus. *Glia* 64, 1350–1362. doi: 10.1002/glia.23008

Wan, S., Cheng, Y., Jin, H., Guo, D., Hua, Y., Keep, R. F., et al. (2016). Microglia activation and polarization after intracerebral hemorrhage in mice: the role of protease-activated receptor-1. *Transl. Stroke Res.* 7, 478–487. doi: 10.1007/s12975-016-0472-8

Wang, J. (2010). Preclinical and clinical research on inflammation after intracerebral hemorrhage. *Prog. Neurobiol.* 92, 463–477. doi: 10.1016/j.pneurobio.2010.08.001

Wang, J., and Tsirka, S. E. (2005). Contribution of extracellular proteolysis and microglia to intracerebral hemorrhage. *Neurocrit. Care* 3, 77–85. doi: 10.1385/NCC:3:1:077

Wang, M., Hong, X., Chang, C. F., Li, Q., Ma, B., Zhang, H., et al. (2015). Simultaneous detection and separation of hyperacute intracerebral hemorrhage and cerebral ischemia using amide proton transfer MRI. *Magn. Reson. Med.* 74, 42–50. doi: 10.1002/mrm.25690

Wu, H., Wu, T., Han, X., Wan, J., Jiang, C., Chen, W., et al. (2017). Cerebroprotection by the neuronal PGE2 receptor EP2 after intracerebral hemorrhage in middle-aged mice. *J. Cereb. Blood Flow Metab.* 37, 39–51. doi: 10.1177/0271678X15625351

Wu, H., Wu, T., Xu, X., Wang, J., and Wang, J. (2011). Iron toxicity in mice with collagenase-induced intracerebral hemorrhage. *J. Cereb. Blood Flow Metab.* 31, 1243–1250. doi: 10.1038/jcbfm.2010.209

Wu, H., Zhang, Z., Hu, X., Zhao, R., Song, Y., Ban, X., et al. (2010). Dynamic changes of inflammatory markers in brain after hemorrhagic stroke in humans: a postmortem study. *Brain Res.* 1342, 111–117. doi: 10.1016/j.brainres.2010.04.033

Yang, B., Parsha, K., Schaar, K., Xi, X., Aronowski, J., and Savitz, S. I. (2016). Various cell populations within the mononuclear fraction of bone marrow contribute to the beneficial effects of autologous bone marrow cell therapy in a rodent stroke model. *Transl. Stroke Res.* 7, 322–330. doi: 10.1007/s12975-016-0462-x

Yang, J., Ding, S., Huang, W., Hu, J., Huang, S., Zhang, Y., et al. (2016). Interleukin-4 ameliorates the functional recovery of intracerebral hemorrhage through the alternative activation of microglia/macrophage. *Front. Neurosci.* 10:61. doi: 10.3389/fnins.2016.00061

Yang, J., Li, Q., Wang, Z., Qi, C., Han, X., Lan, X., et al. (2017). Multimodality MRI assessment of grey and white matter injury and blood-brain barrier disruption after intracerebral haemorrhage in mice. *Sci. Rep.* 7:40358. doi: 10.1038/srep40358

Yu, A., Zhang, T., Duan, H., Pan, Y., Zhang, X., Yang, G., et al. (2017). MiR-124 contributes to M2 polarization of microglia and confers brain inflammatory protection via the C/EBP-alpha pathway in intracerebral hemorrhage. *Immunol. Lett.* 182, 1–11. doi: 10.1016/j.imlet.2016.12.003

Zhang, Z., Zhang, Z., Lu, H., Yang, Q., Wu, H., and Wang, J. (2017). Microglial polarization and inflammatory mediators after intracerebral hemorrhage. *Mol. Neurobiol.* 54, 1874–1886. doi: 10.1007/s12035-016-9785-6

Zhou, K., Zhong, Q., Wang, Y. C., Xiong, X. Y., Meng, Z. Y., Zhao, T., et al. (2017). Regulatory T cells ameliorate intracerebral hemorrhage-induced inflammatory injury by modulating microglia/macrophage polarization through the IL-10/GSK3beta/PTEN axis. *J. Cereb. Blood Flow Metab.* 37, 967–979. doi: 10.1177/0271678X16648712

Zhou, Y., Wang, Y., Wang, J., Anne Stetler, R., and Yang, Q. W. (2014). Inflammation in intracerebral hemorrhage: from mechanisms to clinical translation. *Prog. Neurobiol.* 115, 25–44. doi: 10.1016/j.pneurobio.2013.11.003

Zhu, W., Gao, Y., Chang, C. F., Wan, J. R., Zhu, S. S., and Wang, J. (2014). Mouse models of intracerebral hemorrhage in ventricle, cortex, and hippocampus by injections of autologous blood or collagenase. *PLoS One* 9:e97423. doi: 10.1371/journal.pone.0097423

Zhu, W., Gao, Y., Wan, J., Lan, X., Han, X., Zhu, S., et al. (2018). Changes in motor function, cognition, and emotion-related behavior after right hemispheric intracerebral hemorrhage in various brain regions of mouse. *Brain Behav. Immun.* 69, 568–581. doi: 10.1016/j.bbi.2018.02.004

Conflict of Interest Statement: The authors declare that the research was conducted in the absence of any commercial or financial relationships that could be construed as a potential conflict of interest.

frontiers in Cellular Neuroscience

ORIGINAL RESEARCH
published: 09 January 2019
doi: 10.3389/fncel.2018.00525

Activin Receptor-Like Kinase 1 Combined With VEGF-A Affects Migration and Proliferation of Endothelial Cells From Sporadic Human Cerebral AVMs

*Qiang Hao[1,2], Hao Wang[1], Jun-Lin Lu[1,2], Li Ma[1,2], Xiao-Lin Chen[1,2], Xun Ye[1,2], Ya-Hui Zhao[1,2], Ming-Tao Li[1,2], Yu Chen[1,2] and Yuan-Li Zhao[1,2,3,4,5,6]**

[1] Department of Neurosurgery, Beijing Tiantan Hospital, Capital Medical University, Beijing, China, [2] Department of Neurosurgery, Peking University International Hospital, Peking University, Beijing, China, [3] China National Clinical Research Center for Neurological Diseases, Beijing, China, [4] Stroke Center, Beijing Institute for Brain Disorders, Beijing, China, [5] Beijing Key Laboratory of Translational Medicine for Cerebrovascular Disease, Beijing, China, [6] Basic Medical Science Department, Capital Medical University, Beijing, China

OPEN ACCESS

Edited by:
Sriharsha Kantamneni, University of Bradford, United Kingdom

Reviewed by:
Francesco Lodola, Fondazione Istituto Italiano di Technologia, Italy
Vincenza Rita Lo Vasco, Sapienza Università di Roma, Italy

***Correspondence:**
Yuan-Li Zhao
zhaoyuanli@126.com

Received: *29 September 2018*
Accepted: *17 December 2018*
Published: *09 January 2019*

Citation:
Hao Q, Wang H, Lu J-L, Ma L, Chen X-L, Ye X, Zhao Y-H, Li M-T, Chen Y and Zhao Y-L (2019) Activin Receptor-Like Kinase 1 Combined With VEGF-A Affects Migration and Proliferation of Endothelial Cells From Sporadic Human Cerebral AVMs. Front. Cell. Neurosci. 12:525. doi: 10.3389/fncel.2018.00525

Heterozygous loss of activin receptor-like kinase 1 (Alk1) can lead to hereditary hemorrhagic telangiectasia (HHT), which is a kind of vascular disease characterized by direct connections between arteries and veins with the lacking of capillaries, and develops into arteriovenous malformations (AVMs) in later stage. However, the changes of Alk1 in human sporadic cerebral AVMs (cAVMs) remain unknown. In the present study, we used endothelial cells (ECs) derived from human cAVMs (cAVM-ECs) specimens, to explore the characteristics of cAVM-ECs and the relationship between Alk1 and human sporadic cAVMs. Our data showed that there were obvious morphological changes in cAVM-ECs, and they could trans-differentiate into mesenchyme-like cells easily in a short period. In addition, the abilities of migration of cAVM-ECs were poorer than that in human aortic endothelial cells (HA-ECs). The abilities of proliferation of cAVM-ECs in patients with different ages were lower than HA-ECs. Immunofluorescent staining and Western blot showed that the levels of Alk1 mRNA and protein in the HA-ECs were both higher than that in cAVM-ECs. In addition, the levels of Alk1 mRNA had no significant differences between different ages in cAVM-ECs groups. The levels of VEGF-A mRNA in the cAVM were higher than HA-ECs. Besides, levels of VEGF-A mRNA expression were lower in older cAVM patients. Therefore, we conclude that Alk1 might induce the formation of sporadic human cAVMs through affecting migration and proliferation of endothelial cells combined with VEGF-A.

Keywords: cerebral arteriovenous malformation, endothelial cells, morphology, migration, proliferation, activin receptor like kinase 1, VEGF-A

INTRODUCTION

Cerebral arteriovenous malformations are vascular disorders characterized by an anomalous tangle of nidus in vessels, which are characterized by direct connections between arteries and veins with the lacking of capillaries. Hemorrhage is one of the most serious complications (da Costa et al., 2009; Lawton et al., 2015). Therefore, the most important therapeutic strategy is to prevent the rupture of cAVMs. Current clinical treatments include surgical resection, radiotherapy, and embolization. However, all of these treatments may bring high risks of morbidity, leading to serious complications (da Costa et al., 2009). For example, surgical resection may induce neural functional deficits when cAVMs are located in the functional areas; the intervention of radiosurgery may be restricted by sizes of cAVMs (Wang et al., 2016). However, embolization is a minimally invasive treatment, which may be restricted when cAVMs are scattered and/or feeded by small feeding arteries (Sammons et al., 2011). Therefore, biological therapeutic method may be a promising option for cAVMs. Before biological therapies are developed, we should fully understand the pathophysiology and molecular mechanisms of cAVMs. As an important component of vessels in cAVMs, the endothelium has great theoretical potential as a therapeutic target.

Based on the researches of histological properties of cAVMs in patients with hereditary hemorrhagic telangiectasia (HHT), we speculate that the development of cAVMs originate from a focal dilation of a post capillary venues, leading to arteriole dilation progression and subsequent loss of intervening capillaries (Braverman et al., 1990). In previous studies, sub-dermal arteriovenous malformations (AVMs) are induced in wounds of activin receptor-like kinase 1 (Alk1)-mutant mice, which appeared in the form of both arteries and veins elongation followed by arterial-venous connections *de novo* (Kim et al., 2011; Laux et al., 2013; Garrido-Martin et al., 2014). Although these solid findings are confirmed by the longitudinal imaging of vascular growth, they still remained unclear in cellular level. Therefore, abnormal behaviors of endothelial cells (ECs) may cause AVMs and need to be elucidated in the sporadic patients with cAVMs. Considering the possible relationship between Alk1 function and cAVMs development, we hypothesized that Alk1 may play an important role in the formation of cAVMs by trans-differentiation and changes of ability of migration and proliferation in ECs derived from cAVMs.

Therefore, in this study, we isolated ECs from sporadic human cAVMs patients, to explore the potential mechanisms of occurrence and development of cAVMs in sporadic patients and get a better understanding *in vitro*.

MATERIALS AND METHODS

Isolation of ECs

Human surgical specimens were obtained in accordance with The Human Subject Review Committee of Tian Tan Hospital. cAVM-ECs were obtained from four males and four females, aged from 8 to 51 years old (average of 29.6 ± 14.55). Patients who involved in this study had not adopted gamma knife irradiation or embolization, and information was described in the **Table 1**. cAVM-ECs were isolated and selected by Flow cytometer, and identified by detecting ECs special markers (CD31 and CD34). In addition, their functional properties were detected by LDL-uptake and tube formation. All of cAVM-ECs used in this experiment were passaged to the forth generation at most. Human aortic endothelial cells (HA-ECs) were gained from ScienCell Company (ScienCell, Cat No. 6100, United States) and used as control ECs.

Immunocytochemistry

cAVM-ECs and HA-ECs were fixed in 4% paraformaldehyde for 20 min at RT, then blocked in 5% goat serum and incubated at 4°C with the following primary antibody: Rabbit polyclonal anti-human Alk1 (1:200, Cat No. ab68703, Abcam, United States). The slides were then incubated with the appropriate secondary antibody: Anti-Rabbit IgG H&L (Alexa Fluor®488) (1:200, Cat No. ab150077, Abcam, United States) for 1 h. Coverslips with immunostained cells were mounted on glass slides in Vectashield mounting medium containing DAPI (Vector Laboratories, Cat No. H1200, United States). Immunostained cells were counted randomly from five fields under a Nikon Eclipse microscope.

Cell Migration Assay

The ability of ECs migration was detected by scratch test. cAVM-ECs and HA-ECs were seeded into a 12-well plate at the concentration of 0.5×10^5 cells per well, respectively. When cells contacted with each other, they were scratched vertically with a 100 μl-pipette tip. Then, cells were washed twice with PBS and placed in serum-free culture medium. After 6 and 12 h, distances between the two sides of cells were measured under an invert phase-contrast microscope in five random fields, respectively. Each migration test was run in triplicate.

Cell Proliferation Assay

cAVM-ECs from eight patients were successfully passaged to the forth generation. To detect the proliferative ability of these cells, we seeded different patients' cAVM-ECs at the density of 0.1×10^5 per well, and the cells were cultured for 8 days. Then the cAVM-ECs were digested and counted. HA-ECs were used as control.

Western Blot

For preparation of total protein lysates, cells were lysed in cold RIPA buffer and centrifuged at 13,000 × *g* for 5 min at 4°C. Protein lysates were subjected to 10% SDS-PAGE gels, and then were transferred onto PVDF membranes. After blocking with 5% non-fat dried milk for 2 h at RT, membranes were incubated with the primary antibodies overnight at 4°C: Primary antibodies against Alk1 (1:1,000, Cell Signaling Technology, Cat No. 31278, United States) and GAPDH (1:5,000, Cell Signaling Technology, Cat No. 51332, United States), each primary antibody was diluted in blocking buffer and then incubated overnight at 4°C. The membranes were washed three times and incubated with horseradish peroxidase (HRP)-linked secondary antibody at RT

TABLE 1 | Clinical data of cerebral arteriovenous malformations patients who underwent microsurgical cAVMs resection.

Patient No.	Age (years)	Sex	Hemorrhage	cAVM size (cm)	Spetzler-Martin grade	Radiosurgery
1	14	Female	Yes	3	3	No
2	32	Male	No	4	4	No
3	51	Female	No	4	4	No
4	29	Female	Yes	5	5	No
5	17	Female	No	4	4	No
6	44	Male	Yes	6	5	No
7	8	Male	Yes	3	3	No
8	42	Male	No	5	4	No

The cAVMs endothelial cells (cAVMs-ECs) used in this experiment were derived from them.

for 1 h. Membranes were washed three times with TBST at RT. Protein bands were visualized on X-ray film. GAPDH was used as a loading control.

Quantitative Real-Time PCR

According to the manufacturer's protocol, total RNAs were isolated from EC using TRIzol reagent (Invitrogen). cDNAs were synthesized by reverse transcription using SuperScript III First-Strand Synthesis System kit (Invitrogen). TaqMan Gene Expression Assays (Applied Biosystems) was used for qPCR to quantify relative expression of each gene using Mx3000P QPCR System (Agilent Technologies). Predesigned qPCR primers: Alk1 (forward): 5′-CCACTCATTCCTCCTGGGTA-3′, Alk1 (reverse): 5′-ACTTCCTGACTAGGGGAGGAGTAG-3′; VEGF (forward): 5′-CCCACGAAGTGGTGAAGTTCA-3′, VEGF (reverse): 5′-CCACCAGGGTCTCGATGG-3′; GAPDH (forward): 5′-GATGGTGAAGGTCGGAGTGAAC-3′, GAPDH (reverse): 5′-GTCATTGATGGCGACGATGT-3′. RNase free dH_2O was used as the negative control reaction.

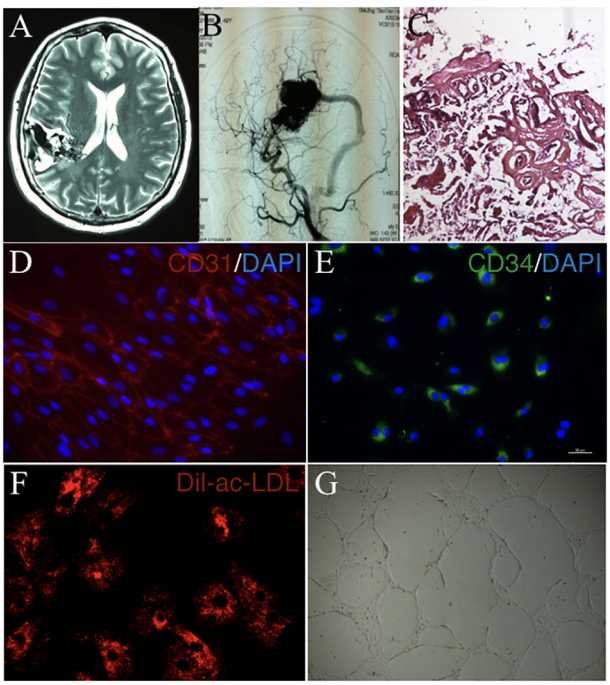

FIGURE 1 | The general characteristics of cAVM and cAVM-ECs. **(A)** T2WI of MRI imaging; **(B)** Digital subtraction angiography (DSA) showed cerebral middle artery provided blood for the cAVM nidus as a feeder artery, which connected to the sigmoid sinus through thick draining vessel; **(C)** Photomicrograph of cAVM with deformed vascular wall, and the nidus of the cAVM had many collagen fibers, lacking of smooth muscle and elastic fibers; **(D,E)** Immunostaining of ECs showed special markers CD31 and CD34 expressed in cAVM-ECs; **(F)** LDL uptake assay of cAVM-ECs; **(G)** Tube formation of cAVM-ECs. Scale bar = 200 μm.

Statistical Analysis

All data were presented as Mean ± SD and subjected to statistical analysis using GraphPad Prism software 6.0 (United States). Student's *t*-test was used for group comparisons between two groups. When there were more than two groups, the one-factor ANOVA (ANOVA) followed by Tukey's *post-hoc* test was used for comparisons between groups. Statistical significance was defined at $p < 0.05$.

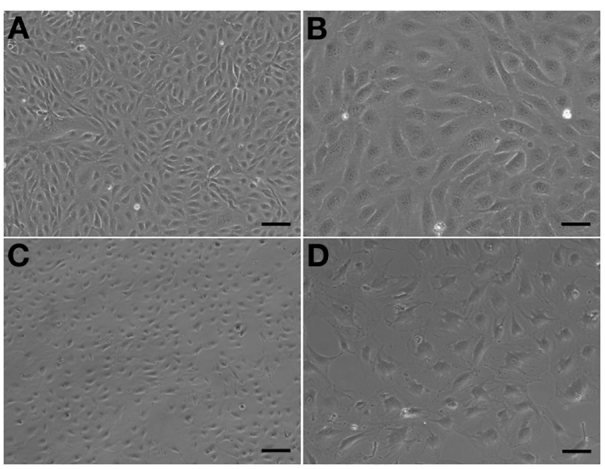

FIGURE 2 | Morphology of human aortic endothelial cells (HA-ECs) and cAVM-ECs. **(A,B)** Morphology of HA-ECs under microscope in **(A)** 40×, Scale bar = 100 μm; **(B)** 100×, Scale bar = 50 μm, showed classical round borders and cobblestone appearance; **(C,D)** showed irregular borders and flatty bodies with smaller nuclei, **(C)** 40×, Scale bar = 100 μm; **(D)** 100×, Scale bar = 50 μm.

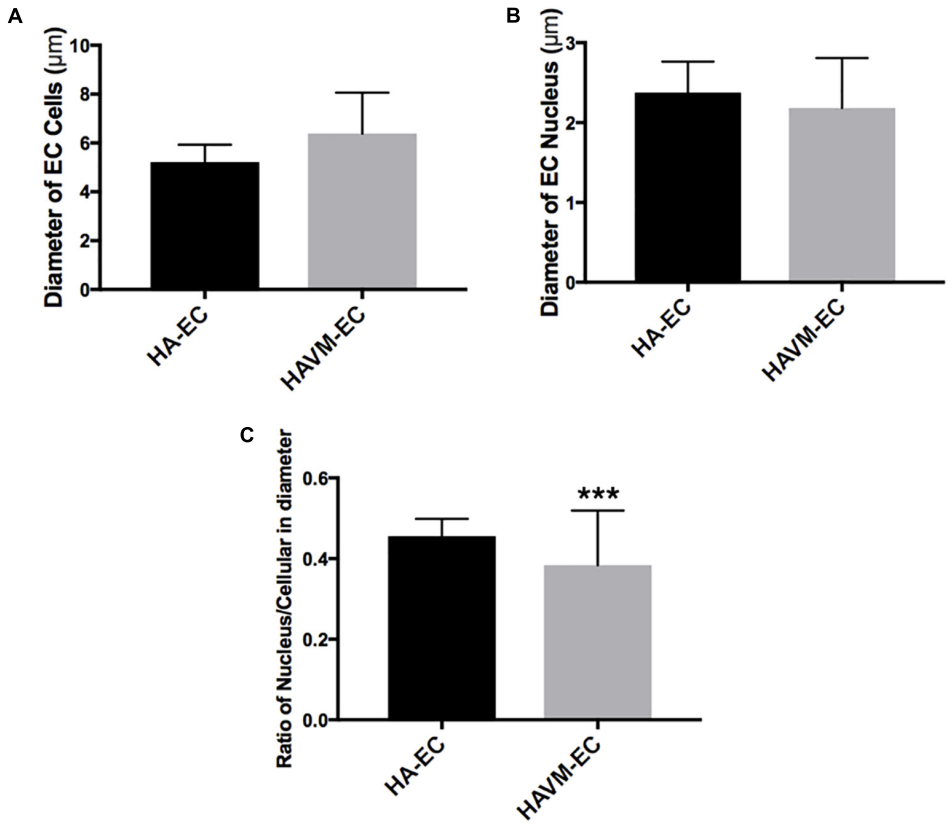

FIGURE 3 | Changes of morphology in cAVM-ECs. **(A)** Average diameters of body in cAVM-ECs and HA-ECs, (6.391 ± 0.5283) μm in cAVM-ECs, were larger than that (5.222 ± 0.2224) μm in HA-ECs ($p > 0.05$); **(B)** The average diameters of nucleus in cAVM-ECs (2.183 ± 0.1981) μm, were smaller than that (2.377 ± 0.1226) μm in HA-ECs ($p > 0.05$); **(C)** Ratios of nucleus to cellular in cAVM-ECs was (0.3437 ± 0.02426), and that in HA-ECs was (0.4557 ± 0.01356), and there was a significant difference between them ($p < 0.05$).

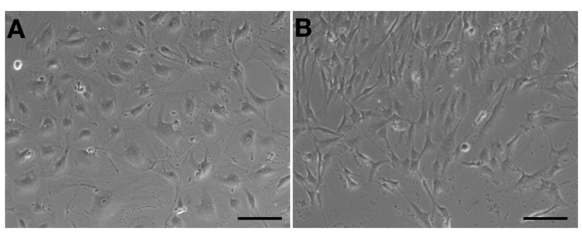

FIGURE 4 | cAVM-ECs trans-differentiated into mesenchyme-like cells in a short period. **(A)** HA-ECs kept the general morphology of ECs when passaged to 7th–8th population without morphological change; **(B)** The morphology of cultured cAVM-ECs changed into spindle-like cells after passaged to the forth generation.

RESULTS

Isolated ECs From Human cAVM (cAVM-ECs)

cAVMs were characterized by conglomerate of tortuous vessels, including feeding arteries and draining veins. We found cluttered vessels flow void in the right temporal-parental area in T2WI of MRI imaging (**Figure 1A**). Digital subtraction angiography (DSA) results showed that cerebral middle artery provided blood for the cAVM nidus as feeder artery, which was connected with the sigmoid sinus through thick draining vessel (**Figure 1B**). Under the operational microscope (Carl Zeiss, Pentero 800, United States), we found abnormal vessels nidus occupied on the brain surface scrabbly (**Figure 1C**). In addition, immunostaining results demonstrated that cAVM-ECs expressed typical EC markers, such as CD31 and CD34 (**Figures 1D,E**). These cells derived from cAVMs also possessed the functional properties of general ECs, including the ability of Dil-Ac-LDL uptake and tube formation on 3D matrigel (**Figures 1F,G**). Therefore, the isolated cAVM-ECs not only have the cellular characteristics in morphology and special markers of ECs, but also have the common functional properties of ECs (Hao et al., 2018).

Morphological Characteristics of cAVM-ECs

Observed under a phase-contrast microscope, the HA-ECs had classical round borders and cobblestone appearances (**Figures 2A,B**). When cAVM-ECs contacted with each other, they showed irregular borders and flatty bodies (**Figures 2C,D**). Compared to HA-ECs, these isolated cells showed rough edges

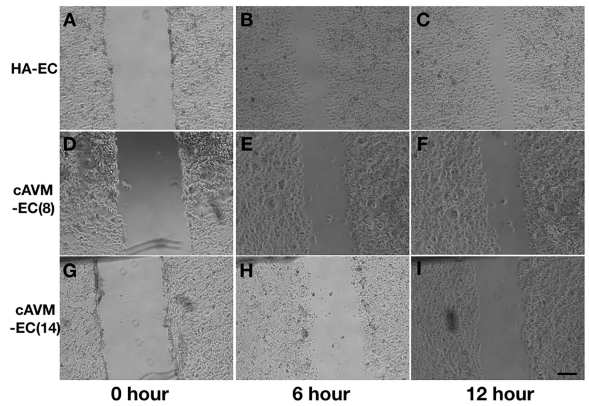

FIGURE 5 | Scratch assay in cAVM-ECs and HA-ECs. When HA-ECs and cAVM-ECs (derived from 8- and 14-year-old patients) were seeded in the 24-well plate, we detected the ability of migration among three groups at 6 and 12 h after seeding, respectively. **(A–C)** Scratch assay in HA-ECs, **(A)** 0 h after Scratched, **(B)** 6 h after Scratched, **(C)** 12 h after Scratched; **(D–F)** Scratch assay in cAVM-ECs (derived from 8-year-old patient), **(D)** 0 h after Scratched, **(E)** 6 h after Scratched, **(F)** 12 h after Scratched; **(G–I)** Scratch assay in cAVM-ECs (derived from 14-year-old patient), **(G)** 0 h after Scratched, **(H)** 6 h after Scratched, **(I)** 12 h after Scratched; Scale bar = 100 μm.

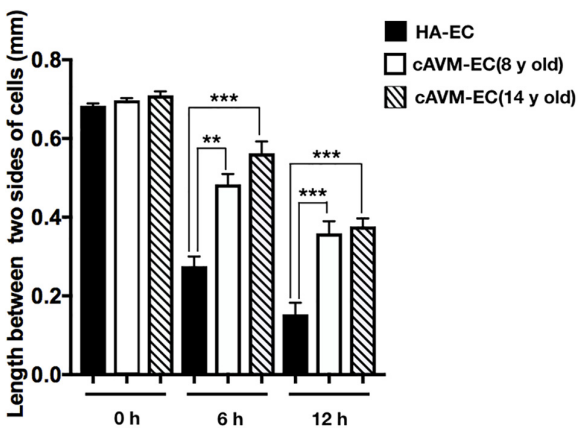

FIGURE 6 | Statistical analysis of scratch assay in cAVM-ECs and HA-ECs. After 6 h, the distances between two sides of scratch in HA-ECs were (0.276 ± 0.024) mm, (0.483 ± 0.026) mm in cAVM-ECs of 8-year-old, and (0.563 ± 0.030) mm in cAVM-ECs of 14-year-old (all $*p < 0.05$). After 12 h, the distances between two sides of scratch in HA-ECs were (0.153 ± 0.029) mm, (0.359 ± 0.030) mm in cAVM-ECs of 8-year-old, (0.376 ± 0.021) mm in and cAVM-ECs of 14-year-old (all $*p < 0.05$). Besides, the distances between two sides of scratch in cAVM of 8- and 14-year-old patients had no significant difference.

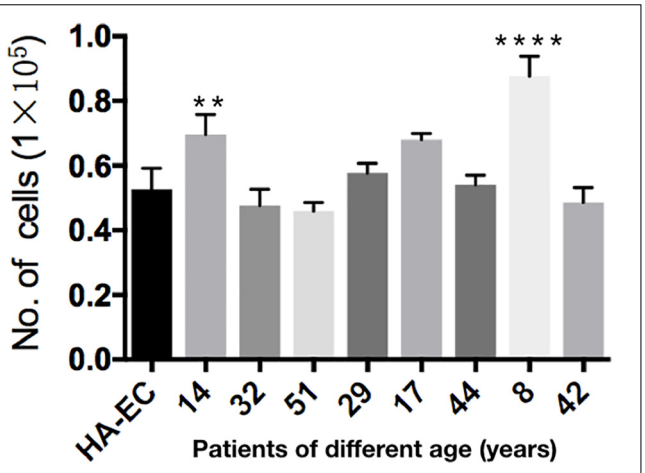

FIGURE 7 | Proliferative ability of HA-ECs and cAVM-ECs with different ages. HA-ECs and cAVM-ECs derived from eight patients were successfully passaged to the forth generation. The results showed that the number of HA-ECs was (0.527 ± 0.065) million, which was less than that in cAVM-ECs from (patient 8-year-old) (0.877 ± 0.06) million and cAVM-ECs from (patient 14-year-old) (0.697 ± 0.061) (all $*p < 0.05$).

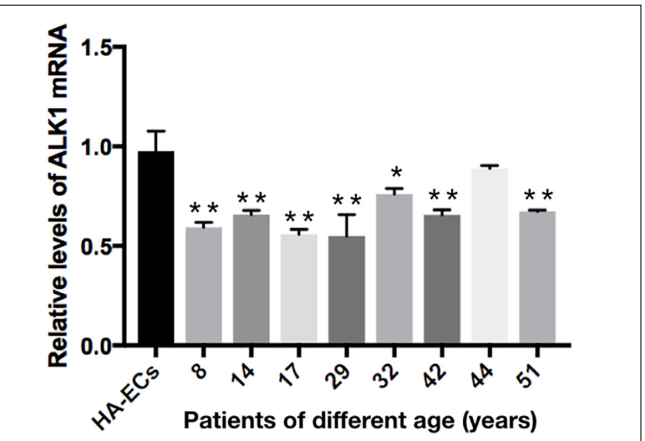

FIGURE 8 | mRNA expression of gene Alk1 in HA-ECs and cAVM-ECs in patients with different ages. Levels of VEGF-A mRNA expression (0.986 ± 0.134) in the HA-ECs were lower than that in cAVM-ECs (8 years) (4.183 ± 0.238) and cAVM-ECs (14 years) (3.834 ± 0.451) (all $*p < 0.05$). In addition, the levels of VEGF-A mRNA expression were (2.92 ± 0.58) in cAVM-ECs (17 years), (3.04 ± 0.79) in cAVM-ECs (29 years), (3.08 ± 0.37) in cAVM-ECs (32 years), (2.08 ± 0.28) in cAVM-ECs (42 years), (1.97 ± 0.24) in cAVM-ECs (44 years), and (1.97 ± 0.25) in cAVM-ECs (51 years), all of that were higher than that (0.986 ± 0.134) in HA-ECs (all $*p < 0.05$).

and had no obvious gloss. In addition, the average diameter of cAVM-ECs body was 6.391 ± 0.5283 μm, which was larger than that in HA-ECs (5.222 ± 0.2224 μm) ($p > 0.05$); the average diameter of nucleus of cAVM-ECs was 2.183 ± 0.1981 μm, which was smaller than that in HA-ECs (2.377 ± 0.1226 μm) ($p > 0.05$). There was no significant difference between cAVM-ECs and HA-ECs. However, the ratio of nucleus to cellular in diameter of cAVM-ECs (0.3437 ± 0.02426) was smaller than that in HA-ECs (0.4557 ± 0.01356), and there was significant difference ($p < 0.05$) (**Figure 3**). These results showed that obvious changes existed in the morphology of cAVM-ECs.

Trans-Differentiation Into Mesenchyme-Like Cells in a Short Period

Human aortic endothelial cells could be passaged to seventh or eighth population without morphological changes (**Figure 4A**).

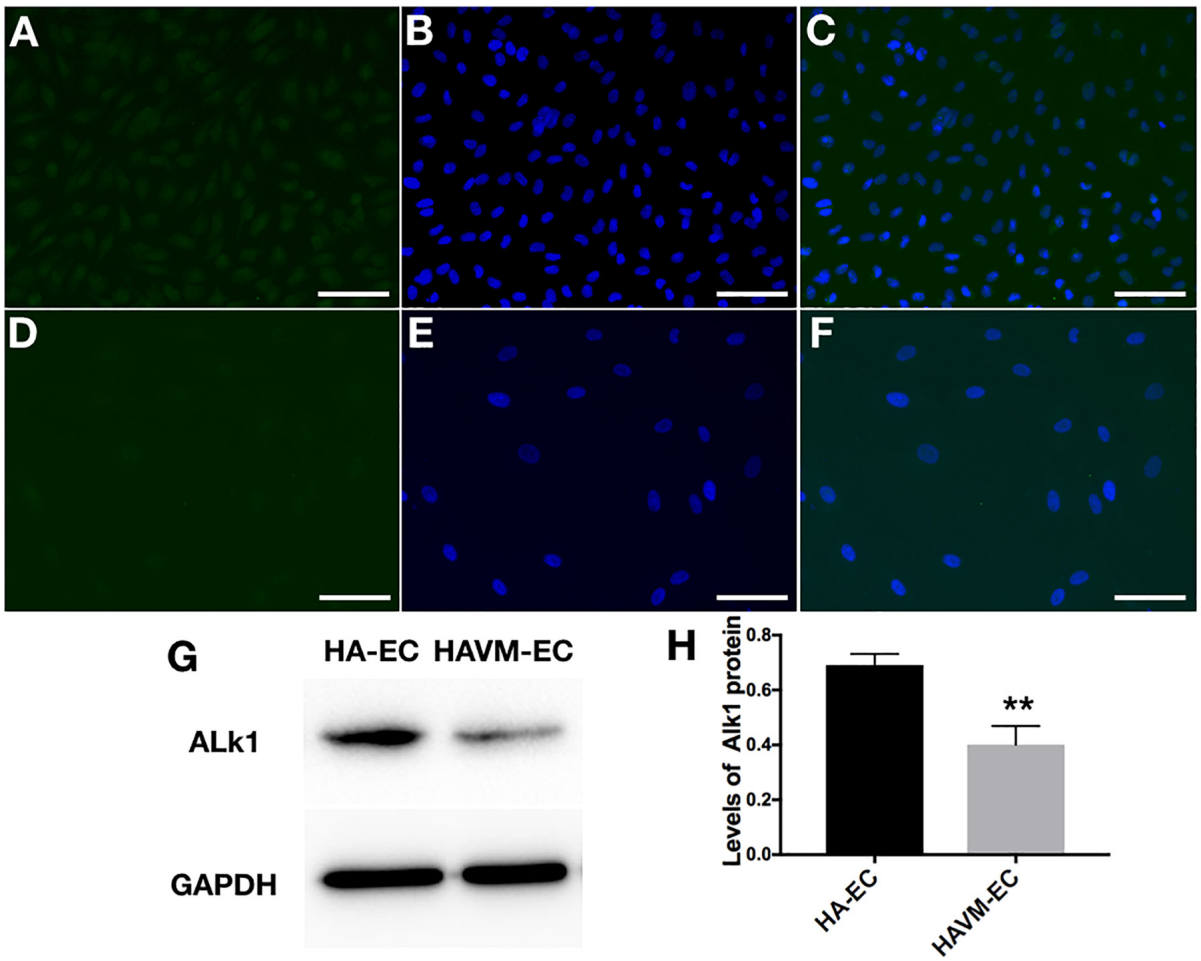

FIGURE 9 | Expression of Alk1 proteins in HA-ECs and cAVM-ECs. **(A–D)** Immunofluorescent staining to detect the Alk1 protein expressed in HA-ECs and cAVM-ECs. **(A–C)** In HA-ECs, **(A)** Alk1 protein was stained by Green fluorescent, **(B)** nuclei was stained by DAPI in Green fluorescent; **(C)** merge; **(D–F)** In cAVM-ECs, **(D)** Alk1 protein was stained by Green fluorescent, **(E)** nuclei was stained by DAPI in Green fluorescent; the fluorescence intensity in cAVM-ECs was obviously lower than in HA-ECs; **(F)** merge. Scale bar = 200 μm; **(G)** Detect the expression of Alk1 by Western blot, **(H)** expression of Alk1 proteins in the HA-ECs cultures were significantly higher than that in cAVM-ECs *in vitro* (*$p < 0.05$).

However, compared to HA-ECs, the morphology of cAVM-ECs changed into spindle-like cells after passaged to the forth generation (**Figure 4B**). These results demonstrate that the cAVM-ECs can not maintain the characteristics of morphology for a long time, and easily trans-differentiate into mesenchyme-like cells in a short period.

Poor Ability of Migration in cAVM-ECs

After HA-ECs and cAVM-ECs (derived from 8- and 14-year-old patients) were seeded in the 24-well plate, we analyzed the ability of migration among three groups in 6 and 12 h, respectively. Because of limitation of cAVM-ECs sources, we just detected cAVM-ECs from 8- to 14-year-old patients. The distances between two sides of scratch in HA-ECs were shorter than that in the other two cAVM-ECs groups, measured, respectively, at 6 and 12 h after seeded. 6 h later, the distances between two sides of scratch in HA-ECs were 0.276 ± 0.024 and 0.483 ± 0.026 mm in cAVM-ECs of 8-year-olds, and 0.563 ± 0.030 mm in cAVM-ECs of 14-year-olds (all*$p < 0.05$). 12 h later, the distances between two sides of scratch in HA-ECs were 0.153 ± 0.029 mm, 0.359 ± 0.030 mm in cAVM-ECs of 8-year-old, and 0.376 ± 0.021 mm in cAVM-ECs of 14-year-old (all *$p < 0.05$). In addition, the distances in cAVM of 8- and 14-year-old patients had no significant difference (**Figures 5**, **6**). These results demonstrate that ability of migration in the cAVM-ECs groups decreases significantly compared to HA-ECs group.

Proliferative Ability of cAVM-ECs Derived From Different Age Patients

Human aortic endothelia cells and cAVM-ECs from eight patients were successfully passaged to the forth generation. To detect the proliferative ability of these cells, we seeded HA-ECs and cAVM-ECs derived from different age patients at the density of 0.1×10^5 per well. Cultured for 8 days later, all of the ECs

were digested and counted. The results showed that the number of HA-ECs was 0.527 ± 0.065 million and less than that in cAVM-ECs (0.877 ± 0.06 million in 8-year-old patient and 0.697 ± 0.061 million in 14-year-old patient) (all $^*p < 0.05$). In addition, there were no significant differences in other patients groups. Besides, the number of cAVM-ECs in 8-year-old patient was higher than that in all the other groups ($^*p < 0.05$) (**Figure 7**).

Lower Expression of Alk1 in cAVM-ECs

The levels of Alk1 mRNA were tested by qRT-PCR. Results showed that the levels of expression of Alk1 mRNA were 0.59 ± 0.03 in cAVM-ECs (8 years), 0.66 ± 0.02 in cAVM-ECs (14 years), 0.66 ± 0.02 in cAVM-ECs (17 years), 0.55 ± 0.1 in cAVM-ECs (29 years), 0.76 ± 0.03 in cAVM-ECs (32 years), 0.66 ± 0.02 in cAVM-ECs (42 years), and 0.67 ± 0.01 in cAVM-ECs (51 years), and all of them were lower than that in HA-ECs (0.98 ± 0.1) (all $^*p < 0.05$). In addition, there were no significant differences between the different cAVM-ECs groups. The levels of Alk1 mRNA in cAVM-ECs (44 years) (0.89 ± 0.01) was lower than that in HA-ECs (0.96 ± 0.1), however, there was no significant difference between them (**Figure 8**). In addition, immunofluorescent staining showed that HA-ECs and cAVM-ECs were Alk1-positive in Cytoplasm. However, the fluorescence intensity in cAVM-ECs was obviously lower than that in HA-ECs (**Figures 9A–F**). Besides, due to the limitation of the cAVM-ECs sources, we combined all of the cAVM-ECs groups to detect the average levels of Alk1 expression. Western blot results also confirmed that the levels of Alk1 proteins in the HA-ECs were higher than that in cAVM-ECs ($^*p < 0.05$) (**Figures 9G,H**).

Increasing Expression of VEGF-A in cAVM-ECs

The levels of VEGF-A gene expression were examined by qRT-PCR analysis. Results showed the levels of VEGF-A mRNA were 0.98 ± 0.13 in the HA-ECs, which was lower than that in cAVM-ECs (8 years) (4.183 ± 0.238) and cAVM-ECs (14 years) (3.834 ± 0.451) (all $^*p < 0.05$). In addition, the levels of VEGF-A mRNA were 2.92 ± 0.58 in cAVM-ECs (17 years), 3.04 ± 0.79 in cAVM-ECs (29 years), 3.08 ± 0.37 in cAVM-ECs (32 years), 2.08 ± 0.28 in cAVM-ECs (42 years), 1.97 ± 0.24 in cAVM-ECs (44 years), and 1.97 ± 0.25 in cAVM-ECs (51 years), which all of those were higher than that in the HA-ECs (0.98 ± 0.13) (all $^*p < 0.05$). These results showed that the levels of VEGF-A in cAVM-ECs were higher than that in HA-ECs. In addition, the levels of VEGF-A in the older patients with cAVM were lower than that in the younger patients (**Figure 10**).

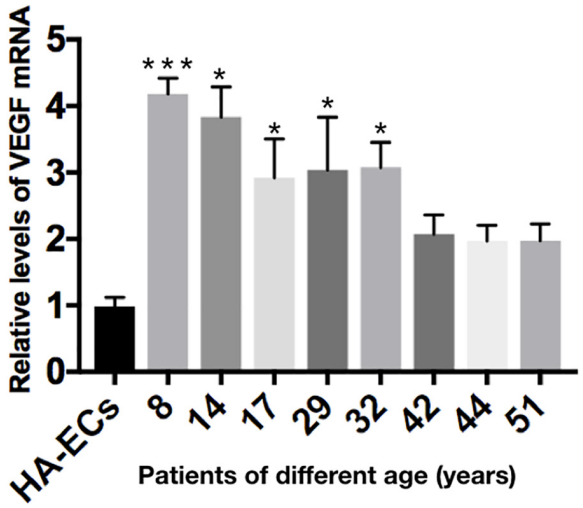

FIGURE 10 | mRNA expression of gene VEGF in HA-ECs and cAVM-ECs with different ages. Level of VEGF-A mRNA expression in the HA-ECs (0.98 ± 0.13) was lower than that in cAVM-ECs (8 years) (4.183 ± 0.238) and cAVM-ECs (14 years) (3.834 ± 0.451) (all $^*p < 0.05$). Level of VEGF-A mRNA expression in cAVM-ECs (17 years) was (2.92 ± 0.58), in cAVM-ECs (29 years) was (3.04 ± 0.79), in cAVM-ECs (32 years) was (3.08 ± 0.37), in cAVM-ECs (42 years) was (2.08 ± 0.28), in cAVM-ECs (44 years) was (1.97 ± 0.24), and in cAVM-ECs (51 years) was (1.97 ± 0.25), all of that were higher than that in the HA-ECs (0.98 ± 0.13) (all $^*p < 0.05$).

DISCUSSION

The isolated human cAVM-ECs owned the general characteristics of ECs, such as cobblestone-like morphology, the special markers of ECs (CD31 and CD34), and the functional properties of LDL intake and tube formation. However, compared with normal HA-ECs, we found some changes of AVM-ECs in morphology, such as irregular borders, smaller nucleus and bigger cell bodies, all of which might induce functional changes of these cells. For instance, in our experiment, we found that AVM-ECs could differentiate into mesenchyme-like cells when passaged into forth generation. In addition, cAVM-ECs proliferated faster and migrated more slowly than that in HA-ECs. These results demonstrate that ECs play an important role in the occurrence and development in sporadic human cAVMs.

In the scratch assay, we found that the speeds of migration in cAVM-ECs were obviously lower than that in HA-ECs. In addition, we detected the levels of Alk1 expression in cAVM-ECs and HA-ECs, using immunofluorescent staining and qRT-PCR, respectively. The results showed that the density of fluorescent of Alk1 positive cells in cAVM-ECs was lower than that in HA-ECs. In addition, levels of Alk1 proteins expression in HA-ECs were higher than that in cAVM-ECs, detected by Western blot assay. Besides, qRT-PCR results were in accordance with Western blot, and there were no significant differences between the different cAVM-ECs groups. Lower levels of Alk1 expression might inhibit the ability of cAVM-ECs migration. Rochon et al. reported, the main role of Alk1-mutant could not alter the arterial EC proliferation, but could alter the movement of arterial ECs in vessels. In Alk1-mutant ECs, directed migration of ECs could be impaired (Rochon et al., 2016). Therefore we speculate that decreased Alk1 expression results in poorer ability of migration in sporadic cAVM-ECs, and Alk1 plays an important role in the formation of cAVMs.

In the proliferation assay, we compared the proliferative ability between the HA-ECs group and cAVM-ECs with different ages groups. The results showed that cAVM-ECs proliferated faster than HA-ECs. We also detected the levels of

VEGF-A expression in HA-ECs and cAVM-ECs with different ages using qRT-PCR. We found that levels of VEGF-A expression in cAVM-ECs were higher than that in HA-ECs. VEGF-A did not only stimulate endothelial migration, but also enhanced the ability of proliferation (Eichmann and Simons, 2012). This conclusion was partly in accordance with our results. However, Pro Gerhardt pointed that neighboring cells contributed to elongation and stability of the new vessel (stalk cells), when some of ECs formed polarized filopodia protrusions and acquire the leading tip position in the nascent sprout (tip cells) (Gerhardt et al., 2003).

In our previous research, we found that the Alk1-mutant mice would not form cAVMs without local VEGF over-expression. Hence, we thought that down-regulation of Alk1 expression combined with the up-regulation of VEGF, could accurately reflect the formation development of cAVMs in the sporadic patients. Actually, we found that the levels of VEGF expression were higher in the sporadic patients than that in normal control in another experiment, detected by ELISA Testing blood samples. The down-regulation of Alk1 expression might influent the ability of migration in ECs, while over-expression of VEGF might enhance the proliferative ability. Both of which could induce the formation of an abnormal vessel nidus. In addition, high doses of VEGF injected in the selected cerebral area of the Alk1-mutant mice could lead to cerebral hemorrhage. Professor Park and Martin reported previously, regional or tissue-specific conditional gene deletion of either Eng or Alk1 could produce AVMs when *de novo* angiogenesis was stimulated by VEGF in mice (Park et al., 2009; Garrido-Martin et al., 2014).

In addition to the above-mentioned, products of ENG and MADH4 were also the receptors or signaling molecules of the TGFβ/BMPs pathway (Urness et al., 2000; Sorensen et al., 2003). They might affect proliferation, differentiation, migration and extracellular matrix formations of ECs, which all played a critical role in the proper development of the blood vessels. Alk1 might promote cell migration and proliferations collaborated with ENG.

In order to further explore the further mechanism of cAVMs formation and development in sporadic patients, we should optimize the methods of isolation and culturing to increase the yield of cAVM-ECs. And the anti-VEGF treatment may be a promising option to treat AVMs. In the future, VEGF might be neutralized to reduce their levels, and to detect whether it could repair the morphology and reduce the rate of hemorrhage induced by cAVMs.

CONCLUSION

Alk1 might induce the formation of sporadic human cAVMs through affecting migration and proliferation of ECs, combined with VEGF-A.

ETHICS STATEMENT

This experiment was approved by the Beijing Tian Tan Hospital Ethics Committee (Beijing, China).

AUTHOR CONTRIBUTIONS

Y-LZ designed the whole experiments and QH participated in the whole proceed. J-LL, HW, X-LC, LM, XY, M-TL, Y-HZ, and YC took part in the collection of AVM tissues and discussion.

FUNDING

This study was supported by grant nos. 81571110, 81271313, and 81500995 to Y-LZ, from The National Natural Science Fund, China, Grant nos. 2017A07 to Y-LZ, from Beijing Bai Qian Wan Talent Engineering Fund, Beijing, China, Grant nos. PX2016034 to HW from Beijing Municipal Administration of Hospitals Incubating Program.

REFERENCES

Braverman, I. M., Keh, A., and Jacobson, B. S. (1990). Ultrastructure and three-dimensional organization of the telangiectases of hereditary hemorrhagic telangiectasia. *J. Invest. Dermatol.* 95, 422–427. doi: 10.1111/1523-1747.ep12555569

da Costa, L., Wallace, M. C., Ter Brugge, K. G., O'Kelly, C., Willinsky, R. A., and Tymianski, M. (2009). The natural history and predictive features of hemorrhage from brain arteriovenous malformations. *Stroke* 40, 100–105. doi: 10.1161/STROKEAHA.108.524678

Eichmann, A., and Simons, M. (2012). VEGF signaling inside vascular endothelial cells and beyond. *Curr. Opin. Cell. Biol.* 24, 188–193. doi: 10.1016/j.ceb.2012.02.002

Garrido-Martin, E. M., Nguyen, H. L., Cunningham, T. A., Choe, S. W., Jiang, Z., Arthur, H. M., et al. (2014). Common and distinctive pathogenetic features of arteriovenous malformations in hereditary hemorrhagic telangiectasia 1 and hereditary hemorrhagic telangiectasia 2 animal models–brief report. *Arterioscler. Thromb Vasc. Biol.* 34, 2232–2236. doi: 10.1161/ATVBAHA.114.303984

Gerhardt, H., Golding, M., Fruttiger, M., Ruhrberg, C., Lundkvist, A., Abramsson, A., et al. (2003). VEGF guides angiogenic sprouting utilizing endothelial tip cell filopodia. *J. Cell Biol.* 161, 1163–1177. doi: 10.1083/jcb.200302047

Hao, Q., Chen, X., Ma, L., Wang, T., Hu, Y., and Zhao, Y. (2018). Procedure for the isolation of isolation of endothelial cells from human cerebral arteriovenous malformation(cAVM) tissues. *Front. Cell. Neurosci.* 12:30. doi: 10.3389/fncel.2018.00030

Kim, H., Su, H., Weinsheimer, S., Pawlikowska, L., and Young, W. L. (2011). Brain arteriovenous malformation pathogenesis: a response-to-injury paradigm. *Acta. Neurochir. Suppl.* 111, 83–92. doi: 10.1007/978-3-7091-0693-8_14

Laux, D. W., Young, S., Donovan, J. P., Mansfield, C. J., Upton, P. D., and Roman, B. L. (2013). Circulating Bmp10 acts through endothelial Alk1 to mediate flow-dependent arterial quiescence. *Development* 140, 3403–3412. doi: 10.1242/dev.095307

Lawton, M. T., Rutledge, W. C., Kim, H., Stapf, C., Whitehead, K. J., Li, D. Y., et al. (2015). Brain arteriovenous malformations. *Nat. Rev. Dis. Primers* 1:15008. doi: 10.1038/nrdp.2015.8

Park, S. O., Wankhede, M., Lee, Y. J., Choi, E. J., Fliess, N., Choe, S. W., et al. (2009). Real-time imaging of de novo arteriovenous malformation in a mouse

model of hereditary hemorrhagic telangiectasia. *J. Clin. Invest.* 119, 3487–3496. doi: 10.1172/JCI39482

Rochon, E. R., Menon, P. G., and Roman, B. L. (2016). Alk1 controls arterial endothelial cell migration in lumenized vessels. *Development* 143, 2593–2602. doi: 10.1242/dev.135392

Sammons, V., Davidson, A., Tu, J., and Stoodley, M. A. (2011). Endothelial cells in the context of brain arteriovenous malformations. *J. Clin. Neurosci.* 18, 165–170. doi: 10.1016/j.jocn.2010.04.045

Sorensen, L. K., Brooke, B. S., Li, D. Y., and Urness, L. D. (2003). Loss of distinct arterial and venous boundaries in mice lacking endoglin, a vascular-specific TGFbeta coreceptor. *Dev. Biol.* 261, 235–250. doi: 10.1016/S0012-1606(03)00158-1

Urness, L. D., Sorensen, L. K., and Li, D. Y. (2000). Arteriovenous malformations in mice lacking activin receptor-like kinase-1. *Nat. Genet.* 26, 328–331. doi: 10.1038/81634

Wang, L., Lin, F., Wu, J., Jiao, Y., Cao, Y., Zhao, Y., et al. (2016). Plasticity of mor function and surgical outcomes in patients with cerebral arterivenous malformation involving primary motor area: insight from fMRI and DTI. *Chin. Neurosurg. J.* 12, 1–9.

Conflict of Interest Statement: The authors declare that the research was conducted in the absence of any commercial or financial relationships that could be construed as a potential conflict of interest.

frontiers in Cellular Neuroscience

ORIGINAL RESEARCH
published: 11 January 2019
doi: 10.3389/fncel.2018.00531

Targeting MAPK Pathways by Naringenin Modulates Microglia M1/M2 Polarization in Lipopolysaccharide-Stimulated Cultures

*Bei Zhang, Yi-Zheng Wei, Guo-Qing Wang, Dai-Di Li, Jing-Shan Shi and Feng Zhang**

Key Laboratory of Basic Pharmacology of Ministry of Education, Joint International Research Laboratory of Ethnomedicine of Ministry of Education, Zunyi Medical University, Zunyi, China

Neuroinflammation is considered to be an important and inevitable pathological process associated with all types of damages to, and disorders of, the central nervous system. The hallmark of neuroinflammation is the microglia activation. In response to different micro-environmental disturbances, microglia could polarize into either an M1 pro-inflammatory phenotype, exacerbating neurotoxicity, or an M2 anti-inflammatory phenotype, exerting neuroprotection. Therefore, shifting the polarization of microglia toward the M2 phenotype could possess a more viable strategy for the neuroinflammatory disorders treatment. Naringenin (NAR) is naturally a grapefruit flavonoid and possesses various kinds of pharmacological activities, such as anti-inflammatory and neuroprotective activities. In the present study, we aimed to investigate the potential effects of NAR on microglial M1/M2 polarization and further reveal the underlying mechanisms of actions. First, NAR inhibited lipopolysaccharide (LPS)-induced microglial activation. Then, NAR shifted the M1 pro-inflammatory microglia phenotype to the M2 anti-inflammatory M2 microglia state as demonstrated by the decreased expression of M1 markers (i.e., inducible TNF-α and IL-1β) and the elevated expression of M2 markers (i.e., arginase 1, IL-4, and IL-10). In addition, the effects of NAR on microglial polarization were dependent on MAPK signaling, particularly JNK inactivation, as evidenced by the fact that the selective activator of JNK abolished NAR-promoted M2 polarization and further NAR-inhibited microglial activation. Together, this study demonstrated that NAR promoted microglia M1/M2 polarization, thus conferring anti-neuroinflammatory effects via the inhibition of MAPK signaling activation. These findings might provide new alternative avenues for neuroinflammation-related disorders treatment.

Keywords: neuroinflammation, microglia polarization, lipopolysaccharide, naringenin, MAPK signaling

OPEN ACCESS

Edited by:
Sriharsha Kantamneni, University of Bradford, United Kingdom

Reviewed by:
Sharon DeMorrow, Texas A&M Health Science Center, United States
Miriam Sciaccaluga, University of Perugia, Italy

***Correspondence:**
Feng Zhang
zhangfengzmc@163.com

Received: *23 October 2018*
Accepted: *24 December 2018*
Published: *11 January 2019*

Citation:
Zhang B, Wei Y-Z, Wang G-Q, Li D-D, Shi J-S and Zhang F (2019) Targeting MAPK Pathways by Naringenin Modulates Microglia M1/M2 Polarization in Lipopolysaccharide-Stimulated Cultures. Front. Cell. Neurosci. 12:531. doi: 10.3389/fncel.2018.00531

INTRODUCTION

Accumulating evidence has confirmed that central nervous system (CNS) is an immunologically privileged site due to the limited inflammatory capacity with the presence of blood-brain barrier and the lack of lymphatic infiltration (Hanisch and Kettenmann, 2007). Recently, neuroinflammation is considered to be an important and inevitable pathological process associated

with all types of damages to, and disorders of, the CNS (Gemma, 2010). As the major cellular elements of neuroinflammation, microglia execute specific immune functions to maintain physiological homoeostasis (Dhama et al., 2015). In response to the pathogenic insult to the CNS, microglia become activated and undergo morphological changes with hypertrophy as well as functional transformations (Ji et al., 2013; Huo et al., 2018). Several lines of studies have indicated that microglia activation plays a pivotal role in the pathogenesis of neurological disorders, including trauma, brain infections coma stroke, ischemia, and neurodegenerative diseases (Nimmo and Vink, 2009). Furthermore, the activated microglia consist of two cell populations which have distinct and even opposing functions. These two microglial polarization extremes are termed as the classically activated M1 (pro-inflammatory) and alternatively activated M2 (anti-inflammatory) phenotypes (Hu et al., 2015). In addition, the two microglial distinct functional polarization states were discerned in the neurodegenerative diseases, such as Parkinson's disease (Bok et al., 2018). Generally, the activated M1 phenotype microglia are characterized by the increased production of pro-inflammatory factors, including tumor necrosis factor-α (TNF-α), interleukin-1β (IL-1β) and the upregulation of inducible nitric oxide synthase (iNOS), CD16, and CD68 (David and Kroner, 2011). Conversely, the activated M2 state microglia are demonstrated to upregulate anti-inflammatory mediators, such as arginase-1 (Arg-1), CD206, and transforming growth factor-β (TGF-β) (Saijo and Glass, 2011). Functionally, the microglia M1 phenotype exacerbates neuronal damage and impedes cellular repair during CNS trauma and disorders. On the contrary, the M2 microglia exert neuroprotection and promote neuronal recovery and remodeling (Mantovani et al., 2013). Therefore, shifting the polarization of microglia toward the M2 phenotype could possess a more viable strategy for the neuroinflammatory disorders treatment.

Naringenin (NAR) is naturally a grapefruit flavonoid and possesses various kinds of pharmacological activities, such as anti-oxidant, anti-inflammatory, cardioprotective and anti-tumor activities (Al-Dosari et al., 2017). The anti-inflammatory effects of NAR are well verified in several different models. NAR protected against airway remodeling after mycoplasma pneumoniae infection via the inhibition of autophagy-mediated lung inflammation and fibrosis (Lin et al., 2018). Also, NAR suppressed the development of precancerous lesions through controlling hyperproliferation and inflammation in the colon of rats (Rehman et al., 2018). Recently, in addition to these beneficial actions, growing interests have been focused on its neuroprotective actions (Kara et al., 2014). First, NAR conferred neuroprotection in Parkinson's disease animal models and attenuated neuroinflammatory reactions (Magalingam et al., 2015). Moreover, NAR produced analgesic effects via inhibiting oxidative stress and oxidation cytokine production (Manchope et al., 2016). However, whether NAR could promote microglial polarization to M2 phenotype and the mechanisms underlying NAR-mediated anti-neuroinflammatory effects remain unilluminated.

In the present study, we aimed to investigate the potential effects of NAR on microglial M1/M2 polarization and further reveal the underlying mechanisms of actions. Specifically, these findings might provide new alternative avenues for neuroinflammation-related disorders treatment.

MATERIALS AND METHODS

Reagents

Naringenin, lipopolysaccharide (LPS) and Anisomycin (ANI) were purchased from Sigma-Aldrich (St. Louis, MO, United States). Enzyme-linked Immunosorbent Assay (ELISA) kits were obtained from R&D Systems (Minneapolis, MN, United States). The fluorescence probe dichlorodihydrofluorescein diacetate (DCFH-DA) were bought from Sangon Biotech (San Diego, CA, United States). SYBR green polymerase chain reaction (PCR) master mix was purchased from Bio-Rad (CA, United States). Anti-mitogen-activated protein kinase (MAPK) signaling pathway antibodies were purchased from Cell signaling Technology (Beverly, MA, United States). Anti-ionize calcium binding adapter molecule 1 (Iba-1), anti-TNF-α, anti-Arg-1, and anti-β-actin antibodies were obtained from Proteintech Group (Chicago, IL, United States).

Cell Culture and Treatment

BV-2 cells, an immortalized murine microglial cell line, were obtained from Wuhan University Cell Library (Wuhan, China). Cells were cultured in DMEM/F12 medium with 10% FBS and 1% penicillin/streptomycin at 37°C in a humidified atmosphere containing 95% air and 5% CO_2. Cells were seeded into 24-well plates at 5×10^5/well or 96-well plates at 1×10^5/well. Cultures were pretreated with NAR (50 μM) for 1 h, and then incubated with or without ANI (5 nM) for another 1 h. Finally, LPS (100 ng/ml) were added to cultures for 24 h. The corresponding indexes were tested.

MTT Assay

Cells were seeded into 96-well plates at 1×10^5/well. MTT (5 mg/ml) solution was added to each well and continued incubation for 4 h at 37°C. After removing the upper medium, dimethyl sulfoxide (DMSO) was added to each well at 37°C to solubilize formazon. Absorbance values were measured at 490 nm.

ELISA

Cells were seeded into 24-well plates at 5×10^5/well. The TNF-α and IL-10 levels in the supernatant were detected using ELISA kit according to the manufacturer's instructions.

Real-Time RT-PCR Assay

Total RNA was extracted with Trizol agent and purified with RNeasy kit. Iba-1, TNF-α, IL-1β, Arg-1, IL-10, and β-actin genes were amplified using the forward and reverse primers. Real-time PCR was performed using a SYBR Green Supermix according to the instruction and then determined on a CFX96 real-time PCR detection system (Bio-Rad, CA, United States). The target gene expression levels were normalized with that of β-actin using the data analysis software provided with the system.

Western Blotting

Cells were lysed in RIPA buffer and the lysates were incubated on ice for 15 min and then centrifuged at 12,000 × g for 15 min at 4°C. The protein concentrations were quantified by BCA assay. A total of 10 μg protein were resolved on 10% Bis-Tris Nu-PAGE gels and transferred to the polyvinylidene difluoride (PVDF) membranes and blocked in 5% fat-free milk at room temperature for 2 h. Membranes were incubated with following primary antibodies: anti-phosphorylated c-Jun Nterminal kinase (p-JNK,1:1000), anti-JNK (1:1000), anti-phosphorylated extracellular signal-regulated kinase1/2 (p-ERK1/2,1:2000), anti-ERK1/2 (1:1000), anti-phosphorylated p38 (p-p38,1:1000), anti-p38 (1:1000), anti-Iba-1 (1:1000), and anti-β-actin (1:2000). The membranes were then incubated with horseradish peroxidase (HRP)-conjugated secondary antibodies at 1:2000 for 1 h. The proteins were detected with ECL substrate.

Immunocytochemical Staining

BV-2 cells were fixed with 4% paraformaldehyde for 30 min at room temperature followed by permeabilization using 0.3% Triton X-100 for 15 min. Cells were then blocked with goat serum at 37°C for 40 min. Cells were concentrated with anti-Iba-1 (1:300), anti-TNF-α (1:300) and anti-Arg-1 (1:300) at 4°C overnight, respectively. The next day, cells were incubated with anti-rabbit-IgG (1: 1500) or anti-mouse-IgG (1: 1500) at 37°C for 1 h. Subsequently, cells were incubated with DAPI for 2 min at room temperature.

Statistical Analysis

Data were presented as mean ± standard error of the mean (SEM). Statistical significance was analyzed by one-way ANOVA through the GraphPad Prism software (GraphPad Software Inc., San Diego, CA, United States). After ANOVA demonstrated the significant differences, pairwise comparisons between means were accessed by Bonferroni's *post hoc* tests with correction. $p < 0.05$ was considered as statistically significant.

RESULTS

NAR Attenuated LPS-Induced Microglial Activation

As shown in **Figures 1A,B**, MTT assay indicated that NAR (100 μM) decreased BV2 cell viability and had cytotoxicity up to the concentration of 200 μM.BV-2 cells were exposed to NAR (50 μM) and LPS (100 ng/ml) for 24 h, cell morphology and cell viability were first determined. In addition, both NAR (50 μM) and LPS (100 ng/ml) had no significant toxic effects on the cell viability. Meanwhile, LPS and NAR had no effect on BV2 cells proliferation (**Supplementary Figure S1**). To discern the effects of NAR on LPS-induced microglial activation, the morphological changes were evaluated via immunostaining using an anti-Iba-1 (a specific microglial marker) antibody. As indicated in **Figure 1C**, in LPS-treated cultures, activated microglia illustrated irregular shapes and amoeboid status. However, NAR attenuated LPS-induced morphological changes of microglia with exhibiting resting round and small cells. In addition, western blot analysis provided quantitative estimation of microglial activation. As shown in **Figures 1D,E**, NAR inhibited LPS-induced increase of Iba-1 mRNA level and protein expression.

NAR Switched Microglial M1 to M2 Polarization

It is well known that TNF-α and IL-1β were used as the marker of M1 polarization, whereas Arg-1 and IL-10 was applied as the marker of M2 polarization. The above observations prompted us to explore whether NAR directly switches microglial M1 to M2 phenotype. As shown in **Figure 2A**, less TNF-α and Arg-1 immunoreactivity was detected in control cultures. Notably, strong TNF-α immunoreactivity and less Arg-1 immunoreactivity were indicated in LPS-treated cultures. After NAR treatment, TNF-α immunoreactivity was decreased, and Arg-1 immunoreactivity was increased. As expected, the increased mRNA and extracellular protein expressions of TNF-α and IL-1β were observed in LPS-treated cultures. NAR-treated microglia expressed higher levels of mRNA and extracellular protein of anti-inflammatory cytokine Arg-1 and IL-10 than those exposed to LPS shown in **Figures 2B,C**. In addition, NAR alone had no significant effect on M1/M2 polarization (**Supplementary Figure S2**).

NAR Inhibited MAPK Signaling Pathway Activation

To determine whether NAR could modulate the MAPK signaling pathway activation, the protein expressions of JNK, p-JNK, ERK1/2, p-ERK1/2, p38 and p-p38 were measured. As shown in **Figure 3**, NAR counteracted the LPS-induced phosphorylation of JNK and ERK1/2. Interestingly, NAR had the most obvious inhibitory effects on JNK activation. However, NAR didn't show the recovery effects on LPS-induced activation of p38. Besides, NAR alone had no significant effect on MAPK signaling pathway (**Supplementary Figure S2**).

NAR Promoted Microglial M1/M2 Polarization Through JNK Inactivation

Naringenin promoted microglia from M1 to M2 polarization and inhibited JNK and ERK1/2 phosphorylation, especially JNK phosphorylation. However, the specific target mediating this action was still unclear. Anisomycin (ANI), a selective agonist of JNK, was thus used to verify the role of JNK activation in NAR-mediated microglial M1/M2 polarization. First, as shown in **Figure 4A**, MTT assay indicated that ANI (5 nM) didn't affect cell viability. In addition, ANI specifically counteracted NAR-elicited downregulation of phosphorylated-JNK but not phosphorylated-ERK1/2 and phosphorylated-p38 as shown in **Figure 4B**.

Next, we assessed and compared the functional recovery between NAR-treated cultures and NAR-ANI co-treated cultures to further determine the role of JNK on NAR-suppressed microglial activation. As shown in **Figure 5A**, NAR and ANI co-treated cultures exhibited irregular shapes and amoeboid status, parallel to the morphological changes in LPS-treated

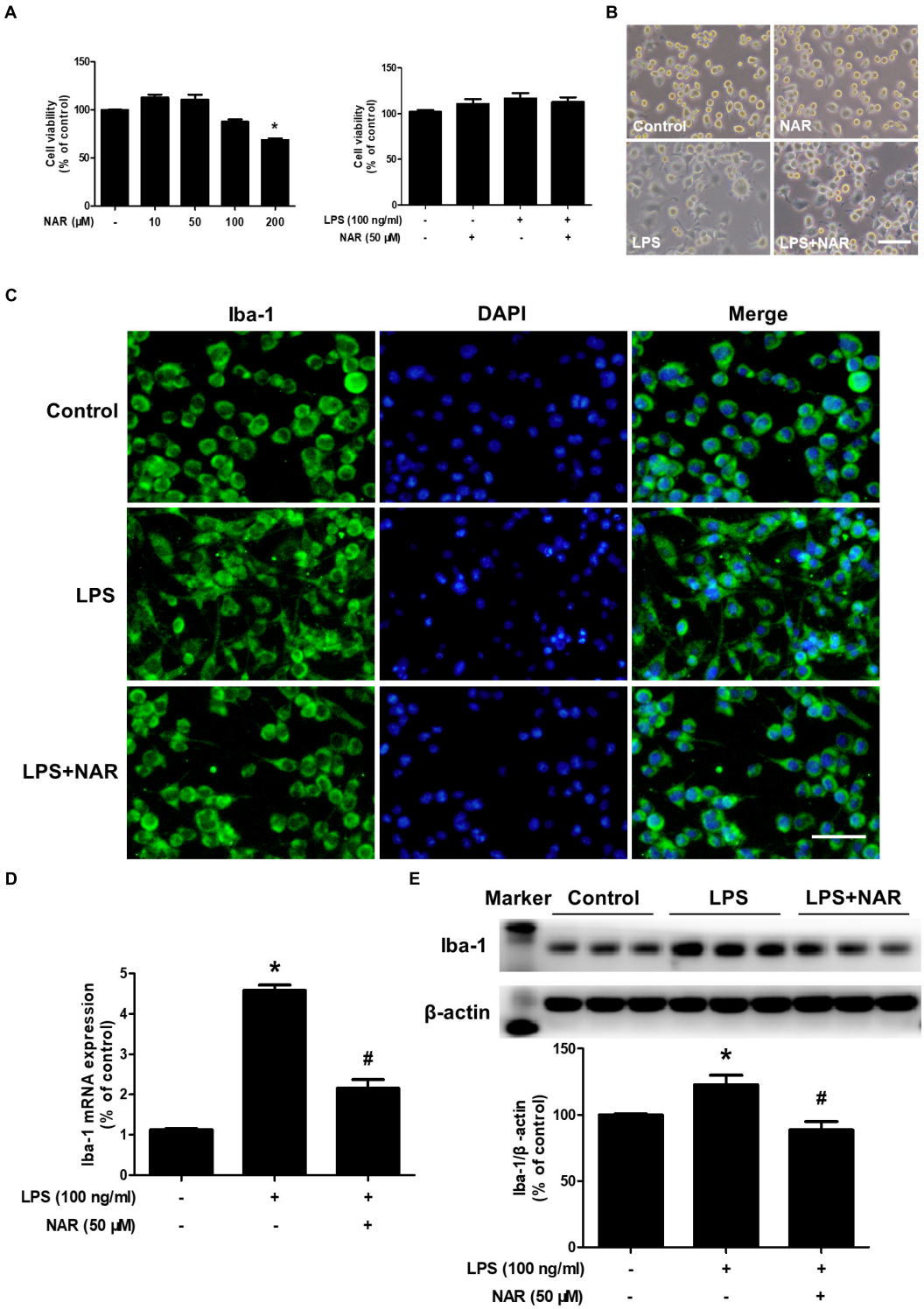

FIGURE 1 | NAR attenuated LPS-induced microglial activation. BV-2 cells were treated with different concentrations of NAR for 24 h, cell viability was measured by MTT assay **(A)**. In addition, BV-2 cells were pretreated with NAR (50 μM) for 1 h and then incubated with LPS (100 ng/ml) for 24 h, cell viability were determined by MTT assay **(A)** and cell morphology was observed via an optical microscopeand **(B)**. Microglial activation was visualized by immunostaining with an anti-Iba-1 antibody **(C)**. Activation of microglia was quantitated by RT-PCR **(D)** and western blot analysis **(E)**. The ratio of densitometry values of Iba1 with β-actin was analyzed and normalized to each respective control cultures. Results were the mean ± SEM from three independent experiments performed in triplicate. $^{*}p < 0.05$ compared to the control cultures. $^{\#}p < 0.05$ compared to LPS-treated cultures. Scale bar = 50 μm.

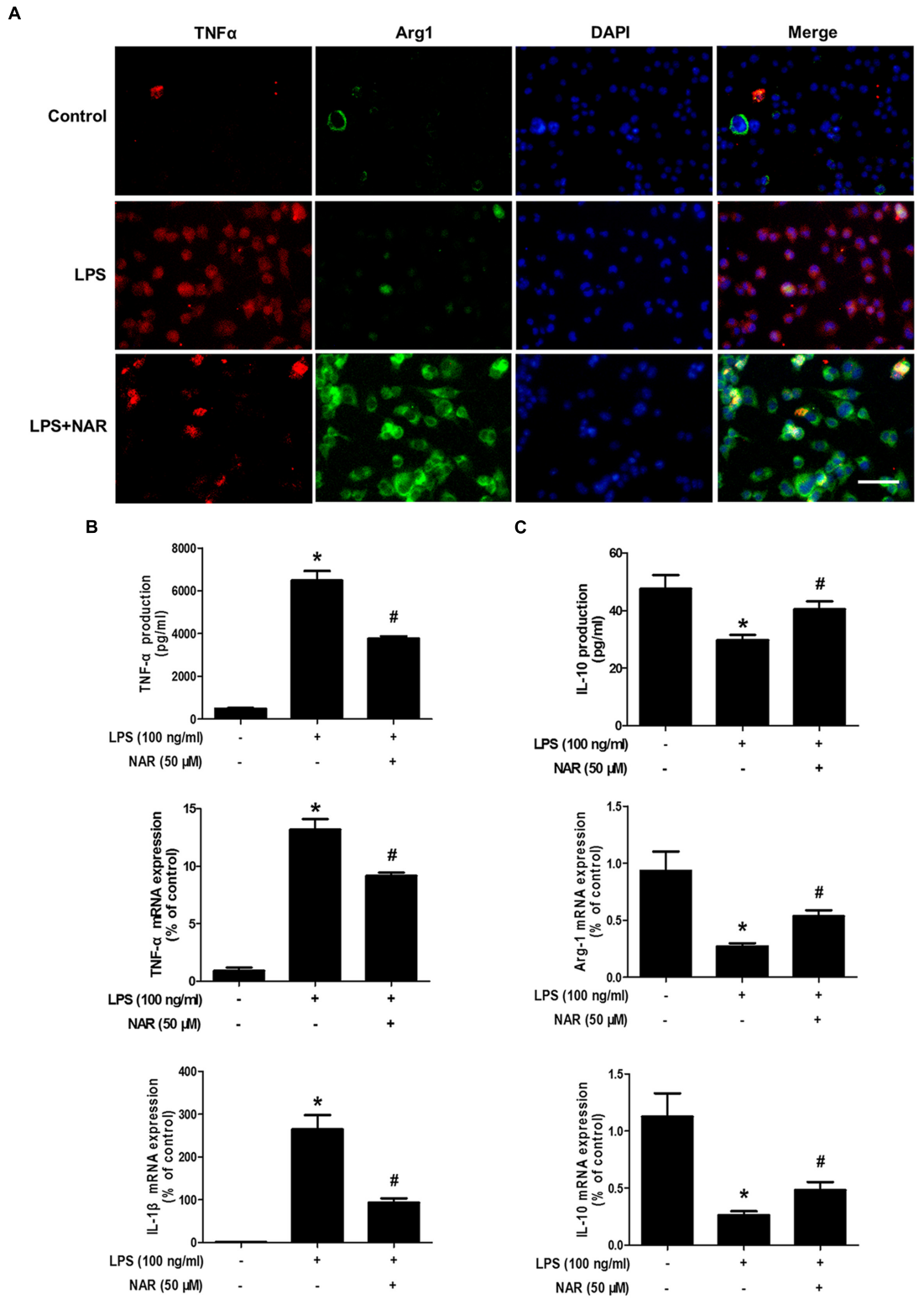

FIGURE 2 | NAR switched microglial M1 to M2 polarization. BV-2 cells were pretreated with NAR (50 μM) for 1 h followed by LPS (100 ng/ml) adminstration for 24 h. Cultures were visualized by immunostaining with anti-TNF-α and Arg-1 antibodies **(A)**. The levels of TNF-α and IL-10 in supernatant were detected by ELISA and the whole cells were collected to detect the gene expressions of TNF-α, IL-1β, Arg-1, and IL-10 by real time RT-PCR **(B,C)**. Results were the mean ± SEM from three independent experiments performed in triplicate. $^{*}p < 0.05$ compared to the control cultures. $^{\#}p < 0.05$ compared to LPS-treated cultures. Scale bar = 50 μm.

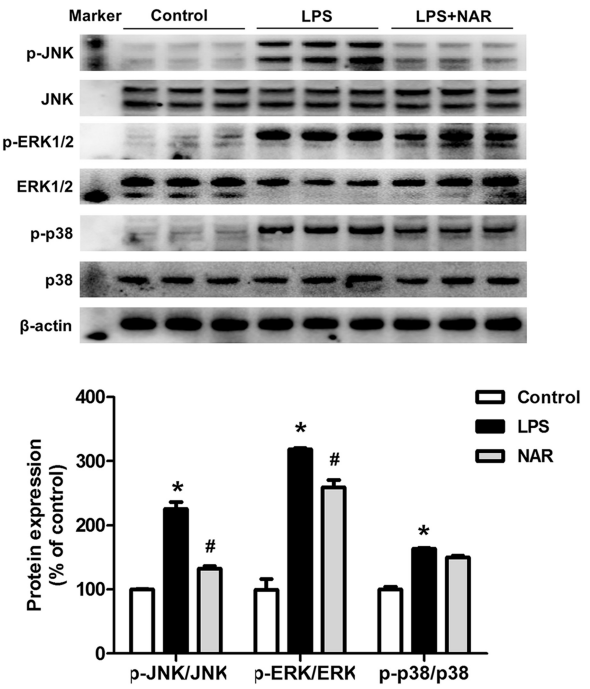

FIGURE 3 | NAR inhibited MAPK signaling pathway activation. BV-2 cells were treated with NAR (50 μM) for 1 h prior to LPS (100 ng/ml) treatment. After LPS (100 ng/ml) stimulation for 24 h, cultures were harvested to detect the protein expressions of JNK, p-JNK, ERK1/2, p-ERK1/2, p38, p-p38 by western blot assay. The ratio of densitometry values of p-ERK1/2, p-JNK and p-p38 with total ERK1/2, JNK and p38 was assessed and normalized to each respective control group. Results were the mean ± SEM from three independent experiments performed in triplicate. $^{*}p < 0.05$ compared to the control cultures. $^{\#}p < 0.05$ compared to LPS-treated cultures.

cultures. Western blot analysis further indicated that NAR-inhibited microglia activation was abrogated by ANI treatment shown in **Figure 5B**. These results pointed out a critical role of the activation of JNK in NAR-inhibited microglial activation.

Further studies were then conducted to evaluate the role of JNK on microglia M1/M2 polarization. As shown in **Figure 6A**, NAR and ANI co-treated cultures exhibited strong TNF-α (M1) immunoreactivity and less Arg-1(M2) immunoreactivity compared with NAR-treated culture. Furtherly, NAR-mediated reversal of LPS-induced downregulation of the M2 marker (Arg-1 and IL-10) and upregulation of the M1 marker (TNF-α and IL-1β) was abrogated by ANI administration as shown in **Figures 6B,C**. Thus, NAR switched microglial M1 to M2 polarization via a JNK-dependent pathway.

DISCUSSION

The current study indicated that NAR shifted the M1 pro-inflammatory microglia phenotype to the M2 anti-inflammatory M2 microglia state, thus inhibiting microglia-mediated neuroinflammation. In addition, the effects of NAR on microglial polarization was dependent on MAPK signaling, particularly JNK inactivation, as evidenced by the fact that the selective activator of JNK abolished NAR-promoted M2 polarization and further NAR-inhibited microglial activation. Together, this study demonstrated that NAR promoted microglia M1/M2 polarization, thus conferring anti-neuroinflammatory effects via MAPK-dependent inactivation.

To date, oxidative stress, mitochondrial dysfunction and environmental exposure have been characterized to be closely associated with the pathogenesis of neurological disorders. However, the underlying mechanisms remain unelucidated. Growing evidence has confirmed that neuroinflammation is involved in the pathogenesis of neurological disorders. The hallmark of neuroinflammation is the glial activation, especially microglial activation (Tentillier et al., 2016). Once activated by brain injury or inflammogen, microglia could release various types of pro-inflammatory and cytotoxic factors. The accumulation of these neurotoxic factors contributed to the surrounding neuronal damage. However, the continuous dying of neurons, in turn induced the secondary activation of microglia and the activated microglia further elicited neuronal damage (Block et al., 2007). Taken together, a vicious cycle leading to the prolonged neuroinflammation and the progressive neuronal loss was created (Gao and Hong, 2008). Thus, inhibition of microglial activation-mediated neuroinflammation might be promising therapeutic strategy for neuroprotection. The present study indicated that NAR inhibited microglia activation-mediated neuroinflammation. These results were consistent with the previous studies that NAR alleviated neuropathic pain through inhibiting microglia-induced neuroinflammation (Hu and Zhao, 2014).

In addition, a great number of studies set out to consider that microglia were highly plastic cells that could assume two diverse phenotypes and participate in different functional programs in response to the pathology of CNS. Recently, similar to the classical M1 phenotype versus the alternative M2 phenotype paradigm defined for macrophages, microglial M1/M2 polarization has been coined and recognized in various neurological disorders, such as traumatic brain injury, stroke, and neurodegenerative diseases (Wang et al., 2013; Wu et al., 2016; Cheon et al., 2017). Typically, the activated M1 phenotype microglia produce various destructive pro- inflammatory factors that result in neuronal damage. As one of the most interesting M1 microglial polarization markers, TNF-α has been confirmed to be implicated in the pathology of neurological disorders (Makuch et al., 2013). IL-1β could be released by activated M1 microglia and the intrathecal administration of IL-1β was discerned to exert algesic actions (Kawasaki et al., 2008). In contrast, the alternatively activated M2 phenotype microglia generate numerous protective and neurotrophic factors and then underly the neuroprotective properties (Prinz and Priller, 2014). Therefore, the pro- and anti-inflammatory responses of microglia phenotype need to be balanced to prevent the potential detrimental activities of an uncontrolled and prolonged inflammation. So far, several lines of evidence presented for the role of neuroinflammation on neurodegenerative diseases pointed to a prolonged and uncontrolled activated microglia M1 state which led to additional continuous neuronal damage (Mantovani et al., 2013). Nevertheless, based on previous

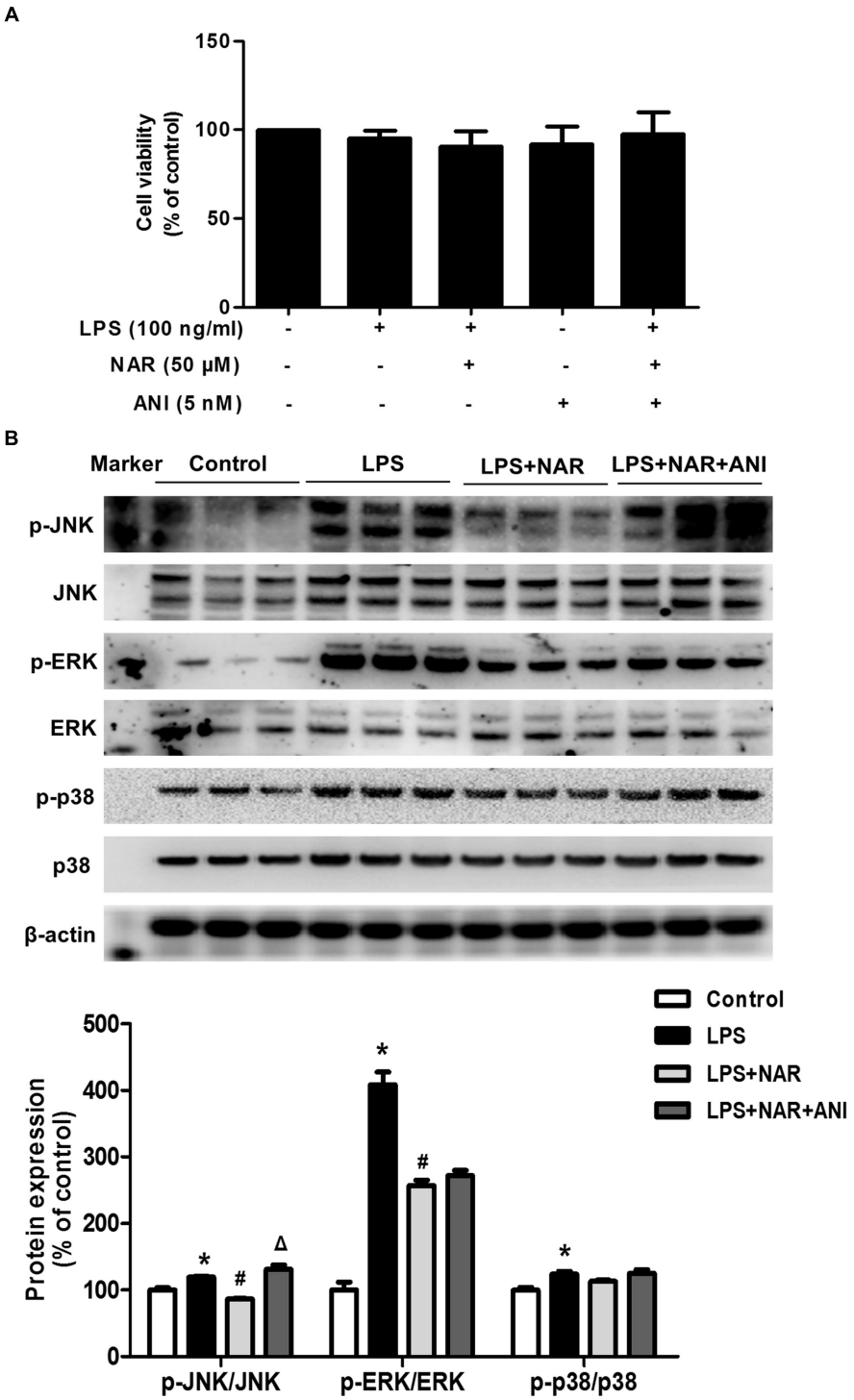

FIGURE 4 | JNK activator attenuated NAR-suppressed JNK activation. BV-2 cells were treated with NAR (50 μM) for 1 h and then ANI (5 nM) for 1 h followed by LPS (100 ng/ml) application for 24 h. Cell viability was determined by MTT assay **(A)**. The protein expressions of JNK, p-JNK, ERK1/2, p-ERK1/2, p38 and p-p38 were detected by western blot assay **(B)**. The ratio of densitometry values of p-ERK1/2, p-JNK and p-p38 with total ERK1/2, JNK and p38 was normalized to each respective control group. Results were the mean ± SEM from three independent experiments performed in triplicate. $^{*}p < 0.05$ compared to the control cultures. $^{\#}p < 0.05$ compared to LPS-treated cultures. $^{\Delta}p < 0.05$ compared to LPS and NAR co-treated cultures.

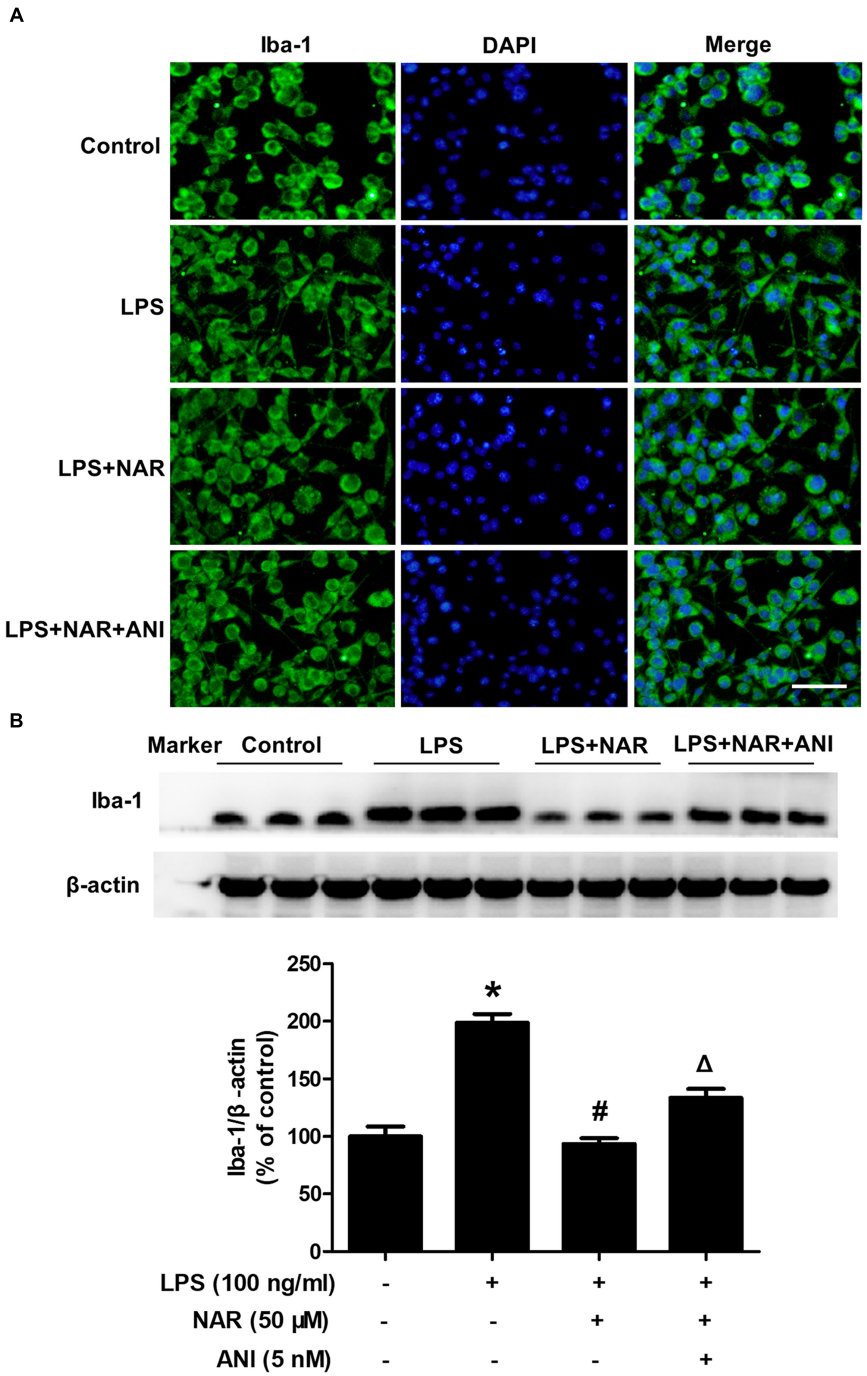

FIGURE 5 | NAR inhibited microglia activation through JNK inactivation. BV-2 cells were treated with ANI (5 nM) for 1h after NAR pretreatment for 1 h. Then, LPS (100 ng/ml) were added into cultures. After LPS stimulation for 24 h, microglial activation was visualized by immunostaining **(A)** and quantitated by western blot analysis **(B)** using an anti-Iba-1 antibody. The ratio of densitometry values of Iba1 with β-actin was analyzed and normalized to each respective control cultures. $^{*}p < 0.05$ compared to the control cultures. $^{\#}p < 0.05$ compared to LPS-treated cultures. $^{\Delta}$ $p < 0.05$ compared to LPS and NAR co-treated cultures. Scale bar = 50 μm.

non-steroidal anti-inflammatory drug and Alzheimer's disease anti-inflammatory prevention trial studies, simply suppressing inflammation via inhibiting M1 activation would likely not exert overall benefits (Becker et al., 2011). On the contrary, promoting the shift of microglial M1 to M2 phenotype while inhibiting microglia M1 state has been emerged as a more promising strategy for neuroinflammation-related disorders treatment (Li et al., 2018). Currently, most of the compounds

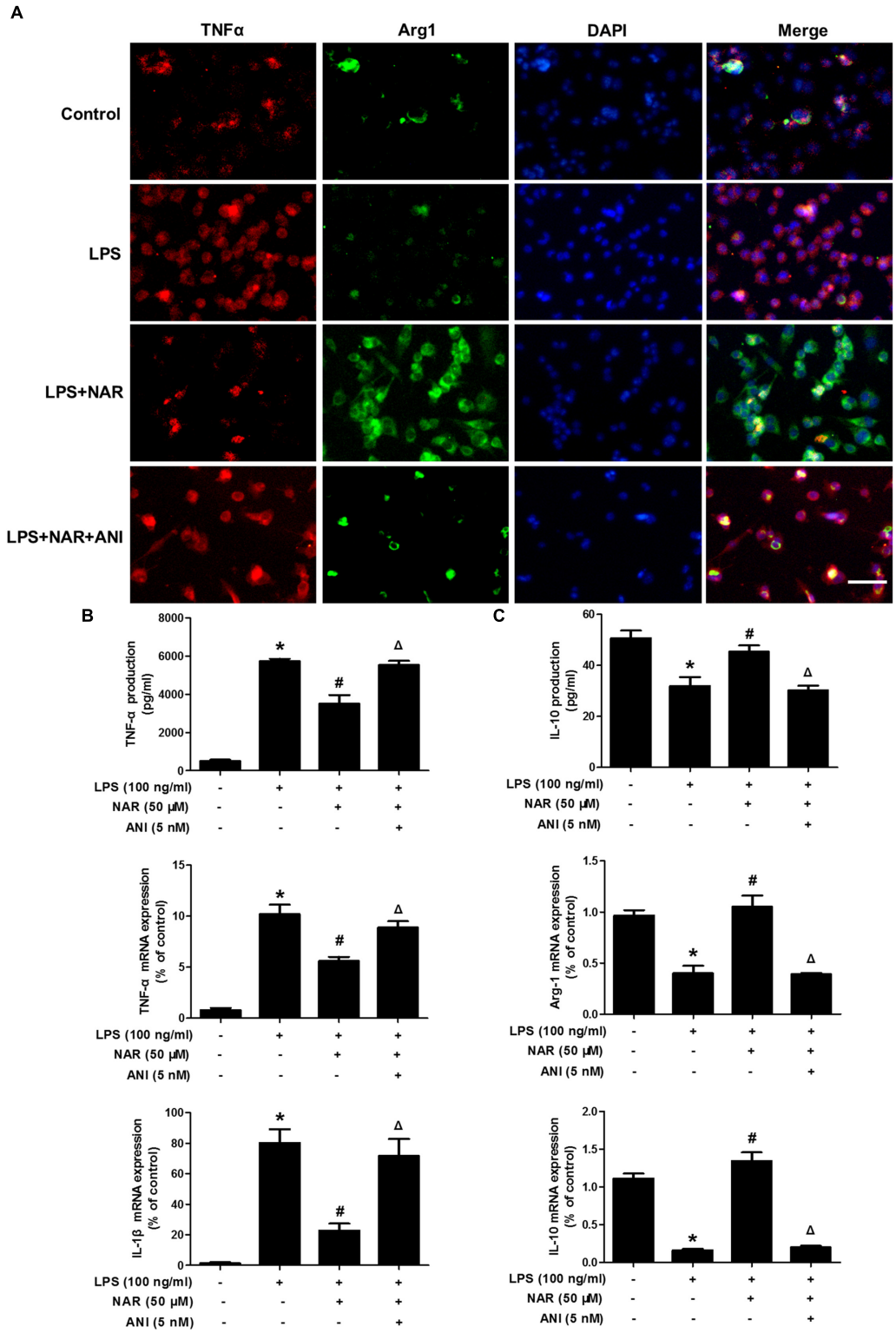

FIGURE 6 | NAR promoted microglial M1/M2 polarization via the inhibition of JNK activation. BV-2 cells were treated with NAR (50 μM) for 1 h and ANI (5 nM) for another 1 h and then stimulated by LPS (100 ng/ml) for 24 h. Cultures were immunostained with anti-TNF-α and anti-Arg-1 antibodies **(A)**. Culture medium was collected to detect the contents of TNF-α and IL-10 by ELISA and the whole cells were collected to measure the gene expressions of TNF-α, IL-1β, Arg-1, and IL-10 by real time RT-PCR **(B,C)**. Results were the mean ± SEM from three independent experiments performed in triplicate. $^{*}p < 0.05$ compared to the control cultures. $^{\#}p < 0.05$ compared to LPS-treated cultures. $^{\Delta}$ $p < 0.05$ compared to LPS and NAR co-treated cultures. Scale bar = 50 μm.

suppressed neuroinflammation via simply inhibiting microglial M1 phenotype. However, few compounds were verified to promote microglial polarization to the M2 phenotype (Huang et al., 2017). Since NAR attenuated neuroinflammatory response, it is of significance to investigate the role of NAR on the modulation of microglial polarization. This study indicated that NAR robustly inhibited microglial M1 phenotype markers expressions and promoted microglia polarization toward the M2 anti-inflammatory phenotype, which might contribute to NAR-mediated neuroprotective actions against neuroinflammation.

Further analysis of cascade signaling events underlying NAR-mediated microglial polarization demonstrates the involvement of mitogen-activated protein kinases (MAPK) signaling pathway. MAPK pathway is a highly conserved family of serine/threonine kinases, including ERK1/2, p38 and JNK isoforms. MAPK signaling not only participates in the regulation of inflammatory responses, but also promotes macrophage/microglia polarization into the M2 stage (Quero et al., 2017). For instance, activation of ERK1/2 and p38 was implicated in the regulation of pro-inflammatory factors production in activated microglia (Zhang et al., 2010a). Moreover, p38 played a crucial role in allowing Ecto-5′-nucleotidase to modulate microglial M1/M2 polarization (Xu et al., 2018). In addition, a common involvement of JNK has also been studied in the regulation of both microglial iNOS and IL-1β expressions (Zhang et al., 2010b). Also, JNK was involved in exosomes-triggered macrophage polarization (Xiao et al., 2018). Thus, MAPK signaling is considered as an attractive target for inflammatory diseases treatment. Recently, some synthetic and natural compounds that could activate MAPK to exert anti-inflammatory effects and promote microglial M2 polarization (Bhatia et al., 2016; Xiang et al., 2018). Therefore, it was of interest to investigate the relationship between NAR-mediated anti-neuroinflammatory actions and MAPK activation. In the present study, we first found that NAR suppressed the phosphorylation of JNK and ERK1/2 in BV-2 cells, while p38 was not altered by NAR after LPS stimulation. Next, we tested whether NAR-mediated microglia polarization toward M2 state was dependent on JNK inactivation. Of note, the specific JNK activator abolished NAR-promoted microglia polarization further inhibiting microglial activation. The current data suggested that NAR-mediated microglial M1/M2 polarization was dependent on the inactivation of MAPK signaling.

In summary, this study demonstrated that NAR administration inhibited the microglial M1 phenotype and shifted the microglial polarization toward M2 state via the inhibition of MAPK signaling activation, which was accompanied by the reduced neuroinflammatory response. The current results supported the potential pharmaceutical application of NAR in neuroinflammation-related neurological disorders therapies.

CONCLUSION

This study illustrates that NAR promoted microglial polarization toward the M2 phenotype through MAPK-dependent inactivation. These findings provide a new evidence that NAR might have considerable value as a potent agent for neuroinflammatory diseases treatment.

AUTHOR CONTRIBUTIONS

FZ conceived and designed the experiments. BZ, G-QW, and Y-ZW participated in the experiments performance. G-QW, D-DL, J-SS, and FZ finished the data analysis. FZ and G-QW wrote, revised, and checked the article. All authors have reviewed the contents of the manuscript, validated the accuracy of the data, and approved the submitted manuscript.

FUNDING

This study was supported by the National Natural Science Foundation of China (Nos. 81460556 and 81760658), the foundation for High-Level Innovative Talents of Guizhou Province (No. 20164027), the Innovation Research Group Project of Education Department of Guizhou Province (No. 2016038), and the Foundation for Excellent Young Talents of Zunyi Medical University (No. 201603).

SUPPLEMENTARY MATERIAL

The Supplementary Material for this article can be found online at: https://www.frontiersin.org/articles/10.3389/fncel.2018.00531/full#supplementary-material

FIGURE S1 | The effects of NAR on cell proliferation. BV-2 cells were treated with NAR (50 μM) for 1 h prior to LPS (100 ng/ml) treatment. After LPS (100 ng/ml) stimulation for 24 h, cultures were harvested to detect the protein expressions of PCNA by western blot assay.

FIGURE S2 | The effects of NAR alone on M1/M2 polarization and MAPK signaling pathway. BV-2 cells were treated with NAR (50 μM) for 24 h. The gene expressions of TNF-α, IL-1β, Arg-1, and IL-10 were detected by real time RT-PCR. The protein expressions of JNK, p-JNK, ERK1/2, p-ERK1/2, p38, p-p38 were measured by western blot assay.

REFERENCES

Al-Dosari, D. I., Ahmed, M. M., Al-Rejaie, S. S., Alhomida, A. S., and Ola, M. S. (2017). Flavonoid naringenin attenuates oxidative stress, apoptosis and improves neurotrophic effects in the diabetic rat retina. *Nutrients* 9:E1161. doi: 10.3390/nu9101161

Becker, C., Jick, S. S., and Meier, C. R. (2011). NSAID use and risk of Parkinson disease: a population-based case-control study. *Eur. J. Neurol.* 18, 1336–1342. doi: 10.1111/j.1468-1331.2011.03399.x

Bhatia, H. S., Baron, J., Hagl, S., Eckert, G. P., and Fiebich, B. L. (2016). Rice bran derivatives alleviate microglia activation: possible involvement of MAPK pathway. *J. Neuroinflammation* 13:148. doi: 10.1186/s12974-016-0615-6

Block, M. L., Zecca, L., and Hong, J. S. (2007). Microglia-mediated neurotoxicity: uncovering the molecular mechanisms. *Nat. Rev. Neurosci.* 8, 57–69. doi: 10.1038/nrn2038

Bok, E., Chung, Y. C., Kim, K. S., Baik, H. H., Shin, W. H., and Jin, B. K. (2018). Modulation of M1/M2 polarization by capsaicin contributes to the survival of dopaminergic neurons in the lipopolysaccharide-lesioned substantia nigra in vivo. *Exp. Mol. Med.* 50:76. doi: 10.1038/s12276-018-0111-4

Cheon, S. Y., Kim, E. J., Kim, J. M., Kam, E. H., Ko, B. W., and Koo, B. N. (2017). Regulation of microglia and macrophage polarization via apoptosis signal-regulating kinase 1 silencing after ischemic/hypoxic injury. *Front. Mol. Neurosci.* 10:261. doi: 10.3389/fnmol.2017.00261

David, S., and Kroner, A. (2011). Repertoire of microglial and macrophage responses after spinal cord injury. *Nat. Rev. Neurosci.* 12, 388–399. doi: 10.1038/nrn3053

Dhama, K., Kesavan, M., Karthik, K., Amarpal, Tiwari, R., Sunkara, L. T., et al. (2015). Neuroimmunomodulation countering various diseases, disorders, infections, stress and aging. *Int. J. Pharmacol.* 11, 76–94. doi: 10.3923/ijp.2015.76.94

Gao, H. M., and Hong, J. S. (2008). Why neurodegenerative diseases are progressive: uncontrolled inflammation drives disease progression. *Trends. Immunol.* 29, 357–365. doi: 10.1016/j.it.2008.05.002

Gemma, C. (2010). Neuroimmunomodulation and aging. *Aging Dis.* 1, 169-172.

Hanisch, U. K., and Kettenmann, H. (2007). Microglia: active sensor and versatile effector cells in the normal and pathologic brain. *Nat. Neurosci.* 10, 1387–1394. doi: 10.1038/nn1997

Hu, C. Y., and Zhao, Y. T. (2014). Analgesic effects of naringenin in rats with spinal nerve ligation-induced neuropathic pain. *Biomed. Rep.* 2, 569–573. doi: 10.3892/br.2014.267

Hu, X., Leak, R. K., Shi, Y., Suenaga, J., Gao, Y., Zheng, P., et al. (2015). Microglial and macrophage polarization-new prospects for brain repair. *Nat. Rev. Neurol.* 11, 56–64. doi: 10.1038/nrneurol.2014.207

Huang, X. P., Peng, J. H., Pang, J. W., Tian, X. C., Li, X. S., Wu, Y., et al. (2017). Peli1 contributions in microglial activation, neuroinflammatory responses and neurological deficits following experimental subarachnoid hemorrhage. *Front. Mol. Neurosci.* 10:398. doi: 10.3389/fnmol.2017.00398

Huo, W., Zhang, Y., Liu, Y., Lei, Y., Sun, R., Zhang, W., et al. (2018). Dehydrocorydaline attenuates bone cancer pain by shifting microglial M1/M2 polarization toward the M2 phenotype. *Mol. Pain* 14:1744806918781733. doi: 10.1177/1744806918781733

Ji, R. R., Berta, T., and Nedergaard, M. (2013). Glia and pain: is chronic pain a gliopathy? *Pain* 154, S10–S28. doi: 10.1016/j.pain.2013.06.022

Kara, S., Gencer, B., Karaca, T., Tufan, H. A., Arikan, S., Ersan, I., et al. (2014). Protective effect of hesperetin and naringenin against apoptosis in ischemia/reperfusion-induced retinal injury in rats. *The Sci. World J.* 2014:797824. doi: 10.1155/2014/797824

Kawasaki, Y., Zhang, L., Cheng, J. K., and Ji, R. R. (2008). Cytokine mechanisms of central sensitization: distinct and overlapping role of interleukin-1beta, interleukin-6, and tumor necrosis factor-alpha in regulating synaptic and neuronal activity in the superficial spinal cord. *J. Neurosci.* 28, 5189–5194. doi: 10.1523/JNEUROSCI.3338-07.2008

Li, C., Zhang, C., Zhou, H., Feng, Y., Tang, F., Hoi, M. P. M., et al. (2018). Inhibitory effects of betulinic acid on LPS-induced neuroinflammation involve M2 microglial polarization via CaMKKβ-dependent AMPK activation. *Front. Mol. Neurosci.* 11:98. doi: 10.3389/fnmol.2018.00098

Lin, Y., Tan, D., Kan, Q., Xiao, Z., and Jiang, Z. (2018). The protective effect of naringenin on airway remodeling after mycoplasma pneumoniae infection by inhibiting autophagy-mediated lung inflammation and fibrosis. *Mediators Inflamm.* 2018, 1–10. doi: 10.1155/2018/8753894

Magalingam, K. B., Radhakrishnan, A. K., and Haleagrahara, N. (2015). Protective mechanisms of flavonoids in Parkinson's Disease. *Oxid. Med. Cell. Longev.* 2015:314560. doi: 10.1155/2015/314560

Makuch, W., Mika, J., Rojewska, E., Zychowska, M., and Przewlocka, B. (2013). Effects of selective and non-selective inhibitors of nitric oxide synthase on morphine-and endomorphin-1-induced analgesia in acute and neuropathic pain in rats. *Neuropharmacology* 75, 445–457. doi: 10.1016/j.neuropharm.2013.08.031

Manchope, M. F., Calixto-Campos, C., Coelho-Silva, L., Zarpelon, A. C., Pinho-Ribeiro, F. A., Georgetti, S. R., et al. (2016). Naringenin inhibits superoxide anion-induced inflammatory pain: role of oxidative stress, cytokines, Nrf-2 and the NO-cGMP-PKG-KATP channel signaling pathway. *PloS One.* 11:e0153015. doi: 10.1371/journal.pone.0153015

Mantovani, A., Biswas, S. K., Galdiero, M. R., Sica, A., and Locati, M. (2013). Macrophage plasticity and polarization in tissue repair and remodeling. *J. Pathol.* 229, 176–185. doi: 10.1002/path.4133

Nimmo, A. J., and Vink, R. (2009). Recent patents in CNS drug discovery: the management of inflammation in the central nervous system. *Recent Pat. CNS Drug Discov.* 4, 86–95. doi: 10.2174/157488909788452997

Prinz, M., and Priller, J. (2014). Microglia and brain macrophages in the molecular age: from origin to neuropsychiatric disease. *Nat. Rev. Neurosci.* 15, 300–312. doi: 10.1038/nrn3722

Quero, L., Hanser, E., Manigold, T., Tiaden, A. N., and Kyburz, D. (2017). TLR2 stimulation impairs anti-inflammatory activity of M2-like macrophages, generating a chimeric M1/M2 phenotype. *Arthritis Res. Ther.* 19:245. doi: 10.1186/s13075-017-1447-1

Rehman, M. U., Rahman Mir, M. U., Farooq, A., Rashid, S. M., Ahmad, B., Bilal Ahmad, S., et al. (2018). Naringenin (4,5,7-trihydroxyflavanone) suppresses the development of precancerous lesions via controlling hyperproliferation and inflammation in the colon of wistar rats. *Environ. Toxicol.* 33, 422–435. doi: 10.1002/tox.22528

Saijo, K., and Glass, C. K. (2011). Microglial cell origin and phenotypes in health and disease. *Nat. Rev. Immunol.* 11, 775–787. doi: 10.1038/nri3086

Tentillier, N., Etzerodt, A., Olesen, M. N., Rizalar, F. S., Jacobsen, J., Bender, D., et al. (2016). Anti-inflammatory modulation of microglia via CD163-targeted glucocorticoids protects dopaminergic neurons in the 6-OHDA Parkinson's disease model. *J. Neurosci.* 36, 9375–9390. doi: 10.1523/JNEUROSCI.1636-16.2016

Wang, G., Zhang, J., Hu, X., Zhang, L., Mao, L., Jiang, X., et al. (2013). Microglia/macrophage polarization dynamics in white matter after traumatic brain injury. *J. Cereb. Blood Flow Metab.* 33, 1864–1874. doi: 10.1523/JNEUROSCI.1636-16.2016

Wu, L. H., Lin, C., Lin, H. Y., Liu, Y. S., Wu, C. Y., Tsai, C. F., et al. (2016). Naringenin suppresses neuroinflammatory responses through inducing suppressor of cytokine signaling 3 expression. *Mol. Neurobiol.* 53, 1080–1091. doi: 10.1007/s12035-014-9042-49

Xiang, B., Xiao, C., Shen, T., and Li, X. (2018). Anti-inflammatory effects of anisalcohol on lipopolysaccharide-stimulated BV2 microglia via selective modulation of microglia polarization and down-regulation of NF-κB p65 and JNK activation. *Mol. Immunol.* 95, 39–46. doi: 10.1016/j.molimm.2018.01.011

Xiao, M., Zhang, J., Chen, W., and Chen, W. (2018). M1-like tumor-associated macrophages activated by exosome-transferred THBS1 promote malignant migration in oral squamous cell carcinoma. *J. Exp. Clin. Cancer Res.* 3:143. doi: 10.1186/s13046-018-0815-2

Xu, S., Zhu, W., Shao, M., Zhang, F., Guo, J., Xu, H., et al. (2018). Ecto-5'-nucleotidase (CD73) attenuates inflammation after spinal cord injury by promoting macrophages/microglia M2 polarization in mice. *Front. J. Neuroinflammation* 15:3155. doi: 10.1186/s12974-018-1183-8

Zhang, F., Qian, L., Flood, P. M., Shi, J. S., Hong, J. S., and Gao, H. M. (2010a). Inhibition of ikappaB kinase-beta protects dopamine neurons against lipopolysaccharide-induced neurotoxicity. *J. Pharmacol. Exp. Ther.* 333, 822–833. doi: 10.1124/jpet.110.165829

Zhang, F., Shi, J. S., Zhou, H., Wilson, B., Hong, J. S., and Gao, H. M. (2010b). Resveratrol protects dopamine neurons against LPS-induced neurotoxicity through its anti-inflammatory actions. *Mol. Pharmacol.* 78, 466–477. doi: 10.1124/mol.110.064535

Conflict of Interest Statement: The authors declare that the research was conducted in the absence of any commercial or financial relationships that could be construed as a potential conflict of interest.

frontiers in Cellular Neuroscience

ORIGINAL RESEARCH
published: 05 February 2019
doi: 10.3389/fncel.2019.00018

Smilagenin Protects Dopaminergic Neurons in Chronic MPTP/Probenecid—Lesioned Parkinson's Disease Models

Xuan He[1†], Shuangshuang Yang[1†], Rui Zhang[1], Lina Hou[1], Jianrong Xu[1], Yaer Hu[1], Rang Xu[2], Hao Wang[1]* and Yongfang Zhang[1]**

[1]*Department of Pharmacology, Institute of Medical Sciences, Shanghai JiaoTong University School of Medicine (SJTUSM), Shanghai, China,* [2]*Scientific Research Center, Xinhua Hospital, Shanghai JiaoTong University School of Medicine (SJTUSM), Shanghai, China*

Current therapies for Parkinson's disease (PD) only offer limited symptomatic alleviation but fail to hamper the progress of the disease. Thus, it is imperative to establish new approaches aiming at protecting or reversing neurodegeneration in PD. Recent work elucidates whether smilagenin (abbreviated SMI), a steroidal sapogenin from traditional Chinese medicinal herbs, can take neuroprotective effect on dopaminergic neurons in a chronic model of 1-methyl-4-phenyl-1,2,3,6-tetrahydropyridine (MPTP) conjuncted with probenecid mice. We reported for the first time that SMI significantly improved the locomotor ability of chronic MPTP/probenecid–lesioned mice. SMI increased the tyrosine hydroxylase (TH) positive and Nissl positive neuron number in the substantia nigra pars compacta (SNpc), augmented striatal DA and its metabolites concentration and elevated striatal dopamine transporter density (DAT). In addition, dopamine receptor D2R not D1R was down-regulated by MPTP/probenecid and slightly raised by SMI prevention. What's more, we discovered that SMI markedly elevated striatal glial cell line-derived neurotrophic factor (GDNF) and brain-derived neurotrophic factor (BDNF) protein levels in SMI prevented mice. And we found that SMI increased GDNF and BDNF mRNA level by promoting CREB phosphorylation in 1-methyl-4-phenylpyridimium (MPP^+) treated SH-SY5Y cells. The results illustrated that SMI could prevent the impairment of dopaminergic neurons in chronic MPTP/probenecid-induced mouse model.

Keywords: brain-derived neurotrophic factor, Chinese herb, dopaminergic neurons, glial cell line-derived neurotrophic factor, Parkinson's disease

OPEN ACCESS

Edited by:
Sriharsha Kantamneni, University of Bradford, United Kingdom

Reviewed by:
Edgar Richard Kramer, Plymouth University, United Kingdom
Yuriko Iwakura, Niigata University, Japan

***Correspondence:**
Yongfang Zhang
zhangyongfang1@yahoo.com
Hao Wang
angela_wanghao@hotmail.com
Rang Xu
rang_xu@hotmail.com

†These authors have contributed equally to this work

Received: *01 November 2018*
Accepted: *16 January 2019*
Published: *05 February 2019*

Citation:
He X, Yang S, Zhang R, Hou L, Xu J, Hu Y, Xu R, Wang H and Zhang Y (2019) Smilagenin Protects Dopaminergic Neurons in Chronic MPTP/Probenecid—Lesioned Parkinson's Disease Models. Front. Cell. Neurosci. 13:18. doi: 10.3389/fncel.2019.00018

INTRODUCTION

Parkinson's disease (PD) is an age-related debilitating neurodegenerative disorder, characterized pathologically by selective loss of dopaminergic neurons in the substantia nigra pars compacta (SNpc) accompanied by a decrease in striatal dopamine level, and intracytoplasmic Lewy bodies aggregated by phosphorylated α-synuclein (αSyn). Additionally, the clinical symptoms such as resting tremor, rigidity, slowness of initial movement do not fully present until there is a loss of

Abbreviations: SMI, smilagenin; MPTP, 1-methyl-4-phenyl-1,2,3 6-tetrahydropyridine; DAT, dopamine transporter density; GDNF, glial cell line-derive neurotrophic factor; BDNF, brain-derived neurotrophic factor; SNpc, substantia nigra pars compacta; α-syn, α-synuclein; PD, Parkinson's disease; TH, tyrosine hydroxylase.

50%–60% SNpc neurons (Przedborski, 2017; Schapira et al., 2017). However current pharmacological therapies for PD, which dopamine replacement is a mainstay of therapeutic strategies, only alleviate symptoms but fail to hamper neurodegeneration process and restore dopaminergic dysfunction. What's worse, the existing therapies for PD after long-term treatment could cause severe adverse effects, such as motor response fluctuations and dyskinetic movements (Tarazi et al., 2014; Pires et al., 2017; Wong and Krainc, 2017). Thus, it is greatly imperative to establish neuroprotective therapy available for PD.

Administration of neurotrophic factors such as brain-derived neurotrophic factor (BDNF) and glial cell line-derived neurotrophic factor (GDNF) are generally recognized as powerful survival factors for the degenerated dopaminergic neurons and the nigro-triatal pathway in PD (Cass et al., 2006; Kramer and Liss, 2015; Sun et al., 2015). Although the potential neuroprotective effects of these neurotrophic factors are undisputed, unfortunately in a randomized controlled trial of intraputamenal infusion of recombinant human GDNF in patients with PD, there is no remarkable improvement in patients receiving GDNF (Lang et al., 2006; Ibáñez and Andressoo, 2017). Owing to its large polypeptide structure and consequent poor bioavailability, it is difficult for these neurotrophic factors to permeate the blood brain barrier (Tarazi et al., 2014; Fan et al., 2016).

Consequently, it is greatly urgent to implement some strategies to stimulate the endogenous expression of neurotrophic factors after oral administration to slow down or reverse the progression of neuronal degeneration. Traditional Chinese medicine have accumulated much knowledge in treatment of PD so that it might be feasible to develop drugs from Chinese medicinal herbs for curing PD (Zhang et al., 2015). Smilagenin (Cogane; 5β, 2α, 25R-spirostan-3β-ol, abbreviated as SMI), with a molecular weight of 416.63 daltons, is a lipid-soluble small-molecule steroidal sapogenin from *Rhizoma anemarrhenae* and *Radix asparagi* widely used in traditional Chinese medicine for treating chronic neurodegeneration diseases (Visanji et al., 2008; Sy et al., 2016). Our previous studies have confirmed that SMI could not only protect the cultures of rat embryonic mesencephalic neurons from 1-methyl-4-phenyl-1,2,3,6-tetrahydropyridine (MPTP) toxicity *in vitro* but also enhance GDNF release as well as motor function of aged rat *in vivo* (Zhang et al., 2008; Li et al., 2013). However, whether SMI could protect dopaminergic neurons *in vivo* in chronic MPTP/probenecid-lesioned mice are unknown. To clarify the protecting effect of SMI on dopaminergic neuron we adopted the chronic MPTP/probenecid mouse model to investigate locomotor ability and the effects of SMI on nigrostriatal dopaminergic system as well as GDNF and BDNF expression (Petroske et al., 2001; Schildknecht et al., 2017; Nonnekes et al., 2018).

MATERIALS AND METHODS

Materials

SMI with a purity of over 98 percent was supplied by Phytopharm plc. UK. One-methyl-4-phenyl-1,2,3,6-tetrahydropyridine hydrochloride (MPTP HCl), 1-methyl-4-phenylpyridimium (MPP^+) was from Sigma, Dulbecco's Modified Eagle Medium was from Gibco (Grand Island, NY, USA), probenecid, hydroxypropyl methyl cellulose (HPMC-Na), Ketanserin, SCH23390, fluoxetine and GBR-12909 and all reagents used in HPLC except acetonitrile were purchased from Sigma. Rabbit anti-mice tyrosine hydroxylase (TH) polyclonal antibody and 3,3′-diaminobenzidine (DAB) were from Chemicon. SABC kit was from Boster Bioengineering Co. Wuhan, China. [^{125}I]-FP-CIT was synthesized using Na[^{125}I] (from Chengdu Gaotong Isotope Co) and FP-CIT (from Jiangsu Institute of Nuclear Medicine) in our laboratory. [^{3}H] SCH23390 (specific activity 80.5 Ci/mmol) and [^{3}H] spiperone (specific activity 16.2 Ci/mmol) were purchased from Perkin Elmer Inc. Acetonitrile was from Merck. BDNF and GDNF ELISA kit were acquired from Promega company. Antibodies against the following proteins were used in the study: anti-BDNF (Abcam), anti-GDNF (Abcam), anti-DAT (Santa Cruz), anti-CREB (Santa Cruz), anti-pCREB (Santa Cruz), anti-D1 receptor (Millipore), anti-D2 receptor (Chemicon), anti-β-actin (Sigma). All primers used in qRT-PCR were designed using Primer Premier 5.0 software and synthesized by Shanghai Sangon Biotech Co. Ltd (Shanghai, China). The SYBR Green PCR Master Mix kit was from ABI (Warrington, UK).

Production of Animal Models and Drug Administration

Male C57BL/6 mice (10 weeks old, 23.80 ± 1.32 g, from Shanghai SIPPR-BK Laboratory Animal Company) were housed five per cage and maintained on a 12 h light-dark cycle in standard conditions. The room temperature and relative humidity were set at 22 ± 2°C and 55% ± 15% respectively, with food and water available *ad libitum*. This study was carried out in accordance with the recommendations of the NIH Guide, Shanghai JiaoTong University Animal Ethic Committee. The protocol was approved by the Shanghai JiaoTong University Animal Ethic Committee. One week period of acclimatization was allowed between delivery of mice and commencement of treatment.

The chronic PD model was produced according to the previous article with slight modifications (Petroske et al., 2001). In brief, 10 doses of MPTP HCL in saline plus probenecid in dimethyl sulfoxide were given in 5 weeks, with an interval of 3.5 days between consecutive injections. Each time, probenecid (250 mg/kg) was given by intraperitoneal injection 30 min prior to subcutaneous injection of MPTP (15 mg/kg; **Figure 1**). The normal control group was injected simultaneously with intraperitoneal injections of DMSO and 30 min later subcutaneous injections of saline. The mice were divided into four groups (seventeen in each group): normal control, MPTP/ probenecid (MPTP/P in figures) control, MPTP/ probenecid treated with SMI at dose of 10 and 26 mg/kg/day. From the third dose of MPTP injection, all mice were administered orally by intragastric administration either SMI or vehicle (HPMC) once daily for 60 days. For the last 3 days,

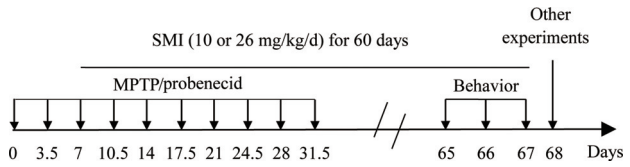

FIGURE 1 | Time schedule of experiments *in vivo*.

locomotor ability of mice is evaluated by the rotarod and open field test.

Rotarod and Open Field Test for Behavioral Assessment

We employed a modification of the procedure described by Rozas using a rotarod apparatus (IITC Life Science, Woodland Hills, CA, USA; Rozas et al., 1998). In general, all mice were trained to be accustomed to the rotarod apparatus at low speed rotation before formal experiment. Then each mouse was tested on rotating rods at a rate of six increments (8, 12, 16, 20, 24, 28 rpm) once per day for 3 days. Duration of each speed does not exceed 150 s. At least a 5 min resting period was required between each speed to alleviate mouse stress and fatigue. The overall rotarod performance for each mouse was obtained by plotting the average time on the rod at each speed vs. the rotating speed, and finally calculating the area under the curve (AUC) to evaluate the mice locomotor ability.

Next, we test spontaneous activity in a white open-field box. First the mice were put into the box to make it accustom to the environment for 5 min. Twenty-four hours later, the mice were placed into the same box and let them freely explore for 5 min. The locomotor activity was recorded by a video camera directly above the box and analyzed by a video track system (Noldus Ethovision).

Tyrosine Hydroxylase Immunohistochemistry and Nissl Staining in the SNpc and Stereological Counting

Coronal sections through the substantia nigra were processed for TH immunohistochemistry and Nissl staining as described previously with minor modifications (Xu et al., 2010). Briefly, mice were euthanized and fixed by 4% paraformaldehyde. Coronal frozen sections (50 μm) from mid brain SN were treated with 0.3% hydrogen peroxidase in methanol and subsequently in 0.3% Triton X-100 and 5% bovine serum albumin. For TH immunostaining, the sections were then incubated with rabbit anti-mouse TH polyclonal antibody (1:600) at 4°C overnight. The following day, sections were treated with biotinylated anti-mouse IgG and then processed with avidin–biotin peroxidase complex. The peroxidase reaction was visualized by 0.05% DAB with 0.03% H_2O_2. For Nissl staining, sections were immersed in Nissl staining solution for 10 min. Finally, TH-positive and Nissl staining areas in SNpc were photographed with a Nikon TE300 inverted microscope. Meanwhile the total number of TH-positive neurons of TH-immunostained sections was quantified by unbiased stereological counting. Briefly, neurons were quantified using an Olympus BX61 microscope with a monitored x-y-z stage linked to the stereo investigator software in every fourth section of each mouse for a total of 8–9 slides through the entire SNpc. As described previously, the software could calculate total numbers of TH-positive neurons automatically (Petroske et al., 2001; Xu et al., 2010).

HPLC Analysis of DA and Its Metabolites

The method adopted from Liang was made some modifications (Liang and Tang, 2006). In brief, striatum was rapidly dissected, weighed, homogenized and centrifuged. The final supernatant was stored at −70°C until HPLC assay. The concentrations of dopamine and its metabolites (DOPAC and HVA) were determined by a Waters 515 HPLC system (Milliford, MA, USA) with an electrochemical detector (HPLC-ECD) and a microbore ODS column (100 × 1 mm i.d.). The mobile phase consisted of 0.1 M NaH_2PO_4, 0.5 mM EDTA, 10 mM NaCl, 1 mM sodium octyl sulfate (pH 3.1) and 5% acetonitrile, and was pumped at 65 μl/min. The sample was diluted 1:4 with the mobile phase to neutralize the pH before chromatography. The calibration materials were assayed in parallel.

Autoradiography of Striatal Dopamine Transporter

Striatal dopamine transporter density (DAT) binding were estimated by [^{125}I]-FP-β-CIT binding autoradiography in coronal frozen sections (20 μm in thickness) prepared from right hemisphere including striatum region. Thawed sections were immersed in binding buffer (50 mM Tris, 120 mM NaCl, 5 mM KCl^-) for 2 × 15 min at room temperature, then incubated in the same buffer containing 50 pM [^{125}I]- FP-β-CIT and 100 nM fluoxetine (to inhibit serotonin binding to the [^{125}I]-FP-β-CIT) for 2 h at 25°C to determine the total binding. Non-specific binding (NSB) was assessed in parallel slices with the addition of 100 μM GBR 12909 (dopamine uptake inhibitor). All sections that were thoroughly washed and air-dried were exposed to X-ray film (Kodak, USA) for 2 d at 4°C. Then the film was developed and fixed. Finally, quantitative analysis of the autoradiographs was performed with a Gel Documentation System (Bio-Rad) by circumscribing the area of striatum on the digitized image and measuring the mean gray level. DAT density was expressed as the mean value of optical density unit.

Radioligand Binding Assay of Dopamine D1 and D2 Receptor Density in Striatum

Densities of Dl and D2 receptor were measured by the radioligand binding assay, using [^{3}H] SCH23390 (SA: 80.5 Ci/mmol) for dopamine Dl receptor and [^{3}H] spiperone (SA: 16.2 Ci/mmol) for dopamine D2 receptor binding, according to the method described previously with minor modifications (Popoli et al., 1998). In brief, the isolated striatum was homogenized in ice-cold buffer containing 50 mM Tris-HCl, 10 mM $MgCl_2$, 0.25 M sucrose, and subsequently centrifuged at 2,000 *g* for 15 min, then at 27,000 *g* for 15 min

at 4°C. The precipitate was suspended with the above buffer without sucrose, and mixed as a membrane protein suspension. Micro-Lowry's method was utilized to quantify sample protein content. Dopamine receptor activity was measured in a parallel set of reaction tubes. A single dose of [^{3}H] SCH23390 at a saturation concentration of 5 nM was selected based on preliminary multipoint saturation analysis for all samples to detect D1 receptor. Parallel tubes with additional 5 μM unlabeled SCH23390 were used for measurement of NSB. D2 receptors were measured using 1.5 nM [^{3}H] spiperone combined with 50 nM ketanserin to block binding to serotonin receptors. NSB was determined in the presence of 80 nM haloperidol. The binding reaction system was incubated at 37°C for 50 min. The reaction was terminated by rinsing in ice-cold distilled water and harvested on a glass fiber filter which was then baked at 80°C, immersed in 0.6% b-PBD xylene scintillator and measured with a liquid scintillation counter (Beckman LS 6500). The density of receptors was determined using the following formula: Receptor density = (Total binding − NSB)/measure efficiency × 60 × specific × protein concentration).

Measurement of BDNF and GDNF Content by ELISA

BDNF and GDNF content were determined using BDNF or GDNF Emax Immunoassay System according to the manufacturer's guidelines. Briefly, the sample dissected from the striatum of unilateral hemisphere was sonicated in cold lysis buffer containing 137 mM NaCl, 20 mM Tris (pH 8.0), 0.5% TritonX-100, 10% glycerol and centrifuged at 10,000 *g* for 10 min at 4°C. Subsequently the supernatants were retained for assay. Then plates were coated with anti-BDNF or GDNF monoclonal antibody overnight. After nonspecific binding was blocked, each well added sample protein, BDNF or GDNF standards were incubated for 2 h (BDNF) or 6 h (GDNF) with shaking at room temperature. After washing, plates were incubated with polyclonal anti-human BDNF or anti-GDNF polyclonal antibody 2 h at room temperature or overnight at 4°C. Anti-IgY HRP-conjugated secondary antibody was added to the washed plates and incubated 1 h for BDNF and 2 h for GDNF at room temperature. Plates were then washed and incubated with TMB One Solution for 10 min or 15 min. Finally, plates were added 1 N hydrochloric acid to terminate the color change reaction and measured the absorbance at 450 nm using a plate reader. Data were expressed as picograms per milligram of protein.

Western Blot

Striatum tissues were homogenized by ultrasonication in 10 volumes of ice-cold RIPA lysis buffer respectively. The homogenates were then centrifuged at 12,000 *g* for 5 min at 4°C. The supernatants were collected and total protein concentration was determined according to the Micro bicinchoninic acid (BCA) procedure. Protein samples (40 μg) were separated by electrophoresis on a 10% PAGE and transferred to PVDF membranes. The membranes were blocked with 5% nonfat dried milk for 2 h at room temperature and then incubated with primary antibody overnight at 4°C. The membranes were rinsed three times with Tris-Buffered Saline with Tween-20 (TBST) and then followed by HRP-conjugated anti-rabbit/mouse IgG for 2 h at room temperature. After rinsing with TBST, the immunocomplexes were visualized by enhanced chemiluminescence using the ECL kit according to the manufacturer's instructions. Densitometric analyses were performed using ImageJ software.

Cell Culture and Treatment

The SH-SY5Y cell line was a kind gift from Dr. H. Zhang of the Shanghai Institute of Materia Medica who bought the cell line from ATCC (Manassas, VA, USA). The cells were seeded at 5×10^5 cells/ml in bottles containing DMEM cultured at 37°C with 5% CO_2. When the cells were 70–80% confluence, SMI was added at a final concentration of 10 μM. Twenty-four hours later, 1 mM MPP^+ was added.

Transfection of SH-SY5Y Cells With CREB siRNA

CREB siRNA and control siRNA were designed as previous described. CREB siRNA: 5′-UACAGCUGGCUAACAAUGG-3′; control siRNA: 5′-UUCUCCGAACGUGUCACGU-3′; Control siRNA showed no significant match and thus served as a non-functional control. Transfection was carried out using the Fugene 6 Transfection Reagent kit (Roche) following instructions in the kit protocol. In brief, when the cells were 70% confluent, 80 nM siRNA and 1 μl transfection reagent were added to 10^5 cells and were then incubated for 4 h to complete the transfection. GDNF and BDNF mRNA were examined 48 h later.

RT-PCR of GDNF and BDNF mRNA

In order to test the effects of MPP^+, SMI and CREB on the expression of GDNF and BDNF, qRT-PCR was carried out using the SYBR Green dye method as described previously (Zhang et al., 2008) with the following primers:

- GDNF; F-5′-CGGGACTCTAAGATGAAGTTATGGGAT GTCGTG-3′,
- R-5′-GGGTCAGATACATCCACACCGTTTAGCGG AATGC-3′,
- BDNF; F-5′-AGCTGAGCGTGTGTGACAGTATTAG-3′
- R-5′-ATTGCTTCAGTTGGCCTTTTGATAC-3′
- GAPDH; F-5′-GACCCCTTCATTGACCTCAACTACA-3′
- R-5′-TCTCGCTCCTGGAAGATGGTGATG-3′.

The amount of GDNF and BDNF mRNA in the SH-SY5Y cells were determined by real time qRT-PCR at 24 h after the addition of MPP^+. Data were finally normalized by respective GAPDH values from the same run and expressed as percent of the control sample.

Statistical Analysis

All data were represented as mean ± SEM. Statistical comparisons of data among the different groups were performed by an analyses of variance (ANOVA) followed by a *post hoc* Newman–Keuls using the SAS software package. $P < 0.05$ was judged to have statistical significance.

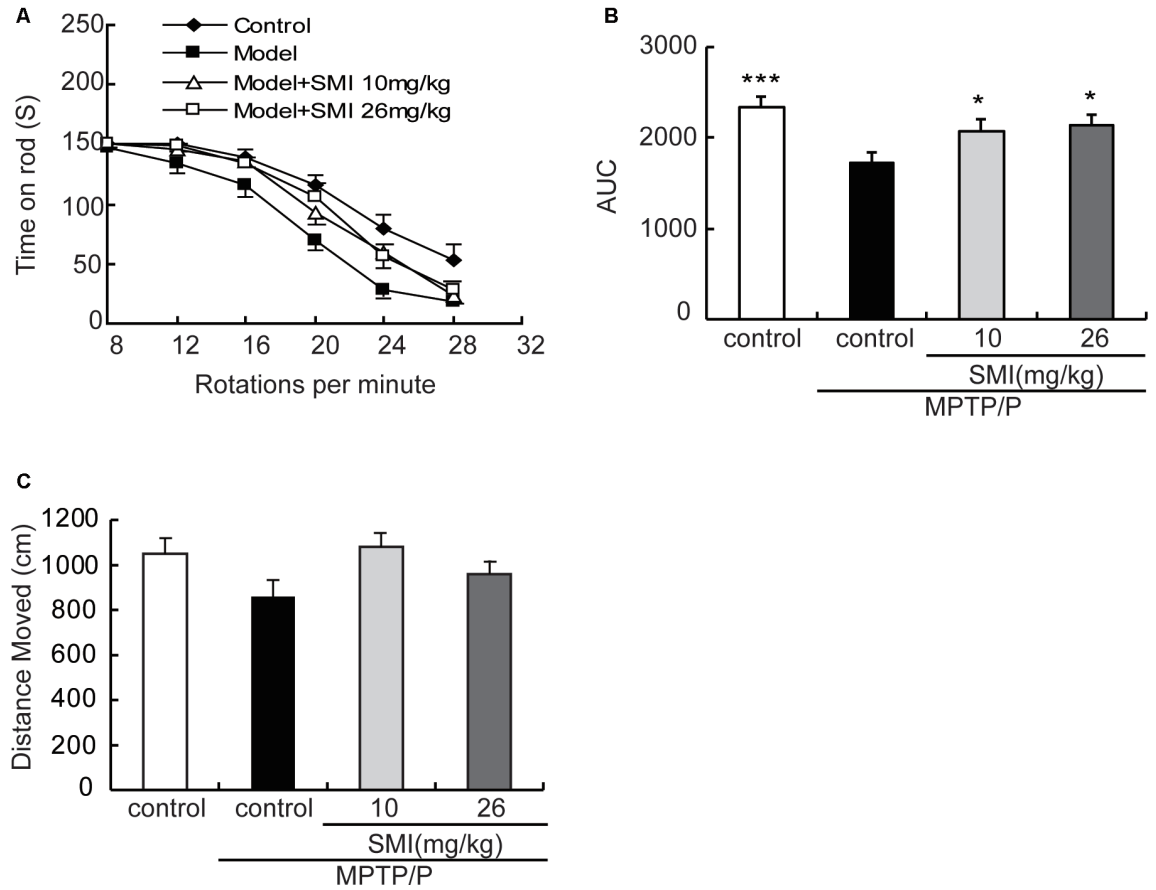

FIGURE 2 | Effects of smilagenin (SMI) on behavioral test of chronic 1-methyl-4-phenyl-1,2,3,6-tetrahydropyridine (MPTP)/probenecid-lesioned mice. **(A)** Time on the rod vs. rotation speed, each point was the mean ± SEM of 3 days consecutive tests. **(B)** Statistical comparisons of area under the curve (AUC) values between groups. **(C)** Total distance moved, measured as centimeters moved in 5 min, data are expressed as mean ± SEM, $n = 10$. *$P < 0.05$ and ***$P < 0.001$ respectively as compared with untreated model group, respectively.

RESULTS

Effect of SMI on Rotarod and Open Field Test for Behavioral Ability in Chronic MPTP/Probenecid-Lesioned Mice

In the present study, we adopted a commonly utilized rotarod test to measure motor coordination in animals and the AUC to reflect the mice on the rotarod movement. The time stayed on the rods for all mice declined with the increase of rotational speed from 8 to 28 rpm in the rotarod apparatus. Generally, the curve dropped most rapidly in the MPTP/probenecid models, followed by SMI treatment, and the normal control mice declined slowest (**Figure 2A**). As indicated in **Figure 2B**, the AUC was significantly declined in MPTP/probenecid-injured mice when compared with normal controls ($P < 0.001$). Meanwhile, SMI at dose of 10 or 26 mg/kg/day significantly ameliorated locomotor ability of MPTP/probenecid-lesioned mice ($P < 0.05$).

As shown in **Figure 2C**, in the open field test, the total distance of MPTP/probenecid injured mice was less than that of control group, but there was no statistically significant difference. There was also no significantly improved locomotor activity with SMI treatment ($P > 0.05$).

Effect of SMI on Tyrosine Hydroxylase Positive and Nissl Positive Neuron Number in Chronic MPTP/Probenecid-Lesioned Mice

According to **Figure 3A**, we can see that the TH-positive neuron number of SNpc was decreased in the model mice compared with normal controls and was increased both in treatment with SMI at 10 and 26 mg/kg/day compared with model mice. **Figure 3B** has indicated the statistical results of TH-positive neuron numbers. Compared with normal control mice, TH-positive neuron number in the SNpc was reduced by 74.4% in chronic MPTP/probenecid injured model mice ($P < 0.001$). Two months' treatment of 10 or 26 mg/kg/day SMI after three doses MPTP/probenecid injection increased TH (+) neurons by 104.1% and 228.8%, respectively when compared with MPTP/probenecid injection alone ($P < 0.01$, $P < 0.001$). On the other hand, Nissl staining showed that

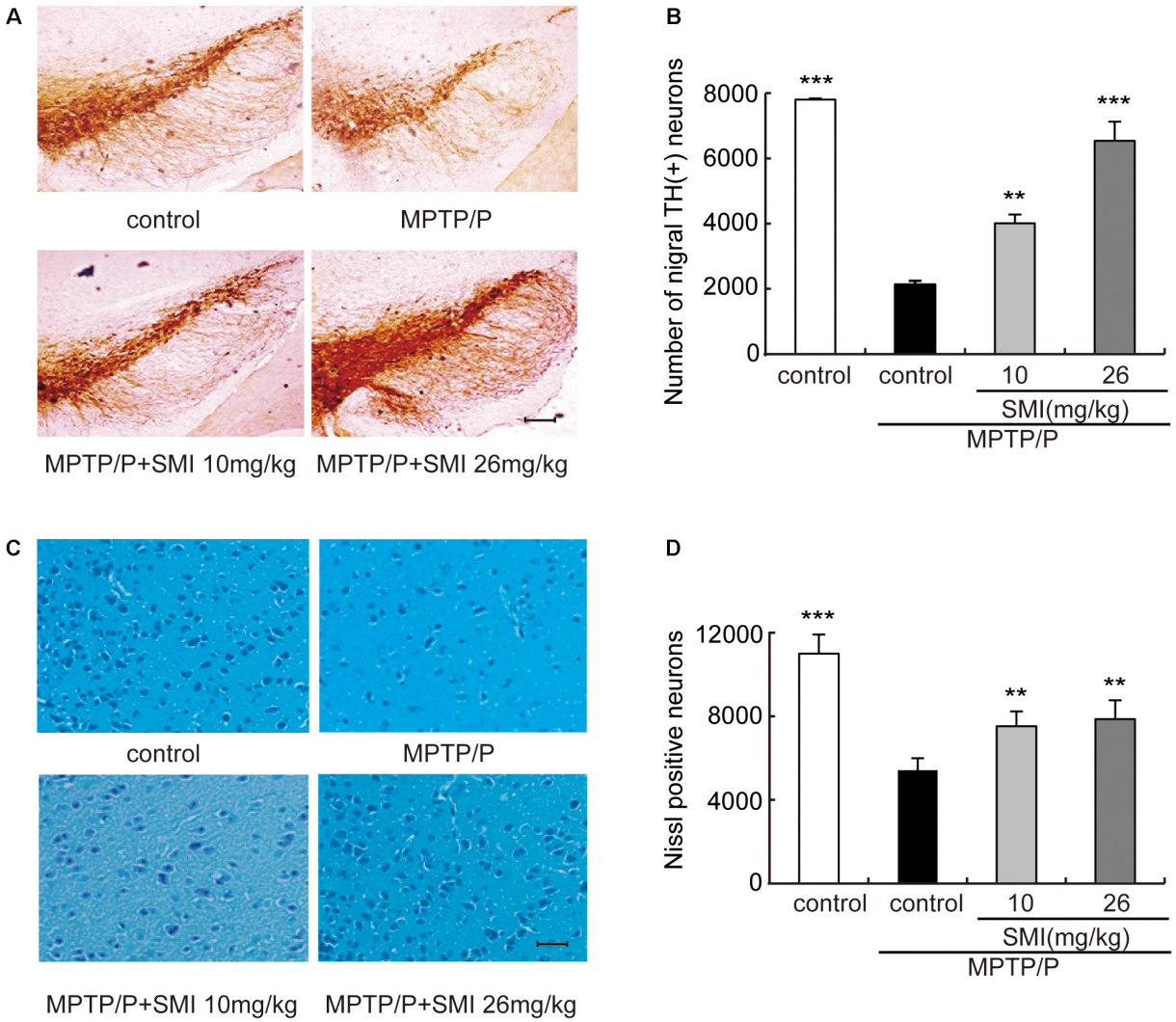

FIGURE 3 | Effect of SMI on tyrosine hydroxylase (TH)-positive and Nissl positive neuron number in chronic MPTP/probenecid-lesioned mice. Panel **(A)** shows the representative slices of the control mice, model mice treated with vehicle, 10 mg/kg/day, and 26 mg/kg/day SMI successively. (×100, scale bar = 100 μm). Panel **(B)** shows the statistical results. Panel **(C)** shows the representative images of Nissl-stained neurons in the substantia nigra pars compacta (SNpc) of the control mice, model mice treated with vehicle, 10 mg/kg/d, and 26 mg/kg/day SMI successively (×100, scale bar = 100 μm). Panel (**D**) shows quantification of Nissl-stained neurons. Number of nigral TH-positive neuron and Nissl-stained neurons in each mouse was quantified at ×100 magnification and then normalized to its corresponding control. Data are expressed as mean ± SEM, $n = 3$. $^{**}P < 0.01$ and $^{***}P < 0.001$, respectively as compared with untreated model group, respectively.

Nissl-stained neurons were reduced in the SNpc of chronic MPTP/probenecid injured model mice compared with controls and was increased after treatment with SMI in model mice (**Figures 3C,D**). These results suggest that administration of SMI may restore the loss of midbrain dopaminergic neurons caused by MPTP/probenecid.

Effect of SMI on Striatal DA and Its Metabolites Concentration in Chronic MPTP/Probenecid-Lesioned Mice

In the chronic PD model induced by MPTP/probenecid, the average concentrations of DA in striatum was only 35.7% of controls ($P < 0.05$). After treatment PD model with SMI for 2 months at dose of 10 or 26 mg/kg/day, DA concentration increased to 50.1% and 54.5% of normal ($P < 0.05$; **Figure 4A**). Besides, the concentrations of the metabolites DOPAC and HVA, which were decreased in the MPTP/probenecid model, were also elevated by SMI (**Figures 4B,C**). For DOPAC/DA, the ratios were 0.149 ± 0.004, 0.149 ± 0.009 and 0.153 ± 0.010, respectively for model and model treated with SMI at dose of 10 or 26 mg/kg/day (**Figure 4D**). For HVA/DOPAC, the ratios were 7.19 ± 0.34, 7.50 ± 0.41 and 7.91 ± 0.23, respectively ($P > 0.05$; **Figure 4E**). We can see SMI has no significant effect on the ratios of DOPAC/DA and HVA/DOPAC. This implicates that SMI did not change the catabolism of DA.

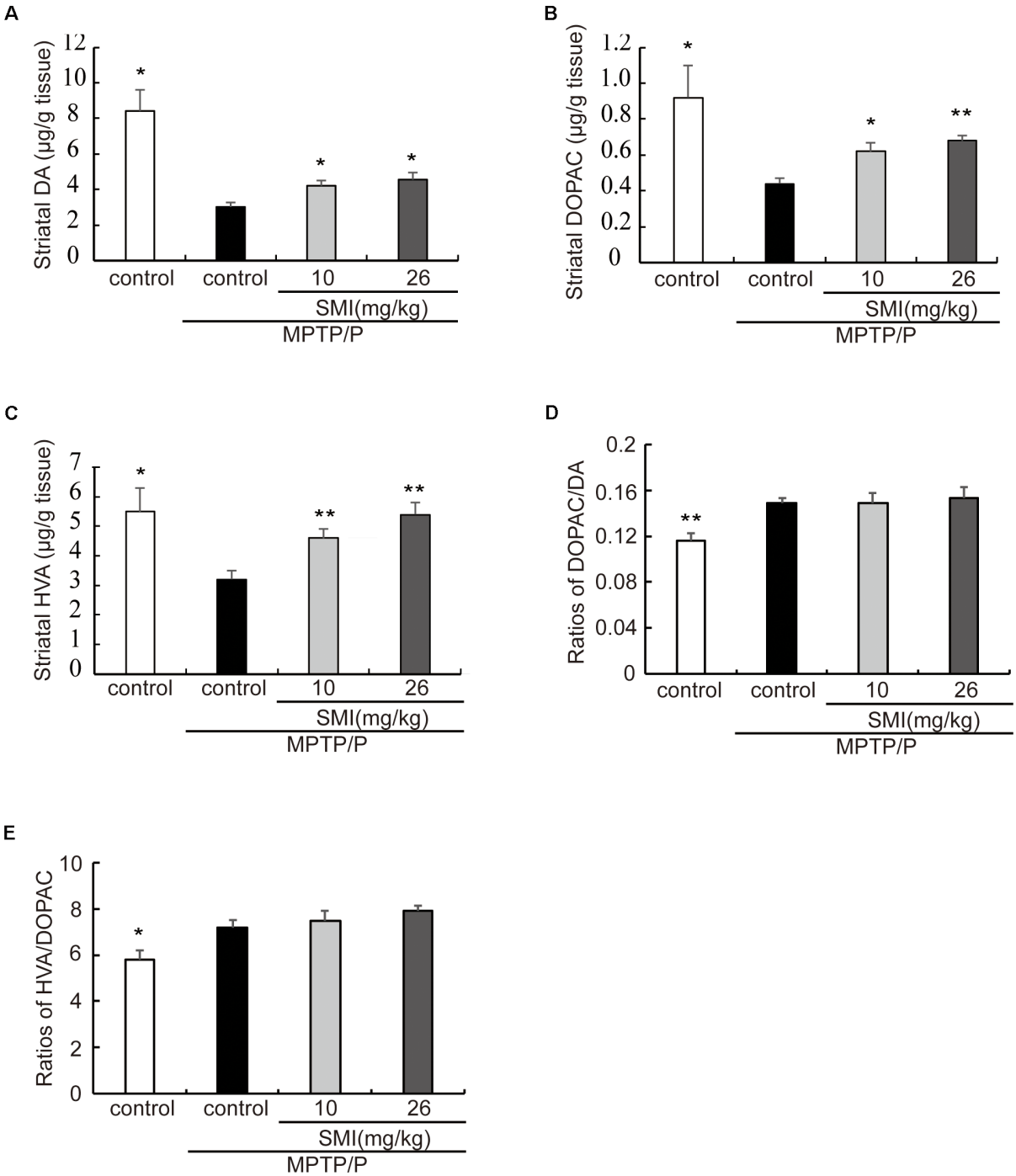

FIGURE 4 | Effect of SMI on striatal DA and its metabolites concentration in chronic MPTP/probenecid-lesioned mice. Panels **(A–C)** show amount of DA and its metabolites in striatum detected by HPLC-ECD. Panel **(D)** shows ratios of DAPOC/DA. Panel **(E)** shows ratios of HVA/DOPAC. Data are expressed as mean ± SEM, $n = 7$. $^{*}P < 0.05$ and $^{**}P < 0.01$, respectively as compared with untreated model group, respectively.

Effect of SMI on Striatal Dopamine Transporter Density and Protein Level in Chronic MPTP/Probenecid-Lesioned Mice

Autoradiography has been utilized to clarify striatal DAT. **Figure 5A** was the representative autoradiographic images. The statistical results revealed in **Figure 5B**, striatal DAT density in MPTP/probenecid-treated mice was significantly reduced by 30.03% ($P < 0.01$), as compared with normal control mice. Additionally, after administration of SMI whatever 10 or 26 mg/kg/day in MPTP/probenecid-injured mice, DAT density

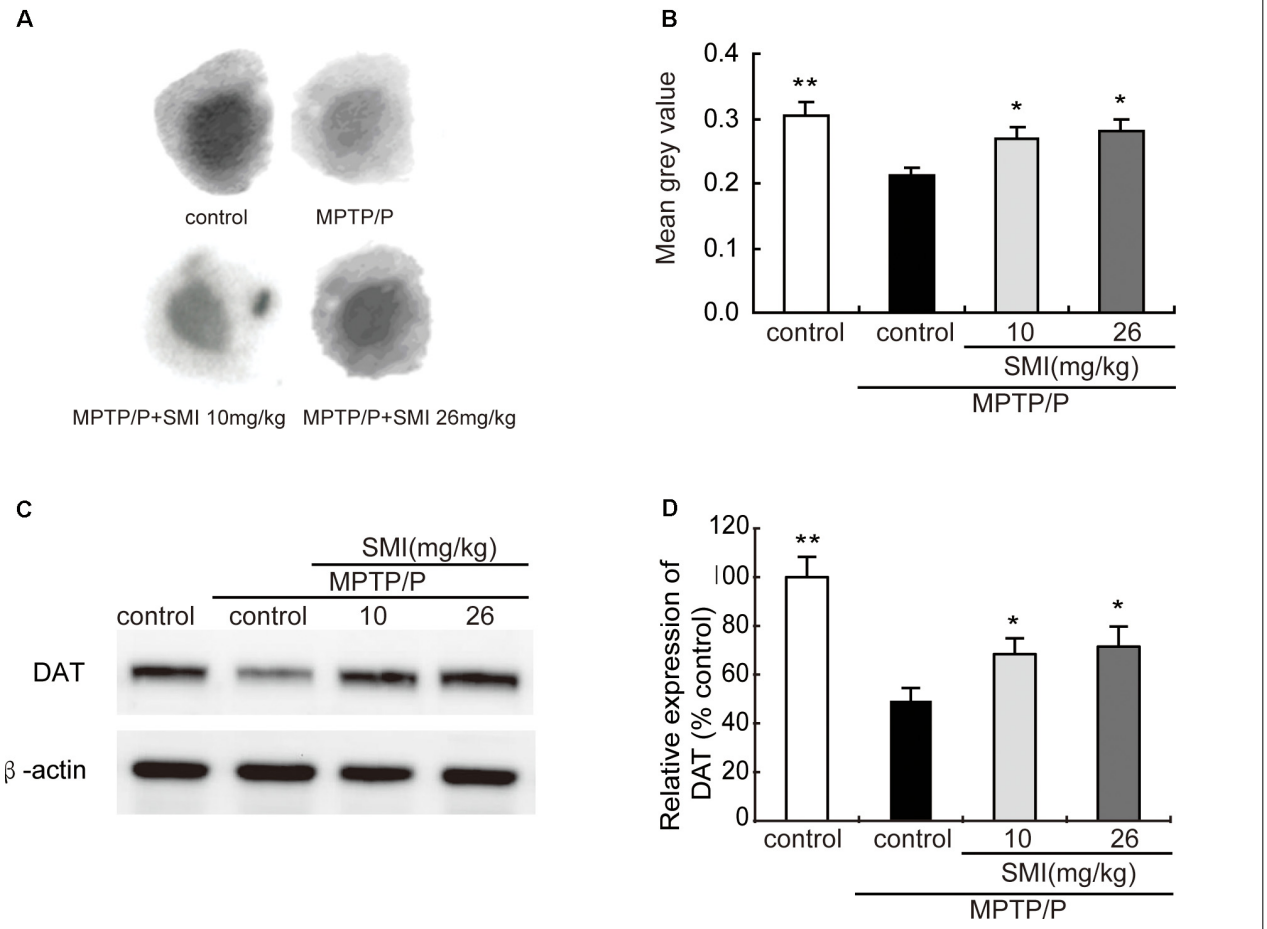

FIGURE 5 | Effect of SMI on striatal dopamine transporter (DAT) density and protein level in chronic MPTP/probenecid-lesioned mice. Panel **(A)** shows representative autoradiographic images of the control mice, model mice treated with vehicle, 10 mg/kg/d, and 26 mg/kg/d SMI successively. Panel **(B)** shows the statistical results (n = 7). Panel **(C)** shows representative western blot bands of DAT. Panel **(D)** shows relative protein expression levels were quantified by densitometry analysis using Image J software on DAT bands (n = 4). Data are expressed as mean ± SEM. *$P < 0.05$ and **$P < 0.01$, respectively as compared with untreated model group, respectively.

in striatum increased by 26.42% and 32.55%, respectively when compared with MPTP/probenecid mice model alone ($P < 0.05$, $P < 0.01$). As shown in **Figures 5C,D**, the same trend was also observed through the Western blot analysis. We found that protein level of DAT significantly downregulated in MPTP/probenecid-treated mice as compared to controls ($P < 0.01$), which was elevated after treatment of SMI ($P < 0.05$).

Effect of SMI on Striatal Dopamine D1 and D2 Receptor Density and Protein Level in Chronic MPTP/Probenecid-Lesioned Mice

Saturation radioligand binding on striatal membranes using ^{3}H-SCH23390 displayed increased D1 receptor density in the model mice compared with normal control and treatment with SMI at dose of 26 mg/kg/day ($P < 0.05$). SMI treatment produced D1 receptor downregulation from 196 to 164 fmol/mg protein in model mice (**Figure 6A**). Conversely, D2 receptor number in MPTP/probenecid-lesioned mice decreased compared with normal ($P < 0.05$); while after administration of SMI at dose of 26 mg/kg/day, there was a significantly increase ($P < 0.01$; **Figure 6B**). As shown in **Figures 6C,D**, we found that protein level of D1 receptor had no significant change through western blot and the reason might be antibody detection was not sensitive enough ($P > 0.05$). On the other hand, D2 receptor expression was downregulated in MPTP/probenecid-treated mice as compared to controls. Meanwhile, SMI at dose of 26 mg/kg/day, not 10 mg/kg/day, significantly restored D2 receptors protein level of MPTP/probenecid-lesioned mice ($P < 0.05$; **Figure 6E**).

Effect of SMI on Striatal GDNF and BDNF in Chronic MPTP/Probenecid-Lesioned Mice

Additionally, to further clarify the underlying mechanism of SMI's neuroprotective effect, we applied ELISA and Western blot to detect striatal GDNF and BDNF protein content. We found that there was a slight reduction but no significant difference in protein contents of GDNF and BDNF in the striatum between the MPTP/probenecid-treated mice and normal control

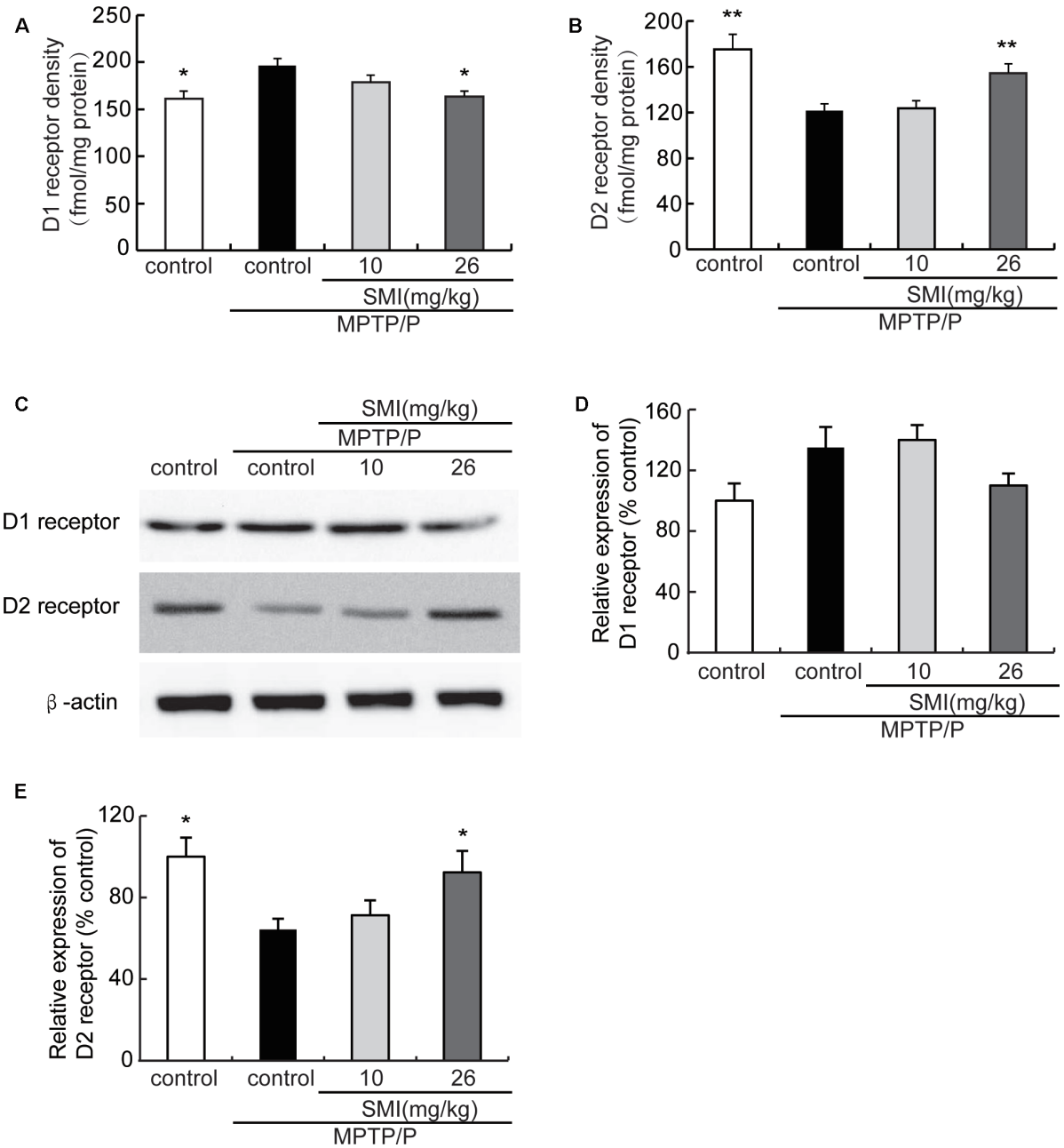

FIGURE 6 | Effect of SMI on striatal dopamine D1 and D2 receptor density and protein level in chronic MPTP/probenecid-lesioned mice. **(A)** D1 receptor density, assessed by ^{3}H-SCH23390 (n = 9). Panel **(B)** D2 receptor density, assessed by ^{3}H-spiperone (n = 9). Panel **(C)** shows representative western blot bands of D1 and D2 receptor. Panels **(D,E)** show relative protein expression levels were quantified by densitometry analysis using Image J software on D1 and D2 receptor bands (n = 4). Data are expressed as mean ± SEM. *P < 0.05 and **P < 0.01, respectively as compared with untreated model group, respectively.

mice (P > 0.05; **Figures 7A–F**). As shown in **Figures 7A,B**, SMI administration elevated the striatal GDNF and BDNF protein content of MPTP/probenecid-induced mice by ELISA analysis (P < 0.01). The same trend was also observed through the Western blot analysis. Meanwhile, we found SMI at dose of 26 mg/kg/day more significantly increased the protein level of GDNF compared with lower dose (P < 0.001; **Figure 7D**).

Effect of SMI on CREB Phosphorylation in Chronic MPTP/Probenecid-Lesioned Mice and CREB siRNA on mRNA Expression of GDNF and BDNF in MPP^{+} Treated SH-SY5Y Cells

Cyclic AMP responsive element binding protein (CREB) is a transcription factor involved in regulation of genes associated

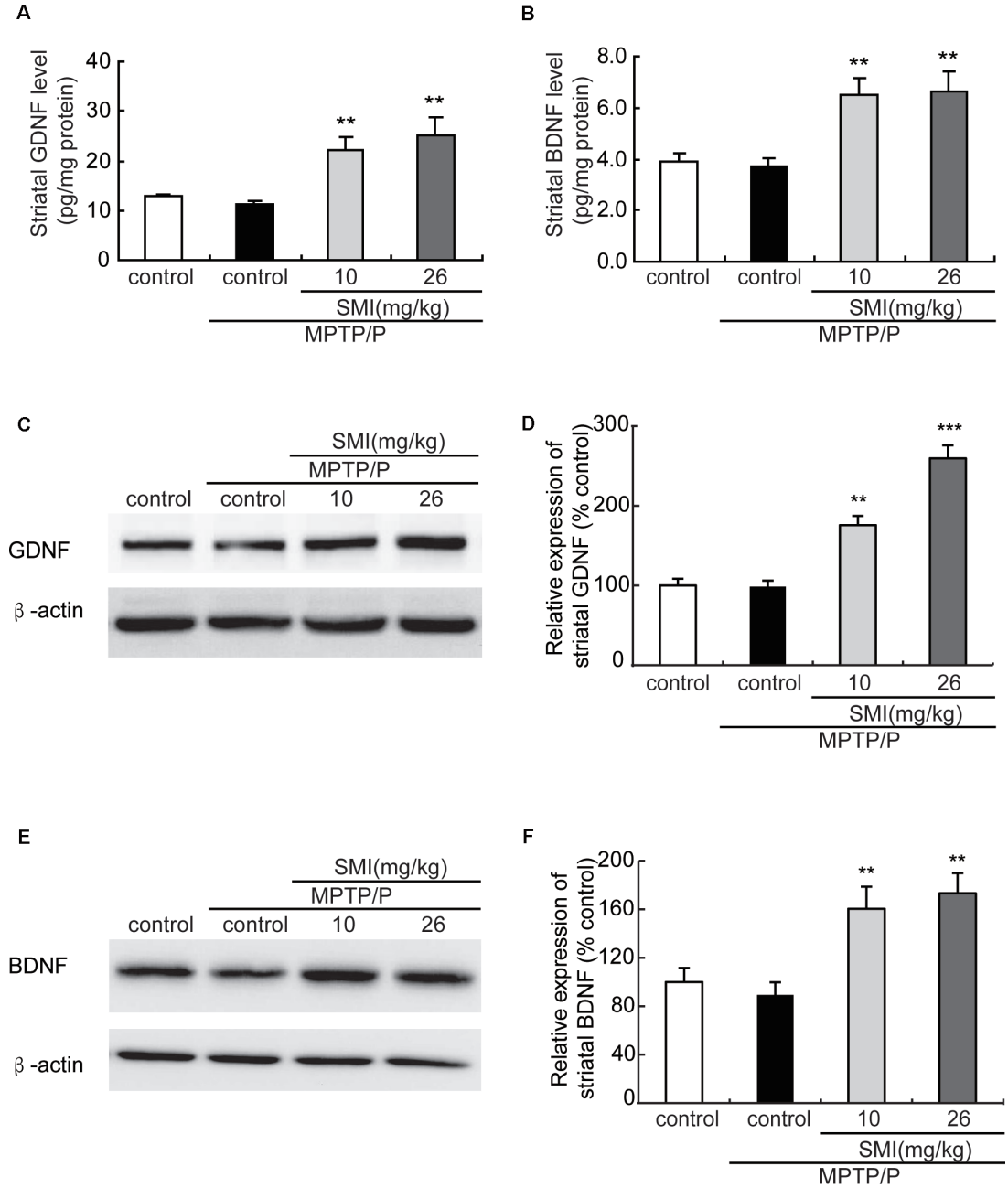

FIGURE 7 | Effect of SMI on striatal glial cell line-derived neurotrophic factor (GDNF) and brain-derived neurotrophic factor (BDNF) levels in chronic MPTP/probenecid-lesioned mice. **(A)** Striatal GDNF levels by ELISA. **(B)** Striatal BDNF levels by ELISA. Panels **(C,E)** show representative western blot bands of GDNF and BDNF. Panels **(D,F)** show relative protein expression levels were quantified by densitometry analysis using Image J software on GDNF and BDNF bands ($n = 4$). Statistical comparisons between groups, data are expressed as mean ± SEM, $^{**}P < 0.01$ and $^{***}P < 0.001$, respectively as compared with untreated model group, respectively.

with synaptic and neural plasticity. The phosphorylation of CREB (pCREB) was necessary for active transcription. CREB has been reported to up-regulate the expression of a set of genes including BDNF and GDNF (Cen et al., 2006; Wang et al., 2017). As shown in **Figure 8A**, Western blot revealed that the expression of pCREB/CREB was reduced in MPTP/probenecid-treated mice as compared with normal control mice ($P < 0.05$). We found SMI treatment elevated the level of CREB phosphorylation and the differences between SMI at dose of 26 mg/kg/day and MPTP control was highly significant ($P < 0.001$; **Figure 8B**). We speculated SMI up-regulated the expression of GDNF and BDNF by increasing the level of CREB phosphorylation. To test this possibility, we blocked CREB by CREB siRNA in MPP^+ treated SH-SY5Y cells and detected

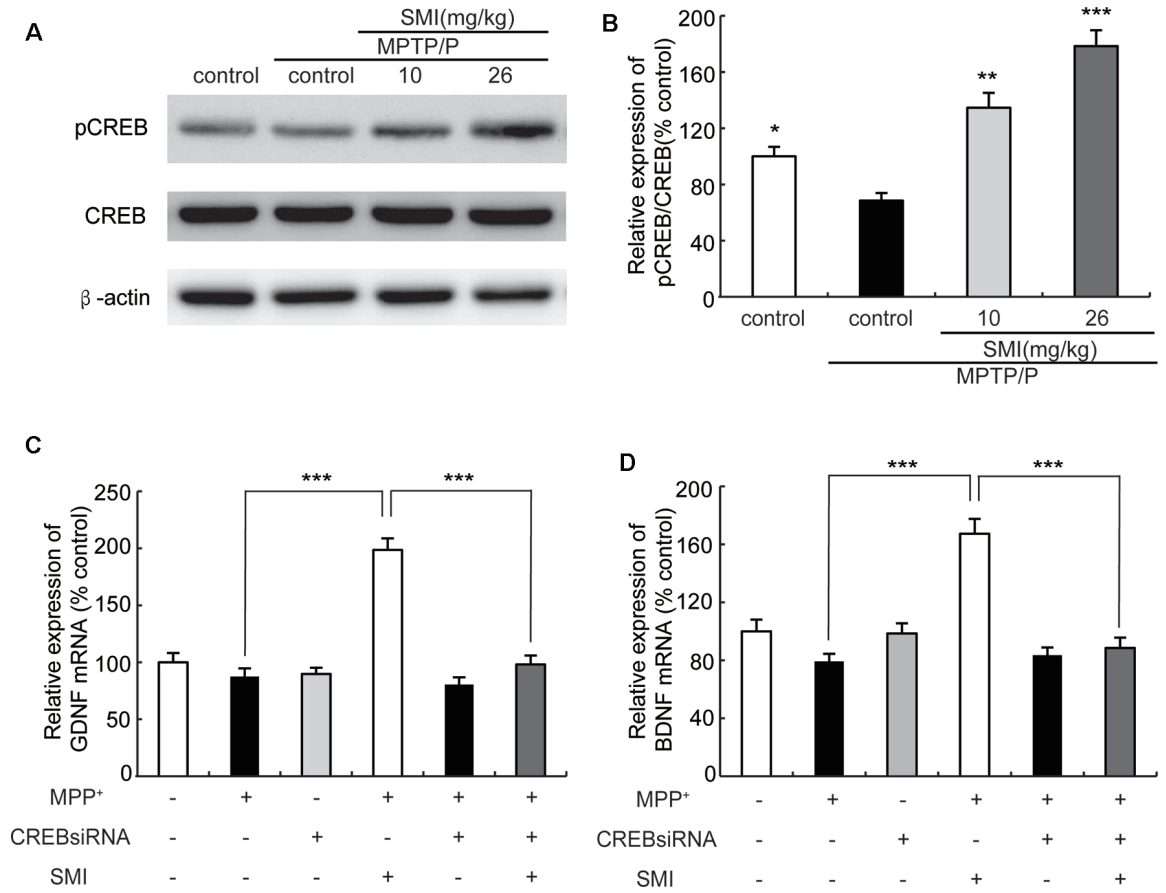

FIGURE 8 | Effect of SMI on cyclic AMP responsive element binding (CREB) phosphorylation in chronic MPTP/probenecid-lesioned mice and CREB siRNA on mRNA expression of GDNF and BDNF in MPP^+ treated SH-SY5Y cells. Panel **(A)** shows western blot bands of CREB and phosphorylation of CREB (pCREB). Panel **(B)** shows relative expression of pCREB/CREB were quantified by densitometry analysis using Image J software on CREB and pCREB bands ($n = 4$). Data are expressed as mean ± SEM, $^*P < 0.05$, $^{**}P < 0.01$ and $^{***}P < 0.001$, respectively as compared with untreated model group, respectively. Panels **(C,D)** show relative expression of GDNF and BDNF mRNA by real time PCR. Data are expressed as mean ± SEM, $^{***}P < 0.001$.

mRNA expression of GDNF and BDNF. We found that there was no significant difference in mRNA expression level of GDNF and BDNF between MPP^+ treated cells and normal control. However, SMI treatment significantly increased GDNF and BDNF transcription in MPP^+ treated cells ($P < 0.001$). After application of CREB siRNA, the elevation effect of SMI on mRNA expression of GDNF and BDNF was abolished. There was no significantly upregulation after SMI treatment ($P > 0.05$, **Figures 8C,D**).

DISCUSSION

It is for the first time that we have evaluated the neuroprotective effects of SMI as well as its effect on locomotor ability in chronic MPTP conjuncted with probenecid lesioned mice model of PD. Given SMI requiring long-term administration to exert well protective effects, the chronic MPTP/probenecid mice model which closely mimics the chronic and progressive neurodegeneration and behavioral deficits observed in human PD was more appropriate for investigating the drug's potent neuroprotective strategies (Peoples et al., 2012; Schildknecht et al., 2017; Nonnekes et al., 2018). Following 60 days' oral administration of SMI when the third dose of MPTP/probenecid injection afterwards.

It was demonstrated that MPTP/probenecid-intoxicated mice gave rise to impaired rotarod performance assessed by means of the rotarod test which is one of the most commonly utilized test to measure motor coordination in animals (Rozas et al., 1998; Petroske et al., 2001; Ayton et al., 2013). In the present study, we observed that rotarod performance was impaired in MPTP/probenecid-lesioned mice compared with the normal control and SMI administration improved MPTP/probenecid-induced motor deficits. The locomotor disorder is considered to be related to the injure of nigrostriatal dopaminergic system.

TH, DA, DAT and dopamine receptors are important hallmarks of the neurodegenerative alterations of nigro striatal dopaminergic neuron in PD (Peoples et al., 2012; Naskar et al., 2015; Zhang et al., 2018). We observed in this article that TH-positive and Nissl positive neuron numbers in SNpc markedly reduced in MPTP-lesioned mice consistent

with previous research reported (Alam et al., 2017; Peng et al., 2018), which can be elevated by administration of SMI starting at the early stage of the model production. TH is a marker of dopaminergic neurons and Nissl body is a marker of neurons. SMI increases the number of TH-positive neuron and Nissl staining cells in the substantia nigra of model mice, reflecting the increase in the number of dopaminergic neurons in the substantia nigra. In addition, the amount of TH in the substantia nigra is increased, which is beneficial to the synthesis of DA. Furthermore, SMI treatment increases striatal DA level of chronic PD mice model and does not change its metabolites concentration. We could speculate that SMI may protect striatal DA at a relatively constant level and does not affect the rate of DA renewal by protecting residual neurons (Xu et al., 2010; Sun et al., 2012). In the case of chronic PD mice model, striatal DAT density was lowered when compared with the vehicle-treated mice (Anandhan et al., 2012; Hong et al., 2015; Miville-Godbout et al., 2016). SMI treatment can reverse the decline of DAT density. This facilitates the ingestion of DA to prepare next release after its release into the synaptic cleft and exerting physiological effects. In addition, DAT is specifically expressed in dopaminergic neurons. Due to the protection of dopamine neurons by SMI, DA synthesis was not significantly reduced, thus avoiding the D1 receptor hypersensitivity and increase in number to some extent. In addition, the up-regulation of D2 receptor density by SMI suggests that SMI may be used in combination with levodopa to improve the down-regulation of D2 receptor density induced by the long-term use of levodopa (Morissette et al., 1996). Thus, we could speculate that SMI exerts effects of elevating nigral TH positive neurons and striatal DAT density in chronic MPTP-intoxicated mice, suggesting that it possesses action of improving dopaminergic neuron loss induced by MPTP and preventing or slowing the process of neuronal degeneration. We also found there was a recovery phenomenon appeared in MPTP/probenecid treated mice after 6 months which suggested us that we could observe the role of SMI in MPTP/probenecid treated mice for a longer period of time and get more information (Petroske et al., 2001).

Although there is undisputed about its significance of the potential neuroprotective effects of both BDNF and GDNF in preclinical studies and GDNF has been shown in some PD patients to have a positive effect (Gill et al., 2003; Love et al., 2005; Lu et al., 2013), unfortunately owing to large polypeptide structure and consequent poor oral bioavailability of exogenous BDNF, in clinical studies using BDNF as a therapeutic agent have been inconclusive (Thoenen and Sendtner, 2002). It is greatly urgent to execute potential strategy to stimulate the endogenous expression of neurotrophic factors after oral administration to slow down or reverse the progression of neuronal degeneration. Our previous study *in vitro* indicated that SMI relied on stimulating the intrinsic GDNF expression to exert neuroprotective effect on primary cultured mesencephalic dopaminergic neurons (Zhang et al., 2008). Hence, we evaluated whether SMI could have an impact on chronic MPTP/probenecid-induced mice *via* enhancing expression of BDNF and GDNF in striatum. In this article, we observed that there were no alterations in striatal BDNF and GDNF protein levels between chronic MPTP/probenecid lesioned mice alone and the vehicle treated mice. However, long-term administration of SMI greatly elevated GDNF and BDNF content in the striatum of MPTP/probenecid-lesioned mice. In addition, we used MPP^+-treated SH-SY5Y cells as an *in vitro* PD model to investigate the mechanism of SMI effect on GDNF and BDNF. We observed SMI treatment significantly increased GDNF and BDNF transcription in MPP^+ treated cells. We also found CREB siRNA abolished the elevation effect of SMI on mRNA expression of GDNF and BDNF in MPP^+-treated cells. We could speculate that SMI increased GDNF and BDNF protein level through promoting the phosphorylation of upstream transcription factor CREB and to increase mRNA expression of GDNF and BDNF. Presently there is a body of evidence revealing that BDNF and GDNF has strong neuroprotective effects on nigrostriatal dopaminergic neurons of animal PD models with 6-OHDA or MPTP, led to a substantial increase in the number of TH-positive neurons in SNpc as well as ameliorated behavioral disorders, stimulated TH positive fiber sprouting and elevated DA content (Biju et al., 2010; Ren et al., 2013). In the present research, it is reasonable to assume SMI protect and repair nigrostriatal dopaminergic system, at least in part, by promoting the phosphorylation of CREB to increase expression of endogenous GDNF and BDNF. GDNF and BDNF exert their neuroprotective effect to increase nigral TH positive neurons and striatal DAT density and subsequently ameliorate motor deficits in chronic MPTP/probenecid-intoxicated mice.

CONCLUSION

In summary, this study demonstrates that administration of the SMI to chronic MPTP/probenecid animals improved the pathological development of disease. The possible mechanism that SMI exerted neuroprotective effects may be partially related to up-regulating CREB phosphorylation which triggers endogenous neurotrophic factors, and ameliorating nigrostriatal dopaminergic system, which is likely to halt the ongoing progression.

DATA AVAILABILITY

All datasets generated for this study are included in the manuscript.

AUTHOR CONTRIBUTIONS

YZ, HW and RX conceived the study. XH and SY performed the experiments and data analyses. RZ, LH and JX provided intellectual inputs. XH and SY wrote the manuscript. All authors edited and approved the manuscript.

FUNDING

This work was supported by The Chinese National Natural Science Foundation (Grant Nos: 81573401, 81373395, 81573415, 81503174, 81503044), Innovative research team of high-level

local universities in Shanghai, Integration of traditional Chinese and western medicine, Construction Project of High Level Local Universities in Shanghai and Pharmacy, Construction Project of High Level Local Universities in Shanghai (XD18015).

ACKNOWLEDGMENTS

We would like to thank all individuals participating in the study.

REFERENCES

Alam, G., Edler, M., Burchfield, S., and Richardson, J. R. (2017). Single low doses of MPTP decrease tyrosine hydroxylase expression in the absence of overt neuron loss. *Neurotoxicology* 60, 99–106. doi: 10.1016/j.neuro.2017.03.008

Anandhan, A., Janakiraman, U., and Manivasagam, T. (2012). Theaflavin ameliorates behavioral deficits, biochemical indices and monoamine transporters expression against subacute 1-methyl-4-phenyl-1,2,3,6-tetrahydropyridine (MPTP)-induced mouse model of Parkinson's disease. *Neuroscience* 218, 257–267. doi: 10.1016/j.neuroscience.2012.05.039

Ayton, S., George, J. L., Adlard, P. A., Bush, A. I., Cherny, R. A., and Finkelstein, D. I. (2013). The effect of dopamine on MPTP-induced rotarod disability. *Neurosci. Lett.* 543, 105–109. doi: 10.1016/j.neulet.2013.02.066

Biju, K., Zhou, Q., Li, G., Imam, S. Z., Roberts, J. L., Morgan, W. W., et al. (2010). Macrophage-mediated GDNF delivery protects against dopaminergic neurodegeneration: a therapeutic strategy for Parkinson's disease. *Mol. Ther.* 18, 1536–1544. doi: 10.1038/mt.2010.107

Cass, W. A., Peters, L. E., Harned, M. E., and Seroogy, K. B. (2006). Protection by GDNF and other trophic factors against the dopamine-depleting effects of neurotoxic doses of methamphetamine. *Ann. N Y Acad. Sci.* 1074, 272–281. doi: 10.1196/annals.1369.024

Cen, X. B., Nitta, A., Ohya, S., Zhao, Y. L., Ozawa, N., Mouri, A., et al. (2006). An analog of a dipeptide-like structure of FK506 increases glial cell line-derived neurotrophic factor expression through cAMP response element-binding protein activated by heat shock protein 90/Akt signaling pathway. *J. Neurosci.* 26, 3335–3344. doi: 10.1523/JNEUROSCI.5010-05.2006

Fan, C. H., Ting, C. Y., Lin, C. Y., Chan, H. L., Chang, Y. C., Chen, Y. Y., et al. (2016). Noninvasive, targeted, and non-viral ultrasound-mediated GDNF-plasmid delivery for treatment of Parkinson's disease. *Sci. Rep.* 6:19579. doi: 10.1038/srep19579

Gill, S. S., Patel, N. K., Hotton, G. R., O'Sullivan, K., McCarter, R., Bunnage, M., et al. (2003). Direct brain infusion of glial cell line-derived neurotrophic factor in Parkinson disease. *Nat. Med.* 9, 589–595. doi: 10.1038/nm850

Hong, J., Sha, S., Zhou, L., Wang, C., Yin, J., and Chen, L. (2015). Sigma-1 receptor deficiency reduces MPTP-induced parkinsonism and death of dopaminergic neurons. *Cell Death Dis.* 6:e1832. doi: 10.1038/cddis.2015.194

Ibáñez, C. F., and Andressoo, J. O. (2017). Biology of GDNF and its receptors—relevance for disorders of the central nervous system. *Neurobiol. Dis.* 97, 80–89. doi: 10.1016/j.nbd.2016.01.021

Kramer, E. R., and Liss, B. (2015). GDNF-Ret signaling in midbrain dopaminergic neurons and its implication for Parkinson disease. *FEBS Lett.* 589, 3760–3772. doi: 10.1016/j.febslet.2015.11.006

Lang, A. E., Gill, S., Patel, N. K., Lozano, A., Nutt, J. G., Penn, R., et al. (2006). Randomized controlled trial of intraputamenal glial cell line-derived neurotrophic factor infusion in Parkinson disease. *Ann. Neurol.* 59, 459–466. doi: 10.1002/ana.20737

Li, J., Xia, Z., Sun, X., Zhang, R., Huang, G., Hickling, R., et al. (2013). Reversal of dopamine neurons and locomotor ability degeneration in aged rats with smilagenin. *Neuroscience* 245, 90–98. doi: 10.1016/j.neuroscience.2013.04.028

Liang, Y. Q., and Tang, X. C. (2006). Comparative studies of huperzine A, donepezil, and rivastigmine on brain acetylcholine, dopamine, norepinephrine and 5-hydroxytryptamine levels in freely-moving rats. *Acta Pharmacol. Sin.* 27, 1127–1136. doi: 10.1111/j.1745-7254.2006.00411.x

Love, S., Plaha, P., Patel, N. K., Hotton, G. R., Brooks, D. J., and Gill, S. S. (2005). Glial cell line-derived neurotrophic factor induces neuronal sprouting in human brain. *Nat. Med.* 11, 703–704. doi: 10.1038/nm0705-703

Lu, B., Nagappan, G. H., Guan, X. M., Nathan, P. J., and Wren, P. (2013). BDNF-based synaptic repair as a disease-modifying strategy for neurodegenerative diseases. *Nat. Rev. Neurosci.* 14, 401–416. doi: 10.1038/nrn3505

Miville-Godbout, E., Bourque, M., Morissette, M., Al-Sweidi, S., Smith, T., Mochizuki, A., et al. (2016). Plasmalogen augmentation reverses striatal dopamine loss in MPTP mice. *PLoS One* 11:e0151020. doi: 10.1371/journal.pone.0151020

Morissette, M., Goulet, M., Calon, F., Falardeau, P., Blanchet, P. J., Bedard, P. J., et al. (1996). Changes of D1 and D2 dopamine receptor mRNA in the brains of monkeys lesioned with 1-methyl-4-phenyl-1,2,3,6-tetrahydropyridine: correction with chronic administration of L-3,4-dihydroxyphenylalanine. *Mol. Pharmacol.* 50, 1073–1079.

Naskar, A., Prabhakar, V., Singh, R., Dutta, D., and Mohanakumar, K. P. (2015). Melatonin enhances L-DOPA therapeutic effects, helps to reduce its dose, and protects dopaminergic neurons in 1-methyl-4-phenyl-1,2,3,6-tetrahydropyridine-induced Parkinsonism in mice. *J. Pineal Res.* 58, 262–274. doi: 10.1111/jpi.12212

Nonnekes, J., Post, B., Tetrud, J. W., Langston, J. W., and Bloem, B. R. (2018). MPTP-induced parkinsonism: an historical case series. *Lancet Neurol.* 17, 300–301. doi: 10.1016/s1474-4422(18)30072-3

Peng, S., Wang, C. P., Ma, J. Y., Jiang, K. T., Jiang, Y. H., Gu, X. S., et al. (2018). Achyranthes bidentata polypeptide protects dopaminergic neurons from apoptosis in Parkinson's disease models both *in vitro* and *in vivo*. *Br. J. Pharmacol.* 175, 631–643. doi: 10.1111/bph.14110

Peoples, C., Shaw, V. E., Stone, J., Jeffery, G., Baker, G. E., and Mitrofanis, J. (2012). Survival of dopaminergic amacrine cells after near-infrared light treatment in MPTP-treated mice. *ISRN Neurol.* 2012:850150. doi: 10.5402/2012/850150

Petroske, E., Meredith, G. E., Callen, S., Totterdell, S., and Lau, Y. S. (2001). Mouse model of Parkinsonism: a comparison between subacute MPTP and chronic MPTP/probenecid treatment. *Neuroscience* 106, 589–601. doi: 10.1016/s0306-4522(01)00295-0

Pires, A. O., Teixeira, F. G., Mendes-Pinheiro, B., Serra, S. C., Sousa, N., and Salgado, A. J. (2017). Old and new challenges in Parkinson's disease therapeutics. *Prog. Neurobiol.* 156, 69–89. doi: 10.1016/j.pneurobio.2017.04.006

Popoli, P., Betto, P., Rimondini, R., Reggio, R., Pézzola, A., Ricciarello, G., et al. (1998). Age-related alteration of the adenosine/dopamine balance in the rat striatum. *Brain Res.* 795, 297–300. doi: 10.1016/s0006-8993(98)00356-4

Przedborski, S. (2017). The two-century journey of Parkinson disease research. *Nat. Rev. Neurosci.* 18, 251–259. doi: 10.1038/nrn.2017.25

Ren, Z., Wang, J., Wang, S., Zou, C., Li, X., Guan, Y., et al. (2013). Autologous transplantation of GDNF-expressing mesenchymal stem cells protects against MPTP-induced damage in cynomolgus monkeys. *Sci. Rep.* 3:2786. doi: 10.1038/srep02786

Rozas, G., López-Martín, E., Guerra, M. J., and Labandeira-García, J. L. (1998). The overall rod performance test in the MPTP-treated-mouse model of Parkinsonism. *J. Neurosci. Methods* 83, 165–175. doi: 10.1016/s0165-0270(98)00078-8

Schapira, A. H. V., Chaudhuri, K. R., and Jenner, P. (2017). Non-motor features of Parkinson disease. *Nat. Rev. Neurosci.* 18:509. doi: 10.1038/nrn.2017.91

Schildknecht, S., Di Monte, D. A., Pape, R., Tieu, K., and Leist, M. (2017). Tipping points and endogenous determinants of nigrostriatal degeneration by MPTP. *Trends Pharmacol. Sci.* 38, 541–555. doi: 10.1016/j.tips.2017.03.010

Sun, Z., Jia, J., Gong, X., Jia, Y., Deng, J., Wang, X., et al. (2012). Inhibition of glutamate and acetylcholine release in behavioral improvement induced by electroacupuncture in parkinsonian rats. *Neurosci. Lett.* 520, 32–37. doi: 10.1016/j.neulet.2012.05.021

Sun, M. K., Nelson, T. J., and Alkon, D. L. (2015). Towards universal therapeutics for memory disorders. *Trends Pharmacol. Sci.* 36, 384–394. doi: 10.1016/j.tips.2015.04.004

Sy, L. K., Lok, C. N., Wang, J. Y., Liu, Y., Cheng, L., Wan, P. K., et al. (2016). Identification of "sarsasapogenin-aglyconed" timosaponins as novel

Aβ-lowering modulators of amyloid precursor protein processing. *Chem. Sci.* 7, 3206–3214. doi: 10.1039/c5sc02377g

Tarazi, F. I., Sahli, Z. T., Wolny, M., and Mousa, S. A. (2014). Emerging therapies for Parkinson's disease: from bench to bedside. *Pharmacol. Ther.* 144, 123–133. doi: 10.1016/j.pharmthera.2014.05.010

Thoenen, H., and Sendtner, M. (2002). Neurotrophins: from enthusiastic expectations through sobering experiences to rational therapeutic approaches. *Nat. Neurosci.* 5, 1046–1050. doi: 10.1038/nn938

Visanji, N. P., Orsi, A., Johnston, T. H., Howson, P. A., Dixon, K., Callizot, N., et al. (2008). PYM50028, a novel, orally active, nonpeptide neurotrophic factor inducer, prevents and reverses neuronal damage induced by MPP^+ in mesencephalic neurons and by MPTP in a mouse model of Parkinson's disease. *FASEB J.* 22, 2488–2497. doi: 10.1096/fj.07-095398

Wang, L., Hu, X. H., Huang, Z. X., Nie, Q., Chen, Z. G., Xiang, J. W., et al. (2017). Regulation of CREB functions by phosphorylation and sumoylation in nervous and visual systems. *Curr. Mol. Med.* 16, 885–892. doi: 10.2174/1566524016666161223110106

Wong, Y. C., and Krainc, D. (2017). α-synuclein toxicity in neurodegeneration: mechanism and therapeutic strategies. *Nat. Med.* 23, 1–13. doi: 10.1038/nm.4269

Xu, G., Xiong, Z., Yong, Y., Wang, Z., Ke, Z., Xia, Z., et al. (2010). Catalpol attenuates MPTP induced neuronal degeneration of nigral-striatal dopaminergic pathway in mice through elevating glial cell derived neurotrophic factor in striatum. *Neuroscience* 167, 174–184. doi: 10.1016/j.neuroscience.2010.01.048

Zhang, Y., Xia, Z., Hu, Y., Orsi, A., and Rees, D. (2008). Role of glial cell derived neurotrophic factor in the protective effect of smilagenin on rat mesencephalic dopaminergic neurons damaged by MPP^+. *FEBS Lett.* 582, 956–960. doi: 10.1016/j.febslet.2008.02.039

Zhang, G. X., Xiong, N., Zhang, Z. T., Liu, L., Huang, J. S., Yang, J. L., et al. (2015). Effectiveness of traditional chinese medicine as an adjunct therapy for Parkinson's disease: a systematic review and meta-analysis. *PLoS One* 10:e0118498. doi: 10.1371/journal.pone.0118498

Zhang, N. S., Yan, F., Liang, X. L., Wu, M. X., Shen, Y. Y., Chen, M., et al. (2018). Localized delivery of curcumin into brain with polysorbate 80-modified cerasomes by ultrasound-targeted microbubble destruction for improved Parkinson's disease therapy. *Theranostics* 8, 2264–2277. doi: 10.7150/thno.23734

Conflict of Interest Statement: The authors declare that the research was conducted in the absence of any commercial or financial relationships that could be construed as a potential conflict of interest.

frontiers in Cellular Neuroscience

ORIGINAL RESEARCH
published: 12 February 2019
doi: 10.3389/fncel.2019.00006

Dose-Dependent Influences of Ethanol on Ischemic Stroke: Role of Inflammation

*Guodong Xu[1,2], Chun Li[1], Anne L. Parsiola[1], Jiyu Li[1], Kimberly D. McCarter[1], Runhua Shi[3], William G. Mayhan[4] and Hong Sun[1]**

[1]*Department of Cellular Biology & Anatomy, Louisiana State University Health Sciences Center-Shreveport, Shreveport, LA, United States,* [2]*Department of Neurology, Hebei General Hospital, Shijiazhuang, China,* [3]*Department of Medicine/Feist-Weiller Cancer Center, Louisiana State University Health Sciences Center-Shreveport, Shreveport, LA, United States,* [4]*Basic Biomedical Sciences, Sanford School of Medicine, The University of South Dakota, Vermillion, SD, United States*

Chronic ethanol consumption dose-dependently affects both incidence and prognosis of ischemic stroke. Our goal was to determine whether the influence of chronic ethanol consumption on ischemic stroke is related to an altered inflammatory profile in the brain. Male C57BL/6J mice were divided into six groups and gavage fed with 0.175, 0.35, 0.7, 1.4, 2.8 g/kg/day ethanol or volume-matched water once a day for 8 weeks. Adhesion molecules, microglial activation, neutrophil infiltration, pro- and anti-inflammatory cytokines/chemokines, blood-brain barrier (BBB) permeability, and matrix metallopeptidases (MMPs) in the cerebral cortex before and following a 90-min unilateral middle cerebral artery occlusion (MCAO)/24-h reperfusion were evaluated. Brain ischemia/reperfusion (I/R) injury was significantly reduced in 0.7 g/kg/day ethanol group (peak blood ethanol concentration: 9 mM) and worsened in 2.8 g/kg/day ethanol group (peak blood ethanol concentration: 37 mM). Baseline E-selectin was downregulated in all ethanol groups, whereas baseline intercellular adhesion molecule-1 (ICAM-1) was only downregulated in 0.35 and 0.7 g/kg/day ethanol groups. Interestingly, baseline vascular cell adhesion molecule-1 (VCAM-1) was upregulated in 0.35, 0.7, and 1.4 g/kg/day ethanol groups. Post-ischemic upregulation of ICAM-1 and E-selectin were suppressed in all ethanol groups. Post-ischemic neutrophil infiltration and microglial activation were significantly less in the low-moderate (0.175–1.4 g/kg/day) ethanol groups but greater in the 2.8 g/kg/day ethanol group compared to the vehicle group. At basal conditions, ethanol increased one pro- and two anti-inflammatory cytokines/chemokines at the 0.7 g/kg/day dose, and 13 pro- and eight anti-inflammatory cytokines/chemokines at the 2.8 g/kg/day dose. After ischemia, 0.7 g/kg/day ethanol suppressed post-ischemic pro-inflammatory cytokines/chemokines and enhanced post-ischemic anti-inflammatory cytokines/chemokines. Moreover, 0.7 g/kg/day ethanol significantly reduced baseline MMP-9 activity and alleviated post-ischemic BBB breakdown. On the other hand,

OPEN ACCESS

Edited by:
Sriharsha Kantamneni, University of Bradford, United Kingdom

Reviewed by:
Ertugrul Kilic, Istanbul Medipol University, Turkey
David F. Werner, Binghamton University, United States

***Correspondence:**
Hong Sun
hsun1@lsuhsc.edu

Received: *19 July 2018*
Accepted: *08 January 2019*
Published: *12 February 2019*

Citation:
Xu G, Li C, Parsiola AL, Li J, McCarter KD, Shi R, Mayhan WG and Sun H (2019) Dose-Dependent Influences of Ethanol on Ischemic Stroke: Role of Inflammation. Front. Cell. Neurosci. 13:6. doi: 10.3389/fncel.2019.00006

2.8 g/kg/day ethanol worsened post-ischemic BBB breakdown. Our findings suggest that low-moderate ethanol consumption may prevent ischemic stroke and reduce brain I/R injury by suppressing inflammation, whereas heavy alcohol consumption may induce ischemic stroke and worsen brain I/R injury by aggravating inflammation.

Keywords: ethanol, ischemic stroke, adhesion molecule, microglia, neutrophil infiltration, cytokine/chemokine, matrix metalloproteinase

INTRODUCTION

Ischemic stroke continues to be one of the leading causes of mortality and permanent disability worldwide (Favate and Younger, 2016; Benjamin et al., 2017). Intravenous recombinant tissue plasminogen activator (tPA) and endovascular therapy are currently used to treat acute ischemic stroke. Both treatments result in recanalization/reperfusion. Although recanalization/reperfusion is critical for restoring normal function, it paradoxically induces and worsens brain injury, called brain ischemia/reperfusion (I/R) injury (Jean et al., 1998). The mechanisms underlying brain I/R injury are complex and involve several interacting elements, including oxidative/nitrosative stress, activation of apoptotic and autophagic pathways, and increased inflammatory response (Jean et al., 1998; Kalogeris et al., 2012; Chen et al., 2014).

Post-ischemic inflammatory responses are characterized by the accumulation of inflammatory cells and mediators in the ischemic brain. The recruitment of leukocytes (including neutrophils) to the ischemic area appears to be a central feature after transient focal cerebral ischemia (Gronberg et al., 2013). When neutrophils are depleted from the circulation the infarct volume is reduced and cerebral blood flow (CBF) is improved during the reperfusion period (Jean et al., 1998; Herz et al., 2015). The recruitment of leukocytes into the ischemic area is facilitated by upregulation of adhesion molecules on endothelial cells prior to and during reperfusion (Supanc et al., 2011). In addition, the recruitment of leukocytes is associated with inflammatory activation of microglia and subsequent production of matrix metallopeptidases (MMPs), chemokines, and cytokines. Microglia are key modulators of the immune response in the brain. After ischemia, microglia rapidly proliferate, transform their morphology and migrate toward injured neurons (Weinstein et al., 2010). Activated microglia directly contribute to brain I/R injury by phagocytosis and producing inflammatory and cytotoxic mediators (Shukla et al., 2017). MMPs are responsible for remodeling extracellular matrix (Bonnans et al., 2014). In addition to microglia, neurons, astrocytes, and endothelial cells also express MMPs (Turner and Sharp, 2016). After transient focal cerebral ischemia, MMPs are upregulated and activated under the influence of inflammatory mediators (Ceulemans et al., 2010). Activated MMPs stimulate leukocyte adherence and transmigration and promote blood-brain barrier (BBB) breakdown and hemorrhagic transformation (Lakhan et al., 2009; Ceulemans et al., 2010). Cytokines are among the principal mediators of the inflammatory response and are involved in virtually every facet of stroke (Kim et al., 2014). Cytokines can be elaborated by leukocytes, macrophages, endothelial cells and resident cells within the brain (Kim et al., 2014). After transient focal cerebral ischemia, pro-inflammatory cytokines, such as interleukin-1 (IL-1), tumor necrosis factor-α (TNF-α), and IL-6, stimulate and aggravate the inflammatory response (Shukla et al., 2017).

Ethanol is one of the most commonly and regularly used chemical substances. Epidemiological studies suggest that low-moderate ethanol intake lowers the incidence of ischemic stroke and reduces mortality and infarct volume from ischemic stroke, whereas heavy ethanol consumption increases the incidence of ischemic stroke and worsens the prognosis of ischemic stroke (Hansagi et al., 1995; Ikehara et al., 2008; Patra et al., 2010; Ronksley et al., 2011; Ducroquet et al., 2013; Zhang et al., 2014). Ischemic stroke is most often caused by atherosclerosis, which has been well recognized as a chronic inflammatory process (Bruno et al., 2008). The relationship between regular ethanol intake and incidence of atherosclerosis appears to be U-shaped (Kiechl et al., 1998). Thus, our goal was to determine whether the influence of ethanol on ischemic stroke is related to an altered inflammatory profile in the brain.

MATERIALS AND METHODS

Animal Models of Ethanol Preconditioning

This study was carried out in accordance with the recommendations of the National Institutes of Health Guide for the Care and Use Laboratory Animals. The protocol was approved by the Institutional Animal Care and Use Committee at the Louisiana State University Health Science Center-Shreveport. One hundred twenty male C57BL/6J mice (20–25 g) were randomly divided into six groups: vehicle (n = 24), 0.175 g/kg/day ethanol (n = 16), 0.35 g/kg/day ethanol (n = 16), 0.7 g/kg/day ethanol (n = 24), 1.4 g/kg/day ethanol (n = 16), and 2.8 g/kg/day ethanol (n = 24). Ethanol groups were gavage fed with 10 ml/kg 1.75% (0.175 g/kg/day ethanol group), 3.5% (0.35 g/kg/day ethanol group), 7% (0.7 g/kg/day ethanol group), 14% (1.4 g/kg/day ethanol group) or 28% (2.8 g/kg/day ethanol group) ethanol once a day for 8 weeks. The vehicle group was gavage fed with 10 ml/kg water. Fasting blood glucose was measured by Bayer Breeze2 Blood Glucose Meter (Bayer HealthCare, Mishawaka, IN, USA). Prior to the measurement, mice were fasted for 12 h during the daytime. To determine whether 8-week feeding changes the peak concentration of blood ethanol, time courses of plasma ethanol concentration in the 0.7 and 2.8 g/kg/day groups were measured using an Ethanol Assay Kit (ab65343, Abcam) at the beginning and end of 8-week feeding period. The measurement

was performed according to the manufacturer's instructions. Same mice were used for same time point in each group. Blood pressure and heart rate were measured using a CODA mouse tail-cuff system (Kent Scientific, Torrington, CT, USA). Prior to the actual measurement, mice were trained for three consecutive days to acclimate to being restrained and to also having the tail cuff placed on them. At the end of 8 weeks of feeding, all mice were subjected to transient focal cerebral ischemia.

Transient Focal Cerebral Ischemia

To avoid a possible effect of acute ethanol, alcohol was not given on the day before the experiment. Transient focal cerebral ischemia was induced by unilateral middle cerebral artery occlusion (MCAO). Since disability-free outcome is better when reperfusion is established less than 90 min after the onset of ischemic stroke (Meretoja et al., 2014), 90-min was selected as the MCAO period. Prior to the procedure, mice were anesthetized with isoflurane (induction at 5% and maintenance at 1.5%) in a gas mixture containing 30% O_2/70% N_2 *via* a facemask. Body temperature was maintained with a temperature controlled heating pad (Harvard Apparatus, March, Germany). A laser-Doppler flow probe (PERIMED, PF 5010 LDPM Unit, Sweden) was attached to the right side of the dorsal surface of the skull to monitor regional CBF (rCBF). The right common and external carotid arteries were exposed and ligated. The MCA was occluded by inserting a silicon rubber-coated monofilament (Doccol Corporation, Sharon, MA, USA) from the basal part of the external carotid artery and advanced cranially into the internal carotid artery to the point where the MCA branched off from the internal artery. The onset of the MCAO was indicated by an immediate drop in rCBF. After the occlusion of the right MCA for 90 min, reperfusion was achieved by withdrawing the suture and reopening the common carotid artery. Animals were allowed to recover for 24 h.

Assessment of Neurological Deficits, Infarct Volume and Edema

A 24-point scoring system was used to evaluate sensorimotor deficits at 24 h of reperfusion (Sun et al., 2008). Sensorimotor testing was graded on a scale of 0–3 each on spontaneous activity, symmetry of movement, response to vibrissae touch, floor walking, beam walking, symmetry of forelimbs, climbing wall of wire cage, reaction to touch on either side of trunk. Neurological scores were assigned as follows: 0, complete deficit; 1, definite deficit with some function; 2, decreased response or mild deficit; 3, no evidence of deficit/symmetrical responses. After neurological evaluation, 30 mice (n = 5 for each group) were euthanized and exsanguinated. The brains were quickly removed and placed in ice-cold saline for 5 min, and cut into six 1.75 mm-thick coronal sections. Sections were stained with 2% 2,3,5-triphenyltetrazolium chloride (TTC; Sigma) for 15 min at 37°C. Sliced images were digitalized, the volumes of infarct lesion, ipsilateral hemisphere and contralateral hemisphere were measured using ImageJ. Total infarct volume was expressed as a percentage of the contralateral hemisphere. Edema was determined by the volume ratio of the ipsilateral hemisphere to the contralateral hemisphere and expressed as a percentage increase of the contralateral hemisphere. All researchers involved in assessing brain injury were blinded to the experimental groups.

Western Blot Analysis

Thirty mice (n = 5 for each group) were euthanized and exsanguinated. Cortical tissues were isolated from the peri-infarct area and contralateral corresponding area to measure protein expression of intercellular adhesion molecule-1 (ICAM-1), vascular cell adhesion molecule-1 (VCAM-1), E-selectin and P-selectin. The brains were cut into six 1.75 mm-thick coronal sections. Under the microscope, the infarct core was identified as an opaque area, and the area bordering 2 mm the infarct core was considered as the peri-infarct area (Choi et al., 2015; McCarter et al., 2017). A researcher who was blinded to the experimental groups collected cortical tissues from the peri-infarct area. The samples were homogenized in ice-cold lysis buffer (150 mmol/l NaCl, 50 mmol/l Tris-HCl, 10 mmol/l EDTA, 0.1% Tween-20, 1% Triton, 0.1% mercaptoethanol, 0.1 mmol/l phenylmethyl sulfonyl fluorides, 5 μg/ml leupeptin, and 5 μg/ml aprotinin, pH 7.4). Lysates were then centrifuged at 12,000× g for 20 min at 4°C, and the supernatants were collected. Protein concentration of the supernatants was determined by the Bradford protein assay (Bio-Rad). SDS-PAGE was performed on a 10% gel on which 20 μg of total protein per well was loaded. After SDS-PAGE, the proteins were transferred to a polyvinylidene difluoride membrane. Immunoblotting was performed using mouse anti-ICAM-1 (sc-8439, Santa Cruz Biotechnology), rabbit anti-VCAM-1 (ab134047, Abcam), rabbit anti-E-selectin (ab18981, Abcam) and goat anti-P-selectin (AF737, R&D systems) as primary antibodies and peroxidase conjugated goat anti-mouse, mouse anti-rabbit, and mouse anti-goat IgG as the secondary antibody. The bound antibody was detected using enhanced chemiluminescence (ECL) detection (Genesee Scientific for ICAM-1, VCAM-1; Thermo Scientific for E-selectin, P-selectin), and the bands were analyzed using ChemiDoc^{TM} MP Imaging System (Bio-Rad). To quantify, protein expression of ICAM-1, VCAM-1, E-selectin and P-selectin was normalized to GAPDH and expressed as percentage changes to the vehicle without I/R.

Immunohistochemistry Staining

Thirty mice (n = 5 for each group) were anesthetized and perfused transcardially with 1× phosphate-buffered saline (PBS), followed by 4% paraformaldehyde in 0.1 mmol/L PBS. The brains were removed, fixed overnight in 4% paraformaldehyde in 0.1 M PBS, dehydrated in a graded series of sugar solutions over the course of 72 h, then embedded in O.C.T. compound (Fisher Scientific) and quick frozen for 5 min in liquid nitrogen. The frozen brains were then cut into 14 μm sections and placed on frost-free slides. The sections were washed with 1× PBS, blocked with 10% bovine serum albumin (BSA) for at least 1 h, and then incubated overnight at 4°C with 1:100 rabbit anti-myeloperoxidase (anti-MPO; Abcam) for visualization of neutrophils or 1:100 rabbit anti-ionized calcium binding adaptor

molecule 1 (anti-Iba1; Wako Chemicals Inc., Richmond, VA, USA) for visualization of microglia as primary antibodies. The sections were then incubated with 1:200 AlexaFluor 555 donkey anti-rabbit (Santa Cruz Technology) for 1 h at room temperature. Sections were mounted with DAPI mounting medium with Vector shield and visualized using a fluorescence microscope. Cells positive for MPO represented infiltrating neutrophils. For quantitative analysis, positive cells were counted in three separate areas per section surrounding the infarct area in at least three slides per mouse in each group. To quantify microglia, cells positive for Iba1 were observed and counted. Resting microglia present with long processes extending from their cell body. Resting microglia present with long processes extending from their cell body. Upon activation, microglia change form from highly ramified to completely lacking processes. In addition, activated microglia show increased Iba1 expression (Taylor and Sansing, 2013; Yang et al., 2015). Thus, microglia with increased Iba1 expression and three processes or less were deemed to be activated (Ahmad et al., 2014; Yang et al., 2015).

Cytokine Array

Expression of cytokines in the right cerebral hemisphere was measured using the Proteome Profiler Mouse Cytokine Array Kit, Panel A (ARY006, R&D Systems) in 24 mice (n = 4 for vehicle, vehicle + I/R, 0.7 g/kg/day ethanol, 0.7 g/kg/day ethanol + I/R, 2.8 g/kg/day ethanol, and 2.8 g/kg/day ethanol + I/R). The array was performed according to the manufacturer's instructions. Results were analyzed using ImageJ software and expressed as percentage change relative to vehicle without I/R.

IgG Staining

Three sections (Bregma 1.21 mm, −0.23 mm and −1.31 mm) per mouse (n = 5 for each group) were blocked with 10% BSA for 1 h. Subsequently, the sections were incubated overnight at 4°C with 1:200 goat anti-mouse IgG (BA-9200, Vector), followed by incubating with 1:200 AlexaFluor 555 (Invitrogen) for 1 h at room temperature. Staining was analyzed with a fluorescence microscope and an image analysis system (NIS-Elements, Nikon). The mean fluorescence intensity of equal size around the infarct core and contralateral corresponding area was measured. IgG staining was normalized to contralateral corresponding area and expressed as percentage changes to the vehicle group.

Gelatin Zymography

MMP activity in the cortical tissues prepared for Western Blot analysis was measured using gelatin zymography. Gelatin zymography was carried out using SDS-polyacrylamide gels containing 0.8% gelatin (Sigma, St. Louis, MO, USA). After electrophoresis, the gels were washed with a buffer (pH 7.5) containing 50 mM Tris-HCl, 5 mM $CaCl_2$, 1 μM $ZnCl_2$, 0.02% NaN_3, and 2.5% Triton X-100 to remove the SDS and renature the gelatinases. Gels were then developed in a buffer (pH 7.5) containing 50 mM Tris-HCl, 5 mM $CaCl_2$, 1 μM $ZnCl_2$, 0.02% NaN_3 for 7 days at 37°C. Enzymatic activity was visualized as negative staining with 0.25% Coomassie Brilliant Blue R-250 (Sigma, St. Louis, MO, USA). The molecular sizes of gelatinolytic activity were determined by comparison to Molecular Weight Markers (Bio-Rad, Hercules, CA, USA). The gel was photographed and analyzed using ChemiDoc™ MP Imaging System (Bio-Rad).

Statistical Analysis

Data are presented as means ± SE. Differences in physiological parameters, cerebral I/R injury, microglia activation, neutrophil infiltration, brain edema, and IgG staining between groups were evaluated by one-way analysis of variance (ANOVA) followed by Dunnett's test for multiple comparisons to the control group. Differences in protein expression of adhesion molecules, cytokines and chemokines, and MMP activity between groups were evaluated by two-way ANOVA followed by Bonferroni's test for multiple within and between group comparisons. All analyses were done using statistical analysis software SAS9.4 for windows (SAS Institute, Cary, NC, USA). $P \leq 0.05$ was considered as statistical significant.

RESULTS

Physiological Parameters

After 8-weeks of gavage feeding there was no significant difference in body weight among six groups (**Table 1**). Since cerebral I/R injury was significantly altered in the 0.7 g/kg/day and 2.8 g/kg/day ethanol groups, mean arterial blood pressure (MABP), heart rate, and fasting blood glucose were measured in the vehicle, 0.7 g/kg/day, and 2.8 g/kg/day ethanol groups. There was no significant difference in MABP, heart rate, or fasting blood glucose among three groups (**Table 1**).

Cerebral I/R Injury

Ethanol altered the total infarct volume at 24 h of reperfusion as indicated by a significant main effect of gavage feeding ($F_{(5,27)}$ = 8.9; p = 0.000043, n = 6). *Post hoc* analysis revealed that 0.7 g/kg/day ethanol reduced infarct volume compared to vehicle (p = 0.010214; **Figures 1A,B**). On the other hand, 2.8 g/kg/day ethanol increased infarct volume

TABLE 1 | Effect of ethanol consumption on body weight, blood pressure, heart rate and fasting blood glucose.

	Vehicle	0.175 g/kg/day	0.35 g/kg/day	0.7 g/kg/day	1.4 g/kg/day	2.8 g/kg/day
Body weight (g)	29.4 ± 0.4	28.6 ± 0.6	27.7 ± 0.6	29.1 ± 0.3	27.9 ± 0.5	28.7 ± 0.5
MABP (mmHg)	81.0 ± 3.8	ND	ND	82.3 ± 2.8	ND	90.6 ± 4.5
Heart rate (bpm)	637 ± 40	ND	ND	564 ± 57	ND	644 ± 17
Fasting blood glucose (mg/dl)	139 ± 8	ND	ND	118 ± 12	ND	156 ± 10

Values are means ± SE for five rats in each group. ND stands for Not Determined.

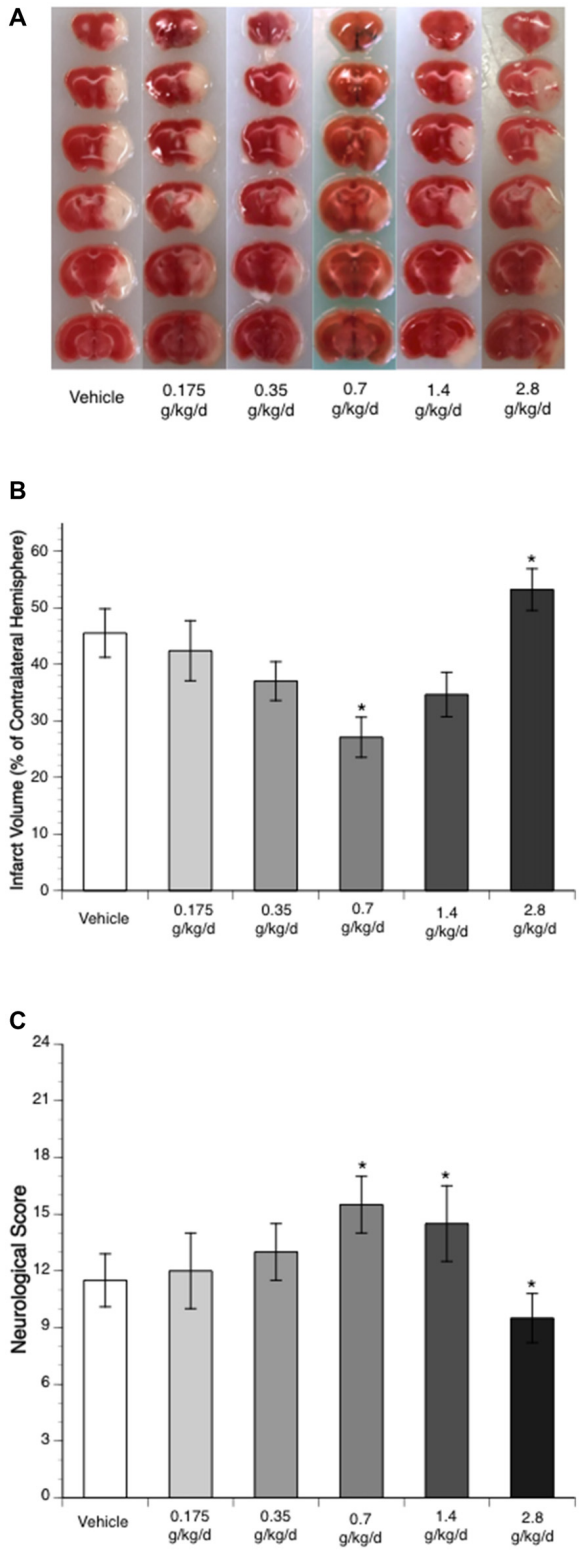

FIGURE 1 | Influence of ethanol on brain injury following a 90-min middle cerebral artery occlusion (MCAO)/24-h reperfusion. **(A)** Representative brain sections stained with 2,3,5-triphenyltetrazolium chloride (TTC). **(B)** Total infarct volume (n = 6). **(C)** Neurological score (n = 15). Values are means ± SE. *P < 0.05 vs. Vehicle.

compared to vehicle (p = 0.036302; **Figure 1B**). Consistently, ethanol altered the neurological deficits at 24 h of reperfusion as indicated by a significant main effect of gavage feeding ($F_{(5,84)}$ = 10.92; p < 0.000001, n = 15). *Post hoc* analysis showed that 0.7 g/kg/day ethanol significantly improved neurological deficits (p = 0.001570), whereas 2.8 g/kg/day ethanol significantly worsened neurological deficits compared to vehicle (p = 0.041920; **Figure 1C**). Interestingly, although the total infarct volume was not significantly reduced (p = 0.193254), neurological deficits significantly improved in the 1.4 g/kg/day ethanol group (p = 0.006; **Figure 1C**). Since both infarct volume and neurological deficits were significantly altered in the 0.7 g/kg/day and 2.8 g/kg/day ethanol groups, plasma ethanol concentration was measured at 15 min, 30 min, 1 h and 2 h after gavage feeding in these two groups. At the beginning of an 8-week feeding period, the peak concentrations (0.7 g/kg/day ethanol group: 9.0 ± 0.4 mM; 2.8 g/kg/day ethanol group: 37.0 ± 1.5 mM) appeared at 15 min in the 0.7 g/kg/day ethanol group and 30 min in the 2.8 g/kg/day ethanol group (**Figure 2**). The ethanol concentration reduced rapidly and approached to zero at 2 h in the 0.7 g/kg/day ethanol group. In contrast, plasma ethanol concentration declined slowly in the 2.8 g/kg/day ethanol group. Eight-week feeding produced a significant decrease and a significant increase in plasma ethanol concentration at 15 min (p = 0.013) and 1 h (p = 0.049), respectively, in the 2.8 g/kg/day ethanol group. However, 8-week feeding did not affect the peak concentration and its time point in both the 0.7 g/kg/day and 2.8 g/kg/day ethanol groups (**Figure 2**).

Protein Expression of Adhesion Molecules

Ethanol altered baseline expression of ICAM-1 as indicated by a significant main effect of gavage feeding ($F_{(5,24)}$ = 4.48; p = 0.005020, n = 5). *Post hoc* analysis showed that 0.35 and 0.7 g/kg/day ethanol significantly downregulated baseline ICAM-1 (p = 0.031723 and p = 0.020119, respectively; **Figure 3A**). A 90-min MCAO significantly upregulated ICAM-1 at 24 h of reperfusion in all groups (Vehicle group: $F_{(1,8)}$ = 81.90; p = 0.000018, n = 5; 0.175 g/kg/day group: $F_{(1,8)}$ = 12.23; p = 0.008117, n = 5; 0.35 g/kg/day group: $F_{(1,8)}$ = 14.85; p = 0.004856, n = 5; 0.7 g/kg/day group: $F_{(1,8)}$ = 15.75; p = 0.004127, n = 5; 1.4 g/kg/day group: $F_{(1,8)}$ = 6.77; p = 0.031492, n = 5; 2.8 g/kg/day group: $F_{(1,8)}$ = 31.23; p = 0.000517, n = 5; **Figure 3A**). There was a significant interaction of ethanol and ischemic stroke on ICAM-1 expression at 24 h of reperfusion ($F_{(11,48)}$ = 15.53; p < 0.000001, n = 5). Mice fed with ethanol had significantly less upregulation in ICAM-1 at 24 h of reperfusion ($F_{(5,24)}$ = 31.54; p < 0.000001, n = 5). *Post hoc* analysis showed that 0.175, 0.35, 0.7, 1.4, and 2.8 g/kg/day ethanol significantly reduced post-ischemic ICAM-1 (p = 0.000223, p < 0.000001, p < 0.000001, p < 0.000001, and p < 0.000001, respectively; **Figure 3A**). In addition to ICAM-1, ethanol also reduced baseline expression of E-selectin as indicated by a significant main effect of gavage feeding ($F_{(5,24)}$ = 32.53; p < 0.000001, n = 5). *Post hoc* analysis showed that 0.175, 0.35, 0.7, 1.4, and

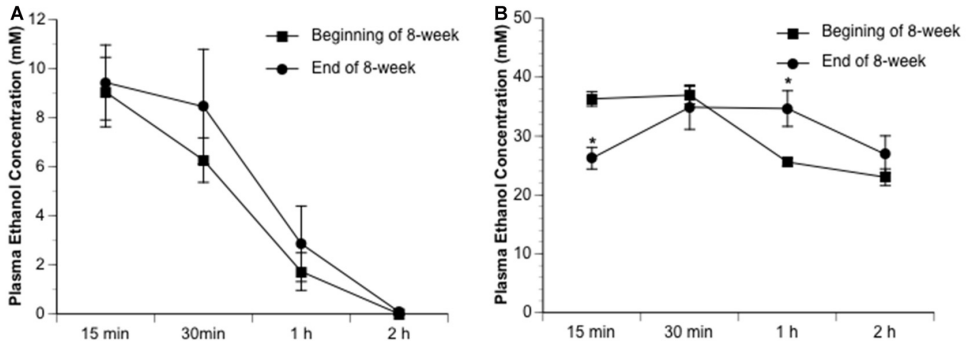

FIGURE 2 | Dynamic change of plasma ethanol concentration in the 0.7 g/kg/day **(A)** and 2.8 g/kg/day **(B)** ethanol groups at the beginning and end of an 8-week feeding period. Values are means ± SE for four mice in each group. $^{*}P < 0.05$ vs. Beginning of 8-week.

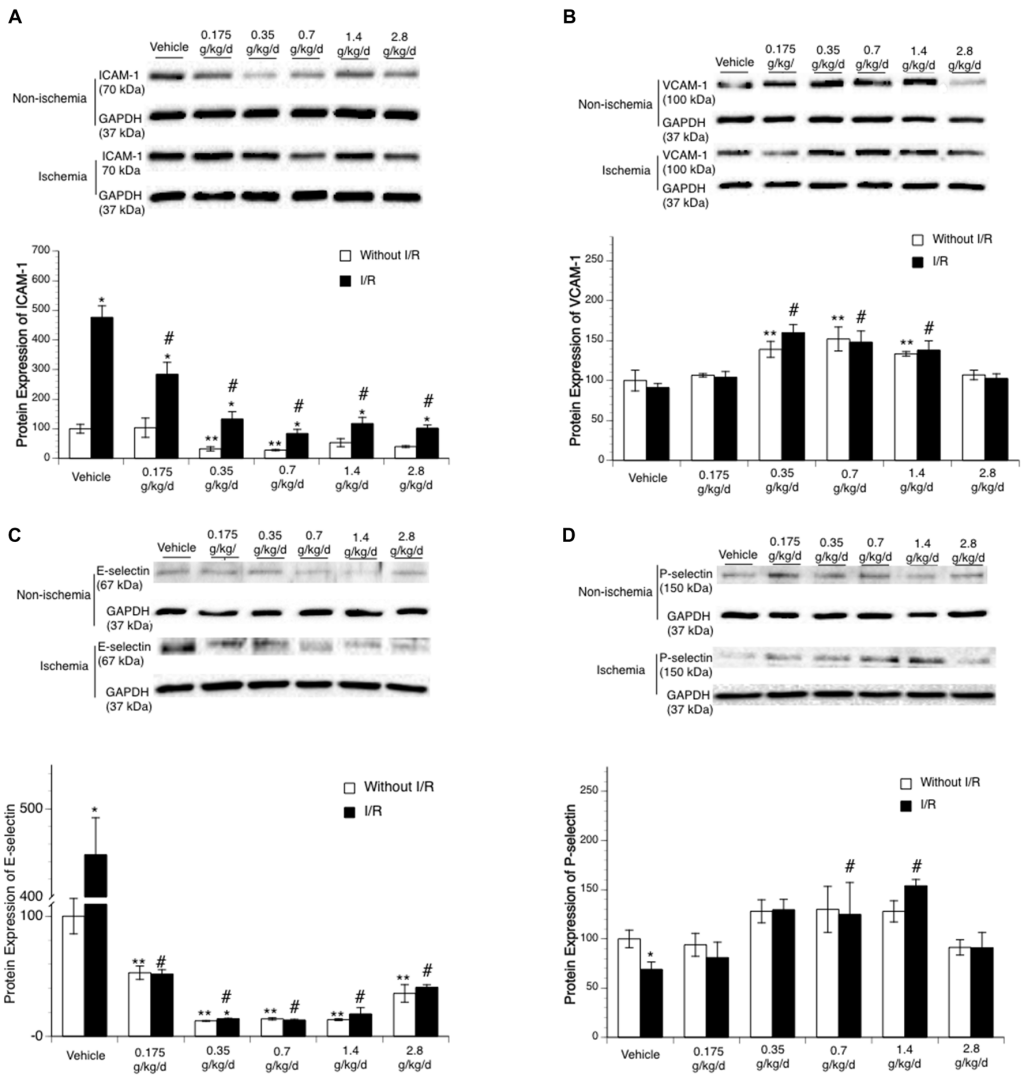

FIGURE 3 | Influence of ethanol on expression of intercellular adhesion molecule-1 (ICAM-1; **A**), vascular cell adhesion molecule-1 (VCAM-1; **B**), E-selectin **(C)** and P-selectin **(D)** following a 90-min MCAO/24-h reperfusion. Values are means ± SE for five mice in each group. Data shown are representative blots for each group. Ischemic side and contralateral side were run on separate gels with two samples from the vehicle group as internal control. $^{**}P < 0.05$ vs. Vehicle without ischemia/reperfusion (I/R). $^{*}P < 0.05$ vs. Without I/R. $^{\#}P < 0.05$ vs. Vehicle with I/R.

2.8 g/kg/day ethanol significantly downregulated baseline E-selectin ($p < 0.00001$, $p < 0.000001$, $p = 0.000163$, $p < 0.000001$, and $p < 0.000001$, respectively; **Figure 3C**). A 90-min MCAO significantly upregulated E-selectin at 24 h of reperfusion in the vehicle group ($F_{(1,8)} = 65.21$; $p = 0.000041$, $n = 5$). There was a significant interaction of ethanol and ischemic stroke on E-selectin expression ($F_{(11,48)} = 62.58$; $p < 0.000001$, $n = 5$). Mice fed with ethanol had significantly less upregulation in E-selectin at 24 h of reperfusion ($F_{(5,24)} = 100.17$; $p < 0.000001$, $n = 5$). *Post hoc* analysis revealed that only 0.35 g/kg/day ethanol significantly upregulated E-selectin at 24 h of reperfusion ($F_{(1,8)} = 10.10$; $p = 0.013023$, $n = 5$; **Figure 3C**). In contrast to ICAM-1 and E-selectin, ethanol upregulated baseline expression of VCAM-1 ($F_{(5,24)} = 23.20$; $p < 0.000001$, $n = 5$). *Post hoc* analysis showed that 0.35, 0.7, and 1.4 g/kg/day ethanol significantly upregulated baseline VCAM-1 ($p = 0.000045$, $p < 0.000001$, and $p = 0.005964$, respectively; **Figure 3B**). Ethanol did not significantly alter baseline expression of P-selectin (**Figure 3D**). In addition, 90-min MCAO did not significantly upregulate either VCAM-1 or P-selectin at 24 h of reperfusion in any group. Interestingly, P-selectin was slightly but significantly downregulated at 24 h of reperfusion in the vehicle group ($F_{(1,8)} = 6.46$; $p = 0.034622$, $n = 5$; **Figure 3D**). Ethanol altered post-ischemic VCAM-1 ($F_{(5,24)} = 11.84$; $p = 0.000008$, $n = 5$) and P-selectin ($F_{(5,24)} = 5.16$; $p = 0.002354$, $n = 5$). *Post hoc* analysis revealed that 0.35, 0.7, and 1.4 g/kg/day ethanol significantly increased post-ischemic VCAM-1 ($p = 0.000171$, $p = 0.000028$, and $p = 0.010020$, respectively; **Figure 3B**). *Post hoc* analysis also revealed that 0.35 and 0.7 g/kg/day ethanol significantly increased post-ischemic P-selectin ($p = 0.001953$ and $p = 0.022819$, respectively; **Figure 3D**). However, there was no significant interaction of ethanol and ischemic stroke on either VCAM-1 ($F_{(11,48)} = 0.40$; $p = 0.846695$, $n = 5$) or P-selectin ($F_{(11,48)} = 0.89$; $p = 0.495995$, $n = 5$).

Microglial Activation

To assess microglial activation, immunofluorescence staining with Iba1 was analyzed. No activated microglia were detected at 24 h of reperfusion in the contralateral hemisphere of ischemic brain. Ethanol altered post-ischemic microglial activation at 24 h of reperfusion in the ipsilateral hemisphere of the ischemic brain as indicated by a significant main effect of gavage feeding ($F_{(5,56)} = 52.23$; $p < 0.000001$, $n = 5$). *Post hoc* analysis showed that 0.175, 0.35, 0.7, and 1.4 g/kg/day ethanol significantly inhibited post-ischemic microglial activation ($p = 0.00004$, $p < 0.000001$, $p < 0.000001$ and $p = 0.000001$, respectively; **Figures 4A,B**). In contrast, 2.8 g/kg/day ethanol significantly promoted post-ischemic microglial activation compared to vehicle ($p = 0.000613$; **Figures 4A,B**).

Neutrophil Infiltration

Immunofluorescence staining with MPO was counted to examine neutrophil infiltration. No neutrophil infiltration was detected at 24 h of reperfusion in the contralateral hemisphere. Ethanol altered post-ischemic neutrophil infiltration at 24 h of reperfusion in the ipsilateral hemisphere of the ischemic brain as indicated by a significant main effect of gavage feeding ($F_{(5,52)} = 53.92$; $p < 0.000001$, $n = 5$). *Post hoc* analysis revealed that 0.175, 0.35, 0.7, and 1.4 g/kg/day ethanol significantly attenuated post-ischemic neutrophil infiltration ($p = 0.022635$, $p = 0.000818$, $p = 0.000002$ and $p = 0.001079$, respectively; **Figures 5A,B**). On the other hand, 2.8 g/kg/day ethanol significantly exacerbated post-ischemic neutrophil infiltration compared to vehicle ($p < 0.000001$; **Figures 5A,B**).

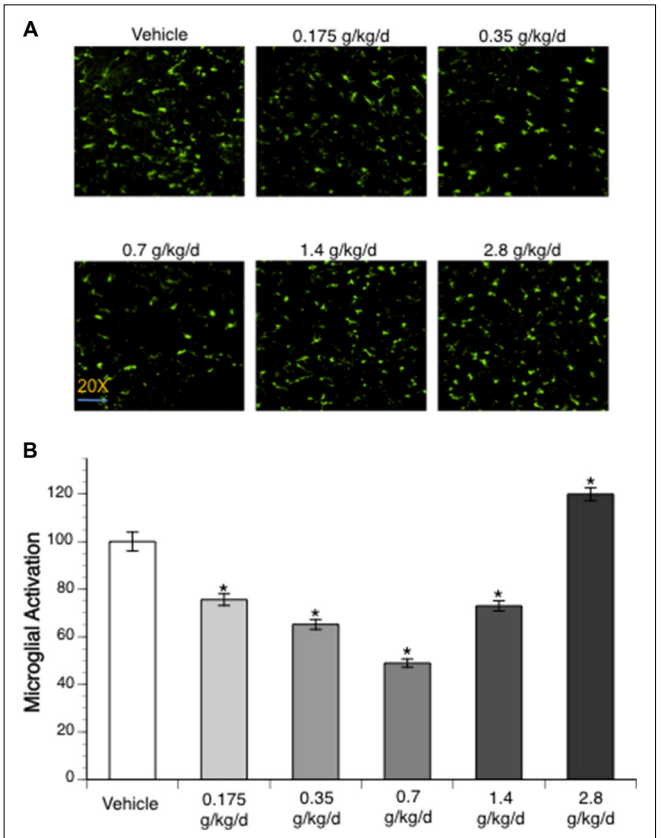

FIGURE 4 | Influence of ethanol on microglial activation following a 90-min MCAO/24-h reperfusion. **(A)** Representative Iba1 staining. **(B)** Values are mean ± SE for five mice in each group. $^*P < 0.05$ vs. Vehicle.

Cytokines and Chemokines

Since cerebral I/R injury was significantly altered in the 0.7 g/kg/day and 2.8 g/kg/day ethanol groups, cytokines and chemokines were only measured in the vehicle, 0.7 g/kg/day, and 2.8 g/kg/day ethanol groups. Thirty-three cytokines/chemokines were detected using the cytokine array (**Figure 6** and **Table 2**). Ethanol altered 13 baseline pro-inflammatory cytokines/chemokines (IL-1β, IL-3, IL-7, IL-17, IL-23, sICAM, TREM-1, CCL3, CCL12, CXCL2, CXCL9, CXCL10, CXCL11) as indicated by significant main effects of gavage feeding (IL-1β: $F_{(2,9)} = 99.16$; $p < 0.000001$, $n = 4$; IL-3: $F_{(2,9)} = 194.83$; $p < 0.000001$, $n = 4$; IL-7: $F_{(2,9)} = 31.09$; $p = 0.000091$, $n = 4$; IL-17: $F_{(2,9)} = 8.77$; $p = 0.007697$, $n = 4$; IL-23: $F_{(2,9)} = 4.15$; $p = 0.052952$, $n = 4$; sICAM: $F_{(2,9)} = 4.19$; $p = 0.051810$, $n = 4$; TREM-1: $F_{(2,9)} = 4.91$; $p = 0.036217$, $n = 4$; CCL3: $F_{(2,9)} = 20.07$;

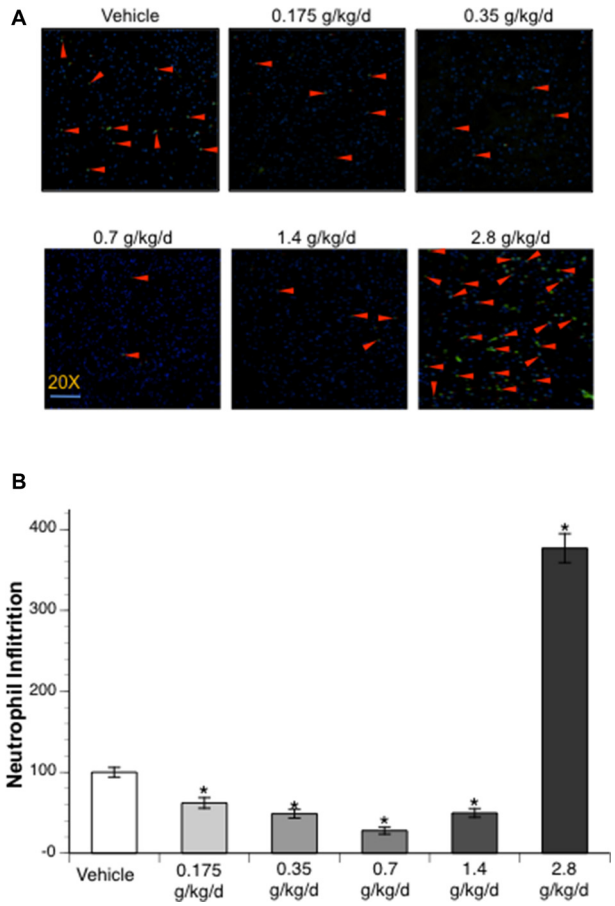

FIGURE 5 | Influence of ethanol on neutrophil infiltration following a 90-min MCAO/24-h reperfusion. **(A)** Representative MPO staining. **(B)** Values are mean ± SE for five mice in each group. *$P < 0.05$ vs. Vehicle.

p = 0.000481, n = 4; CCL12: $F_{(2,9)}$ = 15.38; p = 0.001249, n = 4; CXCL2: $F_{(2,9)}$ = 5.37; p = 0.029185, n = 4; CXCL9: $F_{(2,9)}$ = 13.43; p = 0.001988, n = 4; CXCL10: $F_{(2,9)}$ = 4.79; p = 0.038350, n = 4; CXCL11: $F_{(2,9)}$ = 6.41; p = 0.018620, n = 4). *Post hoc* analysis revealed that 0.7 g/kg/day ethanol only significantly increased baseline CCL12 (p = 0.006008; **Figure 6C**), whereas 2.8 g/kg/day ethanol significantly increased baseline IL-1β ($p < 0.000001$), IL-3 ($p < 0.000001$), IL-7 (p = 0.000116), IL-17 (p = 0.010393), IL-23 (p = 0.037578), sICAM (p = 0.036577), TREM-1 (p = 0.026932), CCL3 (p = 0.000472), CCL12 (p = 0.000965), CXCL2 (p = 0.024882), CXCL9 (p = 0.001251), CXCL10 (p = 0.038815), and CXCL11 (p = 0.013630) compare to vehicle (**Figure 6** and **Table 2**). On the other hand, ethanol altered all eight detected anti-inflammatory cytokines/chemokines (IL-1ra, IL-4, IL-13, IL-27, G-CSF, M-CSF, TIMP-1, and CXCL13) as indicated by significant main effects of gavage feeding (IL-1ra: $F_{(2,9)}$ = 21.21; p = 0.000393, n = 4; IL-4: $F_{(2,9)}$ = 4.97; p = 0.035154, n = 4; IL-13: $F_{(2,9)}$ = 14.60; p = 0.001494, n = 4; IL-27: $F_{(2,9)}$ = 43.65; p = 0.000023, n = 4; G-CSF: $F_{(2,9)}$ = 41.27; p = 0.000029, n = 4; M-CSF: $F_{(2,9)}$ = 5.93; p = 0.022740, n = 4; TIMP-1: $F_{(2,9)}$ = 65.65; p = 0.000004, n = 4; CXCL13: $F_{(2,9)}$ = 31.68; p = 0.000084, n = 4). *Post hoc* analysis revealed that 0.7 g/kg/day ethanol significantly increased baseline IL-27 (p = 0.010523) and TIMP-1 (p = 0.039746; **Figure 6C**), whereas 2.8 g/kg/day ethanol significantly increased baseline IL-1ra (p = 0.000234), IL-4 (p = 0.023458), IL-13 (p = 0.001525), IL-27 (p = 0.000013), G-CSF (p = 0.000026), M-CSF (p = 0.021383), TIMP-1 (p = 0.019979) and CXCL13 (p = 0.000056) compare to vehicle (**Figure 6** and **Table 2**). A 90-min MCAO increased nearly all pro- [IL-1α (p = 0.004446), IL-1β (p = 0.000049), IL-3 (p = 0.003363), IL-6 (p = 0.000427), IL-7 (p = 0.001322), IL-16 (p = 0.006295), IL-17 (p = 0.002063), IL-23 (p = 0.008776), TNFα (p = 0.008415), sICAM (p = 0.005868), C5a (p = 0.002926), TREM-1 (p = 0.000090), IFNγ (p = 0.015976), CCL2 ($p < 0.000001$), CCL3 (p = 0.000165), CCL4 (p = 0.000002), CCL5 (p = 0.000333), CCL12 ($p < 0.000001$), CXCL1 ($p < 0.000001$), CXCL2 (p = 0.000002), CXCL9 (p = 0.001983), CXCL10 (p = 0.003656), CXCL11 (p = 0.017108), CXCL12 (p = 0.003795), and CXCL13 (p = 0.004357)] and anti-(IL-1ra (p = 0.000022), IL-4 (p = 0.006545), IL-13 (p = 0.006153), IL-27 ($p < 0.000001$), G-CSF (p = 0.000538), M-CSF (p = 0.004005), TIMP-1 ($p < 0.000001$) and CXCL13 (p = 0.000056) inflammatory cytokines/chemokines at 24 h of reperfusion in the vehicle group. The number of upregulated pro- and anti-inflammatory cytokines/chemokines at 24 h of reperfusion was less in two ethanol groups. Twelve pro-[IL-1β (p = 0.000325), IL-3 (p = 0.016041), IL-6 (p = 0.012197), IL-16 (p = 0.022580), IL-17 (p = 0.042719), C5a (p = 0.010869), TREM-1 (p = 0.003024), CCL2 (p = 0.000093), CCL3 (p = 0.000472), CCL12 ($p < 0.000001$), CXCL1 (p = 0.000006), and CXCL2 (p = 0.001563)] and four anti-[IL-1ra (p = 0.000008), IL-27 (p = 0.000154), G-CSF (p = 0.008262), and TIMP-1 (p = 0.000185)] inflammatory cytokines/chemokines were increased in the 0.7 g/kg/day ethanol group. Only ten pro- [IL-1β (p = 0.003581), IL-3 (p = 0.009448), IL-6 (p = 0.005024), TREM-1 (p = 0.008930), CCL2 (p = 0.000002), CCL3 (p = 0.040100), CCL4 (p = 0.002640), CCL12 ($p < 0.000001$), CXCL1 (p = 0.000001), and CXCL2 (p = 0.000067)] and three anti-[IL-1ra (p = 0.013861), IL-27 (p = 0.02689), and TIMP-1 (p = 0.000008)] inflammatory cytokines/chemokines were increased in the 2.8 g/kg/day ethanol group (**Figure 6** and **Table 2**). There were significant interactions of ethanol and ischemic stroke on IL-1β ($F_{(5,18)}$ = 25.71; p = 0.000005, n = 4), IL-3 ($F_{(5,18)}$ = 6.00; p = 0.010051, n = 4), CCL12 ($F_{(5,18)}$ = 30.40; p = 0.000002, n = 4), IL-1a ($F_{(5,18)}$ = 5.86; p = 0.010941, n = 4). *Post hoc* analysis revealed that 0.7 g/kg/day ethanol significantly reduced post-ischemic IL-1β (p = 0.020488) and increased IL-1ra (p = 0.047886) at 24 h of reperfusion. *Post hoc* analysis also revealed that 2.8 g/kg/day ethanol significantly increased post-ischemic IL-3 (p = 0.006474), IL-23 (p = 0.034201), and CCL12 (p = 0.000689) at 24 h of reperfusion (**Figure 6** and **Table 2**).

BBB Breakdown

Again, since cerebral I/R injury was significantly altered in the 0.7 g/kg/day and 2.8 g/kg/day ethanol groups, BBB breakdown-related measurements were only conducted in the vehicle, 0.7 g/kg/day, and 2.8 g/kg/day ethanol groups. No IgG leakage

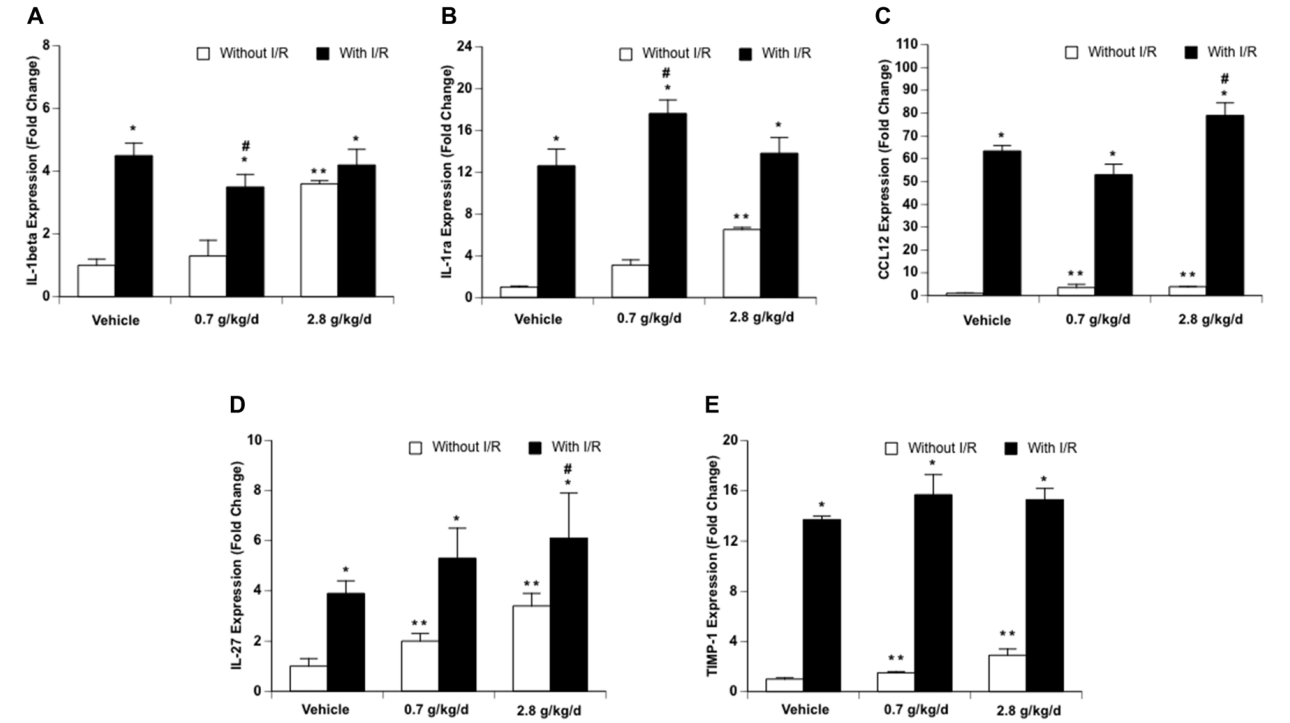

FIGURE 6 | Influence of ethanol on expression of interleukin-1β (IL-1β; **A**), IL-1ra **(B)**, CCL-12 **(C)**, IL-27 **(D)** and TIMP-1 **(E)** following a 90-min MCAO/24-h reperfusion. Values are means ± SE for four mice in each group. $^{**}P < 0.05$ vs. Vehicle without I/R. $^{*}P < 0.05$ vs. Without I/R. $^{\#}P < 0.05$ vs. Vehicle with I/R.

TABLE 2 | Effect of ethanol consumption on cytokines and chemokines in the cerebrum before and following a 90-min middle cerebral artery occlusion (MCAO)/24-h reperfusion.

Cytokines/Chemokines	Vehicle	0.7 g/kg/day	2.8 g/kg/day	Vehicle + I/R	0.7 g/kg/day + I/R	2.8 g/kg/day + I/R
IL-1α	1.0 ± 0.1	1.0 ± 0.2	1.1 ± 0.3	1.8 ± 0.2*	1.6 ± 0.3	1.4 ± 0.5
IL-2	1.0 ± 0.2	2.1 ± 0.5	2.3 ± 0.4	1.2 ± 0.1	1.8 ± 1.2	4.1 ± 2.0
IL-3	1.0 ± 0.2	1.1 ± 0.2	5.1 ± 0.2**	6.0 ± 1.1*	4.0 ± 0.9*	17.8 ± 3.4*#
IL-4	1.0 ± 0.3	2.4 ± 1.1	4.5 ± 1.0**	3.2 ± 0.5*	2.6 ± 0.9	9.8 ± 2.6#
IL-6	ND	ND	ND	1.0 ± 0.1*	1.2 ± 0.3*	0.4 ± 0.1*
IL-7	1.0 ± 0.1	1.2 ± 0.4	3.5 ± 0.2**	2.9 ± 0.3*	2.6 ± 0.7	3.4 ± 0.5
IL-13	1.0 ± 0.1	1.2 ± 0.1	2.5 ± 0.4**	2.0 ± 0.2*	1.7 ± 0.3	1.5 ± 0.8
IL-16	1.0 ± 0.1	1.1 ± 0.2	1.1 ± 0.3	1.8 ± 0.2*	2.1 ± 0.3*	0.8 ± 0.5
IL-17	1.0 ± 0.3	1.0 ± 0.5	3.4 ± 0.5**	2.8 ± 0.2*	2.8 ± 0.4*	2.1 ± 0.5
IL-23	1.0 ± 0.2	2.4 ± 1.1	4.5 ± 1.0**	3.2 ± 0.5*	2.6 ± 0.9	9.8 ± 2.6#
TNFα	1.0 ± 0.6	2.4 ± 1.6	4.7 ± 0.5	12.2 ± 2.8*	16.9 ± 6.9	11.4 ± 6.9
G-CSF	1.0 ± 0.4	1.6 ± 0.4	4.6 ± 0.1**	4.9 ± 0.5*	6.3 ± 1.2*	4.7 ± 1.8
M-CSF	1.0 ± 0.2	1.2 ± 0.3	2.4 ± 0.4**	2.2 ± 0.2*	3.5 ± 1.5	4.5 ± 1.0
sICAM	1.0 ± 0.0	1.3 ± 0.2	1.5 ± 0.2**	1.2 ± 0.1*	1.3 ± 0.1	1.5 ± 0.1
C5a	1.0 ± 0.2	1.5 ± 0.2	1.4 ± 0.4	4.0 ± 0.6*	4.0 ± 0.7*	3.2 ± 0.9
TREM-1	1.0 ± 0.1	1.8 ± 1.1	3.6 ± 0.1**	12.3 ± 1.2*	10.4 ± 1.5*	14.2 ± 2.8*
IFN-γ	1.0 ± 0.2	0.9 ± 0.2	1.5 ± 0.3	2.7 ± 0.4*	2.6 ± 0.9	3.0 ± 1.0
CCL2	1.0 ± 0.1	0.8 ± 0.5	1.5 ± 0.1	8.8 ± 0.1*	8.9 ± 0.7*	7.9 ± 0.3*
CCL3	1.0 ± 0.4	1.9 ± 1.1	6.7 ± 0.2**	8.6 ± 0.8*	9.2 ± 1.0*	10.5 ± 1.5*
CCL4	ND	ND	ND	1.2 ± 0.1*	1.5 ± 0.6	1.4 ± 0.3*
CCL5	1.0 ± 0.4	2.7 ± 1.1	3.8 ± 0.4	6.8 ± 0.7*	5.1 ± 1.8	5.5 ± 1.3
CXCL1	1.0 ± 0.3	0.8 ± 0.2	1.1 ± 0.3	15.8 ± 0.3*	16.1 ± 1.0*	14.1 ± 0.6*
CXCL2	1.0 ± 0.1	1.4 ± 0.1	3.0 ± 0.8**	18.7 ± 1.0*	19.0 ± 3.2*	19.0 ± 1.4*
CXCL9	1.0 ± 0.2	1.6 ± 0.4	2.7 ± 0.1**	3.4 ± 0.4*	3.4 ± 0.9	2.7 ± 0.9
CXCL10	1.0 ± 0.5	4.7 ± 1.1	5.2 ± 1.4**	3.9 ± 0.3*	3.1 ± 1.0	3.4 ± 1.2
CXCL11	1.0 ± 0.1	2.0 ± 0.8	4.4 ± 0.9**	3.1 ± 0.6*	2.5 ± 0.9	2.6 ± 1.9
CXCL12	1.0 ± 0.1	2.2 ± 0.8	2.6 ± 0.5	1.4 ± 0.1*	1.4 ± 0.3	1.5 ± 0.3
CXCL13	1.0 ± 0.3	3.0 ± 0.3	7.5 ± 0.9**	2.5 ± 0.2*	3.2 ± 1.4	6.4 ± 1.0#

Values are means ± SE for four mice in each group. ND stands for Not Detectable. $^{**}P < 0.05$ vs. Vehicle. $^{*}P < 0.05$ vs. Without ischemia/reperfusion (I/R). $^{\#}P < 0.05$ vs. Vehicle + I/R.

was detected at 24 h of reperfusion in the contralateral hemisphere. Ethanol altered post-ischemic IgG leakage at 24 h of reperfusion in the ipsilateral hemisphere of the ischemic brain as indicated by a significant main effect of gavage feeding ($F_{(2,12)}$ = 16.43; p = 0.000366, n = 5). *Post hoc* analysis showed that 0.7 g/kg/day ethanol reduced post-ischemic IgG leakage compared to vehicle (p = 0.015192; **Figure 7B**). In contrast, 2.8 g/kg/day ethanol worsened post-ischemic IgG leakage compared to vehicle (p = 0.044803; **Figures 7A,B**). Ethanol also altered post-ischemic brain edema in the ipsilateral hemisphere of the ischemic brain as indicated by a significant main effect of gavage feeding ($F_{(2,15)}$ = 15.45; p = 0.000229, n = 5). *Post hoc* analysis revealed that 0.7 g/kg/day ethanol significantly alleviated post-ischemic brain edema (p = 0.036270), whereas 2.8 g/kg/day significantly worsened the post-ischemic brain edema (p = 0.018484; **Figure 7C**). Ethanol altered baseline MMP-9 activity as indicated by a significant main effect of gavage feeding ($F_{(2,12)}$ = 6.26; p = 0.013741, n = 5). *Post hoc* analysis showed that 0.7 g/kg/day ethanol significantly reduced baseline MMP-9 activity (p = 0.010701; **Figures 7D,E**). A 90-min MCAO significantly increased MMP-9 activity at 24 h of reperfusion in all three groups (Vehicle group: $F_{(1,8)}$ = 81.90; p = 0.000018, n = 5; 0.7 g/kg/day group: $F_{(1,8)}$ = 20.84; p = 0.001837, n = 5; 2.8 g/kg/day group: $F_{(1,8)}$ = 7.15; p = 0.028171, n = 5; **Figures 7D,E**). There was no significant interaction of ethanol and ischemic stroke on MMP-9 activity at 24 h of reperfusion ($F_{(5,24)}$ = 3.14; p = 0.061657, n = 5). In addition, ethanol did not significantly alter MMP-9 activity at 24 h of reperfusion ($F_{(2,12)}$ = 3.14; p < 0.079986, n = 5; **Figures 7D,E**). In contrast to MMP-9, MMP-2 activity was not altered by ethanol and at 24 h of reperfusion (data not shown).

DISCUSSION

The present study investigated the influence of chronic consumption of low to high doses of ethanol on basal and post-ischemic inflammatory profiles in the brain. There are several new findings from this study. First, 0.35–0.7 g/kg/day ethanol tends to reduce baseline expression of ICAM-1 and E-selectin, but increase baseline expression of VCAM-1. Second, post-ischemic upregulation of ICAM-1 and E-selectin were attenuated in all ethanol groups. Third, low to moderate ethanol alleviated but high-dose ethanol aggravated post-ischemic microglial activation and neutrophil infiltration. Fourth, ethanol tended to dose-dependently increase both pro- and anti-inflammatory cytokines/chemokines at basal conditions. Fifth, low-dose ethanol reduced post-ischemic pro-inflammatory cytokines/chemokines and enhanced post-ischemic anti-inflammatory cytokines/chemokines. Sixth, low-dose ethanol reduced but high-dose ethanol worsened post-ischemic BBB breakdown. Thus, ethanol may affect both basal and post-ischemic inflammatory profiles of the brain in a dose-dependent manner. Low-dose ethanol tends to induce an anti-inflammatory effect, whereas high-dose ethanol produces an inflammatory effect.

Although numerous experimental studies have investigated the effect of ethanol consumption on cardiovascular diseases, there have only been a limited amount of studies investigating the effect of ethanol consumption on ischemic brain damage.

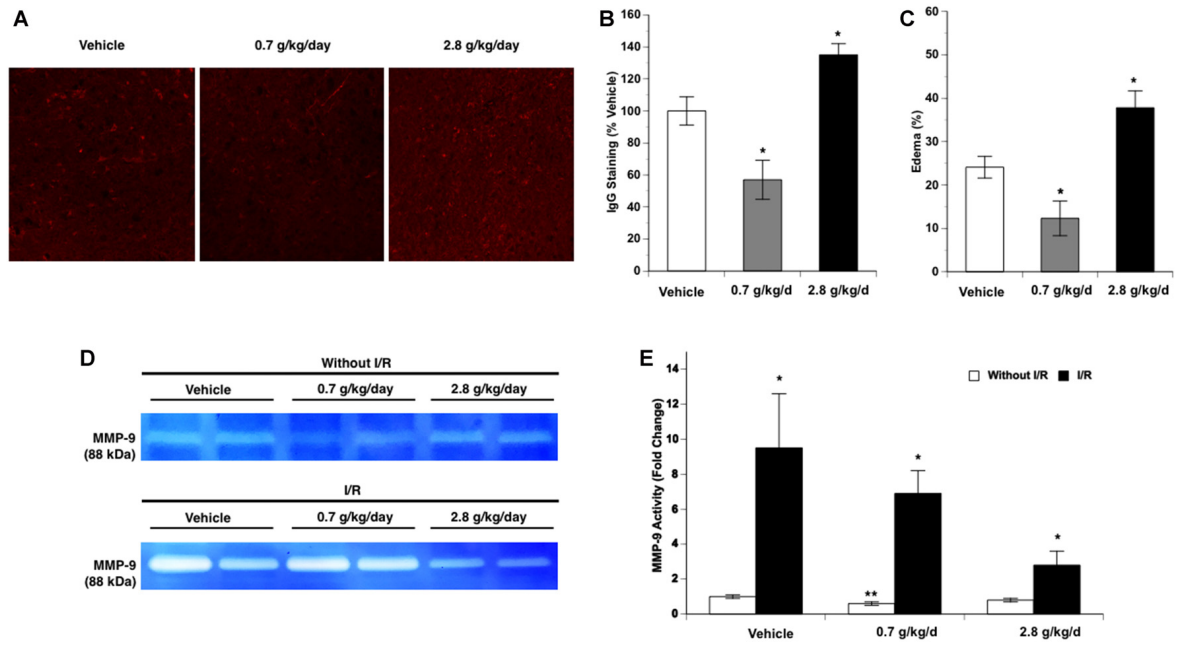

FIGURE 7 | Influence of ethanol on blood-brain barrier (BBB) permeability following a 90-min MCAO/24-h reperfusion. **(A)** Representative IgG staining. **(B)** Values are means ± SE for five mice in each group. **(C)** Values are means ± SE for six mice in each group. **(D)** Representative gelatin zymography. **(E)** Values are means ± SE for five mice in each group. $^{*}P < 0.05$ vs. Vehicle. $^{**}P < 0.05$ vs. Vehicle without I/R. $^{\#}P < 0.05$ vs. Without I/R.

In an early study, Mandybur and Mendenhall (1983) found that chronic alcoholism significantly contributes to the risk of mortality associated with ischemic brain infarction in gerbils. Later, Favalli et al. (2002) found that chronic ethanol consumption leads to an increased excitotoxicity and ischemic brain damage during early withdrawal in rats. Recently, Oliveira et al. (2014) found that heavy ethanol consumption exacerbates post-ischemic motor impairment and cortical neuronal loss in female adolescent rats. Our previous studies have shown that 2-month feeding with a liquid diet containing high-dose ethanol (6.4% v/v) worsened post-ischemic brain damage in rats (Sun et al., 2008; Zhao et al., 2010), whereas the diet containing low-dose ethanol (1% v/v) protected the brain against its I/R injury in both rats and mice (Zhao et al., 2011; Sun et al., 2012). To mimic the drinking pattern of humans, different doses of ethanol were given once a day *via* oral gavage feeding in the present study. We found that 0.7 g/kg/day ethanol significantly protected against brain I/R injury and 2.8 g/kg/day ethanol significantly exacerbated brain I/R injury. The peak blood ethanol concentration of the dose associated with a neuroprotective effect was 9.0 mM, which usually can be seen in a man with average body weight (70 kg or 154 Ibs) after ingestion of one and a half American standard drinks (14 grams of ethanol/each; Fisher et al., 1987). On the other hand, the peak blood ethanol concentration of the dose associated with a detrimental effect was 37.0 mM, which usually can be seen in a man with average body weight after ingestion of slightly more than seven American standard drinks. Therefore, the results of the present study complement and extend that which we have reported previously.

As far as we are aware, the present study is the first to systematically investigate the influence of chronic consumption of low to high doses of ethanol on early post-ischemic inflammation in the brain. We found that transient focal cerebral ischemia increased the expression of ICAM-1 and E-selectin, but not VCAM-1 and P-selectin at 24 h of reperfusion. Interestingly, the magnitude of the increase in ICAM-1 and E-selectin was significantly less in all ethanol groups when compared to the vehicle. The selectins facilitate the diapedesis of leukocytes on the endothelial surface while the immunoglobulin superfamily mediates the firm adhesion and transendothelial migration of leukocytes (Langer and Chavakis, 2009). Animals deficient in ICAM-1 or treated with strategies that block ICAM-1 have decreased ischemic damage and less brain neutrophil infiltration (Kitagawa et al., 1998). In addition, E-selectin inhibition is associated with improved neurological outcome (Huang et al., 2000). Of the various types of leukocytes, neutrophils are among the first to infiltrate the ischemic brain (Gronberg et al., 2013). Neutrophils may worsen brain I/R injury by obstructing capillaries resulting in reduced blood flow during reperfusion as well as by releasing cytotoxic products. Numerous studies have shown that inhibition of neutrophil infiltration is associated with a decrease in brain I/R injury (Egashira et al., 2013; Herz et al., 2015). In the present study, neutrophil infiltration was significantly inhibited in the 0.175–1.4 g/kg/day ethanol groups. The maximum inhibition was observed in the 0.7 g/kg/day ethanol group, in which the brain I/R injury was significantly reduced. Therefore, the neuroprotective effect of low-dose ethanol may be related to a reduction in expression of adhesion molecules and subsequent neutrophil infiltration.

Microglia are resident immune cells of the brain and are important modulators of homeostasis and immune response in the brain (Ziebell et al., 2015). Upon stimulation, microglia become activated and undergo several key morphological changes characterized by an amoeboid shape with little to no extending processes (Ziebell et al., 2015). Activated microglia may contribute to brain I/R injury *via* phagocytosis and elaboration of neuroinflammatory mediators toxic to cells (Ceulemans et al., 2010). In the present study, although post-ischemic microglia activation was significantly attenuated in the 0.175–1.4 g/kg/day ethanol groups, the maximum reduction occurred in the 0.7 g/kg/day ethanol group. Therefore, the neuroprotective effect of low-dose ethanol may be linked to a reduction in microglial activation.

Following transient focal cerebral ischemia, cytokines/chemokines are elaborated from injured neurons, infiltrated leukocytes, activated astrocytes, microglia, and endothelial cells (Kim et al., 2014). Pro-inflammatory cytokines, such as IL-1β, TNFα, and IL-6, contribute to brain I/R injury by stimulating pro-apoptotic signaling and cytotoxic proteins, activating microglia, and increasing the expression of adhesion molecules (Doll et al., 2014). In contrast, anti-inflammatory cytokines, such as IL-1ra, IL-4, and IL-10, inhibit post-ischemic inflammation by inhibiting pro-inflammatory cytokines and suppressing cytokine receptor expression and downstream signaling (Kim et al., 2014). Chemokines play a crucial role in the infiltration of leukocytes under inflammatory conditions (Kim et al., 2014). In the present study, one pro-inflammatory mediator, IL-1β, was less and one anti-inflammatory cytokine, IL-1ra, was greater in the 0.7 g/kg/day ethanol group compared to the vehicle group. IL-1 is a strong neurotoxic mediator and has two isoforms, IL-1α and IL-1β. However, IL-1β rather than IL-1α is considered to be more engaged in ischemic brain damage (Boutin et al., 2001). IL-1ra is an endogenous inhibitor of IL-1. Overexpression of IL-1ra as well as treatment with IL-1ra led to reduced ischemic brain damage (Mulcahy et al., 2003). Thus, it is conceivable that the neuroprotective effect of low-dose ethanol may also be related to an altered post-ischemic expression of cytokines/chemokines.

In the present study, post-ischemic inflammatory response produced conflicting results in the 2.8 g/kg/day ethanol group where the cerebral I/R injury was significantly exacerbated. Surprisingly, although neutrophil infiltration and microglial activation were increased, post-ischemic upregulation in adhesion molecules was reduced. Furthermore, both pro-inflammatory and anti-inflammatory cytokines/chemokines were increased after ischemic stroke. In addition to adhesion molecules, pro-inflammatory cytokines/chemokines and BBB breakdown can also influence the infiltration of neutrophils (Kim et al., 2014). In the present study, post-ischemic increase in three pro-inflammatory (IL-3, IL-23, and CCL12) was significant greater in the 2.8 g/kg/day ethanol group. Unfortunately,

no studies that we are aware of have attempted to relate alterations of IL-3 and CCL12 to neutrophil infiltration following ischemic stroke. CCL12 is a potent monocyte chemokine homologous to human CCL2 (Sarafi et al., 1997). Although the role of CCL12 in ischemic brain damage has not been elucidated, overexpression of CCL2 worsens ischemic brain damage (Chen et al., 2003). A recent study report that IL-23 can aggravate neuron damage and further impair the integrity of BBB (Wang et al., 2015). In the present study, post-ischemic BBB breakdown was significantly worsened in the 2.8 g/kg/day ethanol group. On the other hand, reactive oxygen species (ROS) and extracellular ATP from dying cells have been demonstrated to promote post-ischemic microglial activation (Doll et al., 2014). We previously have found that heavy ethanol consumption exacerbates brain I/R injury by increasing NMDA-mediated excitotoxicity and NAD(P)H oxidase-mediated oxidative stress (Zhao et al., 2010, 2011). Thus, the increased neutrophil infiltration and microglia activation may be resulted from exacerbated cell death and BBB breakdown. Post-ischemic inflammation begins immediately after arterial occlusion and contributes to potential enlargement of the infarct size. In the present study, although we were not able to directly establish the correlation between post-ischemic inflammatory response and infarct volume, we evaluated the inflammatory response in the peri-infarct area at 24 h of reperfusion. Recent studies found that the healing type of activated microglia was predominated in the ischemic core while the pre-inflammatory type of activated microglia was predominated in the peri-infarct area (Denes et al., 2007; Villarreal et al., 2016). The spatial distribution of the microglia phenotypes suggests that the peri-infarct area at early stage may represent the enlargement of injured and damaged brain tissue over time.

In the present study, ethanol did not alter baseline P-selectin, but upregulated baseline VCAM-1 and downregulated baseline ICAM-1 and E-selectin at low-moderate doses. All these adhesion molecules have been extensively linked to atherosclerosis (Galkina and Ley, 2007). Thus, the net effect of low-dose ethanol on these adhesion molecules cannot be estimated. However, it has been reported that combined deficiency of E-selectin and P-selectin could produce the strongest inhibitory effects on atherosclerosis (Galkina and Ley, 2007). In the present study, although low-dose ethanol slightly increased baseline CCL-12, it significantly activated anti-inflammatory mediators, IL-27 and TIMP-1. In addition, low-dose ethanol reduced baseline activity of MMP-9. IL-27 has been previously shown to inhibit atherosclerosis (Hirase et al., 2013). MMP-9 not only contributes to atherosclerotic plaque progression but also associates with cap rupture (Vacek et al., 2015). TIMP-1 is a tissue inhibitor of metalloproteinases. Thus, low-dose ethanol consumption may induce an anti-inflammatory property rather than an inflammatory effect under basal conditions. The relationship between regular ethanol intake and incidence of atherosclerosis appears to be U-shaped (Kiechl et al., 1998). It is possible that the beneficial effect of low-dose ethanol against atherosclerosis as well as subsequent ischemic stroke is related to its anti-inflammatory propensity. In contrast to low-dose ethanol, while high-dose ethanol also activated the anti-inflammatory system, it increased most detected pro-inflammatory cytokines/chemokines, suggesting a propensity towards vascular inflammation.

CONCLUSION

The present study is the first to systematically evaluate the influence of chronic ethanol consumption on the inflammatory profile in the brain under basal conditions and after transient focal cerebral ischemia. We found that the inflammatory profile during low-moderate ethanol consumption tends to prevent ischemic stroke and reduce brain I/R injury. On the other hand, inflammation may contribute to the increased ischemic stroke and exacerbated brain I/R injury during heavy ethanol consumption. Therefore, anti-inflammatory therapeutic strategies may be able to significantly improve prognosis of ischemic stroke in heavy alcohol users but not in low-moderate alcohol users.

AUTHOR CONTRIBUTIONS

HS and WM conceived the experiments. GX, CL, AP, JL, KM and HS conducted the experiments. GX, CL, RS (Biostatistician), and HS analyzed the results. All authors reviewed the manuscript.

FUNDING

This study was supported by a National Institutes of Health Grant (AA023610) and funds from Louisiana State University Health Sciences Center-Shreveport to HS and WM, a postdoctoral fellowship to CL and a predoctoral fellowship to KM from the Center for Cardiovascular Diseases and Sciences, Louisiana State University Health Science Center-Shreveport.

REFERENCES

Ahmad, S., Elsherbiny, N. M., Haque, R., Khan, M. B., Ishrat, T., Shah, Z. A., et al. (2014). Sesamin attenuates neurotoxicity in mouse model of ischemic brain stroke. *Neurotoxicology* 45, 100–110. doi: 10.1016/j.neuro.2014.10.002

Benjamin, E. J., Blaha, M. J., Chiuve, S. E., Cushman, M., Das, S. R., Deo, R., et al. (2017). Heart disease and stroke statistics-2017 update: a report from the american heart association. *Circulation* 135, e146–e603. doi: 10.1161/CIR.0000000000000485

Bonnans, C., Chou, J., and Werb, Z. (2014). Remodelling the extracellular matrix in development and disease. *Nat. Rev. Mol. Cell Biol.* 15, 786–801. doi: 10.1038/nrm3904

Boutin, H., LeFeuvre, R. A., Horai, R., Asano, M., Iwakura, Y., and Rothwell, N. J. (2001). Role of IL-1α and IL-1β in ischemic brain damage. *J. Neurosci.* 21, 5528–5534. doi: 10.1523/JNEUROSCI.21-15-05528.2001

Bruno, A., Kent, T. A., Coull, B. M., Shankar, R. R., Saha, C., Becker, K. J., et al. (2008). Treatment of hyperglycemia in ischemic stroke (THIS): a randomized pilot trial. *Stroke* 39, 384–389. doi: 10.1161/strokeaha.107.493544

Ceulemans, A. G., Zgavc, T., Kooijman, R., Hachimi-Idrissi, S., Sarre, S., and Michotte, Y. (2010). The dual role of the neuroinflammatory response after ischemic stroke: modulatory effects of hypothermia. *J. Neuroinflammation* 7:74. doi: 10.1186/1742-2094-7-74

Chen, Y., Hallenbeck, J. M., Ruetzler, C., Bol, D., Thomas, K., Berman, N. E., et al. (2003). Overexpression of monocyte chemoattractant protein 1 in the brain exacerbates ischemic brain injury and is associated with recruitment of inflammatory cells. *J. Cereb. Blood Flow Metab.* 23, 748–755. doi: 10.1097/01.wcb.0000071885.63724.20

Chen, W., Sun, Y., Liu, K., and Sun, X. (2014). Autophagy: a double-edged sword for neuronal survival after cerebral ischemia. *Neural Regen. Res.* 9, 1210–1216. doi: 10.4103/1673-5374.135329

Choi, D. H., Kim, J. H., Lee, K. H., Kim, H. Y., Kim, Y. S., Choi, W. S., et al. (2015). Role of neuronal NADPH oxidase 1 in the peri-infarct regions after stroke. *PLoS One* 10:e0116814. doi: 10.1371/journal.pone.0116814

Denes, A., Vidyasagar, R., Feng, J., Narvainen, J., McColl, B. W., Kauppinen, R. A., et al. (2007). Proliferating resident microglia after focal cerebral ischaemia in mice. *J. Cereb. Blood Flow Metab.* 27, 1941–1953. doi: 10.1038/sj.jcbfm.9600495

Doll, D. N., Barr, T. L., and Simpkins, J. W. (2014). Cytokines: their role in stroke and potential use as biomarkers and therapeutic targets. *Aging Dis.* 5, 294–306. doi: 10.14336/ad.2014.0500294

Ducroquet, A., Leys, D., Al Saabi, A., Richard, F., Cordonnier, C., Girot, M., et al. (2013). Influence of chronic ethanol consumption on the neurological severity in patients with acute cerebral ischemia. *Stroke* 44, 2324–2326. doi: 10.1161/STROKEAHA.113.001355

Egashira, Y., Suzuki, Y., Azuma, Y., Takagi, T., Mishiro, K., Sugitani, S., et al. (2013). The growth factor progranulin attenuates neuronal injury induced by cerebral ischemia-reperfusion through the suppression of neutrophil recruitment. *J. Neuroinflammation* 10:105. doi: 10.1186/1742-2094-10-105

Favalli, L., Rozza, A., Frattini, P., Masoero, E., Scelsi, R., Pascale, A., et al. (2002). Ischemia-induced glutamate release in rat frontoparietal cortex after chronic alcohol and withdrawal. *Neurosci. Lett.* 326, 183–186. doi: 10.1016/s0304-3940(02)00352-x

Favate, A. S., and Younger, D. S. (2016). Epidemiology of ischemic stroke. *Neurol. Clin.* 34, 967–980. doi: 10.1016/j.ncl.2016.06.013

Fisher, H. R., Simpson, R. I., and Kapur, B. M. (1987). Calculation of blood alcohol concentration (BAC) by sex, weight, number of drinks and time. *Can. J. Public Health* 78, 300–304.

Galkina, E., and Ley, K. (2007). Vascular adhesion molecules in atherosclerosis. *Arterioscler. Thromb. Vasc. Biol.* 27, 2292–2301. doi: 10.1161/atvbaha.107.149179

Gronberg, N. V., Johansen, F. F., Kristiansen, U., and Hasseldam, H. (2013). Leukocyte infiltration in experimental stroke. *J. Neuroinflammation* 10:115. doi: 10.1186/1742-2094-10-115

Hansagi, H., Romelsjö, A., Gerhardsson de Verdier, M., Andréasson, S., and Leifman, A. (1995). Alcohol consumption and stroke mortality. *Stroke* 26, 1768–1773. doi: 10.1161/01.STR.26.10.1768

Herz, J., Sabellek, P., Lane, T. E., Gunzer, M., Hermann, D. M., and Doeppner, T. R. (2015). Role of neutrophils in exacerbation of brain injury after focal cerebral ischemia in hyperlipidemic mice. *Stroke* 46, 2916–2925. doi: 10.1161/strokeaha.115.010620

Hirase, T., Hara, H., Miyazaki, Y., Ide, N., Nishimoto-Hazuku, A., Fujimoto, H., et al. (2013). Interleukin 27 inhibits atherosclerosis *via* immunoregulation of macrophages in mice. *Am. J. Physiol. Heart Circ. Physiol.* 305, H420–H429. doi: 10.1152/ajpheart.00198.2013

Huang, J., Choudhri, T. F., Winfree, C. J., McTaggart, R. A., Kiss, S., Mocco, J., et al. (2000). Postischemic cerebrovascular E-selectin expression mediates tissue injury in murine stroke. *Stroke* 31, 3047–3053. doi: 10.1161/01.str.31.12.3047

Ikehara, S., Iso, H., Toyoshima, H., Date, C., Yamamoto, A., Kikuchi, S., et al. (2008). Alcohol consumption and mortality from stroke and coronary heart disease among Japanese men and women: the Japan collaborative cohort study. *Stroke* 39, 2936–2942. doi: 10.1161/strokeaha.108.520288

Jean, W. C., Spellman, S. R., Nussbaum, E. S., and Low, W. C. (1998). Reperfusion injury after focal cerebral ischemia: the role of inflammation and the therapeutic horizon. *Neurosurgery* 43, 1382–1396; discussion 1396–1387. doi: 10.1227/00006123-199812000-00077

Kalogeris, T., Baines, C. P., Krenz, M., and Korthuis, R. J. (2012). Cell biology of ischemia/reperfusion injury. *Int. Rev. Cell Mol. Biol.* 298, 229–317. doi: 10.1016/B978-0-12-394309-5.00006-7

Kiechl, S., Willeit, J., Rungger, G., Egger, G., Oberhollenzer, F., and Bonora, E. (1998). Alcohol consumption and atherosclerosis: what is the relation? Prospective results from the Bruneck Study. *Stroke* 29, 900–907. doi: 10.1161/01.str.29.5.900

Kim, J. Y., Kawabori, M., and Yenari, M. A. (2014). Innate inflammatory responses in stroke: mechanisms and potential therapeutic targets. *Curr. Med. Chem.* 21, 2076–2097. doi: 10.2174/09298673216613122820514 6

Kitagawa, K., Matsumoto, M., Mabuchi, T., Yagita, Y., Ohtsuki, T., Hori, M., et al. (1998). Deficiency of intercellular adhesion molecule 1 attenuates microcirculatory disturbance and infarction size in focal cerebral ischemia. *J. Cereb. Blood Flow Metab.* 18, 1336–1345. doi: 10.1097/00004647-199812000-00008

Lakhan, S. E., Kirchgessner, A., and Hofer, M. (2009). Inflammatory mechanisms in ischemic stroke: therapeutic approaches. *J. Trans. Med.* 7:97. doi: 10.1186/1479-5876-7-97

Langer, H. F., and Chavakis, T. (2009). Leukocyte-endothelial interactions in inflammation. *J. Cell. Mol. Med.* 13, 1211–1220. doi: 10.1111/j.1582-4934.2009.00811.x

Mandybur, T. I., and Mendenhall, C. L. (1983). The effects of chronic alcoholism on development of ischemic cerebral infarcts following unilateral carotid artery ligation in gerbils. *Alcohol. Clin. Exp. Res.* 7, 357–361. doi: 10.1111/j.1530-0277.1983.tb05481.x

McCarter, K. D., Li, C., Jiang, Z., Lu, W., Smith, H. C., Xu, G., et al. (2017). Effect of low-dose alcohol consumption on inflammation following transient focal cerebral ischemia in rats. *Sci. Rep.* 7:12547. doi: 10.1038/s41598-017-12720-w

Meretoja, A., Keshtkaran, M., Saver, J. L., Tatlisumak, T., Parsons, M. W., Kaste, M., et al. (2014). Stroke thrombolysis: save a minute, save a day. *Stroke* 45, 1053–1058. doi: 10.1161/STROKEAHA.113.002910

Mulcahy, N. J., Ross, J., Rothwell, N. J., and Loddick, S. A. (2003). Delayed administration of interleukin-1 receptor antagonist protects against transient cerebral ischaemia in the rat. *Br. J. Pharmacol.* 140, 471–476. doi: 10.1038/sj.bjp.0705462

Oliveira, G. B., Fontes Ede, A. Jr., de Carvalho, S., da Silva, J. B., Fernandes, L. M., Oliveira, M. C., et al. (2014). Minocycline mitigates motor impairments and cortical neuronal loss induced by focal ischemia in rats chronically exposed to ethanol during adolescence. *Brain Res.* 1561, 23–34. doi: 10.1016/j.brainres.2014.03.005

Patra, J., Taylor, B., Irving, H., Roerecke, M., Baliunas, D., Mohapatra, S., et al. (2010). Alcohol consumption and the risk of morbidity and mortality for different stroke types—a systematic review and meta-analysis. *BMC Public Health* 10:258. doi: 10.1186/1471-2458-10-258

Ronksley, P. E., Brien, S. E., Turner, B. J., Mukamal, K. J., and Ghali, W. A. (2011). Association of alcohol consumption with selected cardiovascular disease outcomes: a systematic review and meta-analysis. *BMJ* 342:d671. doi: 10.1136/bmj.d671

Sarafi, M. N., Garcia-Zepeda, E. A., MacLean, J. A., Charo, I. F., and Luster, A. D. (1997). Murine monocyte chemoattractant protein (MCP)-5: a novel CC chemokine that is a structural and functional homologue of human MCP-1. *J. Exp. Med.* 185, 99–109. doi: 10.1084/jem.185.1.99

Shukla, V., Shakya, A. K., Perez-Pinzon, M. A., and Dave, K. R. (2017). Cerebral ischemic damage in diabetes: an inflammatory perspective. *J. Neuroinflammation* 14:21. doi: 10.1186/s12974-016-0774-5

Sun, H., Xiong, W., Arrick, D. M., and Mayhan, W. G. (2012). Low-dose alcohol consumption protects against transient focal cerebral ischemia in mice: possible role of PPARγ. *PLoS One* 7:e41716. doi: 10.1371/journal.pone.0041716

Sun, H., Zhao, H., Sharpe, G. M., Arrick, D. M., and Mayhan, W. G. (2008). Effect of chronic alcohol consumption on brain damage following transient focal ischemia. *Brain Res.* 1194, 73–80. doi: 10.1016/j.brainres.2007.11.061

Supanc, V., Biloglav, Z., Kes, V. B., and Demarin, V. (2011). Role of cell adhesion molecules in acute ischemic stroke. *Ann. Saudi Med.* 31, 365–370. doi: 10.4103/0256-4947.83217

Taylor, R. A., and Sansing, L. H. (2013). Microglial responses after ischemic stroke and intracerebral hemorrhage. *Clin. Dev. Immunol.* 2013:746068. doi: 10.1155/2013/746068

Turner, R. J., and Sharp, F. R. (2016). Implications of MMP9 for Blood Brain Barrier Disruption and Hemorrhagic Transformation Following Ischemic Stroke. *Front. Cell Neurosci.* 10: 56. doi: 10.3389/fncel.2016.00056

Vacek, T. P., Rehman, S., Neamtu, D., Yu, S., Givimani, S., and Tyagi, S. C. (2015). Matrix metalloproteinases in atherosclerosis: role of nitric oxide, hydrogen sulfide, homocysteine, and polymorphisms. *Vasc. Health Risk Manag.* 11, 173–183. doi: 10.2147/vhrm.s68415

Villarreal, A., Rosciszewski, G., Murta, V., Cadena, V., Usach, V., Dodes-Traian, M. M., et al. (2016). Isolation and characterization of ischemia-derived astrocytes (IDAs) with ability to transactivate quiescent astrocytes. *Front. Cell. Neurosci.* 10:139. doi: 10.3389/fncel.2016.00139

Wang, M., Zhong, D., Zheng, Y., Li, H., Chen, H., Ma, S., et al. (2015). Damage effect of interleukin (IL)-23 on oxygen-glucose-deprived cells of the neurovascular unit *via* IL-23 receptor. *Neuroscience* 289, 406–416. doi: 10.1016/j.neuroscience.2015.01.012

Weinstein, J. R., Koerner, I. P., and Moller, T. (2010). Microglia in ischemic brain injury. *Future Neurol.* 5, 227–246. doi: 10.2217/fnl.10.1

Yang, Y., Salayandia, V. M., Thompson, J. F., Yang, L. Y., Estrada, E. Y., and Yang, Y. (2015). Attenuation of acute stroke injury in rat brain by minocycline promotes blood-brain barrier remodeling and alternative microglia/macrophage activation during recovery. *J. Neuroinflammation* 12:26. doi: 10.1186/s12974-015-0245-4

Zhang, C., Qin, Y. Y., Chen, Q., Jiang, H., Chen, X. Z., Xu, C. L., et al. (2014). Alcohol intake and risk of stroke: a dose-response meta-analysis of prospective studies. *Int. J. Cardiol.* 174, 669–677. doi: 10.1016/j.ijcard.2014.04.225

Zhao, H., Mayhan, W. G., Arrick, D. M., Xiong, W., and Sun, H. (2010). Alcohol-induced exacerbation of ischemic brain injury: role of NAD(P)H oxidase. *Alcohol. Clin. Exp. Res.* 34, 1948–1955. doi: 10.1111/j.1530-0277.2010.01284.x

Zhao, H., Mayhan, W. G., Arrick, D. M., Xiong, W., and Sun, H. (2011). Dose-related influence of chronic alcohol consumption on cerebral ischemia/reperfusion injury. *Alcohol. Clin. Exp. Res.* 35, 1265–1269. doi: 10.1111/j.1530-0277.2011.01461.x

Ziebell, J. M., Adelson, P. D., and Lifshitz, J. (2015). Microglia: dismantling and rebuilding circuits after acute neurological injury. *Metab. Brain Dis.* 30, 393–400. doi: 10.1007/s11011-014-9539-y

Conflict of Interest Statement: The authors declare that the research was conducted in the absence of any commercial or financial relationships that could be construed as a potential conflict of interest.

frontiers in Cellular Neuroscience

ORIGINAL RESEARCH
published: 27 February 2019
doi: 10.3389/fncel.2019.00068

Inhibition of COX2/PGD2-Related Autophagy Is Involved in the Mechanism of Brain Injury in T2DM Rat

*Yang Yang[1†], Qi Chen[2†], Quanfeng Zhao[3†], Ying Luo[1], Ying Xu[4], Weimin Du[1], Hong Wang[1], Huan Li[1], Lu Yang[1], Congli Hu[1], Jiahua Zhang[1], Yuke Li[1], Hui Xia[1], Zhihao Chen[1], Jie Ma[1], Xiaoyan Tian[1] and Junqing Yang[1]**

[1] Department of Pharmacology, Chongqing Medical University, The Key Laboratory of Biochemistry and Molecular Pharmacology, Chongqing, China, [2] Department of Pharmacy, GuiZhou Provincial People's Hospital, Guiyang, China, [3] Department of Pharmacy, Southwest Hospital, First Affiliated Hospital to TMMU, Third Military Medical University (Army Medical University), Chongqing, China, [4] Department of Pharmaceutical Sciences, School of Pharmacy and Pharmaceutical Sciences, University at Buffalo, The State University of New York (SUNY), Buffalo, NY, United States

The present study was designed to observe the effect of COX2/PGD2-related autophagy on brain injury in type 2 diabetes rats. The histopathology was detected by haematoxylin–eosin staining. The learning and memory functions were evaluated by Morris water maze. The levels of insulin and PGD2 were measured by enzyme-linked immunosorbent assay. The expressions of COX2, p-AKT(S473), p-AMPK(T172), Aβ, Beclin1, LC3BII, and p62 were measured by immunohistochemistry and Western blotting. In model rats, we found that the body weight was significantly decreased, the blood glucose levels were significantly increased, the plasma insulin content was significantly decreased, the learning and memory functions were impaired and the cortex and hippocampus neurons showed significant nuclear pyknosis. The levels of COX2, p-AKT(S473), PGD2, Aβ, Beclin1 and p62 were significantly increased, whereas the expression of p-AMPK(T172) and LC3BII was significantly decreased in the cortex and hippocampus of model rats. In meloxicam-treated rats, the body weight, blood glucose and the content of plasma insulin did not significantly change, the learning and memory functions were improved and nuclear pyknosis was improved in the cortex and hippocampus neurons. The expression of p-AMPK(T172), Beclin1 and LC3BII was significantly increased, and the levels of COX2, p-AKT(S473), PGD2, Aβ, and p62 were significantly decreased in the cortex and hippocampus of meloxicam-treated rats. Our results suggested that the inhibition of COX2/PGD2-related autophagy was involved in the mechanism of brain injury caused by type 2 diabetes in rats.

Keywords: cyclooxygenase-2, PGD2, type 2 diabetes, brain injury, autophagy

OPEN ACCESS

Edited by:
Sriharsha Kantamneni, University of Bradford, United Kingdom

Reviewed by:
Marco Segatto, University of Molise, Italy
Xiao-Qiang Li, Fourth Military Medical University, China

***Correspondence:**
Junqing Yang
cqyangjq@cqmu.edu.cn

†Co-first authors

Received: *03 August 2018*
Accepted: *11 February 2019*
Published: *27 February 2019*

Citation:
Yang Y, Chen Q, Zhao Q, Luo Y, Xu Y, Du W, Wang H, Li H, Yang L, Hu C, Zhang J, Li Y, Xia H, Chen Z, Ma J, Tian X and Yang J (2019) Inhibition of COX2/PGD2-Related Autophagy Is Involved in the Mechanism of Brain Injury in T2DM Rat. Front. Cell. Neurosci. 13:68. doi: 10.3389/fncel.2019.00068

INTRODUCTION

The prevalence of type 2 diabetes mellitus (T2DM) is increasing with increased population aging and lifestyle changes. T2DM has become the main reason of disability and death in recent years (Sima, 2010). Diabetes can induce multiple organ damage. The central nervous system damage caused by diabetes has always received attention. A long-term study reported that the

cognitive function declines at an accelerated pace in T2DM patients (Strachan et al., 2003; Wu et al., 2003; Hassing et al., 2004). In the mini-mental state examination test, the T2DM patients' scores were reportedly lower than those of age-, sex- and educational level-matched non-diabetic controls (Ryan and Geckle, 2000; Xu et al., 2004). Studies have shown that the prevalence of cognitive dysfunction caused by diabetes is 25 to 36% (Alagiakrishnan et al., 2013). A major manifestation of brain injury caused by diabetes was attention deficiency, slower information processing, impaired learning ability, and memory decline. Although various factors are reportedly involved in T2DM-induced brain injury, the mechanism of damage is still unclear.

Cyclooxygenase (COX), a rate-limiting enzyme in the synthesis of prostaglandins (PGs), is involved in regulating various functions of the central nervous system (Yagami et al., 2016). COX includes the structural COX1 and the inducible COX2. COX2 increases under various pathological conditions. Many studies have proven that COX2 participates in various chronic central nervous system injuries. Some studies have found that the COX2 expression was significantly increased in Alzheimer disease (AD), Parkinson's disease and amyotrophic lateral sclerosis (Teismann et al., 2003; Consilvio et al., 2004). The selective COX2 inhibitor has a significant protective effect against these diseases. Our previous studies also showed that the COX2 was up-regulated in chronic brain injury in rats caused by aluminum overload (Yu et al., 2014). These results suggested that COX2 has a role in the chronic central nervous system injury. However, its effect on T2DM-induced brain injury is still unclear. COX2 exerts its physiological effects by producing PGs. PGD2 is the most abundant prostaglandin in the brain. PGD2 is involved in the regulation of body temperature, the sleep–wake cycle, blood flow, neurotransmission and pain responses (Abdel-Halim et al., 1980; Chiu and Richardson, 1985). It has been shown that PGD2 has both protective and damaging effects in various models of the central nervous system. Therefore, the effect of PGD2 in brain injury remains controversial. However, to our knowledge, the relationship between COX2/PGD2 and T2DM-induced brain injury has never been reported.

Autophagy is a basic biological process which widely exists in normal cells. It plays an important role in maintaining intracellular homeostasis and the health of the body (Lin et al., 2013). Autophagy is involved in the regulation of cell defense and stress, and it will digest and degrade the unfunctional proteins and organelles within the cell (Kirkin et al., 2009). In cells, autophagy contributes to recycling raw materials, updating organelles and maintaining the cellular microenvironment stability (Klionsky, 2008). Studies have demonstrated that autophagy is involved in tumors, infectious diseases, liver diseases, diabetes, and neurodegenerative diseases (Rubinsztein et al., 2012). Some studies showed that the natural process of brain aging also accompanied a chronic and late-onset deterioration of a neuronal autophagy–lysosomal system in AD (Ling and Salvaterra, 2011). Some studies indicated that the decreased expression of LC3BII and the increased expression of p62 were involved in autism-induced hippocampus injuries (Zhang et al., 2016).

The decrease of autophagy level may be an important factor in T2DM-induced organ damage. A significant increase of p62-positive β-cells was found in the autopsy of T2DM patients, indicating that autophagy was inhibited (Mizukami et al., 2014). The autophagy level was decreased in streptozotocin (STZ)-induced type 2 diabetes heart disease (Wang et al., 2014). Han et al. (1992) first reported that the autophagy level in near-loop tubule was decreased in the STZ-induced rat nephropathy model. In addition, some studies have shown that the autophagy level of podocytes was inhibited in STZ-induced diabetic mice and that the autophagy level of high glucose-cultured podocytes also significantly decreased *in vitro* (Fang et al., 2013). Some studies suggested that the autophagy level was significantly decreased in the animal model of T2DM-induced brain injury (Carvalho et al., 2015; Candeias et al., 2018). However, the mechanism of the decrease of autophagy level in T2DM-induced brain injury is still unclear. It is well known that inflammation and apoptosis are the main reasons of organ damage caused by COX2. A recent study has found that high expression of COX2 lowers the expression of LC3BII (Wang L.F. et al., 2015). Celecoxib, a COX2 inhibitor, significantly increased the LC3BII expression and consequently enhanced the autophagy level (Zhu et al., 2017). These results suggest that the decrease of autophagy level is another important reason for organ damage caused by COX2. The PGD2 is the most abundant prostaglandin in the brain. Therefore, we think that COX2–PGD2 may be involved in the mechanism of T2DM-induced brain injury through inhibiting autophagy.

MATERIALS AND METHODS

Animals

Sprague-Dawley (SD) rats were housed in the barrier housing facility, in keeping with the national standard of "Laboratory Animal-Requirements of Environment and Housing Facilities." The care of the laboratory animal and the animal experimental operation conform to the "Chongqing Administration Rule of Laboratory Animal." The experimental procedures were approved by the animal laboratory administrative center and the institutional ethics committee of Chongqing Medical University (License number: SYXK YU 2012-0001) and are also in accordance with the National Institutes of Health guidelines. The rats were kept in controlled conditions of temperature (24 ± 2°C), relative humidity (60 ± 10%) and 12/12 h light/dark cycle (light from 08:00 am to 08:00 pm).

To establish the rat model of T2DM (Li et al., 2016; Ma et al., 2017), 60 male rats (80–100 g, 4-week old) were a fed high fat diet (HFD) (20% sugar, 10% lard, 10% egg yolk, and 60% basal feed) after a week of normal diet. After 4 weeks, rats were injected once with low-dose STZ (Solarbio, China) (STZ, 30 mg/kg i.p) to induce partial insulin deficiency, and then continuously fed HFD for 4 weeks after injection of STZ. 30 male rats were alive after the completion of modeling. 30 male rats were randomly and equally divided into the following 3 groups: model group, the low

dose meloxicam group (mg·kg^{-1}), and the high dose meloxicam group (3 mg·kg^{-1}), n = 10 for each group. Then the model rats were orally administrated the COX2 inhibitor (meloxicam) for 8 weeks. There were 9 rats remaining in each group when the administration was completed. The rats of the normal group were fed a normal diet. Before the rats were killed, the rats were weighed, the blood glucose levels were tested using Johnson one touch Ultra Test Strips on Johnson Performa blood glucose meter, and plasma was collected.

Morris Water Maze Test

Morris water maze was used to evaluate spatial learning and memory function of rat in each group (Kemppainen et al., 2014; Tian et al., 2016). Rats were given four trials per day for four consecutive days. A different entry site was used for each daily session. During each trial, the rats were introduced into the water where a hidden platform was submerged under the water. If rats failed to reach the platform within 90 s, they were gently guided to it and allowed to remain for 10 s on top of the platform. On the 5th day, following the last day of training, rats were introduced into the pool from the entry site where the last training was performed in order to assess retention of the platform location. During this probe trial, the platform was removed from the maze. The latency for the rat to find the hidden platform and the number of times to cross the platform were recorded, with a maximum of 90 s.

Histopathological Observation

After the Morris water maze test, 3 rats from each group were perfused with heparinized saline (30 ml) to remove blood from the vasculature, and then with 4% paraformaldehyde in phosphate buffered saline (50 ml). The whole brain was then removed and stored in the same fixative. After paraffin embedding, 5-μm sections were obtained and stained with hematoxylin-eosin (H&E). Morphologic changes of hippocampus and cortical neurons were examined using light microscopy. High power fields were sampled from the hippocampus CA1 subfield. Cells with a distinct nucleus and nucleolus were regarded as intact neurons.

Enzyme-Linked Immunosorbent Assay (ELISA)

Rats cortex and hippocampus from each group of rats (n = 6) were removed on the second day after the administration was completed. PGD2 (*Meibiao, Jiangsu, China*) was detected with ELISA kits. Insulin (*Meibiao, Jiangsu, China*) of plasma was detected with ELISA kits (n = 9).

Immunohistochemical Staining Test

Immunohistochemistry was performed to investigate the expression of COX2 in the rat brains. Briefly, brain sections of 3 rats from each group were dewaxed and rehydrated in decreasing concentrations of ethanol. Then the sections were blocked for endogenous peroxidase in 3% H_2O_2 in methanol for 20 min at room temperature. Slides were washed with PBS for three times and pre-incubated in 1% serum for 30 min at room temperature. Thereafter, the sections were incubated with primary antibodies COX2 (dilution 1:50, *Santa, United States*) overnight at 4 C. Then, the sections were incubated with a biotinylated secondary antibody (dilution 1:100) for 30 min at 37°C, and incubated with streptavidin for 20 min, and then rinsed for another 3 min × 3 min with PBS before reaction with the DAB solution. The sections were counterstained with hematoxylin and then observed under a microscope.

Western Blotting Test

Fifty mg of rat cortex and hippocampus (n = 4) were added to 0.5 ml of tissue lysate solution for protein extraction and centrifugation at 12,000 × g for 10 min at 4°C, and the supernatant was used for the detection of protein concentrations with a BCA protein assay kit *(Beyotime, China)*. A 10 μL sample of protein was separated by sodium dodecyl sulphate polyacrylamide gel electrophoresis (SDS-PAGE) and transferred to PVDF membranes (*Millipore, United States*). The membranes were blocked with 5% BSA for 1 h at room temperature and then probed with specific primary antibodies, including anti-Aβ (1:1000; *Abcam, United Kingdom*), COX2 (dilution 1:400, *Santa, United States*), p-AKT(S473, 1:400, *Santa, United States*), p-AMPK(T172, 1:1000; *Abcam, United Kingdom*), Beclin1(1:500; *Abcam, United Kingdom*), LC3BII (1:1000; *CST, United States*), and p62(1:1000; *CST, United States*) and β-actin (1:4000; *Proteintech, United States*) overnight at 4°C. The membranes were washed three times in TBST and incubated with HRP-conjugated secondary antibodies at room temperature for 1 h. Following four washes in TBST, protein signals were visualized by ECL *(Bio-Rad, United States)*.

Statistical Analysis

Data are presented as mean ± standard deviation (SD). Statistical analysis was carried out using SPSS statistics software (Version 20.0) and data were analyzed by performing one-way analysis of variance (ANOVA) followed by *post hoc* Tukey's test. P-value less than 0.05 was considered statistically significant.

RESULTS

Changes of Body Weight, Blood Glucose and Plasma Insulin in T2DM Rat

To determine whether our model was a T2DM model, we measured the body weight, blood glucose, and plasma insulin of the rats. Compared with the normal group, model and meloxicam-treated rat's body weight were significantly decreased. Compared with the normal group, model and meloxicam-treated rats' blood glucose was significantly increased. Compared with the normal group, the plasma insulin was significantly decreased in model and meloxicam-treated rats. The increase of blood glucose and the decrease of body weight and plasma insulin are consistent with the basic pathological features of T2DM. The COX2 inhibitor has no effect on the body weight, blood glucose, and insulin content of T2DM rats (**Figure 1**).

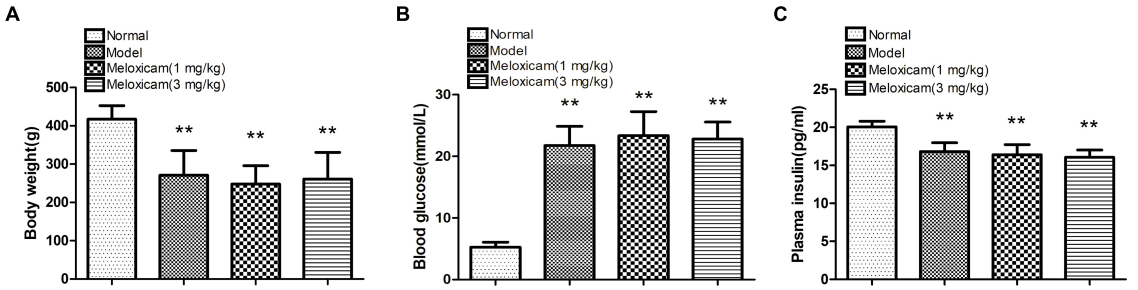

FIGURE 1 | Changes of body weight, blood glucose and plasma insulin in T2DM rat. **(A)** Body weight; **(B)** blood glucose; **(C)** plasma insulin. Rats in the model group showed a significant increase of blood glucose, and a significant decrease of body weight and plasma insulin. The COX2 inhibitor have no effect on the body weight, blood glucose, and plasma insulin. Data are expressed as mean ± SD of nine individual rats in each group, and were analyzed statistically using one-way ANOVA, followed by *post hoc* Tukey's test. $^{**}P < 0.01$ compared with normal group.

Changes of Spatial Learning and Memory Function in T2DM Rat

In order to determine whether rats had neurological impairment, we used the morris water maze to test the learning and memory function of rats. The morris water maze results showed that rats in all groups exhibited a rapid reduction in their escape latencies to find the platform over the 4 training days. Compared with the normal group, rats in the model group showed significantly prolonged escape latency and induced a decrease in the number of platform cross times on 4th and 5th days. Compared with the model group, the escape latency of rats in COX2 inhibitor groups significantly decreased and platform crossing times significantly increased on the 4th and 5th days (**Figures 2**, **3**).

Changes of Neuronal Pathomorphology in T2DM Rat

In order to determine whether the rat's brain had pathological changes, we used HE to test the changes of neuronal pathomorphology in rats' hippocampus and cortex. In the control group, the morphological neuronal structure of the hippocampus and cortex was intact and clear. By comparison, the neuron in the model group showed a remarkable karyopyknosis. COX2 inhibitor significantly improved neuronal karyopycnosis (**Figure 4**).

Changes of COX2 Expression in T2DM Rat Hippocampus and Cortex

COX2 is a rate-limiting enzyme in the synthesis of PGs. In order to determine whether COX2-PGD2 was involved in brain damage in T2DM, we used IHC and WB to test COX2 expression in the rat's cortex and hippocampus. The expression of COX2 in the model rat's cortex and hippocampus were significantly increased compared with the control group. COX2 inhibitor significantly blunted the increase of COX2 protein expression in the model rat's cortex and hippocampus (**Figure 5**).

Changes of PGD2 Content in T2DM Rat Hippocampus and Cortex

In order to determine whether COX2-PGD2 was involved in brain damage in T2DM, we used Elisa to test PGD2 content in the rat's cortex and hippocampus. PGD2 content of the rat's

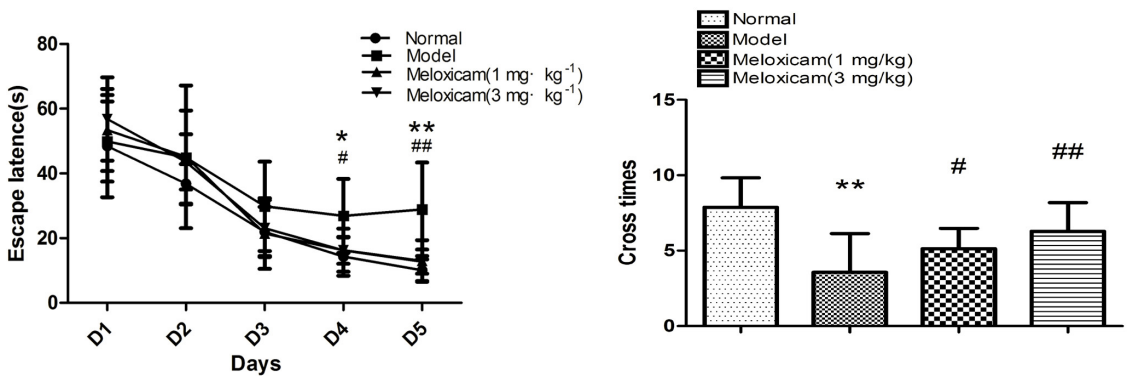

FIGURE 2 | Changes of spatial learning and memory function in T2DM rat. Rats in the model group showed a significant increase of escape latency and a significant decrease of the number of platform cross times. The COX2 inhibitor could significantly blunt those changes caused by T2DM. Data are expressed as mean ± SD of nine individual rats in each group, and were analyzed statistically using one-way ANOVA, followed by *post hoc* Tukey's test. $^{*}P < 0.05$ and $^{**}P < 0.01$ compared with normal group; $^{\#}P < 0.05$ and $^{\#\#}P < 0.01$ compared with model group, respectively.

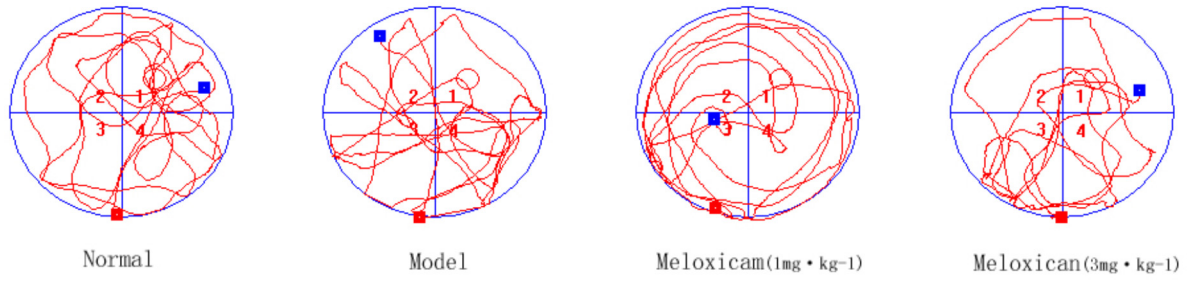

FIGURE 3 | Typical trajectories of the orientation test on day 5 of the water maze test. The circle represents previous platform location in the trace images. The red square represents the starting position of the rat. The blue square represents the end position of the rat.

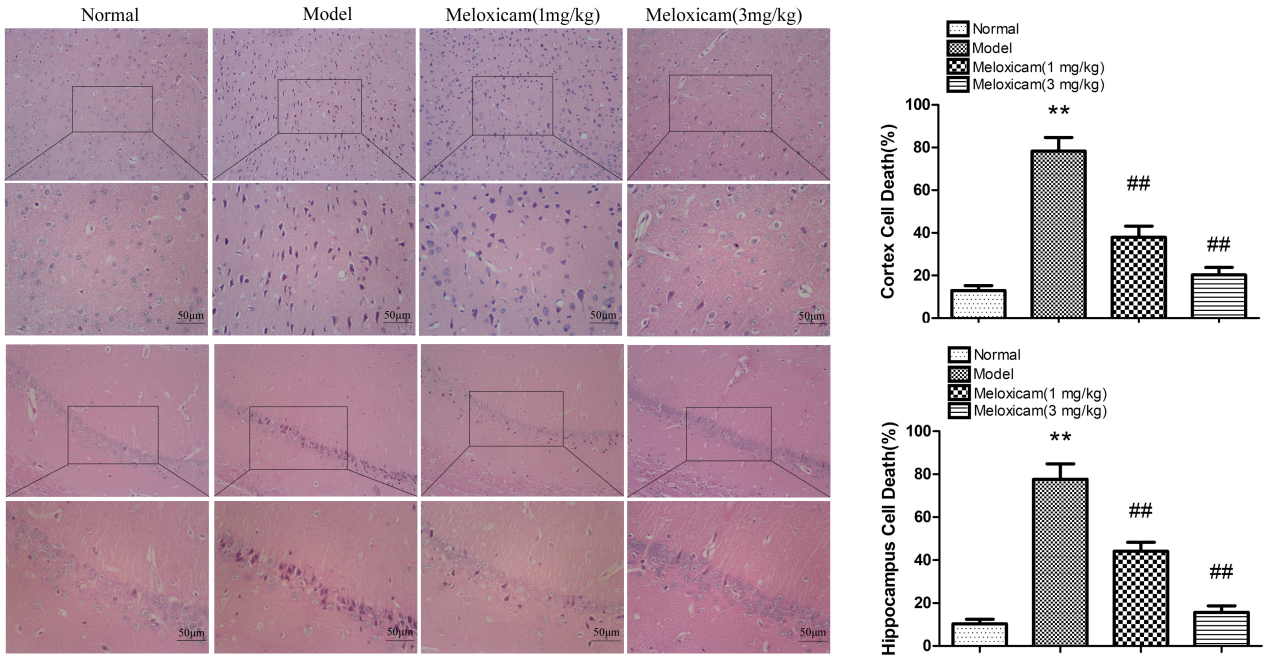

FIGURE 4 | Changes of neuronal pathomorphology in T2DM rat cortex and hippocampus (HE × 200, ×400, Scale bar = 50 μm). The hippocampus and cortical neurons were in distinct and regular structure, and arranged densely and clearly in the normal group. Compared to normal group, neuron in the model group showed a remarkable karyopyknosis. The COX2 inhibitor significantly improved karyopycnosis. Data are expressed as the mean ± SD for three individual rats in each group, and were analyzed statistically using one-way ANOVA, followed by *post hoc* Tukey's test. $^{**}P < 0.01$ compared with normal group; $^{\#\#}P < 0.01$ compared with model group, respectively.

hippocampus and cortex in the model group were significantly increased compared with the control group. The administration of COX2 inhibitor significantly blunted the increase of PGD2 content in diabetes rats (**Figure 6**).

Changes of Aβ, p-AKT(S473), p-AMPK(T172), Beclin1, LC3BII and p62 Expressions in T2DM Rat Hippocampus and Cortex

To determine whether COX2-PGD2 induced T2DM brain injury by affecting p-AKT(S473) and p-AMPK(T172) to inhibit autophagy and reduce the clearance of Aβ, we used WB to detect the related protein expression in the rat's cortex and hippocampus. Compared with the control group, the expressions of p-AKT(S473), Aβ, Beclin1, and p62 were significantly increased, while LC3BII and p-AMPK(T172) expression was significantly decreased in the model rat's cortex and hippocampus. The COX2 inhibitor significantly increased the expression of p-AMPK(T172), Beclin1 and LC3BII, and significantly decreased the expression of p-AKT(S473), Aβ and p62 (**Figure 7**).

DISCUSSION

The increase in the prevalence of T2DM has become an important threat for people's health. T2DM-induced brain injury

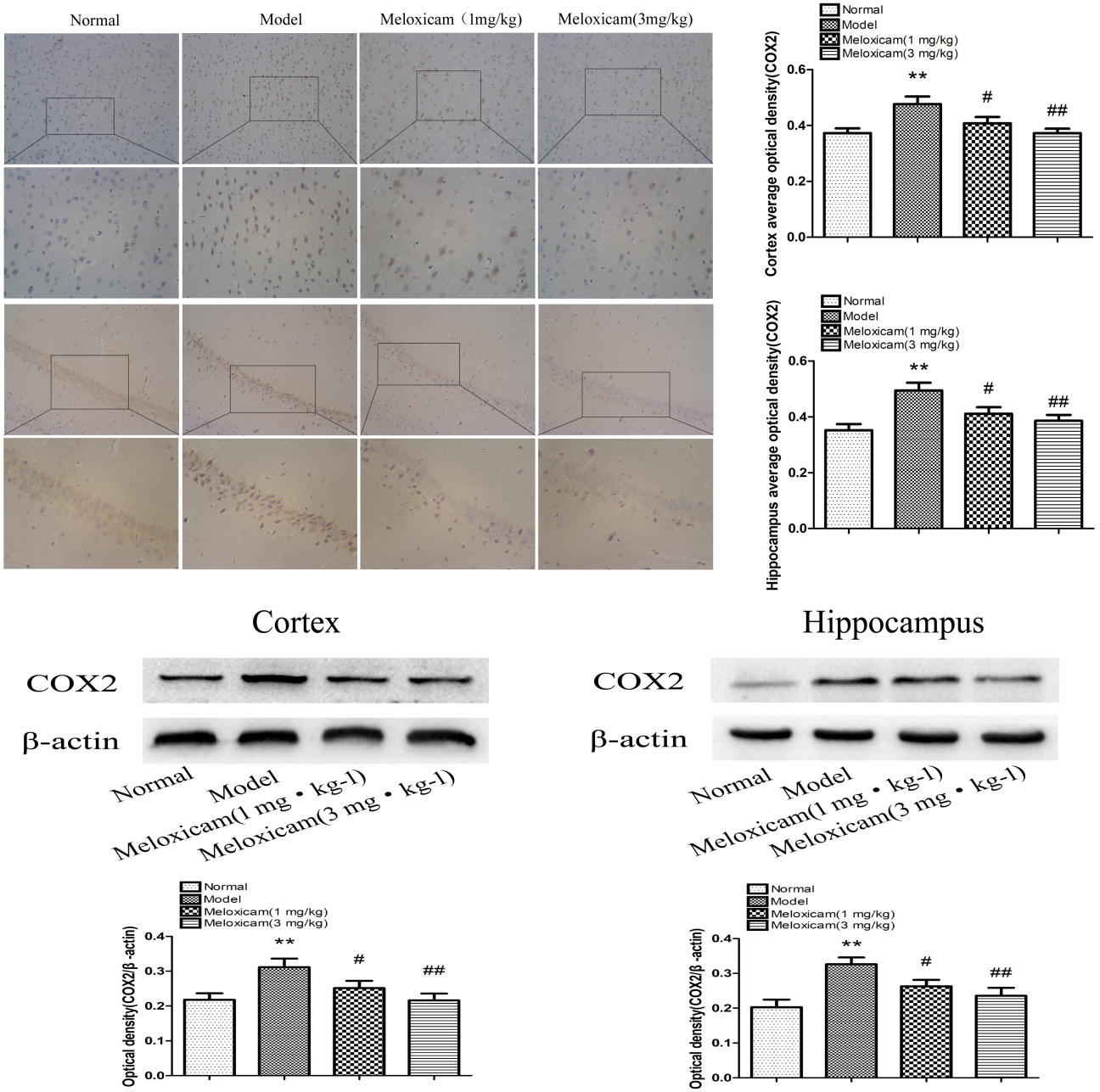

FIGURE 5 | Changes of COX2 expression in T2DM rat cortex and hippocampus (×200, ×400). Compared with normal group, the COX2 expression in cortex and hippocampus were significantly increased compared with normal group. The COX2 inhibitor significantly reversed the increased of cortex and hippocampus COX2 expression. Data are expressed as the mean ± SD for three (IHC) and four (WB) individual rats in each group, and were analyzed statistically using one-way ANOVA, followed by *post hoc* Tukey's test. $^{**}P < 0.01$ compared with normal group; $^{\#}P < 0.05$ and $^{\#\#}P < 0.01$ compared with model group, respectively.

has been a focus in many studies (Sebastião et al., 2014). Many studies have proven that COX2 is involved in various chronic central nervous system injuries, and the mechanism of the damage is related to inflammation and apoptosis. Autophagy is decreased and inversely correlated with COX2 expression in nasal polyps (Wang L.F. et al., 2015). Celecoxib, a COX2 inhibitor, could significantly increase the LC3BII expression to enhance autophagy level in human prostate cancer PC3 cells (Zhu et al., 2017). These results suggested that autophagy inhibition is an injury mechanism of COX2. In our study, we found the functions of learning and memory to be significantly impaired, and the cortex and hippocampus neurons had significant nuclear pyknosis in the model rats. The expressions of COX2, Beclin1 and p62 were significantly increased and that of LC3BII was significantly decreased in the cortex and hippocampus of model rats. The PGD2 content was significantly

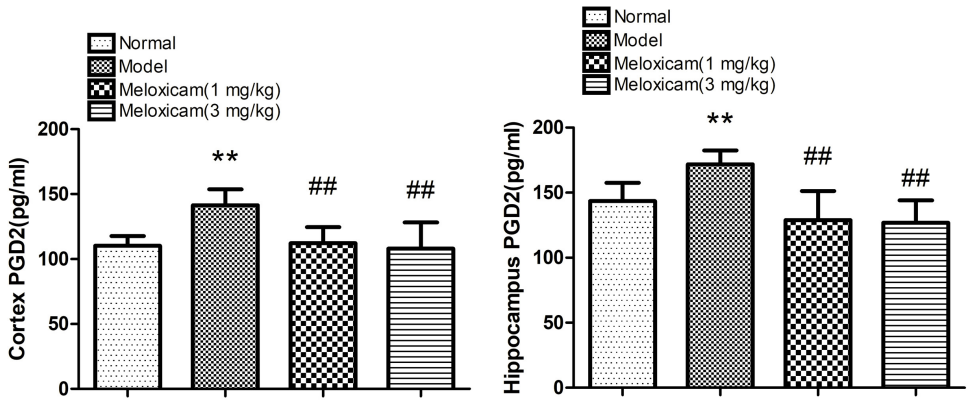

FIGURE 6 | Effect of COX2 inhibitor on changes of hippocampus and cortex PGD2 content in T2DM rat cortex and hippocampus. Compared with that of normal group, the contents of PGD2 significantly increased in model group. Compared with that of model group, the administration of COX2 inhibitor significantly decreased the content of PGD2. Data are expressed as the mean ± SD for six individual rats in each group, and were analyzed statistically using one-way ANOVA, followed by *post hoc* Tukey's test. $^{**}P < 0.01$ compared with normal group. $^{\#\#}P < 0.01$ compared with model group, respectively.

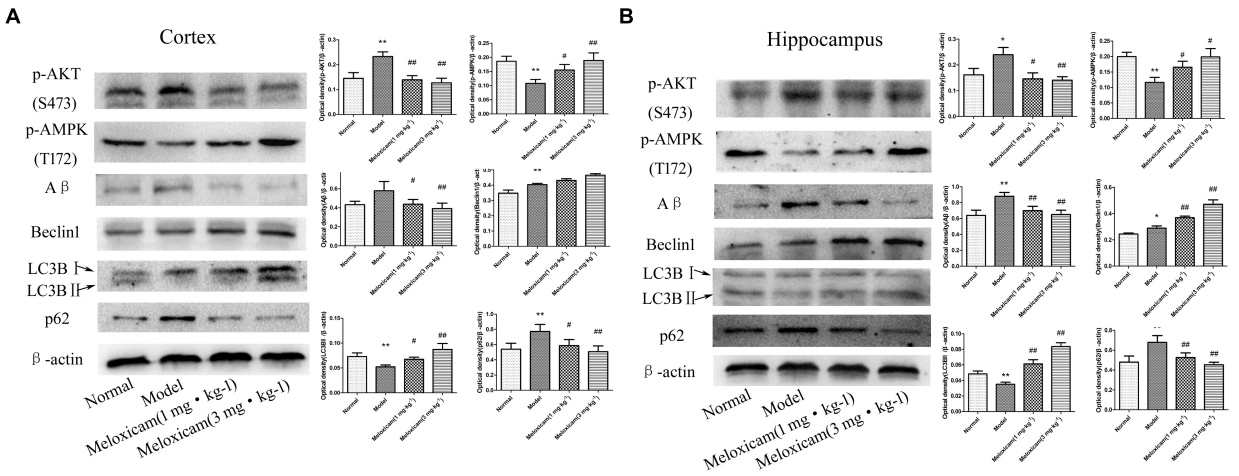

FIGURE 7 | Changes of p-AKT(S473), p-AMPK(T172), Aβ, Beclin1, LC3BII, and p62 expressions in rat cortex and hippocampus. **(A)** The changes of proteins in cortex. **(B)** The changes of proteins in hippocampus. Compared with normal group, the expressions of p-AKT(S473), Aβ, Beclin1, and p62 were significantly increased, while p-AMPK(T172) and LC3BII expression was significantly decreased in the model group. The COX2 inhibitor significantly increased the expression of p-AMPK(T172), Beclin1 and LC3BII, while significantly decreased the expression of p-AKT(S473), Aβ, and p62. The relative protein level was standardized to endogenous β-actin protein for each sample. Data are expressed as mean ± SD of four individual rats in each group, and were analyzed statistically using one-way ANOVA, followed by *post hoc* Tukey's test. $^{*}P < 0.05$ and $^{**}P < 0.01$ compared with normal group; $^{\#}P < 0.05$ and $^{\#\#}P < 0.01$ compared with model group, respectively.

increased in the cortex and hippocampus of model rats. Beclin1 is a key protein in the initial stage of autophagy and promotes the formation of the autophagosome (Reggiori et al., 2005; Mizushima, 2010). However, this autophagosome is still not fully functional. LC3BII represents the effect of strength of the autophagosome, and the degradation of p62 expression by the autophagosome reflects the level of autophagic flux (Klionsky et al., 2010). In the cortex and hippocampus of model rats, we found that the expression of Beclin1 was significantly increased. However, the expression of LC3BII was decreased, thus indicating the lower effect strength of the autophagosome to decrease the degradation of p62, which consequently allowed for significantly increased expression of p62. Therefore, the autophagy level was decreased in the cortex and hippocampus of model rats. Our results suggested that the increase of COX2–PGD2 levels caused the decrease of autophagy in T2DM-induced brain injury.

In agreement with our results, studies showed that platelet-rich plasma induced chondroprotection, which was associated decreased COX2 and increased the autophagy level in human osteoarthritic cartilage (Moussa et al., 2017). Morin hydrate can decrease the COX2 expression and increase the autophagy level in the treatment of atherosclerosis (Zhou et al., 2017). Tart cherries can significantly improve the working memory of normal aged rats; this was accompanied with significantly decreased COX2 expression and significantly increased autophagy level in the hippocampus

(Thangthaeng et al., 2016). Some researchers found that the inhibition of autophagic flux induced M1 microglial phenotype with a higher level of COX2 (Xia et al., 2016) and that M1 microglial phenotype is deleterious (Huang and Feng, 2013). Taken together, these results suggested that the decrease of autophagy may be an important causative factor of tissue injury caused by COX2 overexpression.

COX2-mediated autophagy inhibition may be due to the increase of PG production. Our previous studies found significantly increased COX2 and PGD2 levels in aluminum-overloaded rat brains (Wang H. et al., 2015; Ma et al., 2016). PGD2 may be related to the development and migration of microglia cells, which may be involved in various nerve injuries (Mohri et al., 2003). DP1 and DP2 are the corresponding receptors for PGD2. DP1 can stimulate adenylate cyclase to increase the intracellular cyclic adenosine monophosphate (cAMP) content and then activate PKA. DP2 can stimulate the PI3K/AKT/mTOR pathway (Hata and Breyer, 2004). Some studies indicated that PGD2 could increase the expression of p-AKT(S473) (Wang et al., 2008). Those results suggested that PGD2 increases the expression of AKT through DP2. Although it is known that PKA is involved in the regulation of autophagy (Torres-Quiroz et al., 2015), its exact role in autophagy remains unclear. The PI3K/AKT/mTOR pathway is a classical regulatory pathway of autophagy, and the activation of the PI3K/AKT/mTOR pathway can inhibit the expression of Beclin1 and LC3BII to decrease the autophagy level (Meijer and Codogno, 2006). Our results showed that p-AKT(S473), Beclin1 and p62 expressions were significantly increased, whereas the p-AMPK(T172) and LC3BII expression was significantly decreased in the cortex and hippocampus of model rats. Therefore, Our results suggest that PGD2 is involved in the mechanism of autophagy inhibition.

AMPK is a key protein in the regulation of autophagy. The activation of AMPK can decrease mTOR expression to promote autophagy. Kainuma reported that p-AMPK(T172) is induced by PGD2 in MC3T3-E1 cells (Kainuma et al., 2015). However, in our study, the expression of p-AMPK(T172) was significantly decreased in the cortex and hippocampus of T2DM rats. The reason for the difference in p-AMPK(T172) expression between our's and Kainuma's results may be explained as follows: (1) The tissue material for the detection of p-AMPK(T172) expression is different. Osteoblastic cell lines (MC3T3-E1) were used in Kainuma's study, while rats cortex and hippocampus were used in our study. However, whether this difference in the material used for detection can affect the experimental results is not clear. (2) The stimulating pattern for p-AMPK(T172) expression is not exactly the same. MC3T3-E1 cells were only treated with PGD2 in Kainuma's study. In contrast, in our study, rats were treated with a high-fat diet (HFD) and STZ, which further increased the PGD2 and blood glucose. (3) The cell/rat processing times are different (reflecting the difference between an acute and chronic disease model). The MC3T3-E1 cells were only treated with PGD2 for 1 min to 60 min in Kainuma's study. In contrast, in our study, rats were treated with a HFD for 8 weeks and STZ once during week 4, consistent with a chronic injury model.

Some experimental findings are similar to ours. The effects of PGD2 were different in different models; for example, a decrease of PGD2 was associated with depressive behavior (Chu et al., 2017), and PGD2 promoted apoptosis in transgenic APP/PS1 mice (Guo J.W. et al., 2017). Moreover, the expression of p-AMPK(T172) changes with time in focal cerebral ischemia injury (Fu et al., 2016).

Similar to our results, the expression of p-AMPK(T172) was significantly decreased in the cortex of transgenic db/db DM mice and STZ-induced DM rats (Liu et al., 2016; Peng et al., 2016). The reason for the decrease in p-AMPK(T172) may be related to p-AKT(S473). Moreover, the expression of p-AKT(S473) was significantly increased in the cortex of db/db mice (Peng et al., 2016). We also found that the expression of p-AKT(S473) was significantly increased in the cortex and hippocampus in the rat model. Some studies have demonstrated that p-AKT(S473) can significantly reduce the expression of p-AMPK(T172) by inhibiting liver kinase B1(LKB1) (Kovacic et al., 2003; Soltys et al., 2006). LKB1 can be expressed in the brain, where it has important effects (Ryan et al., 2017).

The massive generation and deposition of Aβ is a major pathological feature in AD brain. It is known that diabetes can significantly increase the risk of AD (Ott et al., 1999). The Aβ expression in rat brain capillaries increased 2.5 times after oxygen and glucose deprivation (Bulbarelli et al., 2012), and the expression of Aβ in the hippocampus also increased significantly in scopolamine-induced memory impairment (Hafez et al., 2017). Taken together, these studies suggested Aβ as a direct reason of central nervous system injury. Our experimental results also showed that the expression of Aβ was significantly increased in T2DM rat brains and that meloxicam significantly decreased the Aβ expression. Similar with our results, it was reported that Aβ level was significantly increased in the brain of T2DM patients (Yang and Song, 2013), and the levels of Aβ and its precursor were significantly increased in the forebrain cortex of T2DM rats (Li et al., 2007). Early studies suggested that fibrous Aβ is neurotoxic and is responsible for the death of nerve cells. However, recent studies have shown that soluble Aβ is an important source of neurotoxicity and is more toxic than fibrous Aβ (Hernandez et al., 2010). Some studies have also shown that soluble Aβ, which is isolated from the brain tissue of AD patients, can induce hyperphosphorylation of tau protein in hippocampal neurons and damage the cytoskeleton of microtubules (Jin et al., 2011).

The inhibition of COX2 may be an effective way to enhance autophagy level by decreasing the PGD2 content, and then, the Aβ will get cleared. In meloxicam-treated rats, the cognitive dysfunction was significantly improved, and the content of PGD2 was significantly decreased in the cortex and hippocampus. Furthermore, the expressions of COX2, p-AKT(S473), Aβ and p62 were significantly decreased, and the expression of p-AMPK(T172), Beclin1 and LC3BII was significantly increased in the cortex and hippocampus. The COX2 inhibitor decreased the PGD2 content to alleviate the activation of DP2. The decreased activation of DP2 is expected to decrease the expression of the PI3K/AKT/mTOR pathway, and then, the increased expression of Beclin1 and LC3BII may improve the levels of autophagy. However, the effect of DP1 (PKA pathway)

on autophagy remains unknown. Some studies indicated that the PKA inhibitor significantly increased the LC3BII expression in the rats hippocampus (Azimi et al., 2016), and another study indicated that neuropeptide Y via PKA stimulates autophagy in hypothalamic neurons to delay aging and produce protective effects against hypothalamic impairments associated with age (Aveleira et al., 2015). The decreased expression of p-AKT(S473) will increase the expression of p-AMPK(T172), and then, the increase expression of Beclin1 and LC3BII may promote autophagy. The effect of DP1 (PKA pathway) on autophagy is still controversial and needs further verification in T2DM-induced brain injury by another experiments. However, our results indicated that the ultimate result of the decrease of PGD2 was increased autophagy levels in T2DM-induced brain injury.

In our studies, we found that Beclin1 expression was not coherent with the behavior of LC3II and p62. Our results found that PGD2 was significantly increased in the cortex and hippocampus of model rats. In many studies, Beclin1 was reported to be increased not only in chronic injuries, such as T2DM-induced brain injury (Carvalho et al., 2015), but also acute injuries, such as cerebral ischemia stroke (Guo D. et al., 2017). These results suggested that Beclin1 may show a compensatory increase in the sustained protection of the cortex and hippocampus of model rats. The decrease in the expression of LC3BII represents the lower efficacy of the autophagosome to decrease the degradation of p62; consequently, the expression of p62 was then significantly increased. Therefore, the expression of Beclin1 and p62 was significantly increased and the expression of LC3BII was significantly decreased in the cortex and hippocampus of model rats compared with the normal rats. The autophagy level was significantly decreased in the cortex and hippocampus of model rats. The expression of Beclin1 and LC3BII was significantly increased when the COX2 inhibitor treatment was performed to decrease the expression of mTOR by decreasing the PGD2 content to decrease the expression of p-AKT(S473) and increase the expression of p-AMPK(T172). The number and effect strength of the autophagosome significantly increased, and then, the expression of p62 significantly decreased. Therefore, compared with the model rats, the expression of Beclin1 and LC3BII was significantly increased and that of p62 was significantly decreased when the COX2 inhibitor treatment was performed in the cortex and hippocampus of meloxicam-treated rats. The autophagy level was increased in the cortex and hippocampus of meloxicam-treated rats. Conversely, recent studies found that p62 stabilizes COX2 protein through the p62 ubiquitin-associated domain (Sample et al., 2017). The increase of p62 can aggravate the COX2/PGD2-induced damage. The inhibition of COX2 not only decreases the expression of COX2 but also reduces the level of p62 by increasing the autophagy levels.

In summary, our present experimental results suggested that the activation of COX2-PGD2 pathway is involved in the mechanism of brain injury caused by T2DM through inhibiting autophagy to decrease the Aβ clearance. These findings pointed out that the COX2-PGD2 pathway is a potential therapeutic target for T2DM brain injury.

AUTHOR CONTRIBUTIONS

JY made substantial contribution to conception, design, and performance of the study. YY, QC, QZ, YLu, YX, WD, HW, HL, LY, CH, JZ, YLi, HX, ZC, JM, and XT participated in performance of all experiments and carried out the data analysis. YY participated in performance of the study and in writing the manuscript. All authors read and approved the final manuscript.

FUNDING

This reported study was supported by research grants from the science and Technology Cooperation Program of Guizhou province LH[2016]7188[QIANKEHELH(2016)7188].

REFERENCES

Abdel-Halim, M. S., Lunden, I., Cseh, G., and Anggard, E. (1980). Prostaglandin profiles in nervous tissue and blood vessels of the brain of various animals. *Prostaglandins* 19, 249–258. doi: 10.1016/0090-6980(80)90023-4

Alagiakrishnan, K., Sankaralingam, S., Ghosh, M., Mereu, L., and Senior, P. (2013). Antidiabetic drugs and their potential role in treating mild cognitive impairment and Alzheimer's disease. *Discov. Med.* 16, 277–286.

Aveleira, C. A., Botelho, M., Carmo-Silva, S., Pascoal, J. F., Ferreira-Marques, M., Nóbrega, C., et al. (2015). Neuropeptide Y stimulates autophagy in hypothalamic neurons. *Proc. Natl. Acad. Sci. U.S.A.* 112, E1642–E1651. doi: 10.1073/pnas.1416609112

Azimi, L., Kachooeian, M., Khodagholi, F., Yans, A., Heysieattalab, S., Vakilzadeh, G., et al. (2016). Protective effects of salicylate on PKA inhibitor (H-89)-induced spatial memory deficit via lessening autophagy and apoptosis in rats. *Pharmacol. Biochem. Behav.* 150-151, 158–169. doi: 10.1016/j.pbb.2016.10.008

Bulbarelli, A., Lonati, E., Brambilla, A., Orlando, A., Cazzaniga, E., Piazza, F., et al. (2012). Aβ42 production in brain capillary endothelial cells after oxygen and glucose deprivation. *Mol. Cell. Neurosci.* 49, 415–422. doi: 10.1016/j.mcn.2012.01.007

Candeias, E., Sebastião, I., Cardoso, S., Carvalho, C., Santos, M. S., Oliveira, C. R., et al. (2018). Brain GLP-1/IGF-1 signaling and autophagy mediate exendin-4 protection against apoptosis in type 2 diabetic rats. *Mol. Neurobiol.* 55, 4030–4050. doi: 10.1007/s12035-017-0622-3

Carvalho, C., Santos, M. S., Oliveira, C. R., and Moreira, P. I. (2015). Alzheimer's disease and type 2 diabetes-related alterations in brain mitochondria, autophagy and synaptic markers. *Biochim. Biophys. Acta* 1852, 1665–1675. doi: 10.1016/j.bbadis.2015.05.001

Chiu, E. K., and Richardson, J. S. (1985). Behavioral and neurochemical aspects of prostaglandins in brain function. *Gen. Pharmacol.* 16, 163–175. doi: 10.1016/0306-3623(85)90064-3

Chu, C., Wei, H., Zhu, W., Shen, Y., and Xu, Q. (2017). Decreased prostaglandin D2 levels in major depressive disorder are associated with depression-like behaviors. *Int J. Neuropsychopharmacol.* 20, 731–739. doi: 10.1093/ijnp/pyx044

Consilvio, C., Vincent, A. M., and Feldman, E. L. (2004). Neuroinflammation, COX-2, and ALS-a dual role? *Exp. Neurol.* 187, 1–10.

Fang, L., Zhou, Y., Cao, H., Wen, P., Jiang, L., He, W., et al. (2013). Autophagy attenuates diabetic glomerular damage through protection of hyperglycemia-induced podocyte injury. *PLoS One* 8:e60546. doi: 10.1371/journal.pone.0060546

Fu, L., Huang, L., Cao, C., Yin, Q., and Liu, J. (2016). Inhibition of AMP-activated protein kinase alleviates focal cerebral ischemia injury in mice: interference with mTOR and autophagy. *Brain Res.* 1650, 103–111. doi: 10.1016/j.brainres.2016.08.035

Guo, D., Ma, J., Yan, L., Li, T., Li, Z., Han, X., et al. (2017). Down-regulation of lncrna MALAT1 attenuates neuronal cell death through suppressing Beclin1-dependent autophagy by regulating Mir-30a in cerebral ischemic stroke. *Cell Physiol. Biochem.* 43, 182–194. doi: 10.1159/000480337

Guo, J. W., Guan, P. P., Ding, W. Y., Wang, S. L., Huang, X. S., Wang, Z. Y., et al. (2017). Erythrocyte membrane-encapsulated celecoxib improves the cognitive decline of Alzheimer's disease by concurrently inducing neurogenesis and reducing apoptosis in APP/PS1transgenic mice. *Biomaterials* 145, 106–127. doi: 10.1016/j.biomaterials.2017.07.023

Hafez, H. S., Ghareeb, D. A., Saleh, S. R., Abady, M. M., El Demellawy, M. A., Hussien, H., et al. (2017). Neuroprotective effect of ipriflavone against scopolamine-induced memory impairment in rats. *Psychopharmacology* 234, 3037–3053. doi: 10.1007/s00213-017-4690-x

Han, K., Lehringer-Polzin, M., Zhou, H., and Pfeifer, U. (1992). Cellular autophagy in proximal tubules of early diabetic rats following insulin treatment and islet transplantation. *Virchows Arch. B Cell Pathol. Incl. Mol. Pathol.* 61, 367–373.

Hassing, L. B., Grant, M. D., Hofer, S. M., Pedersen, N. L., Nilsson, S. E., Berg, S., et al. (2004). Type 2 diabetes mellitus contributes to cognitive decline in old age: a longitudinal population-based study. *J. Int. Neuropsychol. Soc.* 10, 599–607. doi: 10.1017/S1355617704104165

Hata, A. N., and Breyer, R. M. (2004). Pharmacology and signaling of prostaglandin receptors: multiple roles in inflammation and immune modulation. *Pharmacol. Ther.* 103, 147–166. doi: 10.1016/j.pharmthera.2004.06.003

Hernandez, C. M., Kayed, R., Zheng, H., Sweatt, J. D., and Dineley, K. T. (2010). Loss of alpha7 nicotinic receptors enhances beta-amyloid oligomer accumulation, exacerbating early-stage cognitive decline and septohippocampal pathology in a mouse model of Alzheimer's disease. *J. Neurosci.* 30, 2442–2453. doi: 10.1523/JNEUROSCI.5038-09.2010

Huang, Y. C., and Feng, Z. P. (2013). The good and bad of microglia/macrophages: new hope in stroke therapeutics. *Acta Pharmacol. Sin.* 34, 6–7. doi: 10.1038/aps.2012.178

Jin, M., Shepardson, N., Yang, T., Chen, G., Walsh, D., and Selkoe, D. J. (2011). Soluble amyloid beta-protein dimers isolated from Alzheimer cortex directly induce Tau hyperphosphorylation and neuritic degeneration. *Proc. Natl. Acad. Sci. U.S.A.* 108, 5819–5824. doi: 10.1073/pnas.1017033108

Kainuma, S., Tokuda, H., Kuroyanagi, G., Yamamoto, N., Ohguchi, R., Fujita, K., et al. (2015). PGD2 stimulates osteoprotegerin synthesis via AMP-activated protein kinase in osteoblasts: regulation of ERK and SAPK/JNK. *Prostaglandins Leukot Essent Fatty Acids* 101, 23–29. doi: 10.1016/j.plefa.2015.08.003

Kemppainen, S., Hamalainen, E., Miettinen, P. O., Koistinaho, J., and Tanila, H. (2014). Behavioral and neuropathological consequences of transient global ischemia in APP/PS1 Alzheimer model mice. *Behav. Brain Res.* 275, 15–26. doi: 10.1016/j.bbr.2014.08.050

Kirkin, V., McEwan, D. G., Novak, I., and Dikic, I. (2009). A role for ubiquitin in selective autophagy. *Mol. Cell* 34, 259–269. doi: 10.1016/j.molcel.2009.04.026

Klionsky, D. J. (2008). Autophagy revisited: a conversation with Christian de Duve. *Autophagy* 4, 740–743. doi: 10.4161/auto.6398

Klionsky, D. J., Abdelmohsen, K., and Abe, A. (2010). Guidelines for the use and interpretation of assays for monitoring autophagy (3rd edition). *Autophagy* 12, 1–222. doi: 10.1080/15548627.2015.1100356

Kovacic, S., Soltys, C. L., Barr, A. J., Shiojima, I., Walsh, K., and Dyck, J. R. (2003). Akt activity negatively regulates phosphorylation of AMP-activated protein kinase in the heart. *J. Biol. Chem.* 278, 39422–39427. doi: 10.1074/jbc.M305371200

Li, M., Li, H., Zhou, Z., Zhou, Y., Wang, Y., Zhang, X., et al. (2016). Duodenal-jejunal bypass surgery ameliorates glucose homeostasis and reduces endoplasmic reticulum stress in the liver tissue in a diabetic rat model. *Obes. Surg.* 26, 1002–1009. doi: 10.1007/s11695-015-1816-2

Li, Z. G., Zhang, W., and Sima, A. A. (2007). Alzheimer-like changes in rat models of spontaneous diabetes. *Diabetes* 56, 1817–1824. doi: 10.2337/db07-0171

Lin, N. Y., Beyer, C., Giessl, A., Kireva, T., Scholtysek, C., Uderhardt, S., et al. (2013). Autophagy regulates TNFα-mediated joint destruction in experimental arthritis. *Ann. Rheum. Dis.* 72, 761–768. doi: 10.1136/annrheumdis-2012-201671

Ling, D., and Salvaterra, P. M. (2011). Brain aging and $A\beta_{1-42}$ neurotoxicity converge via deterioration in autophagy-lysosomal system: a conditional Drosophila model linking Alzheimer's neurodegeneration with aging. *Acta Neuropathol.* 121, 183–191. doi: 10.1007/s00401-010-0772-0

Liu, P., Yang, X., Hei, C., Meli, Y., Niu, J., Sun, T., et al. (2016). Rapamycin reduced ischemic brain damage in diabetic animals is associated with suppressions of mTOR and ERK1/2 signaling. *Int. J. Biol. Sci.* 12, 1032–1040. doi: 10.7150/ijbs.15624

Ma, J., Li, H., Hu, X., Yang, L., Chen, Q., Hu, C., et al. (2017). CMD-05, a novel promising clinical anti-diabetic drug candidate, in vivo and vitro studies. *Sci. Rep.* 7:46628. doi: 10.1038/srep46628

Ma, J., Yang, Q., Wei, Y., Yang, Y., Ji, C., Hu, X., et al. (2016). Effect of the PGD2-DP signaling pathway on primary cultured rat hippocampal neuron injury caused by aluminum overload. *Sci. Rep.* 6:24646. doi: 10.1038/srep24646

Meijer, A. J., and Codogno, P. (2006). Signalling and autophagy regulation in health, aging and disease. *Mol. Aspects Med.* 27, 411–425. doi: 10.1016/j.mam.2006.08.002

Mizukami, H., Takahashi, K., Inaba, W., Tsuboi, K., Osonoi, S., Yoshida, T., et al. (2014). Involvement of oxidative stress-induced DNA damage, endoplasmic reticulum stress,and autophagy deficits in the decline of β-cell mass in Japanese type 2 diabetic patients. *Diabetes Care* 37, 1966–1974. doi: 10.2337/dc13-2018

Mizushima, N. (2010). The role of the Atg1/ULK1 complex in autophagy regulation. *Curr. Opin. Cell Biol.* 22, 132–139. doi: 10.1016/j.ceb.2009.12.004

Mohri, I., Eguchi, N., Suzuki, K., Urade, Y., and Taniike, M. (2003). Hematopoietic prostaglandin D synthase is expressed in microglia in the developing postnatal mouse brain. *Glia* 42, 263–274. doi: 10.1002/glia.10183

Moussa, M., Lajeunesse, D., Hilal, G., El Atat, O., Haykal, G., Serhal, R., et al. (2017). Platelet rich plasma (PRP) induces chondroprotection via increasing autophagy, anti-inflammatory markers, and decreasing apoptosis in human osteoarthritic cartilage. *Exp. Cell Res.* 352, 146–156. doi: 10.1016/j.yexcr.2017.02.012

Ott, A., Stolk, R. P., van Harskamp, F., Pols, H. A., Hofman, A., and Breteler, M. M. (1999). Diabetes mellitus and the risk of dementia: the rotterdam study. *Neurology* 53, 1937–1942. doi: 10.1212/WNL.53.9.1937

Peng, Y., Liu, J., Shi, L., Tang, Y., Gao, D., Long, J., et al. (2016). Mitochondrial dysfunction precedes depression of AMPK/AKT signaling in insulin resistance induced by high glucose in primary cortical neurons. *J. Neurochem.* 137, 701–713. doi: 10.1111/jnc.13563

Reggiori, F., Shintani, T., Nair, U., and Klionsky, D. J. (2005). Atg9 cycles between mitochondria and the pre-autophagosomal structure in yeasts. *Autophagy* 1, 101–109. doi: 10.4161/auto.1.2.1840

Rubinsztein, D. C., Codogno, P., and Levine, B. (2012). Autophagy modulation as a potential therapeutic target for diverse diseases. *Nat. Rev. Drug Discov.* 11, 709–730. doi: 10.1038/nrd3802

Ryan, C. M., and Geckle, M. O. (2000). Circumscribed cognitive dysfunction in middle-aged adults with type 2 diabetes. *Diabetes Care* 23, 1486–1493. doi: 10.2337/diacare.23.10.1486

Ryan, K. E., Kim, P. S., Fleming, J. T., Brignola, E., Cheng, F. Y., Litingtung, Y., et al. (2017). Lkb1 regulates granule cell migration and cortical folding of the cerebellar cortex. *Dev. Biol.* 432, 165–177. doi: 10.1016/j.ydbio.2017.09.036

Sample, A., Zhao, B., Qiang, L., and He, Y. Y. (2017). Adaptor protein p62 promotes skin tumor growth and metastasis and is induced by UVA radiation. *J. Biol. Chem.* 292, 14786–14795. doi: 10.1074/jbc.M117.786160

Sebastião, I., Candeias, E., Santos, M. S., Oliveira, C. R., Moreira, P. I., and Duarte, A. I. (2014). Insulin as a bridge between type 2 diabetes and alzheimer disease–how anti-diabetics could be a solution for dementia. *Front. Endocrinol.* 5:110. doi: 10.3389/fendo.2014.00110

Sima, A. A. (2010). Encephalo pathies the emergeing diabetic copmplications. *Acta Diabetol.* 47, 279–293. doi: 10.1007/s00592-010-0218-0

Soltys, C. L., Kovacic, S., and Dyck, J. R. (2006). Activation of cardiac AMP-activated protein kinase by LKB1 expression or chemical hypoxia is blunted by increased Akt activity. *Am. J. Physiol. Heart Circ. Physiol.* 290, H2472–H2479. doi: 10.1152/ajpheart.01206.2005

Strachan, M. W., Frier, B. M., and Deary, L. J. (2003). Type 2 diabetes and cognitive impairment. *Diabet Med.* 20, 1–2. doi: 10.1046/j.1464-5491.2003.00855.x

Teismann, P., Vila, M., Choi, D. K., Tieu, K., Wu, D. C., Jackson-Lewis, V., et al. (2003). COX-2 and neurodegeneration in Parkinson's disease. *Ann. N. Y. Acad. Sci.* 991, 272–277. doi: 10.1111/j.1749-6632.2003.tb07482.x

Thangthaeng, N., Poulose, S. M., Gomes, S. M., Miller, M. G., Bielinski, D. F., and Shukitt-Hale, B. (2016). Tart cherry supplementation improves working memory, hippocampal inflammation, and autophagy in aged rats. *Age* 38, 393–404. doi: 10.1007/s11357-016-9945-7

Tian, X., Ji, C., Luo, Y., Yang, Y., Kuang, S., Mai, S., et al. (2016). PGE2-EP3 signaling pathway contributes to protective effects of misoprostol on cerebral injury in APP/PS1 mice. *Oncotarget* 7, 25304–25314. doi: 10.18632/oncotarget.8284

Torres-Quiroz, F., Filteau, M., and Landry, C. R. (2015). Feedback regulation between autophagy and PKA. *Autophagy* 11, 1181–1183. doi: 10.1080/15548627.2015.1055440

Wang, B., Yang, Q., Sun, Y. Y., Xing, Y. F., Wang, Y. B., Lu, X. T., et al. (2014). Resveratrol-enhanced autophagic flux ameliorates myocardial oxidative stress injury in diabetic mice. *J. Cell. Mol. Med.* 18, 1599–1611. doi: 10.1111/jcmm.12312

Wang, H., Ye, M., Yu, L., Wang, J., Guo, Y., Lei, W., et al. (2015). Hippocampal neuronal cyclooxygenase-2 downstream signaling imbalance in a rat model of chronic aluminium gluconate administration. *Behav. Brain Funct.* 18:8. doi: 10.1186/s12993-015-0054-z

Wang, L. F., Chien, C. Y., Yang, Y. H., Hour, T. C., Yang, S. F., Chen, H. R., et al. (2015). Autophagy is deficient and inversely correlated with COX-2 expression in nasal polyps: a novel insight into the inflammation mechanism. *Rhinology* 53, 270–276. doi: 10.4193/Rhin14.232

Wang, S., Yang, Q., Fung, K. M., and Lin, H. K. (2008). AKR1C2 and AKR1C3 mediated prostaglandin D2 metabolism augments the PI3K/Akt proliferative signaling pathway in human prostate cancer cells. *Mol. Cell. Endocrinol.* 289, 60–66. doi: 10.1016/j.mce.2008.04.004

Wu, J. H., Haan, M. N., Liang, J., Ghosh, D., Gonzalez, H. M., and Herman, W. H. (2003). Impact of diabetes on cognitive function among older Latinos: a population-based cohort study. *J. Clin. Epidemiol.* 56, 686–693. doi: 10.1016/S0895-4356(03)00077-5

Xia, C. Y., Zhang, S., Chu, S. F., Wang, Z. Z., Song, X. Y., Zuo, W., et al. (2016). Autophagic flux regulates microglial phenotype according to the time of oxygen-glucose deprivation/reperfusion. *Int. Immunopharmacol.* 39, 140–148. doi: 10.1016/j.intimp.2016.06.030

Xu, W. L., Qiu, C. X., Wahlin, A., Winblad, B., and Fratiglioni, L. (2004). Diabetes mellitus and risk of dementia in the Kungsholmen project: a 6-year follow-up study. *Neurology* 63, 1181–1186. doi: 10.1212/01.WNL.0000140291.86406.D1

Yagami, T., Koma, H., and Yamamoto, Y. (2016). Pathophysiological roles of cyclooxygenases and prostaglandins in the central nervous system. *Mol. Neurobiol.* 53, 4754–4771. doi: 10.1007/s12035-015-9355-3

Yang, Y., and Song, W. (2013). Molecular links between Alzheimer's disease and diabetes mellitus. *Neuroscience* 250, 140–150. doi: 10.1016/j.neuroscience.2013.07.009

Yu, L., Jiang, R., Su, Q., Yu, H., and Yang, J. (2014). Hippocampal neuronal metal ion imbalance related oxidative stress in a rat model of chronic aluminum exposure and neuroprotection of meloxicam. *Behav. Brain Funct.* 10:6. doi: 10.1186/1744-9081-10-6

Zhang, J., Zhang, J. X., and Zhang, Q. L. (2016). PI3K/AKT/mTOR-mediated autophagy in the development of autism spectrum disorder. *Brain Res. Bull.* 125, 152–158. doi: 10.1016/j.brainresbull.2016.06.007

Zhou, Y., Cao, Z. Q., Wang, H. Y., Cheng, Y. N., Yu, L. G., Zhang, X. K., et al. (2017). The anti-inflammatory effects of Morin hydrate in atherosclerosis is associated with autophagy induction through cAMP signaling. *Mol. Nutr. Food Res.* 61:1600966. doi: 10.1002/mnfr.201600966

Zhu, X., Zhou, M., Liu, G., Huang, X., He, W., Gou, X., et al. (2017). Autophagy activated by the c-Jun N-terminal kinase-mediated pathway protects human prostate cancer PC3 cells from celecoxib-induced apoptosis. *Exp. Ther. Med.* 13, 2348–2354. doi: 10.3892/etm.2017.4287

Conflict of Interest Statement: The authors declare that the research was conducted in the absence of any commercial or financial relationships that could be construed as a potential conflict of interest.

frontiers in Cellular Neuroscience

ORIGINAL RESEARCH
published: 15 March 2019
doi: 10.3389/fncel.2019.00101

Homer1a Attenuates Endoplasmic Reticulum Stress-Induced Mitochondrial Stress After Ischemic Reperfusion Injury by Inhibiting the PERK Pathway

*Jialiang Wei[1,2†], Xiuquan Wu[1†], Peng Luo[1], Kangyi Yue[1], Yang Yu[1], Jingnan Pu[1], Lei Zhang[1], Shuhui Dai[1], Donghui Han[3] and Zhou Fei[1]**

[1]Department of Neurosurgery, Xijing Hospital, Fourth Military Medical University, Xi'an, China, [2]Department of Health Services, Fourth Military Medical University, Xi'an, China, [3]Department of Urology, Xijing Hospital, Fourth Military Medical University, Xi'an, China

Homer1a is the short form of a scaffold protein that plays a protective role in many forms of stress. However, the role of Homer1a in cerebral ischemia/reperfusion (I/R) injury and its potential mechanism is still unknown. In this study, we found that Homer1a was upregulated by oxygen and glucose deprivation (OGD) and that overexpression of Homer1a alleviated OGD-induced lactate dehydrogenase (LDH) release and cell death in cultured cortical neurons. After OGD treatment, the overexpression of Homer1a preserved mitochondrial function, as evidenced by less cytochrome c release, less reactive oxygen species (ROS) production, less ATP and mitochondrial membrane potential (MMP) loss, less caspase-9 activation, and inhibition of endoplasmic reticulum (ER) stress confirmed by the decreased expression of phosphate-PKR-like ER Kinase (p-PERK)/PERK and phosphate- inositol-requiring enzyme 1 (p-IRE1)/IRE1 and immunofluorescence (IF) staining. In addition, mitochondrial protection of Homer1a was blocked by the ER stress activator Tunicamycin (TM) with a re-escalated ROS level, increasing ATP and MMP loss. Furthermore, Homer1a overexpression-induced mitochondrial stress attenuation was significantly reversed by activating the PERK pathway with TM and p-IRE1 inhibitor 3,5-dibromosalicylaldehyde (DBSA), as evidenced by increased cytochrome c release, increased ATP loss and a higher ROS level. However, activating the IRE1 pathway with TM and p-PERK inhibitor GSK2656157 showed little change in cytochrome c release and exhibited a moderate upgrade of ATP loss and ROS production in neurons. In summary, these findings demonstrated that Homer1a protects against OGD-induced injury by preserving mitochondrial function through inhibiting the PERK pathway. Our finding may reveal a promising target of protecting neurons from cerebral I/R injury.

Keywords: ischemic stroke, homer1a, mitochondrial dysfunction, endoplasmic reticulum stress, PERK kinase

OPEN ACCESS

Edited by:
Sikha Saha,
University of Leeds, United Kingdom

Reviewed by:
Yu-Feng Wang,
Harbin Medical University, China
Francesco Bellanti,
University of Foggia, Italy

****Correspondence:***
Zhou Fei
feizhou@fmmu.edu.cn

†These authors have contributed equally to this work

Received: *21 October 2018*
Accepted: *27 February 2019*
Published: *15 March 2019*

Citation:
Wei J, Wu X, Luo P, Yue K, Yu Y, Pu J, Zhang L, Dai S, Han D and Fei Z (2019) Homer1a Attenuates Endoplasmic Reticulum Stress-Induced Mitochondrial Stress After Ischemic Reperfusion Injury by Inhibiting the PERK Pathway. Front. Cell. Neurosci. 13:101. doi: 10.3389/fncel.2019.00101

INTRODUCTION

Ischemic stroke (IS) is a sudden medical condition in which little or restricted blood flow to the brain results in cell death. IS has high mortality, in which almost half of the patients live less than 1 year, and high morbidity, with up to 75% of patients having physical, mental, and emotional disability (Hankey, 2017; Benjamin et al., 2018). Some mechanisms have been found to be responsible for post-IS neuronal injury, such as excitatory neurotransmitter release, calcium overload and free radical injury. However, few therapies have been discovered to treat IS efficiently (Pandya et al., 2011; Chen et al., 2012). The exact molecular pathways underlying the ischemic reperfusion (I/R) neuronal injury have not been fully illustrated.

Homer proteins are best known as scaffold proteins located at the postsynaptic density and are crucial in regulating neuronal signals (Huang et al., 2008). Homer1a, a short form of Homer protein, contains a conserved EVH1 domain but lacks the CC domain, which enables Homer1a to function as a negative regulator of long forms of Homer protein (Foa and Gasperini, 2009). Several studies have shown that Homer1a plays an important role in sleep management, anti-depression and chronic inflammatory pain (Tappe et al., 2006; Serchov et al., 2016; Diering et al., 2017). Our previous study showed that Homer1a protects neurons against N-Methyl-D-aspartate (NMDA)-induced injury (Wang et al., 2015), and we also found that Homer1a protects retinal ganglion cells against retinal I/R injury (Fei et al., 2015). However, the exact role of Homer1a in cerebral I/R injury and the associated mechanism have not been elucidated.

Mitochondria play pivotal roles in supplying cellular energy, signaling, cellular differentiation, and cell death, as well as maintaining control of the cell cycle and cell growth (Schumacker et al., 2014). As an indispensable energy reservoir, mitochondria control the lifeline of most cells. Dysfunction of mitochondria plays a key role in many nervous system diseases such as stroke and neurodegenerative diseases (Prentice et al., 2015). Studies have revealed the pivotal role of mitochondria in aggravating reperfusion injury *via* producing excessive free radicals (Sanderson et al., 2013). Many studies have focused on therapies such as antioxidants and pro-biogenesis targeting mitochondria, with substantial progress, indicating the importance of mitochondria in I/R injury (Mailloux, 2016; Bhatti et al., 2017). The endoplasmic reticulum (ER) is also an important organelle that is responsible for protein folding and calcium homeostasis. Misfolded protein overload under various stresses results in ER turbulence, which is also known as ER stress (Chen et al., 2017). Previous studies have shown that ER stress is a major mechanism in I/R injury-induced apoptosis in the liver, myocardium and brain (Wang et al., 2016; Imarisio et al., 2017; Wu et al., 2017). Our previous studies showed that Homer1a preserves mitochondrial function in PC12 cells under oxidative stress induced by hydrogen peroxide and regulates the calcium equilibrium in HT22 cells under glutamate-induced injury (Luo et al., 2012a; Rao et al., 2016). However, the underlying mechanism between Homer1a and mitochondria and whether Homer1a influences ER stress after cerebral I/R are still unclear.

In the present study, it is aimed to survey the expression dynamics of Homer1a after neuronal ischemia-reperfusion injury and to determine the effect of Homer1a against IR injury. The effect of Homer1a on mitochondria dysfunction and ERS, as well as the relationship between them are also investigated. Furthermore, drug administration is implemented to inquire the specific mechanism involving PKR-like ER kinase (PERK) and inositolrequiring protein 1 (IRE1) pathways.

MATERIALS AND METHODS

Rat Primary Cultured Cortical Neurons

All procedures and animal manipulations were designed according to the National Institute of Health (NIH) Guide for the Care and Use of Laboratory Animals (No. 85-23) and were approved by the Ethics Committee of the Fourth Military Medical University. Primary cultured neurons were sampled from pregnant C57 mice using specified methods. Briefly, we removed embryos at 15–16 days and subsequently minced the meninges and vessels under a microscope. Then, we separated the cortex from the cerebrum and shredded it. The cortex then was digested in pancreatic enzymes for 20 min at 37°C with gentle shaking every 5 min. The digested neurons were resuspended in NM medium composed of neurobasal medium, 0.5 mM L-glutamine and 2% B27 before being plated onto the Poly-L-Lysine (PLL) pretreated dishes with a density of 1.5×10^6 cells/cm^2. The neurons were cultured in a 5% CO_2 incubator at 37°C, and the culture medium was renewed every 3 days.

Lentivirus Construction and Transfection

The preparation of a Homer1a Lentivirus was described previously (Luo et al., 2012a). The lentivirus overexpression open reading frame was the Pgc-fu-Homer1a cDNA-3FLAG construct (GeneChem Co., Shanghai, China). The primary cultured cortical neurons were cultured 8 days before being transfected with lentivirus for 72 h with an approximate multiplicity of infection (MOI) of 20.

Oxygen and Glucose Deprivation (OGD)

To mimic the I/R injury, the culture medium was renewed with glucose-free Neurobasal after being washed three times with PBS, and the neurons were then cultured in a specific chamber containing 5% CO_2 and 95% N_2 at 37°C for 1 h to simulate ischemic injury. Neurons were then removed from the chamber and washed with PBS three times before being reinfused with NM medium and maintained in a 5% CO_2 incubator at 37°C for a designated time to simulate the reperfusion injury.

Cell Viability Assay

The neurons with or without various interventions were cultured with the Cell Counting Kit-8 (CCK-8; Dojindo, Japan) for 4 h at a concentration of 10 μl/5,000 neurons. The absorbance of each well was determined by a microplate reader (Bio-Rad, Hercules, CA, USA) at 450 nm.

Lactate Dehydrogenase (LDH) Assay

A Cytotoxicity Detection Kit Plus (Roche Applied Bioscience, Indianapolis, IN, USA) was used to measure the release of lactate dehydrogenase (LDH), and all procedures were implemented following the manufacturer's protocol. Each group had its own maximum release group, and the LDH release was calculated in each group as the experimental value/maximum release × 100%.

Antibodies and Reagents

The primary antibodies used are listed as follows: anti-cytochrome c (1:1,000, 10993-1-AP, Proteintech, rosemont, IL, USA), anti-caspase-9 (1:1,000, #9508, Cell Signaling, Danvers, MA, USA), anti-PERK (1:1,000, #3192, Cell Signaling, Danvers, MA, USA), anti-phosphorylated-PERK (anti-p-PERK; Thr982;1:800, DF7576, Affinity Biosciences, Cincinnati, OH, USA), anti-IRE1 (1:500, ab37073, Abcam, Cambridge, MA, USA), anti-p-IRE1 (phosphor S724; 1:1,000, ab48187, Abcam, Cambridge, MA, USA), anti-activating transcription factor 6 (anti-ATF6; 1:1,000, ab203119, Abcam, Cambridge, MA, USA), anti-N'ATF6 (1:800, ab37149, Abcam, Cambridge, MA, USA) and anti-β-actin (1:3,000, GTX109639, GeneTex, Irvine, CA, USA). The ER stress activator Tunicamycin (TM) and the p-PERK inhibitor GSK2656157 were obtained from MedChem Express (Monmouth Junction, NJ, USA). The p-IRE1 inhibitor 3,5-dibromosalicylaldehyde (DBSA) was obtained from Tokyo Chemical Industry (TCI, Tokyo, Japan).

Western Blot Analysis

Neurons were lysed by RIPA with a protease inhibitor cocktail (Roche Applied Bioscience, Indianapolis, IN, USA), and the protein concentration of each sample was measured using a BCA quantification assay (Biosynthesis biotechnology, Beijing, China). Equivalent amounts of protein (30 μg) were separated by 6%–12% SDS-PAGE gels before being transferred onto the methanol pretreated polyvinylidene difluoride (PVDF) membranes. After being soaked in 5% defatted milk dissolved in Tris-phosphate buffer with 0.05% Tween 20 (TBST) for 1 h, the membranes were incubated overnight at 4°C. The membrane was incubated in secondary antibody diluent for 1 h at room temperature before its immunoreactivity was detected using Super Signal West Pico Chemiluminescent Substrate (Thermo Scientific, Rockford, IL, USA). The intensity of the protein bands was calculated *via* ImageJ with normalization to that of β-actin.

Cytoplasmic/Mitochondrial Protein Extraction

This procedure was implemented by using ProteoExtract Cytosol/Mitochondria Fractionation Kit (Calbiochem, Germany) and subjected to the described protocols. Briefly, the neurons were collected with Accutase (Invitrogen, Carlsbad, CA, USA) and centrifuged twice with PBS at 600 *g* for 5 min. Then, the 1× cytoplasmic extraction buffer was used to resuspend the neurons on ice for 10 min before homogenizing the neuron suspension, which was then centrifuged at 700 *g* for 10 min at 4°C. The cytoplasmic protein was obtained by collecting the supernatant after centrifuging the supernatant collected in the last step at 10,000 *g* for 30 min at 4°C. The mitochondrial protein was obtained by resuspending the sediment with mitochondrial extraction buffer and vortexing for 10 s.

Measurement of Reactive Oxygen Species (ROS) Production

The intracellular reactive oxygen species (ROS) was determined using 2,7-dichlorodihydrofluorescein diacetate (H2-DCFDA), an intracellular ROS indicator, as previously reported. Cultured cortical neurons were incubated with 10 nM H2-DCFDA for 1 h at 37°C in a dark place. Then, the neurons were resuspended with PBS before being read by a fluorescence plate reader (excitation wavelength of 480 nm, emission wavelength of 530 nm).

Measurement of Mitochondrial Membrane Potential (MMP)

To monitor the mitochondrial membrane potential (MMP) of each group, the neurons were incubated in 10 mM fluorescent dye rhodamine 123 (RH 123) for 30 min at 37°C. Then, the neurons were washed with PBS three times before reading the fluorescence with a fluorescence plate reader (excitation wavelength of 480 nm, emission wavelength of 530 nm).

Measurement of Intracellular ATP

The ATP level was intraneuronally evaluated using an ATP assay kit (Beyotime, Shanghai, China), and the procedures were performed following the manufacturer's protocol. Briefly, the culture medium in the 96-well plate was removed, and the neurons were resuspended with 100 μl of working solution (ATP detection reagent: diluent = 1:5) for 5 min at room temperature. The ATP indication of each group was obtained *via* a fluorospectrophotometer and modified as a percentage of the control.

Immunofluorescence Staining

Cultured neurons were fixed in 4% paraformaldehyde for 20 min at room temperature in a dark place. Then, the neurons were treated with 0.3% Triton-X-100 for 20 min and blocked by 10% donkey serum for 3 h. After being washed with 1× PBS three times, the neurons were then incubated with rabbit anti-p-PERK (1:200) or rabbit anti-p-IRE1 (1:200) at 4°C overnight. The DAPI nuclei-staining was implemented for 10 min after the incubation of Alexa 594 donkey-anti-rabbit IgG (1:400) for 2 h at room temperature. The neurons were then visualized with a fluorescence microscope. To compare the immunoreactivity between different groups, all images were collected using the identical laser power, exposure time and detector sensitivity. At least five images were acquired by an researcher who was blinded to the experimental details.

Statistical Analysis

All the experimental procedures were performed at least three times. The statistical analysis was conducted using Bonferroni's multiple comparisons or an unpaired *t*-test (two groups) and univariate analyses of variance (ANOVA; more than two groups); the results were plotted with GraphPad Prism Software 6.0.

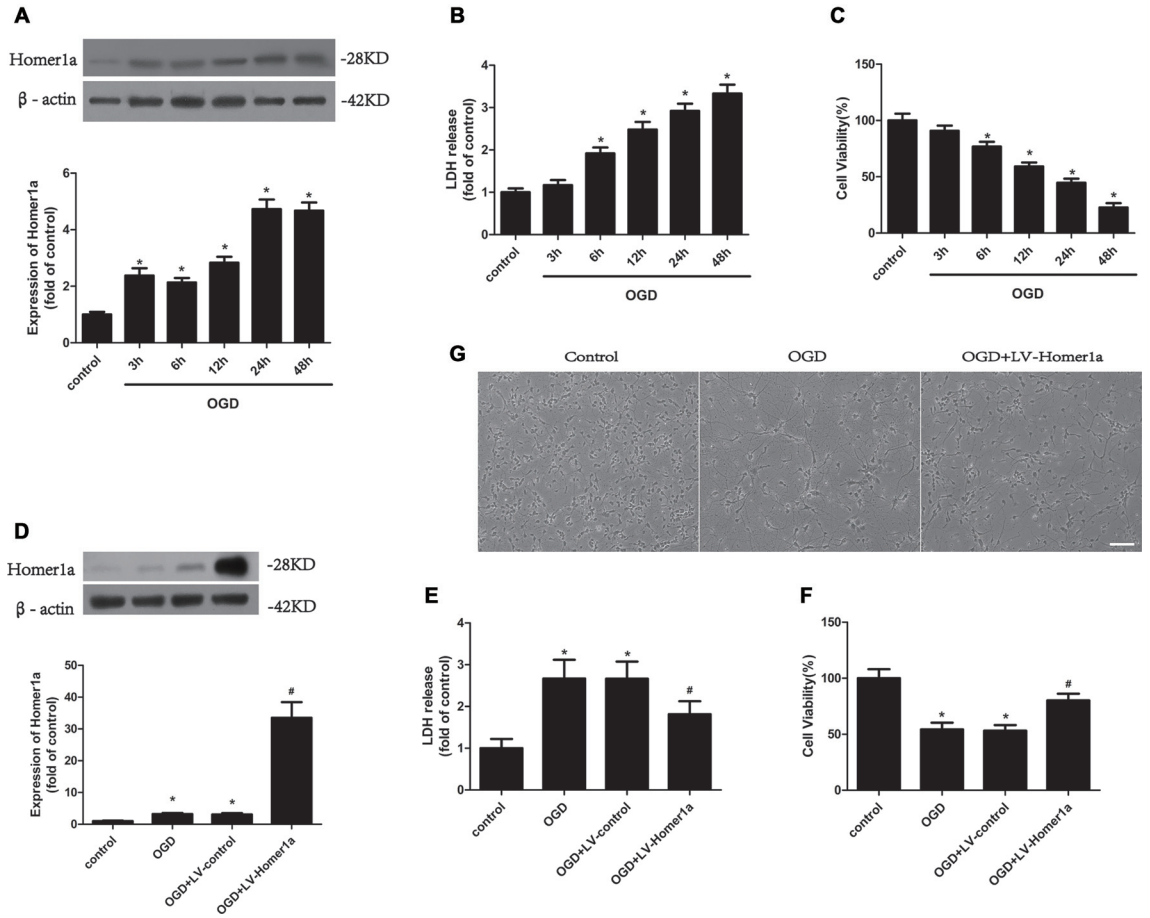

FIGURE 1 | Homer1a protects neurons against ischemia/reperfusion (I/R) injury. Cultured cortical neurons were treated with oxygen and glucose deprivation (OGD) for 1h, and the expression level of Homer1a protein at different reperfusion time points were investigated by Western blot **(A)**. Then the cytotoxicity of neurons was detected by lactate dehydrogenase (LDH) release assay **(B)** and the cell viability was evaluated by CCK-8 test **(C)**. The cortical neurons were then transfected with LV-Homer1a or LV-control for 72 h and exposed to OGD. The Homer1a protein expression was detect by Western blot **(D)**, and cytotoxicity and cell viability were tested in each group **(E,F)**. The cortical neurons were also observed under representative phase photomicrographs **(G)**. The data are represented as means ± SEM. $^{*}p < 0.05$ vs. Control, $^{\#}p < 0.05$ vs. OGD.

RESULTS

Homer1a Protects Neurons Against I/R Injury

To determine the effect of I/R injury on Homer1a, the cultured cortical neurons were treated with oxygen and glucose deprivation (OGD) for 1 h, and the expression level of Homer1a protein at different reoxygenation time points was investigated using Western blot. The results showed that the Homer1a protein levels increased significantly at 6, 12, 24 and 48 h with reperfusion (**Figure 1A**). The I/R injury-induced LDH release (**Figure 1B**) and reduced cell viability of neurons (**Figure 1C**) were elevated in a time-dependent manner. Given that the neuron survival was almost 50%, a 24 h reperfusion after OGD was used in the following experiments. To evaluate the effects of Homer1a, the Homer1a-targeted lentivirus (LV-Homer1a) or the negative control lentivirus (LV-control) was transfected into the neurons for 72 h, and the Western blot results showed that the LV-Homer1a protein expression was significantly increased (**Figure 1D**). The overexpression of Homer1a clearly decreased LDH release (**Figure 1E**) and promoted cell viability (**Figure 1F**) after I/R injury. Furthermore, representative phase photomicrographs exhibited that the LV-Homer1a transfected neurons showed less cell death relative to neurons without LV-Homer1a transfection (**Figure 1G**).

Homer1a Conserves Mitochondrial Function in Neurons After I/R Injury

We also evaluated whether Homer1a conserves the mitochondrial function following I/R injury. We transfected LV-Homer1a 72 h before exposing cultured cortical neurons to the OGD and reperfusion. The results revealed that the overexpression of Homer1a clearly decreased the cytochrome c release from the mitochondria to the cytoplasm (**Figure 2A**) and caspase-9 activation (**Figure 2B**). Additionally, Homer1a expression alleviated MMP loss (**Figure 2C**), reduced the

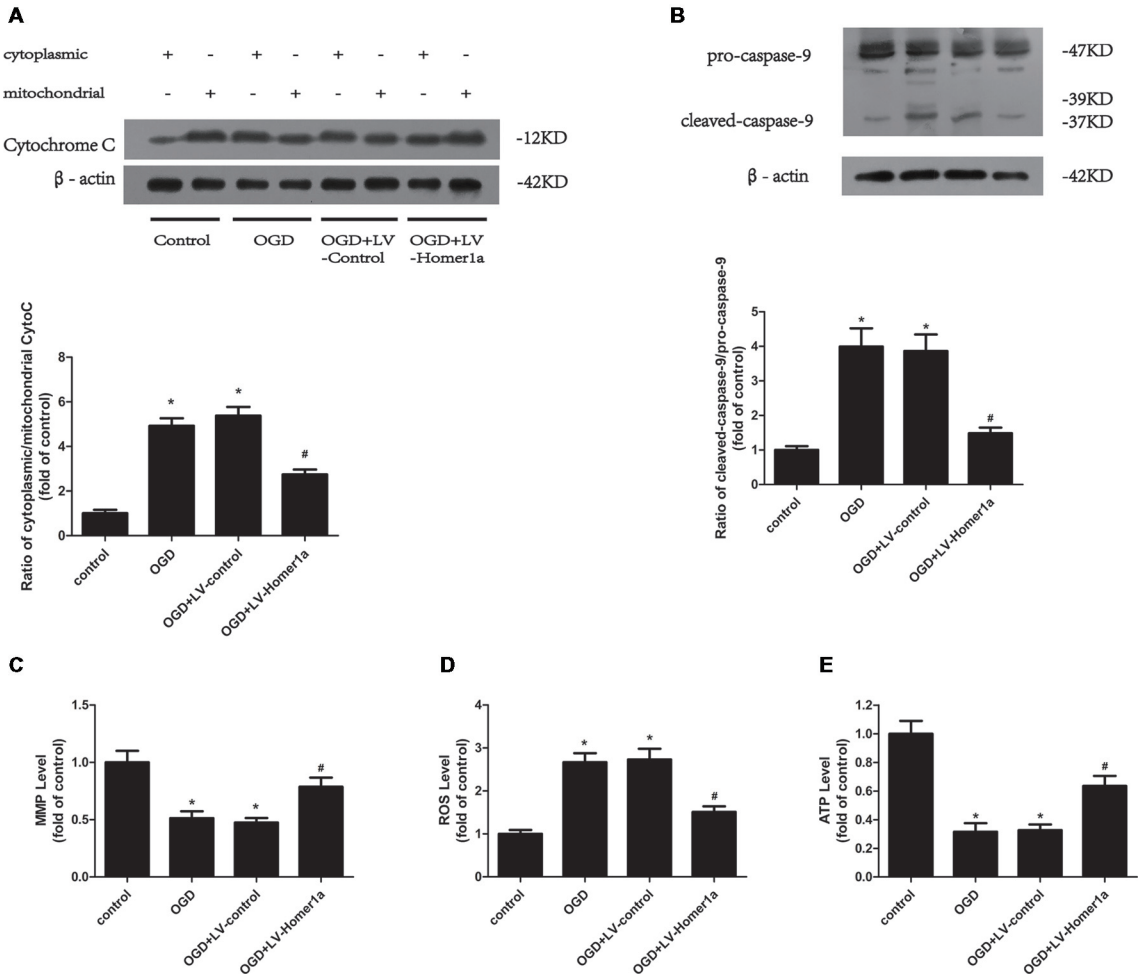

FIGURE 2 | Homer1a conserves mitochondrial function in neurons after I/R injury. Cultured cortical neurons were transfected with LV-Homer1a or LV-control for 72 h and exposed to OGD. The cytochrome c release to cytoplasm and the activation of caspase-9 were detected by Western blot **(A,B)**. The mitochondrial membrane potentials (MMPs) were detected by Rh123 test **(C)**, the intracellular reactive oxygen species (ROS) level was investigated through H_2-DCFDA **(D)** and the intracellular ATP level was measured by ATP assay **(E)**. The data are represented as means ± SEM. $^*p < 0.05$ vs. Control, $^\#p < 0.05$ vs. OGD.

intracellular ROS level (**Figure 2D**) and improved ATP loss (**Figure 2E**) in neurons that underwent I/R injury compared with that in neurons without LV-Homer1a transfection.

Homer1a Reduces ER Stress in Neurons That Underwent I/R Injury

We next examined the effect of Homer1a on ER stress after I/R exposure. The Western blot results showed that under the I/R injury, the ratios of p-PERK/PERK and p-IRE1/IRE1 were both reduced in neurons with Homer1a overexpression compared with neurons without LV-Homer1a lentivirus transfection (**Figure 3A**), whereas the Homer1a overexpression showed little effect on expression of ATF6 and its active form N'ATF6 (**Supplementary Figure S1**). The immunofluorescent results indicated that the effect of I/R injury on neurons significantly increased the fluorescence intensity of p-PERK and p-IRE1. However, neurons with Homer1a overexpression exhibited a significantly decreased fluorescence intensity of p-PERK and p-IRE1 (**Figures 3B,C**). Together, the above data showed that Homer1a overexpression reduced IR-induced ER stress.

Homer1a Alleviates Mitochondria Dysfunction by Reducing ER Stress After I/R Injury

To test whether the Homer1a effect of ER stress reduction is responsible for the conservation of mitochondrial function, we pretreated cortical neurons with 2 μg/L TM, an ER stress activator, 24 h before exposure to the I/R injury to counteract the ER stress reduction of Homer1a overexpression. The Western blot results showed that the TM abolished the reduced p-PERK/PERK and p-IRE1/IRE1 due to Homer1a overexpression (**Figure 4A**). Furthermore, the TM pretreatment of cortical neurons with LV-Homer1a-transfection under I/R injury reversed the ATP loss reduction (**Figure 4B**) and intracellular ROS reduction (**Figure 4C**) achieved by Homer1a

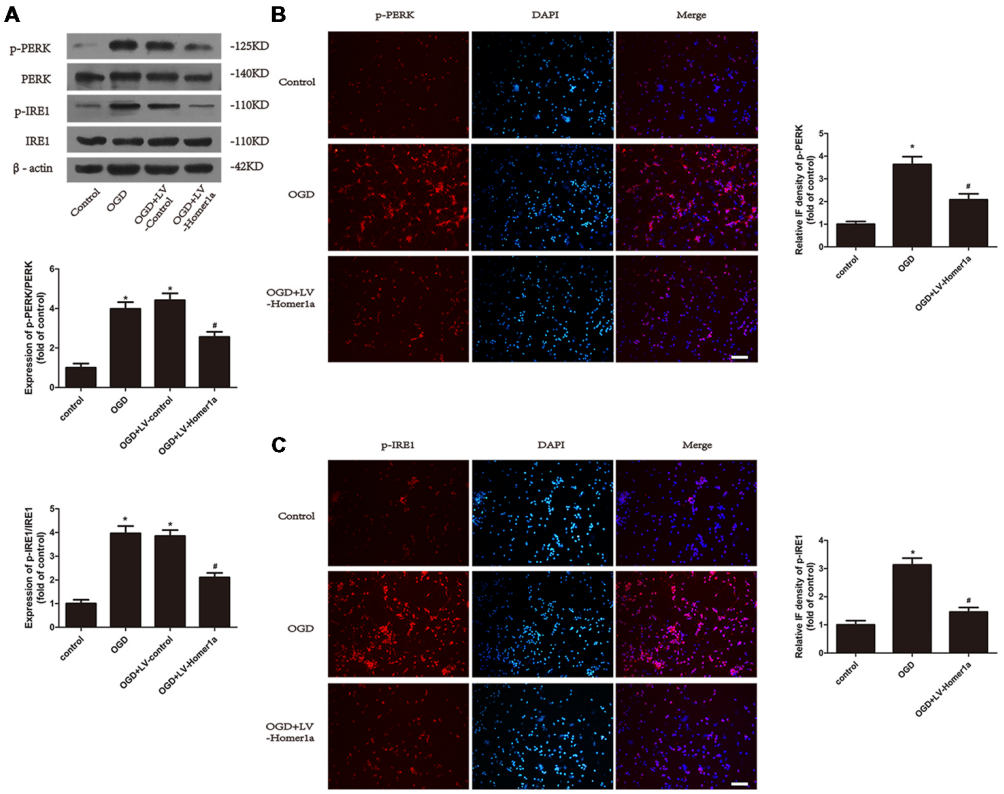

FIGURE 3 | Homer1a reduces endoplasmic reticulum (ER) stress in neurons that underwent I/R injury. Cultured cortical neurons were transfected with LV-Homer1a or LV-control for 72 h and exposed to OGD. Levels of phosphorylated-PKR-like ER kinase (p-PERK), PERK, phosphorylated-IRE1 (p-IRE1) and IRE1 were measured with Western blot **(A)**. The level of p-PERK and p-IRE1 were also determined with immunofluorescence (IF) staining. Images were captured with fluorescence microscope. Red: p-PERK or p-IRE1, blue: nuclei-staining by DAPI. Scale bar = 50 μm. The IF intensity of each group was calculated with ImageJ **(B,C)**. The data are represented as means ± SEM. $^{*}p < 0.05$ vs. Control, $^{\#}p < 0.05$ vs. OGD.

overexpression. Additionally, under I/R injury, LDH release was greater in neurons with LV-Homer1a and TM than in neurons with LV-Homer1a alone (**Figure 4D**).

Homer1a Preserves Mitochondrial Function by Reducing ER Stress Mainly *via* the PERK Pathway After I/R Injury

To further elucidate the mechanisms by which Homer1a reduces the ER stress to preserve mitochondrial function, we pretreated cortical neurons 24 h before any intervention with specific inhibitors to separately test each pathway of ER stress. As the Western blot results showed, 20 μM p-IRE1 specific inhibitor DBSA effectively blocked the phosphorylation of IRE1 (**Figure 5A**), and 5 nM GSK2656157, a specific p-PERK inhibitor, was efficient in reducing the phosphorylation of PERK (**Figure 5B**). As the appropriate dosage of each inhibitor was employed, the Western blot results revealed that neurons pretreated with TM and GSK2656157 showed significant reductions in cytochrome c release from mitochondria to the cytoplasm, whereas neurons pretreated with TM and DBSA showed little change under I/R injury (**Figure 5C**). Furthermore, compared with neurons pretreated with TM and DBSA, neurons pretreated with TM and GSK2656157 exhibited less ATP loss and a lower intracellular ROS level (**Figure 5D**).

DISCUSSION

The involvement of Homer1a in some central neuronal stress conditions has been found in our and previous studies (Luo et al., 2014; Schumacker et al., 2014; Wu et al., 2018). In this study, we revealed that Homer1a protects against neuronal I/R injury by preserving mitochondrial function and regulating ERS in primary cortical neurons. First, upregulated expression of Homer1a alleviated the I/R injury with less neuronal death. Second, upregulation of Homer1a helps restore mitochondrial function and mitigates ER stress activation. Third, the anti-ER stress effects of Homer1a were partially responsible for its pro-mitochondrial roles, which was attained mainly through the PERK pathway.

As an immediate early gene (IEG) that regulates the longer form of the homer gene, Homer1a was minimally expressed in the brain and other areas of the nervous system until the physiological conditions were disturbed. Studies have shown that upregulated Homer1a expression evoked by various forms of

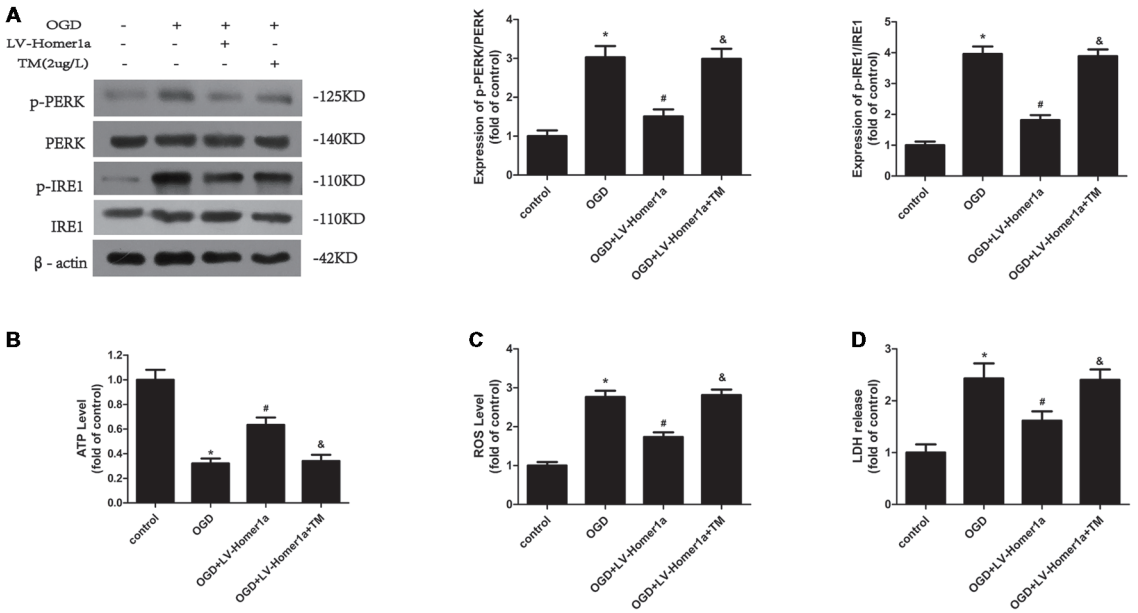

FIGURE 4 | Homer1a alleviates mitochondria dysfunction by reducing ER stress after I/R injury. Cultured cortical neurons were pre-treated with 2 μg/L Tunicamycin (TM) 24 h to activate the ER stress and exposed to I/R injury. The effects of TM were tested by Western blot **(A)**. The intracellular ATP level was measured by ATP assay **(B)** and the intracellular ROS level was investigated through H_2-DCFDA **(C)**. We also investigated the neurons cytotoxicity of each group with LDH release assay **(D)**. The data are represented as means ± SEM. $^{*}p < 0.05$ vs. Control, $^{\#}p < 0.05$ vs. OGD, $^{\&}p < 0.05$ vs. OGD+LV-Homer1a.

stress could help fight against various pathological processes (Tappe et al., 2006; Diering et al., 2017; Leber et al., 2017). Our previous study has shown that Homer1a protects neurons against TNF-a induced injury by interacting with the MAPK pathways (Luo et al., 2012b). Additionally, Wang et al. (2015). found the protective effect of Homer1a against NMDA-induced injury (Rao et al., 2016). Recently, Wu et al. (2018) found that Homer1a contributed a protective effect in HT22 cells under oxidative stress by inducing autophagy. Similarly, our study demonstrated that Homer1a was minimally expressed in rat cortical neurons but rose quickly after the onset of the I/R injury in a time-dependent manner that tended to dynamically stabilize after 24 h of reperfusion. Overexpression of Homer1a with a specific lentivirus increased neuronal survival and decreased LDH release after OGD, which indicated that Homer1a plays a protective role in the neuronal system in I/R conditions.

Because of the high demand for energy, the nervous system is more susceptible to mitochondrial dysfunction that impaired mitochondria is incapable of producing enough ATP to fill neuronal needs (Shulyakova et al., 2017). ROS production by mitochondria occurs in both physiological and pathological processes, and mitochondria dysfunction leads to the burst of ROS production and hinders oxidative phosphorylation as the mitochondrial membrane breaks down and finally leads to apoptotic cell death (Schieber and Chandel, 2014; Martin et al., 2018). Furthermore, the weakened membrane with higher permeability could lead to apoptotic factor release, such as the release of apoptosis-inducing factor and cytochrome c (Niizuma et al., 2010; Leaw et al., 2017). Cytochrome c includes procaspase-9, which is cleaved into caspase-9 and further triggers neuron apoptosis (Bennetts and Pierce, 2010). Our previous studies showed that Homer1a overexpression helps reduce oxidative stress and restore mitochondrial function in PC12 cells and HT-22 cells under oxidative stress (Luo et al., 2012a; Rao et al., 2016). Consistent with these studies, our results showed that Homer1a overexpression reduces ROS production and attenuates ATP and MMP loss in cortical neurons. Additionally, the overexpression of Homer1a reduces cytochrome c release from mitochondria to the cytoplasm as the ratio of cytoplasmic/mitochondrial cytochrome c decreases, which indicates that the Homer1a overexpression prevented the mitochondria from permeabilizing. The apoptic cell death was alleviated as the caspase-9 activation was reduced after Homer1a expression. All these results provide evidence that Homer1a protects mitochondrial function under I/R injury and thus stops neuronal apoptosis.

Three major transmembrane proteins are involved in the ER stress-activated unfolded protein response (UPR): IRE1, PERK and ATF6. All three proteins are coupled with the chaperone protein Bip and stay inactive under physiological conditions. When the UPR is activated, after the Bip dissociation, the IRE1 and PERK oligomerize and phosphorylate to activate their downstream signals, and ATF6 is cleaved by the Golgi and moves into the nucleus to act as a transcription promoter (Darling and Cook, 2014). ER stress is activated after IS and leads to cell damage (Yu et al., 2017). In our study, the results showed that IR significantly activated ER stress as evidenced by the hyperphosphorylation of PERK and IRE1 and enhanced

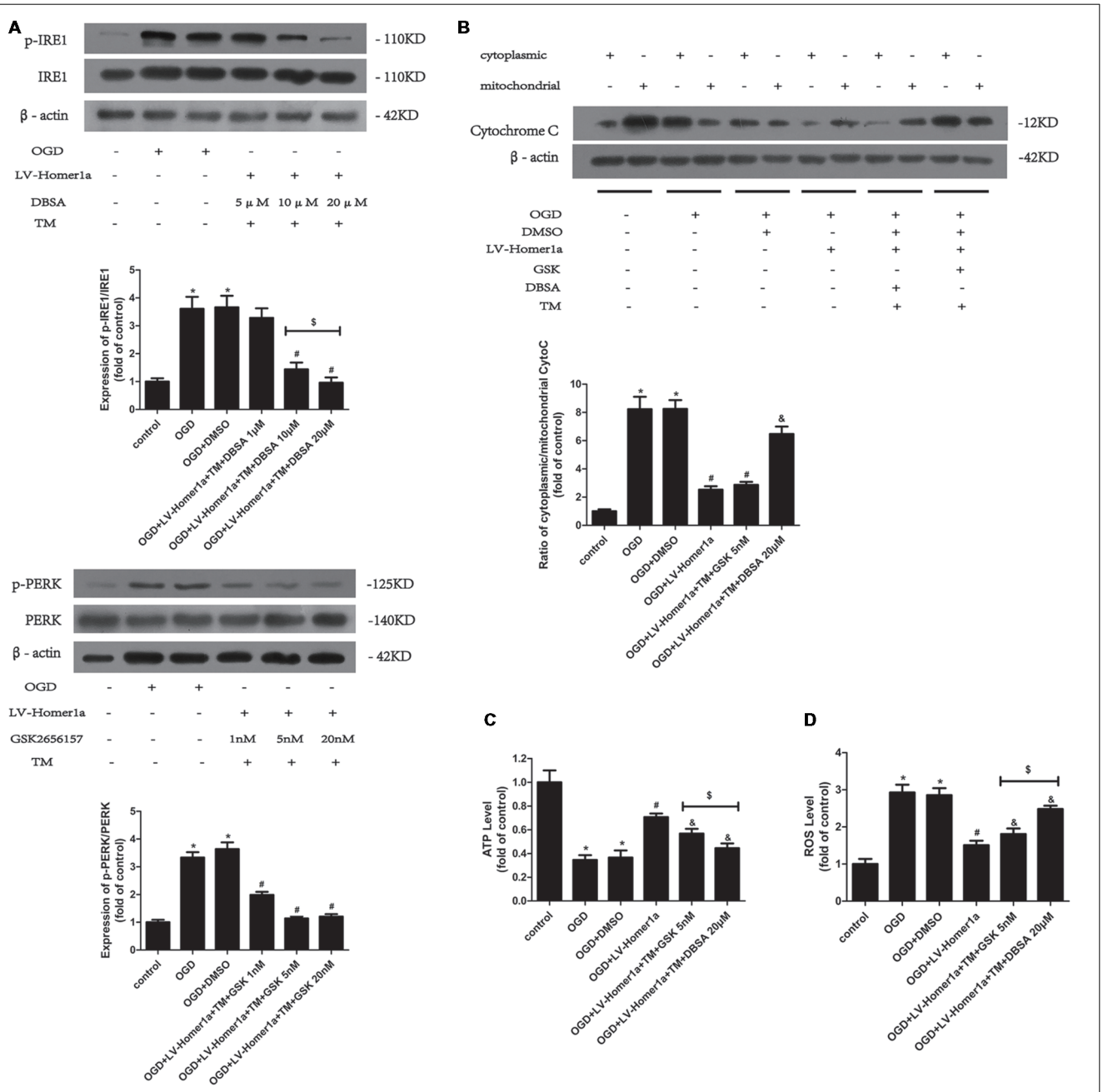

FIGURE 5 | Homer1a preserves mitochondrial function by reducing ER stress mainly *via* the PERK pathway after I/R injury. TM was used to activate the ER stress whereas the GSK2656157 and 3,5-dibromosalicylaldehyde (DBSA) were used to inhibit the PERK and IRE1 respectively. Different DBSA concentrations were tested in cortical neurons and detected by Western blot **(A)** as well as GSK2656157 **(B)**. Then 20 μM DBSA and 5 nM GSK2656157 were chosen to apply to follow experiments. The cytochrome c release to cytoplasm in each group was detected through calculating the ratio of cytoplasmic/mitochondrial cytochrome c by Western blot **(B)**. The intracellular ATP level was measured by ATP assay **(C)** and the intracellular ROS level was investigated through H_2-DCFDA **(D)**. The data are represented as means ± SEM. $^{\$}p < 0.05$, $^{*}p < 0.05$ vs. Control, $^{\#}p < 0.05$ vs. OGD, $^{\&}p < 0.05$ vs. OGD+LV-Homer1a.

fluorescence intensity of p-PERK and p-IRE1. Our previous study showed that downregulation of Homer1b/c, the long form in the homer family that plays an opposite role as Homer1a, inhibited the expression of CHOP, a downstream gene of all three pathways of ER stress, is considered to be a pro-apoptotic protein that mediates ER stress-induced apoptosis (Chen et al., 2012). Similarly, in the present study, our Western blot results showed less phosphorylation of the IRE1 and PERK proteins and reduced fluorescence intensity of phosphorylated IRE1 and PERK. These results demonstrate the anti-ER stress roles of Homer1a. However, our results showed no significant relationship between ATF6 and Homer1a

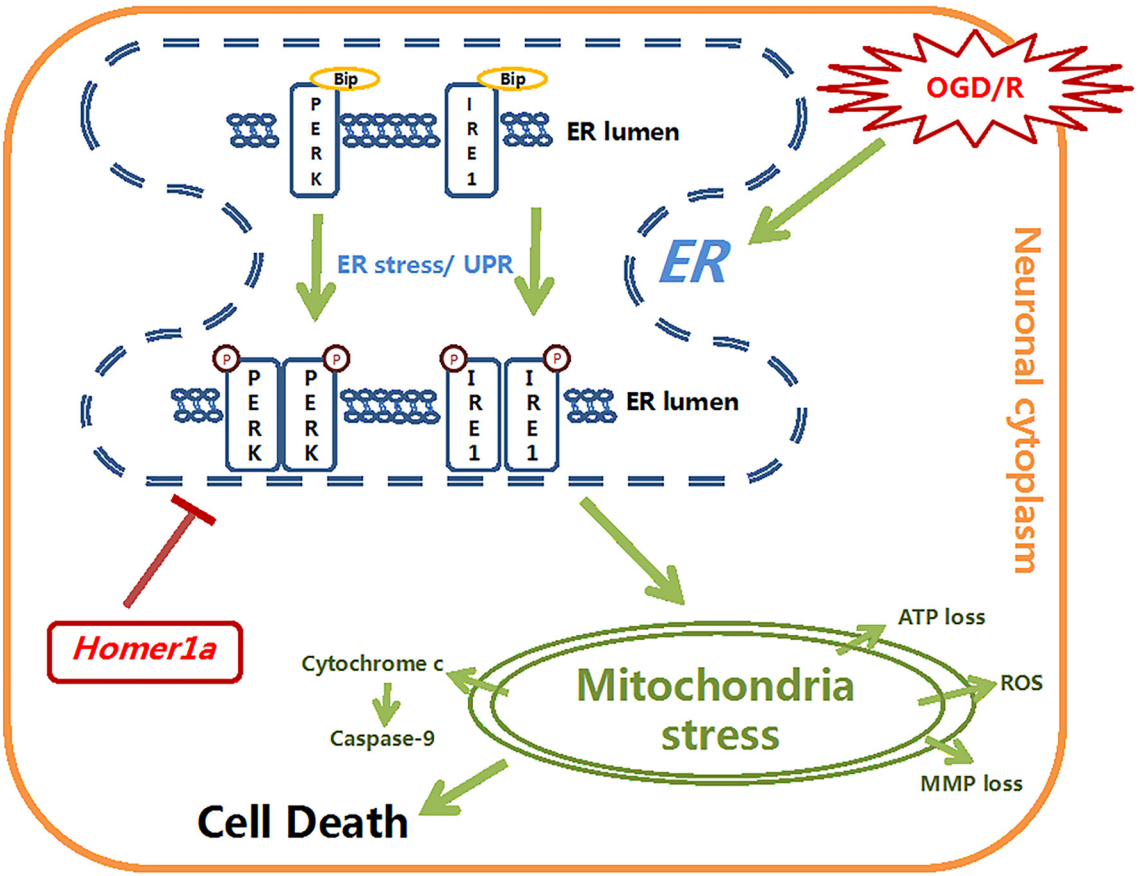

FIGURE 6 | The schematic diagram depicts the molecular mechanisms of homer1a-induced neuron-protection against OGD injury. Homer1a overexpression inhibited the OGD-induced activation of ER stress, which alleviated the secondary mitochondria dysfunction by regulating ATP, MMP, ROS, cytochrome c and caspase-9. In addition, Homer1a-induced preservation of mitochondrial function was achieved mainly *via* inhibiting the PERK pathway.

overexpression which may due to the Homer1a itself, our stroke model, lab environment or other specific details. ATF6 pathway is one of the main branches of ER stress and its activation could upregulates activating transcription factor 4 (ATF4), a cAMP-response element binding protein that could cause retinal and neuronal degeneration (Gully et al., 2016), and CHOP expression (Darling and Cook, 2014). Besides, ATF6 has two isoforms that may be crucial in many scenarios such as embryogenesis (Thuerauf et al., 2007). It is necessary to carry out further experiments to elucidate ATF6's specific roles in brain I/R injury.

ER stress plays different roles in different situations. Under acute or chronic pathologies or stress, ERS elicits UPR, which facilitates the misfolding protein degradation that helps alleviate protein overload that, in turn, helps to avoid cell apoptosis. However, when the cell proteostasis is still not restored, ERS can trigger apoptosis *via* several pathways (Tabas and Ron, 2011). This bifunctional process is essential for maintaining cell homeostasis. Many studies have shown that ERS activation could further aggravate the original pathology, such as pancreatic disease, intestinal inflammation and liver injury (Cunha et al., 2009; Han et al., 2016; Hosomi et al., 2017). In IS, the inhibition of ERS alleviates neuronal injury (Feng et al., 2017). Only a few studies have shown that the activation of ERS protects cells from apoptosis (Tan et al., 2017). In our *in vitro* model, aggravated injury, as demonstrated by increased LDH release, was found in TM-treated neurons. The results indicated that the ERS plays pro-apoptotic roles in cortical neurons under I/R injury.

ER and mitochondria both have dynamic plasticity of their structure in response to cellular requirements, which is the prerequisite for ER-mitochondrial communication functionally and structurally (Bravo-Sagua et al., 2013). The activation of ER stress induced the mitochondrial dysfunction in HT22 cells (Xu et al., 2018), and ER stress sensitized the mitochondria by opening its permeability transition pore in cardiac injury (Chen et al., 2017). Consistent with these studies, our results demonstrate that in cortical neurons under I/R injury, the reactivation of Homer1a overexpression suppressed ER stress *via* TM, which led to increased intracellular calcium load, elevated ROS production and ATP loss. This finding indicated that Homer1a conserves mitochondrial function by inhibiting ER stress under I/R injury in cortical neurons. On the other hand, mitochondria may also have effects on ER stress. Studies showed

that the mitochondria and ER stress has crosstalk in many models (Malhotra and Kaufman, 2011; Senft and Ronai, 2015), and the block of respiratory chain complex with rotenone or antimycin A that leads to mitochondrial dysfunction exerts great effects on ER stress (Lee et al., 2010; Jeon et al., 2017; Heo et al., 2019). Further studies are needed to investigate the effects of mitochondria to ER stress regarding Homer1 protein regulation.

Additionally, we further investigated the mechanism by which Homer1a exerts mitochondrial protection *via* ER stress reduction. According to previous studies, the phosphorylated PERK can activate ATF4 transcription, which in turn promotes the expression of bZIP transcription factor C/EBP homologous protein (CHOP) and then influences mitochondrial function by hyperoxidizing the ER lumen structure by activating ER oxidase 1α (ERO1α; Harding et al., 2000; Song et al., 2008). The oxidized ER activates IP3R-induced calcium release and then activates Ca/calmodulin-dependent protein kinase II (CaMKII), which facilitates calcium transfer into the mitochondria. The increasing mitochondrial calcium uptake leads to MMP loss, cytochrome c release and apoptosis (Kashiwase et al., 2005; Li et al., 2009; Timmins et al., 2009). In this study, compared with neurons with Homer1a overexpression, neurons in which the PERK pathway is activated *via* TM and p-IRE1 inhibitor DBSA under I/R injury showed more cytochrome c release, elevated ATP loss and an increased ROS level, which indicated that the PERK pathway is involved in mitochondrial dysfunction. Previous studies also found that in gastric cancer cells, the phosphorylated IRE1 activated Jun N-terminal protein kinase-1 (JNK-1), which in turn activated the transcription of CHOP and influenced mitochondrial related functions (Kim et al., 2018). However, in our study, activating the IRE1 pathway in neurons under I/R injury with TM and the PERK inhibitor GSK2656157 showed less abortion of Homer1a protection with less ATP loss and ROS production than PERK pathway activation. There was no significant difference in cytochrome c release between neurons in which ER stress was inhibited by Homer1a lentivirus transfection and neurons in which IRE1 was activated by TM and GSK2656157. These discrepancies may be attributed to different models, unknown biological traits of the inhibitors and a potential interaction between Homer1a and IRE1-JNK related pathways. All these results indicate that Homer1a preserves mitochondrial function mainly through the PERK pathway and partially through the IRE1 pathway (**Figure 6**).

A limitation of this study was that Homer1a's effect on mitochondria dysfunction and ER stress under I/R injury was only explored in cultured cortical neurons, lacking the interaction with glial cell signaling. Our lab has already built a Homer1a knockout mouse model in which more experiments will be implemented to further evaluate these observations. Additionally, in this study, we investigated molecular mechanisms in pharmacological ways, and future studies with specific gene modulation should elucidate the exact mechanism of Homer1a in mitochondria protection.

In this study, the primary cultured neurons may contain a small portion of astrocytes and may insert mutual or extra efforts on neuron outcome with OGD/R model. Researches revealed that the astrocyte could protect neurons from I/R injury (Liu et al., 2018), while some suggested that the astrocyte plays harmful roles in IS (Yang et al., 2017). Since the ER stress inhibition *via* Homer1a overexpression could inhibit astrocyte activation (Huang et al., 2017), the roles of astrocyte in our present study are still unclear. Further experiments are needed to find the exact roles of astrocyte in IS.

In conclusion, we suggested that Homer1a may protect against I/R neuronal injury by preserving mitochondrial function though suppressing ER stress. Interestingly, Homer1a's protection of mitochondrial function is mainly by inhibiting the PERK pathway. Taken together, our findings provide novel perceptions about the relationship between Homer1a, ER stress and mitochondrial dysfunction in neurons under I/R conditions.

AUTHOR CONTRIBUTIONS

ZF conceived the idea and designed the experiments. JW and XW carried out most of the experiments and composed the manuscript. PL and KY carried out partial experiments. YY and JP helped in analyzing experimental results. LZ and SD assisted with verifying the results. DH helped revising the manuscript.

FUNDING

This work was supported by the National Natural Science Foundation of China (No. 81771239, No. 81430043).

SUPPLEMENTARY MATERIAL

The Supplementary Material for this article can be found online at: https://www.frontiersin.org/articles/10.3389/fncel.2019.00101/full#supplementary-material

FIGURE S1 | Relationship between Homer1a and ATF6 pathway after I/R injury of neurons. Cultured cortical neurons were transfected with LV-Homer1a or LV-control for 72 h and exposed to OGD. Levels of ATF6 and N'ATF6 were measured with Western blot. The data are represented as means ± SEM. $^{*}p < 0.05$ vs. Control.

REFERENCES

Benjamin, E. J., Virani, S. S., Callaway, C. W., Chamberlain, A. M., Chang, A. R., Cheng, S., et al. (2018). Heart Disease and stroke statistics-2018 update: a report from the american heart association. *Circulation* 137, e67–e492. doi: 10.1161/CIR.0000000000000558

Bennetts, P. S., and Pierce, J. D. (2010). Apoptosis: understanding programmed cell death for the CRNA. *AANA J.* 78, 237–245.

Bhatti, J. S., Bhatti, G. K., and Reddy, P. H. (2017). Mitochondrial dysfunction and oxidative stress in metabolic disorders—a step towards mitochondria based therapeutic strategies. *Biochim. Biophys. Acta Mol. Basis Dis.* 1863, 1066–1077. doi: 10.1016/j.bbadis.2016.11.010

Bravo-Sagua, R., Rodriguez, A. E., Kuzmicic, J., Gutierrez, T., Lopez-Crisosto, C., Quiroga, C., et al. (2013). Cell death and survival through the endoplasmic reticulum-mitochondrial axis. *Curr. Mol. Med.* 13, 317–329. doi: 10.2174/156652413804810781

Chen, T., Fei, F., Jiang, X. F., Zhang, L., Qu, Y., Huo, K., et al. (2012). Down-regulation of Homer1b/c attenuates glutamate-mediated excitotoxicity through endoplasmic reticulum and mitochondria pathways in rat cortical neurons. *Free Radic. Biol. Med.* 52, 208–217. doi: 10.1016/j.freeradbiomed.2011.10.451

Chen, Q., Thompson, J., Hu, Y., Das, A., and Lesnefsky, E. J. (2017). Metformin attenuates ER stress-induced mitochondrial dysfunction. *Transl. Res.* 190, 40–50. doi: 10.1016/j.trsl.2017.09.003

Cunha, D. A., Ladrière, L., Ortis, F., Igoillo-Esteve, M., Gurzov, E. N., Lupi, R., et al. (2009). Glucagon-like peptide-1 agonists protect pancreatic β-cells from lipotoxic endoplasmic reticulum stress through upregulation of BiP and JunB. *Diabetes* 58, 2851–2862. doi: 10.2337/db09-0685

Darling, N. J., and Cook, S. J. (2014). The role of MAPK signalling pathways in the response to endoplasmic reticulum stress. *Biochim. Biophys. Acta* 1843, 2150–2163. doi: 10.1016/j.bbamcr.2014.01.009

Diering, G. H., Nirujogi, R. S., Roth, R. H., Worley, P. F., Pandey, A., and Huganir, R. L. (2017). Homer1a drives homeostatic scaling-down of excitatory synapses during sleep. *Science* 355, 511–515. doi: 10.1126/science.aai8355

Fei, F., Li, J., Rao, W., Liu, W., Chen, X., Su, N., et al. (2015). Upregulation of Homer1a promoted retinal ganglion cell survival after retinal ischemia and reperfusion via interacting with Erk Pathway. *Cell. Mol. Neurobiol.* 35, 1039–1048. doi: 10.1007/s10571-015-0198-2

Feng, D., Wang, B., Wang, L., Abraham, N., Tao, K., Huang, L., et al. (2017). Pre-ischemia melatonin treatment alleviated acute neuronal injury after ischemic stroke by inhibiting endoplasmic reticulum stress-dependent autophagy via PERK and IRE1 signalings. *J. Pineal Res.* 62:3. doi: 10.1111/jpi.12395

Foa, L., and Gasperini, R. (2009). Developmental roles for Homer: more than just a pretty scaffold. *J. Neurochem.* 108, 1–10. doi: 10.1111/j.1471-4159.2008.05726.x

Gully, J. C., Sergeyev, V. G., Bhootada, Y., Mendez-Gomez, H., Meyers, C. A., Zolotukhin, S., et al. (2016). Up-regulation of activating transcription factor 4 induces severe loss of dopamine nigral neurons in a rat model of Parkinson's disease. *Neurosci. Lett.* 627, 36–41. doi: 10.1016/j.neulet.2016.05.039

Han, C. Y., Lim, S. W., Koo, J. H., Kim, W., and Kim, S. G. (2016). PHLDA3 overexpression in hepatocytes by endoplasmic reticulum stress via IRE1-Xbp1s pathway expedites liver injury. *Gut* 65, 1377–1388. doi: 10.1136/gutjnl-2014-308506

Hankey, G. J. (2017). Stroke. *Lancet* 389, 641–654. doi: 10.1016/S0140-6736(16)30962-X

Harding, H. P., Novoa, I., Zhang, Y., Zeng, H., Wek, R., Schapira, M., et al. (2000). Regulated translation initiation controls stress-induced gene expression in mammalian cells. *Mol. Cell* 6, 1099–1108. doi: 10.1016/s1097-2765(00)00108-8

Heo, J. N., Kim, D. Y., Lim, S. G., Lee, K., Suk, K., and Lee, W. H. (2019). ER stress differentially affects pro-inflammatory changes induced by mitochondrial dysfunction in the human monocytic leukemia cell line, THP-1. *Cell Biol. Int.* 43, 313–322. doi: 10.1002/cbin.11103

Hosomi, S., Grootjans, J., Tschurtschenthaler, M., Krupka, N., Matute, J. D., Flak, M. B., et al. (2017). Intestinal epithelial cell endoplasmic reticulum stress promotes MULT1 up-regulation and NKG2D-mediated inflammation. *J. Exp. Med.* 214, 2985–2997. doi: 10.1084/jem.20162041

Huang, G. N., Huso, D. L., Bouyain, S., Tu, J., McCorkell, K. A., May, M. J., et al. (2008). NFAT binding and regulation of T cell activation by the cytoplasmic scaffolding Homer proteins. *Science* 319, 476–481. doi: 10.1126/science.1151227

Huang, R., Zhang, Y., Han, B., Bai, Y., Zhou, R., Gan, G., et al. (2017). Circular RNA *HIPK2* regulates astrocyte activation via cooperation of autophagy and ER stress by targeting *MIR124–2HG*. *Autophagy* 13, 1722–1741. doi: 10.1080/15548627.2017.1356975

Imarisio, C., Alchera, E., Bangalore, R. C., Valente, G., Follenzi, A., Trisolini, E., et al. (2017). Oxidative and ER stress-dependent ASK1 activation in steatotic hepatocytes and Kupffer cells sensitizes mice fatty liver to ischemia/reperfusion injury. *Free Radic. Biol. Med.* 112, 141–148. doi: 10.1016/j.freeradbiomed.2017.07.020

Jeon, Y. M., Lee, S., Kim, S., Kwon, Y., Kim, K., Chung, C. G., et al. (2017). Neuroprotective effects of protein tyrosine phosphatase 1B inhibition against ER stress-induced toxicity. *Mol. Cells* 40, 280–290. doi: 10.14348/molcells.2017.2320

Kashiwase, K., Higuchi, Y., Hirotani, S., Yamaguchi, O., Hikoso, S., Takeda, T., et al. (2005). CaMKII activates ASK1 and NF-κB to induce cardiomyocyte hypertrophy. *Biochem. Biophys. Res. Commun.* 327, 136–142. doi: 10.1016/j.bbrc.2004.12.002

Kim, T. W., Lee, S. Y., Kim, M., Cheon, C., and Ko, S. G. (2018). Kaempferol induces autophagic cell death via IRE1-JNK-CHOP pathway and inhibition of G9a in gastric cancer cells. *Cell Death Dis.* 9:875. doi: 10.1038/s41419-018-0930-1

Leaw, B., Nair, S., Lim, R., Thornton, C., Mallard, C., and Hagberg, H. (2017). Mitochondria, bioenergetics and excitotoxicity: new therapeutic targets in perinatal brain injury. *Front. Cell. Neurosci.* 11:199. doi: 10.3389/fncel.2017.00199

Leber, S. L., Llenos, I. C., Miller, C. L., Dulay, J. R., Haybaeck, J., and Weis, S. (2017). Homer1a protein expression in schizophrenia, bipolar disorder and major depression. *J. Neural Transm.* 124, 1261–1273. doi: 10.1007/s00702-017-1776-x

Lee, J. W., Kim, W. H., Yeo, J., and Jung, M. H. (2010). ER stress is implicated in mitochondrial dysfunction-induced apoptosis of pancreatic β cells. *Mol. Cells* 30, 545–549. doi: 10.1007/s10059-010-0161-5

Li, G., Mongillo, M., Chin, K. T., Harding, H., Ron, D., Marks, A. R., et al. (2009). Role of ERO1-α-mediated stimulation of inositol 1,4,5-triphosphate receptor activity in endoplasmic reticulum stress-induced apoptosis. *J. Cell Biol.* 186, 783–792. doi: 10.1083/jcb.200904060

Liu, X., Tian, F., Wang, S., Wang, F., and Xiong, L. (2018). Astrocyte autophagy flux protects neurons against oxygen-glucose deprivation and ischemic/reperfusion injury. *Rejuvenation Res.* 21, 405–415. doi: 10.1089/rej.2017.1999

Luo, P., Chen, T., Zhao, Y., Xu, H., Huo, K., Zhao, M., et al. (2012a). Protective effect of Homer 1a against hydrogen peroxide-induced oxidative stress in PC12 cells. *Free Radic. Res.* 46, 766–776. doi: 10.3109/10715762.2012.678340

Luo, P., Zhao, Y., Li, D., Chen, T., Li, S., Chao, X., et al. (2012b). Protective effect of Homer 1a on tumor necrosis factor-α with cycloheximide-induced apoptosis is mediated by mitogen-activated protein kinase pathways. *Apoptosis* 17, 975–988. doi: 10.1007/s10495-012-0736-z

Luo, P., Chen, T., Zhao, Y., Zhang, L., Yang, Y., Liu, W., et al. (2014). Postsynaptic scaffold protein Homer 1a protects against traumatic brain injury via regulating group I metabotropic glutamate receptors. *Cell Death Dis.* 5:e1174. doi: 10.1038/cddis.2014.116

Mailloux, R. J. (2016). Application of mitochondria-targeted pharmaceuticals for the treatment of heart disease. *Curr. Pharm. Des.* 22, 4763–4779. doi: 10.2174/1381612822666160629070914

Malhotra, J. D., and Kaufman, R. J. (2011). ER stress and its functional link to mitochondria: role in cell survival and death. *Cold Spring Harb. Perspect. Biol.* 3:a004424. doi: 10.1101/cshperspect.a004424

Martin, J. L., Gruszczyk, A. V., Beach, T. E., Murphy, M. P., and Saeb-Parsy, K. (2018). Mitochondrial mechanisms and therapeutics in ischaemia reperfusion injury. *Pediatr. Nephrol.* doi: 10.1007/s00467-018-3984-5 [Epub ahead of print].

Niizuma, K., Yoshioka, H., Chen, H., Kim, G. S., Jung, J. E., Katsu, M., et al. (2010). Mitochondrial and apoptotic neuronal death signaling pathways in cerebral ischemia. *Biochim. Biophys. Acta* 1802, 92–99. doi: 10.1016/j.bbadis.2009.09.002

Pandya, R. S., Mao, L., Zhou, H., Zhou, S., Zeng, J., Popp, A. J., et al. (2011). Central nervous system agents for ischemic stroke: neuroprotection mechanisms. *Cent. Nerv. Syst. Agents Med. Chem.* 11, 81–97. doi: 10.2174/187152411796011321

Prentice, H., Modi, J. P., and Wu, J. Y. (2015). Mechanisms of neuronal protection against excitotoxicity, endoplasmic reticulum stress and mitochondrial dysfunction in stroke and neurodegenerative diseases. *Oxid. Med. Cell. Longev.* 2015:964518. doi: 10.1155/2015/964518

Rao, W., Peng, C., Zhang, L., Su, N., Wang, K., Hui, H., et al. (2016). Homer1a attenuates glutamate-induced oxidative injury in HT-22 cells through regulation of store-operated calcium entry. *Sci. Rep.* 6:33975. doi: 10.1038/srep33975

Sanderson, T. H., Reynolds, C. A., Kumar, R., Przyklenk, K., and Huttemann, M. (2013). Molecular mechanisms of ischemia-reperfusion injury in brain: pivotal role of the mitochondrial membrane potential in reactive oxygen species generation. *Mol. Neurobiol.* 47, 9–23. doi: 10.1007/s12035-012-8344-z

Schieber, M., and Chandel, N. S. (2014). ROS function in redox signaling and oxidative stress. *Curr. Biol.* 24, R453–R462. doi: 10.1016/j.cub.2014.03.034

Schumacker, P. T., Gillespie, M. N., Nakahira, K., Choi, A. M., Crouser, E. D., Piantadosi, C. A., et al. (2014). Mitochondria in lung biology and pathology: more than just a powerhouse. *Am. J. Physiol. Lung Cell. Mol. Physiol.* 306, L962–L974. doi: 10.1152/ajplung.00073.201

Senft, D., and Ronai, Z. A. (2015). UPR, autophagy, and mitochondria crosstalk underlies the ER stress response. *Trends Biochem. Sci.* 40, 141–148. doi: 10.1016/j.tibs.2015.01.002

Serchov, T., Heumann, R., van Calker, D., and Biber, K. (2016). Signaling pathways regulating Homer1a expression: implications for antidepressant therapy. *Biol. Chem.* 397, 207–214. doi: 10.1515/hsz-2015-0267

Shulyakova, N., Andreazza, A. C., Mills, L. R., and Eubanks, J. H. (2017). Mitochondrial dysfunction in the pathogenesis of rett syndrome: implications for mitochondria-targeted therapies. *Front. Cell. Neurosci.* 11:58. doi: 10.3389/fncel.2017.00058

Song, B., Scheuner, D., Ron, D., Pennathur, S., and Kaufman, R. J. (2008). Chop deletion reduces oxidative stress, improves β cell function, and promotes cell survival in multiple mouse models of diabetes. *J. Clin. Invest.* 118, 3378–3389. doi: 10.1172/JCI34587

Tabas, I., and Ron, D. (2011). Integrating the mechanisms of apoptosis induced by endoplasmic reticulum stress. *Nat. Cell Biol.* 13, 184–190. doi: 10.1038/ncb0311-184

Tan, S. X., Jiang, D. X., Hu, R. C., Dai, A. G., Gan, G. X., Fu, D. Y., et al. (2017). Endoplasmic reticulum stress induces HRD1 to protect alveolar type II epithelial cells from apoptosis induced by cigarette smoke extract. *Cell. Physiol. Biochem.* 43, 1337–1345. doi: 10.1159/000481845

Tappe, A., Klugmann, M., Luo, C., Hirlinger, D., Agarwal, N., Benrath, J., et al. (2006). Synaptic scaffolding protein Homer1a protects against chronic inflammatory pain. *Nat. Med.* 12, 677–681. doi: 10.1038/nm1406

Thuerauf, D. J., Marcinko, M., Belmont, P. J., and Glembotski, C. C. (2007). Effects of the isoform-specific characteristics of ATF6 α and ATF6 β on endoplasmic reticulum stress response gene expression and cell viability. *J. Biol. Chem.* 282, 22865–22878. doi: 10.1074/jbc.m701213200

Timmins, J. M., Ozcan, L., Seimon, T. A., Li, G., Malagelada, C., Backs, J., et al. (2009). Calcium/calmodulin-dependent protein kinase II links ER stress with Fas and mitochondrial apoptosis pathways. *J. Clin. Invest.* 119, 2925–2941. doi: 10.1172/jci38857

Wang, J., Hu, X., and Jiang, H. (2016). ER stress-induced apoptosis: a novel therapeutic target in myocardial ischemia and reperfusion injury. *Int. J. Cardiol.* 214, 233–234. doi: 10.1016/j.ijcard.2016.03.176

Wang, Y., Rao, W., Zhang, C., Zhang, C., Liu, M. D., Han, F., et al. (2015). Scaffolding protein Homer1a protects against NMDA-induced neuronal injury. *Cell Death Dis.* 6:e1843. doi: 10.1038/cddis.2015.216

Wu, X., Luo, P., Rao, W., Dai, S., Zhang, L., Ma, W., et al. (2018). Homer1a attenuates hydrogen peroxide-induced oxidative damage in HT-22 cells through AMPK-dependent autophagy. *Front. Neurosci.* 12:51. doi: 10.3389/fnins.2018.00051

Wu, Y., Wang, X., Zhou, X., Cheng, B., Li, G., and Bai, B. (2017). Temporal expression of apelin/apelin receptor in ischemic stroke and its therapeutic potential. *Front. Mol. Neurosci.* 10:1. doi: 10.3389/fnmol.2017.00001

Xu, Q. H., Song, B. J., Liu, D., Chen, Y. H., Zhou, Y., Liu, W. B., et al. (2018). The MKK7 inhibitor peptide GADD45β-I attenuates ER stress-induced mitochondrial dysfunction in HT22 cells: involvement of JNK-Wnt pathway. *Brain Res.* 1691, 1–8. doi: 10.1016/j.brainres.2018.04.012

Yang, X., Geng, K., Zhang, J., Zhang, Y., Shao, J., and Xia, W. (2017). Sirt3 mediates the inhibitory effect of adjudin on astrocyte activation and glial scar formation following ischemic stroke. *Front. Pharmacol.* 8:943. doi: 10.3389/fphar.2017.00943

Yu, Z., Yi, M., Wei, T., Gao, X., and Chen, H. (2017). KCa3.1 inhibition switches the astrocyte phenotype during astrogliosis associated with ischemic stroke via endoplasmic reticulum stress and MAPK signaling pathways. *Front. Cell. Neurosci.* 11:319. doi: 10.3389/fncel.2017.00319

Conflict of Interest Statement: The authors declare that the research was conducted in the absence of any commercial or financial relationships that could be construed as a potential conflict of interest.

frontiers in Cellular Neuroscience

REVIEW
published: 19 March 2019
doi: 10.3389/fncel.2019.00107

Antiphospholipid Antibodies Overlapping in Isolated Neurological Syndrome and Multiple Sclerosis: Neurobiological Insights and Diagnostic Challenges

*Chiara D'Angelo[1,2,3], Oriol Franch[4], Lidia Fernández-Paredes[1,2], Celia Oreja-Guevara[5], María Núñez-Beltrán[1], Alejandra Comins-Boo[1,2], Marcella Reale[3] and Silvia Sánchez-Ramón[1,2]**

[1]Department of Clinical Immunology and IdISSC, Hospital Clínico San Carlos, Madrid, Spain, [2]Department of Immunology, Ophthalmology and ENT, Complutense University School of Medicine, Madrid, Spain, [3]Department of Medical, Oral and Biotechnological Sciences, University "G. d'Annunzio" Chieti-Pescara, Chieti, Italy , [4]Department of Neurology, Hospital Ruber Internacional, Madrid, Spain, [5]Department of Neurology, Hospital Clínico San Carlos, Madrid, Spain

Antiphospholipid syndrome (APS) is characterized by arterial and venous thrombosis, pregnancy morbidity and fetal loss caused by pathogenic autoantibodies directed against phospholipids (PL) and PL-cofactors. Isolated neurological APS may represent a significant diagnostic challenge, as epidemiological, clinical and neuroimaging features may overlap with those of multiple sclerosis (MS). In an open view, MS could be considered as an organ-specific anti-lipid (phospholipid and glycosphingolipid associated proteins) disease, in which autoreactive B cells and CD8+ T cells play a dominant role in its pathophysiology. In MS, diverse autoantibodies against the lipid-protein cofactors of the myelin sheath have been described, whose pathophysiologic role has not been fully elucidated. We carried out a review to select clinical studies addressing the prevalence of antiphospholipid (aPL) autoantibodies in the so-called MS-like syndrome. The reported prevalence ranged between 2% and 88%, particularly aCL and aβ2GPI, with predominant IgM isotype and suggesting worse MS prognosis. Secondarily, an updated summary of current knowledge on the pathophysiological mechanisms and events responsible for these conditions is presented. We draw attention to the clinical relevance of diagnosing isolated neurological APS. Prompt and accurate diagnosis and antiaggregant and anticoagulant treatment of APS could be vital to prevent or at least reduce APS-related morbidity and mortality.

Keywords: antiphospholipid syndrome, pathogenesis, MS-like syndrome, thrombosis, vasculopathy

OPEN ACCESS

Edited by:
Sriharsha Kantamneni, University of Bradford, United Kingdom

Reviewed by:
Tatsuro Mutoh, Fujita Health University, Japan
Ian P. Giles, University College London, United Kingdom

****Correspondence:***
Silvia Sánchez-Ramón
ssramon@salud.madrid.org

Received: *15 September 2018*
Accepted: *04 March 2019*
Published: *19 March 2019*

Citation:
D'Angelo C, Franch O, Fernández-Paredes L, Oreja-Guevara C, Núñez-Beltrán M, Comins-Boo A, Reale M and Sánchez-Ramón S (2019) Antiphospholipid Antibodies Overlapping in Isolated Neurological Syndrome and Multiple Sclerosis: Neurobiological Insights and Diagnostic Challenges. Front. Cell. Neurosci. 13:107. doi: 10.3389/fncel.2019.00107

CURRENT CHALLENGES IN THE DIAGNOSIS AND MANAGEMENT OF THE ANTIPHOSPHOLIPID SYNDROME

The antiphospholipid syndrome (APS) is a systemic autoimmune disorder characterized by the presence of peripheral procoagulant autoantibodies together with the occurrence of recurrent thrombosis (venous, arterial or both) and/or pregnancy morbidity and fetal loss (Miyakis et al., 2006). The sole presence of autoantibodies does not always lead to thrombosis. APS

can indeed be caused by a diverse array of antiphospholipid (aPL) antibodies that recognize cell surface proteins linked to phospholipids as "non self" within a pro-inflammatory context that has been described as a "second hit" (after infection or tissue damage). This combined effect would in turn activate the clotting cascade in a wide variety of mechanisms that lead to the development of thrombosis (Giannakopoulos and Krilis, 2013; Meroni et al., 2018).

The routine diagnostic aPL antibodies, used according to the 2006 Sydney revised APS classification criteria, are anticardiolipin (aCL), antiβ2-glycoprotein-I (aβ2GPI) and lupus anticoagulant (LA). The non-classic aPL antibodies include anti-phosphatidylserine (aPS), anti-phosphatidylserine-β2GPI (aPS-β2), anti-phosphatidylethanolamine (aPE), anti-prothrombin-prothrombin complex (aPT-PT), anti-phosphatidylserine-prothrombin complex (aPS-PT) and anti-annexin V (aAnV; Shoenfeld et al., 2008).

According to Sydney revision, classification of APS requires at least one clinical manifestation of vascular thrombosis or obstetrical events and the presence of at least two positive laboratory criteria (aCL IgG or IgM and/or aβ2GPI IgG or IgM at moderate titers and/or LA positivity) on two separate occasions at least 12 weeks apart (Miyakis et al., 2006). Persistence of positive aPL was introduced in order to differentiate the aPL antibodies appearing in the setting of infections or other unspecific conditions, in which aPL are transient and non-thrombogenic. Indeed, it is also well known that aPL antibodies fluctuate in blood, which hampers their interpretation (Donohoe et al., 2002; Fonseca and D'Cruz, 2008). To make the picture more complicated, besides the well-recognized obstetric and thrombotic hallmarks, APS can encompass an exceedingly variable clinical spectrum of multiorgan non-thrombotic manifestations, in the so called "extra-criteria" or "non-criteria" manifestations. Among these are the neurological manifestations, such as epilepsy, myelitis, chorea and migraine; hematological manifestations, such as thrombocytopenia and hemolytic anemia; livedo reticularis; pulmonary and osteoarticular manifestations; valvular heart disease; and nephropathy, to mention a few examples that cannot be exclusively explained by prothrombotic phenomena (Gómez-Puerta and Cervera, 2014; Negrini et al., 2017; Garcia and Erkan, 2018). In addition, the extra-criteria manifestations, as well as the classical ones, can occur in the setting of APS without fulfilling the serological criteria, as for instance with low titers' aCL or aβ2GPI antibodies (Cobo-Soriano et al., 1999; Micheloud et al., 2005) or even in the absence of detectable aPL in the so-called "seronegative APS."

APS may be diagnosed as an isolated disease (primary APS) or associated to other autoimmune disorders, mainly systemic lupus erythematous (SLE), rheumatoid arthritis, Sjögren syndrome, autoimmune thyroid disease, systemic sclerosis, systemic vasculitis, dermatopolymyositis, primary biliary cirrhosis and autoimmune hepatitis. It has been estimated that approximately 50% of patients who suffer from APS will develop SLE (Salmon et al., 2007). Nowadays, because of potentially recurrent thrombosis and the hypercoagulability scenario, there is consensus in treating APS patients with long-term oral anticoagulants and, in order to prevent obstetric manifestations, with a combination of low dose aspirin and low molecular weight heparin (LMWH; Empson et al., 2005).

There is a heated debate on the clinically significant titers of aPL antibodies. Investigators are strongly advised to classify patients as affected by APS, when more than one laboratory criterion is present alone or in combination. Specifically, LA presence in plasma; medium or high titer of IgG and/or IgM aCL antibody in serum or plasma (i.e., >40 GPL or MPL, or >the 99th percentile); IgG and/or IgM aβ2GPI antibody in serum or plasma (in titer >the 99th percentile; Miyakis et al., 2006). Growing evidences claim to consider the clinical impact of low level positive aPL antibodies and the necessity to set new cut-off levels, basically—though not exclusively—in obstetric APS (Devreese et al., 2010; Mekinian et al., 2012). The proposal to modify the APS classification criteria, mostly referring to laboratory requirements, is reinforced also by consideration that no differences were observed on obstetric complications, gestational period, arterial and/or venous thrombosis, when comparing pregnant women with aPL-related obstetric complications not fulfilling the Sydney criteria, with those fulfilling them (Arachchillage et al., 2015; Alijotas-Reig et al., 2018). Considering that also atypical (low or non-persistent), aPL antibodies presence may be associated with neurological disorders, such as transient ischemic attacks and migraine, but also epilepsy, transverse myelitis, multiple sclerosis (MS)-like syndrome, visual symptoms, dementia and chorea as well (Islam et al., 2016). The "rigid" adhesion to such criteria in clinical practice might exclude patients with "non-criteria" manifestations of APS in face of diagnostic uncertainty (Abreu et al., 2015; Aggarwal et al., 2015; Joseph and Habboush, 2018; Limper et al., 2018).

Whether anti-aggregant prophylaxis is needed in subjects with persistent positive aPL but without thrombosis history is still unclear. For the identification of the actual thrombotic risk, additional factors should be taken into consideration, such as hypertension, smoking, hypercholesterolemia, overweight or treatment with estrogens. Coexisting SLE and positivity to two or more aPL antibodies should be assessed too (Khamashta et al., 2016).

Isolated Involvement of the Central Nervous System in the Antiphospholipid Syndrome

Neurological features, already predicted in the first description of APS in 1983 (Hughes, 1983), have not been included yet in the APS classification criteria. According to the 2006 APS classification criteria (Miyakis et al., 2006), only transient ischemic attack and stroke have been included as neurological manifestations. Nevertheless, a wide variety of neurological symptoms including cognitive dysfunction, psychosis, chorea and epilepsy cannot be solely explained by thrombotic events or hypercoagulability. These manifestations

represent thus an important challenge in diagnostic practice, with a growing demand to recognize these "non-criteria" neurological manifestations in the classification of the disease (Abreu et al., 2015; Islam et al., 2016; Joseph and Habboush, 2018; Zhang and Pereira, 2018). A special case is the isolated central nervous system (CNS) involvement of APS, given the overlapping clinical and radiological features with MS (Achiron et al., 2004). In fact, isolated CNS APS usually occurs ranging from optical neuritis, chronic headache, migraine, cerebral ischemia, chorea, epilepsy, transverse myelopathy, to dementia and cognitive impairment (Hughes, 2003; Rodrigues et al., 2010). Most of these symptoms are usually referred as MS-like syndrome.

CNS APS and MS may be difficult to distinguish also from an immunological perspective, as the aPL antibody isotypes may involve IgG, IgM or IgA and therefore not always detected as the characteristic mirror pattern (positivity in serum and cerebrospinal fluid, CSF) or even of oligoclonal bands (OCB; predominant intrathecal antibody production; Cuadrado et al., 2000; Vilisaar et al., 2005). The two diseases resemble each other also for the epidemiological features of affected population, the relapsing-remitting course and for their appearance in neuroimaging (**Figure 1**). For both diseases, multifocal white matter lesions in magnetic resonance imaging (MRI) are the most common manifestation within the CNS (Chapman, 2004; Ferreira et al., 2005). In APS subjects, small strokes can occur in the white matter of brain and spinal cord, resulting in lesions that resemble the MS demyelinating plaques. The preferential localization is the subcortical area, and in a recent study, multiple subcortical and cortical infarcts with demyelination, involving both lobes of the brain, have been classified as characteristic MRI features for APS patients. White matter lesions were found in the periventricular area of the brain in almost the totality of the studied cases (Zhu et al., 2014).

Significant correlation between cognitive dysfunction and MRI lesions in primary APS patients has been reported, also in patients without CNS involvement (Tektonidou et al., 2006). In addition, vasculitis and inflammatory changes were also prevalent (Renaud et al., 2014).

Nowadays, the management and the treatment of APS patients with CNS involvement is still a matter of debate. There is good evidence of the benefit of anticoagulation in the typical thrombotic complications of APS, but there is still no consensus on the management with immunosuppression vs. anticoagulant therapy for non-thrombotic complications observed in MS-like syndrome. One might naturally wonder why, in the absence of any evident thrombotic injury on brain imaging, anticoagulant therapy should be used. In a case report by Zhang and Pereira (2018) an elderly woman with 6 months history of headache and intermittent choreiform movements of the face and arm, dramatically improved with warfarin therapy. Her blood tests showed positive LA, weakly positive aCL and negative aβ2GPI, with neither history of pregnancy loss or thrombosis. She received a trial of warfarin in the setting of probable APS, even if further investigation excluded potential secondary APS. After 2 weeks, her aberrant movements resolved as did her headaches, and since then she was symptom free for 18 months (Zhang and Pereira, 2018).

The evidence on how to manage movement disorders associated with APS are insufficient and no superiority of one drug to another has been demonstrated. In the reported case, a clear improvement of the patient's life quality was achieved with anticoagulation, although the pathophysiology of movement disorders in APS, including chorea, as well as of other non-criteria neurological symptoms, remains poorly understood (Joseph and Habboush, 2018).

No standard treatment exists for non-thrombotic neurological manifestations of APS and available evidence mostly derives from retrospective non-randomized trials or

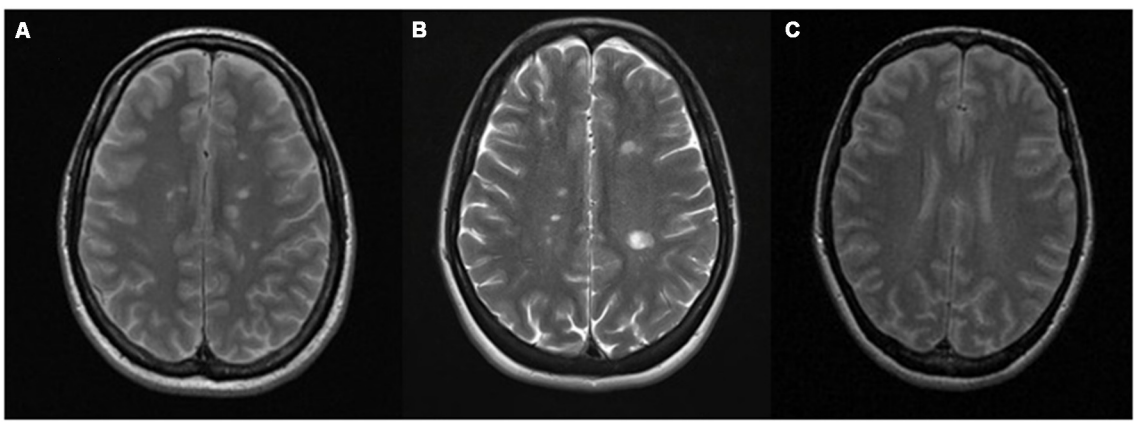

FIGURE 1 | Conventional magnetic resonance imaging (MRI) showing similar demyelinating lesions in: **(A)** multiple sclerosis (MS) and **(B)** antiphospholipid syndrome (APS). **(A)** Gadolinium-enhanced T2-weighted sequence of a patient with MS showing multiple demyelinating lesions in the *supra* and infratentorial white matter, predominantly periventricular, without evidence of postcontrast enhancement. **(B)** T2-weighted sequence of a patient with APS that shows multiple focal demyelinating lesions in periventricular, juxtacortical posterior left parietal (by confluence of several lesions) white matter. that are hyperintense relative to the normal appearing brain tissue, indicating increased permeability of the blood–brain barrier. **(C)** Normal T2 MRI.

case reports. In these studies anticoagulants have proven to be effective for the treatment of conditions that are not primarily thrombotic, such as migraine, transverse myelitis, and neuropsychiatric disturbances (Asherson et al., 2007; Roie et al., 2013).

According to the present state of knowledge, one might consider, under specific conditions, immunosuppressive treatment with corticosteroids, azathioprine and cyclophosphamide in addition to antithrombotic therapy, and combination with symptomatic management with neuroleptics (Cervera et al., 2014; Espinosa and Cervera, 2015; Yelnik et al., 2016). Rituximab, a monoclonal anti-CD20 antibody that depletes B cells, is currently used to treat various autoimmune diseases and hematological malignancies. Several case reports describe the use of rituximab in patients with APS, suggesting a beneficial role in the treatment and monitoring of refractory thrombocytopenia (Gamoudi et al., 2017) and recurrent thrombotic events in APS secondary to SLE (Emmi et al., 2017; Diószegi et al., 2018). The pilot therapeutic trial RITAPS that was designed to evaluate the efficacy and safety of rituximab in non-criteria APS manifestations (cognitive dysfunction, thrombocytopenia, cardiac valve disease, skin ulcers, nephropathy) did not show significant improvement of aPL profiles but a beneficial effect for a few of that conditions, given the small sample size. RITAPS was the first attempt to investigate immunosuppressive treatment in the management of cognitive dysfunction in aPL-positive patients without other systemic autoimmune diseases. The obtained findings indicated improvement in attention, visuomotor speed and flexibility (Erkan et al., 2013).

On the other hand, the rationale for the use of immunosuppressive and/or anticoagulant therapy could be given by the potential aPL-mediated damage considering each specific clinical case and clinical manifestations (Espinosa and Cervera, 2015).

ANTIPHOSPHOLIPID SYNDROME PATHOPHYSIOLOGY

aβ2GPI antibodies are central in many pathogenic APS mechanisms and, although the full pathogenesis of APS is not clear yet, the binding of these aPL antibodies to the antigens on the cell surface of platelets, monocytes, endothelial cells and trophoblasts, triggers intracellular signaling with subsequent activation and alteration of diverse cell functions. Monocytes and endothelial cells' activation determine a pro-aggregation status due to up-regulated expression of adhesion molecules, such as E-selectin, and release of tissue factor (TF) and proinflammatory cytokines (**Figure 2**). Platelets' activation and the subsequent release of thromboxane favor their aggregation. Cellular activation starts after the binding of the complex aβ2GPI antibody/β2GPI to the toll-like or annexin II receptors. Thrombosis at the fine vasculature of the target organ, such as retina or in the CNS, is thought to be more dependent from antibodies against the anticoagulant AnV. The resulting pathological and clinical events include inflammation and vasculitis, thrombus formation and arterial and/or venous vessel-occlusive disease (Pierangeli et al., 2006; Muscal and Brey, 2007; Merashli et al., 2015).

Although APS is considered an autoimmune condition mediated by specific production of autoantibodies and autoreactive T cells, innate immunity defects have been described as essential trigger factors within a multifactorial etiopathogenic scenario. As in most autoimmune diseases, genetically predisposed subjects, exposed to certain environmental agents could develop a specific immune response against self-proteins-binding phospholipids with a subsequent autoantibody production, together with the contribution of innate immunity mediators. Intrinsic alterations of the CNS myelin lipids or their cofactors (target tissue) could play a role in etiopathogenesis as well (Reale and Sanchez-Ramon, 2017). Coming up next, we summarize the events taking place in both innate and adaptive responses concerning APS.

Innate Immune System in Antiphospholipid Syndrome Pathophysiology

APS is characterized by the presence of autoantibodies, but as previously mentioned, aPL antibodies is a necessary but not sufficient condition for the onset of the disease. Additional factors or a "second hit," mediated by innate immunity, would be necessary to trigger the pathogenesis of the disease in the presence of autoantibodies, according to the current accepted theory (Pengo et al., 2011). In this context, certain environmental, proinflammatory or non-immunological procoagulant factors could induce the development of the disease, in genetically susceptible subjects (for instance, HLA-DR4 and HLA-Drw53 are risk factors; Matthey et al., 1989).

It must be also considered that, similarly to MS, several pathogens have been long described as potential triggers of the autoimmune response in APS. Molecular mimicry, with a modified-β2GPI from bacterial or viral structures may contribute to the development of the autoimmune response and the selection of autoantibodies (Cruz-Tapias et al., 2012).

aPL antibodies could be responsible of the specific activation of other innate immune cells and even non-immune cells. Presence of aβ2GPI antibodies induces up-regulation of TLR7 and TLR8 in plasmacytoid dendritic cells (pDCs; Prinz et al., 2011) and activates specific cells through the binding to relevant targets, such as TLR2, 4 and annexin A2 on monocytes and endothelial cells (Lambrianides et al., 2010; Satta et al., 2011; Allen et al., 2012); or ApoE receptor and glycoprotein Iba on platelets (Urbanus et al., 2008), promoting the development of a prothrombotic phenotype. It has indeed been demonstrated that knockout mice for these innate receptors, show a reduced thrombotic response following aPL antibodies administration (Pierangeli et al., 2007; Ramesh et al., 2011).

In addition, aPL antibodies directly promote up-regulation of the TF synthesis in monocytes (Sorice et al., 2007), neutrophils (Ritis et al., 2006) and endothelial cells (Kornberg et al., 2000). This procoagulant condition, not present under normal circumstances, plays an important role in contributing to the

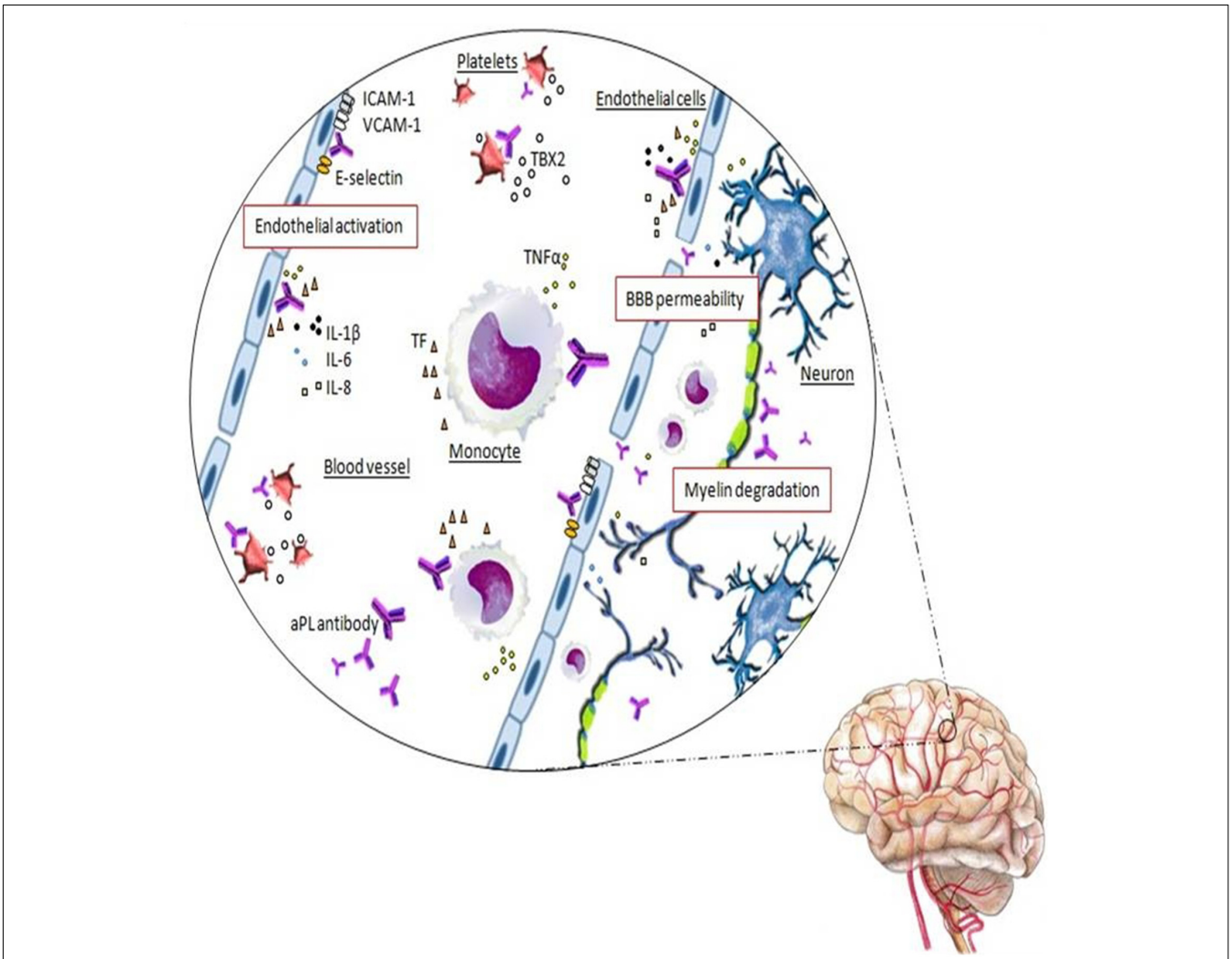

FIGURE 2 | Schematic representation of the autoreactive response in APS in which the thrombus formation is mediated by the interaction of antiphospholipid (aPL) antibodies with the anticoagulant annexinV (AnV) on the surface of the endothelial cells, which are destroyed, accelerating coagulation cascade. Moreover, the binding of aPL antibodies promotes the endothelial cells activation determining an increased expression of adhesion molecules (ICAM-1, VCAM-1, E-selectin) and the release of tissue factor (TF), TNFα, IL-1β, IL-6 and IL-8 proinflammatory cytokines. aPL antibodies promote also platelets and monocytes activation. On the platelets membrane, anti-β2GP1 antibodies lead to platelets activation and thromboxane B2 (TBX2) release. In monocytes, aPL antibodies induce TF expression and TNFα production.The inflammatory condition determined by these events causes a vascular endothelium dysfunction with increased permeability of the blood-brain barrier (BBB). The neurons and myelin become now accessible to the aPL antibodies and their binding may trigger the myelin destruction and the neurodegeneration found in APS with MS-like syndrome.

onset of thrombotic events in cancer, inflammation, angiogenesis and embryogenesis (Mackman, 2009).

aPL antibodies also interfere with the protein C function, especially through the competition for the phospholipid binding site, and therefore predispose to the development of venous thromboembolism (de-Groot et al., 1996).

Activation of the complement pathway is closely linked with thrombosis. Indeed, inhibition of the alternative complement pathway improves clinical outcomes reducing thrombosis risk (Chapin et al., 2016). aPL antibodies have shown to induce complement activation and to promote the upregulation of TF expression on neutrophils mediated by C5a (Ritis et al., 2006).

On the other hand, recent experimental studies on mice models suggest that natural killer T (NKT) cells play an important role in the regulation of aCL antibody production. NKT cells are characterized by their ability to recognize lipid antigens presented by CD1d molecules. Among a wide variety of self- and non-self lipids linked to CD1d in NKT cells, cardiolipin has been identified (Cox et al., 2009). NKT cells expansion was suggested to have a beneficial role in several autoimmune disorders through the release of immunomodulatory cytokines after antigen recognition (Godfrey and Kronenberg, 2004). This recognition of lipids, in the absence of exogenous antigens, is a hallmark of NKT cells and could account for activation and increased numbers of peripheral NKT cells described

in several oncological and autoimmune diseases (Brigl et al., 2003; Darmoise et al., 2010). Although the exact mechanism is not well understood, it has been demonstrated that NKT cells can regulate the activation of autoreactive B cells in a CD1d-dependent manner (Wermeling et al., 2010; Yang et al., 2011). In contrast, absence or reduction of NKT cells or of CD1d-expression on B cells have been related with an increased autoreactive B cells activation and higher aPL release, which raised the hypothesis that aPL antibodies could result from imbalanced NKT population. These data point to NKT cells as an intriguing therapeutic strategy to establish tolerance, a key element for ameliorating autoimmune diseases (Wermeling et al., 2010).

Adaptive Immune System in APS Pathophysiology

Undoubtedly, aPL auto-antibodies production by autoreactive B cells is the key feature of APS, although little is known about their emergence, their overactivation, regulation and about all their pathological effects. In line with the second hit theory, molecular mimicry has been proposed as a potential underlying mechanism for aPL antibodies production (Blank et al., 2002; Gharavi et al., 2002, 2003; Shoenfeld et al., 2006; Martin et al., 2011). In humans, many viral or bacterial infections have been associated with the production of IgM and IgG aPL, which can be persistent in time. As β2GPI has a similar aminoacidic sequence to that of several bacterial and viral components, it has been postulated that subjects with a certain genetic background may produce cross-reactive antibodies (Abdel-Wahab et al., 2016). For many years, aPL antibodies have been considered natural antibodies because of their polyspecific repertoire and other similar characteristics to those produced by B1 cells (Youinou and Renaudineau, 2004; Merrill, 2006). Conversely, aPL antibodies have been shown to be mainly of IgG and IgA isotype (Fanopoulos et al., 1998), hence probably their secretion needs to be T-cell dependent. In fact, a specific T cell-response against β2GPI in APS patients has been reported by several investigators (Kuwana, 2003; Yamaguchi et al., 2007). An increase in IL-17/IL-23 indicating a Th17 response has been described in APS as well (Meroni et al., 2011; Popovic-Kuzmanovic et al., 2013; Jakiela et al., 2016). Although there is no definitive evidence to prove these concepts, it has been demonstrated that antigen driven maturation increases the pathogenic potential of aPL antibodies, although it is not an indispensable prerequisite for pathogenicity (Lieby et al., 2004). In fact, aPL antibodies production induced by infection has not shown to be pathogenic, even if significantly higher number of infected patients with aPL antibodies titer develop thrombotic events. Further, serum collected from healthy individuals can present these autoantibodies too (Uthman et al., 1999; Justo et al., 2011; Nakayama et al., 2014; Abdel-Wahab et al., 2016). To date, it is universally accepted that aPL antibodies cause the typical clinical manifestations of APS, but the causal relationship with the thrombotic events remains speculative.

Besides the diverse effects previously described on innate immune cells, aPL antibodies appear to interfere with the natural antithrombotic processes, by recognition and binding to β2GPI, expressed on the surface membranes of several cell types involved in the coagulation cascade, as well as decidual stromal cells, throphoblast cells, glial cells and neurons (Borghi et al., 2007; Lavazza et al., 2007). The former have been reported to induce defective *in vitro* trophoblast proliferation and differentiation as well as increased apoptosis (Di Simone et al., 2007).

aPL antibodies' prothrombotic effects have also been observed in the CNS. Intrathecal synthesis of aPL antibodies or the disruption of the blood-brain barrier (BBB) could allow aPL autoantibodies to enter the CNS (Martínez-Cordero et al., 1997). Prothrombotic events could be triggered by direct interaction between aPL antibodies and CNS-resident cells. aPL antibodies have been related to astrocyte proliferation and nonspecific permeabilization and depolarization of synaptoneurosomes *in vitro* (Chapman et al., 1999).

The most characteristic features of APS affecting CNS, have been reported to be the connective dysfunction disorder and demyelinization (Espinosa and Cervera, 2008), but the specific role of aPL antibodies in non-thrombotic CNS manifestations of APS or transverse myelitis, remains to be established. Even though studies on small cohorts of patients have shown specific non-thrombogenic effects of aPL antibodies on CNS, with both vascular and non-vascular damage involved in the neurological manifestations of the disease. Data suggest a direct binding of aPL antibodies within the CNS, inducing activation of astrocytes, neurons and brain endotheliocytes (**Figure 2**). However, the binding of aPL antibodies to the membrane phospholipids within the brain has not been extensively studied. Caronti et al. (1998a,b) demonstrated that the neuronal damage might occur by a direct interaction of aPL antibodies with neurons or by functional impairment after their interaction with astrocytes, endothelial cell activation and adherence to CNS cells. These authors showed by indirect immunofluorescence that aβ2GPI antibodies purified from the serum of a patient with SLE/APS specifically bound CNS cells, in particular astrocytes and neurons in culture and in histological sections of human and monkey brain, and to cerebral vascular endothelium.

aCL antibodies' binding was demonstrated also in a cell line of rat astrocytes. In these cells, aCL antibodies exerted an inhibitory effect by decreasing the cells' viability and by depolarizing the cell membrane, impairing the signal transduction (Sun et al., 1992).

Chapman et al. (1999) in 1999 speculated about the potential target site of aPL antibodies at the neuronal synapses. They examined aPL antibodies effects on the plasma membrane function of rat synaptoneurosomes with IgG aPL purified from APS patients' sera. The study was a proof-of-concept describing the functional interaction of IgG purified aPL antibodies from APS subjects with neuronal cell membranes, showing increased depolarization and permeabilization of synaptoneurosomes.

Moreover, it should be considered that by targeting antigens at the BBB and compromising its integrity, aPL antibodies in APS patients gain access to the CNS (**Figure 2**). Further, supporting the hypothesis of a direct role of these autoantibodies in the pathogenesis of neurological manifestations, *in vivo* mice behavioral tests were performed by Shoenfeld et al. (2003).

After direct injection of IgG aPL purified from APS patients into mice brain, worst performances were demonstrated in the animals.

Despite these studies were conducted long-time ago, whether neurological hyperexcitatory manifestations, such as epilepsy and chorea could result from aPL-induced synaptic depolarization or whether the neuronal depolarization might explain the dementia and cognitive dysfunction found in APS, remains unknown.

The CNS involvement in APS might be additionally mediated by a direct neurotoxic effect of aPL antibodies that leads to impaired basal ganglion cell function with the development of neuroinflammation. Possibly, the aPL antibody bond to the cerebral endothelium could also cause endothelial dysfunction and lead to microthrombosis and inflammation of the blood vessels as well. This hypothesis might provide an explanation of why anticoagulation or immunosuppression therapy can represent at present an effective treatment in these aPL positive patients with neurological features. The above-mentioned mechanisms may be relevant not only in APS but in aPL positive MS patients, given the parallel mechanisms that cross between the two conditions.

In addition, a hypothesis proposes that the already described MS-like manifestations in APS patients could depend on the direct reactivity of aPL antibodies and myelin antigens by "molecular mimicry" and cross-reacting with myelin, myelin-related proteins and the cerebral phospholipids cephalin and sphingomyelin (**Figure 2**; Rombos et al., 1990; Karussis et al., 1998; Cikes et al., 2008). MRI studies of APS patients frequently show multiple T2-hyperintense brain lesions. Thus, typical demyelinating lesions of MS, transverse myelitis and optic neuritis, may also be present in the pathological spectrum of APS (Cikes et al., 2008). Moreover, preliminary data showed that the molecular mimicry of aPL-target antigens with myelin, myelin-related proteins and brain phospholipids may lead to cross-reactivity and predispose to a prothrombotic state (Koudriavtseva et al., 2014; Uthman et al., 2015).

PREVALENCE OF NON ORGAN-SPECIFIC ANTIPHOSPHOLIPID ANTIBODIES IN MULTIPLE SCLEROSIS

MS is an autoimmune mediated inflammatory and neurodegenerative disease characterized by multifocal areas of inflammation, due to autoreactive T and B lymphocytes and macrophage infiltrations, which cause demyelination, axonal damage with neuronal loss and gliosis, within both the white and gray matter of the CNS (Machado-Santos et al., 2018). These events lead to the formation of lesions, called plaques, which interfere with nerve impulses' transmission. The nervous transmission alteration accounts for the clinical MS features, such as autonomic and sensory defects, loss or reduction of motor functions and paralysis, fatigue, speech disorders, ataxia, difficulties in concentrating/thinking, learning and memory impairment and psychological problems (Compston and Coles, 2008).

The well-known heterogeneity of MS reflects a myriad of pathogenic mechanisms contributing to the disease. MS pathogenesis is mainly considered to be mediated by Th1 and Th17 autoreactive T cells infiltrating the CNS, which initiate an inflammatory cascade causing destruction of myelin sheath, oligodendrocyte and microglia damage, and finally axonal and neuronal destruction. Lipid-reactive NKT cells have been suggested to primarily drive Th1 and Th17 responses, after activation between certain myelin glycosphingolipids (particularly the derivatives of galactosylceramides) and CD1d glycoprotein (De Libero et al., 2007; Blewett, 2008; Hogan et al., 2013). Phospholipids and glycosphingolipids are the major components of CNS myelin sheath that, under certain circumstances, could become immunogenic and trigger autoimmune responses (Reale and Sanchez-Ramon, 2017). Moreover, invariant NKT (iNKT) cells seem to have a dual proinflammatory vs. counter-regulatory role in MS responses (Podbielska et al., 2018).

To date, B cells and humoral response in MS pathogenesis have reached more importance based on clonally expanded memory B cells and anti-myelin-specific lipids autoantibodies detected in MS patients, as indicated by the diagnostic use of OCB. The presence of the characteristic OCBs in the CSF is one of the main hallmarks of MS although not specific, together with antibody deposition, complement activation and demyelination.

The first and the most common detected autoantibodies in MS recognize the complexes of membrane proteins assembled to myelin lipids, like the transmembrane proteolipid protein (PLP), the extrinsic myelin basic protein (MBP), the myelin oligodendrocyte glycoprotein (MOG) and the myelin associated glycoprotein (MAG; Kanter et al., 2006; Podbielska and Hogan, 2009). Antibodies directed against glycolipids like ganglioside have been reported too (Stevens et al., 1992). Specific autoreactive T-cells and autoantibodies' reactivity directed against lipids such as sulfatide, phosphatidylcholine and sphingomyelin, and also against lipids that are altered by oxidative processes within the brain tissue of MS patients, including cholesterol, phosphatidylcholine, phosphatidyl ethanolamine and lysophosphatidyl ethanolamine have been described (Kanter et al., 2006; Fraussen et al., 2014). These antigenic stimuli from oxidized lipids, may overlap with those involved in the pathophysiology of APS. In MS, it has been evoked the role of capillary and venous hemorrhages that result in extracellular release of hemoglobin and reactive molecules that could induce local oxidative stress, inflammation and tissue damage. In fact, oxidized extracellular hemoglobin cause direct oxidative damage to myelin components, specifically to MBP (Bamm et al., 2017). In this context, vascular pathology could exert a primary event in the induction of a subsequent immunogenic response in MS. In an open view, MS could be considered as an organ-specific aPL disease, in which autoreactive B cells and $CD8^+$ T-cells play a major role in its pathophysiology (Machado-Santos et al., 2018).

The use of MRI and the paramagnetic element gadolinium (Gd) in MS is useful to detect CNS plaques with active inflammation and lesion burden. Gd can only cross the damaged BBB at sites of tissue destruction or inflammation. However, the

correlation between Gd-enhancing lesions and cognitive deficit is weak or absent in MS (Rocca et al., 2015).

Different MS clinical forms have been described, including relapsing remitting (RRMS), the most common subtype (approximately affects 87% of patients), primary progressive (PPMS), secondary progressive (SPMS) and progressive relapsing (PRMS). RRMS is characterized by acute inflammatory attacks, known as exacerbations or relapses, followed by periods of remission between relapses. During every attack, destruction of myelin and nerve fibers occur and accumulate in the long-term. Nearly 65% of patients with RRMS will subsequently develop SPMS, which is considered the second phase of the disease (Ghasemi et al., 2017).

MS different clinical forms are considered to translate into variable pathophysiological pathways, determining different patients' prognosis and treatment decisions. To-date, there is no cure for primary progressive MS, while there are diverse disease-modifying treatments (DMTs) for RRMS and SPMS in current use. The most common strategy of MS management is the "escalation therapy" beginning with interferon-β, glatiramer acetate, and corticosteroids for acute relapses. In patients with demonstrated moderate-to-high-disease activity, early initiation of "high-efficacy" DMTs, such as fingolimod, monoclonal antibodies such as natalizumab and alemtuzumab and new generation monoclonal anti-CD20 antibodies such as ocrelizumab may help to better control the disease (Merkel et al., 2017). These immunomodulatory and anti-inflammatory treatments can partially diminish disease progression and alleviate MS symptoms, by exerting inhibition of immune cell activation and migration through the BBB, lymphocyte proliferation and macrophage-mediated myelin degradation and blocking secretion of proinflammatory cytokines, among other effects (Torkildsen et al., 2016; Ghasemi et al., 2017; Nandoskar et al., 2017).

The hypothesis that aPL antibodies may be involved in the pathogenesis of MS, and the potential association between their presence and specific MS clinical subtypes or clinical phase is not recent (Marchiori et al., 1990; Sugiyama and Yamamoto, 1996; Karussis et al., 1998; Roussel et al., 2000; Horstman et al., 2009). Interestingly, PL/PL-linked cofactor antigens are clinically relevant in MS. We carried out a review in several steps: (1) articles were identified and revised by a computer assisted search of published reports (PubMed, US National Library of Medicine, National Institutes of Health) to locate all cases of MS in which aPL antibodies were analyzed and their positivity was reported. Bibliographies of each article were also scanned for references not identified in the initial search. Only cases with well documented clinical summaries and relevant information were included in the review. Data from these articles were summarized using a standardized data form, including population size, diagnosis and MS clinical phase, sample type, and the percentage of positivity for the specific antibody. According to our review, non organ-specific aPL autoantibodies, particularly aCL and aβ2GPI, that could account for APS patients with MS-like syndrome, occur within a range between 2% and 88% according to the different studies, with predominant IgM over IgG isotype, both in serum and CSF (**Table 1**). Due to the conflicting published levels, the exact prevalence, pathogenic role

TABLE 1 | Summary of relevant studies on the prevalence of aPL in MS patients.

Study	Population	aPL antibodies positivity
Filippidou et al. (2016)	127 MS (Serum); 88 RR, 11 PP, 28 SP	RR: aCL: 10.2% IgM, 18.2% IgG PP: aCL: 36.4% IgM, 18.2% IgG SP: aCL: 35.7% IgM, 32.1% IgG
Mandoj et al. (2015)	100 MS (Serum); 58 REM, 26 REL, 16 SP	REM: aCL: 1.7% IgM, 1.7% IgG, aβ2GPI: 1.7% IgM, aPT: 3.4% IgM, 5.2% IgG, aAnV: 1.7% IgM, 6.9% IgG REL: aCL: 7.7% IgM, 11.5% IgG, aβ2GPI: 26.9% IgM, aPT: 15.4% IgM, 19.2%IgG, aAnV: 3.8% IgM,15.4% IgG SP: aCL: 6.3% IgM, 6.3% IgG, aβ2GPI: 6.3% IgM, aPT: 6.3% IgM, aAnV: 6.3% IgM, 18.8% IgG
Shor et al. (2015)	98 MS (Serum)	aPS-β2: 14.6% IgM, 22.4% IgG, aPT: 46.9% IgM, aPT-PT: 71.4% IgG
Koudriavtseva et al. (2014)	100 MS (Serum)	aCL: 4% IgM, 5% IgG, aβ2GPI: 9% IgM, aPT: 7% IgM, 8% IgG, aAnV: 3% IgM, 11% IgG
Szmyrka-Kaczmarek et al. (2012)	85 MS (Serum)	aβ2GPI: 20% IgM, aCL: 4.7% IgM, 1% IgG
Stosic et al. (2010)	49 MS (Serum)	aCL: 18.4%, aβ2GPI: 10.2%, aPS: 18.4%, aPE: 32.6%
Garg et al. (2007)	111 MS, 27 CIS (Serum)	MS: aCL: 6%, aβ2GPI: 2%, CIS: aβ2GPI: 4%
Bidot et al. (2007)	24 RRMS (Serum); 7 REM, 17 REL	REM: aβ2GPI: 28% IgM, aCL: 28% IgM, aPS: 14% IgM, aPE: 28% IgM, aPC: 14% IgM REL: aβ2GPI: 82% IgM, aCL: 82% IgM, aFVIIa: 59% IgM, aPS: 71% IgM, aPE: 82% IgM, aPC: 76% IgM
Roussel et al. (2000)	89 MS (Serum)	aCL: 4.5% IgM, 16.9% IgG aβ2GPI: 13.5% IgM, 2.2% IgG
Karussis et al. (1998)	170 MS (Serum); 100 atypical, 70 classical	aCL: 27% atypical MS aCL: 5.7% classical MS
Sugiyama and Yamamoto (1996)	32 MS (Serum)	aCL: 44% IgM, 9% IgG
Marchiori et al. (1990)	33 MS (Serum, CSF)	aCL: 46.2% IgG (CSF)

MS, multiple sclerosis; RR, relapsing remitting; PP, primary progressive; SP, secondary progressive; REM, remission; REL, relaps; CIS, clinically isolated syndrome; CSF, cerebrospinal fluid; Acl, anti-cardiolipin; aβ2GPI, anti-β2glycoprotein I; aAnV, anti-annexin V; aPS-β2, anti-phosphatidylserine-β2GPI complex; aPT, anti-prothrombin; aPT-PT, anti-prothrombin complex; aPE, anti-phosphatidylethanolamine; aPS, anti-phosphatidylserine; aPC, anti-phosphatidylcholine; aFVIIa, anti-factor VII activated.

and clinical significance of aPL antibodies in MS remain still unclear and highly debated.

In 2007, two studies found higher aPL antibodies titer in later MS phases, aCL and PE were more common in SPMS when compared to RRMS (Bidot et al., 2007; Garg et al., 2007). By studying MS during the exacerbation phase, Bidot et al. (2007) found a higher titer of IgM aβ2GPI and aCL in 82% of patients with respect to those in remission phase (28%).

Koudriavtseva et al. (2014) found significantly higher frequency of aPL antibodies in MS subjects (32%) compared to healthy controls (7%), with a higher titer in RRMS patients (53.8%). Increased prevalence of IgM β2GPI in MS patients (20%) vs. controls (3.3%), was detected also by Szmyrka-Kaczmarek et al. (2012) of whom 33% were in SPMS patients and 21% in RRMS patients.

More recent studies have focused as well on aPL autoantibodies incidence in MS patients in different clinical phases of the disease, showing at least one IgM aPL or IgG isotype elevated in MS subjects, in RRMS or SPMS phases (Mandoj et al., 2015; Shor et al., 2015; Filippidou et al., 2016).

Positive aPL in the setting of local inflammatory status may induce any of the diverse pathogenetic mechanisms previously mentioned. aPL antibodies may account for antibody-mediated complement deposition in a portion of MS demyelinating lesions and might underline a proportion of approximately 30% of MS patients in which hypoxia-like pathological findings are found (Lucchinetti et al., 2000). Presence of aPL antibodies in SPMS or at later stages of MS might be indicative of a more chronic and worst course of CNS injury. Therefore, positive aPL antibodies in MS might associate to MRI lesions, as their detection could reveal more severe lesions in MS patients with aPL antibodies positivity with respect to those with lower or absent aPL titers (Stosic et al., 2010). However, these correlations still remain to be further investigated.

OVERLAP BETWEEN ANTIPHOSPHOLIPID SYNDROME AND MULTIPLE SCLEROSIS: CLINICAL AND PROGNOSTIC IMPLICATIONS

Nowadays, there are no definite diagnostic tools for distinguishing atypical MS and neurological APS cases, and the occurrence of positive aPL autoantibodies in patients with MS, in the absence of systemic manifestations of autoimmune disease or APS, is of particular concern. Therefore, it seems probable that a small percentage of patients diagnosed with MS, do in fact have a primary neurological APS, a condition with an entirely different pharmacological treatment and that would condition prognosis too. APS misdiagnosis as MS makes a crucial point for the therapeutic approach, given the increased prothrombotic risk (Fernández-Fernández et al., 2006; Donnan and McDonald, 2009; Ahbeddou et al., 2012). Finally, the coexistence of both autoimmune diseases, like APS secondary to MS, could also be possible.

An acute clinical isolated neurological syndrome (CIS) poses the biggest diagnostic challenge, since it is the most common onset of MS, but can also be the only feature or the first manifestation in APS before the occurrence of other features, such as thrombosis or miscarriages (Ferreira et al., 2005). An article published in The Times newspaper reported the results of a survey of the London Lupus Centre suggesting that at least 5% of MS patients were misdiagnosed and suffer from APS instead of MS (Rose, 2006).

APS patients have a generally good clinical outcome under anticoagulant treatment; manifestations such as headache and memory loss often improve drastically, with no further neurological events, when they are properly anticoagulated (Cuadrado et al., 2000).

For the above reasons, APS is recognized as a severe but potentially treatable condition, considering also the neurological complications. However, no standard treatment is available yet for the aPL-associated neurologic manifestations not included in the APS classification criteria, and the effects of immunosuppressive and anti-inflammatory agents, usually used in MS, is unknown in these patients (Espinosa and Cervera, 2015). A careful and correct diagnosis could be vital to avoid or at least reduce APS-related morbidity and mortality.

Despite MS is an incurable neuroinflammatory and neurodegenerative disease, a prompt and adequate treatment, focused on control of MS relapses, partially ameliorates accumulation of physical and neurological disability in the long-term. In fact, relapses timing is unpredictable but during every attack, destruction of myelin occurs and destroyed axonal fibers accumulate in CNS with worsening of patient's clinical condition. The early initiation of DMTs leads to improved stability control of MS disease, when compared to delayed therapy onset (Kavaliunas et al., 2017; Merkel et al., 2017). The presence of aPL antibodies in MS may herald a misdiagnosis of APS or the coexistence with APS, implying the establishment of anticoagulant therapy and the improvement of the prognosis for the individual patient.

CONCLUSION

APS and MS may be both considered as anti-lipid autoimmune diseases with specific pathophysiological mechanisms and events, given the direct role of antiphospholipid in the coagulation cascade, which can cross in the individual patient. Since the time they have been defined, clinical findings cannot clearly distinguish between atypical MS and neurological APS; basic and clinical research is still needed to reduce the misdiagnosis in these difficult cases. In these patients, to date, an accurate diagnosis may only emerge after long-term follow-up. Primary or secondary APS has to be considered an essential differential diagnosis from MS because prompt and correct treatment can improve quality of life and may also reduce morbidity and mortality in the affected patients. Understanding the possible associations between aPL antibodies and non-stroke neurological disabilities warrants further research. The knowledge of new pathogenic mechanisms of aPL might identify novel therapeutic targets and therefore improve the clinical management of atypical APS and aPL-positive MS patients.

AUTHOR CONTRIBUTIONS

CDA and SS-R designed the work and wrote the first draft of the article. LF-P and MR substantially contributed to writing. All authors have revised and approved the manuscript.

ACKNOWLEDGMENTS

We would like to thank the reviewers for their thoughtful comments and efforts towards improving our manuscript.

REFERENCES

Abdel-Wahab, N., Lopez-Olivo, M. A., Pinto-Patarroyo, G. P., and Suarez-Almazor, M. E. (2016). Systematic review of case reports of antiphospholipid syndrome following infection. *Lupus* 25, 1520–1531. doi: 10.1177/0961203316640912

Abreu, M. M., Danowski, A., Wahl, D. G., Amigo, M. C., Tektonidou, M., Pacheco, M. S., et al. (2015). The relevance of "non-criteria" clinical manifestations of antiphospholipid syndrome: 14th international congress on antiphospholipid antibodies technical task force report on antiphospholipid syndrome clinical features. *Autoimmun. Rev.* 14, 401–414. doi: 10.1016/j.autrev.2015.01.002

Achiron, A., Mandel, M., and Shoenfeld, Y. (2004). Multiple sclerosis and anti-phospholipid syndrome—one or two diseases? *Harefuah* 143, 724–766, 766, 765.

Aggarwal, R., Ringold, S., Khanna, D., Neogi, T., Johnson, S. R., Miller, A., et al. (2015). Distinctions between diagnostic and classification criteria? *Arthritis Care Res.* 67, 891–897. doi: 10.1002/acr.22583

Ahbeddou, N., Ait Ben Haddou, E., Hammib, S., Slimani, C., Regragui, W., Benomar, A., et al. (2012). Multiple sclerosis associated with antiphospholipid syndrome: diagnostic and therapeutic difficulties. *Rev. Neurol.* 168, 65–69. doi: 10.1016/j.neurol.2011.01.021

Alijotas-Reig, J., Esteve-Valverde, E., Ferrer-Oliveras, R., LLurba, E., Ruffatti, A., Tincani, A., et al. (2018). Comparative study between obstetric antiphospholipid syndrome and obstetric morbidity related with antiphospholipid antibodies. *Med. Clin.* 151, 215–222. doi: 10.1016/j.medcli.2017.11.017

Allen, K. L., Fonseca, F. V., Betapudi, V., Willard, B., Zhang, J., and McCrae, K. R. (2012). A novel pathway for human endothelial cell activation by antiphospholipid/anti-β2 glycoprotein I antibodies. *Blood* 119, 884–893. doi: 10.1182/blood-2011-03-344671

Arachchillage, D. R., Machin, S. J., Mackie, I. J., and Cohen, H. (2015). Diagnosis and management of non-criteria obstetric antiphospholipid syndrome. *Thromb. Haemost.* 113, 13–19. doi: 10.1160/th14-05-0416

Asherson, R. A., Giampaulo, D., Singh, S., and Sulman, L. (2007). Dramatic response of severe headaches to anticoagulation in a patient with antiphospholipid syndrome. *J. Clin. Rheumatol.* 13, 173–174. doi: 10.1097/rhu.0b013e3180690af6

Bamm, V. V., Henein, M. E. L., Sproul, S. L. J., Lanthier, D. K., and Harauz, G. (2017). Potential role of ferric hemoglobin in MS pathogenesis: effects of oxidative stress and extracellular methemoglobin or its degradation products on myelin components. *Free Radic. Biol. Med.* 112, 494–503. doi: 10.1016/j.freeradbiomed.2017.08.022

Bidot, C. J., Horstman, L. L., Jy, W., Jimenez, J. J., Bidot, C. Jr., Ahn, Y. S., et al. (2007). Clinical and neuroimaging correlates of antiphospholipid antibodies in multiple sclerosis: a preliminary study. *BMC Neurol.* 7:36. doi: 10.1186/1471-2377-7-36

Blank, M., Krause, I., Fridkin, M., Keller, N., Kopolovic, J., Goldberg, I., et al. (2002). Bacterial induction of autoantibodies to β2-glycoprotein-I accounts for the infectious etiology of antiphospholipid syndrome. *J. Clin. Invest.* 109, 797–804. doi: 10.1172/jci200212337

Blewett, M. M. (2008). Hypothesized role of galactocerebroside and NKT cells in the etiology of multiple sclerosis. *Med Hypotheses* 70, 826–830. doi: 10.1016/j.mehy.2007.07.037

Borghi, M. O., Raschi, E., Scurati, S., Grossi, C., Chen, P. P., Pierangeli, S. S., et al. (2007). Effects of Toll-like receptor antagonist and anti-annexin A2 antibodies on binding and activation of decidual cells by anti-b2-glycoprotein I antibodies. Proceedings of the 12th international congress on antiphospholipid antibodies; 2007 Apr 18–21; Florence, Italy. *Clin. Exp. Rheumatol.* 25:157.

Brigl, M., Bry, L., Kent, S. C., Gumperz, J. E., and Brenner, M. B. (2003). Mechanism of CD1d- restricted natural killer T cell activation during microbial infection. *Nat. Immunol.* 4, 1230–1237. doi: 10.1038/ni1002

Caronti, B., Calderaro, C., Alessandri, C., Conti, F., Tinghino, R., Pini, C., et al. (1998a). Serum anti- β2-glycoprotein I antibodies from patients with antiphospholipid antibody syndrome bind central nervous system cells. *J. Autoimmun.* 11, 425–429. doi: 10.1006/jaut.1998.0214

Caronti, B., Pittoni, V., Palladini, G., and Valesini, G. (1998b). Anti-β2-glycoprotein I antibodies bind to central nervous system. *J. Neurol. Sci.* 156, 211–219. doi: 10.1016/s0022-510x(98)00027-6

Cervera, R., Rodríguez-Pintó, I., Colafrancesco, S., Conti, F., Valesini, G., Rosário, C., et al. (2014). 14th international congress on antiphospholipid antibodies task force report on catastrophic antiphospholipid syndrome. *Autoimmun. Rev.* 13, 699–707. doi: 10.1016/j.autrev.2014.03.002

Chapin, J., Terry, H. S., Kleinert, D., and Laurence, J. (2016). The role of complement activation in thrombosis and hemolytic anemias. *Transfus. Apher. Sci.* 54, 191–198. doi: 10.1016/j.transci.2016.04.008

Chapman, J. (2004). The interface of multiple sclerosis and antiphospholipid antibodies. *Thromb. Res.* 114, 477–481. doi: 10.1016/j.thromres.2004.06.016

Chapman, J., Cohen-Armon, M., Shoenfeld, Y., and Korczyn, A. D. (1999). Antiphospholipid antibodies permeabilize and depolarize brain synaptoneurosomes. *Lupus* 8, 127–133. doi: 10.1191/096120399678847524

Cikes, N., Bosnic, D., and Sentic, M. (2008). Non-MS autoimmune demyelination. *Clin. Neurol. Neurosurg.* 110, 905–912. doi: 10.1016/j.clineuro.2008.06.011

Cobo-Soriano, R., Sánchez-Ramón, S., Aparicio, M. J., Teijeiro, M. A., Vidal, P., Suárez-Leoz, M., et al. (1999). Antiphospholipid antibodies and retinal thrombosis in patients without risk factors: a prospective case-control study. *Am. J. Ophthalmol.* 128, 725–732. doi: 10.1016/s0002-9394(99)00311-6

Compston, A., and Coles, A. (2008). Multiple sclerosis. *Lancet* 372, 1502–1517. doi: 10.1016/S0140-6736(08)61620-7

Cox, D., Fox, L., Tian, R., Bardet, W., Skaley, M., Mojsilovic, D., et al. (2009). Determination of cellular lipids bound to human CD1d molecules. *PLoS One* 4:e5325. doi: 10.1371/journal.pone.0005325

Cruz-Tapias, P., Blank, M., Anaya, J. M., and Shoenfeld, Y. (2012). Infections and vaccines in the etiology of antiphospholipid syndrome. *Curr. Opin. Rheumatol.* 24, 389–393. doi: 10.1097/bor.0b013e32835448b8

Cuadrado, M. J., Khamashta, M. A., Ballesteros, A., Godfrey, T., Simon, M. J., and Hughes, G. R. (2000). Can Hughes (antiphospholipid) syndrome be distinguished from multiple sclerosis? Analysis of 27 patients and review of the literature. *Medicine* 79, 57–68. doi: 10.1097/00005792-200001000-00006

Darmoise, A., Teneberg, S., Bouzonville, L., Brady, R. O., Beck, M., Kaufmann, S. H. E., et al. (2010). Lysosomal α-galactosidase controls the generation of self lipid antigens for natural killer T cells. *Immunity* 33, 216–228. doi: 10.1016/j.immuni.2010.08.003

De Libero, G., Macdonald, H. R., and Dellabona, P. (2007). T cell recognition of lipids: quo vadis? *Nat. Immunol.* 8, 223–227. doi: 10.1038/ni0307-223

de-Groot, P. G., Horbach, D. A., and Derksen, R. H. (1996). Protein C and other cofactors involved in the binding of antiphospholipid antibodies: relation to the pathogenesis of thrombosis. *Lupus* 5, 488–493. doi: 10.1177/096120339600500532

Devreese, K., Peerlinck, K., and Hoylaerts, M. F. (2010). Thrombotic risk assessment in the antiphospholipid syndrome requires more than the quantification of lupus anticoagulants. *Blood* 115, 870–878. doi: 10.1182/blood-2009-09-244426

Di Simone, N., Meroni, P. L., D'Asta, M., Di Nicuolo, F., D'Alessio, M. C., and Caruso, A. (2007). Pathogenic role of anti-β2-glycoprotein I antibodies on human placenta: functional effects related to implantation and roles of heparin. *Hum. Reprod. Update* 13, 189–196. doi: 10.1093/humupd/dml051

Diószegi, Á., Tarr, T., Nagy-Vincze, M., Nánásy-Vass, M., Veisz, R., Bidiga, L., et al. (2018). Microthrombotic renal involvement in an SLE patient with concomitant catastrophic antiphospholipid syndrome: the beneficial effect of rituximab treatment. *Lupus* 27, 1552–1558. doi: 10.1177/0961203318768890

Donnan, P. T., and McDonald, M. J. (2009). Patients' experiences of a diagnosis of Hughes' syndrome. *Clin. Rheumatol.* 28, 1091–1100. doi: 10.1007/s10067-009-1196-x

Donohoe, S., Quenby, S., Mackie, I., Panal, G., Farquharson, R., Malia, R., et al. (2002). Fluctuations in levels of antiphospholipid antibodies and increased coagulation activation markers in normal and heparin-treated antiphospholipid syndrome pregnancies. *Lupus* 11, 11–20. doi: 10.1191/0961203302lu132oa

Emmi, G., Urban, M. L., Scalera, A., Becatti, M., Fiorillo, C., Silvestri, E., et al. (2017). Repeated low-dose courses of rituximab in SLE-associated antiphospholipid syndrome: data from a tertiary dedicated centre. *Semin. Arthritis Rheum.* 46, e21–e23. doi: 10.1016/j.semarthrit.2016.08.002

Empson, M., Lassere, M., Craig, J., and Scott, J. (2005). Prevention of recurrent miscarriage for women with antiphospholipid antibody or lupus anticoagulant. *Cochrane Database Syst. Rev.* 2:CD002859. doi: 10.1002/14651858.cd002859.pub2

Erkan, D., Vega, J., Ramón, G., Kozora, E., and Lockshin, M. D. (2013). A pilot open-label phase II trial of rituximab for non-criteria manifestations of antiphospholipid syndrome. *Arthritis Rheum.* 65, 464–471. doi: 10.1002/art.37759

Espinosa, G., and Cervera, R. (2008). Antiphospholipid syndrome. *Arthritis Res. Ther.* 10:230. doi: 10.1186/ar2536

Espinosa, G., and Cervera, R. (2015). Current treatment of antiphospholipid syndrome: lights and shadows. *Nat. Rev. Rheumatol.* 11, 586–596. doi: 10.1038/nrrheum.2015.88

Fanopoulos, D., Teodorescu, M. R., Varga, J., and Teodorescu, M. (1998). High frequency of abnormal levels of IgA anti-β2-glycoprotein I antibodies in patients with systemic lupus erythematosus: relationship with antiphospholipid syndrome. *J. Rheumatol.* 25, 675–680.

Fernández-Fernández, F. J., Rivera-Gallego, A., de la Fuente-Aguado, J., Pérez-Fernández, S., and Muñoz-Fernández, D. (2006). Antiphospholipid syndrome mimicking multiple sclerosis in two patients. *Eur. J. Intern. Med.* 17, 500–502. doi: 10.1016/j.ejim.2006.02.018

Ferreira, S., D'Cruz, D. P., and Hughes, G. R. (2005). Multiple sclerosis, neuropsychiatric lupus and antiphospholipid syndrome: where do we stand? *Rheumatology* 44, 434–442. doi: 10.1093/rheumatology/keh532

Filippidou, N., Krashias, G., Pericleous, C., Rahman, A., Ioannou, Y., Giles, I., et al. (2016). The association between IgG and IgM antibodies against cardiolipin, 2-glycoprotein I and Domain I of 2-glycoprotein I with disease profile in patients with multiple sclerosis. *Mol. Immunol.* 75, 161–167. doi: 10.1016/j.molimm.2016.05.022

Fonseca, A. G., and D'Cruz, D. P. (2008). Controversies in the antiphospholipid syndrome: can we ever stop warfarin? *J. Autoimmune Dis.* 5:6. doi: 10.1186/1740-2557-5-6

Fraussen, J., Claes, N., de Bock, L., and Somers, V. (2014). Targets of the humoral autoimmune response in multiple sclerosis. *Autoimmun. Rev.* 13, 1126–1137. doi: 10.1016/j.autrev.2014.07.002

Gómez-Puerta, J. A., and Cervera, R. (2014). Diagnosis and classification of the antiphospholipid syndrome. *J. Autoimmun.* 48–49, 20–25. doi: 10.1016/j.jaut.2014.01.006

Gamoudi, D., Cutajar, M., Gamoudi, N., Camilleri, D. J., and Gatt, A. (2017). Achieving a satisfactory clinical and biochemical response in antiphospholipid syndrome and severe thrombocytopenia with rituximab: two case reports. *Clin. Case Rep.* 5, 845–848. doi: 10.1002/ccr3.946

Garcia, D., and Erkan, D. (2018). Diagnosis and management of the antiphospholipid syndrome. *N. Engl. J. Med.* 378, 2010–2021. doi: 10.1056/NEJMra1705454

Garg, N., Zivadinov, R., Ramanathan, M., Vasiliu, I., Locke, J., Watts, K., et al. (2007). Clinical and MRI correlates of autoreactive antibodies in multiple sclerosis patients. *J. Neuroimmunol.* 187, 159–165. doi: 10.1016/j.jneuroim.2007.04.008

Gharavi, A. E., Pierangeli, S. S., Espinola, R. G., Liu, X., Colden-Stanfield, M., and Harris, E. N. (2002). Antiphospholipid antibodies induced in mice by immunization with a cytomegalovirus-derived peptide cause thrombosis and activation of endothelial cells *in vivo*. *Arthritis Rheum.* 46, 545–552. doi: 10.1002/art.10130

Gharavi, A. E., Pierangeli, S. S., and Harris, E. N. (2003). Viral origin of antiphospholipid antibodies: endothelial cell activa-tion and thrombus enhancement by CMV peptide-induced APL antibodies. *Immunobiology* 207, 37–42. doi: 10.1078/0171-2985-00216

Ghasemi, N., Razavi, S. H., and Nikzad, E. (2017). Multiple sclerosis: pathogenesis, symptoms, diagnoses, and cell-based therapy. *Cell J.* 19, 1–10. doi: 10.22074/cellj.2016.4867

Giannakopoulos, B., and Krilis, S. A. (2013). The pathogenesis of the antiphospholipid syndrome. *N. Engl. J. Med.* 368, 1033–1044. doi: 10.1056/NEJMra1112830

Godfrey, D. I., and Kronenberg, M. (2004). Going both ways: immune regulation via CD1d-dependent NKT cells. *J. Clin. Invest.* 114, 1379–1388. doi: 10.1172/jci23594

Hogan, E. L., Podbielska, M., and O'Keeffe, J. (2013). Implications of lymphocyte anergy to glycolipids in multiple sclerosis (MS): iNKT cells may mediate the MS infectious trigger. *J. Clin. Cell. Immunol.* 4:144. doi: 10.4172/2155-9899.1000144

Horstman, L. L., Yj, W., Bidot, C. J., Ahn, Y. S., Kelley, R. E., Zivadinov, R., et al. (2009). Antiphospholipid antibodies: paradigm in transition. *J. Neuroinflammation* 6:3. doi: 10.1186/1742-2094-6-3

Hughes, G. R. V. (1983). Thrombosis, abortion, cerebral disease, and the lupus anticoagulant. *Br. Med. J.* 287, 1088–1089. doi: 10.1136/bmj.287.6399.1088

Hughes, G. R. V. (2003). Migraine, memory loss, and "multiple sclerosis". Neurological features of the antiphospholipid (Hughes') syndrome. *Postgrad. Med. J.* 79, 81–83. doi: 10.1136/pmj.79.928.81

Islam, M. A., Alam, F., Kamal, M. A., Wong, K. K., Sasongko, T. H., and Gan, S. H. (2016). 'Non-criteria' neurologic manifestations of antiphospholipid syndrome: a hidden kingdom to be discovered. *CNS Neurol. Disord. Drug Targets* 15, 1253–1265. doi: 10.2174/1871527315666160920122750

Jakiela, B., Iwaniec, T., Plutecka, H., Celinska-Lowenhoff, M., Dziedzina, S., and Musial, J. (2016). Signs of impaired immunoregulation and enhanced effector T-cell responses in the primary antiphospholipid syndrome. *Lupus* 25, 389–398. doi: 10.1177/0961203315618267

Joseph, F. G., and Habboush, H. W. (2018). The antiphospholipid syndrome and its 'non-criteria' manifestations. *Pract. Neurol.* 18, 82–83. doi: 10.1136/practneurol-2017-001846

Justo, D., Finn, T., Atzmony, L., Guy, N., and Steinvil, A. (2011). Thrombosis associated with acute cytomegalo-virus infection: a meta-analysis. *Eur. J. Intern. Med.* 22, 195–199. doi: 10.1016/j.ejim.2010.11.006

Kanter, J. L., Narayana, S., Ho, P. P., Catz, I., Warren, K. G., Sobel, R. A., et al. (2006). Lipid microarrays identify key mediators of autoimmune brain inflammation. *Nat. Med.* 12, 138–143. doi: 10.1038/nm1344

Karussis, D., Leker, R. R., Ashkenazi, A., and Abramsky, O. (1998). A subgroup of multiple sclerosis patients with anticardiolipin antibodies and unusual clinical manifestations: do they represent a new nosological entity? *Ann. Neurol.* 44, 629–634. doi: 10.1002/ana.410440408

Kavaliunas, A., Manouchehrinia, A., Stawiarz, L., Ramanujam, R., Agholme, J., Hedstrom, A. K., et al. (2017). Importance of early treatment initiation in the clinical course of multiple sclerosis. *Mult. Scler.* 23, 1233–1240. doi: 10.1177/1352458516675039

Khamashta, M., Taraborelli, M., Sciascia, S., and Tincani, A. (2016). Antiphospholipid syndrome. *Best Pract. Res. Clin. Rheumatol.* 30, 133–148. doi: 10.1016/j.berh.2016.04.002

Kornberg, A., Renaudineau, Y., Blank, M., Youinou, P., and Shoenfeld, Y. (2000). Anti-β 2-glycoprotein I antibodies and anti-endothelial cell antibodies induce tissue factor in endothelial cells. *Isr. Med. Assoc. J.* 2, 27–31.

Koudriavtseva, T., D'Agosto, G., Mandoj, C., Sperduti, I., and Cordiali-Fei, P. (2014). High frequency of antiphospholipid antibodies in relapse of multiple sclerosis: a possible indicator of inflammatory-thrombotic processes. *Neurol. Sci.* 35, 1737–1741. doi: 10.1007/s10072-014-1823-4

Kuwana, M. (2003). Autoreactive $CD4^+$ T cells to β_2-glycoprotein I in patients with antiphospholipid syndrome. *Autoimmun. Rev.* 2, 192–198. doi: 10.1016/s1568-9972(03)00007-7

Lambrianides, A., Carroll, C. J., Pierangeli, S. S., Pericleous, C., Branch, W., Rice, J., et al. (2010). Effects of polyclonal IgG derived from patients with different clinical types of the antiphospholipid syndrome on monocyte

signaling pathways. *J. Immunol.* 184, 6622–6628. doi: 10.4049/jimmunol.0902765

Lavazza, T., Dipinto, A., Borghi, M. O., Usuelli, V., Bergamaschi, A., Zimarino, V., et al. (2007). Antiphospholipid antibodies and central nervous system involvement: direct autoantibody binding to neuronal cells. Proceedings of the 12th international congress on antiphospholipid antibodies; 2007 Apr 18–21; Florence, Italy. *Clin. Exp. Rheumatol.* 25:147.

Lieby, P., Poindron, V., Roussi, S., Klein, C., Knapp, A. M., Garaud, J. C., et al. (2004). Patho-genic antiphospholipid antibody: an antigen-selected needle in a haystack. *Blood* 104, 1711–1715. doi: 10.1182/blood-2004-02-0462

Limper, M., Scirè, C. A., Talarico, R., Amoura, Z., Avcin, T., Basile, M., et al. (2018). Antiphospholipid syndrome: state of the art on clinical practice guidelines. *RMD Open* 4:e000785. doi: 10.1136/rmdopen-2018-000785

Lucchinetti, C., Brück, W., Parisi, J., Scheithauer, B., Rodriguez, M., and Lassmann, H. (2000). Heterogeneity of multiple sclerosis lesions: implications for the pathogenesis of demyelination. *Ann. Neurol.* 47, 707–717. doi: 10.1002/1531-8249(200006)47:6<707::aid-ana3>3.0.co;2-q

Machado-Santos, J., Saji, E., Tröscher, A. R., Paunovic, M., Liblau, R., Gabriely, G., et al. (2018). The compartmentalized inflammatory response in the multiple sclerosis brain is composed of tissue-resident CD8+ T lymphocytes and B cells. *Brain* 41, 2066–2082. doi: 10.1093/brain/awy151

Mackman, N. (2009). The many faces of tissue factor. *J. Thromb. Haemost.* 7, 136–139. doi: 10.1111/j.1538-7836.2009.03368.x

Mandoj, C., Renna, R., Plantone, D., Sperduti, I., Cigliana, G., Conti, L., et al. (2015). Anti-annexin antibodies, cholesterol levels and disability in multiple sclerosis. *Neurosci. Lett.* 606, 156–160. doi: 10.1016/j.neulet.2015.08.054

Marchiori, P. E., Dos Reis, M., Quevedo, M. E., Callegaro, D., Hirata, M. T., Scaff, M., et al. (1990). Cerebrospinal fluid and serum antiphospholipid antibodies in multiple sclerosis, Guillain-Barre syndrome and systemic lupus erythematosus. *Arq. Neuropsiquiatr.* 48, 465–468. doi: 10.1590/s0004-282x1990000400010

Martin, E., Winn, R., and Nugent, K. (2011). Catastrophic antiphospholipid syndrome in a community-acquired methicillin-resistant Staphylococcus aureus infection: a review of pathogenesis with a case for molecular mimicry. *Autoimmun. Rev.* 10, 181–188. doi: 10.1016/j.autrev.2010.09.023

Martínez-Cordero, E., Rivera García, B. E., and Aguilar León, D. E. (1997). Anticardiolipin antibodies in serum and cerebrospinal fluid from patients with systemic lupus erythematosus. *J. Investig. Allergol. Clin. Immunol.* 7, 596–601.

Matthey, F., Walshe, K., Mackie, I. J., and Machin, S. J. (1989). Familial occurrence of the antiphospholipid syndrome. *J. Clin. Pathol.* 42, 495–497. doi: 10.1136/jcp.42.5.495

Mekinian, A., Loire-Berson, P., Nicaise-Roland, P., Lachassinne, E., Stirnemann, J., Boffa, M. C., et al. (2012). Outcomes and treatment of obstetrical antiphospholipid syndrome in women with low antiphospholipid antibody levels. *J. Reprod. Immunol.* 94, 222–226. doi: 10.1016/j.jri.2012.02.004

Merashli, M., Noureldine, M. H., Uthman, I., and Khamashta, M. (2015). Antiphospholipid syndrome: an update. *Eur. J. Clin. Invest.* 45, 653–662. doi: 10.1111/eci.12449

Merkel, B., Butzkueven, H., Traboulsee, A. L., Havrdova, E., and Kalincik, T. (2017). Timing of high-efficacy therapy in relapsingremitting multiple sclerosis: a systematic review. *Autoimmun. Rev.* 16, 658–665. doi: 10.1016/j.autrev.2017.04.010

Meroni, P. L., Borghi, M. O., Grossi, C., Chighizola, C. B., Durigutto, P., and Tedesco, F. (2018). Obstetric and vascular antiphospholipid syndrome: same antibodies but different diseases? *Nat. Rev. Rheumatol.* 14, 433–440. doi: 10.1038/s41584-018-0032-6

Meroni, P. L., Borghi, M. O., Raschi, E., and Tedesco, F. (2011). Pathogenesis of antiphos- pholipid syndrome: understanding the antibodies. *Nat. Rev. Rheumatol.* 7, 330–339. doi: 10.1038/nrrheum.2011.52

Merrill, J. T. (2006). Do antiphospholipid antibodies develop for a purpose? *Curr. Rheumatol. Rep.* 8, 109–113. doi: 10.1007/s11926-006-0050-2

Micheloud, D., Sánchez-Ramón, S., Carbone, J., Rodríguez Molina, J. J., Fernández-Cruz, E., López-Longo, F. J., et al. (2005). Discordance between anti-β2-glycoprotein-I and anti-cardiolipin antibodies in patients with clinical criteria of antiphospholipid syndrome. *Clin. Exp. Rheumatol.* 23, 525–528.

Miyakis, S., Lockshin, M. D., Atsumi, T., Branch, D. W., Brey, R. L., Cervera, R., et al. (2006). International consensus statement on an update of the classification criteria for definite antiphospholipid syndrome (APS). *J. Thromb. Haemost.* 4, 295–306. doi: 10.1111/j.1538-7836.2006.01753.x

Muscal, E., and Brey, R. L. (2007). Neurological manifestations of the antiphospholipid syndrome: risk assessments and evidence-based medicine. *Int. J. Clin. Pract.* 61, 1561–1568. doi: 10.1111/j.1742-1241.2007.01478.x

Nakayama, T., Akahoshi, M., Irino, K., Kimoto, Y., Arinobu, Y., Niiro, H., et al. (2014). Transient antiphospholipid syndrome associated with primary cytomegalovirus infection: a case report and literature review. *Case Rep. Rheumatol.* 2014:271548. doi: 10.1155/2014/271548

Nandoskar, A., Raffel, J., Scalfari, A. S., Friede, T., and Nicholas, R. S. (2017). Pharmacological approaches to the management of secondary progressive multiple sclerosis. *Drugs* 77, 885–910. doi: 10.1007/s40265-017-0726-0

Negrini, S., Pappalardo, F., Murdaca, G., Indiveri, F., and Puppo, F. (2017). The antiphospholipid syndrome: from pathophysiology to treatment. *Clin. Exp. Med.* 17, 257–267. doi: 10.1007/s10238-016-0430-5

Pengo, V., Ruffatti, A., Legnani, C., Testa, S., Fierro, T., De Marongiu, F., et al. (2011). Incidence of a first thromboembolic event in asymptomatic carriers of high-risk antiphospholipid antibody profile: a multicenter prospective study. *Blood* 118, 4714–4718. doi: 10.1182/blood-2011-03-340232

Pierangeli, S. S., Chen, P. P., and González, E. B. (2006). Antiphospholipid antibodies and the antiphospholipid syndrome: an update on treatment and pathogenic mechanisms. *Curr. Opin. Hematol.* 13, 366–375. doi: 10.1097/01.moh.0000239710.47921.d2

Pierangeli, S. S., Vega-Ostertag, M. E., Raschi, E., Liu, X., Romay-Penabad, Z., De Micheli, V., et al. (2007). Toll-like receptor and antiphospholipid mediated thrombosis: *in vivo* studies. *Ann. Rheum. Dis.* 66, 1327–1333. doi: 10.1136/ard.2006.065037

Podbielska, M., and Hogan, E. L. (2009). Molecular and immunogenic features of myelin lipids: incitants or modulators of multiple sclerosis? *Pharmacol. Res.* 15, 1011–1029. doi: 10.1177/1352458509106708

Podbielska, M., O'Keeffe, J., and Hogan, E. L. (2018). Autoimmunity in multiple sclerosis: role of sphingolipids, invariant NKT cells and other immune elements in control of inflammation and neurodegeneration. *J. Neurol. Sci.* 385, 198–214. doi: 10.1016/j.jns.2017.12.022

Popovic-Kuzmanovic, D., Novakovic, I., Stojanovich, L., Aksentijevich, I., Zogovic, N., Tovilovic, G., et al. (2013). Increased activity of interleukin-23/interleukin-17 cytokine axis in primary antiphospholipid syndrome. *Immunobiology* 218, 186–191. doi: 10.1016/j.imbio.2012.03.002

Prinz, N., Clemens, N., Strand, D., Pütz, I., Lorenz, M., Daiber, A., et al. (2011). Antiphospholipid antibodies induce translocation of TLR7 and TLR8 to the endosome in human monocytes and plasmacytoid dendritic cells. *Blood* 118, 2322–2332. doi: 10.1182/blood-2011-01-330639

Ramesh, S., Morrell, C. N., Tarango, C., Thomas, G. D., Yuhanna, I. S., Girardi, G., et al. (2011). Antiphospholipid antibodies promote leukocyte-endothelial cell adhesion and thrombosis in mice by antagonizing eNOS via β2GPI and apoER2. *J. Clin. Invest.* 121, 120–131. doi: 10.1172/JCI39828

Reale, M., and Sanchez-Ramon, S. (2017). Lipids at the cross-road of autoimmunity in multiple sclerosis. *Curr. Med. Chem.* 24, 176–192. doi: 10.2174/0929867324666161123093606

Renaud, M., Aupy, J., Uring-Lambert, B., Chanson, J. B., Collongues, N., Blanc, F., et al. (2014). Isolated anti-β2-glycoprotein I antibodies in neurology: a frontier syndrome between multiple sclerosis and antiphospholipid syndrome? *Eur. J. Neurol.* 21, 901–906. doi: 10.1111/ene.12408

Ritis, K., Doumas, M., Mastellos, D., Micheli, A., Giaglis, S., Magotti, P., et al. (2006). A novel C5a receptor-tissue factor crosstalk in neutrophils links innate immunity to coagulation pathways. *J. Immunol.* 177, 4794–4802. doi: 10.4049/jimmunol.177.7.4794

Rocca, M. A., Amato, M. P., De Stefano, N., Enzinger, C., Geurts, J. J., Penner, I. K., et al. (2015). Clinical and imaging assessment of cognitive dysfunction in multiple sclerosis. *Lancet Neurol.* 14, 302–317. doi: 10.1016/S1474-4422(14)70250-9

Rodrigues, C. E., Carvalho, J. F., and Shoenfeld, Y. (2010). Neurological manifestations of antiphospholipid syndrome. *Eur. J. Clin. Invest.* 40, 350–359. doi: 10.1111/j.1365-2362.2010.02263.x

Roie, E. V., Labarque, V., Renard, M., Van Geet, C., and Gabriels, L. (2013). Obsessive-compulsive behavior as presenting symptom of primary antiphospholipid syndrome. *Psychosomat. Med.* 75, 326–330. doi: 10.1097/psy.0b013e31828acfbc

Rombos, A., Evangelopoulou-Katsiri, E., Leventakou, A., Voumvourakis, K., Triantafyllou, N., and Papageorgiou, C. (1990). Serum IgG and IgM anticardiolipin antibodies in neurological diseases. *Acta Neurol. Scand.* 81, 43–45. doi: 10.1111/j.1600-0404.1990.tb00975.x

Rose, D. (2006). *Hundreds Wrongly Told they are MS Sufferers.* The Times of London, August 22 2006. www.thesundaytimes.co.uk

Roussel, V., Yi, F., Jauberteau, M. O., Couderq, C., Lacombe, C., Michelet, V., et al. (2000). Prevalence and clinical significance of anti-phospholipid antibodies in multiple sclerosis: a study of 89 patients. *J. Autoimmun.* 14, 259–265. doi: 10.1006/jaut.2000.0367

Salmon, J. E., Girardi, G., and Lockshin, M. D. (2007). The antiphospholipid syndrome as a disorder initiated by inflammation: implications for the therapy of pregnant patients. *Nat. Clin. Pract. Rheumatol.* 3, 140–147. doi: 10.1038/ncprheum0432

Satta, N., Kruithof, E. K., Fickentscher, C., Dunoyer-Geindre, S., Boehlen, F., Reber, G., et al. (2011). Toll-like receptor 2 mediates the activation of human monocytes and endothelial cells by antiphospholipid antibodies. *Blood* 117, 5523–5531. doi: 10.1182/blood-2010-11-316158

Shoenfeld, Y., Blank, M., Cervera, R., Font, J., Raschi, E., and Meroni, P. L. (2006). Infectious origin of the antiphospholipid syndrome. *Ann. Rheum. Dis.* 65, 2–6. doi: 10.1136/ard.2005.045443

Shoenfeld, Y., Nahum, A., Korczyn, A. D., Dano, M., Rabinowitz, R., Beilin, O., et al. (2003). Neuronal-binding antibodies from patients with antiphospholipid syndrome induce cognitive deficits following intrathecal passive transfer. *Lupus* 12, 436–442. doi: 10.1191/0961203303lu409oa

Shoenfeld, Y., Twig, G., Katz, U., and Sherer, Y. (2008). Autoantibody explosion in antiphospholipid syndrome. *J. Autoimmun.* 30, 74–83. doi: 10.1016/j.jaut.2007.11.011

Shor, D. B.-A., Weiss, G. A., Barzilai, O., Ram, M., Anaya, L.-M., Shoenfeld, Y., et al. (2015). Prevalence of classic and non-classic antiphospholipid antibodies in multiple sclerosis. *Isr. Med. Assoc. J.* 17, 559–562.

Sorice, M., Longo, A., Capozzi, A., Garofalo, T., Misasi, R., Alessandri, C., et al. (2007). Anti-β2-glycoprotein I antibodies induce monocyte release of tumor necrosis factor α and tissue factor by signal transduction pathways involving lipid rafts. *Arthritis Rheum.* 56, 2687–2697. doi: 10.1002/art.22802

Stevens, A., Weller, M., and Wiethölter, H. (1992). CSF and serum ganglioside antibody patterns in MS. *Acta Neurol. Scand.* 86, 485–489. doi: 10.1111/j.1600-0404.1992.tb05129.x

Stosic, M., Ambrus, J., Garg, N., Weinstock-Guttman, B., Ramanathan, M., Kalman, B., et al. (2010). MRI characteristics of patients with antiphospholipid syndrome and multiple sclerosis. *J. Neurol.* 257, 63–71. doi: 10.1007/s00415-009-5264-6

Sugiyama, Y., and Yamamoto, T. (1996). Characterization of serum anti-phospholipid antibodies in patients with multiple sclerosis. *Tohoku J. Exp. Med.* 178, 203–215. doi: 10.1620/tjem.178.203

Sun, K. H., Liu, W. T., Tsai, C. Y., Liao, T. S., Lin, W. M., and Yu, C. L. (1992). Inhibition of astrocyte proliferation and binding to brain tissue of anticardiolipin antibodies purified from lupus serum. *Ann. Rheum. Dis.* 51, 707–712. doi: 10.1136/ard.51.6.707

Szmyrka-Kaczmarek, M., Pokryszko-Dragan, A., Pawlik, B., Gruszka, E., Korman, L., Podemski, R., et al. (2012). Antinuclear and antiphospholipid antibodies in patients with multiple sclerosis. *Lupus* 21, 412–420. doi: 10.1177/0961203311427550

Tektonidou, M. G., Varsou, N., Kotoulas, G., Antoniou, A., and Moutsopoulos, H. M. (2006). Cognitive deficits in patients with antiphospholipid syndrome: association with clinical, laboratory, and brain magnetic resonance imaging findings. *Arch. Intern. Med.* 166, 2278–2284. doi: 10.1001/archinte.166.20.2278

Torkildsen, Ø., Myhr, K. M., and Bø, L. (2016). Disease-modifying treatments for multiple sclerosis—a review of approved medications. *Eur. J. Neurol.* 23, 18–27. doi: 10.1111/ene.12883

Urbanus, R. T., Pennings, M. T., Derksen, R. H., and de Groot, P. G. (2008). Platelet activation by dimeric β2-glycoprotein I requires signalling via both glycoprotein Ibα and apolipoprotein E receptor 2ι. *J. Thromb. Haemost.* 6, 1405–1412. doi: 10.1111/j.1538-7836.2008.03021.x

Uthman, I., Noureldine, M. H. A., Berjawi, A., Skaf, M., Haydar, A. A., Merashli, M., et al. (2015). Hughes syndrome and Multiple sclerosis. *Lupus* 24, 115–121. doi: 10.1177/0961203314555539

Uthman, I., Tabbarah, Z., and Gharavi, A. E. (1999). Hughes syndrome associated with cytomegalovirus infection. *Lupus* 8, 775–777. doi: 10.1191/096120399678841034

Vilisaar, J., Wilson, M., Niepel, G., Blumhardt, L. D., and Constantinescu, C. S. (2005). A comparative audit of anticardiolipin antibodies in oligoclonal band negative and positive multiple sclerosis. *Mult. Scler.* 11, 378–380. doi: 10.1191/1352458505ms1208oa

Wermeling, F., Lind, S. M., Jordö, E. D., Cardell, S. L., and Karlsson, M. C. I. (2010). Invariant NKT cells limit activation of autoreactive CD1d-positive B cells. *J. Exp. Med.* 207, 943–952. doi: 10.1084/jem.20091314

Yamaguchi, Y., Seta, N., Kaburaki, J., Kobayashi, K., Matsuura, E., and Kuwana, M. (2007). Excessive exposure to anionic surfaces maintains autoantibody response to b2-glycoprotein I in patients with antiphospholipid syndrome. *Blood* 110, 4312–4318. doi: 10.1182/blood-2007-07-100008

Yang, J.-Q., Wen, X., Kim, P. J., and Singh, R. R. (2011). Invariant NKT cells inhibit autoreactive B cells in a contact- and CD1d-dependent manner. *J. Immunol.* 186, 1512–1520. doi: 10.4049/jimmunol.1002373

Yelnik, C. M., Kozora, E., and Appenzeller, S. (2016). Non-stroke central neurologic manifestations in antiphospholipid syndrome. *Curr. Rheumatol. Rep.* 18:11. doi: 10.1007/s11926-016-0568-x

Youinou, P., and Renaudineau, Y. (2004). The antiphospholipid syndrome as a model for B cell-induced autoimmune diseases. *Thromb. Res.* 114, 363–369. doi: 10.1016/j.thromres.2004.06.019

Zhang, L., and Pereira, A. C. (2018). Oromandibular chorea in antiphospholipid syndrome. *Pract. Neurol.* 18, 132–133. doi: 10.1136/practneurol-2017-001824

Zhu, D.-S., Fu, J., Zhang, Y., Li, S. X., Zhang, G. X., Guan, Y. T., et al. (2014). Neurological antiphospholipid syndrome: clinical, neuroimaging, and pathological characteristics. *J. Neurol. Sci.* 346, 138–144. doi: 10.1016/j.jns.2014.08.010

Conflict of Interest Statement: The authors declare that the research was conducted in the absence of any commercial or financial relationships that could be construed as a potential conflict of interest.

frontiers in Neurology

ORIGINAL RESEARCH
published: 19 March 2019
doi: 10.3389/fneur.2019.00251

There Is Selective Increase in Pro-thrombotic Circulating Extracellular Vesicles in Acute Ischemic Stroke and Transient Ischemic Attack: A Study of Patients From the Middle East and Southeast Asia

Abdelali Agouni[1†], Aijaz S. Parray[2†], Naveed Akhtar[2], Fayaz A. Mir[3], Paula J. Bourke[2], Sujata Joseph[2], Deborah M. Morgan[2], Mark D. Santos[2], Muhammad F. Wadiwala[2], Saadat Kamran[2], Siveen K. Sivaraman[3] and Ashfaq Shuaib[2,4]*

[1] Department of Pharmaceutical Sciences, College of Pharmacy, Qatar University, Doha, Qatar, [2] The Stroke Program, The Neuroscience Institute, Academic Health System, Hamad Medical Corporation, Doha, Qatar, [3] Interim Translational Institute, Academic Health System, Hamad Medical Corporation, Doha, Qatar, [4] Department of Medicine (Neurology), University of Alberta, Edmonton, AB, Canada

Stroke attacks were found to be present at a younger age in patients from Southeast Asia (SE) and the Middle East (ME) resident in the state of Qatar. Extracellular vesicles (EVs), which are small membrane vesicles with pro-thrombotic properties, may contribute to the high risk of stroke in this population. Thus, total and cell-specific medium size EVs were counted by flow cytometry in platelet-free plasma from healthy volunteers and patients with transient ischemic attacks (TIA) and acute ischemic stroke (AIS) from SE and ME. Acutely, within 48 h of attacks, there was an increase in total endothelial EVs in TIA (6.73 ± 1.77; $P = 0.0156$; $n = 21$) and AIS (11.23 ± 1.95; $P = 0.0007$; $n = 66$) patients compared to controls (2.04 ± 0.78; $n = 24$). Similar increases were also evident in EVs originating from platelets, erythrocytes, granulocytes, and leukocytes. Compared to controls, there was also an increase in EVs derived from activated endothelial cells, platelets, granulocytes, leukocytes, and pro-coagulant EVs (Annexin V^+) at 5 and 30-days following the acute events, while a decrease was observed in erythrocyte-derived EVs. This is the first study characterizing EVs in TIA and AIS patients from ME and SE showing an increase in EVs associated with endothelial and platelet cell activation, which may contribute to the elevated risk of stroke at a younger age in this population.

Keywords: extracellular vesicles (EVs), acute ischemic stroke (AIS), transient ischemic attacks (TIA), thrombosis, biomarkers

OPEN ACCESS

Edited by:
Sriharsha Kantamneni, University of Bradford, United Kingdom

Reviewed by:
Johannes Zipperle, Ludwig Boltzmann Institute for Experimental and Clinical Traumatology, Austria
Xu Cui, Henry Ford Hospital, United States

***Correspondence:**
Abdelali Agouni
aagouni@qu.edu.qa

†These authors have contributed equally to this work

Specialty section:
This article was submitted to Neurodegeneration, a section of the journal Frontiers in Neurology

Received: *31 October 2018*
Accepted: *25 February 2019*
Published: *19 March 2019*

Citation:
Agouni A, Parray AS, Akhtar N, Mir FA, Bourke PJ, Joseph S, Morgan DM, Santos MD, Wadiwala MF, Kamran S, Sivaraman SK and Shuaib A (2019) There Is Selective Increase in Pro-thrombotic Circulating Extracellular Vesicles in Acute Ischemic Stroke and Transient Ischemic Attack: A Study of Patients From the Middle East and Southeast Asia. Front. Neurol. 10:251. doi: 10.3389/fneur.2019.00251

INTRODUCTION

Acute ischemic stroke (AIS) is the leading cause of disability and the second most common cause of death and dementia worldwide. The incidence of AIS is particularly high in Southeast Asia (SE) and the Middle East (ME) where the prevalence of hypertension and diabetes is high and an increasing proportion of the population are obese and suffer from metabolic syndrome (1–3).

Enhanced platelet aggregation and cell activation are important contributors to the pathophysiology and progression of AIS and are closely associated with stroke risk factors such as hypertension and diabetes. In addition, loss of vascular homeostasis and low-grade inflammation can further contribute to endothelial dysfunction and atherogenesis, a primary factor in the pathogenesis of AIS (4). In this context, circulating extracellular vesicles (EVs), particularly the endoplasmic membrane-derived microparticles or microvesicles, owing to their crucial pro-coagulant role may contribute to the onset and development of AIS (5).

EVs are membrane-containing vesicles that are released from activated or apoptotic cells of any type. EVs are classified into three main categories based on their size and their mechanism of cellular release: exosomes (30–130 nm), microparticles or microvesicles (100–1,000 nm), and the larger apoptotic bodies (>1,000 nm) (6). Based on the most recent position statement of the International Society for Extracellular Vesicles (ISEV), the term EVs was adopted throughout this article as a generic term to refer to lipid membrane-delineated, replication-defective, and not carrying a functional nucleus, naturally cell-shed vesicles (7). Elevated circulating levels of EVs, particularly those of medium size (microparticles), were reported in many cardiovascular diseases associated with inflammation and thrombotic alterations including stroke and coronary artery disease (8, 9). Total numbers of circulating EVs or those deriving from specific cell populations were found to correlate with the presence and severity of multiple disorders and are thus considered as biomarkers for the monitoring of disease progression. For instance, EVs originating from platelets were found to correlate with atypical carotid intima/media thickness in obese patients (10). In addition, high plasma numbers of pro-coagulant EVs were reported in patients suffering from metabolic syndrome (11, 12). Levels of EVs shed from endothelial cells (13) and platelets (14) were reported to increase in AIS. In another study, circulating EVs from platelets, endothelial cells, erythrocytes, leukocytes, lymphocytes, monocytes, and smooth muscle cells increased at the onset, and at 7 and 90 days in patients suspected with AIS compared to controls (15). Recently, however, Landers-Ramos et al. (16) reported that EVs levels of endothelial origin were not increased in chronic stroke patients compared to young and old healthy volunteers. Nonetheless, chronic stroke patients also suffering from diabetes had higher plasma levels of endothelial-derived EVs in comparison to those free of diabetes (16).

Studies that have investigated EVs in stroke were mostly conducted in small numbers of patients and in homogenous ethnic populations. There are currently no reports available of EVs in stroke patients from ME and SE. Furthermore, none of the available studies has investigated the levels of circulating EVs in patients with TIA, a major precursor and risk factor for AIS. Another crucial point, is that most previous studies only looked at the expression of select sub-populations of EVs in stroke patients.

The aim of the present study was therefore to count the number of circulating medium size EVs and phenotype them according to their cellular origins in patients with TIA and AIS patients from SE and ME origins resident the state of Qatar, at onset (within 48 h of attacks), 5 and 30-days following the initiation of appropriate pharmacotherapy.

MATERIALS AND METHODS

Patients

The study was reviewed and approved by the Institutional Ethical Board (IRB) of Hamad Medical Corporation (#15304/15) and fully adhered to the principles of the declaration of Helsinki. All participants of the study gave written informed consent prior to their enrolment in the investigation. Patients were enrolled in the study within 48 h of stroke onset. Individuals aged 18 years and older and who gave written informed consent were included. Stroke was defined according to World Health Organization (WHO) criteria as "rapidly developing clinical signs of focal (or global) disturbance of cerebral function, with symptoms lasting 24 h or longer or leading to death, with no apparent cause other than vascular origin." TIA was defined as a brief episode of neurologic dysfunction resulting from transient cerebral ischemia but that is not accompanied by cerebral infarction. All AIS and TIA patients received at Hamad General hospital were eligible for inclusion.

Data Collection

The baseline medical history includes age, gender, ethnicity, nationality, marital status, household income, employment status, smoking status, alcohol intake, medical comorbidities (including a history of diabetes, dyslipidemia, coronary artery disease, peripheral vascular disease, chronic kidney disease, heart failure, and sleep apnea), and all current prescription and over-the-counter medications (including dosage, frequency and timing of administration). The cerebrovascular event type (AIS vs. TIA) was documented using the Trial of Org 10,172 in Acute Stroke Treatment (TOAST) classification and the date of stroke was recorded. This information is currently recorded routinely in the stroke database. We also recorded the type of work, duration of time since they moved to Qatar (for expatriate subjects) and the circumstances when the stroke occurred.

Physical examination included automated office blood pressure (BP) [taken with a BPTru® automated monitor by measuring six readings in the arm with the higher BP, discarding the first reading and averaging the latter two], height, weight, and waist circumference.

Laboratory tests included a complete blood count, electrolytes (sodium, potassium, chloride, total carbon dioxide), creatinine, fasting glucose, glycated hemoglobin (A1c), fasting lipid profile, c-reactive protein, and urine microalbumin. Computerized tomography (CT) head scan, echocardiogram, and standard (not

3D) carotid ultrasound results were performed as part of routine clinical care at the time of stroke were recorded in the case record forms (CRF). These tests are performed as part of routine clinical care.

Isolation of Platelet-Free Plasma (PFP) From Whole Blood

Peripheral venous blood (10 mL) from control subjects, AIS, and TIA patients was obtained in ethylenediaminetetraacetic acid tubes (Vacutainers; Becton Dickinson) by using a 21-gauge needle to reduce platelet stimulation. Samples were assayed within 2 h of collection at room temperature. Blood samples were then subjected low speed centrifugation (270 × *g*) for 20 min to separate platelet-rich plasma from whole blood. Following this, platelet-rich plasma was centrifuged for further 20 min at a speed of 1,500 × *g* to collect PFP, which was then frozen and stored at −80°C until subsequent analysis for EVs content (11, 12, 17, 18).

Count and Identification of Cellular Origins of EVs

Specific cellular subpopulations of medium size EVs were identified in PFP according the expression of surface-specific proteins as previously done by us (11, 12, 17, 18). Specific fluorescent antibodies targeting the following surface antigens were used in this study: PE-CD146 (endothelial cells), PE-CD41 (platelets), PC7-CD45 (leukocytes), PC7-CD235a (erythrocytes), PE-CD62E (E-Selectin$^+$ EVs), and PE-CD62P (P-Selectin$^+$ EVs) (Beckman Coulter through Sedeer Medical, Doha, Qatar). Irrelevant human IgG were used as isotype-matched negative controls for each sample (Beckman Coulter). To count medium size EVs and determine plasma concentrations for each cell origin, separate assays for each surface marker were conducted. Briefly, 10 μL of PFP from healthy controls or patients were incubated with 5 μL of each specific antibody for 45 min protected from light. Then, samples were suspended in 300 μL of 0.9% saline solution and 10 μL Flowcount microbeads (Beckman Coulter), a mix of fluorescent beads with known concentration used to calculate absolute counts, were mixed before samples were analyzed by flow cytometry using a BD LSRFortessa analyzer (BD Biosciences, USA) as previously shown by us (11, 12, 17, 18).

For the identification of the number of pro-coagulant EVs (expressing phosphatidylserine), separate assays were conducted to determine Annexin V binding. Briefly, 2 μL of Annexin V (Beckman Coulter) were incubated with 5 μL PFP from each participant for 30 min protected from light. Then, samples were suspended in 300 μL of Annexin-V labeling buffer, and 5 μL (equal volume to sample) of Flowcount microbeads (Beckman Coulter) were added before the analysis of samples by flow cytometry using a BD LSRFortessa analyzer (BD Biosciences) as previously shown by us (11, 12, 17, 18).

Statistical Data Analysis

Data are expressed as mean ± SEM or mean ± SD; *n* indicates the number of subjects included in each experimental group. Statistical analyses were performed by Mann-Whitney *U* or analysis of one-way variance (ANOVA) for repeated measures and subsequent Tukey's *post-hoc* test. $P < 0.05$ was accepted as statistically significant. Analyses were performed using GraphPad Prism 7 software (GraphPad Software Inc., San Diego, USA).

RESULTS

Patients Baseline Characteristics

Between September 2016 and May 2018, we recruited 24 healthy controls and a total of 119 patients with suspected acute stroke, of whom 87 patients (66 [76%] AIS and 21 [24%] TIA) were eventually included in the study after exclusion of stroke mimics.

The baseline characteristics of the 24 healthy volunteers and the 87 patients included in the study are shown in **Table 1**. Similar to previous experience, the average age in both TIA (48.6 ± 9.5) and AIS patients (50.5 ± 11.1) was young (3). The patient population was predominantly male in AIS patients (95.5%). In terms of disease classification, most AIS patients suffered from a small vessel disease (59.1%), followed by cardio-embolic attacks (16.7%) and large vessel disease (15.2%) (**Table 1**).

Total Number of Circulating of EVs and Their Cellular Origins at Onset of Attacks

The count of total EVs regardless of their cellular origin did not differ between controls, TIA and AIS patients (**Figure 1**) within 48 h of onset of attacks. TIA and AIS patients had significantly higher percentage of circulating EVs derived from endothelial cells (CD146$^+$; **Figure 2A**) and activated endothelial cells that express E-selectin (CD62E$^+$; **Figure 2B**) compared to healthy volunteers. Furthermore, there was a trend for AIS patients to express more of total and activated endothelial-derived EVs compared to TIA patients **(Figures 2A,B)**.

Whereas, platelet-derived EVs (CD41$^+$) were not significantly different between controls, TIA, or AIS patients **(Figure 2C)**, the number of EVs derived from activated platelets expressing P-selectin (CD62P$^+$) was significantly higher in TIA and AIS patients compared to controls **(Figure 2D)**. Interestingly, AIS patients exhibited a significantly higher percentage of activated platelets-derived EVs compared to TIA patients **(Figure 2D)**.

EVs derived from erythrocytes (CD235a$^+$) were found to be significantly higher in the blood from both TIA and AIS patients compared to healthy volunteers **(Figure 2E)**. Similarly, EVs derived from circulating immune cells, granulocytes (CD66$^+$; **Figure 2F**) and leukocytes (CD45$^+$; **Figure 2G**), were also significantly higher in TIA and AIS patients compared to controls although there was a non-significant trend for AIS patients to express more of these two EV subtypes compared to TIA patients **(Figures 2F,G)**. Finally, the percentage of pro-coagulant EVs expressing Annexin V at their surface was not significantly different between the three groups within 48 h of onset of attacks **(Figure 2H)**.

The Total Number of EVs Increased Over Time in AIS and TIA Patients as a Percentage of Onset Levels

To investigate the impact of disease progression and the initiation of treatment on the expression of EVs, we assessed the

TABLE 1 | Baseline Characteristics of subjects enrolled in the study.

	Controls ($n = 24$)	Transient Ischemic Attack ($n = 21$)	Acute Ischemic Stroke ($n = 66$)	*P* value
Age (years)	47.7 ± 7.4	48.6 ± 9.5	50.5 ± 11.1	0.485
GENDER				
Male	18 (75)	17 (81.0)	63 (95.5)	0.033
Female	6 (25)	4 (19.0)	3 (4.5)	
ETHNICITY				
ME	6 (29)	12 (57.1)	22 (33.3)	0.013
SE	18 (71)	9 (42.9)	44 (66.7)	
Prior use of statins	0	7 (33.3)	8 (12.1)	0.025
Prior use of anti-hypertensive	0	6 (28.6)	12 (18.2)	0.306
Prior use of anti-diabetic medications	0	3 (14.3)	10 (15.2)	0.923
Diabetic on admission	0	7 (33.3)	27 (40.9)	0.535
Hypertensive on admission	0	13 (61.9)	45 (68.2)	0.595
Dyslipidemia on admission	0	15 (71.4)	38 (57.6)	0.257
Previous stroke	0	1 (4.8)	2 (3.0)	0.705
Coronary artery disease	0	2 (9.5)	6 (9.1)	0.952
Atrial fibrillation	0	1 (4.8)	3 (4.5)	0.967
Smoking history	0	6 (28.6)	29 (43.9)	0.211
IV thrombolysis received	0	2 (9.5)	12 (18.2)	0.347
PROGNOSIS AT DISCHARGE				
Good (mRS 0–2)		21 (100.0)	48 (72.7)	0.007
Poor (mRS 3–6)		0.0	18 (27.3)	
PROGNOSIS AT 90-DAYS				
Good (mRS 0–2)		20 (95.2)	57 (86.4)	0.267
Poor (mRS 3–6)		1 (4.8)	9 (13.6)	
TOAST CLASSIFICATION				
Small vessel disease			39 (59.1)	
Large vessel disease			10 (15.2)	
Cardio-embolic			11 (16.7)	
Stroke of determined origin			3 (4.5)	
Stroke of undetermined origin			3 (4.5)	
OTHER				
Small vessel disease present		11 (52.4)	39 (59.1)	0.588
Silent infarct present		4 (19.0)	25 (37.9)	0.111
White matter ischemia present		14 (66.7)	52 (78.0)	0.258
Cerebral micro-bleeds present		4 (19.0)	20 (30.3)	0.315
Admission NIHSS		1.67 ± 2.1	3.35 ± 3.4	0.035
Systolic blood pressure		162.4 ± 26.1	157.4 ± 33.1	0.522
Diastolic blood pressure		94.7 ± 17.1	93.9 ± 21.0	0.883
Body Mass Index		27.6 ± 3.1	27.1 ± 3.9	0.634
HbA1c levels		6.4 ± 1.4	6.7 ± 2.1	0.545
Cholesterol levels		4.9 ± 1.3	5.2 ± 1.2	0.557
Triglyceride levels		1.9 ± 1.0	1.6 ± 0.9	0.353
HDL levels		1.1 ± 0.7	0.9 ± 0.2	0.031
LDL levels		3.1 ± 1.0	3.5 ± 1.0	0.086

Results are presented as mean ± SD or number (%) as appropriate. P-value from one-way ANOVA for quantitative variables and from Chi-square analysis for qualitative variables. mRS, modified Rankin scale; NIHSS, national institutes of health stroke scale.

progression of numbers of total EVs over time at 5- and 30-days post-attacks **(Figure 3)**. The counts of EVs are expressed either as absolute numbers or as percentage of increase compared to the levels observed at onset of attacks for every patient. As shown in **Figure 3A**, the absolute number of total EVs continued to increase over time in both TIA and AIS patients, with the levels

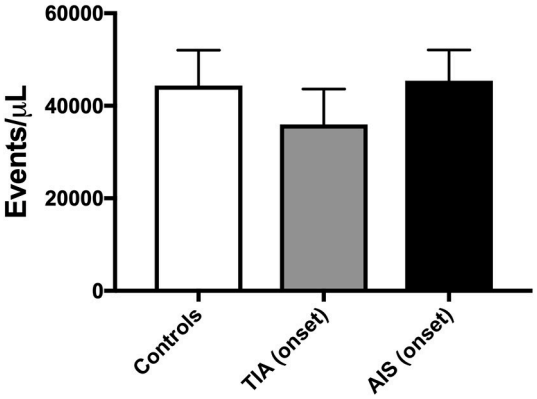

FIGURE 1 | Circulating total EV levels, at onset of attacks, in patients with TIA and AIS compared to healthy controls. Histograms represent events/μL in plasma poor in platelets (PFP) expressed as mean ± SEM. Controls, $n = 24$; TIA, $n = 21$; AIS, $n = 66$.

at the 30-days' time point being the most significant increase. As observed in **Figure 3B**, the number of total EVs, expressed as percentage of onset levels, also steadily increased over time at 5- and 30-days post-attacks both in TIA and AIS patients.

EVs From Selected Cellular Origins Increased Over Time Compared to Onset Levels

The increase in EVs at 5- and 30-days post-attacks varied depending on their cells of origin. TIA and AIS patients had higher levels of EVs derived from endothelial ($CD146^+$; **Figure 4A**) and activated endothelial cells ($CD62E^+$; **Figure 4B**) at 5- and 30-days compared to onset levels. The increase in EVs from activated endothelial cells ($CD62E^+$; **Figure 4B**) was highest in AIS patients, indicating a stronger activation of endothelial cells as the disease progresses in AIS patients compared to TIA patients. Similarly, EVs derived from both platelets ($CD41^+$; **Figure 4C**) and activated platelets ($CD62P^+$; **Figure 4D**) also significantly increased over time at 5- and 30-days in both TIA and AIS patients, indicating a sustained activation of platelets despite appropriate treatment being started. The expression of EVs derived from immune cells, granulocytes ($CD66b^+$; **Figure 4F**) and leukocytes ($CD45^+$; **Figure 4G**), also increased over time in both TIA and AIS patients, indicating a sustained activation of these cell types on the short-term following the start of pharmacotherapy. However, the levels of erythrocyte-derived EVs ($CD235a^+$; **Figure 4E**) decreased significantly over time at 5- and 30-days post-attacks in both TIA and AIS patients, suggesting a reduction in the activation of these cells over time following the initiation of therapy.

Although at onset of attacks, circulating levels of pro-coagulant EVs (Annexin V^+) were not different between controls, TIA and AIS **(Figure 2)**, the numbers of Annexin V^+ EVs, expressed as a proportion of onset levels, increased with time in both TIA and AIS patients at 5- and 30-days post-attacks **(Figure 4H)**, indicating that the shedding of pro-coagulant EVs increased over time.

As a Proportion of Total EVs at Each Time Point, the Initiation of Treatment Did Not Affect the Short-Term Expression of EVs Both in TIA and AIS Patients

As shown in **Figure 5**, the levels of circulating EVs, expressed as a percentage of total EVs at each time point, from all the cell origins investigated did not change in AIS patients over the monitored period (5- and 30-days post-attacks). Similar pattern was observed with TIA patients, where circulating levels of EVs from all cell origins studied did not vary, as a percentage of total EVs for each time point, after 5- and 30-days following the initiation of the pharmacotherapy (**Figure 6**). These data demonstrate that, as a percentage of total EVs at each time point, circulating levels of EVs from various cellular origins were constant over time (at 5- and 30-days) although their numbers have increased compared to onset time point. The increased number of total EVs over time drives the increase of specific populations of EVs without affecting their overall proportion in blood. Together, these findings further indicate that in both TIA and AIS patients, cellular activation continued to be elevated on the short-term despite the management of risk factors and the administration of appropriate pharmacotherapy to the patients.

DISCUSSION

For many decades, EVs were considered as inert cell debris or platelet dust derived from platelets which are rich in phospholipids and endowed of pro-coagulant capacity (8). Later, it was found that EVs could transport cargo content including secretable and non-secretable biological molecules such as active lipids, nucleic acids (microRNA and mRNA) in addition to membrane and cytosolic proteins to target cells (8, 19, 20). Circulating EVs derive from platelets, red and white blood cells, endothelial cells, and monocytes; however, most EVs found in the blood are from platelet origin (8, 9). EVs regulate inflammation and have pro-coagulant properties (21). Plasma numbers of EVs are elevated in cardiovascular disorders associated with thrombotic alterations including stroke and coronary artery disease (8, 9). Plasma levels of total EVs or those deriving from specific cell populations were found to correlate with the presence and severity of multiple disorders and are thus considered as biomarkers for the monitoring of disease progression and hence can provide a signature for changes occurring inside the body (11, 12, 22).

We report in the current study that although the total number of EVs did not differ between TIA and AIS patients compared to controls within 48 h of attacks onset, both TIA and AIS patients had higher circulating levels of EVs derived from endothelial cells ($CD146^+$), activated endothelial cells ($CD62E^+$), activated platelets ($CD62P^+$), granulocytes ($CD66b^+$), and leukocytes ($CD45^+$) compared to controls; however, AIS patients had higher

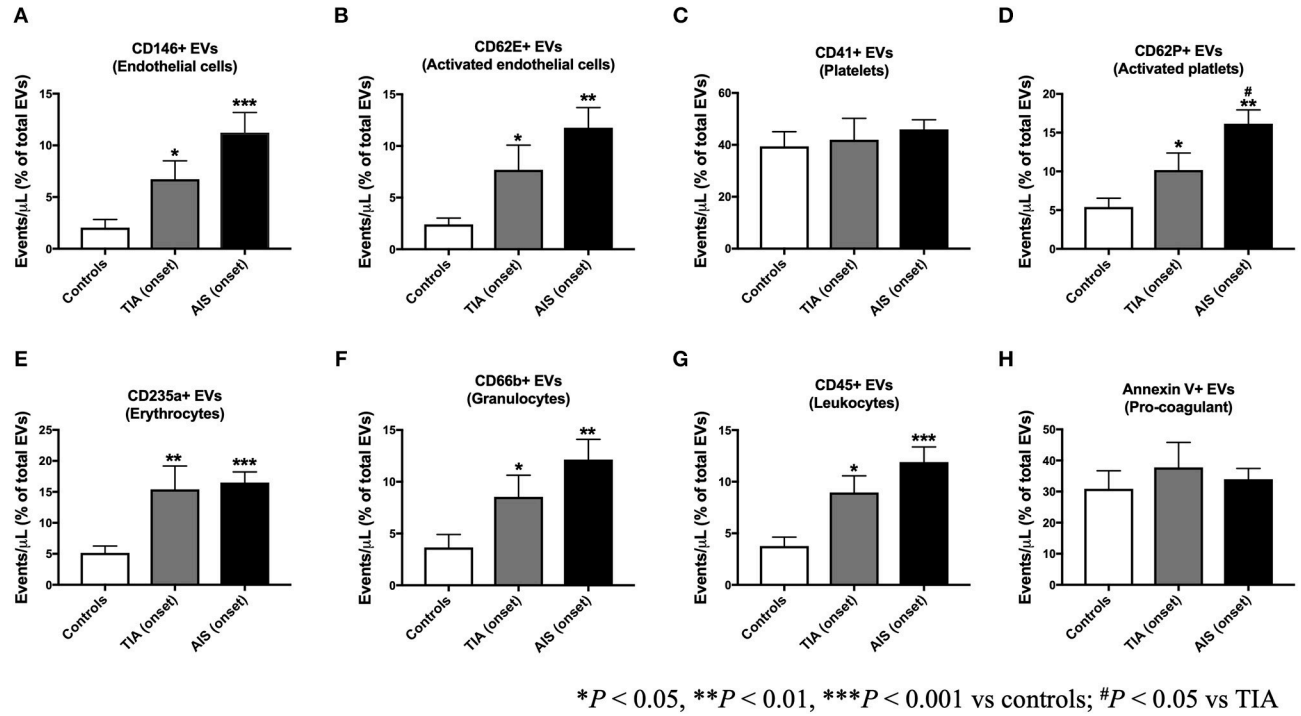

FIGURE 2 | Circulating EV levels, expressed as percentage of total EVs, at onset of attacks, in patients with TIA and AIS compared to healthy controls. Histograms represent circulating levels of EVs derived from: **(A)** endothelial cells ($CD146^+$), **(B)** activated endothelial cells ($CD62E^+$), **(C)** platelets (CD41), **(D)** activated platelets ($CD62P^+$), **(E)** erythrocytes ($CD235a^+$), **(F)** granulocytes ($CD66b^+$), **(G)** leukocytes ($CD45^+$), **(H)** and pro-coagulant (Annexin V^+) origins. Histograms represent events/μL (% of total EVs) in PFP expressed as mean ± SEM. Controls, $n = 24$; TIA, $n = 21$; AIS, $n = 66$. $^*P < 0.05$, $^{**}P < 0.01$, $^{***}P < 0.001$ vs. controls; $^{\#}P < 0.05$ vs. TIA.

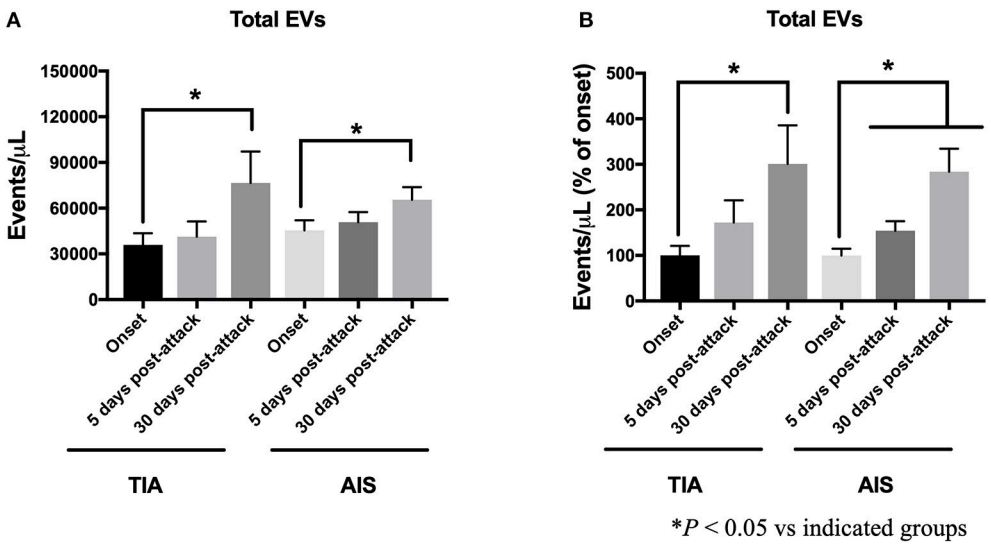

FIGURE 3 | Circulating total EV levels, at onset, 5-days and 30-days post-attacks in patients with TIA and AIS patients. **(A)** Histograms represent total EVs expressed as events/μL in PFP. **(B)** Histograms represent total EVs expressed as events/μL (% of onset levels) in PFP. Data are expressed as mean ± SEM. Controls, $n = 24$; TIA, $n = 21$; AIS, $n = 66$. $^*P < 0.05$ vs. indicated groups.

numbers compared to TIA patients. While there are few reports regarding the phenotype of expression of circulating EVs in AIS, there is a severe paucity of information regarding EVs numbers in blood from TIA patients and how they differ compared to AIS patients. To the best of our knowledge, this is the first report to determine circulating levels of EVs from various cell origins

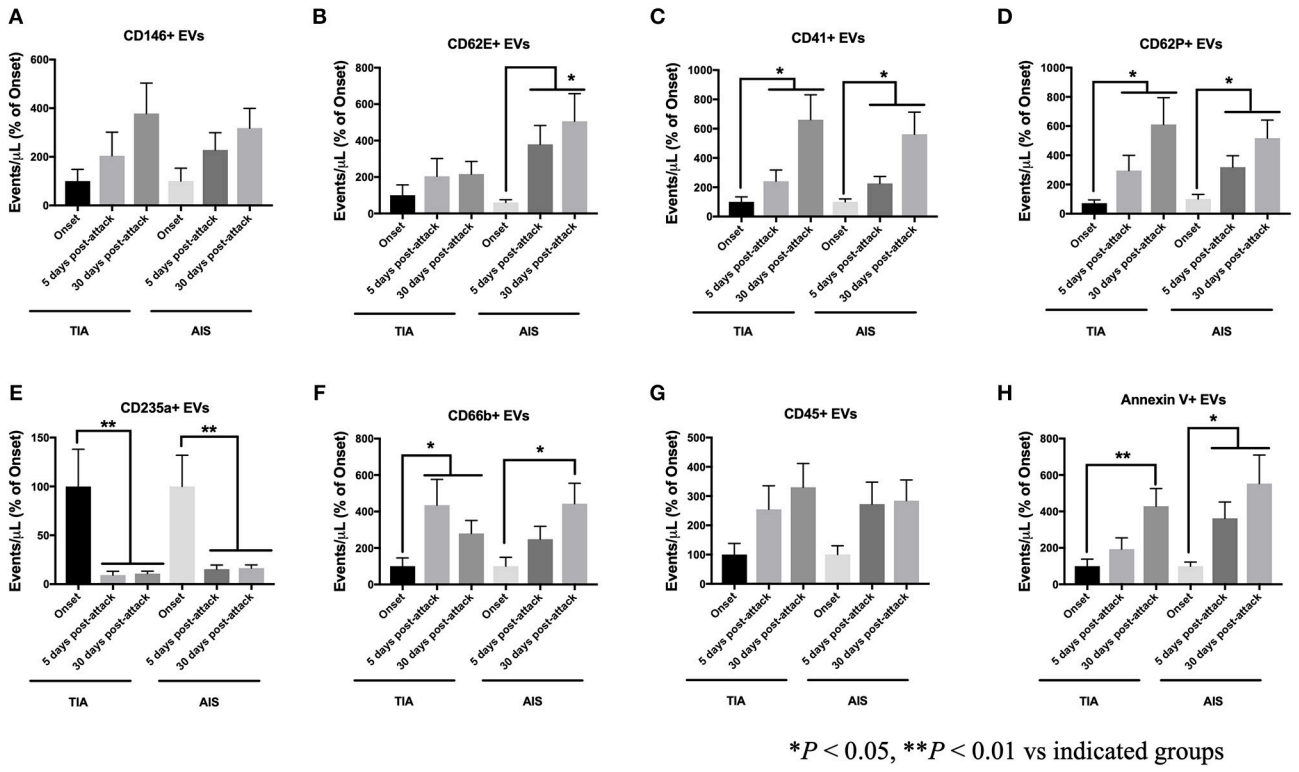

FIGURE 4 | Circulating EV levels, expressed as events/μL (% of onset levels), at onset, 5-days and 30-days post attacks, in PFP from patients with TIA and AIS. Histograms represent circulating levels of EVs derived from: **(A)** endothelial cells ($CD146^+$), **(B)** activated endothelial cells ($CD62E^+$), **(C)** platelets (CD41), **(D)** activated platelets ($CD62P^+$), **(E)** erythrocytes ($CD235a^+$), **(F)** granulocytes ($CD66b^+$), **(G)** leukocytes ($CD45^+$), **(H)** and pro-coagulant (Annexin V^+) origins. Data are expressed as mean ± SEM. Controls, $n = 24$; TIA, $n = 21$; AIS, $n = 66$. $^*P < 0.05$, $^{**}P < 0.01$ vs. indicated groups.

in TIA patients and compare them to AIS patients and healthy controls. Only one previous publication could be found reporting increased levels of platelet-derived EVs in TIA compared to controls (23).

In relation to AIS, our findings are partly in agreement with the few previous studies which investigated EVs levels in AIS patients. Li et al. (13) have studied EVs in a cohort composed of patients with AIS and gender-matched healthy volunteers. In accordance with our data, authors reported that patients had higher levels of endothelial-derived EVs and EVs carrying markers of cell activation ($CD62E^+$); however, no differences in platelet-derived EVs were noted (13). Another study, reported in a cohort of AIS patients that platelet-derived EVs were, however, increased compared to control subjects (14). Recently, it was observed that plasma levels of endothelial-derived EVs were not increased in chronic stroke patients compared to younger and old healthy volunteers (16). These findings are in contrast with our observations and the discrepancy may be attributable to the ethnic differences between the study cohorts [Chinese in Chen et al. (14) vs. SE and ME in our study]. In addition, the study by Chen et al. (14), determined the levels of platelet-derived EVs using anti-CD61 antibody, while in our study we have used an anti-CD41 antibody. Both CD41 and CD61 are platelet-specific glycoproteins, which were widely used as surface markers for the detection of EVs from platelet origin (24, 25). However, in our hands, we have observed similar results to those observed with CD41 when CD61 was used as a surface marker to detect platelet-derived EVs (data not shown for CD61) and hence the discrepancy between the **two** studies may be more related to the ethnic differences in study populations.

More recently, circulating EVs from platelets, endothelial cells, erythrocytes, leukocytes, lymphocytes, monocytes, and smooth muscle cells were analyzed in patients with suspected AIS at the onset of attacks, and then at 7 and 90 days. In line with our observations reported here, authors observed that EVs from all these cell origins were increased in stroke patients compared to controls at onset of attacks and that their levels remained high at 7 and 90 days following the acute events (15). In our hands, we observed that, by contrast to Chiva-Blanch et al. (15), the number of EVs from endothelial cells, activated endothelial cells, platelets, activated platelets, granulocytes, leukocytes, and pro-coagulant origin, expressed as percentage of onset levels, all increased in both TIA and AIS patients after 5 and 30 days post-attacks and the initiation of treatment and the management of risk factors (e.g., diabetes or hypertension). These data, show an escalated cell activation, particularly in endothelial cells and platelets, acutely after the attacks in both

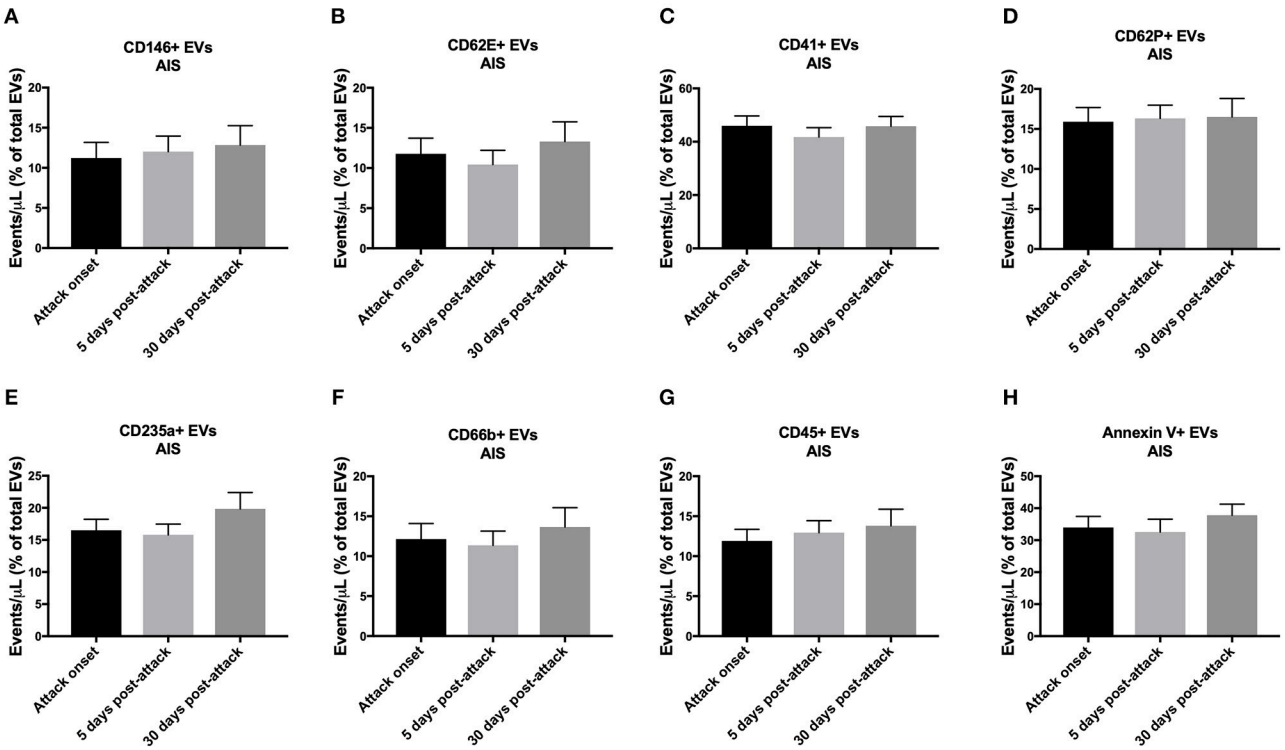

FIGURE 5 | Circulating EV levels, expressed as events/μL (% of total EVs), at onset, 5-days and 30-days post-attacks in PFP from patients with AIS. Histograms represent circulating levels of EVs derived from: **(A)** endothelial cells ($CD146^+$), **(B)** activated endothelial cells ($CD62E^+$), **(C)** platelets (CD41), **(D)** activated platelets ($CD62P^+$), **(E)** erythrocytes ($CD235a^+$), **(F)** granulocytes ($CD66b^+$), **(G)** leukocytes ($CD45^+$), **(H)** and pro-coagulant (Annexin V^+) origins. Data are expressed as mean ± SEM. AIS, $n = 66$.

TIA and AIS patients, which may contribute to heightened endothelial and pro-thrombotic activities contributing thus to an elevated risk of stroke recurrence. However, we cannot rule out that the elevation of EVs levels following the attacks and the start of pharmacotherapy might be related to the resolution of thrombi and the secondary consequences of ischemic episodes. Thus, a longer follow-up of these patients is warranted to determine the long-term changes of EVs and further ascertain the prognostic value of circulating EVs levels in TIA and AIS patients with regards to the risk of recurrence.

Of particular interest, in our study, plasma levels of EVs from platelets ($CD41^+$), activated platelets ($CD62P^+$), and pro-coagulant (Annexin V^+) origins increased, as a percentage of onset numbers, on the short-term (at 5- and 30-days after acute attacks), indicating a higher number of EVs with pro-thrombotic activity, which may contribute to the increased risk of recurrence of stroke in these patients, including those with no major consequences (TIA). EVs from platelet origin are indeed strongly pro-thrombotic (21). It has been reported that one single platelet-derived EV had nearly the same pro-coagulant activity as one activated platelet despite the surface area was 2 orders of magnitude smaller, suggesting that the surface of platelet-derived EVs is 50 to 100–fold more pro-coagulant than that of activated platelets (26). Furthermore, though not directly assessed in this study, EVs expressing tissue factor (TF) may also enhance the coagulation process in stroke patients. EVs carrying TF were found to be highly expressed in several ischemic conditions such as atherosclerosis and acute coronary syndromes (27). It was reported that the expression of TF at the surface of EVs enhanced their pro-coagulant response (28). Higher circulating levels of EVs expressing TF were observed in AIS patients compared to healthy controls. Moreover, 1 week after the diagnosis, the activity of EVs was found to be more elevated in stroke patients not treated with tissue plasminogen activator compared to their basal activity at the onset of attacks (29).

While we have observed that erythrocyte-derided EVs ($CD235a^+$) were increased to the same extent in both TIA and AIS compared to controls within 48 h of onset of attacks, we found that their levels, expressed as a proportion of onset levels, decreased in both TIA and AIS patients at 5- and 30-days following the initiation of pharmacotherapy. In contrast with our observation, Chiva-Blanch et al. (15), found that erythrocyte-derived EVs were higher in AIS patients compared to controls and continued to be high at 7 and 90 days post-stroke attacks (15). Our data suggest that the administration of treatment to patients led to a decrease in the expression of erythrocyte-derided EVs, which were previously linked to hypercoagulable states. Consistent with our observations, Tan et al. (30), observed that high circulating levels of phosphatidylserine-positive erythrocyte-derived EVs, which were highly pro-coagulant, in patients suffering from

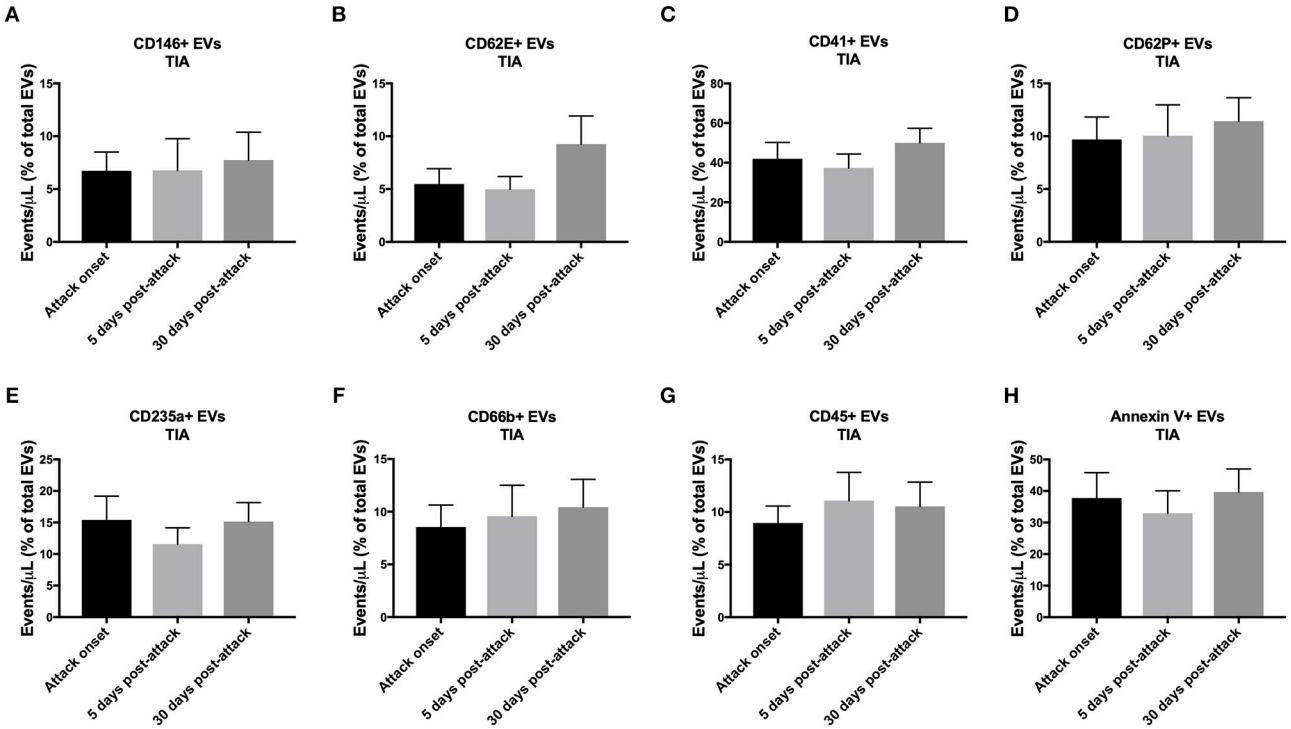

FIGURE 6 | Circulating EV levels, expressed as events/μL (% of total EVs), at onset, 5-days and 30-days post-attacks in PFP from patients with TIA. Histograms represent circulating levels of EVs derived from: **(A)** endothelial cells ($CD146^+$), **(B)** activated endothelial cells ($CD62E^+$), **(C)** platelets (CD41), **(D)** activated platelets ($CD62P^+$), **(E)** erythrocytes ($CD235a^+$), **(F)** granulocytes ($CD66b^+$), **(G)** leukocytes ($CD45^+$), **(H)** and pro-coagulant (Annexin V^+) origins. Data are expressed as mean ± SEM. TIA, $n = 21$.

the hypercoagulable status of polycythemia vera and that the treatment of patients with hydroxyurea was associated with a decrease in the shedding of EVs from erythrocytes (30).

Our data characterized for the **first** time circulating EVs in patients with AIS and compared them to TIA in a multiethnic population from SE and ME origins. We provided here, a very comprehensive analysis of most circulating EVs from vascular wall, blood, and immune cells. We found here that EVs of various origins, especially those associated with endothelial cell injury and platelet activation, are increased in TIA and AIS patients and that their levels persist to be high on the short-term up to 30-days post-attacks, indicating a sustained cellular activation, which may be associated with a heightened risk of recurrence of acute events. Therefore, longer follow-up studies are required to ascertain the value of EVs as biomarkers for the risk of stroke recurrence, especially in a population presenting with stroke at young age like this one.

DATA AVAILABILITY

The datasets generated for this study are available on request to the corresponding author.

AUTHOR CONTRIBUTIONS

AA and AS wrote the article and all authors contributed to the drafting of the manuscript and its critical revision for intellectual content. AA, AS, and ASP were involved in the study conception and design and in the interpretation of data. AA and AS acquired funding and supervised the experiments. AA, ASP, FM, and SS conducted sample analysis, and data acquisition, processing, statistical analysis, and interpretation. AS oversaw the whole clinical process and contributed to the analysis and interpretation of data. NA, PB, SJ, DM, MS, MW, and SK collected clinical data, refined diagnosis, and collected clinical samples for the study. NA contributed to the interpretation of clinical data.

ACKNOWLEDGMENTS

This work was supported by a Qatar University high collaborative grant (QUCG-CPH-2018\2019-2) to AA. The publication of this article was funded by Qatar National Library. The statements made herein are solely the responsibility of the authors.

REFERENCES

1. Brainin M, Teuschl Y, Kalra L. Acute treatment and long-term management of stroke in developing countries. *Lancet Neurol.* (2007) 6:553–61. doi: 10.1016/S1474-4422(07)70005-4
2. Feigin VL, Roth GA, Naghavi M, Parmar P, Krishnamurthi R, Chugh S, et al. Global burden of stroke and risk factors in 188 countries, during 1990–2013: a systematic analysis for the Global Burden of Disease Study 2013. *Lancet Neurol.* (2016) 15:913–24. doi: 10.1016/S1474-4422(16)30073-4
3. Akhtar N, Salam A, Kamran S, D'Souza A, Imam Y, Own A, et al. Pre-existing Small vessel disease in patients with acute stroke from the Middle East, Southeast Asia, and Philippines. *Transl Stroke Res.* (2018) 9:274–82. doi: 10.1007/s12975-017-0578-7
4. Jensen HA, Mehta JL. Endothelial cell dysfunction as a novel therapeutic target in atherosclerosis. *Expert Rev Cardiovasc Ther.* (2016) 14:1021–33. doi: 10.1080/14779072.2016.1207527
5. Wang B, Cai W, Zhang Z, Zhang H, Tang K, Zhang Q, et al. Circulating microparticles in patients after ischemic stroke: a systematic review and meta-analysis. *Rev Neurosci.* (2018). doi: 10.1515/revneuro-2017-0105. [Epub of print].
6. Chiang CY, Chen C. Toward characterizing extracellular vesicles at a single-particle level. *J Biomed Sci.* (2019) 26:9. doi: 10.1186/s12929-019-0502-4
7. Thery C, Witwer KW, Aikawa E, Alcaraz MJ, Anderson JD, Andriantsitohaina R, et al. Minimal information for studies of extracellular vesicles 2018 (MISEV2018): a position statement of the International Society for Extracellular Vesicles and update of the MISEV2014 guidelines. *J Extracell Vesicles*. (2018) 7:1535750. doi: 10.1080/20013078.2018.1535750
8. Agouni A, Andriantsitohaina R, Martinez MC. Microparticles as biomarkers of vascular dysfunction in metabolic syndrome and its individual components. *Curr Vasc Pharmacol.* (2014) 12:483–92. doi: 10.2174/15701611126661404232231 48
9. Chen Y, Li G, Liu ML. Microvesicles as Emerging biomarkers and therapeutic targets in cardiometabolic diseases. *Genomics Proteomics Bioinformatics*. (2018) 16:50–62. doi: 10.1016/j.gpb.2017.03.006
10. Csongradi E, Nagy B Jr, Fulop T, Varga Z, Karanyi Z, Magyar MT, et al. Increased levels of platelet activation markers are positively associated with carotid wall thickness and other atherosclerotic risk factors in obese patients. *Thromb Haemost*. (2011) 106:683–92. doi: 10.1160/TH11-01-0030
11. Agouni A, Lagrue-Lak-Hal AH, Ducluzeau PH, Mostefai HA, Draunet-Busson C, Leftheriotis G, et al. Endothelial dysfunction caused by circulating microparticles from patients with metabolic syndrome. *Am J Pathol.* (2008) 173:1210–9. doi: 10.2353/ajpath.2008.080228
12. Agouni A, Ducluzeau PH, Benameur T, Faure S, Sladkova M, Duluc L, et al. Microparticles from patients with metabolic syndrome induce vascular hyporeactivity via Fas/Fas-ligand pathway in mice. *PLoS ONE*. (2011) 6:e27809. doi: 10.1371/journal.pone.0027809
13. Li P, Qin C. Elevated circulating VE-cadherin^{+}CD144^{+}endothelial microparticles in ischemic cerebrovascular disease. *Thromb Res.* (2015) 135:375–81. doi: 10.1016/j.thromres.2014.12.006
14. Chen Y, Xiao Y, Lin Z, Xiao X, He C, Bihl JC, et al. The role of circulating platelets microparticles and platelet parameters in acute ischemic stroke patients. *J Stroke Cerebrovasc Dis.* (2015) 24:2313–20. doi: 10.1016/j.jstrokecerebrovasdis.2015.06.018
15. Chiva-Blanch G, Suades R, Crespo J, Pena E, Padro T, Jimenez-Xarrie E, et al. Microparticle shedding from neural progenitor cells and vascular compartment cells is increased in ischemic stroke. *PLoS ONE*. (2016) 11:e0148176. doi: 10.1371/journal.pone.0148176
16. Landers-Ramos RQ, Serra MC, Blumenthal JB, Ryan AS, Hafer-Macko CE, Prior SJ. Type 2 diabetes and older age contribute to elevated plasma microparticle concentrations independent of chronic stroke. *Exp. Physiol.* (2018) 103:1560–70. doi: 10.1113/EP087116
17. Mostefai HA, Meziani F, Mastronardi ML, Agouni A, Heymes C, Sargentini C, et al. Circulating microparticles from patients with septic shock exert protective role in vascular function. *Am J Respir Crit Care Med.* (2008) 178:1148–55. doi: 10.1164/rccm.200712-1835OC
18. Priou P, Gagnadoux F, Tesse A, Mastronardi ML, Agouni A, Meslier N, et al. Endothelial dysfunction and circulating microparticles from patients with obstructive sleep apnea. *Am J Pathol.* (2010) 177:974–83. doi: 10.2353/ajpath.2010.091252
19. Tual-Chalot S, Leonetti D, Andriantsitohaina R, Martinez MC. Microvesicles: intercellular vectors of biological messages. *Mol Interv.* (2011) 11:88–94. doi: 10.1124/mi.11.2.5
20. Zaborowski MP, Balaj L, Breakefield XO, Lai CP. Extracellular vesicles: composition, biological relevance, and methods of study. *Bioscience*. (2015) 65:783–97. doi: 10.1093/biosci/biv084
21. Morel O, Jesel L, Freyssinet JM, Toti F. Cellular mechanisms underlying the formation of circulating microparticles. *Arterioscler Thromb Vasc Biol.* (2011) 31:15–26. doi: 10.1161/ATVBAHA.109.200956
22. Sinning JM, Jansen F, Hammerstingl C, Meier A, Losch J, Rohwer K, et al. Circulating microparticles decrease after cardiac stress in patients with significant coronary artery stenosis. *Clin Cardiol.* (2016) 39:570–7. doi: 10.1002/clc.22566
23. Lee YJ, Jy W, Horstman LL, Janania J, Reyes Y, Kelley RE, et al. Elevated platelet microparticles in transient ischemic attacks, lacunar infarcts, and multiinfarct dementias. *Thromb Res.* (1993) 72:295–304.
24. Bennett JS, Berger BW, Billings PC. The structure and function of platelet integrins. *J Thromb Haemost.* (2009) 7(Suppl. 1):200–5. doi: 10.1111/j.1538-7836.2009.03378.x
25. Nolan JP, Jones JC. Detection of platelet vesicles by flow cytometry. *Platelets*. (2017) 28:256–62. doi: 10.1080/09537104.2017.1280602
26. Sinauridze EI, Kireev DA, Popenko NY, Pichugin AV, Panteleev MA, Krymskaya OV, et al. Platelet microparticle membranes have 50- to 100-fold higher specific procoagulant activity than activated platelets. *Thromb Haemost.* (2007) 97:425–34. doi: 10.1160/TH06-06-0313
27. Morel O, Toti F, Hugel B, Bakouboula B, Camoin-Jau L, Dignat-George F, et al. Procoagulant microparticles: disrupting the vascular homeostasis equation? *Arterioscler Thromb Vasc Biol.* (2006) 26:2594–604. doi: 10.1161/01.ATV.0000246775.14471.26
28. Owens APIII, Mackman N. Microparticles in hemostasis and thrombosis. *Circ Res.* (2011) 108:1284–97. doi: 10.1161/CIRCRESAHA.110.233056
29. Switonska M, Slomka A, Sinkiewicz W, Zekanowska E. Tissue-factor-bearing microparticles (MPs-TF) in patients with acute ischaemic stroke: the influence of stroke treatment on MPs-TF generation. *Eur J Neurol.* (2015) 22:e328–99. doi: 10.1111/ene.12591
30. Tan X, Shi J, Fu Y, Gao C, Yang X, Li J, et al. Role of erythrocytes and platelets in the hypercoagulable status in polycythemia vera through phosphatidylserine exposure and microparticle generation. *Thromb Haemost.* (2013) 109:1025–32. doi: 10.1160/TH12-11-0811

Conflict of Interest Statement: The authors declare that the research was conducted in the absence of any commercial or financial relationships that could be construed as a potential conflict of interest.

frontiers in Cellular Neuroscience

ORIGINAL RESEARCH
published: 16 May 2019
doi: 10.3389/fncel.2019.00209

Impairment and Restoration of Homeostatic Plasticity in Cultured Cortical Neurons From a Mouse Model of Huntington Disease

*Amy I. Smith-Dijak[1,2], Wissam B. Nassrallah[1,2], Lily Y. J. Zhang[2], Michal Geva[3†], Michael R. Hayden[3,4†] and Lynn A. Raymond[2]**

[1] Graduate Program in Neuroscience, The University of British Columbia, Vancouver, BC, Canada, [2] Department of Psychiatry, Djavad Mowafaghian Centre for Brain Health, The University of British Columbia, Vancouver, BC, Canada, [3] Research and Development, Teva Pharmaceutical Industries Ltd., Netanya, Israel, [4] Centre for Molecular Medicine and Therapeutics, The University of British Columbia, Vancouver, BC, Canada

OPEN ACCESS

Edited by:
Sriharsha Kantamneni,
University of Bradford,
United Kingdom

Reviewed by:
C. Andrew Frank,
The University of Iowa, United States
Corette J. Wierenga,
Utrecht University, Netherlands

***Correspondence:**
Lynn A. Raymond
lynn.raymond@ubc.ca

†Present address:
Michal Geva and
Michael R. Hayden,
Prilenia Therapeutics Development
Ltd., Herzliya, Israel

Specialty section:
This article was submitted to
Cellular Neuropathology,
a section of the journal
Frontiers in Cellular Neuroscience

Received: 27 October 2018
Accepted: 24 April 2019
Published: 16 May 2019

Citation:
Smith-Dijak AI, Nassrallah WB,
Zhang LYJ, Geva M, Hayden MR and
Raymond LA (2019) Impairment
and Restoration of Homeostatic
Plasticity in Cultured Cortical Neurons
From a Mouse Model of Huntington
Disease.
Front. Cell. Neurosci. 13:209.
doi: 10.3389/fncel.2019.00209

Huntington disease (HD) is an inherited neurodegenerative disorder caused by a mutation in the *huntingtin* gene. The onset of symptoms is preceded by synaptic dysfunction. Homeostatic synaptic plasticity (HSP) refers to processes that maintain the stability of networks of neurons, thought to be required to enable new learning and cognitive flexibility. One type of HSP is synaptic scaling, in which the strength of all of the synapses onto a cell increases or decreases following changes in the cell's level of activity. Several pathways implicated in synaptic scaling are dysregulated in HD, including brain-derived neurotrophic factor (BDNF) and calcium signaling. Here, we investigated whether HSP is disrupted in cortical neurons from an HD mouse model. We treated cultured cortical neurons from wild-type (WT) FVB/N or YAC128 HD mice with tetrodotoxin (TTX) for 48 h to silence action potentials and then recorded miniature excitatory postsynaptic currents. In WT cultures, these increased in both amplitude and frequency after TTX treatment, and further experiments showed that this was a result of insertion of AMPA receptors and formation of new synapses, respectively. Manipulation of BDNF concentration in the culture medium revealed that BDNF signaling contributed to these changes. In contrast to WT cortical neurons, YAC128 cultures showed no response to action potential silencing. Strikingly, we were able to restore the TTX-induced changes in YAC128 cultures by treating them with pridopidine, a drug which enhances BDNF signaling through stimulation of the sigma-1 receptor (S1R), and with the S1R agonist 3-PPP. These data provide evidence for disruption of HSP in cortical neurons from an HD mouse model that is restored by stimulation of S1R. Our results suggest a potential new direction for developing therapy to mitigate cognitive deficits in HD.

Keywords: Huntington disease, homeostatic, synaptic, plasticity, calcium, BDNF, pridopidine

INTRODUCTION

Huntington disease (HD) is an autosomal dominant neurodegenerative disorder caused by an expansion of the CAG repeat region in the first exon of the gene encoding the protein huntingtin (Htt) (MacDonald et al., 1993). Neurodegeneration in HD begins with the death of striatal spiny projection neurons (SPNs), but is preceded by altered function at the corticostriatal synapse (Cepeda et al., 2007; Milnerwood and Raymond, 2010; Plotkin and Surmeier, 2015), and altered cortical activity and plasticity, which has been documented in humans a decade before disease onset (Cepeda et al., 2007; Schippling et al., 2009; Milnerwood and Raymond, 2010; Orth et al., 2010). It has also been found that knocking out mutant Htt (mHtt) in the cortex of HD model mice ameliorates their behavioral changes (Estrada-Sánchez et al., 2015). This suggests that, while striatal neurons are the first to die in HD, cortical neurons are also important in early HD pathophysiology.

Wild-type (WT) Htt interacts with hundreds of proteins involved in many aspects of cellular function, and the presence of mHtt disrupts a correspondingly large number of processes (Shirasaki et al., 2012; Saudou and Humbert, 2016). One of these processes which has received little attention, but which has recently been highlighted as being of potential interest (Wang et al., 2017), is homeostatic synaptic plasticity (HSP). HSP refers to a group of processes, such as synaptic scaling and metaplasticity, which maintain the level of activity of a network of neurons around a set point. Without these processes, a network which could only undergo the classical plasticity processes of long-term potentiation (LTP) and long-term depression (LTD) would eventually become either hyper- or hypoconnected; with either state resulting in neuronal dysfunction and death (Marder and Goaillard, 2006; Turrigiano, 2007; Watt and Desai, 2010). The set of genes involved in HSP overlaps with those involved in multiple neurodegenerative disorders, including several types of episodic ataxia, spinocerebellar ataxia type 19, and fragile X syndrome, as well as HD (Wang et al., 2017).

One point of overlap between HSP and HD is brain-derived neurotrophic factor (BDNF). While Htt does not directly interact with BDNF, it does interact with many proteins involved in BDNF transport and signaling, and BDNF signaling through the TrkB receptor is reduced in HD (Zuccato and Cattaneo, 2007; Milnerwood and Raymond, 2010; Shirasaki et al., 2012; Plotkin and Surmeier, 2015; Saudou and Humbert, 2016). BDNF signaling is also involved in synaptic scaling, a type of HSP. Synaptic scaling is a phenomenon wherein the strength of all of the synapses onto a neuron increases or decreases in response to a change in a neuron's overall level of activity. In excitatory neurons, such as cortical pyramidal neurons (CPNs), increased activity results in decreased synaptic strength, referred to as synaptic down-scaling. Decreased activity results in increased synaptic strength, referred to as synaptic up-scaling (Turrigiano et al., 1998). BDNF is released in an activity-dependent manner, and it is thought that reduced activation of the TrkB receptor by BDNF is a signal for synaptic up-scaling (Rutherford et al., 1998; Turrigiano, 2007; Watt and Desai, 2010). If this signaling is disrupted, as is the case in HD, it could interfere with synaptic up-scaling.

Another notable point of overlap between HD and HSP is calcium homeostasis (Shirasaki et al., 2012; Ryskamp et al., 2017; Wang et al., 2017). Cytoplasmic calcium concentration has been shown to be increased in SPNs from HD model mice as a result of increased entry through *N*-methyl-D-aspartate receptors (NMDARs), whose subunit composition and localisation in these cells is altered (Milnerwood et al., 2010, 2012), and sensitisation of the inositol 1,4,5-trisphosphate receptor (IP3R), which results in increased release of Ca^{2+} from the endoplasmic reticulum (ER) (Tang et al., 2003; Ryskamp et al., 2017). Dysregulated cytoplasmic Ca^{2+} is thought to contribute to the early dysfunction and eventual death of SPNs in HD (Milnerwood and Raymond, 2010). Calcium signaling has been implicated in multiple types of HSP (Marder and Goaillard, 2006; Turrigiano, 2007; Watt and Desai, 2010), and elevated cytoplasmic Ca^{2+} could interfere with any of them.

Together, this suggested to us that the disruption of BDNF and calcium homeostasis in HD may interfere with HSP. The drug pridopidine, which has been investigated as a treatment for HD (Kieburtz et al., 2018), has been shown to normalize both of these signaling pathways (Geva et al., 2016; Ryskamp et al., 2017). We therefore set out to investigate whether HSP, and specifically synaptic scaling, is disrupted in cortical neurons from the YAC128 HD mouse model, and whether pridopidine could restore any such deficit.

MATERIALS AND METHODS

Cell Culture

FVB/N WT or YAC128 (line 55) mice (Slow et al., 2003) were bred and maintained in the University of British Columbia Animal Resource Unit according to guidelines of the Canadian Council on Animal Care, under the approved protocol A15-0069. Cortical neurons were isolated from mouse pups as previously described (Milnerwood et al., 2012). If the culture was being prepared for electrophysiology, 2.7 million cells were suspended in 12 mL D minimum essential medium (DMEM, GIBCO) with 10% FBS (DMEM+). For cultures prepared for immunohistochemistry, 2 million cells were suspended in 100 μL electroporation buffer (Mirus Bio) with a plasmid encoding GFP (Addgene plasmid 37825). This solution was placed in a cuvette, electroporated (AMAXA nucleofector I: program 03), and resuspended in 12 mL DMEM+ with 0.7 million non-transfected cells. Cells were plated at a density of 1.125×10^5 cells per cm^2 in a 24-well plate. After 3 h, DMEM+ was replaced with 0.5 mL plating medium (PM; 2% B27, Invitrogen; penicillin/streptomycin; 2 mM α-glutamine; neurobasal medium, GIBCO). An additional 0.5 mL/well PM was added at 3 days *in vitro* (DIV), half of the culture's PM was replaced at DIV10 and again 4 days before recording or fixation.

Drug Treatment

For experiments involving pridopidine or R(+)-3-(3-Hydroxyphenyl)-*N*-propylpiperidine (3-PPP; Sigma), cells were treated with 0.1, 1, or 10 μM pridopidine (Teva

Pharmaceuticals Ltd.), or 1 μM 3-PPP (Sigma) during the half-medium change 4 days before recording or fixation. To test induction of HSP, cells were treated with 2 μM tetrodotoxin (TTX; Affix Scientific) vs. dH_2O (vehicle) with or without 25 ng/mL BDNF (Thermo Fisher Scientific), or else with 1.5 μg/mL TrkB-Fc (R&D Systems) 2 days before recording or fixation. TTX was stored and handled in accordance with the University of British Columbia's chemical and biological safety standards.

Electrophysiology

Miniature excitatory postsynaptic currents (mEPSCs) were recorded using an Axopatch 200B, Axon Digidata 1550B or MultiClamp 700A amplifier and pClamp 10.2, 10.3, or 10.6 software (Molecular Devices, Palo Alto, CA, United States). CPNs were identified by morphology and recordings were made at DIV 20–22. Cells were voltage clamped at −70 mV, and their intrinsic membrane properties were determined using a 10 mV hyperpolarizing pulse immediately after whole-cell access was achieved. Cells were accepted for recording if they had a holding current more positive than −500 pA and a series resistance of up to 25 MΩ, with most cells' series resistance under 20 MΩ. mEPSCs were recorded for up to 5 min. If the series resistance changed by more than 20% during the course of the recording, or if the holding current fell below −500 pA, events were not analyzed beyond the point where this threshold was exceeded. Cells were excluded from analysis if their series resistance changed by more than 20%, or their holding current fell below −500 pA, during the first 30 s of the recording, or if they had fewer than 50 events with an amplitude of greater than 10 pA. Cells were recorded in artificial cerebrospinal fluid (ACSF) containing (mM): 167 NaCl, 2.4 KCl, 10 Glucose, 10 HEPES, 2 $CaCl_2$, 1 $MgCl_2$, 0.05 picrotoxin (PTX; Tocris), 0.0005 TTX (Affix Scientific), pH 7.3 with NaOH, 310–320 mOsm (all chemicals from Sigma except for PTX and TTX). The recording electrode (3–6 MΩ) was filled with an internal solution containing (mM): 145 K-Gluconate, 1 $MgCl_2$, 10 HEPES, 1 EGTA, 2 MgATP, 0.5 Na_2GTP, pH 7.3 with KOH, 280–290 mOsm. mEPSC recordings were analyzed with Clampfit 10.2 and 10.7, using its template search function.

Peak-Scaled Non-stationary Noise Analysis of AMPAR-Miniature EPSCs

To measure mean AMPAR channel conductance (γ) and the number of channels exposed to glutamate (N) per synapse, peak scaled noise analysis of AMPAR-miniature EPSCs (mEPSCs) was performed using Clampfit 10.2 (Molecular Devices). The peak of each mEPSC in a recording was scaled to the average mEPSC waveform for that recording, and the variance of current around the mean for each time point was calculated. The data were fit with the following parabolic equation:

$$\sigma^2 = iI - I^2/N + \sigma_b^2$$

where σ^2 = variance, I = mean current, i = single-channel current, N = number of open channels at peak current, and σ_b^2= background variance. From this equation, γ was calculated by dividing i by the driving force (−70 mV; AMPAR reversal potential was ∼0 mV with the recording solutions used). Recordings were discarded if the parabolic fits of the current variance plots had R^2 <0.5 (Traynelis et al., 1993; Hartveit and Veruki, 2007).

Immunohistochemistry and Image Analysis

Cells were transfected with GFP at plating, as described above. For excitatory synaptic puncta analysis, they were stained for GluA2 and VGLUT1, imaged and analyzed as previously described (Buren et al., 2016). Briefly, they were live stained on DIV 20–22 with a mouse anti-GluA2 primary antibody (Millipore), fixed, and stained with an Alexa-Fluor 568 donkey anti-mouse secondary antibody (Invitrogen), followed by incubation with a guinea pig anti-VGLUT1 primary antibody (Millipore), and then an AMCA-conjugated donkey anti-guinea pig secondary antibody (Jackson ImmunoResearch Laboratories). GFP-positive cells were imaged as a Z-stack using a Zenn Axiovert 200 M fluorescent microscope at 63× magnification with a numerical aperture of 1.4, and flattened within the ZEN 2012 program using the extended depth of focus function. These flattened images were transferred as TIFF files to ImageJ[1] and split into red, green and blue channels. The background of each channel was removed using the ImageJ subtract background tool, and each channel was manually thresholded. The density of puncta in the red and blue channels, that were at least 40 μm from the cell body and colocalised with a green fluorescent dendritic process connected with the cell being analyzed, was measured using the Analyze Particles tool in ImageJ. Colocalised puncta were defined as contiguous pixels that were above threshold in both the red and blue channels, and were analyzed using the Analyze Particles tool and the colocalization plugin (see footnote 1) in ImageJ.

For spine analysis, cells were fixed on DIV 20–22 by incubation for 20 min with 4% paraformaldehyde (PFA) + 4% sucrose, washing three times with phosphate buffered saline (PBS), and mounted on glass slides (Corning, 2948-75 × 25) using Fluoromount G (SouthernBiotech, 0100-01). Cells were imaged using a Zeiss Axioplan 2 confocal microscope running the ZEN 2009 program, with a single picture being taken of each cell body, as well as three Z stacks, each centered on a segment of a different secondary dendrite which served as the regions of interest (ROIs). These images were exported as TIFFs, and the Z stacks were flattened in ImageJ using the Z project function. Background and noise were removed from the images of the ROIs using the ImageJ subtract background and despeckle functions, respectively. They were then opened in NeuronStudio[2], and spines along the ROIs were classified using NeuronStudio's spine classifier tool. The density of each type of spine was calculated for each ROI, and then the densities were

[1]https://imagej.nih.gov/ij/plugins/colocalization.html

[2]http://research.mssm.edu/cnic/tools-ns.html

averaged across three ROIs per cell to obtain the densities of each spine type for each cell.

Statistics

All statistics were performed using GraphPad Prism, with one- and two-way ANOVAs and unpaired, two-tailed *t*-tests were performed throughout, as reported in the text. Bonferroni post-tests were applied to test for differences between groups following ANOVAs. All experiments were performed on cells obtained from at least three independent cultures, and "*n*" is the number of cells analyzed. Error bars in all figures represent standard error values of the mean calculated from the number of cells analyzed.

RESULTS

HSP Is Impaired in YAC128 Cortical Pyramidal Neurons (CPNs)

To assess the capacity for HSP, cultured CPNs were treated with tetrodotoxin (TTX) or vehicle control (water) for 48 h, after which mEPSCs were recorded (mEPSCs; **Figure 1A**). mEPSC frequency increased ($^{*}p < 0.05$) and mEPSC amplitude tended to increase ($p = 0.08$) in WT CPNs (**Figures 1B,C**). However, there was no change in mEPSC frequency or amplitude in YAC128 CPNs (**Figures 1B,C**), suggesting that YAC128 CPNs are impaired in synaptic upscaling. A non-stationary noise analysis performed on the subset of these traces which also met the standards described above for this analysis (Methods, 2.4) found a significant increase in the number of AMPARs per synapse in WT ($^{*}p < 0.05$) but not YAC128 CPNs treated with TTX (**Figures 1D,F**). TTX treatment did not alter AMPAR conductance in CPNs of either genotype (**Figures 1E,F**).

Before investigating possible mechanisms of this impairment, we sought to better understand the synaptic changes that accompanied the increased mEPSC amplitude and frequency in WT CPNs, and whether or not these properties were altered in YAC128 CPNs under TTX treatment. Cultured CPNs were transfected with GFP and immunostained for the AMPA receptor subunit GluA2 and the vesicular glutamate transporter VGLUT1 (**Figure 2A**). GluA2 served as a postsynaptic marker and marker of AMPA receptor (AMPAR) localisation, and VGLUT1 represented a presynaptic marker and marker of glutamate-containing vesicles. Quantification showed that the density of colocalised GluA2 and VGLUT1 puncta was increased ($^{*}p < 0.05$) in WT CPNs treated with TTX relative to those that were not (**Figure 2B**). These data are consistent with a model in which an increase in synapse density underlies the increase in mEPSC frequency observed in WT CPNs after TTX treatment. Although this would not be considered synaptic scaling, as it involves changing the number of synapses onto a cell rather than the strength of those synapses(Marder and Goaillard, 2006; Watt and Desai, 2010), it is still a form of homeostatic plasticity, as it modifies the properties of cells within a network to preserve the stability of that network (Turrigiano, 2007; Watt and Desai, 2010). Strikingly, there was also a significant increase in density of colocalised puncta ($^{***}p < 0.001$) and VGLUT1 ($^{**}p < 0.01$), as well as GluA2 ($^{*}p < 0.05$), in YAC128 relative to WT CPNs within the control condition (**Figure 2B**). Given that there is no difference in any of these measures between control and TTX-treated YAC128 CPNs (**Figure 2B**), this suggests a ceiling effect in which synapse density onto YAC128 CPNs is already increased in response to some other signal before they are exposed to TTX. If so, it is possible that YAC128 CPN synapse density failed to increase in response to TTX because this effect was already saturated.

In addition to modifying the properties of existing synapses, HSP can also occur via addition or elimination of spines and synapses (Tian et al., 2010; Cohen et al., 2011; Mendez et al., 2018). Furthermore, the morphology of spines can also give an indication of their function. For example, mushroom spines are the most stable type of spine, while thin spines are less so (Chidambaram et al., 2019). Given the change in mEPSC frequency observed, spine density and morphology were also examined (**Figures 2C,D**). WT control CPNs had a higher density of mushroom spines than TTX-treated WT CPNs ($^{*}p < 0.05$). On the other hand, WT control CPNs had a lower density of longneck mushroom spines (defined as mushroom spines with a neck >1 μm long) and filopodia/thin spines than TTX-treated WT CPNs (longneck mushroom: $^{**}p < 0.01$; filopodia/thin: $^{***}p < 0.001$) and YAC128 control CPNs (longneck mushroom: $^{*}p < 0.05$; filopodia/thin: $^{***}p < 0.001$). WT control CPNs also had a lower total spine density than TTX-treated WT CPNs ($^{*}p < 0.05$) and YAC128 control CPNs ($^{*}p < 0.05$; **Figure 2D**).

BDNF Modulates mEPSC Frequency Increase in Response to Activity Suppression

BDNF signaling is thought to be involved in HSP (Rutherford et al., 1998; Turrigiano, 2007; Watt and Desai, 2010). Specifically, BDNF is released in an activity-dependent manner (Poo, 2001), such that suppression of activity in a network of CPNs reduces BDNF release in that network. This reduction in BDNF signaling is thought to be a trigger for synaptic scaling-up (Rutherford et al., 1998; Watt and Desai, 2010). To investigate whether reduced BDNF signaling is required for the changes in mEPSC amplitude and frequency that we observed in our WT cortical cultures at DIV 21 (Rutherford et al., 1998; Watt and Desai, 2010), we first attempted to block homeostatic plasticity in WT CPNs by treating them with BDNF along with TTX. If the effect of TTX is mediated through reduced BDNF signaling, then adding exogenous BDNF at the same time as TTX should block the effect of TTX (Rutherford et al., 1998). Exogenous BDNF did block the increase in mEPSC frequency in response to TTX (**Figures 3A,C** and **Supplementary Figure S1B**). However, it did not block the increase in mEPSC amplitude. While there was no significant difference by Bonferroni *post hoc* test between TTX and control cells in either the BDNF or the control group, both groups showed strong trends toward increased mEPSC amplitude in TTX-treated cells (control: $p = 0.08$; BDNF: $p = 0.12$), and there was a significant overall effect of TTX by two-way ANOVA ($^{**}p < 0.01$; **Figure 3B** and **Supplementary Figure S1A**). To further investigate the role of BDNF in the homeostatic plasticity that we observed, we

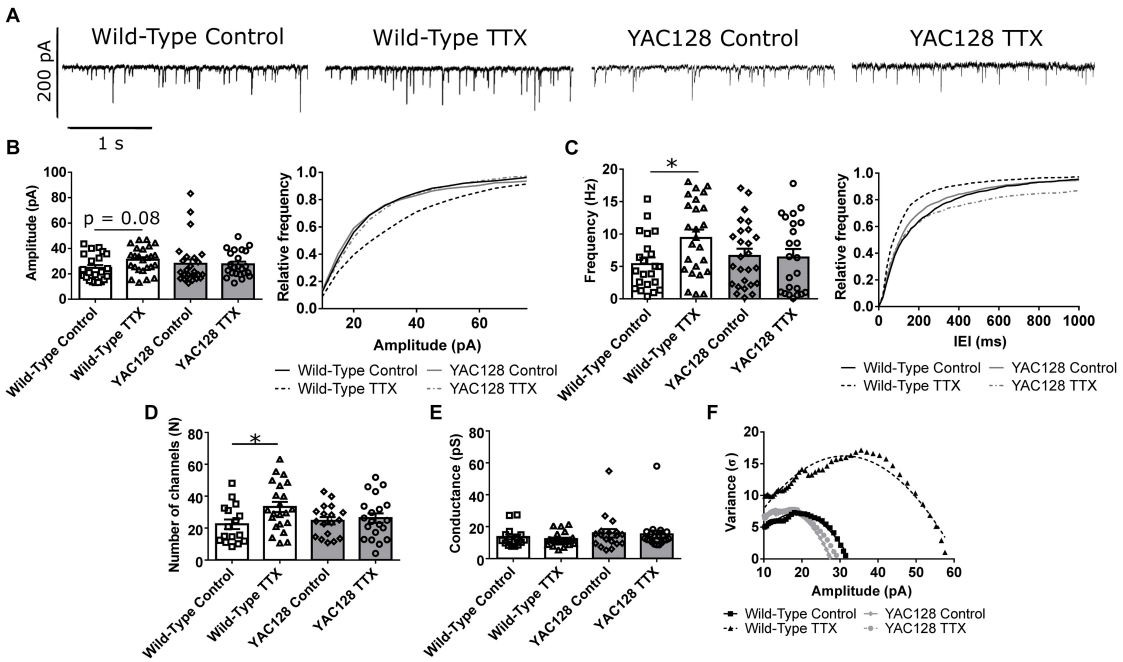

FIGURE 1 | Impaired homeostatic plasticity in YAC128 cortical pyramidal neurons (CPNs). **(A)** Representative traces of miniature excitatory postsynaptic currents (mEPSC) recordings from wild-type (WT) and YAC128 CPNs treated with tetrodotoxin (TTX) or vehicle control. **(B)** mEPSC average amplitude (left panel) and amplitude cumulative probability (right panel). There is a trend toward increased mEPSC amplitude in WT CPNs treated with TTX ($p = 0.08$, Bonferroni *post hoc* *t*-test), but not in YAC128 CPNs treated with TTX ($p > 0.99$, Bonferroni *post hoc* *t*-test). **(C)** mEPSC average frequency (left panel) and inter-event interval (IEI) cumulative probability (right panel). There is increased mEPSC frequency in WT CPNs treated with TTX ($^*p < 0.05$, Bonferroni *post hoc* *t*-test), but not in YAC128 CPNs treated with TTX ($p > 0.99$, Bonferroni *post hoc* *t*-test; TTX $p = 0.07$, genotype/TTX interaction $p < 0.05$, two-way ANOVA). For **(B)** and **(C)**, cell numbers are WT control $n = 22$, WT TTX $n = 25$, YAC128 control $n = 26$, YAC128 TTX $n = 23$; culture batch $N = 6$. **(D)** Number of AMPARs per synapse. WT CPNs treated with TTX had more AMPARs per synapse ($^*p < 0.05$, Bonferroni *post hoc* *t*-test), while YAC128 CPNs treated with TTX did not ($p > 0.99$; TTX $p < 0.05$, two-way ANOVA). **(E)** AMPAR conductance. There was no significant difference in AMPAR conductance between any groups (WT control vs. WT TTX: $p > 0.99$; YAC128 control vs. YAC128 TTX: $p > 0.99$; WT control vs. YAC128 control: $p = 0.87$; WT TTX vs. YAC128 TTX: $p = 0.50$). For **(D)** and **(E)**, cell numbers are WT control $n = 16$, WT TTX $n = 22$, YAC128 control $n = 18$, YAC128 TTX $n = 20$; culture batch $N = 6$. **(F)** Representative current-variance plots for WT and YAC128 CPNs treated with TTX or vehicle control.

attempted to reproduce the effect of TTX by scavenging BDNF from our culture medium using TrkB-Fc (Rutherford et al., 1998; Buren et al., 2014). When WT CPNs were treated with TTX or TrkB-Fc for 48 h, both TTX ($^{**}p < 0.01$) and TrkB-Fc ($^*p < 0.05$) increased mEPSC frequency (**Figures 3D,F** and **Supplementary Figure S1D**). TrkB-Fc also had a similar effect as TTX on mEPSC amplitude (**Figures 3D,E** and **Supplementary Figure S1C**). Together, these data suggested that, in our DIV 21 WT cortical cultures, reduced BDNF signaling is a trigger for HSP in response to activity suppression.

Pridopidine Restores Homeostatic Plasticity in YAC128 CPNs Through Stimulation of the Sigma-1 Receptor

We hypothesized that the homeostatic plasticity deficit observed in YAC128 CPNs is a result of the disruption of a signaling pathway(s) involved in this process that is also known to be impaired in HD. This disruption leads CPNs to undergo a homeostatic increase in synapse density under baseline conditions and prevents activity blockade from inducing further HSP. Specifically, since BDNF signaling is impaired in HD (Zuccato and Cattaneo, 2007), we speculate that the level of BDNF signaling in YAC128 CPNs is low enough under baseline conditions to prevent any further reduction from engaging HSP pathways. It is also possible that reduced BDNF signaling engages these pathways under baseline conditions in YAC128 CPNs, leading to the increased synapse and spine density we showed in **Figure 2**. In addition to BDNF, another key process involved in HSP is regulation of somatic calcium levels (Watt and Desai, 2010; Turrigiano, 2011). In this regard, the drug pridopidine, which has shown promise for the treatment of HD motor symptoms in clinical trials (Kieburtz et al., 2018) is of interest. Recent research has demonstrated that pridopidine boosts the BDNF signaling pathway and is involved in stabilizing ER calcium signaling (Geva et al., 2016; Ryskamp et al., 2017). Therefore, we hypothesized that pridopidine might restore homeostatic plasticity in response to suppression of activity in YAC128 CPNs by normalizing BDNF and/or calcium signaling under baseline conditions.

We treated WT CPNs with 1 μM pridopidine. Given that pridopidine upregulates BDNF signaling (Geva et al., 2016) and that exogenous BDNF at least partially blocked HSP (**Figures 3A–C**), pridopidine might be expected to have a

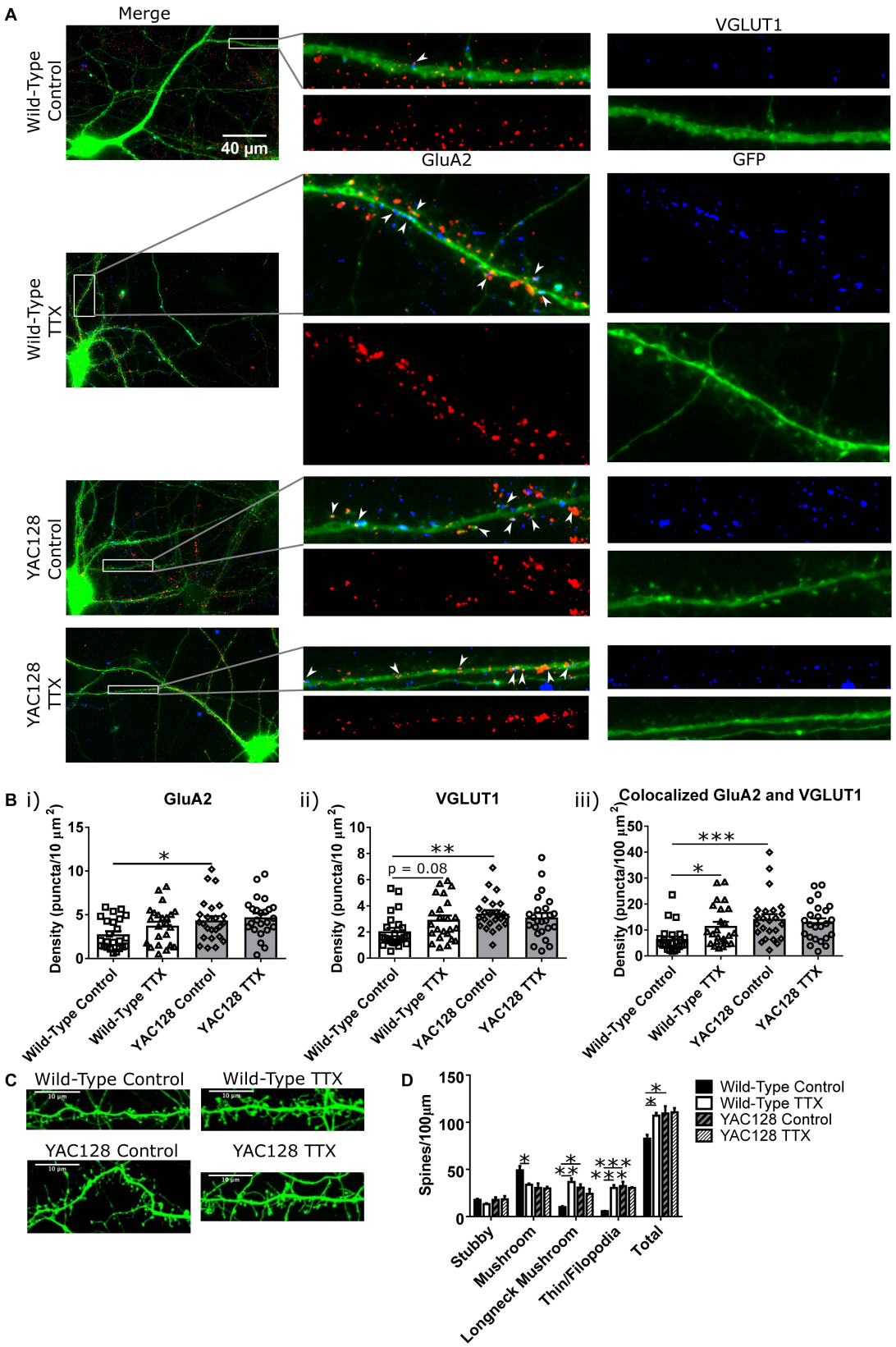

FIGURE 2 | Continued

FIGURE 2 | Synaptic changes underlying homeostatic plasticity. **(A)** Representative images of CPNs filled with GFP (green), and stained for GluA2 (red), and VGLUT1 (blue). **(B)** Density of **(i)** GluA2 (genotype $p < 0.01$, two-way ANOVA), **(ii)** VGLUT1 (genotype $p < 0.05$, genotype/TTX interaction $p < 0.05$, two-way ANOVA), and **(iii)** colocalised GluA2 and VGLUT1 puncta (genotype $p < 0.01$, genotype/TTX interaction $p < 0.05$, two-way ANOVA) on CPN dendrites. YAC128 control CPNs had a higher density of all three types of puncta than WT control CPNs (GluA2 $^{*}p < 0.05$, Bonferroni *post hoc t*-test; VGLUT1 $^{**}p < 0.01$, Bonferroni *post hoc t*-test; colocalised $^{***}p < 0.001$, Bonferroni *post hoc t*-test). WT CPNs treated with TTX also showed a tendency to increased VGLUT1 density ($p = 0.08$, Bonferroni *post hoc t*-test) and significantly increased density of colocalised GluA2 and VGLUT1 puncta ($^{*}p < 0.05$, Bonferroni *post hoc t*-test) relative to WT control CPNs. YAC128 CPNs treated with TTX did not differ from either YAC128 control CPNs or WT CPNs treated with TTX ($p > 0.99$, Bonferroni *post hoc t*-test; cells per group $n = 24$, culture batch $N = 3$). **(C)** Representative images of spines on CPNs filled with GFP. **(D)** Spine density, grouped by morphology. WT control CPNs had a higher density of mushroom spines than TTX-treated WT CPNs ($^{*}p < 0.05$, Bonferroni *post hoc t*-test; genotype $p < 0.05$, two-way ANOVA), as well as fewer longneck mushroom spines (mushroom spines with necks > 1 μm in length; $^{**}p < 0.01$, Bonferroni *post hoc t*-test) and filopodia/thin spines ($^{***}p < 0.001$, Bonferroni *post hoc t*-test). Compared to YAC128 control CPNs, WT control CPNs also had fewer longneck mushroom spines ($^{*}p < 0.05$, Bonferroni *post hoc t*-test; TTX $p < 0.05$, TTX/genotype interaction $p < 0.01$, two-way ANOVA) and filopodia/thin spines ($^{***}p < 0.001$, Bonferroni *post hoc t*-test; TTX $p < 0.01$, genotype $p < 0.01$, TTX/genotype $p < 0.01$, two-way ANOVA). WT control CPNs also had a lower total spine density than TTX-treated WT CPNs ($^{*}p < 0.05$, Bonferroni *post hoc t*-test) and YAC128 control CPNs ($^{*}p < 0.05$, Bonferroni *post hoc t*-test; TTX $p < 0.05$, genotype $p < 0.05$, two-way ANOVA; culture batches $N = 3$).

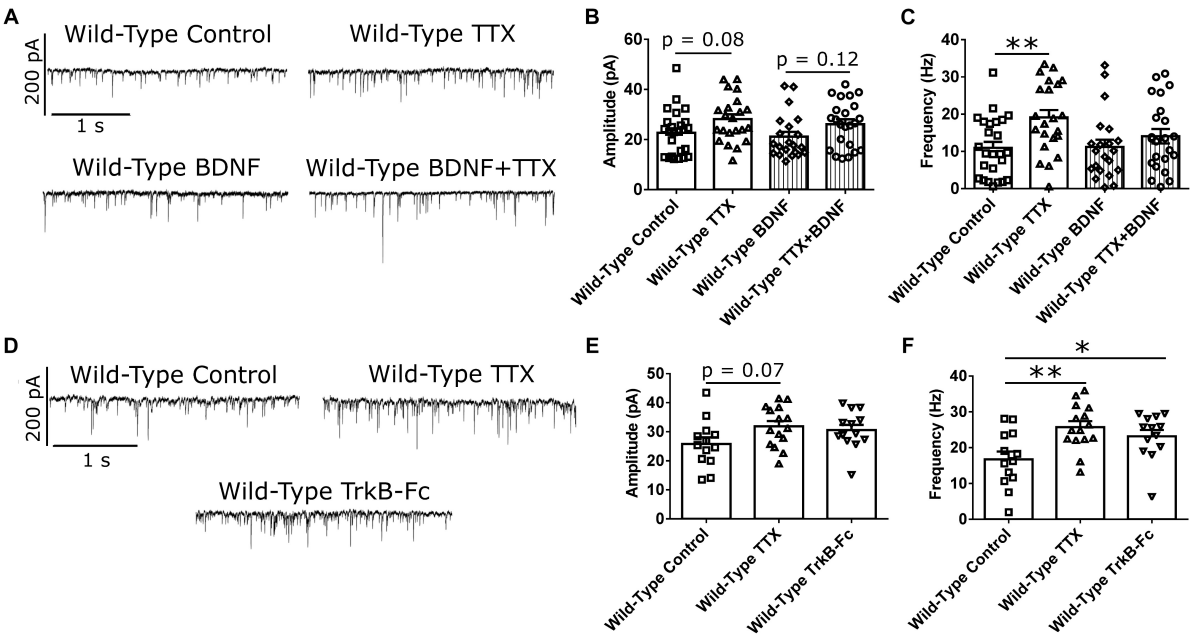

FIGURE 3 | BDNF signaling modulates mEPSC frequency in WT CPNs. **(A)** Representative traces of mEPSC recordings from WT CPNs treated with TTX and/or BDNF. **(B)** mEPSC amplitude of WT CPNs treated with TTX and/or BDNF. By two-way ANOVA, there was no significant *post hoc* difference between any groups, but there was a significant overall effect of TTX ($p < 0.01$); moreover, TTX-treated cells tended to have larger mEPSCs in both vehicle control ($p = 0.08$, Bonferroni *post hoc t*-test) and BDNF-treated ($p = 0.12$, Bonferroni *post hoc t*-test) groups. **(C)** mEPSC frequency of WT CPNs treated with TTX and/or BDNF. Cells treated with only TTX had more frequent mEPSCs than those treated with only vehicle control ($^{**}p < 0.01$, Bonferroni *post hoc t*-test; TTX $p < 0.01$, two-way ANOVA). For **(B)** and **(C)**, control $n = 24$, TTX $n = 22$, BDNF $n = 22$, TTX + BDNF = 23, culture batch $N = 8$). **(D)** Representative traces of mEPSC recordings from WT CPNs treated with TTX, TrkB-Fc, or vehicle control. **(E)** mEPSC amplitude of WT CPNs treated with TTX, TrkB-Fc, or vehicle control. TTX-treated cells tended to have larger mEPSCs than those treated with vehicle control ($p = 0.07$, Bonferroni *post hoc t*-test) while TrkB-Fc did not ($p = 0.24$, Bonferroni *post hoc t*-test; $p = 0.09$, one-way ANOVA). **(F)** mEPSC frequency of WT CPNs treated with TTX, TrkB-Fc, or vehicle control. Cells treated with TTX ($^{**}p < 0.01$, Bonferroni *post hoc t*-test), and TrkB-Fc ($^{*}p < 0.05$, Bonferroni *post hoc t*-test) both had more frequent mEPSCs than cells treated with vehicle control ($p < 0.01$, one-way ANOVA).

blunting effect on homeostatic plasticity in WT CPNs, which have a higher baseline level of BDNF signaling than do YAC128 CPNs. These cells showed increased mEPSC amplitude in response to TTX regardless of whether they were ($^{**}p < 0.01$) or were not ($^{**}p < 0.01$) treated with pridopidine (**Figures 4A,B** and **Supplementary Figure S2A**). However, whereas cells treated with only TTX had increased mean mEPSC frequency relative to those treated with vehicle control ($^{***}p < 0.001$), the difference in mean mEPSC frequency between cells treated with both TTX and pridopidine or with pridopidine alone did not reach statistical significance ($p = 0.06$), suggesting an attenuated effect of TTX on mEPSC frequency (**Figure 4C** and **Supplementary Figure S2B**). These data are consistent with a model in which 1 μM pridopidine impaired HSP in response to TTX in WT CPNs.

To test the effect of pridopidine on HSP in YAC128 CPNs, cultured CPNs were treated with pridopidine (0.1, 1, or 10 μM) or vehicle control (water) for 48 h before TTX or vehicle control was also added to the culture medium. After treatment with TTX, mEPSCs were recorded from these neurons. In cultures treated with either the 0.1 or 10 μM pridopidine concentration, YAC128 CPNs showed increased mEPSC amplitude in response to TTX ($^{*}p < 0.05$), but mean mEPSC frequency remained

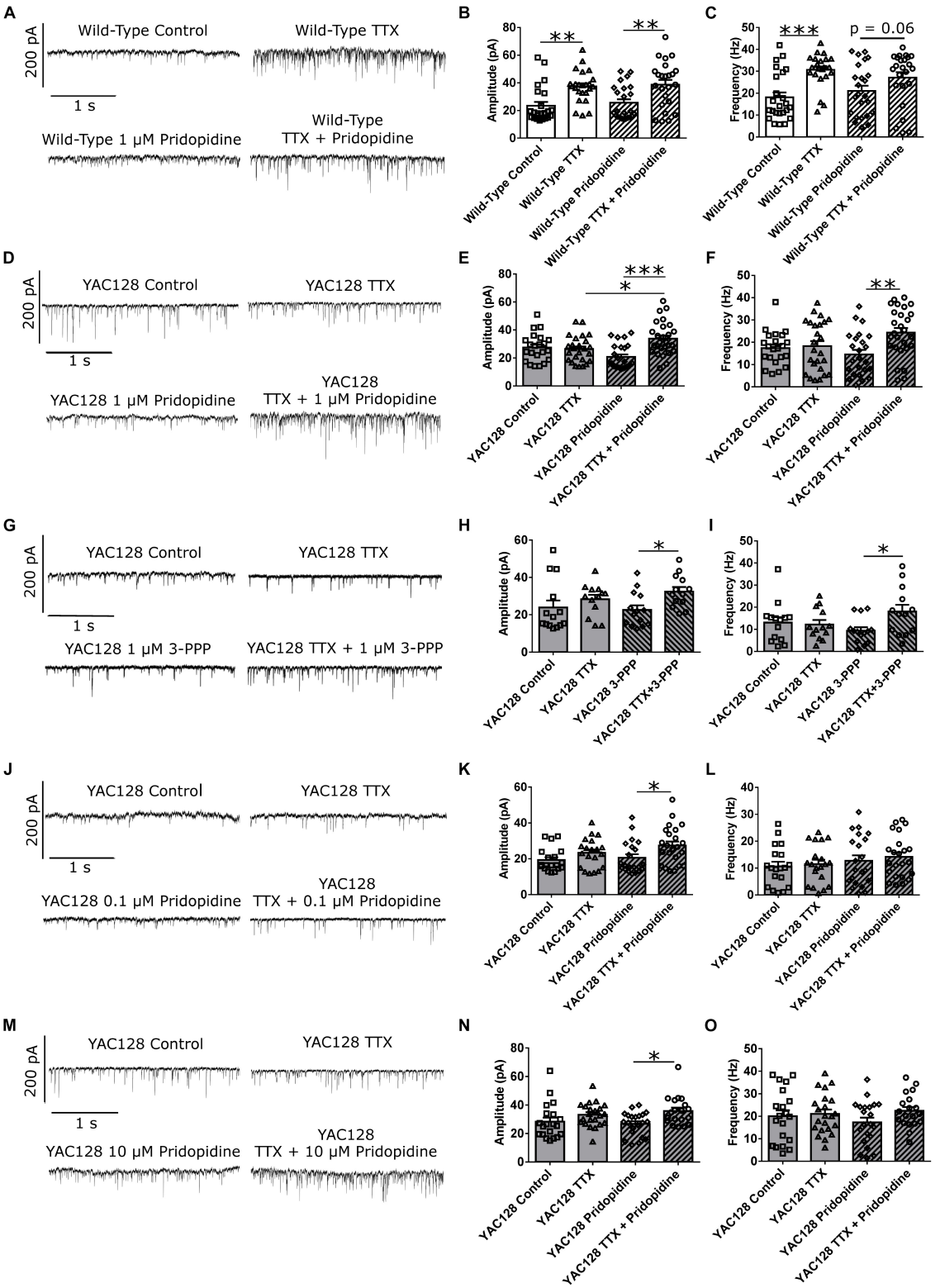

FIGURE 4 | Pridopidine and S1R agonist 3-PPP both restore homeostatic plasticity at a 1 μM concentration. **(A)** Representative traces of mEPSC recordings from WT CPNs treated with TTX and/or 1 μM pridopidine. **(B)** mEPSC amplitude of WT CPNs treated with TTX and/or 1 μM pridopidine. Cells treated with only TTX had larger mEPSCs than those treated with only vehicle control (**$p < 0.01$, Bonferroni *post hoc t*-test), and cells treated with TTX and pridopidine had larger mEPSCs than those treated with only pridopidine (**$p < 0.01$, Bonferroni *post hoc t*-test; TTX $p < 0.001$, two-way ANOVA). **(C)** mEPSC frequency of WT CPNs treated with

(Continued)

FIGURE 4 | Continued
TTX and/or 1 μM pridopidine. Cells treated with only TTX had more frequency mEPSCs than those treated with only vehicle control (***$p < 0.001$, Bonferroni *post hoc t*-test), while those treated with both TTX and pridopidine showed a non-significant trend toward more frequent mEPSCs than those treated with only pridopidine ($p = 0.06$, Bonferroni *post hoc t*-test; TTX $p < 0.001$, two-way ANOVA). For both **(B)** and **(C)**, cells per group $n = 24$, culture batch $N = 4$. **(D)** Representative traces of mEPSC recordings from YAC128 CPNs treated with TTX and/or 1 μM pridopidine. **(E)** mEPSC amplitude of YAC128 CPNs treated with TTX and/or 1 μM pridopidine. Cells treated with both TTX and pridopidine had higher amplitude mEPSCs than those treated with only TTX (*$p < 0.05$, Bonferroni *post hoc t*-test), or pridopidine (***$p < 0.001$, Bonferroni *post hoc t*-test; TTX $p < 0.01$, TTX/pridopidine interaction $p < 0.001$, two-way ANOVA). **(F)** mEPSC frequency of YAC128 CPNs treated with TTX and/or 1 μM pridopidine. Cells treated with both TTX and pridopidine had more frequent mEPSCs than those treated with pridopidine alone (**$p < 0.01$, Bonferroni *post hoc t*-test; TTX $p < 0.05$, TTX/pridopidine interaction $p < 0.05$, two-way ANOVA). For **(E)** and **(F)**, control $n = 22$, TTX $n = 25$, pridopidine $n = 24$, TTX + pridopidine $n = 27$, culture batch $N = 4$. **(G)** Representative traces of mEPSC recordings from YAC128 CPNs treated with TTX and/or 3-PPP. **(H)** mEPSC amplitude from YAC128 CPNs treated with TTX and/or 3-PPP. Cells treated with both 3-PPP and TTX had larger mEPSCs than those treated with only 3-PPP (*$p < 0.05$, Bonferroni *post hoc t*-test; TTX $p < 0.05$, two-way ANOVA). **(I)** mEPSC frequency from YAC128 CPNs treated with TTX and/or 3-PPP. Cells treated with both 3-PPP and TTX had more frequent mEPSCs than those treated with only 3-PPP (*$p < 0.05$, Bonferroni *post hoc t*-test; TTX/3-PPP interaction $p < 0.05$, TTX $p = 0.09$, two-way ANOVA).; For **(H)** and **(I)**, control $n = 14$, TTX $n = 13$, 3-PPP $n = 14$, TTX/3-PPP $n = 13$, culture batch $N = 12$. **(J)** Representative traces of mEPSC recordings from YAC128 CPNs treated with TTX and/or 100 nM pridopidine. **(K)** mEPSC amplitude of YAC128 CPNs treated with TTX and/or 100 nM pridopidine. YAC128 CPNs treated with both TTX and pridopidine had higher mEPSC amplitude than those treated with only pridopidine (*$p < 0.05$, Bonferroni *post hoc t*-test; TTX $p < 0.01$, two-way ANOVA). **(L)** mEPSC frequency of YAC128 CPNs treated with TTX and/or 100 nM pridopidine. There was no difference in mEPSC frequency between any groups (control vs. TTX: $p > 0.99$; pridopidine vs. pridopidine+TTX: $p > 0.99$; control vs. pridopidine: $p = 0.83$; TTX vs. pridopidine+TTX: $p = 0.56$, Bonferroni *post hoc t*-test). For **(K)** and **(L)**, control $n = 19$, TTX $n = 20$, pridopidine $n = 21$, TTX + pridopidine $n = 23$, culture batch $N = 4$. **(M)** Representative traces of mEPSC recordings from YAC128 CPNs treated with TTX and/or 10 μM pridopidine. **(N)** mEPSC amplitude of YAC128 CPNs treated with TTX and/or 10 μM pridopidine. Cells treated with both TTX and pridopidine had larger mEPSCs than those treated with only pridopidine (*$p < 0.05$, Bonferroni *post hoc t*-test; TTX $p < 0.01$, two-way ANOVA). **(O)** mEPSC frequency of YAC128 CPNs treated with TTX and/or 10 μM pridopidine. There was no difference in frequency between any groups (control vs. TTX: $p = 0.92$; pridopidine vs. pridopidine+TTX: $p = 0.18$; control vs. pridopidine: $p = 0.72$; TTX vs. pridopidine+TTX: $p > 0.99$, Bonferroni *post hoc t*-test). For **(N)** and **(O)**, control $n = 20$, TTX $n = 22$, pridopidine $n = 21$, TTX + pridopidine = 19; culture batch $N = 4$.

unchanged (**Figures 4J–O** and **Supplementary Figures S3C–F**). In contrast, YAC128 CPNs treated with 1 μM pridopidine showed increases in both mean mEPSC amplitude (***$p < 0.001$) and frequency (**$p < 0.01$; **Figures 4D–F** and **Supplementary Figures S3A,B**) in response to TTX. Consistent with our previous results, cells treated with vehicle control instead of pridopidine did not show increased mEPSC amplitude or frequency in response to TTX. These results indicate that pridopidine restores homeostatic plasticity in response to activity suppression in YAC128 CPNs. This restoration occurs in a dose-dependent manner, with maximal effect at 1 μM and decreasing efficacy at higher and lower doses.

Pridopidine is an agonist of the sigma-1 receptor (S1R) (Geva et al., 2016; Ryskamp et al., 2017), which, among other functions, regulates both BDNF signaling (Kikuchi-Utsumi and Nakaki, 2008; Fujimoto et al., 2012) and calcium signaling between the mitochondria and ER (Hayashi and Su, 2007; Ryskamp et al., 2017), which could influence homeostatic plasticity (Marder and Goaillard, 2006; Turrigiano, 2007; Watt and Desai, 2010). With this in mind, we attempted to restore TTX-induced homeostatic plasticity in YAC128 CPNs by treating cultures with 3-PPP, another S1R agonist (Ryskamp et al., 2017). Cells that were treated with 1 μM 3-PPP and TTX showed higher mean mEPSC amplitude (*$p < 0.05$) and frequency (*$p < 0.05$) than those treated with only 3-PPP (**Figures 4G–I** and **Supplementary Figure S4**). There was no difference in mean mEPSC amplitude or frequency between TTX-treated and control cells that were not treated with 3-PPP. This suggests that S1R agonism contributes to pridopidine's restoration of homeostatic plasticity in YAC128 CPNs.

Other aspects of the observed homeostatic plasticity were also analyzed. Spine density and morphology showed increased density of both longneck mushroom (***$p < 0.001$) and filopodia/thin spines (***$p < 0.001$), as well as total spine density (**$p < 0.01$; **Figures 5A,B**) in TTX-treated YAC128 CPNs that had first been incubated for 48 h with 1 μM pridopidine. Non-stationary noise analysis also revealed that at the 1 μM dose, cells treated with both pridopidine and TTX had more AMPARs at each synapse than cells treated with only TTX (**$p < 0.01$) or only pridopidine (*$p < 0.05$, **Figures 5C–E**), suggesting that pridopidine affects AMPAR trafficking pathways typically associated with synaptic upscaling (Rutherford et al., 1998; Turrigiano et al., 1998; Marder and Goaillard, 2006; Turrigiano, 2007; Watt and Desai, 2010). In addition, we tested whether YAC128 CPNs' response to BDNF scavenging was also impaired, as would be expected if BDNF signaling is reduced in these cells under baseline conditions, and whether pridopidine could restore this. We treated YAC128 CPNs with 1 μM pridopidine for 48 h, and then with TrkB-Fc (together with pridopidine) for 48 h. Cells treated with both pridopidine and TrkB-Fc had higher mean mEPSC frequency than cells treated with only TrkB-Fc (**$p < 0.01$) or pridopidine (*$p < 0.05$; **Figures 5F,H** and **Supplementary Figure S5**), although there was no significant difference in mean mEPSC amplitude between any groups (**Figure 5G**). There was also no difference in number of AMPARs per synapse or the peak conductance of those receptors, as determined by non-stationary noise analysis (**Figures 5I–K**). This suggests that the effect of pridopidine on TTX-induced increase in mEPSC frequency is mediated by its effect on the BDNF signaling pathway.

DISCUSSION

We investigated functional synaptic responses to a homeostatic plasticity stimulus in cortical neurons from a mouse model of HD. After 48 h of TTX treatment, cultured CPNs from WT FVB/N mice showed increased mEPSC frequency and a

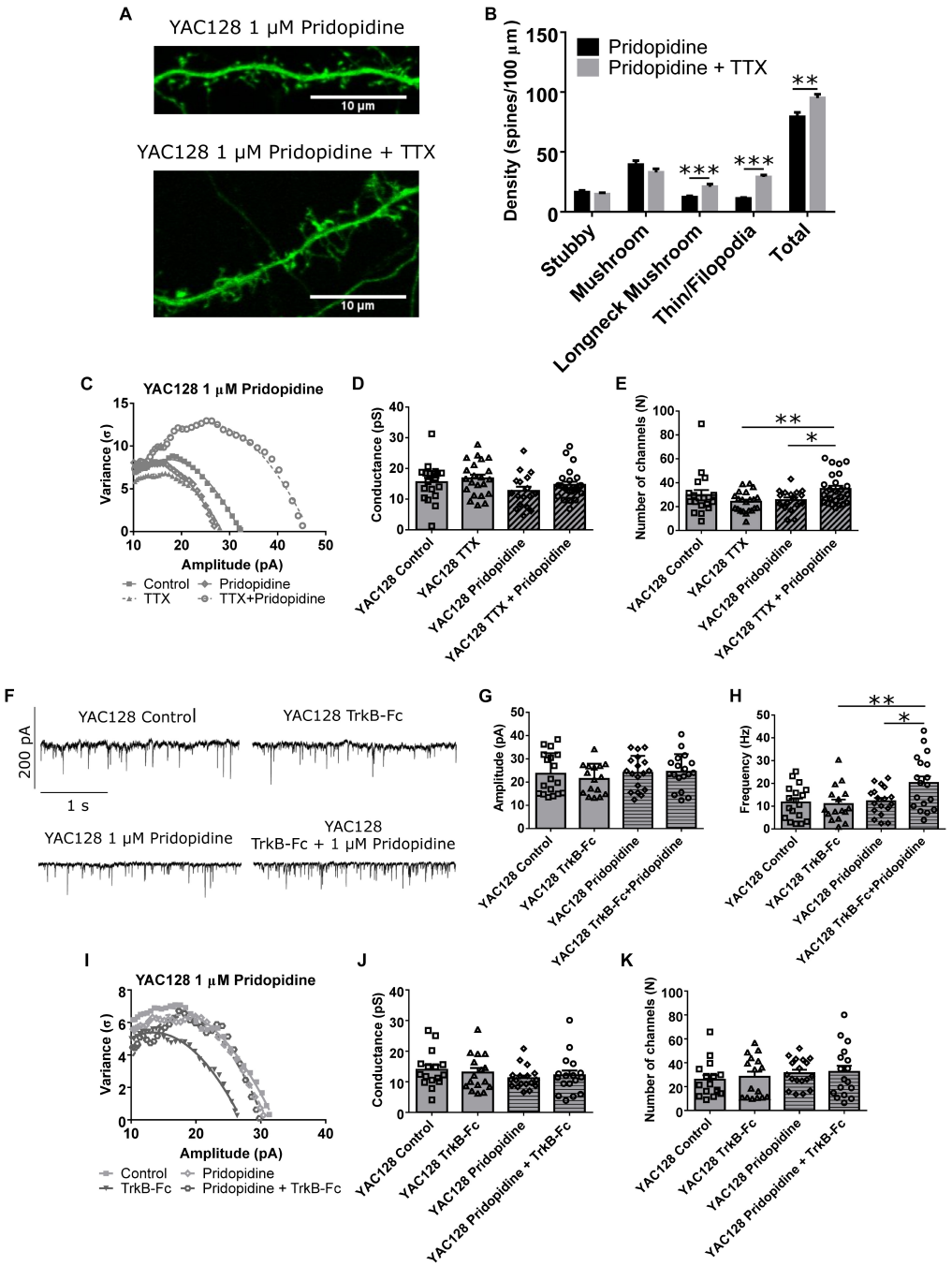

FIGURE 5 | Pridopidine restores other aspects of homeostatic plasticity. **(A)** Representative images of spines on CPNs filled with GFP. **(B)** Spine density of YAC128 CPNs treated with 1 μM pridopidine and TTX or vehicle control. Cells treated with TTX and pridopidine had a higher density of longneck mushroom spines (***$p < 0.001$, unpaired *t*-test) and filopodia/thin spines (***$p < 0.001$, unpaired *t*-test), as well as a higher total spine density (**$p < 0.01$, unpaired *t*-test) than those treated with only pridopidine (cells per group $n = 18$, culture batches $N = 3$) **(C)** Representative current-variance plots from YAC128 CPNs treated with TTX and/or 1 μM pridopidine. **(D)** Peak conductance of synapses onto YAC128 CPNs treated with TTX and/or 1 μM pridopidine, as determined by non-stationary noise analysis. There was no significant difference between any groups (control vs. TTX: $p = 0.95$; pridopidine vs. pridopidine+TTX: $p = 0.51$; control vs. pridopidine: $p = 0.25$; TTX vs. pridopidine+TTX: $p = 0.40$, Bonferroni *post hoc t*-test), although there was a significant effect of pridopidine on conductance (pridopidine $p < 0.05$, two-way ANOVA). **(E)** Number of AMPARs per synapse onto YAC128 CPNs treated with TTX and/or 1 μM pridopidine, as determined by non-stationary noise analysis. There were more AMPARs in cells treated with both TTX and pridopidine than in cells treated with only TTX (**$p < 0.01$, Bonferroni *post hoc t*-test) or pridopidine (*$p < 0.05$, Bonferroni *post hoc t*-test; TTX/pridopidine interaction $p < 0.01$, two-way ANOVA). For **(D)** and **(E)**, control $n = 19$, TTX $n = 20$, pridopidine $n = 21$, TTX + pridopidine $n = 23$, culture batch $N = 4$. **(F)** Representative traces of mEPSC recordings from YAC128 CPNs treated with TrkB-Fc and/or pridopidine. **(G)** mEPSC amplitude of YAC128 CPNs treated with TrkB-Fc and/or pridopidine. There was no significant difference between groups (control vs. TrkB-Fc: $p = 0.81$;

(Continued)

FIGURE 5 | Continued
pridopidine vs. TrkB-Fc: $p > 0.99$; control vs. pridopidine: $p > 0.99$; TrkB-Fc vs. pridopidine+TrkB-Fc: $p = 0.49$, Bonferroni *post hoc t*-test). **(H)** mEPSC frequency of YAC128 CPNs treated with TrkB-Fc and/or pridopidine. Cells treated with TrkB-Fc and pridopidine had more frequent mEPSCs than both those treated with only TrkB-Fc (**$p < 0.01$, Bonferroni *post hoc t*-test) or only pridopidine (*$p < 0.05$, Bonferroni *post hoc t*-test; pridopidine $p < 0.05$, TrkB-Fc/pridopidine interaction $p < 0.05$, two-way ANOVA). **(I)** Representative current-variance plots from YAC128 CPNs treated with TrkB-Fc and/or pridopidine. **(J)** Peak conductance of synapses onto YAC128 CPNs treated with TrkB-Fc and/or pridopidine, as determined by non-stationary noise analysis. There was no significant difference between any groups (control vs. TrkB-Fc: $p > 0.99$; pridopidine vs. pridopidine+TrkB-Fc: $p > 0.99$; control vs. pridopidine: $p = 0.31$; TrkB-Fc vs. pridopidine+TrkB-Fc: $p > 0.99$). **(K)** Number of AMPARs per synapse onto YAC128 CPNs treated with TrkB-Fc and/or pridopidine, as determined by non-stationary noise analysis. There was no significant difference between any groups (control vs. TrkB-Fc: $p > 0.99$; pridopidine vs. pridopidine+TrkB-Fc: $p > 0.99$; control vs. pridopidine: $p = 0.68$; TrkB-Fc vs. pridopidine+TrkB-Fc: $p = 0.97$). For **(G)**, **(H)**, **(J)**, and **(K)**, control $n = 18$, TrkB-Fc $n = 16$, pridopidine $n = 18$, TrkB-Fc + pridopidine $n = 18$; culture batch $N = 6$.

strong trend, which was significant in some sets of experiments, toward increased mEPSC amplitude. The neurons also exhibited increased synapse and spine density, and number of AMPARs per synapse. YAC128 CPNs, in contrast, did not change in any of these measures, suggesting a deficit in homeostatic plasticity. BDNF was involved in the observed effect of TTX on mEPSC frequency in WT CPNs. We were able to restore TTX treatment-induced homeostatic plasticity in YAC128 CPNs with pridopidine, a drug which improved motor deficits in HD clinical trials and significantly enhances BDNF signaling in rodents (Geva et al., 2016; Kieburtz et al., 2018). Our quantification show that pridopidine restored homeostatic plasticity in a dose-dependent manner, with maximum effect at 1 μM. Consistent with pridopidine's proposed mechanism of action (Geva et al., 2016; Ryskamp et al., 2017), homeostatic plasticity was also restored by the S1R agonist 3-PPP.

TTX Induced Multiple Forms of Homeostatic Plasticity

After 48 h of treatment with TTX we expected to see synaptic scaling. This is a form of homeostatic plasticity in which the strength of all of the synapses onto a neuron increases or decreases in response to changes in the neuron's level of activity. In excitatory neurons such as CPNs, a prolonged decrease in activity results in increased synaptic strength (Rutherford et al., 1998; Marder and Goaillard, 2006; Turrigiano, 2007; Watt and Desai, 2010). This is usually assessed by measuring the amplitude and frequency of mEPSCs, small inward currents produced by the stochastic release of individual glutamate-containing synaptic vesicles and mediated by AMPAR activation. Increased mEPSC amplitude is typically interpreted as reflecting postsynaptic changes, while increased frequency is considered to reflect presynaptic changes. Neurons undergoing synaptic scaling at or before DIV 14 typically exhibit only postsynaptic changes. However, between DIV 14 and 18 they undergo a shift toward mixed pre- and postsynaptic scaling (Wierenga et al., 2006). Consistent with this, the WT cells used in our study, which were recorded at DIV 21, showed increases in both mEPSC amplitude and frequency, with frequency changes occurring more consistently. Non-stationary noise analysis indicated that WT CPNs had an increased number of AMPARs per synapse after treatment with TTX, a typical mechanism of mEPSC synaptic up-scaling. These same cells also showed increased spine and synapse density, consistent with the observed increase in mEPSC frequency. While not consistent with synaptic scaling, this has been documented as another form of homeostatic plasticity (Kirov et al., 1999; Turrigiano, 2007). The morphology of spines on TTX-treated WT CPNs was also shifted toward types which appeared less mature and suggested the formation of novel synapses (Kirov et al., 1999). Thus, at DIV 20–22 in our culture system WT CPNs treated with TTX for 48 h increase both AMPAR number per synapse and synapse density.

Impairment of Synapse Density Change in Response to TTX in YAC128 CPNs Is Mediated by Altered BDNF Signaling

While WT CPNs underwent homeostatic plasticity in response to activity suppression by TTX treatment, YAC128 CPNs' mEPSCs did not change in amplitude or frequency. Further examination showed that both control and TTX-treated YAC128 CPNs exhibited synapse and spine density, and spine morphology, more similar to that of TTX-treated than control WT CPNs. This suggests that a homeostatic increase in synapse density is occluded in YAC128 CPNs.

BDNF signaling is impaired in HD (Zuccato and Cattaneo, 2007; Plotkin and Surmeier, 2015) and has been reported to play a critical role in HSP. BDNF is released from CPNs in an activity-dependent manner, and reduced BDNF is thought to be a trigger for synaptic up-scaling after activity suppression (Rutherford et al., 1998; Turrigiano, 2007; Watt and Desai, 2010). Our data in WT CPNs, showing that scavenging BDNF from the medium with TrkB-Fc over 48 h mimics the effect of TTX, and that exogenous BDNF in the medium prevents the TTX-induced increase in mEPSC frequency, support this model. Thus, we hypothesized that a baseline deficit in BDNF signaling in YAC128 CPNs renders them insensitive to further reductions in BDNF, thereby occluding TTX-induced homeostatic plasticity. Moreover, reduced BDNF signaling may underlie a homeostatic increase in synaptogenesis during development in culture, resulting in the elevated density of immature-appearing spines and synapses on DIV 20–22 YAC128 CPNs, and preventing further modulation of synapse density following TTX. Supporting this idea, we found that YAC128 CPNs treated with 1 μM pridopidine, a drug previously shown to upregulate BDNF signaling (Geva et al., 2016), exhibited a similar synapse morphology and density as control WT CPNs, and also responded to 48 h TTX treatment with an increase in synapses as found in TTX-treated WT CPNs. It is interesting that YAC128 CPNs pre-treated with 1 μM pridopidine showed increased mEPSC frequency but not amplitude following BDNF

scavenging, suggesting that modulation of BDNF signaling plays a larger role in regulating synapse numbers than AMPAR content. Together, these data suggest that reduced BDNF signaling in HD impairs a homeostatic increase in synapse number, but not strengthening of those synapses. Synaptic up-scaling by insertion of AMPARs appears to be largely mediated by some other pathway, which is also impaired in HD and restored by pridopidine.

Pridopidine Restores Homeostatic Plasticity in YAC128 CPNs by Stimulating the Sigma-1 Receptor

Pridopidine is a drug which has been investigated as a possible treatment for HD (Kieburtz et al., 2018). It was initially identified as a dopamine stabilizer (Dyhring et al., 2010), but recent studies suggest that its effect on HD is largely mediated through the S1R (Sahlholm et al., 2013, 2015). Stimulation of S1R by pridopidine normalizes multiple biochemical pathways which are disrupted in HD, including normalization of BDNF signaling and calcium homeostasis (Geva et al., 2016; Ryskamp et al., 2017). Furthermore, while the mechanisms by which pridopidine normalizes these pathways is still under study, recent data suggest that its agonism of S1R enhances BDNF axonal transport (Ionescu et al., 2019) and elevates BDNF transcripts (Geva, unpublished results). Thus, pridopidine treatment should not only increase the level of BDNF signaling in YAC128 CPNs, but should also restore their ability to dynamically modulate BDNF release. As these pathways in particular are involved in homeostatic plasticity, this suggested that pridopidine might restore homeostatic plasticity.

The pridopidine concentrations used in these experiments were selected based on the known binding affinity to the S1R, which we hypothesized would be the receptor driving the effects in our experimental system. The EC50 of pridopidine to the S1R is $\sim$ 100 nM as determined by *in vitro* binding assays (Johnston et al., 2018). In previous experiments we demonstrated various effects which were mediated by the S1R, and potent at the range of 100 nM–1 μM. These effects include upregulation of the BDNF pathway (Geva et al., 2016), rescue of spines and calcium homeostasis (Ryskamp et al., 2017, 2019), and enhancement of axonal BDNF transport (Ionescu et al., 2019). In addition, these concentrations correlate to the drug brain exposure levels of pridopidine used in clinical trials (Geva, unpublished data). Specifically, these concentrations show a very selective target engagement of the S1R *in vivo* (Geva et al., 2016; Ryskamp et al., 2017; Ionescu et al., 2019). In a recently completed phase 2 trial in HD patients, the low dose (45 mg twice a day), which shows selective S1R brain occupancy, showed significant slowing of functional decline, while the higher doses were less effective (Reilmann et al., 2018).

We found that pre-treatment with pridopidine restored homeostatic plasticity in YAC128 CPNs in a concentration-dependent manner. While all tested pridopidine concentrations (0.1, 1, and 10 μM) restored the mean mEPSC amplitude increase in response to TTX treatment, only pre-treatment with 1 μM pridopidine was able to restore the increase in mean mEPSC frequency. Furthermore, in WT CPNs, pridopidine pre-treatment did not impact the mean mEPSC amplitude increase in response to 48 h TTX exposure, but it did attenuate the increase in mean mEPSC frequency after activity deprivation. Taken together, these data suggest that the mEPSC frequency response to 48 h TTX is more sensitive to BDNF levels than the amplitude response. As previous work showed BDNF signaling is reduced in HD (Zuccato and Cattaneo, 2007; Plotkin and Surmeier, 2015), it is possible that baseline BDNF signaling must be within a certain range in order for its reduction in response to 48 h TTX treatment to increase synapse density. If so, then its level may be too low in YAC128 CPNs, but elevated to a healthy range by 1 μM pridopidine; further, 10 μM pridopidine may increase BDNF in YAC128 CPNs to a level no longer within this range. 1 μM pridopidine may achieve the same effect in WT CPNs. Alternatively, high concentrations of pridopidine may engage other pathways which inhibit the homeostatic modulation of synapse density, differentially in WT and YAC128 CPNs. Further experiments are required to test these possibilities.

This leaves the question of how pridopidine restores the effect of TTX treatment on synaptic AMPAR content. BDNF signaling is only one of the pathways that pridopidine normalizes through stimulation of the S1R (Geva et al., 2016). We found that the S1R agonist 3-PPP also restored both mEPSC amplitude and frequency increases in response to TTX. This suggests that another process downstream of the S1R, in addition to BDNF, is involved in the restoration of homeostatic plasticity. Of interest to us is calcium homeostasis, which is also restored by pridopidine (Ryskamp et al., 2017). Calcium signaling is involved in homeostatic plasticity through a number of pathways, including CamKIV (Ibata et al., 2008) and Homer1a (Diering et al., 2017); the latter pathway is involved in HSP via regulating ER calcium release. Calcium homeostasis is disrupted in HD through mechanisms such as sensitisation of the IP3R, affecting ER calcium release (Tang et al., 2003), and altered NMDAR localisation and subunit composition (Milnerwood and Raymond, 2010; Milnerwood et al., 2010, 2012). S1R agonists have been found to modulate both of these pathways (Liang and Wang, 1998; Ryskamp et al., 2017). We consider calcium homeostasis to be the most likely pathway by which pridopidine restores the synaptic up-scaling (amplitude) response to TTX.

Homeostatic Plasticity, S1R, and HD

While most HD research has focused on the striatum, which is the first brain structure in which cell death occurs (MacDonald et al., 1993), the cortex is known to play an important role in the disease's early cognitive and psychiatric symptoms (Thu et al., 2010; Estrada-Sánchez et al., 2015). The deficit in CPN homeostatic plasticity reported here could contribute to these symptoms. Drugs like pridopidine, which normalize this process, could improve these symptoms.

Another neurodegenerative disease in which homeostatic plasticity has been implicated is Alzheimer's disease (AD) (Small, 2008). HSP in healthy cells to compensate for synaptic

dysfunction in unhealthy cells is hypothesized to contribute both to cognitive dysfunction in AD and spread of neuronal dysfunction to other brain areas. Aberrant cortical HSP in HD could also, in theory, contribute to pathology in brain areas outside of the cortex. The deficit which we documented has the potential to decrease the overall level of activity of affected cortical areas (Watt and Desai, 2010). Such a decrease would lead to reduced activity-dependent release of BDNF by CPNs onto striatal SPNs, compounding the BDNF secretion deficit mediated by reduced expression and axonal transport (Zuccato and Cattaneo, 2007; Virlogeux et al., 2018), and contributing to decreased neurotrophic support of SPNs, which has been proposed to cause the death of these cells through 'withering' (Plotkin and Surmeier, 2015).

Homeostatic plasticity has also been investigated in sleep. Homer1a-dependent synaptic down-scaling, reduction of the strength of all of the synapses onto a cell, has been reported during sleep (Diering et al., 2017). Factors involved in up- and down-scaling do not overlap greatly (Turrigiano, 2011), so our finding of impairment in TTX-induced homeostatic plasticity does not necessarily imply that down-scaling is also impaired in HD. However, evidence from clinical neurostimulation does support this idea (Calabresi et al., 2016). Further, Homer1a is part of the BDNF signaling pathway, and its expression is decreased in the Q175 HD mouse model, and restored by pridopidine (Geva et al., 2016).

Finally, our findings add to growing evidence for S1R as a potential pharmacological target for the treatment of HD and other neurodegenerative disorders. S1R agonists have been found to improve symptoms of depression and anxiety, which are among the most common psychiatric symptoms of HD (Berrios et al., 2001). S1R is a relatively recently discovered receptor, but it has already been associated with many pathways implicated in neurodegenerative diseases, including calcium homeostasis, neurotrophic support and synaptic transmission (Kourrich et al., 2012; Geva et al., 2016; Ryskamp et al., 2017). Together with our results, these studies suggest that S1R is a promising pharmacological target for HD, as well as for other neurodegenerative disorders.

AUTHOR CONTRIBUTIONS

AS-D was involved in the design of all the experiments included in this manuscript, acquired and analyzed the data for the majority of those experiments, and wrote the majority of this manuscript. WN acquired and analyzed the data for experiments included in this manuscript, and contributed to writing the section "Materials and Methods". LZ acquired and analyzed the data for experiments included in this manuscript. MG and MH contributed to the design of experiments included in this manuscript. LR conceived the research questions, contributed to the design of experiments, supervised the data analysis, and contributed to the manuscript writing and revision. All authors reviewed and approved the manuscript.

FUNDING

This work was supported by the Canadian Institutes of Health Research (CIHR) operating grant to LR (FDN-143210) and from Teva Pharmaceuticals Ltd. (research contract to LR), and by the CIHR operating grant to MH (FDN-154278) and the Canada Research Chair to MH. AS-D holds a CIHR Canadian Graduate Scholarship Award. WN holds a UBC-CIHR-MDPhD Program award.

ACKNOWLEDGMENTS

We are grateful to Rujun Kang for technical assistance in the experiments reported here, and to Marja Sepers, Matthew Parsons, and Karolina Kolodziejczyk for training and in assistance with electrophysiological and immunocytochemical techniques.

SUPPLEMENTARY MATERIAL

The Supplementary Material for this article can be found online at: https://www.frontiersin.org/articles/10.3389/fncel.2019.00209/full#supplementary-material

REFERENCES

Berrios, G. E., Wagle, A. C., Marková, I. S., Wagle, S. A., Ho, L. W., Rubinsztein, D. C., et al. (2001). Psychiatric symptoms and CAG repeats in neurologically asymptomatic Huntington's disease gene carriers. *Psychiatry Res.* 102, 217–225. doi: 10.1016/S0165-1781(01)00257-8

Buren, C., Parsons, M. P., Smith-Dijak, A., and Raymond, L. A. (2016). Impaired development of cortico-striatal synaptic connectivity in a cell culture model of Huntington's disease. *Neurobiol. Dis.* 87, 80–90. doi: 10.1016/j.nbd.2015.12.009

Buren, C., Wang, L., Smith-Dijak, A., and Raymond, L. A. (2014). Region-specific pro-survival signaling and global neuronal protection by wild-type huntingtin. *J. Huntingt. Dis.* 3, 365–376. doi: 10.3233/JHD-140122

Calabresi, P., Pisani, A., Rothwell, J., Ghiglieri, V., Obeso, J. A., and Picconi, B. (2016). Hyperkinetic disorders and loss of synaptic downscaling. *Nat. Neurosci.* 19, 868–875. doi: 10.1038/nn.4306

Cepeda, C., Wu, N., André, V. M., Cummings, D. M., and Levine, M. S. (2007). The corticostriatal pathway in Huntington's disease. *Prog. Neurobiol.* 81, 253–271. doi: 10.1016/j.pneurobio.2006.11.001

Chidambaram, S. B., Rathipriya, A. G., Bolla, S. R., Bhat, A., Ray, B., Mahalakshmi, A. M., et al. (2019). Dendritic spines: revisiting the physiological role. *Prog. Neuropsychopharmacol. Biol. Psychiatry* 92, 161–193. doi: 10.1016/j.pnpbp.2019.01.005

Cohen, J. E., Lee, P. R., Chen, S., Li, W., and Fields, R. D. (2011). MicroRNA regulation of homeostatic synaptic plasticity. *Proc. Natl. Acad. Sci. U.S.A.* 108, 11650–11655. doi: 10.1073/pnas.1017576108

Diering, G. H., Nirujogi, R. S., Roth, R. H., Worley, P. F., Pandey, A., and Huganir, R. L. (2017). Homer1a drives homeostatic scaling-down of excitatory synapses during sleep. *Science* 355, 511–515. doi: 10.1126/science.aai8355

Dyhring, T., Nielsen, E. Ø., Sonesson, C., Pettersson, F., Karlsson, J., Svensson, P., et al. (2010). The dopaminergic stabilizers pridopidine (ACR16) and (-)-OSU6162 display dopamine D2 receptor antagonism and fast receptor

dissociation properties. *Eur. J. Pharmacol.* 628, 19–26. doi: 10.1016/j.ejphar.2009.11.025

Estrada-Sánchez, A. M., Burroughs, C. L., Cavaliere, S., Barton, S. J., Chen, S., Yang, X. W., et al. (2015). Cortical efferents lacking mutant huntingtin improve striatal neuronal activity and behavior in a conditional mouse model of huntington's disease. *J. Neurosci.* 35, 4440–4451. doi: 10.1523/JNEUROSCI.2812-14.2015

Fujimoto, M., Hayashi, T., Urfer, R., Mita, S., and Su, T.-P. (2012). Sigma-1 receptor chaperones regulate the secretion of brain-derived neurotrophic factor. *Synapse* 66, 630–639. doi: 10.1002/syn.21549

Geva, M., Kusko, R., Soares, H., Fowler, K. D., Birnberg, T., Barash, S., et al. (2016). Pridopidine activates neuroprotective pathways impaired in Huntington disease. *Hum. Mol. Genet.* 25, 3975–3987. doi: 10.1093/hmg/ddw238

Hartveit, E., and Veruki, M. L. (2007). Studying properties of neurotransmitter receptors by non-stationary noise analysis of spontaneous postsynaptic currents and agonist-evoked responses in outside-out patches. *Nat. Protoc.* 2, 434–448. doi: 10.1038/nprot.2007.47

Hayashi, T., and Su, T.-P. (2007). Sigma-1 receptor chaperones at the ER-mitochondrion interface regulate Ca2+ signaling and cell survival. *Cell* 131, 596–610. doi: 10.1016/j.cell.2007.08.036

Ibata, K., Sun, Q., and Turrigiano, G. G. (2008). Rapid synaptic scaling induced by changes in postsynaptic firing. *Neuron* 57, 819–826. doi: 10.1016/j.neuron.2008.02.031

Ionescu, A., Gradus, T., Altman, T., Maimon, R., Saraf Avraham, N., Geva, M., et al. (2019). Targeting the sigma-1 receptor via pridopidine ameliorates central features of ALS pathology in a SOD1G93A model. *Cell Death Dis.* 10:210. doi: 10.1038/s41419-019-1451-2

Johnston, T. H., Geva, M., Steiner, L., Orbach, A., Papapetropoulos, S., Savola, J.-M., et al. (2018). Pridopidine, a clinic-ready compound, reduces 3,4-dihydroxyphenylalanine-induced dyskinesia in Parkinsonian macaques. *Mov. Disord.* doi: 10.1002/mds.27565 [Epub ahead of print].

Kieburtz, K., Reilmann, R., and Olanow, C. W. (2018). Huntington's disease: current and future therapeutic prospects. *Mov. Disord.* 33, 1033–1041. doi: 10.1002/mds.27363

Kikuchi-Utsumi, K., and Nakaki, T. (2008). Chronic treatment with a selective ligand for the sigma-1 receptor chaperone, SA4503, up-regulates BDNF protein levels in the rat hippocampus. *Neurosci. Lett.* 440, 19–22. doi: 10.1016/j.neulet.2008.05.055

Kirov, S. A., Sorra, K. E., and Harris, K. M. (1999). Slices have more synapses than perfusion-fixed hippocampus from both young and mature rats. *J. Neurosci.* 19, 2876–2886. doi: 10.1523/JNEUROSCI.19-08-02876.1999

Kourrich, S., Su, T.-P., Fujimoto, M., and Bonci, A. (2012). The sigma-1 receptor: roles in neuronal plasticity and disease. *Trends Neurosci.* 35, 762–771. doi: 10.1016/j.tins.2012.09.007

Liang, X., and Wang, R. Y. (1998). Biphasic modulatory action of the selective sigma receptor ligand SR 31742A on N-methyl-d-aspartate-induced neuronal responses in the frontal cortex. *Brain Res.* 807, 208–213. doi: 10.1016/s0006-8993(98)00797-5

MacDonald, M. E., Ambrose, C. M., Duyao, M. P., Myers, R. H., Lin, C., Srinidhi, L., et al. (1993). A novel gene containing a trinucleotide repeat that is expanded and unstable on Huntington's disease chromosomes. *Cell* 72, 971–983. doi: 10.1016/0092-8674(93)90585-E

Marder, E., and Goaillard, J.-M. (2006). Variability, compensation and homeostasis in neuron and network function. *Nat. Rev. Neurosci.* 7, 563–574. doi: 10.1038/nrn1949

Mendez, P., Stefanelli, T., Flores, C. E., Muller, D., and Lüscher, C. (2018). Homeostatic plasticity in the hippocampus facilitates memory extinction. *Cell Rep.* 22, 1451–1461. doi: 10.1016/j.celrep.2018.01.025

Milnerwood, A. J., Gladding, C. M., Pouladi, M. A., Kaufman, A. M., Hines, R. M., Boyd, J. D., et al. (2010). Early increase in extrasynaptic NMDA receptor signaling and expression contributes to phenotype onset in Huntington's disease mice. *Neuron* 65, 178–190. doi: 10.1016/j.neuron.2010.01.008

Milnerwood, A. J., Kaufman, A. M., Sepers, M. D., Gladding, C. M., Zhang, L., Wang, L., et al. (2012). Mitigation of augmented extrasynaptic NMDAR signaling and apoptosis in cortico-striatal co-cultures from Huntington's disease mice. *Neurobiol. Dis.* 48, 40–51. doi: 10.1016/j.nbd.2012.05.013

Milnerwood, A. J., and Raymond, L. A. (2010). Early synaptic pathophysiology in neurodegeneration: insights from Huntington's disease. *Trends Neurosci.* 33, 513–523. doi: 10.1016/j.tins.2010.08.002

Orth, M., Schippling, S., Schneider, S. A., Bhatia, K. P., Talelli, P., Tabrizi, S. J., et al. (2010). Abnormal motor cortex plasticity in premanifest and very early manifest Huntington disease. *J. Neurol. Neurosurg. Psychiatry* 81, 267–270. doi: 10.1136/jnnp.2009.171926

Plotkin, J. L., and Surmeier, D. J. (2015). Corticostriatal synaptic adaptations in Huntington's disease. *Curr. Opin. Neurobiol.* 33, 53–62. doi: 10.1016/j.conb.2015.01.020

Poo, M. (2001). Neurotrophins as synaptic modulators. *Nat. Rev. Neurosci.* 2, 24–32. doi: 10.1038/35049004

Reilmann, R., McGarry, A., Grachev, I. D., Savola, J.-M., Borowsky, B., Eyal, E., et al. (2018). Safety and efficacy of pridopidine in patients with Huntington's disease (PRIDE-HD): a phase 2, randomised, placebo-controlled, multicentre, dose-ranging study. *Lancet Neurol.* 18, 165–176. doi: 10.1016/S1474-4422(18)30391-0

Rutherford, L. C., Nelson, S. B., and Turrigiano, G. G. (1998). BDNF has opposite effects on the quantal amplitude of pyramidal neuron and interneuron excitatory synapses. *Neuron* 21, 521–530. doi: 10.1016/s0896-6273(00)80563-2

Ryskamp, D., Wu, J., Geva, M., Kusko, R., Grossman, I., Hayden, M., et al. (2017). The sigma-1 receptor mediates the beneficial effects of pridopidine in a mouse model of Huntington disease. *Neurobiol. Dis.* 97, 46–59. doi: 10.1016/j.nbd.2016.10.006

Ryskamp, D., Wu, L., Wu, J., Kim, D., Rammes, G., Geva, M., et al. (2019). Pridopidine stabilizes mushroom spines in mouse models of Alzheimer's disease by acting on the sigma-1 receptor. *Neurobiol. Dis.* 124, 489–504. doi: 10.1016/j.nbd.2018.12.022

Sahlholm, K., Århem, P., Fuxe, K., and Marcellino, D. (2013). The dopamine stabilizers ACR16 and (-)-OSU6162 display nanomolar affinities at the σ-1 receptor. *Mol. Psychiatry* 18, 12–14. doi: 10.1038/mp.2012.3

Sahlholm, K., Sijbesma, J. W. A., Maas, B., Kwizera, C., Marcellino, D., Ramakrishnan, N. K., et al. (2015). Pridopidine selectively occupies sigma-1 rather than dopamine D2 receptors at behaviorally active doses. *Psychopharmacology* 232, 3443–3453. doi: 10.1007/s00213-015-3997-8

Saudou, F., and Humbert, S. (2016). The Biology of Huntingtin. *Neuron* 89, 910–926. doi: 10.1016/j.neuron.2016.02.003

Schippling, S., Schneider, S. A., Bhatia, K. P., Münchau, A., Rothwell, J. C., Tabrizi, S. J., et al. (2009). Abnormal motor cortex excitability in preclinical and very early Huntington's disease. *Biol. Psychiatry* 65, 959–965. doi: 10.1016/j.biopsych.2008.12.026

Shirasaki, D. I., Greiner, E. R., Al-Ramahi, I., Gray, M., Boontheung, P., Geschwind, D. H., et al. (2012). Network organization of the huntingtin proteomic interactome in mammalian brain. *Neuron* 75, 41–57. doi: 10.1016/j.neuron.2012.05.024

Slow, E. J., van Raamsdonk, J., Rogers, D., Coleman, S. H., Graham, R. K., Deng, Y., et al. (2003). Selective striatal neuronal loss in a YAC128 mouse model of Huntington disease. *Hum. Mol. Genet.* 12, 1555–1567. doi: 10.1093/hmg/ddg169

Small, D. H. (2008). Network dysfunction in Alzheimer's disease: does synaptic scaling drive disease progression? *Trends Mol. Med.* 14, 103–105. doi: 10.1016/j.molmed.2007.12.006

Tang, T.-S., Tu, H., Chan, E. Y. W., Maximov, A., Wang, Z., Wellington, C. L., et al. (2003). Huntingtin and huntingtin-associated protein 1 influence neuronal calcium signaling mediated by inositol-(1,4,5) triphosphate receptor type 1. *Neuron* 39, 227–239. doi: 10.1016/S0896-6273(03)00366-0

Thu, D. C. V., Oorschot, D. E., Tippett, L. J., Nana, A. L., Hogg, V. M., Synek, B. J., et al. (2010). Cell loss in the motor and cingulate cortex correlates with symptomatology in Huntington's disease. *Brain* 133, 1094–1110. doi: 10.1093/brain/awq047

Tian, X., Kai, L., Hockberger, P. E., Wokosin, D. L., and Surmeier, D. J. (2010). MEF-2 regulates activity-dependent spine loss in striatopallidal medium spiny neurons. *Mol. Cell. Neurosci.* 44, 94–108. doi: 10.1016/j.mcn.2010.01.012

Traynelis, S. F., Angus Silver, R., and Cull-Candy, S. G. (1993). Estimated conductance of glutamate receptor channels activated during EPSCs at the cerebellar mossy fiber-granule cell synapse. *Neuron* 11, 279–289. doi: 10.1016/0896-6273(93)90184-S

Turrigiano, G. (2007). Homeostatic signaling: the positive side of negative feedback. *Curr. Opin. Neurobiol.* 17, 318–324. doi: 10.1016/j.conb.2007.04.004

Turrigiano, G. (2011). Homeostatic synaptic plasticity: local and global mechanisms for stabilizing neuronal function. *Cold Spring Harb. Perspect. Biol.* 4:a005736. doi: 10.1101/cshperspect.a005736

Turrigiano, G. G., Leslie, K. R., Desai, N. S., Rutherford, L. C., and Nelson, S. B. (1998). Activity-dependent scaling of quantal amplitude in neocortical neurons. *Nature* 391, 892–896. doi: 10.1038/36103

Virlogeux, A., Moutaux, E., Christaller, W., Genoux, A., Bruyère, J., Fino, E., et al. (2018). Reconstituting corticostriatal network on-a-chip reveals the contribution of the presynaptic compartment to Huntington's disease. *Cell Rep.* 22, 110–122. doi: 10.1016/j.celrep.2017.12.013

Wang, J. K. T., Langfelder, P., Horvath, S., and Palazzolo, M. J. (2017). Exosomes and homeostatic synaptic plasticity are linked to each other and to Huntington's, Parkinson's, and other neurodegenerative diseases by database-enabled analyses of comprehensively curated datasets. *Front. Neurosci.* 11:149. doi: 10.3389/fnins.2017.00149

Watt, A. J., and Desai, N. S. (2010). Homeostatic plasticity and STDP: keeping a neuron's cool in a fluctuating world. *Front. Synaptic Neurosci.* 2:5. doi: 10.3389/fnsyn.2010.00005

Wierenga, C. J., Walsh, M. F., and Turrigiano, G. G. (2006). Temporal regulation of the expression locus of homeostatic plasticity. *J. Neurophysiol.* 96, 2127–2133. doi: 10.1152/jn.00107.2006

Zuccato, C., and Cattaneo, E. (2007). Role of brain-derived neurotrophic factor in Huntington's disease. *Prog. Neurobiol.* 81, 294–330. doi: 10.1016/j.pneurobio.2007.01.003

Conflict of Interest Statement: MG and MH were employed by Teva Pharmaceutical Industries Ltd. This company also provided financial and material support to LR in the form of research funding, and the drug pridopidine, used to support some of the experiments conducted in this study.

The remaining authors declare that the research was conducted in the absence of any commercial or financial relationships that could be construed as a potential conflict of interest.

Advantages of publishing in Frontiers

OPEN ACCESS
Articles are free to read for greatest visibility and readership

FAST PUBLICATION
Around 90 days from submission to decision

HIGH QUALITY PEER-REVIEW
Rigorous, collaborative, and constructive peer-review

TRANSPARENT PEER-REVIEW
Editors and reviewers acknowledged by name on published articles

Frontiers
Avenue du Tribunal-Fédéral 34
1005 Lausanne | Switzerland

Visit us: www.frontiersin.org
Contact us: info@frontiersin.org | +41 21 510 17 00

REPRODUCIBILITY OF RESEARCH
Support open data and methods to enhance research reproducibility

DIGITAL PUBLISHING
Articles designed for optimal readership across devices

FOLLOW US
@frontiersin

IMPACT METRICS
Advanced article metrics track visibility across digital media

EXTENSIVE PROMOTION
Marketing and promotion of impactful research

LOOP RESEARCH NETWORK
Our network increases your article's readership